NUCLEAR PHYSICS

JOURNAL DEVOTED TO THE EXPERIMENTAL AND THEORETICAL STUDY OF THE FUNDAMENTAL CONSTITUENTS OF MATTER AND THEIR INTERACTIONS

EDITOR: L. ROSENFELD - COPENHAGEN
ASSOCIATE EDITOR: O. NATHAN - COPENHAGEN

VOLUME XX

NORTH-HOLLAND PUBLISHING COMPANY - AMSTERDAM

NUCLEAR PHYSICS

EDITORIAL BOARD

AUSTRALIA & NEW ZEALAND:	H. Messel (Sydney), M. L. Oliphant (Canberra)
AUSTRIA:	B. Karlik (Vienna), H. Thirring (Vienna)
BELGIUM:	M. de Hemptinne (Louvain), J. Verhaeghe (Ghent)
CANADA:	G. Volkoff (Vancouver)
DENMARK:	C. Møller (Copenhagen), S. Rozental (Copenhagen), G. E. Brown (Copenhagen)
FINLAND:	L. Simons (Helsinki)
FRANCE:	A. Berthelot (Saclay), S. Gorodetzky (Strasbourg)
GERMANY (DEM. REP.):	G. Hertz (Leipzig)
GERMANY (FED. REP.):	W. Gentner (Freiburg i. B.), J. H. D. Jensen (Heidelberg)
GREAT BRITAIN:	S. Devons (Manchester), T. H. R. Skyrme (Harwell)
HUNGARY:	L. Janossy (Budapest)
INDIA:	H. Bhabha (Bombay), R. Ramanna (Trombay)
IRISH REPUBLIC:	J. McConnell (Maynooth)
ISRAEL:	G. Racah (Jerusalem)
ITALY:	E. Amaldi (Rome)
JAPAN:	S. Kikuchi (Tokyo), S. Tomonaga (Tokyo)
MEXICO:	M. Moshinsky (Mexico)
NETHERLANDS:	H. Brinkman (Groningen), S. R. de Groot (Leiden)
NORWAY:	E. Hylleraas (Oslo), A. Lundby (Oslo), H. Wergeland (Trondheim)
POLAND:	L. Infeld (Warsaw)
PORTUGAL:	J. M. Araújo (Porto), J. R. de Almeida Santos (Coimbra)
SOUTH AMERICA:	G. Beck (Saõ Paulo), J. Leite Lopes (Rio de Janeiro)
SPAIN:	J. M. Otero (Madrid), C. Sanchez del Rio (Madrid)
SWEDEN:	O. Klein (Stockholm), K. Siegbahn (Uppsala), I. Waller (Uppsala)
SWITZERLAND:	P. Huber (Basel), P. Scherrer (Zürich)
U.A.R. & ARAB COUNTRIES:	F. El Bedewi (Alexandria), M. G. Nooh (Cairo)
U.S.A.:	H. H. Barschall (Madison, Wisconsin), V. Weisskopf (Cambridge, Mass.)
U.S.S.R.:	M. A. Markov (Moscow), I. S. Shapiro (Moscow), D, V. Skobeltzyn (Moscow)
YUGOSLAVIA:	I. Supek (Zagreb)

NUCLEAR PHYSICS

JOURNAL DEVOTED TO THE EXPERIMENTAL AND THEORETICAL STUDY OF THE FUNDAMENTAL CONSTITUENTS OF MATTER AND THEIR INTERACTIONS

EDITOR: L. ROSENFELD - COPENHAGEN

VOLUME XX

OCTOBER 1960—NOVEMBER 1960

NORTH-HOLLAND PUBLISHING COMPANY-AMSTERDAM

PRINTED IN THE NETHERLANDS

10.C

Nuclear Physics **20** (1960) 1—9; © *North-Holland Publishing Co., Amsterdam*

Not to be reproduced by photoprint or microfilm without written permission from the publisher

DONALD J. HUGHES

(1915—1960)

JOHN A. HARVEY

Oak Ridge National Laboratory, Oak Ridge, Tennessee, USA

Received 12 July 1960

The untimely death of Donald J. Hughes at Brookhaven, New York, on April 12, 1960, at the age of 45 came as a profound shock to his friends and to scientists throughout the world. His unexpected death resulted from a coronary thrombosis which occurred on April 5.

Don Hughes was known throughout the world as an expert in the field of low energy neutron physics. His experimental researches in neutron physics produced results of great importance to the field of nuclear physics. He was responsible for the collection, evaluation and publication of information relating to the interaction of neutrons with matter. He travelled extensively in the United States and Europe as a lecturer, and was an invited speaker at many international conferences on nuclear physics. In addition to many publications in scientific journals, he wrote several books, both of a technical nature and for the general public.

Donald Hughes was born in Chicago, on April 2, 1915. He attended the University of Chicago and was awarded his Ph. D. degree in Physics in 1940. After receiving his degree, he remained at the University to teach and in 1941 was a member of a cosmic-ray expedition to South America. In 1942 he joined the Naval Ordnance Laboratory and directed a section on underwater research on mine and torpedo detectors. Early in 1943 he joined the Manhattan Project at the University of Chicago and spent 1944 at Hanford, Washington. In 1945 he returned to Chicago and became the Director of the Nuclear Physics Division at the Argonne National Laboratory. He left Argonne in 1949 to become a senior physicist in charge of a pile neutron research group at the Brookhaven National Laboratory, a position he held until his death.

Don Hughes' research activities began in the field of cosmic rays under Professor A. H. Compton, at the University of Chicago. His early experiments in 1940—41 were concerned with studies of cosmic rays underground, and the results were published in 1943[1]). During the expedition to South America, cloud chamber photographs were taken of heavy particles at high altitudes. Some results of initial measurements of the photographs were reported in 1941[2]), but a complete publication of the work was delayed until 1946[3]) due to war research. In 1946 he reviewed the cosmic-ray measurements of the meson mass and con-

cluded that "the results were statistically reconcilable with a single mass" [4]).

During the war, Dr. Hughes conducted many pile neutron experiments of a classified nature at the Metallurgical Laboratory of the University of Chicago. These experiments included such measurements as the diffusion lengths of thermal neutrons in uranium, beryllium, and beryllium oxide; the resonace absorption integrals of uranium and thorium; and the study of delayed neutrons from the fission of U^{233} and U^{235}. The neutron periods and abundances of the delayed neutrons from U^{235} were published in 1948 [5]) and have served as a standard of comparison for all subsequent delayed neutron studies on U^{235} and other fissionable isotopes. Measurements were also made, using a hydrogen filled cloud chamber, of the energy distributions of neutrons from several photoneutron sources [6]).

Dr. Hughes carried out experiments of almost every kind that is possible to do with a reactor. These experiments made use of the many properties of the neutron, such as its wave nature, its magnetic moment, its spin, its internal structure, etc. Hughes' interest ranged from measurements with fission and resonance energy neutrons for nuclear physics research to work with thermal and cold neutrons for solid and liquid state physics experiments. At Argonne, Dr. Hughes developed a technique for measuring capture cross sections of nucleides for fission neutrons by producing an intense source of fission energy neutrons, free from low energy neutrons, by means of a U^{235} converter plate in a thermal neutron beam from a reactor [7]). Results obtained with this technique at Argonne [8]) were some of the first nuclear data to show the effect of "magic numbers". Measurements were continued at Brookhaven [9]), and average nuclear level spacings deduced from the data were compared to level densities predicted from the statistical model of the nucleus.

Dr. Hughes' research with thermal and cold neutrons included experiments with polarized neutrons and work in the field of neutron optics. His initial neutron polarization studies were made using a transmission method, in which a neutron beam passes through a large thickness of magnetized iron. The results showed that the experimental value of the polarization was higher than the original theoretical calculations, but later theoretical calculations agreed with these experimental results [10]). Since the polarization produced was extremely sensitive to small deviations from magnetic saturation, this transmission technique was used to study the approach to magnetic saturation of iron and several iron alloys [10]). In the course of these experiments the phenomenon of small angle scattering of thermal neutrons was first observed [11]). It was found that a well-collimated beam of thermal neutrons, in passing through a plate of iron, was spread when the iron was unmagnetized but was not spread when the iron was magnetized. These results were interpreted in terms of the refraction which occurred at domain boundaries, the spreading of the collimated beam being determined by the domain size. Investigations were also made on the size of

magnetic domains using a double transmission method and measuring the depolarization produced by the passage of thermal neutrons through thin samples [12]).

For experiments on the reflection of neutrons from neutron mirrors, he developed a filter technique, which produced a sharp discontinuity in the spectrum of low energy neutrons. In addition to measurements with a beryllium mirror, some definitive work was done with magnetic mirrors. His experiment with a mirror of magnetized iron showed the existence of two critical angles, thus confirming that the spin of the neutron was $\frac{1}{2}$ [13]). This experiment also showed that the effective field acting upon the neutrons in the mirror was the magnetic induction. There had been considerable theoretical discussion as to whether the neutron-electron magnetic interaction was of a dipole-dipole nature or an Amperian current nature and this mirror experiment showed the Amperian current picture to be correct. Mirror experiments with an unmagnetized iron mirror were also performed which showed that the coherent averaging takes place over many domains. By using a magnetized cobalt mirror, Hughes demonstrated that an intense beam of completely polarized neutrons could be produced [13]).

The mirror technique was also used for an accurate determination of the coherent neutron-proton scattering amplitude. This experiment was the first mirror experiment to use a balancing technique in order to increase the sensitivity of the measurement [14]). Neutron mirrors of liquid hydrocarbons were used in which the hydrogen scattering amplitude was somewhat overbalanced by the carbon, which has an accurately known scattering amplitude. Careful measurements resulted in a scattering amplitude for hydrogen accurate to about $\frac{1}{2}$ % [15]), nearly 10 times more accurate than those obtained by other methods. When this scattering amplitude was combined with other nuclear data it showed that the neutron-proton interaction in the singlet state was equal to the proton-proton interaction in the same state; hence, the charge independence of nuclear forces. The mirror technique was also used at Brookhaven for an accurate measurement of the neutron-electron electrostatic interaction [16]). In this experiment a balancing technique was again invoked to increase the accuracy; the reflection of a beam of neutrons from the interface of a bismuth and liquid oxygen mirror was studied. Although a few theoretical papers on this neutron-electron interaction had been published before this experiment was carried out, the accurate result of this experiment motivated many theoreticians to investigate its implication upon meson theories.

Dr. Hughes is probably best known to nuclear physicists for his research with resonance energy neutrons and his work on the systematics of neutron resonances. Soon after arriving at Brookhaven, he initiated a program to develop a "fast chopper" which greatly extended the energy range of accurate total neutron cross section measurements [17]). Measurements with this instrument

showed the constancy of radiation widths of resonances [18]), and the dependence of the radiation widths upon atomic weight [19]). He developed a procedure for the area analysis of resonances [20]) and his group produced the first low energy resonance [21]) data to show that the black-nucleus model was incorrect, and that the data favored the more sophisticated models. Measurements of low energy resonances were continued and a technique was developed to determine strength functions directly from measurements of the average cross section in the region of a few keV, and by 1958 the data [22]) were in good agreement with the predictions of the distorted, diffuse-surface nuclear model. From extensive measurements of many resonances in several heavy nucleides came the discovery that the neutron widths of resonances in a single nucleide fluctuated widely from resonance to resonance, and had approximately an exponential size distribution [23]). A more detailed analysis of the data resulted in a size distribution which. corresponded to a chi-squared distribution with only one degree of freedom [24]). Accurate measurements of the total cross section of U^{235} were made and analyzed to give the fission widths of the resonances up to 20 eV. From these data came the conclusion that the fission width distribution of U^{235} approximately followed an exponential law, corresponding to a chi-squared distribution with two degrees of freedom [25]). A careful analysis was made of the distribution of spacings between neutron resonances with the conclusion that there was a definite repulsion between levels [26]), and that the distribution agreed with a theoretical prediction by Wigner. Measurements and analyses were made to determine the nuclear radii of many elements and the results confirmed the predictions of the deformed diffuse-surface model of the nucleus [27]). In the past 2 years Hughes' interest in neutron spectroscopy was concentrated on the gamma rays from neutron capture in resonances [28]). The interest in these measurements was the determination of the transition probabilities of high-energy gamma rays from nuclear states excited by neutron capture [29]). At the present time, results from Dr. Hughes' group at Brookhaven indicate only a small variation of this partial radiation width from resonance to resonance [30]), a result which is very surprising and in contradiction to predictions of nuclear theories. Hughes would certainly have wanted to be able to shed light on this conflict.

In addition to this prominent work with resonance neutrons, Dr. Hughes still found time for measurements of neutron cross sections of a more applied nature and of interest in reactor design. These included accurate measurements of the absorption cross sections of boron, gold, and U^{235} [31]), and of the energy variation of the number of fission neutrons per absorption in the thermal energy range [32]).

During his 10 years at Brookhaven, Dr. Hughes developed techniques for studying the motions of atoms in solids by the use of "cold" neutrons. Early measurements at Argonne and Brookhaven [33]) on magnetic inelastic scattering in iron led Dr. Hughes to apply the time-of-flight technique to this field of

neutron physics [34]). This technique was used to study both optical and acoustical vibrations in many crystals such as V, Al, Ge and Si [34–39]). Recently, Dr. Hughes used this technique for studying atomic motions in water, with the startling result that there appeared to be a "jump-time" for diffusion, suggesting that a water molecule remains in its initial position for a number of vibrations before jumping over several molecules [40]).

Much of the research which Hughes initiated was designed to settle questions or conflicts arising from nuclear theories. In all his research, Hughes was always able to stimulate considerable activity among theoretical physicists concerning the interpretation and understanding of the results of his experiments.

At a very early stage in his neutron studies, Dr. Hughes realized the importance of collecting and evaluating data on neutron cross sections. He was the driving force in establishing the Compilation Group at Brookhaven (Sigma Center, as he liked to call it) which collected neutron cross section data from all over the world. The presentation of the vast amount of low energy cross section data has appeared as the Neutron Cross Section Compilation [41]) and is known to nuclear physicists through the world. In connection with his interest in neutron cross sections, Dr. Hughes served as a member and chairman of the Nuclear Cross Sections Advisory Group of the U. S. Atomic Energy Commission.

In addition to the many publications on his research, Dr. Hughes wrote several review articles and books on subjects with which he was very familiar. To collect techniques used at reactors, he wrote several review articles on reactor neutron research [42, 43]) and in 1943 published a comprehensive book entitled *Pile Neutron Research* [44]). To summarize the experiments making use of the wave properties of thermal neutrons, he wrote a review article on neutron optics [45]) and a book entitled *Neutron Optics* [46]). He has written several reviews on the systematics of neutron resonance parameters of heavy nuclei [47–51]). At the 1958 Geneva Conference on the Peaceful Uses of Atomic Energy, he prepared a paper on recent cross sections of interest in reactor design [52]). His book on *Neutron Cross Sections* [53]) was written for the many individuals who need to use cross section data but are not experts in nuclear theory. He contributed an article on neutrons to the American Institute of Physics Handbook [54]) and another on experimental neutron physics to the Nuclear Engineering Handbook [55]). Dr. Hughes was an editor for several series of books including *Progress in Nuclear Energy, Monographs on Nuclear Energy* (Div. II, Nuclear Physics), and the *Encyclopaedic Dictionary of Physics*, all published by the Pergamon Press. He had recently been appointed the editor of the scientific journal Reactor Science.

Don Hughes was also active as a teacher and lecturer. During 1953—54 he was a Fulbright Professor at Oxford University in England. During the period from 1954 to 1956 he served as a lecturer to the U. S. Information Service and lectured in many European countries. In the preface of his book *On Nuclear*

Energy [56]), in reference to his lectures to lay groups, he wrote, "I have always been impressed with the real eagerness of the listeners" and that "it was gratifying that the listeners could gain a real understanding of the basic principles in a short time." Anyone who had heard Don present a lecture knows how clearly and enthusiastically he could introduce new and complex ideas. This ability was also reflected in his writings and, particularly, in his books. His latest book was *The Neutron Story* [57]), and was written for high school students and the interested general public.

As can be seen from the list of his principal publications, Don Hughes was very prolific and his research produced significant results in nuclear physics. With the passing of Don Hughes, nuclear physics has lost one of its most lively minds and its most excellent expositor of neutron physics.

Principal Publications

1) Cloud-chamber and counter studies of cosmic rays underground (V. C. Wilson and D. J. Hughes), Phys. Rev. **63** (1943) 161
2) Cloud chamber photograph of slow mesotron pair, Phys. Rev. **60** (1941) 414
3) Cloud chamber photographs of heavy particles at high altitudes, Phys. Rev. **69** (1946) 371
4) The mass of the mesotron as determined by cosmic ray measurements, Phys. Rev. **71** (1947) 387
5) Delayed neutrons from fission of U^{235} (Hughes, Dabbs, Cahn and Hall), Phys. Rev. **73** (1948) 111
6) Cloud-chamber energy measurement of photo-neutron sources (D. J. Hughes and C. Eggler), Phys. Rev. **72** (1947) 902
7) Capture cross sections for fast neutrons (D. J. Hughes, W. D. B. Spatz and N. Goldstein), Phys. Rev. **75** (1949) 1781
8) Fast neutron cross sections and nuclear shells (D. J. Hughes and D. Sherman), Phys. Rev. **78** (1950) 632
9) Fast neutron cross sections and nuclear level density (D. J. Hughes, R. C. Garth and J. S. Levin) Phys. Rev. **91** (1953) 1423
10) Neutron polarization (D. J. Hugnes, J. R. Wallace and R. H. Holtzman), Phys. Rev. **73** (1948) 1277
11) Magnetic refraction of neutrons at domain boundaries (Hughes, Burgy, Heller and Wallace) Phys. Rev. **75** (1949) 565
12) Double transmission and depolarization of neutrons (Burgy, Hughes, Wallace, Heller and Woolf), Phys. Rev. **80** (1950) 953
13) Reflection and polarization of neutrons by magnetized mirrors (D. J. Hughes and M. T. Burgy), Phys. Rev. **76** (1949) 1413;
Reflection of neutrons from magnetized mirrors (D. J. Hughes and M. T. Burgy), Phys. Rev. **81** (1951) 498

14) Coherent neutron-proton scattering by liquid mirror reflection (D. J. Hughes, M. T. Burgy and G. R. Ringo), Pnys. Rev. **77** (1950) 291
15) Coherent neutron-proton scattering by liquid mirror reflection (M. T. Burgy, G. R. Ringo and D. J. Hughes), Phys. Rev. **84** (1951) 1160
16) The neutron-electron interaction (Hughes, Harvey, Goldberg and Stafne), Phys. Rev. **90** (1953) 497
17) "Fast chopper" time-of-flight measurement of neutron resonances (Seidl, Hughes, Palvesky, Levin, Kato and Sjöstrand), Phys. Rev. **95** (1954) 476
18) Radiation widths of nuclear energy levels (D. J. Hughes and J. A. Harvey), Nature **173** (1954) 942
19) Radiation widths of nuclear energy levels (J. S. Levin and D. J. Hughes), Phys. Rev. **101** (1956) 1328
20) A method for rapid analysis of neutron resonances, J. Nuclear Energy **1** (1955) 237
21) Ratio of $\overline{\Gamma_n^0}/D$ for slow neutron resonances (Carter, Harvey, Hughes and Pilcher), Phys. Rev. **96** (1954) 113
22) Strengtn functions for deformed nuclei (D. J. Hughes, R. L. Zimmerman and R. E. Chrien), Phys. Rev. Letters **1** (1958) 461
23) Spacings and neutron widths of nuclear energy levels (Harvey, Hughes, Carter and Pilcher), Phys. Rev. **99** (1955) 10
24) Size distribution of neutron widths (D. J. Hughes and J. A. Harvey), Phys. Rev. **99** (1955) 1032
25) Neutron resonance parameters of U^{235} (V. E. Pilcher, J. A. Harvey and D. J. Hugnes), Phys. Rev. **103** (1956) 1342
26) Spacings of nuclear energy levels (J. A. Harvey and D. J. Hughes), Phys. Rev. **109** (1958) 471
27) Nuclear radii by scattering of low-energy neutrons (Seth, Hughes, Zimmerman and Garth), Phys. Rev. **110** (1958) 692
28) Measurement of spins of levels excited by slow neutron capture (Fox, Zimmerman, Hughes, Palevsky, Brussel and Chrien), Phys. Rev. **110** (1958) 1472
29) Strength of high-energy capture gamma rays in W^{184} (Hughes, Brussel, Fox and Zimmerman), Phys. Rev. Letters **2** (1959) 505
30) Transition probabilities of capture gamma rays in U^{239} (Hughes, Palevsky, Chrien and Bolotin), Bull. Am. Phys. Soc. **5** (1960) 295
31) Thermal neutron absorption cross sections of boron and gold (Carter, Palevsky, Myers and Hughes), Phys. Rev. **92** (1953) 716;
Neutron absorption cross section of U^{235} at 2200 m/sec (Palevsky, Carter, Eisberg and Hughes), Phys. Rev. **94** (1954) 1088
32) Direct measurement of the energy variation of η for U^{233}, U^{235} and Pu^{239} (Palevsky, Hughes, Zimmerman and Eisberg), J. Nuclear Energy **3** (1957) 177

33) Scattering and polarization of neutrons in an iron single crystal (D. J. Hughes, M. T. Burgy and W. C. Woolf), Phys. Rev. **80** (1950) 481;
Magnetic inelastic scattering of slow neutrons (H. Palevsky and D. J. Hughes), Phys. Rev. **92** (1953) 202
34) Inelastic scattering of low-energy neutrons by lattice vibrations of vanadium (R. S. Carter, D. J. Hugnes and H. Palevsky), Phys. Rev. **104** (1956) 271
35) Inelastic scattering of slow neutrons by lattice vibrations in aluminium R. S. Carter, H. Palevsky and D. J. Hughes), Phys. Rev. **106** (1957) 1168
36) Detection of optical lattice vibrations in Ge and ZrH by scattering of cold neutrons (Pelah, Eisenhauer, Hughes and Palevsky), Phys. Rev. **108** (1957) 1091
37) Measurements of lattice vibrations in Vanadium by neutron scattering (Eisenhauer, Pelah, Hughes and Palevsky), Phys. Rev. **109** (1958) 1046
38) Lattice vibrations in Germanium by scattering of cold neutrons (Ghose, Palevsky, Hughes, Pelah and Eisenhauer), Phys. Rev. **113** (1959) 49
39) Lattice vibrations in Silicon by scattering of cold neutrons (Palevsky, Hughes, Kley and Tunkelo), Pnys. Rev. Letters **2** (1959) 258
40) Atomic motions in water by scattering of cold neutrons (Hughes, Palevsky, Kley and Tunkelo), Phys. Rev. Letters **3** (1959) 91
41) Neutron cross sections (D. J. Hughes and J. A. Harvey), Brookhaven National Laboratory Report, BNL-325 (1955); idem (D. J. Hughes and R. B. Schwartz), Brookhaven National Laboratory Report, BNL-325, Suppl. 1 (1957); idem (D. J. Hughes and R. B. Schwartz), Brookhaven National Laboratory Report, BNL-325, 2nd Ed. (1958); idem (D. J. Hughes, B. A. Magurno and M. K. Brussel), Brookhaven National Laboratory Report, BNL-325, 2nd. Ed., Suppl. 1 (1960);
Neutron cross sections: angular distributions (D. J. Hughes and R. S. Carter), Brookhaven National Laboratory Report, BNL-400 (1956)
42) Pile neutron research techniques. Nucleonics **6**, No. 2, 5; **6**, No. 5, 38; **6**, No. 6, 50 (1950);
The reactor as a neutron source. Nucleonics **11**, No. 1, 30 (1953)
43) Research techniques, Handbuch für Physik LXIV (Springer, Berlin, 1959), p. 390
44) Pile neutron research (Addison-Wesley Press, Cambridge, Mass., 1953)
45) Neutron optics, Annual Review of Nuclear Science **3** (1953) 93
46) Neutron optics, Interscience tracts in physics and astronomy No. 1 (Interscience Publishers Inc., New York, 1954)
47) Neutron spectroscopy, Progress in nuclear physics **4** (1955) 330
48) Resonance structure of U^{233}, U^{235} and Pu^{239} (P. A. Egelstaff and D. J. Hughes), Prog. of Nuclear Energy, Series I, Phys. and Math., **1** 55 (Pergamon Press, London, 1956)

49) Neutrons and nuclear structure, Physica **22** (1956) 994
50) Systematics of neutron resonance parameters (D. J. Hughes and R. L. Zimmerman), Proc. Sec. Int. Conf. on the Peaceful Uses of Atomic Energy (Geneva 1958), **14** p. 135
51) Neutron resonances in heavy nuclei (D. J. Hughes and R. L. Zimmerman), Chapter VIII of *Nuclear Reactions* (North-Holland Publishing Company, Amsterdam, (1959)
52) Recent cross sections of interest in reactor design, Proc. Sec. Int. Conf. on the Peaceful Uses of Atomic Energy (Geneva 1958), **16**, p. 8;
Prog. of Nuclear Energy, Series I, Phys. and Math., **3** 1 (Pergamon Press, London, 1959)
53) Neutron Cross sections (Pergamon Press, London, 1957)
54) Neutrons (D. J. Hughes and J. A. Harvey), American Institute of Physics Handbook, Section 8—129 (McGraw Hill Book Company, New York, 1957)
55) Experimental neutron physics (D. J. Hughes and J. A. Harvey), Nuclear Engineering Handbook 5—53 (McGraw Hill Book Company, New York, 1958)
56) On Nuclear Energy (Harvard University Press, Cambridge, Mass., 1957)
57) The Neutron Story (Doubleday Anchor Books, Garden City, New York, 1959)

1.D.3:
1.E.4

Nuclear Physics **20** (1960) 10—14; © *North-Holland Publishing Co., Amsterdam*
Not to be reproduced by photoprint or microfilm without written permission from the publisher

REDUCED WIDTHS IN O^{16} AND GAMMA TRANSITION PROBABILITIES IN F^{19}

B. ROTH † and K. WILDERMUTH

Florida State University, Tallahassee, Florida ††

Received 20 May 1960

Abstract: Reduced widths in O^{16} and γ transition probabilities in F^{19}, qualitatively predicted by the cluster model, are compared with experimental data.

1. Introduction

Since the cluster model has had success in explaining the ordering of low energy levels in light nuclei, with their spins and parities [1–3]), it is worthwhile investigating in some examples how well the dynamical properties of excited states, that is their gamma transition probabilities and their reduced widths, can be explained by this model. Here we shall discuss the α particle reduced widths of the low lying states of O^{16} and the gamma transition probabilities of the low lying states of F^{19}. We start with a consideration of the reduced widths.

2. Reduced widths in O^{16}

The low energy states of O^{16} can be described by an α cluster in relative motion to a C^{12} cluster, the latter being in its ground or first excited state †††. Fig. 1 shows the cluster structure of these states which was derived on the basis of energetical arguments [2, 3]). When the single resonance formula for nuclear reactions applies, the partial width $\Gamma_{\lambda c}$ of a level E_λ for its disintegration through a channel c, is expressed in terms of the reduced width $\gamma_{\lambda c}$ by the realation $\Gamma_{\lambda c} = 2P\,\gamma_{\lambda c}^2$, where P is the penetrability. If the internal wave function belonging to E_λ is X_λ, then $\gamma_{\lambda c}$ is an expansion coefficient in the series expressing X_λ in terms of surface functions ψ_c in the configuration space of the nucleus [4]), i.e.

$$\gamma_{\lambda c} \propto \int \psi_c^* X_\lambda \mathrm{d}S. \tag{1}$$

Therefore $\gamma_{\lambda c}^2$ is a measure of the relative probability of finding the fragments

† On leave from Oklahoma State University, Stillwater, Oklahoma.

†† Work supported in part by a grant from the Office of Naval Research.

††† In these states no α particle cluster is broken up.

belonging to channel c at the surface which separates the internal from the external region of the nucleus in configuration space, when the nucleus is in the state E_λ. The $\gamma_{\lambda c}^2$ satisfy the sum rule $\sum_c \gamma_{\lambda c}^2 = 3\hbar^2/2\mu R$ (the Wigner limit). From eq. (1) it follows that in the scattering of α's on C^{12} we expect $\theta_\alpha^2 = \gamma_\alpha^2(3\hbar^2/2\mu R)^{-1}$ to be an appreciable fraction of 1 for those O^{16} states which have an unexcited C^{12} cluster. For those states which have an excited C^{12} cluster, we expect $\theta_\alpha^2 \ll 1$. Fig. 1 shows [5]) that θ_α^2 behaves in accord with the cluster model predictions.

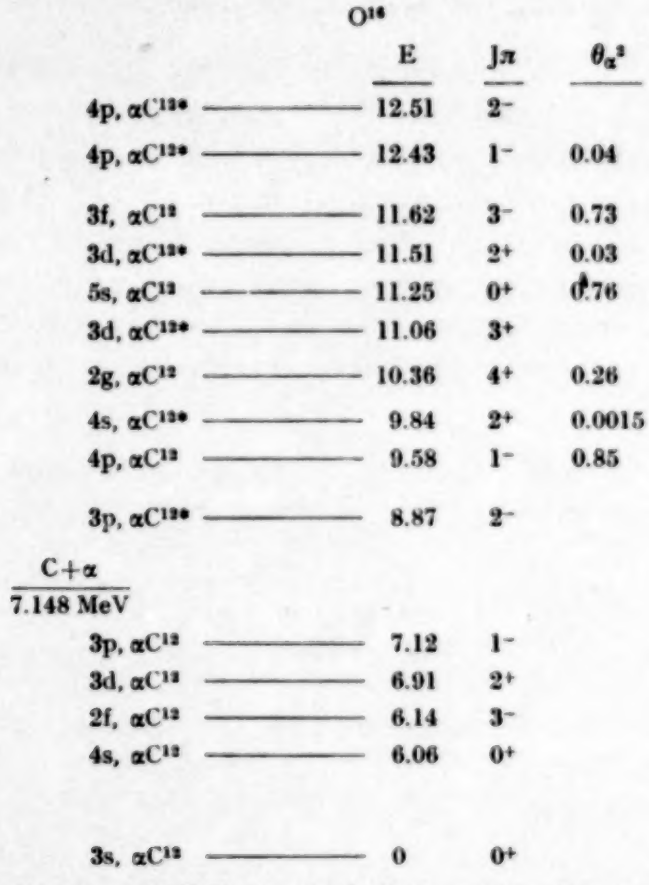

Fig. 1. The low lying states of O^{16}. The states of relative motion of the two clusters are given in the left hand column. A detailed explanation of these states is given in refs. [2, 3]). C^{12*} refers to the first excited state of C^{12}. $\theta_\alpha^2 = \gamma_\alpha^2(3\hbar^2/2\mu R)^{-1}$ is the reduced α particle width in units of the Wigner limit.

It is interesting to note that the proton reduced widths for the 12.43 and 12.51 states † are only [5]) 4 % of the Wigner limit. These relatively small values are to be expected from the cluster structure of these states. The 12.51 state has, in fact, been found [6]) to decay into an α and a C^{12*} as well as decaying by γ and proton emission. This again is expected from the cluster structure of the state. It would be worthwhile to measure the reduced width for the decay of this state into an α and a C^{12*}. Also, it would be interesting to look for the decay of

† States below 12.43 MeV cannot be reached by elastic scattering of protons on N^{15}.

the 12.43 state into an α and a C^{12*}, which is expected on this model. This would probably be difficult to observe as the penetrability factor for this reaction is very small. The 12.51, 11.06 and 8.87 states cannot be reached by scattering of the α particles on C^{12} because of spin and parity reasons. The cluster structure of the 10.98, 0^- state is not clear to us and was therefore not included in fig. 1. We also excluded from our discussion the 12.02 state since its spin and parity are not known.

3. Gamma Radiations from F^{19}

Now we discuss the γ radiations from the low lying states of F^{19}. The cluster structure of these states [2]) and relative γ transition probabilities [5]) are shown in fig. 2. When the spins and parities are not uniquely given by experiment we have chosen those predicted by the cluster model [2, 3]). The γ-transitions from these states are divided into four groups, each group, except the last, corresponding to one initial state. The branching ratios from these states are designated by numbers on the transition lines. The multipolarity and type of radiation shown in fig. 2 is that which is expected to be most probable. For the

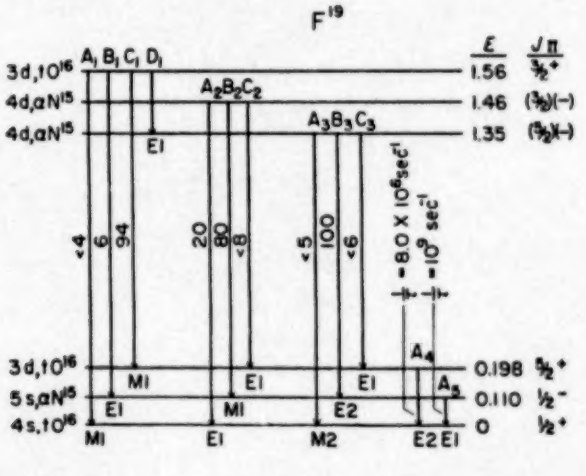

Fig. 2. γ transitions of the low lying states of F^{19}. Numbers on the transition lines indicate branching ratios. Letters A_1, B_1, ..., A_5 are used in the text for identifying transitions.

transitions in the last group (0.198 → g.s. and 0.110 → g.s.) the absolute probabilities are known from experiment. Table 1 compares transition probabilities given by experiment to those expected on the basis of the single particle † model [7, 8]). Since only the branching ratios are known experimentally for the first three groups, we disignate the largest probability in each of these groups by the letters p, q, r. The last column of the table shows immediately that for the first three groups the largest fractions $W_{exp}/W_{s.p.}$ occur for transitions

† In the single particle model, as is well known, a complete overlapping of the radial wave function of the radiating nucleon in the initial and final states is assumed.

between states of the same cluster structure. These fractions are considerably reduced for transitions between states of different cluster structure. That this should be so is evident from the general formulas for γ transition matrix elements, given for example in ref. [7]), p. 599. For, when a cluster structure changes in a transition the overlapping of the initial and final state wave functions is greatly reduced. It is interesting to compare transitions C_1 and A_1: in both of them there is no change of cluster structure; but in the C_1 transition the initial and final states have the same state of relative motion of the clusters, and only a spin flip is involved, whereas in the A_1 transition there is, in addition to the spin flip, a change in the state of relative motion. Therefore, on the basis of the formulas in ref. [7]), one expects that the ratio for the A_1 transition is reduced considerably in comparison to the ratio for the C_1 transition. The data of table 1 are in accord with this conclusion. For the A_4 and A_5 transitions the absolute probabilities are given. For transition A_4 one expects a probability close to the single particle value since the proton in the triton cluster is essentially responsible for the E2 radiation †. The data in table 1 bear this out. For the A_5

TABLE 1

Transition probabilities of the low energy states of F^{19}

Transition	W_{exp}	$W_{s.p.}$	$W_{exp}/W_{s.p.}$
C_1	p	7.1×10^{13}	$1.4\times10^{-14}\,p = \lvert M(C_1)\rvert^2$
D_1	$<0.053p$	9.9×10^{12}	$<0.38\lvert M(C_1)\rvert^2$
B_1	$0.064p$	3.3×10^{15}	$1.4\times10^{-3}\lvert M(C_1)\rvert^2$
A_1	$<0.043p$	1.1×10^{14}	$<2.8\times10^{-3}\lvert M(C_1)\rvert^2$
B_2	q	6.9×10^{13}	$1.4\times10^{-14}\,q = \lvert M(B_2)\rvert^2$
A_2	$0.25q$	3.3×10^{15}	$5.4\times10^{-3}\lvert M(B_2)\rvert^2$
C_2	$<0.10q$	2.1×10^{15}	$<3.4\times10^{-3}\lvert M(B_2)\rvert^2$
B_3	r	2.4×10^{10}	$4.2\times10^{-11}\,r = \lvert M(B_3)\rvert^2$
A_3	$<0.05r$	3.8×10^{9}	$<0.31\lvert M(B_3)\rvert^2$
C_3	$<0.06r$	1.6×10^{15}	$<0.9\times10^{-6}\lvert M(B_3)\rvert^2$
A_4	8.0×10^{6}	2.6×10^{6}	3.1
A_5	1.0×10^{9}	1.4×10^{12}	0.72×10^{-3}

W_{exp}, $W_{s.p.}$ are experimental and single particle transition probabilities.

transition one expects again a severe reduction from the single particle value since the cluster structure changes, and this too is in accord with the data of table 1.

† The shell model calculation of Elliott and Flowers (ref. [9])) also gives a value close to the single particle result.

4. Conclusions

As we have seen, the qualitative cluster model predictions for reduced widths and γ transition probabilities agree very well with the experimental data. But we should note that the experimental data are very meager except for the nuclei considered here. Therefore many more measurements of reduced particle widths † and radiative widths, especially in light and medium weight nuclei are highly desirable. The γ transitions in O^{16}, for instance, could be examined in the same way as for F^{19} if more data were available. It would also be very interesting if more reduced widths † for bound states (for instance, in O^{16}) were measured by stripping reactions [10]).

Most of the data referred to in this apaper were taken from the compilation by F. Ajzenberg-Selove and T. Lauritsen.

Similar questions from a phenomenological approach are now being investigated by G. C. Phillips and collaborators [11]).

† For the neutron, proton, triton, α particle, etc.

References

1) K. Wildermuth and Th. Kanellopoulos, Nuclear Physics **7** (1958) 159; **9** (1958/59) 449
2) CERN Rept. 59—23 (1959)
3) R. K. Sheline and K. Wildermuth, to be published Nuclear Physics,
4) E. P. Wigner and L. Eisenbud, Phys. Rev. **72** (1947) 29;
G. Breit, Theory of Resonance Reactions and Allied Topics, Handbuch der Physik, (Springer, Berlin) Vol. XLI/1 sect. **30**;
Lane and Thomas, Revs. Mod. Phys. **30** (1958) 257;
E. Vogt, in Nuclear Reactions, edited by Endt and Demeur (North-Holland Publishing Co., Amsterdam, 1959) Vol. I, ch. 5
5) F. Ajzenberg-Selove and T. Lauritsen, Nuclear Physics **11** (1959) 1
6) Kraus, French, Fowler nd Lauritsen Phys. Rev. **89** (1953) 299;
Hornyak and Sherr, Phys. Rev. **100** (1955) 1409
7) Blatt and Weisskopf, Theoretical Nuclear Physics (John Wiley and Sons, New York, 1952) Chap. 12
8) S. A. Moszkowski, in Beta and Gamma Ray Spectroscopy, edited by K. Siegbahn (North-Holland Publishing Co., Amsterdam, 1955) Chap. XIII;
B. Stech, Z. Naturfosch. **7a** (1952) 401
9) J. P. Elliott and B. H. Flowers, Proc. Roy. Soc. A **229** (1955) 536
10) W. Zimmerman, Phys. Rev. **104** (1956) 387;
E. K. Warburton and J. N. McGruer, Phys. Rev. **105** (1957) 639;
J. B. French and A. Fujii, Phys. Rev. **105** (1957) 652
11) G. C. Phillips *et al.*, Physical Review, to be published (preprint 1960)

9.B

Nuclear Physics **20** (1960) 15—128; © *North-Holland Publishing Co., Amsterdam*

Not to be reproduced by photoprint or microfilm without written permission from the publisher

ELECTRON NUMBER DISTRIBUTION IN ELECTRON-PHOTON SHOWERS IN AIR AND ALUMINIUM ABSORBERS

J. C. BUTCHER † and H. MESSEL

School of Physics ††, *The University of Sydney, Sydney, N.S.W.*

Received 15 May 1960

Abstract: Numerical results for the number distribution, average numbers and variance of electrons above a given energy due to primary electrons and photons are presented for air and aluminium absorbers. The 276 tables cover the cases for electron and photon primary energies $E_0 = 50$, 100, 200, 500, 1000, 2000, 5000, 10 000, 20 000 and 50 000 MeV, and electron secondary energies $E = 5$, 10, 20, 50, 100, 200, 500, 1000, 2000, 5000, 10 000 and 20 000 MeV with depths ranging from zero to 10 radiation lengths.

The more accurate Bethe-Heitler cross-sections at low energies are used and collision losses and Compton effect are taken into account. Scattering at low energies is neglected for the present low atomic number absorbers.

The results were obtained using Monte Carlo methods on the electronic digital computer SILLIAC. In every case at least 1000 showers were followed to obtain the present numerical values.

1. Introduction

Preliminary results on the electron number distribution in electron-photon cascades have been presented by Butcher and Messel [1, 1a]), using Monte Carlo techniques with the electronic digital computer SILLIAC. The present paper gives completed numerical results for the particle number distribution function Φ in the form of 276 tables. Physically Φ represents the probability of finding a given number of particles of a particular kind, above a given energy E, at a certain depth t below the cascade origin; the cascade having been originated in a given absorber by a given type of particle with a particular primary energy E_0.

The 276 tables cover the cases of air and aluminium absorbers; the critical energy in the case of the former being 98 MeV and in the latter 52 MeV. The value of $Z = 7.4$, $A = 15$ was used for air and $Z = 13$, $A = 27$ for aluminium. Both photon and electron primaries have been used with primary energies $E_0 = 50$, 100, 200, 500, 1000, 2000, 5000, 10 000, 20 000 and 50 000 MeV but only the results for the electron number distribution are presented; those for the photon distribution will form the subject of a separate publication.

Secondary electrons with energies greater than $E = 5$, 10, 20, 50, 100, 200, 500, 1000, 2000, 5000, 10 000 and 20 000 MeV at depths ranging from zero to

† Now in the Department of Applied Mathematics, University of Sydney.

†† Also supported by the Nuclear Research Foundation within the University of Sydney.

10 radiation lengths are considered in this paper. The energy ranges used, thus cover a broad and overlapping region covered both by cosmic ray and accelerator experiments. Since this energy range is one in which the Bethe-Heitler cross-sections for bremsstrahlung and pair production are quite strongly energy dependent, the more accurate expressions for these cross-sections were used. In addition ionization loss and Compton effect were taken into account; however, because of the low atomic number of air and aluminium, scattering at low energies was neglected.

A natural consequence of the results for the number distribution are results for the average numbers and variances, and these likewise are given in the present paper. These cover energy ranges wherein, in the past, it has been most difficult to obtain meaningful numerical results.

In section 2, we discuss the method used to obtain the present results; in section 3 the results are given, and in section 4 we give a short discussion on some of their outstanding features. The equivalent 276 tables for the photon number distribution are in the course of being prepared as well as results using hydrogen and CH_2 absorbers.

2. Simulating The Physical Processes

We assume that there are only four processes taking place

(a) bremsstrahlung,
(b) pair production,
(c) Compton effect, and
(d) ionization loss.

For the first two of these we take (for light elements only) the Bethe-Heitler cross sections given by Rossi [2]). For bremsstrahlung

$$\Phi_1(E,\varepsilon) = \frac{4\alpha N Z^2 r_0^2 \rho}{A}\,\frac{1}{\varepsilon}\{[1+(1-\varepsilon)^2][\tfrac{1}{4}f_1(\delta)-\tfrac{1}{3}\ln Z] - \tfrac{2}{3}(1-\varepsilon)[\tfrac{1}{4}f_2(\delta)-\tfrac{1}{3}\ln Z]\}, \tag{1}$$

and for pair production

$$\Phi_2(E,\varepsilon) = \frac{4\alpha N Z^2 r_0^2 \rho}{A}\{[\varepsilon^2+(1-\varepsilon)^2][\tfrac{1}{4}f_1(\delta)-\tfrac{1}{3}\ln Z] + \tfrac{2}{3}\varepsilon(1-\varepsilon)[\tfrac{1}{4}f_2(\delta)-\tfrac{1}{3}\ln Z]\}, \tag{2}$$

where Φ_1 is the differential cross section per unit distance for bremsstrahlung, that is for the production of a photon of energy εE by an electron of primary energy E. Φ_2 is the differential cross section per unit distance for a photon of energy E producing a pair of electrons one of which has energy εE. The quantities N, α and r_0 are, respectively, Avogadro's number, the fine structure constant and

the classical electron radius e^2/m (m is expressed in energy units throughout). A and Z are the atomic weight and number of the absorbing medium. ρ is the density of the absorber.

To correct for the effect of the atomic electrons on these processes we shall replace Z^2 by $Z(Z+0.8)$ in Φ_1 and Φ_2 (see Heitler [3]) †.

δ is a variable which depends on the influence of the screening effect of the outer electrons on the electromagnetic interaction, being given in the bremsstrahlung case by ††

$$\delta = 136\, Z^{-\frac{1}{3}} \frac{m}{E} \frac{\varepsilon}{1-\varepsilon}, \tag{3}$$

and in the pair production case by

$$\delta = 136\, Z^{-\frac{1}{3}} \frac{m}{E} \frac{1}{\varepsilon(1-\varepsilon)}. \tag{4}$$

f_1 and f_2 are numerically tabulated functions which become in the full screening case ($\delta = 0$)

$$f_1(0) = 4 \ln 183,$$
$$f_2(0) = f_1(0) - \tfrac{2}{3}.$$

These two functions can be approximated with insignificant error by the expressions †††:
for $\delta \leqq 1$,

$$f_1(\delta) = 20.867 - 3.242\delta + 0.625\delta^2, \tag{5}$$

$$f_2(\delta) = 20.209 - 1.930\delta - 0.086\delta^2; \tag{6}$$

for $\delta > 1$

$$f_1(\delta) = f_2(\delta) = 21.12 - 4.184 \ln (\delta + 0.952). \tag{7}$$

If we measure distances in terms of radiation lengths, where a radiation length R is defined by

$$1/R = 4\alpha N r_0^2 Z(Z+0.8)\rho \ln (183 Z^{-\frac{1}{3}})/A,$$

the cross sections are simplified in that the dependence on the nature of the absorber is almost completely removed.

We generalize the treatment given in ref. [1]) for an element and now consider an absorber consisting of a compound or mixture where the proportion of each kind of nuclei (Z_i, A_i) by number is proportional to some number n_i. In the case of a compound this can be taken as the number of atoms of the given type

† In our calculations for air and aluminium absorbers the Z^2 factor was retained. Thus we have used radiation lengths of 73 and 26.3 gm/cm² for air and aluminium respectively rather then 38.8 and 24.7 gm/cm² which would be the case onr using $Z(Z+0.8)$. For our forthcoming results on hydrogen and paraffin absorbers the $Z(Z+0.8)$ factor is used.

†† In eqs. (1) and (2) Rossi used the variable $\gamma = \frac{100}{136}\delta$.

††† In ref. [1]) we used slightly different expressions, quartic in form. Since then, it has been found that the quadratic expressions given in the present paper are equally accurate.

in the molecule of the absorber; for a mixture it may be taken as the relative number of the different kinds of nuclei.

Define the following five quantities:

$$\begin{aligned} a &= (\ln 183)\sum n_i Z_i(Z_i+0.8), \\ b &= \sum n_i Z_i(Z_i+0.8)\ln Z_i^{-\frac{1}{2}}, \\ c &= \sum n_i Z_i, \\ d &= \sum n_i Z_i \ln Z_i^{-2}, \\ M &= \sum n_i A_i, \end{aligned} \tag{8}$$

where the summations are over the various nuclei in the absorber. For a compound, M is the molecular weight and c the total number of protons in a molecule of the absorber.

The expressions (8) enable us to write simply the cross sections for the various interactions in absorbers other than a pure element.

The radiation length is now given by

$$1/R = 4\alpha N r_0^2 \rho(a+b)/M = 1.396\times 10^{-3}\rho(a+b)/M \text{ cm}^{-1},$$

where ρ is in g/cm^3.

It is convenient to define various ratios of the quantities in (8), i.e.

$$\begin{aligned} p &= b/a, \\ q &= c/(a+b), \\ s &= d/(a+b). \end{aligned} \tag{9}$$

Writing φ_1, φ_2 for $R\Phi_1$, $R\Phi_2$, the cross sections, where distance is measured in terms of R, become on rearranging:

$$\begin{aligned} \varphi_1(E,\varepsilon) = R\Phi_1(E,\varepsilon) &= \left[\ln 2\left(\frac{4}{3}+\frac{1}{(9\ln 183)(1+p)}\right)\right]\left[\frac{1}{\ln 2}\left(\frac{1-\varepsilon}{\varepsilon}\right)\right] \\ &\times[A(\delta')]+[\tfrac{1}{2}][2\varepsilon][B(\delta')], \end{aligned} \tag{10}$$

$$\begin{aligned} \varphi_2(E,\varepsilon) = R\Phi_2(E,\varepsilon) &= \left[\frac{2}{3}-\frac{1}{(36\ln 183)(1+p)}\right][1][C(\delta')] \\ &+\left[\frac{1}{12}\left(\frac{4}{3}+\frac{1}{(9\ln 183)(1+p)}\right)\right][12(\varepsilon-\tfrac{1}{2})^2][A(\delta')], \end{aligned} \tag{11}$$

where

$$A(\delta') = \frac{3f_1(\delta')-f_2(\delta')+8p\ln 183}{3f_1(0)-f_2(0)+8p\ln 183}, \tag{12}$$

$$B(\delta') = \frac{f_1(\delta')+4p\ln 183}{f_1(0)+4p\ln 183}, \tag{13}$$

$$C(\delta') = \frac{3f_1(\delta') + f_2(\delta') + 16p \ln 183}{3f_1(0) + f_2(0) + 16p \ln 183}. \tag{14}$$

δ' is defined as:

$$\delta' = (136)(183^p)\frac{m\varepsilon}{E(1-\varepsilon)} \qquad \text{(bremsstrahlung)},$$

and

$$\delta' = (136)(183^p)\frac{m}{E\varepsilon(1-\varepsilon)} \qquad \text{(pair production)}.$$

Note that for an element $\delta' = \delta$. In absorbers with greatly differing values of Z among the different nuclei, the use of an average value of δ' in this way, leads to a small error only in the cases where δ' is very large. This can be seen from an examination of the expressions (5), (6), and (7). For simplicity we shall in future write δ instead of δ'.

The reason for writing the terms of φ_1, φ_2 as the product of three brackets will become evident later.

The cross section for Compton effect, in terms of the radiation length, is given by

$$\varphi_3(E, \varepsilon) = \frac{\pi m}{4\alpha(Z+0.8)\ln(183Z^{-\frac{1}{3}})}\frac{1}{E\varepsilon}[1+\varepsilon^2-\varepsilon\sin^2\theta], \tag{15}$$

and can be written in the form

$$\varphi_3(E, \varepsilon) = \frac{\pi m}{4\alpha}\frac{q}{E\varepsilon}[1+\varepsilon^2-\varepsilon\sin^2\theta]$$

$$= \left[\frac{\pi m}{4\alpha}\frac{q}{E}\ln 2\right]\left[\frac{1}{\ln 2}\frac{1}{\varepsilon}\right]\left[1-\frac{\varepsilon\sin^2\theta}{1+\varepsilon^2}\right] + \left[\frac{\pi m}{4\alpha}\frac{q}{E}\frac{1}{2}\right][2\varepsilon]\left[1-\frac{\varepsilon\sin^2\theta}{1+\varepsilon^2}\right], \tag{16}$$

where the scattering angle θ is defined by the relation

$$m(1-\varepsilon) = \varepsilon E(1-\cos\theta).$$

Here E is the primary photon energy and εE is the energy of the scattered photon. The kinetic energy imparted to an electron, previously considered to be at rest, is hence given by $(1-\varepsilon)E$.

Ionization loss is allowed for by subtracting from the electron energy, after each flight through a distance t radiation lengths, the quantity

$$E_0 - E = \frac{\pi m}{2\alpha(Z+0.8)\ln(183Z^{-\frac{1}{3}})}\left[20.2+3\ln\frac{E_0}{m}-2\ln Z\right]t,$$

$$= \frac{\pi m}{2\alpha}\left[20.2q+s+3q\ln\frac{E_0}{m}\right]t, \tag{17}$$

where E_0 was the energy at the beginning of the flight and E the corrected energy. Formula (17) is based on eq. (1.12) of ref. [2]), but differs by a negligible amount in that E_0 in the logarithmic term replaces the momentum of the electron, and that it is assumed that the rate of energy loss is constant as the electron moves through the small distance t.

To simulate the various processes, we are considering it is essential to have a method of producing some random event in a computer. As in most computers (and in particular SILLIAC) all machine operations give completely deterministic results. It is thus necessary to content oneself with pseudo-random events. That is to say, events which though they conform to a deterministic pattern, this pattern is so complicated that ordinary statistical test on the events would not reveal this fact.

For convenience in use and ease of generation, the pseudo-random events that one sought, are numbers uniformly distributed between 0 and 1. In future we shall refer to such numbers as 'random numbers'. It is also assumed that we have an endless supply of such numbers. In actual fact, 50 million numbers have been generated and tested using one method on SILLIAC. We shall denote such numbers by the symbols ξ, ξ_1, ξ_2, ... as required.

A theorem that makes it possible in principle to write down a rule for computing variates from any distribution is that if $F(x)$ be the cumulative distribution function of a variate x then $F(x)$ is itself distributed uniformly. $F(x)$ is defined by the property that if x is sampled from the corresponding distribution, the probability that the value of x will be less than x' is $F(x')$. $F(x)$ is a monotonically increasing function of x and hence:

$$\begin{aligned}\Pr\left(F(x) < F(x')\right) &= \Pr\left(x < x'\right)\\ &= F(x').\end{aligned}$$

$F(x)$ is therefore uniformly distributed between 0 and 1. Thus we may draw variates from this distribution by drawing a uniform random number ξ, and solving the equation

$$F(x) = \xi.$$

In the important case of the exponential distribution,

$$F(x) = 1-e^{-x/\bar{x}},$$

and the general method yields:

$$x = \bar{x} \log\left(\frac{1}{1-\xi}\right)$$

or more simply replacing $1-\xi$ by ξ:

$$x = \bar{x} \log\left(\frac{1}{\xi}\right).$$

This method is the one used to compute exponential variates in our programme. However, as a rule, it is advantageous to proceed less directly. Two general methods sometimes called "the composition method" and "the rejection method" may be combined in the applications we have made of them to the following (see ref. [1]).

If the frequency function of a distribution is $f(x)$ and if $f(x)$ can be written:

$$f(x) = \sum_{i=1}^{n} \alpha_i f_i(x) g_i(x), \tag{18}$$

where

$$0 \leqq g_i(x) \leqq 1,$$
$$\alpha_i > 0,$$
$$f_i(x) \geqq 0,$$
$$\int f_i(x)\mathrm{d}x = 1,$$

then samples may be drawn from the required distribution by choosing an integer from 1 to n with probability proportional to α_i of being i. This may be done by drawing a uniform variate and forming in turn

$$x_1 = \xi - \frac{\alpha_1}{\alpha_1+\alpha_2+\ldots\alpha_n},$$

$$x_2 = x_1 - \frac{\alpha_2}{\alpha_1+\alpha_2+\ldots\alpha_n},$$

$$x_3 = x_2 - \frac{\alpha_3}{\alpha_1+\alpha_2+\ldots\alpha_n},$$

and terminating the process for the first x_i that becomes negative and choosing the corresponding i. Having selected the value of i a sample is drawn from the distribution function with frequency function $f_i(x)$ and the value is accepted or rejected by computing the value of $g_i(x)$ and comparing with a random variate ξ.

If

$$\xi > g_i(x) \quad \text{reject } x,$$
$$\xi \leqq g_i(x) \quad \text{accept } x,$$

so that the probability of accepting x is $g_i(x)$.

In the case of rejection the process is repeated again and again until a value is finally accepted.

The value of the method lies in the fact that a decomposition of the frequency function as in (18) can usually be found without much difficulty such that n is a low number, $f_i(x)$ corresponds to a distribution easily sampled, and $g_i(x)$ is never much less than 1 (so that rejection of a sample is a rare event).

Examples of distributions easily sampled are those with frequency function of the form:

$$f(x) = \frac{(m+n+1)!}{m!\,n!}\,x^m(1-x)^n \qquad 0 < x \leqq 1$$

where m and n are positive integers for such a distribution may be realised by drawing $m+n+1$ uniform random numbers, ordering them in increasing order say

$$\xi_1 \leqq \xi_2 \leqq \xi_3 \leqq \cdots \leqq \xi_{m+n+1}$$

and selecting as the value of x the number ξ_{m+1}. For the joint frequency function of $\xi_1, \xi_2, \ldots \xi_{m+n+1}$ is

$$(m+n+1)!$$

and hence the frequency function of $x = \xi_{m+1}$ is

$$f(x) = (m+n+1)! \int_0^x d\xi_1 \int_{\xi_1}^x d\xi_2 \cdots \int_{\xi_{m-1}}^x d\xi_m \int_x^1 d\xi_{m+2} \int_{\xi_{m+2}}^1 d\xi_{m+3} \cdots \int_{\xi_{m+n}}^1 d\xi_{m+n+1}$$

$$= \frac{(m+n+1)!}{m!\,n!}\,x^m(1-x)^n.$$

The reason for the factorisation of the pair production cross section (11) is now obvious for we may set

$$\alpha_1 = \frac{2}{3} - \frac{1}{(36 \ln 183)(1+p)},$$

$$\alpha_2 = \frac{1}{12}\left(\frac{4}{3} + \frac{1}{(9 \ln 183)(1+p)}\right),$$

$$f_1 = 1,$$

$$f_2 = 12(\varepsilon - \tfrac{1}{2})^2,$$

$$g_1 = C(\delta),$$

$$g_2 = A(\delta).$$

The distribution corresponding to f_1, is simply the uniform distribution and that corresponding to f_2 may be sampled by drawing three uniform random numbers and selecting the one that differs by most from one half.

For bremsstrahlung, the cross section is of course not so simple. An artificial cutoff must be introduced to avoid the infra red catastrophe so for convenience we replace the term

$$\frac{1}{\ln 2}\,\frac{1-\varepsilon}{\varepsilon}$$

by a function $f_0(\varepsilon)$ say, which has this value for

$$2^{-r} \leqq \varepsilon \leqq 1$$

and has the constant value

$$\frac{1}{\ln 2}(2^r-1) \quad \text{for} \quad \varepsilon \leqq 2^{-r}.$$

If we now define

$$f_i(\varepsilon) = \begin{cases} 0, & \varepsilon \geqq 2^{1-i}, \\ \dfrac{1}{\ln 2}\dfrac{(1-\varepsilon 2^{i-1})}{\varepsilon}, & 2^{-i} \leqq \varepsilon \leqq 2^{1-i}, \\ \dfrac{1}{\ln 2}2^{i-1}, & \varepsilon \leqq 2^{-i}, \end{cases}$$

$$\text{for } i = 1, 2, \ldots r$$

then we have

$$f_0(\varepsilon) = \sum_{i=1}^{r} f_i(\varepsilon).$$

Furthermore all the $f_i(\varepsilon)$ have unit integral and a variate from the f_i distribution may be drawn multiplying a variate from the f_1 distribution by 2^{1-i}.

Thus we have as a suitable decomposition of the bremsstrahlung cross section:

$$\sum_{i=1}^{r+1} \alpha_i f_i(\varepsilon) g_i(\varepsilon)$$

where

$$\alpha_i = \ln 2\left(\frac{4}{3} + \frac{1}{(9 \ln 183)(1+p)}\right) \qquad (i = 1, 2, \ldots r),$$

$$\alpha_{r+1} = \tfrac{1}{2}.$$

The f_i are as defined for $i = 1, 2, \ldots r$ and

$$f_{r+1}(\varepsilon) = 2\varepsilon.$$

Also

$$g_i(\varepsilon) = A(\delta) \qquad (i = 1, 2, \ldots r),$$

$$g_{r+1}(\varepsilon) = B(\delta).$$

Variates from the distribution with frequency function 2ε may be drawn by taking the higher of two random numbers or more simply on a computer by drawing two random numbers ξ_1, and ξ_2 and computing ε thus:

$$\varepsilon = 1 - |\xi_1 - \xi_2|.$$

We need now consider only how to draw variates from the distribution with frequency function:

$$f(\varepsilon) = \begin{cases} \dfrac{1}{\ln 2}\,\dfrac{1-\varepsilon}{\varepsilon}, & \frac{1}{2} \leqq \varepsilon \leqq 1 \\ \dfrac{1}{\ln 2}, & 0 \leqq \varepsilon \leqq \frac{1}{2}. \end{cases}$$

As

$$\Pr\,(\varepsilon < \tfrac{1}{2}) = \frac{1}{2 \ln 2} \approx 0.72$$

we may first compare a random number ξ_1, with $1/(2 \ln 2)$ and if

$$\frac{1}{2 \ln 2} \geqq \xi_1$$

we may take as our value of ε:

$$\varepsilon = \tfrac{1}{2}\xi_2.$$

When

$$\frac{1}{2 \ln 2} < \xi_1$$

we must draw from the distribution with frequency function:

$$f(\varepsilon) = \begin{cases} \dfrac{1}{(\ln 2) - \frac{1}{2}}\,\dfrac{1-\varepsilon}{\varepsilon}, & \frac{1}{2} \leqq \varepsilon \leqq 1. \\ 0 & \varepsilon < \frac{1}{2}. \end{cases}$$

If we substitute $\varepsilon = 1 - \frac{1}{2}x$ so that x will range from zero to 1 we have as the frequency function of x, $h(x)$ say:

$$h(x) = \frac{1}{(4 \ln 2) - 2}\,\frac{x}{1 - \frac{1}{2}x}, \quad 0 \leqq x \leqq 1.$$

We can write this as

$$h(x) = \alpha' f'(x) g'(x),$$

where the usual restrictions apply to these symbols if

$$\alpha' = \frac{1}{4 \ln 2 - 2} = 1.294,$$

$$f'(x) = 2x,$$

$$g'(x) = \frac{1}{2 - x}.$$

We have already considered how to sample from a distribution with frequency function $f'(x)$ so sampling from $h(x)$ becomes trivial.

The Compton effect cross section can be written in the form

$$\sum_{i=1}^{n+1} \alpha_i f_i(\varepsilon) g_i(\varepsilon), \tag{19}$$

where

$$\alpha_i = \frac{\pi m q}{4\alpha E} \ln 2, \qquad (1 \leqq i \leqq n),$$

$$\alpha_{n+1} = \frac{\pi m q}{4\alpha E} \frac{1}{2},$$

$$f_i(\varepsilon) = \frac{1}{\ln 2} \frac{1}{\varepsilon}, \qquad (2^{-i} \leqq \varepsilon < 2^{1-i}, \quad 1 \leqq i \leqq n),$$

$$f_{n+1}(\varepsilon) = 2\varepsilon, \qquad (0 \leqq \varepsilon < 1),$$

$$g_i = 1 - \frac{\varepsilon \sin^2\theta}{1+\varepsilon^2}, \quad (1 \leqq i \leqq n+1),$$

where

$$m(1-\varepsilon) = \varepsilon E(1 - \cos\theta)$$

and g_i is put equal to zero in the cases where θ is not a real angle.

n is the next integer above $\log (E/2m')$ and m' is the lowest energy which the scattered photon can have according to the criterion:

$$\cos\theta > -1,$$

$$m' = \frac{m}{2 + \frac{m}{E'}}.$$

Here E' is the lowest energy particle which we shall ever follow using the programme. We shall use $m' = 0.24$ MeV corresponding to $E' = 4$ MeV.

The sampling of $f_{n+1}(\varepsilon)$ has already been considered as it is the same as $f_{r+1}(\varepsilon)$ in the bremsstrahlung cross section. To sample from $f_i(\varepsilon)$, $i \leqq n$ draw a random number ξ and form ε as:

$$\varepsilon = 2^{1-i} 2^{-\xi}.$$

We have seen how to sample from the distribution of secondary energies as defined by the cross sections for the various events. However, the task of computing the total cross section for a given primary energy still appears to remain. This problem may be completely avoided by observing that if we assume the

cross-sections to have the form

$$f(\varepsilon) = \sum_{i=1}^{n} \alpha_i f_i(\varepsilon) g_i(\varepsilon)$$

where the restrictions applying to the functions as in eq. (13) are satisfied then taking the total cross section as $\sum_{i=1}^{n} \alpha_i$ introduces no error if we proceed as follows:

Draw an exponential variate with total cross section $\sum_{i=1}^{n} \alpha_i$ i.e. with mean free path $1/(\sum_{i=1}^{n} \alpha_i)$.

Simulate the movement of the particle being considered through this distance.

Draw a sample of ε as previously described either accepting or rejecting the value of ε by comparing a random number with the appropriate $g_i(\varepsilon)$. However, in the event of rejection, instead of assuming that the distance that the particle has moved is to be rejected too, suppose that the particle has moved but is to be moved again and again until a value of ε is accepted.

If the true cross section is σ and the value of $\sum_{i=1}^{n} \alpha_i$ is σ' then clearly the probability of acceptance of the ε at a given step will be just σ/σ'.

Thus if we require n attempts before acceptance, the distance travelled t will be distributed as

$$\frac{(\sigma')^n t^{n-1} e^{-\sigma' t}}{(n-1)!}.$$

But the probability of having exactly n attempts is

$$\frac{\sigma}{\sigma'}\left(1-\frac{\sigma}{\sigma'}\right)^{n-1}.$$

Hence the distance travelled will be distributed as:

$$\sum_{n=1} \frac{(\sigma')^n t^{n-1} e^{-\sigma' t}}{(n-1)!} \frac{\sigma}{\sigma'}\left(1-\frac{\sigma}{\sigma'}\right)^{n-1} = \sigma e^{-\sigma t}.$$

Thus the effective cross section is correct.

For Compton effect, the cross section, φ_3, is strongly dependent on energy so a value of σ'_3 is computed each time a photon is considered. Referring to eq. (19) we see that this is:

$$\sigma'_3 = \frac{\pi m q}{4\alpha E}(n \ln 2 + \tfrac{1}{2}). \tag{20}$$

To simulate the motion of a photon we compute its mean free path as

$$\frac{1}{\sigma'_2 + \sigma'_3}$$

σ'_2 having the constant value

$$\frac{7}{9} - \frac{1}{(54 \ln 183)(1+p)}$$

and σ'_3 having the value given by (20).

Having simulated the motion of the photon through a random distance corresponding to that mean free path, we consider either pair production or Compton effect according as a random number ξ is less than or greater than $\sigma'_2/(\sigma'_2+\sigma'_3)$. In the case of rejection by the pair-production process or by the Compton effect process we return to simulate the movement through an additional distance.

3. The Calculation and its Results

In our Monte Carlo calculation the electrons and photons had numbers associated with them, representing the position, orientation, and energy of the 'particles'. Each particle had a certain probability of suffering a given type of 'collision' while traversing a given distance, determined according to the procedure outlined in section 2.

All the particles which were produced were considered in turn, and the whole process continued until all particles had moved outside the region of energies and positions that interested us. At the end of each shower, the number of electrons that had energies above a given value at a given depth was assessed and added into a histogram.

A new shower with a specified primary particle and energy was then started and the whole process repeated. In each instance at least 1000 showers were followed in order to obtain the present results, thus the standard error in a probability whose value is p is $[p(1-p)/1000]^{\frac{1}{2}}$, or about 0.016 for values near 0.5 and 0.0095 for values near 0.1 (see section 4).

A difficulty which obviously arises if one carries out straightforwardly the above procedure, is that of keeping track of all the particles that are produced, in the limited storage space of the computer.

The following procedure was therefore followed by us, overcoming all the obvious difficulties.

A directory was kept of all particles that were to be considered. When, because of a collision, two particles replaced one, the particle of higher energy had its information stored at the end of the directory, and the other was the next considered. When a particle was to be taken from the directory the last one in the directory was always chosen. It is seen that doing as we have described puts a limit on the total number of sets of entries that were ever needed in the directory. In fact, the number cannot exceed the integral part of $\log_2(E_0/E)$.

Our results, which required about 2000 hours of machine time to obtain, are given in the form of 276 tables. Each table gives the values of a probability

distribution function $\Phi^{i,1}_{abs}(E_0, E, n, t)$, namely the probability of finding exactly n electrons with energies greater than E at a depth of t cascade units in a 'given absorber', due to primary particle i ($i = 1$ for electrons and 2 for photons) of energy E_0. We have used 20 different values of the depth variable t, running from 0 to 10 radiation lengths in steps of one half of a radiation length.

There are thus four sets of tables $\Phi^{1,1}_{air}$, $\Phi^{2,1}_{air}$, $\Phi^{1,1}_{al}$, $\Phi^{2,1}_{al}$, each set containing 69 tables according to the combination of primary energies E_0 and secondary energies E chosen. The tables furthermore also give the values for the mean number of particles

$$N^{i,1}_{abs}(E_0, E, t) = \sum_{n=0}^{\infty} n\Phi^{i,1}_{abs}$$

and the variance

$$V^{i,1}_{abs}(E_0, E, t) = \sum_{n=0}^{\infty} n^2\Phi^{i,1}_{abs} - (N^{i,1}_{abs})^2.$$

For purposes of ready comparison we have numbered the tables so that the lowest energy ratios E_0/E come first and that results for corresponding cases in air and aluminium are in consecutive tables. Reference to Index 1, 2 or 3 allows one to readily find any given case.

INDEX 1

Results for a given value of primary electron energy E_0 and secondary electron energy E (both in MeV) may be found in the table number given in the square appropriate to these values. Odd numbered tables are for air absorbers, even numbered ones, for an aluminium absorber.

Primary electron

E \ E_0	50	100	200	500	1000	2000	5000	10 000	20 000	50 000
5	41, 42	61, 62	79, 80	95, 96	109, 110	121, 122	131, 132			
10	27, 28	43, 44	63, 64	85, 86	97, 98	111, 112	125, 126	133, 134		
20	13, 14	29, 30	45, 46	73, 74	87, 88	99, 100	117, 118	127, 128	135, 136	
50		1, 2	21, 22	47, 48	65, 66	81, 82	101, 102	113, 114	123, 124	137, 138
100			3, 4	31, 32	49, 50	67, 68	89, 90	103, 104	115, 116	129, 130
200				15, 16	33, 34	51, 52	75, 76	91, 92	105, 106	119, 120
500					5, 6	23, 24	53, 54	69, 70	83, 84	107, 108
1000						7, 8	35, 36	55, 56	71, 72	93, 94
2000							17, 18	37, 38	57, 58	77, 78
5000								9, 10	25, 26	59, 60
10 000									11, 12	39, 40
20 000										19, 20

INDEX 2

Results for a given value of primary photon energy E_0 and secondary electron energy E (both in MeV) may be found in the table number given in the square appropriate to these values. Odd numbered tables are for air absorbers, even numbered ones, for an aluminium absorber.

Primary photon

E \ E_0	50	100	200	500	1000	2000	5000	10 000	20 000	50 000
5	179, 180	199, 200	217, 218	233, 234	247, 248	259, 260	269, 270			
10	165, 166	181, 182	201, 202	223, 224	235, 236	249, 250	263, 264	271, 272		
20	151, 152	167, 168	183, 184	211, 212	225, 226	237, 238	255, 256	265, 266	273, 274	
50		139, 140	159, 160	185, 186	203, 204	219, 220	239, 240	251, 252	261, 262	275, 276
100			141, 142	169, 170	187, 188	205, 206	227, 228	241, 242	253, 254	267, 268
200				153, 154	171, 172	189, 190	213, 214	229, 230	243, 244	257, 258
500					143, 144	161, 162	191, 192	207, 208	221, 222	245, 246
1000						145, 146	173, 174	193, 194	209, 210	231, 232
2000							155, 156	175, 176	195, 196	215, 216
5000								147, 148	163, 164	197, 198
10 000									149, 150	177, 178
20 000										157, 158

The results from the computer give $\Phi(n)$ for all values of n, but when n gets large, it would be of little value to print out $\Phi(n)$ for all n up to the maximum number determined by E_0/E since most of the values are equal to zero. Furthermore one is usually only interested in knowing the exact value of n for small n and not large n. Thus it could be of interest to know the probability of finding exactly zero particles instead of 1 particle, or 3 particles instead of 4, but relatively unimportant to know the probability of finding exactly 39 particles rather than 40. For this reason we have printed out the tables for individual values of n for values $n = 0, 1, \ldots, 9$; and above 9 we have grouped the particles in fives where applicable.

In each table the results for the largest value of n shown, are given as the probability of finding 'exactly n or more' particles. Usually the complete value of this probability is contributed by $\Phi(n)$ itself; (that is the probability of finding exactly n particles). The probability of finding more than this value of n is thus usually very small. A quick check can be carried out by simply working out the mean from the results given for $\Phi(n)$ and comparing it with the value of the mean given in the table; the tabulated values of the mean and variance having been accurately obtained using $\Phi(n)$ for all values of n without grouping.

INDEX 3

Table numbers for electron and photon primaries of energy E_0 and secondary electrons of energy E are given for both air and aluminium absorbers and for the various energy ratios E_0/E. Energies E_0 and E are given in MeV

E_0/E			Electron		Photon	
	E_0	E	Air	Aluminium	Air	Aluminium
	100	50	1	2	139	140
	200	100	3	4	141	142
	1 000	500	5	6	143	144
2	2 000	1 000	7	8	145	146
	10 000	5 000	9	10	147	148
	20 000	10 000	11	12	149	150
	50	20	13	14	151	152
$2\frac{1}{2}$	500	200	15	16	153	154
	5 000	2 000	17	18	155	156
	50 000	20 000	19	20	157	158
	200	50	21	22	159	160
4	2 000	500	23	24	161	162
	20 000	5 000	25	26	163	164
	50	10	27	28	165	166
	100	20	29	30	167	168
	500	100	31	32	169	170
5	1 000	200	33	34	171	172
	5 000	1 000	35	36	173	174
	10 000	2 000	37	38	175	176
	50 000	10 000	39	40	177	178
	50	5	41	42	179	180
	100	10	43	44	181	182
	200	20	45	46	183	184
	500	50	47	48	185	186
10	1 000	100	49	50	187	188
	2 000	200	51	52	189	190
	5 000	500	53	54	191	192
	10 000	1 000	55	56	193	194
	20 000	2 000	57	58	195	196
	50 000	5 000	59	60	197	198
	100	5	61	62	199	200
	200	10	63	64	201	202
20	1 000	50	65	66	203	204
	2 000	100	67	68	205	206
	10 000	500	69	70	207	208
	20 000	1 000	71	72	209	210
	500	20	73	74	211	212
25	5 000	200	75	76	213	214
	50 000	2 000	77	78	215	216
	200	5	79	80	217	218
40	2 000	50	81	82	219	220
	20 000	500	83	84	221	222

INDEX 3 (Continued)

E_0/E			Electron		Photon	
	E_0	E	Air	Aluminium	Air	Aluminium
	500	10	85	86	223	224
	1 000	20	87	88	225	226
50	5 000	100	89	90	227	228
	10 000	200	91	92	229	230
	50 000	1 000	93	94	231	232
	500	5	95	96	233	234
	1 000	10	97	98	235	236
	2 000	20	99	100	237	238
100	5 000	50	101	102	239	240
	10 000	100	103	104	241	242
	20 000	200	105	106	243	244
	50 000	500	107	108	245	246
	1 000	5	109	110	247	248
200	2 000	10	111	112	249	250
	10 000	50	113	114	251	252
	20 000	100	115	116	253	254
250	5 000	20	117	118	255	256
	50 000	200	119	120	257	258
400	2 000	5	121	122	259	260
	20 000	50	123	124	261	262
	5 000	10	125	126	263	264
500	10 000	20	127	128	265	266
	50 000	100	129	130	267	268
	5 000	5	131	132	269	270
1000	10 000	10	133	134	271	272
	20 000	20	135	136	273	274
	50 000	50	137	138	275	276

4. Discussion of Results

Perhaps the most surprising feature shown by the tables here presented is the high energies that must be considered before Approximation A becomes at all accurate. This may be seen for instance by choosing one particular value of the ratio E_0/E, one type of primary and one of the two absorbers and comparing the table entries for increasing values of E. It will be seen that only when E is more than about ten times the critical energy of the absorber do successive tables show little variation. Comparison with tables of Approximation A average numbers given by Janossy and Messel [4]) will show that when the variation has ceased the agreement with these tables is close.

However, with the higher energy ratios such as 1000 /1 this agreement is never reached in the tables presented here and in ratios such as 100/1 it is only

just reached. These general statements are true for both types of primaries and both absorbers. An example of this change in the average number behaviour is illustrated in fig. 1 in which curves are shown for three cases corresponding to photon initiated showers in air with $E_0/E = 100$. As can be seen the position of the shower maximum and the value of the maximum attained differ widely between the three cases even though the intermediate case, $E_0 = 10\,000$ MeV, $E = 100$ MeV has E equal to the critical energy.

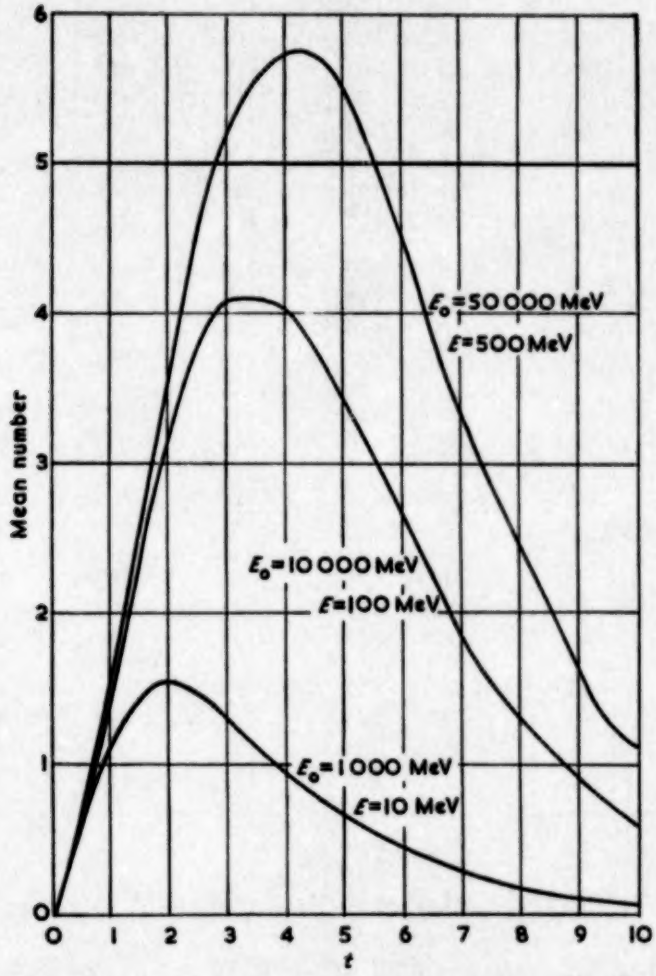

Fig. 1. The average number of electrons with energies greater than $E = 10$, 100 and 500 MeV is plotted against the depth t in radiation lengths, for three typical cases of photon initiated showers with primary energies $E_0 = 1000$, 10 000 and 50 000 MeV in air. In the three cases $E_0/E = 100$ and the values of E_0 and E are attached to the curves.

Although the variation of the results with energy is considerable there is nevertheless a close agreement at quite low energies between the tables for air and for aluminium if the values of E_0 and E for the air cases are about twice those for the aluminium cases. This is not surprising considering that the critical energies for air and for aluminium are in the ratio 2/1. What is generally observed for the photon primary cases is that agreement in this sense is excellent

as long as E is at least of the same order as the critical energy = 100 MeV for air and 50 MeV for aluminium. For electron primaries the energies involved can be lower still and there is for example quite good agreement for the electron primary cases: air, $E_0 = 1000$ MeV, $E = 10$ MeV and: aluminium, $E_0 = 500$ MeV, $E = 5$ MeV for which results are given in tables 97 and 96.

These considerations suggest that the results presented here will be useful for describing showers in all absorbers intermediate between air and aluminium

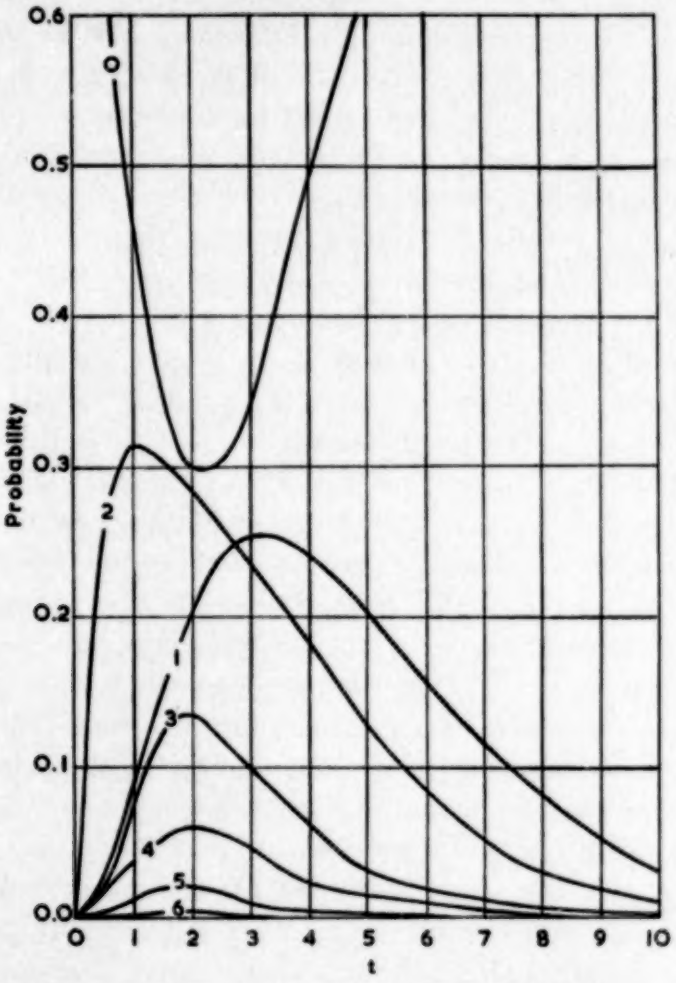

Fig. 2. The probability of finding exactly n electrons for n (attached to the curves) = 0, 1, 2, 3, 4, 5 and 6 is plotted against the depth t in radiation lengths in an air absorber. The shower is initiated by a photon with primary energy $E_0 = 1000$ MeV and each of the n electrons must have an energy greater than 10 MeV.

and perhaps even a little outside this range provided that all energies are scaled by the corresponding critical energies.

An effect which complicates any attempt that might be made to explain results of the type presented here in terms of empirical distributions results from the fact that electrons are normally produced in pairs and thus the parity of the number of electrons at different depths in a shower tends to be

preserved. This we shall refer to as the "odd-even" effect. We would expect to find a bias towards odd numbers of electrons in an electron initiated shower and towards an even number in a photon initiated shower but we would expect such an effect to disappear as the depth increased. In fact these things are what we observe on examination of the tables although for the photon primary cases especially, the effects persevere till well past the shower maximum.

The most striking example of this is the case: photon primary, aluminium absorber, $E_0 = 50\,000$ MeV, $E = 50$ MeV (table 276) where the effect seems to be present as far as the depth tabulated extends. For the electron primary cases, apart from the strong probability of one electron that extends to a considerable depth, the "odd-even" effect as a whole dies out within a few radiation lengths in every case. A typical example shown in fig. 2 is for the case: air absorber, photon primary, $E_0 = 1000$ MeV, $E = 10$ MeV. It is seen that at 2.5 radiation lengths the probability of a single electron is lower than either the probability of zero electrons or of two electrons but that the odd-even effect disappears completely after this depth.

A further example of the odd-even effect is given in fig. 3 for the case: aluminium absorber, electron primary, $E_0 = 50\,000$ MeV, $E = 500$ MeV. A number of other interesting points are also brought out in this example, which, due to the small value of the average number of electrons, are not apparent in fig. 2. In ref. [1]) we drew attention to the two-maxima behaviour for the curves $n = 2$, 3, 4 and higher numbers. As mentioned there the number development of the shower builds up through the small values of n, eventually reaching the maximum value for a certain depth t, (about 6.5 at a depth of 3.5 radiation lengths in the present case), and then the numbers decrease as the particles die off. Hence before and after the cascade maximum the probability of finding n electrons, where n is less than the average number at the maximum, must be greater than at the cascade maximum. The value of the depth t for which each curve reaches its maximum value must therefore also approach more and more closely to the value of the depth at the cascade maximum as n approaches the value at the cascade maximum. Near and beyond the average number at the shower maximum there is only one peak for the curve — namely near the cascade maximum. It is interesting to note that immediately past the cascade maximum the value of the probability of finding $n = 0$, 1, 2, 3, 4 electrons (n less than the average value of the maximum) increases with increasing n. This behaviour is understandable since the odd-even effect brought about by pair production becomes masked as the other shower factors come into play and overshadow pair production effects. On the other hand, at sufficiently great depths the order mentioned above is completely reversed.

It is very tempting to suppose that in some rows of almost every table, the slight fluctuation with depth of the quantity tabulated represents a real effect. Let us consider for example the case: photon primary, aluminium absorber,

$E_0 = 200$ MeV, $E = 100$ MeV (table 142). It will be seen that the probability of one electron generally decreases with increasing depth but that there appears to be a deviation from this general behaviour between $t = 3.5$ and $t = 4.0$. That the true value of the probability of one electron actually decreases smoothly can be found by an examination of table 277 where the same results are given, but for 10 000 rather than for 1000 showers. The increase in accuracy is sufficient to remove any peculiarity of this type and a steady decrease is observed.

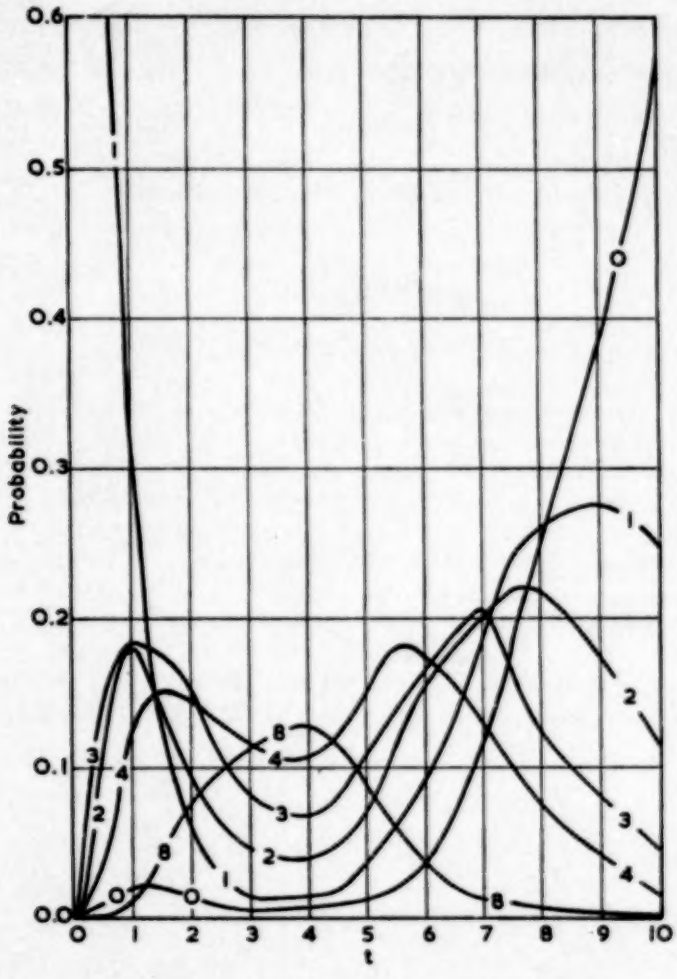

Fig. 3. The probability of finding exactly n electrons for n (attached to the curves) = 0, 1, 2, 3, 4 and 8 is plotted against the depth t in radiation lengths in an aluminium absorber. The shower is initiated by an electron with primary energy $E_0 = 50\,000$ MeV and each of the n electrons must have an energy greater than 500 MeV.

Although the number of irregularities of the sort just described appears to be higher than we would expect for random errors, the fact that the results given for differing depths are found from the same showers and the likelihood that within a single shower there may be a negative auto-correlation between some shower properties at a lag of half a radiation length makes this state of affairs explicable.

The accuracy of the results in general can be found from the theory of the binomial distribution. If p is the probability of an event estimated from N observations, the standard error is $\delta p = (p(1-p)/N)^{\frac{1}{2}}$. In the case of the present calculations $N = 1000$ and a table of δp against p is given as table 278.

As mentioned previously, this estimate of error should be used with care in comparing probabilities for an event at differing depths.

For the accuracy of the means we may use as a standard error the value of $(\sigma^2/1000)^{\frac{1}{2}}$ where σ^2 is the corresponding variance. As a rough estimate for the accuracy of the variance it is sufficient to use for the standard error for this quantity $\sigma^2/(500)^{\frac{1}{2}}$, based on the assumption that the distributions are approximately normal. Thus the percentage error in σ^2 is $(20)^{\frac{1}{2}}$ or about $4\frac{1}{2}$ %.

We wish to thank H. A. Shavers for help in checking the tables.

References

1) J. C. Butcher and H. Messel, Phys. Rev. **112** (1958) 2096

1a) J. C. Butcher and H. Messel, Proceedings of the I.U.P.A.P. Conference on Cosmic Rays, Moscow, 1959. After sending our paper to Moscow, a tape punching error was found (results were due to this mistake for an absorber with atomic number 73 instead of 7.3) effecting the calculations of both ref. [1]) and the paper which had been sent. A revised manuscript pointing this fact out and containing the corrections was sent on to Moscow, well in advance of the conference. On the recent appearance of the Proceedings of the conference, it was discovered that the Moscow editors had mistakenly published the original incorrect manuscript. The corrected version therefore never appeared!

2) B. Rossi, High Energy Particles (Prentice-Hall, Inc., Englewood Cliffs, New Jersey, 1952) also see B. Rossi and K. Preisen, Rev. Mod. Phys. **13** (1941) 290

3) W. Heitler, The quantum theory of radiation, 3rd edition (Clarendon Press, Oxford 1954)

4) L. Janossy and H. Messel, Proc. Roy. Irish Acad. A **54** (1951) 217

TABLE 1

Primary electron E_0 = 100 MeV.
Secondary electrons E = 50 MeV.

Absorber: air, Z = 7.4, A = 15,
Radiation length = 43 g/sq.cm,
Critical energy = 98 MeV.

n \ t	0.5	1.0	1.5	2.0	2.5	3.0	3.5	4.0	4.5	5.0	5.5	6.0	6.5	7.0	7.5	8.0	8.5	9.0	9.5	10.0
0	0.996	0.999	1.000	0.999	1.000	1.000	1.000	1.000	1.000	1.000	1.000	1.000	1.000	1.000	1.000	1.000	1.000	1.000	1.000	1.000
≥1	0.004	0.001	0.000	0.001	0.000	0.000	0.000	0.000	0.000	0.000	0.000	0.000	0.000	0.000	0.000	0.000	0.000	0.000	0.000	0.000
MEAN	0.00	0.00	0.00	0.00	0.00	0.00	0.00	0.00	0.00	0.00	0.00	0.00	0.00	0.00	0.00	0.00	0.00	0.00	0.00	0.00
VAR	0.0	0.0	0.0	0.0	0.0	0.0	0.0	0.0	0.0	0.0	0.0	0.0	0.0	0.0	0.0	0.0	0.0	0.0	0.0	0.0

TABLE 2

Primary electron E_0 = 100 MeV.
Secondary electrons E = 50 MeV.

Absorber: al, Z = 13, A = 27,
Radiation length = 26.3 g/sq.cm = 9.74 cm,
Critical energy = 52 MeV.

n \ t	0.5	1.0	1.5	2.0	2.5	3.0	3.5	4.0	4.5	5.0	5.5	6.0	6.5	7.0	7.5	8.0	8.5	9.0	9.5	10.0
0	0.563	0.996	0.998	1.000	0.998	1.000	1.000	0.999	1.000	1.000	1.000	1.000	0.999	1.000	1.000	1.000	1.000	1.000	1.000	1.000
≥1	0.437	0.004	0.002	0.000	0.002	0.000	0.000	0.001	0.000	0.000	0.000	0.000	0.001	0.000	0.000	0.000	0.000	0.000	0.000	0.000
MEAN	0.44	0.00	0.00	0.00	0.00	0.00	0.00	0.00	0.00	0.00	0.00	0.00	0.00	0.00	0.00	0.00	0.00	0.00	0.00	0.00
VAR	0.2	0.0	0.0	0.0	0.0	0.0	0.0	0.0	0.0	0.0	0.0	0.0	0.0	0.0	0.0	0.0	0.0	0.0	0.0	0.0

TABLE 3

Primary electron E_0 = 200 MeV.
Secondary electrons E = 100 MeV.

Absorber: air, Z = 7.4, A = 15,
Radiation length = 43 g/sq.cm,
Critical energy = 98 MeV.

n \ t	0.5	1.0	1.5	2.0	2.5	3.0	3.5	4.0	4.5	5.0	5.5	6.0	6.5	7.0	7.5	8.0	8.5	9.0	9.5	10.0
0	0.552	0.989	0.998	0.999	0.998	0.997	0.999	1.000	1.000	0.999	1.000	1.000	1.000	1.000	1.000	1.000	1.000	1.000	1.000	1.000
≥1	0.448	0.011	0.002	0.001	0.004	0.003	0.001	0.000	0.000	0.001	0.000	0.000	0.000	0.000	0.000	0.000	0.000	0.000	0.000	0.000
MEAN	0.45	0.01	0.00	0.00	0.00	0.00	0.00	0.00	0.00	0.00	0.00	0.00	0.00	0.00	0.00	0.00	0.00	0.00	0.00	0.00
VAR	0.2	0.0	0.0	0.0	0.0	0.0	0.0	0.0	0.0	0.0	0.0	0.0	0.0	0.0	0.0	0.0	0.0	0.0	0.0	0.0

TABLE 4

Primary electron E_0 = 200 MeV.
Secondary electrons E = 100 MeV.

Absorber: al, Z = 13, A = 27,
Radiation length = 26.3 g/sq.cm = 9.74 cm,
Critical energy = 52 MeV.

n \ t	0.5	1.0	1.5	2.0	2.5	3.0	3.5	4.0	4.5	5.0	5.5	6.0	6.5	7.0	7.5	8.0	8.5	9.0	9.5	10.0
0	0.463	0.879	0.993	0.997	0.999	0.998	0.997	0.998	1.000	1.000	0.999	0.999	1.000	1.000	0.999	1.000	1.000	1.000	1.000	1.000
≥1	0.537	0.121	0.007	0.003	0.001	0.002	0.003	0.002	0.000	0.000	0.001	0.001	0.000	0.000	0.001	0.000	0.000	0.000	0.000	0.000
MEAN	0.54	0.12	0.01	0.00	0.00	0.00	0.00	0.00	0.00	0.00	0.00	0.00	0.00	0.00	0.00	0.00	0.00	0.00	0.00	0.00
VAR	0.2	0.1	0.0	0.0	0.0	0.0	0.0	0.0	0.0	0.0	0.0	0.0	0.0	0.0	0.0	0.0	0.0	0.0	0.0	0.0

TABLE 5

Primary electron E_0 = 1 000 MeV.
Secondary electrons E = 500 MeV.

Absorber: air, Z = 7.4, A = 15,
Radiation length = 43 g/sq.cm,
Critical energy = 98 MeV.

n \ t	0.5	1.0	1.5	2.0	2.5	3.0	3.5	4.0	4.5	5.0	5.5	6.0	6.5	7.0	7.5	8.0	8.5	9.0	9.5	10.0
0	0.391	0.765	0.941	0.984	0.996	0.993	0.995	0.998	0.996	1.000	0.999	0.998	0.998	0.999	0.999	1.000	1.000	1.000	1.000	1.000
≥1	0.609	0.235	0.059	0.016	0.004	0.007	0.005	0.002	0.004	0.000	0.001	0.002	0.002	0.001	0.001	0.000	0.000	0.000	0.000	0.000
MEAN	0.61	0.24	0.06	0.02	0.00	0.01	0.01	0.00	0.00	0.00	0.00	0.00	0.00	0.00	0.00	0.00	0.00	0.00	0.00	0.00
VAR	0.2	0.2	0.1	0.0	0.0	0.0	0.0	0.0	0.0	0.0	0.0	0.0	0.0	0.0	0.0	0.0	0.0	0.0	0.0	0.0

TABLE 6

Primary electron E_0 = 1 000 MeV.
Secondary electrons E = 500 MeV.

Absorber: al, Z = 13, A = 27,
Radiation length = 26.3 g/sq.cm = 9.74 cm,
Critical energy = 52 MeV.

n \ t	0.5	1.0	1.5	2.0	2.5	3.0	3.5	4.0	4.5	5.0	5.5	6.0	6.5	7.0	7.5	8.0	8.5	9.0	9.5	10.0
0	0.379	0.686	0.887	0.964	0.988	0.970	0.997	0.996	0.996	0.999	1.000	0.996	1.000	1.000	1.000	1.000	1.000	1.000	1.000	1.000
≥1	0.621	0.314	0.113	0.036	0.012	0.030	0.003	0.004	0.004	0.001	0.000	0.004	0.000	0.000	0.000	0.000	0.000	0.000	0.000	0.000
MEAN	0.62	0.31	0.11	0.04	0.01	0.03	0.00	0.00	0.00	0.00	0.00	0.00	0.00	0.00	0.00	0.00	0.00	0.00	0.00	0.00
VAR	0.2	0.2	0.1	0.0	0.0	0.0	0.0	0.0	0.0	0.0	0.0	0.0	0.0	0.0	0.0	0.0	0.0	0.0	0.0	0.0

TABLE 7

Primary electron E_0 = 2 000 MeV.
Secondary electron E = 1 000 MeV.

Absorber: air, Z = 7.4, A = 15,
Radiation length = 43 g/sq.cm,
Critical energy = 98 MeV.

n \ t	0.5	1.0	1.5	2.0	2.5	3.0	3.5	4.0	4.5	5.0	5.5	6.0	6.5	7.0	7.5	8.0	8.5	9.0	9.5	10.0
0	0.358	0.697	0.878	0.953	0.992	0.994	0.989	0.997	0.994	0.999	1.000	0.999	1.000	0.999	0.999	1.000	1.000	1.000	1.000	1.000
≥1	0.642	0.303	0.122	0.047	0.008	0.006	0.011	0.003	0.006	0.001	0.000	0.001	0.000	0.001	0.001	0.000	0.000	0.000	0.000	0.000
MEAN	0.64	0.30	0.12	0.05	0.01	0.01	0.01	0.00	0.01	0.00	0.00	0.00	0.00	0.00	0.00	0.00	0.00	0.00	0.00	0.00
VAR	0.2	0.2	0.1	0.0	0.0	0.0	0.0	0.0	0.0	0.0	0.0	0.0	0.0	0.0	0.0	0.0	0.0	0.0	0.0	0.0

TABLE 8

Primary electron E_0 = 2 000 MeV.
Secondary electrons E = 1 000 MeV.

Absorber: al, Z = 13, A = 27,
Radiation length = 26.3 g/sq.cm = 9.74 cm,
Critical energy = 52 MeV.

n \ t	0.5	1.0	1.5	2.0	2.5	3.0	3.5	4.0	4.5	5.0	5.5	6.0	6.5	7.0	7.5	8.0	8.5	9.0	9.5	10.0
0	0.372	0.684	0.866	0.951	0.977	0.983	0.991	0.996	0.996	0.998	1.000	0.998	1.000	1.000	1.000	1.000	1.000	1.000	1.000	1.000
≥1	0.628	0.316	0.134	0.049	0.023	0.017	0.009	0.004	0.004	0.002	0.000	0.002	0.000	0.000	0.000	0.000	0.000	0.000	0.000	0.000
MEAN	0.63	0.32	0.13	0.05	0.02	0.02	0.01	0.00	0.00	0.00	0.00	0.00	0.00	0.00	0.00	0.00	0.00	0.00	0.00	0.00
VAR	0.2	0.2	0.1	0.0	0.0	0.0	0.0	0.0	0.0	0.0	0.0	0.0	0.0	0.0	0.0	0.0	0.0	0.0	0.0	0.0

TABLE 9

Primary electron E_0 = 10 000 MeV.
Secondary electrons E = 5 000 MeV.

Absorber: air, Z = 7.4, A = 15,
Radiation length = 43 g/sq.cm,
Critical energy = 98 MeV.

n \ t	0.5	1.0	1.5	2.0	2.5	3.0	3.5	4.0	4.5	5.0	5.5	6.0	6.5	7.0	7.5	8.0	8.5	9.0	9.5	10.0
0	0.380	0.668	0.847	0.934	0.974	0.983	0.989	0.994	0.995	0.998	0.999	1.000	0.998	1.000	1.000	0.999	1.000	1.000	1.000	1.000
≥1	0.620	0.332	0.153	0.066	0.026	0.017	0.011	0.006	0.005	0.002	0.001	0.000	0.002	0.000	0.000	0.001	0.000	0.000	0.000	0.000
MEAN	0.62	0.33	0.15	0.07	0.03	0.02	0.01	0.01	0.01	0.00	0.00	0.00	0.00	0.00	0.00	0.00	0.00	0.00	0.00	0.00
VAR	0.2	0.2	0.1	0.1	0.0	0.0	0.0	0.0	0.0	0.0	0.0	0.0	0.0	0.0	0.0	0.0	0.0	0.0	0.0	0.0

TABLE 10

Primary electron E_0 = 10 000 MeV.
Secondary electrons E = 5 000 MeV.

Absorber: al, Z = 13, A = 27,
Radiation length = 26.3 g/sq.cm = 9.74 cm,
Critical energy = 52 MeV.

n \ t	0.5	1.0	1.5	2.0	2.5	3.0	3.5	4.0	4.5	5.0	5.5	6.0	6.5	7.0	7.5	8.0	8.5	9.0	9.5	10.0
0	0.338	0.660	0.842	0.945	0.975	0.991	0.993	0.997	0.998	0.996	0.999	0.999	0.999	1.000	1.000	1.000	0.999	1.000	1.000	1.000
≥1	0.662	0.340	0.158	0.055	0.025	0.009	0.007	0.003	0.002	0.004	0.001	0.001	0.001	0.000	0.000	0.000	0.001	0.000	0.000	0.000
MEAN	0.66	0.34	0.16	0.06	0.03	0.01	0.01	0.00	0.00	0.00	0.00	0.00	0.00	0.00	0.00	0.00	0.00	0.00	0.00	0.00
VAR	0.2	0.2	0.1	0.1	0.0	0.0	0.0	0.0	0.0	0.0	0.0	0.0	0.0	0.0	0.0	0.0	0.0	0.0	0.0	0.0

TABLE 11

Primary electron E_0 = 20 000 MeV.
Secondary electrons E = 10 000 MeV.

Absorber: air, Z = 7.4, A = 15,
Radiation length = 43 g/sq.cm,
Critical energy = 98 MeV.

n \ t	0.5	1.0	1.5	2.0	2.5	3.0	3.5	4.0	4.5	5.0	5.5	6.0	6.5	7.0	7.5	8.0	8.5	9.0	9.5	10.0
0	0.343	0.660	0.831	0.931	0.976	0.985	0.993	0.995	0.994	0.998	0.999	0.997	1.000	1.000	1.000	1.000	1.000	1.000	1.000	0.999
⩾1	0.657	0.340	0.169	0.069	0.024	0.015	0.007	0.005	0.006	0.002	0.001	0.003	0.000	0.000	0.000	0.000	0.000	0.000	0.000	0.001
MEAN	0.66	0.34	0.17	0.07	0.02	0.02	0.01	0.01	0.01	0.00	0.00	0.00	0.00	0.00	0.00	0.00	0.00	0.00	0.00	0.00
VAR	0.2	0.2	0.1	0.1	0.0	0.0	0.0	0.0	0.0	0.0	0.0	0.0	0.0	0.0	0.0	0.0	0.0	0.0	0.0	0.0

TABLE 12

Primary electron E_0 = 20 000 MeV.
Secondary electrons E = 10 000 MeV.

Absorber: al, Z = 13, A = 27,
Radiation length = 26.3 g/sq.cm = 9.74 cm,
Critical energy = 52 MeV.

n \ t	0.5	1.0	1.5	2.0	2.5	3.0	3.5	4.0	4.5	5.0	5.5	6.0	6.5	7.0	7.5	8.0	8.5	9.0	9.5	10.0
0	0.317	0.625	0.822	0.931	0.974	0.991	0.991	0.996	0.994	0.999	0.997	0.999	1.000	1.000	1.000	0.999	1.000	1.000	1.000	1.000
⩾1	0.683	0.375	0.178	0.069	0.026	0.009	0.009	0.004	0.006	0.001	0.003	0.001	0.000	0.000	0.000	0.001	0.000	0.000	0.000	0.000
MEAN	0.68	0.38	0.18	0.07	0.03	0.01	0.01	0.00	0.01	0.00	0.00	0.00	0.00	0.00	0.00	0.00	0.00	0.00	0.00	0.00
VAR	0.2	0.2	0.1	0.1	0.0	0.0	0.0	0.0	0.0	0.0	0.0	0.0	0.0	0.0	0.0	0.0	0.0	0.0	0.0	0.0

TABLE 13

Primary electron E_0 = 50 MeV.
Secondary electrons E = 20 MeV.

Absorber: air, Z = 7.4, A = 15,
Radiation length = 43 g/sq.cm,
Critical energy = 98 MeV.

n \ t	0.5	1.0	1.5	2.0	2.5	3.0	3.5	4.0	4.5	5.0	5.5	6.0	6.5	7.0	7.5	8.0	8.5	9.0	9.5	10.0
0	0.999	0.999	1.000	0.999	1.000	1.000	1.000	1.000	0.999	1.000	1.000	1.000	1.000	1.000	1.000	1.000	1.000	1.000	1.000	1.000
⩾1	0.001	0.001	0.000	0.001	0.000	0.000	0.000	0.000	0.001	0.000	0.000	0.000	0.000	0.000	0.000	0.000	0.000	0.000	0.000	0.000
MEAN	0.00	0.00	0.00	0.00	0.00	0.00	0.00	0.00	0.00	0.00	0.00	0.00	0.00	0.00	0.00	0.00	0.00	0.00	0.00	0.00
VAR	0.0	0.0	0.0	0.0	0.0	0.0	0.0	0.0	0.0	0.0	0.0	0.0	0.0	0.0	0.0	0.0	0.0	0.0	0.0	0.0

TABLE 14

Primary electron E_0 = 50 MeV.
Secondary electrons E = 20 MeV.

Absorber: al, Z = 13, A = 27,
Radiation length = 26.3 g/sq.cm = 9.74 cm,
Critical energy = 52 MeV.

n \ t	0.5	1.0	1.5	2.0	2.5	3.0	3.5	4.0	4.5	5.0	5.5	6.0	6.5	7.0	7.5	8.0	8.5	9.0	9.5	10.0
0	0.749	0.999	0.999	0.997	0.999	0.998	1.000	1.000	1.000	1.000	0.999	1.000	1.000	1.000	1.000	1.000	1.000	1.000	1.000	1.000
⩾1	0.251	0.001	0.001	0.003	0.001	0.002	0.000	0.000	0.000	0.000	0.001	0.000	0.000	0.000	0.000	0.000	0.000	0.000	0.000	0.000
MEAN	0.25	0.00	0.00	0.00	0.00	0.00	0.00	0.00	0.00	0.00	0.00	0.00	0.00	0.00	0.00	0.00	0.00	0.00	0.00	0.00
VAR	0.2	0.0	0.0	0.0	0.0	0.0	0.0	0.0	0.0	0.0	0.0	0.0	0.0	0.0	0.0	0.0	0.0	0.0	0.0	0.0

TABLE 15

Primary electron E_0 = 500 MeV.
Secondary electrons E = 200 MeV.

Absorber: air, Z = 7.4, A = 15,
Radiation length = 43 g/sq.cm,
Critical energy = 98 MeV.

n \ t	0.5	1.0	1.5	2.0	2.5	3.0	3.5	4.0	4.5	5.0	5.5	6.0	6.5	7.0	7.5	8.0	8.5	9.0	9.5	10.0
0	0.290	0.691	0.936	0.986	0.992	0.991	0.996	0.999	0.998	0.997	1.000	0.997	0.998	1.000	1.000	1.000	1.000	1.000	1.000	1.000
1	0.710	0.309	0.065	0.014	0.008	0.009	0.004	0.001	0.002	0.003	0.000	0.003	0.002	0.000	0.000	0.000	0.000	0.000	0.000	0.000
⩾2	0.000	0.000	0.000	0.000	0.000	0.000	0.000	0.000	0.000	0.000	0.000	0.000	0.000	0.000	0.000	0.000	0.000	0.000	0.000	0.000
MEAN	0.71	0.31	0.07	0.01	0.01	0.01	0.00	0.00	0.00	0.00	0.00	0.00	0.00	0.00	0.00	0.00	0.00	0.00	0.00	0.00
VAR	0.2	0.2	0.1	0.0	0.0	0.0	0.0	0.0	0.0	0.0	0.0	0.0	0.0	0.0	0.0	0.0	0.0	0.0	0.0	0.0

TABLE 16

Primary electron E_0 = 500 MeV.
Secondary electrons E = 200 MeV.

Absorber: al, Z = 13, A = 27,
Radiation length = 26.3 g/sq.cm = 9.74 cm,
Critical energy = 52 MeV.

n \ t	0.5	1.0	1.5	2.0	2.5	3.0	3.5	4.0	4.5	5.0	5.5	6.0	6.5	7.0	7.5	8.0	8.5	9.0	9.5	10.0
0	0.296	0.632	0.856	0.967	0.985	0.991	0.989	0.994	0.994	0.999	0.999	0.998	1.000	1.000	0.997	1.000	1.000	1.000	0.999	1.000
1	0.703	0.368	0.144	0.033	0.015	0.009	0.011	0.006	0.006	0.001	0.001	0.002	0.000	0.000	0.003	0.000	0.000	0.000	0.001	0.000
⩾ 2	0.001	0.000	0.000	0.000	0.000	0.000	0.000	0.000	0.000	0.000	0.000	0.000	0.000	0.000	0.000	0.000	0.000	0.000	0.000	0.000
MEAN	0.71	0.37	0.14	0.03	0.02	0.01	0.01	0.01	0.01	0.00	0.00	0.00	0.00	0.00	0.00	0.00	0.00	0.00	0.00	0.00
VAR	0.2	0.2	0.1	0.0	0.0	0.0	0.0	0.0	0.0	0.0	0.0	0.0	0.0	0.0	0.0	0.0	0.0	0.0	0.0	0.0

TABLE 17

Primary electron E_0 = 5 000 MeV.
Secondary electrons E = 2 000 MeV.

Absorber: air, Z = 7.4, A = 15,
Radiation length = 43 g/sq.cm,
Critical energy = 98 MeV.

n \ t	0.5	1.0	1.5	2.0	2.5	3.0	3.5	4.0	4.5	5.0	5.5	6.0	6.5	7.0	7.5	8.0	8.5	9.0	9.5	10.0
0	0.291	0.554	0.760	0.878	0.939	0.958	0.975	0.988	0.995	0.997	0.998	0.998	0.998	0.999	1.000	1.000	1.000	1.000	1.000	1.000
1	0.708	0.445	0.240	0.122	0.061	0.042	0.025	0.012	0.005	0.003	0.002	0.002	0.002	0.001	0.000	0.000	0.000	0.000	0.000	0.000
⩾ 2	0.001	0.001	0.000	0.000	0.000	0.000	0.000	0.000	0.000	0.000	0.000	0.000	0.000	0.000	0.000	0.000	0.000	0.000	0.000	0.000
MEAN	0.71	0.45	0.24	0.12	0.06	0.04	0.03	0.01	0.01	0.00	0.00	0.00	0.00	0.00	0.00	0.00	0.00	0.00	0.00	0.00
VAR	0.2	0.3	0.2	0.1	0.1	0.0	0.0	0.0	0.0	0.0	0.0	0.0	0.0	0.0	0.0	0.0	0.0	0.0	0.0	0.0

TABLE 18

Primary electron E_0 = 5 000 MeV.
Secondary electrons E = 2 000 MeV.

Absorber: al, Z = 13, A = 27,
Radiation length = 26.3 g/sq.cm = 9.74 cm,
Critical energy = 52 MeV.

n \ t	0.5	1.0	1.5	2.0	2.5	3.0	3.5	4.0	4.5	5.0	5.5	6.0	6.5	7.0	7.5	8.0	8.5	9.0	9.5	10.0
0	0.254	0.536	0.746	0.882	0.929	0.952	0.978	0.989	0.993	0.994	0.999	0.996	0.996	0.998	1.000	0.999	1.000	1.000	1.000	1.000
1	0.743	0.464	0.253	0.117	0.071	0.048	0.022	0.011	0.007	0.006	0.001	0.004	0.004	0.002	0.000	0.001	0.000	0.000	0.000	0.000
⩾ 2	0.003	0.000	0.001	0.001	0.000	0.000	0.000	0.000	0.000	0.000	0.000	0.000	0.000	0.000	0.000	0.000	0.000	0.000	0.000	0.000
MEAN	0.75	0.46	0.26	0.12	0.07	0.05	0.02	0.01	0.01	0.01	0.00	0.00	0.00	0.00	0.00	0.00	0.00	0.00	0.00	0.00
VAR	0.2	0.2	0.2	0.1	0.1	0.0	0.0	0.0	0.0	0.0	0.0	0.0	0.0	0.0	0.0	0.0	0.0	0.0	0.0	0.0

TABLE 19

Primary electron E_0 = 50 000 MeV.
Secondary electrons E = 20 000 MeV.

Absorber: air, Z = 7.4, A = 15,
Radiation length = 43 g/sq.cm,
Critical energy = 98 MeV.

n \ t	0.5	1.0	1.5	2.0	2.5	3.0	3.5	4.0	4.5	5.0	5.5	6.0	6.5	7.0	7.5	8.0	8.5	9.0	9.5	10.0
0	0.278	0.542	0.738	0.886	0.932	0.971	0.978	0.991	0.993	0.993	0.997	0.996	0.997	1.000	0.999	0.999	0.999	1.000	1.000	1.000
1	0.722	0.458	0.262	0.114	0.068	0.029	0.021	0.008	0.007	0.007	0.003	0.004	0.003	0.000	0.001	0.001	0.001	0.000	0.000	0.000
⩾ 2	0.000	0.000	0.000	0.000	0.000	0.000	0.001	0.001	0.000	0.000	0.000	0.000	0.000	0.000	0.000	0.000	0.000	0.000	0.000	0.000
MEAN	0.72	0.46	0.26	0.11	0.07	0.03	0.02	0.01	0.01	0.01	0.00	0.00	0.00	0.00	0.00	0.00	0.00	0.00	0.00	0.00
VAR	0.2	0.2	0.2	0.1	0.1	0.0	0.0	0.0	0.0	0.0	0.0	0.0	0.0	0.0	0.0	0.0	0.0	0.0	0.0	0.0

TABLE 20

Primary electron E_0 = 50 000 MeV.
Secondary electrons E = 20 000 MeV.

Absorber: al, Z = 13, A = 27,
Radiation length = 26.3 g/sq.cm = 9.74 cm,
Critical energy = 52 MeV.

n \ t	0.5	1.0	1.5	2.0	2.5	3.0	3.5	4.0	4.5	5.0	5.5	6.0	6.5	7.0	7.5	8.0	8.5	9.0	9.5	10.0
0	0.273	0.547	0.734	0.879	0.930	0.970	0.980	0.986	0.989	0.994	0.996	0.994	0.994	0.997	0.997	0.998	1.000	0.999	0.999	1.000
1	0.726	0.452	0.266	0.121	0.070	0.030	0.020	0.014	0.011	0.006	0.004	0.006	0.006	0.003	0.003	0.002	0.000	0.001	0.001	0.000
⩾ 2	0.001	0.001	0.000	0.000	0.000	0.000	0.000	0.000	0.000	0.000	0.000	0.000	0.000	0.000	0.000	0.000	0.000	0.000	0.000	0.000
MEAN	0.73	0.45	0.27	0.12	0.07	0.03	0.02	0.01	0.01	0.01	0.00	0.01	0.01	0.00	0.00	0.00	0.00	0.00	0.00	0.00
VAR	0.2	0.2	0.2	0.1	0.1	0.0	0.0	0.0	0.0	0.0	0.0	0.0	0.0	0.0	0.0	0.0	0.0	0.0	0.0	0.0

TABLE 21

Primary electron E_0 = 200 MeV.
Secondary eletrons E = 50 MeV.

Absorber: air, Z = 7.4, A = 15,
Radiation length = 43 g/sq.cm,
Critical energy = 98 MeV.

n \ t	0.5	1.0	1.5	2.0	2.5	3.0	3.5	4.0	4.5	5.0	5.5	6.0	6.5	7.0	7.5	8.0	8.5	9.0	9.5	10.0
0	0.275	0.782	0.980	0.986	0.992	0.987	0.995	0.992	0.998	0.996	0.996	1.000	1.000	1.000	1.000	1.000	1.000	1.000	1.000	1.000
1	0.723	0.218	0.019	0.012	0.008	0.013	0.005	0.008	0.002	0.004	0.003	0.000	0.000	0.000	0.000	0.000	0.000	0.000	0.000	0.000
⩾2	0.002	0.000	0.001	0.002	0.000	0.000	0.000	0.000	0.000	0.000	0.001	0.000	0.000	0.000	0.000	0.000	0.000	0.000	0.000	0.000
MEAN	0.73	0.22	0.02	0.02	0.01	0.01	0.01	0.01	0.00	0.00	0.01	0.00	0.00	0.00	0.00	0.00	0.00	0.00	0.00	0.00
VAR	0.2	0.2	0.0	0.0	0.0	0.0	0.0	0.0	0.0	0.0	0.0	0.0	0.0	0.0	0.0	0.0	0.0	0.0	0.0	0.0

TABLE 22

Primary electron E_0 = 200 MeV.
Secondary electrons E = 50 MeV.

Absorber: al, Z = 13, A = 27,
Radiation length = 26.3 g/sq.cm = 9.74 cm,
Critical energy = 52 MeV.

n \ t	0.	1.0	1.5	2.0	2.5	3.0	3.5	4.0	4.5	5.0	5.5	6.0	6.5	7.0	7.5	8.0	8.5	9.0	9.5	10.0
0	0.200	0.543	0.856	0.963	0.973	0.984	0.988	0.985	0.996	0.997	0.996	0.999	1.000	1.000	0.999	0.999	1.000	1.000	1.000	1.000
1	0.795	0.456	0.142	0.036	0.026	0.016	0.011	0.014	0.004	0.003	0.004	0.001	0.000	0.000	0.000	0.001	0.000	0.000	0.000	0.000
⩾2	0.005	0.001	0.002	0.001	0.001	0.000	0.001	0.001	0.000	0.000	0.000	0.000	0.000	0.000	0.001	0.000	0.000	0.000	0.000	0.000
MEAN	0.81	0.46	0.15	0.04	0.03	0.02	0.01	0.02	0.00	0.00	0.00	0.00	0.00	0.00	0.00	0.00	0.00	0.00	0.00	0.00
VAR	0.2	0.3	0.1	0.0	0.0	0.0	0.0	0.0	0.0	0.0	0.0	0.0	0.0	0.0	0.0	0.0	0.0	0.0	0.0	0.0

TABLE 23

Primary electron E_0 = 2 000 MeV.
Secondary electrons E = 500 MeV.

Absorber: air, Z = 7.4, A = 15,
Radiation length = 43 g/sq.cm,
Critical energy = 98 MeV.

n \ t	0.5	1.0	1.5	2.0	2.5	3.0	3.5	4.0	4.5	5.0	5.5	6.0	6.5	7.0	7.5	8.0	8.5	9.0	9.5	10.0
0	0.180	0.422	0.615	0.754	0.861	0.928	0.943	0.967	0.977	0.984	0.990	0.989	0.995	0.995	0.997	1.000	0.999	0.998	0.998	1.000
1	0.798	0.559	0.373	0.232	0.136	0.069	0.056	0.032	0.023	0.016	0.010	0.011	0.005	0.005	0.002	0.000	0.001	0.002	0.002	0.000
⩾2	0.022	0.019	0.012	0.014	0.003	0.003	0.001	0.001	0.000	0.000	0.000	0.000	0.000	0.000	0.001	0.000	0.000	0.000	0.000	0.000
MEAN	0.84	0.60	0.40	0.26	0.14	0.08	0.06	0.03	0.02	0.02	0.01	0.01	0.01	0.01	0.00	0.00	0.00	0.00	0.00	0.00
VAR	0.2	0.3	0.3	0.2	0.1	0.1	0.1	0.0	0.0	0.0	0.0	0.0	0.0	0.0	0.0	0.0	0.0	0.0	0.0	0.0

TABLE 24

Primary electron E_0 = 2 000 MeV.
Secondary electrons E = 500 MeV.

Absorber: al, Z = 13, A = 27,
Radiation length = 26.3 g/sq.cm = 9.74 cm,
Critical energy = 52 MeV.

n \ t	0.5	1.0	1.5	2.0	2.5	3.0	3.5	4.0	4.5	5.0	5.5	6.0	6.5	7.0	7.5	8.0	8.5	9.0	9.5	10.0
0	0.182	0.395	0.572	0.758	0.844	0.902	0.935	0.963	0.961	0.971	0.984	0.986	0.995	0.996	0.998	0.999	0.998	0.999	0.999	0.998
1	0.793	0.574	0.419	0.236	0.152	0.097	0.061	0.037	0.038	0.026	0.016	0.013	0.004	0.004	0.002	0.001	0.002	0.001	0.001	0.002
⩾2	0.025	0.031	0.009	0.006	0.004	0.001	0.004	0.000	0.001	0.003	0.000	0.001	0.001	0.000	0.000	0.000	0.000	0.000	0.000	0.000
MEAN	0.84	0.64	0.44	0.25	0.16	0.10	0.07	0.04	0.04	0.03	0.02	0.02	0.01	0.00	0.00	0.00	0.00	0.00	0.00	0.00
VAR	0.2	0.3	0.3	0.2	0.1	0.1	0.1	0.0	0.0	0.0	0.0	0.0	0.0	0.0	0.0	0.0	0.0	0.0	0.0	0.0

TABLE 25

Primary electron E_0 = 20 000 MeV.
Secondary electrons E = 5 000 MeV.

Absorber: air, Z = 7.4, A = 15,
Radiation length = 43 g/sq.cm,
Critical energy = 98 MeV.

n \ t	0.5	1.0	1.5	2.0	2.5	3.0	3.5	4.0	4.5	5.0	5.5	6.0	6.5	7.0	7.5	8.0	8.5	9.0	9.5	10.0
0	0.160	0.351	0.526	0.677	0.787	0.869	0.907	0.945	0.962	0.978	0.982	0.986	0.988	0.994	0.995	0.999	0.998	1.000	1.000	0.999
1	0.803	0.610	0.451	0.311	0.203	0.126	0.092	0.053	0.037	0.022	0.018	0.014	0.012	0.006	0.005	0.001	0.002	0.000	0.000	0.001
⩾2	0.037	0.039	0.023	0.012	0.010	0.005	0.001	0.002	0.001	0.000	0.000	0.000	0.000	0.000	0.000	0.000	0.000	0.000	0.000	0.000
MEAN	0.88	0.69	0.50	0.34	0.22	0.14	0.09	0.06	0.04	0.02	0.02	0.01	0.01	0.01	0.01	0.00	0.00	0.00	0.00	0.00
VAR	0.2	0.3	0.3	0.2	0.2	0.1	0.1	0.1	0.0	0.0	0.0	0.0	0.0	0.0	0.0	0.0	0.0	0.0	0.0	0.0

TABLE 26

Primary electron E_0 = 20 000 MeV.
Secondary electrons E = 5 000 MeV.

Absorber: al, Z = 13, A = 27,
Radiation length = 26.3 g/sq.cm = 9.74 cm,
Critical energy = 52 MeV.

n \ t	0.5	1.0	1.5	2.0	2.5	3.0	3.5	4.0	4.5	5.0	5.5	6.0	6.5	7.0	7.5	8.0	8.5	9.0	9.5	10.0
0	0.133	0.321	0.496	0.660	0.808	0.874	0.915	0.954	0.960	0.971	0.981	0.986	0.989	0.991	0.993	0.997	0.997	1.000	1.000	1.000
1	0.837	0.644	0.480	0.325	0.183	0.120	0.082	0.045	0.039	0.028	0.019	0.014	0.011	0.009	0.007	0.003	0.003	0.000	0.000	0.000
⩾2	0.030	0.035	0.024	0.015	0.009	0.006	0.003	0.001	0.001	0.001	0.000	0.000	0.000	0.000	0.000	0.000	0.000	0.000	0.000	0.000
MEAN	0.90	0.71	0.53	0.36	0.20	0.13	0.09	0.05	0.04	0.03	0.02	0.01	0.01	0.01	0.01	0.00	0.00	0.00	0.00	0.00
VAR	0.2	0.3	0.3	0.3	0.2	0.1	0.1	0.0	0.0	0.0	0.0	0.0	0.0	0.0	0.0	0.0	0.0	0.0	0.0	0.0

TABLE 27

Primary electron E_0 = 50 MeV.
Secondary electrons E = 10 MeV.

Absorber: air, Z = 7.4, A = 15,
Radiation length = 43 g/sq.cm,
Critical energy = 98 MeV.

n \ t	0.5	1.0	1.5	2.0	2.5	3.0	3.5	4.0	4.5	5.0	5.5	6.0	6.5	7.0	7.5	8.0	8.5	9.0	9.5	10.0
0	0.994	0.996	1.000	0.997	0.999	0.999	1.000	1.000	0.998	1.000	1.000	1.000	1.000	1.000	1.000	1.000	1.000	1.000	1.000	1.000
1	0.005	0.003	0.000	0.003	0.001	0.001	0.000	0.000	0.002	0.000	0.000	0.000	0.000	0.000	0.000	0.000	0.000	0.000	0.000	0.000
⩾2	0.001	0.001	0.000	0.000	0.000	0.000	0.000	0.000	0.000	0.000	0.000	0.000	0.000	0.000	0.000	0.000	0.000	0.000	0.000	0.000
MEAN	0.01	0.01	0.00	0.00	0.00	0.00	0.00	0.00	0.00	0.00	0.00	0.00	0.00	0.00	0.00	0.00	0.00	0.00	0.00	0.00
VAR	0.0	0.0	0.0	0.0	0.0	0.0	0.0	0.0	0.0	0.0	0.0	0.0	0.0	0.0	0.0	0.0	0.0	0.0	0.0	0.0

TABLE 28

Primary electron E_0 = 50 MeV.
Secondary electrons E = 10 MeV.

Absorber: al, Z = 13, A = 27,
Radiation length = 26.3 g/sq.cm = 9.74 cm,
Critical energy = 52 MeV.

n \ t	0.5	1.0	1.5	2.0	2.5	3.0	3.5	4.0	4.5	5.0	5.5	6.0	6.5	7.0	7.5	8.0	8.5	9.0	9.5	10.0
0	0.377	0.994	0.996	0.995	0.998	0.995	0.997	1.000	0.998	1.000	0.997	0.998	0.999	1.000	1.000	1.000	1.000	1.000	1.000	1.000
1	0.622	0.006	0.002	0.004	0.002	0.005	0.003	0.000	0.002	0.000	0.003	0.002	0.001	0.000	0.000	0.000	0.000	0.000	0.000	0.000
⩾2	0.001	0.000	0.002	0.001	0.000	0.000	0.000	0.000	0.000	0.000	0.000	0.000	0.000	0.000	0.000	0.000	0.000	0.000	0.000	0.000
MEAN	0.62	0.01	0.01	0.01	0.00	0.01	0.00	0.00	0.00	0.00	0.00	0.00	0.00	0.00	0.00	0.00	0.00	0.00	0.00	0.00
VAR	0.2	0.0	0.0	0.0	0.0	0.0	0.0	0.0	0.0	0.0	0.0	0.0	0.0	0.0	0.0	0.0	0.0	0.0	0.0	0.0

TABLE 29

Primary electron E_0 = 100 MeV.
Secondary electrons E = 20 MeV.

Absorber: air, Z = 7.4, A = 15,
Radiation length = 43 g/sq.cm,
Critical energy = 98 MeV.

n \ t	0.5	1.0	1.5	2.0	2.5	3.0	3.5	4.0	4.5	5.0	5.5	6.0	6.5	7.0	7.5	8.0	8.5	9.0	9.5	10.0
0	0.390	0.982	0.995	0.989	0.988	0.994	0.995	0.999	0.997	0.998	1.000	1.000	1.000	1.000	1.000	1.000	1.000	0.998	1.000	1.000
1	0.609	0.017	0.005	0.011	0.012	0.005	0.005	0.001	0.003	0.002	0.000	0.000	0.000	0.000	0.000	0.000	0.000	0.002	0.000	0.000
⩾2	0.001	0.001	0.000	0.000	0.000	0.001	0.000	0.000	0.000	0.000	0.000	0.000	0.000	0.000	0.000	0.000	0.000	0.000	0.000	0.000
MEAN	0.61	0.02	0.01	0.01	0.01	0.01	0.01	0.00	0.00	0.00	0.00	0.00	0.00	0.00	0.00	0.00	0.00	0.00	0.00	0.00
VAR	0.2	0.0	0.0	0.0	0.0	0.0	0.0	0.0	0.0	0.0	0.0	0.0	0.0	0.0	0.0	0.0	0.0	0.0	0.0	0.0

TABLE 30

Primary electron E_0 = 100 MeV.
Secondary electrons E = 20 MeV.

Absorber: al, Z = 13, A = 27,
Radiation length = 26.3 g/sq.cm = 9.74 cm,
Critical energy = 52 MeV.

n \ t	0.5	1.0	1.5	2.0	2.5	3.0	3.5	4.0	4.5	5.0	5.5	6.0	6.5	7.0	7.5	8.0	8.5	9.0	9.5	10.0
0	0.225	0.743	0.974	0.986	0.983	0.988	0.994	0.995	0.996	0.994	0.999	1.000	0.996	0.999	1.000	1.000	0.999	1.000	0.999	1.000
1	0.768	0.249	0.025	0.014	0.017	0.011	0.006	0.005	0.004	0.006	0.001	0.000	0.004	0.001	0.000	0.000	0.000	0.000	0.001	0.000
⩾2	0.007	0.008	0.001	0.000	0.000	0.001	0.000	0.000	0.000	0.000	0.000	0.000	0.000	0.000	0.000	0.000	0.001	0.000	0.000	0.000
MEAN	0.78	0.27	0.03	0.01	0.02	0.01	0.01	0.01	0.00	0.01	0.00	0.00	0.00	0.00	0.00	0.00	0.00	0.00	0.00	0.00
VAR	0.2	0.2	0.0	0.0	0.0	0.0	0.0	0.0	0.0	0.0	0.0	0.0	0.0	0.0	0.0	0.0	0.0	0.0	0.0	0.0

TABLE 31

Primary electron E_0 = 500 MeV.
Secondary electrons E = 100 MeV.

Absorber: air, Z = 7.4, A = 15,
Radiation length = 43 g/sq.cm,
Critical energy = 98 MeV.

n \ t	0.5	1.0	1.5	2.0	2.5	3.0	3.5	4.0	4.5	5.0	5.5	6.0	6.5	7.0	7.5	8.0	8.5	9.0	9.5	10.0
0	0.137	0.404	0.701	0.887	0.956	0.987	0.989	0.983	0.985	0.987	0.994	0.993	0.992	0.997	0.997	1.000	0.999	1.000	1.000	1.000
1	0.835	0.580	0.293	0.098	0.041	0.032	0.029	0.017	0.014	0.012	0.006	0.007	0.007	0.003	0.003	0.000	0.001	0.000	0.000	0.000
⩾2	0.028	0.016	0.006	0.005	0.003	0.001	0.002	0.000	0.001	0.001	0.000	0.000	0.001	0.000	0.000	0.000	0.000	0.000	0.000	0.000
MEAN	0.89	0.61	0.31	0.11	0.05	0.03	0.03	0.02	0.02	0.01	0.01	0.01	0.01	0.00	0.00	0.00	0.00	0.00	0.00	0.00
VAR	0.2	0.3	0.2	0.1	0.1	0.0	0.0	0.0	0.0	0.0	0.0	0.0	0.0	0.0	0.0	0.0	0.0	0.0	0.0	0.0

TABLE 32

Primary electron E_0 = 500 MeV.
Secondary electrons E = 100 MeV.

Absorber: al, Z = 13, A = 27,
Radiation length = 26.3 g/sq.cm = 9.74 cm,
Critical energy = 52 MeV.

n \ t	0.5	1.0	1.5	2.0	2.5	3.0	3.5	4.0	4.5	5.0	5.5	6.0	6.5	7.0	7.5	8.0	8.5	9.0	9.5	10.0
0	0.147	0.355	0.573	0.759	0.893	0.935	0.954	0.967	0.976	0.990	0.989	0.990	0.991	0.996	0.993	0.996	0.996	0.998	0.999	0.998
1	0.823	0.609	0.413	0.237	0.095	0.060	0.044	0.030	0.022	0.009	0.011	0.010	0.009	0.003	0.007	0.004	0.004	0.002	0.001	0.002
⩾2	0.030	0.036	0.014	0.004	0.012	0.005	0.002	0.003	0.002	0.001	0.000	0.000	0.000	0.001	0.000	0.000	0.000	0.000	0.000	0.000
MEAN	0.88	0.68	0.44	0.25	0.12	0.07	0.05	0.04	0.03	0.01	0.01	0.01	0.01	0.01	0.01	0.00	0.00	0.00	0.00	0.00
VAR	0.2	0.3	0.3	0.2	0.1	0.1	0.0	0.0	0.0	0.0	0.0	0.0	0.0	0.0	0.0	0.0	0.0	0.0	0.0	0.0

TABLE 33

Primary electron E_0 = 1 000 MeV.
Secondary electrons E = 200 MeV.

Absorber: air, Z = 7.4, A = 15,
Radiation length = 43 g/sq.cm,
Critical energy = 98 MeV.

n \ t	0.5	1.0	1.5	2.0	2.5	3.0	3.5	4.0	4.5	5.0	5.5	6.0	6.5	7.0	7.5	8.0	8.5	9.0	9.5	10.0
0	0.130	0.342	0.590	0.778	0.891	0.936	0.962	0.957	0.971	0.978	0.988	0.990	0.995	0.996	1.000	0.998	1.000	1.000	0.998	0.999
1	0.836	0.626	0.386	0.213	0.106	0.061	0.037	0.043	0.029	0.019	0.011	0.010	0.005	0.004	0.000	0.002	0.000	0.000	0.002	0.001
⩾2	0.034	0.032	0.024	0.011	0.003	0.003	0.001	0.000	0.000	0.003	0.001	0.000	0.000	0.000	0.000	0.000	0.000	0.000	0.000	0.000
MEAN	0.91	0.69	0.43	0.24	0.11	0.07	0.04	0.04	0.03	0.03	0.01	0.01	0.01	0.00	0.00	0.00	0.00	0.00	0.00	0.00
VAR	0.2	0.3	0.3	0.2	0.1	0.1	0.0	0.0	0.0	0.0	0.0	0.0	0.0	0.0	0.0	0.0	0.0	0.0	0.0	0.0

TABLE 34

Primary electron E_0 = 1 000 MeV.
Secondary electrons E = 200 MeV.

Absorber: al, Z = 13, A = 27,
Radiation length = 26.3 g/sq.cm = 9.74 cm,
Critical energy = 52 MeV.

n \ t	0.5	1.0	1.5	2.0	2.5	3.0	3.5	4.0	4.5	5.0	5.5	6.0	6.5	7.0	7.5	8.0	8.5	9.0	9.5	10.0
0	0.132	0.309	0.506	0.690	0.812	0.890	0.929	0.957	0.970	0.976	0.983	0.983	0.992	0.991	0.988	0.990	0.997	0.997	0.997	0.998
1	0.825	0.638	0.455	0.296	0.184	0.107	0.064	0.038	0.026	0.022	0.017	0.016	0.007	0.009	0.012	0.010	0.003	0.003	0.003	0.002
⩾2	0.043	0.053	0.039	0.014	0.004	0.003	0.007	0.005	0.004	0.002	0.000	0.001	0.001	0.000	0.000	0.000	0.000	0.000	0.000	0.000
MEAN	0.91	0.74	0.53	0.32	0.19	0.11	0.08	0.05	0.03	0.03	0.02	0.02	0.01	0.01	0.01	0.01	0.00	0.00	0.00	0.00
VAR	0.2	0.3	0.3	0.3	0.2	0.1	0.1	0.1	0.0	0.0	0.0	0.0	0.0	0.0	0.0	0.0	0.0	0.0	0.0	0.0

TABLE 35

Primary electron E_0 = 5 000 MeV.
Secondary electrons E = 1 000 MeV.

Absorber: air, Z = 7.4, A = 15,
Radiation length = 43 g/sq.cm,
Critical energy = 98 MeV.

n \ t	0.5	1.0	1.5	2.0	2.5	3.0	3.5	4.0	4.5	5.0	5.5	6.0	6.5	7.0	7.5	8.0	8.5	9.0	9.5	10.0
0	0.148	0.292	0.461	0.628	0.758	0.820	0.889	0.924	0.940	0.959	0.973	0.987	0.980	0.989	0.994	0.995	0.996	0.998	1.000	0.998
1	0.814	0.651	0.492	0.344	0.221	0.167	0.102	0.072	0.058	0.038	0.026	0.011	0.020	0.011	0.006	0.004	0.004	0.002	0.000	0.002
⩾2	0.038	0.057	0.047	0.028	0.021	0.013	0.009	0.004	0.002	0.003	0.001	0.002	0.000	0.000	0.000	0.001	0.000	0.000	0.000	0.000
MEAN	0.89	0.77	0.59	0.40	0.26	0.19	0.12	0.08	0.06	0.04	0.03	0.02	0.02	0.01	0.01	0.01	0.00	0.00	0.00	0.00
VAR	0.2	0.3	0.3	0.3	0.2	0.2	0.1	0.1	0.1	0.0	0.0	0.0	0.0	0.0	0.0	0.0	0.0	0.0	0.0	0.0

TABLE 36

Primary electron E_0 = 5 000 MeV.
Secondary electrons E = 1 000 MeV.

Absorber: al, Z = 13, A = 27,
Radiation length = 26.3 g/sq. cm = 9.74 cm,
Critical energy = 52 MeV.

n \ t	0.5	1.0	1.5	2.0	2.5	3.0	3.5	4.0	4.5	5.0	5.5	6.0	6.5	7.0	7.5	8.0	8.5	9.0	9.5	10.0
0	0.117	0.274	0.445	0.604	0.730	0.809	0.878	0.923	0.939	0.955	0.973	0.986	0.987	0.991	0.991	0.996	0.996	0.996	0.997	0.997
1	0.828	0.660	0.503	0.363	0.248	0.182	0.114	0.073	0.060	0.045	0.026	0.014	0.013	0.008	0.008	0.005	0.005	0.004	0.003	0.003
⩾2	0.055	0.066	0.052	0.033	0.022	0.009	0.008	0.004	0.001	0.000	0.001	0.000	0.000	0.001	0.001	0.000	0.000	0.000	0.000	0.000
MEAN	0.94	0.79	0.61	0.43	0.29	0.20	0.13	0.08	0.06	0.05	0.03	0.01	0.01	0.01	0.01	0.01	0.01	0.00	0.00	0.00
VAR	0.2	0.3	0.4	0.3	0.3	0.2	0.1	0.1	0.1	0.0	0.0	0.0	0.0	0.0	0.0	0.0	0.0	0.0	0.0	0.0

TABLE 37

Primary electron E_0 = 10 000 MeV.
Secondary electrons E = 2 000 MeV.

Absorber: air, Z = 7.4, A = 15,
Radiation length = 43 g/sq. cm,
Critical energy = 98 MeV.

n \ t	0.5	1.0	1.5	2.0	2.5	3.0	3.5	4.0	4.5	5.0	5.5	6.0	6.5	7.0	7.5	8.0	8.5	9.0	9.5	10.0
0	0.122	0.281	0.439	0.607	0.710	0.801	0.867	0.926	0.939	0.955	0.976	0.981	0.986	0.992	0.992	0.992	0.997	0.999	0.999	0.999
1	0.814	0.654	0.502	0.362	0.273	0.191	0.124	0.068	0.058	0.045	0.024	0.018	0.014	0.008	0.008	0.006	0.002	0.001	0.001	0.001
⩾2	0.064	0.065	0.059	0.031	0.017	0.008	0.009	0.006	0.003	0.000	0.000	0.001	0.000	0.000	0.000	0.002	0.001	0.000	0.000	0.000
MEAN	0.95	0.79	0.62	0.42	0.31	0.21	0.14	0.08	0.06	0.05	0.02	0.02	0.01	0.01	0.01	0.01	0.00	0.00	0.00	0.00
VAR	0.2	0.3	0.4	0.3	0.2	0.2	0.1	0.1	0.1	0.0	0.0	0.0	0.0	0.0	0.0	0.0	0.0	0.0	0.0	0.0

TABLE 38

Primary electron E_0 = 10 000 MeV.
Secondary electrons E = 2 000 MeV.

Absorber: al, Z = 13, A = 27,
Radiation length = 26.3 g/sq. cm = 9.74 cm,
Critical energy = 52 MeV.

n \ t	0.5	1.0	1.5	2.0	2.5	3.0	3.5	4.0	4.5	5.0	5.5	6.0	6.5	7.0	7.5	8.0	8.5	9.0	9.5	10.0
0	0.119	0.262	0.418	0.589	0.696	0.798	0.860	0.887	0.940	0.963	0.976	0.985	0.991	0.990	0.989	0.998	0.998	0.998	0.997	0.998
1	0.834	0.653	0.515	0.374	0.282	0.192	0.130	0.110	0.059	0.045	0.023	0.015	0.009	0.010	0.010	0.004	0.004	0.002	0.003	0.002
⩾2	0.047	0.085	0.067	0.037	0.022	0.010	0.010	0.003	0.001	0.002	0.001	0.000	0.000	0.000	0.001	0.000	0.000	0.000	0.000	0.000
MEAN	0.93	0.83	0.65	0.45	0.33	0.21	0.15	0.12	0.06	0.05	0.03	0.02	0.01	0.01	0.01	0.00	0.00	0.00	0.00	0.00
VAR	0.2	0.3	0.4	0.3	0.3	0.2	0.1	0.1	0.1	0.1	0.0	0.0	0.0	0.0	0.0	0.0	0.0	0.0	0.0	0.0

TABLE 39

Primary electron E_0 = 50 000 MeV.
Secondary electrons E = 10 000 MeV.

Absorber: air, Z = 7.4, A = 15,
Radiation length = 43 g/sq. cm,
Critical energy = 98 MeV.

n \ t	0.5	1.0	1.5	2.0	2.5	3.0	3.5	4.0	4.5	5.0	5.5	6.0	6.5	7.0	7.5	8.0	8.5	9.0	9.5	10.0
0	0.132	0.273	0.437	0.587	0.688	0.787	0.864	0.910	0.926	0.947	0.968	0.977	0.978	0.986	0.989	0.993	0.995	0.994	0.994	0.997
1	0.818	0.646	0.498	0.372	0.288	0.203	0.128	0.085	0.073	0.050	0.031	0.020	0.020	0.012	0.010	0.005	0.003	0.004	0.005	0.003
⩾2	0.050	0.081	0.065	0.041	0.024	0.010	0.008	0.005	0.001	0.003	0.001	0.003	0.002	0.002	0.001	0.002	0.002	0.002	0.001	0.000
MEAN	0.92	0.81	0.63	0.46	0.34	0.22	0.14	0.10	0.08	0.06	0.03	0.03	0.02	0.02	0.01	0.01	0.01	0.01	0.01	0.00
VAR	0.2	0.3	0.4	0.3	0.3	0.2	0.1	0.1	0.1	0.1	0.0	0.0	0.0	0.0	0.0	0.0	0.0	0.0	0.0	0.0

TABLE 40

Primary electron E_0 = 50 000 MeV.
Secondary electrons E = 10 000 MeV.

Absorber: al, Z = 13, A = 27,
Radiation length = 26.3 g/sq. cm = 9.74 cm,
Critical energy = 52 MeV.

n \ t	0.5	1.0	1.5	2.0	2.5	3.0	3.5	4.0	4.5	5.0	5.5	6.0	6.5	7.0	7.5	8.0	8.5	9.0	9.5	10.0
0	0.135	0.283	0.429	0.584	0.692	0.794	0.882	0.913	0.926	0.948	0.969	0.978	0.982	0.985	0.986	0.993	0.994	0.993	0.995	0.995
1	0.806	0.642	0.500	0.373	0.277	0.192	0.107	0.083	0.069	0.049	0.029	0.021	0.018	0.015	0.013	0.007	0.006	0.007	0.005	0.005
⩾2	0.059	0.075	0.071	0.043	0.031	0.014	0.011	0.004	0.005	0.003	0.002	0.001	0.000	0.000	0.001	0.000	0.000	0.000	0.000	0.000
MEAN	0.93	0.79	0.64	0.46	0.34	0.22	0.13	0.09	0.08	0.06	0.03	0.02	0.02	0.02	0.02	0.01	0.01	0.01	0.01	0.01
VAR	0.2	0.3	0.4	0.3	0.3	0.2	0.1	0.1	0.1	0.1	0.0	0.0	0.0	0.0	0.0	0.0	0.0	0.0	0.0	0.0

TABLE 41

Primary electron E_0 = 50 MeV.
Secondary electrons E = 5 MeV.

Absorber: air, Z = 7.4, A = 15,
Radiation length = 43 g/sq. cm,
Critical energy = 98 MeV.

n \ t	0.5	1.0	1.5	2.0	2.5	3.0	3.5	4.0	4.5	5.0	5.5	6.0	6.5	7.0	7.5	8.0	8.5	9.0	9.5	10.0
0	0.980	0.995	0.998	0.996	0.997	0.995	0.998	1.000	0.997	1.000	1.000	1.000	1.000	0.999	1.000	1.000	1.000	1.000	1.000	1.000
1	0.018	0.004	0.006	0.004	0.003	0.005	0.002	0.000	0.003	0.000	0.000	0.000	0.000	0.001	0.000	0.000	0.000	0.000	0.000	0.000
2	0.002	0.001	0.001	0.000	0.000	0.000	0.000	0.000	0.000	0.000	0.000	0.000	0.000	0.000	0.000	0.000	0.000	0.000	0.000	0.000
≥3	0.000	0.000	0.000	0.000	0.000	0.000	0.000	0.000	0.000	0.000	0.000	0.000	0.000	0.000	0.000	0.000	0.000	0.000	0.000	0.000
MEAN	0.02	0.01	0.01	0.00	0.00	0.01	0.00	0.00	0.00	0.00	0.00	0.00	0.00	0.00	0.00	0.00	0.00	0.00	0.00	0.00
VAR	0.0	0.0	0.0	0.0	0.0	0.0	0.0	0.0	0.0	0.0	0.0	0.0	0.0	0.0	0.0	0.0	0.0	0.0	0.0	0.0

TABLE 42

Primary electron E_0 = 50 MeV.
Secondary electrons E = 5 MeV.

Absorber: al, Z = 13, A = 27,
Radiation length = 26.3 g/sq. cm = 9.74 cm,
Critical energy = 52 MeV.

n \ t	0.5	1.0	1.5	2.0	2.5	3.0	3.5	4.0	4.5	5.0	5.5	6.0	6.5	7.0	7.5	8.0	8.5	9.0	9.5	10.0
0	0.221	0.983	0.984	0.989	0.991	0.987	0.989	0.998	0.992	0.998	0.997	0.996	0.998	0.997	1.000	1.000	1.000	1.000	1.000	1.000
1	0.768	0.014	0.014	0.010	0.009	0.011	0.010	0.002	0.007	0.001	0.003	0.004	0.002	0.003	0.000	0.000	0.000	0.000	0.000	0.000
2	0.010	0.003	0.002	0.001	0.000	0.002	0.001	0.000	0.001	0.001	0.000	0.000	0.000	0.000	0.000	0.000	0.000	0.000	0.000	0.000
≥3	0.001	0.000	0.000	0.000	0.000	0.000	0.000	0.000	0.000	0.000	0.000	0.000	0.000	0.000	0.000	0.000	0.000	0.000	0.000	0.000
MEAN	0.79	0.02	0.02	0.01	0.01	0.02	0.01	0.00	0.01	0.00	0.00	0.00	0.00	0.00	0.00	0.00	0.00	0.00	0.00	0.00
VAR	0.2	0.0	0.0	0.0	0.0	0.0	0.0	0.0	0.0	0.0	0.0	0.0	0.0	0.0	0.0	0.0	0.0	0.0	0.0	0.0

TABLE 43

Primary electron E_0 = 100 MeV.
Secondary electrons E = 10 MeV.

Absorber: air, Z = 7.4, A = 15,
Radiation length = 43 g/sq. cm,
Critical energy = 98 MeV.

n \ t	0.5	1.0	1.5	2.0	2.5	3.0	3.5	4.0	4.5	5.0	5.5	6.0	6.5	7.0	7.5	8.0	8.5	9.0	9.5	10.0
0	0.250	0.966	0.982	0.982	0.982	0.991	0.993	0.996	0.993	0.995	0.999	1.000	0.998	1.000	1.000	1.000	1.000	0.997	1.000	1.000
1	0.736	0.031	0.018	0.014	0.014	0.005	0.006	0.003	0.007	0.005	0.001	0.000	0.002	0.000	0.000	0.000	0.000	0.003	0.000	0.000
2	0.014	0.003	0.000	0.004	0.004	0.004	0.001	0.001	0.000	0.000	0.000	0.000	0.000	0.000	0.000	0.000	0.000	0.000	0.000	0.000
≥3	0.000	0.000	0.000	0.000	0.000	0.000	0.000	0.000	0.000	0.000	0.000	0.000	0.000	0.000	0.000	0.000	0.000	0.000	0.000	0.000
MEAN	0.76	0.04	0.02	0.02	0.02	0.01	0.01	0.01	0.01	0.01	0.00	0.00	0.00	0.00	0.00	0.00	0.00	0.00	0.00	0.00
VAR	0.2	0.0	0.0	0.0	0.0	0.0	0.0	0.0	0.0	0.0	0.0	0.0	0.0	0.0	0.0	0.0	0.0	0.0	0.0	0.0

TABLE 44

Primary electron E_0 = 100 MeV.
Secondary electrons E = 10 MeV.

Absorber: al, Z = 13, A = 27,
Radiation length = 26.3 g/sq. cm = 9.74 cm,
Critical energy = 52 MeV.

n \ t	0.5	1.0	1.5	2.0	2.5	3.0	3.5	4.0	4.5	5.0	5.5	6.0	6.5	7.0	7.5	8.0	8.5	9.0	9.5	10.0
0	0.138	0.545	0.933	0.969	0.967	0.966	0.978	0.982	0.983	0.989	0.994	0.995	0.991	0.996	0.996	0.999	0.997	0.999	0.995	0.999
1	0.826	0.436	0.056	0.028	0.027	0.027	0.020	0.015	0.016	0.011	0.006	0.005	0.008	0.002	0.004	0.001	0.002	0.001	0.005	0.001
2	0.031	0.019	0.011	0.003	0.006	0.007	0.002	0.003	0.001	0.000	0.000	0.000	0.001	0.002	0.000	0.000	0.001	0.000	0.000	0.000
≥3	0.005	0.000	0.000	0.000	0.000	0.000	0.000	0.000	0.000	0.000	0.000	0.000	0.000	0.000	0.000	0.000	0.000	0.000	0.000	0.000
MEAN	0.90	0.47	0.08	0.03	0.04	0.04	0.02	0.02	0.02	0.01	0.01	0.01	0.01	0.01	0.00	0.00	0.00	0.00	0.01	0.00
VAR	0.2	0.3	0.1	0.0	0.1	0.1	0.0	0.0	0.0	0.0	0.0	0.0	0.0	0.0	0.0	0.0	0.0	0.0	0.0	0.0

TABLE 45

Primary electron E_0 = 200 MeV.
Secondary electrons E = 20 MeV.

Absorber: air, Z = 7.4, A = 15,
Radiation length = 43 g/sq. cm,
Critical energy = 98 MeV.

n \ t	0.5	1.0	1.5	2.0	2.5	3.0	3.5	4.0	4.5	5.0	5.5	6.0	6.5	7.0	7.5	8.0	8.5	9.0	9.5	10.0
0	0.147	0.530	0.896	0.963	0.960	0.974	0.979	0.978	0.982	0.988	0.987	0.998	0.998	0.998	1.000	0.996	1.000	1.000	1.000	0.999
1	0.817	0.457	0.096	0.042	0.036	0.024	0.016	0.020	0.015	0.010	0.011	0.002	0.001	0.002	0.000	0.004	0.000	0.000	0.000	0.001
2	0.034	0.013	0.009	0.005	0.004	0.002	0.005	0.002	0.003	0.002	0.002	0.000	0.001	0.000	0.000	0.000	0.000	0.000	0.000	0.000
⩾3	0.002	0.000	0.001	0.000	0.000	0.000	0.000	0.000	0.000	0.000	0.000	0.000	0.000	0.000	0.000	0.000	0.000	0.000	0.000	0.000
MEAN	0.89	0.48	0.12	0.05	0.04	0.03	0.03	0.02	0.02	0.01	0.02	0.00	0.00	0.00	0.00	0.00	0.00	0.00	0.00	0.00
VAR	0.2	0.3	0.1	0.1	0.1	0.0	0.0	0.0	0.0	0.0	0.0	0.0	0.0	0.0	0.0	0.0	0.0	0.0	0.0	0.0

TABLE 46

Primary electron E_0 = 200 MeV.
Secondary electrons E = 20 MeV.

Absorber: al, Z = 13, A = 27,
Radiation length = 26.3 g/sq. cm = 9.74 cm,
Critical energy = 52 MeV.

n \ t	0.5	1.0	1.5	2.0	2.5	3.0	3.5	4.0	4.5	5.0	5.5	6.0	6.5	7.0	7.5	8.0	8.5	9.0	9.5	10.0
0	0.089	0.312	0.585	0.823	0.905	0.940	0.952	0.950	0.977	0.987	0.982	0.993	0.993	0.994	0.992	0.996	0.999	0.999	0.999	0.998
1	0.857	0.633	0.380	0.163	0.083	0.049	0.043	0.040	0.021	0.012	0.016	0.006	0.006	0.006	0.005	0.004	0.001	0.001	0.001	0.001
2	0.038	0.052	0.034	0.014	0.012	0.011	0.005	0.010	0.002	0.001	0.002	0.001	0.001	0.000	0.003	0.000	0.000	0.000	0.000	0.001
⩾3	0.016	0.003	0.001	0.000	0.000	0.000	0.000	0.000	0.000	0.000	0.000	0.000	0.000	0.000	0.000	0.000	0.000	0.000	0.000	0.000
MEAN	0.98	0.75	0.45	0.19	0.11	0.07	0.05	0.06	0.03	0.01	0.02	0.01	0.01	0.01	0.01	0.00	0.00	0.00	0.00	0.00
VAR	0.2	0.3	0.3	0.2	0.1	0.1	0.1	0.1	0.0	0.0	0.0	0.0	0.0	0.0	0.0	0.0	0.0	0.0	0.0	0.0

TABLE 47

Primary electron E_0 = 500 MeV.
Secondary electrons E = 50 MeV.

Absorber: air, Z = 7.4, A = 15,
Radiation length = 43 g/sq. cm,
Critical energy = 98 MeV.

n \ t	0.5	1.0	1.5	2.0	2.5	3.0	3.5	4.0	4.5	5.0	5.5	6.0	6.5	7.0	7.5	8.0	8.5	9.0	9.5	10.0
0	0.086	0.245	0.526	0.739	0.886	0.898	0.946	0.954	0.962	0.975	0.971	0.980	0.992	0.993	0.996	0.998	0.998	0.998	0.998	0.998
1	0.844	0.658	0.424	0.232	0.103	0.090	0.047	0.041	0.035	0.025	0.025	0.020	0.008	0.006	0.003	0.002	0.002	0.001	0.001	0.002
2	0.052	0.088	0.046	0.029	0.011	0.012	0.007	0.005	0.003	0.000	0.004	0.000	0.000	0.001	0.001	0.000	0.000	0.001	0.001	0.000
⩾3	0.018	0.009	0.004	0.000	0.000	0.000	0.000	0.000	0.000	0.000	0.000	0.000	0.000	0.000	0.000	0.000	0.000	0.000	0.000	0.000
MEAN	1.00	0.86	0.53	0.29	0.13	0.11	0.06	0.05	0.04	0.03	0.03	0.02	0.01	0.01	0.01	0.00	0.00	0.00	0.00	0.00
VAR	0.2	0.4	0.4	0.3	0.1	0.1	0.1	0.1	0.0	0.0	0.0	0.0	0.0	0.0	0.0	0.0	0.0	0.0	0.0	0.0

TABLE 48

Primary electron E_0 = 500 MeV.
Secondary electrons E = 50 MeV.

Absorber: al, Z = 13, A = 27,
Radiation length = 26.3 g/sq. cm = 9.74 cm,
Critical energy = 52 MeV.

n \ t	0.5	1.0	1.5	2.0	2.5	3.0	3.5	4.0	4.5	5.0	5.5	6.0	6.5	7.0	7.5	8.0	8.5	9.0	9.5	10.0
0	0.080	0.220	0.364	0.546	0.716	0.842	0.880	0.905	0.933	0.950	0.971	0.977	0.971	0.983	0.989	0.992	0.991	0.993	0.999	0.996
1	0.833	0.652	0.537	0.380	0.251	0.140	0.110	0.082	0.055	0.045	0.026	0.021	0.029	0.017	0.011	0.008	0.008	0.007	0.001	0.003
2	0.065	0.103	0.089	0.070	0.032	0.018	0.010	0.013	0.012	0.005	0.003	0.002	0.000	0.000	0.000	0.000	0.001	0.000	0.000	0.001
⩾3	0.022	0.020	0.010	0.004	0.001	0.000	0.000	0.000	0.000	0.000	0.000	0.000	0.000	0.000	0.000	0.000	0.000	0.000	0.000	0.000
MEAN	1.03	0.93	0.75	0.53	0.32	0.18	0.13	0.11	0.08	0.06	0.03	0.03	0.03	0.02	0.01	0.01	0.01	0.01	0.00	0.01
VAR	0.2	0.4	0.4	0.4	0.3	0.2	0.1	0.1	0.1	0.1	0.0	0.0	0.0	0.0	0.0	0.0	0.0	0.0	0.0	0.0

TABLE 49

Primary electron E_0 = 1 000 MeV.
Secondary electrons E = 100 MeV.

Absorber: air, Z = 7.4, A = 15,
Radiation length = 43 g/sq. cm,
Critical energy = 98 MeV.

n \ t	0.5	1.0	1.5	2.0	2.5	3.0	3.5	4.0	4.5	5.0	5.5	6.0	6.5	7.0	7.5	8.0	8.5	9.0	9.5	10.0
0	0.082	0.217	0.380	0.556	0.702	0.804	0.846	0.905	0.929	0.946	0.959	0.975	0.966	0.981	0.984	0.990	0.994	0.996	0.997	0.997
1	0.833	0.643	0.509	0.381	0.259	0.172	0.127	0.077	0.060	0.042	0.039	0.024	0.031	0.017	0.015	0.010	0.006	0.004	0.002	0.002
2	0.064	0.125	0.104	0.060	0.038	0.021	0.027	0.018	0.010	0.012	0.002	0.001	0.003	0.002	0.001	0.000	0.000	0.000	0.001	0.001
⩾3	0.021	0.015	0.007	0.003	0.001	0.003	0.000	0.000	0.001	0.000	0.000	0.000	0.000	0.000	0.000	0.000	0.000	0.000	0.000	0.000
MEAN	1.03	0.94	0.74	0.51	0.34	0.22	0.18	0.11	0.08	0.07	0.04	0.03	0.04	0.02	0.02	0.01	0.01	0.00	0.00	0.00
VAR	0.2	0.4	0.4	0.4	0.3	0.2	0.2	0.1	0.1	0.1	0.0	0.0	0.0	0.0	0.0	0.0	0.0	0.0	0.0	0.0

TABLE 50

Primary electron E_0 = 1 000 MeV.
Secondary electrons E = 100 MeV

Absorber: al, Z = 13, A = 27,
Radiation length = 26.3 g/sq. cm = 9.74 cm,
Critical energy = 52 MeV.

n \ t	0.5	1.0	1.5	2.0	2.5	3.0	3.5	4.0	4.5	5.0	5.5	6.0	6.5	7.0	7.5	8.0	8.5	9.0	9.5	10.0
0	0.069	0.146	0.284	0.411	0.580	0.675	0.789	0.837	0.872	0.912	0.931	0.955	0.973	0.969	0.976	0.982	0.993	0.996	0.996	0.999
1	0.836	0.676	0.541	0.470	0.353	0.269	0.179	0.144	0.112	0.073	0.063	0.038	0.024	0.028	0.022	0.017	0.007	0.003	0.004	0.001
2	0.071	0.143	0.143	0.102	0.060	0.050	0.031	0.019	0.015	0.014	0.006	0.007	0.003	0.003	0.002	0.001	0.000	0.001	0.000	0.000
⩾3	0.024	0.035	0.032	0.017	0.007	0.006	0.001	0.000	0.001	0.001	0.000	0.000	0.000	0.000	0.000	0.000	0.000	0.000	0.000	0.000
MEAN	1.05	1.07	0.93	0.73	0.50	0.39	0.24	0.18	0.15	0.10	0.08	0.05	0.03	0.03	0.03	0.02	0.01	0.01	0.00	0.00
VAR	0.2	0.4	0.6	0.5	0.4	0.4	0.3	0.2	0.2	0.1	0.1	0.1	0.0	0.0	0.0	0.0	0.0	0.0	0.0	0.0

TABLE 51

Primary electron E_0 = 2 000 MeV.
Secondary electrons E = 200 MeV.

Absorber: air, Z = 7.4, A = 15,
Radiation length = 43 g/sq. cm,
Critical energy = 98 MeV.

n \ t	0.5	1.0	1.5	2.0	2.5	3.0	3.5	4.0	4.5	5.0	5.5	6.0	6.5	7.0	7.5	8.0	8.5	9.0	9.5	10.0
0	0.072	0.189	0.300	0.423	0.560	0.685	0.760	0.830	0.880	0.924	0.934	0.964	0.966	0.972	0.978	0.980	0.988	0.994	0.995	0.995
1	0.819	0.629	0.515	0.436	0.358	0.265	0.216	0.149	0.111	0.066	0.058	0.035	0.032	0.025	0.020	0.019	0.008	0.006	0.005	0.005
2	0.081	0.138	0.160	0.127	0.078	0.047	0.022	0.021	0.009	0.010	0.008	0.001	0.002	0.003	0.002	0.001	0.004	0.000	0.000	0.000
⩾3	0.028	0.044	0.025	0.014	0.004	0.003	0.002	0.000	0.000	0.000	0.000	0.000	0.000	0.000	0.000	0.000	0.000	0.000	0.000	0.000
MEAN	1.07	1.04	0.91	0.73	0.53	0.37	0.27	0.19	0.13	0.09	0.07	0.04	0.04	0.03	0.02	0.02	0.02	0.01	0.01	0.01
VAR	0.3	0.5	0.6	0.5	0.4	0.3	0.3	0.2	0.1	0.1	0.1	0.0	0.0	0.0	0.0	0.0	0.0	0.0	0.0	0.0

TABLE 52

Primary electron E_0 = 2 000 MeV.
Secondary electrons E = 200 MeV.

Absorber: al, Z = 13, A = 27,
Radiation length = 26.3 g/sq. cm = 9.74 cm,
Critical energy = 52 MeV.

n \ t	0.5	1.0	1.5	2.0	2.5	3.0	3.5	4.0	4.5	5.0	5.5	6.0	6.5	7.0	7.5	8.0	8.5	9.0	9.5	10.0
0	0.079	0.173	0.262	0.387	0.493	0.594	0.708	0.786	0.842	0.860	0.894	0.927	0.954	0.961	0.975	0.981	0.978	0.987	0.985	0.990
1	0.814	0.631	0.538	0.436	0.383	0.336	0.236	0.171	0.135	0.117	0.096	0.062	0.039	0.033	0.020	0.017	0.020	0.012	0.012	0.008
2	0.078	0.151	0.164	0.144	0.113	0.062	0.052	0.030	0.022	0.022	0.010	0.010	0.007	0.006	0.004	0.002	0.002	0.001	0.003	0.002
⩾3	0.029	0.045	0.036	0.033	0.011	0.008	0.004	0.004	0.001	0.001	0.000	0.001	0.000	0.000	0.001	0.000	0.000	0.000	0.000	0.000
MEAN	1.06	1.07	0.98	0.82	0.64	0.48	0.35	0.24	0.18	0.16	0.12	0.09	0.05	0.05	0.03	0.02	0.02	0.01	0.02	0.01
VAR	0.3	0.5	0.6	0.6	0.5	0.4	0.4	0.3	0.2	0.2	0.1	0.1	0.1	0.1	0.0	0.0	0.0	0.0	0.0	0.0

TABLE 53

Primary electron E_0 = 5 000 MeV.
Secondary electrons E = 500 MeV.

Absorber: air, Z = 7.4, A = 15,
Radiation length = 43 g/sq. cm,
Critical energy = 98 MeV.

n \ t	0.5	1.0	1.5	2.0	2.5	3.0	3.5	4.0	4.5	5.0	5.5	6.0	6.5	7.0	7.5	8.0	8.5	9.0	9.5	10.0
0	0.080	0.151	0.246	0.342	0.461	0.577	0.668	0.750	0.831	0.880	0.886	0.923	0.946	0.961	0.977	0.981	0.993	0.990	0.994	0.996
1	0.807	0.645	0.528	0.458	0.405	0.340	0.275	0.213	0.145	0.121	0.101	0.065	0.047	0.037	0.021	0.018	0.007	0.009	0.006	0.004
2	0.081	0.161	0.191	0.171	0.119	0.078	0.054	0.034	0.023	0.016	0.013	0.012	0.007	0.002	0.002	0.001	0.000	0.001	0.000	0.000
⩾3	0.032	0.043	0.035	0.029	0.015	0.005	0.003	0.003	0.001	0.003	0.000	0.000	0.000	0.000	0.000	0.000	0.000	0.000	0.000	0.000
MEAN	1.07	1.10	1.02	0.89	0.69	0.51	0.39	0.29	0.19	0.16	0.13	0.09	0.06	0.04	0.03	0.02	0.01	0.01	0.01	0.00
VAR	0.3	0.5	0.6	0.6	0.5	0.4	0.4	0.3	0.2	0.2	0.1	0.1	0.1	0.0	0.0	0.0	0.0	0.0	0.0	0.0

TABLE 54

Primary electron E_0 = 5 000 MeV.
Secondary electrons E = 500 MeV.

Absorber: al, Z = 13, A = 27,
Radiation length = 26.3 g/sq. cm = 9.74 cm,
Critical energy = 52 MeV.

n \ t	0.5	1.0	1.5	2.0	2.5	3.0	3.5	4.0	4.5	5.0	5.5	6.0	6.5	7.0	7.5	8.0	8.5	9.0	9.5	10.0
0	0.060	0.144	0.202	0.283	0.385	0.501	0.628	0.717	0.792	0.840	0.881	0.901	0.940	0.948	0.962	0.970	0.977	0.980	0.986	0.994
1	0.833	0.631	0.534	0.475	0.428	0.392	0.305	0.252	0.181	0.140	0.101	0.088	0.055	0.047	0.033	0.029	0.022	0.019	0.014	0.005
2	0.076	0.173	0.222	0.198	0.160	0.086	0.060	0.028	0.024	0.018	0.017	0.011	0.005	0.005	0.005	0.001	0.001	0.001	0.000	0.001
⩾3	0.031	0.052	0.042	0.044	0.027	0.021	0.007	0.003	0.003	0.002	0.001	0.000	0.000	0.000	0.000	0.000	0.000	0.000	0.000	0.000
MEAN	1.08	1.14	1.11	1.01	0.83	0.63	0.45	0.32	0.24	0.18	0.14	0.11	0.07	0.06	0.04	0.03	0.02	0.02	0.01	0.01
VAR	0.3	0.5	0.6	0.7	0.6	0.5	0.4	0.3	0.3	0.2	0.2	0.1	0.1	0.1	0.1	0.0	0.0	0.0	0.0	0.0

TABLE 55

Primary electron E_0 = 10 000 MeV.
Secondary electrons E = 1 000 MeV.

Absorber: air, Z = 7.4, A = 15,
Radiation length = 43 g/sq. cm,
Critical energy = 98 MeV.

n \ t	0.5	1.0	1.5	2.0	2.5	3.0	3.5	4.0	4.5	5.0	5.5	6.0	6.5	7.0	7.5	8.0	8.5	9.0	9.5	10.0
0	0.070	0.159	0.264	0.315	0.414	0.497	0.605	0.716	0.778	0.840	0.880	0.890	0.926	0.953	0.963	0.977	0.983	0.987	0.990	0.997
1	0.817	0.627	0.478	0.441	0.389	0.372	0.309	0.237	0.189	0.138	0.106	0.094	0.063	0.042	0.033	0.023	0.016	0.012	0.010	0.003
2	0.073	0.169	0.206	0.209	0.176	0.112	0.078	0.044	0.031	0.020	0.013	0.015	0.011	0.005	0.003	0.000	0.001	0.001	0.000	0.000
⩾3	0.040	0.045	0.052	0.035	0.021	0.019	0.008	0.003	0.002	0.002	0.001	0.001	0.000	0.000	0.001	0.000	0.000	0.000	0.000	0.000
MEAN	1.08	1.10	1.05	0.97	0.80	0.65	0.49	0.33	0.28	0.18	0.14	0.13	0.09	0.05	0.04	0.02	0.02	0.01	0.01	0.00
VAR	0.3	0.5	0.7	0.7	0.6	0.6	0.5	0.3	0.3	0.2	0.1	0.1	0.1	0.1	0.1	0.0	0.0	0.0	0.0	0.0

TABLE 56

Primary electron E_0 = 10 000 MeV.
Secondary electrons E = 1 000 MeV.

Absorber: al, Z = 13, A = 27,
Radiation length = 26.3 g/sq. cm = 9.74 cm,
Critical energy = 52 MeV.

n \ t	0.5	1.0	1.5	2.0	2.5	3.0	3.5	4.0	4.5	5.0	5.5	6.0	6.5	7.0	7.5	8.0	8.5	9.0	9.5	10.0
0	0.075	0.151	0.241	0.311	0.398	0.485	0.572	0.665	0.755	0.833	0.884	0.900	0.922	0.938	0.960	0.972	0.982	0.983	0.992	0.994
1	0.818	0.603	0.489	0.467	0.415	0.387	0.333	0.274	0.201	0.141	0.100	0.094	0.070	0.055	0.038	0.026	0.016	0.016	0.008	0.006
2	0.082	0.193	0.213	0.187	0.166	0.115	0.090	0.057	0.043	0.023	0.016	0.006	0.008	0.007	0.002	0.002	0.002	0.001	0.000	0.000
⩾3	0.025	0.053	0.057	0.035	0.021	0.013	0.005	0.004	0.001	0.003	0.000	0.000	0.000	0.000	0.000	0.000	0.000	0.000	0.000	0.000
MEAN	1.06	1.15	1.09	0.95	0.81	0.66	0.53	0.40	0.29	0.20	0.13	0.11	0.09	0.07	0.04	0.03	0.02	0.02	0.01	0.01
VAR	0.3	0.5	0.7	0.6	0.6	0.5	0.5	0.4	0.3	0.2	0.1	0.1	0.1	0.1	0.0	0.0	0.0	0.0	0.0	0.0

TABLE 57

Primary electron E_0 = 20 000 MeV.
Secondary electrons E = 2 000 MeV.

Absorber: air, Z = 7.4, A = 15,
Radiation length = 43 g/sq. cm,
Critical energy = 98 MeV.

n \ t	0.5	1.0	1.5	2.0	2.5	3.0	3.5	4.0	4.5	5.0	5.5	6.0	6.5	7.0	7.5	8.0	8.5	9.0	9.5	10.0
0	0.073	0.151	0.225	0.296	0.391	0.475	0.590	0.675	0.743	0.805	0.847	0.901	0.922	0.942	0.964	0.976	0.979	0.986	0.987	0.990
1	0.818	0.612	0.509	0.466	0.414	0.379	0.329	0.273	0.210	0.170	0.136	0.088	0.069	0.047	0.030	0.023	0.019	0.012	0.013	0.010
2	0.075	0.188	0.210	0.204	0.160	0.124	0.072	0.046	0.045	0.024	0.016	0.009	0.009	0.011	0.006	0.001	0.002	0.002	0.000	0.000
⩾3	0.034	0.049	0.056	0.034	0.035	0.022	0.009	0.006	0.002	0.001	0.001	0.002	0.000	0.000	0.000	0.000	0.000	0.000	0.000	0.000
MEAN	1.07	1.14	1.10	0.98	0.85	0.69	0.50	0.38	0.31	0.22	0.17	0.11	0.09	0.07	0.04	0.03	0.02	0.02	0.01	0.01
VAR	0.3	0.5	0.7	0.7	0.7	0.6	0.4	0.4	0.3	0.2	0.2	0.1	0.1	0.1	0.1	0.0	0.0	0.0	0.0	0.0

TABLE 58

Primary electron E_0 = 20 000 MeV.
Secondary electrons E = 2 000 MeV.

Absorber: al, Z = 13, A = 27,
Radiation length = 26.3 g/sq. cm = 9.74 cm,
Critical energy = 52 MeV.

n \ t	0.5	1.0	1.5	2.0	2.5	3.0	3.5	4.0	4.5	5.0	5.5	6.0	6.5	7.0	7.5	8.0	8.5	9.0	9.5	10.0
0	0.071	0.140	0.207	0.296	0.401	0.504	0.574	0.676	0.753	0.811	0.859	0.887	0.914	0.939	0.969	0.973	0.980	0.984	0.987	0.991
1	0.825	0.617	0.499	0.478	0.406	0.358	0.329	0.263	0.203	0.153	0.117	0.098	0.078	0.057	0.041	0.026	0.018	0.014	0.012	0.008
2	0.071	0.171	0.233	0.181	0.168	0.123	0.084	0.058	0.043	0.035	0.024	0.015	0.008	0.004	0.000	0.001	0.002	0.002	0.001	0.001
⩾3	0.033	0.072	0.061	0.045	0.025	0.015	0.013	0.003	0.001	0.001	0.000	0.000	0.000	0.000	0.000	0.000	0.000	0.000	0.000	0.000
MEAN	1.07	1.18	1.15	0.98	0.82	0.65	0.54	0.39	0.29	0.23	0.17	0.13	0.09	0.07	0.04	0.03	0.02	0.02	0.01	0.01
VAR	0.3	0.6	0.7	0.7	0.6	0.6	0.5	0.4	0.3	0.3	0.2	0.1	0.1	0.1	0.0	0.0	0.0	0.0	0.0	0.0

TABLE 59

Primary electron E_0 = 50 000 MeV.
Secondary electrons E = 5 000 MeV.

Absorber: air, Z = 7.4, A = 15,
Radiation length = 43 g/sq. cm,
Critical energy = 98 MeV.

n \ t	0.5	1.0	1.5	2.0	2.5	3.0	3.5	4.0	4.5	5.0	5.5	6.0	6.5	7.0	7.5	8.0	8.5	9.0	9.5	10.0
0	0.076	0.159	0.230	0.298	0.389	0.497	0.584	0.674	0.754	0.824	0.852	0.890	0.921	0.937	0.958	0.966	0.969	0.974	0.984	0.989
1	0.820	0.608	0.492	0.479	0.428	0.372	0.333	0.259	0.202	0.151	0.133	0.100	0.066	0.058	0.038	0.033	0.027	0.025	0.015	0.010
2	0.082	0.185	0.230	0.183	0.157	0.111	0.077	0.063	0.042	0.024	0.015	0.009	0.012	0.005	0.004	0.001	0.004	0.001	0.001	0.001
⩾3	0.022	0.048	0.048	0.040	0.026	0.020	0.006	0.004	0.002	0.001	0.000	0.001	0.001	0.000	0.000	0.000	0.000	0.000	0.000	0.000
MEAN	1.06	1.13	1.11	0.97	0.82	0.65	0.51	0.40	0.29	0.20	0.16	0.12	0.09	0.07	0.05	0.04	0.04	0.03	0.02	0.01
VAR	0.2	0.5	0.7	0.7	0.6	0.6	0.4	0.4	0.3	0.2	0.2	0.1	0.1	0.1	0.1	0.0	0.0	0.0	0.0	0.0

Table 60

Primary electron E_0 = 50 000 MeV.
Secondary electrons E = 5 000 MeV.

Absorber: al, Z = 13, A = 27,
Radiation length = 26.3 g/sq. cm = 9.74 cm,
Critical energy = 52 MeV.

n \ t	0.5	1.0	1.5	2.0	2.5	3.0	3.5	4.0	4.5	5.0	5.5	6.0	6.5	7.0	7.5	8.0	8.5	9.0	9.5	10.0
0	0.067	0.156	0.233	0.278	0.346	0.441	0.564	0.656	0.724	0.804	0.868	0.893	0.923	0.939	0.959	0.976	0.980	0.982	0.989	0.992
1	0.822	0.596	0.488	0.470	0.453	0.410	0.341	0.274	0.238	0.174	0.119	0.092	0.068	0.053	0.034	0.021	0.018	0.016	0.010	0.008
2	0.081	0.182	0.216	0.203	0.178	0.139	0.085	0.065	0.035	0.021	0.013	0.015	0.008	0.008	0.006	0.003	0.002	0.002	0.001	0.000
⩾3	0.030	0.066	0.063	0.049	0.025	0.010	0.010	0.005	0.003	0.001	0.000	0.000	0.001	0.000	0.001	0.000	0.000	0.000	0.000	0.000
MEAN	1.08	1.17	1.12	1.03	0.88	0.72	0.64	0.42	0.32	0.22	0.15	0.12	0.09	0.07	0.05	0.03	0.02	0.02	0.01	0.01
VAR	0.3	0.6	0.7	0.7	0.6	0.5	0.5	0.4	0.3	0.2	0.2	0.1	0.1	0.1	0.1	0.0	0.0	0.0	0.0	0.0

TABLE 61

Primary electron E_0 = 100 MeV.
Secondary electrons E = 5 MeV.

Absorber: air, Z = 7.4, A = 15,
Radiation length = 43 g/sq. cm,
Critical energy = 98 MeV.

n \ t	0.5	1.0	1.5	2.0	2.5	3.0	3.5	4.0	4.5	5.0	5.5	6.0	6.5	7.0	7.5	8.0	8.5	9.0	9.5	10.0
0	0.175	0.947	0.968	0.970	0.976	0.988	0.989	0.994	0.990	0.991	0.999	0.999	0.998	1.000	0.999	1.000	1.000	0.997	1.000	1.000
1	0.788	0.045	0.030	0.024	0.020	0.007	0.008	0.002	0.008	0.008	0.001	0.001	0.002	0.000	0.001	0.000	0.000	0.003	0.000	0.000
2	0.034	0.008	0.002	0.006	0.004	0.005	0.003	0.004	0.002	0.001	0.000	0.000	0.000	0.000	0.000	0.000	0.000	0.000	0.000	0.000
⩾3	0.003	0.000	0.000	0.000	0.000	0.000	0.000	0.000	0.000	0.000	0.000	0.000	0.000	0.000	0.000	0.000	0.000	0.000	0.000	0.000
MEAN	0.87	0.06	0.03	0.04	0.03	0.02	0.01	0.01	0.01	0.01	0.00	0.00	0.00	0.00	0.00	0.00	0.00	0.00	0.00	0.00
VAR	0.2	0.1	0.0	0.0	0.0	0.0	0.0	0.0	0.0	0.0	0.0	0.0	0.0	0.0	0.0	0.0	0.0	0.0	0.0	0.0

TABLE 62

Primary electron E_0 = 100 MeV.
Secondary electrons E = 5 MeV.

Absorber: al, Z = 13, A = 27,
Radiation length = 26.3 g/sq. cm = 9.74 cm,
Critical energy = 52 MeV.

n \ t	0.5	1.0	1.5	2.0	2.5	3.0	3.5	4.0	4.5	5.0	5.5	6.0	6.5	7.0	7.5	8.0	8.5	9.0	9.5	10.0
0	0.085	0.432	0.858	0.935	0.938	0.950	0.961	0.970	0.975	0.977	0.988	0.990	0.988	0.994	0.994	0.998	0.995	0.998	0.993	0.998
1	0.856	0.523	0.123	0.055	0.050	0.042	0.034	0.024	0.020	0.021	0.011	0.009	0.010	0.003	0.005	0.001	0.003	0.002	0.006	0.002
2	0.045	0.040	0.018	0.010	0.012	0.008	0.005	0.006	0.005	0.002	0.001	0.001	0.002	0.003	0.001	0.001	0.002	0.000	0.001	0.000
⩾3	0.014	0.005	0.001	0.000	0.000	0.000	0.000	0.000	0.000	0.000	0.000	0.000	0.000	0.000	0.000	0.000	0.000	0.000	0.000	0.000
MEAN	0.99	0.62	0.16	0.08	0.07	0.06	0.04	0.04	0.03	0.03	0.01	0.01	0.01	0.01	0.01	0.00	0.01	0.00	0.01	0.00
VAR	0.2	0.3	0.2	0.1	0.1	0.1	0.1	0.0	0.0	0.0	0.0	0.0	0.0	0.0	0.0	0.0	0.0	0.0	0.0	0.0

TABLE 63

Primary electron E_0 = 200 MeV.
Secondary electrons E = 10 MeV.

Absorber: air, Z = 7.4, A = 15,
Radiation length = 43 g/sq. cm,
Critical energy = 98 MeV.

n \ t	0.5	1.0	1.5	2.0	2.5	3.0	3.5	4.0	4.5	5.0	5.5	6.0	6.5	7.0	7.5	8.0	8.5	9.0	9.5	10.0
0	0.104	0.402	0.802	0.912	0.931	0.958	0.964	0.970	0.971	0.976	0.983	0.989	0.995	0.997	0.998	0.996	0.999	1.000	1.000	0.999
1	0.825	0.543	0.174	0.075	0.060	0.037	0.024	0.025	0.023	0.019	0.012	0.010	0.004	0.003	0.002	0.003	0.001	0.000	0.000	0.001
2	0.063	0.053	0.022	0.013	0.008	0.005	0.012	0.005	0.006	0.005	0.005	0.001	0.001	0.000	0.000	0.001	0.000	0.000	0.000	0.000
3	0.007	0.002	0.001	0.000	0.001	0.000	0.000	0.000	0.000	0.000	0.000	0.000	0.000	0.000	0.000	0.000	0.000	0.000	0.000	0.000
⩾4	0.001	0.000	0.001	0.000	0.000	0.000	0.000	0.000	0.000	0.000	0.000	0.000	0.000	0.000	0.000	0.000	0.000	0.000	0.000	0.000
MEAN	0.98	0.66	0.23	0.10	0.08	0.05	0.05	0.04	0.04	0.03	0.02	0.01	0.01	0.00	0.00	0.01	0.00	0.00	0.00	0.00
VAR	0.2	0.3	0.2	0.1	0.1	0.1	0.1	0.0	0.0	0.0	0.0	0.0	0.0	0.0	0.0	0.0	0.0	0.0	0.0	0.0

TABLE 64

Primary electron E_0 = 200 MeV.
Secondary electrons E = 10 MeV.

Absorber: al, Z = 13, A = 27,
Radiation length = 26.3 g/sq. cm = 9.74 cm,
Critical energy = 52 MeV.

n \ t	0.5	1.0	1.5	2.0	2.5	3.0	3.5	4.0	4.5	5.0	5.5	6.0	6.5	7.0	7.5	8.0	8.5	9.0	9.5	10.0
0	0.056	0.199	0.464	0.708	0.831	0.888	0.918	0.914	0.944	0.971	0.967	0.978	0.985	0.991	0.985	0.988	0.996	0.997	0.994	0.998
1	0.853	0.666	0.442	0.245	0.127	0.092	0.067	0.066	0.052	0.024	0.025	0.020	0.012	0.006	0.011	0.011	0.004	0.003	0.004	0.001
2	0.063	0.108	0.079	0.043	0.040	0.020	0.015	0.019	0.003	0.005	0.008	0.002	0.003	0.004	0.004	0.001	0.000	0.000	0.002	0.001
3	0.028	0.025	0.015	0.003	0.002	0.000	0.000	0.001	0.001	0.000	0.000	0.000	0.000	0.000	0.000	0.000	0.000	0.000	0.000	0.000
⩾4	0.000	0.002	0.000	0.001	0.000	0.000	0.000	0.000	0.000	0.000	0.000	0.000	0.000	0.000	0.000	0.000	0.000	0.000	0.000	0.000
MEAN	1.06	0.97	0.65	0.34	0.21	0.13	0.10	0.11	0.06	0.03	0.04	0.02	0.02	0.01	0.02	0.01	0.00	0.00	0.01	0.00
VAR	0.2	0.4	0.5	0.3	0.3	0.2	0.1	0.1	0.1	0.0	0.1	0.0	0.0	0.0	0.0	0.0	0.0	0.0	0.0	0.0

TABLE 65

Primary electron E_0 = 1 000 MeV.
Secondary electrons E = 50 MeV.

Absorber: air, Z = 7.4, A = 15,
Radiation length = 43 g/sq. cm,
Critical energy = 98 MeV.

n \ t	0.5	1.0	1.5	2.0	2.5	3.0	3.5	4.0	4.5	5.0	5.5	6.0	6.5	7.0	7.5	8.0	8.5	9.0	9.5	10.0
0	0.044	0.120	0.193	0.325	0.515	0.654	0.731	0.807	0.846	0.875	0.902	0.942	0.958	0.963	0.978	0.981	0.987	0.991	0.988	0.988
1	0.842	0.617	0.526	0.454	0.351	0.252	0.216	0.159	0.119	0.096	0.082	0.050	0.037	0.031	0.021	0.015	0.012	0.009	0.009	0.010
2	0.067	0.160	0.208	0.177	0.116	0.085	0.052	0.034	0.033	0.027	0.016	0.008	0.005	0.006	0.001	0.004	0.001	0.000	0.003	0.002
3	0.043	0.089	0.056	0.043	0.017	0.008	0.001	0.000	0.002	0.002	0.000	0.000	0.000	0.000	0.000	0.000	0.000	0.000	0.000	0.000
4	0.004	0.014	0.014	0.001	0.001	0.001	0.000	0.000	0.000	0.000	0.000	0.000	0.000	0.000	0.000	0.000	0.000	0.000	0.000	0.000
⩾5	0.000	0.000	0.003	0.000	0.000	0.000	0.000	0.000	0.000	0.000	0.000	0.000	0.000	0.000	0.000	0.000	0.000	0.000	0.000	0.000
MEAN	1.12	1.26	1.18	0.94	0.64	0.45	0.32	0.23	0.19	0.16	0.11	0.07	0.05	0.04	0.02	0.02	0.01	0.01	0.02	0.01
VAR	0.3	0.7	0.8	0.7	0.6	0.5	0.3	0.2	0.2	0.2	0.1	0.1	0.1	0.1	0.0	0.0	0.0	0.0	0.0	0.0

TABLE 66

Primary electron E_0 = 1 000 MeV.
Secondary electrons E = 50 MeV.

Absorber: al, Z = 13, A = 27,
Radiation length = 26.3 g/sq. cm = 9.74 cm,
Critical energy = 52 MeV.

n \ t	0.5	1.0	1.5	2.0	2.5	3.0	3.5	4.0	4.5	5.0	5.5	6.0	6.5	7.0	7.5	8.0	8.5	9.0	9.5	10.0
0	0.039	0.095	0.155	0.217	0.317	0.459	0.608	0.673	0.757	0.805	0.849	0.899	0.918	0.940	0.943	0.953	0.967	0.972	0.982	0.984
1	0.811	0.580	0.473	0.442	0.438	0.374	0.282	0.247	0.179	0.159	0.122	0.081	0.070	0.045	0.048	0.044	0.031	0.025	0.015	0.013
2	0.090	0.197	0.248	0.240	0.206	0.140	0.098	0.069	0.057	0.033	0.025	0.018	0.011	0.014	0.008	0.003	0.002	0.002	0.003	0.002
3	0.058	0.111	0.102	0.079	0.032	0.025	0.009	0.011	0.006	0.002	0.004	0.002	0.001	0.001	0.001	0.000	0.000	0.001	0.000	0.001
4	0.002	0.013	0.020	0.021	0.007	0.002	0.002	0.000	0.001	0.001	0.000	0.000	0.000	0.000	0.000	0.000	0.000	0.000	0.000	0.000
⩾5	0.000	0.004	0.002	0.001	0.000	0.000	0.001	0.000	0.000	0.000	0.000	0.000	0.000	0.000	0.000	0.000	0.000	0.000	0.000	0.000
MEAN	1.17	1.38	1.37	1.25	0.97	0.74	0.52	0.42	0.32	0.24	0.18	0.12	0.10	0.08	0.07	0.05	0.04	0.03	0.02	0.02
VAR	0.4	0.8	0.9	0.9	0.7	0.6	0.5	0.4	0.4	0.3	0.2	0.2	0.1	0.1	0.1	0.1	0.0	0.0	0.0	0.0

TABLE 67

Primary electron E_0 = 2 000 MeV.
Secondary electrons E = 100 MeV.

Absorber: air, Z = 7.4, A = 15,
Radiation length = 43 g/sq. cm,
Critical energy = 98 MeV.

n \ t	0.5	1.0	1.5	2.0	2.5	3.0	3.5	4.0	4.5	5.0	5.5	6.0	6.5	7.0	7.5	8.0	8.5	9.0	9.5	10.0
0	0.049	0.097	0.152	0.237	0.323	0.447	0.573	0.651	0.762	0.816	0.862	0.887	0.917	0.932	0.952	0.960	0.963	0.972	0.984	0.987
1	0.806	0.559	0.467	0.422	0.408	0.375	0.310	0.258	0.183	0.149	0.113	0.090	0.063	0.054	0.038	0.033	0.033	0.026	0.015	0.011
2	0.092	0.209	0.250	0.247	0.210	0.150	0.101	0.079	0.049	0.031	0.023	0.022	0.020	0.014	0.008	0.006	0.004	0.002	0.001	0.002
3	0.046	0.118	0.110	0.083	0.049	0.021	0.016	0.011	0.008	0.004	0.002	0.001	0.000	0.000	0.001	0.001	0.000	0.000	0.000	0.000
4	0.006	0.016	0.016	0.010	0.009	0.005	0.000	0.001	0.000	0.000	0.000	0.000	0.000	0.000	0.001	0.000	0.000	0.000	0.000	0.000
⩾5	0.002	0.001	0.005	0.001	0.001	0.002	0.000	0.000	0.000	0.000	0.000	0.000	0.000	0.000	0.000	0.000	0.000	0.000	0.000	0.000
MEAN	1.16	1.40	1.39	1.21	1.02	0.77	0.56	0.45	0.30	0.22	0.17	0.14	0.10	0.08	0.06	0.05	0.04	0.03	0.02	0.02
VAR	0.4	0.8	0.9	0.9	0.8	0.7	0.5	0.5	0.3	0.3	0.2	0.2	0.1	0.1	0.1	0.1	0.0	0.0	0.0	0.0

TABLE 68

Primary electron E_0 = 2 000 MeV.
Secondary electrons E = 100 MeV.

Absorber: al, Z = 13, A = 27,
Radiation length = 26.3 g/sq. cm = 9.74 cm,
Critical energy = 52 MeV.

n \ t	0.5	1.0	1.5	2.0	2.5	3.0	3.5	4.0	4.5	5.0	5.5	6.0	6.5	7.0	7.5	8.0	8.5	9.0	9.5	10.0
0	0.036	0.082	0.119	0.155	0.255	0.321	0.428	0.548	0.634	0.724	0.797	0.832	0.883	0.912	0.930	0.936	0.949	0.954	0.968	0.980
1	0.792	0.554	0.415	0.381	0.379	0.397	0.394	0.313	0.263	0.202	0.154	0.133	0.098	0.071	0.055	0.050	0.044	0.038	0.030	0.019
2	0.094	0.212	0.261	0.297	0.240	0.216	0.141	0.112	0.086	0.063	0.046	0.033	0.016	0.016	0.015	0.013	0.007	0.006	0.002	0.001
3	0.071	0.125	0.151	0.123	0.105	0.057	0.032	0.023	0.017	0.007	0.003	0.001	0.003	0.001	0.000	0.001	0.000	0.002	0.000	0.000
4	0.003	0.019	0.044	0.037	0.018	0.009	0.007	0.004	0.000	0.004	0.000	0.001	0.000	0.000	0.000	0.000	0.000	0.000	0.000	0.000
≥5	0.004	0.008	0.010	0.007	0.003	0.000	0.000	0.000	0.000	0.000	0.000	0.000	0.000	0.000	0.000	0.000	0.000	0.000	0.000	0.000
MEAN	1.23	1.47	1.62	1.53	1.26	1.04	0.80	0.62	0.49	0.37	0.26	0.21	0.14	0.11	0.09	0.08	0.06	0.05	0.03	0.02
VAR	0.5	0.9	1.2	1.1	1.1	0.8	0.7	0.6	0.5	0.4	0.3	0.2	0.2	0.1	0.1	0.1	0.1	0.1	0.0	0.0

TABLE 69

Primary electron E_0 = 10 000 MeV.
Secondary electrons E = 500 MeV.

Absorber: air, Z = 7.4, A = 15,
Radiation length = 43 g/sq. cm,
Critical energy = 98 MeV.

n \ t	0.5	1.0	1.5	2.0	2.5	3.0	3.5	4.0	4.5	5.0	5.5	6.0	6.5	7.0	7.5	8.0	8.5	9.0	9.5	10.0
0	0.034	0.077	0.100	0.123	0.162	0.242	0.325	0.410	0.502	0.610	0.682	0.768	0.825	0.857	0.884	0.912	0.939	0.948	0.960	0.975
1	0.809	0.548	0.403	0.331	0.341	0.354	0.352	0.374	0.333	0.271	0.253	0.178	0.138	0.120	0.092	0.073	0.047	0.043	0.033	0.022
2	0.099	0.211	0.260	0.309	0.314	0.269	0.233	0.171	0.127	0.099	0.056	0.045	0.032	0.019	0.021	0.014	0.012	0.009	0.005	0.002
3	0.054	0.127	0.164	0.165	0.126	0.116	0.071	0.038	0.032	0.018	0.008	0.007	0.004	0.003	0.003	0.001	0.002	0.000	0.002	0.001
4	0.003	0.029	0.049	0.057	0.043	0.018	0.016	0.006	0.005	0.002	0.001	0.000	0.001	0.001	0.000	0.000	0.000	0.000	0.000	0.000
≥5	0.001	0.008	0.024	0.015	0.014	0.001	0.003	0.001	0.001	0.000	0.000	0.002	0.000	0.000	0.000	0.000	0.000	0.000	0.000	0.000
MEAN	1.19	1.51	1.74	1.75	1.59	1.32	1.11	0.86	0.71	0.53	0.39	0.30	0.22	0.17	0.14	0.10	0.08	0.06	0.05	0.03
VAR	0.4	0.9	1.4	1.3	1.3	1.1	1.0	0.8	0.7	0.6	0.4	0.4	0.3	0.2	0.2	0.1	0.1	0.1	0.1	0.0

TABLE 70

Primary electron E_0 = 10 000 MeV.
Secondary electrons E = 500 MeV.

Absorber: al, Z = 13, A = 27,
Radiation length = 26.3 g/sq. cm = 9.74 cm,
Critical energy = 52 MeV.

n \ t	0.5	1.0	1.5	2.0	2.5	3.0	3.5	4.0	4.5	5.0	5.5	6.0	6.5	7.0	7.5	8.0	8.5	9.0	9.5	10.0
0	0.034	0.073	0.109	0.129	0.165	0.199	0.271	0.398	0.480	0.566	0.641	0.706	0.761	0.804	0.859	0.883	0.902	0.933	0.953	0.953
1	0.810	0.544	0.378	0.325	0.310	0.351	0.369	0.356	0.337	0.296	0.252	0.210	0.187	0.157	0.117	0.097	0.087	0.057	0.039	0.040
2	0.090	0.214	0.270	0.307	0.320	0.285	0.257	0.180	0.142	0.106	0.092	0.074	0.040	0.033	0.021	0.017	0.010	0.010	0.007	0.007
3	0.055	0.125	0.173	0.175	0.147	0.133	0.091	0.057	0.031	0.026	0.012	0.008	0.010	0.006	0.003	0.003	0.001	0.000	0.001	0.000
4	0.008	0.032	0.054	0.048	0.044	0.027	0.011	0.007	0.008	0.006	0.003	0.002	0.002	0.000	0.000	0.000	0.000	0.000	0.000	0.000
≥5	0.003	0.012	0.016	0.016	0.014	0.005	0.001	0.002	0.002	0.000	0.000	0.000	0.000	0.000	0.000	0.000	0.000	0.000	0.000	0.000
MEAN	1.20	1.54	1.74	1.74	1.64	1.46	1.21	0.93	0.76	0.61	0.48	0.39	0.31	0.24	0.17	0.14	0.11	0.08	0.06	0.05
VAR	0.4	1.0	1.3	1.3	1.3	1.2	1.0	0.9	0.8	0.7	0.5	0.5	0.4	0.3	0.2	0.2	0.1	0.1	0.1	0.1

TABLE 71

Primary electron E_0 = 20 000 MeV.
Secondary electrons E = 1 000 MeV.

Absorber: air, Z = 7.4, A = 15,
Radiation length = 43 g/sq. cm,
Critical energy = 98 MeV.

n \ t	0.5	1.0	1.5	2.0	2.5	3.0	3.5	4.0	4.5	5.0	5.5	6.0	6.5	7.0	7.5	8.0	8.5	9.0	9.5	10.0
0	0.032	0.064	0.080	0.098	0.136	0.179	0.268	0.372	0.465	0.550	0.647	0.722	0.806	0.835	0.881	0.903	0.912	0.941	0.962	0.968
1	0.793	0.506	0.391	0.346	0.351	0.351	0.368	0.365	0.333	0.301	0.249	0.201	0.155	0.135	0.097	0.077	0.072	0.048	0.033	0.029
2	0.104	0.246	0.285	0.303	0.293	0.296	0.251	0.189	0.153	0.115	0.080	0.065	0.035	0.028	0.019	0.020	0.014	0.011	0.005	0.002
3	0.067	0.143	0.172	0.173	0.168	0.134	0.096	0.057	0.040	0.029	0.020	0.010	0.004	0.004	0.003	0.000	0.001	0.000	0.000	0.001
4	0.003	0.027	0.063	0.062	0.047	0.033	0.014	0.013	0.007	0.005	0.003	0.002	0.000	0.000	0.000	0.000	0.000	0.000	0.000	0.000
≥5	0.001	0.014	0.009	0.018	0.006	0.007	0.003	0.004	0.002	0.000	0.001	0.000	0.000	0.000	0.000	0.000	0.000	0.000	0.000	0.000
MEAN	1.22	1.61	1.78	1.81	1.65	1.51	1.23	0.99	0.80	0.64	0.49	0.37	0.24	0.20	0.14	0.12	0.10	0.07	0.04	0.04
VAR	0.4	1.0	1.2	1.3	1.2	1.2	1.0	1.0	0.8	0.7	0.6	0.4	0.3	0.2	0.2	0.1	0.1	0.1	0.1	0.0

TABLE 72

Primary electron E_0 = 20 000 MeV.
Secondary electrons E = 1 000 MeV.

Absorber: al, Z = 13, A = 27,
Radiation length = 26.3 g/sq.cm = 9.74 cm,
Critical energy = 52 MeV.

n \ t	0.5	1.0	1.5	2.0	2.5	3.0	3.5	4.0	4.5	5.0	5.5	6.0	6.5	7.0	7.5	8.0	8.5	9.0	9.5	10.0
0	0.046	0.069	0.088	0.101	0.132	0.193	0.271	0.351	0.440	0.511	0.608	0.707	0.757	0.814	0.872	0.904	0.925	0.944	0.959	0.965
1	0.775	0.522	0.373	0.307	0.295	0.329	0.376	0.381	0.350	0.337	0.294	0.214	0.194	0.156	0.108	0.078	0.064	0.045	0.034	0.032
2	0.110	0.202	0.281	0.304	0.305	0.286	0.231	0.183	0.171	0.120	0.078	0.071	0.035	0.028	0.019	0.016	0.009	0.010	0.007	0.003
3	0.064	0.155	0.177	0.199	0.209	0.142	0.088	0.070	0.034	0.027	0.016	0.008	0.012	0.002	0.001	0.001	0.002	0.001	0.000	0.000
4	0.005	0.033	0.069	0.069	0.051	0.041	0.028	0.014	0.005	0.005	0.004	0.000	0.002	0.000	0.000	0.001	0.000	0.000	0.000	0.000
≥5	0.000	0.019	0.012	0.020	0.008	0.009	0.008	0.001	0.000	0.000	0.000	0.000	0.000	0.000	0.000	0.000	0.000	0.000	0.000	0.000
MEAN	1.21	1.62	1.80	1.89	1.78	1.54	1.25	1.02	0.81	0.68	0.51	0.38	0.31	0.22	0.15	0.12	0.09	0.07	0.05	0.04
VAR	0.4	1.1	1.3	1.4	1.3	1.3	1.2	1.0	0.8	0.7	0.5	0.4	0.4	0.2	0.2	0.2	0.1	0.1	0.1	0.0

TABLE 73

Primary electron E_0 = 500 MeV.
Secondary electrons E = 20 MeV.

Absorber: air, Z = 7.4, A = 15,
Radiation length = 43 g/sq. cm,
Critical energy = 98 MeV.

n \ t	0.5	1.0	1.5	2.0	2.5	3.0	3.5	4.0	4.5	5.0	5.5	6.0	6.5	7.0	7.5	8.0	8.5	9.0	9.5	10.0
0	0.041	0.152	0.334	0.549	0.741	0.802	0.868	0.893	0.91	0.943	0.941	0.960	0.965	0.985	0.990	0.991	0.993	0.996	0.993	0.995
1	0.819	0.616	0.498	0.340	0.207	0.153	0.107	0.083	0.065	0.045	[illegible]	0.031	0.033	0.012	0.006	0.007	0.007	0.003	0.005	0.005
2	0.085	0.165	0.132	0.102	0.048	0.040	0.023	0.023	0.019	0.012	0.014	0.009	0.002	0.003	0.003	0.002	0.000	0.001	0.001	0.000
3	0.053	0.063	0.035	0.008	0.003	0.005	0.002	0.000	0.001	0.000	0.000	0.000	0.000	0.000	0.001	0.000	0.000	0.000	0.001	0.000
4	0.002	0.004	0.001	0.001	0.001	0.000	0.000	0.001	0.000	0.000	0.000	0.000	0.000	0.000	0.000	0.000	0.000	0.000	0.000	0.000
≥5	0.000	0.000	0.000	0.000	0.000	0.000	0.000	0.000	0.000	0.000	0.000	0.000	0.000	0.000	0.000	0.000	0.000	0.000	0.000	0.000
MEAN	1.16	1.15	0.87	0.57	0.32	0.25	0.16	0.13	0.11	0.07	0.07	0.05	0.04	0.02	0.02	0.01	0.01	0.01	0.01	0.01
VAR	0.3	0.6	0.6	0.5	0.3	0.3	0.2	0.2	0.1	0.1	0.1	0.1	0.0	0.0	0.0	0.0	0.0	0.0	0.0	0.0

TABLE 74

Primary electron E_0 = 500 MeV.
Secondary electrons E = 20 MeV.

Absorber: al, Z = 13, A = 27,
Radiation length = 26.3 g/sq. cm = 9.74 cm,
Critical energy = 52 MeV.

n \ t	0.5	1.0	1.5	2.0	2.5	3.0	3.5	4.0	4.5	5.0	5.5	6.0	6.5	7.0	7.5	8.0	8.5	9.0	9.5	10.0
0	0.035	0.110	0.196	0.335	0.475	0.637	0.738	0.774	0.840	0.872	0.896	0.931	0.936	0.950	0.957	0.976	0.974	0.974	0.987	0.987
1	0.822	0.589	0.502	0.422	0.355	0.259	0.198	0.172	0.124	0.103	0.081	0.054	0.055	0.045	0.033	0.021	0.022	0.024	0.010	0.012
2	0.078	0.189	0.223	0.184	0 143	0.097	0.053	0.045	0.033	0.023	0.021	0.014	0.009	0.005	0.009	0.003	0.004	0.002	0.003	0.001
3	0.057	0.089	0.064	0.055	0.023	0.005	0.010	0.006	0.003	0.002	0.002	0.001	0.000	0.000	0.001	0.000	0.000	0.000	0.000	0.000
4	0.003	0.020	0.014	0.004	0.004	0.002	0.000	0.003	0.000	0.000	0.000	0.000	0.000	0.000	0.000	0.000	0.000	0.000	0.000	0.000
≥5	0.005	0.003	0.001	0.000	0.000	0.000	0.001	0.000	0.000	0.000	0.000	0.000	0.000	0.000	0.000	0.000	0.000	0.000	0.000	0.000
MEAN	1.19	1.33	1.20	0.97	0.73	0.48	0.34	0.29	0.20	0.16	0.13	0.09	0.07	0.06	0.05	0.03	0.03	0.03	0.02	0.01
VAR	0.4	0.8	0.8	0.8	0.7	0.5	0.4	0.4	0.2	0.2	0.2	0.1	0.1	0.1	0.1	0.0	0.0	0.0	0.0	0.0

TABLE 75

Primary electron E_0 = 5 000 MeV.
Secondary electrons E = 200 MeV.

Absorber: air, Z = 7.4, A = 15,
Radiation length = 43 g/sq. cm,
Critical energy = 98 MeV.

n \ t	0.5	1.0	1.5	2.0	2.5	3.0	3.5	4.0	4.5	5.0	5.5	6.0	6.5	7.0	7.5	8.0	8.5	9.0	9.5	10.0
0	0.034	0.074	0.102	0.135	0.166	0.242	0.314	0.417	0.501	0.603	0.687	0.743	0.800	0.837	0.882	0.915	0.932	0.949	0.963	0.970
1	0.792	0.516	0.342	0.307	0.316	0.338	0.339	0.329	0.330	0.302	0.225	0.182	0.143	0.125	0.104	0.068	0.056	0.046	0.033	0.027
2	0.100	0.206	0.269	0.290	0.303	0.268	0.231	0.176	0.122	0.076	0.075	0.063	0.052	0.033	0.014	0.012	0.012	0.004	0.003	0.002
3	0.066	0.146	0.189	0.171	0.157	0.120	0.089	0.063	0.037	0.015	0.012	0.011	0.005	0.004	0.000	0.005	0.000	0.001	0.001	0.001
4	0.004	0 043	0.069	0.079	0.044	0.029	0.023	0.013	0.009	0.004	0.001	0.001	0.000	0.001	0.000	0.000	0.000	0.000	0.000	0.000
≥5	0.004	0.015	0.029	0.018	0.014	0.003	0.004	0.002	0.001	0.000	0.000	0.000	0.000	0.000	0.000	0.000	0.000	0.000	0.000	0.000
MEAN	1.23	1.62	1.87	1.81	1.64	1.37	1.18	0.93	0.73	0.52	0.42	0.35	0.26	0.21	0.13	0.11	0.08	0.06	0.04	0.03
VAR	0.4	1.1	1.5	1.5	1.3	1.2	1.1	1.0	0.8	0.5	0.5	0.4	0.3	0.3	0.1	0.2	0.1	0.1	0.1	0.0

TABLE 76

Primary electron E_0 = 5 000 MeV.
Secondary electrons F = 200 MeV.

Absorber: al, Z = 13, A = 27,
Radiation length = 26.3 g/sq. cm = 9.74 cm,
Critical energy = 52 MeV.

n \ t	0.5	1.0	1.5	2.0	2.5	3.0	3.5	4.0	4.5	5.0	5.5	6.0	6.5	7.0	7.5	8.0	8.5	9.0	9.5	10.0
0	0.032	0.058	0.077	0.092	0.124	0.167	0.226	0.318	0.416	0.530	0.655	0.695	0.776	0.797	0.852	0.897	0.910	0.924	0.946	0.957
1	0.785	0.514	0.328	0.285	0.290	0.294	0.333	0.358	0.369	0.314	0.254	0.233	0.170	0.157	0.116	0.086	0.075	0.063	0.047	0.037
2	0.089	0.222	0.299	0.310	0.260	0.296	0.262	0.220	0.160	0.122	0.074	0.056	0.045	0.038	0.028	0.015	0.014	0.013	0.007	0.005
3	0.085	0.154	0.197	0.200	0.206	0.165	0.137	0.078	0.043	0.029	0.014	0.014	0.009	0.007	0.003	0.002	0.001	0.000	0.000	0.000
4	0.009	0.037	0.071	0.085	0.091	0.055	0.035	0.019	0.009	0.004	0.003	0.002	0.000	0.001	0.001	0.000	0.000	0.000	0.000	0.001
≥5	0.000	0.015	0.028	0.028	0.029	0.023	0.007	0.007	0.003	0.001	0.000	0.000	0.000	0.000	0.000	0.000	0.000	0.000	0.000	0.000
MEAN	1.25	1.64	1.95	2.00	1.96	1.72	1.44	1.15	0.87	0.67	0.46	0.40	0.29	0.26	0.19	0.12	0.11	0.09	0.06	0.05
VAR	0.5	1.1	1.4	1.5	1.7	1.5	1.3	1.1	0.9	0.7	0.5	0.5	0.3	0.3	0.2	0.1	0.1	0.1	0.1	0.1

TABLE 77

Primary electron E_0 = 50 000 MeV.
Secondary electrons E = 2 000 MeV.

Absorber: air, Z = 7.4, A = 15,
Radiation length = 43 g/sq. cm,
Critical energy = 98 MeV.

n \ t	0.5	1.0	1.5	2.0	2.5	3.0	3.5	4.0	4.5	5.0	5.5	6.0	6.5	7.0	7.5	8.0	8.5	9.0	9.5	10.0
0	0.036	0.053	0.077	0.081	0.107	0.116	0.165	0.240	0.332	0.407	0.491	0.583	0.639	0.692	0.774	0.823	0.874	0.898	0.937	0.941
1	0.774	0.483	0.327	0.267	0.246	0.287	0.307	0.345	0.354	0.344	0.313	0.287	0.257	0.236	0.184	0.139	0.109	0.082	0.048	0.049
2	0.103	0.237	0.251	0.268	0.327	0.293	0.287	0.237	0.197	0.172	0.142	0.101	0.083	0.058	0.036	0.032	0.015	0.013	0.013	0.008
3	0.077	0.142	0.200	0.221	0.190	0.187	0.159	0.123	0.090	0.061	0.049	0.025	0.019	0.013	0.004	0.006	0.002	0.007	0.002	0.002
4	0.006	0.055	0.100	0.116	0.088	0.089	0.066	0.039	0.021	0.009	0.005	0.004	0.001	0.001	0.002	0.000	0.000	0.000	0.000	0.000
⩾5	0.004	0.030	0.045	0.047	0.042	0.028	0.016	0.016	0.006	0.007	0.000	0.000	0.001	0.000	0.000	0.000	0.000	0.000	0.000	0.000
MEAN	1.26	1.76	2.07	2.18	2.04	1.93	1.70	1.43	1.13	0.94	0.76	0.58	0.49	0.40	0.28	0.22	0.15	0.13	0.08	0.07
VAR	0.5	1.3	1.7	1.8	1.6	1.6	1.5	1.4	1.2	1.0	0.8	0.6	0.6	0.4	0.3	0.3	0.2	0.2	0.1	0.1

TABLE 78

Primary electron E_0 = 50 000 MeV.
Secondary electrons E = 2 000 MeV.

Absorber: al, Z = 13, A = 27,
Radiation length = 26.3 g/sq. cm = 9.74 cm,
Critical energy = 52 MeV.

n \ t	0.5	1.0	1.5	2.0	2.5	3.0	3.5	4.0	4.5	5.0	5.5	6.0	6.5	7.0	7.5	8.0	8.5	9.0	9.5	10.0
0	0.025	0.059	0.065	0.064	0.072	0.097	0.154	0.226	0.318	0.403	0.509	0.598	0.669	0.729	0.795	0.826	0.864	0.906	0.928	0.949
1	0.780	0.473	0.294	0.248	0.234	0.288	0.293	0.335	0.352	0.358	0.311	0.271	0.248	0.197	0.155	0.141	0.112	0.079	0.061	0.043
2	0.105	0.228	0.287	0.285	0.298	0.305	0.292	0.257	0.209	0.174	0.127	0.108	0.059	0.058	0.040	0.027	0.021	0.013	0.010	0.008
3	0.077	0.163	0.215	0.230	0.215	0.190	0.183	0.134	0.083	0.048	0.036	0.021	0.018	0.011	0.006	0.004	0.002	0.002	0.001	0.000
4	0.013	0.052	0.101	0.110	0.110	0.100	0.066	0.041	0.030	0.014	0.017	0.002	0.005	0.004	0.004	0.002	0.001	0.000	0.000	0.000
⩾5	0.000	0.025	0.038	0.063	0.071	0.040	0.022	0.007	0.008	0.005	0.000	0.000	0.001	0.001	0.000	0.000	0.000	0.000	0.000	0.000
MEAN	1.27	1.76	2.11	2.27	2.29	2.06	1.76	1.45	1.18	0.93	0.74	0.56	0.45	0.37	0.27	0.22	0.16	0.11	0.08	0.06
VAR	0.5	1.3	1.5	1.7	1.8	1.7	1.5	1.3	1.2	1.0	0.9	0.6	0.6	0.5	0.4	0.3	0.2	0.1	0.1	0.1

TABLE 79

Primary electron E_0 = 200 MeV.
Secondary Electrons E = 5 MeV.

Absorber: air, Z = 7.4, A = 15,
Radiation length = 43 g/sq. cm,
Critical energy = 98 MeV.

n \ t	0.5	1.0	1.5	2.0	2.5	3.0	3.5	4.0	4.5	5.0	5.5	6.0	6.5	7.0	7.5	8.0	8.5	9.0	9.5	10.0
0	0.078	0.342	0.736	0.889	0.899	0.937	0.955	0.969	0.963	0.974	0.978	0.987	0.994	0.996	0.997	0.994	0.998	0.999	1.000	0.999
1	0.825	0.548	0.223	0.088	0.079	0.051	0.027	0.031	0.031	0.018	0.017	0.010	0.005	0.004	0.002	0.003	0.002	0.001	0.000	0.001
2	0.072	0.096	0.038	0.022	0.021	0.012	0.017	0.010	0.006	0.008	0.005	0.003	0.001	0.000	0.001	0.003	0.000	0.000	0.000	0.000
3	0.023	0.014	0.003	0.001	0.001	0.000	0.001	0.000	0.000	0.000	0.000	0.000	0.000	0.000	0.000	0.000	0.000	0.000	0.000	0.000
⩾4	0.002	0.000	0.002	0.000	0.000	0.000	0.000	0.000	0.000	0.000	0.000	0.000	0.000	0.000	0.000	0.000	0.000	0.000	0.000	0.000
MEAN	1.05	0.78	0.31	0.14	0.12	0.08	0.06	0.05	0.04	0.03	0.03	0.02	0.01	0.00	0.00	0.01	0.00	0.00	0.00	0.00
VAR	0.3	0.4	0.3	0.2	0.2	0.1	0.1	0.1	0.1	0.0	0.0	0.0	0.0	0.0	0.0	0.0	0.0	0.0	0.0	0.0

TABLE 80

Primary electron E_0 = 200 MeV.
Secondary electrons E = 5 MeV.

Absorber: al, Z = 13, A = 27,
Radiation length = 26.3 g/sq. cm = 9.74 cm,
Critical energy = 52 MeV.

n \ t	0.5	1.0	1.5	2.0	2.5	3.0	3.5	4.0	4.5	5.0	5.5	6.0	6.5	7.0	7.5	8.0	8.5	9.0	9.5	10.0
0	0.038	0.147	0.371	0.621	0.771	0.840	0.878	0.886	0.919	0.950	0.945	0.961	0.973	0.984	0.984	0.981	0.991	0.994	0.990	0.997
1	0.844	0.646	0.473	0.297	0.163	0.118	0.093	0.081	0.064	0.037	0.040	0.032	0.024	0.009	0.010	0.015	0.007	0.005	0.007	0.000
2	0.069	0.147	0.122	0.071	0.059	0.041	0.029	0.032	0.016	0.013	0.015	0.007	0.003	0.007	0.006	0.004	0.002	0.001	0.003	0.003
3	0.049	0.053	0.032	0.007	0.006	0.001	0.000	0.001	0.001	0.000	0.000	0.000	0.000	0.000	0.000	0.000	0.000	0.000	0.000	0.000
≥4	0.000	0.007	0.002	0.004	0.001	0.000	0.000	0.000	0.000	0.000	0.000	0.000	0.000	0.000	0.000	0.000	0.000	0.000	0.000	0.000
MEAN	1.13	1.13	0.82	0.48	0.30	0.20	0.15	0.15	0.10	0.06	0.07	0.05	0.03	0.02	0.02	0.02	0.01	0.01	0.01	0.01
VAR	0.3	0.6	0.6	0.5	0.4	0.3	0.2	0.2	0.1	0.1	0.1	0.1	0.0	0.0	0.0	0.0	0.0	0.0	0.0	0.0

TABLE 81

Primary electron E_0 = 2 000 MeV.
Secondary electrons E = 50 MeV.

Absorber: air, Z = 7.4, A = 15,
Radiation length = 43 g/sq. cm,
Critical energy = 98 MeV.

n \ t	0.5	1.0	1.5	2.0	2.5	3.0	3.5	4.0	4.5	5.0	5.5	6.0	6.5	7.0	7.5	8.0	8.5	9.0	9.5	10.0
0	0.026	0.059	0.094	0.132	0.169	0.279	0.398	0.480	0.603	0.684	0.749	0.791	0.832	0.879	0.891	0.925	0.932	0.952	0.959	0.976
1	0.777	0.491	0.353	0.325	0.342	0.357	0.320	0.304	0.251	0.218	0.187	0.160	0.114	0.094	0.085	0.056	0.050	0.036	0.034	0.019
2	0.106	0.224	0.266	0.270	0.293	0.222	0.186	0.160	0.116	0.077	0.049	0.042	0.050	0.020	0.017	0.015	0.017	0.011	0.005	0.005
3	0.078	0.169	0.194	0.181	0.139	0.107	0.066	0.044	0.025	0.016	0.014	0.007	0.003	0.006	0.005	0.002	0.001	0.001	0.002	0.000
4	0.011	0.039	0.059	0.070	0.034	0.026	0.023	0.011	0.005	0.003	0.001	0.000	0.000	0.001	0.002	0.002	0.000	0.000	0.000	0.000
5	0.000	0.016	0.033	0.018	0.021	0.007	0.006	0.000	0.000	0.002	0.000	0.000	0.001	0.000	0.000	0.000	0.000	0.000	0.000	0.000
6	0.002	0.002	0.001	0.004	0.002	0.001	0.001	0.001	0.000	0.000	0.000	0.000	0.000	0.000	0.000	0.000	0.000	0.000	0.000	0.000
≥7	0.000	0.000	0.000	0.000	0.000	0.001	0.000	0.000	0.000	0.000	0.000	0.000	0.000	0.000	0.000	0.000	0.000	0.000	0.000	0.000
MEAN	1.28	1.69	1.87	1.80	1.60	1.27	1.02	0.81	0.58	0.44	0.33	0.27	0.23	0.16	0.14	0.10	0.09	0.06	0.05	0.03
VAR	0.5	1.1	1.5	1.5	1.4	1.3	1.2	0.9	0 7	0.6	0.4	0.3	0.3	0.2	0.2	0.2	0.1	0.1	0.1	0.0

TABLE 82

Primary electron E_0 = 2 000 MeV.
Secondary electrons E = 50 MeV.

Absorber: al, Z = 13, A = 27,
Radiation length = 26.3 g/sq. cm = 9.74 cm,
Critical energy = 52 MeV.

n \ t	0.5	1.0	1.5	2.0	2.5	3.0	3.5	4.0	4.5	5.0	5.5	6.0	6.5	7.0	7.5	8.0	8.5	9.0	9.5	10.0
0	0.021	0.041	0.063	0.082	0.104	0.156	0.215	0.309	0.404	0.519	0.581	0.681	0.751	0.794	0.840	0.862	0.896	0.899	0.927	0.939
1	0.773	0.487	0.293	0.243	0.239	0.289	0.321	0.340	0.322	0.286	0.277	0.227	0.169	0.154	0.122	0.101	0.086	0.078	0.055	0.052
2	0.086	0.197	0.259	0.279	0.291	0.270	0.275	0.221	0.182	0.132	0.106	0.072	0.064	0.046	0.034	0.035	0.017	0.019	0.014	0.008
3	0.102	0.192	0.224	0.233	0.212	0.170	0.125	0.095	0.067	0.049	0.022	0.019	0.015	0.003	0.004	0.001	0.000	0.002	0.004	0.001
4	0.013	0.051	0.099	0.099	0.092	0.089	0.045	0.027	0.019	0.010	0.012	0.000	0.000	0.002	0.000	0.001	0.001	0.002	0.000	0.000
5	0.005	0.023	0.038	0.047	0.045	0.021	0.014	0.007	0.004	0.004	0.002	0.001	0.001	0.000	0.000	0.000	0.001	0.000	0.000	0.000
6	0.000	0.006	0.017	0.014	0.015	0.004	0.005	0.001	0.002	0.000	0.000	0.000	0.000	0.001	0.000	0.000	0.000	0.000	0.000	0.000
≥7	0.000	0.003	0.007	0.003	0.002	0.001	0.000	0.000	0.000	0.000	0.000	0.000	0.000	0.000	0.000	0.000	0.000	0.000	0.000	0.000
MEAN	1.33	1.83	2.22	2.24	2.15	1.83	1.53	1.22	1.00	0.76	0.61	0.43	0.35	0.27	0.20	0.18	0.13	0.13	0.10	0.07
VAR	0.6	1.4	1.9	1.9	1.9	1.7	1.5	1.2	1.1	0.9	0.8	0.5	0.5	0.4	0.3	0.2	0.2	0.2	0.1	0.1

TABLE 83

Primary electron E_0 = 20 000 MeV.
Secondary electrons E = 500 MeV.

Absorber: air, Z = 7.4, A = 15,
Radiation length = 43 g/sq. cm,
Critical energy = 98 MeV.

n \ t	0.5	1.0	1.5	2.0	2.5	3.0	3.5	4.0	4.5	5.0	5.5	6.0	6.5	7.0	7.5	8.0	8.5	9.0	9.5	10.0
0	0.020	0.032	0.045	0.042	0.052	0.046	0.074	0.102	0.171	0.240	0.344	0.413	0.527	0.600	0.674	0.743	0.775	0.828	0.858	0.905
1	0.750	0.429	0.255	0.181	0.137	0.156	0.175	0.232	0.264	0.317	0.317	0.314	0.293	0.267	0.238	0.176	0.158	0.132	0.114	0.077
2	0.120	0.221	0.218	0.214	0.232	0.226	0.270	0.278	0.283	0.234	0.199	0.174	0.110	0.093	0.064	0.066	0.055	0.032	0.023	0.012
3	0.091	0.194	0.209	0.258	0.246	0.245	0.226	0.220	0.166	0.120	0.094	0.070	0.051	0.029	0.021	0.013	0.009	0.008	0.005	0.002
4	0.016	0.069	0.139	0.146	0.182	0.177	0.155	0.113	0.076	0.062	0.030	0.017	0.013	0.010	0.003	0.002	0.003	0.000	0.000	0.002
5	0.003	0.041	0.082	0.088	0.087	0.101	0.064	0.041	0.032	0.025	0.012	0.011	0.003	0.000	0.000	0.000	0.000	0.000	0.000	0.000
6	0.000	0.009	0.036	0.048	0.049	0.035	0.026	0.008	0.006	0.002	0.003	0.001	0.003	0.000	0.000	0.000	0.000	0.000	0.000	0.001
⩾7	0.000	0.005	0.016	0.023	0.015	0.014	0.010	0.006	0.002	0.000	0.001	0.000	0.000	0.001	0.000	0.000	0.000	0.000	0.000	0.000
MEAN	1.34	2.02	2.62	2.86	2.91	2.87	2.56	2.20	1.84	1.53	1.20	1.00	0.75	0.59	0.44	0.36	0.31	0.22	0.18	0.12
VAR	0.6	1.7	2.6	2.7	2.5	2.4	2.3	1.9	1.8	1.7	1.5	1.2	1.0	0.8	0.5	0.5	0.4	0.3	0.2	0.2

TABLE 84

Primary electron E_0 = 20 000 MeV.
Secondary electrons E = 500 MeV.

Absorber: al, Z = 13, A = 27,
Radiation length = 26.3 g/sq. cm = 9.74 cm
Critical energy = 52 MeV.

n \ t	0.5	1.0	1.5	2.0	2.5	3.0	3.5	4.0	4.5	5.0	5.5	6.0	6.5	7.0	7.5	8.0	8.5	9.0	9.5	10.0
0	0.025	0.034	0.035	0.037	0.046	0.058	0.064	0.088	0.147	0.181	0.267	0.365	0.462	0.542	0.617	0.692	0.738	0.801	0.845	0.890
1	0.737	0.408	0.231	0.149	0.111	0.132	0.165	0.208	0.242	0.303	0.327	0.334	0.306	0.300	0.267	0.210	0.193	0.151	0.117	0.081
2	0.108	0.201	0.231	0.212	0.222	0.209	0.280	0.287	0.276	0.259	0.229	0.186	0.154	0.116	0.079	0.066	0.054	0.037	0.032	0.027
3	0.108	0.210	0.231	0.238	0.225	0.241	0.208	0.208	0.200	0.161	0.110	0.071	0.061	0.030	0.030	0.020	0.011	0.010	0.006	0.002
4	0.015	0.085	0.144	0.177	0.173	0.184	0.138	0.111	0.083	0.066	0.046	0.036	0.014	0.010	0.006	0.007	0.004	0.001	0.000	0.000
5	0.007	0.037	0.091	0.105	0.141	0.105	0.100	0.070	0.037	0.022	0.016	0.007	0.003	0.002	0.000	0.003	0.000	0.000	0.000	0.000
6	0.000	0.016	0.018	0.052	0.055	0.050	0.031	0.017	0.011	0.005	0.004	0.001	0.000	0.000	0.001	0.002	0.000	0.000	0.000	0.000
⩾7	0.000	0.009	0.019	0.030	0.027	0.021	0.014	0.011	0.004	0.003	0.001	0.000	0.000	0.000	0.000	0.000	0.000	0.000	0.000	0.000
MEAN	1.37	2.13	2.66	3.05	3.16	2.99	2.69	2.38	2.01	1.73	1.41	1.10	0.87	0.67	0.55	0.46	0.35	0.26	0.20	0.14
VAR	0.7	1.9	2.4	2.8	2.8	2.7	2.5	2.3	2.0	1.7	1.6	1.3	1.0	0.8	0.7	0.7	0.4	0.3	0.3	0.2

TABLE 85

Primary electron E_0 = 500 MeV.
Secondary electrons E = 10 MeV.

Absorber: air, Z = 7.4, A = 15,
Radiation length = 43 g/sq. cm,
Critical energy = 98 MeV.

n \ t	0.5	1.0	1.5	2.0	2.5	3.0	3.5	4.0	4.5	5.0	5.5	6.0	6.5	7.0	7.5	8.0	8.5	9.0	9.5	10.0
0	0.027	0.113	0.257	0.453	0.662	0.735	0.806	0.847	0.877	0.910	0.918	0.941	0.952	0.979	0.979	0.987	0.989	0.995	0.990	0.993
1	0.805	0.567	0.496	0.371	0.238	0.187	0.144	0.107	0.088	0.072	0.062	0.045	0.037	0.017	0.014	0.010	0.009	0.004	0.007	0.007
2	0.086	0.202	0.179	0.148	0.088	0.064	0.047	0.042	0.033	0.017	0.020	0.014	0.009	0.004	0.006	0.003	0.002	0.001	0.002	0.000
3	0.073	0.099	0.058	0.025	0.011	0.011	0.003	0.003	0.001	0.000	0.000	0.000	0.002	0.000	0.001	0.000	0.000	0.000	0.001	0.000
4	0.009	0.017	0.008	0.003	0.001	0.003	0.000	0.001	0.001	0.001	0.000	0.000	0.000	0.000	0.000	0.000	0.000	0.000	0.000	0.000
⩾5	0.000	0.002	0.002	0.000	0.000	0.000	0.000	0.000	0.000	0.000	0.000	0.000	0.000	0.000	0.000	0.000	0.000	0.000	0.000	0.000
MEAN	1.23	1.36	1.07	0.75	0.45	0.36	0.25	0.20	0.16	0.11	0.10	0.07	0.06	0.03	0.03	0.02	0.01	0.01	0.01	0.01
VAR	0.4	0.8	0.8	0.7	0.5	0.5	0.3	0.3	0.2	0.1	0.1	0.1	0.1	0.0	0.0	0.0	0.0	0.0	0.0	0.0

TABLE 86

Primary electron E_0 = 500 MeV.
Secondary electrons E = 10 MeV.

Absorber: al, Z = 13, A = 27,
Radiation length = 26.3 g/sq. cm = 9.74 cm,
Critical energy = 52 MeV.

n \ t	0.5	1.0	1.5	2.0	2.5	3.0	3.5	4.0	4.5	5.0	5.5	6.0	6.5	7.0	7.5	8.0	8.5	9.0	9.5	10.0
0	0.020	0.070	0.130	0.242	0.378	0.512	0.623	0.687	0.756	0.790	0.837	0.888	0.899	0.911	0.934	0.963	0.963	0.959	0.979	0.980
1	0.787	0.646	0.448	0.387	0.329	0.298	0.252	0.210	0.174	0.141	0.118	0.082	0.075	0.070	0.047	0.030	0.032	0.036	0.016	0.017
2	0.109	0.198	0.251	0.244	0.211	0.156	0.099	0.082	0.055	0.058	0.038	0.029	0.024	0.018	0.016	0.007	0.005	0.005	0.003	0.003
3	0.071	0.132	0.118	0.102	0.066	0.032	0.021	0.014	0.014	0.010	0.006	0.001	0.001	0.001	0.002	0.000	0.000	0.000	0.002	0.000
4	0.007	0.041	0.044	0.021	0.012	0.008	0.003	0.006	0.001	0.001	0.001	0.000	0.001	0 000	0.001	0.000	0.000	0.000	0.000	0.000
⩾ 5	0.006	0.013	0.009	0.004	0.004	0.000	0.002	0.001	0.000	0.000	0.000	0 000	0.000	0.000	0.000	0.000	0.000	0.000	0.000	0.000
MEAN	1.28	1.57	1.53	1.29	1.02	0.73	0.54	0.45	0.33	0.29	0.22	0.14	0.13	0.11	0.09	0.04	0.04	0.05	0.03	0.02
VAR	0.5	1.1	1.1	1.1	1.0	0.8	0.7	0.6	0.4	0.4	0.3	0.2	0.2	0.1	0.1	0.1	0.1	0.1	0.0	0.0

TABLE 87

Primary electron E_0 = 1 000 MeV.
Secondary electrons E = 20 MeV.

Absorber: air, Z = 7.4, A = 15,
Radiation length = 43 g/sq. cm,
Critical energy = 98 MeV.

n \ t	0.5	1.0	1.5	2.0	2.5	3.0	3.5	4.0	4.5	5.0	5.5	6.0	6.5	7.0	7.5	8.0	8.5	9.0	9.5	10.0
0	0.023	0.072	0.108	0.197	0.334	0.475	0.580	0.673	0.737	0.789	0.823	0.880	0.927	0.932	0.943	0.960	0.972	0.973	0.974	0.978
1	0.808	0.558	0.438	0.380	0.349	0.292	0.263	0.225	0.176	0.136	0.127	0.093	0.056	0.048	0.048	0.031	0.021	0.022	0.022	0.019
2	0.070	0.179	0.230	0.261	0.218	0.180	0.122	0.084	0.071	0.063	0.044	0.027	0.016	0.017	0.008	0.008	0.007	0.005	0.004	0.003
3	0.086	0.138	0.148	0.123	0.081	0.043	0.028	0.013	0.014	0.010	0.006	0.000	0.000	0.002	0.001	0.001	0.000	0.000	0.000	0.000
4	0.010	0.039	0.050	0.033	0.016	0.007	0.005	0.005	0.002	0.002	0.000	0.000	0.001	0.001	0.000	0.000	0.000	0.000	0.000	0.000
5	0.003	0.011	0.023	0.006	0.002	0.003	0.002	0.000	0.000	0.000	0.000	0.000	0.000	0.000	0.000	0.000	0.000	0.000	0.000	0.000
6	0.000	0.003	0.002	0.000	0.000	0.000	0.000	0.000	0.000	0.000	0.000	0.000	0.000	0.000	0.000	0.000	0.000	0.000	0.000	0.000
7	0.000	0.000	0.001	0.000	0.000	0.000	0.000	0.000	0.000	0.000	0.000	0.000	0.000	0.000	0.000	0.000	0.000	0.000	0.000	0.000
⩾ 8	0.000	0.000	0.000	0.000	0.000	0.000	0.000	0.000	0.000	0.000	0.000	0.000	0.000	0.000	0.000	0.000	0.000	0.000	0.000	0.000
MEAN	1.26	1.56	1.68	1.43	1.10	0.82	0.62	0.45	0.37	0.30	0.23	0.15	0.09	0.09	0.07	0.05	0.04	0.03	0.03	0.03
VAR	0.5	1.1	1.4	1.2	1.0	0.9	0.7	0.6	0.5	0.4	0.3	0.2	0.1	0.1	0.1	0.1	0.0	0.0	0.0	0.0

TABLE 88

Primary electron E_0 = 1 000 MeV.
Secondary electrons E = 20 MeV.

Absorber: al, Z = 13, A = 27,
Radiation length = 26.3 g/sq. cm = 9.74 cm,
Critical energy = 52 MeV.

n \ t	0.5	1.0	1.5	2.0	2.5	3.0	3.5	4.0	4.5	5.0	5.5	6.0	6.5	7.0	7.5	8.0	8.5	9.0	9.5	10.0
0	0.017	0.045	0.079	0.110	0.154	0.234	0.356	0.445	0.548	0.638	0.699	0.772	0.806	0.843	0.881	0.909	0.918	0.920	0.946	0.961
1	0.776	0.493	0.348	0.303	0.302	0.344	0.335	0.285	0.259	0.217	0.196	0.160	0.139	0.117	0.088	0.074	0.069	0.065	0.040	0.027
2	0.101	0.205	0.255	0.280	0.290	0.247	0.209	0.181	0.152	0.114	0.080	0.057	0.050	0.032	0.023	0.017	0.012	0.012	0.014	0.010
3	0.094	0.176	0.194	0.189	0.169	0.130	0.084	0.067	0.032	0.026	0.023	0.008	0.005	0.006	0.006	0.000	0.001	0.001	0.000	0.002
4	0.011	0.052	0.081	0.076	0.057	0.034	0.011	0.020	0.008	0.005	0.002	0.003	0.000	0.002	0.002	0.000	0.000	0.002	0.000	0.000
5	0.001	0.024	0.030	0.028	0.023	0.009	0.004	0.002	0.001	0.000	0.000	0.000	0.000	0.000	0.000	0.000	0.000	0.000	0.000	0.000
6	0.000	0.005	0.010	0.011	0.004	0.002	0.000	0.000	0.002	0.000	0.001	0.000	0.000	0.000	0.000	0.000	0.000	0.000	0.000	0.000
7	0.000	0.000	0.002	0.003	0.001	0.000	0.001	0.000	0.000	0.000	0.000	0.000	0.000	0.000	0.000	0.000	0.000	0.000	0.000	0.000
⩾ 8	0.000	0.000	0.001	0.000	0.000	0.000	0.000	0.000	0.000	0.000	0.000	0.000	0.000	0.000	0.000	0.000	0.000	0.000	0.000	0.000
MEAN	1.31	1.79	2.00	1.96	1.76	1.42	1.08	0.94	0.71	0.54	0.44	0.31	0.25	0.21	0.16	0.11	0.10	0.10	0.07	0.05
VAR	0.5	1.3	1.7	1.7	1.6	1.3	1.1	1.1	0.9	0.7	0.6	0.4	0.3	0.3	0.2	0.1	0.1	0.1	0.1	0.1

TABLE 89

Primary electron E_0 = 5 000 MeV.
Secondary electrons E = 100 MeV.

Absorber: air, Z = 7.4, A = 15,
Radiation length = 43 g/sq. cm.
Critical energy = 98 MeV.

n \ t	0.5	1.0	1.5	2.0	2.5	3.0	3.5	4.0	4.5	5.0	5.5	6.0	6.5	7.0	7.5	8.0	8.5	9.0	9.5	10.0
0	0.020	0.044	0.055	0.069	0.075	0.109	0.150	0.205	0.287	0.393	0.475	0.546	0.628	0.685	0.748	0.805	0.850	0.885	0.902	0.929
1	0.765	0.426	0.256	0.166	0.180	0.196	0.225	0.282	0.293	0.309	0.280	0.268	0.229	0.197	0.191	0.156	0.109	0.089	0.074	0.056
2	0.096	0.201	0.220	0.233	0.252	0.274	0.254	0.249	0.247	0.180	0.182	0.131	0.098	0.086	0.048	0.025	0.036	0.025	0.021	0.012
3	0.097	0.216	0.217	0.212	0.229	0.201	0.200	0.149	0.105	0.078	0.061	0.040	0.034	0.024	0.011	0.013	0.005	0.001	0.000	0.003
4	0.014	0.059	0.142	0.157	0.145	0.127	0.104	0.081	0.051	0.032	0.018	0.012	0.010	0.006	0.002	0.000	0.000	0.000	0.002	0.000
5	0.008	0.039	0.068	0.097	0.074	0.067	0.039	0.025	0.013	0.004	0.003	0.002	0.001	0.002	0.000	0.001	0.000	0.000	0.001	0.000
6	0.000	0.011	0.024	0.048	0.033	0.023	0.023	0.008	0.004	0.002	0.001	0.001	0.000	0.000	0.000	0.000	0.000	0.000	0.000	0.000
7	0.000	0.003	0.012	0.012	0.009	0.002	0.003	0.000	0.000	0.002	0.000	0.000	0.000	0.000	0.000	0.000	0.000	0.000	0.000	0.000
⩾8	0.000	0.001	0.006	0.006	0.003	0.001	0.002	0.001	0.000	0.000	0.000	0.000	0.000	0.000	0.000	0.000	0.000	0.000	0.000	0.000
MEAN	1.34	2.00	2.53	2.80	2.61	2.35	2.12	1.73	1.40	1.08	0.88	0.71	0.57	0.48	0.33	0.25	0.20	0.14	0.13	0.09
VAR	0.6	1.7	2.5	2.8	2.4	2.3	2.3	1.9	1.6	1.4	1.1	0.9	0.8	0.7	0.4	0.3	0.3	0.2	0.2	0.1

TABLE 90

Primary electron E_0 = 5 000 MeV.
Secondary electrons E = 100 MeV.

Absorber: al, Z = 13, A = 27,
Radiation length = 26.3 g/sq. cm = 9.74 cm,
Critical energy = 52 MeV.

n \ t	0.5	1.0	1.5	2.0	2.5	3.0	3.5	4.0	4.5	5.0	5.5	6.0	6.5	7.0	7.5	8.0	8.5	9.0	9.5	10.0
0	0.016	0.030	0.040	0.038	0.049	0.059	0.067	0.110	0.166	0.248	0.367	0.449	0.519	0.614	0.678	0.741	0.789	0.826	0.863	0.892
1	0.757	0.434	0.226	0.151	0.136	0.122	0.175	0.216	0.276	0.314	0.319	0.291	0.289	0.233	0.226	0.173	0.146	0.133	0.097	0.085
2	0.085	0.194	0.234	0.207	0.197	0.204	0.243	0.277	0.250	0.213	0.197	0.166	0.127	0.095	0.077	0.069	0.057	0.029	0.037	0.017
3	0.121	0.206	0.223	0.250	0.227	0.240	0.238	0.203	0.158	0.140	0.076	0.071	0.042	0.047	0.011	0.015	0.005	0.010	0.002	0.004
4	0.014	0.083	0.131	0.176	0.188	0.180	0.143	0.121	0.092	0.066	0.031	0.018	0.018	0.009	0.006	0.002	0.002	0.002	0.001	0.002
5	0.005	0.037	0.082	0.100	0.110	0.110	0.086	0.050	0.041	0.014	0.009	0.004	0.003	0.002	0.002	0.000	0.001	0.000	0.000	0.000
6	0.002	0.008	0.045	0.047	0.059	0.051	0.033	0.017	0.012	0.005	0.000	0.000	0.001	0.000	0.000	0.000	0.000	0.000	0.000	0.000
7	0.000	0.008	0.017	0.016	0.027	0.023	0.011	0.004	0.005	0.000	0.001	0.000	0.001	0.000	0.000	0.000	0.000	0.000	0.000	0.000
⩾8	0.000	0.000	0.002	0.015	0.007	0.011	0.004	0.002	0.002	0.000	0.000	0.001	0.000	0.000	0.000	0.000	0.000	0.000	0.000	0.000
MEAN	1.38	2.06	2.70	3.04	3.11	3.08	2.69	2.26	1.94	1.52	1.12	0.94	0.77	0.61	0.45	0.36	0.29	0.23	0.18	0.14
VAR	0.7	1.8	2.6	2.8	2.9	3.0	2.5	2.2	2.2	1.7	1.3	1.2	1.0	0.9	0.6	0.5	0.4	0.3	0.2	0.2

TABLE 91

Primary electron E_0 = 10 000 MeV.
Secondary electrons E = 200 MeV.

Absorber: air, Z = 7.4, A = 15,
Radiation length = 43 g/sq. cm.
Critical energy = 98 MeV.

n \ t	0.5	1.0	1.5	2.0	2.5	3.0	3.5	4.0	4.5	5.0	5.5	6.0	6.5	7.0	7.5	8.0	8.5	9.0	9.5	10.0
0	0.021	0.039	0.032	0.038	0.043	0.054	0.081	0.119	0.152	0.230	0.333	0.438	0.523	0.596	0.671	0.722	0.777	0.837	0.871	0.906
1	0.755	0.421	0.250	0.153	0.120	0.131	0.154	0.230	0.266	0.302	0.306	0.273	0.277	0.254	0.217	0.197	0.172	0.123	0.097	0.072
2	0.094	0.187	0.231	0.205	0.207	0.218	0.259	0.251	0.265	0.239	0.207	0.181	0.118	0.105	0.084	0.066	0.040	0.030	0.028	0.020
3	0.111	0.202	0.213	0.210	0.252	0.254	0.232	0.214	0.192	0.144	0.096	0.071	0.064	0.028	0.027	0.015	0.008	0.008	0.003	0.001
4	0.012	0.091	0.130	0.189	0.184	0.184	0.146	0.111	0.078	0.059	0.038	0.024	0.016	0.011	0.006	0.008	0.003	0.002	0.001	0.001
5	0.003	0.040	0.086	0.118	0.112	0.097	0.080	0.061	0.037	0.023	0.016	0.012	0.001	0.004	0.003	0.001	0.000	0.000	0.000	0.000
6	0.003	0.016	0.035	0.050	0.050	0.034	0.030	0.014	0.010	0.002	0.004	0.001	0.001	0.002	0.000	0.001	0.000	0.000	0.000	0.000
7	0.001	0.003	0.016	0.029	0.022	0.020	0.010	0.008	0.000	0.000	0.000	0.000	0.000	0.000	0.001	0.000	0.000	0.000	0.000	0.000
⩾8	0.000	0.001	0.007	0.008	0.010	0.008	0.008	0.002	0.000	0.001	0.000	0.000	0.000	0.000	0.000	0.000	0.000	0.000	0.000	0.000
MEAN	1.36	2.09	2.68	3.11	3.13	2.96	2.67	2.23	1.93	1.58	1.26	1.01	0.78	0.62	0.48	0.40	0.29	0.22	0.17	0.12
VAR	0.7	1.9	2.7	3.0	2.8	2.6	2.6	2.3	1.9	1.7	1.6	1.3	1.0	0.9	0.7	0.6	0.4	0.3	0.2	0.2

TABLE 92

Primary electron E_0 = 10 000 MeV.
Secondary electrons E = 200 MeV.

Absorber: al, Z = 13, A = 27,
Radiation length = 26.3 g/sq. cm = 9.74 cm,
Critical energy = 52 MeV.

n \ t	0.5	1.0	1.5	2.0	2.5	3.0	3.5	4.0	4.5	5.0	5.5	6.0	6.5	7.0	7.5	8.0	8.5	9.0	9.5	10.0
0	0.014	0.024	0.037	0.049	0.045	0.054	0.051	0.086	0.135	0.186	0.257	0.341	0.420	0.514	0.572	0.640	0.707	0.771	0.795	0.834
1	0.751	0.403	0.213	0.143	0.109	0.108	0.127	0.161	0.229	0.270	0.283	0.300	0.296	0.264	0.241	0.229	0.209	0.156	0.154	0.123
2	0.104	0.225	0.232	0.195	0.193	0.180	0.196	0.259	0.242	0.247	0.235	0.200	0.168	0.143	0.122	0.099	0.052	0.050	0.037	0.035
3	0.104	0.180	0.207	0.211	0.192	0.231	0.259	0.215	0.186	0.177	0.127	0.097	0.061	0.054	0.043	0.024	0.026	0.019	0.010	0.007
4	0.016	0.094	0.158	0.177	0.198	0.198	0.196	0.161	0.125	0.076	0.060	0.044	0.037	0.016	0.019	0.006	0.005	0.004	0.003	0.001
5	0.009	0.058	0.084	0.108	0.129	0.125	0.103	0.074	0.054	0.033	0.031	0.012	0.012	0.005	0.003	0.002	0.001	0.000	0.001	0.000
6	0.001	0.012	0.045	0.068	0.093	0.064	0.042	0.033	0.023	0.007	0.005	0.005	0.004	0.002	0.000	0.000	0.000	0.000	0.000	0.000
7	0.001	0.002	0.014	0.032	0.026	0.024	0.020	0.009	0.006	0.004	0.001	0.001	0.002	0.002	0.000	0.000	0.000	0.000	0.000	0.000
⩾8	0.000	0.002	0.010	0.017	0.015	0.016	0.007	0.002	0.001	0.000	0.001	0.000	0.000	0.000	0.000	0.000	0.000	0.000	0.000	0.000
MEAN	1.39	2.16	2.80	3.19	3.37	3.27	3.04	2.62	2.22	1.83	1.57	1.26	1.06	0.83	0.71	0.53	0.42	0.33	0.28	0.22
VAR	0.7	1.9	2.8	3.4	3.3	3.2	2.6	2.5	2.4	2.0	1.9	1.6	1.5	1.2	1.0	0.7	0.6	0.5	0.4	0.3

TABLE 93

Primary electron E_0 = 50 000 MeV.
Secondary electrons E = 1 000 MeV.

Absorber: air, Z = 7.4, A = 15,
Radiation length = 43 g/sq. cm,
Critical energy = 98 MeV.

n \ t	0.5	1.0	1.5	2.0	2.5	3.0	3.5	4.0	4.5	5.0	5.5	6.0	6.5	7.0	7.5	8.0	8.5	9.0	9.5	10.0
0	0.025	0.032	0.043	0.028	0.035	0.030	0.036	0.055	0.084	0.128	0.182	0.255	0.332	0.400	0.489	0.578	0.676	0.724	0.795	0.830
1	0.718	0.374	0.213	0.127	0.092	0.093	0.083	0.132	0.176	0.223	0.255	0.279	0.307	0.294	0.292	0.254	0.200	0.192	0.157	0.130
2	0.107	0.223	0.191	0.193	0.175	0.164	0.197	0.209	0.2[illegible]	0.238	0.241	0.250	0.205	0.184	0.136	0.112	0.082	0.060	0.035	0.028
3	0.129	0.199	0.202	0.202	0.207	0.231	0.231	0.239	0.187	0.197	0.167	0.129	0.092	0.086	0.054	0.036	0.036	0.016	0.007	0.008
4	0.010	0.092	0.136	0.170	0.185	0.194	0.201	0.165	0.148	0.120	0.092	0.044	0.038	0.024	0.023	0.015	0.004	0.004	0.005	0.004
5	0.009	0.046	0.110	0.134	0.143	0.139	0.135	0.114	0.092	0.060	0.042	0.028	0.019	0.011	0.004	0.004	0.002	0.003	0.001	0.000
6	0.000	0.017	0.054	0.075	0.090	0.082	0.068	0.055	0.035	0.029	0.013	0.009	0.005	0.001	0.002	0.000	0.000	0.000	0.000	0.000
7	0.001	0.014	0.027	0.041	0.044	0.039	0.034	0.019	0.012	0.003	0.006	0.005	0.002	0.000	0.000	0.001	0.000	0.000	0.000	0.000
8	0.001	0.001	0.018	0.021	0.023	0.017	0.012	0.008	0.004	0.002	0.002	0.001	0.000	0.000	0.000	0.000	0.000	0.001	0.000	0.000
9	0.000	0.001	0.005	0.007	0.004	0.007	0.002	0.001	0.001	0.000	0.000	0.000	0.000	0.000	0.000	0.000	0.000	0.000	0.000	0.000
⩾10	0.000	0.001	0.001	0.002	0.002	0.004	0.001	0.003	0.000	0.000	0.000	0.000	0.000	0.000	0.000	0.000	0.000	0.000	0.000	0.000
MEAN	1.42	2.24	3.01	3.46	3.61	3.59	3.42	3.06	2.65	2.28	1.95	1.58	1.28	1.08	0.85	0.67	0.50	0.40	0.27	0.23
VAR	0.8	2.2	3.6	3.7	3.6	3.4	3.0	3.0	2.8	2.5	2.3	2.0	1.7	1.3	1.1	1.0	0.7	0.6	0.4	0.3

TABLE 94

Primary electron E_0 = 50 000 MeV.
Secondary electrons E = 1 000 MeV.

Absorber: al, Z = 13, A = 27,
Radiation length = 26.3 g/sq. cm = 9.74 cm,
Critical energy = 52 MeV.

n \ t	0.5	1.0	1.5	2.0	2.5	3.0	3.5	4.0	4.5	5.0	5.5	6.0	6.5	7.0	7.5	8.0	8.5	9.0	9.5	10.0
0	0.015	0.031	0.024	0.024	0.021	0.026	0.034	0.038	0.066	0.106	0.177	0.225	0.312	0.416	0.502	0.566	0.646	0.698	0.770	0.818
1	0.737	0.387	0.186	0.092	0.079	0.064	0.065	0.107	0.156	0.231	0.267	0.296	0.311	0.318	0.282	0.275	0.237	0.209	0.162	0.137
2	0.096	0.201	0.206	0.176	0.152	0.137	0.153	0.200	0.221	0.260	0.246	0.255	0.215	0.166	0.141	0.114	0.073	0.067	0.050	0.037
3	0.125	0.198	0.228	0.210	0.170	0.181	0.204	0.236	0.240	0.203	0.167	0.136	0.098	0.060	0.051	0.026	0.033	0.021	0.015	0.005
4	0.016	0.100	0.154	0.187	0.194	0.205	0.211	0.177	0.145	0.119	0.085	0.048	0.041	0.027	0.019	0.014	0.007	0.004	0.003	0.002
5	0.010	0.047	0.110	0.143	0.156	0.184	0.151	0.131	0.097	0.049	0.041	0.030	0.017	0.010	0.002	0.004	0.001	0.001	0.000	0.001
6	0.001	0.024	0.055	0.093	0.123	0.111	0.097	0.063	0.052	0.022	0.012	0.007	0.006	0.003	0.003	0.002	0.003	0.000	0.000	0.000
7	0.000	0.007	0.023	0.050	0.069	0.058	0.043	0.028	0.020	0.008	0.003	0.002	0.000	0.000	0.000	0.001	0.000	0.000	0.000	0.000
8	0.000	0.003	0.011	0.017	0.026	0.020	0.018	0.012	0.003	0.002	0.002	0.001	0.000	0.000	0.000	0.000	0.000	0.000	0.000	0.000
9	0.000	0.002	0.003	0.005	0.007	0.009	0.004	0.006	0.000	0.000	0.000	0.000	0.000	0.000	0.000	0.000	0.000	0.000	0.000	0.000
≥10	0.000	0.000	0.002	0.003	0.003	0.005	0.000	0.002	0.000	0.000	0.000	0.000	0.000	0.000	0.000	0.000	0.000	0.000	0.000	0.000
MEAN	1.42	2.25	3.07	3.66	3.97	3.99	3.87	3.32	2.86	2.29	1.91	1.62	1.32	1.01	0.82	0.67	0.53	0.43	0.32	0.24
VAR	0.8	2.2	3.1	3.5	3.8	3.6	3.3	3.2	2.8	2.3	2.2	1.8	1.6	1.3	1.1	1.0	0.8	0.6	0.4	0.3

TABLE 95

Primary electron E_0 = 500 MeV.
Secondary electrons E = 5 MeV.

Absorber: air, Z = 7.4, A = 15,
Radiation length = 43 g/sq. cm,
Critical energy = 98 MeV.

n \ t	0.5	1.0	1.5	2.0	2.5	3.0	3.5	4.0	4.5	5.0	5.5	6.0	6.5	7.0	7.5	8.0	8.5	9.0	9.5	10.0
0	0.017	0.098	0.218	0.391	0.605	0.681	0.755	0.808	0.848	0.879	0.894	0.920	0.942	0.972	0.968	0.980	0.983	0.991	0.986	0.991
1	0.788	0.546	0.464	0.374	0.256	0.208	0.176	0.129	0.101	0.089	0.075	0.059	0.042	0.019	0.024	0.017	0.012	0.008	0.010	0.009
2	0.099	0.182	0.206	0.175	0.118	0.091	0.064	0.054	0.047	0.030	0.030	0.019	0.014	0.009	0.007	0.003	0.005	0.001	0.003	0.000
3	0.085	0.143	0.087	0.049	0.017	0.016	0.004	0.008	0.002	0.001	0.001	0.002	0.002	0.000	0.001	0.000	0.000	0.000	0.001	0.000
4	0.010	0.024	0.019	0.010	0.003	0.003	0.001	0.001	0.002	0.001	0.000	0.000	0.000	0.000	0.000	0.000	0.000	0.000	0.000	0.000
5	0.001	0.006	0.006	0.001	0.001	0.001	0.000	0.000	0.000	0.000	0.000	0.000	0.000	0.000	0.000	0.000	0.000	0.000	0.000	0.000
≥6	0.000	0.001	0.000	0.000	0.000	0.000	0.000	0.000	0.000	0.000	0.000	0.000	0.000	0.000	0.000	0.000	0.000	0.000	0.000	0.000
MEAN	1.29	1.47	1.24	0.92	0.56	0.48	0.32	0.27	0.21	0.16	0.14	0.10	0.08	0.04	0.04	0.02	0.02	0.01	0.02	0.01
VAR	0.5	1.0	1.0	0.9	0.6	0.6	0.4	0.4	0.3	0.2	0.2	0.1	0.1	0.1	0.1	0.0	0.0	0.0	0.0	0.0

TABLE 96

Primary electron E_0 = 500 MeV.
Secondary electrons E = 5 MeV.

Absorber: al, Z = 13, A = 27,
Radiation length = 26.3 g/sq. cm = 9.74 cm,
Critical energy = 52 MeV.

n \ t	0.5	1.0	1.5	2.0	2.5	3.0	3.5	4.0	4.5	5.0	5.5	6.0	6.5	7.0	7.5	8.0	8.5	9.0	9.5	10.0
0	0.016	0.058	0.101	0.182	0.302	0.407	0.527	0.602	0.687	0.723	0.771	0.835	0.859	0.869	0.907	0.934	0.939	0.941	0.965	0.968
1	0.781	0.514	0.385	0.355	0.308	0.326	0.268	0.222	0.212	0.179	0.152	0.122	0.097	0.092	0.060	0.049	0.042	0.044	0.027	0.025
2	0.107	0.189	0.258	0.256	0.242	0.180	0.144	0.133	0.097	0.075	0.060	0.040	0.038	0.036	0.029	0.017	0.019	0.015	0.006	0.007
3	0.098	0.176	0.157	0.139	0.114	0.082	0.049	0.033	0.017	0.017	0.013	0.003	0.004	0.002	0.002	0.000	0.000	0.000	0.002	0.000
4	0.010	0.055	0.071	0.052	0.027	0.019	0.007	0.008	0.007	0.005	0.002	0.000	0.001	0.001	0.002	0.000	0.000	0.000	0.000	0.000
5	0.006	0.020	0.017	0.011	0.006	0.006	0.003	0.002	0.000	0.001	0.002	0.000	0.000	0.000	0.000	0.000	0.000	0.000	0.000	0.000
6	0.001	0.004	0.009	0.004	0.001	0.000	0.001	0.000	0.000	0.000	0.000	0.000	0.001	0.000	0.000	0.000	0.000	0.000	0.000	0.000
7	0.001	0.002	0.002	0.001	0.000	0.000	0.001	0.000	0.000	0.000	0.000	0.000	0.000	0.000	0.000	0.000	0.000	0.000	0.000	0.000
≥8	0.000	0.002	0.000	0.000	0.000	0.000	0.000	0.000	0.000	0.000	0.000	0.000	0.000	0.000	0.000	0.000	0.000	0.000	0.000	0.000
MEAN	1.35	1.75	1.81	1.58	1.28	0.98	0.77	0.63	0.49	0.41	0.33	0.21	0.20	0.17	0.13	0.08	0.08	0.07	0.05	0.04
VAR	0.6	1.4	1.5	1.4	1.3	1.1	1.0	0.8	0.6	0.6	0.5	0.3	0.3	0.2	0.2	0.1	0.1	0.1	0.1	0.1

TABLE 97

Primary electron E_0 = 1 000 MeV.
Secondary electrons E = 10 MeV.

Absorber: air, Z = 7.4, A = 15.
Radiation length = 43 g/sq. cm.
Critical energy = 98 MeV.

n \ t	0.5	1.0	1.5	2.0	2.5	3.0	3.5	4.0	4.5	5.0	5.5	6.0	6.5	7.0	7.5	8.0	8.5	9.0	9.5	10.0
0	0.011	0.048	0.113	0.173	0.269	0.392	0.486	0.562	0.672	0.717	0.780	0.810	0.849	0.883	0.896	0.925	0.953	0.962	0.955	0.980
1	0.771	0.487	0.354	0.315	0.329	0.322	0.274	0.242	0.202	0.177	0.151	0.134	0.105	0.071	0.073	0.048	0.035	0.023	0.033	0.014
2	0.092	0.204	0.264	0.259	0.239	0.184	0.177	0.140	0.100	0.091	0.056	0.058	0.038	0.038	0.024	0.025	0.012	0.015	0.012	0.006
3	0.108	0.176	0.169	0.170	0.111	0.082	0.047	0.042	0.017	0.011	0.010	0.007	0.005	0.007	0.005	0.002	0.000	0.000	0.000	0.000
4	0.012	0.057	0.060	0.058	0.037	0.028	0.012	0.012	0.008	0.004	0.002	0.001	0.003	0.000	0.002	0.000	0.000	0.000	0.000	0.000
5	0.004	0.020	0.033	0.017	0.012	0.008	0.002	0.001	0.001	0.000	0.001	0.000	0.000	0.001	0.000	0.000	0.000	0.000	0.000	0.000
6	0.002	0.006	0.006	0.004	0.003	0.004	0.002	0.001	0.000	0.000	0.000	0.000	0.000	0.000	0.000	0.000	0.000	0.000	0.000	0.000
7	0.000	0.001	0.001	0.003	0.000	0.000	0.000	0.000	0.000	0.000	0.000	0.000	0.000	0.000	0.000	0.000	0.000	0.000	0.000	0.000
⩾8	0.000	0.001	0.000	0.001	0.000	0.000	0.000	0.000	0.000	0.000	0.000	0.000	0.000	0.000	0.000	0.000	0.000	0.000	0.000	0.000
MEAN	1.36	1.80	1.84	1.71	1.37	1.05	0.84	0.71	0.49	0.41	0.31	0.27	0.21	0.17	0.14	0.10	0.06	0.05	0.06	0.03
VAR	0.6	1.4	1.6	1.7	1.4	1.3	1.0	0.9	0.7	0.5	0.4	0.4	0.3	0.3	0.2	0.2	0.1	0.1	0.1	0.0

TABLE 98

Primary electron E_0 = 1 000 MeV.
Secondary electrons E = 10 MeV.

Absorber: al, Z = 13, A = 27,
Radiation length = 26.3 g/sq. cm = 9.74 cm.
Critical energy = 52 MeV.

n \ t	0.5	1.0	1.5	2.0	2.5	3.0	3.5	4.0	4.5	5.0	5.5	6.0	6.5	7.0	7.5	8.0	8.5	9.0	9.5	10.0
0	0.009	0.039	0.056	0.070	0.109	0.157	0.228	0.307	0.412	0.515	0.601	0.656	0.699	0.772	0.807	0.843	0.878	0.898	0.924	0.948
1	0.765	0.443	0.292	0.234	0.239	0.242	0.276	0.258	0.286	0.263	0.231	0.210	0.197	0.139	0.136	0.112	0.083	0.073	0.052	0.039
2	0.073	0.208	0.211	0.244	0.238	0.291	0.237	0.238	0.186	0.150	0.128	0.094	0.066	0.072	0.046	0.037	0.033	0.026	0.021	0.012
3	0.128	0.178	0.219	0.221	0.185	0.186	0.154	0.125	0.080	0.053	0.026	0.030	0.029	0.013	0.010	0.005	0.005	0.001	0.003	0.001
4	0.017	0.080	0.128	0.126	0.129	0.076	0.072	0.055	0.027	0.017	0.012	0.008	0.007	0.002	0.000	0.003	0.001	0.002	0.000	0.000
5	0.008	0.039	0.063	0.067	0.065	0.039	0.030	0.012	0.006	0.002	0.001	0.002	0.001	0.001	0.001	0.000	0.000	0.000	0.000	0.000
6	0.000	0.009	0.020	0.028	0.027	0.006	0.003	0.005	0.003	0.000	0.001	0.000	0.001	0.001	0.000	0.000	0.000	0.000	0.000	0.000
7	0.000	0.003	0.007	0.006	0.005	0.003	0.000	0.000	0.000	0.000	0.000	0.000	0.000	0.000	0.000	0.000	0.000	0.000	0.000	0.000
8	0.000	0.001	0.002	0.004	0.002	0.000	0.000	0.000	0.000	0.000	0.000	0.000	0.000	0.000	0.000	0.000	0.000	0.000	0.000	0.000
⩾9	0.000	0.000	0.002	0.000	0.001	0.000	0.000	0.000	0.000	0.000	0.000	0.000	0.000	0.000	0.000	0.000	0.000	0.000	0.000	0.000
MEAN	1.40	1.99	2.40	2.47	2.33	1.94	1.67	1.42	1.05	0.80	0.62	0.53	0.46	0.34	0.28	0.21	0.17	0.14	0.10	0.07
VAR	0.7	1.7	2.3	2.4	2.5	1.9	1.8	1.7	1.3	1.0	0.8	0.8	0.7	0.5	0.4	0.3	0.2	0.2	0.2	0.1

TABLE 99

Primary electron E_0 = 2 000 MeV.
Secondary electrons E = 20 MeV.

Absorber: air, Z = 7.4, A = 15,
Radiation length = 43 g/sq. cm.
Critical energy = 98 MeV.

n \ t	0.5	1.0	1.5	2.0	2.5	3.0	3.5	4.0	4.5	5.0	5.5	6.0	6.5	7.0	7.5	8.0	8.5	9.0	9.5	10.0
0	0.013	0.041	0.067	0.079	0.105	0.147	0.216	0.301	0.375	0.499	0.573	0.655	0.732	0.779	0.812	0.863	0.875	0.927	0.932	0.946
1	0.731	0.414	0.248	0.179	0.201	0.234	0.283	0.288	0.293	0.252	0.234	0.192	0.190	0.156	0.121	0.098	0.086	0.052	0.054	0.041
2	0.106	0.189	0.219	0.261	0.255	0.289	0.236	0.235	0.211	0.157	0.131	0.115	0.063	0.052	0.051	0.030	0.030	0.015	0.011	0.010
3	0.120	0.197	0.223	0.238	0.202	0.163	0.173	0.109	0.079	0.065	0.044	0.030	0.010	0.008	0.011	0.008	0.008	0.006	0.003	0.003
4	0.017	0.083	0.137	0.116	0.135	0.099	0.059	0.052	0.035	0.016	0.015	0.006	0.004	0.005	0.004	0.001	0.000	0.000	0.000	0.000
5	0.012	0.054	0.067	0.084	0.064	0.047	0.020	0.012	0.003	0.010	0.001	0.002	0.001	0.000	0.001	0.000	0.001	0.000	0.000	0.000
6	0.000	0.017	0.023	0.027	0.028	0.016	0.010	0.003	0.003	0.001	0.002	0.000	0.000	0.000	0.000	0.000	0.000	0.000	0.000	0.000
7	0.001	0.004	0.010	0.010	0.009	0.004	0.003	0.000	0.001	0.000	0.000	0.000	0.000	0.000	0.000	0.000	0.000	0.000	0.000	0.000
8	0.000	0.001	0.003	0.006	0.001	0.001	0.000	0.000	0.000	0.000	0.000	0.000	0.000	0.000	0.000	0.000	0.000	0.000	0.000	0.000
9	0.000	0.000	0.002	0.000	0.000	0.000	0.000	0.000	0.000	0.000	0.000	0.000	0.000	0.000	0.000	0.000	0.000	0.000	0.000	0.000
⩾10	0.000	0.000	0.001	0.000	0.000	0.000	0.000	0.000	0.000	0.000	0.000	0.000	0.000	0.000	0.000	0.000	0.000	0.000	0.000	0.000
MEAN	1.44	2.12	2.50	2.58	2.42	2.06	1.69	1.37	1.13	0.88	0.71	0.55	0.37	0.30	0.28	0.19	0.18	0.10	0.09	0.07
VAR	0.8	2.0	2.5	2.5	2.5	2.2	1.9	1.6	1.4	1.2	1.0	0.8	0.5	0.4	0.4	0.3	0.3	0.2	0.1	0.1

TABLE 100

Primary electron E_0 = 2 000 MeV.
Secondary electrons E = 20 MeV.

Absorber: al, Z = 13, A = 27,
Radiation length = 26.3 g/sq. cm = 9.74 cm,
Critical energy = 52 MeV.

n \ t	0.5	1.0	1.5	2.0	2.5	3.0	3.5	4.0	4.5	5.0	5.5	6.0	6.5	7.0	7.5	8.0	8.5	9.0	9.5	10.0
0	0.012	0.023	0.037	0.060	0.059	0.070	0.084	0.133	0.207	0.259	0.342	0.424	0.498	0.592	0.640	0.695	0.767	0.811	0.859	0.877
1	0.726	0.405	0.221	0.150	0.139	0.126	0.159	0.198	0.248	0.252	0.293	0.266	0.261	0.231	0.221	0.186	0.154	0.133	0.095	0.071
2	0.079	0.169	0.169	0.178	0.192	0.230	0.224	0.274	0.252	0.236	0.204	0.180	0.151	0.117	0.089	0.094	0.055	0.041	0.033	0.041
3	0.147	0.215	0.219	0.188	0.214	0.198	0.243	0.194	0.148	0.137	0.086	0.087	0.065	0.039	0.032	0.017	0.013	0.009	0.009	0.008
4	0.021	0.089	0.156	0.178	0.160	0.180	0.162	0.104	0.076	0.074	0.052	0.019	0.021	0.014	0.012	0.005	0.006	0.004	0.003	0.002
5	0.009	0.047	0.087	0.103	0.096	0.094	0.072	0.050	0.036	0.027	0.016	0.011	0.008	0.005	0.004	0.002	0.003	0.001	0.001	0.001
6	0.004	0.025	0.049	0.060	0.057	0.049	0.032	0.024	0.017	0.010	0.005	0.006	0.003	0.001	0.001	0.001	0.001	0.001	0.000	0.000
7	0.001	0.013	0.027	0.035	0.034	0.025	0.014	0.012	0.008	0.003	0.001	0.003	0.002	0.001	0.001	0.000	0.001	0.000	0.000	0.000
8	0.001	0.007	0.015	0.020	0.020	0.013	0.008	0.006	0.004	0.001	0.001	0.002	0.001	0.000	0.000	0.000	0.000	0.000	0.000	0.000
9	0.000	0.004	0.009	0.012	0.012	0.007	0.002	0.003	0.002	0.001	0.000	0.001	0.000	0.000	0.000	0.000	0.000	0.000	0.000	0.000
≥ 10	0.000	0.003	0.011	0.016	0.018	0.008	0.002	0.002	0.002	0.000	0.000	0.001	0.000	0.000	0.000	0.000	0.000	0.000	0.000	0.000
MEAN	1.49	2.34	3.08	3.35	3.33	3.09	2.72	2.32	1.91	1.66	1.29	1.11	0.89	0.68	0.58	0.46	0.36	0.27	0.21	0.19
VAR	1.0	2.8	4.2	4.8	5.0	3.8	2.8	2.9	2.7	2.2	1.7	1.8	1.4	1.0	0.9	0.7	0.6	0.4	0.3	0.3

TABLE 101

Primary electron E_0 = 5 000 MeV.
Secondary electrons E = 50 MeV.

Absorber: air, Z = 7.4, A = 15,
Radiation length = 43 g/sq. cm,
Critical energy = 98 MeV.

n \ t	0.5	1.0	1.5	2.0	2.5	3.0	3.5	4.0	4.5	5.0	5.5	6.0	6.5	7.0	7.5	8.0	8.5	9.0	9.5	10.0
0	0.014	0.026	0.034	0.033	0.039	0.049	0.058	0.094	0.134	0.172	0.257	0.357	0.455	0.529	0.612	0.671	0.735	0.786	0.826	0.871
1	0.702	0.391	0.209	0.115	0.098	0.091	0.135	0.168	0.206	0.231	0.274	0.269	0.270	0.259	0.238	0.209	0.174	0.142	0.128	0.100
2	0.090	0.172	0.168	0.167	0.161	0.176	0.220	0.236	0.237	0.246	0.225	0.196	0.155	0.135	0.097	0.090	0.066	0.056	0.033	0.022
3	0.157	0.198	0.210	0.196	0.183	0.183	0.211	0.198	0.185	0.168	0.139	0.102	0.076	0.038	0.028	0.020	0.017	0.014	0.009	0.007
4	0.021	0.098	0.157	0.181	0.199	0.183	0.158	0.142	0.134	0.103	0.055	0.047	0.026	0.025	0.019	0.004	0.005	0.002	0.003	0.000
5	0.013	0.073	0.101	0.128	0.135	0.143	0.118	0.096	0.063	0.047	0.033	0.016	0.007	0.008	0.004	0.004	0.002	0.000	0.001	0.000
6	0.001	0.026	0.060	0.094	0.101	0.091	0.057	0.040	0.026	0.023	0.016	0.009	0.008	0.003	0.002	0.001	0.001	0.000	0.000	0.000
7	0.001	0.006	0.036	0.049	0.046	0.048	0.025	0.021	0.010	0.007	0.001	0.002	0.003	0.002	0.000	0.000	0.000	0.000	0.000	0.000
8	0.000	0.007	0.016	0.025	0.024	0.021	0.013	0.006	0.001	0.003	0.000	0.002	0.000	0.001	0.000	0.001	0.000	0.000	0.000	0.000
9	0.001	0.003	0.007	0.008	0.008	0.010	0.003	0.000	0.002	0.000	0.000	0.000	0.000	0.000	0.000	0.000	0.000	0.000	0.000	0.000
≥ 10	0.000	0.000	0.002	0.004	0.006	0.005	0.002	0.000	0.002	0.000	0.000	0.000	0.000	0.000	0.000	0.000	0.000	0.000	0.000	0.000
MEAN	1.52	2.37	3.13	3.62	3.69	3.63	3.10	2.71	2.36	2.09	1.63	1.32	1.02	0.82	0.62	0.50	0.39	0.30	0.24	0.17
VAR	1.0	2.6	3.7	4.0	4.0	4.1	3.4	3.0	2.8	2.6	2.1	1.9	1.6	1.3	1.0	0.8	0.6	0.4	0.4	0.2

TABLE 102

Primary electron E_0 = 5 000 MeV.
Secondary electrons E = 50 MeV.

Absorber: al, Z = 13, A = 27,
Radiation length = 26.3 g/sq. cm = 9.74 cm,
Critical energy = 52 MeV.

n \ t	0.5	1.0	1.5	2.0	2.5	3.0	3.5	4.0	4.5	5.0	5.5	6.0	6.5	7.0	7.5	8.0	8.5	9.0	9.5	10.0
0	0.015	0.020	0.024	0.020	0.026	0.020	0.025	0.033	0.054	0.080	0.131	0.196	0.272	0.367	0.452	0.537	0.580	0.643	0.713	0.755
1	0.712	0.347	0.187	0.077	0.049	0.048	0.069	0.085	0.111	0.170	0.221	0.234	0.282	0.283	0.275	0.238	0.253	0.227	0.173	0.169
2	0.099	0.187	0.154	0.141	0.113	0.101	0.108	0.149	0.201	0.231	0.235	0.230	0.198	0.176	0.164	0.141	0.098	0.084	0.083	0.054
3	0.137	0.249	0.200	0.170	0.160	0.156	0.147	0.197	0.200	0.186	0.173	0.171	0.132	0.107	0.064	0.057	0.044	0.025	0.019	0.019
4	0.020	0.092	0.163	0.168	0.168	0.184	0.200	0.181	0.167	0.154	0.130	0.092	0.071	0.041	0.027	0.015	0.018	0.014	0.007	0.001
5	0.013	0.054	0.136	0.162	0.167	0.172	0.165	0.141	0.121	0.085	0.055	0.047	0.027	0.016	0.013	0.007	0.005	0.006	0.001	0.001
6	0.001	0.029	0.067	0.106	0.123	0.137	0.108	0.105	0.084	0.054	0.038	0.019	0.012	0.005	0.002	0.003	0.002	0.000	0.003	0.000
7	0.003	0.017	0.039	0.062	0.099	0.089	0.092	0.053	0.032	0.023	0.007	0.005	0.005	0.004	0.002	0.002	0.000	0.001	0.001	0.001
8	0.000	0.004	0.020	0.035	0.049	0.055	0.047	0.034	0.021	0.013	0.005	0.003	0.000	0.001	0.001	0.000	0.000	0.000	0.000	0.000
9	0.000	0.001	0.006	0.019	0.025	0.026	0.020	0.016	0.004	0.002	0.004	0.002	0.001	0.000	0.000	0.000	0.000	0.000	0.000	0.000
⩾10	0.000	0.000	0.004	0.020	0.021	0.012	0.019	0.006	0.005	0.002	0.001	0.001	0.000	0.000	0.000	0.000	0.000	0.000	0.000	0.000
MEAN	1.49	2.44	3.36	4.22	4.53	4.56	4.41	3.88	3.37	2.86	2.37	2.01	1.61	1.27	1.00	0.82	0.69	0.56	0.45	0.35
VAR	0.9	2.4	3.9	4.9	5.0	4.6	5.0	4.3	3.9	3.5	3.0	2.7	2.2	1.8	1.5	1.3	1.0	0.9	0.8	0.5

TABLE 103

Primary electron E_0 = 10 000 MeV.
Secondary electrons E = 100 MeV.

Absorber: air, Z = 7.4, A = 15,
Radiation length = 43 g/sq. cm,
Critical energy = 98 MeV.

n \ t	0.5	1.0	1.5	2.0	2.5	3.0	3.5	4.0	4.5	5.0	5.5	6.0	6.5	7.0	7.5	8.0	8.5	9.0	9.5	10.0
0	0.012	0.017	0.027	0.021	0.027	0.026	0.024	0.036	0.046	0.073	0.115	0.185	0.241	0.346	0.424	0.530	0.573	0.660	0.722	0.789
1	0.696	0.364	0.192	0.096	0.055	0.049	0.050	0.082	0.097	0.137	0.191	0.245	0.287	0.299	0.298	0.246	0.235	0.207	0.186	0.154
2	0.094	0.175	0.159	0.119	0.123	0.104	0.119	0.148	0.173	0.248	0.226	0.229	0.204	0.180	0.148	0.120	0.115	0.094	0.067	0.035
3	0.156	0.211	0.191	0.160	0.156	0.156	0.173	0.192	0.202	0.198	0.206	0.145	0.138	0.086	0.064	0.053	0.042	0.023	0.019	0.017
4	0.017	0.102	0.146	0.168	0.162	0.170	0.187	0.189	0.177	0.144	0.114	0.098	0.078	0.062	0.041	0.034	0.017	0.011	0.003	0.004
5	0.022	0.076	0.115	0.142	0.158	0.167	0.173	0.134	0.138	0.096	0.069	0.060	0.037	0.015	0.016	0.010	0.013	0.003	0.002	0.000
6	0.002	0.033	0.077	0.124	0.124	0.116	0.107	0.113	0.096	0.056	0.047	0.025	0.008	0.007	0.006	0.002	0.004	0.001	0.001	0.001
7	0.001	0.012	0.051	0.091	0.089	0.105	0.086	0.056	0.042	0.030	0.024	0.010	0.005	0.005	0.001	0.004	0.001	0.001	0.000	0.000
8	0.001	0.006	0.028	0.042	0.052	0.058	0.034	0.035	0.017	0.007	0.008	0.004	0.004	0.000	0.002	0.001	0.000	0.000	0.000	0.000
9	0.000	0.004	0.010	0.023	0.032	0.030	0.030	0.013	0.007	0.006	0.000	0.001	0.000	0.000	0.000	0.000	0.000	0.000	0.000	0.000
⩾10	0.000	0.000	0.004	0.014	0.022	0.019	0.017	0.002	0.005	0.005	0.000	0.000	0.000	0.000	0.000	0.000	0.000	0.000	0.000	0.000
MEAN	1.56	2.50	3.42	4.27	4.52	4.60	4.38	3.87	3.57	2.99	2.58	2.08	1.71	1.32	1.09	0.88	0.76	0.54	0.41	0.30
VAR	1.1	2.7	4.4	5.1	5.4	5.1	4.7	4.1	3.9	3.6	3.2	2.9	2.3	1.9	1.7	1.6	1.3	0.8	0.6	0.5

TABLE 104

Primary electron E_0 = 10 000 MeV.
Secondary electrons E = 100 MeV.

Absorber: al, Z = 13, A = 27,
Radiation length = 26.3 g/sq. cm = 9.74 cm,
Critical energy = 52 MeV.

n \ t	0.5	1.0	1.5	2.0	2.5	3.0	3.5	4.0	4.5	5.0	5.5	6.0	6.5	7.0	7.5	8.0	8.5	9.0	9.5	10.0
0	0.009	0.010	0.015	0.015	0.017	0.017	0.012	0.015	0.025	0.042	0.067	0.111	0.166	0.234	0.318	0.368	0.462	0.554	0.648	0.690
1	0.706	0.335	0.153	0.085	0.042	0.023	0.038	0.038	0.066	0.088	0.131	0.176	0.225	0.240	0.251	0.309	0.294	0.242	0.203	0.200
2	0.090	0.187	0.143	0.109	0.095	0.081	0.084	0.096	0.102	0.147	0.182	0.200	0.226	0.211	0.220	0.179	0.125	0.118	0.086	0.072
3	0.162	0.222	0.173	0.160	0.123	0.129	0.110	0.145	0.159	0.174	0.192	0.205	0.157	0.146	0.117	0.084	0.074	0.054	0.043	0.024
4	0.018	0.106	0.179	0.151	0.145	0.141	0.144	0.175	0.165	0.167	0.167	0.134	0.106	0.081	0.058	0.036	0.026	0.020	0.007	0.010
5	0.010	0.070	0.142	0.155	0.154	0.167	0.165	0.160	0.170	0.144	0.099	0.103	0.070	0.043	0.019	0.013	0.009	0.009	0.010	0.002
6	0.005	0.030	0.084	0.097	0.142	0.133	0.159	0.144	0.130	0.103	0.081	0.043	0.036	0.027	0.013	0.009	0.007	0.001	0.002	0.002
7	0.000	0.021	0.057	0.098	0.118	0.117	0.105	0.098	0.088	0.071	0.036	0.012	0.010	0.014	0.003	0.000	0.003	0.001	0.001	0.000
8	0.000	0.013	0.025	0.049	0.078	0.084	0.076	0.060	0.049	0.030	0.024	0.008	0.000	0.002	0.000	0.001	0.000	0.001	0.000	0.000
9	0.000	0.004	0.017	0.041	0.045	0.056	0.057	0.041	0.024	0.018	0.014	0.006	0.004	0.002	0.001	0.001	0.000	0.000	0.000	0.000
≥10	0.000	0.002	0.012	0.040	0.041	0.052	0.050	0.028	0.022	0.011	0.007	0.002	0.000	0.000	0.000	0.000	0.000	0.000	0.000	0.000
MEAN	1.52	2.64	3.77	4.62	5.11	5.32	5.29	4.86	4.49	3.96	3.36	2.72	2.24	1.93	1.48	1.20	0.98	0.79	0.60	0.48
VAR	0.9	3.1	4.7	6.3	6.1	6.1	6.0	5.2	5.1	4.9	4.5	3.5	3.1	3.0	2.1	1.7	1.5	1.3	1.1	0.8

TABLE 105

Primary electron E_0 = 20 000 MeV.
Secondary electrons E = 200 MeV.

Absorber. air, Z = 7.4, A = 15,
Radiation length = 43 g/sq. cm,
Critical energy = 98 MeV.

n \ t	0.5	1.0	1.5	2.0	2.5	3.0	3.5	4.0	4.5	5.0	5.5	6.0	6.5	7.0	7.5	8.0	8.5	9.0	9.5	10.0
0	0.008	0.023	0.020	0.028	0.020	0.014	0.020	0.021	0.019	0.029	0.058	0.086	0.142	0.217	0.285	0.371	0.456	0.540	0.625	0.698
1	0.700	0.330	0.147	0.060	0.043	0.034	0.031	0.049	0.058	0.080	0.114	0.193	0.217	0.249	0.274	0.274	0.278	0.263	0.215	0.190
2	0.103	0.182	0.136	0.118	0.076	0.053	0.067	0.088	0.110	0.156	0.184	0.200	0.242	0.205	0.206	0.191	0.139	0.117	0.101	0.074
3	0.146	0.201	0.200	0.146	0.102	0.092	0.122	0.145	0.157	0.177	0.216	0.176	0.162	0.149	0.127	0.086	0.070	0.044	0.036	0.017
4	0.029	0.103	0.156	0.144	0.165	0.140	0.154	0.153	0.189	0.176	0.169	0.144	0.103	0.091	0.062	0.054	0.025	0.019	0.010	0.008
5	0.012	0.089	0.130	0.155	0.177	0.181	0.167	0.152	0.156	0.145	0.121	0.094	0.065	0.050	0.028	0.014	0.017	0.009	0.008	0.006
6	0.002	0.035	0.090	0.114	0.126	0.165	0.148	0.145	0.118	0.120	0.065	0.066	0.041	0.029	0.012	0.004	0.009	0.005	0.003	0.003
7	0.000	0.024	0.057	0.100	0.104	0.128	0.123	0.108	0.091	0.059	0.035	0.027	0.019	0.005	0.003	0.003	0.005	0.003	0.002	0.000
8	0.000	0.007	0.025	0.059	0.079	0.081	0.071	0.072	0.049	0.033	0.020	0.007	0.004	0.002	0.000	0.001	0.001	0.000	0.000	0.000
9	0.000	0.005	0.023	0.031	0.050	0.056	0.049	0.083	0.030	0.018	0.014	0.004	0.004	0.003	0.001	0.001	0.000	0.000	0.000	0.001
≥10	0.000	0.001	0.016	0.045	0.068	0.056	0.048	0.034	0.023	0.007	0.004	0.003	0.001	0.000	0.002	0.001	0.000	0.000	0.000	0.000
MEAN	1.53	2.64	3.82	4.71	5.24	5.51	5.26	4.89	4.53	3.99	3.37	2.87	2.38	1.97	1.58	1.27	1.05	0.80	0.64	0.48
VAR	0.9	3.1	5.1	6.5	6.5	5.7	5.9	5.6	5.0	4.5	4.1	3.7	3.3	2.9	2.3	2.0	1.8	1.3	1.1	0.9

TABLE 106

Primary electron E_0 = 20 000 MeV.
Secondary electrons E = 200 MeV.

Absorber: al, Z = 13, A = 27,
Radiation length = 26.3 g/sq. cm = 9.74 cm,
Critical energy = 52 MeV.

n \ t	0.5	1.0	1.5	2.0	2.5	3.0	3.5	4.0	4.5	5.0	5.5	6.0	6.5	7.0	7.5	8.0	8.5	9.0	9.5	10.0
0	0.010	0.020	0.022	0.019	0.018	0.011	0.012	0.010	0.018	0.017	0.034	0.055	0.103	0.154	0.206	0.299	0.372	0.462	0.558	0.629
1	0.735	0.333	0.130	0.066	0.045	0.027	0.014	0.023	0.033	0.047	0.067	0.114	0.161	0.203	0.266	0.285	0.294	0.267	0.233	0.224
2	0.090	0.153	0.127	0.094	0.068	0.080	0.043	0.064	0.074	0.104	0.142	0.164	0.233	0.220	0.221	0.192	0.153	0.142	0.140	0.087
3	0.128	0.241	0.189	0.158	0.092	0.076	0.084	0.096	0.134	0.145	0.167	0.199	0.181	0.191	0.122	0.100	0.100	0.081	0.049	0.035
4	0.018	0.095	0.153	0.121	0.130	0.120	0.119	0.146	0.154	0.171	0.182	0.163	0.135	0.108	0.096	0.068	0.041	0.028	0.013	0.019
5	0.015	0.079	0.124	0.147	0.135	0.126	0.144	0.156	0.153	0.178	0.152	0.133	0.095	0.066	0.046	0.020	0.018	0.010	0.003	0.003
6	0.004	0.042	0.107	0.114	0.129	0.145	0.148	0.149	0.164	0.125	0.108	0.081	0.046	0.034	0.023	0.019	0.016	0.005	0.003	0.002
7	0.000	0.022	0.067	0.110	0.123	0.128	0.136	0.128	0.117	0.095	0.065	0.053	0.027	0.013	0.012	0.009	0.001	0.003	0.000	0.001
8	0.000	0.008	0.037	0.068	0.096	0.106	0.108	0.104	0.074	0.065	0.044	0.022	0.008	0.008	0.006	0.007	0.002	0.000	0.000	0.000
9	0.000	0.005	0.016	0.042	0.078	0.072	0.073	0.070	0.039	0.026	0.024	0.011	0.005	0.001	0.001	0.000	0.002	0.001	0.001	0.000
≥10	0.000	0.002	0.028	0.061	0.086	0.109	0.119	0.054	0.040	0.027	0.015	0.005	0.006	0.002	0.001	0.001	0.001	0.001	0.000	0.000
MEAN	1.47	2.67	4.03	5.00	5.71	5.98	6.20	5.64	5.14	4.72	4.17	3.54	2.82	2.37	1.98	1.59	1.30	1.03	0.75	0.61
VAR	0.9	3.2	5.6	7.3	7.8	7.6	6.9	5.9	5.6	5.1	5.0	4.3	3.8	3.3	3.0	2.7	2.2	1.7	1.1	1.0

TABLE 107

Primary electron E_0 = 50 000 MeV.
Secondary electrons E = 500 MeV.

Absorber: air, Z = 7.4, A = 15,
Radiation length = 43 g/sq. cm,
Critical energy = 98 MeV.

n \ t	0.5	1.0	1.5	2.0	2.5	3.0	3.5	4.0	4.5	5.0	5.5	6.0	6.5	7.0	7.5	8.0	8.5	9.0	9.5	10.0
0	0.006	0.013	0.018	0.012	0.015	0.013	0.012	0.018	0.021	0.015	0.029	0.054	0.094	0.126	0.193	0.270	0.348	0.423	0.504	0.583
1	0.703	0.295	0.123	0.079	0.036	0.033	0.019	0.020	0.029	0.050	0.082	0.121	0.163	0.204	0.245	0.255	0.262	0.264	0.263	0.229
2	0.098	0.193	0.121	0.079	0.068	0.050	0.065	0.052	0.073	0.111	0.117	0.150	0.183	0.211	0.233	0.208	0.178	0.154	0.127	0.108
3	0.149	0.218	0.189	0.148	0.100	0.080	0.075	0.091	0.114	0.139	0.154	0.199	0.162	0.188	0.138	0.132	0.116	0.077	0.053	0.046
4	0.029	0.122	0.183	0.139	0.111	0.109	0.110	0.127	0.129	0.165	0.180	0.148	0.169	0.120	0.094	0.060	0.053	0.041	0.038	0.019
5	0.015	0.083	0.134	0.138	0.152	0.142	0.149	0.163	0.174	0.147	0.137	0.126	0.097	0.074	0.049	0.046	0.025	0.026	0.008	0.006
6	0.000	0.047	0.095	0.120	0.140	0.136	0.145	0.152	0.136	0.124	0.119	0.102	0.065	0.049	0.018	0.017	0.013	0.008	0.005	0.006
7	0.000	0.016	0.057	0.107	0.127	0.125	0.132	0.121	0.127	0.098	0.099	0.051	0.032	0.017	0.019	0.007	0.003	0.004	0.001	0.001
8	0.000	0.008	0.028	0.068	0.089	0.114	0.118	0.096	0.091	0.076	0.034	0.026	0.015	0.006	0.007	0.003	0.000	0.003	0.001	0.002
9	0.000	0.003	0.030	0.060	0.080	0.083	0.068	0.087	0.061	0.037	0.030	0.013	0.015	0.001	0.003	0.002	0.001	0.000	0.000	0.000
≥10	0.000	0.002	0.022	0.050	0.082	0.115	0.107	0.073	0.045	0.038	0.019	0.010	0.005	0.004	0.001	0.000	0.001	0.000	0.000	0.000
MEAN	1.54	2.75	4.03	5.03	5.75	6.15	6.09	5.81	5.36	4.86	4.33	3.64	3.10	2.55	2.08	1.73	1.42	1.20	0.91	0.75
VAR	0.9	3.0	5.3	7.0	7.5	8.0	7.3	6.4	5.9	5.9	5.3	4.8	4.6	3.5	3.2	2.7	2.3	2.1	1.5	1.4

TABLE 108

Primary electron E_0 = 50 000 MeV.
Secondary electrons E = 500 MeV.

Absorber: al, Z = 13, A = 27,
Radiation length = 26.3 g/sq. cm = 9.74 cm,
Critical energy = 52 MeV.

n \ t	0.5	1.0	1.5	2.0	2.5	3.0	3.5	4.0	4.5	5.0	5.5	6.0	6.5	7.0	7.5	8.0	8.5	9.0	9.5	10.0
0	0.009	0.020	0.020	0.010	0.010	0.004	0.006	0.009	0.009	0.008	0.019	0.039	0.069	0.125	0.169	0.254	0.313	0.379	0.467	0.562
1	0.685	0.322	0.134	0.063	0.029	0.013	0.016	0.013	0.017	0.042	0.059	0.098	0.141	0.184	0.244	0.247	0.266	0.277	0.266	0.245
2	0.112	0.181	0.138	0.087	0.069	0.045	0.043	0.038	0.050	0.068	0.119	0.172	0.183	0.189	0.219	0.223	0.198	0.170	0.154	0.117
3	0.136	0.184	0.176	0.153	0.110	0.079	0.081	0.067	0.078	0.131	0.155	0.157	0.188	0.206	0.145	0.117	0.115	0.083	0.059	0.044
4	0.032	0.125	0.150	0.146	0.113	0.114	0.119	0.101	0.125	0.145	0.181	0.173	0.161	0.125	0.106	0.070	0.053	0.054	0.028	0.014
5	0.021	0.073	0.137	0.133	0.112	0.132	0.122	0.138	0.150	0.161	0.139	0.136	0.101	0.071	0.056	0.047	0.032	0.021	0.012	0.008
6	0.003	0.051	0.091	0.113	0.145	0.148	0.128	0.151	0.156	0.148	0.116	0.095	0.071	0.048	0.031	0.023	0.012	0.009	0.008	0.008
7	0.001	0.024	0.062	0.098	0.129	0.127	0.115	0.142	0.121	0.101	0.096	0.060	0.047	0.032	0.013	0.013	0.006	0.002	0.004	0.000
8	0.000	0.011	0.046	0.076	0.099	0.109	0.116	0.129	0.114	0.087	0.053	0.040	0.015	0.012	0.008	0.003	0.003	0.001	0.002	0.001
9	0.001	0.007	0.019	0.060	0.072	0.077	0.102	0.095	0.078	0.052	0.037	0.020	0.015	0.003	0.003	0.003	0.001	0.003	0.000	0.001
≥10	0.000	0.002	0.027	0.061	0.112	0.152	0.152	0.117	0.102	0.057	0.026	0.010	0.009	0.005	0.006	0.000	0.001	0.001	0.000	0.000
MEAN	1.58	2.75	4.04	5.13	5.98	6.46	6.51	6.46	6.11	5.32	4.59	3.89	3.33	2.73	2.25	1.84	1.54	1.30	1.02	0.77
VAR	1.1	3.5	5.9	7.2	8.2	7.5	7.8	6.8	6.8	6.1	5.7	5.0	4.7	4.1	3.6	3.0	2.5	2.3	1.7	1.4

TABLE 109

Primary electron E_0 = 1 000 MeV.
Secondary electrons E = 5 MeV.

Absorber: air, Z = 7.4, A = 15,
Radiation length = 43 g/sq. cm,
Critical energy = 98 MeV.

n \ t	0.5	1.0	1.5	2.0	2.5	3.0	3.5	4.0	4.5	5.0	5.5	6.0	6.5	7.0	7.5	8.0	8.5	9.0	9.5	10.0
0	0.017	0.058	0.074	0.122	0.203	0.328	0.416	0.516	0.589	0.669	0.706	0.778	0.859	0.872	0.895	0.919	0.940	0.952	0.954	0.965
1	0.743	0.481	0.320	0.275	0.279	0.289	0.278	0.272	0.240	0.188	0.186	0.151	0.095	0.081	0.081	0.062	0.046	0.039	0.034	0.027
2	0.096	0.175	0.249	0.255	0.272	0.201	0.194	0.135	0.118	0.109	0.085	0.058	0.039	0.038	0.022	0.018	0.013	0.007	0.011	0.007
3	0.115	0.179	0.188	0.196	0.147	0.116	0.072	0.058	0.042	0.025	0.020	0.012	0.005	0.006	0.001	0.000	0.001	0.001	0.000	0.000
4	0.019	0.060	0.092	0.095	0.068	0.042	0.030	0.016	0.010	0.008	0.002	0.001	0.002	0.003	0.001	0.001	0.000	0.001	0.000	0.001
5	0.010	0.029	0.054	0.044	0.021	0.015	0.007	0.001	0.001	0.001	0.001	0.000	0.000	0.000	0.000	0.000	0.000	0.000	0.001	0.000
6	0.000	0.015	0.015	0.011	0.007	0.008	0.001	0.002	0.000	0.000	0.000	0.000	0.000	0.000	0.000	0.000	0.000	0.000	0.000	0.000
7	0.000	0.002	0.007	0.002	0.003	0.001	0.002	0.000	0.000	0.000	0.000	0.000	0.000	0.000	0.000	0.000	0.000	0.000	0.000	0.000
≥8	0.000	0.001	0.001	0.000	0.000	0.000	0.000	0.000	0.000	0.000	0.000	0.000	0.000	0.000	0.000	0.000	0.000	0.000	0.000	0.000
MEAN	1.41	1.87	2.17	2.05	1.70	1.34	1.06	0.80	0.65	0.52	0.43	0.31	0.20	0.19	0.13	0.10	0.08	0.06	0.06	0.05
VAR	0.7	1.7	2.1	2.0	1.8	1.7	1.4	1.1	0.9	0.7	0.6	0.4	0.3	0.3	0.2	0.1	0.1	0.1	0.1	0.1

TABLE 110

Primary electron E_0 = 1 000 MeV.
Secondary electrons E = 5 MeV.

Absorber: al, Z = 13, A = 27,
Radiation length = 26.3 g/sq. cm = 9.74 cm,
Critical energy = 52 MeV.

n \ t	0.5	1.0	1.5	2.0	2.5	3.0	3.5	4.0	4.5	5.0	5.5	6.0	6.5	7.0	7.5	8.0	8.5	9.0	9.5	10.0
0	0.010	0.025	0.037	0.059	0.076	0.107	0.177	0.262	0.309	0.416	0.488	0.585	0.628	0.703	0.739	0.775	0.823	0.835	0.878	0.914
1	0.729	0.409	0.255	0.181	0.150	0.193	0.256	0.241	0.286	0.260	0.256	0.230	0.213	0.173	0.161	0.165	0.116	0.106	0.084	0.060
2	0.096	0.180	0.207	0.217	0.250	0.242	0.230	0.223	0.216	0.181	0.150	0.113	0.111	0.087	0.076	0.051	0.049	0.048	0.034	0.020
3	0.139	0.209	0.202	0.207	0.211	0.204	0.183	0.142	0.109	0.083	0.068	0.051	0.030	0.022	0.015	0.008	0.012	0.006	0.004	0.006
4	0.014	0.077	0.142	0.150	0.136	0.125	0.099	0.087	0.064	0.037	0.029	0.014	0.016	0.013	0.006	0.001	0.000	0.002	0.002	0.000
5	0.011	0.071	0.084	0.100	0.099	0.091	0.032	0.033	0.021	0.012	0.007	0.006	0.001	0.001	0.002	0.000	0.000	0.002	0.000	0.000
6	0.001	0.013	0.048	0.050	0.045	0.023	0.016	0.010	0.003	0.010	0.001	0.001	0.001	0.001	0.000	0.000	0.000	0.000	0.000	0.000
7	0.000	0.011	0.016	0.022	0.018	0.010	0.005	0.002	0.002	0.001	0.001	0.000	0.000	0.000	0.001	0.000	0.000	0.001	0.000	0.000
8	0.000	0.004	0.005	0.007	0.012	0.004	0.001	0.000	0.000	0.000	0.000	0.000	0.000	0.000	0.000	0.000	0.000	0.000	0.000	0.000
9	0.000	0.001	0.000	0.006	0.003	0.000	0.001	0.000	0.000	0.000	0.000	0.000	0.000	0.000	0.000	0.000	0.000	0.000	0.000	0.000
⩾10	0.000	0.000	0.004	0.001	0.000	0.001	0.000	0.000	0.000	0.000	0.000	0.000	0.000	0.000	0.000	0.000	0.000	0.000	0.000	0.000
MEAN	1.46	2.26	2.74	2.91	2.84	2.50	1.97	1.70	1.40	1.15	0.92	0.70	0.60	0.48	0.40	0.30	0.25	0.25	0.17	0.12
VAR	0.8	2.3	3.0	3.3	3.1	2.7	2.3	2.2	1.8	1.7	1.3	1.1	0.9	0.8	0.6	0.4	0.4	0.4	0.3	0.2

TABLE 111

Primary electron E_0 = 2 000 MeV.
Secondary electrons E = 10 MeV.

Absorber: air, Z = 7.4, A = 15,
Radiation length = 43 g/sq. cm,
Critical energy = 98 MeV.

n \ t	0.5	1.0	1.5	2.0	2.5	3.0	3.5	4.0	4.5	5.0	5.5	6.0	6.5	7.0	7.5	8.0	8.5	9.0	9.5	10.0
0	0.008	0.025	0.053	0.061	0.065	0.101	0.150	0.213	0.305	0.406	0.505	0.569	0.621	0.693	0.753	0.809	0.834	0.865	0.879	0.919
1	0.705	0.363	0.211	0.170	0.167	0.193	0.220	0.242	0.279	0.252	0.237	0.239	0.217	0.195	0.161	0.127	0.111	0.097	0.085	0.061
2	0.111	0.208	0.191	0.200	0.225	0.236	0.254	0.237	0.215	0.210	0.171	0.130	0.106	0.076	0.061	0.043	0.041	0.024	0.029	0.017
3	0.144	0.222	0.223	0.194	0.199	0.200	0.180	0.153	0.107	0.092	0.055	0.047	0.037	0.026	0.015	0.013	0.012	0.008	0.006	0.003
4	0.014	0.086	0.149	0.154	0.166	0.140	0.107	0.088	0.056	0.025	0.027	0.011	0.017	0.004	0.008	0.004	0.001	0.004	0.001	0.000
5	0.012	0.065	0.084	0.105	0.093	0.070	0.049	0.042	0.024	0.010	0.003	0.003	0.001	0.004	0.001	0.003	0.001	0.002	0.000	0.000
6	0.003	0.016	0.049	0.065	0.045	0.033	0.024	0.017	0.008	0.001	0.000	0.001	0.000	0.001	0.001	0.000	0.000	0.000	0.000	0.000
7	0.003	0.007	0.024	0.025	0.024	0.016	0.013	0.005	0.006	0.002	0.002	0.000	0.001	0.001	0.000	0.001	0.000	0.000	0.000	0.000
8	0.000	0.008	0.012	0.017	0.011	0.009	0.002	0.003	0.000	0.001	0.000	0.000	0.000	0.000	0.000	0.000	0.000	0.000	0.000	0.000
9	0.000	0.000	0.003	0.008	0.005	0.000	0.000	0.000	0.000	0.001	0.000	0.000	0.000	0.000	0.000	0.000	0.000	0.000	0.000	0.000
⩾10	0.000	0.000	0.001	0.001	0.000	0.002	0.001	0.000	0.000	0.000	0.000	0.000	0.000	0.000	0.000	0.000	0.000	0.000	0.000	0.000
MEAN	1.51	2.32	2.87	3.08	2.91	2.58	2.20	1.90	1.46	1.14	0.88	0.71	0.62	0.47	0.37	0.29	0.24	0.20	0.17	0.10
VAR	0.9	2.2	3.3	3.7	3.3	3.0	2.7	2.5	2.0	1.6	1.2	1.0	0.9	0.8	0.6	0.5	0.4	0.3	0.2	0.1

TABLE 112

Primary electron E_0 = 2 000 MeV.
Secondary electrons E = 10 MeV.

Absorber: al, Z = 13, A = 27,
Radiation length = 26.3 g/sq.cm = 9.74 cm,
Critical energy = 52 MeV.

n \ t	0.5	1.0	1.5	2.0	2.5	3.0	3.5	4.0	4.5	5.0	5.5	6.0	6.5	7.0	7.5	8.0	8.5	9.0	9.5	10.0
0	0.004	0.017	0.018	0.023	0.030	0.034	0.050	0.065	0.090	0.168	0.224	0.323	0.388	0.449	0.524	0.597	0.666	0.716	0.774	0.783
1	0.721	0.377	0.172	0.095	0.055	0.075	0.092	0.129	0.177	0.196	0.253	0.223	0.255	0.295	0.262	0.229	0.202	0.176	0.132	0.145
2	0.087	0.142	0.165	0.130	0.139	0.141	0.180	0.197	0.237	0.229	0.250	0.219	0.188	0.149	0.144	0.121	0.078	0.073	0.065	0.051
3	0.154	0.227	0.214	0.182	0.181	0.182	0.176	0.209	0.202	0.176	0.135	0.125	0.096	0.064	0.032	0.032	0.035	0.024	0.019	0.012
4	0.015	0.107	0.153	0.188	0.161	0.176	0.170	0.167	0.132	0.106	0.067	0.058	0.041	0.025	0.022	0.010	0.012	0.006	0.008	0.005
5	0.015	0.067	0.121	0.131	0.150	0.146	0.136	0.114	0.072	0.073	0.042	0.027	0.016	0.006	0.008	0.010	0.002	0.003	0.001	0.001
6	0.001	0.035	0.071	0.111	0.130	0.117	0.096	0.065	0.050	0.027	0.014	0.017	0.014	0.007	0.004	0.001	0.003	0.001	0.000	0.003
7	0.002	0.016	0.051	0.061	0.068	0.076	0.057	0.025	0.024	0.014	0.009	0.005	0.001	0.003	0.004	0.000	0.001	0.001	0.000	0.000
8	0.000	0.007	0.015	0.049	0.051	0.025	0.026	0.021	0.007	0.007	0.003	0.003	0.001	0.002	0.000	0.000	0.000	0.000	0.000	0.000
9	0.001	0.003	0.013	0.019	0.024	0.016	0.010	0.008	0.007	0.004	0.003	0.000	0.000	0.000	0.000	0.000	0.001	0.000	0.001	0.000
≥10	0.000	0.002	0.007	0.011	0.011	0.010	0.008	0.000	0.002	0.000	0.000	0.000	0.000	0.000	0.000	0.000	0.000	0.000	0.000	0.000
MEAN	1.52	2.53	3.46	4.08	4.26	4.03	3.69	3.19	2.75	2.32	1.83	1.56	1.26	0.99	0.83	0.66	0.56	0.45	0.37	0.33
VAR	1.0	2.9	4.2	4.8	4.8	4.5	4.5	3.7	3.5	3.3	2.6	2.4	2.0	1.6	1.3	1.0	1.0	0.7	0.7	0.6

TABLE 113

Primary electron E_0 = 10 000 MeV.
Secondary electrons E = 500 MeV.

Absorber: air, Z = 7.4, A = 15,
Radiation length = 43 g/sq. cm,
Critical energy = 98 MeV.

n \ t	0.5	1.0	1.5	2.0	2.5	3.0	3.5	4.0	4.5	5.0	5.5	6.0	6.5	7.0	7.5	8.0	8.5	9.0	9.5	10.0
0	0.004	0.015	0.011	0.011	0.012	0.009	0.016	0.016	0.018	0.020	0.041	0.068	0.133	0.200	0.260	0.319	0.403	0.483	0.565	0.642
1	0.694	0.300	0.132	0.054	0.027	0.025	0.016	0.038	0.035	0.054	0.092	0.140	0.165	0.209	0.222	0.241	0.266	0.256	0.235	0.225
2	0.092	0.135	0.120	0.080	0.054	0.046	0.036	0.051	0.063	0.105	0.126	0.196	0.207	0.205	0.218	0.196	0.163	0.143	0.130	0.086
3	0.156	0.232	0.174	0.118	0.076	0.074	0.079	0.078	0.110	0.150	0.170	0.176	0.173	0.152	0.128	0.111	0.084	0.076	0.048	0.030
4	0.027	0.113	0.178	0.116	0.103	0.103	0.118	0.110	0.168	0.162	0.163	0.155	0.113	0.094	0.083	0.065	0.046	0.025	0.008	0.011
5	0.018	0.092	0.133	0.138	0.137	0.134	0.124	0.146	0.151	0.144	0.156	0.093	0.083	0.066	0.041	0.032	0.025	0.005	0.005	0.002
6	0.004	0.058	0.098	0.144	0.133	0.115	0.119	0.133	0.146	0.117	0.095	0.060	0.065	0.036	0.028	0.017	0.006	0.003	0.004	0.003
7	0.004	0.029	0.063	0.091	0.126	0.126	0.129	0.134	0.115	0.101	0.076	0.049	0.032	0.016	0.012	0.011	0.005	0.007	0.002	0.001
8	0.001	0.014	0.055	0.073	0.101	0.116	0.109	0.092	0.073	0.059	0.045	0.028	0.014	0.015	0.001	0.005	0.001	0.001	0.001	0.000
9	0.000	0.008	0.049	0.064	0.080	0.090	0.102	0.076	0.058	0.047	0.022	0.020	0.007	0.003	0.007	0.001	0.000	0.001	0.002	0.000
10-14	0.000	0.004	0.035	0.109	0.145	0.153	0.141	0.123	0.065	0.040	0.014	0.015	0.008	0.004	0.000	0.002	0.001	0.000	0.000	0.000
≥15	0.000	0.000	0.002	0.002	0.006	0.009	0.011	0.003	0.000	0.001	0.000	0.000	0.000	0.000	0.000	0.000	0.000	0.000	0.000	0.000
MEAN	1.60	2.96	4.39	5.62	6.38	6.58	6.53	6.10	5.39	4.82	4.10	3.41	2.84	2.30	1.90	1.64	1.24	0.98	0.78	0.57
VAR	1.2	3.8	7.0	8.7	9.0	9.1	8.6	8.3	6.3	6.2	5.4	5.3	4.6	4.0	3.2	3.0	2.1	1.7	1.3	0.9

TABLE 114

Primary electron E_0 = 10 000 MeV.
Secondary electrons E = 50 MeV.

Absorber: al, Z = 13, A = 27,
Radiation length = 26.3 g/sq. cm = 9.74 cm,
Critical energy = 52 MeV.

n \ t	0.5	1.0	1.5	2.0	2.5	3.0	3.5	4.0	4.5	5.0	5.5	6.0	6.5	7.0	7.5	8.0	8.5	9.0	9.5	10.0
0	0.003	0.009	0.007	0.013	0.010	0.009	0.008	0.012	0.010	0.014	0.014	0.021	0.037	0.065	0.099	0.163	0.207	0.325	0.403	0.450
1	0.667	0.259	0.108	0.033	0.020	0.016	0.018	0.011	0.012	0.018	0.046	0.051	0.084	0.137	0.176	0.212	0.249	0.253	0.240	0.264
2	0.088	0.153	0.088	0.059	0.037	0.032	0.029	0.025	0.041	0.046	0.058	0.094	0.145	0.192	0.196	0.200	0.218	0.150	0.156	0.143
3	0.174	0.243	0.162	0.108	0.055	0.043	0.047	0.045	0.055	0.080	0.108	0.156	0.177	0.159	0.167	0.159	0.118	0.122	0.100	0.066
4	0.030	0.098	0.136	0.127	0.092	0.064	0.056	0.076	0.085	0.113	0.112	0.147	0.174	0.133	0.114	0.109	0.079	0.058	0.053	0.041
5	0.030	0.111	0.155	0.121	0.110	0.089	0.070	0.082	0.101	0.122	0.150	0.147	0.115	0.115	0.108	0.075	0.058	0.036	0.024	0.012
6	0.003	0.058	0.105	0.120	0.098	0.099	0.106	0.116	0.130	0.130	0.147	0.112	0.077	0.079	0.063	0.031	0.027	0.023	0.007	0.013
7	0.005	0.039	0.085	0.103	0.104	0.119	0.104	0.125	0.125	0.149	0.117	0.109	0.075	0.045	0.037	0.021	0.020	0.018	0.009	0.004
8	0.000	0.021	0.062	0.088	0.117	0.101	0.120	0.130	0.124	0.109	0.088	0.063	0.038	0.027	0.015	0.011	0.014	0.011	0.005	0.005
9	0.000	0.004	0.036	0.077	0.098	0.097	0.101	0.117	0.095	0.079	0.070	0.053	0.033	0.017	0.013	0.011	0.004	0.002	0.003	0.002
10-14	0.000	0.005	0.054	0.142	0.239	0.292	0.309	0.237	0.212	0.137	0.087	0.047	0.045	0.030	0.012	0.007	0.006	0.002	0.000	0.000
≥15	0.000	0.000	0.002	0.009	0.020	0.039	0.032	0.024	0.010	0.003	0.003	0.000	0.000	0.001	0.000	0.001	0.000	0.000	0.000	0.000
MEAN	1.69	3.12	4.77	6.17	7.35	7.98	8.04	7.64	7.12	6.38	5.72	4.95	4.26	3.60	3.08	2.51	2.16	1.72	1.36	1.14
VAR	1.3	4.0	7.4	10.1	11.3	12.6	11.8	10.3	9.3	8.1	7.7	6.5	6.8	6.2	5.2	4.5	4.1	3.7	2.6	2.2

TABLE 115

Primary electron E_0 = 20 000 MeV.
Secondary electrons E = 100 MeV.

Absorber: air, Z = 7.4, A = 15,
Radiation length = 43 g/sq. cm,
Critical energy = 98 MeV.

n \ t	0.5	1.0	1.5	2.0	2.5	3.0	3.5	4.0	4.5	5.0	5.5	6.0	6.5	7.0	7.5	8.0	8.5	9.0	9.5	10.0
0	0.008	0.012	0.009	0.010	0.007	0.006	0.006	0.005	0.007	0.008	0.017	0.025	0.040	0.071	0.111	0.167	0.224	0.316	0.393	0.477
1	0.668	0.244	0.107	0.045	0.020	0.013	0.011	0.011	0.011	0.017	0.020	0.050	0.081	0.141	0.178	0.203	0.240	0.256	0.266	0.249
2	0.089	0.134	0.097	0.065	0.033	0.018	0.011	0.021	0.023	0.040	0.068	0.105	0.134	0.154	0.181	0.209	0.208	0.190	0.162	0.140
3	0.178	0.239	0.146	0.099	0.073	0.045	0.043	0.030	0.036	0.063	0.109	0.121	0.151	0.160	0.147	0.160	0.146	0.109	0.077	0.062
4	0.022	0.141	0.150	0.103	0.083	0.052	0.048	0.060	0.083	0.087	0.119	0.146	0.145	0.147	0.135	0.109	0.086	0.067	0.049	0.028
5	0.023	0.123	0.126	0.121	0.105	0.080	0.064	0.083	0.111	0.125	0.151	0.144	0.152	0.108	0.104	0.063	0.047	0.025	0.028	0.019
6	0.007	0.039	0.108	0.130	0.096	0.099	0.115	0.111	0.111	0.133	0.117	0.115	0.092	0.073	0.057	0.041	0.021	0.017	0.011	0.013
7	0.004	0.033	0.094	0.092	0.118	0.121	0.103	0.124	0.136	0.137	0.099	0.117	0.069	0.061	0.032	0.023	0.015	0.008	0.005	0.008
8	0.001	0.020	0.062	0.098	0.104	0.119	0.110	0.120	0.124	0.129	0.096	0.064	0.053	0.034	0.021	0.011	0.006	0.006	0.006	0.001
9	0.000	0.009	0.038	0.075	0.091	0.093	0.128	0.116	0.102	0.095	0.071	0.043	0.042	0.026	0.019	0.008	0.003	0.001	0.001	0.000
10-14	0.000	0.006	0.062	0.150	0.243	0.300	0.326	0.286	0.242	0.156	0.127	0.068	0.040	0.024	0.015	0.006	0.004	0.005	0.002	0.003
≥15	0.000	0.000	0.001	0.012	0.027	0.064	0.035	0.033	0.014	0.010	0.006	0.002	0.001	0.001	0.000	0.000	0.000	0.000	0.000	0.000
MEAN	1.66	3.18	4.81	6.27	7.45	8.36	8.44	8.06	7.52	6.82	6.01	5.12	4.44	3.70	3.11	2.48	2.02	1.62	1.34	1.10
VAR	1.3	3.9	7.6	10.9	12.3	12.9	11.2	10.2	9.2	8.8	8.9	7.7	7.1	6.4	5.5	4.2	3.4	3.1	2.6	2.4

TABLE 11c

Primary electron E_0 = 20 000 MeV.
Secondary electrons E = 100 MeV.

Absorber: al, Z = 13, A = 27,
Radiation length = 26.3 g/sq. cm = 9.74 cm.
Critical energy = 52 MeV.

n \ t	0.5	1.0	1.5	2.0	2.5	3.0	3.5	4.0	4.5	5.0	5.5	6.0	6.5	7.0	7.5	8.0	8.5	9.0	9.5	10.0
0	0.005	0.005	0.009	0.007	0.008	0.008	0.007	0.004	0.005	0.006	0.006	0.006	0.021	0.021	0.048	0.078	0.137	0.194	0.271	0.353
1	0.656	0.260	0.072	0.024	0.013	0.010	0.008	0.005	0.004	0.008	0.013	0.021	0.039	0.069	0.102	0.151	0.162	0.221	0.259	0.257
2	0.092	0.121	0.093	0.035	0.029	0.024	0.014	0.012	0.013	0.017	0.015	0.037	0.071	0.119	0.151	0.171	0.182	0.197	0.184	0.162
3	0.183	0.232	0.157	0.073	0.041	0.026	0.023	0.024	0.031	0.023	0.039	0.091	0.089	0.144	0.157	0.176	0.165	0.148	0.104	0.101
4	0.027	0.120	0.129	0.103	0.055	0.045	0.034	0.029	0.033	0.041	0.087	0.114	0.153	0.163	0.153	0.146	0.135	0.100	0.081	0.054
5	0.027	0.125	0.130	0.109	0.084	0.060	0.049	0.052	0.051	0.071	0.099	0.109	0.127	0.122	0.141	0.079	0.101	0.047	0.043	0.029
6	0.007	0.064	0.122	0.127	0.084	0.072	0.068	0.061	0.073	0.123	0.141	0.158	0.133	0.118	0.083	0.083	0.045	0.038	0.028	0.017
7	0.004	0.037	0.096	0.124	0.108	0.085	0.070	0.083	0.093	0.099	0.111	0.116	0.127	0.093	0.057	0.049	0.027	0.020	0.014	0.011
8	0.000	0.026	0.067	0.087	0.109	0.097	0.097	0.100	0.127	0.123	0.124	0.095	0.092	0.045	0.048	0.026	0.018	0.013	0.009	0.004
9	0.000	0.009	0.040	0.092	0.091	0.095	0.118	0.122	0.109	0.113	0.119	0.079	0.048	0.037	0.027	0.011	0.013	0.012	0.004	0.001
10-14	0.000	0.011	0.084	0.194	0.312	0.381	0.426	0.416	0.393	0.325	0.223	0.164	0.096	0.066	0.034	0.030	0.014	0.010	0.003	0.001
⩾ 15	0.000	0.000	0.001	0.025	0.066	0.097	0.086	0.092	0.068	0.051	0.023	0.010	0.004	0.003	0.002	0.000	0.001	0.000	0.000	0.000
MEAN	1.70	3.29	5.14	7.01	8.45	9.29	9.66	9.64	9.20	8.59	7.57	6.59	5.71	4.82	4.11	3.48	2.96	2.38	1.88	1.52
VAR	1.3	4.5	8.1	11.0	14.2	15.3	14.1	12.8	11.7	11.4	9.9	9.3	8.6	7.6	6.9	6.3	5.5	4.8	3.7	3.3

TABLE 11f

Primary electron E_0 = 5 000 MeV.
Secondary electrons E = 20 MeV.

Absorber: air, Z = 7.4, A = 15,
Radiation length = 33 g/sq. cm,
Critical energy = 98 MeV.

n \ t	0.5	1.0	1.5	2.0	2.5	3.0	3.5	4.0	4.5	5.0	5.5	6.0	6.5	7.0	7.5	8.0	8.5	9.0	9.5	10.0
0	0.004	0.017	0.028	0.020	0.028	0.036	0.034	0.029	0.056	0.090	0.129	0.172	0.263	0.336	0.396	0.493	0.543	0.646	0.715	0.760
1	0.691	0.324	0.130	0.066	0.044	0.032	0.042	0.059	0.096	0.154	0.200	0.218	0.249	0.245	0.250	0.236	0.254	0.202	0.167	0.141
2	0.098	0.129	0.111	0.115	0.076	0.084	0.100	0.143	0.170	0.190	0.172	0.208	0.194	0.199	0.189	0.151	0.125	0.097	0.077	0.063
3	0.151	0.240	0.189	0.136	0.133	0.120	0.139	0.181	0.171	0.178	0.186	0.173	0.134	0.104	0.076	0.060	0.050	0.035	0.028	0.025
4	0.025	0.103	0.143	0.150	0.145	0.155	0.164	0.168	0.166	0.144	0.136	0.106	0.085	0.056	0.053	0.033	0.017	0.011	0.007	0.007
5	0.023	0.105	0.153	0.126	0.129	0.154	0.160	0.131	0.132	0.109	0.088	0.061	0.047	0.028	0.024	0.015	0.006	0.007	0.004	0.000
6	0.006	0.043	0.102	0.101	0.114	0.129	0.129	0.100	0.092	0.066	0.043	0.042	0.015	0.020	0.008	0.010	0.003	0.001	0.002	0.001
7	0.002	0.025	0.064	0.107	0.125	0.119	0.093	0.077	0.053	0.043	0.022	0.006	0.009	0.003	0.003	0.002	0.002	0.000	0.000	0.000
8	0.000	0.009	0.032	0.086	0.081	0.075	0.051	0.055	0.031	0.014	0.013	0.009	0.001	0.006	0.000	0.000	0.000	0.001	0.000	0.000
9	0.000	0.003	0.021	0.037	0.062	0.046	0.048	0.023	0.021	0.008	0.006	0.001	0.002	0.003	0.001	0.000	0.000	0.000	0.000	0.000
10-14	0.000	0.002	0.026	0.056	0.061	0.050	0.042	0.033	0.012	0.004	0.006	0.004	0.001	0.000	0.000	0.000	0.000	0.000	0.000	0.000
⩾ 15	0.000	0.000	0.001	0.000	0.002	0.000	0.000	0.001	0.000	0.000	0.000	0.000	0.000	0.000	0.000	0.000	0.000	0.000	0.000	0.000
MEAN	1.61	2.79	4.06	4.93	5.28	5.10	4.82	4.37	3.76	3.11	2.71	2.30	1.80	1.54	1.27	1.00	0.78	0.59	0.47	0.38
VAR	1.2	3.3	5.9	7.4	7.4	6.4	6.3	5.9	5.0	4.3	4.1	3.5	2.8	2.7	2.1	1.7	1.2	1.0	0.8	0.6

TABLE 118

Primary electron E_0 = 5 000 MeV.
Secondary electrons E = 20 MeV.

Absorber: al, Z = 13, A = 27,
Radiation length = 26.3 g/sq. cm = 9.74 cm,
Critical energy = 52 MeV.

n \ t	0.5	1.0	1.5	2.0	2.5	3.0	3.5	4.0	4.5	5.0	5.5	6.0	6.5	7.0	7.5	8.0	8.5	9.0	9.5	10.0
0	0.006	0.010	0.011	0.011	0.009	0.012	0.005	0.006	0.009	0.018	0.028	0.059	0.100	0.161	0.198	0.322	0.355	0.438	0.523	0.580
1	0.676	0.293	0.115	0.039	0.021	0.019	0.011	0.024	0.030	0.037	0.074	0.106	0.151	0.193	0.245	0.236	0.257	0.269	0.233	0.225
2	0.080	0.129	0.121	0.063	0.057	0.038	0.045	0.043	0.052	0.091	0.134	0.159	0.182	0.191	0.216	0.185	0.181	0.129	0.138	0.113
3	0.187	0.239	0.165	0.120	0.074	0.057	0.067	0.082	0.091	0.144	0.153	0.185	0.187	0.181	0.140	0.108	0.100	0.075	0.060	0.044
4	0.018	0.113	0.131	0.117	0.111	0.067	0.083	0.109	0.124	0.124	0.172	0.146	0.131	0.111	0.094	0.081	0.045	0.061	0.027	0.017
5	0.027	0.117	0.128	0.157	0.108	0.110	0.120	0.138	0.149	0.153	0.146	0.134	0.097	0.074	0.048	0.032	0.029	0.014	0.010	0.007
6	0.006	0.045	0.106	0.119	0.136	0.131	0.116	0.114	0.164	0.134	0.101	0.085	0.075	0.034	0.027	0.013	0.016	0.009	0.004	0.009
7	0.002	0.028	0.078	0.108	0.126	0.110	0.130	0.147	0.107	0.102	0.079	0.060	0.031	0.030	0.017	0.013	0.011	0.003	0.005	0.002
8	0.000	0.013	0.069	0.099	0.095	0.117	0.110	0.110	0.099	0.081	0.051	0.027	0.021	0.014	0.007	0.006	0.004	0.001	0.000	0.003
9	0.000	0.007	0.036	0.053	0.081	0.102	0.092	0.086	0.070	0.050	0.027	0.023	0.014	0.008	0.004	0.002	0.002	0.001	0.000	0.000
10-14	0.000	0.006	0.039	0.106	0.168	0.225	0.214	0.134	0.101	0.064	0.035	0.016	0.011	0.003	0.004	0.002	0.000	0.000	0.000	0.000
≥ 15	0.000	0.000	0.001	0.008	0.014	0.012	0.007	0.008	0.004	0.002	0.000	0.000	0.000	0.000	0.000	0.000	0.000	0.000	0.000	0.000
MEAN	1.65	3.00	4.53	5.81	6.65	7.22	7.04	6.43	5.97	5.26	4.42	3.76	3.16	2.56	2.13	1.87	1.47	1.16	0.91	0.78
VAR	1.2	3.7	7.1	8.5	10.2	10.1	9.2	8.0	7.4	7.1	6.2	5.5	5.0	4.2	3.6	3.2	2.7	2.1	1.6	1.5

TABLE 119

Primary electron E_0 = 50 000 MeV.
Secondary electrons E = 200 MeV.

Absorber: air, Z = 7.4, A = 15,
Radiation length = 43 g/sq. cm,
Critical energy = 98 MeV.

n \ t	0.5	1.0	1.5	2.0	2.5	3.0	3.5	4.0	4.5	5.0	5.5	6.0	6.5	7.0	7.5	8.0	8.5	9.0	9.5	10.0
0	0.005	0.008	0.009	0.005	0.002	0.004	0.002	0.004	0.003	0.001	0.005	0.004	0.003	0.010	0.018	0.049	0.079	0.114	0.164	0.232
1	0.629	0.229	0.091	0.021	0.019	0.006	0.004	0.005	0.004	0.004	0.002	0.003	0.012	0.028	0.054	0.064	0.122	0.157	0.203	0.209
2	0.090	0.120	0.071	0.042	0.028	0.012	0.013	0.002	0.008	0.014	0.008	0.013	0.026	0.047	0.086	0.119	0.134	0.154	0.188	0.206
3	0.212	0.227	0.129	0.065	0.034	0.027	0.012	0.014	0.007	0.014	0.017	0.022	0.056	0.080	0.104	0.123	0.145	0.172	0.131	0.123
4	0.025	0.139	0.115	0.076	0.048	0.028	0.021	0.018	0.018	0.018	0.022	0.056	0.067	0.100	0.127	0.145	0.145	0.120	0.109	0.086
5	0.027	0.105	0.132	0.111	0.066	0.050	0.023	0.031	0.030	0.031	0.052	0.071	0.101	0.127	0.127	0.112	0.120	0.082	0.076	0.057
6	0.005	0.065	0.106	0.106	0.080	0.048	0.043	0.045	0.043	0.046	0.061	0.118	0.113	0.109	0.118	0.105	0.059	0.066	0.047	0.033
7	0.006	0.049	0.088	0.082	0.086	0.075	0.071	0.051	0.053	0.058	0.092	0.102	0.122	0.127	0.101	0.083	0.070	0.058	0.039	0.027
8	0.000	0.021	0.076	0.116	0.085	0.078	0.065	0.066	0.069	0.092	0.083	0.112	0.118	0.105	0.068	0.068	0.044	0.032	0.017	0.011
9	0.001	0.017	0.053	0.086	0.080	0.071	0.069	0.071	0.074	0.092	0.107	0.105	0.096	0.078	0.058	0.045	0.028	0.022	0.007	0.006
10-14	0.000	0.020	0.115	0.223	0.331	0.393	0.389	0.428	0.477	0.448	0.443	0.319	0.250	0.167	0.125	0.083	0.053	0.021	0.018	0.010
15-19	0.000	0.000	0.015	0.063	0.118	0.171	0.243	0.225	0.179	0.161	0.094	0.068	0.036	0.020	0.014	0.004	0.001	0.002	0.001	0.000
≥ 20	0.000	0.000	0.000	0.004	0.023	0.037	0.045	0.040	0.035	0.021	0.014	0.007	0.001	0.002	0.000	0.000	0.000	0.000	0.000	0.000
MEAN	1.76	3.50	5.63	7.75	9.49	10.86	11.78	11.71	11.51	10.88	10.03	8.84	7.80	6.72	5.78	4.96	4.05	3.40	2.76	2.26
VAR	1.4	5.2	11.3	15.4	20.4	21.3	20.3	18.8	17.0	15.7	13.7	12.9	11.8	11.1	10.7	9.5	8.2	7.0	6.0	4.9

TABLE 120

Primary electron E_0 = 50 000 MeV.
Secondary electrons E = 200 MeV.

Absorber: al, Z = 13, A = 27,
Radiation length = 26.3 g/sq.cm = 9.74 cm,
Critical energy = 52 MeV.

n \ t	0.5	1.0	1.5	2.0	2.5	3.0	3.5	4.0	4.5	5.0	5.5	6.0	6.5	7.0	7.5	8.0	8.5	9.0	9.5	10.0
0	0.002	0.004	0.003	0.001	0.001	0.002	0.003	0.002	0.002	0.002	0.002	0.004	0.004	0.002	0.007	0.019	0.039	0.068	0.121	0.151
1	0.638	0.234	0.059	0.011	0.012	0.005	0.003	0.001	0.001	0.001	0.002	0.001	0.008	0.017	0.034	0.051	0.072	0.110	0.171	0.215
2	0.090	0.125	0.060	0.030	0.013	0.008	0.003	0.004	0.008	0.004	0.001	0.006	0.011	0.029	0.061	0.082	0.124	0.157	0.179	0.194
3	0.187	0.228	0.146	0.056	0.015	0.015	0.010	0.014	0.008	0.007	0.006	0.021	0.035	0.065	0.092	0.130	0.146	0.144	0.135	0.158
4	0.040	0.115	0.119	0.070	0.035	0.013	0.015	0.009	0.006	0.012	0.014	0.015	0.043	0.082	0.108	0.112	0.132	0.121	0.127	0.094
5	0.030	0.115	0.145	0.094	0.045	0.029	0.017	0.017	0.017	0.026	0.032	0.043	0.066	0.085	0.124	0.136	0.135	0.124	0.087	0.062
6	0.006	0.064	0.109	0.109	0.064	0.032	0.028	0.029	0.021	0.029	0.034	0.053	0.068	0.100	0.103	0.103	0.113	0.095	0.063	0.044
7	0.007	0.052	0.092	0.078	0.078	0.054	0.040	0.024	0.027	0.039	0.051	0.075	0.099	0.121	0.102	0.113	0.066	0.059	0.037	0.019
8	0.000	0.028	0.074	0.113	0.070	0.070	0.055	0.028	0.040	0.046	0.064	0.106	0.117	0.110	0.099	0.071	0.057	0.045	0.024	0.018
9	0.000	0.017	0.054	0.076	0.098	0.067	0.059	0.041	0.042	0.060	0.093	0.112	0.105	0.098	0.087	0.063	0.036	0.030	0.016	0.019
10-14	0.000	0.018	0.130	0.295	0.386	0.393	0.373	0.408	0.405	0.449	0.469	0.429	0.363	0.255	0.172	0.109	0.073	0.038	0.037	0.025
15-19	0.000	0.000	0.008	0.065	0.156	0.248	0.307	0.334	0.337	0.272	0.203	0.122	0.071	0.034	0.011	0.011	0.006	0.009	0.003	0.001
⩾20	0.000	0.000	0.001	0.004	0.027	0.064	0.087	0.089	0.086	0.053	0.029	0.013	0.010	0.002	0.000	0.000	0.001	0.000	0.000	0.000
MEAN	1.77	3.52	5.82	8.32	10.48	12.15	13.16	13.54	13.52	12.58	11.58	10.37	9.17	7.72	6.50	5.69	4.81	4.14	3.32	2.77
VAR	1.5	5.2	10.3	15.2	19.0	21.5	22.7	20.7	19.9	17.9	15.0	14.2	13.8	12.0	10.7	10.3	9.3	8.6	7.8	6.4

TABLE 121

Primary electron E_0 = 2 000 MeV.
Secondary electrons E = 5 MeV.

Absorber: air, Z = 7.4, A = 15,
Radiation length = 43 g/sq. cm,
Critical energy = 98 MeV.

n \ t	0.5	1.0	1.5	2.0	2.5	3.0	3.5	4.0	4.5	5.0	5.5	6.0	6.5	7.0	7.5	8.0	8.5	9.0	9.5	10.0
0	0.005	0.024	0.045	0.052	0.056	0.067	0.113	0.163	0.243	0.340	0.421	0.497	0.556	0.632	0.705	0.761	0.791	0.833	0.861	0.899
1	0.685	0.346	0.185	0.142	0.126	0.161	0.180	0.224	0.250	0.238	0.243	0.247	0.230	0.213	0.177	0.154	0.136	0.110	0.087	0.072
2	0.105	0.180	0.175	0.177	0.193	0.208	0.229	0.212	0.227	0.208	0.207	0.160	0.130	0.100	0.082	0.052	0.051	0.041	0.039	0.020
3	0.162	0.237	0.210	0.187	0.189	0.200	0.198	0.173	0.141	0.136	0.073	0.065	0.048	0.034	0.021	0.020	0.017	0.004	0.009	0.007
4	0.022	0.083	0.148	0.146	0.168	0.170	0.135	0.108	0.080	0.049	0.031	0.021	0.028	0.009	0.012	0.008	0.003	0.007	0.004	0.002
5	0.012	0.085	0.116	0.117	0.125	0.085	0.075	0.075	0.031	0.015	0.021	0.007	0.007	0.008	0.002	0.003	0.001	0.003	0.000	0.000
6	0.004	0.021	0.051	0.103	0.063	0.057	0.039	0.024	0.018	0.010	0.002	0.003	0.000	0.002	0.000	0.001	0.001	0.001	0.000	0.000
7	0.005	0.014	0.041	0.037	0.047	0.032	0.019	0.013	0.007	0.002	0.001	0.000	0.001	0.001	0.001	0.000	0.000	0.001	0.000	0.000
8	0.000	0.008	0.020	0.017	0.020	0.015	0.010	0.005	0.003	0.000	0.001	0.000	0.000	0.000	0.000	0.001	0.000	0.000	0.000	0.000
9	0.000	0.001	0.006	0.015	0.011	0.001	0.001	0.002	0.000	0.002	0.000	0.000	0.000	0.000	0.000	0.000	0.000	0.000	0.000	0.000
⩾10	0.000	0.001	0.003	0.007	0.002	0.004	0.001	0.001	0.000	0.000	0.000	0.000	0.000	0.001	0.000	0.000	0.000	0.000	0.000	0.000
MEAN	1.59	2.48	3.17	3.45	3.36	3.02	2.61	2.28	1.78	1.43	1.13	0.90	0.79	0.62	0.47	.0.38	0.31	0.26	0.21	0.14
VAR	1.1	2.6	3.9	4.5	4.1	3.6	3.2	3.1	2.5	2.0	1.7	1.3	1.2	1.1	0.8	0.7	0.5	0.5	0.3	0.2

TABLE 122

Primary electron E_0 = 2 000 MeV.
Secondary electrons E = 5 MeV.

Absorber: al, Z = 13, A = 27,
Radiation length = 26.3 g/sq.cm = 9.74 cm,
Critical energy = 52 MeV.

n \ t	0.5	1.0	1.5	2.0	2.5	3.0	3.5	4.0	4.5	5.0	5.5	6.0	6.5	7.0	7.5	8.0	8.5	9.0	9.5	10.0
0	0.002	0.011	0.016	0.021	0.022	0.024	0.034	0.042	0.060	0.105	0.146	0.220	0.291	0.331	0.404	0.506	0.573	0.618	0.698	0.722
1	0.702	0.354	0.148	0.074	0.048	0.047	0.056	0.069	0.106	0.162	0.203	0.207	0.248	0.289	0.279	0.241	0.234	0.212	0.169	0.160
2	0.081	0.122	0.135	0.100	0.075	0.105	0.115	0.161	0.188	0.187	0.222	0.213	0.192	0.181	0.177	0.149	0.118	0.111	0.088	0.085
3	0.174	0.233	0.200	0.150	0.145	0.132	0.165	0.166	0.200	0.191	0.174	0.161	0.142	0.114	0.073	0.056	0.038	0.027	0.025	0.013
4	0.017	0.111	0.141	0.171	0.171	0.146	0.157	0.179	0.164	0.124	0.117	0.087	0.064	0.046	0.036	0.032	0.019	0.021	0.014	0.013
5	0.020	0.087	0.141	0.146	0.150	0.150	0.146	0.146	0.114	0.098	0.071	0.054	0.032	0.017	0.016	0.008	0.011	0.007	0.002	0.003
6	0.001	0.036	0.083	0.104	0.107	0.140	0.102	0.102	0.077	0.067	0.031	0.030	0.018	0.008	0.006	0.006	0.003	0.001	0.003	0.001
7	0.002	0.023	0.067	0.093	0.117	0.117	0.106	0.058	0.049	0.037	0.023	0.014	0.008	0.006	0.005	0.002	0.002	0.002	0.000	0.002
8	0.000	0.013	0.037	0.059	0.068	0.056	0.058	0.043	0.018	0.018	0.007	0.010	0.004	0.005	0.003	0.000	0.000	0.001	0.000	0.001
9	0.001	0.006	0.016	0.036	0.045	0.035	0.027	0.019	0.014	0.008	0.004	0.002	0.001	0.002	0.001	0.000	0.002	0.000	0.001	0.000
10-14	0.000	0.004	0.015	0.045	0.052	0.047	0.025	0.015	0.008	0.003	0.002	0.002	0.000	0.001	0.000	0.000	0.000	0.000	0.000	0.000
⩾15	0.000	0.000	0.001	0.001	0.000	0.001	0.000	0.000	0.000	0.000	0.000	0.000	0.000	0.000	0.000	0.000	0.000	0.000	0.000	0.000
MEAN	1.58	2.76	3.87	4.71	5.04	4.94	4.56	4.02	3.47	3.01	2.45	2.13	1.68	1.42	1.18	0.93	0.77	0.66	0.51	0.46
VAR	1.1	3.5	5.2	6.5	6.4	6.4	5.9	5.0	4.5	4.4	3.5	3.5	2.7	2.3	2.0	1.5	1.4	1.2	0.9	0.9

TABLE 123

Primary electron E_0 = 20 000 MeV.
Secondary electrons E = 50 MeV.

Absorber: air, Z = 7.4, A = 15,
Radiation length = 43 g/sq. cm,
Critical energy = 98 MeV.

n \ t	0.5	1.0	1.5	2.0	2.5	3.0	3.5	4.0	4.5	5.0	5.5	6.0	6.5	7.0	7.5	8.0	8.5	9.0	9.5	10.0
0	0.003	0.008	0.007	0.006	0.005	0.005	0.004	0.004	0.004	0.003	0.005	0.009	0.010	0.015	0.025	0.059	0.096	0.145	0.199	0.286
1	0.639	0.210	0.069	0.032	0.008	0.001	0.004	0.004	0.001	0.006	0.003	0.009	0.018	0.033	0.073	0.087	0.120	0.176	0.217	0.234
2	0.075	0.100	0.070	0.037	0.027	0.012	0.009	0.008	0.007	0.006	0.014	0.032	0.046	0.080	0.102	0.134	0.162	0.190	0.204	0.171
3	0.206	0.234	0.105	0.070	0.033	0.013	0.013	0.009	0.013	0.015	0.023	0.043	0.065	0.107	0.110	0.157	0.192	0.158	0.137	0.120
4	0.029	0.133	0.121	0.081	0.053	0.024	0.022	0.017	0.018	0.028	0.038	0.056	0.097	0.122	0.148	0.147	0.133	0.113	0.093	0.069
5	0.034	0.123	0.133	0.078	0.055	0.046	0.026	0.032	0.021	0.045	0.069	0.073	0.101	0.105	0.115	0.110	0.100	0.078	0.049	0.045
6	0.004	0.072	0.108	0.102	0.070	0.044	0.043	0.032	0.047	0.050	0.090	0.101	0.117	0.118	0.109	0.089	0.067	0.046	0.030	0.028
7	0.006	0.062	0.093	0.086	0.083	0.070	0.050	0.046	0.053	0.080	0.091	0.101	0.113	0.100	0.093	0.061	0.045	0.034	0.030	0.019
8	0.002	0.019	0.084	0.091	0.084	0.076	0.057	0.062	0.084	0.094	0.092	0.119	0.101	0.091	0.073	0.058	0.037	0.021	0.012	0.014
9	0.002	0.019	0.067	0.086	0.094	0.087	0.071	0.079	0.081	0.077	0.100	0.110	0.086	0.054	0.051	0.033	0.019	0.016	0.013	0.006
10-14	0.000	0.019	0.129	0.273	0.336	0.367	0.437	0.457	0.470	0.438	0.359	0.287	0.208	0.155	0.093	0.063	0.027	0.021	0.016	0.009
15-19	0.000	0.001	0.014	0.049	0.127	0.199	0.215	0.207	0.179	0.143	0.107	0.056	0.032	0.019	0.008	0.002	0.002	0.002	0.000	0.001
⩾20	0.000	0.000	0.000	0.009	0.025	0.056	0.049	0.043	0.022	0.015	0.009	0.004	0.006	0.001	0.000	0.000	0.000	0.000	0.000	0.000
MEAN	1.79	3.67	5.92	7.92	9.80	11.36	11.83	11.75	11.27	10.52	9.56	8.34	7.29	6.21	5.30	4.43	3.56	2.96	2.44	2.01
VAR	1.6	5.3	10.9	17.0	20.7	22.0	20.5	18.8	15.8	18.2	15.7	13.7	13.3	11.6	10.0	8.8	6.7	6.4	5.5	4.9

TABLE 12a

Primary electron E_0 = 20 000 MeV.
Secondary electrons E = 50 MeV.

Absorber: al, Z = 13, A = 27,
Radiation length = 26.3 g/sq. cm = 9.74 cm,
Critical energy = 52 MeV.

n \ t	0.5	1.0	1.5	2.0	2.5	3.0	3.5	4.0	4.5	5.0	5.5	6.0	6.5	7.0	7.5	8.0	8.5	9.0	9.5	10.0
0	0.003	0.001	0.004	0.005	0.005	0.003	0.002	0.003	0.002	0.002	0.003	0.001	0.000	0.002	0.006	0.017	0.024	0.041	0.076	0.154
1	0.615	0.214	0.040	0.014	0.005	0.004	0.006	0.003	0.002	0.002	0.002	0.002	0.006	0.010	0.019	0.039	0.071	0.098	0.136	0.190
2	0.086	0.104	0.056	0.019	0.019	0.012	0.003	0.004	0.003	0.005	0.003	0.006	0.009	0.017	0.041	0.057	0.084	0.127	0.184	0.149
3	0.210	0.215	0.138	0.039	0.018	0.009	0.011	0.001	0.004	0.004	0.010	0.010	0.022	0.042	0.062	0.028	0.114	0.147	0.163	0.163
4	0.028	0.123	0.102	0.063	0.036	0.015	0.009	0.016	0.009	0.012	0.010	0.020	0.026	0.063	0.075	0.108	0.136	0.136	0.110	0.098
5	0.042	0.121	0.116	0.073	0.031	0.028	0.020	0.006	0.015	0.010	0.022	0.025	0.047	0.061	0.101	0.111	0.131	0.101	0.092	0.066
6	0.009	0.088	0.096	0.096	0.056	0.028	0.022	0.016	0.018	0.019	0.021	0.057	0.058	0.094	0.117	0.130	0.109	0.096	0.068	0.052
7	0.007	0.048	0.107	0.089	0.057	0.038	0.029	0.027	0.022	0.028	0.033	0.053	0.064	0.104	0.124	0.100	0.089	0.069	0.054	0.039
8	0.000	0.032	0.089	0.094	0.062	0.042	0.038	0.036	0.034	0.032	0.047	0.065	0.094	0.093	0.103	0.085	0.069	0.062	0.035	0.015
9	0.000	0.013	0.079	0.081	0.077	0.068	0.045	0.042	0.038	0.038	0.066	0.083	0.107	0.100	0.086	0.063	0.053	0.041	0.028	0.013
10-14	0.000	0.030	0.150	0.313	0.369	0.346	0.330	0.319	0.331	0.401	0.441	0.435	0.401	0.336	0.215	0.157	0.098	0.073	0.050	0.036
15-19	0.000	0.001	0.021	0.096	0.196	0.267	0.329	0.362	0.382	0.333	0.278	0.189	0.126	0.067	0.043	0.032	0.021	0.007	0.004	0.004
⩾20	0.000	0.000	0.002	0.018	0.069	0.140	0.156	0.165	0.140	0.114	0.064	0.034	0.020	0.011	0.008	0.003	0.001	0.002	0.000	0.001
MEAN	1.84	3.79	6.40	9.07	11.48	13.38	14.33	14.72	14.59	13.90	12.85	11.43	10.22	8.88	7.61	6.56	5.53	4.77	3.86	3.12
VAR	1.6	5.9	12.2	18.5	27.7	28.5	27.6	25.5	23.3	20.8	20.0	17.5	16.0	15.4	14.6	13.9	11.4	10.8	9.0	8.3

TABLE 12b

Primary electron E_0 = 5 000 MeV.
Secondary electrons E = 10 MeV.

Absorber: air, Z = 7.4, A = 15,
Radiation length = 43 g/sq. cm,
Critical energy = 98 MeV.

n \ t	0.5	1.0	1.5	2.0	2.5	3.0	3.5	4.0	4.5	5.0	5.5	6.0	6.5	7.0	7.5	8.0	8.5	9.0	9.5	10.0
0	0.002	0.013	0.025	0.018	0.020	0.025	0.023	0.019	0.030	0.054	0.077	0.107	0.171	0.231	0.301	0.406	0.461	0.547	0.622	0.670
1	0.664	0.289	0.109	0.045	0.035	0.026	0.026	0.036	0.067	0.098	0.141	0.161	0.221	0.214	0.224	0.223	0.244	0.235	0.200	0.186
2	0.095	0.122	0.099	0.093	0.052	0.046	0.065	0.083	0.107	0.130	0.147	0.199	0.186	0.227	0.214	0.176	0.162	0.119	0.107	0.089
3	0.170	0.238	0.154	0.112	0.088	0.092	0.087	0.125	0.136	0.167	0.177	0.163	0.160	0.128	0.116	0.086	0.068	0.054	0.043	0.035
4	0.025	0.106	0.152	0.124	0.140	0.116	0.123	0.157	0.140	0.147	0.156	0.144	0.104	0.094	0.062	0.050	0.032	0.030	0.019	0.012
5	0.030	0.118	0.124	0.119	0.098	0.133	0.134	0.120	0.147	0.132	0.122	0.099	0.081	0.038	0.045	0.031	0.017	0.009	0.005	0.004
6	0.009	0.068	0.114	0.116	0.120	0.126	0.155	0.118	0.124	0.098	0.072	0.051	0.041	0.033	0.021	0.013	0.008	0.003	0.004	0.003
7	0.005	0.031	0.089	0.105	0.113	0.117	0.117	0.115	0.104	0.076	0.037	0.036	0.017	0.016	0.010	0.009	0.004	0.002	0.000	0.001
8	0.000	0.012	0.053	0.095	0.096	0.101	0.083	0.084	0.060	0.050	0.031	0.024	0.012	0.007	0.004	0.005	0.002	0.000	0.000	0.000
9	0.000	0.009	0.029	0.057	0.081	0.082	0.071	0.060	0.040	0.028	0.018	0.005	0.003	0.005	0.003	0.000	0.002	0.000	0.000	0.000
10-14	0.000	0.004	0.051	0.109	0.148	0.132	0.112	0.080	0.044	0.020	0.022	0.011	0.004	0.007	0.000	0.001	0.000	0.001	0.000	0.000
⩾15	0.000	0.000	0.001	0.007	0.009	0.004	0.004	0.003	0.001	0.000	0.000	0.000	0.000	0.000	0.000	0.000	0.000	0.000	0.000	0.000
MEAN	1.70	3.05	4.58	5.67	6.27	6.17	5.94	5.46	4.79	4.09	3.54	3.04	2.42	2.10	1.73	1.38	1.10	0.84	0.67	0.56
VAR	1.4	3.9	7.4	9.3	10.2	8.9	8.5	7.8	6.9	5.9	5.9	4.9	4.0	3.9	3.0	2.7	2.0	1.5	1.1	1.0

TABLE 126

Primary electron E_0 = 5 000 MeV.
Secondary electrons E = 10 MeV.

Absorber: al, Z = 13, A = 27,
Radiation length = 26.3 g/sq. cm = 9.74 cm,
Critical energy = 52 MeV.

n \ t	0.5	1.0	1.5	2.0	2.5	3.0	3.5	4.0	4.5	5.0	5.5	6.0	6.5	7.0	7.5	8.0	8.5	9.0	9.5	10.0
0	0.003	0.007	0.008	0.009	0.003	0.008	0.004	0.003	0.004	0.010	0.009	0.024	0.045	0.069	0.099	0.162	0.213	0.283	0.368	0.429
1	0.646	0.249	0.092	0.027	0.018	0.012	0.005	0.008	0.011	0.012	0.028	0.054	0.078	0.119	0.165	0.206	0.236	0.259	0.244	0.260
2	0.085	0.122	0.091	0.045	0.030	0.022	0.016	0.027	0.022	0.031	0.055	0.077	0.127	0.149	0.196	0.202	0.184	0.187	0.172	0.150
3	0.200	0.239	0.146	0.079	0.062	0.032	0.047	0.033	0.049	0.071	0.091	0.127	0.143	0.181	0.176	0.127	0.139	0.103	0.095	0.073
4	0.019	0.103	0.116	0.107	0.071	0.051	0.043	0.049	0.052	0.081	0.120	0.143	0.138	0.143	0.116	0.125	0.092	0.074	0.064	0.044
5	0.034	0.140	0.124	0.123	0.077	0.068	0.056	0.099	0.070	0.123	0.127	0.147	0.128	0.121	0.087	0.071	0.049	0.043	0.035	0.014
6	0.007	0.052	0.119	0.104	0.093	0.069	0.078	0.104	0.125	0.121	0.142	0.113	0.118	0.075	0.071	0.045	0.037	0.026	0.009	0.011
7	0.006	0.041	0.085	0.111	0.109	0.085	0.090	0.110	0.127	0.124	0.096	0.091	0.083	0.052	0.042	0.023	0.023	0.012	0.004	0.006
8	0.000	0.021	0.068	0.112	0.079	0.106	0.108	0.099	0.123	0.111	0.097	0.079	0.047	0.027	0.022	0.023	0.014	0.007	0.002	0.010
9	0.000	0.013	0.065	0.077	0.117	0.105	0.096	0.110	0.099	0.081	0.097	0.057	0.029	0.028	0.007	0.005	0.006	0.002	0.007	0.002
10-14	0.000	0.013	0.078	0.185	0.281	0.360	0.378	0.307	0.279	0.217	0.128	0.082	0.062	0.036	0.018	0.009	0.007	0.004	0.000	0.001
15-19	0.000	0.000	0.008	0.020	0.054	0.079	0.076	0.051	0.039	0.017	0.009	0.006	0.002	0.000	0.001	0.002	0.000	0.000	0.000	0.000
≥ 20	0.000	0.000	0.000	0.001	0.006	0.003	0.003	0.000	0.000	0.001	0.001	0.000	0.000	0.000	0.000	0.000	0.000	0.000	0.000	0.000
MEAN	1.75	3.35	5.24	6.86	8.16	9.02	9.08	8.40	8.08	7.21	6.33	5.36	4.59	3.81	3.15	2.64	2.26	1.81	1.47	1.24
VAR	1.4	4.6	9.4	11.8	14.6	14.7	13.5	12.5	11.2	10.8	9.7	8.6	7.9	6.7	5.6	5.2	4.5	3.5	2.8	2.7

TABLE 127

Primary electron E_0 = 10 000 MeV.
Secondary electrons E = 20 MeV.

Absorber: air, Z = 7.4, A = 15,
Radiation length = 43 g/sq. cm,
Critical energy = 98 MeV.

n \ t	0.5	1.0	1.5	2.0	2.5	3.0	3.5	4.0	4.5	5.0	5.5	6.0	6.5	7.0	7.5	8.0	8.5	9.0	9.5	10.0
0	0.002	0.006	0.004	0.006	0.010	0.002	0.009	0.011	0.008	0.007	0.012	0.019	0.036	0.077	0.091	0.171	0.215	0.294	0.363	0.450
1	0.651	0.248	0.103	0.028	0.014	0.016	0.010	0.012	0.014	0.009	0.020	0.047	0.080	0.106	0.165	0.176	0.199	0.245	0.248	0.237
2	0.092	0.122	0.081	0.059	0.024	0.024	0.015	0.018	0.022	0.032	0.056	0.074	0.114	0.152	0.157	0.184	0.214	0.183	0.186	0.153
3	0.184	0.221	0.150	0.070	0.044	0.027	0.022	0.028	0.034	0.058	0.089	0.114	0.159	0.155	0.167	0.147	0.146	0.112	0.099	0.095
4	0.023	0.127	0.111	0.082	0.057	0.040	0.047	0.035	0.054	0.080	0.100	0.125	0.130	0.144	0.133	0.117	0.087	0.069	0.058	0.036
5	0.034	0.111	0.124	0.105	0.073	0.079	0.059	0.054	0.079	0.095	0.104	0.134	0.123	0.101	0.098	0.079	0.064	0.052	0.019	0.012
6	0.005	0.059	0.106	0.118	0.095	0.078	0.089	0.097	0.103	0.113	0.132	0.132	0.100	0.090	0.078	0.051	0.047	0.020	0.009	0.009
7	0.007	0.051	0.094	0.102	0.101	0.076	0.081	0.105	0.118	0.128	0.121	0.105	0.074	0.066	0.042	0.023	0.016	0.010	0.006	0.004
8	0.002	0.028	0.061	0.095	0.100	0.115	0.076	0.099	0.115	0.109	0.095	0.071	0.053	0.034	0.030	0.019	0.007	0.010	0.003	0.000
9	0.000	0.013	0.049	0.095	0.102	0.105	0.104	0.107	0.108	0.099	0.090	0.065	0.056	0.034	0.018	0.017	0.007	0.001	0.003	0.002
10-14	0.000	0.014	0.109	0.188	0.309	0.347	0.390	0.354	0.306	0.243	0.170	0.107	0.074	0.041	0.022	0.015	0.008	0.004	0.006	0.002
15-19	0.000	0.000	0.007	0.050	0.067	0.082	0.088	0.074	0.039	0.025	0.011	0.007	0.001	0.000	0.001	0.001	0.000	0.000	0.000	0.000
20-24	0.000	0.000	0.001	0.001	0.004	0.009	0.008	0.006	0.000	0.002	0.000	0.000	0.000	0.000	0.000	0.000	0.000	0.000	0.000	0.000
≥ 25	0.000	0.000	0.000	0.001	0.000	0.000	0.002	0.000	0.000	0.000	0.000	0.000	0.000	0.000	0.000	0.000	0.000	0.000	0.000	0.000
MEAN	1.74	3.43	5.37	7.24	8.55	9.15	9.41	9.08	8.20	7.56	6.59	5.71	4.83	3.99	3.41	2.81	2.28	1.81	1.45	1.16
VAR	1.5	5.1	10.6	14.1	15.1	15.5	15.7	14.6	11.4	11.1	9.8	9.5	9.0	7.6	6.2	6.0	4.3	3.7	2.9	2.2

TABLE 128

Primary electron E_0 = 10 000 MeV.
Secondary electrons E = 20 MeV.

Absorber: al, Z = 13, A = 27,
Radiation length = 26.3 g/sq. cm = 9.74 cm,
Critical energy = 52 MeV.

n \ t	0.5	1.0	1.5	2.0	2.5	3.0	3.5	4.0	4.5	5.0	5.5	6.0	6.5	7.0	7.5	8.0	8.5	9.0	9.5	10.0
0	0.001	0.006	0.005	0.005	0.004	0.004	0.003	0.006	0.005	0.006	0.003	0.005	0.005	0.012	0.017	0.033	0.056	0.118	0.168	0.215
1	0.625	0.211	0.073	0.018	0.010	0.002	0.002	0.004	0.004	0.006	0.001	0.007	0.008	0.028	0.044	0.078	0.116	0.139	0.168	0.230
2	0.076	0.105	0.066	0.027	0.019	0.020	0.011	0.009	0.008	0.010	0.017	0.011	0.027	0.056	0.077	0.137	0.145	0.167	0.182	0.179
3	0.203	0.232	0.116	0.069	0.025	0.019	0.018	0.018	0.008	0.017	0.027	0.038	0.051	0.091	0.128	0.123	0.132	0.154	0.144	0.138
4	0.039	0.108	0.105	0.077	0.034	0.019	0.028	0.012	0.022	0.018	0.028	0.054	0.066	0.112	0.113	0.126	0.146	0.110	0.108	0.087
5	0.042	0.129	0.138	0.100	0.069	0.031	0.028	0.019	0.027	0.044	0.042	0.064	0.100	0.126	0.124	0.118	0.118	0.087	0.076	0.056
6	0.005	0.074	0.107	0.094	0.074	0.056	0.048	0.037	0.032	0.046	0.056	0.091	0.123	0.098	0.106	0.098	0.079	0.073	0.050	0.034
7	0.005	0.065	0.116	0.101	0.071	0.048	0.035	0.044	0.054	0.054	0.060	0.095	0.122	0.120	0.097	0.079	0.066	0.045	0.043	0.022
8	0.004	0.034	0.066	0.077	0.083	0.078	0.046	0.059	0.059	0.087	0.085	0.099	0.110	0.094	0.088	0.061	0.043	0.039	0.016	0.010
9	0.000	0.020	0.059	0.081	0.068	0.075	0.069	0.066	0.079	0.078	0.104	0.112	0.091	0.065	0.057	0.044	0.039	0.030	0.011	0.008
10-14	0.000	0.015	0.130	0.263	0.356	0.363	0.380	0.419	0.436	0.434	0.415	0.346	0.254	0.174	0.136	0.092	0.054	0.035	0.033	0.020
15-19	0.000	0.001	0.018	0.079	0.162	0.216	0.262	0.247	0.217	0.181	0.123	0.074	0.039	0.032	0.014	0.009	0.006	0.002	0.001	0.000
20-24	0.000	0.000	0.001	0.008	0.024	0.059	0.062	0.063	0.044	0.019	0.019	0.003	0.004	0.002	0.000	0.002	0.000	0.001	0.000	0.001
≥25	0.000	0.000	0.000	0.001	0.001	0.010	0.008	0.007	0.005	0.000	0.000	0.001	0.000	0.000	0.000	0.000	0.000	0.000	0.000	0.000
MEAN	1.85	3.73	5.95	8.24	10.25	11.74	12.27	12.19	11.89	10.90	10.23	8.97	7.91	6.71	5.94	5.07	4.31	3.59	2.99	2.38
VAR	1.7	5.6	11.5	17.6	20.8	24.7	23.6	21.5	19.8	17.4	16.1	13.8	12.6	12.9	11.1	11.0	9.0	8.4	7.3	5.8

TABLE 129

Primary electron E_0 = 50 000 MeV.
Secondary electrons E = 100 MeV.

Absorber: air, Z = 7.4, A = 15,
Radiation length = 43 g/sq. cm,
Critical energy = 98 MeV.

n \ t	0.5	1.0	1.5	2.0	2.5	3.0	3.5	4.0	4.5	5.0	5.5	6.0	6.5	7.0	7.5	8.0	8.5	9.0	9.5	10.0
0	0.002	0.004	0.004	0.003	0.002	0.003	0.002	0.001	0.002	0.001	0.001	0.002	0.002	0.001	0.003	0.004	0.010	0.026	0.052	0.073
1	0.596	0.183	0.064	0.014	0.008	0.004	0.002	0.004	0.003	0.001	0.001	0.000	0.000	0.001	0.006	0.012	0.027	0.048	0.071	0.118
2	0.077	0.097	0.046	0.021	0.018	0.007	0.003	0.003	0.001	0.003	0.002	0.004	0.003	0.008	0.010	0.027	0.048	0.090	0.102	0.119
3	0.247	0.231	0.112	0.044	0.014	0.006	0.004	0.003	0.003	0.003	0.002	0.002	0.008	0.009	0.023	0.039	0.058	0.100	0.122	0.140
4	0.023	0.109	0.084	0.050	0.027	0.009	0.011	0.004	0.005	0.006	0.003	0.004	0.013	0.021	0.040	0.066	0.088	0.096	0.103	0.113
5	0.038	0.131	0.100	0.060	0.040	0.023	0.009	0.004	0.005	0.009	0.005	0.004	0.013	0.023	0.051	0.074	0.085	0.096	0.125	0.100
6	0.006	0.084	0.104	0.069	0.033	0.031	0.013	0.014	0.009	0.006	0.008	0.016	0.029	0.038	0.072	0.076	0.109	0.092	0.094	0.079
7	0.008	0.063	0.086	0.080	0.057	0.031	0.019	0.021	0.015	0.013	0.010	0.015	0.025	0.052	0.058	0.089	0.100	0.078	0.084	0.068
8	0.001	0.033	0.089	0.086	0.047	0.028	0.027	0.018	0.007	0.013	0.021	0.034	0.040	0.063	0.084	0.094	0.085	0.087	0.056	0.053
9	0.001	0.027	0.068	0.084	0.078	0.053	0.030	0.020	0.013	0.013	0.027	0.045	0.058	0.086	0.081	0.090	0.060	0.068	0.056	0.041
10-14	0.001	0.037	0.184	0.308	0.307	0.262	0.236	0.212	0.197	0.217	0.267	0.346	0.418	0.411	0.394	0.303	0.251	0.178	0.111	0.079
15-19	0.000	0.001	0.054	0.126	0.224	0.285	0.286	0.280	0.338	0.359	0.366	0.340	0.261	0.211	0.132	0.106	0.067	0.040	0.022	0.013
20-24	0.000	0.000	0.005	0.052	0.103	0.167	0.204	0.257	0.264	0.250	0.227	0.159	0.112	0.063	0.039	0.019	0.012	0.003	0.002	0.004
25-29	0.000	0.000	0.000	0.003	0.038	0.077	0.128	0.118	0.108	0.085	0.060	0.029	0.018	0.013	0.005	0.001	0.000	0.001	0.000	0.000
≥30	0.000	0.000	0.000	0.000	0.004	0.014	0.026	0.041	0.030	0.021	0.000	0.000	0.000	0.000	0.000	0.000	0.000	0.000	0.000	0.000
MEAN	1.89	4.05	6.99	10.01	12.94	15.43	17.26	18.04	18.22	17.58	16.52	15.13	13.56	12.15	10.57	9.18	7.88	6.56	5.44	4.65
VAR	1.7	6.8	17.0	25.4	36.7	40.7	43.0	43.5	35.7	32.1	25.7	24.0	23.8	22.2	22.0	19.6	18.2	16.8	13.7	12.6

TABLE 130

Primary electron E_0 = 50 000 MeV.
Secondary electrons E = 100 MeV.

Absorber: al, Z = 13, A = 27,
Radiation length = 26.3 g/sq. cm = 9.74 cm,
Critical energy = 52 MeV.

n \ t	0.5	1.0	1.5	2.0	2.5	3.0	3.5	4.0	4.5	5.0	5.5	6.0	6.5	7.0	7.5	8.0	8.5	9.0	9.5	10.0
0	0.001	0.002	0.002	0.001	0.000	0.000	0.002	0.001	0.000	0.000	0.000	0.002	0.001	0.000	0.000	0.001	0.002	0.006	0.014	0.024
1	0.610	0.191	0.043	0.007	0.007	0.003	0.001	0.000	0.001	0.001	0.002	0.001	0.000	0.001	0.000	0.003	0.009	0.017	0.039	0.065
2	0.081	0.098	0.038	0.012	0.001	0.006	0.001	0.003	0.003	0.002	0.001	0.001	0.003	0.002	0.004	0.007	0.007	0.037	0.063	0.081
3	0.156	0.198	0.109	0.042	0.009	0.003	0.001	0.000	0.003	0.003	0.001	0.000	0.003	0.006	0.005	0.016	0.030	0.054	0.087	0.112
4	0.043	0.121	0.078	0.039	0.016	0.006	0.003	0.001	0.000	0.002	0.001	0.002	0.001	0.003	0.015	0.028	0.050	0.074	0.102	0.119
5	0.049	0.131	0.111	0.044	0.021	0.011	0.009	0.003	0.002	0.002	0.003	0.003	0.007	0.010	0.024	0.046	0.068	0.081	0.094	0.125
6	0.011	0.088	0.103	0.071	0.026	0.011	0.007	0.009	0.005	0.007	0.004	0.003	0.009	0.016	0.039	0.045	0.090	0.102	0.099	0.113
7	0.009	0.062	0.106	0.071	0.026	0.009	0.008	0.010	0.005	0.005	0.003	0.010	0.007	0.023	0.052	0.061	0.083	0.092	0.079	0.080
8	0.001	0.046	0.088	0.068	0.055	0.024	0.013	0.011	0.010	0.012	0.009	0.006	0.014	0.033	0.048	0.079	0.082	0.096	0.101	0.067
9	0.000	0.021	0.069	0.077	0.044	0.029	0.021	0.009	0.011	0.007	0.008	0.015	0.021	0.036	0.059	0.085	0.090	0.059	0.067	0.041
10-14	0.000	0.040	0.204	0.331	0.335	0.243	0.165	0.102	0.087	0.085	0.114	0.154	0.240	0.326	0.372	0.365	0.329	0.283	0.198	0.126
15-19	0.000	0.002	0.044	0.175	0.259	0.275	0.266	0.233	0.192	0.228	0.308	0.343	0.368	0.359	0.257	0.204	0.124	0.087	0.043	0.040
20-24	0.000	0.000	0.004	0.055	0.137	0.223	0.245	0.299	0.321	0.318	0.339	0.324	0.256	0.146	0.112	0.048	0.032	0.012	0.012	0.006
25-29	0.000	0.000	0.001	0.006	0.050	0.111	0.172	0.198	0.238	0.222	0.207	0.136	0.070	0.039	0.013	0.012	0.004	0.000	0.002	0.001
≥30	0.000	0.000	0.000	0.001	0.014	0.046	0.086	0.121	0.122	0.106	0.000	0.000	0.000	0.000	0.000	0.000	0.000	0.000	0.000	0.000
MEAN	1.91	4.12	7.21	10.92	14.53	17.64	19.93	21.55	22.12	21.76	19.89	18.76	17.04	15.09	13.19	11.58	9.99	8.48	7.15	6.09
VAR	1.9	7.0	15.8	28.8	37.1	45.5	48.7	50.2	45.3	44.6	26.4	26.3	25.8	24.7	24.8	24.0	21.6	19.3	18.1	16.7

TABLE 131

Primary electron E_0 = 5 000 MeV.
Secondary electrons E = 5 MeV.

Absorber: air, Z = 7.4, A = 15,
Radiation length = 43 g/sq. cm,
Critical energy = 98 MeV.

n \ t	0.5	1.0	1.5	2.0	2.5	3.0	3.5	4.0	4.5	5.0	5.5	6.0	6.5	7.0	7.5	8.0	8.5	9.0	9.5	10.0
0	0.003	0.015	0.009	0.015	0.024	0.015	0.011	0.018	0.016	0.027	0.042	0.095	0.137	0.174	0.250	0.325	0.414	0.474	0.557	0.629
1	0.613	0.279	0.125	0.045	0.028	0.020	0.032	0.033	0.043	0.056	0.086	0.110	0.152	0.230	0.232	0.247	0.225	0.226	0.208	0.194
2	0.092	0.122	0.096	0.062	0.045	0.035	0.038	0.053	0.071	0.089	0.131	0.156	0.194	0.186	0.185	0.190	0.147	0.160	0.125	0.114
3	0.202	0.201	0.140	0.107	0.074	0.065	0.071	0.092	0.105	0.136	0.145	0.165	0.156	0.148	0.131	0.114	0.093	0.073	0.065	0.042
4	0.032	0.113	0.130	0.120	0.089	0.089	0.098	0.106	0.144	0.142	0.159	0.135	0.131	0.096	0.089	0.055	0.055	0.042	0.028	0.009
5	0.040	0.115	0.136	0.125	0.112	0.120	0.118	0.126	0.135	0.142	0.120	0.119	0.100	0.073	0.054	0.034	0.038	0.014	0.011	0.011
6	0.008	0.059	0.093	0.103	0.113	0.100	0.128	0.137	0.153	0.114	0.115	0.070	0.056	0.035	0.023	0.018	0.013	0.004	0.003	0.001
7	0.006	0.037	0.086	0.095	0.112	0.113	0.128	0.124	0.095	0.109	0.095	0.061	0.033	0.028	0.020	0.008	0.008	0.003	0.001	0.000
8	0.002	0.032	0.067	0.090	0.101	0.107	0.101	0.114	0.073	0.080	0.042	0.044	0.017	0.011	0.006	0.007	0.004	0.004	0.001	0.000
9	0.002	0.011	0.044	0.080	0.082	0.111	0.092	0.063	0.065	0.039	0.030	0.026	0.009	0.006	0.009	0.000	0.000	0.000	0.000	0.000
10-14	0.000	0.016	0.070	0.139	0.197	0.204	0.177	0.128	0.093	0.064	0.035	0.018	0.015	0.012	0.001	0.001	0.003	0.000	0.001	0.000
15-19	0.000	0.000	0.004	0.018	0.023	0.021	0.008	0.006	0.007	0.002	0.000	0.001	0.000	0.001	0.000	0.001	0.000	0.000	0.000	0.000
≥20	0.000	0.000	0.000	0.001	0.000	0.000	0.000	0.001	0.000	0.000	0.000	0.000	0.000	0.000	0.000	0.000	0.000	0.000	0.000	0.000
MEAN	1.86	3.30	4.86	6.19	6.86	7.12	6.70	6.17	5.65	5.09	4.36	3.69	2.98	2.49	2.04	1.61	1.41	1.08	0.86	0.65
VAR	1.7	5.2	8.5	11.4	12.2	11.0	9.8	9.1	8.5	7.5	6.5	6.5	5.3	5.0	3.8	3.0	3.0	1.9	1.6	1.1

TABLE 132

Primary electron E_0 = 5 000 MeV.
Secondary electrons E = 5 MeV.

Absorber: al, Z = 13, A = 27,
Radiation length = 26.3 g/sq.cm = 9.74 cm,
Critical energy = 52 MeV.

n \ t	0.5	1.0	1.5	2.0	2.5	3.0	3.5	4.0	4.5	5.0	5.5	6.0	6.5	7.0	7.5	8.0	8.5	9.0	9.5	10.0
0	0.002	0.004	0.009	0.007	0.006	0.002	0.003	0.001	0.003	0.005	0.006	0.010	0.022	0.035	0.054	0.095	0.137	0.177	0.251	0.341
1	0.641	0.221	0.087	0.032	0.011	0.006	0.012	0.004	0.007	0.011	0.015	0.020	0.040	0.069	0.102	0.133	0.153	0.181	0.220	0.240
2	0.068	0.112	0.077	0.027	0.027	0.018	0.009	0.009	0.012	0.018	0.036	0.029	0.062	0.127	0.153	0.170	0.197	0.198	0.177	0.157
3	0.207	0.245	0.123	0.064	0.041	0.022	0.023	0.022	0.025	0.031	0.049	0.084	0.105	0.116	0.148	0.155	0.157	0.143	0.132	0.111
4	0.034	0.114	0.121	0 083	0.057	0.041	0.033	0.033	0.039	0.052	0.074	0.099	0.134	0.134	0.132	0.125	0.122	0.117	0.087	0.055
5	0.039	0.139	0.119	0.104	0.063	0.050	0.043	0.045	0.052	0.065	0.088	0.122	0.114	0.119	0.112	0.107	0.079	0.070	0.053	0.042
6	0.003	0.066	0.117	0.097	0.070	0.063	0.072	0.056	0.075	0.091	0.105	0.105	0.120	0.128	0.096	0.071	0.065	0.041	0.027	0.022
7	0.006	0.048	0.096	0.095	0.092	0.075	0.064	0.079	0.092	0.112	0.106	0.118	0.098	0.088	0.065	0.053	0.032	0.029	0.027	0.013
8	0.000	0.019	0.075	0.114	0.081	0.083	0.071	0.078	0.096	0.100	0.105	0.099	0.085	0.068	0.055	0.035	0.026	0.023	0.007	0.008
9	0.000	0.015	0.054	0.084	0.093	0.098	0.082	0.108	0.108	0.105	0.106	0.091	0.074	0.046	0.024	0.021	0.011	0.011	0.011	0.005
10-14	0.000	0.017	0.110	0.244	0.334	0.400	0.403	0.389	0.373	0.347	0.267	0.203	0.135	0.073	0.057	0.032	0.021	0.010	0.008	0.006
15-19	0.000	0.000	0.011	0.045	0.109	0.131	0.156	0.153	0.109	0.057	0.039	0.018	0.011	0.007	0.003	0.003	0.000	0.000	0.000	0.000
20-24	0.000	0.000	0.001	0.003	0.015	0.010	0.029	0.021	0.009	0.006	0.004	0.002	0.000	0.000	0.000	0.000	0.000	0.000	0.000	0.000
25-29	0.000	0.000	0.000	0.001	0.001	0.001	0.000	0.001	0.000	0.000	0.000	0.000	0.000	0.000	0.000	0.000	0.000	0.000	0.000	0.000
⩾30	0.000	0.000	0.000	0.000	0.000	0.000	0.000	0.001	0.000	0.000	0.000	0.000	0.000	0.000	0.000	0.000	0.000	0.000	0.000	0.000
MEAN	1.79	3.54	5.56	7.72	9.26	10.07	10.60	10.57	9.64	8.85	7.86	7.01	6.05	5.06	4.31	3.64	3.05	2.67	2.18	1.71
VAR	1.5	4.9	10.4	15.3	18.6	16.7	19.6	20.1	14.9	13.8	12.7	10.9	10.8	9.0	8.5	7.5	6.0	5.2	4.7	3.9

TABLE 133

Primary electron E_0 = 10 000 MeV.
Secondary electrons E = 10 MeV.

Absorber: air, Z = 7.4, A = 15,
Radiation length = 43 g/sq. cm,
Critical energy = 98 MeV.

n \ t	0.5	1.0	1.5	2.0	2.5	3.0	3.5	4.0	4.5	5.0	5.5	6.0	6.5	7.0	7.5	8.0	8.5	9.0	9.5	10.0
0	0.006	0.003	0.008	0.007	0.006	0.006	0.004	0.005	0.003	0.004	0.006	0.010	0.011	0.032	0.056	0.094	0.153	0.195	0.277	0.342
1	0.598	0.228	0.084	0.027	0.012	0.008	0.004	0.005	0.007	0.008	0.014	0.015	0.042	0.055	0.103	0.138	0.150	0.193	0.230	0.259
2	0.079	0.118	0.080	0.045	0.026	0.014	0.017	0.008	0.005	0.016	0.020	0.041	0.066	0.096	0.128	0.144	0.159	0.183	0.167	0.159
3	0.206	0.198	0.108	0.054	0.036	0.025	0.019	0.024	0.017	0.027	0.035	0.065	0.081	0.106	0.150	0.137	0.143	0.137	0.128	0.099
4	0.053	0.121	0.121	0.087	0.052	0.037	0.029	0.024	0.040	0.036	0.065	0.090	0.112	0.137	0.119	0.151	0.136	0.100	0.072	0.067
5	0.039	0.123	0.116	0.087	0.066	0.046	0.033	0.042	0.034	0.054	0.073	0.099	0.121	0.126	0.120	0.092	0.082	0.077	0.043	0.032
6	0.012	0.064	0.111	0.079	0.064	0.045	0.049	0.053	0.072	0.080	0.087	0.100	0.131	0.108	0.091	0.087	0.064	0.037	0.036	0.021
7	0.004	0.059	0.086	0.106	0.074	0.070	0.059	0.059	0.072	0.098	0.112	0.118	0.086	0.098	0.073	0.060	0.040	0.027	0.022	0.007
8	0.001	0.027	0.068	0.077	0.089	0.080	0.070	0.085	0.084	0.097	0.111	0.104	0.077	0.066	0.041	0.029	0.028	0.017	0.011	0.004
9	0.002	0.030	0.068	0.082	0.088	0.087	0.081	0.077	0.100	0.113	0.092	0.091	0.089	0.059	0.048	0.023	0.014	0.012	0.005	0.005
10-14	0.001	0.026	0.133	0.277	0.349	0.378	0.412	0.425	0.427	0.349	0.318	0.226	0.169	0.107	0.067	0.042	0.034	0.020	0.009	0.005
15-19	0.000	0.003	0.017	0.070	0.120	0.172	0.186	0.169	0.128	0.110	0.064	0.038	0.013	0.010	0.003	0.003	0.007	0.002	0.000	0.000
20-24	0.000	0.000	0.000	0.002	0.016	0.029	0.037	0.023	0.010	0.007	0.003	0.002	0.002	0.000	0.001	0.000	0.000	0.000	0.000	0.000
25-29	0.000	0.000	0.000	0.000	0.002	0.003	0.000	0.001	0.001	0.000	0.001	0.001	0.000	0.000	0.000	0.000	0.000	0.000	0.000	0.000
⩾30	0.000	0.000	0.000	0.000	0.000	0.000	0.000	0.000	0.000	0.000	0.000	0.000	0.000	0.000	0.000	0.000	0.000	0.000	0.000	0.000
MEAN	1.92	3.77	5.85	8.00	9.54	10.64	11.08	10.81	10.27	9.56	8.57	7.49	6.44	5.51	4.51	3.81	3.20	2.66	2.05	1.61
VAR	1.9	6.5	12.2	16.4	19.4	20.9	20.1	18.5	15.4	15.6	14.0	13.4	11.6	10.6	9.4	8.2	8.3	6.3	4.7	3.5

TABLE 134

Primary electron E_0 = 10 000 MeV.
Secondary electrons E = 10 MeV.

Absorber: al, Z = 13, A = 27,
Radiation length = 26.3 g/sq. cm = 9.74 cm,
Critical energy = 52 MeV.

n \ t	0.5	1.0	1.5	2.0	2.5	3.0	3.5	4.0	4.5	5.0	5.5	6.0	6.5	7.0	7.5	8.0	8.5	9.0	9.5	10.0
0	0.000	0.003	0.001	0.002	0.002	0.000	0.001	0.001	0.001	0.000	0.000	0.001	0.002	0.001	0.009	0.006	0.017	0.035	0.081	0.126
1	0.592	0.199	0.062	0.024	0.007	0.003	0.000	0.003	0.000	0.002	0.000	0.001	0.002	0.007	0.015	0.019	0.049	0.080	0.111	0.155
2	0.071	0.095	0.049	0.020	0.013	0.007	0.005	0.003	0.003	0.003	0.005	0.006	0.011	0.016	0.033	0.048	0.071	0.123	0.147	0.173
3	0.233	0.218	0.092	0.050	0.026	0.009	0.009	0.002	0.003	0.007	0.003	0.007	0.019	0.031	0.052	0.094	0.110	0.114	0.150	0.127
4	0.045	0.113	0.103	0.052	0.035	0.021	0.005	0.006	0.005	0.005	0.008	0.019	0.021	0.051	0.070	0.098	0.116	0.138	0.135	0.114
5	0.042	0.133	0.101	0.070	0.037	0.010	0.011	0.013	0.010	0.011	0.029	0.022	0.043	0.067	0.081	0.093	0.121	0.124	0.095	0.092
6	0.008	0.068	0.104	0.072	0.040	0.032	0.028	0.013	0.014	0.017	0.022	0.031	0.044	0.080	0.078	0.121	0.112	0.102	0.072	0.072
7	0.007	0.062	0.096	0.062	0.053	0.043	0.024	0.015	0.015	0.016	0.032	0.045	0.062	0.084	0.105	0.092	0.077	0.083	0.062	0.046
8	0.001	0.035	0.080	0.077	0.066	0.047	0.032	0.035	0.023	0.028	0.035	0.064	0.085	0.103	0.096	0.084	0.081	0.052	0.035	0.023
9	0.001	0.031	0.077	0.068	0.066	0.060	0.047	0.039	0.036	0.044	0.051	0.065	0.082	0.077	0.093	0.078	0.067	0.028	0.031	0.020
10-14	0.000	0.041	0.197	0.334	0.317	0.302	0.277	0.272	0.278	0.333	0.366	0.411	0.417	0.327	0.280	0.224	0.153	0.104	0.072	0.033
15-19	0.000	0.002	0.035	0.128	0.235	0.278	0.332	0.327	0.376	0.329	0.307	0.246	0.169	0.135	0.081	0.041	0.022	0.014	0.007	0.008
20-24	0.000	0.000	0.004	0.035	0.084	0.146	0.162	0.214	0.196	0.165	0.121	0.074	0.038	0.016	0.006	0.004	0.004	0.002	0.001	0.001
25-29	0.000	0.000	0.000	0.006	0.015	0.036	0.058	0.051	0.033	0.034	0.021	0.008	0.005	0.005	0.001	0.000	0.000	0.001	0.001	0.000
≥ 30	0.000	0.000	0.000	0.000	0.004	0.006	0.009	0.006	0.008	0.006	0.000	0.000	0.000	0.000	0.000	0.000	0.000	0.000	0.000	0.000
MEAN	1.94	4.04	6.92	9.79	12.36	14.23	15.48	15.88	15.89	15.20	13.99	12.65	11.20	9.77	8.50	7.29	6.22	5.17	4.27	3.52
VAR	1.8	7.0	15.2	25.0	39.5	33.5	33.4	30.6	26.8	26.9	24.7	22.0	20.5	20.0	17.9	14.3	13.3	12.1	11.0	9.2

TABLE 135

Primary electron E = 20 000 MeV.
Secondary electrons E = 20 MeV.

Absorber: air, Z = 7.4, A = 15
Radiation length = 43 g/sq. cm,
Critical energy = 98 MeV.

n \ t	0.5	1.0	1.5	2.0	2.5	3.0	3.5	4.0	4.5	5.0	5.5	6.0	6.5	7.0	7.5	8.0	8.5	9.0	9.5	10.0
0	0.002	0.003	0.004	0.001	0.002	0.003	0.002	0.005	0.003	0.003	0.002	0.002	0.001	0.001	0.003	0.006	0.021	0.041	0.078	0.123
1	0.581	0.199	0.051	0.021	0.009	0.005	0.002	0.001	0.002	0.000	0.000	0.002	0.003	0.008	0.012	0.028	0.060	0.081	0.118	0.150
2	0.089	0.102	0.047	0.022	0.007	0.009	0.005	0.006	0.002	0.004	0.002	0.002	0.002	0.016	0.021	0.047	0.071	0.126	0.147	0.170
3	0.211	0.192	0.106	0.044	0.021	0.007	0.008	0.006	0.003	0.004	0.001	0.005	0.012	0.019	0.055	0.068	0.108	0.096	0.130	0.135
4	0.043	0.105	0.082	0.054	0.028	0.013	0.007	0.008	0.003	0.005	0.008	0.010	0.028	0.038	0.046	0.090	0.105	0.115	0.118	0.129
5	0.059	0.147	0.119	0.072	0.042	0.022	0.009	0.010	0.014	0.007	0.018	0.019	0.035	0.065	0.079	0.115	0.114	0.113	0.100	0.078
6	0.008	0.072	0.100	0.055	0.035	0.018	0.011	0.009	0.009	0.012	0.016	0.028	0.040	0.061	0.072	0.101	0.104	0.107	0.068	0.067
7	0.007	0.066	0.090	0.072	0.045	0.027	0.020	0.010	0.014	0.019	0.018	0.024	0.069	0.077	0.097	0.097	0.087	0.069	0.061	0.041
8	0.000	0.040	0.069	0.081	0.051	0.037	0.022	0.027	0.037	0.026	0.023	0.046	0.068	0.091	0.100	0.105	0.085	0.071	0.055	0.033
9	0.000	0.028	0.089	0.065	0.065	0.039	0.044	0.022	0.026	0.030	0.048	0.063	0.074	0.091	0.100	0.065	0.047	0.060	0.041	0.021
10-14	0.000	0.044	0.208	0.313	0.324	0.292	0.270	0.259	0.245	0.300	0.400	0.404	0.401	0.342	0.297	0.212	0.171	0.100	0.071	0.048
15-19	0.000	0.002	0.026	0.149	0.239	0.332	0.311	0.326	0.343	0.355	0.315	0.286	0.209	0.153	0.106	0.054	0.026	0.018	0.011	0.004
20-24	0.000	0.000	0.006	0.044	0.111	0.137	0.207	0.220	0.233	0.185	0.125	0.091	0.049	0.035	0.011	0.011	0.001	0.003	0.001	0.001
25-29	0.000	0.000	0.003	0.007	0.017	0.049	0.063	0.081	0.057	0.042	0.024	0.018	0.009	0.003	0.001	0.001	0.000	0.000	0.001	0.000
≥ 30	0.000	0.000	0.000	0.000	0.004	0.010	0.019	0.010	0.009	0.008	0.000	0.000	0.000	0.000	0.000	0.000	0.000	0.000	0.000	0.000
MEAN	1.96	4.13	6.99	10.13	12.81	14.85	16.28	16.61	16.40	15.68	14.46	13.49	11.74	10.41	9.07	7.56	6.31	5.36	4.44	3.58
VAR	1.8	7.5	15.9	26.7	32.7	34.7	36.3	34.0	31.0	28.3	23.1	22.8	21.6	22.0	18.2	17.3	14.7	12.9	12.0	9.5

TABLE 136

Primary electron E = 20 000 MeV.
Secondary electrons E = 20 MeV.

Absorber: al, Z = 13, A = 27,
Radiation length = 26.3 g/sq. cm = 9.74 cm,
Critical energy = 52 MeV.

n \ t	0.5	1.0	1.5	2.0	2.5	3.0	3.5	4.0	4.5	5.0	5.5	6.0	6.5	7.0	7.5	8.0	8.5	9.0	9.5	10.0
0	0.001	0.003	0.001	0.004	0.003	0.005	0.002	0.000	0.002	0.001	0.001	0.001	0.002	0.001	0.001	0.002	0.004	0.004	0.009	0.022
1	0.621	0.172	0.040	0.011	0.007	0.000	0.000	0.002	0.000	0.000	0.001	0.001	0.001	0.001	0.001	0.001	0.003	0.008	0.023	0.044
2	0.080	0.088	0.053	0.019	0.007	0.009	0.003	0.002	0.000	0.002	0.001	0.002	0.000	0.000	0.004	0.002	0.006	0.033	0.063	0.091
3	0.215	0.239	0.077	0.031	0.018	0.005	0.004	0.000	0.000	0.002	0.003	0.002	0.000	[illegible]	0.002	0.012	0.030	0.042	0.079	0.124
4	0.025	0.113	0.081	0.041	0.013	0.007	0.005	0.005	0.005	0.001	0.001	0.000	0.000	0.006	0.012	0.016	0.042	0.062	0.100	0.107
5	0.039	0.118	0.109	0.042	0.025	0.010	0.006	0.004	0.003	0.002	0.003	0.005	0.003	0.008	0.017	0.032	0.061	0.073	0.099	0.105
6	0.005	0.069	0.080	0.066	0.022	0.016	0.009	0.010	0.003	0.002	0.002	0.006	0.004	0.015	0.027	0.052	0.061	0.104	0.082	0.079
7	0.011	0.078	0.108	0.053	0.031	0.016	0.010	0.010	0.004	0.003	0.006	0.001	0.015	0.023	0.032	0.065	0.077	0.070	0.092	0.091
8	0.001	0.037	0.074	0.072	0.030	0.022	0.020	0.014	0.010	0.006	0.002	0.007	0.019	0.028	0.049	0.066	0.064	0.101	0.087	0.079
9	0.001	0.028	0.076	0.064	0.055	0.032	0.011	0.017	0.008	0.005	0.003	0.012	0.022	0.028	0.043	0.072	0.099	0.084	0.066	0.053
10-14	0.001	0.051	0.215	0.325	0.274	0.185	0.128	0.101	0.082	0.105	0.127	0.142	0.199	0.299	0.358	0.359	0.329	0.290	0.196	0.148
15-19	0.000	0.006	0.074	0.168	0.250	0.253	0.220	0.176	0.185	0.187	0.264	0.316	0.358	0.337	0.286	0.223	0.164	0.092	0.086	0.040
20-24	0.000	0.000	0.011	0.078	0.158	0.210	0.251	0.235	0.268	0.291	0.350	0.315	0.284	0.176	0.129	0.074	0.053	0.032	0.016	0.015
25-29	0.000	0.000	0.001	0.022	0.075	0.145	0.184	0.229	0.241	0.239	0.236	0.190	0.093	0.070	0.039	0.024	0.007	0.005	0.002	0.002
⩾30	0.000	0.000	0.000	0.004	0.032	0.085	0.147	0.195	0.189	0.154	0.000	0.000	0.000	0.000	0.000	0.000	0.000	0.000	0.000	0.000
MEAN	1.86	4.26	7.71	11.48	15.31	18.63	21.27	23.01	23.40	22.75	20.31	19.35	17.72	15.86	14.23	12.44	10.87	9.18	7.80	6.53
VAR	1.8	7.9	19.4	34.4	49.4	60.8	64.5	77.4	61.8	49.8	28.3	28.5	26.5	30.0	28.3	27.3	25.6	22.1	21.7	19.5

TABLE 137

Primary electron E_0 = 50 000 MeV.
Secondary electrons E = 50 MeV.

Absorber: air, Z = 7.4, A = 15,
Radiation length = 43 g/sq. cm,
Critical energy = 98 MeV.

n \ t	0.5	1.0	1.5	2.0	2.5	3.0	3.5	4.0	4.5	5.0	5.5	6.0	6.5	7.0	7.5	8.0	8.5	9.0	9.5	10.0
0	0.000	0.000	0.000	0.002	0.001	0.001	0.000	0.001	0.000	0.000	0.000	0.000	0.000	0.000	0.000	0.000	0.000	0.002	0.003	0.022
1	0.574	0.153	0.033	0.007	0.005	0.002	0.002	0.000	0.001	0.001	0.000	0.000	0.000	0.001	0.000	0.001	0.002	0.007	0.013	0.034
2	0.082	0.086	0.026	0.010	0.005	0.003	0.000	0.002	0.002	0.001	0.000	0.001	0.001	0.001	0.003	0.004	0.006	0.021	0.034	0.055
3	0.233	0.201	0.075	0.025	0.006	0.003	0.003	0.002	0.000	0.001	0.002	0.002	0.002	0.000	0.001	0.004	0.012	0.024	0.051	0.062
4	0.041	0.101	0.073	0.029	0.012	0.007	0.003	0.003	0.003	0.001	0.001	0.001	0.004	0.002	0.006	0.011	0.020	0.030	0.075	0.090
5	0.045	0.150	0.092	0.041	0.020	0.010	0.005	0.005	0.003	0.002	0.005	0.003	0.001	0.002	0.005	0.021	0.028	0.049	0.055	0.093
6	0.012	0.087	0.102	0.041	0.019	0.010	0.011	0.003	0.003	0.004	0.002	0.003	0.001	0.003	0.006	0.029	0.036	0.073	0.083	0.083
7	0.010	0.082	0.102	0.070	0.027	0.015	0.008	0.006	0.005	0.004	0.004	0.006	0.004	0.011	0.018	0.029	0.044	0.076	0.078	0.092
8	0.000	0.039	0.082	0.059	0.027	0.013	0.011	0.008	0.006	0.004	0.006	0.002	0.008	0.009	0.027	0.031	0.056	0.060	0.086	0.084
9	0.002	0.037	0.074	0.064	0.039	0.019	0.010	0.009	0.005	0.003	0.001	0.005	0.012	0.018	0.033	0.046	0.058	0.096	0.080	0.072
10-14	0.001	0.059	0.247	0.319	0.255	0.162	0.092	0.065	0.054	0.049	0.054	0.063	0.104	0.179	0.261	0.308	0.346	0.312	0.275	0.204
15-19	0.000	0.004	0.072	0.198	0.258	0.216	0.183	0.133	0.116	0.112	0.141	0.180	0.237	0.293	0.299	0.293	0.226	0.162	0.120	0.081
20-24	0.000	0.001	0.020	0.094	0.177	0.224	0.219	0.206	0.189	0.220	0.237	0.314	0.289	0.276	0.213	0.148	0.105	0.067	0.034	0.025
25-29	0.000	0.000	0.002	0.031	0.093	0.166	0.203	0.224	0.236	0.254	0.290	0.237	0.212	0.132	0.097	0.060	0.034	0.018	0.013	0.002
⩾30	0.000	0.000	0.000	0.010	0.056	0.149	0.250	0.333	0.377	0.344	0.257	0.183	0.125	0.073	0.031	0.015	0.007	0.003	0.000	0.001
MEAN	2.00	4.57	8.26	12.52	16.70	20.66	23.56	25.39	26.52	26.18	25.20	23.69	21.94	19.64	17.26	15.16	13.17	11.23	9.58	8.00
VAR	2.0	8.5	20.3	38.1	54.3	70.0	73.8	68.9	[illegible]	59.1	58.6	51.3	49.7	46.0	38.8	36.3	33.5	30.7	27.6	26.9

TABLE 138

Primary electron E_0 = 50 000 MeV.
Secondary electrons E = 50 MeV.

Absorber: al, Z = 13, A = 27,
Radiation length = 26.3 g/sq. cm = 9.74 cm,
Critical energy = 52 MeV.

n \ t	0.5	1.0	1.5	2.0	2.5	3.0	3.5	4.0	4.5	5.0	5.5	6.0	6.5	7.0	7.5	8.0	8.5	9.0	9.5	10.0
0	0.002	0.004	0.002	0.001	0.000	0.000	0.001	0.000	0.000	0.001	0.001	0.000	0.000	0.000	0.000	0.000	0.000	0.000	0.001	0.002
1	0.570	0.158	0.033	0.008	0.004	0.000	0.002	0.000	0.001	0.000	0.000	0.000	0.000	0.000	0.000	0.000	0.000	0.000	0.001	0.011
2	0.072	0.086	0.033	0.012	0.003	0.003	0.000	0.000	0.000	0.000	0.002	0.000	0.000	0.000	0.001	0.000	0.003	0.003	0.005	0.014
3	0.235	0.193	0.067	0.025	0.008	0.003	0.001	0.001	0.000	0.000	0.000	0.001	0.000	0.000	0.000	0.001	0.003	0.004	0.010	0.028
4	0.033	0.103	0.069	0.025	0.008	0.002	0.002	0.002	0.001	0.000	0.000	0.001	0.001	0.001	0.001	0.001	0.004	0.005	0.017	0.038
5	0.060	0.141	0.091	0.040	0.016	0.006	0.003	0.003	0.001	0.000	0.000	0.001	0.002	0.000	0.001	0.001	0.004	0.011	0.038	0.042
6	0.013	0.088	0.072	0.041	0.020	0.007	0.007	0.001	0.001	0.001	0.002	0.003	0.001	0.002	0.003	0.004	0.005	0.015	0.045	0.062
7	0.010	0.079	0.087	0.050	0.023	0.011	0.005	0.003	0.003	0.001	0.000	0.002	0.001	0.002	0.001	0.004	0.014	0.028	0.040	0.062
8	0.002	0.042	0.093	0.058	0.029	0.014	0.005	0.005	0.004	0.004	0.000	0.000	0.001	0.003	0.006	0.013	0.021	0.041	0.060	0.075
9	0.002	0.049	0.082	0.059	0.031	0.017	0.006	0.003	0.003	0.003	0.003	0.002	0.001	0.002	0.008	0.011	0.025	0.036	0.059	0.066
10-14	0.001	0.068	0.247	0.295	0.206	0.127	0.072	0.034	0.028	0.020	0.016	0.013	0.021	0.032	0.084	0.124	0.210	0.281	0.296	0.318
15-19	0.000	0.009	0.091	0.210	0.229	0.178	0.123	0.079	0.045	0.044	0.035	0.043	0.072	0.117	0.197	0.268	0.280	0.276	0.239	0.177
20-24	0.000	0.000	0.027	0.117	0.192	0.181	0.161	0.135	0.114	0.089	0.108	0.116	0.151	0.221	0.236	0.257	0.228	0.175	0.133	0.064
25-29	0.000	0.000	0.006	0.049	0.126	0.182	0.191	0.160	0.157	0.163	0.167	0.228	0.253	0.277	0.223	0.185	0.117	0.077	0.040	0.031
⩾30	0.000	0.000	0.000	0.010	0.105	0.269	0.421	0.574	0.642	0.674	0.666	0.590	0.496	0.343	0.239	0.131	0.086	0.048	0.016	0.010
MEAN	2.04	4.67	8.66	13.24	18.47	23.36	27.36	30.76	32.56	33.24	38.01	32.92	30.67	27.38	24.33	21.36	19.01	16.66	13.98	11.78
VAR	2.2	9.5	23.9	42.3	68.2	87.5	100.0	98.5	91.7	83.3	229.4	114.6	96.9	74.3	70.1	50.1	57.3	48.4	40.5	36.8

TABLE 139

Primary photon E_0 = 100 MeV.
Secondary electrons E = 50 MeV.

Absorber: air, Z = 7.4, A = 15,
Radiation length = 43 g/sq. cm,
Critical energy = 98 MeV.

n \ t	0.5	1.0	1.5	2.0	2.5	3.0	3.5	4.0	4.5	5.0	5.5	6.0	6.5	7.0	7.5	8.0	8.5	9.0	9.5	10.0
0	0.897	0.939	0.948	0.972	0.980	0.984	0.988	0.983	0.992	0.992	0.997	0.999	0.997	1.000	0.999	0.999	1.000	1.000	0.999	0.999
⩾1	0.103	0.061	0.052	0.028	0.020	0.016	0.012	0.017	0.008	0.008	0.003	0.001	0.003	0.000	0.001	0.001	0.000	0.000	0.001	0.001
MEAN	0.10	0.06	0.05	0.03	0.02	0.02	0.01	0.02	0.01	0.01	0.00	0.00	0.00	0.00	0.00	0.00	0.00	0.00	0.00	0.00
VAR	0.1	0.1	0.0	0.0	0.0	0.0	0.0	0.0	0.0	0.0	0.0	0.0	0.0	0.0	0.0	0.0	0.0	0.0	0.0	0.0

TABLE 140

Primary photon E_0 = 100 MeV.
Secondary electrons E = 50 MeV.

Absorber: al, Z = 13, A = 27,
Radiation length = 26.3 g/sq. cm = 9.74 cm,
Critical energy = 52 MeV.

n \ t	0.5	1.0	1.5	2.0	2.5	3.0	3.5	4.0	4.5	5.0	5.5	6.0	6.5	7.0	7.5	8.0	8.5	9.0	9.5	10.0
0	0.885	0.923	0.937	0.953	0.962	0.969	0.977	0.978	0.988	0.991	0.991	0.994	0.993	0.995	0.997	0.997	0.996	0.999	0.998	1.000
⩾1	0.115	0.077	0.063	0.047	0.038	0.031	0.023	0.022	0.012	0.009	0.009	0.006	0.007	0.005	0.003	0.003	0.004	0.001	0.002	0.000
MEAN	0.12	0.08	0.06	0.05	0.04	0.03	0.02	0.02	0.01	0.01	0.01	0.01	0.01	0.01	0.00	0.00	0.00	0.00	0.00	0.00
VAR	0.1	0.1	0.1	0.0	0.0	0.0	0.0	0.0	0.0	0.0	0.0	0.0	0.0	0.0	0.0	0.0	0.0	0.0	0.0	0.0

TABLE 141

Primary photon E_0 = 200 MeV.
Secondary elecrtons E = 100 MeV.

Absorber: air, Z = 7.4, A = 15,
Radiation length = 43 g/sq. cm,
Critical energy = 98 MeV.

n \ t	0.5	1.0	1.5	2.0	2.5	3.0	3.5	4.0	4.5	5.0	5.5	6.0	6.5	7.0	7.5	8.0	8.5	9.0	9.5	10.0
0	0.868	0.895	0.921	0.944	0.960	0.974	0.978	0.977	0.989	0.995	0.997	0.995	0.999	0.997	0.999	0.999	1.000	0.999	1.000	1.000
⩾1	0.132	0.105	0.079	0.056	0.040	0.026	0.022	0.023	0.011	0.005	0.003	0.005	0.001	0.003	0.001	0.001	0.000	0.001	0.000	0.000
MEAN	0.13	0.11	0.08	0.06	0.04	0.03	0.02	0.02	0.01	0.01	0.00	0.01	0.00	0.00	0.00	0.00	0.00	0.00	0.00	0.00
VAR	0.1	0.1	0.1	0.1	0.0	0.0	0.0	0.0	0.0	0.0	0.0	0.0	0.0	0.0	0.0	0.0	0.0	0.0	0.0	0.0

TABLE 142

Primary photon E_0 = 200 MeV.
Secondary electrons E = 100 MeV.

Absorber: al, Z = 13, A = 27,
Radiation length = 26.3 g/sq. cm = 9.74 cm,
Critical energy = 52 MeV.

n \ t	0.5	1.0	1.5	2.0	2.5	3.0	3.5	4.0	4.5	5.0	5.5	6.0	6.5	7.0	7.5	8.0	8.5	9.0	9.5	10.0
0	0.854	0.869	0.898	0.922	0.943	0.958	0.972	0.969	0.984	0.991	0.996	0.997	0.997	0.997	0.997	0.998	0.997	0.999	0.999	0.999
≥1	0.146	0.131	0.102	0.078	0.057	0.042	0.028	0.031	0.016	0.009	0.004	0.003	0.003	0.003	0.003	0.002	0.003	0.001	0.001	0.001
MEAN	0.15	0.13	0.10	0.08	0.06	0.04	0.03	0.03	0.02	0.01	0.00	0.00	0.00	0.00	0.00	0.00	0.00	0.00	0.00	0.00
VAR	0.1	0.1	0.1	0.1	0.1	0.0	0.0	0.0	0.0	0.0	0.0	0.0	0.0	0.0	0.0	0.0	0.0	0.0	0.0	0.0

TABLE 143

Primary photon E_0 = 1 000 MeV.
Secondary electrons E = 500 MeV.

Absorber: air, Z = 7.4, A = 15,
Radiation length = 43 g/sq. cm,
Critical energy = 98 MeV.

n \ t	0.5	1.0	1.5	2.0	2.5	3.0	3.5	4.0	4.5	5.0	5.5	6.0	6.5	7.0	7.5	8.0	8.5	9.0	9.5	10.0
0	0.791	0.826	0.857	0.898	0.928	0.953	0.958	0.971	0.979	0.988	0.992	0.993	0.997	0.999	0.999	1.000	0.999	1.000	1.000	1.000
≥1	0.209	0.174	0.143	0.102	0.072	0.047	0.042	0.029	0.021	0.012	0.008	0.007	0.003	0.001	0.001	0.000	0.001	0.000	0.000	0.000
MEAN	0.21	0.17	0.14	0.10	0.07	0.05	0.04	0.03	0.02	0.01	0.01	0.01	0.00	0.00	0.00	0.00	0.00	0.00	0.00	0.00
VAR	0.2	0.1	0.1	0.1	0.1	0.0	0.0	0.0	0.0	0.0	0.0	0.0	0.0	0.0	0.0	0.0	0.0	0.0	0.0	0.0

TABLE 144

Primary photon E_0 = 1 000 MeV.
Secondary electrons E = 500 MeV.

Absorber: al, Z = 13, A = 27,
Radiation length = 26.3 g/sq. cm = 9.74 cm,
Critical energy = 52 MeV.

n \ t	0.5	1.0	1.5	2.0	2.5	3.0	3.5	4.0	4.5	5.0	5.5	6.0	6.5	7.0	7.5	8.0	8.5	9.0	9.5	10.0
0	0.819	0.826	0.846	0.874	0.914	0.942	0.954	0.976	0.979	0.985	0.989	0.992	0.996	0.993	0.995	0.997	0.998	0.999	0.997	0.998
≥1	0.181	0.174	0.154	0.126	0.086	0.058	0.046	0.024	0.021	0.015	0.011	0.008	0.004	0.007	0.005	0.003	0.002	0.001	0.003	0.002
MEAN	0.18	0.17	0.15	0.13	0.09	0.06	0.05	0.02	0.02	0.02	0.01	0.01	0.00	0.01	0.01	0.00	0.00	0.00	0.00	0.00
VAR	0.1	0.1	0.1	0.1	0.1	0.0	0.0	0.0	0.0	0.0	0.0	0.0	0.0	0.0	0.0	0.0	0.0	0.0	0.0	0.0

TABLE 145

Primary photon E_0 = 2 000 MeV.
Secondary electrons E = 1 000 MeV.

Absorber: air, Z = 7.4, A = 15,
Radiation length = 43 g/sq. cm,
Critical energy = 98 MeV.

n \ t	0.5	1.0	1.5	2.0	2.5	3.0	3.5	4.0	4.5	5.0	5.5	6.0	6.5	7.0	7.5	8.0	8.5	9.0	9.5	10.0
0	0.789	0.787	0.810	0.859	0.912	0.933	0.955	0.974	0.987	0.984	0.993	0.996	0.996	0.998	1.000	0.999	0.999	0.998	0.999	1.000
≥1	0.211	0.213	0.190	0.141	0.088	0.067	0.045	0.026	0.013	0.016	0.007	0.004	0.004	0.002	0.000	0.001	0.001	0.002	0.001	0.000
MEAN	0.21	0.21	0.19	0.14	0.09	0.07	0.05	0.03	0.01	0.02	0.01	0.00	0.00	0.00	0.00	0.00	0.00	0.00	0.00	0.00
VAR	0.2	0.2	0.2	0.1	0.1	0.1	0.0	0.0	0.0	0.0	0.0	0.0	0.0	0.0	0.0	0.0	0.0	0.0	0.0	0.0

TABLE 146

Primary photon E_0 = 2 000 MeV.
Secondary electrons E = 1 000 MeV.

Absorber: al, Z = 13, A = 27,
Radiation length = 26.3 g/sq. cm = 9.74 cm,
Critical energy = 52 MeV.

n \ t	0.5	1.0	1.5	2.0	2.5	3.0	3.5	4.0	4.5	5.0	5.5	6.0	6.5	7.0	7.5	8.0	8.5	9.0	9.5	10.0
0	0.809	0.771	0.834	0.857	0.896	0.932	0.961	0.963	0.974	0.983	0.989	0.993	0.994	0.996	0.997	0.997	0.999	0.999	1.000	1.000
≥1	0.191	0.229	0.166	0.143	0.104	0.068	0.039	0.037	0.026	0.017	0.011	0.007	0.006	0.004	0.003	0.003	0.001	0.001	0.000	0.000
MEAN	0.19	0.23	0.17	0.14	0.10	0.07	0.04	0.04	0.03	0.02	0.01	0.01	0.01	0.00	0.00	0.00	0.00	0.00	0.00	0.00
VAR	0.2	0.2	0.1	0.1	0.1	0.1	0.0	0.0	0.0	0.0	0.0	0.0	0.0	0.0	0.0	0.0	0.0	0.0	0.0	0.0

TABLE 147

Primary photon E_0 = 10 000 MeV.
Secondary electrons E = 5 000 MeV.

Absorber: air, Z = 7.4, A = 15,
Radiation length = 43 g/sq. cm,
Critical energy = 98 MeV.

n \ t	0.5	1.0	1.5	2.0	2.5	3.0	3.5	4.0	4.5	5.0	5.5	6.0	6.5	7.0	7.5	8.0	8.5	9.0	9.5	10.0
0	0.787	0.746	0.796	0.863	0.906	0.935	0.945	0.966	0.972	0.983	0.993	0.995	0.994	0.994	0.997	0.998	0.999	1.000	1.000	0.999
⩾1	0.213	0.254	0.205	0.137	0.094	0.065	0.055	0.034	0.028	0.017	0.007	0.005	0.006	0.006	0.003	0.002	0.001	0.000	0.000	0.001
MEAN	0.21	0.25	0.21	0.14	0.09	0.07	0.06	0.03	0.03	0.02	0.01	0.01	0.01	0.01	0.00	0.00	0.00	0.00	0.00	0.00
VAR	0.2	0.2	0.2	0.1	0.1	0.1	0.1	0.0	0.0	0.0	0.0	0.0	0.0	0.0	0.0	0.0	0.0	0.0	0.0	0.0

TABLE 148

Primary photon E_0 = 10 000 MeV.
Secondary electrons E = 5 000 MeV.

Absorber: al, Z = 13, A = 27,
Radiation length = 26.3 g/sq. cm = 9.74 cm,
Critical energy = 52 MeV.

n \ t	0.5	1.0	1.5	2.0	2.5	3.0	3.5	4.0	4.5	5.0	5.5	6.0	6.5	7.0	7.5	8.0	8.5	9.0	9.5	10.0
0	0.772	0.760	0.789	0.856	0 905	0.934	0.954	0.971	0.979	0.984	0.984	0.992	0 991	0.998	0.999	0.999	0.999	0.999	0.998	0.999
⩾1	0.228	0.240	0.201	0.144	0.095	0.066	0.046	0.029	0.021	0.016	0.016	0.008	0.009	0.002	0.001	0.001	0.001	0.001	0.002	0.001
MEAN	0.23	0.24	0.20	0.14	0.10	0.07	0.05	0.03	0.02	0.02	0.02	0.01	0.01	0.00	0.00	0.00	0.00	0.00	0.00	0.00
VAR	0.2	0.2	0.2	0.1	0.1	0.1	0.0	0.0	0.0	0.0	0.0	0.0	0.0	0.0	0.0	0.0	0.0	0.0	0.0	0.0

TABLE 149

Primary photon E_0 = 20 000 MeV.
Secondary electrons E = 10 000 MeV.

Absorber: air, Z = 7.4, A = 15,
Radiation length = 43 g/sq. cm,
Critical energy = 98 MeV.

n \ t	0.5	1.0	1.5	2.0	2.5	3.0	3.5	4.0	4.5	5.0	5.5	6.0	6.5	7.0	7.5	8.0	8.5	9.0	9.5	10.0
0	0.796	0.777	0.817	0.833	0.882	0.936	0.950	0.960	0.965	0.981	0.993	0.995	0.994	0.995	0.997	0.999	0.996	0.998	0.997	0.999
⩾1	0.204	0.223	0.183	0.167	0.118	0.064	0.050	0.040	0.035	0.019	0.007	0.005	0.006	0.005	0.003	0.001	0.004	0.002	0.003	0.001
MEAN	0.20	0.22	0.18	0.17	0.12	0.06	0.05	0.04	0.04	0.02	0.01	0.01	0.01	0.01	0.00	0.00	0.00	0.00	0.00	0.00
VAR	0.2	0.2	0.2	0.1	0.1	0.1	0.0	0.0	0.0	0.0	0.0	0.0	0.0	0.0	0.0	0.0	0.0	0.0	0.0	0.0

TABLE 150

Primary photon E_0 = 20 000 MeV.
Secondary electrons E = 10 000 MeV.

Absorber: al, Z = 13, A = 27,
Radiation length = 26.3 g/sq. cm = 9.74 cm,
Critical energy = 52 MeV.

n \ t	0.5	1.0	1.5	2.0	2.5	3.0	3.5	4.0	4.5	5.0	5.5	6.0	6.5	7.0	7.5	8.0	8.5	9.0	9.5	10.0
0	0.805	0.770	0.803	0.837	0.896	0.935	0.945	0.964	0.978	0.981	0.987	0.991	0.995	0.998	0.998	0.998	0.998	0.999	0.999	0.999
⩾1	0.195	0.230	0.197	0.163	0.104	0.065	0.055	0.036	0.022	0.019	0.013	0.009	0.005	0.002	0.002	0.002	0.002	0.001	0.001	0.001
MEAN	0.20	0.23	0.20	0.16	0.10	0.07	0.06	0.04	0.02	0.02	0.01	0.01	0.01	0.00	0.00	0.00	0.00	0.00	0.00	0.00
VAR	0.2	0.2	0.2	0.1	0.1	0.1	0.1	0.0	0.0	0.0	0.0	0.0	0.0	0.0	0.0	0.0	0.0	0.0	0.0	0.0

TABLE 151

Primary photon E_0 = 50 MeV.
Secondary electrons E = 20 MeV.

Absorber: air, Z = 7.4, A = 15,
Radiation length = 43 g/sq. cm,
Critical energy = 98 MeV.

n \ t	0.5	1.0	1.5	2.0	2.5	3.0	3.5	4.0	4.5	5.0	5.5	6.0	6.5	7.0	7.5	8.0	8.5	9.0	9.5	10.0
0	0.934	0.948	0.955	0.974	0.976	0.983	0.986	0.989	0.994	0.997	0.994	0.997	0.999	1.000	1.000	1.000	1.000	1.000	1.000	0.999
1	0.065	0.050	0.044	0.025	0.024	0.017	0.014	0.010	0.006	0.003	0.006	0.003	0.001	0.000	0.000	0.000	0.000	0.000	0.000	0.001
⩾2	0.001	0.002	0.001	0.001	0.000	0.000	0.000	0.001	0.000	0.000	0.000	0.000	0.000	0.000	0.000	0.000	0.000	0.000	0.000	0.000
MEAN	0.07	0.05	0.05	0.03	0.02	0.02	0.01	0.01	0.01	0.00	0.01	0.00	0.00	0.00	0.00	0.00	0.00	0.00	0.00	0.00
VAR	0.1	0.1	0.0	0.0	0.0	0.0	0.0	0.0	0.0	0.0	0.0	0.0	0.0	0.0	0.0	0.0	0.0	0.0	0.0	0.0

TABLE 152

Primary photon E_0 = 50 MeV.
Secondary electrons E = 20 MeV.

Absorber: al, Z = 13, A = 27,
Radiation length = 26.3 g/sq. cm = 9.74 cm.
Critical energy = 52 MeV.

n \ t	0.5	1.0	1.5	2.0	2.5	3.0	3.5	4.0	4.5	5.0	5.5	6.0	6.5	7.0	7.5	8.0	8.5	9.0	9.5	10.0
0	0.892	0.904	0.942	0.954	0.969	0.982	0.977	0.989	0.988	0.987	0.988	0.992	0.998	0.996	1.000	1.000	0.999	1.000	0.998	0.999
1	0.102	0.094	0.057	0.044	0.030	0.017	0.023	0.010	0.012	0.013	0.012	0.008	0.002	0.004	0.000	0.000	0.001	0.000	0.002	0.001
⩾2	0.006	0.002	0.001	0.002	0.001	0.001	0.000	0.001	0.000	0.000	0.000	0.000	0.000	0.000	0.000	0.000	0.000	0.000	0.000	0.000
MEAN	0.11	0.10	0.06	0.05	0.03	0.02	0.02	0.01	0.01	0.01	0.01	0.01	0.00	0.00	0.00	0.00	0.00	0.00	0.00	0.00
VAR	0.1	0.1	0.1	0.0	0.0	0.0	0.0	0.0	0.0	0.0	0.0	0.0	0.0	0.0	0.0	0.0	0.0	0.0	0.0	0.0

TABLE 153

Primary photon E_0 = 500 MeV.
Secondary electrons E = 200 MeV.

Absorber: air, Z = 7.4, A = 15,
Radiation length = 43 g/sq. cm,
Critical energy = 98 MeV.

n \ t	0.5	1.0	1.5	2.0	2.5	3.0	3.5	4.0	4.5	5.0	5.5	6.0	6.5	7.0	7.5	8.0	8.5	9.0	9.5	10.0
0	0.763	0.784	0.825	0.873	0.913	0.931	0.949	0.957	0.975	0.985	0.983	0.989	0.995	0.998	0.998	1.000	1.000	1.000	1.000	1.000
1	0.228	0.203	0.170	0.120	0.085	0.066	0.049	0.042	0.025	0.015	0.017	0.011	0.004	0.002	0.002	0.000	0.000	0.000	0.000	0.000
⩾2	0.009	0.013	0.006	0.007	0.002	0.003	0.002	0.001	0.000	0.000	0.000	0.000	0.001	0.000	0.000	0.000	0.000	0.000	0.000	0.000
MEAN	0.25	0.23	0.18	0.13	0.09	0.07	0.05	0.04	0.03	0.02	0.02	0.01	0.01	0.00	0.00	0.00	0.00	0.00	0.00	0.00
VAR	0.2	0.2	0.2	0.1	0.1	0.1	0.1	0.0	0.0	0.0	0.0	0.0	0.0	0.0	0.0	0.0	0.0	0.0	0.0	0.0

TABLE 154

Primary photon E_0 = 500 MeV.
Secondary electrons E = 200 MeV.

Absorber: al, Z = 13, A = 27,
Radiation length = 26.3 g/sq. cm = 9.74 cm.
Critical energy = 52 MeV.

n \ t	0.5	1.0	1.5	2.0	2.5	3.0	3.5	4.0	4.5	5.0	5.5	6.0	6.5	7.0	7.5	8.0	8.5	9.0	9.5	10.0
0	0.775	0.740	0.794	0.853	0.892	0.919	0.929	0.950	0.961	0.979	0.986	0.988	0.991	0.994	0.991	0.995	0.995	0.997	0.997	1.000
1	0.210	0.253	0.202	0.136	0.105	0.079	0.067	0.049	0.037	0.021	0.014	0.011	0.009	0.006	0.009	0.005	0.005	0.003	0.003	0.000
⩾2	0.015	0.007	0.004	0.011	0.003	0.002	0.004	0.001	0.002	0.000	0.000	0.001	0.000	0.000	0.000	0.000	0.000	0.000	0.000	0.000
MEAN	0.24	0.27	0.21	0.16	0.11	0.08	0.08	0.05	0.04	0.02	0.01	0.01	0.01	0.01	0.01	0.01	0.01	0.00	0.00	0.00
VAR	0.2	0.2	0.2	0.2	0.1	0.1	0.1	0.1	0.0	0.0	0.0	0.0	0.0	0.0	0.0	0.0	0.0	0.0	0.0	0.0

TABLE 155

Primary photon E_0 = 5 000 MeV.
Secondary electrons E = 2 000 MeV.

Absorber: air, Z = 7.4, A = 15,
Radiation length = 43 g/sq. cm,
Critical energy = 98 MeV.

n \ t	0.5	1.0	1.5	2.0	2.5	3.0	3.5	4.0	4.5	5.0	5.5	6.0	6.5	7.0	7.5	8.0	8.5	9.0	9.5	10.0
0	0.745	0.717	0.738	0.805	0.855	0.901	0.925	0.945	0.959	0.968	0.980	0.988	0.991	0.996	0.996	0.997	1.000	0.998	0.999	0.999
1	0.231	0.265	0.254	0.186	0.142	0.097	0.072	0.054	0.040	0.031	0.019	0.012	0.009	0.004	0.004	0.003	0.000	0.002	0.001	0.001
⩾2	0.024	0.018	0.008	0.009	0.003	0.002	0.003	0.001	0.001	0.001	0.001	0.000	0.000	0.000	0.000	0.000	0.000	0.000	0.000	0.000
MEAN	0.28	0.30	0.27	0.20	0.15	0.10	0.08	0.06	0.04	0.03	0.02	0.01	0.01	0.00	0.00	0.00	0.00	0.00	0.00	0.00
VAR	0.3	0.2	0.2	0.2	0.1	0.1	0.1	0.1	0.0	0.0	0.0	0.0	0.0	0.0	0.0	0.0	0.0	0.0	0.0	0.0

TABLE 156

Primary photon E_0 = 5 000 MeV.
Secondary electrons E = 2 000 MeV.

Absorber: al, Z = 13, A = 27,
Radiation length = 26.3 g/sq. cm = 9.74 cm.
Critical energy = 52 MeV.

n \ t	0.5	1.0	1.5	2.0	2.5	3.0	3.5	4.0	4.5	5.0	5.5	6.0	6.5	7.0	7.5	8.0	8.5	9.0	9.5	10.0
0	0.765	0.694	0.725	0.771	0.833	0.881	0.908	0.947	0.958	0.975	0.976	0.977	0.985	0.992	0.995	0.996	0.998	0.999	0.999	1.000
1	0.212	0.288	0.267	0.219	0.160	0.116	0.088	0.050	0.041	0.024	0.024	0.023	0.015	0.008	0.005	0.004	0.002	0.001	0.001	0.000
⩾2	0.023	0.018	0.008	0.010	0.007	0.003	0.004	0.003	0.001	0.001	0.000	0.000	0.000	0.000	0.000	0.000	0.000	0.000	0.000	0.000
MEAN	0.28	0.32	0.28	0.24	0.17	0.12	0.10	0.06	0.04	0.03	0.02	0.02	0.02	0.01	0.01	0.00	0.00	0.00	0.00	0.00
VAR	0.2	0.3	0.2	0.2	0.2	0.1	0.1	0.1	0.0	0.0	0.0	0.0	0.0	0.0	0.0	0.0	0.0	0.0	0.0	0.0

TABLE 157

Primary photon E_0 = 50 000 MeV.
Secondary electrons E = 20 000 MeV.

Absorber: air, Z = 7.4, A = 15,
Radiation length = 43 g/sq. cm,
Critical energy = 98 MeV.

n \ t	0.5	1.0	1.5	2.0	2.5	3.0	3.5	4.0	4.5	5.0	5.5	6.0	6.5	7.0	7.5	8.0	8.5	9.0	9.5	10.0
0	0.770	0.703	0.717	0.774	0.825	0.877	0.901	0.926	0.941	0.967	0.976	0.989	0.990	0.989	0.994	0.996	0.997	0.999	0.998	0.999
1	0.210	0.276	0.269	0.215	0.169	0.119	0.096	0.071	0.056	0.033	0.024	0.011	0.010	0.011	0.006	0.005	0.003	0.001	0.002	0.001
≥2	0.020	0.021	0.014	0.011	0.006	0.004	0.003	0.003	0.003	0.000	0.000	0.000	0.000	0.000	0.000	0.000	0.000	0.000	0.000	0.000
MEAN	0.25	0.32	0.30	0.24	0.18	0.13	0.10	0.08	0.06	0.03	0.02	0.01	0.01	0.01	0.01	0.01	0.00	0.00	0.00	0.00
VAR	0.2	0.3	0.2	0.2	0.2	0.1	0.1	0.1	0.1	0.0	0.0	0.0	0.0	0.0	0.0	0.0	0.0	0.0	0.0	0.0

TABLE 158

Primary photon E_0 = 50 000 MeV.
Secondary electrons E = 20 000 MeV.

Absorber: al, Z = 13, A = 27,
Radiation length = 26.3 g/sq. cm = 9.74 cm,
Critical energy = 52 MeV.

n \ t	0.5	1.0	1.5	2.0	2.5	3.0	3.5	4.0	4.5	5.0	5.5	6.0	6.5	7.0	7.5	8.0	8.5	9.0	9.5	10.0
0	0.766	0.691	0.741	0.797	0.821	0.879	0.907	0.931	0.950	0.964	0.974	0.990	0.994	0.996	0.993	0.996	0.997	1.000	0.999	0.999
1	0.214	0.294	0.248	0.194	0.172	0.120	0.088	0.068	0.049	0.036	0.026	0.010	0.006	0.004	0.007	0.005	0.003	0.000	0.001	0.001
≥2	0.020	0.015	0.011	0.009	0.007	0.001	0.005	0.001	0.001	0.000	0.000	0.000	0.000	0.000	0.000	0.000	0.000	0.000	0.000	0.000
MEAN	0.25	0.32	0.27	0.21	0.19	0.12	0.10	0.07	0.05	0.04	0.03	0.01	0.01	0.00	0.01	0.01	0.00	0.00	0.00	0.00
VAR	0.2	0.2	0.2	0.2	0.2	0.1	0.1	0.1	0.1	0.0	0.0	0.0	0.0	0.0	0.0	0.0	0.0	0.0	0.0	0.0

TABLE 159

Primary photon E_0 = 200 MeV.
Secondary electrons E = 50 MeV.

Absorber: air, Z = 7.4, A = 15,
Radiation length = 43 g/sq. cm,
Critical energy = 98 MeV.

n \ t	0.5	1.0	1.5	2.0	2.5	3.0	3.5	4.0	4.5	5.0	5.5	6.0	6.5	7.0	7.5	8.0	8.5	9.0	9.5	10.0
0	0.754	0.769	0.848	0.859	0.899	0.937	0.954	0.971	0.974	0.981	0.980	0.993	0.994	0.999	0.998	0.997	0.996	0.998	0.998	0.999
1	0.212	0.201	0.135	0.121	0.088	0.055	0.040	0.026	0.022	0.017	0.018	0.004	0.005	0.001	0.002	0.003	0.004	0.001	0.002	0.001
≥2	0.034	0.030	0.017	0.020	0.013	0.008	0.006	0.003	0.004	0.002	0.002	0.003	0.001	0.000	0.000	0.000	0.000	0.001	0.000	0.000
MEAN	0.28	0.26	0.17	0.16	0.11	0.07	0.05	0.03	0.03	0.02	0.02	0.01	0.01	0.00	0.00	0.00	0.00	0.00	0.00	0.00
VAR	0.3	0.3	0.2	0.2	0.1	0.1	0.1	0.0	0.0	0.0	0.0	0.0	0.0	0.0	0.0	0.0	0.0	0.0	0.0	0.0

TABLE 160

Primary photon E_0 = 200 MeV.
Secondary electrons E = 50 MeV.

Absorber: al, Z = 13, A = 27,
Radiation length = 26.3 g/sq. cm = 9.74 cm,
Critical energy = 52 MeV.

n \ t	0.5	1.0	1.5	2.0	2.5	3.0	3.5	4.0	4.5	5.0	5.5	6.0	6.5	7.0	7.5	8.0	8.5	9.0	9.5	10.0
0	0.772	0.723	0.766	0.804	0.862	0.897	0.907	0.929	0.947	0.963	0.977	0.980	0.989	0.986	0.995	0.999	0.999	0.999	0.999	0.998
1	0.175	0.236	0.200	0.172	0.125	0.097	0.076	0.061	0.049	0.033	0.020	0.019	0.009	0.011	0.005	0.001	0.000	0.001	0.001	0.001
≥2	0.053	0.041	0.034	0.024	0.013	0.006	0.017	0.010	0.004	0.004	0.003	0.001	0.002	0.003	0.000	0.000	0.001	0.000	0.000	0.001
MEAN	0.28	0.32	0.27	0.22	0.15	0.11	0.11	0.08	0.06	0.04	0.03	0.02	0.01	0.02	0.01	0.00	0.00	0.00	0.00	0.00
VAR	0.3	0.3	0.3	0.2	0.2	0.1	0.1	0.1	0.1	0.0	0.0	0.0	0.0	0.0	0.0	0.0	0.0	0.0	0.0	0.0

TABLE 161

Primary photon E_0 = 2 000 MeV.
Secondary electrons E = 500 MeV.

Absorber: air, Z = 7.4, A = 15,
Radiation length = 43 g/sq. cm,
Critical energy = 98 MeV.

n \ t	0.5	1.0	1.5	2.0	2.5	3.0	3.5	4.0	4.5	5.0	5.5	6.0	6.5	7.0	7.5	8.0	8.5	9.0	9.5	10.0
0	0.719	0.613	0.587	0.670	0.749	0.815	0.857	0.904	0.937	0.949	0.959	0.974	0.979	0.986	0.995	0.997	0.995	0.995	0.997	0.997
1	0.189	0.315	0.355	0.296	0.228	0.168	0.127	0.085	0.058	0.045	0.038	0.026	0.018	0.014	0.005	0.002	0.004	0.005	0.003	0.003
≥2	0.092	0.072	0.058	0.034	0.023	0.017	0.016	0.011	0.005	0.006	0.003	0.000	0.003	0.000	0.000	0.001	0.001	0.000	0.000	0.000
MEAN	0.37	0.46	0.47	0.36	0.27	0.20	0.16	0.11	0.07	0.06	0.04	0.03	0.02	0.01	0.01	0.00	0.01	0.01	0.00	0.00
VAR	0.4	0.4	0.4	0.3	0.2	0.2	0.2	0.1	0.1	0.1	0.0	0.0	0.0	0.0	0.0	0.0	0.0	0.0	0.0	0.0

TABLE 162

Primary photon E_0 = 2 000 MeV.
Secondary electrons E = 500 MeV.

Absorber: al, Z = 13, A = 27,
Radiation length = 26.3 g/sq. cm = 9.74 cm,
Critical energy = 52 MeV.

n \ t	0.5	1.0	1.5	2.0	2.5	3.0	3.5	4.0	4.5	5.0	5.5	6.0	6.5	7.0	7.5	8.0	8.5	9.0	9.5	10.0
0	0.724	0.597	0.608	0.645	0.737	0.789	0.856	0.895	0.916	0.937	0.954	0.976	0.980	0.987	0.990	0.992	0.994	0.994	0.997	0.999
1	0.179	0.301	0.320	0.306	0.231	0.182	0.132	0.095	0.076	0.055	0.044	0.022	0.020	0.012	0.010	0.007	0.006	0.005	0.003	0.001
≥2	0.097	0.102	0.072	0.049	0.032	0.029	0.012	0.010	0.008	0.008	0.002	0.002	0.000	0.001	0.000	0.001	0.000	0.001	0.000	0.000
MEAN	0.37	0.51	0.46	0.40	0.30	0.24	0.16	0.12	0.09	0.07	0.05	0.03	0.02	0.01	0.01	0.01	0.01	0.01	0.00	0.00
VAR	0.4	0.5	0.4	0.3	0.3	0.2	0.2	0.1	0.1	0.1	0.0	0.0	0.0	0.0	0.0	0.0	0.0	0.0	0.0	0.0

TABLE 163

Primary photon E_0 = 20 000 MeV.
Secondary electrons E = 5 000 MeV.

Absorber: air, Z = 7.4, A = 15,
Radiation length = 43 g/sq. cm,
Critical energy = 98 MeV.

n \ t	0.5	1.0	1.5	2.0	2.5	3.0	3.5	4.0	4.5	5.0	5.5	6.0	6.5	7.0	7.5	8.0	8.5	9.0	9.5	10.0
0	0.719	0.614	0.598	0.627	0.689	0.746	0.796	0.864	0.890	0.922	0.945	0.954	0.970	0.978	0.984	0.996	0.990	0.989	0.992	0.994
1	0.191	0.300	0.347	0.313	0.289	0.228	0.186	0.123	0.100	0.073	0.052	0.043	0.030	0.021	0.015	0.004	0.010	0.011	0.008	0.006
≥2	0.090	0.086	0.055	0.060	0.042	0.026	0.018	0.013	0.010	0.005	0.003	0.003	0.000	0.001	0.001	0.000	0.000	0.000	0.000	0.000
MEAN	0.37	0.47	0.46	0.43	0.37	0.28	0.22	0.15	0.12	0.08	0.06	0.05	0.03	0.02	0.02	0.00	0.01	0.01	0.01	0.01
VAR	0.4	0.4	0.4	0.4	0.3	0.3	0.2	0.2	0.1	0.1	0.1	0.1	0.0	0.0	0.0	0.0	0.0	0.0	0.0	0.0

TABLE 164

Primary photon E_0 = 20 000 MeV.
Secondary electrons E = 5 000 MeV.

Absorber: al, Z = 13, A = 27,
Radiation length = 26.3 g/sq. cm = 9.74 cm,
Critical energy = 52 MeV.

n \ t	0.5	1.0	1.5	2.0	2.5	3.0	3.5	4.0	4.5	5.0	5.5	6.0	6.5	7.0	7.5	8.0	8.5	9.0	9.5	10.0
0	0.717	0.604	0.565	0.598	0.683	0.752	0.820	0.869	0.900	0.925	0.945	0.955	0.969	0.987	0.981	0.987	0.993	0.995	0.995	0.994
1	0.195	0.307	0.364	0.355	0.285	0.227	0.161	0.121	0.093	0.070	0.052	0.041	0.030	0.013	0.019	0.013	0.007	0.005	0.005	0.006
≥2	0.088	0.089	0.071	0.047	0.032	0.021	0.019	0.010	0.007	0.005	0.003	0.004	0.001	0.000	0.000	0.000	0.000	0.000	0.000	0.000
MEAN	0.37	0.49	0.51	0.45	0.35	0.27	0.20	0.14	0.11	0.08	0.06	0.05	0.03	0.01	0.02	0.01	0.01	0.01	0.01	0.01
VAR	0.4	0.4	0.4	0.3	0.3	0.2	0.2	0.1	0.1	0.1	0.1	0.1	0.0	0.0	0.0	0.0	0.0	0.0	0.0	0.0

TABLE 165

Primary photon E_0 = 50 MeV.
Secondary electrons E = 10 MeV.

Absorber: air, Z = 7.4, A = 15,
Radiation length = 43 g/sq. cm,
Critical energy = 98 MeV.

n \ t	0.5	1.0	1.5	2.0	2.5	3.0	3.5	4.0	4.5	5.0	5.5	6.0	6.5	7.0	7.5	8.0	8.5	9.0	9.5	10.0
0	0.885	0.903	0.927	0.955	0.962	0.968	0.977	0.982	0.990	0.994	0.990	0.996	0.997	0.998	1.000	1.000	1.000	0.999	1.000	0.999
1	0.102	0.080	0.060	0.040	0.032	0.028	0.023	0.016	0.009	0.005	0.009	0.004	0.003	0.002	0.000	0.000	0.000	0.001	0.000	0.001
≥2	0.013	0.017	0.013	0.005	0.006	0.004	0.000	0.002	0.001	0.001	0.001	0.001	0.000	0.000	0.000	0.000	0.000	0.000	0.000	0.000
MEAN	0.13	0.11	0.09	0.05	0.04	0.04	0.02	0.02	0.01	0.01	0.01	0.01	0.00	0.00	0.00	0.00	0.00	0.00	0.00	0.00
VAR	0.1	0.1	0.1	0.1	0.1	0.0	0.0	0.0	0.0	0.0	0.0	0.0	0.0	0.0	0.0	0.0	0.0	0.0	0.0	0.0

TABLE 166

Primary photon E_0 = 50 MeV.
Secondary electrons E = 10 MeV.

Absorber: al, Z = 13, A = 27,
Radiation length = 26.3 g/sq. cm = 9.74 cm,
Critical energy = 52 MeV.

n \ t	0.5	1.0	1.5	2.0	2.5	3.0	3.5	4.0	4.5	5.0	5.5	6.0	6.5	7.0	7.5	8.0	8.5	9.0	9.5	10.0
0	0.818	0.840	0.900	0.918	0.943	0.957	0.956	0.973	0.977	0.980	0.982	0.986	0.992	0.993	0.997	0.997	0.999	0.999	0.998	0.999
1	0.150	0.129	0.077	0.070	0.045	0.034	0.036	0.021	0.021	0.017	0.015	0.013	0.007	0.004	0.003	0.002	0.001	0.001	0.002	0.001
≥2	0.032	0.031	0.023	0.012	0.012	0.009	0.008	0.006	0.002	0.003	0.003	0.001	0.001	0.003	0.000	0.001	0.000	0.000	0.000	0.000
MEAN	0.21	0.19	0.12	0.09	0.07	0.05	0.05	0.03	0.03	0.02	0.02	0.02	0.01	0.01	0.00	0.00	0.00	0.00	0.00	0.00
VAR	0.2	0.2	0.2	0.1	0.1	0.1	0.1	0.0	0.0	0.0	0.0	0.0	0.0	0.0	0.0	0.0	0.0	0.0	0.0	0.0

TABLE 167

Primary photon E_0 = 100 MeV.
Secondary electrons E = 20 MeV.

Absorber: air, Z = 7.4, A = 15,
Radiation length = 43 g/sq. cm,
Critical energy = 98 MeV.

n \ t	0.5	1.0	1.5	2.0	2.5	3.0	3.5	4.0	4.5	5.0	5.5	6.0	6.5	7.0	7.5	8.0	8.5	9.0	9.5	10.0
0	0.773	0.843	0.859	0.926	0.946	0.967	0.965	0.972	0.976	0.982	0.986	0.994	0.989	0.998	0.997	0.999	1.000	0.999	0.998	0.999
1	0.178	0.134	0.117	0.066	0.045	0.028	0.030	0.024	0.017	0.017	0.012	0.004	0.007	0.002	0.002	0.001	0.000	0.000	0.002	0.000
≥2	0.049	0.023	0.024	0.008	0.009	0.005	0.005	0.004	0.007	0.001	0.002	0.002	0.004	0.000	0.001	0.000	0.000	0.001	0.000	0.001
MEAN	0.28	0.18	0.17	0.08	0.06	0.04	0.04	0.03	0.03	0.02	0.02	0.01	0.02	0.00	0.00	0.00	0.00	0.00	0.00	0.00
VAR	0.3	0.2	0.2	0.1	0.1	0.0	0.0	0.0	0.0	0.0	0.0	0.0	0.0	0.0	0.0	0.0	0.0	0.0	0.0	0.0

TABLE 168

Primary photon E_0 = 100 MeV.
Secondary electrons E = 20 MeV.

Absorber: al, Z = 13, A = 27,
Radiation length = 26.3 g/sq. cm = 9.74 cm,
Critical energy = 52 MeV.

n \ t	0.5	1.0	1.5	2.0	2.5	3.0	3.5	4.0	4.5	5.0	5.5	6.0	6.5	7.0	7.5	8.0	8.5	9.0	9.5	10.0
0	0.786	0.795	0.846	0.876	0.886	0.926	0.930	0.951	0.959	0.972	0.980	0.974	0.981	0.985	0.990	0.993	0.991	0.994	0.996	1.000
1	0.174	0.173	0.121	0.100	0.101	0.068	0.061	0.040	0.035	0.022	0.017	0.020	0.017	0.012	0.007	0.006	0.008	0.005	0.004	0.000
≥2	0.040	0.032	0.033	0.024	0.013	0.006	0.009	0.009	0.006	0.006	0.003	0.006	0.002	0.003	0.003	0.001	0.001	0.001	0.000	0.000
MEAN	0.29	0.24	0.19	0.15	0.13	0.08	0.08	0.06	0.05	0.03	0.02	0.03	0.02	0.02	0.01	0.01	0.01	0.01	0.00	0.00
VAR	0.3	0.2	0.2	0.2	0.1	0.1	0.1	0.1	0.1	0.0	0.0	0.0	0.0	0.0	0.0	0.0	0.0	0.0	0.0	0.0

TABLE 169

Primary photon E_0 = 500 MeV.
Secondary electrons E = 100 MeV.

Absorber: air, Z = 7.4, A = 15,
Radiation length = 43 g/sq. cm,
Critical energy = 98 MeV.

n \ t	0.5	1.0	1.5	2.0	2.5	3.0	3.5	4.0	4.5	5.0	5.5	6.0	6.5	7.0	7.5	8.0	8.5	9.0	9.5	10.0
0	0.711	0.627	0.672	0.752	0.814	0.860	0.891	0.907	0.947	0.957	0.964	0.973	0.984	0.988	0.991	0.995	0.996	1.000	1.000	0.999
1	0.201	0.292	0.265	0.213	0.157	0.118	0.090	0.081	0.050	0.037	0.032	0.024	0.014	0.011	0.008	0.005	0.004	0.000	0.000	0.001
≥2	0.088	0.081	0.063	0.035	0.029	0.022	0.019	0.012	0.003	0.006	0.004	0.003	0.002	0.001	0.001	0.000	0.000	0.000	0.000	0.000
MEAN	0.38	0.45	0.39	0.28	0.22	0.16	0.13	0.11	0.06	0.05	0.04	0.03	0.02	0.01	0.01	0.01	0.00	0.00	0.00	0.00
VAR	0.4	0.4	0.4	0.3	0.2	0.2	0.1	0.1	0.1	0.1	0.0	0.0	0.0	0.0	0.0	0.0	0.0	0.0	0.0	0.0

TABLE 170

Primary photon E_0 = 500 MeV.
Secondary electrons E = 100 MeV.

Absorber: al, Z = 13, A = 27,
Radiation length = 26.3 g/sq. cm = 9.74 cm,
Critical energy = 52 MeV.

n \ t	0.5	1.0	1.5	2.0	2.5	3.0	3.5	4.0	4.5	5.0	5.5	6.0	6.5	7.0	7.5	8.0	8.5	9.0	9.5	10.0
0	0.738	0.614	0.636	0.688	0.749	0.815	0.854	0.883	0.905	0.929	0.961	0.964	0.974	0.976	0.981	0.991	0.988	0.992	0.993	0.997
1	0.149	0.275	0.303	0.260	0.209	0.163	0.120	0.104	0.083	0.066	0.038	0.030	0.022	0.023	0.017	0.008	0.010	0.008	0.006	0.003
≥2	0.113	0.111	0.061	0.052	0.042	0.022	0.026	0.013	0.012	0.005	0.001	0.006	0.004	0.001	0.002	0.001	0.002	0.000	0.001	0.000
MEAN	0.38	0.50	0.43	0.37	0.29	0.21	0.17	0.13	0.11	0.08	0.04	0.04	0.03	0.03	0.02	0.01	0.01	0.01	0.01	0.00
VAR	0.5	0.5	0.4	0.3	0.3	0.2	0.2	0.1	0.1	0.1	0.0	0.1	0.0	0.0	0.0	0.0	0.0	0.0	0.0	0.0

TABLE 171

Primary photon E_0 = 1 000 MeV.
Secondary electrons E = 200 MeV.

Absorber: air, Z = 7.4, A = 15,
Radiation length = 43 g/sq. cm,
Critical energy = 98 MeV.

n \ t	0.5	1.0	1.5	2.0	2.5	3.0	3.5	4.0	4.5	5.0	5.5	6.0	6.5	7.0	7.5	8.0	8.5	9.0	9.5	10.0
0	0.727	0.608	0.608	0.685	0.750	0.817	0.863	0.891	0.921	0.948	0.965	0.965	0.974	0.983	0.984	0.988	0.987	0.992	0.994	0.995
1	0.167	0.286	0.305	0.259	0.197	0.157	0.119	0.094	0.076	0.046	0.028	0.030	0.022	0.017	0.015	0.010	0.013	0.008	0.006	0.005
≥2	0.106	0.106	0.087	0.056	0.053	0.026	0.018	0.015	0.003	0.006	0.007	0.005	0.004	0.000	0.001	0.002	0.000	0.000	0.000	0.000
MEAN	0.38	0.50	0.48	0.37	0.30	0.21	0.16	0.12	0.08	0.06	0.04	0.04	0.03	0.02	0.02	0.01	0.01	0.01	0.01	0.01
VAR	0.5	0.5	0.4	0.3	0.3	0.2	0.2	0.1	0.1	0.1	0.1	0.0	0.0	0.0	0.0	0.0	0.0	0.0	0.0	0.0

TABLE 172

Primary photon E_0 = 1 000 MeV.
Secondary electrons E = 200 MeV.

Absorber: al, Z = 13, A = 27,
Radiation length = 26.3 g/sq. cm = 9.74 cm,
Critical energy = 52 MeV.

n \ t	0.5	1.0	1.5	2.0	2.5	3.0	3.5	4.0	4.5	5.0	5.5	6.0	6.5	7.0	7.5	8.0	8.5	9.0	9.5	10.0
0	0.715	0.693	0.568	0.618	0.704	0.764	0.813	0.862	0.900	0.923	0.937	0.955	0.965	0.975	0.981	0.983	0.991	0.994	0.997	0.993
1	0.175	0.293	0.342	0.330	0.252	0.201	0.165	0.110	0.086	0.063	0.056	0.038	0.034	0.020	0.017	0.016	0.008	0.006	0.003	0.006
≥2	0.110	0.114	0.090	0.052	0.044	0.035	0.022	0.028	0.014	0.014	0.007	0.007	0.001	0.005	0.002	0.001	0.001	0.000	0.000	0.001
MEAN	0.40	0.52	0.52	0.44	0.34	0.27	0.21	0.17	0.11	0.09	0.07	0.05	0.04	0.03	0.02	0.02	0.01	0.01	0.00	0.01
VAR	0.5	0.5	0.4	0.4	0.3	0.3	0.2	0.2	0.1	0.1	0.1	0.1	0.0	0.0	0.0	0.0	0.0	0.0	0.0	0.0

TABLE 173

Primary photon E_0 = 5 000 MeV.
Secondary electrons E = 1 000 MeV.

Absorber: air, Z = 7.4, A = 15,
Radiation length = 43 g/sq. cm,
Critical energy = 98 MeV.

n \ t	0.5	1.0	1.5	2.0	2.5	3.0	3.5	4.0	4.5	5.0	5.5	6.0	6.5	7.0	7.5	8.0	8.5	9.0	9.5	10.0
0	0.705	0.568	0.537	0.593	0.647	0.729	0.774	0.831	0.881	0.908	0.922	0.950	0.957	0.972	0.981	0.986	0.988	0.995	0.997	0.995
1	0.160	0.296	0.346	0.326	0.293	0.227	0.199	0.148	0.107	0.082	0.071	0.044	0.041	0.026	0.018	0.013	0.012	0.004	0.002	0.005
≥2	0.135	0.136	0.117	0.081	0.060	0.044	0.027	0.021	0.012	0.010	0.007	0.006	0.002	0.002	0.001	0.001	0.000	0.001	0.001	0.000
MEAN	0.43	0.57	0.58	0.49	0.41	0.32	0.25	0.19	0.13	0.10	0.09	0.06	0.05	0.03	0.02	0.02	0.01	0.01	0.00	0.01
VAR	0.5	0.5	0.5	0.4	0.4	0.3	0.2	0.2	0.1	0.1	0.1	0.1	0.0	0.0	0.0	0.0	0.0	0.0	0.0	0.0

TABLE 174

Primary photon E_0 = 5 000 MeV.
Secondary electrons E = 1 000 MeV.

Absorber: al, Z = 13, A = 27,
Radiation length = 26.3 g/sq. cm = 9.74 cm,
Critical energy = 52 MeV.

n \ t	0.5	1.0	1.5	2.0	2.5	3.0	3.5	4.0	4.5	5.0	5.5	6.0	6.5	7.0	7.5	8.0	8.5	9.0	9.5	10.0
0	0.720	0.574	0.535	0.544	0.628	0.688	0.756	0.806	0.864	0.902	0.920	0.935	0.951	0.970	0.971	0.981	0.988	0.994	0.998	0.997
1	0.166	0.295	0.352	0.366	0.314	0.261	0.208	0.173	0.124	0.084	0.068	0.057	0.044	0.026	0.028	0.019	0.012	0.006	0.002	0.003
≥2	0.114	0.131	0.113	0.090	0.058	0.051	0.036	0.021	0.012	0.014	0.012	0.008	0.005	0.004	0.001	0.000	0.000	0.000	0.000	0.000
MEAN	0.40	0.56	0.58	0.55	0.43	0.37	0.28	0.22	0.15	0.11	0.09	0.07	0.05	0.03	0.03	0.02	0.01	0.01	0.00	0.00
VAR	0.5	0.5	0.5	0.4	0.4	0.3	0.3	0.2	0.2	0.1	0.1	0.1	0.1	0.0	0.0	0.0	0.0	0.0	0.0	0.0

TABLE 175

Primary photon E_0 = 10 000 MeV.
Secondary electrons E = 2 000 MeV.

Absorber: air, Z = 7.4, A = 15,
Radiation length = 43 g/sq. cm,
Critical energy = 98 MeV.

n \ t	0.5	1.0	1.5	2.0	2.5	3.0	3.5	4.0	4.5	5.0	5.5	6.0	6.5	7.0	7.5	8.0	8.5	9.0	9.5	10.0
0	0.699	0.528	0.484	0.551	0.627	0.694	0.775	0.822	0.854	0.893	0.927	0.943	0.963	0.966	0.974	0.985	0.990	0.993	0.997	0.994
1	0.190	0.326	0.384	0.369	0.314	0.259	0.178	0.151	0.133	0.097	0.065	0.051	0.035	0.032	0.025	0.014	0.009	0.007	0.003	0.006
≥2	0.111	0.146	0.132	0.080	0.059	0.047	0.047	0.027	0.013	0.010	0.008	0.006	0.002	0.002	0.001	0.001	0.001	0.000	0.000	0.000
MEAN	0.41	0.62	0.65	0.53	0.44	0.35	0.27	0.21	0.16	0.12	0.08	0.06	0.04	0.04	0.03	0.02	0.01	0.01	0.00	0.01
VAR	0.5	0.5	0.5	0.4	0.4	0.3	0.3	0.2	0.2	0.1	0.1	0.1	0.0	0.0	0.0	0.0	0.0	0.0	0.0	0.0

TABLE 176

Primary photon E_0 = 10 000 MeV.
Secondary electrons E = 2 000 MeV.

Absorber: al, Z = 13, A = 27,
Radiation length = 26.3 g/sq. cm = 9.74 cm,
Critical energy = 52 MeV.

n \ t	0.5	1.0	1.5	2.0	2.5	3.0	3.5	4.0	4.5	5.0	5.5	6.0	6.5	7.0	7.5	8.0	8.5	9.0	9.5	10.0
0	0.698	0.558	0.498	0.556	0.624	0.703	0.773	0.812	0.862	0.900	0.905	0.933	0.963	0.969	0.981	0.989	0.990	0.994	0.993	0.996
1	0.170	0.303	0.363	0.367	0.312	0.252	0.183	0.170	0.127	0.090	0.082	0.059	0.035	0.025	0.018	0.009	0.009	0.005	0.006	0.003
≥2	0.132	0.139	0.139	0.077	0.064	0.045	0.044	0.018	0.011	0.010	0.013	0.008	0.002	0.006	0.001	0.002	0.001	0.001	0.001	0.001
MEAN	0.43	0.58	0.64	0.52	0.44	0.34	0.27	0.21	0.15	0.11	0.11	0.08	0.04	0.04	0.02	0.01	0.01	0.01	0.01	0.01
VAR	0.5	0.5	0.5	0.4	0.4	0.3	0.3	0.2	0.1	0.1	0.1	0.1	0.0	0.0	0.0	0.0	0.0	0.0	0.0	0.0

TABLE 177

Primary photon E_0 = 50 000 MeV.
Secondary electrons E = 10 000 MeV.

Absorber: air, Z = 7.4, A = 15,
Radiation length = 43 g/sq. cm,
Critical energy = 98 MeV.

n \ t	0.5	1.0	1.5	2.0	2.5	3.0	3.5	4.0	4.5	5.0	5.5	6.0	6.5	7.0	7.5	8.0	8.5	9.0	9.5	10.0
0	0.733	0.586	0.517	0.551	0.601	0.661	0.728	0.775	0.832	0.895	0.908	0.936	0.958	0.960	0.977	0.985	0.982	0.993	0.993	0.995
1	0.164	0.271	0.346	0.343	0.327	0.289	0.223	0.189	0.147	0.091	0.080	0.055	0.038	0.037	0.020	0.014	0.017	0.006	0.007	0.005
⩾ 2	0.103	0.143	0.137	0.106	0.072	0.050	0.049	0.036	0.021	0.014	0.012	0.009	0.004	0.003	0.003	0.001	0.001	0.001	0.000	0.000
MEAN	0.37	0.56	0.62	0.56	0.47	0.39	0.32	0.26	0.19	0.12	0.10	0.07	0.05	0.04	0.03	0.02	0.02	0.01	0.01	0.01
VAR	0.4	0.5	0.5	0.5	0.4	0.3	0.3	0.3	0.2	0.1	0.1	0.1	0.1	0.0	0.0	0.0	0.0	0.0	0.0	0.0

TABLE 178

Primary photon E_0 = 50 000 MeV.
Secondary electrons E = 10 000 MeV.

Absorber: al, Z = 13, A = 27,
Radiation length = 26.3 g/sq. cm = 9.74 cm,
Critical energy = 52 MeV.

n \ t	0.5	1.0	1.5	2.0	2.5	3.0	3.5	4.0	4.5	5.0	5.5	6.0	6.5	7.0	7.5	8.0	8.5	9.0	9.5	10.0
0	0.728	0.567	0.509	0.532	0.577	0.688	0.727	0.794	0.848	0.892	0.904	0.936	0.956	0.969	0.974	0.978	0.986	0.994	0.993	0.995
1	0.149	0.290	0.358	0.363	0.344	0.262	0.218	0.191	0.142	0.101	0.085	0.056	0.041	0.029	0.024	0.022	0.013	0.005	0.005	0.004
⩾ 2	0.123	0.143	0.133	0.105	0.079	0.050	0.055	0.015	0.010	0.007	0.011	0.008	0.003	0.002	0.002	0.000	0.001	0.001	0.002	0.001
MEAN	0.40	0.58	0.63	0.58	0.50	0.36	0.33	0.22	0.16	0.12	0.11	0.07	0.05	0.03	0.03	0.02	0.02	0.01	0.01	0.01
VAR	0.5	0.5	0.5	0.5	0.4	0.3	0.3	0.2	0.2	0.1	0.1	0.1	0.1	0.0	0.0	0.0	0.0	0.0	0.0	0.0

TABLE 179

Primary photon E_0 = 50 MeV.
Secondary electrons E = 5 MeV.

Absorber: air, Z = 7.4, A = 15,
Radiation length = 43 g/sq. cm,
Critical energy = 98 MeV.

n \ t	0.5	1.0	1.5	2.0	2.5	3.0	3.5	4.0	4.5	5.0	5.5	6.0	6.5	7.0	7.5	8.0	8.5	9.0	9.5	10.0
0	0.855	0.879	0.904	0.938	0.954	0.958	0.969	0.977	0.982	0.988	0.988	0.994	0.996	0.997	0.999	1.000	1.000	0.999	1.000	0.999
1	0.115	0.088	0.074	0.053	0.034	0.037	0.028	0.017	0.016	0.010	0.011	0.004	0.004	0.003	0.001	0.000	0.000	0.001	0.000	0.001
2	0.030	0.033	0.022	0.009	0.012	0.005	0.003	0.006	0.002	0.002	0.001	0.002	0.000	0.000	0.000	0.000	0.000	0.000	0.000	0.000
⩾ 3	0.000	0.000	0.000	0.000	0.000	0.000	0.000	0.000	0.000	0.000	0.000	0.000	0.000	0.000	0.000	0.000	0.000	0.000	0.000	0.000
MEAN	0.18	0.15	0.12	0.07	0.06	0.05	0.03	0.03	0.02	0.01	0.01	0.01	0.00	0.00	0.00	0.00	0.00	0.00	0.00	0.00
VAR	0.2	0.2	0.1	0.1	0.1	0.1	0.0	0.0	0.0	0.0	0.0	0.0	0.0	0.0	0.0	0.0	0.0	0.0	0.0	0.0

TABLE 180

Primary photon E_0 = 50 MeV.
Secondary electrons E = 5 MeV.

Absorber: al, Z = 13, A = 27,
Radiation length = 26.3 g/sq. cm = 9.74 cm,
Critical energy = 52 MeV.

n \ t	0.5	1.0	1.5	2.0	2.5	3.0	3.5	4.0	4.5	5.0	5.5	6.0	6.5	7.0	7.5	8.0	8.5	9.0	9.5	10.0
0	0.792	0.801	0.868	0.899	0.916	0.941	0.946	0.963	0.970	0.975	0.975	0.981	0.989	0.992	0.996	0.997	0.998	0.998	0.998	0.999
1	0.139	0.143	0.093	0.073	0.066	0.039	0.039	0.029	0.024	0.017	0.021	0.014	0.009	0.003	0.003	0.002	0.001	0.000	0.002	0.001
2	0.069	0.056	0.039	0.028	0.018	0.020	0.015	0.008	0.006	0.008	0.004	0.005	0.002	0.005	0.001	0.001	0.001	0.001	0.000	0.000
⩾ 3	0.000	0.000	0.000	0.000	0.000	0.000	0.000	0.000	0.000	0.000	0.000	0.000	0.000	0.000	0.000	0.000	0.000	0.000	0.000	0.000
MEAN	0.28	0.26	0.17	0.13	0.10	0.08	0.07	0.05	0.04	0.03	0.03	0.02	0.01	0.01	0.01	0.00	0.00	0.00	0.00	0.00
VAR	0.3	0.3	0.2	0.2	0.1	0.1	0.1	0.1	0.0	0.0	0.0	0.0	0.0	0.0	0.0	0.0	0.0	0.0	0.0	0.0

TABLE 181

Primary photon E_0 = 100 MeV.
Secondary electrons E = 10 MeV.

Absorber: air, Z = 7.4, A = 15,
Radiation length = 43 g/sq. cm,
Critical energy = 98 MeV.

n \ t	0.5	1.0	1.5	2.0	2.5	3.0	3.5	4.0	4.5	5.0	5.5	6.0	6.5	7.0	7.5	8.0	8.5	9.0	9.5	10.0
0	0.744	0.802	0.828	0.900	0.932	0.956	0.959	0.961	0.967	0.974	[illegible]2	0.994	0.984	0.997	0.996	0.999	0.999	0.998	0.998	0.999
1	0.165	0.155	0.117	0.071	0.048	0.036	0.031	0.027	0.025	0.019	0.013	0.004	0.009	0.002	0.003	0.000	0.001	0.000	0.002	0.000
2	0.089	0.043	0.055	0.028	0.020	0.008	0.010	0.012	0.008	0.006	0.005	0.002	0.007	0.001	0.002	0.001	0.000	0.002	0.000	0.001
⩾3	0.002	0.000	0.000	0.001	0.000	0.000	0.000	0.000	0.000	0.001	0.000	0.000	0.000	0.000	0.000	0.000	0.000	0.000	0.000	0.000
MEAN	0.35	0.24	0.23	0.13	0.09	0.05	0.05	0.05	0.04	0.03	0.02	0.01	0.02	0.00	0.01	0.00	0.00	0.00	0.00	0.00
VAR	0.4	0.3	0.3	0.2	0.1	0.1	0.1	0.1	0.1	0.1	0.0	0.0	0.0	0.0	0.0	0.0	0.0	0.0	0.0	0.0

TABLE 182

Primary photon E_0 = 100 MeV.
Secondary electrons E = 10 MeV.

Absorber: al, Z = 13, A = 27,
Radiation length = 26.3 g/sq. cm = 9.74 cm,
Critical energy = 52 MeV.

n \ t	0.5	1.0	1.5	2.0	2.5	3.0	3.5	4.0	4.5	5.0	5.5	6.0	6.5	7.0	7.5	8.0	8.5	9.0	9.5	10.0
0	0.750	0.734	0.790	0.825	0.841	0.887	0.896	0.922	0.948	0.957	0.969	0.960	0.968	0.978	0.982	0.986	0.988	0.993	0.994	0.996
1	0.131	0.205	0.143	0.123	0.126	0.096	0.080	0.058	0.043	0.034	0.022	0.034	0.026	0.016	0.014	0.013	0.010	0.004	0.006	0.004
2	0.118	0.061	0.065	0.052	0.033	0.017	0.023	0.020	0.009	0.009	0.008	0.006	0.006	0.006	0.004	0.001	0.002	0.003	0.000	0.000
⩾3	0.001	0.000	0.002	0.000	0.000	0.000	0.001	0.000	0.000	0.000	0.001	0.000	0.000	0.000	0.000	0.000	0.000	0.000	0.000	0.000
MEAN	0.37	0.33	0.28	0.23	0.19	0.13	0.13	0.10	0.06	0.05	0.04	0.05	0.04	0.03	0.02	0.02	0.01	0.01	0.01	0.00
VAR	0.5	0.3	0.3	0.3	0.2	0.1	0.2	0.1	0.1	0.1	0.1	0.1	0.0	0.0	0.0	0.0	0.0	0.0	0.0	0.0

TABLE 183

Primary photon E_0 = 200 MeV.
Secondary electrons E = 20 MeV.

Absorber: air, Z = 7.4, A = 15,
Radiation length = 43 g/sq. cm,
Critical energy = 98 MeV.

n \ t	0.5	1.0	1.5	2.0	2.5	3.0	3.5	4.0	4.5	5.0	5.5	6.0	6.5	7.0	7.5	8.0	8.5	9.0	9.5	10.0
0	0.722	0.647	0.753	0.788	0.832	0.884	0.917	0.935	0.960	0.966	0.963	0.976	0.987	0.990	0.996	0.993	0.994	0.997	0.997	0.999
1	0.168	0.254	0.196	0.157	0.126	0.095	0.067	0.055	0.038	0.029	0.030	0.019	0.011	0.008	0.002	0.006	0.004	0.002	0.003	0.000
2	0.109	0.098	0.052	0.055	0.042	0.021	0.015	0.010	0.012	0.005	0.007	0.005	0.002	0.002	0.002	0.001	0.002	0.001	0.000	0.001
⩾3	0.001	0.001	0.000	0.000	0.000	0.000	0.001	0.000	0.000	0.000	0.000	0.000	0.000	0.000	0.000	0.000	0.000	0.000	0.000	0.000
MEAN	0.39	0.45	0.30	0.27	0.21	0.14	0.10	0.08	0.06	0.04	0.04	0.03	0.02	0.01	0.01	0.01	0.01	0.00	0.00	0.00
VAR	0.5	0.5	0.3	0.3	0.2	0.2	0.1	0.1	0.1	0.0	0.1	0.0	0.0	0.0	0.0	0.0	0.0	0.0	0.0	0.0

TABLE 184

Primary photon E_0 = 200 MeV.
Secondary electrons E = 20 MeV.

Absorber: al, Z = 13, A = 27,
Radiation length = 26.3 g/sq cm = 9.74 cm,
Critical energy = 52 MeV.

n \ t	0.5	1.0	1.5	2.0	2.5	3.0	3.5	4.0	4.5	5.0	5.5	6.0	6.5	7.0	7.5	8.0	8.5	9.0	9.5	10.0
0	0.751	0.629	0.627	0.691	0.755	0.800	0.848	0.870	0.897	0.927	0.939	0.952	0.965	0.972	0.976	0.993	0.992	0.997	0.996	0.996
1	0.102	0.251	0.262	0.224	0.193	0.165	0.107	0.091	0.080	0.059	0.050	0.039	0.028	0.023	0.019	0.007	0.006	0.003	0.003	0.004
2	0.145	0.117	0.110	0.084	0.052	0.035	0.044	0.037	0.022	0.014	0.011	0.009	0.007	0.005	0.005	0.000	0.002	0.000	0.001	0.001
⩾3	0.002	0.003	0.001	0.001	0.000	0.000	0.001	0.002	0.001	0.000	0.000	0.000	0.000	0.000	0.000	0.000	0.000	0.000	0.000	0.000
MEAN	0.40	0.49	0.49	0.40	0.30	0.24	0.20	0.17	0.13	0.09	0.07	0.06	0.04	0.03	0.03	0.01	0.01	0.00	0.01	0.01
VAR	0.5	0.5	0.5	0.4	0.3	0.3	0.3	0.2	0.2	0.1	0.1	0.1	0.1	0.0	0.0	0.0	0.0	0.0	0.0	0.0

TABLE 185

Primary photon E_0 = 500 MeV.
Secondary electrons E = 50 MeV.

Absorber: air, Z = 7.4, A = 15,
Radiation length = 43 g/sq. cm,
Critical energy = 98 MeV.

n \ t	0.5	1.0	1.5	2.0	2.5	3.0	3.5	4.0	4.5	5.0	5.5	6.0	6.5	7.0	7.5	8.0	8.5	9.0	9.5	10.0
0	0.708	0.562	0.555	0.662	0.738	0.792	0.828	0.857	0.897	0.922	0.918	0.938	0.962	0.963	0.981	0.980	0.996	0.996	0.996	0.996
1	0.119	0.259	0.312	0.260	0.193	0.153	0.135	0.112	0.078	0.066	0.066	0.052	0.028	0.030	0.017	0.018	0.001	0.004	0.003	0.003
2	0.168	0.177	0.128	0.076	0.066	0.054	0.036	0.031	0.025	0.012	0.015	0.010	0.009	0.007	0.002	0.002	0.003	0.000	0.001	0.001
⩾3	0.005	0.002	0.005	0.002	0.003	0.001	0.003	0.000	0.000	0.000	0.001	0.000	0.001	0.000	0.000	0.000	0.000	0.000	0.000	0.000
MEAN	0.47	0.62	0.58	0.42	0.33	0.26	0.22	0.17	0.13	0.09	0.10	0.07	0.05	0.04	0.02	0.02	0.01	0.00	0.01	0.01
VAR	0.6	0.6	0.5	0.4	0.4	0.3	0.3	0.2	0.2	0.1	0.1	0.1	0.1	0.1	0.0	0.0	0.0	0.0	0.0	0.0

TABLE 186

Primary photon E_0 = 500 MeV.
Secondary electrons E = 50 MeV.

Absorber: al, Z = 13, A = 27,
Radiation length = 26.3 g/sq. cm = 9.74 cm,
Critical energy = 52 MeV.

n \ t	0.5	1.0	1.5	2.0	2.5	3.0	3.5	4.0	4.5	5.0	5.5	6.0	6.5	7.0	7.5	8.0	8.5	9.0	9.5	10.0
0	0.705	0.539	0.500	0.549	0.629	0.678	0.751	0.803	0.841	0.864	0.904	0.911	0.938	0.960	0.971	0.973	0.980	0.978	0.986	0.993
1	0.099	0.247	0.327	0.315	0.274	0.237	0.184	0.144	0.122	0.111	0.077	0.070	0.054	0.033	0.024	0.022	0.017	0.017	0.012	0.006
2	0.190	0.202	0.161	0.126	0.091	0.077	0.065	0.053	0.035	0.024	0.019	0.019	0.007	0.007	0.005	0.005	0.003	0.005	0.001	0.001
⩾3	0.006	0.012	0.012	0.010	0.006	0.008	0.000	0.000	0.002	0.001	0.000	0.000	0.001	0.000	0.000	0.000	0.000	0.000	0.001	0.001
MEAN	0.50	0.69	0.69	0.60	0.47	0.42	0.31	0.25	0.20	0.16	0.12	0.11	0.07	0.05	0.03	0.03	0.02	0.03	0.02	0.01
VAR	0.7	0.7	0.6	0.6	0.5	0.4	0.3	0.3	0.2	0.2	0.1	0.1	0.1	0.1	0.0	0.0	0.0	0.0	0.0	0.0

TABLE 187

Primary photon E_0 = 1 000 MeV.
Secondary electrons E = 100 MeV.

Absorber: air, Z = 7.4, A = 15,
Radiation length = 43 g/sq. cm,
Critical energy = 98 MeV.

n \ t	0.5	1.0	1.5	2.0	2.5	3.0	3.5	4.0	4.5	5.0	5.5	6.0	6.5	7.0	7.5	8.0	8.5	9.0	9.5	10.0
0	0.693	0.513	0.463	0.531	0.598	0.687	0.756	0.803	0.861	0.886	0.909	0.930	0.947	0.961	0.970	0.975	0.980	0.988	0.989	0.992
1	0.114	0.266	0.345	0.331	0.293	0.237	0.174	0.156	0.106	0.091	0.060	0.060	0.046	0.031	0.023	0.023	0.015	0.010	0.011	0.008
2	0.189	0.212	0.182	0.134	0.105	0.072	0.067	0.037	0.033	0.019	0.029	0.010	0.006	0.008	0.006	0.002	0.005	0.001	0.000	0.000
⩾3	0.004	0.009	0.010	0.004	0.004	0.004	0.003	0.004	0.000	0.004	0.002	0.000	0.001	0.000	0.001	0.000	0.000	0.001	0.000	0.000
MEAN	0.51	0.72	0.74	0.61	0.52	0.39	0.32	0.24	0.17	0.14	0.12	0.08	0.06	0.05	0.04	0.03	0.03	0.02	0.01	0.01
VAR	0.7	0.7	0.6	0.5	0.5	0.4	0.4	0.3	0.2	0.2	0.2	0.1	0.1	0.1	0.1	0.0	0.0	0.0	0.0	0.0

TABLE 188

Primary photon E_0 = 1 000 MeV.
Secondary electrons E = 100 MeV.

Absorber: al, Z = 13, A = 27,
Radiation length = 26.3 g/sq. cm = 9.74 cm,
Critical energy = 52 MeV.

n \ t	0.5	1.0	1.5	2.0	2.5	3.0	3.5	4.0	4.5	5.0	5.5	6.0	6.5	7.0	7.5	8.0	8.5	9.0	9.5	10.0
0	0.710	0.553	0.478	0.478	0.503	0.590	0.636	0.737	0.789	0.838	0.856	0.888	0.920	0.938	0.956	0.959	0.965	0.964	0.973	0.983
1	0.092	0.218	0.288	0.313	0.321	0.287	0.279	0.199	0.159	0.127	0.118	0.094	0.066	0.057	0.036	0.031	0.031	0.030	0.024	0.014
2	0.192	0.213	0.222	0.197	0.168	0.114	0.082	0.060	0.047	0.035	0.025	0.016	0.013	0.005	0.008	0.010	0.004	0.006	0.003	0.003
⩾3	0.006	0.016	0.012	0.012	0.008	0.009	0.003	0.004	0.005	0.000	0.001	0.002	0.001	0.000	0.000	0.000	0.000	0.000	0.000	0.000
MEAN	0.50	0.69	0.77	0.74	0.68	0.54	0.45	0.33	0.27	0.20	0.17	0.13	0.10	0.07	0.05	0.05	0.04	0.04	0.03	0.02
VAR	0.7	0.7	0.7	0.7	0.6	0.5	0.4	0.4	0.3	0.2	0.2	0.2	0.1	0.1	0.1	0.1	0.0	0.1	0.0	0.0

TABLE 189

Primary photon E_0 = 2 000 MeV.
Secondary electrons E = 200 MeV.

Absorber: air, Z = 7.4, A = 15,
Radiation length = 43 g/sq. cm,
Critical energy = 98 MeV.

n \ t	0.5	1.0	1.5	2.0	2.5	3.0	3.5	4.0	4.5	5.0	5.5	6.0	6.5	7.0	7.5	8.0	8.5	9.0	9.5	10.0
0	0.699	0.517	0.408	0.418	0.483	0.558	0.641	0.717	0.787	0.841	0.881	0.906	0.923	0.945	0.958	0.974	0.980	0.984	0.988	0.994
1	0.101	0.218	0.326	0.364	0.368	0.317	0.278	0.208	0.163	0.124	0.097	0.072	0.057	0.049	0.038	0.023	0.018	0.016	0.011	0.006
2	0.196	0.248	0.246	0.203	0.136	0.117	0.076	0.069	0.045	0.034	0.020	0.020	0.019	0.004	0.003	0.003	0.002	0.000	0.001	0.000
⩾3	0.004	0.017	0.020	0.015	0.013	0.008	0.005	0.006	0.005	0.001	0.002	0.002	0.001	0.002	0.001	0.000	0.000	0.000	0.000	0.000
MEAN	0.51	0.77	0.88	0.82	0.68	0.58	0.45	0.36	0.27	0.20	0.14	0.12	0.10	0.06	0.05	0.03	0.02	0.02	0.01	0.01
VAR	0.7	0.8	0.7	0.7	0.6	0.5	0.4	0.4	0.3	0.2	0.2	0.2	0.1	0.1	0.1	0.0	0.0	0.0	0.0	0.0

TABLE 190

Primary photon E_0 = 2 000 MeV.
Secondary electrons E = 200 MeV.

Absorber: al, Z = 13, A = 27,
Radiation length = 26.3 g/sq. cm = 9.74 cm,
Critical energy = 52 MeV.

n \ t	0.5	1.0	1.5	2.0	2.5	3.0	3.5	4.0	4.5	5.0	5.5	6.0	6.5	7.0	7.5	8.0	8.5	9.0	9.5	10.0
0	0.706	0.514	0.433	0.396	0.415	0.506	0.566	0.642	0.721	0.792	0.830	0.864	0.905	0.922	0.946	0.960	0.963	0.975	0.979	0.982
1	0.101	0.210	0.282	0.351	0.386	0.343	0.317	0.288	0.222	0.169	0.139	0.112	0.082	0.067	0.046	0.043	0.033	0.019	0.015	0.014
2	0.187	0.259	0.252	0.233	0.182	0.136	0.103	0.064	0.052	0.035	0.030	0.022	0.013	0.010	0.008	0.007	0.004	0.006	0.006	0.004
⩾3	0.006	0.017	0.033	0.021	0.017	0.015	0.014	0.006	0.005	0.004	0.001	0.002	0.000	0.001	0.000	0.000	0.000	0.000	0.000	0.000
MEAN	0.49	0.78	0.89	0.89	0.80	0.66	0.57	0.44	0.34	0.25	0.20	0.16	0.11	0.09	0.06	0.05	0.04	0.03	0.03	0.02
VAR	0.7	0.8	0.8	0.7	0.6	0.6	0.5	0.4	0.4	0.3	0.2	0.2	0.1	0.1	0.1	0.1	0.0	0.0	0.0	0.0

TABLE 191

Primary photon E_0 = 5 000 MeV.
Secondary electrons E = 500 MeV.

Absorber: air, Z = 7.4, A = 15,
Radiation length = 43 g/sq. cm,
Critical energy = 98 MeV.

n \ t	0.5	1.0	1.5	2.0	2.5	3.0	3.5	4.0	4.5	5.0	5.5	6.0	6.5	7.0	7.5	8.0	8.5	9.0	9.5	10.0
0	0.692	0.522	0.423	0.382	0.418	0.478	0.563	0.651	0.724	0.770	0.830	0.865	0.897	0.916	0.929	0.944	0.956	0.969	0.982	0.984
1	0.106	0.215	0.285	0.359	0.363	0.357	0.316	0.257	0.209	0.165	0.131	0.109	0.079	0.068	0.059	0.049	0.038	0.026	0.018	0.014
2	0.196	0.234	0.262	0.237	0.198	0.148	0.109	0.080	0.060	0.056	0.034	0.025	0.024	0.015	0.012	0.006	0.006	0.004	0.002	0.002
⩾3	0.006	0.029	0.030	0.022	0.021	0.017	0.012	0.012	0.007	0.009	0.005	0.001	0.000	0.001	0.000	0.001	0.000	0.001	0.000	0.000
MEAN	0.52	0.77	0.90	0.90	0.83	0.71	0.57	0.45	0.35	0.30	0.21	0.16	0.13	0.10	0.08	0.06	0.05	0.04	0.02	0.02
VAR	0.7	0.8	0.8	0.7	0.7	0.6	0.5	0.5	0.4	0.4	0.3	0.2	0.2	0.1	0.1	0.1	0.1	0.1	0.0	0.0

TABLE 192

Primary photon E_0 = 5 000 MeV.
Secondary electrons E = 500 MeV.

Absorber: al, Z = 13, A = 27,
Radiation length = 26.3 g/sq. cm = 9.74 cm,
Critical energy = 52 MeV.

n \ t	0.5	1.0	1.5	2.0	2.5	3.0	3.5	4.0	4.5	5.0	5.5	6.0	6.5	7.0	7.5	8.0	8.5	9.0	9.5	10.0
0	0.705	0.517	0.419	0.385	0.384	0.469	0.542	0.613	0.676	0.736	0.796	0.850	0.885	0.892	0.917	0.943	0.957	0.964	0.976	0.982
1	0.104	0.223	0.309	0.347	0.394	0.364	0.354	0.289	0.243	0.201	0.150	0.115	0.107	0.091	0.072	0.048	0.036	0.032	0.020	0.014
2	0.184	0.234	0.234	0.226	0.182	0.147	0.090	0.084	0.071	0.053	0.049	0.031	0.024	0.016	0.009	0.008	0.006	0.004	0.003	0.004
⩾3	0.007	0.026	0.038	0.042	0.040	0.020	0.014	0.014	0.010	0.010	0.005	0.004	0.004	0.001	0.002	0.001	0.001	0.000	0.001	0.000
MEAN	0.49	0.77	0.90	0.93	0.88	0.72	0.58	0.50	0.42	0.34	0.26	0.19	0.17	0.13	0.10	0.07	0.05	0.04	0.03	0.02
VAR	0.7	0.8	0.8	0.8	0.7	0.6	0.5	0.5	0.4	0.4	0.3	0.2	0.2	0.1	0.1	0.1	0.1	0.0	0.0	0.0

TABLE 193

Primary photon E_0 = 10 000 MeV.
Secondary electrons E = 1 000 MeV.

Absorber: air, Z = 7.4, A = 15,
Radiation length = 43 g/sq. cm,
Critical energy = 98 MeV.

n \ t	0.5	1.0	1.5	2.0	2.5	3.0	3.5	4.0	4.5	5.0	5.5	6.0	6.5	7.0	7.5	8.0	8.5	9.0	9.5	10.0
0	0.690	0.513	0.392	0.377	0.379	0.470	0.531	0.598	0.665	0.736	0.791	0.845	0.876	0.898	0.930	0.939	0.947	0.962	0.973	0.973
1	0.105	0.217	0.299	0.345	0.390	0.366	0.343	0.297	0.267	0.204	0.167	0.123	0.102	0.090	0.064	0.051	0.042	0.027	0.020	0.021
2	0.199	0.243	0.277	0.244	0.208	0.144	0.114	0.095	0.061	0.052	0.038	0.030	0.019	0.011	0.006	0.009	0.009	0.010	0.007	0.006
≥ 3	0.006	0.027	0.032	0.034	0.023	0.020	0.012	0.010	0.007	0.008	0.004	0.002	0.003	0.001	0.000	0.001	0.002	0.001	0.000	0.000
MEAN	0.52	0.79	0.95	0.94	0.88	0.72	0.61	0.52	0.41	0.33	0.26	0.19	0.15	0.12	0.08	0.07	0.07	0.05	0.03	0.03
VAR	0.7	0.8	0.8	0.8	0.7	0.6	0.6	0.5	0.4	0.4	0.3	0.2	0.2	0.1	0.1	0.1	0.1	0.1	0.0	0.0

TABLE 194

Primary photon E = 10 000 MeV.
Secondary electrons E = 1 000 MeV.

Absorber: al, Z = 13, A = 27,
Radiation length = 26.3 g/sq. cm = 9.74 cm,
Critical energy = 52 MeV.

n \ t	0.5	1.0	1.5	2.0	2.5	3.0	3.5	4.0	4.5	5.0	5.5	6.0	6.5	7.0	7.5	8.0	8.5	9.0	9.5	10.0
0	0.700	0.515	0.421	0.385	0.394	0.448	0.484	0.565	0.652	0.725	0.760	0.814	0.858	0.876	0.909	0.925	0.934	0.944	0.968	0.976
1	0.110	0.203	0.287	0.322	0.360	0.337	0.328	0.303	0.251	0.205	0.188	0.149	0.118	0.099	0.074	0.058	0.059	0.045	0.029	0.018
2	0.179	0.246	0.249	0.254	0.219	0.187	0.167	0.122	0.088	0.066	0.047	0.034	0.020	0.025	0.016	0.014	0.007	0.011	0.003	0.006
≥ 3	0.011	0.036	0.043	0.039	0.027	0.028	0.021	0.010	0.009	0.004	0.005	0.003	0.004	0.000	0.001	0.003	0.000	0.000	0.000	0.000
MEAN	0.50	0.81	0.92	0.95	0.88	0.80	0.73	0.58	0.45	0.35	0.30	0.23	0.17	0.15	0.11	0.10	0.07	0.07	0.04	0.03
VAR	0.7	0.9	0.9	0.8	0.7	0.7	0.7	0.6	0.5	0.4	0.3	0.3	0.2	0.2	0.1	0.1	0.1	0.1	0.0	0.0

TABLE 195

Primary photon E = 20 000 MeV.
Secondary electrons E = 2 000 MeV.

Absorber: air, Z = 7.4, A = 15,
Radiation length = 43 g/sq. cm,
Critical energy = 98 MeV.

n \ t	0.5	1.0	1.5	2.0	2.5	3.0	3.5	4.0	4.5	5.0	5.5	6.0	6.5	7.0	7.5	8.0	8.5	9.0	9.5	10.0
0	0.698	0.509	0.406	0.377	0.388	0.432	0.477	0.551	0.658	0.719	0.754	0.809	0.852	0.867	0.904	0.931	0.942	0.954	0.978	0.979
1	0.110	0.214	0.296	0.339	0.371	0.358	0.352	0.319	0.253	0.211	0.195	0.161	0.128	0.106	0.081	0.058	0.050	0.039	0.020	0.018
2	0.181	0.238	0.247	0.239	0.215	0.191	0.145	0.124	0.078	0.067	0.047	0.027	0.018	0.024	0.014	0.011	0.007	0.006	0.002	0.003
≥ 3	0.011	0.039	0.051	0.045	0.026	0.019	0.026	0.006	0.011	0.008	0.004	0.003	0.002	0.003	0.001	0.000	0.001	0.001	0.000	0.000
MEAN	0.51	0.81	0.95	0.96	0.88	0.80	0.72	0.59	0.44	0.35	0.30	0.22	0.17	0.16	0.11	0.08	0.07	0.05	0.02	0.02
VAR	0.7	0.9	0.9	0.8	0.7	0.7	0.7	0.5	0.5	0.4	0.3	0.2	0.2	0.2	0.1	0.1	0.1	0.1	0.0	0.0

TABLE 196

Primary photon E_0 = 20 000 MeV.
Secondary electrons E = 2 000 MeV.

Absorber: al, Z = 13, A = 27,
Radiation length = 26.3 g/sq. cm = 9.74 cm,
Critical energy = 52 MeV.

n \ t	0.5	1.0	1.5	2.0	2.5	3.0	3.5	4.0	4.5	5.0	5.5	6.0	6.5	7.0	7.5	8.0	8.5	9.0	9.5	10.0
0	0.694	0.507	0.398	0.351	0.376	0.407	0.487	0.561	0.616	0.716	0.763	0.813	0.858	0.886	0.905	0.933	0.956	0.965	0.972	0.977
1	0.113	0.202	0.301	0.352	0.371	0.374	0.345	0.314	0.293	0.213	0.186	0.150	0.111	0.092	0.074	0.053	0.038	0.030	0.026	0.020
2	0.185	0.269	0.270	0.264	0.222	0.193	0.143	0.115	0.080	0.066	0.049	0.031	0.029	0.020	0.020	0.012	0.005	0.004	0.002	0.003
≥ 3	0.008	0.022	0.031	0.033	0.031	0.026	0.025	0.010	0.011	0.005	0.002	0.006	0.002	0.002	0.001	0.002	0.001	0.001	0.000	0.000
MEAN	0.51	0.81	0.94	0.98	0.91	0.84	0.71	0.58	0.49	0.36	0.29	0.23	0.18	0.14	0.12	0.08	0.05	0.04	0.03	0.03
VAR	0.7	0.8	0.8	0.7	0.7	0.7	0.7	0.5	0.5	0.4	0.3	0.3	0.2	0.2	0.2	0.1	0.1	0.1	0.0	0.0

TABLE 197

Primary photon E_0 = 50 000 MeV.
Secondary electrons E = 5 000 MeV.

Absorber: air, Z = 7.4, A = 15,
Radiation length = 43 g/sq.cm,
Critical energy = 98 MeV.

n \ t	0.5	1.0	1.5	2.0	2.5	3.0	3.5	4.0	4.5	5.0	5.5	6.0	6.5	7.0	7.5	8.0	8.5	9.0	9.5	10.0
0	0.695	0.502	0.400	0.373	0.362	0.421	0.482	0.542	0.605	0.683	0.761	0.812	0.846	0.887	0.921	0.935	0.960	0.966	0.979	0.983
1	0.085	0.204	0.283	0.331	0.371	0.390	0.350	0.324	0.293	0.242	0.192	0.150	0.130	0.094	0.064	0.054	0.037	0.032	0.017	0.013
2	0.204	0.269	0.269	0.250	0.226	0.162	0.142	0.118	0.091	0.062	0.038	0.035	0.021	0.017	0.015	0.011	0.007	0.002	0.004	0.004
⩾3	0.016	0.025	0.048	0.046	0.041	0.027	0.026	0.016	0.011	0.013	0.009	0.003	0.003	0.002	0.000	0.000	0.000	0.000	0.000	0.000
MEAN	0.54	0.82	0.97	0.97	0.95	0.80	0.71	0.61	0.51	0.41	0.30	0.23	0.18	0.13	0.09	0.08	0.04	0.04	0.03	0.02
VAR	0.8	0.9	0.9	0.9	0.8	0.7	0.6	0.6	0.5	0.4	0.3	0.3	0.2	0.2	0.1	0.1	0.0	0.0	0.0	0.0

TABLE 198

Primary photon E_0 = 50 000 MeV.
Secondary electrons E = 5 000 MeV.

Absorber: al, Z = 13, A = 27,
Radiation length = 26.3 g/sq.cm = 9.74 cm,
Critical energy = 52 MeV.

n \ t	0.5	1.0	1.5	2.0	2.5	3.0	3.5	4.0	4.5	5.0	5.5	6.0	6.5	7.0	7.5	8.0	8.5	9.0	9.5	10.0
0	0.700	0.486	0.374	0.321	0.331	0.407	0.506	0.559	0.668	0.714	0.777	0.831	0.858	0.879	0.905	0.929	0.945	0.958	0.974	0.984
1	0.101	0.222	0.309	0.364	0.411	0.405	0.353	0.322	0.251	0.218	0.174	0.137	0.119	0.097	0.076	0.061	0.046	0.039	0.022	0.015
2	0.189	0.257	0.268	0.278	0.212	0.174	0.125	0.106	0.070	0.063	0.045	0.026	0.017	0.022	0.016	0.009	0.008	0.003	0.004	0.001
⩾3	0.010	0.035	0.049	0.037	0.046	0.014	0.016	0.013	0.011	0.005	0.004	0.006	0.006	0.002	0.003	0.001	0.001	0.000	0.000	0.000
MEAN	0.51	0.85	1.00	1.04	0.98	0.80	0.65	0.57	0.42	0.36	0.28	0.21	0.17	0.15	0.12	0.08	0.07	0.05	0.03	0.02
VAR	0.7	0.9	0.9	0.8	0.7	0.6	0.6	0.5	0.5	0.4	0.3	0.3	0.2	0.2	0.2	0.1	0.1	0.0	0.0	0.0

TABLE 199

Primary photon E_0 = 100 MeV.
Secondary electrons E = 5 MeV.

Absorber: air, Z = 7.4, A = 15,
Radiation length = 43 g/sq.cm,
Critical energy = 98 MeV.

n \ t	0.5	1.0	1.5	2.0	2.5	3.0	3.5	4.0	4.5	5.0	5.5	6.0	6.5	7.0	7.5	8.0	8.5	9.0	9.5	10.0
0	0.727	0.776	0.805	0.875	0.914	0.946	0.952	0.954	0.960	0.965	0.978	0.992	0.982	0.994	0.993	0.997	0.997	0.998	0.997	0.999
1	0.162	0.166	0.127	0.079	0.060	0.040	0.030	0.030	0.031	0.028	0.015	0.005	0.011	0.004	0.005	0.002	0.003	0.000	0.002	0.000
2	0.108	0.056	0.068	0.045	0.026	0.014	0.018	0.016	0.009	0.006	0.007	0.003	0.007	0.002	0.002	0.001	0.000	0.002	0.001	0.001
3	0.002	0.002	0.000	0.001	0.000	0.000	0.000	0.000	0.000	0.001	0.000	0.000	0.000	0.000	0.000	0.000	0.000	0.000	0.000	0.000
⩾4	0.001	0.000	0.000	0.000	0.000	0.000	0.000	0.000	0.000	0.000	0.000	0.000	0.000	0.000	0.000	0.000	0.000	0.000	0.000	0.000
MEAN	0.39	0.28	0.26	0.17	0.11	0.07	0.07	0.06	0.05	0.04	0.03	0.01	0.03	0.01	0.01	0.00	0.00	0.00	0.00	0.00
VAR	0.5	0.3	0.3	0.2	0.2	0.1	0.1	0.1	0.1	0.1	0.0	0.0	0.0	0.0	0.0	0.0	0.0	0.0	0.0	0.0

TABLE 200

Primary photon E_0 = 100 MeV.
Secondary electrons E = 5 MeV.

Absorber: al, Z = 13, A = 27,
Radiation length = 26.3 g/sq.cm = 9.74 cm,
Critical energy = 52 MeV.

n \ t	0.5	1.0	1.5	2.0	2.5	3.0	3.5	4.0	4.5	5.0	5.5	6.0	6.5	7.0	7.5	8.0	8.5	9.0	9.5	10.0
0	0.740	0.681	0.735	0.784	0.817	0.864	0.875	0.894	0.931	0.939	0.959	0.947	0.962	0.973	0.976	0.984	0.985	0.993	0.991	0.996
1	0.113	0.221	0.180	0.144	0.126	0.106	0.091	0.078	0.050	0.047	0.028	0.041	0.028	0.020	0.017	0.010	0.013	0.003	0.008	0.005
2	0.143	0.098	0.081	0.072	0.056	0.029	0.031	0.028	0.019	0.013	0.011	0.011	0.010	0.007	0.007	0.006	0.002	0.004	0.001	0.000
3	0.004	0.000	0.004	0.000	0.001	0.000	0.003	0.000	0.000	0.001	0.001	0.001	0.000	0.000	0.000	0.000	0.000	0.000	0.000	0.000
⩾4	0.000	0.000	0.000	0.000	0.000	0.001	0.000	0.000	0.000	0.000	0.001	0.000	0.000	0.000	0.000	0.000	0.000	0.000	0.000	0.000
MEAN	0.41	0.42	0.35	0.29	0.24	0.17	0.16	0.13	0.09	0.08	0.06	0.07	0.05	0.03	0.03	0.02	0.02	0.01	0.01	0.01
VAR	0.6	0.4	0.4	0.3	0.3	0.2	0.2	0.2	0.1	0.1	0.1	0.1	0.1	0.0	0.0	0.0	0.0	0.0	0.0	0.0

TABLE 201

Primary photon E_0 = 200 MeV.
Secondary electrons E = 10 MeV.

Absorber: air, Z = 7.4, A = 15,
Radiation length = 43 g/sq. cm,
Critical energy = 98 MeV.

n \ t	0.5	1.0	1.5	2.0	2.5	3.0	3.5	4.0	4.5	5.0	5.5	6.0	6.5	7.0	7.5	8.0	8.5	9.0	9.5	10.0
0	0.716	0.612	0.698	0.742	0.791	0.855	0.890	0.911	0.937	0.949	0.953	0.968	0.981	0.986	0.990	0.990	0.993	0.995	0.995	0.999
1	0.141	0.252	0.217	0.179	0.142	0.115	0.081	0.069	0.042	0.040	0.034	0.023	0.015	0.010	0.008	0.008	0.004	0.003	0.005	0.000
2	0.135	0.131	0.080	0.078	0.064	0.028	0.028	0.018	0.020	0.011	0.013	0.009	0.004	0.004	0.002	0.002	0.003	0.002	0.000	0.001
3	0.008	0.003	0.005	0.001	0.003	0.002	0.001	0.001	0.001	0.000	0.000	0.000	0.000	0.000	0.000	0.000	0.000	0.000	0.000	0.000
⩾4	0.000	0.002	0.000	0.000	0.000	0.000	0.000	0.001	0.000	0.000	0.000	0.000	0.000	0.000	0.000	0.000	0.000	0.000	0.000	0.000
MEAN	0.44	0.53	0.39	0.34	0.28	0.18	0.14	0.11	0.09	0.08	0.08	0.04	0.02	0.02	0.01	0.01	0.01	0.01	0.01	0.00
VAR	0.6	0.6	0.4	0.4	0.3	0.2	0.2	0.2	0.1	0.1	0.1	0.1	0.0	0.0	0.0	0.0	0.0	0.0	0.0	0.0

TABLE 202

Primary photon E_0 = 200 MeV.
Secondary electrons E = 10 MeV.

Absorber: al, Z = 13, A = 27,
Radiation length = 26.3 g/sq. cm = 9.74 cm,
Critical energy = 52 MeV.

n \ t	0.5	1.0	1.5	2.0	2.5	3.0	3.5	4.0	4.5	5.0	5.5	6.0	6.5	7.0	7.5	8.0	8.5	9.0	9.5	10.0
0	0.745	0.601	0.559	0.617	0.692	0.747	0.789	0.816	0.854	0.894	0.909	0.931	0.946	0.953	0.962	0.976	0.982	0.991	0.992	0.992
1	0.073	0.230	0.279	0.244	0.210	0.189	0.146	0.124	0.103	0.084	0.069	0.051	0.042	0.034	0.026	0.023	0.010	0.007	0.005	0.006
2	0.174	0.155	0.154	0.129	0.093	0.059	0.061	0.054	0.0[illegible]	0.022	0.022	0.015	0.012	0.012	0.012	0.001	0.008	0.002	0.003	0.002
3	0.005	0.014	0.007	0.008	0.005	0.004	0.004	0.005	0.002	0.000	0.000	0.003	0.000	0.001	0.000	0.000	0.000	0.000	0.000	0.000
⩾4	0.003	0.000	0.001	0.002	0.000	0.001	0.000	0.001	0.000	0.000	0.000	0.000	0.000	0.000	0.000	0.000	0.000	0.000	0.000	0.000
MEAN	0.45	0.58	0.61	0.53	0.41	0.32	0.28	0.25	0.19	0.13	0.11	0.09	0.07	0.06	0.05	0.03	0.03	0.01	0.01	0.01
VAR	0.7	0.8	0.8	0.8	0.5	0.4	0.3	0.3	0.2	0.2	0.1	0.1	0.1	0.1	0.1	0.0	0.0	0.0	0.0	0.0

TABLE 203

Primary photon E_0 = 1 000 MeV.
Secondary electrons E = 50 MeV.

Absorber: air, Z = 7.4, A = 15,
Radiation length = 43 g/sq. cm,
Critical energy = 98 MeV.

n \ t	0.5	1.0	1.5	2.0	2.5	3.0	3.5	4.0	4.5	5.0	5.5	6.0	6.5	7.0	7.5	8.0	8.5	9.0	9.5	10.0
0	0.717	0.516	0.421	0.408	0.444	0.552	0.624	0.653	0.754	0.800	0.845	0.875	0.894	0.920	0.940	0.952	0.963	0.963	0.969	0.973
1	0.061	0.162	0.265	0.326	0.330	0.266	0.234	0.242	0.174	0.139	0.114	0.085	0.080	0.068	0.038	0.035	0.029	0.030	0.025	0.022
2	0.206	0.291	0.249	0.228	0.196	0.144	0.111	0.090	0.059	0.054	0.033	0.036	0.023	0.011	0.020	0.012	0.008	0.006	0.004	0.005
3	0.013	0.026	0.055	0.031	0.027	0.030	0.026	0.014	0.012	0.007	0.007	0.004	0.003	0.001	0.002	0.001	0.000	0.001	0.002	0.000
4	0.003	0.004	0.010	0.006	0.004	0.008	0.005	0.001	0.001	0.000	0.001	0.000	0.000	0.000	0.000	0.000	0.000	0.000	0.000	0.000
⩾5	0.000	0.001	0.000	0.001	0.000	0.000	0.000	0.000	0.000	0.000	0.000	0.000	0.000	0.000	0.000	0.000	0.000	0.000	0.000	0.000
MEAN	0.52	0.84	0.97	0.90	0.82	0.68	0.55	0.47	0.33	0.27	0.21	0.17	0.14	0.09	0.08	0.06	0.05	0.05	0.04	0.03
VAR	0.8	0.9	1.0	0.8	0.8	0.8	0.7	0.5	0.4	0.3	0.3	0.2	0.2	0.1	0.1	0.1	0.1	0.1	0.1	0.0

TABLE 204

Primary photon E_0 = 1 000 MeV.
Secondary electrons E = 50 MeV.

Absorber: al, Z = 13, A = 27,
Radiation length = 26.3 g/sq. cm = 9.74 cm,
Critical energy = 52 MeV.

n \ t	0.5	1.0	1.5	2.0	2.5	3.0	3.5	4.0	4.5	5.0	5.5	6.0	6.5	7.0	7.5	8.0	8.5	9.0	9.5	10.0
0	0.709	0.524	0.384	0.345	0.352	0.422	0.473	0.564	0.647	0.682	0.734	0.776	0.838	0.865	0.907	0.917	0.940	0.954	0.967	0.974
1	0.048	0.134	0.235	0.302	0.328	0.332	0.316	0.282	0.225	0.205	0.173	0.156	0.124	0.108	0.067	0.061	0.045	0.038	0.029	0.020
2	0.226	0.284	0.306	0.253	0.246	0.197	0.171	0.127	0.101	0.094	0.080	0.059	0.030	0.022	0.025	0.021	0.012	0.006	0.003	0.006
3	0.012	0.039	0.058	0.087	0.063	0.040	0.037	0.024	0.022	0.016	0.013	0.009	0.006	0.005	0.000	0.001	0.003	0.002	0.001	0.000
4	0.005	0.017	0.015	0.011	0.010	0.006	0.003	0.003	0.005	0.003	0.000	0.000	0.002	0.000	0.001	0.000	0.000	0.000	0.000	0.000
⩾5	0.000	0.002	0.002	0.002	0.001	0.003	0.000	0.000	0.000	0.000	0.000	0.000	0.000	0.000	0.000	0.000	0.000	0.000	0.000	0.000
MEAN	0.56	0.90	1.09	1.12	1.05	0.89	0.78	0.62	0.51	0.45	0.37	0.30	0.21	0.17	0.12	0.11	0.08	0.06	0.04	0.03
VAR	0.8	1.1	1.1	1.1	1.0	0.9	0.8	0.7	0.6	0.6	0.5	0.4	0.3	0.2	0.2	0.1	0.1	0.1	0.0	0.0

TABLE 205

Primary photon E_0 = 2 000 MeV.
Secondary electrons E = 100 MeV.

Absorber: air, Z = 7.4, A = 15,
Radiation length = 43 g/sq. cm,
Critical energy = 98 MeV.

n \ t	0.5	1.0	1.5	2.0	2.5	3.0	3.5	4.0	4.5	5.0	5.5	6.0	6.5	7.0	7.5	8.0	8.5	9.0	9.5	10.0
0	0.693	0.510	0.376	0.315	0.341	0.387	0.449	0.556	0.615	0.676	0.761	0.822	0.847	0.874	0.908	0.922	0.940	0.958	0.964	0.975
1	0.053	0.148	0.210	0.328	0.345	0.331	0.317	0.277	0.264	0.236	0.174	0.116	0.108	0.091	0.065	0.060	0.046	0.038	0.030	0.019
2	0.240	0.283	0.333	0.277	0.254	0.225	0.171	0.136	0.091	0.070	0.048	0.052	0.036	0.032	0.024	0.016	0.014	0.003	0.006	0.004
3	0.010	0.042	0.067	0.062	0.050	0.053	0.055	0.024	0.020	0.015	0.016	0.008	0.007	0.003	0.002	0.002	0.000	0.001	0.000	0.002
4	0.003	0.016	0.014	0.018	0.008	0.003	0.007	0.008	0.010	0.002	0.000	0.002	0.001	0.000	0.001	0.000	0.001	0.000	0.000	0.000
⩾5	0.001	0.001	0.000	0.000	0.002	0.001	0.001	0.002	0.000	0.001	0.001	0.000	0.001	0.000	0.000	0.000	0.000	0.000	0.000	0.000
MEAN	0.58	0.91	1.13	1.14	1.06	0.96	0.86	0.65	0.55	0.43	0.32	0.25	0.21	0.16	0.12	0.10	0.08	0.05	0.04	0.03
VAR	0.9	1.1	1.1	1.0	0.9	0.9	0.9	0.7	0.7	0.5	0.4	0.4	0.3	0.2	0.2	0.1	0.1	0.1	0.1	0.1

TABLE 206

Primary photon E_0 = 2 000 MeV.
Secondary electrons E = 100 MeV.

Absorber: al, Z = 13, A = 27,
Radiation length = 26.3 g/sq. cm = 9.74 cm,
Critical energy = 52 MeV.

n \ t	0.5	1.0	1.5	2.0	2.5	3.0	3.5	4.0	4.5	5.0	5.5	6.0	6.5	7.0	7.5	8.0	8.5	9.0	9.5	10.0
0	0.719	0.520	0.394	0.298	0.279	0.292	0.341	0.409	0.471	0.582	0.658	0.722	0.773	0.822	0.851	0.899	0.915	0.935	0.956	0.963
1	0.057	0.133	0.202	0.286	0.323	0.342	0.355	0.339	0.326	0.275	0.232	0.187	0.168	0.140	0.100	0.085	0.068	0.047	0.035	0.032
2	0.209	0.267	0.289	0.303	0.298	0.263	0.217	0.192	0.155	0.108	0.081	0.071	0.059	0.034	0.035	0.024	0.017	0.014	0.007	0.004
3	0.012	0.052	0.092	0.088	0.079	0.081	0.072	0.045	0.038	0.025	0.025	0.019	0.008	0.003	0.003	0.002	0.002	0.003	0.001	0.000
4	0.003	0.020	0.020	0.021	0.020	0.016	0.012	0.013	0.009	0.010	0.004	0.006	0.001	0.001	0.001	0.000	0.000	0.001	0.001	0.000
⩾5	0.000	0.008	0.003	0.004	0.001	0.006	0.003	0.002	0.001	0.000	0.000	0.001	0.000	0.000	0.001	0.000	0.000	0.000	0.000	0.001
MEAN	0.52	0.94	1.15	1.26	1.24	1.21	1.07	0.92	0.79	0.61	0.49	0.40	0.30	0.22	0.20	0.14	0.11	0.09	0.06	0.05
VAR	0.8	1.3	1.3	1.2	1.0	1.1	1.0	0.9	0.8	0.7	0.6	0.6	0.4	0.3	0.3	0.2	0.1	0.1	0.1	0.1

TABLE 207

Primary photon E_0 = 10 000 MeV.
Secondary electrons E = 500 MeV.

Absorber: air, Z = 7.4, A = 15,
Radiation length = 43 g/sq. cm,
Critical energy = 98 MeV.

n \ t	0.5	1.0	1.5	2.0	2.5	3.0	3.5	4.0	4.5	5.0	5.5	6.0	6.5	7.0	7.5	8.0	8.5	9.0	9.5	10.0
0	0.688	0.476	0.338	0.255	0.222	0.219	0.262	0.340	0.429	0.498	0.593	0.668	0.729	0.787	0.816	0.861	0.885	0.909	0.935	0.945
1	0.063	0.123	0.190	0.217	0.254	0.312	0.334	0.343	0.317	0.293	0.243	0.220	0.163	0.137	0.140	0.101	0.087	0.067	0.049	0.043
2	0.227	0.322	0.327	0.308	0.332	0.296	0.261	0.218	0.185	0.151	0.121	0.091	0.066	0.055	0.031	0.030	0.024	0.023	0.015	0.011
3	0.013	0.052	0.104	0.150	0.128	0.124	0.105	0.068	0.050	0.045	0.032	0.016	0.010	0.019	0.010	0.008	0.004	0.001	0.001	0.001
4	0.009	0.023	0.035	0.058	0.066	0.040	0.031	0.028	0.016	0.010	0.009	0.004	0.002	0.002	0.002	0.000	0.000	0.000	0.000	0.000
⩾5	0.000	0.004	0.006	0.012	0.008	0.009	0.007	0.005	0.003	0.003	0.002	0.001	0.000	0.000	0.001	0.000	0.000	0.000	0.000	0.000
MEAN	0.59	1.04	1.33	1.58	1.57	1.48	1.33	1.11	0.92	0.79	0.63	0.47	0.36	0.31	0.25	0.19	0.15	0.12	0.08	0.07
VAR	0.9	1.3	1.4	1.6	1.4	1.3	1.2	1.1	1.0	0.9	0.8	0.6	0.4	0.5	0.4	0.3	0.2	0.2	0.1	0.1

TABLE 208

Primary photon E_0 = 10 000 MeV.
Secondary electrons E = 500 MeV.

Absorber: al, Z = 13, A = 27,
Radiation length = 26.3 g/sq. cm = 9.74 cm,
Critical energy = 52 MeV.

n \ t	0.5	1.0	1.5	2.0	2.5	3.0	3.5	4.0	4.5	5.0	5.5	6.0	6.5	7.0	7.5	8.0	8.5	9.0	9.5	10.0
0	0.674	0.492	0.356	0.260	0.233	0.228	0.251	0.310	0.387	0.477	0.517	0.589	0.658	0.737	0.792	0.831	0.857	0.891	0.907	0.926
1	0.072	0.122	0.167	0.214	0.251	0.291	0.337	0.359	0.337	0.311	0.280	0.257	0.225	0.187	0.150	0.134	0.109	0.080	0.073	0.055
2	0.232	0.293	0.321	0.340	0.311	0.301	0.279	0.228	0.187	0.143	0.154	0.114	0.088	0.061	0.043	0.028	0.027	0.024	0.018	0.018
3	0.016	0.061	0.098	0.130	0.137	0.143	0.096	0.079	0.068	0.055	0.037	0.032	0.025	0.020	0.012	0.006	0.006	0.005	0.002	0.001
4	0.006	0.025	0.047	0.045	0.055	0.030	0.030	0.024	0.020	0.011	0.007	0.007	0.004	0.005	0.001	0.001	0.001	0.000	0.000	0.000
⩾5	0.000	0.007	0.011	0.011	0.013	0.007	0.007	0.000	0.001	0.003	0.005	0.001	0.000	0.000	0.002	0.000	0.000	0.000	0.000	0.000
MEAN	0.61	1.03	1.35	1.52	1.57	1.48	1.34	1.15	1.00	0.82	0.75	0.62	0.49	0.37	0.29	0.21	0.19	0.14	0.12	0.09
VAR	0.9	1.4	1.6	1.4	1.5	1.3	1.2	1.0	1.0	1.0	0.9	0.8	0.6	0.5	0.4	0.3	0.3	0.2	0.2	0.1

TABLE 209

Primary photon E_0 = 20 000 MeV.
Secondary electrons E = 1 000 MeV.

Absorber: air, Z = 7.4, A = 15,
Radiation length = 43 g/sq. cm,
Critical energy = 98 MeV.

n \ t	0.5	1.0	1.5	2.0	2.5	3.0	3.5	4.0	4.5	5.0	5.5	6.0	6.5	7.0	7.5	8.0	8.5	9.0	9.5	10.0
0	0.701	0.515	0.385	0.296	0.265	0.231	0.271	0.279	0.359	0.421	0.481	0.576	0.644	0.704	0.757	0.787	0.839	0.894	0.911	0.924
1	0.064	0.121	0.167	0.228	0.236	0.283	0.284	0.335	0.343	0.307	0.324	0.284	0.232	0.190	0.171	0.155	0.130	0.084	0.074	0.064
2	0.212	0.289	0.305	0.303	0.316	0.301	0.278	0.263	0.206	0.203	0.145	0.106	0.091	0.078	0.053	0.045	0.029	0.019	0.013	0.009
3	0.015	0.051	0.101	0.107	0.116	0.107	0.123	0.101	0.062	0.056	0.040	0.027	0.028	0.022	0.015	0.012	0.001	0.002	0.002	0.008
4	0.007	0.017	0.033	0.052	0.059	0.065	0.037	0.016	0.028	0.011	0.005	0.004	0.004	0.006	0.003	0.001	0.001	0.001	0.000	0.000
⩾5	0.001	0.007	0.009	0.014	0.008	0.013	0.007	0.006	0.002	0.002	0.005	0.003	0.001	0.000	0.001	0.000	0.000	0.000	0.000	0.000
MEAN	0.37	0.96	1.26	1.43	1.49	1.53	1.39	1.26	1.06	0.94	0.78	0.61	0.52	0.44	0.34	0.29	0.20	0.13	0.11	0.09
VAR	0.9	1.3	1.5	1.5	1.5	1.5	1.3	1.1	1.1	1.0	0.9	0.7	0.7	0.6	0.5	0.4	0.2	0.2	0.1	0.1

TABLE 210

Primary photon E_0 = 20 000 MeV.
Secondary electrons E = 1 000 MeV.

Absorber: al, Z = 13, A = 27,
Radiation length = 26.3 g/sq. cm = 9.74 cm,
Critical energy = 52 MeV.

n \ t	0.5	1.0	1.5	2.0	2.5	3.0	3.5	4.0	4.5	5.0	5.5	6.0	6.5	7.0	7.5	8.0	8.5	9.0	9.5	10.0
0	0.686	0.494	0.366	0.273	0.233	0.223	0.248	0.284	0.360	0.420	0.475	0.563	0.610	0.678	0.743	0.782	0.832	0.865	0.885	0.919
1	0.047	0.129	0.172	0.215	0.226	0.289	0.300	0.353	0.325	0.327	0.335	0.276	0.253	0.233	0.194	0.163	0.127	0.107	0.098	0.068
2	0.252	0.278	0.312	0.313	0.327	0.298	0.306	0.227	0.204	0.168	0.135	0.113	0.096	0.069	0.049	0.041	0.030	0.024	0.013	0.007
3	0.010	0.067	0.098	0.124	0.127	0.134	0.098	0.102	0.086	0.068	0.040	0.035	0.033	0.015	0.012	0.012	0.010	0.002	0.003	0.005
4	0.005	0.027	0.035	0.057	0.059	0.045	0.043	0.028	0.025	0.019	0.013	0.011	0.007	0.003	0.002	0.002	0.001	0.002	0.001	0.001
⩾5	0.000	0.005	0.017	0.018	0.018	0.011	0.005	0.006	0.000	0.000	0.002	0.002	0.001	0.002	0.000	0.000	0.000	0.000	0.000	0.000
MEAN	0.60	1.02	1.32	1.54	1.62	1.52	1.41	1.26	1.09	0.94	0.79	0.66	0.58	0.44	0.34	0.29	0.22	0.17	0.14	0.10
VAR	0.9	1.4	1.6	1.6	1.6	1.4	1.3	1.2	1.1	1.0	0.9	0.8	0.7	0.6	0.4	0.4	0.3	0.2	0.2	0.1

TABLE 211

Primary photon E_0 = 500 MeV.
Secondary electrons E = 20 MeV.

Absorber: air, Z = 7.4, A = 15,
Radiation length = 43 g/sq. cm,
Critical energy = 98 MeV.

n \ t	0.5	1.0	1.5	2.0	2.5	3.0	3.5	4.0	4.5	5.0	5.5	6.0	6.5	7.0	7.5	8.0	8.5	9.0	9.5	10.0
0	0.704	0.519	0.468	0.536	0.632	0.686	0.745	0.773	0.837	0.864	0.881	0.892	0.937	0.933	0.955	0.967	0.981	0.983	0.987	0.991
1	0.073	0.201	0.292	0.294	0.230	0.196	0.182	0.145	0.118	0.088	0.082	0.079	0.044	0.048	0.037	0.024	0.015	0.014	0.011	0.008
2	0.209	0.254	0.213	0.146	0.118	0.102	0.065	0.074	0.041	0.042	0.036	0.026	0.016	0.018	0.007	0.008	0.004	0.002	0.002	0.001
3	0.010	0.021	0.025	0.021	0.017	0.016	0.007	0.007	0.004	0.004	0.001	0.003	0.003	0.001	0.001	0.001	0.000	0.001	0.000	0.000
≥4	0.004	0.005	0.002	0.003	0.003	0.000	0.001	0.001	0.000	0.002	0.000	0.000	0.000	0.000	0.000	0.000	0.000	0.000	0.000	0.000
MEAN	0.54	0.79	0.80	0.86	0.53	0.45	0.34	0.32	0.21	0.19	0.16	0.14	0.09	0.09	0.05	0.04	0.02	0.02	0.02	0.01
VAR	0.8	0.9	0.8	0.7	0.6	0.5	0.4	0.4	0.3	0.3	0.2	0.2	0.1	0.1	0.1	0.1	0.0	0.0	0.0	0.0

TABLE 212

Primary photon E_0 = 500 MeV.
Secondary electrons E = 20 MeV.

Absorber: al, Z = 13, A = 27,
Radiation length = 26.3 g/sq. cm = 9.74 cm,
Critical energy = 52 MeV.

n \ t	0.5	1.0	1.5	2.0	2.5	3.0	3.5	4.0	4.5	5.0	5.5	6.0	6.5	7.0	7.5	8.0	8.5	9.0	9.5	10.0
0	0.702	0.508	0.414	0.407	0.485	0.519	0.591	0.650	0.712	0.750	0.806	0.836	0.866	0.911	0.918	0.930	0.948	0.955	0.969	0.976
1	0.056	0.148	0.261	0.307	0.284	0.294	0.240	0.213	0.192	0.167	0.140	0.107	0.103	0.063	0.058	0.052	0.038	0.032	0.025	0.018
2	0.226	0.295	0.270	0.225	0.180	0.154	0.140	0.119	0.082	0.068	0.046	0.047	0.028	0.024	0.020	0.017	0.013	0.011	0.005	0.004
3	0.013	0.037	0.037	0.049	0.041	0.027	0.027	0.015	0.010	0.011	0.007	0.009	0.003	0.002	0.004	0.001	0.001	0.002	0.000	0.001
4	0.003	0.010	0.016	0.012	0.009	0.006	0.002	0.003	0.004	0.004	0.001	0.001	0.000	0.000	0.000	0.000	0.000	0.000	0.001	0.000
≥5	0.000	0.002	0.002	0.000	0.001	0.000	0.000	0.000	0.000	0.000	0.000	0.000	0.000	0.000	0.000	0.000	0.000	0.000	0.000	0.001
MEAN	0.56	0.90	0.99	0.95	0.81	0.71	0.61	0.51	0.40	0.35	0.26	0.23	0.17	0.12	0.11	0.09	0.07	0.06	0.04	0.03
VAR	0.8	1.1	1.0	0.9	0.9	0.8	0.7	0.6	0.5	0.5	0.3	0.3	0.2	0.2	0.2	0.1	0.1	0.1	0.1	0.1

TABLE 213

Primary photon E_0 = 5 000 MeV.
Secondary electrons E = 200 MeV.

Absorber: air, Z = 7.4, A = 15,
Radiation length = 43 g/sq. cm,
Critical energy = 98 MeV.

n \ t	0.5	1.0	1.5	2.0	2.5	3.0	3.5	4.0	4.5	5.0	5.5	6.0	6.5	7.0	7.5	8.0	8.5	9.0	9.5	10.0
0	0.725	0.516	0.370	0.277	0.233	0.224	0.268	0.335	0.413	0.497	0.570	0.620	0.695	0.756	0.792	0.819	0.854	0.892	0.909	0.932
1	0.053	0.099	0.163	0.216	0.234	0.292	0.326	0.321	0.298	0.269	0.260	0.245	0.202	0.168	0.140	0.128	0.120	0.080	0.069	0.050
2	0.197	0.293	0.312	0.311	0.336	0.294	0.256	0.229	0.198	0.168	0.128	0.106	0.070	0.050	0.051	0.043	0.021	0.021	0.017	0.017
3	0.018	0.058	0.097	0.120	0.130	0.142	0.104	0.078	0.069	0.048	0.033	0.021	0.029	0.021	0.012	0.006	0.004	0.005	0.005	0.000
4	0.006	0.026	0.043	0.059	0.049	0.035	0.038	0.032	0.019	0.011	0.011	0.007	0.004	0.004	0.004	0.004	0.001	0.001	0.000	0.001
≥5	0.001	0.008	0.015	0.017	0.018	0.013	0.008	0.006	0.003	0.007	0.000	0.001	0.000	0.001	0.001	0.000	0.000	0.001	0.000	0.000
MEAN	0.53	1.01	1.33	1.52	1.58	1.51	1.34	1.17	0.99	0.83	0.66	0.55	0.45	0.35	0.30	0.25	0.18	0.15	0.12	0.09
VAR	0.8	1.4	1.6	1.6	1.5	1.3	1.3	1.2	1.1	1.0	0.8	0.7	0.6	0.5	0.5	0.4	0.2	0.2	0.2	0.1

TABLE 214

Primary photon E_0 = 5 000 MeV.
Secondary electrons E = 200 MeV.

Absorber: al, Z = 13, A = 27,
Radiation length = 26.3 g/sq. cm = 9.74 cm,
Critical energy = 52 MeV.

n \ t	0.5	1.0	1.5	2.0	2.5	3.0	3.5	4.0	4.5	5.0	5.5	6.0	6.5	7.0	7.5	8.0	8.5	9.0	9.5	10.0
0	0.698	0.473	0.355	0.274	0.210	0.209	0.230	0.268	0.343	0.428	0.504	0.575	0.660	0.700	0.754	0.782	0.841	0.869	0.880	0.923
1	0.042	0.110	0.149	0.179	0.218	0.226	0.277	0.291	0.315	0.312	0.292	0.259	0.205	0.206	0.179	0.162	0.120	0.091	0.092	0.069
2	0.236	0.312	0.308	0.312	0.315	0.316	0.279	0.270	0.226	0.173	0.146	0.111	0.095	0.062	0.047	0.043	0.034	0.033	0.023	0.005
3	0.013	0.064	0.117	0.140	0.154	0.171	0.150	0.120	0.080	0.068	0.038	0.039	0.030	0.026	0.016	0.011	0.003	0.005	0.004	0.002
4	0.011	0.028	0.068	0.071	0.075	0.056	0.048	0.032	0.026	0.016	0.018	0.014	0.008	0.006	0.001	0.002	0.002	0.002	0.000	0.001
≥5	0.000	0.013	0.013	0.024	0.028	0.022	0.016	0.019	0.010	0.003	0.002	0.002	0.002	0.000	0.003	0.000	0.000	0.000	0.001	0.000
MEAN	0.60	1.11	1.42	1.63	1.76	1.71	1.56	1.42	1.16	0.94	0.78	0.67	0.53	0.43	0.34	0.29	0.21	0.18	0.16	0.09
VAR	0.9	1.5	1.7	1.8	1.7	1.6	1.5	1.5	1.3	1.1	0.9	0.9	0.8	0.6	0.5	0.4	0.3	0.3	0.2	0.1

TABLE 215

Primary photon E_0 = 50 000 MeV.
Secondary electrons E = 2 000 MeV.

Absorber: air, Z = 7.4, A = 15,
Radiation length = 43 g/sq. cm,
Critical energy = 98 MeV.

n \ t	0.5	1.0	1.5	2.0	2.5	3.0	3.5	4.0	4.5	5.0	5.5	6.0	6.5	7.0	7.5	8.0	8.5	9.0	9.5	10.0
0	0.684	0.458	0.334	0.254	0.193	0.182	0.203	0.212	0.262	0.341	0.385	0.446	0.548	0.640	0.685	0.750	0.800	0.842	0.874	0.893
1	0.042	0.099	0.141	0.177	0.185	0.213	0.259	0.277	0.289	0.306	0.320	0.325	0.261	0.234	0.200	0.172	0.139	0.109	0.095	0.080
2	0.244	0.328	0.307	0.296	0.304	0.301	0.279	0.276	0.257	0.221	0.199	0.146	0.123	0.091	0.080	0.054	0.047	0.033	0.022	0.019
3	0.017	0.063	0.123	0.147	0.182	0.188	0.166	0.145	0.126	0.094	0.071	0.049	0.046	0.024	0.026	0.018	0.010	0.015	0.006	0.005
4	0.012	0.041	0.072	0.092	0.100	0.079	0.066	0.067	0.049	0.028	0.022	0.027	0.019	0.006	0.007	0.004	0.003	0.001	0.003	0.003
≥5	0.001	0.011	0.023	0.034	0.036	0.037	0.027	0.023	0.017	0.010	0.003	0.007	0.003	0.005	0.002	0.002	0.001	0.000	0.000	0.000
MEAN	0.63	1.17	1.54	1.76	1.93	1.89	1.72	1.65	1.47	1.20	1.03	0.91	0.74	0.54	0.48	0.36	0.28	0.22	0.17	0.15
VAR	1.0	1.6	1.9	2.0	1.9	1.8	1.7	1.7	1.6	1.3	1.1	1.1	1.0	0.8	0.7	0.6	0.4	0.3	0.3	0.2

TABLE 216

Primary photon E_0 = 50 000 MeV.
Secondary electrons E = 2 000 MeV.

Absorber: al, Z = 13, A = 27,
Radiation length = 26.3 g/sq. cm = 9.74 cm,
Critical energy = 52 MeV.

n \ t	0.5	1.0	1.5	2.0	2.5	3.0	3.5	4.0	4.5	5.0	5.5	6.0	6.5	7.0	7.5	8.0	8.5	9.0	9.5	10.0
0	0.708	0.504	0.345	0.235	0.185	0.156	0.172	0.202	0.230	0.277	0.367	0.441	0.531	0.608	0.657	0.723	0.776	0.817	0.861	0.883
1	0.045	0.093	0.129	0.151	0.183	0.229	0.241	0.278	0.304	0.342	0.328	0.316	0.276	0.241	0.213	0.186	0.156	0.142	0.104	0.090
2	0.219	0.295	0.323	0.322	0.308	0.305	0.291	0.293	0.281	0.229	0.198	0.167	0.131	0.101	0.096	0.070	0.056	0.032	0.027	0.020
3	0.020	0.068	0.117	0.164	0.190	0.183	0.189	0.145	0.130	0.105	0.077	0.051	0.039	0.033	0.026	0.018	0.008	0.005	0.005	0.006
4	0.008	0.038	0.055	0.091	0.093	0.095	0.075	0.061	0.046	0.040	0.022	0.016	0.019	0.015	0.008	0.003	0.003	0.003	0.003	0.001
≥5	0.000	0.004	0.031	0.037	0.041	0.032	0.032	0.021	0.009	0.007	0.008	0.009	0.004	0.002	0.000	0.002	0.001	0.001	0.000	0.000
MEAN	0.58	1.05	1.50	1.85	1.96	1.94	1.86	1.65	1.49	1.31	1.09	0.91	0.75	0.61	0.52	0.40	0.31	0.24	0.19	0.15
VAR	0.9	1.5	1.9	2.0	1.9	1.8	1.8	1.6	1.4	1.3	1.2	1.1	1.0	0.9	0.7	0.6	0.4	0.3	0.3	0.2

TABLE 217

Primary photon E_0 = 200 MeV.
Secondary electrons E = 5 MeV.

Absorber: air, Z = 7.4, A = 15.
Radiation length = 43 g/sq.cm,
Critical energy = 98 MeV.

n \ t	0.5	1.0	1.5	2.0	2.5	3.0	3.5	4.0	4.5	5.0	5.5	6.0	6.5	7.0	7.5	8.0	8.5	9.0	9.5	10.0
0	0.714	0.596	0.680	0.710	0.770	0.831	0.866	0.893	0.918	0.935	0.945	0.960	0.976	0.979	0.985	0.988	0.992	0.994	0.993	0.997
1	0.118	0.248	0.211	0.193	0.144	0.126	0.091	0.077	0.061	0.049	0.038	0.030	0.018	0.013	0.011	0.010	0.006	0.003	0.007	0.002
2	0.153	0.145	0.101	0.095	0.076	0.040	0.041	0.027	0.030	0.015	0.016	0.010	0.006	0.007	0.004	0.002	0.003	0.002	0.000	0.001
3	0.013	0.008	0.008	0.002	0.010	0.003	0.002	0.002	0.000	0.001	0.001	0.000	0.000	0.001	0.000	0.000	0.000	0.001	0.000	0.000
4	0.001	0.003	0.000	0.000	0.000	0.000	0.000	0.001	0.001	0.000	0.000	0.000	0.000	0.000	0.000	0.000	0.000	0.000	0.000	0.000
≥5	0.001	0.000	0.000	0.000	0.000	0.000	0.000	0.000	0.000	0.000	0.000	0.000	0.000	0.000	0.000	0.000	0.000	0.000	0.000	0.000
MEAN	0.47	0.57	0.44	0.39	0.33	0.22	0.18	0.14	0.12	0.08	0.07	0.05	0.03	0.03	0.02	0.01	0.01	0.01	0.01	0.00
VAR	0.7	0.6	0.5	0.4	0.4	0.3	0.2	0.2	0.2	0.1	0.1	0.1	0.0	0.0	0.0	0.0	0.0	0.0	0.0	0.0

TABLE 218

Primary photon E_0 = 200 MeV.
Secondary electrons E = 5 MeV.

Absorber: al, Z = 13, A = 27,
Radiation length = 26.3 g/sq.cm = 9.74 cm,
Critical energy = 52 MeV.

n \ t	0.5	1.0	1.5	2.0	2.5	3.0	3.5	4.0	4.5	5.0	5.5	6.0	6.5	7.0	7.5	8.0	8.5	9.0	9.5	10.0
0	0.744	0.580	0.527	0.571	0.641	0.689	0.742	0.780	0.806	0.850	0.868	0.908	0.933	0.931	0.950	0.964	0.972	0.986	0.989	0.990
1	0.051	0.215	0.256	0.246	0.231	0.210	0.171	0.142	0.130	0.121	0.097	0.064	0.047	0.050	0.035	0.029	0.019	0.011	0.008	0.007
2	0.192	0.179	0.192	0.166	0.114	0.088	0.074	0.066	0.061	0.028	0.030	0.023	0.018	0.017	0.014	0.007	0.008	0.003	0.003	0.003
3	0.006	0.021	0.017	0.010	0.013	0.012	0.012	0.009	0.002	0.001	0.005	0.005	0.002	0.002	0.001	0.000	0.001	0.000	0.000	0.000
4	0.006	0.004	0.008	0.007	0.001	0.001	0.001	0.002	0.001	0.000	0.000	0.000	0.000	0.000	0.000	0.000	0.000	0.000	0.000	0.000
≥5	0.001	0.001	0.000	0.000	0.000	0.000	0.000	0.001	0.000	0.000	0.000	0.000	0.000	0.000	0.000	0.000	0.000	0.000	0.000	0.000
MEAN	0.48	0.66	0.72	0.64	0.50	0.43	0.36	0.31	0.26	0.18	0.17	0.13	0.09	0.09	0.07	0.04	0.04	0.02	0.01	0.01
VAR	0.8	0.8	0.8	0.7	0.6	0.5	0.5	0.4	0.3	0.2	0.2	0.2	0.1	0.1	0.1	0.1	0.1	0.0	0.0	0.0

TABLE 219

Primary photon E_0 = 2 000 MeV.
Secondary electrons E = 50 MeV.

Absorber: air, Z = 7.4, A = 15.
Radiation length = 43 g/sq.cm.
Critical energy = 98 MeV.

n \ t	0.5	1.0	1.5	2.0	2.5	3.0	3.5	4.0	4.5	5.0	5.5	6.0	6.5	7.0	7.5	8.0	8.5	9.0	9.5	10.0
0	0.689	0.504	0.351	0.273	0.242	0.253	0.300	0.377	0.450	0.526	0.624	0.703	0.754	0.792	0.844	0.865	0.877	0.918	0.937	0.947
1	0.041	0.090	0.150	0.207	0.245	0.297	0.286	0.291	0.292	0.270	0.229	0.186	0.150	0.136	0.101	0.090	0.092	0.058	0.051	0.037
2	0.245	0.307	0.326	0.320	0.318	0.280	0.271	0.222	0.170	0.146	0.102	0.083	0.063	0.053	0.040	0.032	0.024	0.021	0.011	0.013
3	0.012	0.057	0.109	0.159	0.137	0.113	0.095	0.078	0.063	0.039	0.033	0.021	0.023	0.016	0.011	0.009	0.005	0.002	0.001	0.002
4	0.011	0.032	0.047	0.049	0.048	0.044	0.035	0.024	0.023	0.015	0.009	0.005	0.008	0.002	0.002	0.005	0.002	0.001	0.000	0.001
5	0.001	0.007	0.015	0.019	0.009	0.012	0.012	0.006	0.002	0.003	0.002	0.002	0.002	0.001	0.002	0.000	0.000	0.000	0.000	0.000
6	0.000	0.003	0.002	0.002	0.001	0.001	0.000	0.001	0.000	0.000	0.000	0.000	0.000	0.000	0.000	0.000	0.000	0.000	0.000	0.000
≥7	0.001	0.000	0.000	0.001	0.000	0.000	0.001	0.001	0.000	0.001	0.001	0.000	0.000	0.000	0.000	0.000	0.000	0.000	0.000	0.000
MEAN	0.62	1.06	1.40	1.55	1.54	1.44	1.32	1.11	0.92	0.76	0.59	0.45	0.39	0.30	0.23	0.20	0.16	0.11	0.09	0.07
VAR	1.0	1.5	1.7	1.7	1.4	1.4	1.4	1.3	1.1	1.0	0.8	0.6	0.6	0.5	0.4	0.3	0.2	0.2	0.1	0.1

TABLE 220

Primary photon E_0 = 2 000 MeV.
Secondary electrons E = 50 MeV.

Absorber: al, Z = 13, A = 27,
Radiation length = 26.3 g/sq. cm = 9.74 cm,
Critical energy = 52 MeV.

n \ t	0.5	1.0	1.5	2.0	2.5	3.0	3.5	4.0	4.5	5.0	5.5	6.0	6.5	7.0	7.5	8.0	8.5	9.0	9.5	10.0
0	0.718	0.509	0.372	0.264	0.207	0.180	0.190	0.222	0.281	0.378	0.471	0.522	0.614	0.676	0.738	0.788	0.828	0.856	0.897	0.928
1	0.032	0.087	0.124	0.161	0.201	0.241	0.258	0.308	0.312	0.312	0.274	0.262	0.236	0.216	0.163	0.146	0.123	0.110	0.074	0.051
2	0.224	0.287	0.286	0.295	0.305	0.308	0.298	0.262	0.232	0.166	0.174	0.141	0.104	0.076	0.076	0.050	0.036	0.023	0.025	0.016
3	0.014	0.057	0.124	0.163	0.165	0.162	0.137	0.126	0.111	0.100	0.049	0.037	0.031	0.026	0.017	0.012	0.009	0.006	0.003	0.004
4	0.011	0.035	0.062	0.071	0 087	0.068	0.075	0 058	0.048	0.029	0.025	0.028	0.012	0.005	0.005	0.002	0.002	0.003	0.001	0.000
5	0.000	0.021	0.024	0.032	0.024	0.032	0.026	0.018	0.011	0.012	0.006	0.009	0.002	0.001	0.000	0.002	0.002	0.000	0.000	0.001
6	0.001	0.002	0.006	0.010	0.010	0.008	0.013	0.003	0.003	0.002	0.001	0.001	0.000	0.000	0.001	0.000	0.000	0.002	0.000	0.000
⩾7	0.000	0.002	0.002	0 004	0.001	0.001	0.003	0.003	0.002	0.001	0.000	0.000	0.001	0.000	0.000	0.000	0.000	0.000	0.000	0.000
MEAN	0.57	1.10	1.49	1.77	1.84	1.83	1.80	1.57	1.39	1.14	0.91	0.82	0.60	0.47	0.39	0.30	0.24	0.20	0.14	0.10
VAR	0.9	1.8	2.1	2.2	1.9	1.8	1.9	1.7	1.6	1.5	1.2	1.2	0.9	0.8	0.6	0.4	0.4	0.3	0.2	0 2

TABLE 221

Primary photon E_0 = 20 000 MeV.
Secondary electrons E = 500 MeV.

Absorber: air, Z = 7.4, A = 15,
Radiation length = 43 g/sq. cm,
Critical energy = 98 MeV.

n \ t	0.5	1.0	1.5	2.0	2.5	3.0	3.5	4.0	4.5	5.0	5.5	6.0	6.5	7.0	7.5	8.0	8.5	9.0	9.5	10.0
0	0.700	0.506	0.366	0.267	0.204	0.148	0.120	0.117	0.156	0.179	0.214	0.291	0.380	0.464	0.502	0.584	0.649	0.739	0.784	0.809
1	0.030	0.065	0.085	0.108	0.103	0.120	0.156	0.185	0.194	0.218	0.289	0.310	0.302	0.257	0.264	0.234	0.214	0.158	0.152	0.143
2	0.234	0.306	0.285	0.268	0.251	0.246	0.249	0.270	0.279	0.259	0.234	0.200	0.167	0.167	0.149	0.109	0.087	0.071	0.053	0.036
3	0.019	0.055	0.129	0.153	0.167	0.187	0.203	0.200	0.185	0.192	0.146	0.118	0.088	0.069	0.055	0.047	0.038	0.025	0.007	0.007
4	0.014	0.043	0.069	0.104	0.151	0.141	0.161	0.129	0.111	0.093	0.074	0.052	0.035	0.026	0.021	0.017	0.011	0.005	0.004	0.005
5	0.002	0.015	0.046	0.060	0.077	0.088	0.066	0.064	0.053	0.039	0.026	0.016	0.019	0.013	0.004	0.006	0.001	0.002	0.000	0.000
6	0.001	0.006	0.017	0.030	0.028	0.048	0.028	0.023	0.016	0.013	0.011	0.008	0.007	0.003	0.004	0.002	0.000	0.000	0.000	0.000
⩾7	0.000	0.004	0.003	0.010	0.019	0.022	0.017	0.012	0.006	0.007	0.006	0.005	0.002	0.001	0.001	0.001	0.000	0.000	0.000	0.000
MEAN	0.63	1.15	1.67	2.08	2.40	2.63	2.53	2.39	2.16	2.01	1.73	1.44	1.19	0.99	0.86	0.71	0.55	0.41	0.30	0.26
VAR	1.1	1.9	2.6	3.1	3.2	3.3	2.7	2.5	2.3	2.2	2.1	1.9	1.7	1.5	1.3	1.1	0.8	0.6	0.4	0.4

TABLE 222

Primary photon E_0 = 20 000 MeV.
Secondary electrons E = 500 MeV.

Absorber: al, Z = 13, A = 27,
Radiation length = 26.3 g/sq. cm = 9.74 cm,
Critical energy = 52 MeV.

n \ t	0.5	1.0	1.5	2.0	2.5	3.0	3.5	4.0	4.5	5.0	5.5	6.0	6.5	7.0	7.5	8.0	8.5	9.0	9.5	10.0
0	0.686	0.488	0.352	0.236	0.170	0.132	0.114	0.106	0.126	0.154	0.189	0.253	0.327	0.392	0.483	0.553	0.611	0.684	0.733	0.793
1	0.024	0.065	0.090	0.111	0.093	0.124	0.139	0.179	0.206	0.234	0.279	0.300	0.294	0.289	0.281	0.256	0.220	0.187	0.185	0.139
2	0.266	0.292	0.272	0.274	0.267	0.248	0.253	0.259	0.271	0.260	0.239	0.226	0.214	0.174	0.148	0.112	0.105	0.096	0.056	0.043
3	0.017	0.071	0.123	0.130	0.185	0.193	0.188	0.205	0.180	0.174	0.166	0.133	0.094	0.093	0.057	0.050	0.041	0.019	0.018	0.019
4	0.004	0.056	0.084	0.130	0.136	0.160	0.172	0.146	0.137	0.108	0.083	0.049	0.045	0.036	0.018	0.021	0.014	0.008	0.004	0.005
5	0.001	0.018	0.054	0.074	0.086	0.092	0.071	0.066	0.049	0.049	0.026	0.028	0.019	0.010	0.009	0.006	0.005	0.002	0.001	0.001
6	0.002	0.007	0.015	0.332	0.046	0.034	0.042	0.031	0.021	0.017	0.011	0.006	0.005	0.002	0.002	0.002	0.004	0.002	0.002	0.000
⩾7	0.000	0.003	0.010	0.013	0.017	0.017	0.021	0.008	0.010	0.004	0.007	0.005	0.002	0.004	0.002	0.000	0.000	0.002	0.001	0.000
MEAN	0.64	1.24	1.77	2.23	2.56	2.63	2.66	2.47	2.28	2.09	1.83	1.56	1.32	1.15	0.89	0.76	0.66	0.51	0.39	0.31
VAR	1.0	2.1	2.9	3.2	3.2	2.9	3.0	2.5	2.4	2.3	2.1	1.9	1.7	1 6	1.3	1.1	1.1	0.9	0.6	0.5

TABLE 223

Primary photon E_0 = 500 MeV.
Secondary electrons E = 10 MeV.

Absorber: air, Z = 7.4, A = 15,
Radiation length = 43 g/sq. cm,
Critical energy = 98 MeV.

n \ t	0.5	1.0	1.5	2.0	2.5	3.0	3.5	4.0	4.5	5.0	5.5	6.0	6.5	7.0	7.5	8.0	8.5	9.0	9.5	10.0
0	0.703	0.504	0.440	0.486	0.548	0.619	0.675	0.721	0.802	0.825	0.845	0.863	0.913	0.906	0.933	0.958	0.971	0.973	0.979	0.990
1	0.057	0.176	0.256	0.286	0.270	0.218	0.211	0.171	0.119	0.109	0.103	0.084	0.059	0.062	0.054	0.032	0.024	0.018	0.017	0.008
2	0.218	0.277	0.251	0.179	0.144	0.131	0.097	0.087	0.071	0.053	0.047	0.044	0.021	0.030	0.012	0.008	0.005	0.007	0.004	0.002
3	0.014	0.027	0.040	0.039	0.029	0.029	0.016	0.017	0.006	0.010	0.005	0.008	0.007	0.002	0.001	0.002	0.000	0.002	0.000	0.000
4	0.008	0.013	0.013	0.009	0.007	0.003	0.001	0.003	0.002	0.002	0.000	0.001	0.000	0.000	0.000	0.000	0.000	0.000	0.000	0.000
≥5	0.000	0.003	0.000	0.001	0.002	0.000	0.000	0.001	0.000	0.001	0.000	0.000	0.000	0.000	0.000	0.000	0.000	0.000	0.000	0.000
MEAN	0.57	0.88	0.93	0.80	0.68	0.58	0.46	0.41	0.29	0.26	0.21	0.20	0.12	0.13	0.08	0.05	0.03	0.04	0.03	0.01
VAR	0.9	1.0	1.0	0.9	0.8	0.7	0.6	0.6	0.4	0.4	0.3	0.3	0.2	0.2	0.1	0.1	0.0	0.1	0.0	0.0

TABLE 224

Primary photon E_0 = 500 MeV.
Secondary electrons E = 10 MeV.

Absorber: al, Z = 13, A = 27,
Radiation length = 26.3 g/sq. cm = 9.74 cm,
Critical energy = 52 MeV.

n \ t	0.5	1.0	1.5	2.0	2.5	3.0	3.5	4.0	4.5	5.0	5.5	6.0	6.5	7.0	7.5	8.0	8.5	9.0	9.5	10.0
0	0.702	0.501	0.398	0.356	0.394	0.442	0.506	0.541	0.607	0.667	0.717	0.775	0.815	0.860	0.881	0.892	0.918	0.935	0.957	0.959
1	0.035	0.115	0.187	0.253	0.281	0.276	0.247	0.245	0.238	0.200	0.184	0.132	0.127	0.091	0.077	0.078	0.056	0.044	0.031	0.030
2	0.238	0.304	0.294	0.277	0.222	0.202	0.181	0.160	0.116	0.098	0.072	0.072	0.049	0.043	0.030	0.028	0.023	0.018	0.010	0.008
3	0.014	0.050	0.076	0.080	0.069	0.060	0.050	0.037	0.032	0.025	0.019	0.019	0.008	0.006	0.010	0.001	0.002	0.003	0.001	0.002
4	0.010	0.023	0.034	0.032	0.026	0.018	0.012	0.014	0.005	0.009	0.008	0.002	0.000	0.000	0.002	0.001	0.001	0.000	0.001	0.000
≥5	0.001	0.007	0.011	0.002	0.008	0.002	0.004	0.003	0.002	0.001	0.000	0.000	0.001	0.000	0.000	0.000	0.000	0.000	0.000	0.001
MEAN	0.60	1.00	1.20	1.19	1.08	0.94	0.83	0.75	0.60	0.51	0.42	0.34	0.26	0.20	0.18	0.14	0.11	0.09	0.06	0.06
VAR	1.0	1.3	1.4	1.2	1.3	1.1	1.0	1.0	0.8	0.7	0.6	0.5	0.4	0.3	0.3	0.2	0.2	0.1	0.1	0.1

TABLE 225

Primary photon E_0 = 1 000 MeV.
Secondary electrons E = 20 MeV.

Absorber: air, Z = 7.4, A = 15,
Radiation length = 43 g/sq. cm,
Critical energy = 98 MeV.

n \ t	0.5	1.0	1.5	2.0	2.5	3.0	3.5	4.0	4.5	5.0	5.5	6.0	6.5	7.0	7.5	8.0	8.5	9.0	9.5	10.0
0	0.714	0.507	0.388	0.339	0.335	0.403	0.487	0.519	0.629	0.697	0.742	0.793	0.833	0.862	0.892	0.909	0.922	0.938	0.954	0.980
1	0.039	0.098	0.183	0.243	0.274	0.296	0.244	0.268	0.221	0.180	0.163	0.143	0.111	0.107	0.070	0.058	0.055	0.048	0.033	0.026
2	0.222	0.305	0.285	0.286	0.286	0.203	0.191	0.165	0.114	0.090	0.079	0.051	0.044	0.029	0.030	0.031	0.018	0.011	0.010	0.012
3	0.015	0.065	0.091	0.092	0.076	0.066	0.053	0.037	0.028	0.026	0.012	0.011	0.010	0.001	0.005	0.001	0.004	0.002	0.002	0.001
4	0.010	0.021	0.044	0.035	0.023	0.024	0.022	0.010	0.007	0.005	0.004	0.002	0.001	0.000	0.002	0.001	0.001	0.001	0.001	0.001
5	0.000	0.003	0.006	0.004	0.005	0.007	0.003	0.001	0.001	0.002	0.000	0.000	0.001	0.001	0.000	0.000	0.000	0.000	0.000	0.000
6	0.000	0.001	0.003	0.001	0.001	0.001	0.000	0.000	0.000	0.000	0.000	0.000	0.000	0.000	0.001	0.000	0.000	0.000	0.000	0.000
7	0.000	0.000	0.000	0.000	0.000	0.000	0.000	0.000	0.000	0.000	0.000	0.000	0.000	0.000	0.000	0.000	0.000	0.000	0.000	0.000
≥8	0.000	0.000	0.000	0.000	0.000	0.000	0.000	0.000	0.000	0.000	0.000	0.000	0.000	0.000	0.000	0.000	0.000	0.000	0.000	0.000
MEAN	0.57	1.01	1.25	1.26	1.20	1.04	0.89	0.75	0.57	0.47	0.37	0.29	0.24	0.17	0.16	0.13	0.11	0.08	0.06	0.06
VAR	0.9	1.3	1.5	1.3	1.2	1.2	1.1	0.9	0.7	0.7	0.5	0.4	0.4	0.2	0.3	0.2	0.2	0.1	0.1	0.1

TABLE 226

Primary photon E_0 = 1 000 MeV.
Secondary electrons $\bar{E}$ = 20 MeV.

Absorber: al, Z = 13, A = 27,
Radiation length = 26.3 g/sq.cm = 9.74 cm,
Critical energy = 52 MeV.

n \ t	0.5	1.0	1.5	2.0	2.5	3.0	3.5	4.0	4.5	5.0	5.5	6.0	6.5	7.0	7.5	8.0	8.5	9.0	9.5	10.0
0	0.709	0.514	0.362	0.287	0.244	0.279	0.319	0.383	0.446	0.510	0.591	0.637	0.707	0.763	0.791	0.818	0.866	0.895	0.923	0.932
1	0.024	0.077	0.122	0.166	0.219	0.244	0.265	0.283	0.260	0.244	0.201	0.190	0.189	0.132	0.138	0.119	0.099	0.073	0.053	0.047
2	0.232	0.293	0.334	0.304	0.287	0.268	0.259	0.216	0.180	0.152	0.136	0.119	0.078	0.073	0.053	0.050	0.028	0.025	0.023	0.020
3	0.020	0.054	0.103	0.134	0.152	0.143	0.106	0.078	0.081	0.056	0.057	0.043	0.016	0.021	0.014	0.011	0.005	0.005	0.001	0.000
4	0.014	0.042	0.055	0.068	0.076	0.043	0.039	0.030	0.029	0.031	0.013	0.010	0.007	0.010	0.004	0.002	0.001	0.001	0.000	0.001
5	0.001	0.014	0.020	0.031	0.015	0.018	0.009	0.008	0.002	0.006	0.002	0.001	0.002	0.000	0.000	0.000	0.001	0.001	0.000	0.000
6	0.000	0.006	0.003	0.006	0.005	0.004	0.003	0.001	0.001	0.000	0.000	0.000	0.001	0.001	0.000	0.000	0.000	0.000	0.000	0.000
7	0.000	0.000	0.001	0.004	0.002	0.001	0.000	0.001	0.001	0.001	0.000	0.000	0.000	0.000	0.000	0.000	0.000	0.000	0.000	0.000
≥8	0.000	0.000	0.000	0.000	0.000	0.000	0.000	0.000	0.000	0.000	0.000	0.000	0.000	0.000	0.000	0.000	0.000	0.000	0.000	0.000
MEAN	0.61	1.10	1.44	1.67	1.67	1.50	1.32	1.12	1.00	0.88	0.71	0.60	0.44	0.39	0.30	0.26	0.18	0.15	0.10	0.09
VAR	1.0	1.8	1.8	2.1	1.8	1.7	1.5	1.4	1.3	1.3	1.0	0.9	0.7	0.7	0.4	0.4	0.3	0.2	0.1	0.1

TABLE 227

Primary photon E_0 = 5 000 MeV.
Secondary electrons $\bar{E}$ = 100 MeV.

Absorber: air, Z = 7.4, A = 15,
Radiation length = 43 g/sq.cm,
Critical energy = 98 MeV.

n \ t	0.5	1.0	1.5	2.0	2.5	3.0	3.5	4.0	4.5	5.0	5.5	6.0	6.5	7.0	7.5	8.0	8.5	9.0	9.5	10.0
0	0.725	0.512	0.359	0.253	0.182	0.150	0.146	0.187	0.231	0.282	0.350	0.437	0.509	0.579	0.649	0.685	0.742	0.802	0.841	0.864
1	0.030	0.064	0.087	0.109	0.131	0.155	0.201	0.220	0.247	0.278	0.284	0.257	0.258	0.243	0.193	0.191	0.173	0.126	0.108	0.093
2	0.207	0.302	0.299	0.272	0.262	0.288	0.271	0.259	0.249	0.226	0.204	0.175	0.145	0.104	0.102	0.078	0.060	0.054	0.033	0.032
3	0.024	0.055	0.107	0.154	0.203	0.185	0.178	0.169	0.159	0.115	0.100	0.084	0.050	0.048	0.028	0.035	0.018	0.009	0.009	0.008
4	0.011	0.050	0.095	0.120	0.120	0.134	0.108	0.105	0.078	0.056	0.038	0.034	0.028	0.017	0.018	0.007	0.006	0.007	0.006	0.002
5	0.002	0.019	0.028	0.063	0.056	0.054	0.060	0.047	0.020	0.026	0.014	0.008	0.008	0.006	0.003	0.004	0.001	0.000	0.003	0.000
6	0.001	0.004	0.019	0.016	0.036	0.027	0.026	0.007	0.008	0.011	0.007	0.004	0.002	0.002	0.006	0.000	0.000	0.002	0.000	0.000
7	0.000	0.003	0.004	0.009	0.007	0.006	0.010	0.006	0.007	0.003	0.003	0.001	0.000	0.001	0.001	0.000	0.000	0.000	0.000	0.001
≥8	0.000	0.001	0.002	0.004	0.003	0.001	0.000	0.000	0.001	0.003	0.000	0.000	0.000	0.000	0.000	0.000	0.000	0.000	0.000	0.000
MEAN	0.58	1.17	1.68	2.10	2.31	2.30	2.24	1.98	1.74	1.54	1.28	1.07	0.88	0.71	0.61	0.50	0.38	0.30	0.24	0.20
VAR	1.0	2.0	2.6	2.9	2.8	2.5	2.5	2.2	2.1	2.1	1.7	1.5	1.3	1.1	1.1	0.8	0.6	0.5	0.4	0.3

TABLE 228

Primary photon E_0 = 5 000 MeV.
Secondary electrons $\bar{E}$ = 100 MeV.

Absorber: al, Z = 13, A = 27,
Radiation length = 26.3 g/sq.cm = 9.74 cm,
Critical energy = 52 MeV.

n \ t	0.5	1.0	1.5	2.0	2.5	3.0	3.5	4.0	4.5	5.0	5.5	6.0	6.5	7.0	7.5	8.0	8.5	9.0	9.5	10.0
0	0.598	0.470	0.346	0.248	0.175	0.135	0.112	0.122	0.145	0.185	0.262	0.331	0.426	0.477	0.556	0.613	0.669	0.729	0.765	0.806
1	0.024	0.065	0.080	0.078	0.085	0.098	0.148	0.177	0.206	0.261	0.271	0.274	0.258	0.264	0.248	0.222	0.205	0.172	0.157	0.133
2	0.243	0.307	0.276	0.275	0.246	0.246	0.242	0.235	0.237	0.248	0.241	0.187	0.162	0.146	0.119	0.097	0.092	0.064	0.053	0.047
3	0.015	0.065	0.128	0.144	0.184	0.179	0.193	0.200	0.218	0.161	0.122	0.116	0.083	0.062	0.046	0.044	0.020	0.023	0.017	0.009
4	0.017	0.065	0.088	0.127	0.153	0.177	0.152	0.149	0.099	0.091	0.058	0.054	0.041	0.030	0.018	0.012	0.008	0.008	0.006	0.001
5	0.003	0.015	0.044	0.072	0.087	0.092	0.084	0.069	0.062	0.039	0.029	0.023	0.020	0.011	0.006	0.008	0.004	0.002	0.002	0.001
6	0.000	0.009	0.025	0.038	0.044	0.050	0.045	0.030	0.025	0.011	0.013	0.008	0.008	0.006	0.005	0.001	0.002	0.001	0.000	0.001
7	0.000	0.003	0.007	0.014	0.023	0.017	0.018	0.010	0.002	0.001	0.001	0.005	0.001	0.003	0.001	0.003	0.000	0.001	0.000	0.000
≥8	0.000	0.001	0.006	0.004	0.003	0.006	0.006	0.008	0.006	0.003	0.003	0.002	0.001	0.001	0.001	0.000	0.000	0.000	0.000	0.000
MEAN	0.64	1.29	1.84	2.29	2.63	2.77	2.69	2.51	2.25	1.90	1.61	1.43	1.16	0.98	0.77	0.66	0.51	0.42	0.35	0.28
VAR	1.1	2.2	3.1	3.4	3.4	3.3	3.1	2.9	2.6	2.2	2.2	2.1	1.9	1.6	1.3	1.1	0.8	0.7	0.5	0.4

TABLE 229

Primary photon E_0 = 10 000 MeV.
Secondary electrons E = 200 MeV.

Absorber: air, Z = 7.4, A = 15,
Radiation length = 43 g/sq. cm,
Critical energy = 98 MeV.

n \ t	0.5	1.0	1.5	2.0	2.5	3.0	3.5	4.0	4.5	5.0	5.5	6.0	6.5	7.0	7.5	8.0	8.5	9.0	9.5	10.0
0	0.688	0.472	0.318	0.230	0.162	0.114	0.103	0.105	0.141	0.196	0.252	0.325	0.407	0.513	0.569	0.625	0.698	0.748	0.792	0.834
1	0.023	0.049	0.068	0.081	0.083	0.102	0.137	0.184	0.228	0.240	0.274	0.284	0.278	0.236	0.226	0.209	0.187	0.157	0.143	0.108
2	0.256	0.316	0.311	0.244	0.257	0.248	0.215	0.254	0.230	0.234	0.219	0.194	0.177	0.141	0.115	0.103	0.073	0.067	0.042	0.034
3	0.017	0.084	0.123	0.154	0.171	0.176	0.224	0.190	0.195	0.174	0.128	0.105	0.079	0.058	0.055	0.034	0.030	0.015	0.016	0.015
4	0.015	0.057	0.097	0.146	0.148	0.181	0.162	0.137	0.111	0.083	0.074	0.056	0.034	0.037	0.018	0.020	0.010	0.009	0.006	0.007
5	0.001	0.012	0.054	0.090	0.096	0.107	0.109	0.078	0.056	0.048	0.030	0.021	0.016	0.011	0.011	0.006	0.001	0.003	0.000	0.002
6	0.000	0.007	0.019	0.033	0.048	0.041	0.034	0.027	0.023	0.014	0.013	0.008	0.005	0.003	0.003	0.000	0.001	0.001	0.001	0.000
7	0.000	0.002	0.009	0.014	0.026	0.022	0.008	0.015	0.013	0.009	0.010	0.003	0.003	0.000	0.001	0.002	0.000	0.000	0.000	0.000
⩾8	0.000	0.001	0.001	0.008	0.010	0.009	0.008	0.010	0.003	0.002	0.000	0.004	0.001	0.001	0.002	0.001	0.000	0.000	0 000	0.000
MEAN	0.65	1.29	1.90	2.43	2.73	2.86	2.76	2.55	2.25	1.97	1.69	1.42	1.15	0.92	0.79	0.65	0.47	0.39	0.31	0.26
VAR	1.0	2.0	2.9	3.6	3.6	3.2	2.9	2.9	2.7	2.5	2.3	2.1	1.7	1.5	1.4	1.1	0.7	0.7	0.5	0.5

TABLE 230

Primary photon E_0 = 10 000 MeV.
Secondary electrons E = 200 MeV.

Absorber: al, Z = 13, A = 27,
Radiation length = 26.3 g/sq. cm = 9.74 cm,
Critical energy = 52 MeV.

n \ t	0.5	1.0	1.5	2.0	2.5	3.0	3.5	4.0	4.5	5.0	5.5	6.0	6.5	7.0	7.5	8.0	8.5	9.0	9.5	10.0
0	0.672	0.482	0.325	0.227	0.165	0.124	0.102	0.099	0.094	0.137	0.184	0.246	0.310	0.391	0.464	0.566	0.623	0.686	0.738	0.781
1	0.037	0.046	0.065	0.072	0.096	0.090	0.094	0.117	0.153	0.216	0.229	0.257	0.268	0.270	0.275	0.241	0.211	0.185	0.169	0.143
2	0.249	0.294	0.301	0.265	0.220	0.232	0.224	0.238	0.250	0.253	0.279	0.230	0.188	0.178	0.144	0.112	0.098	0.088	0.058	0.056
3	0.019	0.083	0.110	0.154	0.178	0.170	0.208	0.214	0.236	0.184	0.147	0.139	0.133	0.083	0.066	0.046	0.040	0.023	0.017	0.011
4	0.021	0.062	0.097	0.131	0.147	0.175	0.170	0.177	0.157	0.106	0.088	0.063	0.058	0.043	0.025	0.019	0.018	0.012	0.016	0.007
5	0.001	0.020	0.057	0.073	0.099	0.105	0.104	0.093	0.067	0.068	0.042	0.035	0.026	0.020	0.018	0.009	0.007	0.004	0.001	0.001
6	0.001	0.008	0.025	0.045	0.057	0.064	0.061	0.039	0.030	0.025	0.018	0.018	0.012	0.010	0.006	0.006	0.003	0.002	0.000	0.000
7	0.000	0.004	0.013	0.022	0.024	0.025	0.022	0.015	0.007	0.008	0.007	0.008	0.003	0.002	0.000	0.000	0.000	0.000	0.001	0.000
⩾8	0.000	0.001	0.007	0.011	0.014	0.015	0.015	0.009	0.006	0.003	0.006	0.004	0.002	0.003	0.002	0.001	0.000	0.000	0.000	0.001
MEAN	0.69	1.32	1.97	2.47	2.78	2.98	3.02	2.82	2.60	2.27	2.00	1.76	1.51	1.25	1.00	0.77	0.65	0.51	0.41	0.33
VAR	1.1	2.3	3.4	3.9	3.9	3.8	3.5	2.9	2.5	2.6	2.6	2.5	2.2	2.0	1.6	1.3	1.1	0.8	0.7	0.6

TABLE 231

Primary photon E_0 = 50 000 MeV.
Secondary electrons E = 1 000 MeV.

Absorber: air, Z = 7.4, A = 15,
Radiation length = 43 g/sq cm,
Critical energy = 98 MeV

n \ t	0.5	1.0	1.5	2.0	2.5	3.0	3.5	4.0	4.5	5.0	5.5	6.0	6.5	7.0	7.5	8.0	8.5	9.0	9.5	10.0
0	0.682	0.454	0.323	0.232	0.157	0.132	0.110	0.089	0.093	0.114	0.137	0.171	0.244	0.335	0.383	0.488	0.555	0.627	0.704	0.738
1	0.027	0.056	0.061	0.077	0.069	0.069	0.071	0.093	0.127	0.169	0.196	0.256	0.255	0.263	0.280	0.251	0.239	0.222	0.168	0.155
2	0.248	0.311	0.277	0.237	0.202	0.188	0.190	0.198	0.211	0.192	0.242	0.236	0.222	0.194	0.155	0.144	0.125	0.076	0.095	0.065
3	0.020	0.077	0.128	0.145	0.160	0.175	0.192	0.213	0.206	0.226	0.186	0.174	0.127	0.115	0.101	0.064	0.044	0.044	0.032	0.024
4	0.018	0.063	0.098	0.116	0.104	0.161	0.191	0.159	0.168	0.151	0.124	0.074	0.077	0.045	0.041	0.033	0.020	0.022	0.019	0.009
5	0.004	0.020	0.051	0.094	0.123	0.127	0.112	0.122	0.091	0.079	0.066	0.044	0.033	0.026	0.024	0.013	0.006	0.006	0 008	0.004
6	0.001	0.012	0.040	0.050	0.069	0.084	0.077	0.080	0.062	0.043	0.034	0.026	0.017	0.010	0.006	0.006	0.008	0.002	0.003	0.002
7	0.000	0.006	0.011	0.031	0.034	0.041	0.033	0.026	0.028	0.020	0.011	0.013	0.009	0.007	0.008	0.001	0.001	0.001	0.001	0.001
8	0.000	0.000	0.010	0.014	0.015	0.015	0.016	0.011	0.006	0.004	0.003	0.005	0.004	0.003	0.001	0.001	0.002	0.000	0.000	0.002
9	0.000	0.000	0.000	0.003	0.006	0.006	0.004	0.007	0.003	0.000	0.002	0.001	0.002	0.002	0.001	0.000	0.000	0.000	0.000	0.000
⩾10	0.000	0.001	0.001	0.001	0.004	0.002	0.004	0.002	0.005	0.002	0.000	0.000	0.000	0.000	0.000	0.000	0.000	0.000	0.000	0.000
MEAN	0.68	1.39	2.05	2.59	3.08	3.24	3.25	3.21	2.99	2.68	2.39	2.06	1.78	1.48	1.29	0.97	0.80	0.64	0.54	0.45
VAR	1.2	2.4	3.7	4.4	4.5	4.4	4.0	3.8	3.7	3.2	2.9	2.8	2.7	2.4	2.2	1.6	1.4	1.1	1.1	0.9

TABLE 232

Primary photon E_0 = 50 000 MeV.
Secondary electrons E = 1 000 MeV.

Absorber: al, Z = 13, A = 27,
Radiation length = 26.3 g/sq. cm = 9.74 cm,
Critical energy = 52 MeV.

n \ t	0.5	1.0	1.5	2.0	2.5	3.0	3.5	4.0	4.5	5.0	5.5	6.0	6.5	7.0	7.5	8.0	8.5	9.0	9.5	10.0
0	0.708	0.498	0.333	0.226	0.153	0.111	0.090	0.069	0.065	0.071	0.115	0.170	0.212	0.279	0.353	0.437	0.518	0.584	0.647	0.716
1	0.023	0.060	0.062	0.053	0.057	0.072	0.089	0.102	0.117	0.178	0.203	0.233	0.250	0.288	0.295	0.283	0.240	0.228	0.221	0.179
2	0.223	0.287	0.273	0.249	0.215	0.162	0.162	0.172	0.207	0.230	0.242	0.210	0.219	0.198	0.183	0.139	0.132	0.097	0.078	0.062
3	0.028	0.065	0.120	0.136	0.166	0.203	0.188	0.217	0.224	0.196	0.177	0.180	0.155	0.122	0.082	0.060	0.062	0.056	0.031	0.025
4	0.018	0.059	0.097	0.145	0.164	0.179	0.180	0.185	0.195	0.166	0.140	0.110	0.093	0.062	0.051	0.048	0.029	0.024	0.016	0.013
5	0.000	0.025	0.059	0.088	0.115	0.112	0.143	0.130	0.107	0.095	0.068	0.064	0.039	0.028	0.021	0.026	0.015	0.005	0.003	0.003
6	0.000	0.012	0.031	0.047	0.070	0.084	0.084	0.081	0.048	0.044	0.025	0.028	0.021	0.017	0.008	0.005	0.002	0.006	0.003	0.001
7	0.000	0.004	0.015	0.040	0.035	0.054	0.035	0.026	0.025	0.014	0.023	0.012	0.009	0.004	0.006	0.002	0.002	0.000	0.000	0.000
8	0.000	0.000	0.008	0.010	0.013	0.014	0.017	0.012	0.008	0.005	0.005	0.003	0.002	0.001	0.001	0.000	0.000	0.000	0.001	0.001
9	0.000	0.000	0.001	0.005	0.009	0.005	0.010	0.006	0.003	0.000	0.002	0.000	0.000	0.000	0.000	0.000	0.000	0.000	0.000	0.000
≥10	0.000	0.000	0.001	0.001	0.003	0.004	0.002	0.000	0.001	0.001	0.000	0.000	0.000	0.001	0.000	0.000	0.000	0.000	0.000	0.000
MEAN	0.63	1.28	2.03	2.68	3.10	3.36	3.41	3.31	3.08	2.78	2.49	2.18	1.93	1.59	1.31	1.11	0.91	0.75	0.58	0.46
VAR	1.1	2.3	3.7	4.4	4.5	4.3	4.2	3.5	3.1	2.9	3.0	2.8	2.6	2.3	2.0	1.9	1.5	1.3	1.0	0.8

TABLE 233

Primary photon E_0 = 500 MeV.
Secondary electrons E = 5 MeV.

Absorber: air, Z = 7.4, A = 15,
Radiation length = 43 g/sq. cm,
Critical energy = 98 MeV.

n \ t	0.5	1.0	1.5	2.0	2.5	3.0	3.5	4.0	4.5	5.0	5.5	6.0	6.5	7.0	7.5	8.0	8.5	9.0	9.5	10.0
0	0.703	0.500	0.422	0.456	0.507	0.574	0.632	0.682	0.759	0.787	0.810	0.840	0.891	0.884	0.915	0.961	0.962	0.970	0.973	0.988
1	0.048	0.153	0.238	0.259	0.264	0.229	0.217	0.181	0.144	0.129	0.118	0.092	0.071	0.074	0.067	0.038	0.032	0.020	0.017	0.014
2	0.218	0.295	0.249	0.215	0.177	0.142	0.120	0.103	0.084	0.064	0.064	0.054	0.029	0.037	0.014	0.008	0.005	0.007	0.010	0.003
3	0.023	0.026	0.068	0.049	0.037	0.047	0.025	0.024	0.009	0.011	0.008	0.010	0.007	0.004	0.004	0.003	0.001	0.003	0.000	0.000
4	0.007	0.021	0.020	0.017	0.012	0.007	0.006	0.009	0.003	0.008	0.000	0.004	0.002	0.001	0.000	0.000	0.000	0.000	0.000	0.000
5	0.001	0.003	0.003	0.001	0.003	0.001	0.000	0.001	0.000	0.000	0.000	0.000	0.000	0.000	0.000	0.000	0.000	0.000	0.000	0.000
≥6	0.000	0.002	0.000	0.003	0.000	0.000	0.000	0.000	0.001	0.001	0.000	0.000	0.000	0.000	0.000	0.000	0.000	0.000	0.000	0.000
MEAN	0.59	0.93	1.04	0.93	0.79	0.69	0.56	0.50	0.36	0.33	0.27	0.25	0.16	0.16	0.11	0.06	0.05	0.4	0.04	0.02
VAR	0.9	1.2	1.2	1.1	0.9	0.9	0.7	0.7	0.5	0.5	0.4	0.4	0.3	0.2	0.1	0.1	0.1	0.1	0.1	0.0

TABLE 234

Primary photon E_0 = 500 MeV.
Secondary electrons E = 5 MeV.

Absorber: al, Z = 13, A = 27,
Radiation length = 26.3 g/sq. cm = 9.74 cm,
Critical energy = 52 MeV.

n \ t	0.5	1.0	1.5	2.0	2.5	3.0	3.5	4.0	4.5	5.0	5.5	6.0	6.5	7.0	7.5	8.0	8.5	9.0	9.5	10.0
0	0.702	0.500	0.382	0.330	0.351	0.382	0.434	0.475	0.530	0.598	0.649	0.709	0.766	0.804	0.846	0.846	0.895	0.910	0.945	0.941
1	0.026	0.089	0.154	0.209	0.247	0.257	0.247	0.249	0.251	0.223	0.210	0.165	0.145	0.123	0.096	0.112	0.067	0.063	0.036	0.042
2	0.239	0.300	0.292	0.276	0.246	0.236	0.217	0.189	0.149	0.121	0.100	0.091	0.067	0.062	0.039	0.035	0.027	0.021	0.016	0.014
3	0.017	0.068	0.099	0.123	0.090	0.073	0.069	0.057	0.055	0.041	0.029	0.027	0.019	0.010	0.014	0.005	0.009	0.006	0.001	0.002
4	0.014	0.030	0.048	0.050	0.047	0.041	0.026	0.023	0.010	0.014	0.012	0.006	0.002	0.001	0.005	0.002	0.002	0.000	0.001	0.000
5	0.001	0.006	0.021	0.012	0.016	0.008	0.003	0.006	0.004	0.002	0.000	0.002	0.000	0.000	0.000	0.000	0.000	0.000	0.001	0.001
6	0.000	0.007	0.003	0.000	0.002	0.003	0.004	0.001	0.001	0.001	0.000	0.000	0.001	0.000	0.000	0.000	0.000	0.000	0.000	0.000
7	0.001	0.000	0.001	0.000	0.001	0.000	0.000	0.000	0.000	0.000	0.000	0.000	0.000	0.000	0.000	0.000	0.000	0.000	0.000	0.000
MEAN	0.62	1.09	1.36	1.39	1.30	1.17	1.03	0.93	0.78	0.66	0.55	0.46	0.35	0.28	0.24	0.21	0.16	0.12	0.08	0.08
VAR	1.0	1.6	1.8	1.6	1.6	1.5	1.3	1.2	1.0	1.0	0.8	0.7	0.5	0.4	0.4	0.3	0.3	0.2	0.1	0.1

TABLE 235

Primary photon E_0 = 1 000 MeV.
Secondary electrons E = 10 MeV.

Absorber: air, Z = 7.4, A = 15,
Radiation length = 43 g/sq. cm.
Critical energy = 98 MeV.

n \ t	0.5	1.0	1.5	2.0	2.5	3.0	3.5	4.0	4.5	5.0	5.5	6.0	6.5	7.0	7.5	8.0	8.5	9.0	9.5	10.0
0	0.688	0.476	0.354	0.299	0.302	0.336	0.421	0.480	0.538	0.622	0.679	0.729	0.780	0.812	0.863	0.869	0.904	0.925	0.940	0.954
1	0.024	0.086	0.147	0.194	0.243	0.253	0.259	0.228	0.241	0.202	0.171	0.155	0.136	0.117	0.087	0.090	0.067	0.046	0.042	0.032
2	0.255	0.312	0.306	0.284	0.263	0.251	0.199	0.192	0.152	0.126	0.109	0.082	0.058	0.059	0.036	0.031	0.024	0.022	0.014	0.011
3	0.016	0.078	0.120	0.137	0.114	0.103	0.079	0.069	0.044	0.027	0.026	0.024	0.016	0.007	0.008	0.008	0.005	0.004	0.004	0.002
4	0.017	0.035	0.049	0.060	0.055	0.047	0.032	0.023	0.017	0.021	0.013	0.006	0.008	0.003	0.005	0.002	0.000	0.002	0.000	0.001
5	0.000	0.012	0.020	0.020	0.018	0.008	0.006	0.005	0.006	0.002	0.001	0.002	0.002	0.002	0.001	0.000	0.000	0.000	0.000	0.000
6	0.000	0.000	0.004	0.006	0.003	0.002	0.001	0.003	0.002	0.000	0.001	0.002	0.000	0.000	0.000	0.000	0.000	0.001	0.000	0.000
7	0.000	0.000	0.001	0.000	0.001	0.000	0.003	0.000	0.000	0.000	0.000	0.000	0.000	0.000	0.000	0.000	0.000	0.000	0.000	0.000
8	0.000	0.001	0.000	0.000	0.000	0.000	0.000	0.000	0.000	0.000	0.000	0.000	0.000	0.000	0.000	0.000	0.000	0.000	0.000	0.000
9	0.000	0.000	0.000	0.000	0.000	0.000	0.000	0.000	0.000	0.000	0.000	0.000	0.000	0.000	0.000	0.000	0.000	0.000	0.000	0.000
≥10	0.000	0.000	0.000	0.000	0.001	0.000	0.000	0.000	0.000	0.000	0.000	0.000	0.000	0.000	0.000	0.000	0.000	0.000	0.000	0.000
MEAN	0.65	1.15	1.44	1.55	1.46	1.30	1.08	0.95	0.79	0.63	0.53	0.44	0.34	0.28	0.21	0.18	0.13	0.12	0.08	0.06
VAR	1.0	1.6	1.8	1.8	1.8	1.5	1.4	1.3	1.1	0.9	0.8	0.7	0.6	0.4	0.4	0.3	0.2	0.2	0.1	0.1

TABLE 236

Primary photon E_0 = 1 000 MeV.
Secondary electrons E = 10 MeV.

Absorber: al, Z = 13, A = 27,
Radiation length = 26.3 g/sq. cm = 9.74 cm.
Critical energy = 52 MeV.

n \ t	0.5	1.0	1.5	2.0	2.5	3.0	3.5	4.0	4.5	5.0	5.5	6.0	6.5	7.0	7.5	8.0	8.5	9.0	9.5	10.0
0	0.707	0.518	0.385	0.278	0.237	0.225	0.234	0.271	0.328	0.419	0.478	0.541	0.566	0.640	0.733	0.755	0.810	0.834	0.851	0.875
1	0.011	0.069	0.087	0.116	0.126	0.185	0.201	0.241	0.248	0.255	0.254	0.217	0.231	0.200	0.161	0.144	0.122	0.090	0.097	0.077
2	0.246	0.281	0.294	0.270	0.216	0.279	0.289	0.245	0.222	0.181	0.159	0.149	0.127	0.111	0.069	0.069	0.046	0.056	0.040	0.030
3	0.015	0.060	0.103	0.163	0.167	0.131	0.147	0.127	0.117	0.090	0.067	0.059	0.041	0.030	0.026	0.019	0.011	0.014	0.004	0.008
4	0.020	0.056	0.073	0.100	0.112	0.106	0.084	0.073	0.059	0.032	0.029	0.023	0.021	0.016	0.010	0.009	0.007	0.006	0.007	0.007
5	0.000	0.016	0.041	0.049	0.038	0.053	0.035	0.034	0.027	0.014	0.009	0.005	0.009	0.001	0.001	0.004	0.002	0.000	0.001	0.003
6	0.001	0.007	0.012	0.020	0.018	0.013	0.016	0.007	0.002	0.006	0.003	0.005	0.004	0.000	0.000	0.000	0.002	0.000	0.000	0.000
7	0.000	0.002	0.005	0.003	0.005	0.005	0.003	0.001	0.002	0.002	0.000	0.001	0.001	0.002	0.000	0.000	0.000	0.000	0.000	0.000
8	0.000	0.000	0.000	0.001	0.002	0.002	0.000	0.001	0.000	0.001	0.001	0.000	0.000	0.000	0.000	0.000	0.000	0.000	0.000	0.000
9	0.000	0.000	0.000	0.000	0.000	0.001	0.001	0.000	0.000	0.000	0.000	0.000	0.000	0.000	0.000	0.000	0.000	0.000	0.000	0.000
≥10	0.000	0.001	0.000	0.000	0.000	0.000	0.000	0.000	0.000	0.000	0.000	0.000	0.000	0.000	0.000	0.000	0.000	0.000	0.000	0.000
MEAN	0.63	1.17	1.59	1.94	2.01	1.96	1.86	1.63	1.44	1.14	0.96	0.85	0.77	0.60	0.42	0.40	0.30	0.27	0.22	0.20
VAR	1.1	2.1	2.5	2.7	2.5	2.6	2.3	2.1	1.9	1.7	1.4	1.4	1.3	0.9	0.7	0.7	0.6	0.5	0.4	0.4

TABLE 237

Primary photon E_0 = 2 000 MeV.
Secondary electrons E = 20 MeV.

Absorber: air, Z = 7.4, \ = 15,
Radiation length = 43 g/sq. cm,
Critical energy = 98 MeV.

n \ t	0.5	1.0	1.5	2.0	2.5	3.0	3.5	4.0	4.5	5.0	5.5	6.0	6.5	7.0	7.5	8.0	8.5	9.0	9.5	10.0
0	0.690	0.491	0.319	0.232	0.186	0.188	0.193	0.241	0.303	0.403	0.462	0.542	0.626	0.651	0.717	0.780	0.829	0.863	0.873	0.898
1	0.025	0.054	0.092	0.120	0.139	0.183	0.214	0.209	0.263	0.239	0.269	0.233	0.189	0.202	0.169	0.133	0.103	0.086	0.082	0.074
2	0.248	0.285	0.308	0.263	0.287	0.280	0.262	0.290	0.213	0.206	0.147	0.139	0.116	0.095	0.068	0.062	0.048	0.042	0.037	0.021
3	0.016	0.067	0.114	0.152	0.182	0.170	0.174	0.136	0.114	0.088	0.069	0.055	0.049	0.029	0.028	0.014	0.015	0.006	0.006	0.006
4	0.017	0.063	0.102	0.131	0.124	0.107	0.094	0.083	0.075	0.039	0.035	0.020	0.009	0.015	0.011	0.005	0.005	0.002	0.002	0.001
5	0.003	0.024	0.040	0.057	0.049	0.043	0.038	0.027	0.022	0.015	0.012	0.007	0.005	0.006	0.004	0.003	0.000	0.001	0.000	0.000
6	0.001	0.010	0.015	0.025	0.020	0.017	0.015	0.009	0.007	0.006	0.004	0.003	0.003	0.002	0.002	0.002	0.000	0.000	0.000	0.000
7	0.000	0.004	0.006	0.011	0.008	0.007	0.006	0.003	0.002	0.002	0.001	0.001	0.002	0.001	0.001	0.001	0.000	0.000	0.000	0.000
8	0.000	0.001	0.002	0.005	0.003	0.003	0.002	0.001	0.001	0.001	0.001	0.000	0.001	0.000	0.000	0.000	0.000	0.000	0.000	0.000
9	0.000	0.001	0.001	0.002	0.001	0.001	0.001	0.001	0.000	0.001	0.000	0.000	0.000	0.000	0.000	0.000	0.000	0.000	0.000	0.000
≥10	0.000	0.000	0.001	0.002	0.001	0.001	0.001	0.000	0.000	0.000	0.000	0.000	0.000	0.000	0.000	0.000	0.000	0.000	0.000	0.000
MEAN	0.66	1.30	1.83	2.22	2.22	2.09	1.99	1.76	1.51	1.21	1.01	0.82	0.67	0.59	0.47	0.35	0.26	0.20	0.18	0.14
VAR	1.1	2.4	2.8	3.3	2.7	2.6	2.5	2.1	2.0	1.8	1.6	1.3	1.2	1.0	0.9	0.7	0.4	0.3	0.3	0.2

TABLE 238

Primary photon E_0 = 2 000 MeV.
Secondary electrons E = 20 MeV.

Absorber: al, Z = 13, A = 27,
Radiation length = 26.3 g/sq. cm = 9.74 cm,
Critical energy = 52 MeV.

n \ t	0.5	1.0	1.5	2.0	2.5	3.0	3.5	4.0	4.5	5.0	5.5	6.0	6.5	7.0	7.5	8.0	8.5	9.0	9.5	10.0
0	0.704	0.483	0.347	0.240	0.172	0.133	0.120	0.130	0.150	0.200	0.276	0.314	0.412	0.472	0.560	0.621	0.678	0.747	0.789	0.819
1	0.019	0.038	0.051	0.069	0.083	0.107	0.127	0.157	0.188	0.222	0.243	0.277	0.240	0.240	0.251	0.201	0.193	0.155	0.128	0.115
2	0.238	0.303	0.273	0.255	0.239	0.206	0.224	0.223	0.241	0.241	0.192	0.183	0.179	0.157	0.106	0.116	0.083	0.061	0.057	0.040
3	0.013	0.077	0.123	0.156	0.181	0.190	0.198	0.202	0.177	0.165	0.151	0.129	0.100	0.071	0.048	0.042	0.024	0.017	0.017	0.015
4	0.021	0.065	0.111	0.127	0.125	0.170	0.161	0.137	0.117	0.090	0.068	0.052	0.035	0.033	0.024	0.010	0.013	0.013	0.004	0.005
5	0.002	0.016	0.055	0.072	0.104	0.101	0.100	0.080	0.062	0.052	0.043	0.032	0.017	0.018	0.008	0.006	0.006	0.004	0.002	0.002
6	0.003	0.008	0.029	0.045	0.054	0.056	0.042	0.037	0.045	0.020	0.017	0.007	0.011	0.006	0.003	0.002	0.003	0.002	0.002	0.001
7	0.000	0.006	0.005	0.021	0.028	0.023	0.019	0.018	0.013	0.010	0.007	0.004	0.005	0.003	0.000	0.002	0.000	0.001	0.001	0.003
8	0.000	0.003	0.002	0.013	0.010	0.007	0.005	0.010	0.004	0.000	0.002	0.000	0.001	0.000	0.000	0.000	0.000	0.000	0.000	0.000
9	0.000	0.001	0.004	0.002	0.002	0.005	0.002	0.003	0.003	0.000	0.001	0.002	0.000	0.000	0.000	0.000	0.000	0.000	0.000	0.000
≥10	0.000	0.000	0.000	0.000	0.002	0.002	0.002	0.003	0.000	0.000	0.000	0.000	0.000	0.000	0.000	0.000	0.000	0.000	0.000	0.000
MEAN	0.65	1.34	1.95	2.45	2.76	2.89	2.78	2.64	2.40	2.01	1.74	1.49	1.23	1.05	0.76	0.66	0.53	0.42	0.34	0.30
VAR	1.2	2.4	3.4	3.9	4.0	3.7	3.3	3.5	3.2	2.6	2.7	2.2	2.0	1.8	1.2	1.1	0.9	0.8	0.6	0.6

TABLE 239

Primary photon E_0 = 5 000 MeV.
Secondary electrons E = 50 MeV.

Absorber: air, Z = 7.4, A = 15,
Radiation length = 43 g/sq. cm,
Critical energy = 98 MeV.

n \ t	0.5	1.0	1.5	2.0	2.5	3.0	3.5	4.0	4.5	5.0	5.5	6.0	6.5	7.0	7.5	8.0	8.5	9.0	9.5	10.0
0	0.686	0.491	0.339	0.239	0.181	0.137	0.109	0.108	0.127	0.152	0.215	0.264	0.346	0.429	0.484	0.558	0.642	0.693	0.743	0.786
1	0.021	0.037	0.049	0.043	0.054	0.066	0.121	0.122	0.149	0.199	0.222	0.259	0.261	0.254	0.243	0.224	0.181	0.159	0.160	0.129
2	0.250	0.276	0.264	0.237	0.200	0.190	0.176	0.181	0.216	0.232	0.234	0.201	0.191	0.166	0.131	0.118	0.099	0.076	0.059	0.059
3	0.023	0.078	0.107	0.131	0.143	0.163	0.150	0.211	0.202	0.178	0.152	0.145	0.098	0.068	0.069	0.051	0.040	0.037	0.023	0.017
4	0.013	0.073	0.108	0.124	0.155	0.149	0.172	0.154	0.139	0.134	0.089	0.067	0.061	0.045	0.040	0.027	0.019	0.017	0.010	0.004
5	0.004	0.027	0.072	0.091	0.122	0.130	0.111	0.111	0.080	0.056	0.050	0.035	0.028	0.025	0.014	0.011	0.010	0.009	0.003	0.004
6	0.003	0.009	0.028	0.073	0.092	0.083	0.076	0.053	0.047	0.028	0.016	0.019	0.006	0.010	0.012	0.008	0.004	0.004	0.002	0.000
7	0.000	0.003	0.018	0.037	0.041	0.053	0.051	0.039	0.027	0.017	0.013	0.005	0.007	0.003	0.004	0.002	0.003	0.003	0.000	0.001
8	0.000	0.004	0.007	0.014	0.026	0.011	0.021	0.013	0.009	0.004	0.004	0.003	0.002	0.002	0.002	0.001	0.002	0.001	0.000	0.000
9	0.000	0.000	0.006	0.008	0.010	0.012	0.010	0.005	0.002	0.000	0.002	0.001	0.000	0.000	0.001	0.000	0.000	0.001	0.000	0.000
⩾10	0.000	0.002	0.002	0.003	0.006	0.006	0.003	0.003	0.002	0.000	0.003	0.001	0.000	0.000	0.000	0.000	0.000	0.000	0.000	0.000
MEAN	0.68	1.38	2.11	2.77	3.13	3.31	3.27	3.06	2.72	2.33	2.02	1.73	1.42	1.19	1.07	0.85	0.69	0.60	0.41	0.34
VAR	1.2	2.7	4.2	5.1	5.2	5.0	4.7	4.0	3.6	2.9	3.1	2.6	2.2	2.1	2.1	1.8	1.4	1.4	0.7	0.6

TABLE 240

Primary photon E_0 = 5 000 MeV.
Secondary electrons E = 50 MeV.

Absorber: al, Z = 13, A = 27,
Radiation length = 26.3 g/sq. cm = 9.74 cm,
Critical energy = 52 MeV.

n \ t	0.5	1.0	1.5	2.0	2.5	3.0	3.5	4.0	4.5	5.0	5.5	6.0	6.5	7.0	7.5	8.0	8.5	9.0	9.5	10.0
0	0.701	0.489	0.344	0.229	0.151	0.121	0.096	0.081	0.074	0.086	0.119	0.161	0.203	0.266	0.313	0.393	0.479	0.548	0.597	0.665
1	0.013	0.037	0.045	0.050	0.044	0.051	0.066	0.070	0.096	0.133	0.151	0.186	0.217	0.237	0.242	0.242	0.239	0.239	0.214	0.175
2	0.244	0.275	0.246	0.195	0.174	0.133	0.141	0.157	0.153	0.186	0.216	0.202	0.226	0.205	0.184	0.181	0.137	0.091	0.099	0.080
3	0.018	0.069	0.103	0.134	0.121	0.124	0.134	0.164	0.191	0.167	0.183	0.176	0.126	0.121	0.132	0.088	0.069	0.054	0.036	0.039
4	0.020	0.072	0.118	0.131	0.143	0.157	0.140	0.160	0.165	0.164	0.133	0.114	0.107	0.074	0.057	0.048	0.036	0.035	0.028	0.020
5	0.003	0.031	0.064	0.091	0.138	0.138	0.145	0.127	0.124	0.110	0.090	0.083	0.057	0.057	0.033	0.026	0.022	0.017	0.012	0.011
6	0.001	0.012	0.041	0.083	0.116	0.101	0.102	0.093	0.093	0.075	0.052	0.039	0.038	0.021	0.020	0.016	0.012	0.007	0.010	0.005
7	0.000	0.007	0.017	0.043	0.053	0.083	0.087	0.072	0.060	0.036	0.026	0.020	0.017	0.012	0.013	0.003	0.004	0.003	0.002	0.004
8	0.000	0.004	0.007	0.024	0.030	0.055	0.052	0.043	0.027	0.021	0.016	0.014	0.002	0.001	0.003	0.002	0.000	0.005	0.001	0.000
9	0.000	0.002	0.008	0.011	0.015	0.017	0.019	0.019	0.009	0.015	0.010	0.004	0.006	0.004	0.002	0.001	0.000	0.000	0.001	0.000
⩾10	0.000	0.002	0.007	0.009	0.015	0.020	0.018	0.014	0.009	0.007	0.004	0.001	0.001	0.002	0.001	0.000	0.002	0.001	0.000	0.001
MEAN	0.66	1.43	2.20	3.01	3.62	3.99	4.05	3.88	3.62	3.29	2.87	2.52	2.19	1.87	1.66	1.33	1.09	0.92	0.78	0.66
VAR	1.2	3.1	4.7	5.9	6.2	6.5	6.4	5.6	4.7	4.8	4.3	3.8	3.5	3.2	3.0	2.3	2.2	2.0	1.7	1.5

TABLE 241

Primary photon E_0 = 10 000 MeV.
Secondary electrons E = 100 MeV.

Absorber: air, Z = 7.4, A = 15.
Radiation length = 43 g/sq. cm,
Critical energy = 98 MeV.

s \ t	0.5	1.0	1.5	2.0	2.5	3.0	3.5	4.0	4.5	5.0	5.5	6.0	6.5	7.0	7.5	8.0	8.5	9.0	9.5	10.0
0	0.680	0.486	0.327	0.226	0.163	0.115	0.087	0.064	0.066	0.076	0.101	0.135	0.203	0.282	0.347	0.408	0.477	0.562	0.641	0.674
1	0.014	0.032	0.039	0.036	0.038	0.040	0.049	0.058	0.086	0.109	0.155	0.196	0.225	0.215	0.262	0.276	0.222	0.215	0.176	0.187
2	0.263	0.264	0.241	0.193	0.150	0.137	0.118	0.143	0.149	0.187	0.197	0.216	0.190	0.202	0.177	0.157	0.157	0.113	0.088	0.079
3	0.018	0.077	0.103	0.134	0.131	0.123	0.164	0.162	0.183	0.186	0.182	0.145	0.140	0.127	0.102	0.074	0.062	0.047	0.048	0.031
4	0.021	0.089	0.110	0.128	0.131	0.153	0.170	0.177	0.170	0.157	0.139	0.136	0.100	0.090	0.055	0.036	0.039	0.034	0.020	0.014
5	0.004	0.030	0.066	0.097	0.132	0.144	0.152	0.162	0.143	0.108	0.091	0.084	0.067	0.037	0.024	0.026	0.021	0.015	0.013	0.008
6	0.000	0.014	0.055	0.080	0.098	0.106	0.098	0.089	0.081	0.083	0.061	0.038	0.041	0.023	0.019	0.012	0.011	0.007	0.009	0.006
7	0.000	0.006	0.034	0.038	0.065	0.087	0.084	0.068	0.065	0.041	0.044	0.030	0.018	0.015	0.007	0.007	0.005	0.006	0.004	0.001
8	0.000	0.002	0.011	0.038	0.046	0.048	0.037	0.033	0.033	0.034	0.019	0.010	0.007	0.005	0.003	0.005	0.002	0.000	0.000	0.000
9	0.000	0.000	0.009	0.013	0.025	0.027	0.023	0.025	0.015	0.013	0.008	0.007	0.007	0.002	0.001	0.003	0.002	0.000	0.001	0.000
≥10	0.000	0.000	0.005	0.017	0.021	0.020	0.018	0.019	0.009	0.006	0.003	0.005	0.002	0.002	0.003	0.001	0.002	0.001	0.000	0.000
MEAN	0.70	1.44	2.39	3.18	3.78	4.10	4.09	4.05	3.76	3.45	3.04	2.66	2.27	1.87	1.49	1.29	1.14	0.89	0.73	0.58
VAR	1.2	2.8	5.3	6.7	7.1	6.8	5.7	5.4	4.9	4.8	4.4	4.2	3.9	3.3	2.8	2.6	2.4	1.9	1.7	1.1

TABLE 242

Primary photon E_0 = 10 000 MeV.
Secondary electrons E = 100 MeV.

Absorber: al, Z = 13, A = 27,
Radiation length = 26.3 g/sq. cm = 9.74 cm,
Critical energy = 52 MeV.

s \ t	0.5	1.0	1.5	2.0	2.5	3.0	3.5	4.0	4.5	5.0	5.5	6.0	6.5	7.0	7.5	8.0	8.5	9.0	9.5	10.0
0	0.696	0.489	0.353	0.259	0.184	0.134	0.092	0.071	0.050	0.055	0.068	0.082	0.115	0.167	0.212	0.289	0.360	0.427	0.465	0.565
1	0.016	0.039	0.034	0.029	0.032	0.030	0.047	0.044	0.039	0.072	0.096	0.134	0.151	0.183	0.222	0.245	0.242	0.236	0.248	0.214
2	0.237	0.263	0.237	0.183	0.155	0.130	0.131	0.113	0.114	0.134	0.139	0.188	0.186	0.180	0.189	0.189	0.162	0.154	0.139	0.109
3	0.024	0.075	0.110	0.113	0.098	0.102	0.104	0.117	0.147	0.134	0.166	0.153	0.174	0.169	0.146	0.111	0.111	0.085	0.071	0.051
4	0.024	0.069	0.110	0.110	0.129	0.130	0.130	0.158	0.171	0.187	0.148	0.150	0.132	0.127	0.090	0.061	0.056	0.050	0.039	0.031
5	0.002	0.033	0.058	0.091	0.105	0.122	0.123	0.153	0.163	0.139	0.150	0.109	0.098	0.070	0.066	0.048	0.023	0.024	0.018	0.014
6	0.001	0.020	0.043	0.097	0.092	0.114	0.113	0.140	0.128	0.099	0.084	0.072	0.072	0.048	0.036	0.031	0.025	0.010	0.013	0.008
7	0.000	0.003	0.030	0.041	0.074	0.083	0.115	0.071	0.081	0.076	0.070	0.046	0.036	0.026	0.010	0.013	0.007	0.004	0.006	0.005
8	0.000	0.006	0.014	0.039	0.050	0.072	0.070	0.055	0.044	0.045	0.041	0.039	0.014	0.014	0.019	0.006	0.008	0.006	0.000	0.000
9	0.000	0.003	0.004	0.026	0.032	0.043	0.035	0.038	0.031	0.031	0.022	0.011	0.014	0.010	0.002	0.004	0.004	0.003	0.000	0.001
≥10	0.000	0.000	0.007	0.012	0.049	0.040	0.040	0.040	0.032	0.028	0.016	0.016	0.008	0.006	0.008	0.003	0.002	0.001	0.001	0.002
MEAN	0.67	1.45	2.26	3.18	3.98	4.39	4.55	4.57	4.52	4.25	3.91	3.44	3.07	2.65	2.27	1.83	1.56	1.29	1.12	0.89
VAR	1.2	3.1	5.1	7.3	9.2	8.3	7.8	6.9	5.9	6.1	5.8	5.5	4.9	4.7	4.4	3.6	3.3	2.6	2.2	2.0

TABLE 243

Primary photon E_0 = 20 000 MeV.
Secondary electrons E = 200 MeV.

Absorber: air, Z = 7.4, A = 15,
Radiation length = 43 g/sq. cm,
Critical energy = 98 MeV.

n \ t	0.5	1.0	1.5	2.0	2.5	3.0	3.5	4.0	4.5	5.0	5.5	6.0	6.5	7.0	7.5	8.0	8.5	9.0	9.5	10.0
0	0.691	0.477	0.343	0.248	0.178	0.128	0.090	0.069	0.064	0.050	0.054	0.076	0.111	0.156	0.202	0.281	0.346	0.427	0.511	0.585
1	0.022	0.039	0.037	0.035	0.034	0.033	0.032	0.029	0.034	0.061	0.089	0.126	0.152	0.170	0.236	0.239	0.263	0.251	0.243	0.214
2	0.239	0.265	0.231	0.161	0.134	0.116	0.108	0.104	0.094	0.119	0.159	0.168	0.183	0.217	0.164	0.169	0.147	0.141	0.105	0.096
3	0.014	0.063	0.092	0.119	0.092	0.107	0.099	0.126	0.156	0.171	0.167	0.181	0.157	0.147	0.150	0.123	0.090	0.086	0.062	0.045
4	0.027	0.077	0.115	0.137	0.133	0.105	0.140	0.148	0.149	0.155	0.158	0.140	0.148	0.121	0.096	0.072	0.074	0.043	0.030	0.030
5	0.004	0.043	0.063	0.095	0.129	0.096	0.150	0.157	0.147	0.140	0.137	0.118	0.101	0.071	0.071	0.054	0.047	0.024	0.022	0.016
6	0.003	0.013	0.050	0.075	0.093	0.128	0.131	0.105	0.125	0.115	0.109	0.075	0.067	0.049	0.036	0.029	0.017	0.015	0.015	0.009
7	0.000	0.010	0.030	0.050	0.083	0.108	0.092	0.127	0.100	0.082	0.048	0.059	0.035	0.029	0.017	0.016	0.007	0.008	0.007	0.003
8	0.000	0.008	0.022	0.034	0.058	0.082	0.072	0.062	0.061	0.039	0.039	0.030	0.029	0.025	0.014	0.014	0.004	0.003	0.001	0.001
9	0.000	0.003	0.009	0.028	0.030	0.052	0.036	0.039	0.042	0.038	0.021	0.015	0.006	0.003	0.011	0.002	0.002	0.001	0.002	0.000
≥10	0.000	0.002	0.008	0.018	0.036	0.045	0.050	0.034	0.028	0.030	0.019	0.012	0.011	0.012	0.003	0.001	0.003	0.001	0.002	0.002
MEAN	0.69	1.54	2.40	3.26	4.02	4.63	4.72	4.73	4.64	4.37	3.91	3.52	3.13	2.73	2.33	1.93	1.59	1.27	1.06	0.85
VAR	1.3	3.5	5.7	7.5	8.4	8.9	7.6	6.8	6.4	6.2	5.4	5.3	5.0	4.9	4.4	3.8	3.2	2.6	2.5	2.0

TABLE 244

Primary photon E_0 = 20 000 MeV.
Secondary electrons E = 200 MeV.

Absorber: al, Z = 13, A = 27,
Radiation length = 26.3 g/sq. cm = 9.74 cm,
Critical energy = 52 MeV.

n \ t	0.5	1.0	1.5	2.0	2.5	3.0	3.5	4.0	4.5	5.0	5.5	6.0	6.5	7.0	7.5	8.0	8.5	9.0	9.5	10.0
0	0.686	0.476	0.332	0.230	0.165	0.103	0.072	0.047	0.036	0.031	0.032	0.049	0.074	0.104	0.139	0.207	0.292	0.363	0.439	0.516
1	0.017	0.025	0.028	0.025	0.025	0.029	0.020	0.030	0.021	0.044	0.058	0.084	0.137	0.178	0.189	0.203	0.241	0.253	0.247	0.216
2	0.238	0.271	0.241	0.170	0.143	0.126	0.093	0.074	0.065	0.072	0.132	0.162	0.180	0.175	0.205	0.211	0.174	0.152	0.135	0.140
3	0.022	0.076	0.100	0.107	0.090	0.082	0.079	0.095	0.106	0.133	0.140	0.182	0.154	0.170	0.167	0.145	0.102	0.104	0.076	0.062
4	0.029	0.075	0.100	0.128	0.110	0.113	0.113	0.118	0.148	0.145	0.151	0.147	0.143	0.122	0.110	0.080	0.076	0.056	0.054	0.034
5	0.006	0.042	0.078	0.095	0.124	0.111	0.147	0.141	0.155	0.154	0.140	0.126	0.102	0.096	0.084	0.069	0.045	0.035	0.021	0.011
6	0.002	0.020	0.048	0.085	0.103	0.118	0.125	0.116	0.140	0.146	0.121	0.090	0.087	0.076	0.042	0.032	0.026	0.017	0.015	0.010
7	0.000	0.010	0.028	0.062	0.093	0.096	0.103	0.139	0.122	0.110	0.088	0.063	0.056	0.037	0.026	0.024	0.019	0.010	0.007	0.009
8	0.000	0.004	0.018	0.045	0.051	0.089	0.098	0.088	0.080	0.065	0.065	0.046	0.034	0.024	0.020	0.012	0.010	0.004	0.001	0.001
9	0.000	0.001	0.015	0.032	0.041	0.054	0.065	0.072	0.062	0.049	0.039	0.021	0.013	0.009	0.010	0.009	0.007	0.003	0.004	0.001
≥10	0.000	0.000	0.012	0.021	0.055	0.079	0.085	0.080	0.065	0.051	0.034	0.030	0.020	0.009	0.008	0.008	0.008	0.003	0.001	0.000
MEAN	0.72	1.54	2.49	3.50	4.28	4.97	5.41	5.54	5.43	5.10	4.62	4.03	3.55	3.09	2.73	2.35	1.94	1.53	1.26	1.01
VAR	1.3	3.2	6.0	8.0	9.3	9.5	9.0	8.1	6.8	6.5	6.3	6.1	5.9	5.1	4.7	4.6	4.3	3.2	2.6	2.1

TABLE 245

Primary photon E_0 = 50 000 MeV.
Secondary electrons E = 500 MeV.

Absorber: air, Z = 7.4, A = 15,
Radiation length = 43 g/sq. cm,
Critical energy = 98 MeV.

n \ t	0.5	1.0	1.5	2.0	2.5	3.0	3.5	4.0	4.5	5.0	5.5	6.0	6.5	7.0	7.5	8.0	8.5	9.0	9.5	10.0
0	0.690	0.476	0.316	0.226	0.147	0.109	0.069	0.046	0.028	0.026	0.022	0.036	0.059	0.093	0.133	0.195	0.279	0.359	0.433	0.472
1	0.014	0.020	0.033	0.039	0.022	0.029	0.022	0.014	0.023	0.017	0.042	0.064	0.119	0.161	0.197	0.231	0.243	0.234	0.247	0.256
2	0.237	0.279	0.234	0.174	0.144	0.107	0.080	0.065	0.063	0.080	0.096	0.141	0.165	0.175	0.192	0.169	0.156	0.160	0.141	0.118
3	0.022	0.064	0.091	0.104	0.097	0.077	0.067	0.096	0.084	0.107	0.139	0.141	0.154	0.172	0.154	0.153	0.119	0.100	0.084	0.082
4	0.028	0.085	0.124	0.122	0.116	0.103	0.123	0.117	0.126	0.139	0.144	0.155	0.140	0.120	0.110	0.084	0.077	0.062	0.040	0.037
5	0.005	0.037	0.070	0.084	0.094	0.129	0.129	0.140	0.147	0.158	0.155	0.137	0.128	0.104	0.081	0.062	0.046	0.034	0.031	0.015
6	0.004	0.023	0.055	0.079	0.100	0.103	0.140	0.138	0.160	0.138	0.120	0.114	0.083	0.070	0.046	0.044	0.038	0.022	0.012	0.010
7	0.000	0.007	0.036	0.063	0.092	0.110	0.114	0.123	0.115	0.123	0.114	0.084	0.062	0.040	0.031	0.031	0.022	0.010	0.009	0.001
8	0.000	0.007	0.022	0.042	0.061	0.074	0.093	0.092	0.094	0.083	0.073	0.055	0.043	0.023	0.028	0.014	0.007	0.009	0.001	0.005
9	0.000	0.001	0.006	0.021	0.049	0.063	0.065	0.069	0.067	0.056	0.042	0.031	0.025	0.021	0.016	0.011	0.006	0.004	0.002	0.003
≥ 10	0.000	0.001	0.013	0.036	0.078	0.096	0.098	0.100	0.093	0.073	0.053	0.042	0.022	0.021	0.012	0.006	0.007	0.006	0.000	0.001
MEAN	0.72	1.56	2.57	3.53	4.58	5.15	5.58	5.73	5.76	5.49	5.06	4.51	3.85	3.33	2.88	2.43	2.02	1.64	1.26	1.11
VAR	1.4	3.4	6.0	8.7	10.6	10.6	9.2	8.0	7.3	6.8	6.6	6.4	6.2	6.0	5.5	4.9	4.5	3.7	2.5	2.3

TABLE 246

Primary photon E_0 = 50 000 MeV.
Secondary electrons E = 500 MeV.

Absorber: al, Z = 13, A = 27,
Radiation length = 26.3 g/sq. cm = 9.74 cm,
Critical energy = 52 MeV.

n \ t	0.5	1.0	1.5	2.0	2.5	3.0	3.5	4.0	4.5	5.0	5.5	6.0	6.5	7.0	7.5	8.0	8.5	9.0	9.5	10.0
0	0.694	0.465	0.318	0.212	0.151	0.100	0.078	0.057	0.045	0.037	0.032	0.036	0.049	0.077	0.110	0.164	0.241	0.287	0.375	0.457
1	0.011	0.032	0.040	0.032	0.031	0.028	0.013	0.014	0.022	0.025	0.048	0.081	0.118	0.137	0.180	0.219	0.216	0.245	0.246	0.243
2	0.237	0.292	0.250	0.185	0.135	0.108	0.078	0.065	0.052	0.066	0.093	0.109	0.144	0.155	0.189	0.161	0.188	0.183	0.161	0.139
3	0.020	0.077	0.095	0.096	0.088	0.081	0.075	0.061	0.088	0.090	0.128	0.151	0.150	0.169	0.146	0.147	0.126	0.106	0.086	0.065
4	0.030	0.067	0.108	0.109	0.097	0.087	0.090	0.101	0.117	0.119	0.131	0.163	0.150	0.140	0.135	0.103	0.086	0.073	0.049	0.035
5	0.005	0.037	0.060	0.114	0.088	0.118	0.134	0.110	0.138	0.169	0.169	0.130	0.118	0.107	0.093	0.083	0.048	0.039	0.025	0.030
6	0.002	0.018	0.043	0.067	0.108	0.102	0.122	0.138	0.141	0.132	0.122	0.115	0.104	0.085	0.046	0.038	0.040	0.031	0.027	0.013
7	0.001	0.005	0.039	0.062	0.091	0.100	0.109	0.133	0.129	0.118	0.118	0.077	0.063	0.045	0.039	0.041	0.025	0.013	0.014	0.006
8	0.000	0.001	0.017	0.059	0.071	0.077	0.088	0.117	0.098	0.096	0.078	0.054	0.048	0.041	0.022	0.019	0.012	0.013	0.010	0.004
9	0.000	0.005	0.017	0.028	0.055	0.062	0.076	0.071	0.056	0.069	0.033	0.033	0.029	0.019	0.016	0.010	0.009	0.004	0.002	0.003
≥ 10	0.000	0.001	0.013	0.036	0.085	0.137	0.137	0.133	0.114	0.079	0.050	0.051	0.027	0.025	0.024	0.015	0.009	0.006	0.005	0.001
MEAN	0.71	1.51	2.51	3.66	4.69	5.45	5.86	6.09	5.83	5.63	5.01	4.57	4.05	3.64	3.13	2.73	2.24	1.90	1.56	1.21
VAR	1.4	3.1	6.1	8.8	11.2	11.9	10.9	9.4	8.4	7.7	6.9	7.0	6.4	6.3	6.0	5.7	4.8	4.1	3.7	2.7

TABLE 247

Primary photon E_0 = 1 000 MeV.
Secondary electrons E = 5 MeV.

Absorber: air, Z = 7.4, A = 15,
Radiation length = 43 g/sq. cm,
Critical energy = 98 MeV.

n \ t	0.5	1.0	1.5	2.0	2.5	3.0	3.5	4.0	4.5	5.0	5.5	6.0	6.5	7.0	7.5	8.0	8.5	9.0	9.5	10.0
0	0.711	0.504	0.373	0.304	0.280	0.307	0.376	0.385	0.490	0.569	0.622	0.682	0.739	0.771	0.818	0.846	0.875	0.888	0.920	0.927
1	0.024	0.068	0.113	0.170	0.187	0.224	0.212	0.248	0.237	0.223	0.197	0.197	0.145	0.143	0.105	0.094	0.074	0.077	0.050	0.050
2	0.219	0.274	0.264	0.272	0.290	0.263	0.245	0.213	0.175	0.134	0.130	0.087	0.081	0.062	0.056	0.049	0.037	0.024	0.023	0.019
3	0.025	0.075	0.127	0.139	0.140	0.120	0.091	0.103	0.059	0.047	0.033	0.020	0.024	0.017	0.012	0.007	0.010	0.009	0.002	0.002
4	0.019	0.059	0.078	0.073	0.060	0.055	0.051	0.035	0.030	0.020	0.013	0.012	0.007	0.004	0.005	0.003	0.004	0.002	0.005	0.000
5	0.001	0.014	0.031	0.036	0.032	0.017	0.018	0.012	0.005	0.006	0.003	0.001	0.004	0.002	0.002	0.001	0.000	0.000	0.000	0.002
6	0.001	0.004	0.010	0.006	0.009	0.010	0.004	0.004	0.003	0.000	0.002	0.000	0.000	0.000	0.001	0.000	0.000	0.000	0.000	0.000
7	0.000	0.001	0.001	0.000	0.002	0.003	0.003	0.000	0.001	0.001	0.000	0.001	0.000	0.001	0.001	0.000	0.000	0.000	0.000	0.000
8	0.000	0.000	0.002	0.000	0.000	0.001	0.000	0.000	0.000	0.000	0.000	0.000	0.000	0.000	0.000	0.000	0.000	0.000	0.000	0.000
⩾9	0.000	0.001	0.001	0.000	0.000	0.000	0.000	0.000	0.000	0.000	0.000	0.000	0.000	0.000	0.000	0.000	0.000	0.000	0.000	0.000
MEAN	0.62	1.19	1.58	1.64	1.66	1.50	1.31	1.21	0.93	0.75	0.64	0.49	0.43	0.35	0.30	0.23	0.19	0.16	0.12	0.10
VAR	1.1	2.0	2.5	2.1	2.1	2.0	1.8	1.6	1.4	1.1	1.0	0.8	0.7	0.6	0.6	0.4	0.3	0.3	0.2	0.2

TABLE 248

Primary photon E_0 = 1 000 MeV.
Secondary electrons E = 5 MeV.

Absorber: al, Z = 13, A = 27,
Radiation length = 26.3 g/sq. cm = 9.74 cm,
Critical energy = 52 MeV.

n \ t	0.5	1.0	1.5	2.0	2.5	3.0	3.5	4.0	4.5	5.0	5.5	6.0	6.5	7.0	7.5	8.0	8.5	9.0	9.5	10.0
0	0.708	0.511	0.352	0.265	0.200	0.186	0.183	0.203	0.273	0.312	0.416	0.457	0.499	0.580	0.623	0.684	0.742	0.780	0.826	0.863
1	0.014	0.038	0.065	0.095	0.118	0.145	0.187	0.239	0.226	0.234	0.222	0.216	0.246	0.215	0.196	0.160	0.138	0.144	0.100	0.085
2	0.230	0.282	0.294	0.233	0.224	0.246	0.211	0.260	0.207	0.220	0.166	0.170	0.155	0.115	0.105	0.098	0.085	0.051	0.060	0.041
3	0.022	0.065	0.115	0.154	0.178	0.169	0.205	0.143	0.145	0.093	0.106	0.082	0.064	0.051	0.045	0.040	0.026	0.010	0.007	0.008
4	0.022	0.057	0.091	0.118	0.140	0.133	0.115	0.078	0.087	0.078	0.050	0.051	0.022	0.024	0.021	0.006	0.007	0.011	0.004	0.001
5	0.003	0.030	0.049	0.060	0.071	0.064	0.055	0.051	0.040	0.041	0.029	0.017	0.008	0.011	0.008	0.009	0.002	0.002	0.002	0.001
6	0.000	0.007	0.018	0.046	0.036	0.032	0.023	0.016	0.013	0.011	0.007	0.004	0.003	0.003	0.001	0.001	0.000	0.001	0.001	0.001
7	0.001	0.004	0.009	0.020	0.020	0.011	0.018	0.007	0.005	0.007	0.002	0.003	0.002	0.001	0.001	0.002	0.000	0.001	0.000	0.000
8	0.000	0.005	0.007	0.006	0.008	0.011	0.001	0.002	0.004	0.002	0.001	0.000	0.000	0.000	0.000	0.000	0.000	0.000	0.000	0.000
9	0.000	0.001	0.000	0.003	0.004	0.002	0.002	0.001	0.000	0.002	0.001	0.000	0.001	0.000	0.000	0.000	0.000	0.000	0.000	0.000
⩾10	0.000	0.000	0.000	0.000	0.001	0.001	0.000	0.000	0.000	0.000	0.000	0.000	0.000	0.000	0.000	0.000	0.000	0.000	0.000	0.000
MEAN	0.65	1.29	1.83	2.29	2.48	2.38	2.25	1.93	1.77	1.62	1.29	1.14	0.92	0.77	0.68	0.57	0.42	0.34	0.27	0.21
VAR	1.2	2.6	3.1	3.8	3.7	3.4	3.0	2.5	2.6	2.6	2.2	1.9	1.4	1.4	1.2	1.0	0.7	0.6	0.5	0.4

TABLE 249

Primary photon E_0 = 2 000 MeV.
Secondary electrons E = 10 MeV.

Absorber: air, Z = 7.4, A = 15,
Radiation length = 43 g/sq. cm,
Critical energy = 98 MeV.

n \ t	0.5	1.0	1.5	2.0	2.5	3.0	3.5	4.0	4.5	5.0	5.5	6.0	6.5	7.0	7.5	8.0	8.5	9.0	9.5	10.0
0	0.689	0.497	0.338	0.240	0.184	0.144	0.149	0.196	0.228	0.283	0.350	0.449	0.536	0.584	0.665	0.717	0.760	0.771	0.832	0.873
1	0.020	0.046	0.059	0.087	0.103	0.144	0.178	0.201	0.217	0.233	0.235	0.231	0.206	0.205	0.172	0.143	0.137	0.139	0.112	0.078
2	0.253	0.280	0.284	0.253	0.246	0.257	0.243	0.232	0.248	0.231	0.213	0.181	0.136	0.116	0.101	0.084	0.064	0.067	0.041	0.034
3	0.015	0.076	0.116	0.147	0.162	0.170	0.181	0.161	0.138	0.127	0.100	0.069	0.062	0.051	0.032	0.030	0.025	0.014	0.011	0.007
4	0.017	0.061	0.106	0.117	0.153	0.139	0.136	0.113	0.085	0.075	0.063	0.043	0.032	0.030	0.018	0.019	0.008	0.004	0.003	0.007
5	0.004	0.022	0.057	0.083	0.065	0.084	0.062	0.059	0.055	0.034	0.019	0.017	0.016	0.008	0.005	0.007	0.001	0.002	0.000	0.001
6	0.001	0.012	0.022	0.042	0.038	0.034	0.035	0.023	0.019	0.012	0.016	0.007	0.007	0.006	0.005	0.000	0.004	0.001	0.001	0.000
7	0.000	0.004	0.011	0.018	0.019	0.018	0.010	0.009	0.009	0.004	0.001	0.003	0.003	0.000	0.002	0.000	0.001	0.001	0.000	0.000
8	0.001	0.002	0.006	0.011	0.006	0.009	0.003	0.004	0.001	0.000	0.002	0.000	0.002	0.000	0.000	0.000	0.000	0.001	0.000	0.000
9	0.000	0.000	0.001	0.001	0.003	0.001	0.001	0.001	0.000	0.001	0.001	0.000	0.000	0.000	0.000	0.000	0.000	0.000	0.000	0.000
≥10	0.000	0.000	0.000	0.001	0.001	0.000	0.002	0.001	0.000	0.000	0.000	0.000	0.000	0.000	0.000	0.000	0.000	0.000	0.000	0.000
MEAN	0.67	1.30	1.95	2.40	2.57	2.56	2.39	2.15	1.93	1.66	1.44	1.12	0.95	0.79	0.61	0.51	0.41	0.36	0.25	0.20
VAR	1.2	2.4	3.4	3.9	3.6	3.3	3.0	3.0	2.7	2.3	2.2	1.8	1.8	1.4	1.2	1.0	0.8	0.7	0.4	0.4

TABLE 250

Primary photon E_0 = 2 000 MeV.
Secondary electrons E = 10 MeV.

Absorber: al, Z = 13, A = 27,
Radiation length = 26.3 g/sq. cm = 9.74 cm,
Critical energy = 52 MeV.

n \ t	0.5	1.0	1.5	2.0	2.5	3.0	3.5	4.0	4.5	5.0	5.5	6.0	6.5	7.0	7.5	8.0	8.5	9.0	9.5	10.0
0	0.718	0.505	0.363	0.241	0.175	0.119	0.093	0.082	0.082	0.134	0.155	0.204	0.266	0.351	0.441	0.480	0.565	0.611	0.667	0.727
1	0.009	0.034	0.044	0.068	0.053	0.057	0.069	0.086	0.127	0.143	0.195	0.219	0.244	0.245	0.218	0.234	0.209	0.188	0.176	0.167
2	0.228	0.267	0.254	0.217	0.184	0.154	0.190	0.189	0.192	0.206	0.213	0.219	0.183	0.187	0.143	0.156	0.118	0.118	0.095	0.066
3	0.016	0.069	0.090	0.132	0.125	0.157	0.148	0.160	0.185	0.185	0.165	0.147	0.130	0.102	0.103	0.067	0.059	0.045	0.038	0.021
4	0.023	0.067	0.097	0.125	0.155	0.182	0.165	0.189	0.162	0.134	0.124	0.089	0.077	0.050	0.054	0.030	0.028	0.019	0.012	0.013
5	0.002	0.028	0.064	0.069	0.112	0.115	0.139	0.125	0.105	0.094	0.069	0.054	0.054	0.041	0.026	0.020	0.014	0.011	0.005	0.003
6	0.004	0.018	0.042	0.061	0.091	0.095	0.086	0.079	0.066	0.050	0.041	0.037	0.025	0.015	0.010	0.009	0.004	0.002	0.005	0.001
7	0.000	0.005	0.024	0.039	0.042	0.064	0.057	0.046	0.045	0.027	0.023	0.015	0.008	0.006	0.001	0.001	0.003	0.003	0.001	0.001
8	0.000	0.006	0.015	0.025	0.028	0.030	0.030	0.023	0.022	0.017	0.008	0.010	0.008	0.002	0.003	0.003	0.000	0.001	0.001	0.001
9	0.000	0.001	0.003	0.013	0.011	0.014	0.009	0.010	0.012	0.005	0.005	0.005	0.004	0.001	0.001	0.000	0.000	0.000	0.000	0.000
≥10	0.000	0.000	0.004	0.010	0.024	0.013	0.014	0.011	0.002	0.005	0.002	0.001	0.001	0.000	0.000	0.000	0.000	0.002	0.000	0.000
MEAN	0.64	1.38	2.14	2.80	3.40	3.66	3.63	3.51	3.26	2.84	2.49	2.19	1.90	1.49	1.26	1.05	0.85	0.75	0.60	0.45
VAR	1.2	2.9	4.8	5.8	6.5	5.6	5.2	4.8	4.4	4.3	3.8	3.6	3.4	2.6	2.3	1.9	1.6	1.6	1.2	0.8

TABLE 251

Primary photon E_0 = 10 000 MeV.
Secondary electrons E = 50 MeV.

Absorber: air, Z = 7.4, A = 15,
Radiation length = 43 g/sq. cm,
Critical energy = 98 MeV.

n \ t	0.5	1.0	1.5	2.0	2.5	3.0	3.5	4.0	4.5	5.0	5.5	6.0	6.5	7.0	7.5	8.0	8.5	9.0	9.5	10.0
0	0.686	0.471	0.317	0.219	0.150	0.099	0.074	0.052	0.044	0.033	0.045	0.072	0.083	0.133	0.189	0.237	0.319	0.401	0.476	0.559
1	0.007	0.018	0.012	0.018	0.017	0.014	0.017	0.024	0.035	0.037	0.066	0.104	0.136	0.159	0.212	0.234	0.217	0.249	0.234	0.201
2	0.249	0.263	0.227	0.163	0.136	0.089	0.066	0.063	0.057	0.089	0.114	0.140	0.184	0.188	0.188	0.158	0.188	0.142	0.126	0.108
3	0.021	0.071	0.089	0.080	0.064	0.073	0.070	0.052	0.117	0.133	0.144	0.142	0.140	0.157	0.126	0.133	0.112	0.080	0.077	0.065
4	0.029	0.085	0.116	0.109	0.105	0.102	0.106	0.130	0.127	0.125	0.123	0.123	0.138	0.118	0.098	0.095	0.057	0.045	0.027	0.029
5	0.006	0.031	0.075	0.095	0.114	0.112	0.096	0.129	0.124	0.153	0.133	0.130	0.088	0.089	0.069	0.055	0.042	0.033	0.021	0.013
6	0.002	0.035	0.076	0.093	0.081	0.110	0.129	0.121	0.121	0.118	0.126	0.096	0.080	0.063	0.050	0.036	0.023	0.021	0.015	0.012
7	0.000	0.015	0.040	0.080	0.103	0.106	0.119	0.131	0.102	0.107	0.074	0.075	0.058	0.035	0.017	0.026	0.018	0.011	0.013	0.007
8	0.000	0.005	0.024	0.049	0.073	0.077	0.095	0.090	0.091	0.076	0.060	0.044	0.037	0.029	0.018	0.010	0.010	0.005	0.002	0.001
9	0.000	0.003	0.012	0.041	0.051	0.082	0.078	0.080	0.071	0.050	0.045	0.022	0.027	0.009	0.010	0.006	0.005	0.007	0.005	0.002
10-14	0.000	0.003	0.012	0.051	0.102	0.128	0.144	0.122	0.107	0.078	0.068	0.050	0.027	0.020	0.023	0.010	0.009	0.006	0.004	0.003
≥15	0.000	0.000	0.000	0.002	0.004	0.008	0.006	0.006	0.004	0.001	0.002	0.002	0.002	0.000	0.000	0.000	0.000	0.000	0.000	0.000
MEAN	0.73	1.67	2.74	3.97	4.89	5.66	6.02	6.03	5.69	5.27	4.83	4.19	3.65	3.08	2.61	2.25	1.85	1.49	1.21	0.98
VAR	1.4	4.0	6.7	10.2	11.6	11.7	10.9	10.0	9.4	7.9	8.5	8.1	6.9	6.0	5.9	4.9	4.3	3.8	3.0	2.6

TABLE 252

Primary photon E_0 = 10 000 MeV.
Secondary electrons E = 50 MeV.

Absorber: al, Z = 13, A = 27,
Radiation length = 26.3 g/sq.cm = 9.74 cm,
Critical energy = 52 MeV.

n \ t	0.5	1.0	1.5	2.0	2.5	3.0	3.5	4.0	4.5	5.0	5.5	6.0	6.5	7.0	7.5	8.0	8.5	9.0	9.5	10.0
0	0.672	0.479	0.322	0.220	0.152	0.104	0.076	0.064	0.038	0.028	0.024	0.024	0.035	0.047	0.066	0.120	0.177	0.227	0.286	0.372
1	0.008	0.010	0.014	0.017	0.023	0.007	0.012	0.009	0.006	0.014	0.028	0.044	0.075	0.077	0.129	0.151	0.191	0.208	0.242	0.258
2	0.252	0.242	0.209	0.179	0.104	0.085	0.059	0.053	0.041	0.044	0.053	0.074	0.084	0.135	0.139	0.174	0.180	0.191	0.189	0.148
3	0.020	0.075	0.083	0.064	0.069	0.062	0.041	0.038	0.054	0.064	0.070	0.092	0.122	0.149	0.166	0.156	0.134	0.129	0.105	0.097
4	0.033	0.092	0.116	0.102	0.087	0.069	0.066	0.060	0.072	0.088	0.101	0.125	0.138	0.142	0.127	0.123	0.106	0.098	0.066	0.061
5	0.008	0.040	0.059	0.079	0.080	0.095	0.073	0.082	0.088	0.108	0.129	0.117	0.116	0.111	0.104	0.080	0.072	0.050	0.037	0.030
6	0.007	0.042	0.060	0.064	0.090	0.083	0.104	0.097	0.105	0.113	0.128	0.126	0.102	0.090	0.093	0.066	0.047	0.023	0.025	0.014
7	0.000	0.009	0.044	0.071	0.081	0.078	0.115	0.126	0.126	0.111	0.116	0.111	0.087	0.080	0.055	0.042	0.030	0.034	0.019	0.007
8	0.000	0.005	0.039	0.061	0.081	0.087	0.086	0.112	0.120	0.128	0.115	0.090	0.080	0.055	0.034	0.029	0.023	0.018	0.011	0.007
9	0.000	0.002	0.026	0.044	0.065	0.073	0.083	0.098	0.097	0.096	0.089	0.055	0.049	0.036	0.032	0.022	0.017	0.007	0.008	0.008
10-14	0.000	0.004	0.027	0.092	0.153	0.226	0.255	0.254	0.228	0.196	0.141	0.134	0.104	0.071	0.049	0.035	0.022	0.015	0.010	0.008
≥15	0.000	0.000	0.001	0.007	0.015	0.031	0.030	0.017	0.025	0.010	0.006	0.008	0.008	0.007	0.006	0.002	0.001	0.000	0.002	0.000
MEAN	0.79	1.70	2.97	4.28	5.53	6.57	7.11	7.28	7.30	6.89	6.34	5.90	5.31	4.69	4.10	3.39	2.82	2.37	1.96	1.55
VAR	1.6	4.1	8.7	13.4	16.0	17.0	15.2	12.9	12.0	10.5	9.2	9.9	10.1	9.4	9.1	7.5	6.5	5.5	4.8	3.9

TABLE 253

Primary photon E_0 = 20 000 MeV.
Secondary electrons E = 100 MeV.

Absorber: air, Z = 7.4, A = 15,
Radiation length = 43 g/sq. cm,
Critical energy = 98 MeV.

n \ t	0.5	1.0	1.5	2.0	2.5	3.0	3.5	4.0	4.5	5.0	5.5	6.0	6.5	7.0	7.5	8.0	8.5	9.0	9.5	10.0
0	0.700	0.504	0.356	0.251	0.176	0.121	0.081	0.054	0.040	0.031	0.026	0.0[illegible]	0.034	0.038	0.065	0.1[illegible]	0.154	0.214	0.296	0.359
1	0.009	0.019	0.021	0.021	0.019	0.013	0.017	0.011	0.010	0.018	0.019	0.025	0.054	0.083	0.121	0.127	0.184	0.198	0.234	0.228
2	0.226	0.245	0.217	0.170	0.110	0.096	0.069	0.055	0.045	0.032	0.050	0.052	0.081	0.132	0.152	0.154	0.159	0.176	0.172	0.170
3	0.022	0.069	0.078	0.069	0.058	0.043	0.046	0.041	0.051	0.054	0.062	0.097	0.120	0.130	0.146	0.134	0.133	0.117	0.101	0.088
4	0.028	0.074	0.089	0.091	0.082	0.090	0.078	0.071	0.070	0.097	0.097	0.112	0.120	0.152	0.127	0.123	0.117	0.106	0.058	0.052
5	0.010	0.034	0.061	0.080	0.084	0.059	0.062	0.078	0.097	0.094	0.114	0.118	0.137	0.131	0.114	0.103	0.074	0.072	0.059	0.045
6	0.005	0.023	0.057	0.075	0.074	0.092	0.099	0.096	0.113	0.124	0.135	0.114	0.109	0.084	0.072	0.084	0.070	0.041	0.028	0.022
7	0.000	0.013	0.045	0.069	0.081	0.095	0.085	0.110	0.102	0.109	0.122	0.123	0.100	0.066	0.056	0.062	0.038	0.029	0.026	0.015
8	0.000	0.007	0.026	0.056	0.088	0.088	0.098	0.109	0.102	0.121	0.085	0.098	0.081	0.056	0.047	0.030	0.029	0.017	0.010	0.006
9	0.000	0.008	0.019	0.041	0.055	0.068	0.092	0.093	0.099	0.086	0.087	0.081	0.063	0.044	0.038	0.024	0.020	0.014	0.003	0.004
10-14	0.000	0.004	0.030	0.083	0.157	0.205	0.250	0.259	0.246	0.211	0.191	0.142	0.093	0.079	0.058	0.039	0.020	0.015	0.012	0.010
≥ 15	0.000	0.000	0.001	0.004	0.016	0.031	0.023	0.023	0.025	0.023	0.012	0.008	0.008	0.005	0.004	0.002	0.002	0.001	0.001	0.001
MEAN	0.72	1.58	2.73	4.06	5.41	6.42	6.97	7.29	7.34	7.10	6.72	6.22	5.46	4.75	4.22	3.70	3.09	2.58	2.01	1.72
VAR	1.5	4.2	8.5	13.1	16.5	18.3	16.2	13.8	13.1	11.7	10.6	9.9	9.5	9.1	9.5	8.1	7.0	6.0	5.0	4.5

TABLE 254

Primary photon E_0 = 20 000 MeV.
Secondary electrons E = 100 MeV.

Absorber: al, Z = 13, A = 27,
Radiation length = 26.3 g/sq. cm = 9.74 cm,
Critical energy = 52 MeV.

n \ t	0.5	1.0	1.5	2.0	2.5	3.0	3.5	4.0	4.5	5.0	5.5	6.0	6.5	7.0	7.5	8.0	8.5	9.0	9.5	10.0
0	0.686	0.488	0.347	0.227	0.153	0.102	0.071	0.044	0.032	0.023	0.015	0.009	0.006	0.012	0.029	0.046	0.072	0.115	0.186	0.233
1	0.004	0.013	0.015	0.015	0.013	0.009	0.005	0.007	0.010	0.004	0.011	0.010	0.027	0.041	0.072	0.113	0.126	0.176	0.211	0.232
2	0.259	0.247	0.209	0.161	0.117	0.086	0.066	0.052	0.029	0.028	0.019	0.035	0.049	0.079	0.104	0.124	0.157	0.176	0.156	0.158
3	0.018	0.047	0.060	0.067	0.049	0.041	0.041	0.031	0.026	0.024	0.045	0.053	0.076	0.087	0.112	0.137	0.132	0.128	0.139	0.132
4	0.023	0.102	0.095	0.093	0.087	0.074	0.053	0.052	0.049	0.056	0.069	0.078	0.102	0.111	0.141	0.133	0.130	0.118	0.097	0.059
5	0.007	0.033	0.060	0.074	0.076	0.067	0.051	0.061	0.071	0.058	0.080	0.105	0.112	0.113	0.105	0.117	0.109	0.087	0.066	0.063
6	0.001	0.030	0.070	0.080	0.080	0.072	0.067	0.064	0.084	0.097	0.099	0.112	0.139	0.120	0.099	0.080	0.075	0.056	0.042	0.038
7	0.002	0.016	0.037	0.055	0.073	0.082	0.089	0.092	0.087	0.102	0.102	0.110	0.093	0.109	0.084	0.063	0.063	0.036	0.028	0.033
8	0.000	0.010	0.043	0.067	0.072	0.066	0.069	0.087	0.104	0.086	0.109	0.105	0.108	0.086	0.053	0.055	0.040	0.031	0.021	0.018
9	0.000	0.008	0.024	0.055	0.067	0.086	0.093	0.085	0.091	0.115	0.113	0.101	0.077	0.061	0.062	0.035	0.024	0.022	0.018	0.008
10-14	0.000	0.006	0.038	0.090	0.176	0.257	0.307	0.335	0.349	0.346	0.294	0.246	0.187	0.159	0.126	0.092	0.064	0.047	0.034	0.025
≥ 15	0.000	0.000	0.002	0.016	0.037	0.058	0.088	0.090	0.068	0.061	0.044	0.036	0.024	0.022	0.013	0.005	0.008	0.004	0.002	0.001
MEAN	0.72	1.73	2.99	4.46	5.88	7.19	8.18	8.58	8.66	8.64	8.19	7.67	6.88	6.35	5.49	4.69	4.15	3.49	2.85	2.47
VAR	1.4	4.7	9.8	15.1	18.5	20.8	21.6	19.1	16.1	14.1	13.3	12.6	11.7	12.0	11.7	10.5	9.5	9.0	7.7	6.9

TABLE 255

Primary photon E_0 = 5 000 MeV.
Secondary electrons E = 20 MeV.

Absorber: air, Z = 7.4, A = 15,
Radiation length = 43 g/sq. cm,
Critical energy = 98 MeV.

n \ t	0.5	1.0	1.5	2.0	2.5	3.0	3.5	4.0	4.5	5.0	5.5	6.0	6.5	7.0	7.5	8.0	8.5	9.0	9.5	10.0
0	0.725	0.510	0.348	0.240	0.161	0.114	0.089	0.074	0.070	0.075	0.102	0.136	0.189	0.271	0.313	0.393	0.433	0.515	0.594	0.655
1	0.006	0.017	0.028	0.025	0.038	0.029	0.037	0.047	0.062	0.095	0.116	0.171	0.185	0.204	0.211	0.227	0.248	0.240	0.191	0.184
2	0.210	0.259	0.222	0.174	0.170	0.134	0.108	0.112	0.153	0.167	0.183	0.207	0.197	0.187	0.214	0.164	0.147	0.118	0.122	0 091
3	0.023	0.056	0.090	0.094	0.101	0.097	0.119	0.104	0.146	0.147	0.166	0.146	0.165	0.134	0.103	0.084	0.086	0.065	0.046	0.041
4	0.024	0.070	0.120	0.140	0.122	0.135	0.144	0.168	0.149	0.156	0.130	0.127	0.096	0.084	0.068	0.067	0.035	0.026	0.020	0.012
5	0.008	0.050	0.063	0.087	0.107	0.136	0.140	0.150	0.149	0.120	0.137	0.077	0.063	0.051	0.030	0.028	0.025	0.017	0.020	0.007
6	0.003	0.024	0.048	0.086	0.098	0.118	0.099	0.133	0.097	0.099	0.076	0.052	0.048	0.036	0.025	0.018	0.012	0.011	0.004	0.005
7	0.001	0.006	0.033	0.049	0.066	0.079	0.096	0.092	0.079	0.065	0.046	0.032	0.034	0.017	0.014	0.009	0.009	0.005	0.001	0.002
8	0.000	0.004	0.028	0.048	0.063	0.073	0.072	0.057	0.039	0.035	0.018	0.023	0.009	0.007	0.013	0.005	0.004	0.002	0.001	0.000
9	0.000	0.002	0.011	0.029	0.033	0.038	0.049	0.021	0.023	0.019	0.014	0.016	0.005	0.005	0.002	0.005	0.001	0.000	0.001	0.002
10-14	0.000	0.002	0.009	0.029	0.041	0.046	0.047	0.041	0.033	0.022	0.011	0.013	0.009	0.004	0.007	0.000	0.000	0.001	0.000	0.001
≥15	0.000	0.000	0.000	0.001	0.000	0.001	0.001	0.001	0.000	0.000	0.001	0.000	0.000	0.000	0.000	0.000	0.000	0.000	0.000	0.000
MEAN	0.66	1.49	2.47	3.47	4.00	4.51	4.68	4.56	4.15	3.83	3.37	2.92	2.51	2.06	1.81	1.47	1.24	0.99	0.80	0.65
VAR	1.4	3.5	6.1	8.4	8.6	8.3	7.9	6.9	6.3	5.9	5.3	5.5	4.6	4.0	3.9	3.1	2.5	2.0	1.6	1.4

TABLE 256

Primary photon E_0 = 5 000 MeV.
Secondary electrons E = 20 MeV.

Absorber: al, Z = 13, A = 27,
Radiation length = 26.3 g/sq. cm = 9.74 cm,
Critical energy = 52 MeV.

n \ t	0.5	1.0	1.5	2.0	2.5	3.0	3.5	4.0	4.5	5.0	5.5	6.0	6.5	7.0	7.5	8.0	8.5	9.0	9.5	10.0
0	0.679	0.470	0.337	0.236	0.153	0.110	0.078	0.055	0.046	0.039	0.028	0.050	0.061	0.094	0.143	0.192	0.257	0.319	0.373	0.455
1	0.010	0.019	0.021	0.017	0.018	0.018	0.015	0.018	0.018	0.026	0.053	0.075	0.112	0.155	0.186	0.218	0.197	0.218	0.241	0.223
2	0.234	0.271	0.220	0.163	0.139	0.084	0.069	0.066	0.055	0.071	0.100	0.119	0.167	0.158	0.181	0.181	0.202	0.202	0.159	0.150
3	0.016	0.059	0.073	0.069	0.065	0.056	0.048	0.061	0.075	0.102	0.110	0.144	0.159	0.163	0.147	0.136	0.122	0.103	0.091	0.074
4	0.030	0.088	0.118	0.111	0.096	0.099	0.106	0.093	0.107	0.117	0.158	0.156	0.128	0.124	0.109	0.098	0.086	0.051	0.059	0.047
5	0.006	0.032	0.057	0.065	0.092	0.116	0.091	0.106	0.135	0.150	0.136	0.128	0.110	0.098	0.077	0.050	0.043	0.043	0.034	0.024
6	0.006	0.036	0.052	0.089	0.078	0.084	0.113	0.132	0.116	0.121	0.116	0.106	0.077	0.077	0.050	0.045	0.034	0.022	0.023	0.010
7	0.001	0.015	0.046	0.076	0.079	0.104	0.103	0.108	0.142	0.107	0.102	0.073	0.058	0.040	0.039	0.032	0.024	0.022	0.009	0.009
8	0.000	0.004	0.033	0.064	0.096	0.098	0.105	0.099	0.080	0.098	0.065	0.048	0.039	0.025	0.028	0.018	0.017	0.009	0.004	0.006
9	0.000	0.002	0.018	0.037	0.064	0.069	0.087	0.079	0.085	0.072	0.054	0.031	0.033	0.021	0.019	0.012	0.006	0.003	0.004	0.001
10-14	0.000	0.004	0.025	0.069	0.119	0.156	0.179	0.176	0.132	0.093	0.077	0.067	0.055	0.043	0.019	0.017	0.012	0.008	0.003	0.001
≥15	0.000	0.000	0.000	0.004	0.003	0.006	0.006	0.007	0.009	0.004	0.001	0.003	0.001	0.002	0.002	0.002	0.000	0.000	0.000	0.000
MEAN	0.72	1.67	2.77	4.06	5.04	5.79	6.29	6.39	6.16	5.69	5.16	4.61	4.09	3.59	3.03	2.59	2.22	1.82	1.54	1.24
VAR	1.5	4.0	7.9	11.9	12.7	12.7	12.1	11.6	10.0	8.6	7.8	8.4	8.3	7.8	6.8	6.2	5.1	4.1	3.4	2.7

TABLE 257

Primary photon E_0 = 50 000 MeV.
Secondary electrons E = 200 MeV.

Absorber: air, Z = 7.4, A = 15,
Radiation length = 43 g/sq. cm,
Critical energy = 98 MeV.

n \ t	0.5	1.0	1.5	2.0	2.5	3.0	3.5	4.0	4.5	5.0	5.5	6.0	6.5	7.0	7.5	8.0	8.5	9.0	9.5	10.0
0	0.682	0.452	0.319	0.230	0.151	0.117	0.086	0.058	0.042	0.028	0.020	0.012	0.012	0.014	0.015	0.032	0.045	0.069	0.110	0.168
1	0.006	0.013	0.008	0.009	0.008	0.005	0.001	0.002	0.004	0.002	0.002	0.004	0.010	0.023	0.029	0.045	0.090	0.125	0.165	0.202
2	0.239	0.254	0.172	0.115	0.095	0.056	0.037	0.037	0.030	0.026	0.019	0.019	0.030	0.031	0.054	0.093	0.124	0.151	0.161	0.150
3	0.031	0.063	0.074	0.046	0.047	0.033	0.022	0.015	0.015	0.018	0.017	0.027	0.036	0.061	0.084	0.113	0.125	0.122	0.127	0.130
4	0.026	0.080	0.110	0.091	0.069	0.041	0.050	0.026	0.019	0.019	0.033	0.038	0.044	0.070	0.082	0.105	0.107	0.119	0.111	0.093
5	0.008	0.041	0.070	0.084	0.045	0.054	0.043	0.031	0.024	0.033	0.028	0.047	0.062	0.086	0.090	0.100	0.108	0.112	0.081	0.068
6	0.006	0.040	0.053	0.087	0.076	0.064	0.052	0.055	0.043	0.041	0.050	0.060	0.084	0.086	0.107	0.100	0.078	0.086	0.064	0.054
7	0.001	0.023	0.055	0.057	0.073	0.067	0.051	0.053	0.053	0.049	0.059	0.093	0.111	0.104	0.099	0.086	0.076	0.041	0.036	0.037
8	0.001	0.016	0.040	0.052	0.067	0.070	0.062	0.065	0.065	0.071	0.087	0.089	0.090	0.097	0.101	0.067	0.068	0.039	0.038	0.023
9	0.000	0.007	0.032	0.048	0.052	0.067	0.066	0.059	0.076	0.090	0.097	0.088	0.095	0.070	0.071	0.059	0.046	0.031	0.030	0.021
10-14	0.000	0.011	0.063	0.146	0.233	0.273	0.330	0.369	0.397	0.413	0.398	0.382	0.315	0.284	0.219	0.158	0.105	0.090	0.062	0.040
15-19	0.000	0.000	0.004	0.031	0.068	0.126	0.170	0.197	0.208	0.179	0.164	0.132	0.100	0.071	0.041	0.026	0.027	0.012	0.015	0.014
⩾ 20	0.000	0.000	0.000	0.004	0.016	0.027	0.030	0.033	0.024	0.031	0.026	0.009	0.011	0.003	0.007	0.007	0.001	0.003	0.002	0.000
MEAN	0.77	1.95	3.43	5.18	7.01	8.57	9.72	10.50	10.84	10.84	10.54	9.85	9.06	8.18	7.25	6.21	5.31	4.52	3.91	3.26
VAR	1.6	5.6	11.5	19.8	27.0	30.7	30.4	27.7	23.9	21.7	19.6	17.3	18.0	16.9	15.3	15.6	14.3	13.1	12.4	10.8

TABLE 258

Primary photon E_0 = 50 000 MeV.
Secondary electrons E = 200 MeV.

Absorber: al, Z = 13, A = 27,
Radiation length = 26.3 g/sq. cm = 9.74 cm,
Critical energy = 52 MeV.

n \ t	0.5	1.0	1.5	2.0	2.5	3.0	3.5	4.0	4.5	5.0	5.5	6.0	6.5	7.0	7.5	8.0	8.5	9.0	9.5	10.0
0	0.707	0.497	0.320	0.220	0.149	0.102	0.070	0.044	0.029	0.018	0.012	0.010	0.010	0.005	0.009	0.012	0.016	0.040	0.060	0.108
1	0.007	0.016	0.008	0.007	0.009	0.005	0.001	0.006	0.001	0.002	0.001	0.003	0.005	0.011	0.010	0.029	0.059	0.086	0.092	0.134
2	0.227	0.245	0.200	0.141	0.106	0.065	0.050	0.036	0.025	0.015	0.021	0.007	0.008	0.025	0.030	0.050	0.078	0.093	0.145	0.147
3	0.012	0.053	0.060	0.068	0.034	0.033	0.025	0.018	0.011	0.017	0.008	0.011	0.020	0.032	0.061	0.076	0.094	0.118	0.139	0.124
4	0.037	0.084	0.095	0.080	0.059	0.055	0.036	0.029	0.026	0.016	0.010	0.022	0.030	0.044	0.071	0.068	0.110	0.127	0.115	0.122
5	0.007	0.035	0.062	0.051	0.070	0.045	0.037	0.031	0.024	0.022	0.019	0.032	0.044	0.063	0.078	0.116	0.113	0.101	0.081	0.109
6	0.002	0.030	0.059	0.075	0.062	0.046	0.048	0.040	0.037	0.022	0.038	0.036	0.060	0.069	0.095	0.091	0.105	0.082	0.080	0.058
7	0.001	0.010	0.048	0.057	0.070	0.061	0.055	0.029	0.031	0.045	0.042	0.058	0.073	0.088	0.078	0.086	0.089	0.076	0.072	0.050
8	0.000	0.015	0.039	0.057	0.060	0.067	0.051	0.064	0.045	0.057	0.054	0.072	0.074	0.085	0.089	0.087	0.061	0.062	0.054	0.037
9	0.000	0.005	0.028	0.056	0.063	0.070	0.061	0.050	0.066	0.053	0.075	0.079	0.098	0.109	0.110	0.084	0.058	0.050	0.042	0.037
10-14	0.000	0.009	0.067	0.149	0.224	0.266	0.304	0.344	0.362	0.408	0.431	0.452	0.413	0.323	0.270	0.239	0.169	0.133	0.101	0.060
15-19	0.000	0.001	0.003	0.036	0.082	0.143	0.202	0.244	0.275	0.264	0.245	0.186	0.136	0.126	0.084	0.053	0.045	0.029	0.015	0.013
⩾ 20	0.000	0.000	0.001	0.003	0.012	0.042	0.060	0.065	0.068	0.061	0.044	0.032	0.029	0.020	0.015	0.009	0.003	0.003	0.004	0.001
MEAN	0.70	1.70	3.35	5.24	7.05	8.97	10.48	11.49	12.15	12.29	12.00	11.30	10.55	9.61	8.59	7.62	6.54	5.67	4.92	4.09
VAR	1.4	5.0	12.0	21.0	27.3	33.4	35.4	32.4	28.1	25.4	20.3	18.1	19.0	19.3	18.6	17.2	16.8	15.4	13.6	11.9

TABLE 259

Primary photon E_0 = 2 000 MeV.
Secondary electrons E = 5 MeV.

Absorber: air, Z = 7.4, A = 15,
Radiation length = 43 g/sq. cm,
Critical energy = 98 MeV.

n \ t	0.5	1.0	1.5	2.0	2.5	3.0	3.5	4.0	4.5	5.0	5.5	6.0	6.5	7.0	7.5	8.0	8.5	9.0	9.5	10.0
0	0.689	0.497	0.337	0.238	0.180	0.136	0.132	0.155	0.174	0.243	0.309	0.384	0.476	0.521	0.623	0.661	0.706	0.728	0.791	0.832
1	0.016	0.039	0.051	0.063	0.073	0.104	0.139	0.163	0.199	0.209	0.211	0.228	0.214	0.214	0.171	0.169	0.158	0.149	0.133	0.099
2	0.249	0.287	0.254	0.229	0.223	0.239	0.222	0.234	0.224	0.220	0.217	0.201	0.145	0.137	0.112	0.097	0.085	0.089	0.053	0.046
3	0.018	0.073	0.112	0.146	0.153	0.168	0.176	0.171	0.171	0.143	0.120	0.089	0.071	0.059	0.046	0.039	0.029	0.018	0.018	0.014
4	0.020	0.068	0.122	0.115	0.15(	0.139	0.163	0.130	0.104	0.095	0.077	0.049	0.050	0.036	0.029	0.017	0.013	0.009	0.003	0.006
5	0.005	0.027	0.056	0.099	0.093	0.098	0.075	0.078	0.064	0.047	0.029	0.021	0.027	0.023	0 008	0.011	0.003	0.003	0.001	0.002
6	0.002	0.019	0.034	0.063	0.061	0.060	0.051	0.042	0.040	0.032	0.016	0.018	0.008	0.006	0.007	0.004	0.003	0.002	0.001	0.001
7	0.000	0.006	0.019	0.022	0.037	0.031	0.023	0.016	0.017	0.004	0.013	0.009	0.005	0.002	0.002	0.002	0.003	0 000	0.000	0.000
8	0.001	0.003	0.012	0.019	0.013	0.016	0.013	0.005	0.005	0.005	0.005	0.001	0.002	0.001	0.001	0.000	0.000	0.001	0.000	0.000
9	0.000	0.000	0.002	0.003	0.007	0.006	0.004	0.005	0.002	0.002	0.002	0.000	0.001	0.001	0.000	0.000	0.000	0 001	0.000	0.000
≥10	0.000	0.001	0.001	0.003	0.004	0.003	0.002	0.001	0.000	0.000	0.001	0.000	0.001	0.000	0.001	0.000	0.000	0.000	0 000	0 000
MEAN	0.69	1.39	2.12	2.66	2.90	2.92	2.77	2.51	2.31	1.97	1.71	1.38	1.17	0.99	0.76	0.64	0.52	0.46	0.32	0.27
VAR	1.3	2.9	4.1	4.7	4.7	4.2	3.8	3.5	3.3	3.0	3.0	2.4	2.4	1.9	1.6	1.3	1.0	0.9	0.5	0.5

TABLE 260

Primary photon E_0 = 2 000 MeV.
Secondary electrons E = 5 MeV.

Absorber: al, Z = 13, A = 27,
Radiation length = 26.3 g/sq. cm = 9.74 cm.
Critical energy = 52 MeV.

n \ t	0.5	1.0	1.5	2.0	2.5	3.0	3.5	4.0	4.5	5.0	5.5	6.0	6.5	7.0	7.5	8.0	8.5	9.0	9.5	10.0
0	0.718	0 505	0.359	0.238	0.171	0.116	0.083	0.070	0.060	0.091	0.108	0.135	0.186	0.249	0.347	0.390	0.470	0.500	0.573	0.643
1	0.004	0.024	0.036	0.051	0.033	0.044	0.041	0.050	0.084	0.105	0.144	0.167	0.204	0.230	0.213	0.235	0.224	0.225	0.207	0.198
2	0.227	0.265	0.234	0.206	0.161	0.121	0.149	0.131	0.137	0.145	0.190	0.211	0.197	0.211	0.180	0.170	0.142	0.142	0.119	0.094
3	0.013	0.059	0.081	0.117	0.107	0.135	0.132	0.138	0.175	0.168	0.160	0.153	0.149	0.125	0.111	0.104	0.085	0.071	0.045	0.037
4	0.028	0.078	0.108	0.107	0.130	0.133	0.131	0.167	0.169	0.171	0.138	0.125	0.096	0.072	0.075	0.049	0.031	0.029	0 034	0.017
5	0.002	0.025	0.064	0.080	0.111	0.137	0.149	0.151	0.126	0.118	0.104	0.089	0.075	0.053	0.040	0.020	0.027	0.015	0.012	0.004
6	0.008	0.024	0.050	0.059	0.096	0.112	0.103	0.120	0.104	0.096	0.067	0.047	0.038	0.030	0.017	0.020	0.013	0 008	0.006	0.003
7	0.000	0.010	0.028	0.060	0.077	0.080	0.089	0.071	0.047	0.048	0.041	0.035	0.028	0.018	0.005	0.006	0.006	0.003	0.003	0.001
8	0.000	0.006	0.018	0.032	0.046	0.068	0.056	0.049	0.049	0.027	0.028	0.015	0.012	0.007	0.007	0 003	0.001	0.002	0.001	0 000
9	0.000	0.004	0.014	0.021	0.025	0.024	0.031	0.023	0.029	0.016	0.010	0.011	0.010	0.001	0.005	0.002	0 002	0.003	0.001	0.002
10-14	0.000	0.000	0.008	0.029	0.042	0.029	0.036	0.028	0.020	0.014	0.010	0.012	0.005	0.004	0.000	0.001	0.000	0.002	0.000	0.001
≥15	0.000	0.000	0.000	0.000	0.001	0.001	0.000	0.002	0.000	0.001	0.000	0.000	0.000	0.000	0.000	0.000	0.000	0.000	0 000	0.000
MEAN	0.67	1.47	2.35	3.18	3.94	4.23	4.36	4.30	4.01	3.61	3.19	2.87	2.47	1.99	1.64	1.40	1.16	1.05	0.84	0.64
VAR	1.4	3.4	5.8	7.8	8.6	7.4	7.0	6.4	5.8	5.5	5.2	5.0	4.6	3.6	3.1	2.7	2.3	2.3	1.7	1.3

TABLE 261

Primary photon E_0 = 20 000 MeV.
Secondary electrons E = 50 MeV.

Absorber: air, Z = 7.4, A = 15,
Radiation length = 43 g/sq. cm,
Critical energy = 98 MeV.

n \ t	0.5	1.0	1.5	2.0	2.5	3.0	3.5	4.0	4.5	5.0	5.5	6.0	6.5	7.0	7.5	8.0	8.5	9.0	9.5	10.0
0	0.700	0.504	0.355	0.251	0.174	0.120	0.080	0.052	0.036	0.029	0.021	0.019	0.016	0.014	0.019	0.031	0.056	0.092	0.143	0.193
1	0.007	0.011	0.016	0.011	0.016	0.005	0.008	0.006	0.001	0.003	0.005	0.010	0.014	0.012	0.038	0.068	0.093	0.117	0.151	0.201
2	0.223	0.224	0.193	0.145	0.096	0.078	0.052	0.043	0.034	0.015	0.019	0.011	0.028	0.053	0.066	0.073	0.101	0.156	0.168	0.157
3	0.017	0.065	0.059	0.049	0.038	0.026	0.030	0.021	0.021	0.015	0.020	0.022	0.033	0.073	0.107	0.114	0.127	0.119	0.136	0.120
4	0.033	0.084	0.090	0.082	0.069	0.058	0.052	0.034	0.033	0.028	0.027	0.033	0.058	0.074	0.098	0.111	0.122	0.113	0.098	0.085
5	0.010	0.029	0.054	0.055	0.052	0.045	0.051	0.048	0.031	0.047	0.045	0.065	0.076	0.109	0.114	0.096	0.105	0.094	0.086	0.059
6	0.008	0.031	0.055	0.060	0.065	0.059	0.045	0.035	0.050	0.051	0.075	0.068	0.084	0.098	0.096	0.097	0.080	0.063	0.051	0.051
7	0.002	0.017	0.051	0.059	0.052	0.060	0.041	0.053	0.053	0.064	0.073	0.095	0.096	0.111	0.094	0.089	0.061	0.061	0.040	0.030
8	0.000	0.016	0.034	0.059	0.065	0.068	0.066	0.061	0.067	0.079	0.086	0.101	0.102	0.089	0.063	0.084	0.068	0.049	0.039	0.036
9	0.000	0.008	0.030	0.052	0.063	0.069	0.057	0.077	0.098	0.076	0.088	0.085	0.088	0.082	0.073	0.054	0.046	0.039	0.026	0.025
10-14	0.000	0.009	0.058	0.145	0.238	0.249	0.325	0.349	0.360	0.408	0.396	0.361	0.325	0.221	0.177	0.149	0.120	0.086	0.056	0.035
15-19	0.000	0.002	0.006	0.029	0.061	0.134	0.163	0.187	0.183	0.159	0.127	0.119	0.069	0.058	0.048	0.031	0.017	0.007	0.005	0.007
≥ 20	0.000	0.000	0.000	0.003	0.011	0.029	0.030	0.034	0.033	0.026	0.019	0.011	0.012	0.006	0.007	0.003	0.004	0.004	0.001	0.001
MEAN	0.75	1.77	3.17	4.98	6.75	8.44	9.46	10.26	10.50	10.53	9.99	9.61	8.68	7.62	6.84	6.12	5.27	4.41	3.58	3.06
VAR	1.7	5.6	11.9	20.9	27.1	32.6	30.8	28.0	24.4	21.3	18.7	17.5	16.6	16.0	17.3	15.3	14.3	12.4	10.3	9.7

TABLE 262

Primary photon E_0 = 20 000 MeV.
Secondary electrons E = 50 MeV.

Absorber: al, Z = 13, A = 27,
Radiation length = 26.3 g/sq. cm = 9.74 cm,
Critical energy = 52 MeV.

n \ t	0.5	1.0	1.5	2.0	2.5	3.0	3.5	4.0	4.5	5.0	5.5	6.0	6.5	7.0	7.5	8.0	8.5	9.0	9.5	10.0
0	0.686	0.488	0.347	0.226	0.153	0.102	0.070	0.044	0.031	0.019	0.015	0.007	0.002	0.004	0.003	0.003	0.011	0.029	0.061	0.085
1	0.001	0.009	0.007	0.007	0.003	0.007	0.004	0.001	0.005	0.003	0.001	0.001	0.001	0.004	0.008	0.024	0.029	0.055	0.072	0.117
2	0.253	0.227	0.181	0.138	0.094	0.068	0.057	0.038	0.022	0.011	0.006	0.008	0.013	0.010	0.021	0.036	0.067	0.100	0.109	0.141
3	0.016	0.044	0.050	0.046	0.039	0.030	0.020	0.013	0.010	0.010	0.005	0.005	0.016	0.025	0.048	0.071	0.078	0.106	0.121	0.126
4	0.028	0.094	0.085	0.087	0.063	0.045	0.030	0.034	0.021	0.018	0.022	0.014	0.021	0.039	0.050	0.084	0.090	0.105	0.113	0.099
5	0.008	0.035	0.048	0.051	0.045	0.034	0.028	0.027	0.015	0.015	0.019	0.025	0.033	0.057	0.076	0.094	0.104	0.102	0.103	0.097
6	0.006	0.048	0.070	0.076	0.064	0.051	0.037	0.031	0.026	0.026	0.029	0.035	0.047	0.049	0.079	0.077	0.100	0.099	0.087	0.071
7	0.001	0.020	0.050	0.058	0.059	0.048	0.044	0.032	0.031	0.025	0.030	0.045	0.054	0.085	0.077	0.088	0.084	0.077	0.074	0.048
8	0.001	0.009	0.046	0.042	0.055	0.067	0.040	0.040	0.045	0.049	0.052	0.064	0.066	0.081	0.085	0.097	0.082	0.051	0.064	0.049
9	0.000	0.014	0.034	0.047	0.052	0.046	0.052	0.051	0.050	0.055	0.066	0.076	0.069	0.084	0.090	0.079	0.069	0.053	0.046	0.038
10-14	0.000	0.012	0.074	0.173	0.233	0.258	0.282	0.278	0.305	0.345	0.367	0.404	0.406	0.347	0.297	0.237	0.210	0.161	0.103	0.092
15-19	0.000	0.000	0.009	0.039	0.107	0.171	0.212	0.260	0.314	0.302	0.280	0.231	0.215	0.165	0.132	0.089	0.058	0.047	0.040	0.022
≥ 20	0.000	0.000	0.001	0.010	0.033	0.073	0.124	0.151	0.125	0.122	0.108	0.085	0.057	0.050	0.036	0.021	0.022	0.015	0.007	0.006
MEAN	0.76	1.91	3.55	5.54	7.73	9.69	11.53	12.67	13.23	13.41	13.10	12.52	11.76	10.71	9.69	8.40	7.55	6.45	5.57	4.73
VAR	1.6	6.0	14.4	25.2	34.3	40.3	45.4	42.0	36.0	29.9	26.6	23.6	22.5	23.2	22.5	21.8	20.0	19.7	17.1	16.1

TABLE 263

Primary photon E_0 = 5 000 MeV.
Secondary electrons E = 10 MeV.

Absorber: air, Z = 7.4, A = 15,
Radiation length = 43 g/sq. cm,
Critical energy = 98 MeV.

n \ t	0.5	1.0	1.5	2.0	2.5	3.0	3.5	4.0	4.5	5.0	5.5	6.0	6.5	7.0	7.5	8.0	8.5	9.0	9.5	10.0
0	0.725	0.510	0.348	0.239	0.159	0.111	0.085	0.068	0.056	0.059	0.072	0.081	0.123	0.191	0.227	0.297	0.357	0.420	0.511	0.570
1	0.003	0.011	0.018	0.019	0.026	0.020	0.021	0.031	0.038	0.054	0.072	0.121	0.154	0.174	0.167	0.224	0.218	0.247	0.205	0.204
2	0.206	0.244	0.211	0.155	0.139	0.101	0.085	0.078	0.090	0.119	0.135	0.153	0.168	0.186	0.223	0.164	0.163	0.145	0.123	0.116
3	0.023	0.055	0.080	0.079	0.083	0.080	0.077	0.078	0.115	0.128	0.149	0.179	0.148	0.135	0.141	0.119	0.104	0.077	0.077	0.049
4	0.027	0.075	0.107	0.123	0.114	0.121	0.105	0.113	0.137	0.134	0.152	0.123	0.125	0.111	0.082	0.077	0.065	0.046	0.040	0.032
5	0.009	0.050	0.069	0.100	0.099	0.087	0.123	0.133	0.142	0.128	0.119	0.108	0.105	0.072	0.056	0.046	0.033	0.025	0.022	0.014
6	0.006	0.032	0.051	0.079	0.096	0.109	0.121	0.136	0.119	0.119	0.103	0.072	0.069	0.050	0.041	0.029	0.025	0.020	0.011	0.007
7	0.001	0.009	0.039	0.056	0.071	0.110	0.099	0.112	0.103	0.102	0.070	0.058	0.047	0.037	0.025	0.018	0.020	0.011	0.006	0.002
8	0.000	0.006	0.032	0.048	0.081	0.085	0.085	0.106	0.069	0.049	0.058	0.042	0.029	0.018	0.014	0.008	0.003	0.006	0.001	0.002
9	0.000	0.005	0.021	0.035	0.052	0.067	0.082	0.060	0.064	0.041	0.038	0.027	0.019	0.013	0.008	0.008	0.007	0.002	0.003	0.002
10-14	0.000	0.003	0.024	0.065	0.077	0.106	0.114	0.090	0.076	0.067	0.031	0.035	0.023	0.013	0.016	0.012	0.005	0.001	0.001	0.002
≥15	0.000	0.000	0.000	0.002	0.004	0.003	0.003	0.007	0.001	0.000	0.001	0.001	0.000	0.000	0.000	0.000	0.000	0.000	0.000	0.000
MEAN	0.68	1.59	2.74	3.87	4.60	5.34	5.61	5.55	5.15	4.77	4.26	3.82	3.29	2.72	2.43	2.00	1.71	1.35	1.11	0.89
VAR	1.5	4.1	7.8	10.8	11.3	11.6	10.6	9.7	8.5	8.1	7.2	7.3	6.5	5.8	5.4	4.8	3.9	3.0	2.5	2.1

TABLE 264

Primary photon E_0 = 5 000 MeV.
Secondary electrons E = 10 MeV.

Absorber: al, Z = 13, A = 27,
Radiation length = 26.3 g/sq. cm = 9.74 cm,
Critical energy = 52 MeV.

n \ t	0.5	1.0	1.5	2.0	2.5	3.0	3.5	4.0	4.5	5.0	5.5	6.0	6.5	7.0	7.5	8.0	8.5	9.0	9.5	10.0
0	0.697	0.470	0.337	0.236	0.153	0.108	0.076	0.053	0.043	0.026	0.020	0.024	0.028	0.040	0.077	0.114	0.163	0.187	0.258	0.312
1	0.009	0.011	0.015	0.011	0.010	0.012	0.008	0.012	0.006	0.012	0.017	0.032	0.042	0.083	0.114	0.132	0.142	0.193	0.197	0.235
2	0.223	0.258	0.202	0.146	0.123	0.078	0.052	0.045	0.034	0.039	0.049	0.060	0.106	0.126	0.159	0.167	0.179	0.183	0.174	0.165
3	0.034	0.053	0.054	0.050	0.051	0.038	0.031	0.028	0.031	0.040	0.065	0.105	0.115	0.125	0.135	0.140	0.158	0.152	0.136	0.105
4	0.032	0.094	0.112	0.107	0.081	0.062	0.068	0.065	0.053	0.068	0.091	0.106	0.122	0.122	0.133	0.114	0.104	0.096	0.084	0.068
5	0.004	0.039	0.057	0.059	0.074	0.072	0.053	0.068	0.101	0.101	0.107	0.125	0.124	0.119	0.087	0.094	0.080	0.055	0.047	0.039
6	0.009	0.037	0.060	0.062	0.065	0.081	0.087	0.082	0.079	0.098	0.135	0.118	0.104	0.099	0.075	0.076	0.049	0.044	0.036	0.029
7	0.002	0.017	0.055	0.063	0.068	0.080	0.077	0.086	0.099	0.125	0.107	0.109	0.098	0.078	0.060	0.044	0.033	0.033	0.027	0.014
8	0.000	0.011	0.034	0.062	0.082	0.081	0.115	0.089	0.100	0.114	0.097	0.085	0.072	0.056	0.051	0.039	0.029	0.024	0.015	0.012
9	0.000	0.004	0.017	0.059	0.059	0.080	0.087	0.086	0.113	0.092	0.086	0.073	0.052	0.049	0.045	0.025	0.026	0.012	0.011	0.010
10-14	0.000	0.005	0.056	0.107	0.203	0.258	0.290	0.323	0.297	0.255	0.210	0.134	0.123	0.088	0.050	0.049	0.034	0.021	0.013	0.011
15-19	0.000	0.001	0.001	0.016	0.030	0.049	0.054	0.060	0.038	0.029	0.016	0.029	0.014	0.013	0.014	0.005	0.003	0.000	0.002	0.001
≥20	0.000	0.000	0.000	0.002	0.001	0.001	0.002	0.003	0.006	0.001	0.000	0.000	0.000	0.002	0.000	0.001	0.000	0.000	0.000	0.000
MEAN	0.74	1.79	3.13	4.67	5.97	7.09	7.81	8.16	8.03	7.54	6.96	6.32	5.68	5.06	4.26	3.76	3.22	2.70	2.32	1.94
VAR	1.6	4.8	10.5	16.4	19.0	19.6	18.4	17.8	15.0	12.1	11.2	12.2	11.3	11.3	10.5	9.4	8.2	6.2	5.8	5.0

TABLE 265

Primary photon E_0 = 10 000 MeV.
Secondary electrons E = 20 MeV.

Absorber: air, Z = 7.4, A = 15,
Radiation length = 43 g/sq. cm,
Critical energy = 98 MeV.

n \ t	0.5	1.0	1.5	2.0	2.5	3.0	3.5	4.0	4.5	5.0	5.5	6.0	6.5	7.0	7.5	8.0	8.5	9.0	9.5	10.0
0	0.686	0.471	0.317	0.218	0.148	0.099	0.072	0.049	0.039	0.022	0.023	0.023	0.022	0.044	0.061	0.108	0.154	0.224	0.288	0.375
1	0.004	0.013	0.004	0.010	0.010	0.007	0.008	0.010	0.010	0.010	0.018	0.025	0.048	0.081	0.113	0.138	0.175	0.197	0.228	0.209
2	0.239	0.237	0.201	0.136	0.104	0.066	0.043	0.038	0.025	0.039	0.035	0.065	0.090	0.114	0.149	0.181	0.168	0.164	0.174	0.151
3	0.024	0.066	0.074	0.053	0.051	0.034	0.039	0.019	0.035	0.043	0.079	0.103	0.116	0.114	0.141	0.121	0.155	0.130	0.107	0.101
4	0.036	0.092	0.101	0.087	0.067	0.070	0.044	0.047	0.057	0.066	0.079	0.095	0.131	0.139	0.124	0.113	0.107	0.102	0.061	0.057
5	0.006	0.028	0.069	0.066	0.073	0.068	0.060	0.061	0.052	0.095	0.095	0.111	0.133	0.128	0.113	0.087	0.065	0.051	0.040	0.034
6	0.004	0.042	0.073	0.085	0.066	0.069	0.079	0.081	0.086	0.101	0.105	0.102	0.104	0.096	0.085	0.078	0.044	0.040	0.028	0.034
7	0.001	0.022	0.045	0.069	0.077	0.082	0.082	0.077	0.114	0.104	0.111	0.103	0.074	0.068	0.065	0.049	0.037	0.031	0.024	0.008
8	0.000	0.013	0.042	0.076	0.077	0.083	0.089	0.107	0.102	0.098	0.080	0.108	0.067	0.070	0.041	0.044	0.032	0.022	0.014	0.011
9	0.000	0.007	0.029	0.054	0.073	0.067	0.077	0.087	0.100	0.092	0.084	0.056	0.063	0.045	0.027	0.016	0.023	0.011	0.011	0.007
10-14	0.000	0.008	0.040	0.127	0.217	0.284	0.323	0.338	0.307	0.283	0.249	0.177	0.135	0.087	0.073	0.059	0.034	0.025	0.024	0.009
15-19	0.000	0.001	0.005	0.017	0.035	0.065	0.074	0.080	0.071	0.045	0.042	0.028	0.016	0.012	0.008	0.006	0.006	0.002	0.001	0.004
20-24	0.000	0.000	0.000	0.002	0.002	0.006	0.009	0.006	0.002	0.002	0.000	0.004	0.001	0.002	0.000	0.000	0.000	0.001	0.000	0.000
≥25	0.000	0.000	0.000	0.000	0.000	0.000	0.001	0.000	0.000	0.000	0.000	0.000	0.000	0.000	0.000	0.000	0.000	0.000	0.000	0.000
MEAN	0.76	1.87	3.24	4.97	6.32	7.57	8.30	8.68	8.39	7.91	7.48	6.64	5.82	5.08	4.40	3.83	3.21	2.65	2.17	1.79
VAR	1.5	5.4	10.1	17.1	20.1	21.4	20.7	18.7	16.0	14.0	14.5	13.7	12.0	11.3	10.4	10.0	8.9	7.5	6.4	5.4

TABLE 266

Primary photon E_0 = 10 000 MeV.
Secondary electrons E = 20 MeV.

Absorber: al, Z = 13, A = 27,
Radiation length = 26.3 g/sq. cm = 9.74 cm,
Critical energy = 52 MeV.

n \ t	0.5	1.0	1.5	2.0	2.5	3.0	3.5	4.0	4.5	5.0	5.5	6.0	6.5	7.0	7.5	8.0	8.5	9.0	9.5	10.0
0	0.672	0.479	0.321	0.219	0.152	0.104	0.076	0.052	0.037	0.026	0.018	0.014	0.013	0.015	0.012	0.024	0.038	0.081	0.109	0.155
1	0.006	0.005	0.005	0.009	0.012	0.002	0.004	0.003	0.003	0.004	0.005	0.004	0.010	0.012	0.029	0.055	0.089	0.115	0.150	0.187
2	0.242	0.222	0.174	0.143	0.085	0.058	0.042	0.035	0.021	0.017	0.014	0.015	0.024	0.034	0.052	0.087	0.122	0.121	0.146	0.163
3	0.021	0.048	0.069	0.044	0.037	0.031	0.017	0.016	0.012	0.012	0.019	0.021	0.040	0.066	0.060	0.106	0.100	0.135	0.136	0.126
4	0.042	0.103	0.107	0.081	0.062	0.042	0.041	0.015	0.025	0.024	0.025	0.044	0.058	0.056	0.095	0.104	0.112	0.118	0.133	0.111
5	0.007	0.036	0.050	0.056	0.052	0.058	0.018	0.033	0.026	0.027	0.026	0.046	0.065	0.075	0.108	0.114	0.109	0.107	0.079	0.071
6	0.008	0.053	0.073	0.062	0.058	0.054	0.048	0.037	0.040	0.045	0.052	0.068	0.085	0.115	0.109	0.088	0.101	0.081	0.058	0.053
7	0.001	0.025	0.049	0.054	0.068	0.046	0.056	0.043	0.050	0.057	0.061	0.083	0.083	0.094	0.099	0.086	0.075	0.069	0.048	0.042
8	0.001	0.014	0.037	0.071	0.063	0.049	0.047	0.056	0.053	0.069	0.080	0.089	0.076	0.083	0.089	0.072	0.059	0.031	0.031	0.025
9	0.000	0.005	0.038	0.051	0.064	0.062	0.075	0.053	0.068	0.066	0.085	0.094	0.102	0.080	0.072	0.061	0.039	0.026	0.028	0.020
10-14	0.000	0.009	0.070	0.166	0.227	0.282	0.319	0.386	0.389	0.405	0.422	0.357	0.315	0.268	0.212	0.154	0.117	0.097	0.068	0.037
15-19	0.000	0.001	0.007	0.036	0.100	0.171	0.202	0.214	0.222	0.210	0.167	0.149	0.110	0.089	0.054	0.040	0.034	0.016	0.013	0.010
20-24	0.000	0.000	0.000	0.008	0.018	0.033	0.050	0.056	0.049	0.035	0.024	0.015	0.019	0.013	0.009	0.009	0.005	0.003	0.001	0.000
≥25	0.000	0.000	0.000	0.000	0.002	0.008	0.005	0.001	0.005	0.003	0.002	0.001	0.000	0.000	0.000	0.000	0.000	0.000	0.000	0.000
MEAN	0.82	1.94	3.56	5.51	7.51	9.38	10.52	11.12	11.49	11.23	10.74	10.07	9.27	8.44	7.47	6.41	5.58	4.61	3.96	3.28
VAR	1.7	5.7	12.9	23.2	33.3	37.2	35.9	29.0	28.4	22.6	19.8	19.1	20.1	18.6	17.2	17.3	16.1	13.0	11.8	9.9

TABLE 267

Primary photon E_0 = 50 000 MeV.
Secondary electrons E = 100 MeV.

Absorber: air, Z = 7.4, A = 15,
Radiation length = 43 g/sq. cm.
Critical energy = 98 MeV.

n \ t	0.5	1.0	1.5	2.0	2.5	3.0	3.5	4.0	4.5	5.0	5.5	6.0	6.5	7.0	7.5	8.0	8.5	9.0	9.5	10.0
0	0.682	0.452	0.319	0.230	0.151	0.117	0.086	0.058	0.042	0.028	0.019	0.012	0.009	0.008	0.006	0.005	0.003	0.015	0.025	0.038
1	0.002	0.007	0.003	0.005	0.005	0.002	0.010	0.000	0.000	0.001	0.000	0.000	0.001	0.000	0.002	0.005	0.011	0.034	0.052	0.087
2	0.230	0.233	0.156	0.105	0.078	0.045	0.032	0.032	0.024	0.016	0.012	0.010	0.005	0.009	0.008	0.019	0.036	0.045	0.070	0.120
3	0.026	0.048	0.057	0.030	0.034	0.013	0.010	0.007	0.015	0.011	0.004	0.004	0.002	0.007	0.014	0.024	0.054	0.079	0.107	0.112
4	0.042	0.087	0.078	0.056	0.046	0.035	0.034	0.014	0.011	0.013	0.017	0.006	0.008	0.014	0.029	0.050	0.066	0.091	0.088	0.093
5	0.009	0.048	0.068	0.059	0.033	0.029	0.015	0.015	0.008	0.013	0.007	0.006	0.020	0.023	0.040	0.055	0.080	0.093	0.099	0.101
6	0.004	0.039	0.061	0.072	0.040	0.041	0.030	0.021	0.013	0.007	0.006	0.012	0.023	0.031	0.038	0.059	0.079	0.094	0.090	0.073
7	0.004	0.026	0.059	0.059	0.045	0.039	0.023	0.016	0.013	0.010	0.014	0.020	0.026	0.029	0.052	0.074	0.075	0.065	0.075	0.066
8	0.001	0.019	0.041	0.054	0.060	0.047	0.037	0.024	0.019	0.021	0.021	0.018	0.041	0.053	0.065	0.069	0.085	0.071	0.064	0.065
9	0.000	0.018	0.030	0.055	0.056	0.045	0.039	0.030	0.024	0.021	0.026	0.040	0.032	0.053	0.059	0.079	0.070	0.072	0.056	0.036
10-14	0.000	0.023	0.109	0.174	0.220	0.220	0.223	0.209	0.191	0.198	0.220	0.255	0.300	0.315	0.328	0.308	0.247	0.209	0.170	0.130
15-19	0.000	0.000	0.018	0.080	0.152	0.212	0.207	0.252	0.276	0.300	0.327	0.330	0.309	0.294	0.246	0.174	0.132	0.082	0.069	0.050
20-24	0.000	0.000	0.001	0.019	0.058	0.094	0.166	0.197	0.239	0.248	0.240	0.224	0.175	0.134	0.093	0.065	0.045	0.044	0.026	0.024
25-29	0.000	0.000	0.000	0.002	0.020	0.052	0.079	0.101	0.102	0.097	0.087	0.063	0.049	0.030	0.020	0.014	0.017	0.006	0.009	0.005
≥ 30	0.000	0.000	0.000	0.000	0.002	0.009	0.019	0.024	0.023	0.016	0.000	0.000	0.000	0.000	0.000	0.000	0.000	0.000	0.000	0.000
MEAN	0.81	2.19	4.89	6.43	9.15	11.67	13.86	15.50	16.41	16.64	16.49	16.00	15.03	13.93	12.61	11.04	9.74	8.32	7.37	6.28
VAR	1.8	7.4	17.5	31.9	47.8	60.0	65.6	60.6	55.4	46.7	37.2	32.8	32.4	31.4	30.2	29.5	30.6	28.5	27.3	25.6

TABLE 268

Primary photon E_0 = 50 000 MeV.
Secondary electrons E = 100 MeV.

Absorber: al, Z = 13, A = 27,
Radiation length = 26.3 g/sq. cm = 9.74 cm.
Critical energy = 52 MeV.

n \ t	0.5	1.0	1.5	2.0	2.5	3.0	3.5	4.0	4.5	5.0	5.5	6.0	6.5	7.0	7.5	8.0	8.5	9.0	9.5	10.0
0	0.707	0.496	0.338	0.220	0.149	0.102	0.070	0.044	0.029	0.018	0.012	0.010	0.009	0.005	0.002	0.002	0.002	0.002	0.007	0.011
1	0.004	0.012	0.003	0.004	0.006	0.001	0.001	0.003	0.001	0.000	0.000	0.000	0.000	0.000	0.001	0.002	0.006	0.012	0.018	0.042
2	0.218	0.229	0.182	0.127	0.090	0.064	0.042	0.033	0.017	0.012	0.010	0.003	0.001	0.005	0.004	0.002	0.006	0.020	0.035	0.055
3	0.017	0.039	0.047	0.035	0.026	0.018	0.008	0.006	0.006	0.008	0.007	0.004	0.003	0.000	0.007	0.008	0.023	0.034	0.037	0.068
4	0.039	0.082	0.087	0.091	0.044	0.035	0.027	0.014	0.014	0.012	0.002	0.003	0.007	0.004	0.008	0.012	0.028	0.050	0.065	0.087
5	0.010	0.033	0.049	0.042	0.041	0.039	0.019	0.016	0.016	0.010	0.006	0.005	0.005	0.010	0.012	0.016	0.040	0.047	0.075	0.079
6	0.004	0.049	0.057	0.046	0.049	0.033	0.025	0.021	0.012	0.006	0.006	0.008	0.005	0.009	0.021	0.036	0.040	0.054	0.074	0.076
7	0.000	0.017	0.043	0.045	0.042	0.026	0.028	0.028	0.015	0.011	0.006	0.005	0.011	0.017	0.027	0.042	0.044	0.074	0.088	0.080
8	0.001	0.017	0.042	0.051	0.039	0.041	0.024	0.015	0.019	0.016	0.011	0.009	0.016	0.017	0.033	0.040	0.063	0.074	0.066	0.085
9	0.000	0.009	0.028	0.043	0.048	0.032	0.036	0.020	0.017	0.020	0.019	0.013	0.018	0.025	0.028	0.046	0.068	0.070	0.062	0.049
10-14	0.000	0.015	0.110	0.173	0.216	0.224	0.185	0.154	0.129	0.104	0.113	0.133	0.157	0.224	0.268	0.317	0.314	0.278	0.267	0.232
15-19	0.000	0.002	0.020	0.090	0.149	0.181	0.211	0.223	0.214	0.216	0.248	0.290	0.307	0.333	0.312	0.262	0.210	0.170	0.134	0.088
20-24	0.000	0.000	0.002	0.027	0.071	0.128	0.157	0.193	0.241	0.282	0.285	0.279	0.290	0.220	0.178	0.143	0.109	0.080	0.048	0.034
25-29	0.000	0.000	0.000	0.006	0.027	0.068	0.113	0.141	0.185	0.192	0.205	0.177	0.119	0.102	0.074	0.054	0.033	0.029	0.021	0.011
≥ 30	0.000	0.000	0.000	0.001	0.005	0.018	0.054	0.089	0.085	0.093	0.070	0.061	0.052	0.029	0.025	0.018	0.014	0.006	0.003	0.003
MEAN	0.73	1.91	3.97	6.61	9.43	12.46	15.25	17.56	18.98	19.91	20.21	19.77	18.97	17.50	16.10	14.76	13.04	11.45	10.04	8.49
VAR	1.6	6.6	18.3	38.8	53.8	68.5	79.4	84.6	69.5	62.2	52.2	44.5	45.3	41.0	39.7	38.7	39.7	37.8	33.6	30.3

TABLE 269

Primary photon E_0 = 5 000 MeV.
Secondary electrons E = 5 MeV.

Absorber: air, Z = 7.4, A = 15,
Radiation length = 45 g/sq. cm,
Critical energy = 98 MeV.

n \ t	0.5	1.0	1.5	2.0	2.5	3.0	3.5	4.0	4.5	5.0	5.5	6.0	6.5	7.0	7.5	8.0	8.5	9.0	9.5	10.0
0	0.686	0.490	0.337	0.235	0.169	0.122	0.086	0.069	0.057	0.042	0.042	0.062	0.098	0.121	0.184	0.232	0.325	0.404	0.484	0.517
1	0.006	0.018	0.015	0.013	0.012	0.018	0.016	0.019	0.030	0.041	0.060	0.090	0.115	0.158	0.177	0.200	0.204	0.181	0.191	0.194
2	0.243	0.225	0.202	0.142	0.107	0.083	0.068	0.058	0.062	0.088	0.127	0.132	0.156	0.185	0.165	0.178	0.177	0.153	0.149	0.127
3	0.019	0.062	0.068	0.089	0.073	0.050	0.056	0.068	0.080	0.118	0.133	0.151	0.153	0.150	0.146	0.124	0.097	0.088	0.082	0.073
4	0.032	0.101	0.102	0.092	0.096	0.086	0.076	0.094	0.111	0.136	0.133	0.129	0.140	0.123	0.103	0.100	0.077	0.068	0.042	0.035
5	0.005	0.037	0.073	0.086	0.097	0.079	0.093	0.121	0.120	0.144	0.135	0.126	0.113	0.093	0.082	0.056	0.038	0.031	0.024	0.022
6	0.008	0.035	0.075	0.075	0.085	0.093	0.112	0.118	0.122	0.095	0.109	0.087	0.071	0.064	0.049	0.042	0.029	0.030	0.019	0.012
7	0.000	0.011	0.040	0.067	0.089	0.104	0.106	0.088	0.108	0.089	0.077	0.071	0.056	0.041	0.030	0.019	0.017	0.017	0.008	0.008
8	0.001	0.011	0.036	0.055	0.067	0.090	0.098	0.087	0.096	0.082	0.065	0.061	0.038	0.025	0.019	0.017	0.014	0.008	0.005	0.005
9	0.000	0.003	0.017	0.043	0.065	0.086	0.088	0.082	0.073	0.059	0.047	0.029	0.020	0.013	0.020	0.012	0.007	0.007	0.004	0.003
10-14	0.000	0.007	0.031	0.096	0.124	0.175	0.187	0.180	0.127	0.103	0.065	0.060	0.039	0.025	0.023	0.018	0.013	0.011	0.012	0.004
15-19	0.000	0.000	0.004	0.008	0.016	0.012	0.014	0.015	0.014	0.003	0.007	0.002	0.001	0.002	0.002	0.002	0.002	0.002	0.000	0.000
⩾20	0.000	0.000	0.000	0.000	0.000	0.002	0.000	0.001	0.000	0.000	0.000	0.000	0.000	0.000	0.000	0.000	0.000	0.000	0.000	0.000
MEAN	0.76	1.72	2.97	4.32	5.24	6.08	6.42	6.33	6.00	5.42	4.88	4.41	3.77	3.23	2.89	2.47	1.98	1.76	1.40	1.16
VAR	1.6	4.6	9.2	14.0	15.1	15.2	13.6	12.6	11.3	9.6	8.8	8.3	7.6	6.6	6.9	6.3	5.3	5.2	4.1	3.0

TABLE 270

Primary photon E_0 = 5 000 MeV.
Secondary electrons E = 5 MeV.

Absorber: al, Z = 13, A = 27,
Radiation length = 26.3 g/sq. cm = 9.74 cm.
Critical energy = 52 MeV.

n \ t	0.5	1.0	1.5	2.0	2.5	3.0	3.5	4.0	4.5	5.0	5.5	6.0	6.5	7.0	7.5	8.0	8.5	9.0	9.5	10.0
0	0.701	0.488	0.342	0.225	0.145	0.111	0.084	0.063	0.051	0.035	0.022	0.017	0.019	0.027	0.041	0.050	0.072	0.129	0.167	0.232
1	0.002	0.007	0.009	0.008	0.011	0.008	0.009	0.011	0.007	0.009	0.014	0.015	0.025	0.034	0.070	0.100	0.142	0.161	0.191	0.203
2	0.225	0.225	0.177	0.137	0.091	0.065	0.042	0.043	0.024	0.036	0.032	0.043	0.055	0.079	0.102	0.127	0.157	0.156	0.179	0.157
3	0.019	0.054	0.054	0.051	0.042	0.031	0.033	0.025	0.022	0.023	0.037	0.058	0.070	0.115	0.109	0.140	0.134	0.134	0.130	0.122
4	0.039	0.096	0.103	0.088	0.070	0.059	0.040	0.032	0.041	0.049	0.056	0.080	0.095	0.106	0.115	0.113	0.126	0.103	0.093	0.085
5	0.006	0.041	0.064	0.056	0.064	0.057	0.052	0.052	0.052	0.050	0.076	0.108	0.097	0.116	0.104	0.118	0.100	0.077	0.049	0.052
6	0.005	0.041	0.071	0.082	0.071	0.045	0.059	0.056	0.060	0.079	0.073	0.085	0.121	0.107	0.091	0.073	0.080	0.082	0.055	0.048
7	0.002	0.017	0.056	0.067	0.062	0.074	0.065	0.061	0.078	0.075	0.102	0.107	0.108	0.085	0.078	0.067	0.052	0.040	0.039	0.025
8	0.001	0.009	0.032	0.065	0.082	0.087	0.061	0.074	0.084	0.088	0.113	0.091	0.094	0.085	0.069	0.055	0.031	0.036	0.029	0.024
9	0.000	0.006	0.021	0.043	0.083	0.074	0.069	0.075	0.085	0.108	0.095	0.078	0.072	0.061	0.059	0.042	0.032	0.021	0.017	0.015
10-14	0.000	0.015	0.060	0.145	0.211	0.281	0.323	0.352	0.354	0.341	0.299	0.260	0.201	0.161	0.142	0.094	0.055	0.055	0.048	0.036
15-19	0.000	0.001	0.010	0.029	0.060	0.094	0.141	0.128	0.127	0.100	0.072	0.056	0.040	0.021	0.017	0.021	0.019	0.005	0.005	0.003
20-24	0.000	0.000	0.001	0.004	0.008	0.011	0.022	0.026	0.013	0.006	0.009	0.002	0.003	0.004	0.002	0.002	0.000	0.001	0.000	0.000
⩾25	0.000	0.000	0.000	0.000	0.000	0.003	0.000	0.002	0.002	0.001	0.000	0.000	0.000	0.000	0.001	0.000	0.000	0.000	0.000	0.000
MEAN	0.75	1.88	3.37	5.12	6.78	8.07	9.11	9.43	9.49	9.03	8.53	7.82	7.10	6.27	5.72	4.97	4.17	3.64	3.14	2.72
VAR	1.6	6.0	12.7	19.7	23.5	26.7	27.7	25.9	22.2	18.7	17.1	15.8	14.4	13.8	14.2	13.2	11.2	10.0	9.2	8.3

TABLE 271

Primary photon E_0 = 10 000 MeV.
Secondary electrons E = 10 MeV.

Absorber: air, Z = 7.4, A = 15.
Radiation length = 43 g/sq. cm.
Critical energy = 98 MeV.

n \ t	0.5	1.0	1.5	2.0	2.5	3.0	3.5	4.0	4.5	5.0	5.5	6.0	6.5	7.0	7.5	8.0	8.5	9.0	9.5	10.0
0	0.680	0.486	0.324	0.225	0.156	0.105	0.074	0.054	0.040	0.028	0.022	0.015	0.019	0.035	0.039	0.074	0.104	0.138	0.211	0.219
1	0.005	0.006	0.008	0.009	0.005	0.003	0.008	0.006	0.002	0.006	0.005	0.013	0.033	0.046	0.070	0.088	0.118	0.168	0.175	0.218
2	0.240	0.219	0.178	0.122	0.086	0.067	0.034	0.024	0.025	0.026	0.026	0.036	0.050	0.077	0.099	0.100	0.158	0.173	0.158	0.168
3	0.025	0.052	0.057	0.041	0.037	0.025	0.021	0.019	0.017	0.018	0.030	0.056	0.062	0.076	0.103	0.138	0.114	0.122	0.119	0.127
4	0.039	0.102	0.096	0.083	0.063	0.059	0.044	0.033	0.021	0.033	0.046	0.078	0.098	0.098	0.105	0.121	0.123	0.114	0.101	0.077
5	0.007	0.040	0.051	0.068	0.053	0.047	0.045	0.043	0.046	0.048	0.064	0.080	0.091	0.107	0.119	0.101	0.101	0.070	0.062	0.052
6	0.004	0.035	0.074	0.074	0.079	0.048	0.058	0.042	0.060	0.064	0.071	0.092	0.085	0.088	0.106	0.086	0.073	0.056	0.043	0.042
7	0.000	0.031	0.048	0.057	0.049	0.064	0.060	0.065	0.081	0.084	0.095	0.096	0.104	0.087	0.086	0.079	0.048	0.040	0.038	0.034
8	0.000	0.009	0.044	0.063	0.085	0.068	0.067	0.074	0.061	0.090	0.095	0.086	0.098	0.086	0.072	0.065	0.037	0.040	0.028	0.014
9	0.000	0.009	0.036	0.046	0.053	0.067	0.076	0.092	0.082	0.104	0.094	0.090	0.068	0.082	0.060	0.037	0.029	0.023	0.013	0.014
10-14	0.000	0.010	0.074	0.161	0.216	0.298	0.346	0.377	0.405	0.368	0.348	0.283	0.233	0.182	0.129	0.088	0.079	0.045	0.045	0.028
15-19	0.000	0.001	0.011	0.043	0.091	0.121	0.139	0.139	0.135	0.109	0.096	0.068	0.056	0.028	0.020	0.020	0.015	0.010	0.006	0.007
20-24	0.000	0.000	0.000	0.008	0.025	0.027	0.026	0.029	0.025	0.023	0.008	0.006	0.002	0.008	0.002	0.002	0.001	0.001	0.001	0.000
≥25	0.000	0.000	0.000	0.000	0.002	0.001	0.002	0.003	0.000	0.001	0.000	0.001	0.001	0.000	0.000	0.001	0.000	0.000	0.000	0.000
MEAN	0.78	1.91	3.63	5.54	7.38	8.70	9.50	10.06	10.15	9.72	9.15	8.20	7.48	6.64	5.70	5.01	4.27	3.52	3.06	2.66
VAR	1.5	5.8	13.9	23.3	30.6	30.5	26.9	24.5	21.8	19.8	17.5	16.8	17.0	16.3	13.7	13.7	12.5	10.4	10.0	8.2

TABLE 272

Primary photon E_0 = 10 000 MeV.
Secondary electrons E = 10 MeV.

Absorber: al, Z = 13, A = 27.
Radiation length = 26.3 g/sq. cm = 9.74 cm
Critical energy = 52 MeV.

n \ t	0.5	1.0	1.5	2.0	2.5	3.0	3.5	4.0	4.5	5.0	5.5	6.0	6.5	7.0	7.5	8.0	8.5	9.0	9.5	10.0
0	0.696	0.487	0.352	0.257	0.180	0.129	0.088	0.062	0.041	0.034	0.025	0.019	0.016	0.015	0.010	0.010	0.021	0.029	0.051	0.063
1	0.003	0.002	0.006	0.003	0.005	0.003	0.006	0.001	0.002	0.001	0.001	0.001	0.003	0.006	0.011	0.013	0.023	0.051	0.065	0.102
2	0.221	0.229	0.150	0.097	0.074	0.058	0.049	0.031	0.022	0.014	0.007	0.011	0.010	0.009	0.018	0.039	0.058	0.080	0.086	0.119
3	0.017	0.047	0.049	0.042	0.033	0.023	0.019	0.013	0.009	0.006	0.005	0.009	0.017	0.016	0.031	0.062	0.060	0.081	0.106	0.126
4	0.050	0.089	0.096	0.072	0.054	0.035	0.028	0.030	0.017	0.009	0.016	0.010	0.016	0.024	0.047	0.062	0.076	0.088	0.109	0.115
5	0.006	0.038	0.051	0.049	0.034	0.036	0.023	0.022	0.016	0.019	0.018	0.008	0.021	0.049	0.060	0.072	0.101	0.099	0.099	0.097
6	0.005	0.040	0.067	0.060	0.042	0.034	0.033	0.031	0.031	0.018	0.020	0.038	0.042	0.057	0.056	0.081	0.074	0.112	0.091	0.088
7	0.002	0.024	0.043	0.059	0.051	0.042	0.047	0.032	0.028	0.022	0.027	0.033	0.057	0.066	0.081	0.079	0.087	0.085	0.081	0.058
8	0.000	0.021	0.044	0.065	0.053	0.048	0.038	0.041	0.044	0.046	0.028	0.047	0.051	0.068	0.086	0.066	0.079	0.053	0.068	0.040
9	0.000	0.009	0.043	0.047	0.057	0.054	0.042	0.039	0.034	0.037	0.040	0.059	0.069	0.073	0.075	0.081	0.069	0.068	0.055	0.042
10-14	0.000	0.012	0.086	0.169	0.222	0.243	0.225	0.247	0.253	0.286	0.325	0.352	0.358	0.338	0.313	0.270	0.228	0.170	0.124	0.104
15-19	0.000	0.002	0.012	0.066	0.139	0.187	0.213	0.241	0.285	0.318	0.317	0.273	0.236	0.208	0.141	0.121	0.100	0.063	0.055	0.077
20-24	0.000	0.000	0.002	0.013	0.048	0.080	0.139	0.151	0.158	0.155	0.136	0.118	0.082	0.063	0.061	0.037	0.016	0.016	0.007	0.007
25-29	0.000	0.000	0.000	0.001	0.008	0.021	0.045	0.052	0.052	0.029	0.035	0.022	0.022	0.008	0.010	0.007	0.008	0.005	0.003	0.002
≥30	0.000	0.000	0.000	0.000	0.000	0.007	0.005	0.007	0.008	0.006	0.000	0.000	0.000	0.000	0.000	0.000	0.000	0.000	0.000	0.000
MEAN	0.77	1.97	3.74	5.97	8.36	10.43	12.24	13.38	14.17	14.27	14.13	13.45	12.54	11.54	10.50	9.32	8.31	7.12	6.20	5.30
VAR	1.7	6.5	15.8	29.2	42.2	51.6	56.0	52.4	45.0	37.2	32.2	29.9	29.2	27.9	28.0	27.2	25.3	23.6	20.2	18.3

TABLE 273

Primary photon E_0 = 20 000 MeV.
Secondary electrons E = 20 MeV.

Absorber: air, Z = 7.4, A = 15,
Radiation length = 43 g/sq. cm,
Critical energy = 98 MeV.

n \ t	0.5	1.0	1.5	2.0	2.5	3.0	3.5	4.0	4.5	5.0	5.5	6.0	6.5	7.0	7.5	8.0	8.5	9.0	9.5	10.0
0	0.691	0.476	0.343	0.248	0.174	0.126	0.087	0.061	0.049	0.033	0.024	0.015	0.011	0.008	0.005	0.006	0.016	0.034	0.051	0.066
1	0.004	0.007	0.007	0.007	0.006	0.003	0.000	0.002	0.003	0.002	0.000	0.001	0.002	0.002	0.008	0.023	0.031	0.060	0.060	0.110
2	0.229	0.220	0.158	0.097	0.079	0.052	0.046	0.033	0.013	0.017	0.007	0.010	0.010	0.015	0.019	0.035	0.063	0.078	0.119	0.120
3	0.014	0.039	0.042	0.033	0.025	0.012	0.012	0.012	0.014	0.010	0.010	0.007	0.008	0.016	0.031	0.050	0.070	0.082	0.113	0.119
4	0.039	0.092	0.080	0.066	0.041	0.043	0.028	0.014	0.016	0.008	0.012	0.007	0.016	0.028	0.035	0.056	0.086	0.080	0.105	0.133
5	0.008	0.037	0.058	0.065	0.042	0.032	0.021	0.024	0.011	0.013	0.020	0.018	0.017	0.038	0.049	0.052	0.090	0.086	0.091	0.089
6	0.011	0.063	0.062	0.053	0.041	0.038	0.024	0.024	0.015	0.020	0.022	0.023	0.028	0.040	0.067	0.086	0.073	0.101	0.076	0.081
7	0.001	0.017	0.053	0.063	0.053	0.032	0.033	0.032	0.026	0.020	0.028	0.029	0.039	0.050	0.083	0.074	0.066	0.065	0.068	0.039
8	0.003	0.016	0.053	0.044	0.049	0.041	0.035	0.030	0.035	0.027	0.028	0.035	0.060	0.083	0.063	0.078	0.060	0.066	0.066	0.039
9	0.000	0.014	0.027	0.044	0.050	0.045	0.042	0.034	0.021	0.023	0.036	0.051	0.067	0.075	0.076	0.074	0.061	0.063	0.042	0.036
10-14	0.000	0.016	0.095	0.182	0.210	0.238	0.230	0.208	0.249	0.259	0.274	0.336	0.366	0.330	0.323	0.270	0.245	0.182	0.144	0.114
15-19	0.000	0.003	0.019	0.077	0.159	0.195	0.235	0.259	0.277	0.306	0.329	0.309	0.234	0.208	0.165	0.143	0.103	0.078	0.041	0.043
20-24	0.000	0.000	0.002	0.019	0.047	0.113	0.136	0.202	0.205	0.210	0.163	0.128	0.121	0.085	0.058	0.044	0.027	0.024	0.020	0.006
25-29	0.000	0.000	0.001	0.002	0.022	0.023	0.059	0.059	0.060	0.043	0.047	0.031	0.021	0.022	0.018	0.009	0.009	0.001	0.004	0.005
⩾30	0.000	0.000	0.000	0.000	0.002	0.007	0.012	0.006	0.006	0.009	0.000	0.000	0.000	0.000	0.000	0.000	0.000	0.000	0.000	0.000
MEAN	0.80	2.10	3.96	6.26	8.85	11.14	13.00	14.24	14.92	15.17	14.77	14.14	13.25	12.14	11.01	9.81	8.48	7.30	6.26	5.37
VAR	1.9	7.5	18.5	32.0	47.8	55.9	59.0	53.5	47.7	41.7	35.6	30.3	29.5	30.7	29.8	29.1	28.4	25.4	23.8	21.1

TABLE 274

Primary photon E_0 = 20 000 MeV.
Secondary electrons E = 20 MeV.

Absorber: al, Z = 13, A = 27,
Radiation length = 26.3 g/sq. cm = 9.74 cm,
Critical energy = 52 MeV.

n \ t	0.5	1.0	1.5	2.0	2.5	3.0	3.5	4.0	4.5	5.0	5.5	6.0	6.5	7.0	7.5	8.0	8.5	9.0	9.5	10.0
0	0.686	0.476	0.330	0.228	0.161	0.098	0.068	0.044	0.029	0.021	0.014	0.009	0.006	0.005	0.002	0.000	0.000	0.001	0.014	0.010
1	0.003	0.008	0.004	0.003	0.002	0.000	0.000	0.000	0.000	0.000	0.000	0.001	0.000	0.000	0.000	0.000	0.004	0.010	0.014	0.037
2	0.217	0.192	0.152	0.111	0.076	0.067	0.035	0.026	0.015	0.007	0.008	0.005	0.002	0.001	0.003	0.009	0.007	0.019	0.024	0.051
3	0.024	0.040	0.037	0.029	0.015	0.016	0.013	0.010	0.005	0.008	0.005	0.003	0.002	0.001	0.003	0.006	0.022	0.032	0.051	0.072
4	0.047	0.101	0.089	0.069	0.046	0.033	0.020	0.022	0.012	0.006	0.007	0.004	0.005	0.003	0.005	0.013	0.023	0.045	0.066	0.085
5	0.003	0.050	0.053	0.046	0.032	0.024	0.023	0.009	0.010	0.006	0.004	0.002	0.004	0.007	0.009	0.016	0.036	0.046	0.053	0.077
6	0.017	0.038	0.050	0.044	0.043	0.034	0.025	0.010	0.013	0.009	0.007	0.005	0.005	0.006	0.014	0.026	0.047	0.049	0.075	0.091
7	0.003	0.032	0.047	0.043	0.040	0.027	0.017	0.025	0.014	0.011	0.008	0.007	0.013	0.016	0.020	0.035	0.050	0.057	0.066	0.078
8	0.000	0.018	0.061	0.048	0.051	0.027	0.030	0.023	0.011	0.006	0.007	0.009	0.013	0.018	0.035	0.049	0.062	0.068	0.085	0.063
9	0.000	0.013	0.032	0.043	0.039	0.041	0.024	0.011	0.015	0.011	0.008	0.008	0.011	0.022	0.043	0.044	0.059	0.064	0.061	0.063
10-14	0.000	0.030	0.107	0.192	0.204	0.187	0.163	0.134	0.109	0.103	0.099	0.103	0.147	0.218	0.259	0.303	0.280	0.298	0.254	0.220
15-19	0.000	0.002	0.033	0.096	0.151	0.191	0.198	0.193	0.187	0.204	0.195	0.246	0.278	0.291	0.283	0.255	0.228	0.172	0.131	0.091
20-24	0.000	0.000	0.004	0.037	0.080	0.127	0.175	0.226	0.233	0.234	0.280	0.300	0.278	0.225	0.193	0.142	0.123	0.095	0.067	0.040
25-29	0.000	0.000	0.001	0.005	0.044	0.078	0.124	0.152	0.199	0.219	0.224	0.188	0.157	0.140	0.089	0.076	0.041	0.027	0.028	0.015
⩾30	0.000	0.000	0.000	0.006	0.016	0.050	0.085	0.115	0.148	0.155	0.134	0.110	0.079	0.047	0.042	0.026	0.018	0.017	0.011	0.007
MEAN	0.84	2.23	4.33	7.24	10.24	13.54	16.44	18.69	20.51	21.48	21.55	21.09	19.87	18.35	16.88	15.28	13.59	12.12	10.80	8.85
VAR	2.0	8.2	21.5	55.1	65.2	86.6	90.7	90.0	82.0	74.6	59.7	52.6	46.8	42.6	46.3	43.4	43.0	43.7	41.8	35.4

TABLE 275

Primary photon E_0 = 50 000 MeV.
Secondary electrons E = 50 MeV.

Absorber: air, Z = 7.4, A = 15.
Radiation length = 43 g/sq. cm.
Critical energy = 98 MeV.

n \ t	0.5	1.0	1.5	2.0	2.5	3.0	3.5	4.0	4.5	5.0	5.5	6.0	6.5	7.0	7.5	8.0	8.5	9.0	9.5	10.0
0	0.691	0.477	0.316	0.225	0.151	0.109	0.070	0.044	0.029	0.020	0.009	0.004	0.001	0.000	0.000	0.000	0.000	0.000	0.000	0.000
1	0.004	0.003	0.006	0.002	0.004	0.002	0.001	0.002	0.000	0.000	0.000	0.001	0.000	0.000	0.000	0.000	0.001	0.006	0.014	0.018
2	0.215	0.201	0.155	0.109	0.076	0.045	0.037	0.025	0.013	0.012	0.008	0.006	0.006	0.000	0.001	0.001	0.005	0.010	0.021	0.042
3	0.016	0.040	0.038	0.030	0.021	0.012	0.008	0.008	0.010	0.002	0.001	0.000	0.001	0.001	0.000	0.001	0.005	0.020	0.036	0.053
4	0.052	0.094	0.082	0.056	0.035	0.033	0.023	0.019	0.016	0.008	0.007	0.002	0.003	0.002	0.003	0.006	0.012	0.029	0.045	0.073
5	0.007	0.042	0.047	0.036	0.039	0.022	0.015	0.012	0.008	0.006	0.002	0.004	0.000	0.006	0.007	0.009	0.020	0.027	0.049	0.077
6	0.008	0.046	0.057	0.055	0.044	0.026	0.019	0.014	0.014	0.005	0.004	0.002	0.003	0.002	0.006	0.010	0.022	0.035	0.069	0.083
7	0.004	0.019	0.048	0.039	0.034	0.027	0.019	0.015	0.007	0.005	0.005	0.003	0.007	0.003	0.007	0.021	0.045	0.063	0.060	0.068
8	0.002	0.028	0.049	0.043	0.038	0.027	0.018	0.017	0.013	0.012	0.008	0.007	0.006	0.010	0.008	0.024	0.040	0.056	0.070	0.070
9	0.000	0.016	0.039	0.051	0.040	0.030	0.028	0.010	0.009	0.011	0.003	0.006	0.004	0.012	0.026	0.033	0.053	0.045	0.064	0.065
10-14	0.001	0.031	0.116	0.172	0.173	0.167	0.131	0.102	0.083	0.069	0.070	0.058	0.069	0.120	0.186	0.216	0.280	0.276	0.261	0.222
15-19	0.000	0.003	0.035	0.118	0.155	0.156	0.160	0.146	0.128	0.117	0.112	0.143	0.188	0.220	0.248	0.272	0.205	0.204	0.153	0.127
20-24	0.000	0.000	0.011	0.043	0.101	0.145	0.167	0.182	0.180	0.197	0.220	0.260	0.258	0.278	0.235	0.206	0.159	0.108	0.084	0.061
25-29	0.000	0.000	0.001	0.016	0.056	0.113	0.138	0.169	0.205	0.226	0.265	0.232	0.237	0.179	0.158	0.120	0.100	0.058	0.045	0.022
≥30	0.000	0.000	0.000	0.006	0.033	0.086	0.168	0.235	0.285	0.310	0.286	0.272	0.217	0.167	0.115	0.081	0.053	0.043	0.029	0.016
MEAN	0.83	2.28	4.59	7.68	11.19	14.93	18.37	21.22	23.07	24.27	25.49	25.20	24.06	22.93	20.48	18.48	16.14	14.02	12.23	10.22
VAR	2.0	8.8	24.0	50.0	79.2	103.4	120.1	120.4	105.2	88.7	93.9	75.8	68.9	84.7	66.3	56.2	59.4	56.5	55.2	43.7

TABLE 276

Primary photon E_0 = 50 000 MeV.
Secondary electrons E = 50 MeV.

Absorber: al, Z = 13, A = 27.
Radiation length = 26.3 g/sq. cm = 9.74 cm.
Critical energy = 52 MeV.

n \ t	0.5	1.0	1.5	2.0	2.5	3.0	3.5	4.0	4.5	5.0	5.5	6.0	6.5	7.0	7.5	8.0	8.5	9.0	9.5	10.0
0	0.693	0.474	0.324	0.225	0.153	0.102	0.076	0.052	0.038	0.026	0.020	0.012	0.009	0.005	0.003	0.003	0.003	0.002	0.003	0.001
1	0.003	0.005	0.003	0.001	0.002	0.001	0.000	0.000	0.000	0.000	0.000	0.000	0.000	0.000	0.000	0.000	0.000	0.001	0.004	0.002
2	0.224	0.217	0.162	0.118	0.071	0.045	0.026	0.022	0.012	0.011	0.007	0.009	0.003	0.002	0.002	0.000	0.000	0.002	0.002	0.011
3	0.016	0.038	0.034	0.022	0.023	0.019	0.009	0.005	0.003	0.000	0.003	0.001	0.002	0.002	0.001	0.000	0.001	0.003	0.005	0.010
4	0.043	0.087	0.076	0.053	0.045	0.034	0.026	0.011	0.009	0.006	0.007	0.003	0.003	0.003	0.002	0.000	0.001	0.004	0.010	0.025
5	0.007	0.045	0.047	0.031	0.031	0.017	0.014	0.011	0.007	0.004	0.001	0.003	0.003	0.004	0.001	0.002	0.005	0.002	0.014	0.034
6	0.008	0.042	0.066	0.044	0.031	0.029	0.013	0.014	0.012	0.006	0.003	0.002	0.002	0.001	0.003	0.002	0.007	0.014	0.014	0.040
7	0.002	0.029	0.040	0.040	0.037	0.027	0.020	0.010	0.006	0.006	0.005	0.003	0.003	0.002	0.001	0.006	0.005	0.016	0.029	0.046
8	0.003	0.019	0.040	0.043	0.030	0.028	0.017	0.012	0.011	0.009	0.005	0.003	0.002	0.003	0.004	0.005	0.016	0.021	0.044	0.035
9	0.001	0.011	0.043	0.043	0.029	0.021	0.019	0.013	0.008	0.006	0.004	0.003	0.000	0.006	0.004	0.008	0.014	0.028	0.036	0.057
10-14	0.000	0.029	0.118	0.182	0.157	0.123	0.112	0.080	0.062	0.049	0.025	0.029	0.029	0.035	0.056	0.093	0.142	0.207	0.245	0.274
15-19	0.000	0.003	0.033	0.114	0.160	0.139	0.116	0.104	0.079	0.069	0.058	0.051	0.065	0.076	0.135	0.181	0.226	0.231	0.222	0.193
20-24	0.000	0.001	0.011	0.052	0.121	0.137	0.140	0.128	0.124	0.107	0.102	0.110	0.128	0.165	0.189	0.228	0.193	0.172	0.169	0.131
25-29	0.000	0.000	0.003	0.021	0.071	0.132	0.146	0.139	0.148	0.131	0.169	0.169	0.211	0.234	0.223	0.189	0.175	0.144	0.103	0.076
≥30	0.000	0.000	0.000	0.005	0.039	0.146	0.266	0.399	0.481	0.570	0.591	0.602	0.540	0.462	0.376	0.283	0.212	0.153	0.100	0.065
MEAN	0.80	2.22	4.59	7.90	12.00	16.63	20.84	24.78	27.60	29.61	33.61	39.68	32.19	31.17	28.21	25.33	22.62	20.10	17.76	15.31
VAR	1.9	8.6	25.4	53.3	91.7	131.2	157.7	168.5	160.9	143.7	229.2	387.1	164.4	166.7	124.7	103.6	88.8	78.5	74.2	64.4

TABLE 277

Primary photon, E_0 = 200 MeV. Aluminium absorber
Secondary electrons E = 100 MeV. Results for 10 000 showers

t	Prob. of 1 electron	t	Prob. of 1 electron
0.5	0.1494	5.5	0.0086
1.0	0.1421	6.0	0.0063
1.5	0.0994	6.5	0.0035
2.0	0.0706	7.0	0.0030
2.5	0.0496	7.5	0.0019
3.0	0.0390	8.0	0.0022
3.5	0.0301	8.5	0.0014
4.0	0.0202	9.0	0.0009
4.5	0.0147	9.5	0.0001
5.0	0.0088	10.0	0.0003

TABLE 278

Standard error in an estimate of a probability p based on 1000 showers

p	δp	p	δp
0.001	0.0010	0.600	0.0155
0.003	0.0017	0.800	0.0126
0.006	0.0024	0.900	0.0095
0.010	0.0031	0.940	0.0075
0.030	0.0054	0.970	0.0054
0.060	0.0075	0.990	0.0031
0.100	0.0095	0.994	0.0024
0.200	0.0126	0.997	0.0017
0.400	0.0155	0.999	0.0010

7.A

Nuclear Physics **20** (1960) 129—135; © *North-Holland Publishing Co., Amsterdam*

Not to be reproduced by photoprint or microfilm without written permission from the publisher

A DISCUSSION OF DUAL DIAGRAMS IN PERTURBATION THEORY

P. V. LANDSHOFF

St. John's College, Cambridge †

Received 8 June 1960

Abstract: A discussion is given of the dimensions of the space in which dual diagrams are drawn and of restrictions arising for singularities in scattering processes in which more than one particle is produced.

1. Introduction

Anomalous thresholds in perturbation theory were first discovered for simple vertex graphs by Karplus, Sommerfield and Wichmann [1]). Methods for determining singularities in the contributions from other Feynman graphs have been given by Landau [2]) and by J. C. Taylor [3]), though the arguments of these authors, who use a dual diagram analysis, only apply to real singularities. They have been extended by Polkinghorne and Screaton [4]) to cover also complex singularities, the dual diagrams now being drawn in a complex space which, for convenience, may be taken as Euclidean. We give a further discussion of the construction of dual diagrams.

In section 2 we summarise the general theory on which the analysis rests, and then in section 3 we consider the dimensions of the space in which dual diagrams are to be drawn. The two basic types of dual diagram are briefly discussed in section 4 and finally, in section 5, we mention the limitations on singularities imposed by the dimensionality of space.

2. General Theory

The contribution to the S-matrix corresponding to a given Feynman graph G in perturbation theory is a multiple integral

$$I = \int_{-\infty}^{\infty} \int_{0}^{1} \prod_j \mathrm{d}^4 k_j \prod_i \mathrm{d}\alpha_i \frac{\delta(\sum \alpha_i - 1)}{f^n}, \tag{1}$$

where

$$f = \sum_i \alpha_i (q_i^2 - m_i^2). \tag{2}$$

† Work supported in part by the United States Air Force, Research and Development Command, Europe

Here α_i, q_i, m_i are respectively the Feynman parameter, the momentum 4-vector and the mass associated with the ith internal line of G. A set of independent closed loops is chosen in G, and the integration variable k_j is the momentum running round the jth such loop.

The integral I is a function of the complex variables z which are the scalar invariants for the graph G. By the analysis of Polkinghorne and Screaton [4]) it is found that I has a singularity at a point in z-space if for that point there is a "pinch" in each of the k- and α-integrations. Thus I has a singularity on most of its sheets if it is possible to find a set of internal momenta q_i such that momentum is conserved at each vertex of G and, for each j

$$\frac{\partial f}{\partial k_j} = 0, \tag{3}$$

with, for each i,

$$\frac{\partial f}{\partial \alpha_i} = 0. \tag{4}$$

These conditions are equivalent to

$$\sum_j \alpha_i q_i = 0 \tag{5}$$

and

$$q_i^2 = m_i^2 \tag{6}$$

where, in (5), $\sum_j$ indicates summation round each closed loop of G.

Singularities of this type are known as leading singularities of G. There are additional singularities at which for some i we have $\alpha_i = 0$ instead of (4) and (6). These are leading singularities for the graphs obtained from G by contracting the corresponding internal lines.

We may note that satisfying eq. (3) is essentially equivalent to performing the k-integration [4]), and that the result of so doing is independent of the dimensions of the vectors k_j. However, the possibility of satisfying (3) and (4) simultaneously may depend on the dimensions. This is discussed further in the next section.

3. Dimensionality of Dual Diagrams

The conditions (5) and (6) lead to the dual diagram analysis of Landau [2]) and of J. C. Taylor [3]). This has been further discussed by Okun and Rudik [5]).

Since the integrations over the internal loop momenta k_j in the Feynman integral (1) are four-dimensional, dual diagrams are at first sight to be drawn in four-dimensional complex space. However this may be modified by use of (5). For example, the dual diagram corresponding to the third order single loop

graph is shown in fig. 1. The condition (5) implies that there is a vanishing linear combination of the vectors OA, OB, OC, so that they must be coplanar.

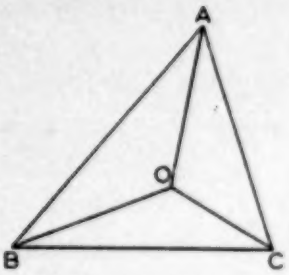

Fig. 1.

But it is not always the case that dual diagrams are drawn in a space of the same dimensions as that spanned by the external vectors. Thus for fig. 3, which corresponds to the Feynman graph of fig. 2, the diagram is overdetermined in the plane when AB, BC, say, are fixed, but may be drawn in three dimensions with one degree of freedom. This degree of freedom is taken up when condition (5) is applied.

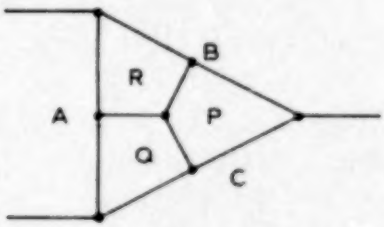

Fig. 2.

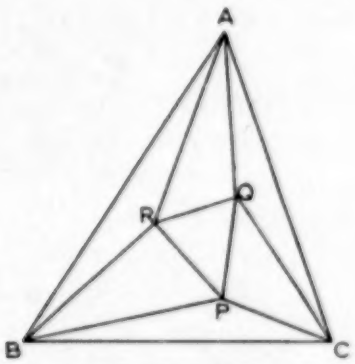

Fig. 3.

It is of interest to examine further the case when the dual diagram is drwan in a space of greater dimensions than that spanned by the external vectors, since the possibility of this being allowed is at first sight somewhat surprising (see ref. [2, 3, 5]).

Condition (5) takes the form of a set of linear vector equations in the loop momenta k and the external momenta p. We write this in matrix form,

$$Ak = Bp, \tag{7}$$

where the matrices A, B are functions of the α_i only.

If the vectors p span a space of less than four dimensions (that is, they are less than five in number), we may take their fourth components, say, as zero. Then the fourth component of the equations (7) gives a solution with the fourth components of the k not all zero if and only if

$$\det A = 0. \tag{8}$$

When this holds either the first three components of eq. (7) cannot be satisfied, or the eq. (7) are not independent. Since, however, they clearly are satisfied in the case we are considering, we conclude that it must be the latter which is true here.

This has the consequence that when all but two of the k-integrations in (1) have been performed, what is left is essentially

$$\frac{1}{[(ak_1+bk_2+c)^2+d]^p},$$

where a, b are functions of the α_i and c, d are functions of α_i, p. The k_1-integration simply yields a power of $1/d$, which, being independent of k_2, gives a divergence when the k_2-integration is performed.

Hence the situation $\det A = 0$ must be avoided by distorting the contours of α-integration. Here, however, this distortion cannot be made because of "pinches", and we have a singularity which would not have occurred if the dimensions of the k-integration had been equal to those of the space spanned by the external momenta.

We observe, however, that his situation does not arise when all the α_i are positive, because $\det A$ has been shown by Symanzik [6] † and by Bjorken [7] to be the *sum* of products of the α_i. Thus conclusions of previous authors [2, 3, 5] concerning those singularities of propagators and vertex functions which are on the physical sheet are unaffected, though there are additional singularities off the physical sheet.

4. Proper and Improper Dual Diagrams

We term a dual diagram proper when the corresponding Feynman graph may be drawn such that its lines are joined wherever they cross. The dual diagram may then be constructed using the standard notation invented by Bow for finding stresses in rigid frameworks. Such a diagram is characterised by the fact that one line in the Feynman graph G corresponds to one line in the dual diagram, and the vectors round any loop of G all converge at one point in the dual diagram.

We may note that our previous result, that diagrams drawn in a space of greater dimensions than that spanned by the external vectors cannot yield all positive α_i, may be seen very easily for proper dual diagrams. This is because in the real subspace one of the points of the diagram is "furthest away" from the real subspace spanned by the external momenta, so that the vectors converging at that point cannot have a vanishing linear combination with all the coefficients α_i positive.

† Note that the parameters α used by Symanzik are essentially the inverse of our Feynman parameters.

A Feynman graph which only has an improper dual diagram † cannot be drawn with all lines joined where they cross. The lines in the dual diagram which correspond to those round a closed loop in the graph G do not necessarily all converge at the same point, and one line in G may have to correspond to several lines in the dual diagram. A simple example is the graph of fig. 4, with its dual diagram in fig. 5.

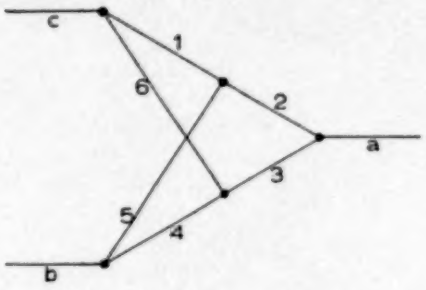

Fig. 4.

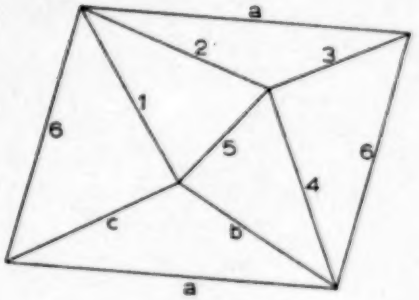

Fig. 5.

It is graphs having only improper dual diagrams which present most of the difficulties encountered in seeking singularities in perturbation theory. For example, for proper graphs corresponding to scattering processes only two of the invariants r, s, t can appear in the denominator of the integral I in (1) after the k-integration has been performed, but for improper graphs all three invariants may appear. This is the difficulty in a proof of the Mandelstam representation such as is proposed by Eden [8]). Also, the argument given by Taylor [3]), that all the singularities for the vertex function are determined by a few of the simplest graphs, does not cover improper graphs. However, the situation is saved here by the fact that improper dual diagrams cannot be drawn in a plane, so that, by the results of the last section, for the vertex function they do not give singularities on the physical sheet.

5. Restrictions Arising from the Dimensionality of Space

The fact that not more than four dimensions are available for the construction of dual diagrams implies that those corresponding to graphs having many external lines in general are overdetermined if all but one of the scalar invariants is fixed in advance. (It has been shown elsewhere [9]) that complex singularities arise on the physical sheet if more than one invariant is allowed to vary.)

For example, the dual diagram corresponding to the fifth order single-loop graph is shown in fig. 6, which is to be drawn in four-space. Here the invariants corresponding to the lengths AD, DB, BE, EC have been fixed, and the con-

† Cf. ref. [5]). It is pointed out there that the dual diagram for an improper graph G is apparently similar to the diagram for the graph obtained from G by making all lines join where they cross. However, the application of eq. 5 gives different results in the two cases.

struction gives the value of AC at the singularity. For the dual diagram of the six-point graph (fig. 8) extra lines must be added to fig. 7. Since for n external lines there are $(3n-10)$ independent invariants (excluding the external masses),

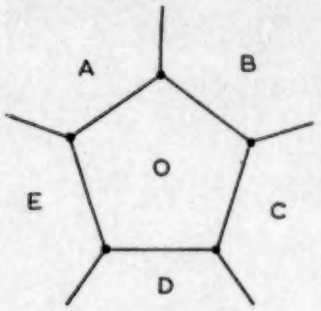

Fig. 6.

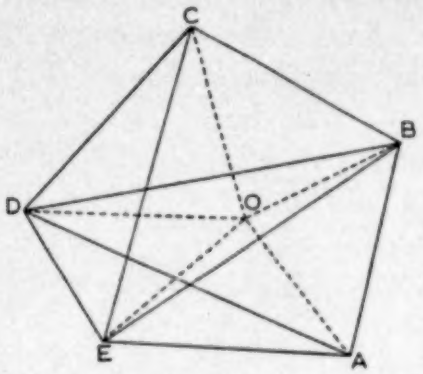

Fig. 7.

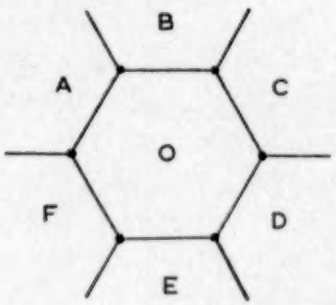

Fig. 8.

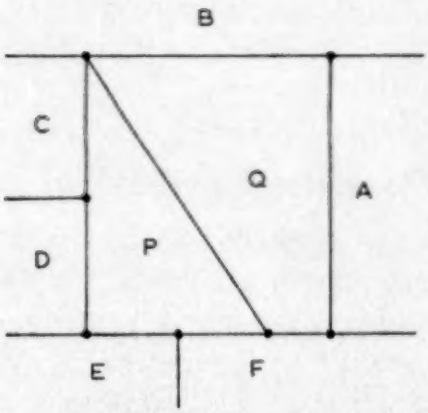

Fig. 9.

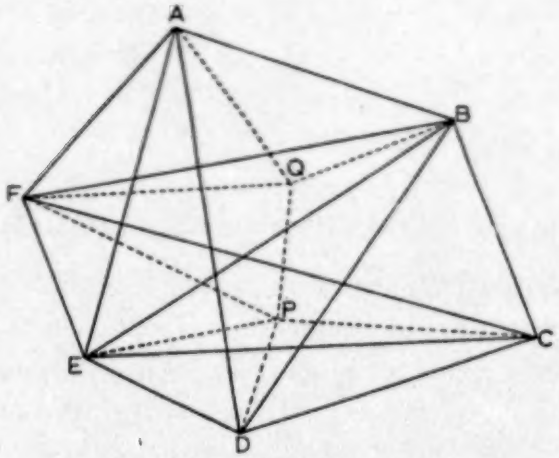

Fig. 10.

the values of seven of the invariants must now be chosen. These may conveniently be AD, DB, BE, EC as before, with also EA, FB, FC. The addition of the lines FE, FA, FB, FC to fig. 7 is sufficient to determine the position of the point F, so that, except for fortuitous choices of the fixed invariants, there cannot also be inserted the line FO.

This argument may be extended to the addition of external lines to any graph whose dual diagram is already fully determined in four-space. It does not imply, however, that all dual diagrams for graphs having more than five external lines are over-determined, as it is not valid when the original dual diagram is only determined by application of condition (5). An example of this is the diagram of fig. 10, corresponding to the Feynman graph of fig. 9.

I am grateful to Dr. J. C. Polkinghorne for help and encouragement, and to Mr. M. Fowler and Mr. R. W. Lardner for stimulating discussions. This work was done while I was receiving grants from the D.S.I.R. and the Amy Mary Preston Read Bequest.

References

1) R. Karplus, C. M. Sommerfield and E. H. Wichmann, Phys. Rev. **111** (1958) 1187
2) L. D. Landau, Nuclear Physics **13** (1959) 181 or JETP **37** (10), 45 (1960)
3) J. C. Taylor, Phys. Rev. **117** (1960) 261
4) J. C. Polkinghorne and G. R. Screaton, Nuovo Cim. **15** (1960) 289, 925
5) L. B. Okun and A. P. Rudik, Nuclear Physics **15** (1960) 261
6) K. Symanzik, Prog. Theor. Phys. **20** (1958) 690
7) J. D. Bjorken, preprint (Stanford)
8) R. J. Eden, preprint (Berkeley)
9) M. Fowler, P. V. Landshoff and R. W. Lardner, preprint (Cambridge)

2.I:
2.J

Nuclear Physics **20** (1960) 136—154; © *North-Holland Publishing Co., Amsterdam*
Not to be reproduced by photoprint or microfilm without written permission from the publisher

ANGULAR DISTRIBUTIONS IN PHOTOFISSION OF URANIUM

BENGT FORKMAN and SVEN A. E. JOHANSSON
Department of Physics, University of Lund, Lund, Sweden

Received 23 June 1960

Abstract: The angular distributions in photofission of natural uranium have been measured. Bremsstrahlung with maximum energies of 10 and 20 MeV and monoenergetic gamma radiation of 6.1, 6.9 and 7.1 MeV energy were used as photon sources. The fission fragments were detected in two ways. One method was to irradiate nuclear emulsions containing uranium. In the other method a scintillation counter was used to detect the fission fragments. The first method is more tedious but has a considerably better angular resolution. The two methods give results which agree very well.

The following results have been obtained: The angular distribution at 6.1 MeV is of the form $0.07+\sin^2\theta+0.37\ \sin^2 2\theta$. At 6.9 MeV the distribution $1+0.70\ \sin^2\theta+0.05\ \sin^2 2\theta$ was obtained. The distribution at 7.1 MeV is similar but somewhat more isotropic. The angular distribution obtained by 10 MeV bremsstrahlung is of the form $1+0.85\ \sin^2\theta+0.13\ \sin^2 2\theta$. Irradiation with 20 MeV bremsstrahlung gives an isotropic angular distribution.

The results of the present work are compared with the theory of A. Bohr. They agree very well with this theory. It is also possible to use these results to separate the photonuclear absorption at 6 MeV into a dipole and a quadrupole part. The quadrupole absorption in particular is discussed and compared with theoretical estimates.

1. Introduction

It has been known for some time that there is an anisotropy in the angular distribution of the fragments in photofission. It was found by Winhold and Halpern [1]) that when foils of uranium and thorium were bombarded by bremsstrahlung from a linear accelerator the fission fragments were preferentially emitted at 90°. The anisotropy increased with decreasing bremsstrahlung energy. Within the rather large statistical errors the angular distributions had the form $1+\alpha\ \sin^2\theta$. This is the distribution expected for dipole absorption of the photons. Baz *et al.* [2]) irradiated nuclear emulsions soaked with a uranium salt in the beam of an electron synchrotron at various energies. They obtained similar results. At a bombarding energy of 9.4 MeV, however, the angular distribution also contained a term of the form $\sin^2\theta\ \cos^2\theta$, which corresponds to quadrupole absorption. The emulsion technique was also used by Faissner and Gönnenwein [3]), who investigated thorium at a bremsstrahlung energy of 16 MeV.

Baerg *et al.* [4]) measured angular distributions of several actinide and transuranium isotopes. The radiation source was a betatron, and an ionization chamber was used as detector. The odd-mass nuclei gave an isotropic distribution at

all energies. The even nuclei gave anisotropic distributions, with the greatest anisotropy at low energy. The distributions could be described by an equation of the form $1+\alpha \sin^2\theta$ indicating dipole absorption.

The anisotropy in photofission is difficult to understand on the basis of the liquid drop model. Recently A. Bohr [5]) has suggested a theory that can account for the anisotropy. The basic assumption is that the fissioning nucleus is cold when passing over the top of the potential barrier, since the greater part of the excitation energy is used up in the deformation of the nucleus. Hence less energy is left to excite the nucleus. This implies that the level spectrum at the saddle point should be rather simple for excitation energies slightly greater

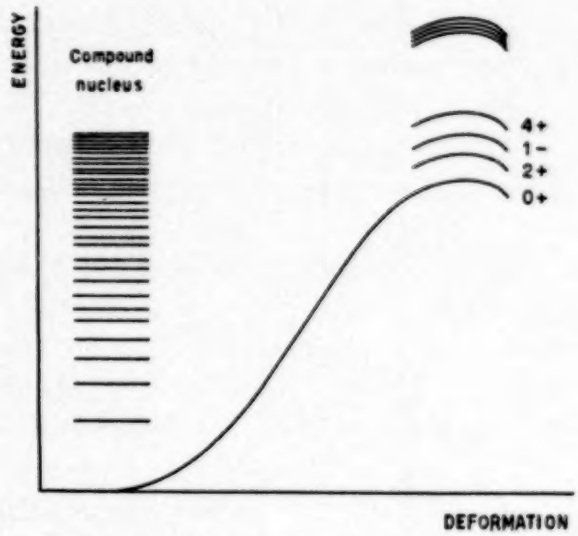

Fig. 1. Schematic picture of the levels in a nucleus during the fission process. The figure is not intended to show the exact position of the levels at the saddle point.

than the barrier height. It is further assumed that at the saddle point the level spectrum is similar to that of a deformed nucleus at the equilibrium deformation. The situation is especially simple for even nuclei. It is illustrated in fig. 1. The lowest levels belong to a rotational band with $K = 0$ and even parity based on the ground state. The spin values are 0, 2, 4, ... Slightly higher in energy comes another type of collective excitation, a rotational band with $K = 0$ and odd parity. The spin values are 1, 3, 5, ...When the energy is increased to about 1 MeV above the 0+ level, nucleonic excitation will be possible and the level density will soon become quite high.

Hence there are not one but many barrier curves, each of which defines a fission channel. If the nucleus is excited to a certain energy in the compound state (to the left in fig. 1), it can fission if there is available at the saddle point a channel with the proper spin and parity. It is then easy to understand the anisotropy in photofission. Photonuclear reactions are known to occur mainly by electric dipole absorption. This means that in an even nucleus 1− levels

will be excited. In fig. 1 it can be seen that there is a 1− channel available among the lowest channels. The fragments are further assumed to be emitted in the direction of the symmetry axis. For a state $I = 1$, $K = 0$ the angular distribution will be of the form $\sin^2\theta$. At higher energies there will be many more 1− channels, corresponding to various excited configurations. These channels will have K equal to both 0 and 1, however. The average angular distribution of these states will then be isotropic. The anisotropy is hence limited to an energy range of about 1 MeV above the threshold. The angular distribution will be of the form $1+\alpha \sin^2\theta$. The constant α is expected to decrease with increasing bombarding energy. This is in agreement with the experimental results.

A similar situation exists for the electric quadrupole absorption. In an even nucleus electric quadrupole absorption leads to a 2+ state. Among the lowest channels there is one with $I = 2$, even parity and $K = 0$. The corresponding angular distribution will be of the form $\sin^2 2\theta$. The higher 2+ channels will have the K values 2, 1 and 0. The average angular distribution for these channels will be isotropic.

In order to test the theory it is desirable to investigate the photofission close to threshold where the number of channels is small and their properties are well known. It is difficult to do this with a continuous bremsstrahlung spectrum, however. Monoenergetic gamma rays of suitable energy and sufficiently high intensity would be better. Fortunately the reaction $F^{19}(p, \alpha\gamma)O^{16}$ provides a gamma-ray source with the required properties. This reaction produces gamma rays with the energy values 6.1, 6.9 and 7.1 MeV. Since the height of the barrier in U^{238} is 5.8 MeV, these gamma rays are ideal for an investigation of the photofission of uranium. The intensity ratio of the three gamma rays can be varied by proper selection of proton energy and target thickness.

In the study of the angular distribution of fission fragments, several different techniques are possible. One technique is to catch the fragments on foils mounted around the target. This requires a rather high gamma-ray intensity, however. Another possibility is to detect the fragments by means of a suitable counter, such as a proportional counter or a scintillation counter. This method is more sensitive than the previous one. However the counting rate is small with the available gamma-ray sources. The angular resolution will necessarily be rather poor. A third method is to bombard nuclear emulsions containing uranium. The fission fragments give heavy, easily detectable tracks in the emulsion. The orientation of the tracks can be measured quite accurately. This method has, therefore, a very good angular resolution. A disadvantage is that both the scanning of the emulsions and the measurements on the tracks are very tedious.

In the present work, our principal interest has been in the photofission near the threshold, but we have also investigated the angular distributions at higher

energies. The photon sources were a 30 MeV electron synchrotron and a 4 MeV electrostatic generator. The synchrotron was run at two different energies, 10 and 20 MeV. The proton energy of the electrostatic generator was varied in order to change the ratio between the three gamma rays at 6.1, 6.9 and 7.1 MeV.

Both the emulsion technique and the counter technique were used. The emulsion experiments give the most detailed results. The counter experiments give additional data and also serve as a check on the correctness of the results obtained by the emulsions.

2. Emulsions

Emulsions of the type Ilford K_1_ with a thickness of 50 μm were used. It would be desirable to use thicker emulsions. It was found, however, that the thicker emulsions had a tendency to crack after soaking and drying. Uranium was introduced into the emulsions by soaking them for 12 h in a solution with 5.2 g sodium citrate in 50 ml water, 15 g uranyl nitrate, and 1.2 g sodium hydroxide in 30 ml water.

The plates were washed in water for several minutes and were allowed to dry for one hour. They were then wrapped in thin aluminium foil. After the exposure the plates were washed in water for one hour and were then developed in the usual way.

The mounting of the plates is a very important problem in an experiment of the present type. One possibility is to mount them perpendicular to the direction of the incident gamma radiation. The orientation of the fission tracks relative to the direction of the incident radiation is determined by measuring the dip and the projected length of the tracks. In calculating the angular distribution from the measured values, one must know the shrinkage factor fairly accurately. This presents some problems which will be discussed later. Another disadvantage of this mounting is that tracks with a large dip must also be included in the measurements. The scanning of the plates must be done meticulously to avoid losses of steep tracks. Even then one cannot get reliable results for angles of less than 10° to 15°.

Another way of mounting the plates is to let the gamma radiation impinge parallel to the plane of the plate. One then measures only tracks having a dip less than a certain limit. If this limit is sufficiently small, the direction of the tracks is practically the same as the direction of the projection of the tracks on the plane of the plate. Hence it is not necessary to know the shrinkage factor accurately, provided that it is the same all over the plate. The scanning of the plates is easy, since all the accepted tracks are almost horizontal. The great disadvantage of this method of measuring is that only a small part of the total number of tracks can be accepted. If the intensity of the gamma radiation is low, the number of tracks might not be enough to give a reasonable statistical

accuracy. If one increases the dip limit in order to accept more tracks, the advantages of this method will soon be lost and the two ways of mounting the plates will be almost equivalent.

In the present work we have used mainly the perpendicular mounting. It is of course, possible to use this type of mounting in the cases where the gamma-ray intensity is low and the parallel mounting in the other cases. Since this might introduce systematic differences between the different exposures, we chose to use the same mounting in all cases. Later, however, we checked the angular distribution at 6.1 MeV by an experiment using the parallel mounting. As will be shown later, the results agree well. Since the systematic errors should not be the same in the two experiments, this indicates that systematic errors are not too important in the present work.

The scanning of the plates was performed with Leitz microscopes. Scanning presents no particular problems for the plates irradiated with monoenergetic gamma rays. The background is low and the tracks including those with a large dip are easily detectable. The situation is less favourable when plates are irradiated with bremsstrahlung from the synchrotron. The background is higher, making it more difficult to find the steep tracks. The plates were therefore scanned a second time particularly for these tracks. We feel that the scanning losses are small and without significance. A good check is provided by the angular distribution from the irradiation with 20 MeV bremsstrahlung (shown in fig. 11). This distribution is known to be practically isotropic. There is no sign of loss of tracks for small angles. No results will be presented for the angular interval of 0° to 10°. The number of tracks is very low in this interval and the statistical errors are consequently large. Furthermore, the scanning losses can probably not be neglected in this interval.

It is important to determine accurately the shrinkage factor of the emulsions. We have used two different methods. The first one is straightforward. A nuclear plate was soaked in the uranium salt solution in the usual way and was then dried. It was glued to a well-polished, plane parallel glass plate. The total thickness of glass plate and nuclear emulsion was measured by means of a micrometer. The anvil of the micrometer was a spherical surface with a fairly small curvature, designed to avoid deforming the emulsion during the measurements. There was no sign of such an effect. Next the emulsion was developed and the thickness was again determined. Finally, the emulsion was removed and the thickness of the glass determined. These three measurements give the shrinkage factor directly. Two completely independent series of measurements were performed. The uranium solution and the developer were not the same. The results were 1.54 ± 0.08 and 1.56 ± 0.06. The good agreement indicates that the shrinkage factor is the same in different runs.

The shrinkage factor was also determined by a second method, based on the fact that the fission tracks in the emulsion have an almost constant length.

The length distribution is a narrow peak at about 24 μm with a full width of half maximum of 2.8 μm. The squares of the horizontal and vertical projections of each track are plotted in a diagram. Mean values are taken in a number of intervals. The resulting diagram is shown in fig. 2. The points fall nicely on a straight line as expected. The slope of the line is equal to K^2, where K is the shrinkage factor. The result is 1.62 ± 0.02. It is in satisfactory agreement with the result of the first method. We have used a weighted mean: 1.60 ± 0.05. The

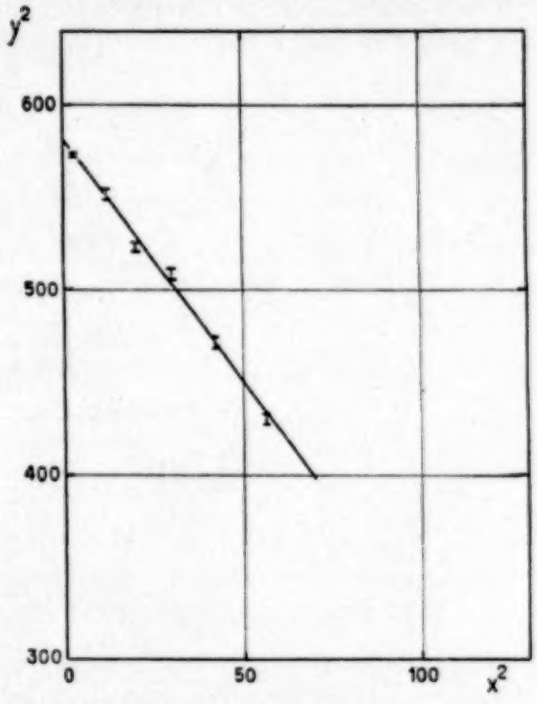

Fig. 2. Diagram for determination of the shrinkage factor of the emulsions. The square of the horizontal projection of the tracks is plotted against the square of the vertical projection.

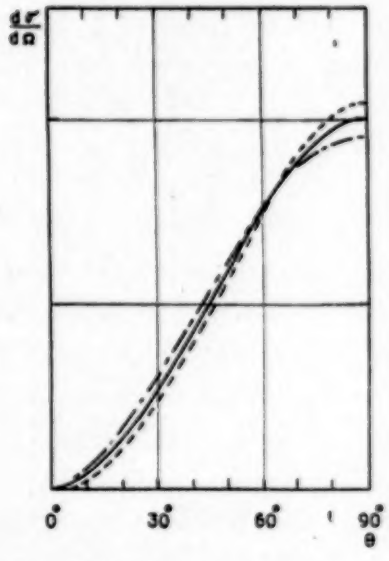

Fig. 3. The influence of an error in the shrinkage factor on the angular distribution. The dashed lines show the deviations from a $\sin^3\theta$ distribution (full line) caused by a 5 % error in the shrinkage factor.

errors are estimated from the various uncertainties of the measurements. Of course, one cannot exclude the possibility of systematic errors. It would be rather strange, however, if they influenced the measurements in the same way in the two methods used. A further check on the shrinkage factor is provided by the angular distribution obtained in the irradiation with 20 MeV bremsstrahlung. The angular distribution should be isotropic and within the statistical errors, the experimental points agree with such a form. If there were a substantial error in the determination of the shrinkage factor, it would cause a deviation of the points from the isotropic distribution. Therefore we estimate that the error in the shrinkage factor is less than 5 %.

It is instructive to examine the consequences of an error in the shrinkage factor. In fig. 3 we show the effect of a 5 % error on a distribution of the form

$\sin^2\theta$. Obviously the effect is very small. Even a 10 % error would not change the angular distributions radically.

The measured orientation of the tracks gives the angular distribution after obvious corrections for the geometrical factors of the experimental arrangements. There are some small errors and uncertainties which influence the angular distribution and which therefore must be corrected for. They are

1) Errors of measurement: The various quantities (length, dip, and angle of the tracks) which are measured in the present experiment have certain errors. These errors were determined by repeated measurements on a number of selected tracks.

2) Scattering of the fission tracks: The orientation of a fission track has been determined by measuring the position of the end points. What we want to determine is the orientation of the central part of the track, which contains the point of origin of the fragments. Hence, because of the scattering, a certain error is introduced, We therefore made a study of the scattering of a number of tracks selected at random.

3) Extension of the gamma-ray source: In the ideal case a point source is assumed. In the present case we have a source of finite size. Its dimensions are determined by the cross-section of the proton beam.

All the mentioned factors will tend to smear out the angular distributions and increase the isotropic part. We have calculated a correction for all of these factors and have applied it to the data. The calculation is straightforward but somewhat tedious and will not be described here. The correction will be of greatest importance for the points close to 0° and for steep distributions, i.e., distributions with a small isotropic part. For such points it amounts to 20 to 30 %. In general it is much less.

3. Scintillation Counter

The scintillation counter arrangement is shown schematically in fig. 4. The counter consists of a photomultiplier, type DuMont 6292, and a screen of zinc sulfide powder mounted directly on the face of the multiplier. The thickness of the screen is 7 mg/cm^2 and the mean grain size is 5 μm.

The pulse height spectrum of the counter is shown in fig. 5. To the left in the figure is the steeply rising distribution of the α-particles. To the right are the fission pulses. A background spectrum is also shown. The position of the counter in the background run was such that the zinc sulfide screen was irradiated with the same gamma-ray flux as in the actual measurements. The position of the uranium target relative to the gamma-ray source was such, however, that very few fission pulses were obtained. As can be seen, the counter is practically insensitive to gamma irradiation. The α-particle distribution is well limited on the high energy side. It is apparently quite easy to get a good separation of the fission pulses.

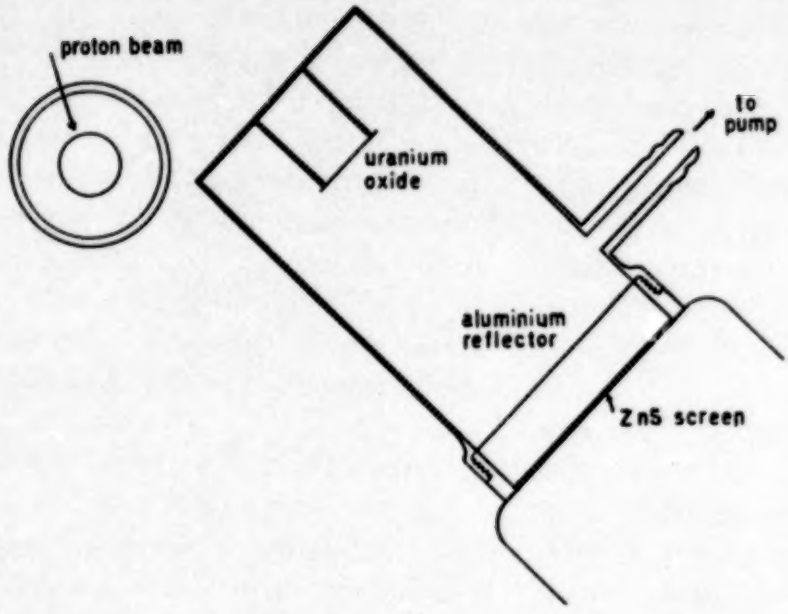

Fig. 4. A schematic diagram of the scintillation counter arrangement.

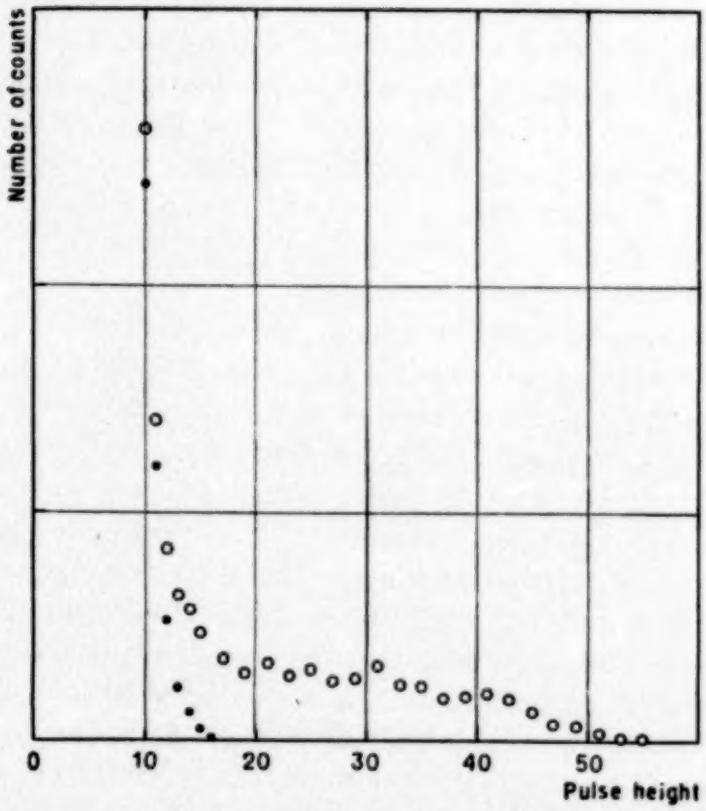

Fig 5. Pulse-height distribution of the scintillation counter. Open circles: total spectrum. Dots: alpha-particle background.

The experimental arrangement is shown in fig. 4. The uranium target, consisting of a thin layer of uranium oxide, is mounted inside a light-tight container covering the top of the photomultiplier. The container is evacuated. The multiplier is movable around an axis through the uranium target, perpendicular to the plane of the figure. Hence the counter can be set in different positions relative to the direction of the gamma rays irradiating the uranium target. Readings were taken at three angles only 0°, 45° and 90°. The reason for this is that the measurements are very time consuming. It was not feasible to extend them to other angles.

The cross-sections for photofission of uranium at 6 and 7 MeV are unfortunately very small (about 10 mb). The gamma-ray intensity is limited by target deterioration. The distances between the calcium fluoride target and the uranium oxide layer and between the scintillation screen and the oxide layer cannot be too small if one wants a reasonable angular resolution. With the geometry shown in fig. 4, the counting rate of fission pulses varied from about 100 per hour with the 7 MeV gamma rays to about 10 per hour with the 6 MeV gamma rays. This clearly requires long counting periods. It is necessary to have the counter as stable as possible and to check it frequently. The pulses were displayed on a 100-channel analyzer. The stability of the counter could easily be checked by monitoring the pulse-height spectrum. The spectrum was plotted separately for each run in order to make sure that it had the normal shape.

The measurements were performed in the following way. Each run had a duration of one to two hours. Then the counter was moved to another position and a new run was started. This was repeated until there were many runs for each angle. In this way the influence of any drift in the apparatus should be eliminated. The results of different runs at the same angle agreed within the statistical errors. There is apparently no serious drift. There was no sign of spurious pulses or of other disturbances.

The most serious source of error is probably that the intensity distribution in the proton beam is not absolutely constant. It is slightly affected by the small adjustments of the extraction voltage and the focusing voltage which are necessary during the operation of the electrostatic generator. This causes the effective distance between the gamma-ray source and the uranium foil to change. The fluctuations in counting rate caused by this effect are estimated to be less than 10 %. There are many runs for each angle, however, and they are spread out over the whole counting time. This error is therefore largely eliminated.

The angular resolution of the counter is determined mainly by the geometry of the experimental arrangement. It is also affected by the scattering of the fragments in the uranium target. As mentioned above we have studied the scattering of the fragments in nuclear emulsions. The results of this study allow us to calculate the scattering in uranium. The correction of the angular resolution for the scattering can then be performed.

4. Radiation Sources

The gamma radiation for the present work was obtained in two ways. Some experiments were peformed using a 35 MeV electron synchrotron as a source of high energy bremsstrahlung. In most experiments the reaction $F^{19}(p, \alpha\gamma)O^{16}$ was used as a gamma-ray source. Protons from a 4 MeV van de Graaff generator bombarded a calcium fluoride target. By varying the proton energy and the target thickness, one can change the composition of the gamma radiation.

The gamma radiation from the fluorine reaction consists of three components with the energy values 6.1, 6.9 and 7.1 MeV. In order to analyze the measured

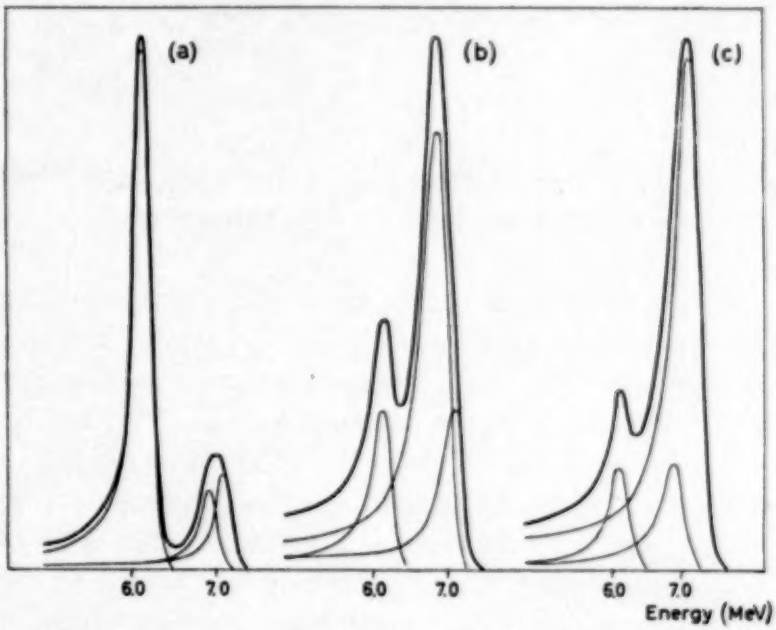

Fig. 6. Gamma ray spectra from the reaction $F^{19}(p, \alpha\gamma)O^{16}$ resolved in three components with the energy values 6.1, 6.9 and 7.1 MeV. (a) thick target and 1.45 MeV protons, (b) 300 keV target and 2.5 MeV protons, (c) 300 keV target and 2.2 MeV protons.

angular distributions it is necessary to know the composition of the gamma radiation fairly well. This has therefore been investigated by means of a three crystal scintillation spectrometer [6]). The gamma-ray spectra are shown in fig. 6. They have been resolved into the three components. The spectrum shown in fig. 6(a) is obtained by bombarding a thick target with protons of 1.45 MeV energy. The intensity ratios between the 6.1, 6.9 and 7.1 MeV components are 1 : 0.15 : 0.17. Fig. 6(b) shows the spectrum of the gamma radiation emitted in the bombardment of a 300 keV thick target with protons of 2.5 MeV energy. The intensity ratios in this case are 0.31 : 1 : 0.37. Fig. 6(c) shows the spectrum of the gamma radiation emitted with a proton energy of 2.2 MeV and with the same target thickness, 300 keV. The intensity ratios are 0.17 : 0.21 : 1. It can be seen that by changing the proton energy one can obtain a gamma-ray source emitting predominantly 6.1, 6.9 or 7.1 MeV gamma rays. These energy values

are well suited to an investigation of the photofission of uranium, since they cover the interesting region just above the threshold. No other monoenergetic gamma-ray sources of sufficient intensity are available.

A proton current of 30 μA was used. The limitation on the current was set, not by the current available from the machine, but by the deterioration of the targets. Higher currents caused a slight evaporation of the calcium fluoride. This changes the intensity and the composition of the gamma radiation and would have been very disturbing in the measurements.

The gamma-ray intensity was monitored by a scintillation spectrometer with a sodium iodide crystal of 10×12.5 cm. Pulses above a height corresponding to 3 MeV were counted.

5. Results

In order to analyze the experimental results, it is necessary to know the shape of the cross-section curve, especially in the region 6 to 7 MeV. There are several measurements but they do not agree too well. Winhold and Halpern [1]) and Schmitt and Duffield [7]) found a rather pronounced peak at 6 MeV but Katz *et al.* [8]) found only a plateau between 6 and 7 MeV. Measurements by Clarke [9]), by means of the fluorine radiation, showed the cross-section at 6 MeV to be higher than at 7 MeV, but more recent measurements [13]) gave approximately the same cross-section for these two energies. We have assumed that the more recent measurements are correct and that the cross-sections are equal at 6 and 7 MeV. The cross-section enter in only in a fairly small correction of the experimental curves and exact values are therefore not needed.

We will first present the results obtained with the emulsion technique.

Fig. 7 shows the angular distribution obtained by irradiation with 6 MeV gamma rays. The distribution has been corrected for the presence of the 7 MeV gamma rays in the radiation source. The emulsions were mounted perpendicular to the impinging radiation. The experimental points have been fitted with a curve of the form $(1.00\pm 0.05)\sin^2\theta+(0.35\pm 0.05)\sin^2 2\theta$. In order to fit curves to the experimental points we have used the method of maximum likelihood. In the figure the curve has been resolved into its two components.

In order to test the result of this experiment we repeated it in another geometry, using emulsions mounted parallel to the impinging radiation. The result is shown in fig. 8. The distribution now has the form $(0.07\pm 0.08)+(1.00\pm 0.10)\sin^2\theta+(0.50\pm 0.12)\sin^2 2\theta$. The two experiments are in satisfactory agreement, which indicates that there are no serious systematic errors in the experimental technique. Furthermore, it is evident that there is a considerable quadrupole component in the angular distribution.

The hypothesis that an angular distribution with isotropic, dipole and quadrupole components is statistically consistent with the experimental

data has been tested with the χ^2-method giving $\chi^2_{14} = 8.3$ corresponding to a probability of 0.9. The hypothesis that an angular distribution with only isotropic and dipole components is consistent with the data gives $\chi^2_{15} = 30$ corresponding to a probability of 0.01. This test confirms the conclusion that the angular distribution has a considerable quadrupole component.

In all of the following experiments with the emulsion technique the emulsions were mounted perpendicular to the incident radiation.

Fig. 9 shows the angular distribution obtained with protons of 2.5 MeV

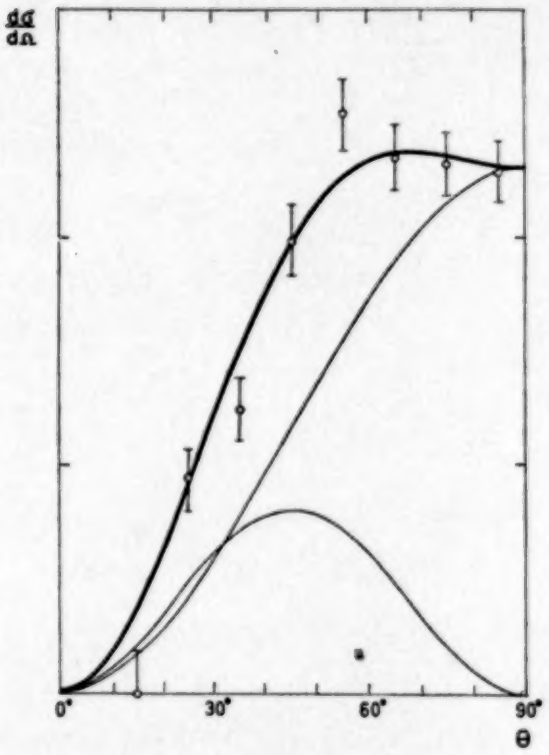

Fig. 7. Angular distribution obtained by the 6.1 MeV gamma rays with the emulsion mounted perpendicular to the incident radiation. The distribution is corrected for the 7 MeV component of the radiation. The fitted curve (heavy line) has the equation $\sin^2\theta + 0.35 \sin^2 2\theta$. The fine lines show the curve resolved in its two components.

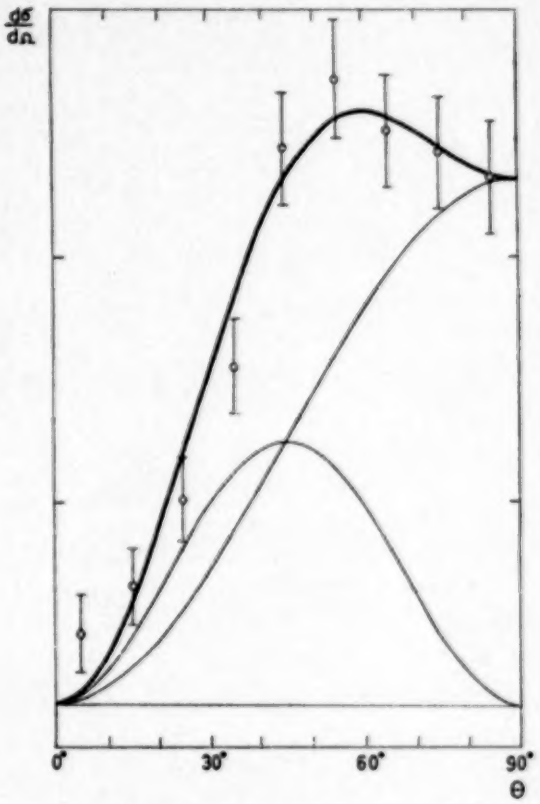

Fig. 8. Angular distribution obtained by the 6.1 MeV gamma rays with the emulsion mounted parallel to the incident radiation. The distribution is corrected for the 7 MeV component of the radiation. The fitted curve (heavy line) has the equation $0.07 + \sin^2\theta + 0.50 \sin^2 2\theta$. The fine lines show the three components of the curve.

energy. The gamma radiation consists mainly of the 6.9 MeV component. The distribution is corrected for the presence of the 6.1 MeV gamma ray. The influence of the 7.1 MeV gamma ray is small since, as will be shown later, it gives an angular distribution similar to that obtained for the 6.9 MeV gamma ray. The fitted curve in fig. 9 has the equation $(1 \pm 0.22) + (0.70 \pm 0.22) \sin^2\theta + (0.05 \pm 0.20) \sin^2 2\theta$. The anisotropy is smaller than at 6 MeV, as expected.

When the emulsions were bombarded with 10 MeV bremsstrahlung, the

angular distribution of fig. 10 was obtained. The fitted curve has the equation $1+(0.85\pm0.28)\sin^2\theta+(0.13\pm0.14)\sin^2 2\theta$.

Fig. 11 shows the result of the irradiation with 20 MeV bremsstrahlung. The angular distribution is known experimentally and theoretically to be very nearly isotropic. The experimental points agree within the statistical errors with an isotropic distribution. This is an important result, since it indicates strongly that there are no serious systematic errors in the method used in the present work.

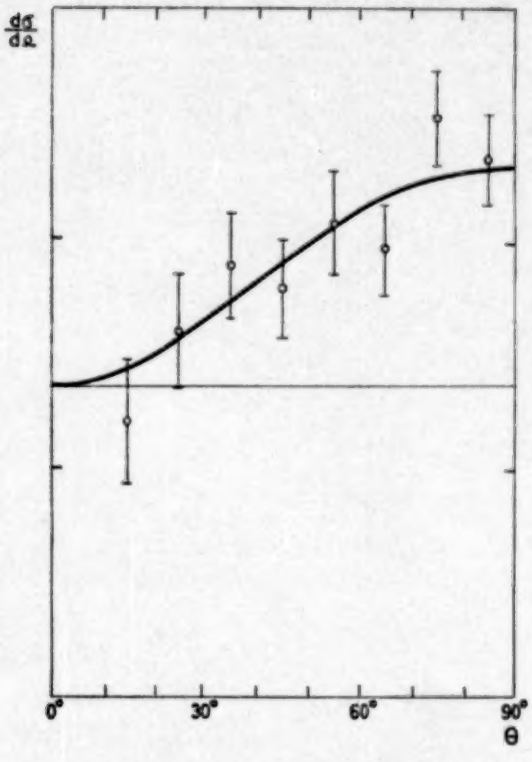

Fig. 9. Angular distribution obtained by the 6.9 MeV gamma rays. The distribution is corrected for the 6.1 MeV component of the radiation. The fitted curve (heavy line) has the equation $1+0.70\sin^2\theta+0.05\sin^2 2\theta$. The fine line shows the isotropic component of the curve.

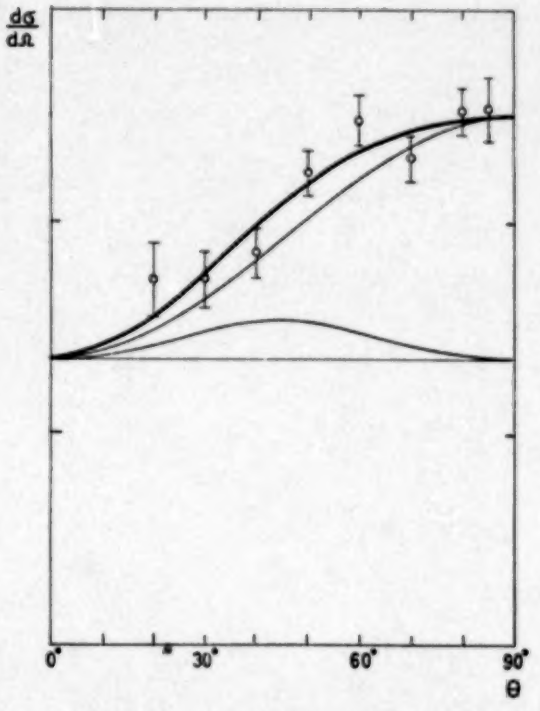

Fig. 10. Angular distribution obtained by 10 MeV bremsstrahlung. The fitted curve (heavy line) has the equation $1+0.85\sin^2\theta+0.13\sin^2 2\theta$. The fine lines show the components of the curve.

The experiments with the scintillation counter gave the following results:

In one experiment the scintillation counter was used to record the angular distribution in the irradiation with 6 MeV gamma rays. This experiment is similar to that described in fig. 7. The main difficulty is the correction for the limited angular resolution. It introduces a considerable uncertainty so that the experimental points do not give the details of the angular distribution very accurately. Therefore in the angular resolution correction we assumed the angular distribution to be that given by the curve in fig. 7. The corrected

experimental points are shown in fig. 12(a). The curve in the figure is from fig. 7. The agreement between the points and the curve is reasonably good. This experiment does not give any independent determination of the angular distribution but is consistent with the emulsion experiment.

Figs. 12(b) and 12(c) show distributions obtained with gamma rays of 6.9 and 7.1 MeV, respectively. They have been corrected for the presence of the 6.1 MeV component in the radiation. The errors are fairly large but there is an indication that the anisotropy is smaller at 7.1 MeV. The distribution in fig. 12(b) agrees

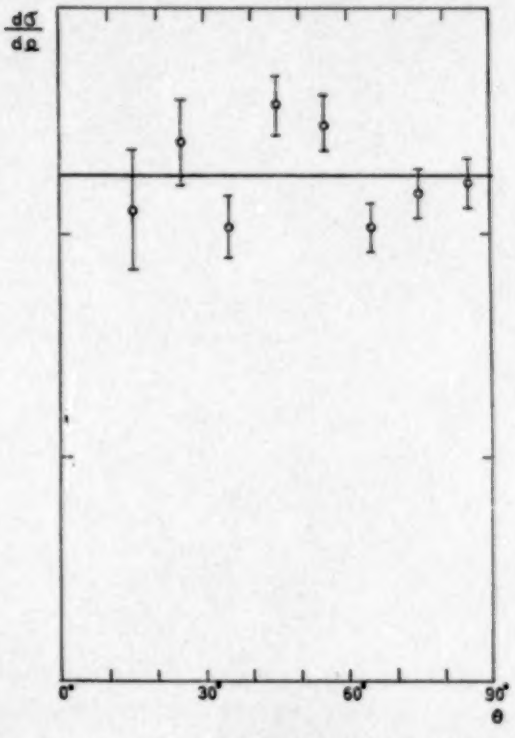

Fig. 11. Angular distribution obtained by 20 MeV bremsstrahlung.

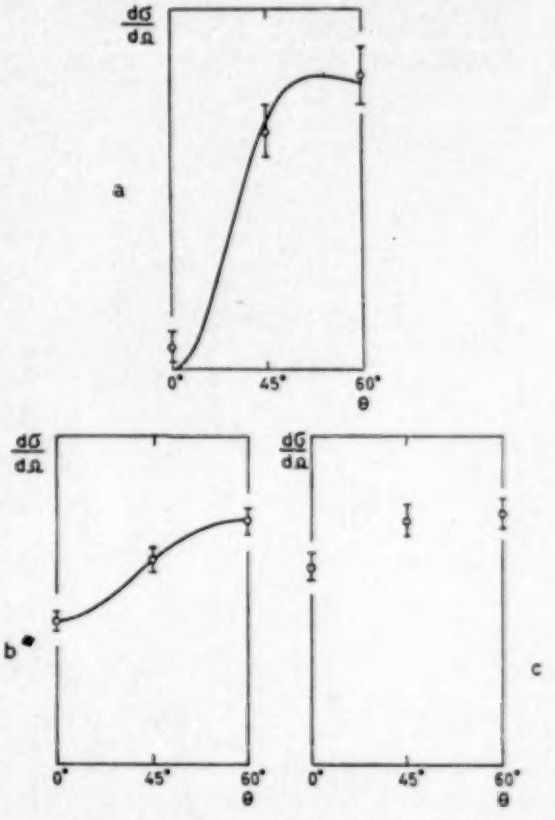

Fig. 12. Angular distributions obtained by the scintillation counter in irradiations with (a) the 6.1 MeV gamma rays (the curve is the angular distribution of the corresponding emulsion experiment of fig. 7), (b) the 6.9 MeV gamma rays (the curve is the angular distribution of the corresponding emulsion experiment of fig. 9), (c) the 7.1 MeV gamma rays.

well with the corresponding distribution obtained by emulsions, which is shown in fig. 9. The curve in fig. 12(b) is the fitted curve from fig. 9.

The interpretation of angular distributions obtained by irradiation with bremsstrahlung is difficult, because of the continuous nature of the bremsstrahlung spectrum. We have made an attempt to analyze the distribution in fig. 10 in more detail. It is obtained by 10 MeV bremsstrahlung. The photo-

fission cross-section curve is fairly well known [1,7,8]). It has been weighted by the bremsstrahlung spectrum. We then assume that in the energy interval below 6.5 MeV the angular distribution can be represented by the distribution obtained at 6.1 MeV. In the range 6.5 to 7.5 MeV the distribution is assumed to be represented by the distribution at 6.9 MeV. In the 10 MeV distribution, the contribution from photons below 7.5 MeV can then be subtracted. The remaining distribution, which represents the range 7.5 to 10 MeV, is shown in fig. 13. The points are scattered but the distribution appears fairly isotropic. Hence the angular anisotropy in photofission is concentrated in a region 1 to 2 MeV above the threshold. The present analysis of the 10 MeV distribution is rather crude,

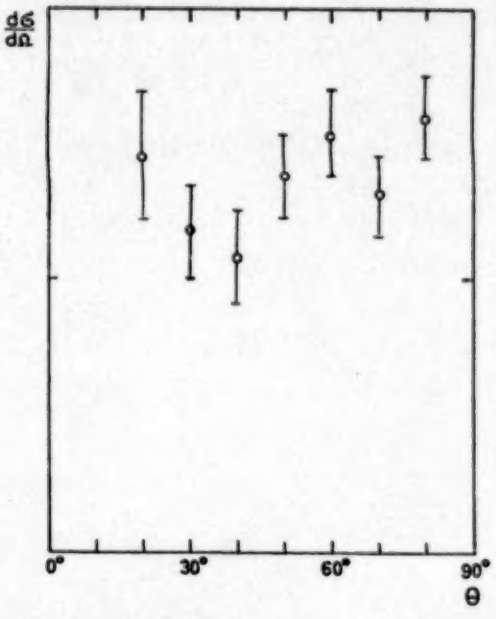

Fig. 13. Angular distribution corresponding to photons in the energy range 7.5 to 10 MeV. This distribution has been obtained from the distribution in fig. 10 by subtracting the contribution of the photons in the range 6 to 7.5 MeV.

since the subdivision in energy intervals is somewhat arbitrary. This will probably not change the results qualitatively.

The results of the present investigation can be summarized in the following way: At 6.1 MeV the angular distribution is strongly anisotropic. The isotropic term amounts to less than 10 %. There is a considerable quadrupole term, which corresponds to a quadrupole cross-section of 21 % of the total photofission cross-section.

At 7 MeV the anisotropy is less; the isotropic part is 67 % of the total cross-section. There is a small but significant tendency for the anisotropy to decrease when the energy is increased from 6.9 to 7.1 MeV. Because of the statistical errors not very much can be said regarding the quadrupole part in the angular distributions at 7 MeV. It seems to be definitely smaller than that at 6 MeV.

At energies above 7 MeV, the anisotropy rapidly decreases. To account for the shape of the angular distribution obtained in the experiment with 10 MeV bremsstrahlung, one must assume that it is already quite small at 7.5 MeV.

It is of interest to compare the present work with previous investigations. Since no work has been reported using monoenergetic gamma radiation, one has to compare this work with the investigations which have been performed by bremsstrahlung irradiation. If the maximum energy of the bremsstrahlung is set at about 6.5 MeV, the main contribution to photofission comes from photons in a narrow region around 6 MeV. The distribution obtained by Baz *et al.* [2]) at a maximum energy of 6.5 MeV and by Baerg *et al.* [4]) at 6.3 MeV should be comparable with our distribution obtained by 6.1 MeV gamma radiation. Baz *et al.* report a distribution of the form $1+(4.2\pm1.8)\sin^2\theta+(3.1\pm3.2)\sin^2\theta\cos^2\theta$. If we normalize our distribution to have the same coefficient for the dipole term, we get $(0.3\pm0.3)+(4.2\pm0.2)\sin^2\theta+(6.2\pm0.8)\sin^2\theta\cos^2\theta$. Our isotropic part is smaller but that can be explained by the fact that, in the bremsstrahlung experiment, part of the photofission occurs in the region 6 to 6.5 MeV in which the isotropic term is rapidly increasing. No definite conclusion regarding the quadrupole term can be drawn from the distribution of Baz *et al.* because of the large statistical uncertainty. Within the errors, however, their distribution is consistent with the one obtained in the present work.

Bearg *et al.* report an angular distribution of the form $1+(8.5\pm3.2)\sin^2\theta-(1.6\pm3.1)\sin^4\theta$. Rewriting our distribution, we get $(0.2\pm0.3)+(8.5\pm0.7)\sin^2\theta-(5.1\pm0.6)\sin^4\theta$. In this case again the large errors prevent any detailed comparison but there is no inconsistency. Neither of the two mentioned experiments excludes a quadrupole term of the size we have found.

Our distribution, obtained by 10 MeV bremsstrahlung, can be compared with the distributions of Baz *et al.* and Baerg *et al.* at 9.4 MeV. They have the form $1+(0.85\pm0.28)\sin^2\theta+(0.51\pm0.56)\sin^2\theta\cos^2\theta$, $1+(0.54\pm0.08)\sin^2\theta+(1.43\pm\pm0.24)\sin^2\theta\cos^2\theta$ and $1+(0.43\pm0.16)\sin^2\theta+(0.01\pm0.16)\sin^4\theta$, respectively. As far as the dipole term is concerned, these three measurements agree within the statistical errors. There seems to be a discrepancy regarding the quadrupole term. Baz *et al.* report a large quadrupole term, but the other two distributions show only a small one. In order to explain this large quadrupole term, Baz *et al.* postulate that in the region 7 to 8 MeV the photofission is due mainly to quadrupole absorption. This assumption is in definite disagreement with the present work which shows that at 7 MeV the quadrupole term in the angular distribution is quite small.

6. Discussion

We can now compare the results of the present investigation with the Bohr theory. As discussed in the introduction, the lowest fission channels are predic-

ted to be 1− and 2+ and, in fact, the angular distribution at 6.1 MeV shows both a dipole and a quadrupole term.

It is interesting to note that the 6.1 MeV angular distribution contains a small isotropic term. Theoretically it should be zero but this is only under the condition that K is a perfectly good quantum number from the saddle point to the point of scission. This is not likely and the presence of a small isotropic term is therefore quite natural. Its size might give some indication of the extent to which K remains a good quantum number.

Baerg *et al.* [4]) assume that the isotropic term in fission near the threshold arises from fission channels in the region 1 MeV above the 0+ channel. These channels can contribute to fission near the threshold because of the barrier penetration. Baerg *et al.* try to use the size of the isotropic term in order to estimate the position of the high energy 1− channels with $K = 1$ relative to the low lying 1− channel with $K = 0$. This evidently requires the assumption that K is a good quantum number during the fission process. Since one cannot assume this a priori, such an estimate is rather uncertain.

There is an energy gap of a little less than 1 MeV between the low lying 1− and 2+ states and states of the same spin and parity due to nucleonic excitation. The barrier height corresponding to the lower states is experimentally determined to be about 5.8 MeV [8]). Hence barriers from about 6.6 MeV and upwards correspond to the higher states. Due to the barrier penetration, these fission channels will start to appear as low as at about 6.4 MeV. Since these channels have all the possible K values, the pure angular distributions characteristic for $K = 0$, which are found at 6.1 MeV, will be smeared out. The level density increases rapidly above the energy gap and one therefore expects the smearing out process to proceed quite rapidly. Experimentally, we have found that already at 6.9 MeV most of the anisotropy has disappeared. There even seems to be an indication that the anisotropy is smaller at 7.1 MeV than at 6.9 MeV. This also shows that it is decreasing quite rapidly in this region.

So far one can make theoretical prediction they seem to be verified by the present experiment. It is evident that in order to make a quantitative comparison one needs a more detailed theory. First of all it is necessary to know the position of the low lying 1− and 2+ states. There is no reason to assume them to have the same position at the saddle point as at the equilibrium deformation. Furthermore, it would be desirable to know something about the properties and position of the channles above the energy gap.

The present experiment gives information about the fission channels close to threshold but is also of interest from the point of view of photon absorption. Since one can separate a dipole and a quadrupole term in the angular distribution, one can obtain values of the cross-section for electric dipole and quadrupole photon absorption at 6 MeV. This is of particular interest, since there does not seem to be any other method of getting information about the relative

amounts of dipole and quadrupole absorption of high energy photons. The only information one has on this point is limited to light nuclei where spin and parity of single levels can be determined. This is of course a rather special case.

It is necessary to be cautious in interpreting the angular distribution obtained by the 6.1 MeV gamma rays. The reason is that nothing is known with certainty about the energy spread of the gamma rays. The excited oxygen nucleus formed in the reaction $F^{19}(p, \alpha)O^{16}$ recoils after the α-particle emission, but the life time of the 6.1 MeV state is so long that the excited nucleus is practically stopped before the emission of the gamma radiation [10]). Hence the recoil broadening of the gamma radiation might be quite low. The question now is how many levels in the uranium nucleus are excited by the gamma radiation. If the gamma-ray width is of the same order of magnitude as the level spacing, only one or a few levels in the uranium nucleus are excited. They cannot be expected to give a typical picture of the properties of the levels in this energy region. It is possible, for example, that relatively many 2+ levels are excited. This would give an abnormally high quadrupole absorption. If, on the other hand, the width is considerably greater than the level spacing, the photon absorption will be characteristic for the average properties of the levels.

Information on this point is provided by a comparison of the cross-section for photofission at 6.1 MeV obtained from measurements by bremsstrahlung and by the 6.1 MeV gamma rays. Such measurements have been made for several nuclei (Th^{232}, U^{233}, U^{238}, Np^{237}) [8, 9]). The values of the cross-section for these two different ways of excitation are the same within the experimental accuracy. This agreement indicates strongly that so many levels are excited by the 6.1 MeV gamma rays that these levels represent an average of the level properties at this energy. In the following we will assume this to be the case.

It should be mentioned that this uncertainty does not exist for the gamma rays at 6.9 and 7.1 MeV. The corresponding levels in O^{16} are known to have such a short life time that these two gamma rays are considerably broadened by the recoil [10]).

In the present work we obtain the result that 21 % of the photofission at 6.1 MeV goes via quadrupole absorption. This corresponds to a quadrupole cross-section of about 2 mb. In order to get the total quadrupole cross-section, one has to add the elastic and inelastic scattering cross-sections. They are not known so well but normally one does not expect gamma-ray emission to compete strongly with fission. Hence the total absorption cross section should be about the same as the fission cross-section.

It is of interest to compare our experimental value with theoretical estimates. Blatt and Weisskopf give the following expression for the electric quadrupole absorption cross-section:

$$\sigma = 1.2(\hbar\omega)^3 \left(\frac{R}{6\times 10^{-13}}\right)^4 10^{-30}\ \mathrm{cm}^2, \qquad (1)$$

where $\hbar\omega$ is measured in MeV and the radius R in cm. Using a radius constant $r_0 = 1.2\times10^{-13}$ cm we get $\sigma = 0.6\times10^{-27}$ cm^2. This value shoud be somewhat increased due to collective enhancement of the transition probability. In view of the uncertainties in the theoretical estimate, the agreement is surprisingly good.

Another way of estimating the order of magnitude of the quadrupole absorption is to use a sum rule. Levinger and Bethe [12]) have derived a sum rule for the electric quadrupole absorption. The expression contains the average kinetic energy and the mean square displacement in the ground state of the nucleons. If one makes crude estimates of these quantities, the following expression is obtained

$$\int_0^\infty \frac{\sigma}{E}\,\mathrm{d}E \approx 30\ \text{mb}. \qquad (2)$$

In order to get cross-section values from a sum rule, it is necessary to know the shape of the cross-section curve. We will assume that the cross-section varies with the energy according to expression (1). Following Blatt and Weisskopf we further assume that the cross-section goes down to zero for higher energies (around 25 MeV). With these assumptions we can use the sum rule (2) to calculate the cross-section at 6 MeV. The result 1 mb is obtained.

The experimental value thus agrees well with the theoretical estimates. As a matter of fact the agreement is better than one can reasonably expect since the theoretical expressions are probably uncertain within one order of magnitude. This comparison shows, however, that our experimental value is not unreasonable from the theoretical point of view.

We are greatly indebted to Professor A. Bohr and Professor B. Mottelson for stimulating discussions. We would like to thank Mr L. Ask for performing the measurements with the three-crystal spectrometer.

References

1) E. J. Winhold and I. Halpern, Phys. Rev. **103** (1956) 990
2) A. I. Baz, N. M. Kulikova, L. E. Lazareva, N. V. Nikitina and V. A. Semenov, Second U. N. Intern. Conf. on the Peaceful Uses of Atomic Energy (United Nations, Geneva, 1958), p. 2037
3) H. Faissner and F. Gönnenwein, Z. f. Physik **153** (1958) 257
4) A. P. Baerg, R. M. Bartholomew, F. Brown, L. Katz and S. B. Kovalski, Can. J. Phys. **37** (1959) 1418
5) A. Bohr, First U. N. Intern. Conf. on the Peaceful Uses of Atomic Energy (United Nations, Geneva, 1955), p. 911
6) L. Ask, Univ. of Lund (private communication)
7) R. A. Schmitt and R. B. Duffield, Phys. Rev. **105** (1957) 1277
8) L. Katz, A. P. Baerg and F. Brown, Second U. N. Intern. Conf. on the Peaceful Uses of Atomic Energy (United Nations, Geneva, 1958), p. 200
9) K. M. Clarke, Argonne National Laboratory report ANL-5853
10) S. Devons, G. Manning and D. P. Bunbury, Proc. Phys. Soc. A **68** (1955) 18
11) J. M. Blatt and V. F. Weisskopf, Theoretical nuclear physics (Wiley, New York, 1952)
12) J. S. Levinger and H. A. Bethe, Phys. Rev. **78** (1950) 115
13) J. R. Huizenga, private communication

4.E:6.A

Nuclear Physics **20** (1960) 155—158; © *North-Holland Publishing Co., Amsterdam*

Not to be reproduced by photoprint or microfilm without written permission from the publisher

BALANCED ION CHAMBER MEASUREMENT OF HALF-LIVES OF SEVERAL RADIOISOTOPES

H. T. EASTERDAY † and R. L. SMITH

University of Oregon, Eugene, Oregon ††

Received 4 June 1960

Abstract: Half-lives of six gamma emitters have been measured using a Balanced Ion Chamber arrangement with one chamber driven by a radium source. Data analyzed by least squares yielded the following results: Se^{75}, 120.4±0.2 d; Zn^{65}, 245.7±1.1 d; Ru^{106}, 265.8±1.7 d; Ag^{110m}, 255.0±0.8 d; Cs^{134}, 2.05±0.05 y; Ce^{144}, 277±4 d.

A precision measurement of the half-life of a radioactive isotope by conventional techniques requires the observations to be extended over a period of time comparable to the half-life. Even for moderately long half-lives this is not only time consuming but introduces many experimental difficulties: The sensitivity of the detector may change in time, the source detector geometry may not be reproducible, and the background may vary during the experiment. More important, a slight variation in apparent half-life due to impurities in the sample is difficult to detect during the course of the observations.

The Balanced Ion Chamber technique [1]) does not suffer from the above difficulties. By using large cylindrical ion chambers and by introducing the source along the symmetry axis, the counters are made less sensitive to changes in geometry than conventional end window counters with external sources. Any change in background will produce an equal effect in both chambers. Hence, the current reading which is the difference current (refer to fig. 1) remains unchanged. A half-life in the region of 1 year can be measured to an accuracy of 1 % by observations extending over a period of roughly 10 days. This relatively rapid measurement permits several independent half-life determinations to be made on a given sample, and any slight variation with time of the measured half-life is readily detectable.

The Balanced Ion Chambers and components are shown schematically in fig. 1. Chambers are filled to a pressure of 3 atm with argon and are connected to a common manifold to maintain equal pressure in the chambers. The two detectors are isolated from each other by placing 10 cm of lead between the units. A Ra^{226} source is placed in one of the chambers at the start of a run; the strength of the unknown source (sources are in liquid form) can be adjusted

† Now at Oregon State College, Corvallis, Oregon.

†† Work supported by the U. S. Atomic Energy Commission.

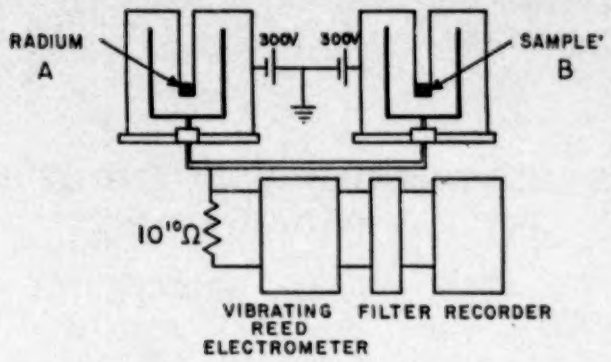

Fig. 1. Schematic diagram of the Balanced Ion Chamber Apparatus.

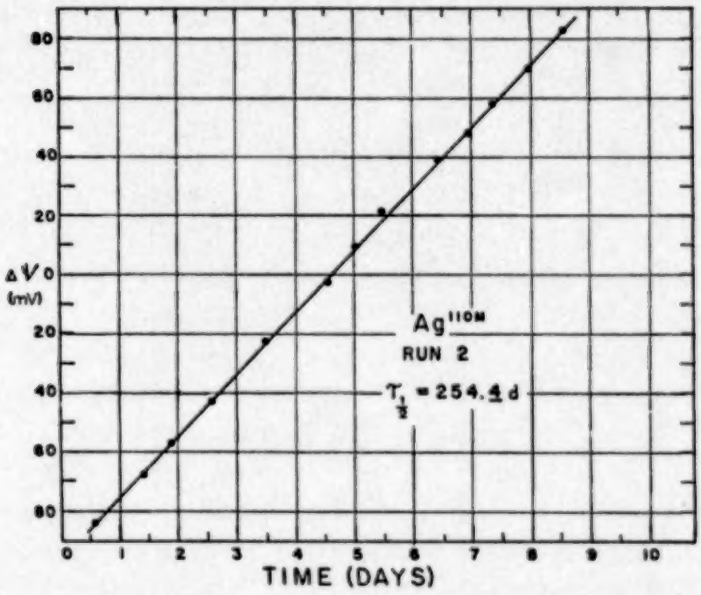

Fig. 2. A typical difference voltage vs time plot for one sample of Ag^{110m}.

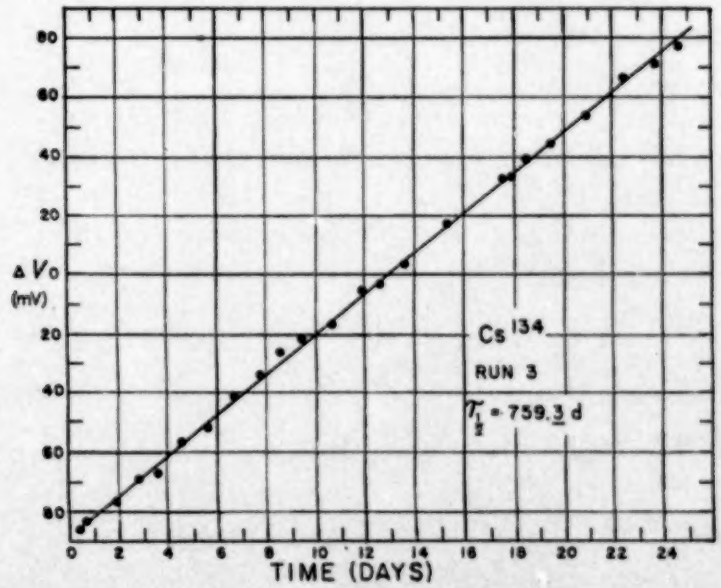

Fig. 3. Difference voltage versus time for Cs^{134}.

so the output or difference current is zero to one part in 10^4 of the single chamber output current:

$$i = i_A - i_B = 0 \quad \text{at} \quad t = 0.$$

$i_A = i_0$ is considered constant during the run since $\tau_{\frac{1}{2}} = 1620$ y for Ra^{226}. As the unknown source decays in time, the difference current becomes finite:

$$i = i_0(1 - e^{-\lambda t}).$$

The observation period is kept short so the condition $\lambda t \ll 1$ is satisfied thus allowing the neglect of second order and higher terms in the expansion of the exponential:

$$i = i_0 \lambda t \quad \text{or} \quad \lambda = \frac{1}{V_0}\frac{dV}{dt},$$

since the vibrating reed electrometer measures voltages. The permissible time duration of an observation is increased by adding an excess of the unknown activity at the start of a run rather than balancing the chambers. The output voltages observed then extend from negative values through balance to positive values. It is not necessary that the time of balance be known exactly since this does not enter the expression for λ. Data plotted from two typical runs are shown in figs. 2 and 3. Results are given in table 1.

TABLE 1

Results

Isotope	Half-life	Previous Measurements	Reference
Se^{75}	120.4 ±0.2 d	120 d	[a]
		128 d	[b]
Zn^{65}	245.7 ±1.1 d	243.5 ±0.8 d	[c]
		245.0 ±0.5 d	[a]
Ru^{106}	365.8 ±1.7 d	366.6 ±0.9 d	[d]
		1.02 y	[e]
Ag^{110m}	255.0 ±0.8 d	252.5 ±1.5 d	[c]
		270 ±4 d	[f]
Cs^{134}	2.05±0.02 y	2.07±0.02 y	[c]
		2.19 y	[g]
Ce^{144}	277 ±4 d	284.5 ±1.0 d	[d]
		290 d	[g]

[a]) H. W. Wright *et al.*, Nucl. Sci. Eng. **2** (1957) 427
[b]) M. J. Cork *et al.*, Phys. Rev. **79** (1950) 889
[c]) K. W. Geiger, Phys. Rev. **105** (1957) 1539
[d]) R. P. Schuman, M. E. Jones and A. C. Mewherter, J. Inorg. Chem. **3** (1956) 160
[e]) W. F. Merritt, P. J. Campion and R. C. Hawkins, Can. J. Phys. **35** (1957) 16
[f]) J. R. Gum and M. R. Pool, Phys. Rev. **80** (1950) 315
[g]) F. Joliot, Compt. Rend. **218** (1944) 733

Half-lives quoted are from a least squares analysis of the data. Four or more determinations were made for each sample, and the error indicated is the standard deviation of the mean. Samples were obtained from Oak Ridge.

The authors wish to thank the staff of the Cyclotron at Oregon State College for a zinc bombardment.

Reference

1) J. Tobailem, Ann. Phys. **10**, 783 (1955)

2.B

Nuclear Physics **20** (1960) 159—168; © *North-Holland Publishing Co., Amsterdam*

Not to be reproduced by photoprint or microfilm without written permission from the publisher

ANGULAR CORRELATION MEASUREMENTS IN Ba^{136}

Z. GRABOWSKI †, S. GUSTAFSSON and I. MARKLUND

Institute of Physics, Uppsala

and

I. B. HÄLLER

The Gustaf Werner Institute for Nuclear Chemistry, Uppsala

Received 18 June 1960

Abstract: The angular correlation of cascading transitions between levels in Ba^{136} excited from Cs^{136} have been investigated with an automatic gamma-gamma directional correlation apparatus and with an electron-gamma correlation apparatus. The measured cascades are (keV): 1065—830, 1255—830, 337—1065 and 270—1065. They give the following spins of energy levels in Ba^{136} (keV (I, π)): 0(0+), 830(2+), 1900(4+), 2090(4+), 2170(5+) and 2240(6+).

1. Level Scheme

The nucleide $_{56}Ba^{136}_{80}$ has two holes in a closed shell of 82 neutrons. Its level scheme has been investigated in the decay of Cs^{136}($T_{\frac{1}{2}} = 13$ d) by J. L. Olsen and G. D. O'Kelley [1]) and more recently by R. K. Girgis and R. van Lieshout [2]). Olsen and O'Kelley used a beta-spectrometer, a proportional counter and a gamma-gamma coincidence spectrometer and arrived at the decay scheme shown to the left in fig. 1. Later, O'Kelley reported to the editor of the Nuclear Data Sheets that the 830 keV gamma ray (placed in their decay scheme between 2198 keV and 1376 keV levels) was the most intense instead of the 1041 keV gamma ray. Their decay scheme thus became doubtful.

Girgis and van Lieshout have reinvestigated the decay scheme of Cs^{136} using only scintillation techniques (single spectra, sumspectra and gamma-gamma coincidences). As confirmed by their measurements the 830 keV gamma-ray is the most intense. The 830 keV line was also the only strong gamma ray found[2]) in the decay of La^{136} to Ba^{136}. It corresponds to the transition from the first excited state to the ground state in Ba^{136}. Such an excitation energy of the first excited state is in agreement with the level systematics [3]) of the even isotopes of Xe and Ba. The decay scheme proposed by Girgis and van Lieshout is presented to the right in fig. 1.

We have measured the gamma-gamma and electron-gamma directional correlation of four cascades in Ba^{136} in order to assign definite spin values to

† On leave from: Instytut Badán Jadrowych, Kraków, Poland.

the corresponding excited states. The decay scheme of Girgis and van Lieshout, to the right in fig. 1, is accepted as the most probable one. The gamma rays, indicated with circles, were selected in the present angular correlation measurements. The resulting spin assignments are also given in fig. 1. The single scintillation spectrum of Cs^{136} in the energy range 200 keV to 1300 keV is presented in fig. 2. The analyser settings used are indicated.

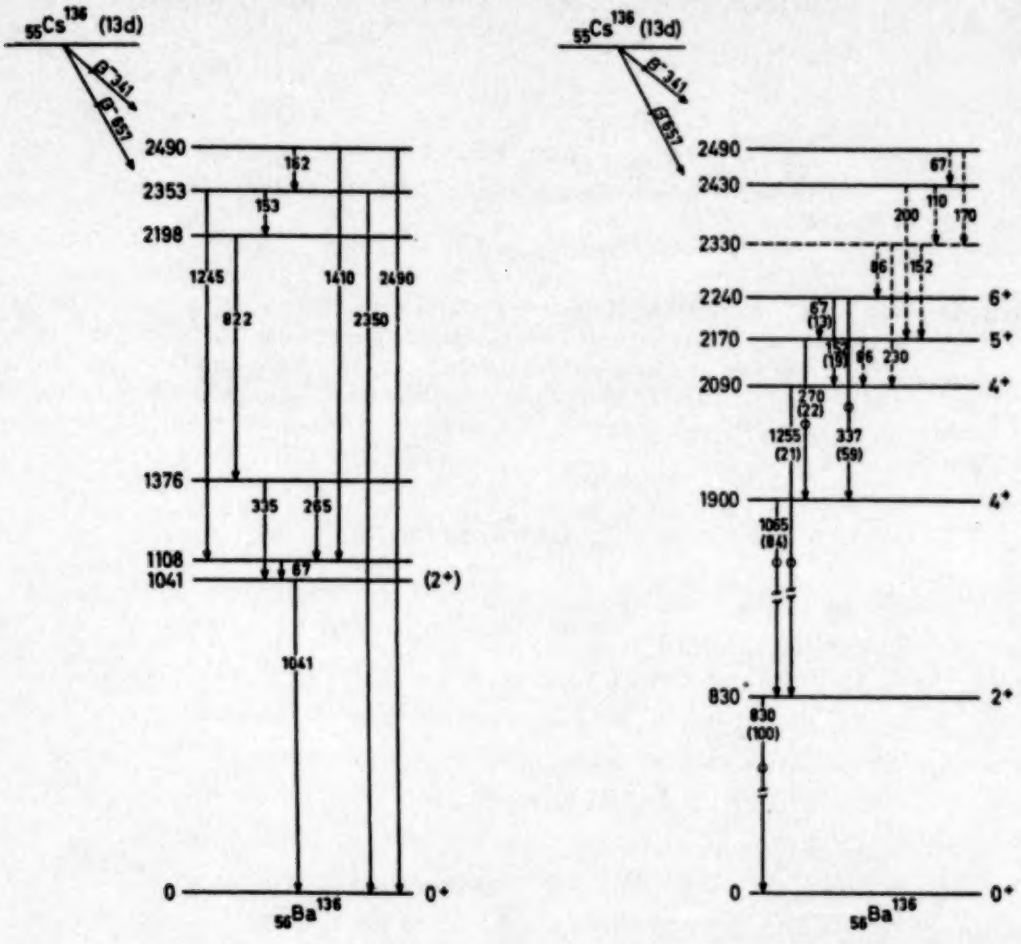

Fig. 1. The decay scheme of Cs^{136}. To the left is shown the decay scheme proposed by J. L. Olsen and G. D. O'Kelley [1]), to the right decay scheme proposed by R. K. Girgis and R. van Lieshout [2]). The gamma rays indicated with circles were selected in the present experiment. Our resulting spin assignments are included.

2. Source Preparation

The Cs^{136} source was prepared by bombarding a $BaCO_3$ target with 25 MeV deuterons in the synchrocyclotron at Birmingham. The target material was enriched in Ba^{138} to 98 %.

After irradiation the $BaCO_3$ target was dissolved in diluted hydrochloric acid and CO_2 was boiled off. Ba was precipitated as $BaCl_2 \cdot H_2O$ by the drop-by-drop addition of concentrated HCl with vigorous stirring. The precipitate was centrifuged off. The supernate was boiled down to a small volume and

cleaned off all Ba by a total of three $BaCl_2$ precipitations, each of which was carried out by the drop-by-drop addition with stirring. The final supernate was evaporated and transferred to a small polyethylene source holder. The source for the beta spectrometer measurement was prepared using the drop method. As a backing, zapon film was used with a very thin layer of silver deposited on it.

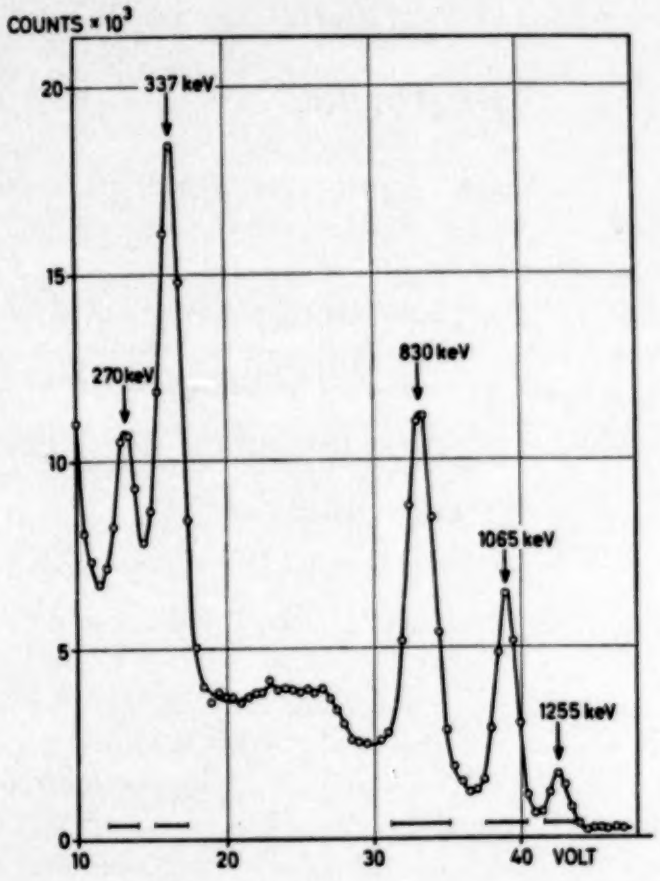

Fig. 2. A single scintillation spectrum of Cs^{136} in the energy range 200 keV to 1300 keV with indicated channel settings.

The source preparation was finished within four hours. The efficiency of the chemical method [3]) was found to be better than 90 %.

3. Experimental Procedure

The directional correlation function of two successive gamma transitions between levels with spins I_1, I_2 and I_3 can always be written

$$W(\theta) = \sum_{\nu} A_\nu P_\nu(\cos\theta) = 1 + A_2 P_2(\cos\theta) + A_4 P_4(\cos\theta), \qquad (1)$$

where $P_\nu(\cos\theta)$ are the Legendre polynomials.

When a radiation is a mixture of two multipoles L and $L' = L+1$, the

mixing parameter δ is the ratio of the respective matrix elements

$$\delta = \frac{\langle L' \rangle}{\langle L \rangle},$$

and δ^2 is the intensity ratio of the two multipoles.

If we assume that only the first transition in the cascade is mixed, we can denote the cascade as $I_1(L_1L'_1)I_2(L_2)I_3$. The coefficients A_ν are then [4,5])

$$A_\nu = \frac{1}{1+\delta^2}[F_\nu(L_1L_1I_1I_2) + 2\delta F_\nu(L_1L'_1I_1I_2) + \delta^2 F_\nu(L'_1L'_1I_1I_2)]F_\nu(L_2L_2I_2I_3). \quad (2)$$

In the case of electron-gamma angular correlation the A_ν coefficients have the form

$$A_\nu = \frac{1}{1+\bar{\delta}^2}[F_\nu(L_1L_1I_1I_2)b_\nu(L_1L_1) + 2\bar{\delta}F_\nu(L_1L'_1I_1I_2)b_\nu(L_1L'_1) + \bar{\delta}^2 F_\nu(L'_1L'_1I_1I_2)b_\nu(L'_1L'_1)]F_\nu(L_2L_2I_2I_3). \quad (3)$$

The mixing parameter $\bar{\delta}$ is related to δ by the simple formula

$$\bar{\delta} = \sqrt{\frac{\alpha(L')}{\alpha(L)}}\,\delta,$$

where α are the conversion coefficients. The F_ν and b_ν coefficients are tabulated in refs. [4,5]).

For the gamma-gamma angular correlation measurements an automatic coincidence spectrometer has been used [6]). This spectrometer is provided with two 3.8 cm by 3.8 cm. NaI(Tl) crystals and a coincidence circuit with resolving time $2\tau = 3 \times 10^{-8}$ s. The source to crystal distances were 50 mm. The counters were shielded frontally by 5 mm of aluminium and a lateral lead shielding was employed to eliminate coincidences due to scattering.

The A_2 and A_4 coefficients in the correlation function (1) were calculated using the method of Gimmi *et al.* [7]). Corrections for the finite solid angle of the counters were applied using an earlier, experimentally determined curve for the same geometry [6]). We have used the graphs representing A_2 and A_4 versus δ given in ref. [8]) for the interpretation of the experimentally obtained A_2 and A_4 values

The errors quoted for the A_2 and A_4 coefficients are always standard deviations, using the formulas of Gimmi *et al.* [7]), and when corrections are applied these additional errors are included.

The electron-gamma directional correlation measurements were performed with a medium thick lens spectrometer adopted for electron-gamma angular correlation measurements [9]). The gamma rays were selected in a 5.1 cm high by 6.4 cm diameter NaI(Tl) scintillation detector. We have measured the

coincidences at three angles, 90°, 180° and 270°. Using these data the anisotropy was computed after correction for the single channel counting rates, N_e and N_γ, taken for each position of the gamma counter.

4. Results

4.1. 1065 keV—830 keV CORRELATION

The settings of both the differential discriminators are indicated in fig. 2. With these settings the coincidence contribution from the 1255 keV—830 keV cascade was estimated to be 8 %. Taking into account that this contributing cascade has the same angular correlation pattern as the 1065 keV—830 keV cascade, it does not change the result. The correlation coefficients after solid angle correction were found to be

$$A_2 = +0.100 \pm 0.008 \quad \text{and} \quad A_4 = +0.008 \pm 0.018.$$

They give the following possibilities for the spin of the 1900 keV level:

Spin of the 1900 keV level	δ for the 1065 keV gamma-ray
2	$-2.5\times10^{-1} \leqq \delta \leqq -1.9\times10^{-1}$
3	$-2.6\times10^{-1} \leqq \delta \leqq -2.2\times10^{-1}$
4	$\lvert\delta\rvert \leqq 10^{-2}$

The $2\pm$ and $3\pm$ spin possibilities for the 1900 keV level can be excluded from our results for the 337 keV—1065 keV correlation. See fig. 1 and subsection 4.3. Let us for a moment assume the 1900 keV level to have a spin $2\pm$ or $3\pm$. The 2240 keV level has a most probable spin $I > 2$, as no transition to the ground state or first excited state is observed. The 337 keV—1065 keV cascade should then have the possible spin sequences:

$$I \to 2+ \to 2+ \quad \text{with} \quad I = 3\pm \text{ or } 4\pm \quad \text{or}$$
$$I' \to 3\pm \to 2+ \quad \text{with} \quad I' = 3+, 4+ \text{ or } 5+.$$

None of these spin sequences fit our gamma-gamma and electron-gamma correlation measurements for the 337 keV—1065 keV cascade. This conclusion was drawn after a careful analysis of eighteen graphs of A_2 versus $\bar{\delta}$, similar to the six curves shown in fig. 3, for all the above-mentioned sequences. These curves are, however, not included in the present article.

A $2+$ assignment to the 1900 keV level should require a predominantly M1 character of the $2+ \to 2+$ transition (95 % M1) in contrast to the predominantly E2 character of the other known transitions of this type [10, 11]). The absence of any cross-over transition is also in favour of a spin 4 assignment, although an E2 transition from the 1900 keV level to the ground state is expected to be strongly suppressed from the theoretical point of view.

Because of the above-mentioned reasons we can assign a spin 4 to the 1900 keV level. Positive parity is most probable.

4.2. 1255 keV—830 keV CORRELATION

The differential discriminators selected the 1255 keV and 830 keV photopeaks respectively. The result after solid angle correction is

$$A_2 = +0.105 \pm 0.010 \quad \text{and} \quad A_4 = +0.003 \pm 0.011.$$

This angular correlation result gives the following possible spin assignments for the 2090 keV level:

Spin of the 2090 keV level	δ for the 1255 keV gamma-ray
2	$-2.1\times10^{-1} \leqq \delta \leqq -1.9\times10^{-1}$
3	$-2.8\times10^{-1} \leqq \delta \leqq -2.2\times10^{-1}$
4	$\lvert\delta\rvert \leqq 2\times10^{-2}$

The absence of any cross-over transition from the 2090 keV level to the ground state indicates a spin value higher than 2. The relatively strong feeding to this level from the 2240 keV level, which we will later assign as 6+(4.3.2), definitely excludes a spin 2 or 3 assignment to the 2090 keV level. The unobserved transition of 190 keV between the 2090 keV (4+) level and the 1900 keV (4+) level is expected to be weak as competing with the 1255 keV gamma ray.

We are thus left with spin 4 as the only possible spin value for the 2090 keV level. Positive parity seems to be reasonable from point of view of the relative intensities of the gamma transitions.

4.3. 337 keV—1065 keV CORRELATION

4.3.1. Gamma-gamma angular correlation measurement

The settings of the differential discriminators can be found in fig. 2. For these settings the coincidence contribution from the 1065 keV—830 keV cascade was found to be 14 %. This contribution changed the result very little, as the 1065 keV—830 keV correlation has the same angular distribution (4.1). The result of the measurement of the 337 keV—1065 keV cascade, corrected for coincident contribution and finite solid angle, is

$$A_2 = +0.103 \pm 0.006 \quad \text{and} \quad A_4 = -0.003 \pm 0.013.$$

This result is in agreement with the following spin values for the 2240 keV level:

Spin of the 2240 keV level	δ for the 337 keV gamma ray
3	$\delta \approx 3.0\times10^{-1}$
4	$-2.8\times10^{-1} \leqq \delta \leqq -2.2\times10^{-1}$
5	$-3.0\times10^{-1} \leqq \delta \leqq -2.6\times10^{-1}$
6	$\lvert\delta\rvert \leqq 10^{-2}$

From the gamma-gamma angular correlation alone it is thus impossible to give any definite spin assignment for the 2240 keV level. Only spin 1 and 2 are excluded. To reduce the number of possibilities for the spin of this level, we have measured electron-gamma angular correlation for the same cascade.

4.3.2. Electron-gamma angular correlation measurement

The lens spectrometer was focused on the K-conversion line of the 337 keV transition and the differential discriminator of the gamma channel was set to accept the 1065 keV photopeak. The measured anisotropy was corrected for the coincident background from the continuous beta spectrum. This background was found to give an almost isotropic correlation pattern. The energy resolution of the beta spectrometer was 4 %. For this condition the coincident background contribution to the measurement was 51 %. The measured A_2 coefficient, corrected for this background and for the solid angles of the beta spectrometer and gamma detector, was found to be

$$A_2 = 0.190 \pm 0.025.$$

In fig. 3 the theoretical curve for the A_2 coefficient for an electron-gamma correlation is drawn versus δ for the spin sequence $I_1 \rightarrow 4+ \overset{E2}{\rightarrow} 2+$ with $I_1 = 3+$, $4+$ and $5+$. The possible spin value $I_1 = 6+$ gives a pure E2 transition and will be discussed later. From fig. 3 it is easy to see that the high

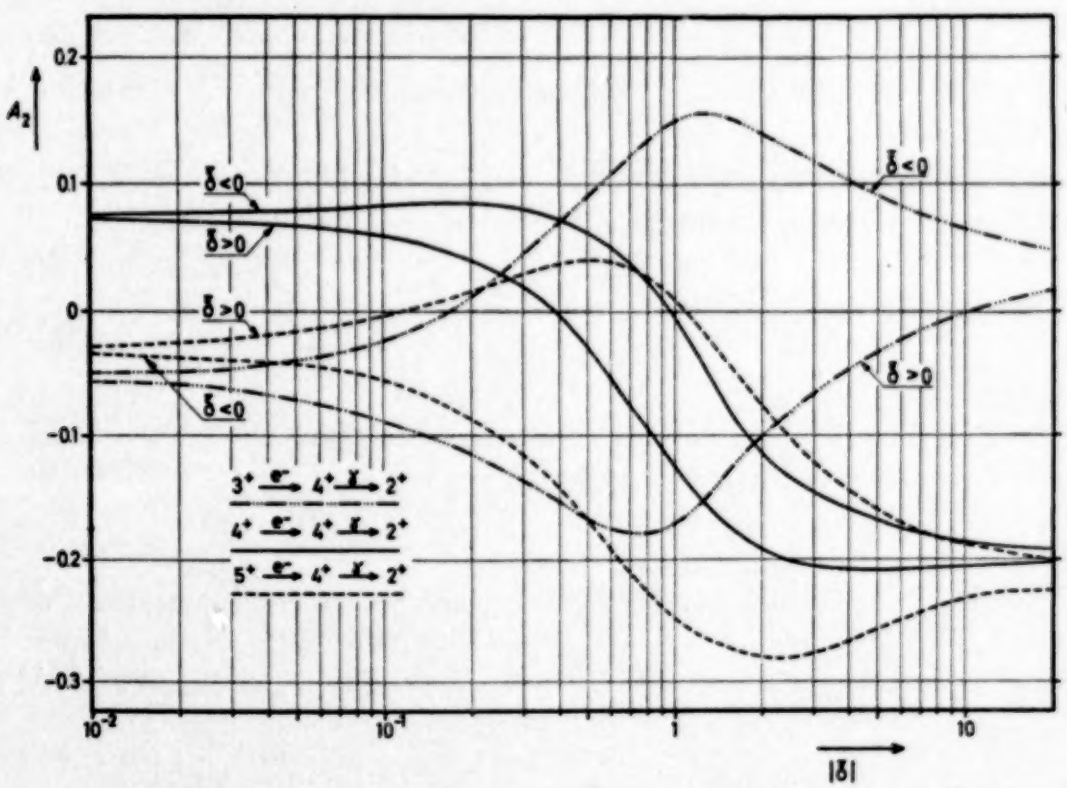

Fig. 3. The theoretical coefficients A_2 in eq. (1) versus $\bar{\delta}$ for the spin sequence $I_1 \underset{E}{\overset{\gamma}{\rightarrow}} 4+ \overset{E2}{\rightarrow} 2+$ with $I = 3+$, $4+$ and $5+$, computed for the 337 keV—1065 keV correlation.

value of the experimental A_2 coefficient excludes the spin values 3+, 4+ and 5+. The only remaining possibility from the gamma-gamma angular correlation measurement (for even parity) is 6+. In this case the 337 keV transition should have a pure E2 character according to the experimental result. The theoretical A_2 value for the electron-gamma correlation with a spin sequence $6+ \xrightarrow[e^-]{E1} 4+ \xrightarrow[\gamma]{E2} 2+$ is

$$A_2^{\text{theory}} = +0.170.$$

This value is in a good agreement with our experimental result.

When considering the odd parity possibilities for the sequence $I_1 \xrightarrow[e^-]{E1} 4+ \xrightarrow[\gamma]{E2} 2+ (I_1 = 3-, 4-, 5-)$ one finds that only 3− is in agreement with the measured value of A_2. The theoretical value of A_2 is in this case $A_2^{\text{theory}} = +0.196$. We have however excluded the 3− possibility for the 2240 ke Vlevel for several reasons, e.g.:

a) In that case the 337 keV gamma ray should have E1 character in disagreement with the measured K/L ratio for this transition [1]).

b) Taking into account that the 337 keV transition, which in this case should have an E1 character, is comparatively strong, it should appear a much stronger transition of 1410 keV of E1 character between the 2240 keV level and the first excited level (2+). Such a transition is not observed [2]).

c) The high log *ft* value of 8.0 for the 657 keV beta transition should then, if it is feeding the 2240 keV level, require positive parity for the ground state of Cs^{136}. If this was the case the 4+ level at 1900 keV or the 2+ level at 830 keV should be strongly populated with a beta branch from Cs^{136} and such beta branches are not observed.

The theoretical value of A_2 for the $I_1 = 6-$ possibility with an upper transition of pure M2 character (see the gamma-gamma correlation result) is

$$(A_2^{\text{theory}})_{e^- - \gamma} = +0.126.$$

Our experimental electron-gamma correlation result also excludes this possibility.

Taking into account all the above-mentioned arguments, we can assign the 2240 keV level a spin-parity value of 6+.

4.4. 270 keV—1065 keV CORRELATION

In this case the 337 keV—1065 keV cascade gives a coincident contribution. This contribution for the channel settings indicated in fig. 2 was estimated to be 35 %. The result of the gamma-gamma correlation measurement, corrected for this coincident background and for the solid angle of the counters, is

$$A_2 = -0.104 \pm 0.009 \quad \text{and} \quad A_4 = -0.003 \pm 0.018.$$

This result gives as possible spin values for the 2170 keV level, 3 ($2.8 \times 10^{-2} \leqq$

$\leqq \delta \leqq 5.3\times10^{-2}$) and 5 ($3.2\times10^{-2} \leqq \delta \leqq 6.5\times10^{-2}$). The first possibility is excluded, as a 67 keV transition feeds this level from the 2240 keV 6+ level. Positive parity for the 2170 keV level is in agreement with the observed intensity ratios of the transitions from the 2240 keV level. If we assign 5+ as the spin value for the 2170 keV level a large admixture of E2 is required for the 67 keV transition to fulfill the intensity conditions. This is in a good agreement with the rather low value of K/L = 3.5 reported for this transition [1]). The 2170 keV level thus has a spin-parity 5+, and the 270 keV transition is an almost pure M1 transition ($\geqq$ 99.6 % M1).

The absence of any observed 80 keV transition (5+ → 4+) can be easily explained from the energy dependence, which favours the 270 keV 5+ → 4+ M1 transition. If we assume that the 80 keV 5+ → 4+ transition also has pure M1 character, the Weisskopf formula [5]) gives the intensity ratio

$$\frac{I_{80}^{M1}}{I_{270}^{M1}} \approx \frac{1}{40},$$

that means a relative intensity of the 80 keV ray $\approx$ 0.5 in the decay scheme.

5. Conclusion

The levels in Ba^{136} excited from Cs^{136} are found to have the spin-parities from ground 0+(0 keV), 2+(830), 4+(1900), 4+(2090), 5+(2170) and 6+(2240). (See fig. 1). Only the last one of these levels is fed directly [1, 2]) by a beta branch from Cs^{136}. The reported energy of 657 keV and intensity of 7 % for the highest beta branch gives log ft = 8.0 indicating a first forbidden or unique first forbidden transition. All the experimental data thus point towards a negative parity and a spin higher than 6 for ${}_{55}Cs_{81}^{136}$. If we assume that the 657 keV beta branch is feeding the 1900 keV level and the 341 keV branch the 2240 keV level, the spin-parity of this last level should have a spin-parity of 3− according to our experimental result. This possibility is, however, already excluded. See the discussion in subsection 4.3. We thus conclude that the 657 keV beta branch is probably feeding the 2240 keV level.

The neighbouring odd cesium isotopes ${}_{55}Cs_{78}^{133}$, ${}_{55}Cs_{80}^{135}$ and ${}_{55}Cs_{82}^{137}$ all have a directly measured spin of $I = \frac{7}{2}$ in their ground states. The 55th proton is then likely to stay in the same shell model orbit $g_{\frac{7}{2}}$ also in the nucleus ${}_{55}Cs_{81}^{136}$. A neutron orbit of $h_{\frac{11}{2}}$ is reasonable because of the experimentally expected negative parity and high spin value. When coupling the momenta of these two odd nucleons [12]) we can arrive at a probable spin-parity assignment of 8− for Cs^{136} compatible with the experimental data. This assignment is strengthened by the directly measured spin of Cs^{134m}, I = 8−. Cs^{136} seems thus to have the same nucleon configuration as Cs^{134m} but for an additional pair of neutrons.

It is a pleasure to express our gratitude to Professor Kai Siegbahn for his stimulating interest in this work. The English correction was made by Mr. W. Parker. This investigation was financially supported by the U. S. Air Research and Development Command.

References

1) J. L. Olsen and G. D. O'Kelley, Phys. Rev. **95** (1954) 1539
2) R. K. Girgis and R. van Lieshout, Nuclear Physics **12** (1959) 204
3) C. D. Coryell and N. Sugerman (editors), Radiochemical Studies: The Fission Products (Nuclear Energy Series), Div. IV, Vol. 9, p. 1654
4) L. C. Biedenharn and M. E. Rose, Rev. Mod. Phys. **25** (1953) 729
5) A. H. Wapstra, G. J. Nijgh and R. van Lieshout, Nuclear Spectroscopy Tables (North-Holland Publishing Company, Amsterdam, 1959)
6) T. Lindqvist, Arkiv f. Fysik **12** (1957) 495
7) F. Gimmi, E. Heer and P. Scherrer, Helv. Phys. Acta **29** (1956) 147
8) I. Marklund, B. van Nooijen and Z. Grabowski, Nuclear Physics **15** (1960) 553
9) T. R. Gerholm and B. G. Pettersson, Nuclear Instruments **4** (1959) 107
10) S. S. Melik, V. R. Potnis and C. E. Mandeville, Nuclear Physics **11** (1959) 691
11) D. M. van Patter, Nuclear Physics **14** (1959) 42
12) C. J. Gallagher and S. A. Moszkowski, Phys. Rev. **111** (1958) 1282

1.E.1:
4.E

Nuclear Physics **20** (1960) 169—182; © *North-Holland Publishing Co., Amsterdam*
Not to be reproduced by photoprint or microfilm without written permission from the publisher

DER β-ZERFALL DES NEODYM-147

HANS-DIETRICH WENDT und PETER KLEINHEINZ

I. Institut für Experimentalphysik, Physikalisches Staatsinstitut Hamburg

Eingegangen am 18. Mai 1960

Abstract: The β-decay of Nd^{147} has been investigated using a double-lens spectrometer and fast-slow $\beta-\gamma$ coincidence technique, showing a total of five β-transitions, of which one has not been reported previously. Their end-point energies, partial intensities and log ft values are: 809 keV (64.7 %), log ft = 7.6; 719 keV (10.4 %), log ft = 8.1; 480 keV (0.5 %), log ft = 9.0; 370 keV (12.1 %), log ft = 7.3 and 215 keV (12.3 %), log ft = 6.5. A level scheme in agreement with the observed data is proposed and spins are discussed for the daughter nucleus Pm^{147}.

1. Einleitung

Der Zerfall von Neodym-147 in Promethium-147 ist seit der Auffindung einer 10 Tage-Aktivität bei dem Beschuß von natürlichem Neodym mit verschiedenen schweren Teilchen durch Law *et al.* [1]) von zahlreichen Autoren untersucht worden.

Marinsky *et al.* [2]) und Hayden [3]) ordneten dieser Aktivität das Isotop mit der Massenzahl 147 zu. Weitere Untersuchungen [4–8]) ergaben die Grundzüge des Zerfallsschemas. Bothe [4]) bestimmte die Halbwertzeit mit guter Genauigkeit zu 11.1 ± 0.2 d. Rutledge *et al.* [9]) fanden Konversionslinien von 11 γ-Übergängen.

Untersuchungen von Hans *et al.* [10]) mit Szintillationszählern und einer γ—γ-Koinzidenzanordnung ergaben ein Zerfallsschema mit 9 γ-Übergängen. Aus Intensitätsbetrachtungen schlossen die Autoren, daß das komplexe β-Spektrum aus 4 Komponenten besteht.

$\beta-\gamma$-Koinzidenzmessungen von Ewan *et al.* [11]) ergaben β-Übergänge mit Zerfallsenergien von 818 ± 7 keV, 368 ± 10 keV und 214 ± 15 keV.

Die Untersuchungen durch Lindqvist *et al.* [12]) bestätigten Teile der Ergebnisse von Hans [10]).

Eine Wiederholung der Messungen von Rutledge [9]) durch Cork *et al.* [13]) in Verbindung mit γ—γ-Koinzidenzen führte zu einer Erweiterung des Schemas von Hans [10]). Das β-Spektrum wurde aufgelöst in 3 Komponenten, deren Energien und relative Häufigkeiten 812 ± 30 keV (66 %), 380 ± 50 keV (18 %) und 230 ± 50 keV (16 %) betragen. Die Intensität weiterer β-Komponenten mit Zerfallsenergien zwischen 500 und 600 keV wurde auf kleiner als 2 % geschätzt.

Sehr sorgfältige Messungen mit Hilfe von β—γ-Koinzidenzen führte Evans [14]) durch. Seine Ergebnisse stimmen im allgemeinen gut mit denen von Cork [13]) überein. Unterschiede bestehen im Zerfallsschema durch die Berücksichtigung der Ergebnisse von Rutledge [9]) sowie in den Intensitäten der β-Komponenten. Hier fand Evans folgende Werte: 802 keV (76 %), 362 keV (20 %), 220 keV (2.8 %). Dazu wurde noch ein β-Übergang von 404 keV mit 1.2 % Intensität vermutet.

In Übereinstimmung mit Hans [10]) stehen die Ergebnisse von Mitchell *et al.* [15]) hinsichtlich der γ-Übergänge. Die Analyse des β-Spektrums lieferte Komponenten mit Endpunktsenergien von 801 keV, 472 keV und 374 keV; Anteile mit kleinerer Energie könnten unter dem 225 keV β-Übergang des Tochterkerns Pm^{147} verborgen sein.

Berenyi [16]) untersuchte das β-Spektrum mit β—γ-Koinzidenzen und fand Anteile mit Zerfallsenergien von 815 ± 10 keV, 529 ± 25 keV, 365 ± 15 keV und 215 ± 15 keV.

Schließlich führten Bodenstedt *et al.* [17]) sehr genaue γ—γ-Koinzidenzmessungen aus und bestätigten die Ergebnisse von Cork [13]).

Obgleich der Zerfall des Neodym-147 gerade in letzter Zeit mit modernen Techniken untersucht wurde, ließ sich bisher noch immer kein eindeutiges Zerfallsschema aufstellen. Besonders große Diskrepanzen bestanden hinsichtlich der Anzahl, der Maximalenergie und der nur selten gemessenen relativen Intensitäten der β-Übergänge. Aus diesem Grunde erschien es angebracht, den β-Zerfall des Nd^{147} erneut zu untersuchen.

2. Apparatur

Die Messungen wurden mit einem Doppellinsen-β-Spektrometer und einem NaJ(Tl)-Szintillationsspektrometer in Verbindung mit einer Fast-Slow-Koinzidenzapparatur durchgeführt [18–20]).

Die Auflösungszeit der schnellen Koinzidenzstufe war bei allen Messungen $2\tau \approx 12$ ns. Die Anzahl der zufälligen Koinzidenzen blieb dadurch stets klein gegen die wahre Koinzidenzrate und beeinflußte die Meßgenauigkeit nicht.

Der Raumwinkel, unter dem die Strahlung in das Spektrometer eintrat, betrug 2 % von 4π, die Impulsauflösung war $\Delta p/p = 2.5\,\%$.

Das aktive Material in Form von Neodymchlorid wurde aus Harwell, Berkshire, England, bezogen.

Vorbereitende Messungen wurden mit einer dicken Quelle gemacht. Sie bestand aus ca. 1 mg/cm² natürlichem Neodymchlorid auf einer 5 μm dicken Aluminiumunterlage. Das Neodym war 4 Wochen bei einem Neutronenfluß von etwa 10^{12} Neutronen pro sec pro cm² bestrahlt worden. Den Zerfall dieser Quelle verfolgten wir über 3 Halbwertszeiten. Dabei konnten keine störenden Verunreinigungen festgestellt werden.

Die Analyse der Gesamt- und Koinzidenzspektren ergab die bereits bekannten β-Komponenten mit Endpunktsenergien von etwa 800 keV, 500 keV, 360 keV und 210 keV. Darüber hinaus ergab sich aus den Gesamtspektren sowie aus einem Koinzidenzspektrum mit dem 91.5 keV γ-Übergang eine neue β-Komponente, deren Endpunktsenergie etwa 700 keV betrug.

Für die endgültigen Messungen wurden zwei dünne Quellen von einigen $\mu g/cm^2$ auf 0.4 μm dicken Zaponlack-Folien benutzt. Diese Quellen waren aus *einer* Lieferung von trägerfreiem Neodym-147 hergestellt worden. Die Verfolgung des Zerfalls über 3 Halbwertszeiten ergab ebenfalls keine störenden Verunreinigungen.

Die Stärke einer frischen Quelle betrug etwa 10 μc. Sie war begrenzt durch das Auflösungsvermögen des γ-Spektrometers, dessen Gesamtzählrate 10^4 s^{-1} nicht wesentlich übersteigen sollte.

3. Meßmethode

Der γ-Einkanal wurde auf einen geeigneten Teil des γ-Spektrums eingestellt und ein $\beta-\gamma$-Koinzidenzspektrum aufgenommen. Gleichzeitig wurde die β-Einzelzählrate registriert, um ein β-Gesamtspektrum zu erhalten. Die γ-Einzelzählrate diente zur Kontrolle der γ-Kanal-Einstellung.

Die schnellen Koinzidenz-Kanäle wurden mit Hilfe von Kabelkombinationen gegeneinander verzögert, um Laufzeitunterschiede koinzidenter Signale zu kompensieren. Die notwendigen Verzögerungszeiten als Funktion des Spektrometerstroms und der γ-Kanal-Einstellung wurden experimentell bestimmt.

Die Auflösungszeit der Koinzidenzapparatur wurde für jede Koinzidenzmessung neu gemessen. Zu diesem Zweck wurde die Verzögerung in einem der schnellen Koinzidenzkanäle so groß gemacht, daß keine wahren Koinzidenzen registriert werden konnten. Aus der zufälligen Koinzidenzrate und den Einzelzählraten wurde dann die Auflösungszeit berechnet.

Die Meßdauer je Meßpunkt betrug 50 oder 100 Minuten, die Zeit für die Aufnahme eines Spektrums 2 bis 6 Tage. Die Messungen wurden ohne Unterbrechung durchgeführt; ständige Kontrollen sicherten ein konstantes Arbeiten der Apparatur. Während einer Meßreihe wurde die Netzspannung auf ± 1 ‰, die Raumtemperatur auf $\pm 0.5°$ C konstant gehalten.

4. Ergebnisse

Die Kurie-Analyse der Gesamtspektren ergab für den höchstenergetischen β-Übergang eine Endpunktsenergie von 809 ± 9 keV (Fig. 1) und einen Anteil am Gesamtzerfall des Nd^{147} von 64.7 ± 3.4 %. Die Maximalenergie stimmt mit den Ergebnissen anderer Autoren innerhalb der Fehler überein [11, 13–16].

Für die relative Intensität fanden Emmerich [8]) und Cork [13]) 66 %, dagegen Evans [14]) 76 %.

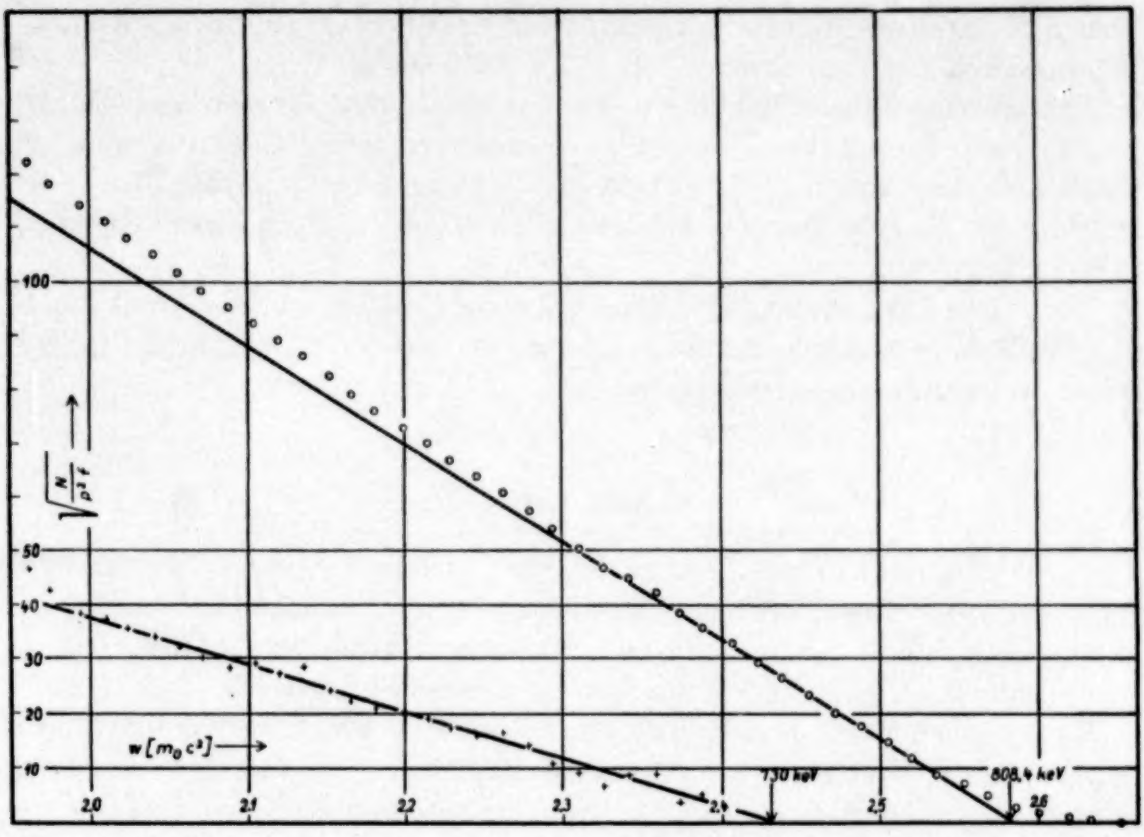

Fig. 1. Kurie-Plot eines hochenergetischen β-Gesamtspektrums mit den Übergängen von 809 keV und 719 keV.

Der 809 keV β-Übergang führt nicht zum Grundniveau des Tochterkerns Pm^{147}. Daher suchten wir nach einer β-Strahlung, deren Endpunktsenergie größer als 809 keV ist. In Übereinstimmung mit anderen Autoren [14]) fanden wir keinen solchen Übergang. Falls ein Zerfall in den Grundzustand Pm^{147} stattfindet, ist er mit weniger als 1 % am Gesamtzerfall beteiligt.

Nach Abzug des 809 keV-Partialspektrums fanden wir in den Gesamtspektren einen bisher noch nicht bekannten Übergang von 719 ± 26 keV Maximalenergie und 10.4 % relativer Intensität (Fig. 1). Das Intensitätsverhältnis der beiden β-Übergänge mit 809 keV und 719 keV blieb über 3 Halbwertszeiten des Neodym-147 innerhalb der Meßgenauigkeit konstant.

Um die Existenz des neugefundenen 719 keV β-Übergangs zu sichern, wurden mehrere Koinzidenzspektren im hochenergetischen Bereich des β-Spektrums mit verschiedener Einstellung des γ-Kanals gemessen. Die Energien der zur Koinzidenz gewählten γ-Strahlen und die Ergebnisse sind in Tabelle 1 einander gegenübergestellt.

TABELLE 1

$\beta-\gamma$-Koinzidenzmessungen mit Elektronen hoher Energie

β-Spektrum in Koinzidenz mit	Ergebnis
(1) 91.5 keV γ-Strahlen	719 keV β-Übergang gegenüber dem 809 keV β-Übergang schwächer als im Gesamtspektrum
(2) 91.5 keV $< E_\gamma \leqq$ 240 keV, ein kleiner Teil des 91.5 keV γ-Peaks liegt noch im γ-Kanal	719 keV Übergang gegenüber dem 809 keV Übergang stärker als im Gesamtspektrum
(3) 140 keV $\leqq E_\gamma \leqq$ 250 keV	nur noch 719 keV Übergang, mit viel geringerer Intensität als bei (2).

Aus diesen Messungen ergibt sich, daß der 719 keV β-Zerfall in Koinzidenz mit dem 91.5 keV γ-Übergang und einer γ-Strahlung zwischen 140 keV und 250 keV ist.

Der Versuch, die Energie des zweiten γ-Übergangs genauer zu bestimmen, scheiterte an der geringen Intensität dieser Strahlung.

Auf Grund unserer Ergebnisse ordneten wir den 719 keV β-Übergang dem Zerfall des Nd^{147} zu.

Die weitere Analyse der Gesamtspektren zeigte eine β-Komponente von etwa 520 keV Maximalenergie, deren Anteil am Gesamtzerfall kleiner als 1 % ist. Frühere Untersuchungen ergaben die Endpunktsenergie zu 529 $\pm$25 keV (Berenyi [16]), bzw. 472 keV (Mitchell [15]). Aus γ-Intensitätsmessungen hatten Hans *et al.* [10]) auf einen β-Übergang von etwa 500 keV Endpunktsenergie mit einer relativen Intensität von ungefähr 3 % geschlossen.

In unseren Gesamtspektren ergab dieser Übergang keinen geraden Kurie-Plot; die Meßpunkte lagen vielmehr auf einer Kurve stark wechselnder Krümmung. Die Ansicht, es könne sich hier um einen eindeutig einfach verbotenen Übergang handeln, wie sie Berenyi [16]) geäußert hat, erscheint uns allerdings nicht vertretbar. Die Krümmung ist zu stark und erstreckt sich nur über ein kurzes Stück des Kurie-Plots, an das sich ein gerader Teil anschließt. Wird nur dieser Teil linear bis zur Abszisse extrapoliert, so ergibt sich eine Endpunktsenergie von etwa 480 keV.

Ein Vergleich mit Koinzidenzmessungen zeigte, daß an dieser Stelle das Spektrum durch Elektronen, die nicht zur β-Strahlung des Nd^{147} gehören, verdeckt wird. Hervorgerufen wird diese Störung durch Photoelektronen, die von der sehr intensiven 530 keV γ-Strahlung an den Blenden des β-Spektrometers ausgelöst werden. Sie machte eine weitere Analyse des Gesamtspektrums sehr unsicher. Da außerdem durch das zweimalige Subtrahieren der Teilspektren erhebliche Fehler entstanden sein konnten, stützten wir uns bei der Unter-

suchung der übrigen β-Komponenten auf 6 mit verschiedenen γ-Energien aufgenommene Koinzidenzspektren.

Für den erwähnten β-Übergang fanden wir eine Endpunktsenergie von 480 ± 80 keV; sein Anteil am Gesamtzerfall ist 0.5 ± 0.1 % (Fig. 2). Die

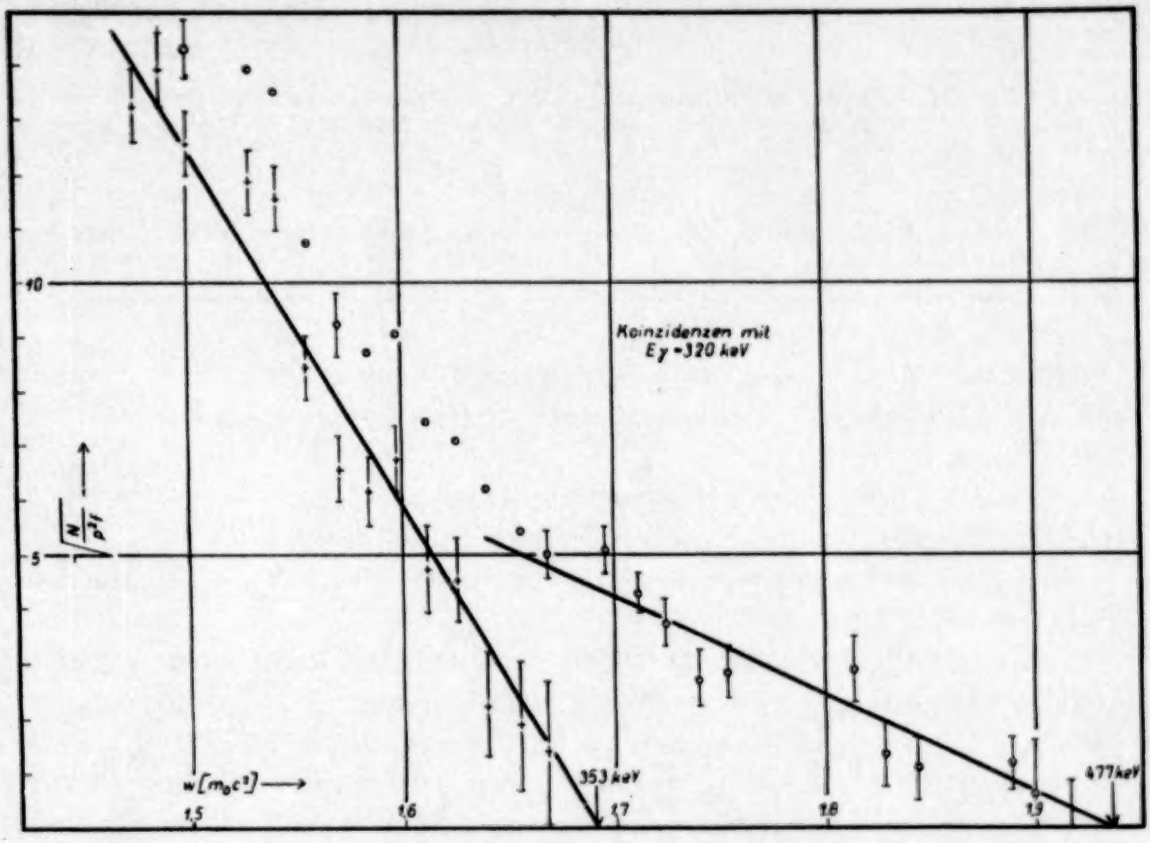

Fig. 2. Kurie-Plot eines β-Koinzidenzspektrums ($E_\gamma = 320$ keV) mit den Übergängen von 480 keV und 370 keV.

Maximalenergie der letzten beiden Komponenten erhielten wir zu 370 ± 9 keV und 215 ± 9 keV in Übereinstimmung mit früheren Arbeiten [13–16]). Die relativen Intensitäten betragen 12.1 ± 1.8 % bzw. 12.3 ± 1.8 % (Fig. 3).

Die Meßergebnisse sind noch einmal in Tabelle 2 zusammengestellt. Neben den Maximalenergien und Anteilen am Gesamtzerfall sind die log *ft* Werte angegeben. Aus ihrer Größe und der Tatsache, daß alle Kurie-Plots innerhalb der Meßgenauigkeit linear sind, lassen sich die beobachteten β-Übergänge als einfach verboten mit erlaubtem Spektrum klassifizieren. Eine Ausnahme macht möglicherweise der 480 keV Übergang, bei dem die Meßergebnisse mit einer zu großen Unsicherheit behaftet sind.

In der vierten Spalte stehen die γ-Übergänge, mit denen die β-Komponenten eindeutig in Koinzidenz gefunden wurden. Die letzte Spalte enthält Hinweise

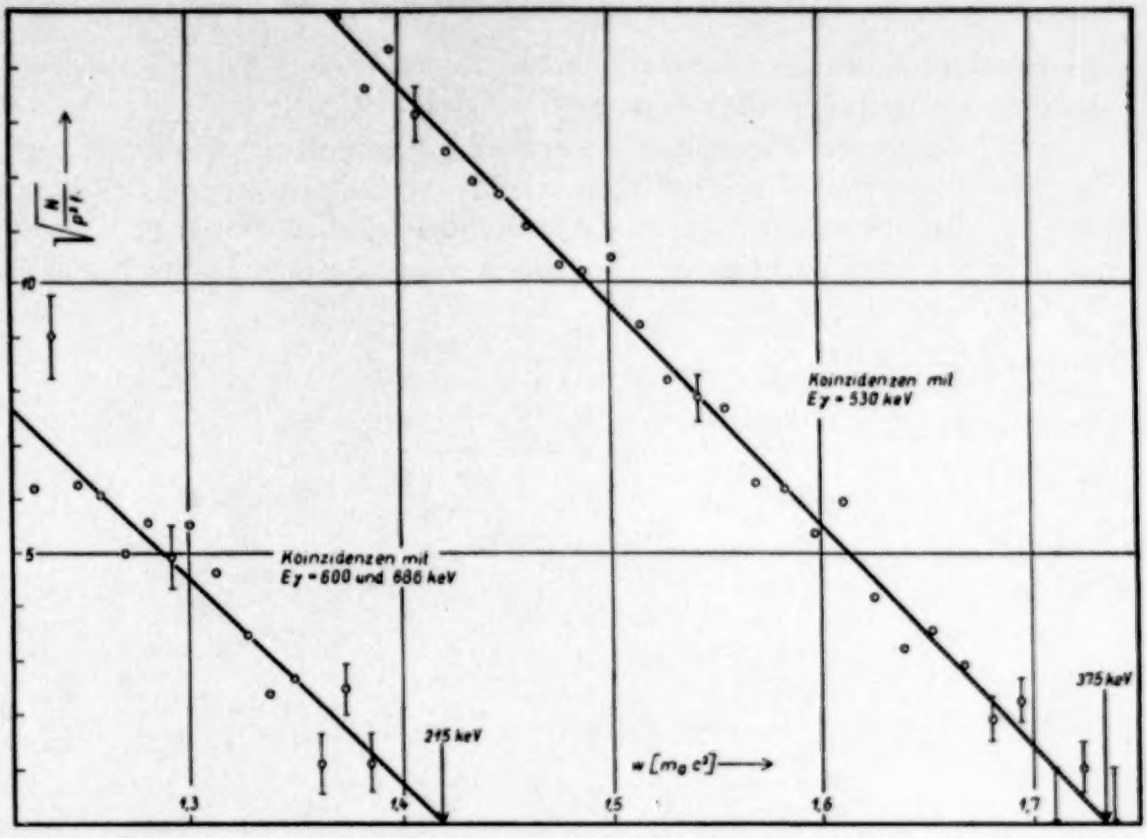

Fig. 3. Kurie-Plot zweier Koinzidenzspektren (E_γ = 530 keV bzw. 600 keV) mit den Übergängen 370 keV und 215 keV.

TABELLE 2

Die β-Übergänge des Nd^{147} Zerfalls

Endpunktsenergie in keV	Beteiligung am Gesamtzerfall in %	log *ft*	koinzident mit γ-Übergang (Energie in keV)	Beobachtungsmethoden † (Energie in keV)
809± 9	64.7±3.4	7.6	91.5	Gesamtspektrum, Koinz.-Spektrum mit $E_\gamma = 91.5$
719±26	10.4±1.4	8.1	91.5 $140 \leqq E_\gamma \leqq 240$	Gesamtspektrum, Koinz.-Spektren mit $E_\gamma = 91.5$, $92 < E_\gamma \leqq 240$, $140 \leqq E_\gamma \leqq 250$
480±80	0.5±0.1	9.0	320	Gesamtspektrum, Koinz.-Spektrum mit $E_\gamma = 320$
370± 9	12.1±1.8	7.3	530 440	Koinz.-Spektren mit $E_\gamma = 530$, $E_\gamma = 440$, $298 \leqq E_\gamma \leqq 350$, $258 \leqq E_\gamma \leqq 293$, $198 \leqq E_\gamma \leqq 277$
215± 9	12.3±1.8	6.5	686 595	Koinz. Spektren mit $E_\gamma = 595$ und 686, $298 \leqq E_\gamma \leqq 350$, $258 \leqq E_\gamma \leqq 293$, $198 \leqq E_\gamma \leqq 277$, $385 \leqq E_\gamma \leqq 473$, $480 \leqq E_\gamma \leqq 580$
>809	<1.0	>9.5		Übergang zum Grundzustand, im Gesamtspektrum nicht gefunden

† Bei Koinzidenzmessungen, die nur durch den Bereich der zugelassenen γ-Energien gekennzeichnet sind, ist mindestens ein Teil der Koinzidenzen durch die Comptonverteilung einer γ-Strahlung höherer Energie hervorgerufen.

auf die Untersuchungsmethode. Alle Fehler sind mittlere Fehler der nach der Methode kleinster Quadrate berechneten Werte.

Aus Messungen zur Einstellung der schnellen Koinzidenzstufe ergeben sich für einige angeregte Niveaus des Tochterkerns Pm^{147} obere Grenzen der Halbwertszeit. Zusammen mit der bereits von Graham und Bell [21]) und Bodenstedt *et al.* [22]) gemessenen Halbwertszeit des 91.5 keV Niveaus sind die Ergebnisse in Tabelle 3 aufgetragen.

TABELLE 3

Lebensdauer angeregter Niveaus von Pm^{147}

Niveau (keV)	$T_{\frac{1}{2}}$ (10^{-9} sec)
91.5	2.45 ± 0.2 (2.44 nach Ref. [21, 22])
410	<0.7
530	<0.6
686	<0.8

5. Das Zerfallsschema des Neodym-147

Auf Grund der Ergebnisse unserer β—γ-Koinzidenzmessungen haben wir ein neues Zerfallsschema für das Neodym-147 aufgestellt (Fig. 4). Es enthält einen

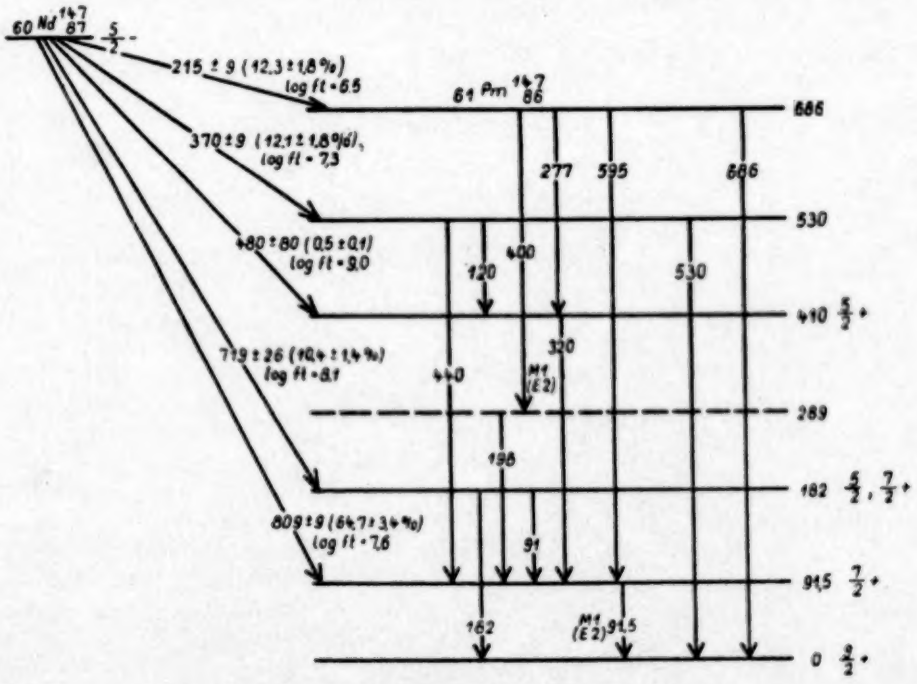

Fig. 4. Zerfallsschema des Nd^{147}.

β-Übergang und ein angeregtes Niveau mehr als früher angegebene Schemata [13, 14]).

Bei der Einordnung der γ-Übergänge benutzten wir auch noch die Ergebnisse von Cork [13]) und die $\gamma-\gamma$-Koinzidenzmessungen von Bodenstedt [17]).

Der 91.5 keV γ-Übergang muß wegen seiner großen Intensität auf den Grundzustand des Pm^{147} führen [14]). Aus unseren Koinzidenzmessungen folgt damit, daß der 809 keV β-Übergang das erste angeregte Niveau von 91.5 keV erreicht. Aus den Endpunktsenergien der übrigen β-Übergänge ergeben sich dann angeregte Niveaus von 182 keV, 410 keV, 530 keV und 686 keV.

Das Niveau bei 289 keV ist nur durch die Tripelkaskade der 400 keV–198 keV–91.5 keV γ-Übergänge bestimmt. Die im Schema angegebene Reihenfolge der beiden γ-Strahlungen von 400 keV und 198 keV ist von Cork [13]) vorgeschlagen worden, während Evans [14]) durch Annahme der umgekehrten Reihenfolge zu einem Niveau bei 490 keV gelangte. Aus unseren Messungen lassen sich keine Aussagen über die Lage dieses Niveaus machen. Wir haben daher den Vorschlag von Cork in unser Schema übernommen.

Die Einordnung der γ-Übergänge von 91.5 keV, 91 keV, 182 keV, 320 keV, 440 keV, 530 keV, 595 keV und 686 keV erfolgte nach unseren $\beta-\gamma$-Koinzidenzmessungen. Alle anderen wurden nach den Ergebnissen der $\gamma-\gamma$-Koinzidenzmessungen von Bodenstedt [17]) und Cork [13]) eingefügt. Die Energien 91 keV und 182 keV der beiden γ-Strahlungen, die das 182 keV Niveau entregen, sind aus den Energieunterschieden der beteiligten Niveaus entnommen.

6. Diskussion der Spins beim Promethium-147

Auf Grund von Winkelkorrelationsmessungen ordneten Lindqvist *et al.* [12]) den Niveaus von Pm^{147} Spins zu. Sie gingen dabei von der Annahme aus, daß der bis dahin noch nicht gemessene Spin des Nd^{147}-Grundzustandes dem Schalenmodell entsprechend $\frac{9}{2}-$ sei†. Später bestimmten Kedzie *et al.* [23]) jedoch dessen Spin mit der Methode der paramagnetischen Kernresonanz zu $\frac{5}{2}$ mit negativer Parität (Strominger *et al.* [24])). Auf dieser Grundlage erscheint eine neue Diskussion der Spinzuordnung angebracht.

Der β-Übergang zum ersten angeregten Niveau des Pm^{147} hat erlaubte Form; der log *ft* Wert klassifiziert ihn als einfach verboten. Damit ergibt sich als Spin für das 91.5 keV Niveau $I = \frac{7}{2}+$, $\frac{5}{2}+$ oder $\frac{3}{2}+$.

Der 91.5 keV Übergang ist von Lindqvist *et al.* [12]) sowie Bodenstedt [17]) als M1(E2)-Strahlung identifiziert worden. Der β-Übergang vom Grundzustand des Pm^{147} zum Grundzustand des Sm^{147} ist einfach verboten mit erlaubter Form [25]). Der Spin des Sm^{147}-Grundzustandes ist $I = \frac{7}{2}-$ [24, 26]).

Aus diesen Befunden ergibt sich für den Spin des Pm^{147}-Grundzustandes $\frac{5}{2}$, $\frac{7}{2}$ oder $\frac{9}{2}$ mit positiver Parität. Da jedoch der β-Übergang zum Grundzustand des Pm^{147} nicht mit merklicher Intensität auftritt, kann dessen Spin nur $\frac{9}{2}+$ betragen. Für das 91.5 keV Niveau ergibt sich daraus $I = \frac{7}{2}+$.

† Siehe Anmerkung bei der Korrektur.

Auch der 719 keV β-Übergang ist einfach verboten ($\log ft = 8.1$) mit erlaubter Form. Von den dadurch möglichen Werten $\frac{3}{2}+$, $\frac{5}{2}+$, $\frac{7}{2}+$ für den Spin des 182 keV Niveaus ist $\frac{3}{2}+$ unwahrscheinlich, weil der 182 keV γ-Übergang zum Grundniveau mit verhältnismäßig großer Intensität auftritt.

Bodenstedt *et al.* [17]) bestimmten den Multipolcharakter der 320 keV γ-Strahlung zu M1(E2) und schlossen auf $I = \frac{5}{2}+$ für den Spin des 410 keV Niveaus; dieser Wert ist mit $\log ft = 9.0$ für den 480 keV β-Übergang verträglich.

Der Spin $\frac{9}{2}$ des Pm^{147}-Grundzustandes ist nicht in Übereinstimmung mit den Voraussagen des Schalenmodells, das für das unpaarige Proton eine $1g_{\frac{7}{2}}$-Konfiguration erwarten läßt. Auch die Annahme einer Deformation liefert mit Nielsson's [27]) Modell keine Erklärung.

Wir danken dem Direktor des Instituts, Herrn Professor Dr. H. Neuert, für sein stetes Interesse und seine Hilfsbereitschaft. Wertvolle Ratschläge für den Bau und Betrieb der Koinzidenzapparatur gaben Herr Dr. H. J. Stuckenberg und Herr Dr. E. Bodenstedt und seine Mitarbeiter, die uns auch freundlicherweise ihre Ergebnisse vor der Veröffentlichung überließen.

Diese Arbeit wurde durch Mittel der Deutschen Forschungsgemeinschaft unterstützt.

Anhang

1. BESTIMMUNG DER RELATIVEN β-INTENSITÄTEN AUS DEN GESAMTSPEKTREN

Aus den gemessenen Gesamtspektren lassen sich die relativen Intensitäten der durch Kurie-Analyse gefundenen β-Übergänge leicht ermitteln. Bedeutet $N(p)$ die auf das Impulsintervall Eins reduzierte β-Einzelzählrate und

$$N_{\beta E}(p) = p^2 F(p, Z)(a+bW)^2 = p^2 F(p, Z) b^2 (W_0 - W)^2$$

das aus der Kurie-Analyse gewonnene Partialspektrum mit der Endpunktsenergie $E = (W_0 - 1)$, $W_0 = -a/b$,
so ist die relative Intensität des β-Übergangs mit der Endpunktsenergie E

$$I_{\beta E} = \frac{\int N_{\beta E}(p)\,dp}{\int N(p)\,dp} = \frac{\bar{N}_{\beta E}}{\bar{N}}. \tag{1}$$

Die Integrale zur Berechnung von $I_{\beta E}$ erhielten wir durch graphische Integration.

Der Fehler von $I_{\beta E}$ wird im wesentlichen durch die Fehler Δa und Δb der Parameter a und b bestimmt, die in das Integral des Zählers eingehen. Nach dem Fehlerfortpflanzungsgesetz ist dessen Fehler

$$\Delta \bar{N}_{\beta E} = \left\{ \left(\frac{\partial \bar{N}_{\beta E}}{\partial a} \right)^2 (\Delta a)^2 + \left(\frac{\partial \bar{N}_{\beta E}}{\partial b} \right)^2 (\Delta b)^2 \right\}^{\frac{1}{2}}. \tag{2}$$

Zu seiner Abschätzung berechnen wir

$$\frac{\partial \bar{N}_{\beta E}}{\partial a} = -2b \cdot \int_0^{p_0} p^2 F(p, Z)(W_0 - W)\mathrm{d}p, \tag{3}$$

$$\frac{\partial \bar{N}_{\beta E}}{\partial b} = 2\left\{\frac{1}{b}\bar{N}_{\beta E} + a\int_0^{p_0} p^2 F(p, Z)(W_0 - W)\mathrm{d}p\right\}. \tag{4}$$

Das in den partiellen Ableitungen (3) und (4) auftretende Integral

$$\int_0^{p_0} p^2 F(p, Z)(W_0 - W)\mathrm{d}p \tag{5}$$

läßt sich ebenfalls durch graphische Integration ermitteln. Um aber diese sehr mühsame Arbeit zu umgehen, schätzen wir es nach oben ab.

Wie man leicht zeigen kann, ist $W_0 - W \leqq p_0 - p$ im Intervall $0 \leqq p \leqq p_0$. Das Produkt $p^2 F(p, Z)$ hat als Funktion von p einen nach oben konkaven Verlauf und verschwindet für $p = 0$; daher gilt im Bereich $0 \leqq p \leqq p_0$

$$p^2 F(p, Z) \leqq p_0 F(p_0, Z) p.$$

Daraus ergibt sich für den Integranden

$$p^2 F(p, Z)(W_0 - W) \leqq p_0 F(p_0, Z) p(p_0 - p),$$

und das Integral (5) wird

$$\int_0^{p_0} p^2 F(p, Z)(W_0 - W)\mathrm{d}p \leqq \int_0^{p_0} p_0 F(p_0, Z) p(p_0 - p)\mathrm{d}p = p_0^2 F(p_0, Z)\frac{p_0}{6}. \tag{6}$$

Der Fehler (2) der relativen Intensität $I_{\beta E}(1)$ ergibt sich dann mit (3), (4) und (6) zu

$$\Delta I_{\beta E} \leqq \frac{2}{\bar{N}}\left\{\left(b p_0^2 F(p_0, Z)\frac{p_0^2}{6}\right)^2 (\Delta a)^2 + \left(\frac{\bar{N}_{\beta E}}{b} + a p_0^2 F(p_0, Z)\frac{p_0^2}{6}\right)^2 (\Delta b)^2\right\}^{\frac{1}{2}}. \tag{7}$$

2. BESTIMMUNG DER RELATIVEN β-INTENSITÄTEN AUS DEN KOINZIDENZSPEKTREN

Eine Kurie-Analyse der Koinzidenzspektren liefert zunächst nur die Endpunktsenergien der einzelnen β-Komponenten. Um auch die Intensitäten der β-Übergänge zu bestimmen, müssen die Einzelzählraten des γ-Kanals berücksichtigt werden.

In dem Szintillationsspektrum eines Zerfalls mit zahlreichen γ-Übergängen sitzen die Photopeaks der γ-Strahlen mittlerer und niedriger Energie stets auf einer breiten Compton-Verteilung, die von γ-Strahlen höherer Energie erzeugt wird. Es ist daher unmöglich, durch die Einstellung des γ-Einkanals auf einen solchen Photopeak die Signale dieser Strahlung von den Signalen eines γ-

Übergangs mit hoher Energie zu trennen. In diesem Fall erscheint in einem β-Koinzidenzspektrum mit dem Photopeak einer γ-Strahlung nicht nur die hiermit koinzidente β-Komponente allein. Über die Anteile der Compton-Verteilungen, die in den γ-Einkanal fallen, erhält man alle zu γ-Übergängen höherer Energie gehörende β-Anteile, die durch eine Kurie-Analyse voneinander getrennt werden können. Nur bei den γ-Strahlungen mit den größten Energien, deren Photopeaks nicht auf einer Compton-Verteilung sitzen, lassen sich die zugehörigen β-Übergänge in den Koinzidenzspektren rein erhalten.

Eine Trennung der in den γ-Kanal fallenden Signale in die verschiedenen Photopeaks- und Compton-Anteile ist sehr schwierig. Es müßten nämlich nicht nur die Photo- und Compton-Prozesse im γ-Szintillator berücksichtigt werden, sondern z.B. auch die Comptonstreuung der den Szintillator umgebenden Teile des Spektrometers, der Einfluß des Lichtleiters auf die Signalgröße und die Koinzidenzverluste in der Nachweisapparatur. Hierzu käme noch eine Bestimmung der relativen Intensitäten aller γ-Übergänge, die zu einem bestimmten angeregten Niveau hinführen bzw. von ihm wegführen. Da viele dieser Größen nur ungenau bekannt sind, würden die so gewonnenen Ergebnisse mit einer erheblichen Unsicherheit behaftet sein.

Eine genaue Untersuchung der Beziehungen zwischen der γ-Einzelzählrate und den in dem Koinzidenzspektrum vorhandenen β-Komponenten zeigt indes, daß eine detaillierte Kenntnis dieser Daten zur Bestimmung der relativen β-Intensitäten nicht notwendig ist.

Es sei

N_0 die absolute Quellenstärke,

ε die Wahrscheinlichkeit, daß ein Elektron mit dem Impuls p, das die Quelle verläßt, im β-Kanal registriert wird, wenn das β-Spektrometer Elektronen mit dem Impuls p fokussiert,

$I_{\beta E}$ die relative Intensität des β-Übergangs mit der Endpunktsenergie E,

$i_{\beta E}(p)$ die Wahrschienlichkeit, daß ein Elektron des β-Anteils mit der Endpunktsenergie E gerade den Impuls p besitzt, mit der Normierung $\int i_{\beta E}(p)\mathrm{d}p = 1$,

$N_{\beta E}(p)$ die aus dem Kurie-Plot des Koinzidenzspektrums ermittelte Zählrate des β-Anteils der Endpunktsenergie E,

$P^{\gamma}_{\beta E}$ die relative Intensität, mit der γ-Quanten, die mit dem β-Übergang der Endpunktsenergie E koinzident sind, im γ-Kanal des Spektrometers registriert werden.

Dann ergibt sich die Koinzidenzrate zu

$$N_{\beta E}(p) = N_0 \varepsilon I_{\beta E} i_{\beta E}(p) P^{\gamma}_{\beta E} \tag{8}$$

für jeden in dem Koinzidenzspektrum vertretenen β-Übergang. Durch Integration erhält man aus (8)

$$\int N_{\beta E}(p)\mathrm{d}p = \bar{N}_{\beta E} = N_0 \varepsilon I_{\beta E} P^{\gamma}_{\beta E}. \tag{9}$$

Da jeder γ-Übergang mit *genau einem* β-Übergang koinzidiert, setzt sich die γ-Einzelzählrate N_γ additiv aus den Anteilen $N_0 P^\gamma_{\beta E}$ zusammen. Hinzu kommt noch die Untergrundzählrate C, die natürlich mit keinem β-Übergang koinzident ist:

$$N_\gamma = \sum_{\beta E} N_0 P^\gamma_{\beta E} + C. \tag{10}$$

Löst man (9) nach $N_0 P^\gamma_{\beta E}$ auf und setzt in (10) ein, so ergibt sich

$$N_\gamma = \sum_{\beta E} \frac{\bar{N}_{\beta E}}{\varepsilon I_{\beta E}} + C \tag{11}$$

für jedes einzelne Koinzidenzspektrum.

Hierin sind bekannt die γ-Einzelzählrate N_γ, die Größen $\bar{N}_{\beta E}$ aus der Kurie-Analyse und die Untergrundzählrate C, die bei $N_\gamma \gg C$ vernachlässigt werden kann.

Um die Produkte $\varepsilon I_{\beta E}$ berechnen zu können, benötigt man mindestens so viele von einander unabhängige Koinzidenzspektren, wie β-Komponenten in ihnen auftreten. Sind mehr Koinzidenzspektren gemessen worden, so daß das Gleichungssystem (11) überbestimmt ist, müssen die Größen $\varepsilon I_{\beta E}$ durch Ausgleichsrechnung ermittelt werden.

Die Kenntnis von ε ist nicht notwendig. Da trivialerweise $\sum I_{\beta E} = 1$ ist, wenn über alle am Zerfall beteiligten β-Übergänge summiert wird, brauchen nur die Verhältnisse der Intensitäten bekannt zu sein. Die Fehler der Intensitäten ergeben sich aus (7) und gegebenenfalls aus der Ausgleichsrechnung.

Anmerkung bei der Korrektür: In einer kurzlich veroffentlichten Arbeit bestimmten Klinkenberg und Tomkins [28]) den Spin des Grundzugstandes von Promethium-147 zu $\frac{7}{2}$ durch die Untersuchung der optischen Hyperfeinstruktur. Ebenso finden Bodenstedt *et al.* [29]), daß ein Spin von $\frac{7}{2}+$ für den Grundzustand und $\frac{5}{2}+$ für das 91.5 keV Niveau ihren g-Faktormessungen besser entspricht. Weiterhin geben sie auf Grund von $\gamma-\gamma$-Winkelkorrelationsmessungen Spins für folgende angeregte Zustünde im Pm^{147} an: 410 keV $\frac{5}{2}+$; 530 keV $\frac{3}{2}+$ oder $\frac{7}{2}+$; 686 keV $\frac{7}{2}+$ oder $\frac{3}{2}+$. Diese Ergebnisse sind mit unseren Messungen verträglich, jedoch ist es nur schwer zu verstehen, warum der β-Übergang vom Nd^{147} mit dem Spin $\frac{5}{2}-$ zum Grundzustand des Pm^{147} nicht mit merklicher Intensität auftritt. Ein Spin von $\frac{3}{2}-$ des Nd^{147}-Grundzustandes würde diese Schwierigkeiten beseitigen.

Literaturverzeichnis

1) H. B. Law, M. L. Pool, J. D. Kurbatov und L. L. Quill, Phys. Rev. **59** (1941) 936
2) J. A. Marinsky, L. E. Glendenin und C. D. Coryell, J. Am. Chem. Soc. **69** (1947) 2781
3) R. J. Hayden, Phys. Rev. **74** (1948) 650
4) W. Bothe, Z. Naturforsch. **1** (1946) 179

5) J. M. Cork, R. G. Shreffler und C. M. Fowler, Phys. Rev. **74** (1948) 240
6) C. E. Mandeville und E. Shapiro, Phys. Rev. **79** (1951) 391
7) E. Kondaiah und K. Siegbahn, Phys. Rev. **81** (1951) 1056;
E. Kondaiah, Arkiv för Fysik **4** (1952) 81
8) W. Emmerich und J. D. Kurbatov, Phys. Rev. **81** (1951) 1062; **83** (1951) 40
9) W. C. Rutledge, J. M. Cork und S. B. Burson, Phys. Rev. **86** (1952) 775
10) H. S. Hans, B. Saraf und C. E. Mandeville, Phys. Rev. **97** (1955) 1267; **98** (1955) 1173
11) G. T. Ewan, M. A. Clark und J. W. Knowles, AECL PR-P-30 (1956) (zitiert nach Berenyi [16]))
12) T. Lindqvist und E. Karlsson, Arkiv för Fysik **12** (1957) 519
13) J. M. Cork, M. K. Brice, R. G. Helmer und R. M. Woods, Phys. Rev. **110** (1958) 526
14) P. R. Evans, Phil. Mag. **3** (1958) 1061
15) A. C. G. Mitchell, C. B. Creager und C. W. Kocher, Phys. Rev. **111** (1958) 1343
16) D. Berenyi, Nuclear Physics **8** (1958) 607
17) E. Bodenstedt, H. J. Körner und E. Matthias, Priv. Mitt. (1959)
18) R. H. Siemssen, Diplomarbeit, Hamburg (1958)
19) H.-D. Wendt, Dissertation, Hamburg (1959)
20) P. Kleinheinz, Diplomarbeit, Hamburg (1960) (in Vorbereitung)
21) R. L. Graham und R. E. Bell, Can. J. Phys. **31** (1953) 377
22) E. Bodenstedt, E. Matthias, H. J. Körner und R. H. Siemssen, Z. Naturforsch. **13a** (1958) 425
23) R. W. Kedzie, M. Abraham und C. D. Jeffries, Phys. Rev. **108** (1957) 54
24) D. Strominger, J. M. Hollander und G. T. Seaborg, Rev. Mod. Phys. **30** (1958) 585
25) H. Agnew, Phys. Rev. **77** (1950) 655;
T. D. Nainan, H. G. Deware und A. Mukerji, Proc. Indian Acad. Sci. **44A** (1956) 111
26) G. S. Bogle und H. E. D. Scovil, Proc. Phys. Soc. A **65** (1952) 360;
K. Mukarawa, Phys. Rev. **93** (1954) 1232;
K. Mukarawa und S. Suwa, Rep. Inst. Sci. Technol. Univ. of Tokyo **6** (1952) 209
27) S. G. Nielsson, Mat. Fys. Medd. Dan. Vid. Selsk. **29** Nr. 16 (1955)
28) P. F. A. Klinkenberg und F. S. Tomkins, Physica **26** (1960) 103
29) E. Bodenstedt, H. J. Körner, F. Friesius, D. Hovestadt und E. Gerdau,
Zs. f. Physik (erscheint demnächst)

2.A.1

Nuclear Physics **20** (1960) 183—187; © *North-Holland Publishing Co., Amsterdam*

Not to be reproduced by photoprint or microfilm without written permission from the publisher

THERMAL NEUTRON CROSS SECTIONS FOR PRODUCING ISOMERS (II)

H. S. HANS, M. L. SEHGAL and P. S. GILL

Department of physics, Muslim University, Aligarh, India

Received 13 June 1960

Abstract: Thermal neutron cross sections for the production of isomers have been measured for the following cases, by making irradiations with the swimming pool reactor at Trombay, Bombay:

Se^{78} $(n, \gamma)Se^{79m}$, Sr^{84} $(n, \gamma)Sr^{85m}$, Sr^{84} $(n, \gamma)Sr^{85}$,
Rb^{85} $(n, \gamma)Rb^{86m}$, $Ba^{132}(n, \gamma)Ba^{133m}$, $Ba^{134}(n, \gamma)Ba^{135m}$
$Ba^{136}(n, \gamma)Ba^{137m}$, Os^{190} $(n, \gamma)Os^{191, 191m}$ and some others.

Activation method was employed using scintillation technique. Isomeric ratios seem to follow the rule of Mateosian and Goldhaber [10]).

1. Introduction

The cross-sections for the production of isomers by the absorption of thermal neutrons have been measured earlier by us using scintillation technique [1]). The measurements reported herein are in continuation of the earlier ones [1, 2]). The procedure is the same as described before. Irradiations were made both in the thermal column as well as near the core of the reactor. The substances studied in the present case were obtained from Johnson Mathey and Co.,Ltd. (London) and had a purity of better than 99.9 %. Au^{197} was used as the standard substance with an absorption cross-section of 98 ± 1 barns [3]). In those cases, in which irradiations were made near the core, percentage of resonance neutrons was taken into account by usual cadmium ratio.

2. Measurements

2.1. $Se^{76}(n, \gamma)Se^{77m}$ and $Se^{78}(n, \gamma)Se^{79}$

For measuring the above cross-section, selenium was taken in the metallic form and irradiations were made in the irradiation pipe near the core for 5 min at a low power level of the reactor. After irradiation, the total integrated counting rate for γ-rays above the pulse height of 1 V was measured as a function of time. The background activity due to Se^{81m}, with a half-life of 57 min was subtracted from the main decay curve, giving two activities, one of 3.85 min for Se^{79m}, and other of 18 s for Se^{77m}. The decay scheme of Se^{77m} and

Se^{79m}, and also the value of the conversion coefficient of 96 keV γ-ray is taken from Strominger, Hollander and Seaborg [4]). The internal conversion coefficient for 160 keV γ-ray due to the decay of Se^{77m}, was calculated from the conversion table of Rose [5]).

2.2. $Rb^{85}(n, \gamma)Rb^{86m}$

For measuring the cross-section of 1 min activity due to Rb^{86m}, rubidium chloride was taken in the powder form and the irradiations were made near the core at low power level of the reactor. The integrated counting rate above 3 V, was plotted as function of time and the 18 min activity due to Rb^{88m}, was subtracted which gave us an activity of 1.06 min due to Rb^{86m}. The correction was applied for counts between zero to 3 V. Although the type of 560 keV γ-ray is not known, plausibly it may be taken as either E3 or E4 from shell model considerations. In any case, as the energy of the γ-ray is quite high (560 keV), the error introduced due to internal conversion coefficient will be less than 2 %.

2.3. $Sr^{84}(n, \gamma)Sr^{85m}$, $Sr^{84}(n, \gamma)Sr^{85}$ and Sr^{86} $(n, \gamma)Sr^{87m}$

The cross-section for $Sr^{84}(n, \gamma)Sr^{85m}$ reaction was measured by bombarding Sr CO_3 near the core. The γ-ray spectrum was taken at different times and the decay curve was drawn for the integrated counts from which 70 min activity due to Sr^{85m} could be separated and the cross-section was determined as usual. The decay scheme and conversion coefficient were taken from Sunyar *et al.* [6]).

The cross-section for $Sr^{84}(n, \gamma)Sr^{85}$ was measured by irradiating a separate sample for 1 h near the core. The spectrum was taken after 16 d, such that the activities due to Sr^{85m} and Sr^{87m} had decayed. The area under the Photo-peak of 513 keV γ-ray gives the contribution from $Sr^{84}(n, \gamma)Sr^{85}$ as well as from the subsequent decay of Sr^{85m}, into Sr^{85}. The latter could be taken into account as the cross-section for $Sr^{84}(n, \gamma)Sr^{85m}$ was measured separately.

For measuring the cross-section for $Sr^{86}(n, \gamma)Sr^{87m}$, irradiations were made still with a fresh sample. The cross-section for this reaction was found from the area under the photo peak of 388 keV γ-ray.

2.4. $Ba^{136}(n, \gamma)Ba^{137m}$, $Ba^{132}(n, \gamma)Ba^{133m}$ and $Ba^{134}(n, \gamma)Ba^{135m}$

For the cross-section of $Ba^{136}(n, \gamma)Ba^{137m}$, reaction Ba CO_3 was irradiated, and taking the integrated counting rate, for γ-ray pulses above 6 V, the 2.6 min activity due to Ba^{137m} was separated from the decay curve. The correction due to counts between 0 and 6 V was applied with the help of a standard Cs^{137} source.

For measuring the cross-sections for $Ba^{132}(n, \gamma)Ba^{133m}$, and $Ba^{134}(n, \gamma)Ba^{135m}$ reactions, irradiations were made for a longer time near the core. The short life activities due to Ba^{137m} and Ba^{139} were first allowed to decay and the spectrum was taken on different days. From these spectra the decay curve was drawn by

taking the area under the photo-peak of the 276 keV γ-ray. After subtracting background activity of 12 d due to Ba^{131} an activity of 39 h was obtained which was assigned to Ba^{133m}. The 28 h activity due to Ba^{135m}, was too small to be distinctly separated, so only an upper limit was put for the cross-section of $Ba^{134}(n, \gamma)Ba^{135m}$. For measuring the cross-section for $Ba^{132}(n, \gamma)Ba^{133m}$ reaction, the percentage abundance of Ba^{132} is taken 0.19 % as given by Akishin *et al.* [7]), instead of 0.097 % as given by Nier [8]). The value of the internal conversion coefficient of the 276 keV γ-ray was got from the result of Hill and Cork [9]).

2.5. $Os^{190}(n, \gamma)Os^{191m, 191}$ and $Os^{189}(n, \gamma)Os^{190m}$

The cross-section for the combined reaction $Os^{190}(n, \gamma)Os^{191m}$ and $Os^{190}(n, \gamma)Os^{191}$ was measured by bombarding osmium metal sponge in the thermal column and studying its γ-ray spectrum at various intervals of time. Only the combined cross-section could be measured, because of the uncertainty about the K-conversion coefficient of the 74 keV γ-ray.

To measure the cross-section for $Os^{189}(n, \gamma)Os^{190m}$, a different sample of osmium sponge was bombarded with neutrons in the thermal column. Only the upper limit for its cross-section could be obtained.

The results of all the measurements are given in table 1.

TABLE 1

Experimental results

Reaction	Half life measured or used	Cross-section (barns)	
		this work	other authors [3])
$Se^{76}(n, \gamma)Se^{77m}$	17.0 s	10 ± 3	7 ± 3
$Se^{78}(n, \gamma)Se^{79m}$	3.9 min	0.12 ± 0.04	
$Sr^{84}(n, \gamma)Sr^{85m}$	65 d	0.4 ± 0.2	
$Sr^{84}(n, \gamma)Sr^{84m}$	70 m	0.6 ± 0.2	1 ± 0.3
$Sr^{86}(n, \gamma)Sr^{87m}$	2.8 h	0.8 ± 0.25	1.3 ± 0.4
$Rb^{85}(n, \gamma)Rb^{86m}$	1.06 min	0.007 ± 0.002	
$Ba^{132}(n, \gamma)Ba^{133m}$	39 h	4.1 ± 1.5	
$Ba^{134}(n, \gamma)Ba^{135m}$	28 h	< 0.05	
$Ba^{136}(n, \gamma)Ba^{137m}$	2.6 min	0.016 ± 0.005	
$Eu^{151}(n, \gamma)Eu^{152}$	9.2 h	1700 ± 250	1400 ± 300
$Os^{189}(n, \gamma)Os^{190m}$	10 min	< 0.02	
$Os^{190}(n, \gamma)Os^{191, 191m}$		40 ± 10	

3. Discussion

Isomeric ratios, defined as the ratio of the cross-sections for the production of each isomeric state in a given reaction have been investigated by Mateosian and Goldhaber [10]) for the case of thermal neutron capture. They have proposed a semi-empirical rule stating that the ratio of the cross-sections for the produc-

tion of two isomeric states by slow neutron capture is such that the isomeric state with spin close to that of the compound nucleus is favoured. In fig. 1 we have plotted for even target nuclei the fraction of the cascade populating the isomeric state with lower spin difference (defined as the ratio of the cross-section for the isomeric state with lower spin difference to the sum of the cross-sections for the two isomeric states) versus Z, the atomic number of the compound nucleus. These values are obtained partly as a result of our measurements and partly from ref. [3]). Naturally the cases plotted are such that the spins of the compound nucleus after neutron capture may be taken as $\frac{1}{2}$. In the case of osmium the value of the cross-section for $Os^{190}(n, \gamma)Os^{191}$ reaction was taken from the results of Nablo *et al.* [11]), and the isomeric ratio was determined with

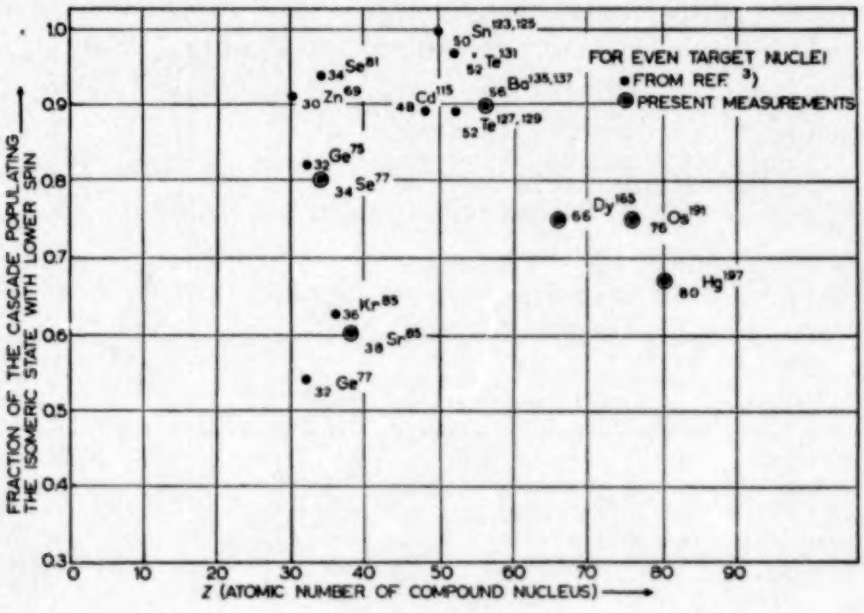

Fig. 1.

the help of the present results. Evidently the rule of Mateosian and Goldhaber seems to hold good for all these cases. The cases of target nuclei of Se^{78} and Ba^{132}, for which the cross-sections for the metastable states have been measured by us, do not seem to follow the above rule, if the values of cross-sections for other states as given in literature are accepted. These cross-sections may require further investigation.

It should be pointed out here that because of the comparatively large errors involved in the thermal neutron cross-sections measurements, the fractions plotted in fig. 1, have large errors. Only the most probable values are plotted in that figure.

The points in the figure do not seem to follow any special trend. They seem to lie mostly around or above the value 0.8 except a few cases having comparatively low values.

The authors are thankful to the Department of Atomic Energy, Government of India, and specially to Dr. Ramanna, for providing the facilities at Trombay. The authors are also thankful to the operating staff of the "Apsara" reactor for their kind cooperation. One of the authors (M. L. S.) is thankful to the Tata Institute of Fundamental Research Bombay, for providing him facilities during the course of the present work.

References

1) M. L. Sehgal, H. S. Hans and P. S. Gill, Nuclear Physics **12** (1959) 261
2) M. L. Sehgal, Ind. J. Physics **31** (1957) 630
3) Neutron cross-sections, compiled by D. J. Hughes and J. A. Hervey, Brookhaven National Laboratory Report BNL-325 (1955)
4) D. Strominger, J. M. Hollander and G. T. Seaborg, Rev. Mod. Phys. **30** (1958)
5) M. E. Rose, Internal conversion coefficient tables (North-Holland Publishing Co., Amsterdam, 1958)
6) A. W. Sunyar, J. W. Mihelich, G. S. Goldhaber and M. Goldhaber, Phys. Rev. **86** (1952) 1023
7) P. A. Akishin, G. M. Panchenkov, N. N. Vasil'ev and O. T. Nikitien, Zhur. Fig. Nank. **30** (1956) 1387
8) A. O. Nier, Phys. Rev. **54** (1938) 275
9) R. D. Hill and F. R. Metzger, Phys. Rev. **83** (1951) 455
10) E. der Mateoasian and M. Goldhaber, Phys. Rev. **108** (1951) 766 (all other references are to be found in this paper together with that of ref. [9]))
11) S. V. Nablo, J. W. Johns, A. Artna and R. H. Goodman, Canad. J. Physics **36** (1958) 1409

2.H

Nuclear Physics **20** (1960) 188—201; © *North-Holland Publishing Co., Amsterdam*

Not to be reproduced by photoprint or microfilm without written permission from the publisher

EFFECT OF FINITE LIFE OF UPPER LEVEL ON PROBABILITY OF COULOMB EXCITATION

G. BREIT and R. L. GLUCKSTERN

Yale University, New Haven, Conn. †

Received 4 June 1960

Abstract: The effect of the finite life of the upper level on the probability of Coulomb excitation is calculated in the semiclassical approximation. The problem is first treated by considering the upper level to be coupled to the continuum by means of a matrix element as in the Weisskopf-Wigner treatment of emission and absorption in radiation theory. Equations for the excitation probability at intermediate times are worked out. The overall transition probability from the ground state to the continuum is transformed in terms of an integral over energies for a transition to a level with infinite life time. The result is then interpreted and generalized in terms of direct transitions to the continuum of stationary states without making use of the division of the nuclear Hamiltonian into parts which provided the matrix element of the first treatment. The second approximation provides a more accurate formula for the overall transition probability and relates the Coulomb excitation probability directly to the Einstein absorption probabilities per unit frequency range. A schematic illustration is given for the increase in the number of transitions from the ground state.

1. Introduction and Notation

The probability P of Coulomb excitation is well known to be strongly affected by the excitation energy which enters formulae for the cross section through the parameter

$$\xi = \eta_f - \eta_i \approx \eta E/(2E_0)$$

in the usual notation and with E representing the excitation energy. For $\xi \gg 1$ the cross section is small, the collision becoming adiabatic. The adiabatic nature of the collision results from the presence of a factor $\exp(i\omega t)$, $\omega = E/\hbar$, whicn for large ω gives alternately positive and negative contributions of nearly equal absolute value to the excitation amplitude. This is the situation as long as the mean life τ of the upper state is large in comparsion with the collision time t_{coll} as is usually assumed in treatments of Coulomb excitation. If the life is not long in comparison with t_{coll}, the excitation amplitude accumulated during the early stage of the collision is decreased through the decay of the upper level and the cancellation of negative and positive parts may be expected to be less severe. The number of decayed upper levels as measured by observing

† This research was supported in part by the United States Air Force under Contract AF 18 (600)—771 monitored by the AF Office of Scientific Research of the Air Research and Development Command and by the U. S. Atomic Energy Commission under Contract AT (30-1)-1807.

the decay products may be expected therefore to increase as long as shortening τ reduces the cancellation of parts of the amplitude but not beyond the point of preventing the build up during a half cycle of the oscillation of exp $(i\omega t)$. Since in the bombardment of high Z targets by light and intermediate weight ions such as Li^6 the conditions for Coulomb excitation of the projectile are favoured by the high Z of the target, the question of the approximate magnitude of the effect of $\tau \neq \infty$ becomes of interest. This is especially true because of the existence of diffuse energy levels in a number of the lighter nuclei [1]).

The calculations reported below employ an approximate treatment of the effect of diffuseness of the excited level. It is in particular essential for the simplifications made in the calculations that the part of the wave function of the upper level which matters for the calculation of the matrix element $\mathcal{M}$ of the Coulomb excitation electromagnetic multipole retain its shape through the decay time of the excited state. In terms of a sharply defined energy treatment a practically equivalent assumption is that the part of the wave function responsible for the calculation of $\mathcal{M}$ retains its shape [2,3]) as the energy is varied.

It will be found below that for large E the effect of increasing the width of the upper level γ is to give a larger P. The influence of γ is most pronounced when the excitation energy and the level width are roughly comparable.

Below, we give a list of the symbols used in this paper.

$Z_1 e,\ Z_2 e$	charges of projectile and of target,
v_{rel}	relative velocity of projectile and target,
η	$= \dfrac{Z_1 Z_2 e^2}{\hbar v_{\mathrm{rel}}}$,
E_0	kinetic energy of projectile and target in centre-of-mass system,
$E = \hbar\omega_{\mu 0} = \hbar(\omega_\mu - \omega_0)$	excitation energy of nuclear level with magnetic quantum number μ,
τ	mean life of excited nuclear state,
$\Gamma = \hbar\gamma$	half width of excited nuclear state,
C_μ	probability amplitude for excited state with magnetic quantum number μ,
$c_{s\mu}$	probability amplitude for continuum state with magnetic quantum number μ,
c_0	probability amplitude for ground state,
$H^{\mathrm{C}}_{\mu 0}\ (t)$	Coulomb excitation interaction energy for state with magnetic quantum number μ,
P_μ	transition probability to sublevel μ,
$\sigma_\mu(\omega_{\mu 0}, \gamma)$	cross section for Coulomb excitation to state of energy $\hbar\omega_{\mu 0}$, sublevel μ, half value width $2\hbar\gamma$,
v	relative velocity of disintegrating fragments,

v_r relative velocity of disintegrating fragments at resonance energy,

E_r resonant energy of nuclear level,

ψ_μ^J many body wave function of disintegrating system with angular momentum J, magnetic quantum number μ,

$f(E, E_r)$ energy dependent factor in ψ_μ^J,

$\kappa = \omega/c$.

2. Coupling to a Continuum

The disintegration of the upper state will be pictured as taking place on account of the coupling of the free waves representing the disintegration products to a part of the upper state function responsible for the Coulomb excitation multipoles. Thus in the case of Coulomb excitation of $Li^6 \rightarrow He^4 + H^2$ the dissociated states of Li^6 consisting of non-interacting $He^4 + H^2$ will form the free waves. These are supposed to be coupled to an excited state Li^{6*} which is made stable through the introduction of an auxiliary potential. The treatment is in this respect similar to the Weisskopf-Wigner [4]) treatment of light emission and absorption and resembles an early discussion [5]) of a two-channel nuclear resonance. Although it appears to be not altogether general, it is possible to supply this lack of formal rigour without much trouble by bearing in mind the analogy to the spontaneous emission of alpha particles and the possibility of constructing for the latter time decaying wave packets [6]) of the same type as those explicitly constructed for the one body problem [2]). The essential feature of the treatment below is the possibility of constructing elementary solutions with an exponential time decay of the inner part of the wave function and the more formal considerations give therefore the same results as those below. As in ref. [5]) the equations may be written

$$\begin{aligned} &dC_\mu/idt + \omega_\mu C_\mu + [H^C_{\mu 0}(t)/\hbar]c_0 + \sum_s (H'_{\mu s}/\hbar)c_{s\mu} = 0, \\ &dc_{s\mu}/idt + \omega_s c_{s\mu} + (H'_{\mu s}/\hbar)C_\mu = 0. \end{aligned} \tag{1}$$

Here C_μ is the probability amplitude of the sublevel of upper state n, having magnetic quantum number μ, the c_s are probability amplitudes of the states in the continuum made discrete through the introduction of a fundamental volume. The Coulomb excitation part of the Hamiltonian H is denoted by H^C and the ground state of the nucleus is referred to by 0. The explicit introduction of magnetic substates of the ground state is not needed because the return to the ground state which is caused by $H^C_{\mu 0}$ is neglected, being a higher order effect of Coulomb excitation. Similarly the effect of gamma emission from $n \rightarrow 0$ will be neglected, the probability of electromagnetic processes being small whenever the width of n caused by mechanical break up is at all comparable

with the excitation energy. Neglecting the $H^{C}_{\mu 0}$ a solution of the emission type has the form

$$C_{\mu}^{e}(t, t') = \exp\{-i(\omega_{\mu}-i\gamma)(t-t')\}, \tag{1.1}$$

$$c^{e}_{s\mu}(t, t') = -\frac{B_{s\mu}\{\exp[-i(\omega_{\mu}-i\gamma)(t-t')]-\exp[-i\omega_{s}(t-t')]\}}{\omega_{s}-\omega_{\mu}+i\gamma}, \tag{1.2}$$

$$B_{s\mu} = H'_{s\mu}/\hbar, \quad \gamma = \Gamma/\hbar, \tag{1.3}$$

$$\Gamma = \frac{\langle|H'_{s\mu}|^2\rangle}{2\hbar\Delta\nu_{s}}, \quad \gamma = \frac{\pi\langle|B_{s\mu}|^2\rangle}{\Delta\omega_{s}} = \frac{\pi\langle|H'_{\mu s}|^2\rangle}{\hbar^2\Delta\omega_{s}}, \tag{1.4}$$

where $1/\Delta\nu_{s}$ is the number of discrete states per unit frequency range representing the continuum in the fundamental volume and the $\langle\rangle$ indicates averaging of $|H'_{\mu s}|^2$ over all directions of relative motion of the disintegration fragments. The solution of (1) can be constructed by superposing the emission solutions (1.1) and (1.2) in the form

$$C_{\mu}(t) = \int^{t} C_{\mu}^{e}(t, t')f(t')\mathrm{d}t', \quad c_{s\mu}(t) = \int^{t} c^{e}_{s\mu}(t, t')f(t')\mathrm{d}t', \tag{2}$$

which when substituted into (1) satisfies the second equation directly and on substitution into the first gives

$$f(t) = -(i/\hbar)H^{C}_{\mu 0}(t)c_{0}(t). \tag{2.1}$$

From (1.1), (2) and (2.1) it follows that

$$\frac{\mathrm{d}C_{\mu}}{i\mathrm{d}t} + (\omega_{\mu}-i\gamma)C_{\mu} + \frac{H^{C}_{\mu 0}(t)}{\hbar}c_{0} = 0, \tag{2.2}$$

from which it follows that in the absence of $H^{C}_{\mu 0}$ there are decaying states with the mean life

$$\tau = \frac{1}{2\gamma}. \tag{2.3}$$

Independently of the validity of (1) one could postulate (2.2) on the grounds that for a quasistationary state with mean life τ, uncoupled to the ground state, it is the correct equation and that the last term in it gives the effect of the Coulomb field. This term has to be assumed to be of the same form as though the substate μ were a true stationary state. This assumption implies [2, 3, 6]) that the shape of the continuum wave functions $\psi_{\mu}(\mathbf{r}, s, E)$ in an analysis in terms of stationary continuum states is sufficiently constant throughout the level width to make $H^{C}_{\mu 0}(t)$ the same for a fixed normalization of the ψ_{μ} in the interior nuclear region. If one were concerned with the ejection of α-particles this restriction would mean that the shape of the many body nuclear wave function

is assumed to be sufficiently energy independent of the α-particle energy through the resonance width. This assumption is not quite correct and especially so in the outer parts of the Coulomb barrier. Since these do not overlap with the ground state appreciably the assumption is a good one from a practical standpoint.

The probability amplitude c_0 of the ground state sublevel 0 is affected by coupling to the sublevels μ of the upper state as in the equation

$$\frac{\mathrm{d}c_0}{i\mathrm{d}t}+\omega_0 c_0+\frac{1}{\hbar}\sum_\mu H^{\mathrm{C}}_{0\mu}C_\mu=0. \tag{3}$$

If the presence of other sublevels of the nuclear ground state may be neglected then from (3) and its complex conjugate it follows that

$$\frac{\mathrm{d}|c_0|^2}{\mathrm{d}t}=\frac{i}{\hbar}\sum_\mu(H^{\mathrm{C}}_{\mu 0}c_0C_\mu^{*}-H^{\mathrm{C}}_{0\mu}c_0^{*}C_\mu)=2\,\mathrm{Re}\left(\frac{i}{\hbar}\sum_\mu H^{\mathrm{C}}_{\mu 0}c_0C_\mu^{*}\right), \tag{3.1}$$

which together with the first part of eq. (2) gives the rate at which nuclei leave the ground state. For other sublevels of the ground state 0′ a similar relation holds but with $0\to 0'$. Since for moderate $H^{\mathrm{C}}_{\mu 0}$ the $c_{0'}$ are small their contributions will be neglected below †. From (1) and (3) it follows that

$$\frac{\mathrm{d}}{\mathrm{d}t}\left[|c_0|^2+\sum_\mu|C_\mu|^2+\sum_{\mu s}|c_{s\mu}|^2\right]=0, \tag{3.2}$$

an equation expressing the conservation of total probability. From (3.1) and (3.2)

$$\frac{\mathrm{d}}{\mathrm{d}t}\left[\sum_\mu|C_\mu|^2+\sum_{\mu s}|c_{s\mu}|^2\right]=2\,\mathrm{Re}\left(\frac{i}{\hbar}\sum_\mu H^{\mathrm{C}}_{0\mu}c_0^{*}C_\mu\right). \tag{3.3}$$

This equation gives the rate of change of the total probability of there being either an excitation to one of the excited sublevels or of that excitation having been followed by a disintegration. Working to the lowest order in H^{C} one has

$$\mathrm{d}c_0/i\mathrm{d}t+\omega_0 c_0=0, \tag{3.4}$$

so that one may use

$$c_0=\exp(-i\omega_0 t). \tag{3.5}$$

This approximate expression gives from (2.2)

$$C_\mu(t)\exp(i\omega_0 t)=-\frac{i}{\hbar}\int_{-\infty}^{t}H^{\mathrm{C}}_{\mu 0}(t')\exp[-i(\omega_{\mu 0}-i\gamma)(t-t')]\mathrm{d}t'. \tag{3.6}$$

†) The approximation implied in this assumption is not always a good one because higher order effects in Coulomb excitation are not always negligible as pointed out by G. Breit and J. P. Lazarus [7]). Work on higher order effects has been done by Breit, Gluckstern and Russell [7]), and Alder *et al.* [8]); cf also a discussion by Breit and Gluckstern [7]) of unpublished work on the reorientation effect by J. P. Lazarus

Substitution in (3.3) yields

$$\frac{\mathrm{d}}{\mathrm{d}t}[\sum_{\mu}|C_{\mu}|^2+\sum_{\mu s}|c_{s\mu}|^2]=\frac{2}{\hbar^2}\mathrm{Re}[H^{\mathrm{c}}_{0\mu}(t)\int_{-\infty}^{t}H^{\mathrm{c}}_{\mu 0}(t')\exp[i(\omega_{\mu 0}-i\gamma)(t'-t)]\mathrm{d}t']. \quad (3.7)$$

This formula is convenient since after integration over t it gives the total chance that an excitation has taken place. It is also desirable to have a breakdown into probabilities of excitation and disintegration. From (3.6) the probability of excitation to a sublevel μ is available as

$$|C_{\mu}(t)|^2=\frac{1}{\hbar^2}\left|\int_{-\infty}^{t}H^{\mathrm{c}}_{\mu 0}(t')\exp[-i(\omega_{\mu 0}-i\gamma)(t-t')]\mathrm{d}t'\right|^2 \quad (4)$$

and since according to (2.3) the number of disintegrations per second from sublevel μ is $2\gamma|C_{\mu}|^2$,

$$\frac{\mathrm{d}}{\mathrm{d}t}\sum_{s}|c_{s\mu}|^2=2\gamma|C_{\mu}(t)|^2. \quad (4.1)$$

This relation can also be obtained from eq. (1). By a straightforward transformation one verifies that (3.7) follows from (4) and (4.1). A special reason for writing out expressions enabling the computation of excitation and disintegration probabilities separately is that for large values of γ the breakup may take place during the collision leading to an alteration of the angular and energy distributions of the disintegration products as compared to what it would be if all disintegrations took place definitely after the collision. This alteration may be partly caused by the interception of the disintegration fragments by the projectile. Thus in the bombardment of Au by Li^6 and the breakup of Li^6 the usual Coulomb excitation terminology is restored by regarding Au as the projectile. The alpha particles from the Li^6 breakup may be intercepted by the Au in this case.

3. Overall Transition Probability

Integrating (3.7) over the whole collision time one obtains the overall transition probability for a transition to sublevel μ

$$P_{\mu}=\frac{2}{\hbar^2}\mathrm{Re}\int_{-\infty}^{+\infty}\mathrm{d}tH^{\mathrm{c}}_{0\mu}(t)\int_{-\infty}^{t}\mathrm{d}t'\,H^{\mathrm{c}}_{\mu 0}(t')\exp[-i(\omega_{\mu 0}-i\gamma)(t-t')]. \quad (5)$$

This expression differs from the one for a discrete state only through the presence of the factor $\exp[-\gamma(t-t')]$. In order to reduce the problem to that of the discrete level for which there are extensive tabulations [8]) the extra factor will be used in the form

$$\exp[-\gamma|t-t'|]=\frac{1}{\pi}\int_{-\infty}^{+\infty}\frac{\exp[i\gamma|t-t'|y]}{1+y^2}\mathrm{d}y. \quad (5.1)$$

When this is inserted in (5) and the complex conjugate of the integral over t' is added to that integral so as to evaluate the real part, the integrals over t and t' combine to give a double integral over t and t', both variables covering the range $-\infty$ to $+\infty$. This simplification is not accidental because the insertion of (5.1) in (5) gives in the exponent $-i(\omega_{\mu 0}-\gamma y)(t-t')$ so that the form of the double integral is just like that for a discrete level. For the latter however $P_\mu = |C_\mu(\infty)|^2$ which according to (3.6) is such a double integral. One thus obtains

$$P_\mu = \sum_s |c_{s\mu}(\infty)|^2 = \frac{\gamma}{\pi\hbar^2}\int_{-\infty}^{+\infty}\frac{d\omega}{\gamma^2+\omega^2}\left|\int_{-\infty}^{+\infty} H^c_{0\mu}(t)\exp\left[-i(\omega_{\mu 0}-\omega)t\right]dt\right|^2. \quad (5.2)$$

For $\gamma \to 0$ the integrand has a sharp maximum at $\omega = 0$ so that the integration may be performed treating the quantity between bars as constant. In that case

$$(P_\mu)_{\gamma=0} = \frac{1}{\hbar^2}\left|\int_{-\infty}^{+\infty} H^c_{0\mu}(t)\exp\left(-i\omega_{\mu 0}t\right)dt\right|^2, \quad (5.3)$$

in agreement with (4). The cross section for Coulomb excitation to sublevel μ and subsequent disintegration may therefore be written

$$\sigma_\mu(\omega_{\mu 0},\gamma) = \frac{1}{\pi}\int_{-\infty}^{+\infty}\sigma_\mu(\omega_{\mu 0}-\omega, 0)\frac{\gamma d\omega}{\gamma^2+\omega^2}. \quad (5.4)$$

In this form there occurs the cross section for Coulomb excitation to a discrete level which is here denoted by $\sigma_\mu(\omega_{\mu 0}-\omega, 0)$ and for this quantity there exist the tabulations previously mentioned [8]). If $\omega > \omega_{\mu 0}$ the argument of this function becomes negative. In such cases the integrals such as the $S_\mu^{(2)}$ of Alder and Winther [8]) become interchanged for positive and negative μ and the tabulations can still be used. Expressions similar to (5.4) can be derived for the angular distribution of decay products. One is usually concerned with

$$P = \sum_\mu P_\mu, \quad \sigma = \sum_\mu \sigma_\mu, \quad (5.5)$$

the sum of transition probabilities over all sublevels and the cross section σ. In their evaluation there enter $P(\omega_{\mu 0}-\omega, 0)$ and $\sigma(\omega_{\mu 0}-\omega, 0)$. The existing tabulations apply to these quantities directly, the interchanges $\mu \to -\mu$ being immaterial. This is in agreement with the fact that the probability of de-excitation is the same as the probability of excitation if the absolute value of the energy difference between the initial and final levels and the transition moments are the same.

Although there is formally no difficulty in evaluating (5.4), the consideration of limitations of (5.4) by means of stationary states shows, however, that the part of (5.4) arising from values of $\omega > \omega_{\mu 0}$ is given only very crudely by (5.4) and that it cannot consistently be claimed to give rise to disintegrations.

In eq. (5.4) the cross section appears in the form of contributions from energy regions $\hbar d(\omega_{\mu 0}-\omega)$ to non-decaying states. This suggests an interpretation and generalization of the answer in terms of transitions to the continuum. The states under consideration will now be defined for the *complete Hamiltonian without removal of H'*. This treatment is closely related to that of resonant radiative capture [2]). An equivalent treatment is possible by means of the $\mathscr{R}$-matrix but is somewhat more involved. Eq. (47.23) of ref. [9]) will be rewritten as

$$\lambda = v_r \Big/ \Big[\int_{I,b} |\psi^J_{L\mu}|^2 d\tau\Big] \quad (E = E_r). \tag{6}$$

Here v_r is the velocity of relative motion of the disintegrating fragments at the resonance energy, $\psi^J_{L,\mu}$ is the many body wave function of the whole system with total angular momentum J, magnetic quantum number μ composed of parts that can be coupled to states of relative orbital angular momentum L in the exterior region. The subscripts I, b indicate that the integration is taken over the interior region (I) as well as through the disintegration channel up to $r = b$. The integral is evaluated at the resonance energy E_r. The restriction to coupling only to one L of the channel is not essential and the suffix L will be dropped therefore. The integration is supposed to include a summation over spin coordinates. For simplicity there is supposed to be only one open channel. As the energy is varied there develops a maximum of $\psi_\mu{}^J$ in I for fixed normalization in the remote portions of the exterior region. As in the alpha-emission problem discussed in ref. [9]), the resonance energy corresponds to that maximum and, similarly to the discussion of resonant gamma capture in connection with fig. 1 of section 4 of ref. [3]), a resonant compound state will be defined as

$$w_\mu = (\psi_\mu{}^J)_r \Big/ \Big[\int_{I,b} |\psi_\mu{}^J|^2 d\tau\Big]^{\frac{1}{2}}_r. \tag{6.1}$$

The quantities on the right hand side are all at the resonance energy as indicated by suffix r. This definition is similar to that of the state denoted by φ_L in section 4 of ref. [3]). The matrix elements of Coulomb excitation multipoles select regions of $\psi_\mu{}^J$ which overlap the ground state and are essentially in I. It will be supposed that the shape of $\psi_\mu{}^J$ is insensitive to E so that one may write

$$\psi_\mu{}^J = f(E, E_r)(\psi_\mu{}^J)_r \tag{6.2}$$

for the part of configuration space for which $\psi_\mu{}^J$ is needed in the calculation of the transition probability. Although (6.2) is very far from being correct in the exterior region of configuration space it is a reasonable approximation through most of I in a rather wide energy range.

The whole system is put in a quantizing sphere of very large radius R. The function $\psi_\mu{}^J$ is first normalized so that for coupling to only one L in the channel it is expressed by eq. (47.6) of ref. [9]). Accordingly the normalized wave

function in the quantizing sphere is

$$(2/R)^{\frac{1}{2}}\psi^J_{\mu k}. \tag{6.3}$$

The dependence on the energy is shown here by the suffix k, the wave number of the channel fragments being designated by $k/2\pi$. The relevant part of H^C will be provided with necessary constant factors to give the transition probability from ground state u_0 to a discrete level v_μ at energy E as

$$P(v_\mu, E-E_0) = \int |(v_\mu, \mathscr{M}(t)u_0)|^2 \exp[-i\omega_{\mu 0}t]\mathrm{d}t, \tag{6.4}$$

$\mathscr{M}$ standing for $H^C/\hbar$. The transition probability to the state (6.3) is then

$$P_{k\mu} \equiv P((2/R)^{\frac{1}{2}}\psi^J_{\mu k}, E-E_0) = \frac{2}{R}f^2(E, E_r)P((\psi_\mu{}^J)_r, E-E_0). \tag{6.5}$$

The total transition probability is the sum of all P_k. Since the k are very closely spaced the sum may be replaced by an integral. In this conversion there enters the spacing between successive levels

$$\Delta k = \pi/R, \tag{6.6}$$

which corresponds to the vanishing of $\mathscr{F}$ at $r = R$. Expressing $\mathrm{d}k$ in terms of $\mathrm{d}E$ leads to

$$P_\mu = \sum_k P_{k\mu} = \frac{R}{\pi}\int P_k \frac{\mathrm{d}E}{\hbar v}, \tag{6.7}$$

where v is the relative velocity of disintegration fragments at energy E. Substitution of $P_{k\mu}$ by means of (6.5) gives

$$P_\mu = \frac{2}{\pi}\int f^2(E, E_r)\left[\int_{1,b} |\psi_\mu{}^J|^2 \mathrm{d}\tau\right]_r P((\psi_\mu{}^J)_r, E-E_0)\frac{\mathrm{d}E}{\hbar v}. \tag{6.7'}$$

Replacement of the integral in terms of λ by means of (6) and substitution for λ by means of

$$\lambda = 2\Gamma/\hbar \tag{6.8}$$

gives

$$P_\mu = \frac{1}{\pi}\int \frac{v_r}{v\Gamma} f^2(E, E_r)P(w_\mu, E-E_0)\mathrm{d}E. \tag{7}$$

In order to see the connection with (5.5) it is convenient to set

$$E = E_r - \hbar\omega \tag{7.1}$$

so that

$$P_\mu = \frac{\hbar}{\pi}\int \frac{v_r}{v\Gamma} f^2(E, E_r)P(w_\mu, \hbar(\omega_{r0}-\omega))\mathrm{d}\omega. \tag{7.2}$$

In the approximation

$$f^2(E, E_r) \approx \frac{\Gamma^2}{(E-E_r)^2+\Gamma^2}, \tag{7.3}$$

and with the replacement of Γ in terms of γ by means of (1.3)

$$P_\mu = \frac{1}{\pi}\int \frac{v_r}{v}\frac{\gamma}{\gamma^2+\omega^2} P(w_\mu, \hbar(\omega_{r0}-\omega))\mathrm{d}\omega, \tag{7.4}$$

which corresponds to (5.4) provided in addition to the other approximations one sets $v_r/v = 1$. To (7.2) there corresponds

$$\sigma_\mu(\omega_{\mu 0}, \gamma) = \frac{\hbar}{\pi}\int \frac{v_r}{v\Gamma} f^2(E, E_r)\sigma(\omega_{r0}-\omega, 0)\mathrm{d}\omega. \tag{7.5}$$

The part of the integral with $\omega > \omega_{\mu 0}-\omega_{d0}$, where $\hbar\omega_{d0}$ is the energy difference between the energy E_d of the barely dissociated state and the ground state energy E_0, should be omitted in the calculation of the disintegration probability because the final state is then below the ground state. The contribution to the integral in (7.5) from positive but small $\omega_{\mu 0}-\omega$ may be non-negligible because of the relatively non-adiabatic character of the collisions to which these values correspond. The employment of (7.3) in this case, i.e., of (5.4) modified through the insertion of the factor (v_r/v), is justifiable only if $\omega_{\mu 0}$ is not too large compared to γ. Otherwise there is no reason to expect (7.3) to hold. For $\omega > \omega_{\mu d}$ the integral in (7.5) should be replaced by a sum over discrete levels of the cross sections for excitation to the discrete levels below the energy E_d.

The increase in $\sigma_\mu(\omega_{\mu 0}, \gamma)$ caused by γ being $\neq 0$ is due largely to $\sigma(\omega_{r0}-\omega, 0)$ increasing rapidly as ω increases from $\omega = 0$. This increase is more marked than the decrease caused by ω decreasing from $\omega = 0$. The increase in $\sigma_\mu(\omega_{\mu 0}, \gamma)$ has been expected according to arguments concerning the adiabatic character of the collision which have been presented in the introduction.

The function $f(E, E_r)$ has an approximate relationship to the phase shift δ_J for the channel under consideration. Since

$$\mathscr{F}_J = F_L \cos\delta_J + G_L \sin\delta_J \tag{8}$$

and since the shape of the function through the interior is approximately energy independent

$$f^2(E, E_r) \approx (F_L \cos\delta_J + G_L \sin\delta_J)^2/(G_L^2)_r, \tag{8.1}$$

where all quantities are evaluated at the channel radius. If the channel radius is taken to be too big, the formula loses accuracy because the shape of G_L is then not energy independent in the whole channel. A reason for pointing out the approximate relation (8.1) is that data on disintegration of a projectile like Li^6 contain information regarding the energy distribution of the fragments.

Their interpretation may be helped therefore by having some other experimental material such as scattering for comparison. In the example of Li^6 bombardment of a heavy target the scattering of d by He^4 is of interest and is in fact available together with a phase shift analysis [10]). The reduced transition probabilities to parts of the continuum are also available in measurements of photodisintegration but mostly for somewhat heavier nuclei. If the giant resonance caused by dipole effects is dominant the Coulomb disintegration consisting in the ejection of a single nucleon is directly related to the photodisintegration cross section, the reduced transition probabilities $B(E1)$ applying to the same differentials of the kinetic energies of the disintegration products in the two cases.

For electric multipoles of order λ,

$$B_{if}=\frac{4\pi^2(\lambda+1)}{\hbar^2\lambda[(2\lambda+1)!!]^2}\,\kappa^{2\lambda-2}[B_i^f\uparrow]_{CE}. \tag{8.2}$$

In this equation the left hand side is the Einstein transition probability from the lower level i to the upper level f defined so that $B_{if}\rho(\nu)$ is the chance per second of a transition, with $\rho(\nu)d\nu$ standing for the radiation density in frequency interval $d\nu$. On the right hand side $[B_i^f\uparrow]_{CE}$ is the reduced transition probability for Coulomb excitation. In applying (8.2) to the continuum one may replace the transition probabilities by the sum of transition probabilities over a finite energy range on both sides of the equation. Eq. (8.2) is readily obtained from eq. (IIA.56) of the Copenhagen review article on Coulomb excitation [11]) as well as by other calculations. In this article a proof is found of the equivalence within a constant factor of the radiative and Coulomb excitation matrix elements for electric as well as magnetic multipoles. The employment of B_{if} in (4) making use of (8.2) is independent of the validity of resonance considerations.

4. Transients and Approximate Magnitudes

In formulae giving the cross section for the whole collision the existence of a level is seen not to enter the final result, the only quantity of interest being the reduced transition probability per unit energy range of the continuum. If the process of excitation is inspected before the collision is over the phase relations between amplitudes of excitation enter also and additional confirmation of the presence of a level becomes in principle available. It is probable that clear evidence of it will be hard to obtain on account of the simultaneous presence of several nuclear reaction mechanisms. It could be observed for instance by the interception of one of the fragments by the nucleus supplying the electric field, a transfer reaction with virtual Coulomb excitation [12]). The quantity of interest for such processes is $|C_\mu(t)|^2$ which is available in eq. (4). On account of the limitations on the interpretation of eq. (5.5) which have become obvious in the

discussion following eq. (7.5) a literal employment of eqs. (3.6), eq. (4) is justifiable only if γ is sufficiently small compared with the distance of E_r from other levels and from E_d. It will suffice, therefore, to give a simple example having some similarity to the conditions for Coulomb excitation. Representing schematically H^C_{n0} by

$$H^C_{n0}(t) = V \exp(-\alpha|t|), \tag{9}$$

with a constant V one has

$$C_\mu(t) \exp(i\omega_0 t) = -\frac{iV}{\hbar}\left\{\frac{2\alpha \exp[-(i\omega_{\mu 0}+\gamma)t]}{\alpha^2-(\gamma+i\omega_{\mu 0})^2} - \frac{\exp(-\alpha t)}{\alpha-\gamma-i\omega_{\mu 0}}\right\}, \quad (t>0), \tag{9.1}$$

$$|C_\mu(0)|^2 = \frac{V^2/\hbar^2}{(\alpha+\gamma)^2+\omega^2_{\mu 0}}, \tag{9.2}$$

$$\int_{-\infty}^{0} 2\gamma |C_\mu(t)|^2 \mathrm{d}t = \frac{\gamma V^2/(\alpha\hbar^2)}{(\alpha+\gamma)^2+\omega^2_{\mu 0}}, \tag{9.3}$$

$$\int_{-\infty}^{+\infty} 2\gamma |C_\mu(t)|^2 \mathrm{d}t = \frac{2V^2}{\hbar^2}\left\{\frac{\gamma/\alpha}{(\alpha+\gamma)^2+\omega^2_{\mu 0}} + \frac{2(\alpha+\gamma)^2}{[(\alpha+\gamma)^2+\omega^2_{\mu 0}]^2}\right\}. \tag{9.4}$$

These formulae show the main effects of γ on the various quantities of interest. According to (9.2) the probability of excitation at the middle of the collision $t = 0$ is decreased by increasing the level width. On the other hand, according to (9.3) the number of disintegrations which have taken place at $t = 0$ at first increases approximately as γ, as γ increases, but at large γ decreases as $1/\gamma$. Comparing by means of (9.3) values for the number of disintegrations that have taken place at $t = \infty$ for $\gamma = 0$ and $\gamma = \alpha$ and taking the ratio of the former to the latter, one finds for it $\frac{8}{3}$ for $\omega_{\mu 0} = 0$, approximately 1 for $\omega_{\mu 0} = \alpha$ and $\frac{8}{25}$ for $\omega_{\mu 0} = 2\alpha$. There is thus indeed a marked increase in the effectiveness of fragment production at $t = +\infty$ as the width of the upper level is increased. However, it should be mentioned again that some of the increase for large γ which is expected according to (9.4) has to be calculated with modifications discussed in connection with (7.5).

The simplified example of eq. (9) can be compared with conditions for actual Coulomb excitation by equating the time constant $1/\alpha$ to the collision time. The latter is not sharply defined. Somewhat arbitrarily one may use as a criterion the doubling of the distance from its minimum value. This criterion gives

$$C\xi = \omega_{\mu 0}/\alpha \tag{10}$$

with $C \approx 4.6$ for close collisions. On the other hand

$$\gamma/\alpha = C\xi\gamma/\omega_{\mu 0}. \tag{10.1}$$

Eq. (9.4) becomes then

$$\int_{-\infty}^{+\infty} 2\gamma|C_\mu(t)|^2\,\mathrm{d}t = \frac{2V^2}{\hbar^2\alpha^2}\left\{\frac{\gamma/\alpha}{[1+(\gamma/\alpha)]^2+C^2\xi^2}+\frac{2[1+(\gamma/\alpha)]^2}{([1+(\gamma/\alpha)]^2+C^2\xi^2)^2}\right\}, \quad (10.2)$$

with γ/α as in (10.1). For small scattering angles θ the value of C is larger than for large θ and the adiabaticity effect is more serious. At the same time according to (10.1) γ/α is larger and hence for large ξ and small θ the effect of γ can be to increase the overall probability of disintegration.

According to (5.4) and (7.5) some of the increase is caused by there being relatively more transitions to the lower energy part of the continuum than the factor $1/(\gamma^2+\omega^2)$ would indicate. This increase is caused by the variation of $\sigma(\omega_{r0}-\omega, 0)$ in these equations and partly by the factor $1/v$ in (7.5). Hence one may expect somewhat more low energy disintegration products than corresponds to the shape of the resonance curve as observed by scattering of one disintegration product by the other. In order that this effect be pronounced ξ and the collision time must be large enough for the resonance energy. Otherwise no appreciable gain in $\sigma(\omega_{r0}-\omega, 0)$ is obtained by lowering the excitation energy $\hbar(\omega_{r0}-\omega)$. In the region $0 < \xi < 0.6$

$$f_2(\xi) = 0.90\exp(-4.61\,\xi^2)$$

represents f_2 reasonably well. Employing this approximation in eq. (5.4) which is an approximation to eq. (7.5) the necessary integral is found to be of the same form as that tabulated by Zemansky [13]). With the aid of his values table 1 results for the ratio of the overall cross section to that cross section for $\gamma = 0$.

TABLE 1

Values of $\sigma(\omega_{\mu 0}, \gamma)/\sigma(\omega_{\mu 0}, 0)$

$\Gamma/\Delta E$ \ ξ	0.23	0.47	0.70	0.93	1.40
0.0	1.0	1.0	1.0	1.0	1
0.05	1.0	1.0	1.2	2.2	90
0.10	1.0	1.0	1.5	3.3	180
0.25	0.9	1.0	1.9	5.7	
0.50	0.8	0.9	2.0	7.8	

For the larger ξ the Gaussian approximation loses accuracy. The numbers obtained are recorded nevertheless in order to give an idea of the approximate magnitudes involved.

References

1) F. Ajzenberg-Selove and T. Lauritsen, Nuclear Physics **11** (1959) 1
2) G. Breit and F. L. Yost, Phys. Rev. **48** (1935) 205
3) G. Breit, Encyclopedia of Physics **41/1** (1959), Sections 3 and 4

4) V. Weisskopf and E. Wigner, Z. Physik **63** (1930) 54;
G. Breit, Revs. Mod. Phys. **5** (1933) 91
5) G. Breit and E. Wigner, Phys. Rev. **49** (1936) 519
6) G. Breit, Encylopedia of Physics **41**/1 (1959), Sect. 47, pp. 358–359
7) G. Breit and J. P. Lazarus, Phys. Rev. **100** (1955) 942;
Breit, Gluckstern and Russell, Phys. Rev. **103** (1956) 727; **105** (1957) 1121;
G. Breit and R. L. Gluckstern, Encyclopedia of Physics **41**/1 (1959), Sect. 8
8) Biedenharn, Goldstein, McHale and Thaler, Phys. Rev. **101** (1956) 662;
Alder, Bohr, Huus, Mottelson and Winther, Revs. Mod. Phys. **28** (1956) 432;
G. Breit and R. L. Gluckstern, Encyclopedia of Physics **41**/1 (1959), p. 532
9) G. Breit, Encyclopedia of Physics **41**/1 (1959), Sect. 47
10) A. Galonsky and M. T. McEllistrem, Phys. Rev. **98** (1955) 590
11) Alder, Bohr, Huus, Mottelson and Winther, Revs. Mod. Phys. **28** (1956) 432, Sect. II
12) G. Breit and M. E. Ebel, Phys. Rev. **104** (1956) 1030
13) M. Zemansky, Phys. Rev. **36** (1930) 219

2.A.1

Nuclear Physics **20** (1960) 202—219; © *North-Holland Publishing Co., Amsterdam*

Not to be reproduced by photoprint or microfilm without written permission from the publisher

ABSOLUTE NEUTRON ABSORPTION CROSS SECTIONS FOR Sb-Be PHOTONEUTRONS

H. W. SCHMITT

Oak Ridge National Laboratory, Oak Ridge, Tennessee

and

C. W. COOK

Convair, San Diego, California

Received 10 June 1960

Abstract: Absolute absorption cross sections of Cu, Zn, Ag, Cd, In, Sb, I, Au, Hg and Pb have been measured for Sb-Be photoneutrons the average energy of which is given as 24.0±2.2 keV. A specially designed antimony-beryllium neutron source was used in spherical shell transmission measurements. A detailed account of the method, including discussion of the experimental measurements and analysis of data, is given. Absorption cross sections obtained are as follows: Cu, 42±15 mb; Zn, 64±20 mb; Ag, 1185±80 mb; Cd, 515±70 mb; In, 823±60 mb; Sb, 565±45 mb; I, 885±90 mb; Au, 585±60 mb; Hg, 380±100 mb; Pb, 3±9 mb.

1. Introduction

Interest in neutron capture cross sections in the keV energy range has been increasing in recent years, particularly because of their importance both in reactor technology [1]) and in synthesis of elements [2, 3]). Relative measurements of neutron capture cross sections [4]) and activation cross sections [5–7]) of certain nucleides as a function of energy in the keV energy range have been made. Also relative cross sections of various nucleides using photoneutron sources have been measured [8–13]). Absolute capture cross section measurements in this energy range include two activation measurements [8, 14]) and an absorption measurement [15]) the results of which will be discussed in another section.

To provide independent absolute values of capture cross sections of certain elements, and to provide calibration for relative measurements, a set of careful measurements has been made to determine absolute neutron capture cross sections of a few elements at an energy of 24.0±2.2 keV. Neutrons of this energy were obtained from a specially designed antimony-beryllium source. The method employed for these measurements is the spherical-shell transmission method, discussed principally by Bethe *et al.* [16]) and Beyster *et al.* [17]) in connection with inelastic cross section measurements using neutrons in the energy range of several MeV. The method was used as early as 1936 by Collie and Griffiths [18]).

2. Absorption Cross Section Measurements by the Shell Transmission Method

For purposes of clarity, let us first distinguish between several terms. The term "capture" or "capture cross section," σ_c, as used in this report refers only to the (n, γ) process. The term "absorption" or "absorption cross section," σ_a, refers to all processes by which a neutron is removed, including the (n, γ) process. In the keV energy range the (n, charged-particle) cross sections for medium and heavy nuclei are very small; hence in this case σ_c and σ_a are used interchangeably. In the work of Beyster *et al.* [17]) the term "inelastic collision cross section", σ_{in}, is used; this refers to all processes except elastic scattering; thus inelastic scattering and all absorption processes are included. In general therefore, we have $\sigma_{in} \geqq \sigma_a \geqq \sigma_c$.

In shell transmission measurements, the use of a neutron detector whose response is *flat* as a function of neutron energy permits determination of *absorption* cross sections. In the keV energy range, for medium-weight and heavy nuclei, this is equivalent to the capture cross section.

The most striking advantage of the shell-transmission method for absorption cross-section measurements, aside from its simplicity-in-principle, is that *absolute values are obtained from neutron transmission measurements into which absolute detection efficiencies do not enter.* An additional advantage for reactor applications is that effective absorption cross sections of composite structural materials may be measured directly. The most important disadvantage is that relatively thick samples are necessary; thus in the kilovolt energy range the effect of resonance self-protection must be considered. In later sections a distinction is made between the "effective absorption cross section" $\bar{\sigma}_a$ corresponding to thick-sample measurements and the absorption cross section per nucleus σ_a.

3. Apparatus and Method

3.1. GENERAL METHOD

A diagram of the apparatus used in these measurements is shown schematically in fig. 1. In a typical shell-on measurement, the source is brought automatically to a fixed pre-determined position; the shells, supported from movable tables as shown, are carefully closed around the source, with the source at the center of the shell. In a typical shell-off measurement, the source is brought into position and the tables are closed below the source. Successive runs of 10 to 20 min duration were made, alternating between shell-on, shell-off and background measurements. All transmissions were determined to an accuracy of ± 0.005 or better.

3.2. NEUTRON SOURCE

The design of the neutron source was the result of compromise between two conditions: (a) to approximate "ideal" geometry with a source as small as

possible, (b) to obtain sufficient intensity for the experiment. The neutron source, shown in fig. 1, is a spherical antimony-beryllium source of about 2.5 cm diameter. The beryllium sphere was made as thin as practical (0.076 cm) in order to minimize neutron energy degradation by multiple scattering in the beryllium. For this source, about 88 % of the photoneutrons escape without an interaction in the beryllium; the average energy loss for the remaining 12 %

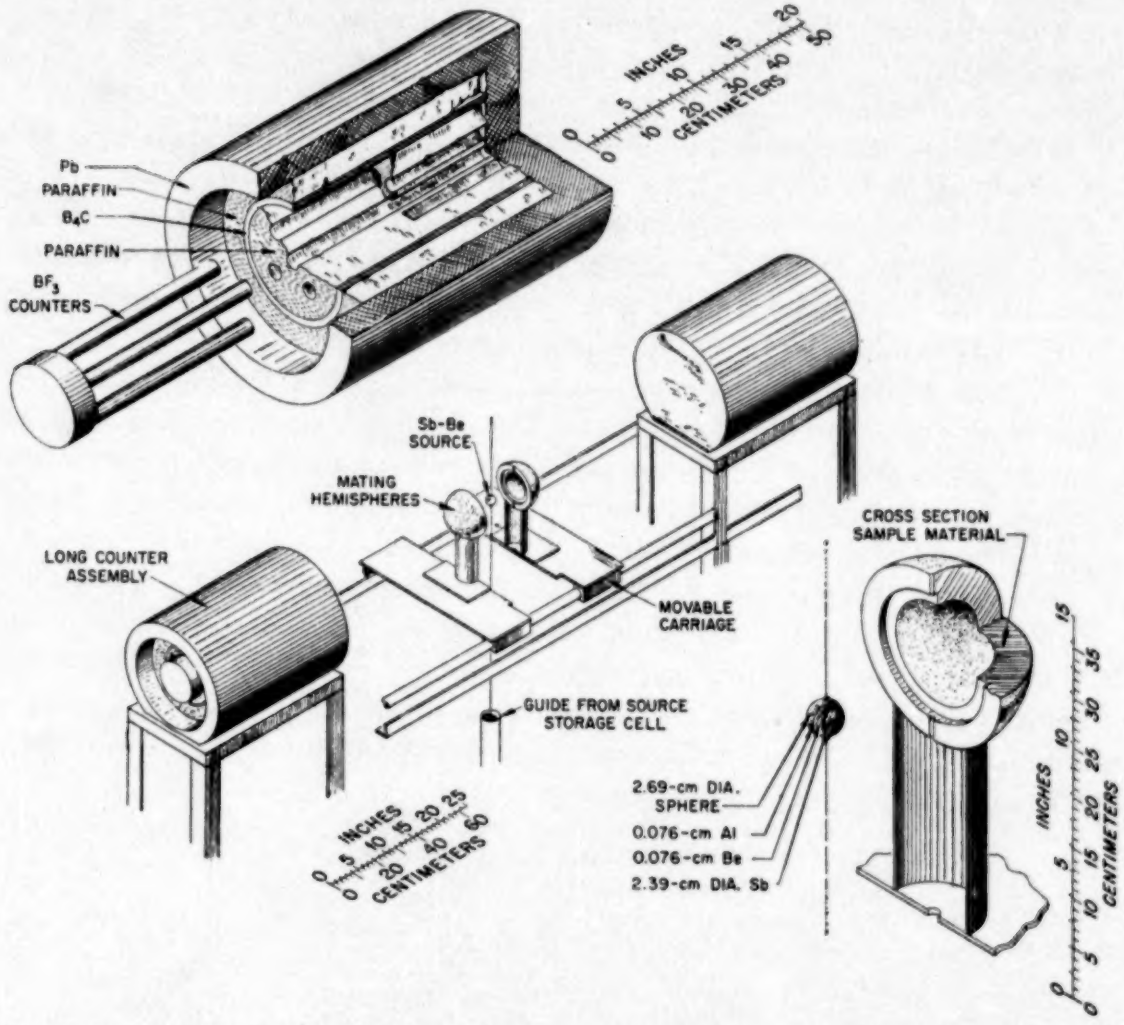

Fig. 1. Apparatus for the measurement of absorption cross sections for Sb-Be photoneutrons by the spherical shell transmission method.

which is scattered in the beryllium, is about 4 keV †. The maximum energy spread of primary neutrons from the source, due to gamma-ray momentum and consequent center-of-mass motion in the $Be^9(\gamma, n)$ reaction, was calculated to

† These figures may be compared with similar ones for typical Sb-Be sources such as the standard ORNL cylindrical Sb-Be source in which the beryllium is 0.45 cm thick. For this source only about 62 % of the neutrons escape without interaction in the source, and the average energy loss for the remaining 38 % is about 7 keV. Further discussion of this subject appears in the accompanying paper [19]).

be 2.7 keV. This neutron source emits neutrons isotropically, as indicated from the design and as demonstrated in experimental tests.

The mean energy of the principal Sb-Be neutron group from this source is 24.0 ± 2.2 keV [19]). Gamma rays which are Compton-scattered in the source give an entirely negligible low-energy tail in the spectrum. There is a weak neutron group [20]) at about 380 keV whose effect is taken into account (see sect. 4), so that in the present experiment 24.0 keV neutron absorption cross sections are determined.

3.3. SAMPLE SHELLS

The shells whose transmissions were measured varied in size and thickness, depending on the material. Most of the solid shells were about 15 cm in outside diameter and from 1 to 5 cm thick. Care was taken in obtaining pure materials and uniform matching hemispheres. For example, all of the solid hemispheres were radiographed, and all samples were spectrochemically analyzed.

In the case of iodine, the sample was in the form of crushed iodine crystals contained in matched hemispherical containers of 1.5 mm thick aluminium. The containers were filled in a dry-box and scaled. In the case of mercury, a similar pair of containers was filled with triple-distilled liquid mercury and sealed. The use of such containers required a correction term to be included in the analysis, as will be discussed in sect. 4. The transmission of an unfilled aluminium container was found to be unity within an uncertainty of 0.3 %.

Sample shell data are included in the table of results, sect. 8.

3.4. NEUTRON DETECTORS

The detectors were modified long counters surrounded by a 5 cm thick cylinder of lead and shielded from the source by an 8 cm thickness of lead, as shown in fig. 1. This heavy shielding was included to reduce the already small gamma-ray sensitivity of the detector, a necessary step since the ratio of gamma rays to neutrons from the present source was about 8×10^4. Periodic transmission measurements of a thick lead shell indicated a gamma-ray sensitivity of the detectors less than 4×10^{-8} relative to the neutron sensitivity. The five BF_3 counters in each detector were connected in parallel. Shell transmissions were measured independently by the two detectors, respectively located about 90 and 120 cm from the source.

In an auxiliary experiment using photoneutrons from Sb-Be (24.0 keV), ThC″—D_2O (195 keV), and Ra-Be (480 keV) sources, responses of the two detectors were measured relative to the known energy response [21]) of a standard long counter. The responses of the detectors were determined only as functions of energy; there was no attempt to determine the absolute efficiencies. Results indicated that the responses varied 20 % or less from 24 keV to 480 keV.

3.5. EXTERNAL CONDITIONS

The present measurements were made in a large room, where the source was at least 3 m from the ground, ceiling and walls. The supports for the shells were made of thin aluminium and the remainder of the supporting framework was kept light. Shell-off measurements were made with and without bare aluminium supports in place; no difference in counting rate was found. Air scattering was not negligible (estimated to be a few per cent); however, it was essentially the same, percentage-wide, in the shell-on and shell-off measurements. The counting rate in the detectors was measured with and without 0.076 cm thick cadmium surrounding the detector; no difference in counting rate was observed.

4. Analysis of Transmission Data

4.1. GENERAL

The theory of the transmission of spherical shells has been developed by Bethe, Beyster and Carter [16]) in connection with fast (MeV energy range) neutron experiments. The primary analysis is general and can be applied in the present experiment with only a few minor changes. The "corrections", however, are different for the present experiment, and it is the purpose of this section to discuss the corrections for (1) source shape and finite source size, (2) neutron absorption in the source, and (3) finite source-to-detector distance.

In the keV energy range the spacing of neutron resonances is in general larger than the widths, hence the effect of resonance self-protection must also be taken into account. This effect is treated separately in sect. 5 and a correction is applied to results of the transmission analysis of this section.

First let us review the relation between absorption cross section and transmission for the case of an isotropic point source at the centre of a spherical shell and an isotropic, flat-response detector located at a large distance from the source and shell. For this case we have

$$(1-T) = (1-T_0)\frac{\bar{\sigma}_a}{\sigma_t}\left[1+\frac{\bar{\sigma}_s}{\sigma_t}(1-P_1)+\frac{(1-P_1)(1-P_2)\bar{\sigma}_s^2}{\sigma_t(\bar{\sigma}_a+\bar{\sigma}_s P_m)}\right], \qquad (4.1)$$

or equivalently

$$T = T_0+(1-T_0)\frac{\bar{\sigma}_s}{\sigma_t}\left[P_1+(1-P_1)P_2\frac{\bar{\sigma}_s}{\sigma_t}+\frac{(1-P_1)(1-P_2)\bar{\sigma}_s^2 P_m}{\sigma_t(\bar{\sigma}_a+\bar{\sigma}_s P_m)}\right], \qquad (4.2)$$

where T is the shell transmission for the specified conditions (T = (shell-on counts — background)/(shell-off counts — background)), $T_0 = \exp[-n\sigma_t(r_2-r_1)]$, n is the number of atoms/cm^3 in the sample shell, r_2 the outside radius of the shell, r_1 the inside radius of the shell, $\bar{\sigma}_a$ the effective absorption cross section of shell material, $\bar{\sigma}_s$ the effective scattering cross section of shell material, $\sigma_t = \bar{\sigma}_a+\bar{\sigma}_s$ the measured total cross section of shell material, P_1 the probability

of escape for a neutron after one collision in the shell, P_2 the probability of escape for a neutron after two collisions in the shell, and, finally, P_m the probability of escape for a neutron after three or more collisions in the shell. The term in square brackets in eq. (4.2) is referred to occasionally as B_e. The escape probabilities $P_i (i = 1, 2, m)$ are independent of the source geometry (except for the corrections mentioned above) and have to do only with escape after interactions in the shell. The P_i are therefore general functions and have been calculated [16]) as functions of the shell characteristics r_1/r_2 and $n\sigma_t(r_2-r_1)$. These calculations were made for shells up to 1.6 mean free paths thick, in which the neutron distribution after i collisions converges to the normal mode distribution rapidly as i increases. For shells much thicker than one mean free path the escape probability may be calculated using diffusion or transport theory or Monte Carlo methods. The P_i are also sensitive to the angular distribution of elastic scattering in the shell material. In the keV energy range elastic scattering is essentially isotropic in the center of mass system, as has been assumed in the calculation of the escape probabilities; thus the total and total transport cross sections are equivalent.

For thin shells, it can be shown that $P_1 \approx P_2 \approx P_m$. In this case eq. (4.1) becomes

$$(1-T) = (1-T_0)\frac{\bar{\sigma}_a}{\bar{\sigma}_a+\bar{\sigma}_s P_m}. \tag{4.3}$$

This equation is convenient to use in the evaluation of errors and also allows a simple physical interpretation. Thus, a neutron may be removed from the shell in two ways: by absorption, the probability for which is proportional to $\bar{\sigma}_a$, and by escape, the probability for which is proportional to $\bar{\sigma}_s P_m$. The fraction of neutrons absorbed is then given by eq. (4.3).

4.2. EFFECT OF SOURCE SHAPE AND FINITE SOURCE SIZE

In the present experiment the neutron source is in the form of a thin spherical shell of beryllium as indicated in fig. 1 and sect. 3. The transmission equation, corrected for this effect, is given in sect. 6. Minimized in the design of the present experiment, this effect depends on the value of the transmission as well as on specific shell characteristics; it is, however, at most a few per cent in $\bar{\sigma}_a$.

4.3. EFFECT OF NEUTRON ABSORPTION IN THE SOURCE

The transmission equation is not affected by absorption in the source since, to first order, only the source strength is altered. The escape probabilities P_i, however, are affected since they depend on transmission of neutrons through the cavity of the shell.

The escape probability $P_i (i = 1, 2, m)$ will be altered by absorption in the source by an amount ΔP_i given as follows:

$$\Delta P_i = P_\Omega P_C P_a P_e, \tag{4.4}$$

where P_Ω is the average probability that ith-scattered neutrons are scattered into Ω, the solid angle subtended by the source at scattering points in the shell; P_C is the probability that a neutron having scattered into Ω will enter the shell cavity, P_a the probability of absorption in the source and P_e the probability of escape from the opposite side of the shell after a neutron has traversed the cavity. In order to obtain a realistic estimate of the maximum value of ΔP_i, we assume that the neutrons are all scattered from the inside surface of the shell. Then for shells of 10.16 cm inside diameter and a source 2.54 cm in diameter, we have $P_\Omega = 0.016$. P_C will be unity and P_a will have a value of about 0.02 assuming $\bar{\sigma}_a \approx 0.50$ barns for antimony. Values of P_e are in the range 0.2 to 0.6 for the present experiments. The product then yields in this case $\Delta P_i \leqq 0.0002$. The smallest value of P_i encountered in the present experiment is ≈ 0.13, hence an error of at most 0.2 % in P_i is introduced. It can be seen from the simplified transmission formula (4.3) that $\Delta P_m/P_m \approx \Delta\bar{\sigma}_a/\bar{\sigma}_a$, hence a maximum error of only 0.2 % is introduced in $\bar{\sigma}_a$ by this effect.

In the present series of measurements one shell of 5 cm inside diameter was used. For this case the value of P_Ω is 0.07, whence $\Delta P_i = 0.0014$. The maximum 1 % error introduced in σ_a in this case is included in the quoted experimental uncertainty.

4.4. EFFECT OF FINITE SOURCE-TO-DETECTOR DISTANCE

If the source-to-detector distance is large compared to the shell radius, the effect of finite source-to-detector distance is small and may therefore be considered independently of the effects of source shape and size and source absorption. As in the case of source absorption, the effect is only to alter the escape probabilities P_i and is taken into account if we alter B_e to give

$$\bar{B}_e = \bar{P}_1 + (1-P_1)\bar{P}_2\frac{\bar{\sigma}_s}{\sigma_t} + \frac{(1-P_1)(1-P_2)\bar{P}_m\bar{\sigma}_s^2}{(\bar{\sigma}_a+\bar{\sigma}_s P_m)\sigma_t}, \tag{4.5}$$

where

$$\bar{P}_i = P_i + \frac{1}{2b^2}P_i^* + \frac{3}{8b^4}P_i^{**}. \tag{4.6}$$

The source-to-detector distance b as used in this correction must be expressed in mean free paths. Bethe *et al.* [16]) have shown that the third term in eq. (4.6) becomes important only when the source-to-detector distance is of the order of the shell diameter. In the present experiments the P_i^* are in general of the order of unity, hence here even the second term is small, of the order of 10^{-4} to 10^{-3}. The P_i^* have been calculated [16]) as a function of r_1/r_2 and $n\sigma_t(r_2-r_1)$. These calculations are used in cases where the correction is important.

4.5. EFFECT OF 380-keV NEUTRON GROUP FROM Sb-Be SOURCE

In the measurement of neutron capture cross sections at 24 keV using an Sb-Be source, account must be taken of the neutron group at 380 keV. The

ratio of the intensity of this group to that of the primary group is 0.046 [20]). In the present experiment the 380 keV group is taken into account by making a simple correction to the measured transmission. Thus if the transmission of the principal group is T and if the transmission of the 380 keV group is T_1, then the measured transmission T_m is given by

$$T_m = \frac{T + (0.046)\varepsilon T_1}{1 + (0.046)\varepsilon}, \tag{4.7}$$

where ε is the ratio of detection efficiency for 380 keV neutrons to that for 24 keV neutrons. For a flat-response detector, $\varepsilon = 1$; for the present work, $\varepsilon \approx 1.2$. It is possible to calculate T_1 from known or estimated absorption cross sections at 380 keV using the developments of this section, as summarized in sect. 6, eqs. (6.1)—(6.6). The value of T_1 thus obtained together with the measured transmission T_m may be substituted into eq. 4.7 to obtain the observed transmission T for the primary neutron group. It is this value of T which is used in the analysis to obtain 24 keV absorption cross sections. The effect of this correction can be seen in the table of results, section 8.

5. Resonance Self Protection

The effect of self protection must be considered in experiments in which thick samples are used. The effect of resonance self protection arises in the present experiment for the reason that in the keV energy range the average level spacings are larger than the level widths, and samples may be thick to the resonances. The entire question of resonance absorption has been considered by Dresner [22]), and his results are used directly in the following description.

The problem which Dresner has solved is that of a convex lump of absorbing material in an isotropic sea of neutrons. This is not the problem at hand in the present experiment; nevertheless his solution may be adapted to the present case. In this solution the geometric configuration enters only through a parameter $n\sigma_p l$, where n is the density of absorbing nuclei, σ_p is the potential scattering cross section of the absorbing nuclei, and l is the "effective path length" of neutrons in the lump. Under the conditions of the present experiment the dependence of the resonance self-protection correction factor on the parameter $n\sigma_p l$ is very weak. Thus the correction factor is well-defined and any uncertainty in the analysis arises principally from uncertainties in some of the assumptions made [22]). Uncertainty in the results also includes that arising from uncertainty in the resonance parameters. Doppler broadening of the resonances and the distribution of widths are important factors in the evaluation of this effect.

The quantity of interest in evaluating the resonance self-protection correction is the effective resonance absorption integral, defined for a single isolated

resonance by the relation

$$I = \int_{\text{res}} \frac{b\Sigma_p}{\Sigma_s+\Sigma_a+b\Sigma_p}\,\sigma_a\,dE, \tag{5.1}$$

where Σ_p, Σ_s and Σ_a are, respectively, the macroscopic potential scattering, resonance scattering and absorption cross sections of the absorbing nuclei and where

$$b = 1+(n\sigma_p l)^{-1}. \tag{5.2}$$

The effective absorption cross section $\bar{\sigma}_a$, obtained from the analysis of sect. 4, is just the effective resonance absorption integral averaged over many levels, taking account of Doppler broadening and of the Porter-Thomas distribution of widths; this averaged resonance absorption integral is denoted by $\langle I\rangle$. The quantity desired is $\langle I_\infty\rangle$, called the "infinite dilution" resonance absorption integral (equivalent to the corrected average absorption cross section σ_a) averaged over many levels and which, incidentally, is independent of Doppler broadening of levels. Thus the corrected average absorption cross section σ_a for the present case is given by

$$\sigma_a = \frac{\bar{\sigma}_a}{\langle I\rangle/\langle I_\infty\rangle}. \tag{5.3}$$

Dresner [22]) has arrived at an expression for the factor $\langle I_J\rangle/\langle I_{J\infty}\rangle$, where the subscript J indicates a particular value of the total angular momentum of the compound state; thus

$$\langle I_J\rangle/\langle I_{J\infty}\rangle = \frac{(2/\pi)b\beta_0\langle J(\xi, b\beta)\rangle}{\langle\beta_0/\beta\rangle}, \tag{5.4}$$

where

$$\beta_0 = \sigma_p/\sigma_0, \quad \beta = \sigma_p/\sigma_t, \tag{5.5}$$

$$\xi_0 = \Gamma/\Delta, \tag{5.6}$$

and

$$\langle J(\xi, b\beta)\rangle = \left\langle \int_{x=0}^{\infty} \frac{\psi(\xi, x)}{\psi(\xi, x)+b\beta}\,dx \right\rangle. \tag{5.7}$$

In eq. (5.5), σ_p is the potential scattering cross section and σ_0 is the peak cross section at resonance, given by

$$\sigma_0 = 4\pi\lambda\!\!\!^{-2}\,\frac{2J+1}{2(2I+1)}\,\frac{\Gamma_n}{\Gamma}, \tag{5.8}$$

where $\lambda\!\!\!^{-}$ is the reduced wavelength of the incident neutron in the centre-of-mass system, I is the target spin, Γ_n and Γ are the average neutron and total widths respectively, and where the braces indicate an average over the statistical distribution of neutron widths. In eq. (5.6), Δ is the Doppler width, and

$\psi(\xi, x)$ in eq. (5.7) is the Doppler-broadened line shape.Note ξ is the average lethargy change per collision; the lethargy u is defined as $u \equiv \ln (E_{\text{reference}}/E)$. Methods for evaluating $\langle J(\xi, b\beta)\rangle$ have been given by Dresner [22]); various simplifying approximations are useful depending on the ranges of interest of the variables. The tables of Dressner [22]) and Adler [23]) are useful in this evaluation.

For each element calculations of $1/(\langle I_J\rangle/\langle I_{J\infty}\rangle)$ were made corresponding to each J for s-wave neutrons, and to each J for p-wave neutrons. The results in each case were weighted and averaged according to the statistical factor $2J+1$, assuming for simplicity that the quantity $\langle I_J\rangle/D_J$ is independent of J. Thus two factors, $(\langle I\rangle/\langle I_\infty\rangle)_{l=0}$ and $(\langle I\rangle/\langle I_\infty\rangle)_{l=1}$, are obtained. The correction factor $\langle I\rangle/\langle I_\infty\rangle$ to be applied to the effective cross section $\bar{\sigma}_a$ is then given by

$$\frac{\langle I\rangle}{\langle I_\infty\rangle} = \frac{\sigma_{a(l=0)}\left(\frac{\langle I\rangle}{\langle I_\infty\rangle}\right)_{l=0} + \sigma_{a(l=1)}\left(\frac{\langle I\rangle}{\langle I_\infty\rangle}\right)_{l=1}}{\sigma_{a(l=0)}+\sigma_{a(l=1)}}. \tag{5.9}$$

In this equation $\sigma_{a(l=0)}$ and $\sigma_{a(l=1)}$ are respectively the s-wave and p-wave contributions to the absorption cross section σ_a. The s-wave contribution is computed from average resonance parameters measured at low neutron energies, usually by means of neutron velocity selectors or choppers; the p-wave contribution is obtained along with the quantity $\langle I\rangle/\langle I_\infty\rangle$ from eqs. (5.3) and (5.9). Values of $\langle I\rangle/\langle I_\infty\rangle$ for 24.0 keV neutrons are as follows: Ag, 0.85 ± 0.05; Cd, 0.68 ± 0.10; In, 0.93 ± 0.06; Sb-1, 0.88 ± 0.06; Sb-2, 0.88 ± 0.06; I, 0.85 ± 0.07; Au-1, 0.94 ± 0.06; Au-2, 0.93 ± 0.06; Hg, 0.75 ± 0.20. No correction factors were calculated for Cu, Zn and Pb. In the case of Cu and Zn, the total cross sections [24, 25]) exhibit resonance structure whose width is comparable to or broader than that of the resolution function of the present measurements; thus the effect of resonance self protection is in doubt and only relatively large uncertainties are included. In the case of lead the cross section results are not altered by resonance self protection.

Uncertainties in the correction factors listed above are due to uncertainty in the initial assumptions, as discussed above, and to uncertainties in the resonance parameters; the magnitudes of the uncertainties also depend slightly upon the relative s- and p-wave contributions. Estimates of the total uncertainty range from about 30 to 100 % of the difference from unity of the correction factors.

6. Determination of Absorption Cross Section

The transmission equation, corrected for source shape, finite source size, and finite source-to-detector distance, is as follows:

$$T = T_0'' + (1-T'_0)\left(1-\frac{r_0^2}{3b^2}\right)\left(\frac{\bar{\sigma}_s}{\sigma_t}\right)\left[\bar{P}_1 + (1-P_1)\bar{P}_2\frac{\bar{\sigma}_s}{\sigma_t} + \frac{(1-P_1)(1-P_2)\bar{P}_m\bar{\sigma}_s^2}{(\bar{\sigma}_a+\bar{\sigma}_s P_m)\sigma_t}\right], \tag{6.1}$$

where

$$T''_0 = T'_0 + \frac{n\sigma_t r_0^4}{9b^2}\left(\frac{1}{r_1} - \frac{1}{r_2}\right) T_0, \tag{6.2}$$

$$T'_0 = T_0\left[1 - \frac{n\sigma_t r_0^2}{3}\left(\frac{1}{r_1} - \frac{1}{r_2}\right)\right], \tag{6.3}$$

$$T_0 = e^{-n\sigma_t(r_2 - r_1)}, \tag{6.4}$$

and

$$\bar{P}_i = P_i + \frac{1}{2b^2} P_i^*(i = 1, 2, m). \tag{6.5}$$

Knowing (a) the effective total cross section of the shell material, (b) the dimensions and atomic density of the shell, (c) the radius r_0 of the source, and (d) the source-to-detector distance, and using the relation

$$\sigma_t = \bar{\sigma}_a + \bar{\sigma}_s, \tag{6.6}$$

all quantities in eq. (6.1) can be determined and the effective absorption cross section calculated for any given value of T.

For the analysis of the iodine and mercury data, eq. (6.1) must be modified slightly to account for the fact that aluminium replaces the sample material in the region of the equator of the sphere, where the hemispheres come together. The loss of neutrons through the aluminium container walls at the equator was estimated by measuring the transmission of the shells filled with lead shot of very high purity. Since lead has a very low absorption cross section in this energy region ($\approx$ 3 mb) [4]†, the difference from unity of this transmission is an approximate measure of neutron loss in the equatorial plane. Although it would be difficult to include this effect explicitly in the analysis, the transmission of the shells, to a sufficiently good approximation, may be corrected by replacing the first factor on the right hand side of eq. (6.1) by

$$(1 - \delta - T'_0). \tag{6.7}$$

For each aluminium shell the quantity δ is adjusted so that eq. (6.1) satisfies the results of the transmission measurement in which the lead shot replaces the sample material; δ is, within 1 %, equal to the difference from unity of the transmission of the lead-filled shell. It is noted that a correction of the form indicated would not be valid if diffusion considerations (large numbers of collisions per neutron within the shell) were required. The present approximation for the correction is justified, however, on the basis that more than 90 and 60 % of the incident neutrons are transmitted or captured with less than 4 collisions in the iodine and mercury shells respectively.

† See also results quoted in this paper.

The resonance self-protection correction is applied as a multiplicative factor, the form of which is given and values for which are listed in sect. 5.

7. Evaluation of Errors and Uncertainties

Errors and uncertainties in the present experiment may be conveniently divided into two classes: (1) those which are associated with the experimental measurements and enter into the determination of transmissions, and (2) those which are associated with the analysis and enter into the determination of absorption cross sections from measured transmissions.

In the first group we list the following: (a) statistical uncertainties in shell-on and shell-off counts, (b) uncertainties arising from electronic drifts or other external sources, (c) uncertainty due to scattering of neutrons by the surroundings, and (d) uncertainty in the effect of the 380 keV neutron group including the uncertainty in ε (eq. (4.7)). It was found that uncertainties arising from drifts or similar external sources other than counting statistics were small; the effect of scattering of neutrons by the surroundings was negligible. The effect of the 380 keV neutron group has been calculated for each shell and is indicated in the table of results (sect. 8); the corresponding uncertainty in transmission of the 24 keV neutron group is estimated and included. Each of these four effects is treated as an independent source of error, and the r.m.s. combination of uncertainties in transmission for each shell is given in the table. Standard deviations are used throughout.

In the second group of uncertainties we list the following: (a) uncertainty in shell dimensions, (b) uncertainty in number of atoms per cm^3 of sample material, (c) uncertainty in the $P_i (i = 1, 2, m)$, (d) uncertainty in total cross section, (e) uncertainty in the analysis arising from approximations, and (f) uncertainty in the resonance self-protection correction. Shell dimensions were measured directly using standard precision instruments; shell weights were obtained with an accuracy 0.3 % or better. The volume of each shell was computed, or in the case of the hollow shells measured directly, and the atomic density obtained. Each shell was radiographed to determine that the density was uniform, and each sample material was spectroscopically analyzed for impurities. Uncertainties in the P_i values of this experiment are about ± 0.003 or less for most cases, corresponding to an uncertainty in absorption cross section of less than 2 %. Uncertainty in total cross section is, for a shell whose measured transmission is significantly different from 1.00, one of the primary contributions to the uncertainty in absorption cross section. This uncertainty is included, and sensitivity to total cross section is discussed in sect. 8. Uncertainty in the analysis arises primarily because of the approximation of the neutron distribution in the shell to the normal mode distribution after three or more collisions. Bethe *et al.* [16] have stated that an uncertainty of 1 % in cross section should be included. In

the cases of I and Hg, additional uncertainty in the correction for walls of the containers at the equatorial plane gives rise to an additional 1 % uncertainty in σ_a. Uncertainty in the resonance self-protection correction has been discussed in sect. 5.

Of the errors indicated in the previous paragraph, only errors (a) and (b) are interdependent. These, however, are small relative to errors (d) and (f); hence all uncertainties have been r.m.s. combined as independent sources of error.

TABLE 1

Individual contributions to the uncertainties in absorption cross sections. Uncertainties in items listed at heads of columns give rise to the tabulated uncertainties in absorption cross sections. Cross section values are given in table 2.

Element	Uncertainty in absorption cross section in mb						Quoted uncertainty in absorption cross section (mb)
	(Shell dimensions and density)	(P_t)	(σ_t)	(Analysis approximations)	(Transmission of 24 keV neutrons (Group 1, text))	(Resonance self-protection)	
Ag	negl. †	16	30	10	25	66	80
Cd	negl.	5	9	3.5	13	67	70
In	negl.	6	20	8	27	50	60
Sb-1	negl.	5	13	5	23	36	45
Sb-2	negl.	5	10	5	23	37	45
I	24	6.5	14	10	64	68	90
Au-1	negl.	5	44	6	26	35	60
Au-2	negl.	54	60	16	14	35	90
Hg	10	14	19	6	10	95	100
Pb	negl.	negl.	negl.	negl.	9		9

† negligible

Other negligible uncertainties considered but not listed include those due to small errors in background determination, source position, and closure of the shells about the source. A compilation of individual uncertainties is given in table 1; all known uncertainties have been pessimistically evaluated and r.m.s. combined to give overall uncertainties (standard deviations) in absorption cross sections.

8. Results and Discussion

The results of the present measurements are given in table 2. Shell data are given in columns 1 to 5, including total cross section values [24–31]) used in the analysis. Pertinent transmission values are given in columns 6 and 7 and absorption cross sections are given in columns 8 and 9. The uncertainty in transmission of the primary neutron group given in column 7 is that obtained by combining those uncertainties listed in group (1) of sect. 7. Uncertainties in the absorption cross sections of column 9 were obtained by combining all

TABLE 2

Shell transmission data and results (see text for discussion)

Element	σ_t(24.0 keV) (barns)	Shell dimensions			Measured transmission	Transmission of 24 keV neutrons	Absorption cross section (mb)	
		r_1(cm)	r_2(cm)	$n\sigma_t(r_2-r_1)$			Uncorrected for resonance self-protection	Corrected for resonance self-protection
Cu	9 ±1 [24, 25])	5.03	7.58	1.92	0.972±0.004	0.971±0.004	42±15	
Zn	10 ±2 [26, 27])	4.96	7.97	1.97	0.963±0.005	0.961±0.005	64±20	
Ag	7.3±0.3 [24, 28])	4.30	7.46	1.34	0.703±0.003	0.694±0.004	1013±45	1185± 80
Cd	7.0±0.4 [29, 30])	3.80	8.30	1.46	0.864±0.004	0.859±0.004	352±17	515± 70
In	6.6±0.3 [28])	3.80	7.10	0.83	0.858±0.004	0.853±0.005	766±36	823± 60
Sb-1	6.3±0.3 [28])	2.54	7.62	1.05	0.877±0.005	0.873±0.005	490±27	555± 45
Sb-2	6.3±0.3 [28])	4.62	7.62	0.62	0.927±0.003	0.925±0.003	506±26	573± 45
I	6.0±0.4 [28])	4.96	11.21	0.46	0.926±0.005	0.923±0.006	754±70	885± 90
Au-1	12 ±1.5 [24])	5.93	7.62	1.19	0.880±0.005	0.876±0.005	553±52	589± 60
Au-2	12 ±1.5 [24])	5.08	7.62	1.79	0.806±0.004	0.800±0.004	537±83	579± 90
Hg	11.0±1.0 [29, 30])	4.99	8.80	1.71	0.879±0.004	0.875±0.004	286±28	380±100
Pb	10.2±0.5 [31])	5.08	9.21	1.38	0.999±0.003	0.999±0.003	3± 9	

known uncertainties; standard deviations are used throughout. The neutron energy is given as 24.0 ± 2.2 keV [19]). In the case of Cu and Zn, the resonance self-protection correction was not applied since, as discussed above, the width of observed resonance structure in the total cross sections in the neighborhood of 24 keV is comparable with that of the neutron resolution function. Correspondingly large uncertainties are, however, included in the absorption cross section results.

Two measurements each were made for antimony and gold, in each case using shells of different thicknesses. Good agreement between the two cross section values thus obtained for each element respectively is evidence of consistency in the measurements and analysis.

For any element the fractional change in σ_a may be related to the fractional change in σ_t approximately as follows:

$$\frac{\Delta\sigma_a}{\sigma_a} \approx -k\frac{\Delta\sigma_t}{\sigma_t}. \tag{8.1}$$

The value of k for each element (Cu, Zn, and Pb excepted) is as follows: Ag, 0.65; Cd, 0.60; In, 0.50; Sb, 0.46; I, 1.15; Au, 0.65; Hg, 0.70. These numbers are insensitively dependent upon the assumed value of σ_t; k changes by only about 1 % for a 15 % change in σ_t. This relation may be used to change the absorption cross sections obtained in these measurements, should more accurate total cross sections become available, provided that $\Delta\sigma_t/\sigma_t$ is not too large.

Results of the present experiment are compared with those of other investigators in table 3.

The measurements of Macklin *et al.* [10]), Booth *et al.* [11]), Hamermesh *et al.* [8, 9]) and recently by Kononov *et al.* [33]) were made using Sb-Be photoneutron sources and activation techniques. For In and Sb, the activation results are not internally consistent, and no general comparison can be made. In the case of iodine, agreement between the present result and that of the absolute measurement of Macklin [14]) is satisfactory; recent less precise results [6, 32]) for iodine are consistent with these results. In the case of copper and gold the activation results appear to be consistent, but are in disagreement both with shell transmission results and with time-of-flight results (see discussion later in this section). Studies are in progress at this Laboratory to ascertain the source of these discrepancies.

The experiments of Belanova were carried out using an Sb-Be source in spherical shell transmission measurements. The analysis of Belanova was based on an "average path length" determination using the assumption that the distribution of path lengths of neutrons which undergo an elastic scattering in the shell is an exponential distribution. Transmission values were not reported; however, this analysis, applied to data of the present experiment using equations given by Belanova, resulted in "effective absorption cross section" values

TABLE 3

Neutron capture cross sections for 24 keV neutrons. Results of the present experiment are tabulated and compared with those of other investigators. (See text for further discussion).

Z	Element	Neutron capture cross sections for Sb-Be photoneutrons (mb)					
		Present work	Macklin *et al.*[10])	Booth *et al.*[11])	Hamermesh *et al.*[8, 9])[a])	Belanova[15])[a])	Others
29	Cu	42± 15	94± 9	94± 17	105± 25	32± 3	
30	Zn	64± 20				29± 2	
47	Ag	1185± 80					
48	Cd	515± 70				321± 7	
49	In	823± 60	805± 80[b])	980±220[b])			590±120[b])[33])
51	Sb	565± 45	739± 65	562±150		444± 4	
53	I	885± 90	820± 60[14])		2000±400	1097±39	910±160[6]) / 720±140[32])
79	Au	585± 60	1120±110	890±190	1500±225		960±200[32])
80	Hg	380±100				202± 9	
82	Pb	3± 9				13± 3	

[a]) These results are included for completeness (see text for discussion)
[b]) In^{115} (54-min half-life activation) only.

20 to 30 % lower than those reported in table 2. Also, the effect of resonance self-protection was not mentioned by Belanova. As to the uncertainties assigned, it was stated in text by Belanova that a 3 to 5 % effect was beyond the limits of accuracy of the results. The results of Belanova are included in table 3 for completeness.

Recently Neiler *et al.* [4]) have measured neutron capture cross sections in the keV range for certain elements by means of a large liquid scintillation tank for neutron time-of-flight measurements with direct detection of capture gamma rays. These measurements were made relative to the absorption cross section of U^{235}; associated uncertainties are about ± 20 %. Elements measured include all those listed in table 3 except mercury. Results are in good agreement with results of the present experiment.

In conclusion, the average neutron capture cross sections at 24.0 keV for s-wave neutrons have been calculated using neutron and radiation widths and level spacings obtained at lower energies [27]). The following values were obtained Ag, 446 mb; In, 322 mb; Sb, 199 mb; I, 311 mb; Au, 331 mb. These values are uncertain because of the large uncertainties in strength functions, level spacings or level parameters; nevertheless, the differences between these values and the measured cross sections in all cases are significant and are large. These differences are attributed to p-wave capture in this energy range [34]).

The authors are pleased to acknowledge many helpful discussions with L. Dresner concerning the problem of resonance absorption. The assistance of C. N. Inskeep and N. H. Fuchs in taking some of the transmission data is gratefully acknowledged. We wish to thank J. H. Gibbons for his participation in early phases of the experiment.

References

1) For example, see A. M. Weinberg and E. P. Wigner, The physical theory of neutron chain reactors (University of Chicago Press, 1958)
2) Burbidge, Burbidge, Fowler, and Hoyle, Revs. Modern Phys. **29** (1957) 547
3) A. G. W. Cameron, Bull. Am. Phys. Soc. **4** (1959) 247
4) Neiler, Macklin, Gibbons and Miller, Bull. Am. Phys. Soc. **4** (1959) 43, 474
5) Bilpuch, Weston, Newson, Rohrer and Jones, Bull. Am. Phys. Soc. **2** (1957) 218; for additional references, see D. J. Hughes and R. B. Schwartz, Report BNL-325, 2nd Edition (Superintendent of Documents, U. S. Government Printing Office, Washington D. C., 1958)
6) S. J. Bame, Jr. and R. L. Cubitt, Phys. Rev. **113** (1959) 256
7) Miskel, Marsh, Lindner and Nagle, Bull. Am. Phys. Soc. **4** (1959) 475
8) V. Hummel and B. Hamermesh, Phys. Rev. **82** (1951) 67
9) C. Kimball and B. Hamermesh, Phys. Rev. **89** (1953) 1306
10) Macklin, Lazar and Lyon, Phys. Rev. **107** (1957) 504
11) Booth, Ball and MacGregor, Phys. Rev. **112** (1958) 226
12) Leipunsky *et al.*, Proceedings of the Second United Nations International Conference on the Peaceful Uses of Atomic Energy **15** (1958) 50
13) J. F. Vervier, Nuclear Physics **9** (1959) 569

14) Described in appendix I of ref. [19])
15) T. S. Belanova, JETP **34** (1958) 574
16) Bethe, Beyster and Carter, J. Nucl. Energy **3** (1956) 207, 273; **4** (1957) 3, 147 (originally written as Los Alamos Report LA-1429 (1955))
17) Beyster, Henkel, Nobles and Kister, Phys. Rev. **98** (1955) 1216
18) C. H. Collie and J. H. E. Griffiths, Proc. Roy. Soc. A **155** (1936) 434
19) H. W. Schmitt, Nuclear Physics **20** (1960) 220
20) Gibbons, Macklin, Marion and Schmitt, Phys. Rev. **114** (1959) 1319
21) W. D. Allen, in Fast neutron physics, edited by J. B. Marion and J. L. Fowler (Interscience Publishers, New York, 1960), Ch. IIIA
22) L. Dresner, Report ORNL 2659, 1959 (unpublished)
23) F. T. Adler and L. W. Nordheim, Report GA-377, 1958 (unpublished)
24) Newson, Gibbons, Marshak, Williamson, Mobley, Patterson and Nichols, Phys. Rev. **105** (1957) 198
25) H. Marshak and H. W. Newson, Phys. Rev. **106** (1957) 110
26) H. W. Newson, private communication (1958)
27) See D. J. Hughes and R. B. Schwartz, ref. [8])
28) Bockelman, Peterson, Adair and Barschall, Phys. Rev. **76** (1949) 277
29) Walt, Becker, Okazaki and Fields, Phys. Rev. **89** (1953) 1271
30) R. R. Palmer and L. M. Bollinger, Phys. Rev. **102** (1956) 228
31) Good, Neiler and Gibbons, Phys. Rev. **109** (1958) 926
32) Gabbard, Davis and Bonner, Phys. Rev. **114** (1959) 201
33) Kononov, Stavisskii and Tolstikov, Reactor Science **11** (1960) 46
34) See, for example, papers of Weston *et al.*, Moldauer, and others, the Topical Conference on Neutron Capture Reactions, Bull. Am. Phys. Soc. **4** (1959) 472

2.A.1

Nuclear Physics **20** (1960) 220—226; © *North-Holland Publishing Co., Amsterdam*

Not to be reproduced by photoprint or microfilm without written permission from the publisher

DETERMINATION OF THE ENERGY OF ANTIMONY-BERYLLIUM PHOTONEUTRONS

H. W. SCHMITT

Oak Ridge National Laboratory, Oak Ridge, Tennessee

Received 10 June 1960

Abstract: The transmission of a spherical shell of enriched B^{10} has been measured and used to determine the average energy of neutrons from a spherical antimony-beryllium source. Analysis of the transmission data in terms of the known absorption and total cross sections of B^{10}, including effects of single and multiple neutron scattering in the shell and source, permits determination of the effective energy of neutrons in the shell, the average energy of neutrons emitted from the particular source, and an estimate of the initial antimony-beryllium photoneutron energy. The average energy of neutrons from the neutron source of this experiment is 24.0 ± 2.2 keV; the initial energy of the primary group of antimony-beryllium photoneutrons is 24.8 ± 2.4 keV. A discussion of the source neutron energy as a function of source dimensions is included.

1. Introduction

Neutrons from antimony-beryllium photoneutron sources have been used extensively in measurements of activation cross sections [1–4]) and recently in absolute measurements of neutron absorption cross sections [5]). A number of studies of the energy of neutrons from Sb-Be sources have been made [6–10]), from which it is apparent that the effective neutron energy from a source depends upon the dimensions and construction of the source. The principal effect giving rise to this dependence is that of neutron energy degradation by single and multiple scattering in the beryllium and surrounding materials. In this paper a new determination of the energy of neutrons from an Sb-Be source will be described; the source is that which was used in the absolute absorption cross section measurements of the accompanying paper [5]). The dependence of source energy on source dimensions is discussed; and a determination of the energy of the initial Sb-γ-Be photoneutrons is given.

2. Method

In principle, the neutron energy determination is as follows. The transmission T of a spherical shell of enriched B^{10} for neutrons from a spherically symmetric Sb-Be source is measured. A correction is made for the neutron group (4.4 % intensity [11])) at 380 keV to obtain the transmission for the primary neutron group, whose energy is to be determined. The absorption cross section for the boron sample is determined by means of the analysis described in the preceding

paper [5]); the known absorption cross section as a function of energy for the present sample, as discussed later, is then used to arrive at the effective energy of neutrons absorbed in the boron shell. The ratio of this effective energy to the average initial energy of neutrons from the Sb-Be source is readily obtained through the analysis of single and multiple scattering in the shell, taking into account the $1/v$ absorption cross section of the boron; thus the average energy of neutrons from the source is determined. Similarly, neutron scattering and energy degradation in the source are taken into account to estimate the initial Sb-γ-Be photoneutron energy.

The method and apparatus for this measurement were as described in the preceding paper [5]). The Sb-Be source consisted of a 2.54 cm inside diameter, 0.076 cm thick spherical shell of beryllium surrounding a solid 2.54 cm diameter antimony sphere; the flat-response detectors and the positioning apparatus were the same. In the present measurement, however, the sample was elemental boron powder. Matched hemispherical containers of 1.6 mm thick aluminium were used to contain the boron powder; the transmission of the unfilled aluminium shell was measured and was found to be unity within an uncertainty of 0.3 %. The containers were of approximately 10 cm inside diameter and 14 cm outside diameter; they were filled through openings at the top, a vibrator being used to assure as uniform packing of the powder as possible. Direct weight and volume measurements were made to determine the atomic density of the sample. The sample was chemically determined to contain 98 % boron; a spectrochemical analysis indicated less than 0.1 % metallic and rare-earth impurities. Mass spectrometric analysis showed the isotopic abundance of B^{10} and B^{11} in the boron to be 91.2 ± 0.1 and 8.8 ± 0.1 %, respectively. Alternating shell-on, shell-off and background counts were made as in the preceding paper.

3. Analysis and Energy Determination

Analysis of spherical shell transmission measurements to determine absorption cross sections is discussed and a summary is given in the preceding paper. Analysis for the present case is the same as that described for iodine and mercury in the preceding paper, including the small correction for neutron loss through the aluminium container walls at the sphere equator. In the present case 2 % or less of the neutrons interact three or more times in the shell, hence the approximate form of the correction is justified.

Since in the present experiment the source energy and hence total cross section of the sample are initially unknown, it is necessary to solve simultaneously two equations relating the total and absorption cross sections of the sample:

$$T = T_0'' + (1-\delta-T'_0)\left(1-\frac{r_0^2}{3b^2}\right)\frac{\sigma_s}{\sigma_t}\bar{B}_e, \tag{1}$$

$$\sigma_a = \sigma_t - \sigma_s. \tag{2}$$

The first of these is the transmission equation taken from the preceding paper, to which we refer for definitions and explanations of symbols. The total, absorption and scattering cross sections for the sample are given by σ_t, σ_a and σ_s respectively.

A graphical solution of eqs. (1) and (2) is shown in fig. 1. The measured transmission for the boron shell was 0.503 ± 0.003; correcting for the 4.4 % abundant 380 keV neutron group [11]), the transmission T of the primary neutron group is found to be 0.487 ± 0.005. The curve giving σ_a versus σ_t from eq. (1) is marked "Experimental: $T = 0.487$."

To determine the relation given in eq. (2) for the present sample of boron, an effective cross section is used for the sample which contains B^{10}, B^{11} and oxygen. Consider now the cross sections of each of these nuclei in turn.

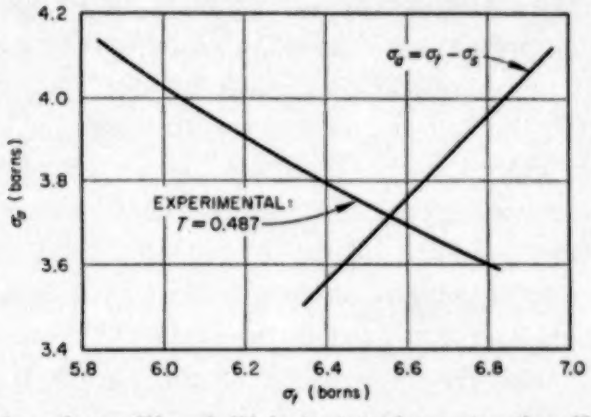

Fig. 1. Graphical solution of eqs. (1) and (2) in text to determine the effective cross section for neutrons in the boron sample shell.

The total cross section of B^{10} has been measured by Newson and Bilpuch [12]) in the energy range from 3 keV to 100 keV. This cross section follows the relation

$$\sigma_t(B^{10}) = \frac{a}{\sqrt{E}} + b, \tag{3}$$

where E is the neutron energy and a and b are constants, in the energy range from 3 keV to at least 70 keV [12]).

The absorption cross section for B^{10}, i.e. the sum of the (n, α) and (n, $\alpha\gamma$) reaction cross sections, is determined from the following measurements:

(a) Absolute measurements [13, 14]) of the total cross section of B^{10} in the thermal neutron energy range have indicated $1/v$ behaviour to an accuracy of ± 1 %; since the scattering cross section is less than 1 % of the total cross section in this energy range, σ_a follows the relation, quoted with an accuracy of ± 1 % or better [13, 14]),

$$\sigma_a = \frac{612}{\sqrt{E}} \text{b} \tag{4}$$

in the thermal neutron energy range.

(b) It has been shown experimentally by Bichsel and Bonner [15]) that the cross section for $B^{10}(n, \alpha)$ plus $B^{10}(n, \alpha\gamma)$ reactions follows the $1/v$ relation for neutron energies in the range $20 \leqq E \leqq 100$ keV. No uncertainties were attached to the "shape" of the cross-section versus energy curve; only a 25 % uncertainty in absolute value was quoted. Considering, however, the maximum spread (± 3 %) of the published data points in the range up to 100 keV together with the response of long counters as discussed by Allen [16]), a maximum deviation of ± 3 % from $1/v$ behaviour may be estimated for the energy range of interest. Similar measurements by Bilpuch, Weston and Newson [17]) in which a careful comparison between the response of a long counter, that of a bare BF_3 counter, and that of a proton recoil counter was carried out, confirm this result to ± 3 % [18]) for neutron energies up to about 100 keV.

(c) The shape of the total cross section of B^{10} from thermal neutron energies to the keV range has been accurately measured [12, 19]), and no resonance behaviour has been found. Thorough evaluation of all of these considerations leads quite naturally to the assumption that σ_a for B^{10} follows the relation given by eq. (4) from thermal neutron energies to at least 70 keV, and an uncertainty in σ_a for B^{10} of ± 5 % in the keV energy range is indicated. Should this conclusion not be correct, and if the various measurements are required to be consistent, then one or more unlikely irregularities must occur in the B^{10} scattering and/or absorption cross sections between a few eV and a few keV. The constant scattering cross section then, determined from total cross section measurements [12]) and from the absorption cross section of eq. (4), with appropriate uncertainties included, is given as 2.6 ± 0.5 barns, in agreement with an early measurement of Hibdon and Muelhause [20]).

The total cross section of B^{11} in the keV energy range is computed from the measured total cross sections of B^{10} and natural boron [12]). It is found that σ_t, or σ_s, for B^{11} is approximately constant over the limited energy range of interest (15 to 30 keV) and is equal to 5.0 ± 0.5 barns. The total or scattering cross section for oxygen has been measured [21]) to be 3.7 ± 0.3 barns in the energy range of interest here. Thus, using the sample data above together with these cross section values we find that for this sample the effective cross sections are

$$\sigma_a(\text{sample}) = \frac{551}{\sqrt{E(\text{eV})}} \text{ barns}, \tag{5}$$

$$\sigma_s(\text{sample}) = 2.84 \text{ barns}. \tag{5'}$$

Using the result of eq. (5') in eq. (2) yields the curve marked "$\sigma_a = \sigma_t - \sigma_s$" in fig. 1. The intersection of the two curves of fig. 1 gives $\sigma_a = 3.72$ barns, $\sigma_t = 6.56$ barns.

The values of σ_a and σ_t thus obtained are "effective" cross sections for neutrons in the boron shell. If it is assumed, for simplicity, that each elastic collision of a neutron with an atom in the shell causes the neutron to lose a fraction of energy equal to the average fractional energy loss $(1-\varepsilon)$ per collision, then the effective absorption cross section $\bar{\sigma}_a$ may be written:

$$\bar{\sigma}_a = n_0\sigma_{a0}+n_1\sigma_{a1}+n_2\sigma_{a2}+\ldots, \tag{6}$$

where n_i is the fractional number of neutrons captured after i collisions, σ_{ai} is the absorption cross section for neutrons having suffered i collisions. Each of these quantities is dependent on the initial energy E_s of the source neutrons and on the quantity ε. The first three n_i are given as follows:

$$\begin{aligned} n_0 &= (1-T'_0)\frac{\sigma_{a0}}{\sigma_{t0}}, \quad n_1 = (1-T'_0)\frac{\sigma_{s0}}{\sigma_{t0}}(1-P_1)\frac{\sigma_{a1}}{\sigma_{t1}}, \\ n_2 &= (1-T'_0)\frac{\sigma_{s0}}{\sigma_{t0}}(1-P_1)\frac{\sigma_{s1}}{\sigma_{t1}}(1-P_2)\frac{\sigma_{a2}}{\sigma_{t2}}, \end{aligned} \tag{7}$$

where σ_{ti} and σ_{si} are the total and scattering cross sections respectively for neutrons having suffered i collisions, P_i is the probability of escape without further interaction of a neutron having suffered i collisions. The P_i are functions of shell thickness in total mean free paths and shell dimensions; P_i values are obtained directly from the computations of Bethe, Beyster and Carter [22]). Using eq. (7) and succeeding members of the sequence n_i, together with eqs. (2), (4) and (5), and $\varepsilon = 0.838$ in eq. (6), it is found that $\sigma_{a0} = 3.56$ barns. The source energy is then obtained using this value in eq. (5): the result is $E_s = 24.0$ keV.

The uncertainty which must be attached to the source energy is a combination of the following: (a) uncertainty in the transmission T of the order of 1 % giving rise to an energy uncertainty of ± 0.8 keV; (b) uncertainty in the correction for the container walls at the sphere equator, causing an energy uncertainty of ± 0.3 keV; (c) uncertainty in the total and scattering cross sections for the sample, leading to an energy uncertainty of ± 0.7 keV (this includes uncertainty in sample content, but does not include uncertainty in the assumption that $\sigma_{n,\alpha}$ is proportional to $1/v$ from thermal to keV neutron energies); and (d) uncertainty in the analysis of multiple scattering and energy degradation, giving rise to an energy uncertainty of ± 0.3 keV. On this basis, an estimate of the energy uncertainty is ± 1.2 keV. If the uncertainty in $1/v$ behaviour of $\sigma_{n,\alpha}$ is included, giving rise to about ± 5 % uncertainty in $\sigma_{n,\alpha}$ in the region of interest at 20—25 keV, then the comined energy uncertainty is 2.2 keV. Thus the source energy must be given as

$$E_s = 24.0 \pm 2.2 \text{ keV}. \tag{8}$$

The initial energy E_0 of Sb-γ-Be photoneutrons has been estimated by taking account of neutron scattering and energy degradation in the beryllium. This analysis is similar to that outlined above for the boron shell. The assumption is made, however, that no neutrons interact in the antimony, a sufficiently good assumption when the average path length of neutrons in the antimony is small compared with the mean free path of neutrons in antimony. The total and scattering cross sections of Be^9 were assumed to be equal; the value was assumed to be 5.85 ± 0.20 barns [19]). The result of this calculation gives for the initial energy of Sb-γ-Be photoneutrons

$$E_0 = 24.8 \pm 2.4 \text{ keV}. \tag{9}$$

The uncertainty given applies to the quoted average neutron energy; there is an inherent maximum spread of about ± 1.4 keV in neutron energy due to the center-of-mass motion of the $Be^9 + \gamma$ system.

4. Discussion

The results of the present experiment giving 24.0 ± 2.2 keV as the effective neutron energy of the source and 24.8 ± 2.4 keV as the initial Sb-γ-Be photo-

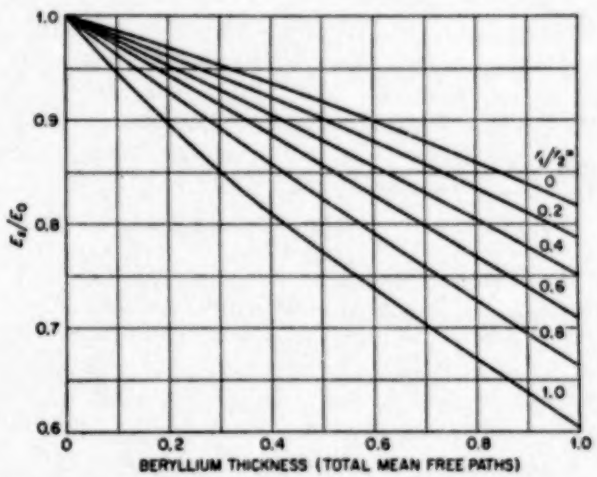

Fig. 2. Ratio of effective source energy to initial Sb-γ-Be photo-neutron energy vs. beryllium thickness for various source dimensions. These results apply to spherical sources; r_1 = inside radius and r_2 = outside radius of beryllium. Simplifying assumptions have been made as discussed in text.

neutron energy may be compared with the neutron energy determined from the gamma ray energy and the $Be^9(\gamma, n)Be^8$ threshold energy. Thus, the Q-value for the $Be^9(\gamma, n)Be^8$ reaction is given by Connors and Miller [23]) as -1.664 ± 0.004 MeV; the energy of the primary neutron-producing Te^{124} gamma ray is given by Strominger, Hollander and Seaborg [24]) to be 1.692 MeV; the neutron energy deduced is then 28 ± 4 keV. The present results may also be compared with the following previously published source neutron energies: Wattenberg [6]), 24 ± 15 keV; Hughes and Eggler [7]), 35 ± 10 keV; Hanson [8]), 24 ± 3 keV; Roberts *et al.* [9]), 20 ± 4 keV; Culp and Hamermesh [10]), 24.5 ± 4 keV.

The calculation of effective neutron energy from a spherical Sb-Be source, as outlined in sect. 3, has been carried out as a function of source dimensions. Again the assumption that no neutrons interact in the antimony is made, and the beryllium total and scattering cross sections are assumed to be the same and equal to 5.85 barns. The fractional energy lost by a neutron in each collision in the beryllium is assumed to be equal to the average fractional energy lost per collision. Because the above simplifications have been made in the calculations, some care is indicated in the use of the results shown in fig. 2. For thick sources, for example, the neutron energy spread may be large and the "effective" energy may depend on the particular experiment.

The author gratefully acknowledges the assistance of N. H. Fuchs in taking some of the transmission data and in carrying out many of the calculations. J. R. Sites has provided the mass spectrometric analysis of the boron sample. Helpful discussions with J. L. Fowler and C. W. Cook are gratefully acknowledged.

References

1) V. Hummel and B. Hamermesh, Phys. Rev. **82** (1951) 67
2) C. Kimball and B. Hamermesh, Phys. Rev. **89** (1953) 1306
3) Macklin, Lazar and Lyon, Phys. Rev. **107** (1957) 504
4) Booth, Ball and MacGregor, Phys. Rev. **112** (1958) 226
5) H. W. Schmitt and C. W. Cook, Nuclear Physics **20** (1960) 202
6) A. Wattenberg, Phys. Rev. **71** (1947) 497
7) D. Hughes and C. Eggler, Phys. Rev. **72** (1947) 902
8) A. O. Hanson, Phys. Rev. **75** (1949) 1794
9) Roberts, Hill and McCammon, Phys. Rev. **80** (1950) 6
10) R. Culp and B. Hamermesh, Phys. Rev. **93** (1954) 1025
11) Gibbons, Macklin, Marion and Schmitt, Phys. Rev. **114** (1959) 1319
12) H. W. Newson and E. Bilpuch, private communication (1959)
13) Schmitt, Block and Bailey, Nuclear Physics, **17** (1960) 109
14) Safford, Taylor, Rustad and Havens, Bull. Am. Phys. Soc. **5** (1960) 288
15) H. Bichsel and T. W. Bonner, Phys. Rev. **108** (1957) 1025
16) W. D. Allen, in Fast neutron physics, edited by J. B. Marion and J. L. Fowler (Interscience Publishers, New York, 1960), Ch. IIIA, p. 361
17) Bilpuch, Weston and Newson, Annals of Physics, in press
18) L. W. Weston, private communication (1960)
19) Unpublished work, included in Hughes and Schwartz, Report BNL-325, Second Edition, Supt. of Documents, U. S. Printing Office, Washington, D. C. (1958)
20) C. T. Hibdon and C. O. Muelhause, Argonne National Laboratory Report ANL 4552 (unpublished)
21) C. K. Bockelman, Phys. Rev. **80** (1950) 1011
22) Bethe, Beyster and Carter, J. Nucl. Energy **3** (1956) 207, 273; **4** (1957) 3, 147 (originally written as Los Alamos Report LA-1429 (1955))
23) D. R. Connors and W. C. Miller, Bull. Am. Phys. Soc. **1** (1956) 340
24) Strominger, Hollander and Seaborg, Revs. Mod. Phys. **30** (1958) 585

8.A

Nuclear Physics **20** (1960) 227—253; © *North-Holland Publishing Co., Amsterdam*

Not to be reproduced by photoprint or microfilm without written permission from the publisher

EINE SYSTEMATISCHE UNTERSUCHUNG π^--MESONISCH ZERFALLENDER HYPERFRAGMENTE, DIE DURCH K^--MESONEN ERZEUGT WURDEN

J. TIETGE

Max-Planck-Institut für Physik und Astrophysik, München

Eingegangen am 27. Mai 1960

Abstract: A stack of nuclear emulsions (Ilford G5), exposed to the 300 MeV/c K^--beam of the Berkeley Bevatron, has been scanned systematically for hyperfragments. 36 hyperfragments decaying by the π^--mesonic mode were found. 24 of these hyperfragments could be analyzed uniquely in the sense of the criteria given. Binding energies are obtained for ${}_\Lambda H^3$, ${}_\Lambda H^4$, ${}_\Lambda He^4$, ${}_\Lambda He^5$, ${}_\Lambda Li^8$ and ${}_\Lambda Li^9$. Angular, energy and momentum distributions of the ${}_\Lambda He^5$ decay products are studied and compared with the corresponding theoretical distributions given by Byers and Cottingham. The mean lifetime for ${}_\Lambda H^4$-hyperfragments is calculated. Finally, the nuclear capture of a Σ^--hyperon is described, from which a hydrogen nucleus (very probably a proton) and a π^--meson were emitted.

1. Einleitung

Bei den Wechselwirkungen von K^--Mesonen mit Nukleonen können Λ^0- und Σ-Hyperonen entstehen, zum Beispiel

$$K^- + N \to \begin{cases} \Lambda^0 + \pi \\ \Sigma + \pi \end{cases} \quad \text{oder} \quad K^- + N + N \to \begin{cases} \Lambda^0 + N \\ \Sigma + N. \end{cases}$$

Die Σ-Hyperonen können durch sekundäre Reaktionen wiederum in Λ^0-Hyperonen übergehen:

$$\Sigma^0 \to \Lambda^0 + \gamma, \quad \Sigma^\pm + \begin{pmatrix} n \\ p \end{pmatrix} \to \Lambda^0 + \begin{pmatrix} p \\ n \end{pmatrix}.$$

Von den Λ^0-Hyperonen ist bekannt, daß sie an Kernfragmente gebunden werden und somit Hyperfragmente bilden können. Das in einem Hyperfragment gebundene Λ^0 hat im wesentlichen drei Reaktionsmöglichkeiten. Es kann zerfallen wie ein freies Λ^0,

$$\Lambda^0 \to \begin{cases} p + \pi^- + 37.2\ \text{MeV} \\ n + \pi^0 + 40.5\ \text{MeV}, \end{cases}$$

oder es kann mit einem Nukleon im Hyperfragment reagieren und sich dabei in ein Neutron umwandeln,

$$\Lambda^0 + N \to n + N + 175.6\ \text{MeV}.$$

Jede der drei Reaktionen bedeutet den Zerfall des Hyperfragments; man unterscheidet entsprechend π^--mesonische, π^0-mesonische und nichtmesonische Hyperfragmentzerfälle. In der vorliegenden Arbeit sollen nur die Hyperfragmente mit π^--mesonischem Zerfall untersucht werden.

2. Experiment

Ein Paket trägerfreier Kernemulsionen vom Typ Ilford G 5, das aus 105 Emulsionsschichten mit den Dimensionen 8.9 cm × 14.0 cm × 600 μm bestand, wurde im 300 MeV/c K^--Mesonen-Strahl am Bevatron in Berkeley exponiert.

2.1. DURCHMUSTERUNG

In den einzelnen Emulsionsschichten wurden die K^--Spuren 3 mm von der Eintrittskante entfernt aufgesucht und bis zu ihrem irgendwo im Emulsionspaket liegenden Ende verfolgt. Von den so verfolgten 8912 K^--Mesonen machten 1805 eine Reaktion oder einen Zerfall im Fluge; die restlichen 7107 kamen zur Ruhe und wurden von einem Atomkern der Emulsion eingefangen. Alle von den K^--Flug- und Einfangreaktionen ausgehenden Spuren (außer denen mit Minimum- oder nahezu Minimumionisation) wurden bis zu ihrem Ende verfolgt. Fand dort eine Wechselwirkung statt, von der mehr als minimal ionisierende Sekundärspuren ausgingen, so wurden auch diese bis zu ihrem Ende verfolgt. Auf diese Weise wurden 37 mögliche Hyperfragmente mit π^--mesonischem Zerfall gefunden. Bei 36 Ereignissen hiervon waren die Meßergebnisse mit der Deutung dieser Ereignisse als Hyperfragmente vereinbar (siehe Tab. 1). Das restliche Ereignis (Ereignis 25) stellte den Kerneinfang eines Σ^--Hyperons dar, bei dem ein Wasserstoffkern und ein π^--Meson emittiert wurden.

Für die π^--mesonisch zerfallenden Hyperfragmente stimmt innerhalb der statistischen Schwankungen das Ladungsspektrum bei Erzeugung durch Ruheeinfänge negativer K-Mesonen, wie es sich aus Tab. 1 ergibt, mit dem Ladungsspektrum bei Erzeugung durch 4.5 GeV π^--Mesonen [1]) überein.

2.2. MESSUNGEN UND DEREN UNSICHERHEITEN

An jedem möglichen Hyperfragment und den Spuren seiner geladenen Zerfallsprodukte wurden Reichweite- und Winkelmessungen durchgeführt. Für alle einfach geladenen Teilchen wurde die Energie-Reichweite-Beziehung von W. H. Barkas [2]) verwendet. Nach dieser $E-R$-Beziehung soll die Reichweite der μ^+-Mesonen aus den Ruhezerfällen $\pi^+ \to \mu^+ + \nu$ gleich 602.2±1.5 μm sein. Zum Vergleich wurden 50 solche μ^+-Mesonen ausgemessen. Als Mittelwert ihrer Reichwerten ergab sich

$$R(\mu^+) = 601.9 \pm 3.6\ \mu\text{m}.$$

Korrektionen, die das Bremsvermögen der benutzten Emulsionen dem Brems-

vermögen, das der Barkas'schen Energie-Reichweite-Beziehung zugrunde liegt, angleichen, waren also nicht notwendig.

Für mehrfach geladene Kerne ($Z \geqq 2$) mit kleinen Geschwindigkeiten ($\beta \lesssim Z/137$), für die die Barkas'sche $E-R$-Beziehung nicht mehr zuverlässig ist, wurden die Energie-Reichweite-Kurven von J. J. Wilkins [3]) benutzt.

Die bei den Reichweitemessungen vorhandenen Unsicherheiten wurden mit einem Meßfehler von 2 % in der gesamten Reichweite berücksichtigt. Typische Meßfehler bei den Winkelmessungen an Spuren länger als etwa 50 μm sind zum Beispiel: 0.5° bis 1° beim projizierten Winkel α (das ist der Winkel zwischen den Projektionen zweier Spuren in die horizontale Ebene) und 1° bis 2.5° beim Tauchwinkel θ (das ist der Neigungswinkel einer Spur gegen die horizontale Ebene in der ungeschrumpften Emulsion).

3. Analyse der Hyperfragmentzerfälle

Es wurde versucht, aus den Reichweite- und Winkelmessungen an den Zerfallsspuren die Zerfallsschemata der Hyperfragmente zu bestimmen.

3.1. ANALYSE DER RUHEZERFÄLLE

3.1.1. *Zerfälle mit zwei kollinearen Sekundärspuren*

Aus der Kollinearität der beiden Spuren wurde geschlossen, daß die Zerfälle Ruhezerfälle waren, und daß bei ihnen keine neutralen Zerfallsprodukte emittiert wurden:

$$\mathrm{Hf} \rightarrow \mathrm{Fr} + \pi^- .$$

Die jeweils sehr kurze Reichweite $R(\mathrm{Fr})$ des Atomkerns Fr wurde folgendermaßen bestimmt:

$$R(\mathrm{Fr}) = \frac{R_{\mathrm{proj}}(\mathrm{Fr})}{\cos\theta(\pi^-)} .$$

$R_{\mathrm{proj}}(\mathrm{Fr})$ bedeutet die Länge der Projektion der Fr-Spur in die horizontale Ebene, und $\theta(\pi^-)$ ist der Tauchwinkel der π^--Spur. $\theta(\pi^-)$ ist stets sehr viel genauer meßbar als $\theta(\mathrm{Fr})$, der Tauchwinkel der Fr-Spur.

Der Kern Fr hat dem Betrage nach den gleichen Impuls wie das π^--Meson. Nun wurden für Fr alle möglichen Kerne angenommen (beginnend mit He^3) und die zugehörigen Reichweiten berechnet. Für die beiden Kerne K_1 und K_2 seien die so berechneten Reichweiten $R_b(\mathrm{Fr} \equiv K_1)$ und $R_b(\mathrm{Fr} \equiv K_2)$. $R_b(\mathrm{Fr} \equiv K_1)$ möge der gemessenen Reichweite R (Fr) am nächsten liegen, und $R_b(\mathrm{Fr} \equiv K_2)$ liege $R(\mathrm{Fr})$ am zweitnächsten. Der Hyperfragmentzerfall ist dann als eindeutig analysiert anzusehen, d.h., es ist ihm das Zerfallsschema

$$\mathrm{Hf} \rightarrow K_1 + \pi^-$$

zuzuordnen, wenn die folgenden drei Bedingungen erfüllt sind:

$$|R_b(\mathrm{Fr} \equiv \mathrm{K}_1) - R_b(\mathrm{Fr} \equiv \mathrm{K}_2)| = D \geqq 1\mu\mathrm{m}, \tag{1}$$

$$|R_b(\mathrm{Fr} \equiv \mathrm{K}_1) - R(\mathrm{Fr})| \leqq \mathrm{Min}(2\mu\mathrm{m}, \tfrac{1}{3}D), \tag{2}$$

$$B_\Lambda > 0 \text{ (innerhalb der Fehlergrenzen).} \tag{3}$$

B_Λ ist die Bindungsenergie des Λ^0 im Hyperfragment.

3.1.2. *Zerfälle mit drei komplanaren Sekundärspuren*

Die drei Sekundärspuren wurden als komplanar angesehen, wenn der kleinste Winkel, den eine Spur mit der Ebene der beiden anderen nach den Meßergebnissen bildete, kleiner als 6° war (bei den Zerfällen, deren drei Sekundärspuren nicht komplanar waren, betrug dieser Winkel stets mehr als 15°). Aus der Komplanarität der Spuren wurde geschlossen, daß die Hyperfragmente in Ruhe zerfielen, und daß bei diesen Zerfällen keine neutralen Zerfallsprodukte auftraten:

$$\mathrm{Hf} \rightarrow \mathrm{Fr}_1 + \mathrm{Fr}_2 + \pi^-.$$

Die beiden längsten Reichweiten (die π^--Reichweite und die Fr_2-Reichweite) wurden direkt gemessen. Die kürzeste Reichweite (die Fr_1-Reichweite) wurde nach folgender Gleichung bestimmt:

$$R(\mathrm{Fr}_1) = \frac{R_{\mathrm{proj}}(\mathrm{Fr}_1)}{\cos\theta_c(\mathrm{Fr}_1)}. \tag{4}$$

$R_{\mathrm{proj}}(\mathrm{Fr}_1)$ ist die Länge der Projektion der Fr_1-Spur in die horizontale Ebene. $\theta_c(\mathrm{Fr}_1)$ ist der aus den Tauchwinkeln $\theta(\pi^-)$ und $\theta(\mathrm{Fr}_2)$ und den projizierten Winkeln $\alpha(\pi^-, \mathrm{Fr}_2)$ und $\alpha(\pi^-, \mathrm{Fr}_1)$ unter Benutzung der Komplanarität von π^--, Fr_1- und Fr_2-Spur berechnete Tauchwinkel der Fr_1-Spur. Wegen der Kürze der Fr_1-Reichweiten ist ihre Bestimmung nach Gleichung (4) genauer als die durch direkte Messungen.

Für Fr_1 und Fr_2 wurden alle möglichen Kerne angenommen. Aus dem Impuls des π^--Mesons und des für Fr_2 angenommenen Kerns sowie aus dem Winkel zwischen der π^-- und der Fr_2-Spur folgt der Impuls des für Fr_1 angenommenen Kerns, und daraus läßt sich die zugehörige Fr_1-Reichweite $R_b(\mathrm{Fr}_1)$ berechnen. Auf diese Weise wurden alle möglichen Zerfallsschemata durchgerechnet. Im Zerfallsschema Z_1 sei für Fr_1 der Kern K_1 und für Fr_2 der Kern K_3 gesetzt; im Zerfallsschema Z_2 entspreche Fr_1 der Kern K_2 und Fr_2 der Kern K_4. Von den bei der Durchrechnung aller möglichen Zerfallsschemata erhaltenen Fr_1-Reichweiten möge die aus dem Zerfallsschema Z_1 folgende $R_b(\mathrm{Fr}_1 \equiv \mathrm{K}_1)$ der Reichweite $R(\mathrm{Fr}_1)$ am nächsten liegen, und die aus dem Zerfallsschema Z_2 folgende $R_b(\mathrm{Fr}_1 \equiv \mathrm{K}_2)$ möge ihr am zweitnächsten liegen. Der untersuchte Hyperfragmentzerfall gilt dann als eindeutig analysiert, d.h., es ist ihm das

Zerfallsschema Z_1,

$$Hf \rightarrow K_1 + K_3 + \pi^-,$$

zuzuordnen, falls die drei Eindeutigkeitskriterien (1), (2) und (3) erfüllt sind; für das dortige Fr setze man hier Fr_1.

3.1.3. *Kompliziertere Zerfälle*

Bei hinreichend langen Hyperfragmentspuren ($\gtrsim 20\,\mu$m) kann man an der Ionisation und der Streuung im allgemeinen erkennen, ob ein Ruhezerfall vorliegt oder nicht. Ist eine Hyperfragmentspur kürzer als etwa 20 μm, so ist eine derartige Unterscheidung praktisch nicht mehr möglich.

Nur das π^--Meson konnte sicher identifiziert werden. Für die übrigen Zerfallsspuren wurden alle möglichen Kerne angenommen und die zugehörigen kinetischen Energien und Impulse aus den gemessenen Reichweiten bestimmt. Danach wurde für jedes mögliche Zerfallsschema ohne und mit Neutronen der Restimpuls P_r der geladenen Zerfallsprodukte berechnet (das ist die Summe der Impulse der geladenen Zerfallsprodukte). Wie aus Tab. 1 zu ersehen ist, ergaben die eindeutig analysierten Hyperfragmentzerfälle mit drei komplanaren Sekundärspuren für die richtigen Zerfallsschemata Restimpulse bis zu 30 MeV/c. Die komplizierteren (d.h., weder kollinearen noch komplanaren) Ruhezerfälle von Hyperfragmenten mußten nun eine der folgenden drei Bedingungen erfüllen, um als eindeutig analysiert angesehen zu werden:

1) Alle Zerfallsschemata mit einem und mehr Neutronen ergeben negative Bindungsenergien B_Λ, bzw. negative obere Grenzen von B_Λ. Unter den Zerfallsschemata ohne Neutronen gibt es nur eins mit einem Restimpuls $P_r < 30$ MeV/c und $B_\Lambda > 0$.

2) Alle Zerfallsschemata mit zwei und mehr Neutronen ergeben negative obere Grenzen von B_Λ. Alle Zerfallsschemata ohne Neutronen ergeben, wenn überhaupt positive B_Λ, dann nur gleichzeitig mit Restimpulsen $P_r > 45$ MeV/c. Unter den Zerfallsschemata mit einem Neutron gibt es nur eins, für das B_Λ positiv wird.

3) Alle Zerfallsschemata mit einem Neutron ergeben negative B_Λ. Alle Zerfallsschemata ohne Neutronen ergeben höchstens positive B_Λ, wenn gleichzeitig $P_r > 45$ MeV/c wird. Unter den Zerfallsschemata mit zwei und mehr Neutronen gibt es nur eins, für das die obere Grenze von B_Λ positiv wird.

Die Bedingungen für die Bindungsenergie B_Λ brauchten natürlich auch hier nur innerhalb der Fehlergrenzen erfüllt zu sein.

3.2. ANALYSE DER FLUGZERFÄLLE

Jeder der drei sicheren Hyperfragment-Flugzerfälle, die gefunden wurden, zeigte drei Zerfallsspuren. Es wurden alle möglichen Zerfallsschemata ohne Neutronen durchgerechnet:

$$Hf \rightarrow Fr_1 + Fr_2 + \pi^-.$$

TABELLE

Experimentelle Daten der Hyperfragmente π^--

Ereignis Nr.	Hyperfragment				laden
	Zerfallsschema	Reichw. [μm] [a]	Eigenflugzeit [10^{-12} sec] [b]	Teilchen	Reic [μ
1	${}_\Lambda H^{2,3,4} \rightarrow H^{1,2,3} + H^1 + \pi^-$	496	(24.0)	π^- H^1 $H^{1,2,3}$	1642 19
2	${}_\Lambda H^4 \rightarrow H^3 + H^1 + \pi^-$	415	23.3	π^- H^1 H^3	105 5
3	${}_\Lambda He^5 \rightarrow He^4 + H^1 + \pi^-$	28.1	2.5	π^- H^1 He^4	104 2
4	${}_\Lambda Li^9 \rightarrow He^4 + He^4 + n + \pi^-$	33.0	2.5	π^- He^4 He^4	173
5	${}_\Lambda He^5 \rightarrow He^4 + H^1 + \pi^-$	10.8	1.2	π^- H^1 He^4	16
6	${}_\Lambda He^5 \rightarrow He^4 + H^1 + \pi^-$	45.4	3.5	π^- H^1 He^4	13
7	${}_\Lambda He^4 \rightarrow He^3 + H^1 + \pi^-$	122	6.9	π^- H^1 He^3	7
8	(?)	41.2	(2.9)	π^- (?) (?)	1
9	${}_\Lambda H^4 \rightarrow H^3 + H^1 + n + \pi^-$ oder ${}_\Lambda H^4 \rightarrow H^1 + H^1 + n + n + \pi^-$	57.3	6.3	π^- $H^{1,2}$ $H^{1,2}$	1
10	${}_\Lambda He^5 \rightarrow He^4 + H^1 + \pi^-$	75.0	4.9	π^- H^1 He^4	

[a]) Bei den Flugzerfällen (24, 35, 36) ist in Klammern die berechnete Restreichweite des Hyperfragments im Zerfallspunkt angegeben. Darüber steht jeweils die Weglänge vom K^--Einfang bis zum Zerfallspunkt.

[b]) Die Eigenflugzeit ist immer dann in Klammern angegeben, wenn Ladung und Masse des Hyperfragments nicht eindeutig bestimmt werden konnten. In allen diesen Fällen ist der angegebene Wert das arithmetische Mittel der verschiedenen möglichen Eigenflugzeiten. War das Zerfallsschema ganz unbekannt ((?) in Spalte (1)), so wurde die Eigenflugzeit eines Protons mit der Reichweite des Hyperfragments angegeben.

t π^--mesonischem Zerfall

ladene Zerfallsprodukte			P_T	$\lvert\vec{\pi}[\vec{Fr}_1 \times \vec{Fr}_2]\rvert$	K⁻-Reaktion	
Reichw. [μm]	Θ [Grad] [c]	ϕ [Grad]	$\left[\frac{MeV}{c}\right]$ [d]	oder $\sin\psi(\pi^-, Fr)$ [e]	Ruheeinfang oder Flug-reaktion	Anzahl der erzeugten Spuren (ohne Hf.)
16426	−13.3	343.5				
196	+16.6	162.7			F	1+π
0						
10594	+12.2	135.7				
575	−40.2	311.8	8	0.020	R	4+π
8.6	+71.1	126.4				
10449	+36.8	68.0				
272	+16.7	46.5	9	0.021	R	4
19.2	−26.6	231.9				
17347	+50.9	84.8				
13.9	+35.3	67.5			R	3
15.0	−42.0	262.1				
16645	+9.0	290.7				
14.0	+34.3	230.7	20	0.056	R	2
7.6	−17.1	105.1				
13310	−4.7	120.8				
124	−59.7	165.3	29	0.035	R	3
11.1	+27.3	308.7				
7773	−2.5	186.0				
719	+64.7	24.7	25	0.076	R	2+π
11.4	−73.7	352.7				
14073	+9.9	108.1				
48.2	−62.6	294.1			R	3
2.8	+44.5	287.3				
10598	+7.1	149.2				
28.2	+11.9	311.0			R	1
7.1	+36.0	347.4				
9875	−40.6	307.6				
315	−33.6	240.1	9	0.039	R	4
17.3	+38.5	85.7				

[c]) Bei einem positiven Tauchwinkel Θ wird das betreffende Zerfallsprodukt in den oberen Halbraum (zur Emulsionsoberfläche) emittiert, bei negativem Θ wird es in den unteren Halbraum (zum Glas) emittiert.

[d]) Der Restimpuls P_T ist für alle eindeutig analysierten Ruhezerfälle mit nur geladenen Zerfallsprodukten angegeben (ausgenommen die Ereignisse 19 und 29).

[e]) Für die komplanaren Dreikörper-Zerfälle ist das Parallelepipedon-Volumen $\lvert\vec{\pi}[\vec{Fr}_1 \times \vec{Fr}_2]\rvert$ angegeben. $\vec{\pi}$, $\vec{Fr}_1$ und $\vec{Fr}_2$ sind die Einheitsvektoren in Richtung der π^--, der Fr_1- und der Fr_2-Spur. Für die kollinearen Zweikörper-Zerfälle ist $\sin\psi(\pi^-, Fr)$ angegeben. $\psi(\pi^-, Fr)$ ist der Winkel zwischen der π^-- und der Fr-Spur.

TABELLE (Forts.)

Ereignis Nr.	Hyperfragment			Teilchen	(Fortsetzung)
	Zerfallsschema	Reichw. [μm] [a]	Eigenflugzeit [10^{-12} sec] [b]		Reichw. [μm]
11	${}_{\Lambda}He^{5} \rightarrow He^{4}+H^{1}+\pi^{-}$	80.1	5.2	π^{-} H^{1} He^{4}	163
12	${}_{\Lambda}He^{4} \rightarrow He^{3}+H^{1}+\pi^{-}$	163	7.9	π^{-} H^{1} He^{3}	154
13	(?)	22.4	(2.0)	π^{-} (?)	21
14	${}_{\Lambda}Li^{8} \rightarrow Be^{7}+n+\pi^{-}$ oder ${}_{\Lambda}Li^{9} \rightarrow Be^{7}+n+n+\pi^{-}$	11.4	1.0	π^{-} Be^{7}	5
15	(?)	2.7	(0.4)	π^{-} (?) (?)	10
16	${}_{\Lambda}He^{5} \rightarrow He^{4}+H^{1}+\pi^{-}$	10.6	1.2	π^{-} H^{1} He^{4}	14
17	${}_{\Lambda}He^{4} \rightarrow H^{2}+H^{1}+H^{1}+\pi^{-}$	81.7	4.9	π^{-} H^{1} H^{1} H^{2}	6
18	${}_{\Lambda}H^{4} \rightarrow He^{3}+n+\pi^{-}$	255	16.7	π^{-} He^{3}	17
19	${}_{\Lambda}H^{4} \rightarrow He^{4}+\pi^{-}$	514	27.0	π^{-} He^{4}	
20	(?)	4.2	(0.6)	π^{-} (?) (?)	
21	${}_{\Lambda}He^{5} \rightarrow He^{4}+H^{1}+\pi^{-}$	60.3	4.3	π^{-} H^{1} He^{4}	
22	(?)	1174	(30.5)	π^{-} (?) (?)	1
23	${}_{\Lambda}He^{5} \rightarrow He^{4}+H^{1}+\pi^{-}$	28.3	2.5	π^{-} H^{1} He^{4}	

Siehe Fußnoten auf Seiten 232, 233.

ortsetzung)

eladene Zerfallsprodukte			P_r	$\lvert\vec{\pi}[\vec{Fr}_1 \times \vec{Fr}_2]\rvert$	K⁻-Reaktion	
Reichw. [μm]	Θ [Grad] [c]	ϕ [Grad]	$\left[\frac{MeV}{c}\right]$ [d]	oder $\sin\psi(\pi^-, Fr)$ [e]	Ruheeinfang oder Flug-reaktion	Anzahl der erzeugten Spuren (ohne Hf.)
16380	−5.6	9.6				
37.8	+11.7	102.9	9	0.005	R	1+π
5.6	0	216.9				
15455	−5.3	69.7				
51.1	−64.3	197.0	21	0.059	R	3
7.5	+29.0	264.0				
21660	+6.4	kollinear		≈ kollinear	R	2
2.2	<0					
5339	+8.0	29.1			R	1
3.6	−31.3	155.6				
10532	+29.0	299.0				
12.2	+11.2	53.5			R	1
2.4	0.	201.0				
14158	+6.5	330.0				
59.1	−17.7	27.0	19	0.111	R	3
9.9	+11.3	171.0				
6924	−15.8	131.5				
177	+67.6	296.4	12		R	3+π
55.2	+47.3	300.3				
64.8	−76.8	85.6				
17712	+11.2	94.1			R	2+π^+
8.2	0	264.0				
	0	118.5		0.061	R	2
8.2	0	302.0				
1172	+12.8	3.0				
1038	+1.7	159.0			R	1+π
0						
7953	−50.4	121.8				
496	−32.8	43.9	15	0.060	R	4+π
18.3	+49.3	244.4				
18101	−12.7	141.1				
47.3	+18.4	339.9			R	4
1.1						
7857	+74.9	53.0				
746	−33.0	117.3	12	0.039	R	2+π
9.3	0	286.4				

TABELLE (Forts

Ereignis Nr.	Hyperfragment				Gelad
	Zerfallsschema	Reichw. [μm] [a])	Eigenflugzeit [10^{-12} sec] [b])	Teilchen	Re [μ
24	${}_{\Lambda}H^{3} \rightarrow H^{2}+H^{1}+\pi^{-}$ Flugzerfall	1801 (3468)	31.2	π^{-} H^{1} H^{2}	14 3 1
26	${}_{\Lambda}He^{5} \rightarrow He^{4}+H^{1}+\pi^{-}$	116	6.7	π^{-} H^{1} He^{4}	2 1
27	${}_{\Lambda}H^{4} \rightarrow He^{3}+n+\pi^{-}$	169	12.8	π^{-} He^{3}	12
28	${}_{\Lambda}Li^{8} \rightarrow He^{4}+He^{4}+\pi^{-}$	93.1	5.1	π^{-} He^{4} He^{4}	15
29	${}_{\Lambda}H^{4} \rightarrow He^{4}+\pi^{-}$	32.9	3.9	π^{-} He^{4}	
30	(?)	20.3	(1.9)	π^{-} (?) (?)	1
31	${}_{\Lambda}H^{4} \rightarrow H^{3}+H^{1}+\pi^{-}$	430	23.9	π^{-} H^{1} H^{3}	1
32	(?)	10.0	(1.1)	π^{-} (?) (?) (?)	1
33	${}_{\Lambda}He^{4} \rightarrow He^{3}+H^{1}+\pi^{-}$ oder ${}_{\Lambda}He^{5} \rightarrow He^{4}+H^{1}+\pi^{-}$	30.2	(2.5)	π^{-} H^{1} $He^{3,4}$	
34	${}_{\Lambda}He^{4} \rightarrow He^{3}+H^{1}+\pi^{-}$ oder ${}_{\Lambda}He^{5} \rightarrow He^{4}+H^{1}+\pi^{-}$	193	(9.2)	π^{-} H^{1} $He^{3,4}$	
35	${}_{\Lambda}H^{4} \rightarrow H^{3}+H^{1}+\pi^{-}$ Flugzerfall	7930 (4007)	128.2	π^{-} H^{1} H^{3}	
36	${}_{\Lambda}H^{4} \rightarrow H^{3}+H^{1}+\pi^{-}$ Flugzerfall	648 (260)	22.7	π^{-} H^{1} H^{3}	
37	${}_{\Lambda}He^{5} \rightarrow He^{4}+H^{1}+\pi^{-}$	78.8	5.2	π^{-} H^{1} He^{4}	

Siehe Fußnoten auf Seiten 232, 233.

LLE (Fortsetzung)

Geladene Zerfallsprodukte			P_r $\left[\frac{MeV}{c}\right]$ [d]	$\lvert\vec{\pi}[\vec{Fr}_1 \times \vec{Fr}_2]\rvert$ oder $\sin\varphi$ (π^-, Fr) [e]	K$^-$-Reaktion	
Reichw. [μm]	Θ [Grad] [c]	ϕ [Grad]			Ruheeinfang oder Flugreaktion	Anzahl der erzeugten Spuren (ohne Hf.)
14001	+38.3	359.1				
3568	+8.0	232.7			R	3
1892	+10.9	243.7				
2534	+76.9	250.3				
1466	+42.3	210.0	13	0.019	R	2
34.5	−53.1	31.4				
12999	−33.1	307.0				
23.2	+18.3	118.8			R	4
15888	−12.2	318.4				
60.4	−39.0	163.0	19	0.052	R	1
38.8	+59.6	358.2				
	−40.0	21.8		0.058	R	5
8.5	+36.7	201.7				
15978	+56.1	272.0				
90.6	−80.0	272.0			R	2
0						
14821	+56.2	1.8				
174	−56.5	225.5	3	0.003	R	3
3.1	0	115.0				
10819	+21.6	207.1				
29.5	−5.3	70.4			R	2
8.1	0	303.8				
2.2	0	113.0				
3282	+24.6	137.0				
1714	+40.8	291.0	29	0.026	R	3
24.8	−49.4	101.9				
11330	+23.4	262.9				
553	−20.9	77.8			R	3+π^-
0						
4210	+39.1	306.5				
2216	−28.3	183.8			R	4
5093	−11.1	139.6				
12859	+24.2	151.2				
1108	−26.3	25.0			R	3
109	−33.7	83.5				
15057	−20.0	274.4				
31.6	−5.4	298.6	3	0.006	R	2
10.5	+15.1	104.9				

Im Laborsystem (L-System) folgen die Impuse des π^--Mesons und der verschiedenen für Fr_1 und Fr_2 angenommenen Kerne aus den entsprechenden Reichweiten. Die kinetische Energie $\hat{E}$ eines Zerfallsproduktes im Schwerpunktsystem (S-System) folgt aus seinem Impuls $\hat{p}$ im L-System, seiner Ruhemasse m, seiner Gesamtenergie U im L-System, dem Winkel ϑ zwischen seiner Flugrichtung und der Flugrichtung des Hyperfragments in L-System und der Geschwindigkeit β des Hyperfragments (im Augenblick des Zerfalls):

$$\hat{E} = \frac{U - \hat{p}\beta\cos\vartheta}{\sqrt{1-\beta^2}} - m.$$

(Die Lichtgeschwindigkeit c wurde hier, wie auch im folgenden stets gleich 1 gesetzt.)

β ergab sich aus dem Impuls P des Hyperfragments im L-System und seiner Ruhemasse M. P wurde als Vektorsumme der Impulse der drei Zerfallsprodukte im L-System berechnet.

Jeder der drei Hyperfragmentzerfälle im Fluge galt dann als eindeutig analysiert, wenn es nur ein Zerfallsschema ohne Neutronen gab, für das die beiden folgenden Bedingungen erfüllt waren:

1) Die Komponente des Gesamtimpulses der drei Zerfallsprodukte in der horizontalen Ebene, senkrecht zur Flugrichtung des Hyperfragments, mußte innerhalb der doppelten Fehlergrenzen verschwinden.

2) Die Bindungsenergie B_Λ mußte innerhalb der Fehlergrenzen positiv sein.

An den Spuren von Ereignis 24 und Ereignis 36 waren zusätzlich direkte Massenund Ladungsbestimmungen notwendig, um die Zerfallsschemata für diese beiden Flugzerfälle eindeutig festlegen zu können.

Zerfallsschemata mit Neutronen wurden bei der Analyse der Flugzerfälle nicht berücksichtigt, da bei jedem emittierten Neutron Betrag und Richtung seines Impulses unbekannt sind und daher die für die Transformation vom L- ins S-System benötigte Geschwindigkeit β des Hyperfragments nicht berechnet werden kann.

4. Ergebnisse und Diskussion

4.1. BINDUNGSENERGIEN B_Λ

Die Bindungsenergie B_Λ des Λ^0-Hyperons in einem Hyperfragment wird gegeben durch

$$B_\Lambda = (M + m_{\Lambda^0}) - (\sum_i m_i + Q_{\mathrm{kin}}).$$

M ist die Masse des Kernfragments und m_{Λ^0} die Masse des Λ^0 (Kernfragment und Λ^0 zusammen bilden das Hyperfragment). $\sum_i m_i$ ist die Summe der Massen

aller Zerfallsprodukte, und Q_{kin} ist die gesamte beim Zerfall des Hyperfragments freiwerdende kinetische Energie.

Die Massen der Atomkerne wurden aus den von A. H. Wapstra [4]) gegebenen Kernbindungsenergien unter Verwendung der Protonenmasse [5])

$$m_p = 938.21 \pm 0.01 \text{ MeV}$$

und der Neutronenmasse [5])

$$m_n = 939.51 \pm 0.01 \text{ MeV}$$

berechnet.

Die Masse des Λ^0-Hyperons wird gegeben durch

$$m_{\Lambda^0} = m_p + m_{\pi^-} + Q(\Lambda^0).$$

Die Masse des π^--Mesons ist sehr genau bekannt [5]):

$$m_{\pi^-} = 139.63 \pm 0.06 \text{ MeV}.$$

Für $Q(\Lambda^0)$ wurde der Wert

$$Q(\Lambda^0) = 37.22 \pm 0.20 \text{ MeV}$$

benutzt [1]).

Im folgenden werden die Bindungsenergien B_Λ für alle diejenigen Hyperfragmente gegeben, die eindeutig analysiert werden konnten.

4.1.1. *Wasserstoff-Hyperfragmente*

a) $_\Lambda H^3$-Hyperfragment

Für den Flugzerfall von Ereignis 24 lieferte die Analyse zwei mögliche Zerfallsschemata:

$$_\Lambda H^{2,3} \rightarrow H^{1,2} + H^1 + \pi^-.$$

Streumessungen an der entscheidenden Zerfallsspur ergaben, daß sie von einem Deuteron erzeugt worden war:

$$_\Lambda H^3 \rightarrow H^2 + H^1 + \pi^-.$$

Die gesamte beim Zerfall freiwerdende kinetische Energie betrug im Schwerpunktsystem des $_\Lambda H^3$

$$\bar{Q}_{\text{kin}} = 36.93 \text{ MeV}.$$

Damit folgte

$$B_\Lambda = 0.29 \pm 0.96 \text{ MeV}.$$

Der angegebene Fehler ΔB_Λ ist der aus der Bohrschwankung der Reichweiten und den Unsicherheiten in den Reichweite- und Winkelmessungen berechnete.

b) ${}_\Lambda H^4$-Hyperfragmente

i) Den Ereignissen 19 und 29 konnte sicher der Zweikörper-Zerfall

$$ {}_\Lambda H^4 \rightarrow He^4 + \pi^- $$

zugeordnet werden. Da aber das π^--Meson bei Ereignis 19 nach etwa 3 cm aus dem Emulsionspaket lief und bei Ereignis 29 nach ungefähr 1.5 mm im Fluge verschwand (Ladungsaustausch), wurde in beiden Fällen seine kinetische Energie $E(\pi^-)$ aus Blobdichte-Messungen bestimmt. Wegen der dadurch entstehenden großen Unsicherheiten sind die Bindungsenergien B_Λ in beiden Fällen wertlos.

Ereignis Nr.	$E(\pi^-)$ [MeV]	$E(He^4)$ [MeV]
19	$50.1^{+5.2}_{-4.5}$	2.39 ± 0.05
29	$52.7^{+7.9}_{-5.8}$	2.47 ± 0.05

Eine Mikrophotographie von Ereignis 19 ist in Abb. 1 gezeigt.

${}_\Lambda H^4 \rightarrow He^4 + \pi^- + (53 \pm 5)$MeV.

Abb. 1. Mikrophotographie von Ereignis 19.

ii) Zwei ${}_\Lambda H^4$-Hyperfragmente (Ereignisse 18 und 27) zerfielen folgendermaßen:

$$ {}_\Lambda H^4 \rightarrow He^3 + n + \pi^- . $$

Ereignis Nr.	Q_{kin} [MeV]	B_Λ [MeV]	ΔB_Λ [MeV]
18	35.25	1.21	0.85
27	35.69	0.77	0.62

iii) Für die Ereignisse 2, 31, 35 und 36 ergab die Analyse das Zerfallsschema

$$ {}_\Lambda H^4 \rightarrow H^3 + H^1 + \pi^- . $$

Ereignis Nr.	Q_{kin} [MeV]	B_Λ [MeV]	ΔB_Λ [MeV]	$R(H^3)$ [μm]	$R_b(H^3)$ [μm]
2	35.09	2.13	0.54	8.6	10.2
31	34.44	2.78	0.62	3.1	3.1
35	35.70 †	1.52	1.06	Flugzerfall	
36	36.21 †	1.01	0.64	Flugzerfall	

† Es ist dies die gesamte beim Zerfall freiwerdende kinetische Energie im Schwerpunktsystem des ${}_\Lambda H^4$-Hyperfragments.

4.1.2. *Helium-Hyperfragmente*

a) ${}_\Lambda He^4$-Hyperfragmente

i) Der Vierkörper-Zerfall von Ereignis 17 konnte als Zerfall eines ${}_\Lambda He^4$-Hyperfragments identifiziert werden:

$$ {}_\Lambda He^4 \rightarrow H^2 + H^1 + H^1 + \pi^- , $$

mit

$$ Q_{kin} = 29.62 \text{ MeV}, \quad B_\Lambda = 2.11 \pm 0.41 \text{ MeV}. $$

ii) Den komplanaren Zerfällen der Ereignisse 7 und 12 konnte eindeutig das Zerfallsschema

$$ {}_\Lambda He^4 \rightarrow He^3 + H^1 + \pi^- $$

zugeordnet werden.

Ereignis Nr.	Q_{kin} [MeV]	B_Λ [MeV]	ΔB_Λ [MeV]	$R(He^3)$ [μm]	$R_b(He^3)$ [μm]
7	34.67	2.55	0.46	11.4	11.8
12	34.29	2.93	0.61	7.5	7.1

b) ${}_{\Lambda}He^5$-Hyperfragmente

Es wurden 10 ${}_{\Lambda}He^5$-Hyperfragmente identifiziert. Das Zerfallsschema war in allen Fällen

$${}_{\Lambda}He^5 \rightarrow He^4 + H^1 + \pi^-.$$

Ereignis Nr.	Q_{kin} [MeV]	B_Λ [MeV]	ΔB_Λ [MeV]	$R(He^4)$ [μm]	$R_b(He^4)$ [μm]
3	35.12	2.10	0.52	19.2	20.0
5	34.37	2.85	0.64	7.6	7.2
6	34.50	2.72	0.59	11.1	11.1
10	34.37	2.85	0.51	17.3	17.0
11	34.55	2.67	0.65	5.6	5.3
16	33.63	3.59	0.60	9.9	9.3
21	34.17	3.05	0.46	18.3	18.7
23	34.50	2.72	0.46	9.3	8.8
26	34.90	2.32	0.35	34.5	33.6
37	34.13	3.09	0.61	10.5	10.4

In Abb. 2 ist eine Mikrophotographie von Ereignis 37 gezeigt.

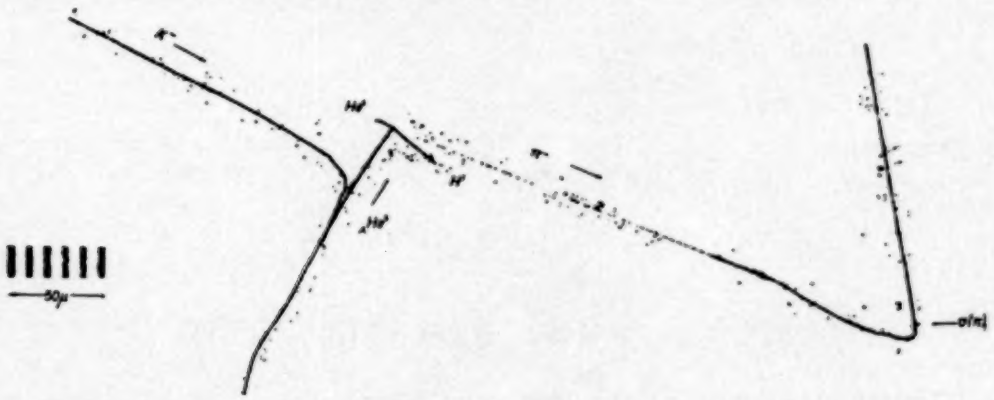

${}_{\Lambda}He^5 \rightarrow He^4 + H^1 + \pi^- + (34{,}1 \pm 0{,}6)\,MeV$

Abb. 2. Mikrophotographie von Ereignis 37.

4.1.3. *Lithium-Hyperfragmente*

a) ${}_{\Lambda}Li^8$-Hyperfragment

Ereignis 28 wurde als ${}_{\Lambda}Li^8$-Hyperfragment mit dem Zerfallsschema

$${}_{\Lambda}Li^8 \rightarrow He^4 + He^4 + \pi^-$$

identifiziert. Es war

$$Q_{\text{kin}} = 48.06\ \text{MeV}, \quad B_\Lambda = 6.51 \pm 0.67\ \text{MeV},$$
$$R(\text{He}^4) = 38.8\,\mu\text{m}, \quad R_b(\text{He}^4) = 37.1\ \mu\text{m}.$$

b) $_\Lambda\text{Li}^9$-Hyperfragment

Ereignis 4 ließ sich nur als Zerfall eines $_\Lambda\text{Li}^9$-Hyperfragments erklären. Die Zuordnung des Zerfallsschemas war eindeutig:

$$_\Lambda\text{Li}^9 \rightarrow \text{He}^4 + \text{He}^4 + \text{n} + \pi^-.$$

Es war

$$Q_{\text{kin}} = 44.52\ \text{MeV}, \quad B_\Lambda = 8.01 \pm 1.06\ \text{MeV}.$$

4.1.4. *Zusammenfassung*

Die Verteilungen der Bindungsenergien B_Λ für die verschiedenen Hyperfragmente sind in Abb. 3 gezeigt. Die gewichteten Mittelwerte $\bar{B}_\Lambda$ der Bindungs-

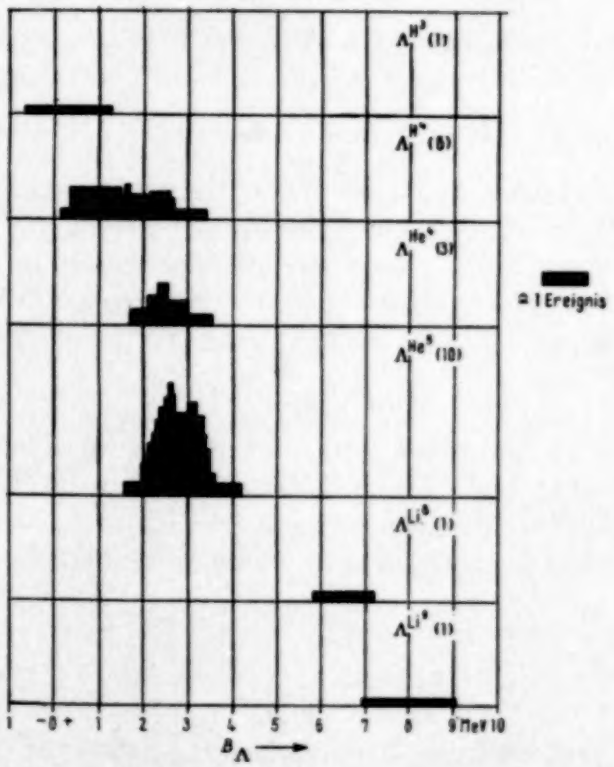

Abb. 3. Verteilungen der Bindungsenergien B_Λ für die verschiedenen Hyperfragmente. Jedem Ereignis entspricht ein Rechteck konstanten Flächeninhalts, dessen Grundlinie dem jeweiligen ΔB_Λ proportional ist.

energien sind in Tab. 2 gegeben. Es ist:

$$\bar{B}_\Lambda = \frac{\sum_i \frac{B_\Lambda^{(i)}}{(\Delta B_\Lambda^{(i)})^2}}{\sum_i \frac{1}{(\Delta B_\Lambda^{(i)})^2}}, \quad \Delta\bar{B}_\Lambda = \left\{\sum_i \frac{1}{(\Delta B_\Lambda^{(i)})^2}\right\}^{-\frac{1}{2}}.$$

TABELLE 2

Gewichtete Mittelwerte $\bar{B}_\Lambda$ der Bindungsenergien für die verschiedenen Hyperfragmente

Hyperfragment	$\bar{B}_\Lambda$ [MeV]	$\Delta\bar{B}_\Lambda$ [MeV]	Anzahl der gemittelten Ereignisse
${}_\Lambda H^3$	0.29	0.96	1
${}_\Lambda H^4$	1.65	0.27	6
${}_\Lambda He^4$	2.43	0.27	3
${}_\Lambda He^5$	2.72	0.16	10
${}_\Lambda Li^8$	6.51	0.67	1
${}_\Lambda Li^9$	8.01	1.06	1

Wie in allen bisher veröffentlichten Arbeiten über Hyperfragmente, so wurde auch in der vorliegenden weder ein ${}_\Lambda H^2$ noch ein ${}_\Lambda He^3$ gefunden. Die Zerfälle

$${}_\Lambda H^2 \to H^1 + H^1 + \pi^- \quad \text{und} \quad {}_\Lambda He^3 \to H^1 + H^1 + H^1 + \pi^-$$

wären leicht zu erkennen und auch eindeutig zu analysieren. Man darf also annehmen, daß die Wechselwirkung eines Λ^0-Hyperons mit 1 oder 2 Protonen in diesen Fällen nicht stark genug ist, um eine Bindung zu erzeugen.

Ebenso wurden Hyperfragmente mit der Baryonenzahl 6 (${}_\Lambda He^6$ und ${}_\Lambda Li^6$) bis jetzt nicht gefunden. Der am häufigsten zu erwartende Zerfall für ${}_\Lambda Li^6$ wäre

$${}_\Lambda Li^6 \to He^4 + H^1 + H^1 + \pi^-.$$

Zerfälle dieser Art können nicht übersehen werden und müßten auch einmal eindeutig analysierbar sein (Ereignis 32 stellt mit Sicherheit kein ${}_\Lambda Li^6$ dar). ${}_\Lambda Li^6$-Hyperfragmente werden also, wenn überhaupt, nur sehr selten vorkommen.

Für ${}_\Lambda He^6$ wäre ein energetisch sehr günstiges Zerfallsschema

$${}_\Lambda He^6 \to He^4 + H^1 + n + \pi^-.$$

Wenn der Impuls des Neutrons nicht zu groß ist, lassen sich solche Zerfälle von den Zerfällen ${}_\Lambda He^5 \to He^4 + H^1 + \pi^-$ nicht unterscheiden. Will man die Abweichungen von der exakten Komplanarität nicht auf Meßunsicherheiten zurückführen sondern als tatsächlich ansehen, so kann man alle 10 ${}_\Lambda He^5$-Zerfälle der vorliegenden Arbeit auch als ${}_\Lambda He^6 \to He^4 + H^1 + n + \pi^-$ interpretieren.

In der vorliegenden Arbeit ist das schwerste Hyperfragment, für das die Bindungsenergie B_Λ bestimmt werden konnte, ein ${}_\Lambda Li^9$. Das schwerste Hyperfragment mit π^--mesonischem Zerfall, das bisher überhaupt innerhalb der Fehlergrenzen eindeutig analysiert werden konnte [6]), ist ein ${}_\Lambda B^{12}$. Da das Verhältnis der nichtmesonischen zu den π^--mesonischen Zerfällen mit wachsender Kernladung Z der Hyperfragmente sehr stark ansteigt [7]), ist man zur Bestimmung der Bindungsenergien B_Λ von noch schwereren Hyperfragmenten praktisch auf die Untersuchung nichtmesonischer Zerfälle angewiesen.

4.2. ENERGIE-, IMPULS- UND WINKELVERTEILUNGEN DER ZERFALLSPRODUKTE

In diesem Abschnitt werden nur diejenigen Hyperfragmentzerfälle berücksichtigt, die sicher das folgende Zerfallsschema haben:

$$Hf \rightarrow Fr + H^1 + \pi^-.$$

Proton und π^--Meson wurden als die Zerfallsprodukte eines fiktiven „Λ^0"-Hyperons angesehen. Dann lassen sich für diese „Λ^0"-Hyperonen die $Q_{„\Lambda"}$-Werte berechnen. $Q_{„\Lambda"}$ ist die Summe der kinetischen Energien von Proton und π^--Meson im Ruhesystem des „Λ^0":

$$Q_{„\Lambda"} = (m_p + m_\pi) \cdot \left\{ \left(1 + \frac{2Q^*}{m_p + m_\pi} \right)^{\frac{1}{2}} - 1 \right\},$$

mit

$$Q^* = \frac{U_p U_\pi - m_p m_\pi - p_p p_\pi \cos \psi}{m_p + m_\pi}.$$

m_p und m_π sind die Ruhemassen von Proton und π^--Meson. U_p und p_p sind Gesamtenergie und Impuls des Protons im Ruhesystem des Hyperfragments. U_π und p_π sind die entsprechenden Größen für das π^--Meson. ψ ist der Winkel zwischen den Flugrichtungen von Proton und π^--Meson im Ruhesystem des Hyperfragments.

Abb. 4 zeigt die Verteilung der $Q_{„\Lambda"}$-Werte aus der vorliegenden Arbeit.

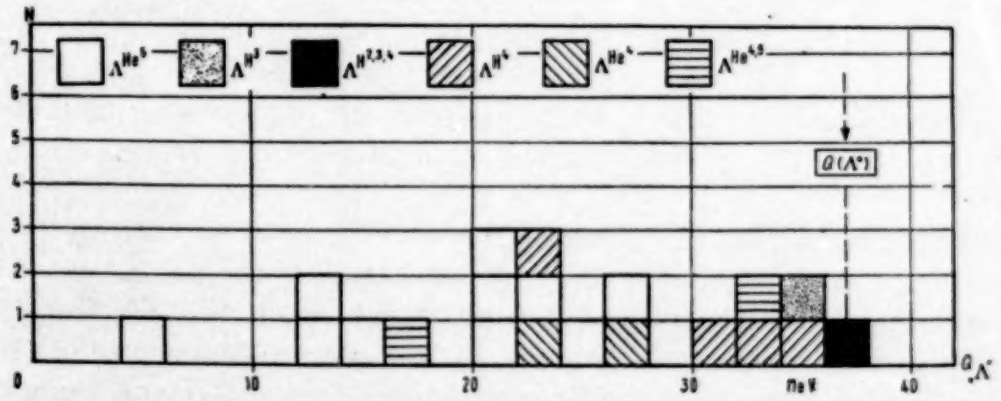

Abb. 4. Häufigkeitsverteilung der $Q_{„\Lambda"}$-Werte aus dem vorliegenden Experiment.

In Abb. 5 sind diese Werte mit denen der Weltstatistik [8]) zusammengefaßt und die $Q_{„\Lambda"}$-Verteilungen für die verschiedenen Hyperfragmente getrennt dargestellt.

Unter der Annahme, daß keine merklichen Wechselwirkungen zwischen Proton, π^--Meson und dem Kern Fr bestehen, sollte man in jedem Fall eine $Q_{„\Lambda"}$-Verteilung mit einem ausgeprägten Maximum nahe $Q(\Lambda^0)-B_\Lambda$ erwarten. Die $Q_{„\Lambda"}$-Verteilung in Abb. 4 läßt ein solches Maximum nicht erkennen. Von den $Q_{„\Lambda"}$-Verteilungen in Abb. 5 ist die für ${}_\Lambda\mathrm{He}^5$ statistisch am besten fundiert.

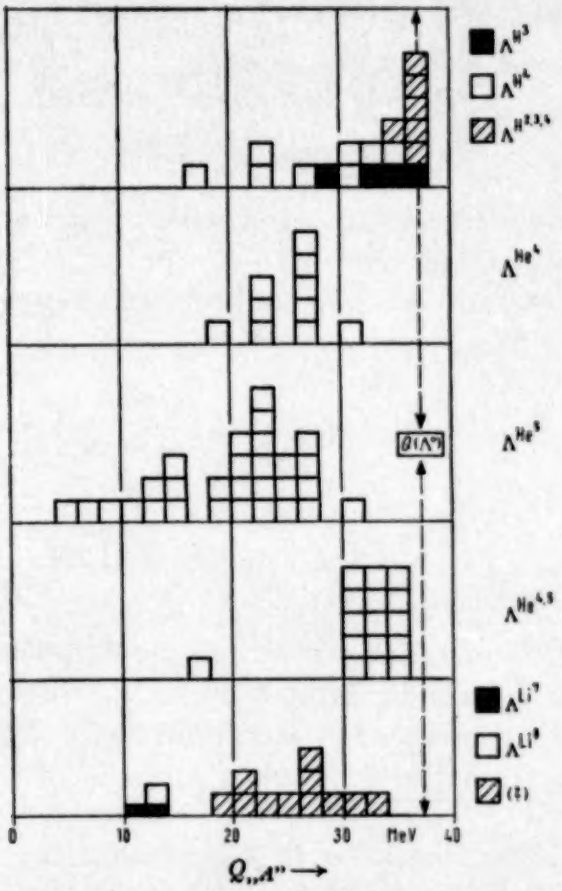

Abb. 5. Häufigkeitsverteilungen der $Q_{„\Lambda"}$-Werte für die verschiedenen Hyperfragmente (Zusammenfassung des vorliegenden Experiments mit der Weltstatistik [8])).

Die Breite dieser Verteilung und die Lage ihres Maximums bei etwa 23 MeV sind als Folge von Wechselwirkungen zwischen Proton, π^--Meson und He^4 aufzufassen.

Byers und Cottingham [9]) haben die Verteilungen von $\cos\Theta_{\pi\Lambda}$ und $P_{„\Lambda"}$ untersucht und gefunden, daß die Form dieser Verteilungen hauptsächlich bestimmt wird durch die in der Proton-He^4-Streuung bei 1.8 MeV liegende $P_{\frac{3}{2}}$-Resonanz. $P_{„\Lambda"}$ ist der Impuls des „Λ^0", also die Vektorsumme der Impulse von Proton und π^--Meson im Ruhesystem des Hyperfragments. Dem Betrage nach ist $P_{„\Lambda"}$ gleich dem Impuls des He^4 oder allgemeiner des Kerns Fr.

$\Theta_{\pi\Lambda}$ ist der Winkel zwischen der Flugrichtung des π^--Mesons im Ruhesystem des „Λ^0" und der Richtung von $P_{„\Lambda^0"}$ (siehe Abb. 6).

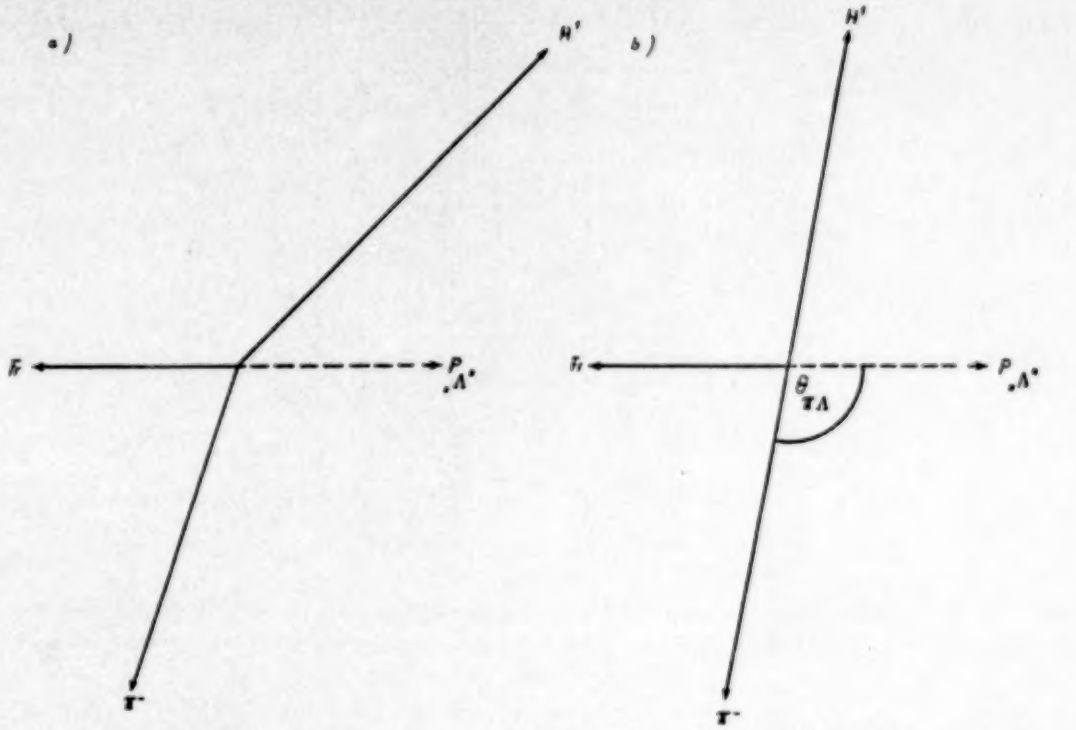

Abb. 6. Zur Definition des Winkels $\Theta_{\pi\Lambda}$. a) Zerfallsbild im Ruhesystem des Hyperfragments. b) Zerfallsbild im Ruhesystem des „Λ^0".

$\Theta_{\pi\Lambda}$ wurde berechnet aus dem Winkel ϑ (im Ruhesystem des Hyperfragments) zwischen der Flugrichtung des π^--Mesons und der Richtung von $P_{„\Lambda^0"}$:

$$\operatorname{tg}\Theta_{\pi\Lambda} = \sqrt{1-\beta^2}\,\frac{\sin\vartheta}{\cos\vartheta - \dfrac{\beta U_\pi}{p_\pi}}.$$

U_π und p_π sind die Gesamtenergie und der Impuls des π^--Mesons im Ruhesystem des Hyperfragments, und β ist die Geschwindigkeit des „Λ^0" in diesem System.

In Abb. 7 ist die $\cos\Theta_{\pi\Lambda}$-Verteilung für alle ${}_\Lambda\mathrm{He}^5$-Hyperfragmente aus der vorliegenden Arbeit und der Weltstatistik [8]) zusammengestellt. Die eingezeichnete Kurve ist die von Byers und Cottingham berechnete Verteilung für $\cos\Theta_{\pi\Lambda}$. Die qualitative Übereinstimmung der experimentellen mit der theoretischen Verteilung ist offensichtlich.

In Abb. 8 ist die aus der vorliegenden Arbeit und der Weltstatistik [8]) bestimmte $P_{„\Lambda^0"}$-Verteilung für die ${}_\Lambda\mathrm{He}^5$-Zerfälle mit der von Byers und Cottingham berechneten verglichen. Ein He^4-Kern mit einem Impuls $P_{„\Lambda^0"} = 100$ MeV/c hat eine Reichweite von 4.5 μm; bei einem Impuls von 80 MeV/c beträgt die Reichweite des He^4-Kerns 3.0 μm. Diese kurzen Reichweiten sind der Grund dafür, daß kein ${}_\Lambda\mathrm{He}^5$-Zerfall mit einem $P_{„\Lambda^0"} < 80$ MeV/c eindeutig

analysiert werden konnte. Alle in diesem Bereich liegenden ${}_{\Lambda}He^{5}$-Zerfälle sind in der Gruppe der zweideutigen ${}_{\Lambda}He^{4,5}$-Zerfälle enthalten. Auf die insgesamt 29 eindeutig analysierten Zerfälle ${}_{\Lambda}He^{5} \rightarrow He^{4}+H^{1}+\pi^{-}$ kommen 10 eindeutig

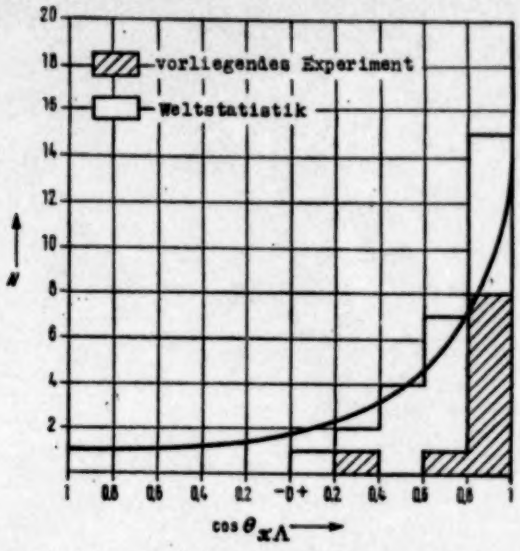

Abb. 7. cos $\Theta_{\pi\Lambda}$-Verteilung für die ${}_{\Lambda}He^{5}$-Hyperfragmente aus dem vorliegenden Experiment und der Weltstatistik [8]). Die eingezeichnete Kurve ist die von Byers und Cottingham [9]) berechnete cos $\Theta_{\pi\Lambda}$-Verteilung für ${}_{\Lambda}He^{5}$.

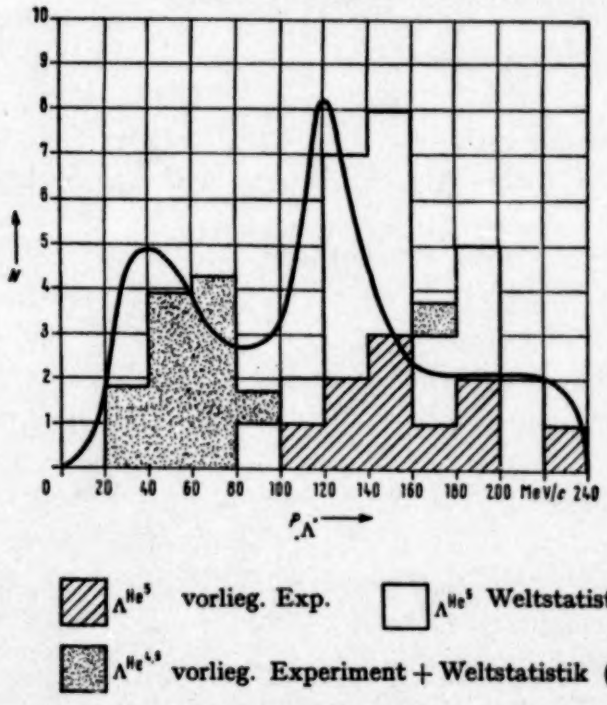

Abb. 8. Korrigierte P_{Λ}-Verteilung für die ${}_{\Lambda}He^{5}$-Hyperfragmente aus dem vorliegenden Experiment und der Weltstatistik [8]). Die eingezeichnete Kurve ist die von Byers und Cottingham [9]) berechnete P_{Λ}-Verteilung für ${}_{\Lambda}He^{5}$.

analysierte Zerfälle ${}_{\Lambda}He^{4} \rightarrow He^{3}+H^{1}+\pi^{-}$. Es wurde daher angenommen, daß unter den 16 Zerfällen ${}_{\Lambda}He^{4,5} \rightarrow He^{3,4}+H^{1}+\pi^{-}$ elf ${}_{\Lambda}He^{5}$-Zerfälle sind. Dementsprechend wurde in der Abb. 8 jeder der 16 ${}_{\Lambda}He^{4,5}$-Zerfälle 0.7-fach als ${}_{\Lambda}He^{5}$-

Zerfall gezählt. Die Formen der experimentellen und der theoretischen Verteilung sind einander offenbar sehr ähnlich, wenn auch die beiden Maxima der experimentellen Verteilung gegenüber denen der theoretischen etwas nach höheren $P_{„\Lambda"}$-Werten hin verschoben erscheinen.

Für die Zerfälle der verschiedenen anderen Hyperfragmente ist eine ähnliche Untersuchung der $Q_{„\Lambda"}$-, $\cos\Theta_{\pi\Lambda}$- und $P_{„\Lambda"}$-Verteilungen noch sinnlos, da die Statistiken zu klein sind.

In der Tab. 3 sind die Zahlenwerte von $Q_{„\Lambda"}$, $\cos\Theta_{\pi\Lambda}$ und $P_{„\Lambda"}$ für die einzelnen Hyperfragmentzerfälle aus der vorliegenden Arbeit gegeben.

TABELLE 3

$Q_{„\Lambda"}$, $\cos\Theta_{\pi\Lambda}$ und $P_{„\Lambda"}$ für die Hyperfragmentzerfälle der vorliegenden Arbeit

Hyperfragment	Ereignis Nr.	$Q_{„\Lambda"}$ [MeV]	$\cos\Theta_{\pi\Lambda}$	$P_{„\Lambda"}$ $\left[\frac{\text{MeV}}{c}\right]$
${}_\Lambda H^3$	24	35.78	+0.443	43.00
${}_\Lambda H^4$	2	31.58	−0.503	74.85
	31	33.41	+0.162	39.47
	35	23.28	+0.427	139.71
	36	34.17	−0.454	58.40
${}_\Lambda H^{2,3,4}$	1	36.32	−0.274	6.32
${}_\Lambda He^4$	7	23.60	+0.059	132.7
	12	27.16	+0.784	106.44
${}_\Lambda He^5$	3	13.90	+0.960	189.9
	5	25.11	+0.953	125.4
	6	21.13	+0.844	151.1
	10	15.63	+0.847	178.6
	11	27.38	+0.834	110.91
	16	21.99	+0.897	140.5
	21	13.90	+0.785	185.7
	23	23.60	+0.259	138.9
	26	4.31	+0.863	227.6
	37	21.34	+0.983	147.8
${}_\Lambda He^{4,5}$	33	16.81	−0.068	178.5
	34	33.63	−0.969	50.66

4.3. MITTLERE LEBENSDAUERN

Zur Abschätzung der Lebensdauern der Hyperfragmente sind die betreffenden Ergebnisse des vorliegenden Experiments in Tab. 4 zusammengestellt. $\sum t_i$ ist die Summe aller Abbremszeiten (für Ruhezerfälle) bzw. Flugzeiten (für Flugzerfälle). t_i ist die Zeit im Eigensystem des betreffenden Hyperfragments.

TABELLE 4

Zur Abschätzung der Hyperfragment-Lebensdauern

Hyperfragment	${}_\Lambda H^3$	${}_\Lambda H^4$	${}_\Lambda H^{2,3,4}$	${}_\Lambda He^4$	${}_\Lambda He^5$	${}_\Lambda He^{4,5}$	${}_\Lambda Li^8$	${}_\Lambda Li^9$	${}_\Lambda Li^{8,9}$	(?)
Σt_i [10^{-10} sec]	0.312	2.648	0.240	0.197	0.372	0.117	0.051	0.025	0.010	0.394
Anzahl der Flugzerfälle	1	2								

Entsprechend den drei Zerfallsmöglichkeiten setzt sich die Zerfallsrate für ein Hyperfragment additiv aus den drei Zerfallsraten für π^--mesonischen, π^0-mesonischen und nichtmesonischen Zerfall zusammen:

$$\frac{1}{\tau} = \frac{1}{\tau_{\pi^- \text{-mes.}}} + \frac{1}{\tau_{\pi^0 \text{-mes.}}} + \frac{1}{\tau_{\text{nichtmes.}}}.$$

τ ist die gesamte mittlere Lebensdauer, und $\tau_{\pi^- \text{-mes.}}$, $\tau_{\pi^0 \text{-mes.}}$, $\tau_{\text{nichtmes.}}$ sind die mittleren Lebensdauern gegenüber den drei Zerfallsmöglichkeiten.

Berechnet wurde die mittlere Lebensdauer der ${}_\Lambda H^4$-Hyperfragmente. Es sei

$$S(\tau) = \frac{\frac{1}{\tau}\sum t_i - n}{\sqrt{n}},$$

wobei n die Anzahl der Flugzerfälle sein soll. Nimmt τ für $S(\tau) = 0, +1, -1$ beziehentlich die Werte τ_0, τ_+, τ_- an, so folgt als wahrscheinlichster Wert für die mittlere Lebensdauer [10])

$$\tau = \tau_{0-(\tau_0-\tau_+)}^{+(\tau_--\tau_0)}.$$

Berücksichtigt man nur die sicher identifizierten ${}_\Lambda H^4$-Hyperfragmente, so ergibt sich

$$\tau_{\pi^- \text{-mes.}}({}_\Lambda H^4) = (1.3^{+3.2}_{-0.5}) \times 10^{-10} \text{ sec}.$$

Werden zusätzlich alle Hyperfragmente berücksichtigt, die möglicherweise ${}_\Lambda H^4$ sein könnten (${}_\Lambda H^{2,3,4}$ und (?)), dann erhält man

$$\tau^*_{\pi^- \text{-mes.}}({}_\Lambda H^4) = (1.6^{+3.9}_{-0.7}) \times 10^{-10} \text{ sec}.$$

Für freie Λ^0-Hyperonen ist innerhalb der Fehlergrenzen das Verzweigungsverhältnis [11])

$$\frac{\Lambda^0 \to p + \pi^-}{\Lambda^0 \to n + \pi^0} = 2.$$

Wenn man die nichtmesonischen Zerfälle des ${}_\Lambda H^4$ vernachlässigt und für die im ${}_\Lambda H^4$ gebundenen Λ^0-Hyperonen das gleiche Verzweigungsverhältnis wie für die freien Λ^0-Hyperonen annimmt, so folgt

$$\tau({}_\Lambda H^4) = (0.9^{+2.1}_{-0.3}) \times 10^{-10}\,\text{sec}$$

und

$$\tau^*({}_\Lambda H^4) = (1.1^{+2.6}_{-0.5}) \times 10^{-10}\,\text{sec}.$$

Eine Zusammenfassung mit den Ergebnissen der von Slater [1]) durchgeführten systematischen Untersuchung liefert

$$\tau({}_\Lambda H^4) = (0.9^{+1.9}_{-0.5}) \times 10^{-10}\,\text{sec}, \quad \tau^*({}_\Lambda H^4) = (1.1^{+2.3}_{-0.6}) \times 10^{-10}\,\text{sec}.$$

Die mittlere Lebensdauer des freien Λ^0 beträgt [11])

$$\tau(\Lambda^0_{\text{frei}}) = (2.60^{+0.16}_{-0.14}) \times 10^{-10}\,\text{sec}.$$

Trotzdem es so aussieht, als ob $\tau({}_\Lambda H^4) < \tau(\Lambda^0_{\text{frei}})$ wäre, stimmen beide mittlere Lebensdauern innerhalb der Fehlergrenzen noch überein.

4.4. EREIGNIS 25

Beim Ruheeinfang eines K^--Mesons wurden vier geladene Teilchen emittiert (keines war ein π-Meson). Vom Ende der 737 μm langen Spur eines dieser Teilchen gehen die Spur eines Wasserstoffkerns und die Spur eines π^--Mesons aus. Die Reichweite des Wasserstoffkerns beträgt 3765 μm, die Reichweite des π^--Mesons 3900 μm. Wasserstoffspur und π^--Spur bilden einen Winkel von 62.2° miteinander.

Für das π^--Meson ergibt sich als kinetische Energie

$$E_{\text{kin}}(\pi^-) = 13.45\ \text{MeV}.$$

Der Wasserstoffkern war sehr wahrscheinlich ein Proton. Die kinetische Energie für das Proton beträgt

$$E_{\text{kin}}(H^1) = 29.94\ \text{MeV}.$$

Für ein Deuteron bzw. Triton wären die kinetischen Energien $E_{\text{kin}}(H^2) = 40.28$ MeV und $E_{\text{kin}}(H^3) = 47.81$ MeV.

Allein aus den kinetischen Energien von π^--Meson und Wasserstoffkern folgt, daß Ereignis 25 kein Hyperfragment-Zerfall in Ruhe sein kann, da für

jedes Zerfallsschema die Bindungsenergie B_Λ stark negativ wird. Die Änderung der Ionisation längs der 737 μm langen Primärspur und besonders die Streuungen nahe ihrem Ende schließen einen Hyperfragment-Flugzerfall aus; das Primärteilchen kam zur Ruhe. δ-Strahl-Zählungen an der Primärspur ergaben eine Ladung $Z = 1$.

Setzt man für den Wasserstoffkern ein Proton, was sehr wahrscheinlich richtig ist, so kann Ereignis 25 folgendermaßen erklärt werden: Das K^--Meson reagierte im komplexen Atomkern mit einem Neutron und erzeugte dabei ein Σ^--Hyperon:

$$K^- + n \rightarrow \Sigma^- + \pi^0.$$

Das Σ^- reagierte am Ende seiner Reichweite in dem einfangenden Atomkern mit einem Proton:

$$\Sigma^- + p \rightarrow \Lambda^0 + n \quad \text{oder} \quad \Sigma^- + p \rightarrow \Sigma^0 + n \rightarrow \Lambda^0 + \gamma + n.$$

(Für den Σ^--Einfang sprechen auch ein Blob und ein Auger-Elektron.) Das Λ^0 zerfiel nach einer unmeßbar kurzen Wegstrecke in Proton und π^--Meson. Für die Summe Q der kinetischen Energien von Proton und π^--Meson im Ruhesystem des Λ^0 erhält man

$$Q = 9.5 \text{ MeV}.$$

Dieser niedrige Q-Wert bedeutet, daß das Λ^0 nicht frei zerfallen sein kann, sondern daß sein Zerfall zum Beispiel durch den komplexen Atomkern, in dem es erzeugt wurde, gestört worden ist, oder daß das Λ^0 in einem Hyperfragment gebunden war, welches im Fluge zerfiel, noch bevor es eine meßbare Weglänge zurückgelegt hatte.

Abschließend soll bemerkt werden, daß Kerneinfänge kurzreichweitiger Σ^--Hyperonen, bei denen wie im Ereignis 25 neben anderen geladenen Zerfallsprodukten auch ein π^--Meson emittiert wird, sicherlich nicht immer von π^--mesonischen Hyperfragmentzerfällen in Ruhe unterschieden werden können.

Herrn Prof. Dr. W. Heisenberg und Herrn Dr. K. Gottstein danke ich für die mir im Max-Planck-Institut für Physik und Astrophysik gebotenen Arbeitsmöglichkeiten und für die Anregung zu dieser Arbeit. Frl. M. Ankermann, Frau H. Baumbach, Frl. U. Kaulfuss und Frl. H. Neu möchte ich für ihre Hilfe bei der Durchmusterung der Platten danken. Herrn Dr. H. Heckman und Herrn Dr. M. Cresti vom Lawrence Radiation Laboratory in Berkeley bin ich für die Exposition des Emulsionspaketes zu Dank verpflichtet.

Anmerkung bei der Korrektur: Unter Berücksichtigung der Ergebnisse neuester Experimente [12]) erhält man für $Q(\Lambda^0)$ als zur Zeit besten Wert 37.58 ± 0.15 MeV. Bei Zugrundelegung dieses Wertes sind zu allen in der vorliegenden Arbeit berechneten Bindungsenergien 0.36 MeV zu addieren.

Literatur

1) W. E. Slater, Nuovo Cim. Suppl. **10** (1958) 1
2) W. H. Barkas, P. H. Barrett, P. Cüer, H. Heckman, F. M. Smith und H. K. Ticho, Nuovo Cim. **8** (1958) 185;
   W. H. Barkas, Nuovo Cim. **8** (1958) 201
3) J. J. Wilkins, A.E.R.E. G/R (1951) 664
4) A. H. Wapstra, Physica **21** (1955) 367
5) W. H. Barkas und A. H. Rosenfeld, UCRL-8030 (1958)
6) R. Ammar, R. Levi Setti, W. E. Slater, S. Limentani, P. E. Schlein und P. H. Steinberg, Nuovo Cim. **15** (1960) 181
7) E. M. Silverstein, Nuovo Cim. Suppl. **10** (1958) 41
8) R. Levi Setti, W. E. Slater und V. L. Telegdi, Nuovo Cim. Suppl. **10** (1958) 68
9) N. Byers und W. N. Cottingham, Nuclear Physics **11** (1959) 554
10) C. Castagnoli, G. Cortini und C. Franzinetti, Nuovo Cim. Suppl. **12** (1954) 297
11) Proc. Ann. Int. Conf. on High Energy Physics at CERN (1958)
12) R. Ammar, R. Levi Setti, W. E. Slater, S. Limentani, P. E. Schlein und P. H. Steinberg, Nuovo Cim. **15** (1960) 181;
    E. B. Brucker, Thesis, The John Hopkins University (1960);
    J. Lodge, F. Anderson, E. B. Brucker, A. Pevsner und R. Strand, noch nicht veröffentlicht;
    J. Bogdanowicz, M. Danysz, A. Filipkowsky, E. Marquit, E. Skrzypczak, A. Wroblewski und J. Zakrzewski, Nuovo Cim. **11** (1959) 727;
    W. H. Barkas, P. C. Giles, H. H. Heckman, F. W. Inman, C. J. Mason und F. M. Smith, Padua-Venice Conference Report (1957) VI-41

8.A

Nuclear Physics **20** (1960) 254—274; © *North-Holland Publishing Co., Amsterdam*

Not to be reproduced by photoprint or microfilm without written permission from the publisher

DIE MITTLERE LEBENSDAUER GELADENER Σ-HYPERONEN UND UNTERSUCHUNGEN ÜBER WEITERE EIGENSCHAFTEN DIESER TEILCHEN

W. PÜSCHEL

Max Planck Institut für Physik und Astrophysik, München

Eingegangen am 27. Mai 1960

Abstract: The apparent discrepancy in the mean lifetime of the Σ-hyperons in emulsions has been investigated by using decays in flight only and decays both in flight and at rest. All our Σ's came from K^--absorptions from which apart from the Σ only one fast particle was emitted. For the $\Sigma^+ \to p+\pi^0$ decay mode using 127 decays at rest and in flight we find $\tau = (0.98^{+0.16}_{-0.13}) \times 10^{-10}$ sec. Using the 48 decays in flight only, $\tau = (0.60^{+0.43}_{-0.17}) \times 10^{-10}$ sec. For the mixture of $\Sigma^\pm$-hyperons from decays in flight only by the mode $\Sigma^\pm \to n+\pi^\pm$ the same maximum likelihood estimates lead to $\tau = (0.91^{+0.45}_{-0.19}) \times 10^{-10}$ sec. By combining data from this laboratory (191 decays), Istituto di Fisica Bologna (114) decays, École Polytechnique Paris (74 decays), and Istituto di Fisica Parma (68 decays) it is shown that there is no evidence for a lifetime doublet. Comparison with other data is also made and it is concluded that the best value for the Σ^+-hyperon lifetime is $\tau = (0.95^{+0.07}_{-0.05}) \times 10^{-10}$ sec.

Angular distributions in Σ decay are analysed for information on parity conservation in Σ production. No evidence for a parity non-conservation in Σ production is found. Measurements of the masses of the charged Σ-hyperons and the K^--meson are reported. The terminal behaviour of the Σ^--hyperons was also studied.

1. Bereitstellung des Versuchsmaterials

Für die vorliegenden Untersuchungen stand uns ein aus 105 Kernemulsionen vom Typ Ilford G5 bestehendes Plattenpaket mit den Ausmaßen $13.9 \times 8.9 \times 6.3$ cm³ zur Verfügung. Der „Stack" wurde 1957 im 300 MeV/c K^--Mesonenstrahl des Bevatrons exponiert.

Die durch K^--Mesonen hervorgerufenen Spuren wurden beim Eintritt in die Emulsion 3 mm vom Rand entfernt gesucht und dann verfolgt. Wir fanden 8912 K^--Mesonen.

Für die Arbeit wurden nun K^--Mesonen-Wechselwirkungen ausgesucht, die dem folgenden Kriterium genügten: Es durften nur 2 sichtbare Teilchen in der Reaktion erzeugt werden, von denen das eine Teilchen eine Minimumspur, das andere dagegen eine schwarze oder graue Spur hervorriefen. Mit dieser Auswahl wollten wir nur diejenigen K^--Einfangreaktionen erfassen, bei denen ein geladenes Σ-Hyperon und gleichzeitig ein entgegengesetzt geladenes π-Meson ($K^- + p \to \Sigma^\pm + \pi^\mp$) erzeugt wurden und keine weiteren Sekundärprozesse stattfanden, wie z.B. die Emission von Protonen aus dem komplexen Einfang-

kern. Diese K^--Einfänge nennen wir (Σ, π)-Ereignisse. Damit war die Möglichkeit gegeben, rasch eine große Anzahl von positiven und negativen Hyperonen zu erhalten. Außerdem hofften wir, mit dieser Auswahl unbeeinflußte Ereignisse zu bekommen. Falls nämlich mehrere schwarze Spuren in einer K^--Reaktion erzeugt werden, von denen jede das Hyperon sein könnte, besteht die Gefahr, daß Σ-Zerfälle übersehen werden.

Da Minimumspuren beim Durchmustern leicht übersehen werden können, wurden alle gefundenen K^--Einfangreaktionen mit einer schwarzen oder grauen Spur sorgfältig überprüft. Unter 882 solchen Ereignissen wurden 159 gefunden, bei denen das π-Meson übersehen worden war.

Die schwarzen oder grauen Spuren wurden alle verfolgt, bis die Teilchen zerfielen, eingefangen wurden oder zur Ruhe kamen.

Auf diese Weise wurden identifiziert:

63 Flugzerfälle $\Sigma^{\pm} \to \pi^{\pm} + n$,
84 Ruhezerfälle $\Sigma^{+} \to \pi^{+} + n$,
48 Flugzerfälle $\Sigma^{+} \to \pi^{0} + p$,
79 Ruhezerfälle $\Sigma^{+} \to \pi^{0} + p$.

591 Ereignisse ohne typische Merkmale am Ende der grauen oder schwarzen Spur (die Spurenden wurden sorgfältig auf das Vorhandensein von Minimumspuren geprüft);

4 Teilchen verschwanden im Flug (dies können Ladungsaustauschreaktionen oder Flugreaktionen von Hyperonen oder Protonen sein);

87 sichere Σ^--Einfänge (beim Einfang der Σ^--Hyperonen an komplexen Kernen wurde dabei die Emission von geladenen Teilchen mit einer Reichweite $\geqq 5\,\mu$m verlangt);

160 nicht sicher zu identifizierende Einfänge von negativen Hyperonen mit „Auger Elektronen", „Blobs" oder „Recoils".

In Abb. 1 und 2 werden Mikrophotographien von K^--Mesoneneinfängen durch Wasserstoffatomkerne gebracht.

2. Die mittlere Lebensdauer geladener Hyperonen und die Verzweigungsverhältnisse des Σ^+-Zerfalls

2.1. DIE MITTLERE LEBENSDAUER DER Σ-HYPERONEN BESTIMMT AUS DEN $\Sigma^+ \to p + \pi^0$ und $\Sigma^{\pm} \to \pi^{\pm} + n$ ZERFÄLLEN

Bestimmt man die mittlere Lebensdauer der positiven Σ-Hyperonen, indem man Ruhe- und Flugzerfälle dazu benutzt, so ergeben Kernemulsions- und Blasenkammeruntersuchungen gut übereinstimmende Werte, deren Mittelwert zwischen 0.9×10^{-10} sec und 1.0×10^{-10} sec liegt.

Werden dagegen allein die Flugzerfälle zur Bestimmung der Lebensdauer benutzt, so variieren die Werte verschiedener Autoren von 0.95×10^{-10} sec bis zu einem 8 mal kleineren Wert.

Die Ladung der Σ-Hyperonen aus den Flugzerfällen der Art $\Sigma^{\pm} \to \pi^{\pm}+\mathrm{n}$ wurde in den meisten Fällen bei Kernemulsionsuntersuchungen nicht bestimmt. Lebensdauerbestimmungen für die $\Sigma^{\pm}$, also für ein Gemisch positiver und negativer Hyperonen, ergeben zum Teil ebenfalls kleine Werte von etwa 0.3×10^{-10} sec (Ausführliche Literaturangaben in den Tabellen 1 bis 4).

Dies überraschende Ergebnis zweier verschiedener Lebensdauern für die geladenen Σ-Hyperonen ließe sich erklären, falls die Hyperonen aus einem Gemisch kurzlebiger und langlebiger Teilchen bestehen würden; denn die kurzlebigen Teilchen spielen natürlich eine größere Rolle bei den Flugzerfällen.

Hauptziel dieser Arbeit war, mit einer größeren Anzahl von Σ-Hyperonen als bisher die Lebensdauern dieser Teilchen erneut zu bestimmen und damit die Frage zu untersuchen, ob die Hyperonen tatsächlich aus einem Gemisch von Teilchen mit verschiedenen Lebensdauern bestehen.

Zur Bestimmung der mittleren Lebensdauer der Σ-Hyperonen benutzen wir Bartletts „Maximum Likelihood"-Methode. Die Anwendung dieser Methode für Nebelkammern sowie für Kernemulsionen wird ausführlich in der Literatur behandelt [1–4]).

Die mittlere Lebensdauer für die Σ-Hyperonen wurde dann aus den Formeln

$$\bar{\tau}_{\mathrm{r,f}} = \frac{1}{n_{\mathrm{f}}} \left(\sum_{i=1}^{n_{\mathrm{f}}} t_i + \sum_{j=1}^{n_{\mathrm{r}}} T_j\right), \tag{1}$$

$$\bar{\tau}_{\mathrm{f}} = \frac{1}{n_{\mathrm{f}}} \sum_{i=1}^{n_{\mathrm{f}}} \left(t_i + \frac{T_i}{\exp\{T_i/\bar{\tau}_{\mathrm{f}}\}-1}\right) \tag{2}$$

berechnet (r Ruhezerfall, f Flugzerfall, n_{f} Zahl der Flugzerfälle, n_{r} Zahl der Ruhezerfälle, t_i Flugzeit des im Flug zerfallenden Teilchens i, T_j Flugzeit des in Ruhe zerfallenden Teilchens j, T_i Flugzeit des im Flug zerfallenden Teilchens i, wenn es nicht zerfallen wäre). Formel (1) ist gültig für die Berechnung der mittleren Lebensdauer unter Benutzung der Ruhe- und Flugzerfälle, Formel (2) unter Benutzung allein der Flugzerfälle.

Wir erhielten:

1) Für 79 Ruhe- und 48 Flugzerfälle $\Sigma^{+} \to \mathrm{p}+\pi^{0}$:
$\bar{\tau}_{\mathrm{r,f}} = (0.98^{+0.16}_{-0.12}) \times 10^{-10}$ sec,

2) für die 48 Flugzerfälle $\Sigma^{+} \to \mathrm{p}+\pi^{0}$: $\bar{\tau}_{\mathrm{f}} = (0.60^{+0.42}_{-0.17}) \times 10^{-10}$ sec,

3) für 63 Flugzerfälle $\Sigma^{\pm} \to \mathrm{n}+\pi^{\pm}$: $\bar{\tau}_{\mathrm{f}} = (0.91^{+0.45}_{-0.19}) \times 10^{-10}$ sec.

Die Ruhezerfälle $\Sigma^{+} \to \mathrm{p}+\pi^{0}$ lassen sich infolge der Reichweite des Protons ($R_{\mathrm{p}} \approx 1670$ μm in „G5" Kernemulsionen) leicht als solche erkennen. Nur Einfänge negativer Σ-Hyperonen mit einer Sekundärspur von etwa 1670 μm könnten die Auswahl der $\Sigma^{+} \to \mathrm{p}+\pi^{0}$ Ruhezerfälle beeinflussen, die diesbezügliche Korrektur ist jedoch unbedeutend. In Abb. 3 wird bei allen zur Ruhe kommenden Σ-Hyperonen mit einer „schwarzen" oder „grauen" Sekundärspur

länger als 300 μm die Längenverteilung dieser Sekundärspuren gebracht. Wie man aus der Abb. 3 sieht, werden wir unter den 80 identifizierten Ruhezerfällen nicht mehr als 1 Σ^- zu erwarten haben (1 Hyperon mit einer Sekundarspur von 1518 μm wurde auf Grund eines Blobs und eines Auger Elektrons bereits als Σ^- identifiziert).

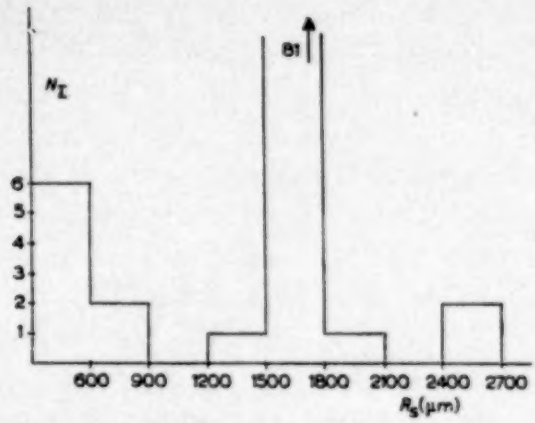

Abb. 3. Längenverteilung der Sekundärspuren aller zu Ruhe kommender Σ-Hyperonen mit einer grauen oder schwarzen Sekundärspur (2 Ereignisse mit $R_s > 2700$ μm).

Bei den $\Sigma^+ \to p+\pi^0$ Flugzerfällen ist der Emissionswinkel und aus Reichweitemessungen die Geschwindigkeit des Protons im Laborsystem bekannt. Aus der Kinematik folgen dann 2 Lösungen für die Energie des Σ^+ Hyperons im Augenblick des Zerfalls. Die richtige der beiden Lösungen wurde anhand von Lückendichtemessungen ausgewählt.

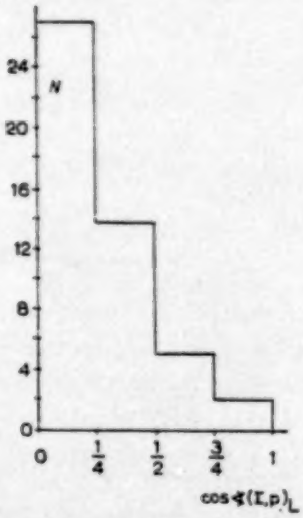

Abb. 4. Winkelverteilung der Protonen aus den $\Sigma^+ \to p+\pi^0$ Flugzerfällen in Bezug auf die Σ-Flugrichtung im Laborsystem.

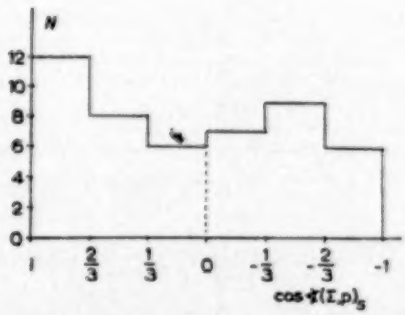

Abb. 5. Winkelverteilung der Protonen aus den $\Sigma^+ \to p+\pi^0$ Flugzerfällen in Bezug auf die Σ-Flugrichtung im Schwerpunktssystem.

In Abb. 4 und 5 sind die Winkelverteilungen der Protonen aus den $\Sigma \to p$ Flugzerfällen in Bezug auf die Σ-Flugrichtungen im Labor- und Schwerpunkts-

system angegeben. Falls beim K^--Mesoneneinfang (starke Wechselwirkung!) die Parität verletzt wird, sollte man für die Zerfallsteilchen der Hyperonen eine Vorwärts- und Rückwärtsasymmetrie beobachten (siehe Sekt. 4). Tatsächlich haben wir für die $\Sigma \to p$ Flugzerfälle keine derartige Asymmetrie gefunden. Wir fanden, daß von 48 Flugzerfällen 26 Protonen in die vordere und 22 in die hintere Hemisphäre emittiert wurden. Diese Tatsache spricht zugleich für die richtige Auswahl der Flugzerfälle. Wird nämlich das Zerfallsproton im Schwerpunktssystem nach vorn emittiert, so ist die Geschwindigkeit des Protons im Laborsystem größer als die des Σ-Hyperons; dies macht sich in einer geringeren Ionisation bemerkbar. Diese Fälle wird man leicht visuell unter dem Mikroskop als Flugzerfälle identifizieren können. Falls jedoch das Proton im Schwerpunktssystem nach hinten emittiert wird, so ist die Geschwindigkeit des Protons im Laborsystem kleiner als die des Hyperons. Diese Fälle sind oft nicht leicht von Streuungen eines Protons zu unterscheiden. Meistens wird man diese Ereignisse mit Hilfe der Zerfallskinematik des $\Sigma \to p$ Flugzerfalls entscheiden können. Unglücklicherweise können nun aber auch einige Protonenstreuungen derart beschaffen sein, daß die Zerfallskinematik auch hierfür vernünftige Werte liefert. In unserer Winkelverteilung wäre eine „Spitze" nach hinten zu erwarten, falls wir einige Protonenstreuungen als $\Sigma \to p$ Flugzerfälle identifiziert hätten. Dagegen sehen wir eine kleine Spitze nach vorn in unserer Verteilung, die noch in den Fehlergrenzen der Statistik liegt. In Abb. 6 ist die Winkelverteilung der

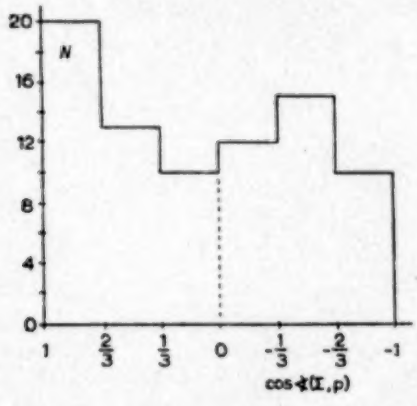

Abb. 6. Winkelverteilung der Protonen aus den $\Sigma^+ \to p+\pi^0$ Ruhezerfällen in Bezug auf die Anfangsflugrichtung des Σ-Hyperons.

Protonen aus den Ruhezerfällen $\Sigma^+ \to p+\pi^0$ in Bezug auf die Anfangsflugrichtung des Σ-Hyperons wiedergegeben. Auch hier finden wir keine asymmetrische Verteilung. Auf Grund dieser Untersuchungen glauben wir, daß sich keine systematischen Fehler bei der Auswahl der $\Sigma^+ \to p+\pi^0$ Zerfälle (weder der Ruhe- noch Flugzerfälle) eingeschlichen haben.

Abb. 7 und 8 geben die Winkelverteilungen der Mesonen aus den $\Sigma^\pm \to \pi^\pm + n$ Flugzerfällen in Bezug auf die Hyperonenflugrichtung im Labor- und Schwer-

punktssystem wieder. Infolge der hohen Geschwindigkeit des π-Mesons beim Zerfall des Hyperons im Schwerpunktssystem beobachtet man bereits im Laborsystem fast eine symmetrische Winkelverteilung. Die gut symmetrische Winkelverteilung im Schwerpunktssystem beweist, daß keine systematischen Fehler beim Auffinden der $\Sigma^{\pm} \to \pi^{\pm}+\mathrm{n}$ Flugzerfälle entstanden sind. Zur

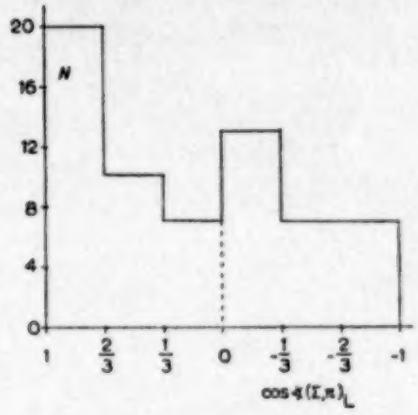

Abb. 7. Winkelverteilung der π-Mesonen aus den $\Sigma^{\pm} \to \mathrm{n}+\pi^{\pm}$ Flugzerfällen in Bezug auf die Σ-Flugrichtung im Laborsystem.

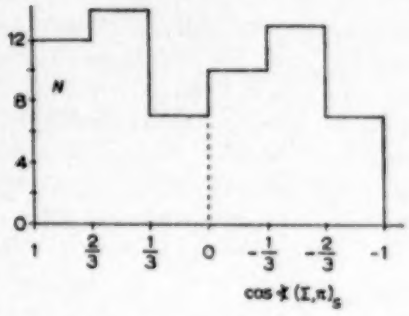

Abb. 8. Winkelverteilung der π-Mesonen aus den $\Sigma^{\pm} \to \mathrm{n}+\pi^{\pm}$ Flugzerfällen in Bezug auf die Σ-Flugrichtung im Schwerpunktssystem.

Verbesserung der Statistik wurden unsere Ereignisse (190 Zerfälle) mit den Ereignissen von 3 anderen Instituten † (Ecole Polytechnique Paris: 74 Zerfälle; Istituto di Fisica Bolgona: 114 Zerfälle; Istituto di Fisica Parma: 68 Zerfälle) zusammengefaßt, die unter ähnlichen Bedingungen (analoge Durchmusterung und Auswahl der Ereignisse, gleichzeitige bzw. analoge Exposition und Entwicklung der Kernemulsionen) wie unsere gewonnen wurden. Die Zusammenfassung ergibt dann für

185 Ruhe- und 99 Flugzerfälle $\Sigma^{+} \to \mathrm{p}+\pi^{0}$: $\bar{\tau}_{\mathrm{r,f}} = (0.99^{+0.11}_{-0.09}) \times 10^{-10}$ sec,

99 Flugzerfälle $\Sigma^{+} \to \mathrm{p}+\pi^{0}$: $\bar{\tau}_{\mathrm{f}} = (0.75^{+0.42}_{-0.20}) \times 10^{-10}$ sec,

162 Flugzerfälle $\Sigma^{\pm} \to \pi^{\pm}+\mathrm{n}$: $\bar{\tau}_{\mathrm{f}} = (0.66^{+0.14}_{-0.13}) \times 10^{-10}$ sec.

Da jedoch für die $\Sigma^{\pm} \to \pi^{\pm}+\mathrm{n}$ Flugzerfälle die Energie und damit Flugzeit der Σ-Hyperonen nur aus Lückendichtemessungen bestimmt wurde (die π-Mesonen können wegen der geringen Minimumkorndichte nur unter großen Mühen und Zeitverlusten verfolgt werden; die meisten von ihnen verlassen außerdem das Plattenpaket, und Reichweitestreuungen der π-Mesonen äußern sich in einem großen Fehler der berechneten Σ-Hyperonen-Energie), wird man Flugzerfälle mit einer Restreichweite kleiner als 300 μm nicht mehr sicher als Flugzerfälle identifizieren können. Um sicher zu sein, Flugzerfälle nicht als Ruhezerfälle und umgekehrt identifiziert zu haben, führten wir eine Abschneideenergie von 8 MeV ein, entsprechend einer Restreichweite von 300 μm und möglichen Ab-

† Private Mitteilungen.

bremszeit von $T'_i = 0.128 \times 10^{-10}$ sec †. Für 137 Flugzerfälle $\Sigma^{\pm} \to \pi^{\pm} + n$ erhielten wir dann

$$\bar{\tau}_{I\ (cut\ off)} = (0.77^{+0.23}_{-0.16}) \times 10^{-10}\ \text{sec}.$$

2.2. ZUSAMMENFASSUNG DER BISHER GEFUNDENEN LEBENSDAUERN FÜR DIE GELADENEN Σ-HYPERONEN

Die folgenden Tabellen enthalten alle uns bekannten, bisher veröffentlichten Werte für die mittlere Lebensdauer der geladenen Σ-Hyperonen.

Folgende Abkürzungen wurden verwendet:

Genf 1958:	1958 Annual International Conference on High Energy Physics at CERN
Kiew 1959:	1959 Annual International Conference on High Energy Physics at Kiew
ML:	"Maximum Likelihood" Methode von Bartlett
FA:	Flugzeit-Abfall-Methoden
RT:	"Residual-Time" Methode
H.B.C.	Wasserstoff-Blasenkammer
P.B.C.:	Propan-Blasenkammer
M.C.C.:	Magnet-Nebelkammer
C.C.:	Nebelkammer
$(p)_{F,R}$:	$\Sigma^+ \to p + \pi^0$ Flug- und Ruhezerfälle,
$(\pi^{\pm})_F$:	$\Sigma^{\pm} \to n + \pi^{\pm}$ Flugzerfälle, u.s.w.
Co:	"Cut off"; Ereignisse, bei denen eine Abschneideenergie eingeführt wurde.

Emulsionsgruppen

Wisconsin:	W. F. Fry, J. Schneps, G. A. Snow, M. S. Swami, D. C. Wold, C. J. Mason, N. A. Nickols, F. M. Smith
European Collaboration:	B. Bhowmik, D. Evans, D. Falla, F. Hassan, A. A. Kamal, K. K. Nagpaul, D. J. Prowse (Bristol) M. Rene (Brüssel) G. Alexander, R. H. W. Johnston, C. O'Ceallaigh (Dublin I.A.S.) D. Keefe (Dublin U.C.) E. H. S. Burhop, D. H. Davis, R. C. Kumar, W. B. Lasich, M. A. Shaukat, F. R. Stannard (London U.C.) M. Bacchella, A. Bonetti, C. Dilworth, G. Occhialini, L. Scarsi (Mailand) M. Merlin, A. Salandin, M. Grilli, L. Guerriero, L. v. Lindern (Padua)
Livermore I :	S. White, G. Gilbert, S. C. Freden
N.R.L.:	R. G. Glaser, N. Seeman, G. A. Snow
Rochester:	T. F. Hoang, M. Kaplon, T. Yamanouchi
Parma:	G. Dascola, S. Mora
Paris:	J. Crussard, J. Hennessy
Bologna:	W. Alles, N. N. Biswas, M. Ceccarelli, R. Gessaroli, G. Quareni
Livermore II:	S. C. Freden, H. N. Kornblum, R. S. White

Blasenkammergruppen

Berkeley:	N. Horwitz, D. Miller, J. Murray, A. Rosenfeld, F. Solmitz, R. Tripp
Michigan:	J. Brown, D. Glaser, C. Graves, M. Perl, J. Cronin, J. Vandervelde
Alvarez u.a. (Berkeley):	L. W. Alvarez, H. Bradner, P. Falk-Vairant, J. D. Gow, A. H. Rosenfeld, F. T. Solmitz, R. D. Tripp
Columbia:	F. Eisler, R. Plano, A. Prodell, N. Samios, M. Schwartz, J. Steinberger
Bologna:	P. Bassi, V. Borelli, G. Puppi, G. Tanaka, P. Waloschek, V. Zobuli
Pisa:	M. Conversi, P. Franzini, I. Manelli, R. Santangelo, V. Silvestrini

† Falls die Σ-Hyperonen aus einem Gemisch kurzlebiger und langlebiger Teilchen bestehen würden, sollte ein "cut off' das Ergebnis zugunsten der kürzeren Lebensdauer beeinflussen.

TABELLE 1

Σ^+-Lebensdauer, bestimmt aus Flug- und Ruhezerfällen

Autorengruppe	Technik	Primärstrahl	Zerfallsart	Anzahl der Σ	Auswahl d. Ereignisse	Methode	Lebensdauer in 10^{-10} sec	Literatur
1) Alles	Emulsion	K^-	$(p)_{F,R}$	29 R 12 F	(Σ, π)	ML	$1.11\ ^{+0.50}_{-0.27}$	Diplomarbeit Max Planck Institut für Physik Göttingen, 1957
2) Alles	Emulsion	K^-	$(\pi^+)_{F,R}$	24 R 12 F	(Σ, π)	ML	$1.34\ ^{+0.54}_{-0.30}$	
3) Wisconsin	Emulsion	K^-	$(p)_{F,R}$	26 R 14 F	alle K^--Reaktionen	ML	$0.96\ ^{+0.37}_{-0.21}$	Phys. Rev. **107** (1957) 257 Genf 1958
4) Berkeley	Emulsion		$(p)_{F,R}$				$0.94\ ^{+0.23}_{-0.15}$	Genf 1958
5) European Collabaration I	Emulsion	K^-	$(p)_{F,R}$				$0.84\ ^{+0.20}_{-0.13}$	Genf 1958
6) Livermore I	Emulsion		$(p)_{F,R}$				$0.61\ ^{+0.18}_{-0.11}$	Genf 1958
7) N.R.L.	Emulsion	K^-	$(p)_{F,R}$		alle K^--Reaktionen	ML	$1.25\ ^{+0.51}_{-0.28}$	Phys. Rev. **107** (1957) 277 Genf 1958
8) Rochester	Emulsion		$(p)_{F,R}$				$0.95\ ^{+0.16}_{-0.16}$	Genf 1958
9) München, Paris, Parma, Bologna	Emulsion	K^-	$(p)_{F,R}$	186 R 99 F	(Σ, π)	ML	$0.99\ ^{+0.11}_{-0.09}$	diese Arbeit
10) München	Emulsion	K^-	$(\pi^+)_{F,R}$	84 R 51 F	(Σ, π)	ML	$0.86\ ^{+0.14}_{-0.14}$	diese Arbeit
11) Livermore II	Emulsion	K^-	$(p)_{F,R}$	68 R 49 F	(Σ, π)	ML	$0.35\ ^{+0.14}_{-0.11}$	UCRL-5724 1959
12) European Collaboration II	Emulsion	K^-	$(p)_{F,R}$	51R+F		ML	$0.82\ ^{+0.31}_{-0.20}$	Kiew 1959

Σ^+-Lebensdauer, bestimmt aus den Flugzerfällen allein

Autorengruppe	Technik	Primärstrahl	Zerfallsart	Anzahl der Σ^+	Auswahl d. Ereignisse	Methode	Lebensdauer in 10^{-10} sec	Literatur
1) Berkeley	H.B.C.	K^-	$(p, \pi)_F$				$0.69\ ^{+0.1}_{-0.1}$	Genf 1958
2) Michigan	P.B.C.		$(p, \pi)_F$				$0.95\ ^{+0.37}_{-0.23}$	Genf 1958
3) Alvarez u.a.	H.B.C.	K^-	$(p)_F$	27	alle K^- Reaktionen	FA	$0.86\ ^{+0.17}_{-0.17}$	Nuovo Cim. **5** (1957) 1026
4) Alles	Emulsion	K^-	$(p)_F$	12	(Σ, π)	ML	$2.76\ ^{+\infty}_{-2.14}$	Diplomarbeit M.P.I. für Physik, Göttingen, 1957
5) European Collaboration	Emulsion	K^-	$(p)_F$				$0.86\ ^{+0.57}_{-0.25}$	Genf 1958
6) Rochester	Emulsion		$(p)_F$				$0.81\ ^{+0.75}_{-0.15}$	Genf 1958
7) Wisconsin	Emulsion	K^-	$(\pi^+)_F$	12	alle K^--Reaktionen	ML	$0.94\ ^{+0.35}_{-0.35}$	Phys. Rev. **107** (1957) 257
8) Wisconsin	Emulsion	K^-	$(p)_F$	14	(Σ, π)	ML	$0.47\ ^{+0.44}_{-0.15}$	Phys. Rev. **107** (1957) 257 Genf 1958
9) Livermore I	Emulsion		$(p)_F$				$0.54\ ^{+0.58}_{-0.11}$	Genf 1958
10) Livermore I	Emulsion		$(p)_{F\,\infty}$				$0.12\ ^{+0.07}_{-0.04}$	Genf 1958
11) Livermore I	Emulsion		$(\pi^+)_F$				$0.16\ ^{+0.08}_{-0.03}$	Genf 1958
12) München, Paris, Bologna, Parma	Emulsion	K^-	$(p)_F$	99	(Σ, π)	ML	$0.75\ ^{+0.42}_{-0.20}$	diese Arbeit
13) Livermore II	Emulsion	K^-	$(p)_F$	49	(Σ, π)	ML	$0.95\ ^{+1.87}_{-0.40}$	UCRL-(5724-1959
14) Livermore II	Emulsion	K^-	$(\pi^+)_F$	37	(Σ, π)	ML	$0.60\ ^{+0.68}_{-0.20}$	UCRL-5724-1959

TABELLE 3

$\Sigma^\pm$-Lebensdauer, bestimmt aus Flugzerfällen (und Ruhezerfällen)

TABELLE 3

$\Sigma^{\pm}$-Lebensdauer, bestimmt aus Flugzerfällen (und Ruhezerfällen)

Autorengruppe	Technik	Primärstrahl	Zerfallsart	Anzahl der $\Sigma^{\pm}$	Auswahl d. Ereignisse	Methode	Lebensdauer in 10^{-10} sec	Literatur
1) Amaldi u. s.	Emulsion	Höhenstrahlung	$(p, \pi)_{F,R}$		alle gefundenen Σ	ML, RT	$0.5 < \tau < 3$	Nuov. Cim **12** (1954) 668
2) Dahanayake u.a.	Emulsion	Höhenstrahlung	$(\pi^{\pm})_F$	4		ML	$0.5\,^{+3.3}_{-0.33}$	Nuov. Cim. **1** (1955) 888
3) Cooper u.a.	M.C.C.	Höhenstrahlung	$(\pi^{\pm})_F$	13	alle gefundenen Σ	ML	$0.63\,^{+0.30}_{-0.30}$	Nuov. Cim. **4** (1956) 390
4) Davies u.a.	Emulsion	Höhenstrahlung	$(\pi^{\pm})_F$	11		ML	$0.35\,^{+0.15}_{-0.11}$	Nuov. Cim. **4** (1956) 472
5) Webb u.a.	Emulsion	K^-	$(\pi^{\pm})_F$	8	alle K^--Reaktionen	ML	$0.81\,^{+1.25}_{-0.34}$	Nuov. Cim. **8** (1958) 899
6) Alles	Emulsion	K^-	$(\pi^{\pm})_F$	24	(Σ, π)	ML	$2.62\,^{+\infty}_{-2.14}$	Diplomarbeit M.P.I. für Physik. Göttingen, 1957
7) European Collaboration I	Emulsion	K^-	$(\pi^{\pm})_F$				$0.81\,^{+0.22}_{-0.15}$	Genf 1958
8) Berkeley	Emulsion	K^-	$(\pi^{\pm})_F$				0.51 ± 0.2	Genf 1958
9) Livermore I	Emulsion		$(\pi^{\pm})_F$				$0.33\,^{+0.11}_{-0.04}$	Genf 1958
10) N.R.L.	Emulsion	K^-	$(\pi^{\pm})_F$	6	alle K^--Reaktionen	ML	$0.31\,^{+0.32}_{-0.10}$	Phys. Rev. **107** (1957) 277 Genf 1958)
11) Wisconsin	Emulsion	K^-	$(\pi^{\pm})_F$	26	all K^--Reaktionen	ML	$0.32\,^{+0.11}_{-0.07}$	Phys. Rev. **107** (1957) 257 Genf 1958
12) München, Paris, Parma, Bologna	Emulsion	K^-	$(\pi^{\pm})_F$	162	(Σ, π)	ML	$0.66\,^{+0.14}_{-0.13}$	diese Arbeit
13) München, Paris, Parma, Bologna	Emulsion	K^-	$(\pi^{\pm})_{F\,co}$	137	(Σ, π)	ML	$0.77\,^{+0.23}_{-0.16}$	diese Arbeit
14) European Collaboration II	Emulsion	K^-	$(\pi^{\pm})_F$	70		ML	$0.80\,^{+0.29}_{-0.15}$	Kiew 1959

TABELLE 4

Σ^--Lebensdauer

Autorengruppe	Technik	Primärstrahl	Zerfallsart	Anzahl der Σ	Auswahl d. Ereignisse	Methode	Lebensdauer in 10^{-10} sec	Literatur
1) Alles	Emulsion	K^-	$(\pi)_{F,R}$	29 R 16 F	(Σ, π)	ML	$1.93\ ^{+0.64}_{-0.39}$	Diplomarbeit M.P.I. für Physik, Göttingen, 1957
2) Wisconsin	Emulsion	K^-	$(\pi)_{F,R}$	115 R 14 F	alle K^--Reaktionen	ML	$2.5\ ^{+0.8}_{-0.8}$	Phys. Rev. **107** (1957) 257 Genf 1958
3) Livermore	Emulsion		$(\pi)_F$				$0.34\ ^{+0.37}_{-0.07}$	Genf 1958
4) München	Emulsion	K^-	$(\pi)_{F,R}$	15 R 2 F	K^--Einfang an freien Protonen	ML	$1.86\ ^{+0.69}_{-0.71}$	diese Arbeit
5) Trilling u.a.	C.C.	Höhenstrahlung					$1.5\ ^{+0.38}_{-0.25}$	Nuov. Com. Suppl. **6** (1957) 561
6) Michigan	P.B.C.		$(\pi)_F$				$1.67\ ^{+0.40}_{-0.28}$	Genf 1958
7) Berkeley	H.B.C.		$(\pi)_{F,R}$				1.60 ± 0.2	Genf 1958
8) Columbia, Pisa, Bologna	P.B.C.		$(\pi)_F$	107			$1.89\ ^{+0.33}_{-0.25}$	Nuov. Cim. **10** (1958) 150 Genf 1958

2.3. DISKUSSION DER ERGEBNISSE FÜR DIE LEBENSDAUERN

Lee und Yang [5]) hatten 1956 die Existenz von Paritätsdubletts für alle Teilchen ungerader Strangeness erörtert. Es war dann zu erwarten, daß die das Dublett bildenden Hyperonen verschiedene Lebensdauern hätten.

In der Tat fanden einige Autoren (s. Tabellen 1—3) Anzeichen für die Existenz zweier verschiedener Lebensdauern für die Σ^+- und $\Sigma^\pm$-Hyperonen. Da aber keine weiteren experimentellen Beweise für die Theorie von Lee und Yang gefunden wurden (z.B. eine asymmetrische Winkelverteilung der Zerfallsprodukte der Hyperonen [6,7]) und wir und einige Autoren die zwei verschiedenen Lebensdauern nicht beobachteten, liegt es nahe, die Ursache der Diskrepanz für die verschiedenen Lebensdauerwerte in irgendwelchen systematischen Meßfehlern oder in einem falschen Auswertverfahren zu suchen. Da in den meisten Fällen die „Maximum Likelihood Methode" von Bartlett benutzt wurde, die von Kaplon u.a. [8]) mit Hilfe einer Monte Carlo Rechnung nachgeprüft und für das vorliegende Problem als zulässig befunden wurde, ist die Diskrepanz bezüglich der verschiedenen Lebensdauern offenbar in experimentellen Fehlern zu suchen.

Bei den Bestimmungen der Lebensdauern kommen nur Reichweite-, Winkel- und Lückendichtemessungen in Betracht. Reichweite- und Winkelmessungen dürften kaum Anlaß zu fehlerhaften Ergebnissen geben. Lückendichtemessungen dagegen, auf denen die Energiebestimmungen bei den Flugzerfällen $\Sigma^\pm \to \pi^\pm + n$ meistens beruhen, können mit großen Fehlern und subjektiven Beeinflußungen behaftet sein.

Falls die Energie im Augenblick des Zerfalls zu groß bestimmt wird und/oder Flugzerfälle als Ruhezerfälle identifiziert werden (dies ist leicht möglich, wenn die Restreichweite der Flugzerfälle nur noch klein ist) so können diese fehlerhaften Beobachtungen zu merklich zu kurzen Lebensdauern führen, falls man versucht, die Lebensdauern aus den Flugzerfällen allein zu bestimmen.

Da wir für die Flugzerfälle $\Sigma^\pm \to \pi^\pm + n$ eine „Abschneideenergie" einführten, wird der von uns bestimmte Lebensdauerwert von $\bar{\tau}_{f\,(\text{cut off})} = (0.77^{+0.23}_{-0.16}) \times 10^{-10}$ sec (s. oben) nicht durch eine falsche Identifizierung von Flugzerfällen als Ruhezerfälle oder umgekehrt beeinflußt worden sein. Wir glauben auch nicht, daß wir die Energien beim Zerfall der Hyperonen zu klein bestimmt haben, da wir unsere Lückendichtemessungen mit Hilfe der Flugzerfälle $\Sigma^+ \to p + \pi^0$ überprüft haben und in den meisten Fällen gute Übereinstimmung der aus der Kinematik berechneten Energien mit den aus Lückendichtemessungen bestimmten Energien fanden.

Den von Fry *et al.* [7]) angegebenen „kurzen" Lebensdauerwert der Hyperonen aus $\Sigma^\pm \to \pi^\pm + n$ Flugzerfällen haben wir ebenfalls auf diese angegebenen möglichen Fehlerquellen untersucht. Da diese Autoren im Gegensatz zu uns alle in der Emulsion vorkommenden K^--Mesoneneinfänge benutzten, haben wir ihre Ergebnisse mit denen der K^- Kollaboration [9]) verglichen; Fry *et al.* fanden

0.85 ± 0.25 für das Verhältnis der Anzahl der Ruhezerfälle $\Sigma^+ \to \pi^+ + n$ zur Anzahl der Flugzerfälle $\Sigma^\pm \to \pi^\pm + n$, die K^- Kollaboration für das gleiche Verhältnis 0.66 ± 0.13. Infolge dieser guten Übereinstimmung glauben wir, daß die von Fry *et al.* angegebene kurze Lebensdauer nicht auf eine falsche Identifizierung der Flugzerfälle als Ruhezerfälle beruht, da die von der K^- Kollaboration angegebene Lebensdauer sich nicht wesentlich von unserem Wert unterscheidet (s. Tabelle 3). Betrachten wir dagegen die Energiespektren der Hyperonen aus den Flugzerfällen $\Sigma^\pm \to \pi^\pm + n$ beider Arbeiten, so sehen wir, daß Fry *et al.* im Bereich 0—55 MeV 13 Hyperonen, im Bereich 55—100 MeV 13 Hyperonen, die K^- Kollaboration für entsprechende Intervalle 43 und 13 Hyperonen fanden; dies bedeutet, daß Fry *et al.* bedeutend mehr energiereiche Hyperonen gefunden haben. Falls etwa demnach diese Autoren tatsächlich die Energien für die Hyperonen zu groß bestimmt hätten, wäre damit eine Erklärung für ihren kurzen Lebensdauerwert gegeben.

Die von uns gefundene Übereinstimmung der mittleren Lebensdauer für die $\Sigma^\pm$-Hyperonen von $\bar{\tau}_{\tau,t}$ und $\bar{\tau}_t$ besagt, daß keine Anzeichen für die Existenz einer 2. Sorte von Hyperonen mit kurzer Lebensdauer vorhanden sind. Zur genauen Bestimmung der mittleren Lebensdauer des Σ^+-Hyperons, wird man Flug- und Ruhezerfälle benutzen, da bei den Energien der meisten Experimente T_f und T_t in der Größenordnung der mittleren Lebensdauer liegen, sodaß bei ihrer Berechnung aus den Flugzerfällen allein mit einem größeren statistischen Fehler gerechnet werden muß. Um aus den angegebenen Werten der verschiedenen Autoren (s. Tabellen) den besten Mittelwert für die mittlere Lebensdauer der Σ^+-Hyperonen zu erhalten, haben wir die Werte von der Tabelle 1 zusammengefaßt.

Berücksichtigen wir dort nicht 2) und 10), da die Anzahl der Hyperonen in diesen Fällen ($\Sigma^+ \to \pi^+ + n$) auf Abschätzungen beruht und ebenfalls nicht 5) und 6), da beide Gruppen inzwischen neuere Werte (s. 11) und 12)) veröffentlichten, so erhalten wir

$$\bar{\tau}_{t,\tau} = \left(0.95^{+0.07}_{-0.05}\right) \times 10^{-10} \text{ sec}$$

als wohl bisher genauesten Wert für die mittlere Lebensdauer des Σ^+-Hyperons.

2.4. Die Verzweigungsverhältnisse des Σ-Zerfalls und die Lebensdauer des Σ^+-Hyperons bestimmt aus dem Zerfall $\Sigma^+ \to \pi^+ + n$

Mehrere Autoren [10, 11]) haben auf das theoretische Interesse hingewiesen, das der Wert des Verzweigungsverhältnisses R(= Anzahl der $\Sigma^+ \to p + \pi^0$ Zerfälle/ Anzahl der $\Sigma^+ \to \pi^+ + n$ Zerfälle) besitzt. Falls man die Auswahlregel $T = \pm \frac{1}{2}$ für den Σ-Zerfall annimmt, so folgt eine Beziehung zwischen R und dem Verhältnis der Lebensdauern des Σ^+- und Σ^--Hyperons. Über die experimentellen Ergebnisse bezüglich dieses Punktes berichten ausführlich Alvarez u.a. [6, 7]).

Wir beobachteten 79 Ruhezerfälle $\Sigma^+ \to p + \pi^0$ und 84 Ruhezerfälle $\Sigma^+ \to \pi^+ + n$

wobei wir glauben, daß wir alle $\Sigma^+ \to \pi^+ + n$ Zerfälle beobachtet haben, so daß keine Korrektion für einen Durchmusterungsverlust notwendig ist. Wir erhalten somit

$$R = \frac{\Sigma^+ \to p + \pi^0}{\Sigma^+ \to \pi^+ + n} = 79/84 = 0.94 \pm 0.15,$$

in guter Übereinstimmung mit anderen Autoren [6, 7, 12]).

Mit Hilfe dieses Verzweigungsverhältnisses können wir nun die Anzahl der positiven und negativen Hyperonen der $\Sigma^\pm \to \pi^\pm + n$ Flugzerfälle abschätzen. Da wir 48 $\Sigma^+ \to p + \pi^0$ Flugzerfälle gefunden haben, können wir annehmen, daß unter den 63 $\Sigma^\pm$ Flugzerfällen 51 ± 11 positive Hyperonen sind.

Man kann nun die Lebensdauer der positiven Hyperonen aus der Zerfallsart $\Sigma^+ \to \pi^+ + n$ abschätzen, indem man die Gesamtflugzeit der 63 Σ^+ auf 51 Σ^+ reduziert.

Wie wir aus Blasenkammeruntersuchungen wissen, (s. Tabelle 4) ist die mittlere Lebensdauer des Σ^- Hyperons etwa doppelt so groß wie die für das Σ^+ Hyperon. Für $\tau_{\Sigma^-} = 2\tau_{\Sigma^+}$ erhalten wir aus den 84 Ruhezerfällen und 51 Flugzerfällen

$$\bar{\tau}_{r,f} = (0.86 \pm 0.14) \times 10^{-10} \text{ sec};$$

für $\tau_{\Sigma^-} = \tau_{\Sigma^+}$ würde folgen $\bar{\tau}_{r,f} = (0.93 \pm 0.14) \times 10^{-10}$ sec. Diese hier bestimmte Lebensdauer stimmt gut überein mit der aus den $\Sigma^+ \to p + \pi^0$ Zerfällen bestimmte.

Für die Häufigkeit des Zerfalls $\Sigma^+ \to p + \gamma$ [13]) können wir eine obere Grenze angeben. Für einen derartigen Zerfall in Ruhe besitzt das Proton eine Reichweite von etwa 3 mm in der Emulsion. Unter den 79 Ruhezerfällen $\Sigma^+ \to p + \pi^0$ und unter den als Σ^--Einfänge identifizierten Ereignissen, konnten wir kein Ereignis finden, das mit dem Zerfall $\Sigma^+ \to p + \gamma$ vereinbar ist. Für das Verhältnis der Anzahl der $\Sigma^+ \to p + \gamma$ zur Anzahl der $\Sigma^+ \to p + \pi^0$ Zerfälle folgt

$$\frac{\Sigma^+ \to p + \gamma}{\Sigma^+ \to p + \pi^0} < 1.3\ \%.$$

Die theoretischen Angaben für das Verzweigungsverhältnis variieren von 10^{-2} zu 10^{-4}, sodaß die hier angegebenen Daten nicht inkonsistent mit der Theorie sind [14, 15]).

3. K^--Mesoneneinfänge durch freie Protonen

3.1. DIE ERZEUGUNGSRATE FÜR DIE Σ^- UND Σ^+-HYPERONEN UND EINE METHODE ZUR BESTIMMUNG DER MITTLEREN LEBENSDAUER VON Σ^--HYPERONEN IN KERNEMULSIONEN

Wir fanden 24 K^--Mesoneneinfänge in Ruhe durch freie Protonen. Diese Ereignisse sind leicht zu identifizieren, da die Spuren der erzeugten Σ-Hypero-

nen und π-Mesonen kollinear sind und die Reichweite des Σ^+ Hyperons etwa 820 μm und die des Σ^- Hyperons etwa 724 μm in der Kernemulsion beträgt. Wir identifizierten als „Wasserstoffereignisse"

4 Ruhezerfälle $\Sigma^+ \to p+\pi^0$,
2 Ruhezerfälle $\Sigma^+ \to n+\pi^+$,
0 Flugzerfälle $\Sigma^+ \to p+\pi^0$,
3 Flugzerfälle $\Sigma^\pm \to n+\pi^\pm$,
15 Einfänge negativer Hyperonen.

Für das Verhältnis der beim Einfang der K^--Mesonen durch freie Protonen erzeugten Hyperonen erhalten wir somit unter den extremen Annahmen, daß alle 3 Hyperonen der Flugzerfälle $\Sigma^\pm \to \pi^+ + n$ negativ oder positiv geladen sind,

$$\frac{\text{Anzahl der } \Sigma^-}{\text{Anzahl der } \Sigma^+} = \begin{cases} \frac{18}{6} = 3.0 \pm 1.4, \\ \frac{15}{9} = 1.7 \pm 0.7. \end{cases}$$

Dieses Ergebnis bestätigt Werte anderer Autoren, die in Blasenkammern gewonnen wurden [6]).

Diese „Wasserstoffereignisse" könnte man benutzen, um die Lebensdauer für die Σ-Hyperonen zu bestimmen. Die Bestimmung der mittleren Lebensdauer in Kernemulsionen aus Flug- und Ruhezerfällen der in komplexen Kernen erzeugten Σ^--Hyperonen, wird dadurch erschwert, daß man nicht die Zahl der zur Ruhe kommenden Σ^--Hyperonen kennt, die ohne Einfangsmerkmale, wie Emission von Sekundärspuren, eingefangen werden. Diese Zahl kann nur abgeschätzt werden. Bei den „Wasserstoffereignissen" können die Σ^--Hyperonen neben den Einfangsmerkmalen noch infolge ihrer Reichweite identifiziert werden, sodaß man genau die Zahl der zur Ruhe kommenden Σ^--Hyperonen kennt. Leider konnten wir wegen der geringen Korndichte und der kleinen Ausmaße des Emulsionspaketes nicht die Ladung der 3 Flugzerfälle $\Sigma^\pm \to \pi^\pm + n$ bestimmen, so daß eine Lebensdauerbestimmung in unserem Fall für das Σ^--Hyperon nicht möglich ist.

3.2. MASSENBESTIMMUNGEN DER $\Sigma^\pm$-HYPERONEN UND K^--MESONEN

Die Reichweiteverteilung der μ-Mesonen aus 50 $\pi^+ \to \mu+\nu$ Zerfällen ergibt $\bar{R}(\mu^+) = (601.9 \pm 3.6)\mu$m. Auf Grund der guten Übereinstimmung unseres Wertes mit dem von Barkas u.a. gefundenen benutzen wir die neuen Reichweitetabellen von Barkas [16]).

In Abb. 9 ist die Reichweiteverteilung von 80 Protonen aus Ruhezerfällen der Art $\Sigma^+ \to p+\pi^0$ wiedergegeben. Der Mittelwert der Reichweiten der Protonen ergibt $\bar{R}_p = 1666.8 \pm 5.7$ μm. Die Reichweite-Energie-Beziehung von Barkas ergibt eine entsprechende Energie von $T_p = 18.78 \pm 0.05$ MeV. Mit Hilfe des Impuls- und Energiesatzes und der Werte $m_p = 938.215 \pm 0.010$ MeV und $m_{\pi^0} = 135.04 \pm 0.16$ MeV erhalten wir

$$m_{\Sigma^+} = 1189.00 \pm 0.22 \text{ MeV} = 2326 \pm 0.47 m_e.$$

Wir identifizierten 6 K^--Mesoneneinfänge an freien Protonen mit Erzeugung von positiven Hyperonen ($K^-+H \rightarrow \Sigma^+ + \pi^-$). Da die Masse des positiven Hyperons (s. oben) bekannt ist, läßt sich mit diesen „Wasserstoffereignissen" und der

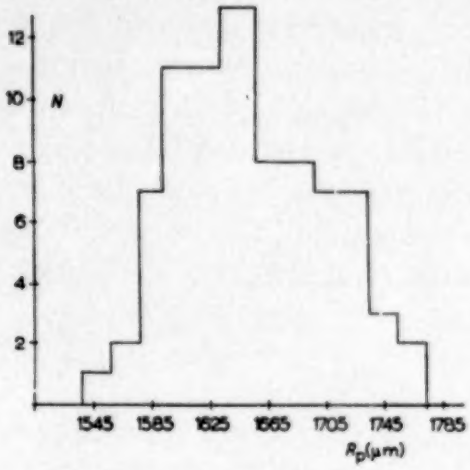

Abb. 9. Reichweiteverteilung der Protonen aus 80 $\Sigma^+ \rightarrow p+\pi^0$ Ruhezerfällen.

Reichweite der 6 Hyperonen leicht die Masse des K^--Mesons bestimmen. Aus der mittleren Reichweite von 821.2 ± 9.3 μm für das Σ^+-Hyperon erhielten wir $m_{K^-} = 493.0\pm0.6$ MeV $= 969.9\pm1.2 m_e$.

15 K^--Mesoneneinfänge an freien Protonen mit Erzeugung von negativen Hyperonen ($K^-+H \rightarrow \Sigma^- + \pi^+$) wurden gefunden. Die Massendifferenz zwischen Σ und Σ^+ läßt sich aus der Reichweitedifferenz beider Teilchen nach Barkas *et al.* [17]) berechnen. Wir erhielten mit $R_{\Sigma^-} = 724.0\pm5.8$ μm,

$$m_{\Sigma^-} - m_{\Sigma^+} = 5.67\pm0.61 \text{ MeV},$$
$$m_{\Sigma^-} = 1194.7\pm0.7 \text{ MeV} = 2338.1\pm1.0\, m_e.$$

Die hier gefundenen Massenwerte stimmen gut mit früher angegebenen überein [17, 29]).

4. Vorwärts-Rückwärts-Asymmetrie im Zerfall der Σ-Hyperonen

Experimentelle Untersuchungen über eine Vorwärts-Rückwärts-Asymmetrie im Hyperonenzerfall können Aufschluß geben über die Gültigkeit der Paritätserhaltung in starken Wechselwirkungen bei der „Strange Particle" Erzeugung. Experimente über Kern-Energie-Zustände zeigten, daß die Parität in hohem Grade in starken Wechselwirkungen zwischen Atomkernen erhalten bleibt [18, 19]). Soloview [20]), und Pais [21]) wiesen jedoch darauf hin, daß diese Experimente wenig darüber besagen, ob die Parität in starken Wechselwirkungen erhalten bleibt, falls „Strange Particles" daran beteiligt sind.

Falls die Parität in starken Wechselwirkungen der „Strange Particles" erhalten bleibt, so steht ein möglicher Polarisationsvektor der Hyperonen nur

senkrecht auf der Erzeugungsebene, während eine Nichterhaltung der Parität dagegen eine Polarisationskomponente in der Erzeugungsebene hervorruft, die zu einer Zerfallsasymmetrie in dieser Ebene führt.

Vorwärts-Rückwärts-Asymmetrieen wurden bei Λ^0-Hyperonen angegeben, die durch Höhenstrahlen in komplexen Kernen erzeugt wurden [22, 23, 24]). Durch π-Mesonen in Blei und Kohlenstoff erzeugte Λ^0-Hyperonen zeigten ebenfalls eine solche Asymmetrie [25]), während jedoch in einem neueren Experiment bei durch 1.33 GeV/c π-Mesonen in Kohlenstoff erzeugten Λ^0-Hyperonen diese Asymmetrie nicht beobachtet wurde [26]). Auch die Wasserstoff-Blasenkammer-Gruppe in Berkeley [27, 28]), erbrachte mit ihren Untersuchungen an Λ^0-Hyperonen Ergebnisse, die konsistent sind mit der Erhaltung der Parität in der „assoziierten" Erzeugung

$$\pi^- + \mathrm{p} \rightarrow \bar{\mathrm{K}}^0 + \Lambda^0.$$

Wir untersuchten die Winkelverteilungen der sichtbaren Zerfallsprodukte der Σ-Hyperonen in Bezug auf die $\mathbf{p}_\Sigma$-Richtung. Falls das Σ-Hyperon den Spin $\frac{1}{2}$ hat, muß die Winkelverteilung des Zerfalls im Ruhesystem des Σ-Hyperons die Form $1+\alpha\bar{P}\cos\vartheta$ haben, wobei ϑ der Winkel zwischen dem Zerfallsteilchen und der Flugrichtung des Σ-Hyperons im Schwerpunktssystem des Hyperons sein soll.

Eine Gleichung für den Wert $\alpha\bar{P}$ für N Zerfälle wird gegeben durch

$$\alpha\bar{P} = \frac{3}{N}\sum_{n=1}^{N}(\cos\vartheta)_n \pm (3/N)^{\frac{1}{2}}.$$

Wir erhielten für

79 Ruhezerfälle	$\Sigma^+ \rightarrow \mathrm{p}+\pi^0$:	$\alpha\bar{P} = -0.26 \pm 0.19$	(Abb. 6),
84 Ruhezerfälle	$\Sigma^+ \rightarrow \mathrm{n}+\pi^+$:	$\alpha\bar{P} = +0.10 \pm 0.19$	(Abb. 10),
48 Flugzerfälle	$\Sigma^+ \rightarrow \mathrm{p}+\pi^0$:	$\alpha\bar{P} = -0.27 \pm 0.25$	(Abb. 5),
63 Flugzerfälle	$\Sigma^\pm \rightarrow \mathrm{n}+\pi^+$:	$\alpha\bar{P} = +0.20 \pm 0.22$	(Abb. 8).

Eine „Vorwärts-Rückwärts"-Asymmetrie für die Zerfallsprodukte der Σ-Hyperonen in Bezug auf die Flugrichtung der Hyperonen konnten wir also nicht beobachten. Die $\alpha\bar{P}$ wurden berechnet, indem für alle 4 Zerfallsarten die Winkelverteilungen der Zerfalls-π-Mesonen benutzt wurden.

5. Einfänge negativer Σ-Hyperonen

Beim Einfang von Σ^--Hyperonen sind folgende Reaktionen möglich:

$$\Sigma^- + \mathrm{p} \rightarrow \Lambda^0 + \mathrm{n} + 80\ \mathrm{MeV}, \quad \Sigma^- + \mathrm{p} \rightarrow \Sigma^0 + \mathrm{n} + 4\ \mathrm{MeV}.$$

Abb. 11 zeigt die Spurenverteilung der Σ-Einfang-Sterne, deren Σ^--Hyperonen in K^--Einfängen in Ruhe und im Flug an freien Protonen erzeugt wurden.

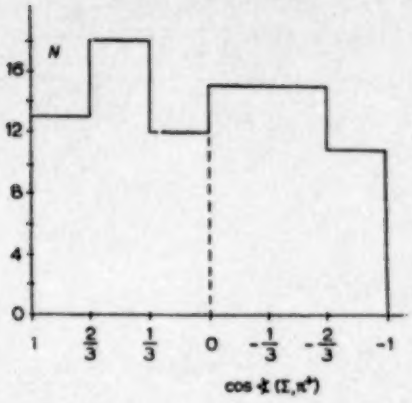

Abb. 10. Winkelverteilung der π-Mesonen aus den $\Sigma^+ \to n+\pi^+$ Ruhezerfällen in Bezug auf die Anfangsflugrichtung des Σ-Hyperons.

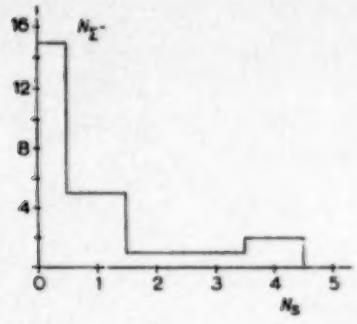

Abb. 11. Spurenverteilung der Σ^--Einfänge, deren Hyperonen in K^--Einfängen durch freie Protonen erzeugt wurden (N_S ist die Anzahl der Sekundärspuren, N_{Σ^-} die Anzahl der Σ^--Einfänge).

Die folgende Tabelle zeigt die Merkmale der Einfänge ohne jede sichtbare Sekundärspur.

Anzahl der Ereignisse	Merkmale
2	2 Elektronen und Blob
5	Blob
3	ohne Elektronen und Blobs
2	1 Elektron
3	1 Elektron und Blob

Die freiwerdende sichtbare Energie für die Σ^--Einfang-Sterne, deren Σ^--Hyperonen in K^--Einfängen an freien Protonen erzeugt wurden, zeigt Abb. 12 unter der Annahme, daß alle sichtbaren emittierten Teilchen Protonen sind.

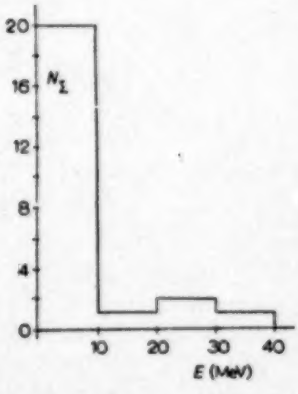

Abb. 12. Die „sichtbare" Energieverteilung für die in Abb. 8 angeführten Ereignisse, und zwar unter der Annahme, daß alle sichtbaren Sekundärteilchen Protonen sind.

Abb. 13 gibt die Spurenverteilung aller übrigen Σ^--Einfang-Sterne, also der Σ^--Einfang-Reaktionen an komplexen Kernen. Übertragen wir die Anzahl der Einfänge ohne jede sichtbare Sekundärspur, die länger als 5 μm ist, von den „Wasserstoff-Ereignissen" auf diese Verteilung, indem wir die Anzahl der

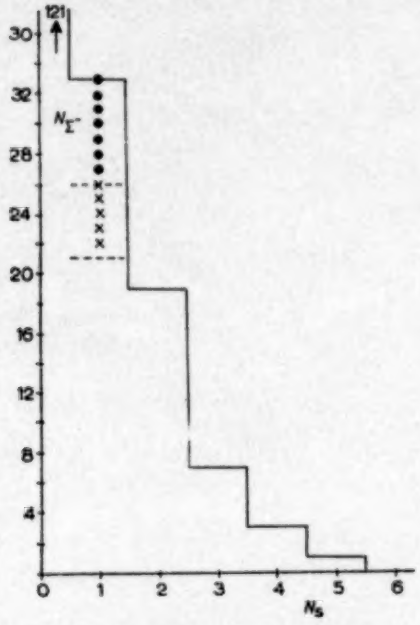

Abb. 13. Spurenverteilung der Σ-Einfänge an komplexen Kernen (die Kreuze stellen Σ^--Einfänge vor, deren eine Sekundärspur kleiner als 50 μm, jedoch größer als 5 μm ist; die Punkte beziehen sich auf Σ^--Einfänge mit einer Sekundärspur oder mögliche Protonstreuungen).

identifizierten Sterne mit 1 oder mehr Sekundärspuren zur Normierung benutzen, so erhalten wir 121 ± 53 Sterne ohne Sekundärspuren. Die sichtbare Energieverteilung für die Σ^--Einfänge an komplexen Kernen gibt die Abb. 14a, b wieder.

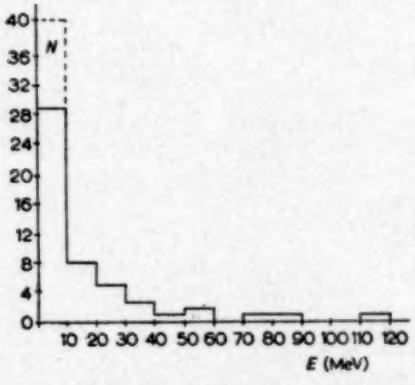

Abb. 14a. Sichtbare Energieverteilung der Σ-Einfänge an komplexen Kernen, wieder unter der Annahme, daß alle sichtbaren Sekundärteilchen Protonen sind.

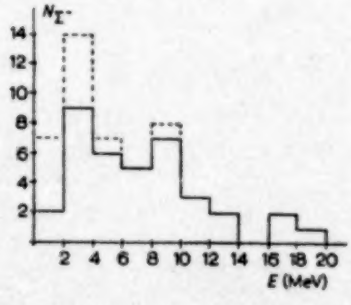

Abb. 14b. Das Energieintervall 0—20 MeV der Abb. 14a wird in Intervalle von 2 MeV unterteilt wiedergegeben (die gestrichelten Linien der Abb. 14a, b geben die in Abb. 13 mit Punkte oder Kreuze gekennzeichneten Einfänge wieder).

In der folgenden Tabelle sind die Spurenverteilungen der von einigen anderen Autoren und von uns gefundenen Σ^--Einfänge (die Σ^--Einfänge an freien Protonen und an komplexen Kernen wurden in unserer Arbeit zusammengefaßt) wiedergegeben.

Zahl der sichtbaren Sekundärspuren des Σ^--Einfanges	Anzahl der Σ^--Einfänge				
	Alles [30])	Chadwick *et al.* [31])	European Collaboration [9])	Fry *et al.* [7])	diese Arbeit
0	57		192	65	136
1	9	17	53	31	38
2	4	8	30	13	20
3	4	5	8	5	8
4	2	0	3	1	5
5	0	0	0	0	1

Alles und die „European Collaboration" schätzten die Anzahl ihrer Σ^--Einfänge ohne sichtbaren Sekundärspuren aus der Winkelverteilung der Σ-Hyperonen und π-Mesonen, Fry u.a. schätzten die Anzahl dieser Sterne aus der Einfangwahrscheinlichkeit in leichten und schweren Kernen und der Produktionswahrscheinlichkeit für Auger Elektronen, während wir zur Abschätzung die „Wasserstoffereignisse" benutzten. Wie wir sehen, stimmen die Spurenverteilungen für die Σ^--Einfänge von der Europäischen Kollaboration und von uns gut überein. Berücksichtigen wir in unserer Arbeit auch noch die Zerfälle negativer Hyperonen, so erhalten wir für die insgesamt in den (Σ, π)-Ereignissen emittierten negativen Hyperonen eine Anzahl von 220 ± 56. Für das Verhälnis der Anzahl der positiven Σ-Hyperonen zur Anzahl der negativen Σ-Hyperonen, die im K^--Einfang an gebundenen Protonen erzeugt wurden und den Kern verließen ohne Emission sichtbarer sekundärer Teilchen ((Σ, π) Ereignisse) erhalten wir somit 1.3 ± 0.3.

Ich danke Herrn Prof. Dr. W. Heisenberg und Herrn Dr. K. Gottstein für die Möglichkeit, die vorliegende Arbeit im Max-Planck-Institut für Physik und Astrophysik in München anzufertigen und für die Anregung zu dieser Arbeit. Den Beobachterinnen der Emulsionsgruppe, besonders Frl. Frentzel-Beyme und Frl. Arndt, sei für das Verfolgen der K^--Mesonen und Herrn Dr. H. Heckman und Herrn Dr. M. Cresti für die Exposition der Kernemulsionen gedankt. Den Emulsionsgruppen von Bologna (W. Alles, N. N. Biswas, M. Ceccarelli, R. Gessaroli und G. Quareni), Parma (G. Dascola und S. Mora) und Paris (J. Crussard und J. Hennessy) möchte ich noch für die Mitteilung ihrer unveröffentlichten Ergebnisse der Σ-Lebensdauern danken.

Literatur

1) M. S. Bartlett, Phil. Mag. **44** (1953) 249
2) E. Amaldi, C. Castagnoli, G. Cortini und C. Franzinetti, Nuovo Cim. **12** (1954) 668
3) C. Castagnoli, G. Cortini und C. Franzinetti, Nuovo Cim. Suppl. **12** (1954) 279
4) C. Franzinetti und G. Morpurgo, Nuovo Cim. Suppl. **6** (1957) 577
5) C. N. Yang, und T. D. Lee, Phys. Rev. **102** (1956) 290
6) L. Alvarez, H. Bradner, P. Falk-Vairant, J. D. Gow, A. H. Rosenfeld, F. T. Solmitz und R. D. Tripp, Nuovo Cim. **5** (1957) 1026
7) W. F. Fry, J. Schneps, G. A. Snow, M. S. Swami und D. C. Wold, Phys. Rev. **107** (1957) 257
8) M. F. Kaplon, T. Yamanouchi und A. C. Melissinos. Bull. Am. Phys. Soc. **4** (1959) 289
9) European K^- Stack Collaboration, Nuovo Cim. **14** (1957) 315
10) R. Gatto, Nuovo Cim. **3** (1956) 318
11) D'Espagnat und J. Prentki, Nuovo Cim. **3** (1956) 1045
12) S. C. Freden, H. N. Kornblum und R. S. White, UCRL-5724-T
13) G. Quareni, A. Quareni-Vigundelli, G. Dascola und S. Mora, Nuovo Cim. **14** (1959) 1179
14) R. F. Behrends, Phys. Rev. **111** (1958) 1691
15) P. Prakash und A. H. Zimermann, Nuovo Cim. **11** (1959) 869
16) W. H. Barkas, P. H. Barret, P. Cüer, H. Heckman und F. M. Smith, Nuovo Cim. **8** (1958) 185; W. H. Barkas, Nuovo Cim. **8** (1958) 201
17) W. H. Barkas, J. N. Dyer, P. C. Giles, H. H. Heckman, C. J. Mason, N. A. Nickols und F. M. Smith, Phys. Rev. **112** (1959) 622
18) N. Tanner, Phys. Rev. **107** (1957) 1203
19) D. H. Wilkinson, Phys. Rev. **109** (1958) 1603
20) V. G. Soloview, Nuovo Cim. **13** (1959) 442
21) A. Pais, Phys. Rev. Lett. **1** (1958) 418
22) W. A. Cooper, H. Filthuth, L. Montanet, J. A. Newth, G. Petrucci, R. A. Salmeron und A. Zichichi, Nuovo Cim. **8** (1958) 471
23) G. Alexander, C. Ballario, R. Bizzarri, B. Brunelli, E. DiCapua, A. Michelini, G. C. Monetti und A. Z. Zichichi, Nuovo Cim. **9** (1958) 624
24) P. A. Glaser, Report on the Conference on High Energy Physics at Kiew, 1959
25) H. Blumenfeld, W. Chinowsky und L. M. Ledermann, Nuovo Cim. **8** (1958) 296
26) P. Franzini, S. Fußnote bei R. A. Salmeron und A. Zichichi, Nuovo Cim. **11** (1959) 461
27) F. S. Crawford, M. Cresti, M. L. Good, F. T. Schmitz und M. L. Stevenson, Phys. Rev. Lett. **1** (1958) 209
28) F. S. Crawford, M. Cresti, M. L. Good, F. T. Schmitz und M. L. Stevenson, Phys. Rev. Lett. **2** (1959) 11
29) M. Gell-Mann und A. H. Rosenfeld, Ann. Rev. Phys. **7** (1957) 407
30) W. Alles, Diplomarbeit 1957, M. P. I. für Physik, Göttingen; Zeitschr. f. Naturf. **13a** (1958) 740
31) G. B. Chadwick, S. A. Durrani, P. B. Jones, J. W. G. Wignali und D. H. Wilkinson, Phil. Mag. **3** (1958) 1193

2.C

Nuclear Physics **20** (1960) 275—308; © *North-Holland Publishing Co., Amsterdam*

Not to be reproduced by photoprint or microfilm without written permission from the publisher

TERTIARY AND GENERAL-ORDER COLLISIONS (II)

L. M. DELVES †

Department of Physics and Laboratory for Nuclear Science, Massachusetts Institute of Technology, Cambridge, Massachusetts ††

Received 13 June 1960

Abstract: The basis introduced in a previous paper for describing collisions involving more than two free particles in ingoing or outgoing channels is discussed in more detail. With this formalism channel wavefunctions for many-particle channels are formally identical to the usual two-particle wavefunctions and require no special treatment. The scattering matrix referring to open channels is unitary and symmetric when many-particle channels are included; its symmetries in the complex k-plane are also discussed. Long-range effects in many-particle channels are considered, and it is shown that these can modify the threshold behaviour of matrix elements given previously. Effective range expansions, valid for many-particle channels, are given for the reactance matrix and eigenphaseshifts.

1. Introduction

In a previous paper [1]), hereafter referred to as (I), a representation was introduced for describing states of a system involving many free particles which had the advantage that the scattering matrix in such a representation is discrete. The paper (I) was chiefly concerned with deriving the threshold properties of reactions involving many-particle channels, and gave a discussion of the energy variation of observables such as cross-sections, polarization, and energy spectra at energies near that for a threshold in one or more such channels. We wish here to discuss this representation further. We first develop the formalism in somewhat greater detail than in (I), and show that the wavefunction for many-particle channels outside the interaction region can be written in a way which is formally identical to that for two-particle channels. Channels are labelled by the set of quantum numbers introduced in (I); however, the radial part of the channel wave function carries only one quantum number, the "order" of the channel. For two-particle channels this is the relative orbital angular momentum of the particles; for N-particle channels it is an integer or half integer according as N is even or odd, which plays the role of an angular momentum in determining such things as threshold properties and barrier heights, and the asymptotic form of the channel wavefunctions. It is defined in section 2.

† Permanent address: Clarendon Laboratory, Oxford, England

†† This work was performed during the tenure of a scholarship from the Shell Petroleum Company, and was supported in part through AEC Contract AT(30-1)-2098, by funds provided by the U. S. Atomic Energy Commission, the Office of Naval Research and the Air Force Office of Scientific Research.

The total channel wavefunction is a product of the radial wavefunction and a surface wavefunction. This surface wavefunction contains the intrinsic wavefunctions of all the particles in the channel, together with the various angle and spin functions, and is normalized to unity over the surface of the hypersphere; a systematic method of building up these surface functions is also discussed in section 2.

Section 3 deals with the scattering matrix in this representation. The usual properties of the submatrix referring to open channels (unitarity and symmetry) are maintained; symmetries in the complex plane are also discussed and differ slightly from those in the two-particle case due to the presence of half-integer channel orders (channels with an odd number of particles). Many-particle bound states can occur; the condition for these is given.

Section 4 deals with the behaviour of S near thresholds; the results of (I) are summarized, and limitations on the form of the interactions involved for them to be valid are given. For the case of two-particle scattering involving the rather long-range Van der Waals forces (such as e—H scattering), these conditions are violated for states with $l \geqq 1$, leading to a modified threshold behaviour for such states; for many-particle channels they may be violated in some states even when only short range two-particle forces are present, leading again to a modification of the threshold behaviour given in (I). This modification should be observable experimentally. For situations such that the conditions are not violated, effective range expansions are given for the reactance matrix K and eigenphaseshifts cot δ valid even for coupled many-particle channels.

2. Formalism

2.1. NOTATION

We must first introduce the basic notation we shall use; minor items will be defined as they are introduced.

We shall be concerned with *states* of a system of *bodies*; by body we shall mean an entity represented in the Schrödinger equation by three and only three space coordinates. It may have internal degrees of freedom such as spin. The system considered is then an M-body system satisfying a $3M$ dimensional non-relativistic Schrödinger equation in the laboratory system. Two or more of the bodies may form a bound state; we shall call such a bound subsystem a *particle* when it is one of the initial or final products of a reaction, and this word will also be used to describe single bodies in such circumstances. In general we shall find our attention focussed on the particles rather than the bodies as individuals.

Those regions of configuration space corresponding to a number of well-separated particles we call collectively the external region; a single such region corresponding to a given set of particles in a given state is called a channel. A channel is labelled by the set of quantum numbers describing the particles

in it and their relative motion: we shall use a single Greek letter ($\alpha, \beta, \gamma \ldots$) for this set. This description includes the number of particles in the channel and we speak in general of an N-particle channel when it contains N free particles. As an example consider the reaction

$$p+\mathrm{Be}^9 \to \alpha+\alpha+p+n; \to p+\mathrm{Be}^9.$$

The system is a 10-body system; the initial (entrance) channels are two-particle channels while the final (exit) channels contain either two or four particles. Note that the description $\alpha+\alpha+p+n$ covers many channels: we must also specify the state of relative motion of the various particles in the channel, and a prime purpose of this paper is to discuss in detail one convenient scheme for doing this.

Thus we wish to consider solutions Ψ of the wave equation

$$H\Psi = (T+V)\Psi = E\Psi, \tag{2.1}$$

where

$$T = -\sum_{i=1}^{M} \frac{\hbar^2}{2m_{\mathrm{b}i}} \nabla^2(\mathbf{r}_{\mathrm{b}i});$$

$\mathbf{r}_{\mathrm{b}i}$ is the position vector of the i^{th} body of mass $m_{\mathrm{b}i}$, and the centre-of-mass motion has not been factored out. In those parts of configuration space corresponding to an N-particle channel, which we label by a single suffix α, the solutions Ψ have the form

$$\Psi^{\alpha} = \psi_{\alpha}(F) \prod_{i=1}^{N} \psi_{\alpha i}(\mathrm{int}), \tag{2.2}$$

where $\psi_{\alpha i}(\mathrm{int})$ is the internal wave function of the i^{th} particle of channel α in its own centre-of-mass system and $\psi_{\alpha}(F)$ describes the motion of the centre of masses of the N particles. If the interaction between the particles is identically zero in these regions of space, $\psi_{\alpha}(F)$ obeys the N-body force-free Schrödinger equation

$$(T_{\alpha}-E_{\alpha})\psi_{\alpha}(F) = 0, \quad T_{\alpha} = -\sum_{i=1}^{N} \frac{\hbar^2}{2m_{\mathrm{p}i}} \nabla^2(\mathbf{r}_{\mathrm{p}i}), \tag{2.3}$$

where $m_{\mathrm{p}i}$ is the mass of the i^{th} particle, whose centre of mass has position vector $\mathbf{r}_{\mathrm{p}i}$. E_{α} is given in terms of the total energy E of (2.1) by

$$E_{\alpha} = E-\sum_{i=1}^{N} E_{i\alpha}, \tag{2.4}$$

where $E_{i\alpha}$ is the internal energy of the i^{th} particle in the channel; that is, the binding energy of the i^{th} particle is $-E_{i\alpha}$. We have not yet taken out the centre-of-mass motion; but if we assume that the centre of mass is at rest, we shall call E_{α} the *channel energy*. Note also that there are many independent solutions

of (2.3) so that the channel is not yet specified uniquely; however, all channels corresponding to a given set of particles have the same channel energy (for a given total energy). The problem of including many-particle channels is that of finding a convenient set of solutions of (2.3) in order to specify the channels in a useful manner. One such set was described in (I); we repeat the arguments here in order to give the formalism in more detail, and in such a way as to complete the analogy with two-particle channels. This section may therefore be read independently of (I). To introduce the method it is convenient first to recall the form of solution used to describe two-particle channels; we then discuss the methods used in (I) as applied to three-particle channels and later give the generalization to N-particles.

2.2. TWO-PARTICLE CHANNELS

We go over to the centre-of-mass system; that is, we write

$$\mathbf{r}_{\mathrm{cm}} = \frac{m_{\mathrm{p1}}\mathbf{r}_{\mathrm{p1}}+m_{\mathrm{p2}}\mathbf{r}_{\mathrm{p2}}}{m_{\mathrm{p1}}+m_{\mathrm{p2}}}, \quad \mathbf{r} = \mathbf{r}_{\mathrm{p1}}-\mathbf{r}_{\mathrm{p2}}, \quad \psi_\alpha(F) = \psi_{\mathrm{cm}}(\mathbf{r}_{\mathrm{cm}})R_\alpha(\mathbf{r}), \quad (2.5)$$

and obtain

$$\left[\frac{\hbar^2}{2\mu_\alpha}\nabla^2(\mathbf{r})+E_\alpha\right]R_\alpha(\mathbf{r}) = 0, \quad (2.6)$$

where we used the reduced mass $\mu_\alpha = m_{\mathrm{p1}}m_{\mathrm{p2}}/(m_{\mathrm{p1}}+m_{\mathrm{p2}})$.
The simplest set of solutions of (2.6) are the plane wave set

$$R_\alpha(\mathbf{r}) = \exp(\pm i\mathbf{k}_\alpha\cdot\mathbf{r}), \quad \hbar^2k_\alpha{}^2 = 2\mu_\alpha E_\alpha,$$

but these are not a denumerable set and do not, therefore, give a discrete scattering matrix; the standard procedure is to make a partial wave analysis and write

$$R_\alpha(\mathbf{r}) = R_\alpha(r)Y_l{}^m(\theta,\phi), \quad (2.7)$$

$$\left[\frac{1}{r^2}\frac{\partial}{\partial r}\left(r^2\frac{\partial}{\partial r}\right)-\frac{l_\alpha(l_\alpha+1)}{r^2}+k_\alpha{}^2\right]R_\alpha(r) = 0, \quad (2.8)$$

which has as a set of independent solutions

$$R_\alpha(r) = Ar^{-1}F_{l_\alpha}(k_\alpha r)+Br^{-1}G_{l_\alpha}(k_\alpha r),$$

where $F_l(kr)$, $G_l(kr)$ are the usual regular and irregular solutions satisfying equations of the type

$$\left[\frac{\mathrm{d}^2}{\mathrm{d}r^2}-\frac{l(l+1)}{r^2}+k^2\right]F = 0. \quad (2.9)$$

Their relevant properties are listed in the appendix. The asymptotic form of the

total wavefunction (2.2) for large r in channel α is then given by

$$\Psi^{\alpha} = \mu_{\alpha}^{\frac{1}{2}} k_{\alpha}^{-\frac{1}{2}} [A_{\alpha} F_{\alpha}(k_{\alpha} r) + B_{\alpha} G_{\alpha}(k_{\alpha} r)] r^{-1} Y_{l_{\alpha}}^{m_{\alpha}}(\theta, \phi) \psi_{\alpha 1}(\text{int}) \psi_{\alpha 2}(\text{int}), \quad (2.10)$$

where the normalization is the conventional one (see later). The internal wavefunctions of particles 1 and 2, $\psi_{\alpha 1}$ and $\psi_{\alpha 2}$, include the spins of the particles if any; so that (2.10) gives the asymptotic form in a completely decoupled representation, i.e. the channel α is characterized by a definition of particles 1 and 2 including their spins S_1 and S_2; the orbital angular momentum l and its Z-component $m = m_l$, and m_{s1}, m_{s2}, the Z-components of the two spins which are needed to complete the definitions of $\psi_{\alpha 1}$, $\psi_{\alpha 2}$. This is not usually the most convenient representation; we would generally use $\mathbf{J} = \mathbf{l} + \mathbf{s}_1 + \mathbf{s}_2$, $\mathbf{S} = \mathbf{s}_1 + \mathbf{s}_2$, l and $M = m_l + m_{s1} + m_{s2}$. However, the actual coupling scheme used is not of importance here; methods for coupling the various angular momentum and spin wavefunctions are well known.[2]) We note only that such recoupling affects only the part $r^{-1} Y_l^m(\theta, \phi) \psi_{\alpha 1}(\text{int}) \psi_{\alpha 2}(\text{int})$ of (2.10) since we assume that l is used as one of the quantum numbers; for an arbitrary coupling scheme, with this proviso, we can write (2.10) as

$$\Psi^{\alpha} = \mu_{\alpha}^{\frac{1}{2}} k_{\alpha}^{-\frac{1}{2}} [A_{\alpha} F_{\alpha} + \beta_{\alpha} G_{\alpha}] \phi_{\alpha}, \quad (2.10a)$$

where the ϕ_{α} contains the internal wave functions of the two particles, all the spin and angle functions, and the factor r^{-1}. With the internal wavefunctions and the various spin and orbital functions separately normalized in their own spaces, ϕ_{α} is normalized and orthogonal over the hypersurface at infinity; that is, writing the total volume element including spins as $d\tau = dr\, dS$ we have

$$\int \phi_{\alpha}^* \phi_{\beta} dS = \delta_{\alpha\beta} \quad (2.11)$$

for all two-particle channels α, β; and we shall see later that the orthogonality extends also to the many-particle channels. For channels containing the same particles 1 and 2 the orthogonality follows from that of the spin and angle functions; if the channels contain different particles, their internal wavefunctions have no overlap on the surface at infinity. We shall write (2.10a) for brevity as

$$\Psi^{\alpha} = R_{\alpha} \phi_{\alpha} \quad (2.10b)$$

and refer to R_{α} as the channel or radial function and ϕ_{α} as the surface wavefunction in channel α.

2.3. THREE-PARTICLE CHANNELS

We wish now to consider solutions of (2.3) with $N = 3$, and again it is a convenient time to go over into the centre-of-mass system; that is, we define a coordinate system $\mathbf{r}_1$, $\mathbf{r}_2$, $\mathbf{r}_{cm}$ where $\mathbf{r}_1$ is the radius vector from the centre of

mass of particle 1 to that of particle 2; $\mathbf{r}_2$ is the radius vector from the centre of mass of particle 3 to the combined centre of mass of particles 1 and 2:

$$\mathbf{r}_1 = \mathbf{r}_{p2} - \mathbf{r}_{p1}, \quad \mathbf{r}_2 = \mathbf{r}_{p3} - \frac{m_{p1}}{m_{p1}+m_{p2}}\mathbf{r}_{p1} - \frac{m_{p2}}{m_{p1}+m_{p2}}\mathbf{r}_{p2},$$

$$(m_{p1}+m_{p2}+m_{p3})\mathbf{r}_{cm} = m_{p1}\mathbf{r}_{p1}+m_{p2}\mathbf{r}_{p2}+m_{p3}\mathbf{r}_{p3}.$$

Then, writing $\psi_\alpha(F) = \psi_{cm}(\mathbf{r}_{cm})R_\alpha(\mathbf{r}_1, \mathbf{r}_2)$ we have

$$\left(\frac{\hbar^2}{2\mu_1}\nabla^2(\mathbf{r}_1) + \frac{\hbar^2}{2\mu_2}\nabla^2(\mathbf{r}_2) + E_\alpha\right) R_\alpha(\mathbf{r}_1, \mathbf{r}_2) = 0, \tag{2.12}$$

where the reduced masses are given by

$$\mu_1 = m_{p1}m_{p2}/(m_{p1}+m_{p2}), \quad \mu_2 = m_{p3}(m_{p1}+m_{p2})/(m_{p1}+m_{p2}+m_{p3}).$$

As discussed in (I) we look for a set of solutions of (2.12) which is denumerable. This condition is imposed because we wish the scattering matrix to be discrete, and rules out the use of a plane wave set such as

$$R(\mathbf{r}_1, \mathbf{r}_2) = \exp(\pm i\mathbf{k}_1 \cdot \mathbf{r}_1 \pm i(\mathbf{k}_2 \cdot \mathbf{r}_2)), \quad \frac{\hbar^2 k_1^2}{2\mu_1} + \frac{\hbar^2 k_2^2}{2\mu_2} = E_\alpha.$$

Instead, as in the two-particle case, we take out first the angular parts of $\mathbf{r}_1 = (r_1, \Omega_1)$ and $\mathbf{r}_2 = (r_2, \Omega_2)$ and write

$$R(\mathbf{r}_1, \mathbf{r}_2) = R(r_1, r_2)Y_1(\Omega_1)Y_2(\Omega_2)$$

with

$$\left[\frac{\hbar^2}{2\mu_1 r_1^2}\frac{\partial}{\partial r_1}\left(r_1^2\frac{\partial}{\partial r_1}\right) + \frac{\hbar^2}{2\mu_2 r_2^2}\frac{\partial}{\partial r_2}\left(r_2^2\frac{\partial}{\partial r_2}\right) - \frac{\hbar^2 l_1(l_1+1)}{2\mu_1 r_1^2} - \frac{\hbar^2 l_2(l_2+1)}{2\mu_2 r_2^2} + E_\alpha\right] \times R(r_1, r_2) = 0. \tag{2.13}$$

Again, the obvious extension of the two-particle case is got by writing

$$R(r_1, r_2) = \frac{R_{l_1}(k_1 r_1)R_{l_2}(k_2 r_2)}{r_1 r_2}, \quad \frac{\hbar^2 k_1^2}{2\mu_1} + \frac{\hbar^2 k_2^2}{2\mu_2} = E_\alpha,$$

where $R_l(kr)$ obeys (2.9); and again, this is not a convenient set of solutions because of the continuous range of k_1, k_2. We can find a denumerable set of solutions of (2.13) by making a further change of variable: write

$$r_1 = \left(\frac{m}{\mu_1}\right)^{\frac{1}{2}} r \sin\alpha, \quad r_2 = \left(\frac{m}{\mu_2}\right)^{\frac{1}{2}} r \cos\alpha, \tag{2.14}$$

where m is some standard mass which may be chosen arbitrarily. The physical significance of the angle α and the eigenfunctions belonging to it are discussed

later. In terms of r, α (2.13) becomes [3])

$$\left[\frac{1}{r^5}\frac{\partial}{\partial r}\left(r^5\frac{\partial}{\partial r}\right)+\frac{1}{r^2\sin^2\alpha\cos^2\alpha}\frac{\partial}{\partial\alpha}\left(\sin^2\alpha\cos^2\alpha\frac{\partial}{\partial\alpha}\right)\right.$$
$$\left.-\frac{l_1(l_1+1)}{r^2\sin^2\alpha}-\frac{l_2(l_2+1)}{r^2\cos^2\alpha}+k^2\right]R(r,\alpha)=0,\quad \hbar^2k^2=2mE_a. \tag{2.15}$$

The volume element $\mathrm{d}\mathbf{r}_1\mathrm{d}\mathbf{r}_2$ in these coordinates is

$$\mathrm{d}\mathbf{r}_1\mathrm{d}\mathbf{r}_2=m^3(\mu_1\mu_2)^{-\frac{3}{2}}r^5\sin^2\alpha\cos^2\alpha\sin\theta_1\sin\theta_2\mathrm{d}\theta_1\mathrm{d}\theta_2\mathrm{d}\phi_1\mathrm{d}\phi_2\mathrm{d}r\mathrm{d}\alpha \tag{2.16}$$

and it is convenient to choose m so that $\mu_1\mu_2=m^2$. Eq. (2.15) can be separated; if we write

$$R(r,\alpha)=r^{-\frac{5}{2}}\sin^{-1}\alpha\cos^{-1}\alpha Y(\alpha)R(r), \tag{2.17}$$

we obtain for the α equation

$$\left[\frac{\mathrm{d}^2}{\mathrm{d}\alpha^2}+4-\frac{l_1(l_1+1)}{\sin^2\alpha}-\frac{l_2(l_2+1)}{\cos^2\alpha}\right]Y(\alpha)=-BY(\alpha) \tag{2.18}$$

and the solutions regular at $\alpha=0,\frac{1}{2}\pi$ are

$$B=(l_1+l_2+\lambda)(l_1+l_2+2\lambda+4)$$

$$Y(l_1,l_2,\lambda;\alpha)=A\sin^{l_1+1}\alpha\cos^{l_2+1}\alpha\ {}_2F_1(-\lambda,l_1+l_2+\lambda+2;l_1+\tfrac{3}{2};\sin^2\alpha), \tag{2.19}$$

where A is a normalizing constant and $\lambda=0,1,2\ldots$.

The $Y(l_1,l_2,\lambda;\alpha)$ are orthogonal in λ between 0 and $\frac{1}{2}\pi$ with unit weight, and we take them normalized:

$$\int_0^{\frac{1}{2}\pi}Y(l_1,l_2,\lambda_1;\alpha)Y(l_1,l_2,\lambda_2;\alpha)\mathrm{d}\alpha=\delta_{\lambda_1\lambda_2}.$$

The normalizing constant and other properties of these functions are given in the appendix. The equation for $R(r)$ is, for this choice of separation constant B,

$$\left(\frac{\mathrm{d}^2}{\mathrm{d}r^2}-\frac{l(l+1)}{r^2}+k^2\right)R(r)=0, \tag{2.20}$$

where

$$l=l_1+l_2+2\lambda+\tfrac{3}{2}. \tag{2.21}$$

This has exactly the same form as that for the two-particle channel functions, (2.9), with the (half-integral) $l_1+l_2+2\lambda+\frac{3}{2}$ playing the part of the orbital angular momentum; and the solutions have exactly the same form (A3). We can therefore write the asymptotic form of the total wavefunction (2.2) along a

3-particle channel α, in the completely decoupled representation, as

$$\Psi^{\alpha} = m_{\alpha}^{\frac{1}{2}} k_{\alpha}^{-\frac{1}{2}} [A_{\alpha} F_{\alpha} + B_{\alpha} G_{\alpha}] \times \frac{Y_{l_1}^{m_1}(\Omega_1) Y_{l_2}^{m_2}(\Omega_2) Y(l_1, l_2, \lambda; \alpha) \psi_{\alpha 1}(\text{int}) \psi_{\alpha 2}(\text{int}) \psi_{\alpha 3}(\text{int})}{r^{\frac{5}{2}} \sin\alpha \cos\alpha}, \quad (2.22)$$

where again the ψ_{α} (int) are the internal wavefunctions of the channel particles. The reason for the choice of normalization of (2.22), that is the factor $m_{\alpha}^{\frac{1}{2}} k_{\alpha}^{-\frac{1}{2}}$, is the same as for the two-particle channels and is discussed in section 3. As for the two-particle channels, (2.22) can be written in the form (2.10a), where the surface function is now

$$\phi_{\alpha} = Y_{l_1}^{m_1}(\Omega_1) Y_{l_2}^{m_2}(\Omega_2) Y(l_1, l_2, \lambda; \alpha) \psi_{\alpha 1} \psi_{\alpha 2} \psi_{\alpha 3} r^{-\frac{5}{2}} \sin^{-1}\alpha \cos^{-1}\alpha \quad (2.23)$$

and satisfies the orthonormality condition (2.11) over the surface at infinity, with respect to both 2- and 3-particle channels. This result is again independent of the coupling scheme used to couple together l_1, l_2, the spins of the particles, and λ, provided that $l = l_1 + l_2 + 2\lambda + \frac{3}{2}$ is used as one quantum number.

We have thus shown that it is possible to write the asymptotic form of the total wavefunction along three-particle channels in a way which is formally identical with that for two-particle channels. This convenient result arises from two causes. Firstly, we chose a discrete basis for the three-body channels; this is the most important step. Secondly, we factored out the quantity $r^{\frac{5}{2}} \sin\alpha \cos\alpha$ from the wavefunction. The removal of this factor put the radial part of the wave equation into the same form as for the two-particle channels, and at the same time gave the orthonormality of the surface wavefunctions over the hypersurface at infinity. Strictly speaking, both these results require the factoring out only of $r^{-\frac{5}{2}}$; the definition of the $Y(l_1 l_2, \lambda; \alpha)$ would then include the extra $\sin^{-1}\alpha \cos^{-1}\alpha$ and they would be orthonormal with weight function $\sin^2\alpha \cos^2\alpha$. The $\sin^{-1}\alpha \cos^{-1}\alpha$ was taken out to make the transition to many-particle channels straightforward; note in this respect that the same result would have been obtained had we first factored out $(r_1 r_2)^{-1}$ from (2.13), and then a further $r^{-\frac{1}{2}}$.

It is convenient to have a name for the quantity $l = l_1 + l_2 + 2\lambda + \frac{3}{2}$ which replaces the orbital angular momentum of two-particle channels. It can without ambiguity be called the channel angular momentum, but in case this should cause confusion we shall call it here the *channel order*. This nomenclature has some justification in that it was shown in (I) that this quantity determines the threshold properties of the channel.

2.4. *N*-PARTICLE CHANNELS

It is now a simple matter to extend the formalism to cover N-particle channels. The function $\psi_{\alpha}(F)$ for an N-body channel satisfies (2.3) in the laboratory system; there are, however, many ways of choosing centre of mass coordinates.

One systematic way is to choose as coordinates the radius vector between the centre of masses of particles 1 and 2; the radius vector between the centre of mass of particle 3 and the combined centre of mass of 1 and 2; and so on for the N particles, the i^{th} radius vector $\mathbf{x}_i$ chosen being that between the centre of mass of particle $i+1$ and the combined centre of mass of particles $1 \ldots i$. Then writing $\psi(F) = \psi_{\text{cm}} R(\mathbf{x}_1 \ldots \mathbf{x}_{N-1})$ we have

$$\left[\sum_{i=1}^{N-1} \frac{\hbar^2}{2\mu_i} \nabla^2(\mathbf{x}_i) + E_\alpha\right] R(\mathbf{x}_1 \ldots \mathbf{x}_{N-1}) = 0, \tag{2.24}$$

where the i^{th} reduced mass is

$$\mu_i = m_{\text{p}(i+1)} \left[\sum_{j=1}^{i} m_{\text{p}j}\right] \Big/ \sum_{j=1}^{i+1} m_{\text{p}j}.$$

Such coordinates have been used before [1, 4]; apart from the arbitrary order in which the particles are numbered, this is by no means the only possible set giving an equation of the form (2.24) for R. This set groups the particles together successively in one increasing cluster; however, such a cluster can be stopped at any stage and another started with other particles in the same way, final coordinates being the radius vector joining the centre of masses of the built-up clusters. In each case, the reduced mass associated with the radius vector joining the centre of masses of two clusters of total masses m_1, m_2 is $\mu = m_1 m_2/(m_1+m_2)$ exactly as if the clusters were single bodies; and the resulting equation is of the form (2.24). This result, which is of course also the basis for separating out the internal wavefunctions of the separate particles in the channel region to give (2.2) and (2.3), is trivially proved by induction. Fig. 1 gives two possible coupling schemes for the radius vectors to give a C.M. coordinate system for a 6-particle system where the particles all have equal mass.

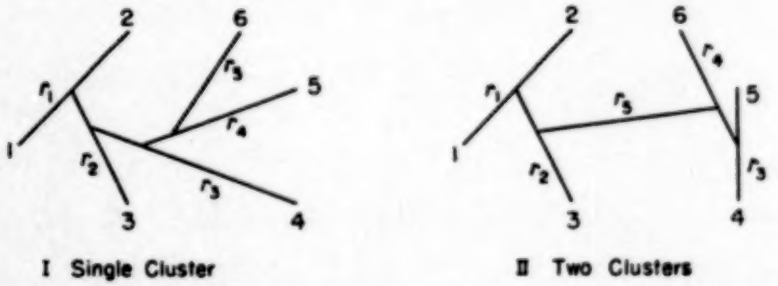

Fig. 1. Two possible sets of C.M. coordinates for a 6-particle system.

I. Particles successively coupled in a single cluster.

II. Two clusters formed from particles (1, 2, 3) and (4, 5, 6), followed by coupling of the clusters.

This lack of uniqueness of the coordinate system occurs even for three particles, when we arbitrarily labelled the particles 1, 2, and 3; however, we shall be finally left with one radial coordinate r, which will be independent of

the particular coordinate system chosen; the arbitrariness is then contained in the choice of angular variables; that is, in the surface wavefunctions for the channel.

The occurrence in (2.24) of different reduced masses μ_i is a nuisance; they were eliminated in the three-particle case by the transformation (2.14), and we again eliminate them here by a scale change. We write in (2.24)

$$\mathbf{x}_i = \left(\frac{m}{\mu_i}\right)^{\frac{1}{2}} \mathbf{r}_i, \quad (m)^{N-1} = \prod_{i=1}^{N-1} \mu_i = \prod_{i=1}^{N} m_{pi} \Big/ \sum_{i=1}^{N} m_{pi} \tag{2.24a}$$

and we obtain for (2.24)

$$\left[\sum_{i=1}^{N-1} \nabla^2(\mathbf{r}_i) + k^2\right] R(\mathbf{r}_1 \cdots \mathbf{r}_{N-1}) = 0, \quad \hbar^2 k^2 = 2mE_\alpha. \tag{2.24b}$$

The choice of m is of course arbitrary; however, it is convenient to define it in such a way as to leave the volume element unchanged,

$$d\tau = \prod_{i=1}^{N-1} d\mathbf{x}_i = \prod_{i=1}^{N-1} d\mathbf{r}_i,$$

and this is what we have done.

Now to find a suitable discrete set of solutions of (2.24b) we first take out the angular parts of $\mathbf{r}_1 \ldots \mathbf{r}_{N-1}$, and at the same time a factor r_i^{-1} for each i; that is, we write

$$R_\alpha(\mathbf{r}_1 \ldots \mathbf{r}_{N-1}) = R_\alpha(r_1 \ldots r_{N-1}) \prod_{i=1}^{N-1} r_i^{-1} Y_i(\Omega_i), \tag{2.25}$$

where we write for brevity (as elsewhere) $Y_{l_i}^{m_i}(\Omega_i) = Y_i(\Omega_i)$. We obtain

$$\left[\sum_{i=1}^{N-1} \left(\frac{\partial^2}{\partial r_i^2} - \frac{l_i(l_i+1)}{r_i^2}\right) + k_\alpha^2\right] R_\alpha(r_1 \ldots r_{N-1}) = 0. \tag{2.26}$$

We now treat the coordinates r_i two at a time as for the three-body case; that is, we write first

$$\begin{aligned} r_1 &= r^{(1)} \sin \alpha_1, \quad r_2 = r^{(1)} \cos \alpha_1, \\ R_\alpha(r_1 \ldots r_{N-1}) &= [r^{(1)}]^{-\frac{1}{2}} Y(l_1, l_2, \lambda_1; \alpha_1) R_\alpha(r^{(1)}; r_3 \ldots r_{N-1}), \end{aligned} \tag{2.27}$$

and obtain

$$\left\{\left[\frac{\partial^2}{\partial [r^{(1)}]^2} - \frac{l^{(1)}(l^{(1)}+1)}{[r^{(1)}]^2}\right] + \sum_{i=3}^{N-1} \left(\frac{\partial^2}{\partial r_i^2} - \frac{l_i(l_i+1)}{r_i^2}\right) + k_\alpha^2\right\} R_\alpha(r^{(1)}; r_3 \ldots r_{N-1}) = 0, \tag{2.28}$$

where $l^{(1)} = l_1 + l_2 + 2\lambda_1 + \frac{3}{2}$.

Eq. (2.28) has exactly the same form as (2.26), but with one fewer variable; we can therefore repeat the process, replacing at the j^{th} stage two (any two) radial variables by a single radial variable $r^{(j)}$ and an angular variable α_j with an angular wave function of the form (2.19), with quantum numbers depending on the order in which we couple the radial coordinates. If for definiteness we carry out the coupling from left to right in the arguments of $R(r_1 \ldots r_{N-1})$ then the j^{th} angular function is $Y(l^{(j)}, l_{j+1}, \lambda_j; \alpha_j)$, where

$$r^{(j-1)} = r^{(j)} \sin \alpha_j, \quad r_{j+1} = r^{(j)} \cos \alpha_j,$$
$$l^{(j)} = \sum_{i=1}^{j+1} l_i + 2 \sum_{i=1}^{j} \lambda_i + \tfrac{3}{2} j. \tag{2.29}$$

The process continues until we have only a single radial variable $r \equiv r^{(N-2)}$ with wavefunction $R_\alpha(r)$ satisfying

$$\left[\frac{\mathrm{d}^2}{\mathrm{d}r^2} - \frac{l_\alpha(l_\alpha+1)}{r^2} + k_\alpha^2\right] R_\alpha(r) = 0,$$

where

$$l_\alpha \equiv l^{(N-2)} = \sum_{i=1}^{N-1} l_i + 2 \sum_{i=1}^{N-2} \lambda_i + \tfrac{3}{2}(N-2). \tag{2.30}$$

The quantum number l_α is the N-particle equivalent of the orbital angular momentum; as for the three-particle channels we shall refer to it as the channel order. It is integral for N even, and half integral for N odd.

We have, altogether, then

$$R_\alpha(\mathbf{r}_1 \ldots \mathbf{r}_{N-1}) = R_\alpha(r) \prod_{i=1}^{N-2} [[r^{(i)}]^{-\frac{1}{2}} Y(l^{(i)}, l_{i+1}, \lambda_i; \alpha_i)] \prod_{i=1}^{N-1} r_i^{-1} Y_i(\Omega_i). \tag{2.31}$$

We may write, in terms of r and α_i,

$$\prod_{i=1}^{N-1} (r_i) = r^{N-1} \prod_{i=1}^{N-2} \sin \alpha_i \cos \alpha_i, \quad \prod_{i=1}^{N-2} (r^{(i)}) = r^{N-2} \prod_{i=2}^{N-2} \sin^{(i-1)} \alpha_i, \tag{2.32}$$

so that (2.31) becomes

$$R_\alpha(\mathbf{r}_1 - \mathbf{r}_{N-1}) = R_\alpha(r) r^{\frac{1}{2}(4-3N)} \prod_{i=1}^{N-1} Y_i(\Omega_i)$$
$$\times \prod_{i=1}^{N-2} [Y(l^{(i)}, l_{i+1}, \lambda_i; \alpha_i) \sin^{-1} \alpha_i \cos^{-1} \alpha_i] \prod_{i=2}^{N-2} [\sin^{(1-i)} \alpha_i]^{\frac{1}{2}}. \tag{2.33}$$

The volume element is

$$\mathrm{d}\mathbf{r}_1 \ldots \mathrm{d}\mathbf{r}_{N-1} = r^{3N-4} \mathrm{d}r \prod_{i=1}^{N-2} \sin^2 \alpha_i \cos^2 \alpha_i \mathrm{d}\alpha_i \prod_{i=2}^{N-2} \sin^{(i-1)} \alpha_i \prod_{i=1}^{N-1} \sin \theta_i \, \mathrm{d}\theta_i \, \mathrm{d}\phi_i. \tag{2.34}$$

The complication of these formulae is more apparent than real; the weight

function in the volume element cancels the same factor in the square of the wave function so that for most purposes we can consider the wavefunction to be

$$R_a(\mathbf{r}_1 \ldots \mathbf{r}_{N-1}) = R_a(r) \prod_{i=1}^{N-1} Y_i(\Omega_i) \prod_{i=1}^{N-2} Y(l^{(i)}, l_{i+1}, \lambda_i; \alpha_i)$$

and the volume element

$$\mathrm{d}r \prod_{i=1}^{N-2} \mathrm{d}\alpha_i \prod_{i=1}^{N-1} \mathrm{d}\Omega_i.$$

This was one of the reasons for taking out such factors; the other, related, reason is that had we not done so the definition of the $Y(l_1, l_2, \lambda; \alpha)$ would have depended on the number of particles in the channel.

With this basis for the N-particle channels it is possible to write down the channel wavefunction for an arbitrary channel at sight; this is obviously very convenient. Moreover, we have now in the general case a split of the asymptotic form of the total state wavefunction, Ψ^γ, along an N-particle channel γ, into a radial and a normalized surface wavefunction exactly as in (2.10a) with the F_l, G_l obeying (2.9) for integral or half integral channel order l, and the surface function being, in the uncoupled scheme we have given,

$$\phi_\gamma = r^{\frac{1}{2}(4-3N)} \prod_{i=1}^{N-1} Y_i(\Omega_i) \prod_{i=1}^{N-2} Y(l^{(i)}, l_{i+1}, \lambda_i; \alpha_i) \times \sin^{-1}\alpha_i \cos^{-1}\alpha_i \prod_{i=2}^{N-2} [\sin^{(1-i)}\alpha_i]^{\frac{1}{2}} \prod_{i=1}^{N} \psi_{\gamma i}(\mathrm{int}). \quad (2.35)$$

All the quantum numbers in (2.35) of course carry a suffix γ depending on the channel. These surface wavefunctions obey the orthonormality conditions (2.11) between all channels α, β and as usual the form of the results is unchanged if a set of surface functions differing in the coupling of the various l's is used, provided that the channel order is retained.

The surface wavefunctions depend not only on the coupling scheme used to recouple the various angular momentum functions $Y_i(\Omega_i)$ and spins, but on the set of C.M. coordinates $\mathbf{x}_i$ originally chosen in (2.24), that is on the renormalized $\mathbf{r}_i$ of (2.24b), and further on the order in which the r_i are coupled together to define the α_i through (2.27). However, the radial variable r is independent of these choices; we have

$$r^2 = \sum_{i=1}^{N-1} r_i^2 = \frac{1}{m} \sum_{i=1}^{N-1} \mu_i x_i^2 = \frac{1}{m} \sum_{i=1}^{N} m_{\mathrm{p}i} r_{0i}^2, \quad (2.36)$$

where $\mathbf{r}_{0i}$ is the vector from the centre of mass of particle i to the centre of mass of the whole system.

With this formalism we have a complete analogy between the channel wave functions for two and many particle channels, so that most results which are

generally proved for two-particle channels go through unchanged also when many-particle channels are included (slight modifications sometimes arise from the possibility of half-integer channel orders). One such result is the discussion of threshold effects given in (I); others, given in later sections of this paper, are the symmetry properties of the scattering matrix S, effective range expansions of S, and a discussion of the effect of long-range potentials.

3. The Scattering Matrix and the N-Particle Current Operator

3.1. DEFINITION OF S AND S^{++}

The scattering matrix S is defined by the asymptotic form of the state function Ψ when this is written not in terms of the "standing waves" F and G as in (2.10a) but in terms of "ingoing" and "outgoing" waves I and O (see appendix A2):

$$\Psi^\gamma = m_\gamma^{\frac{1}{4}} k_\gamma^{-\frac{1}{2}} [A_\gamma I_\gamma - B_\gamma O_\gamma] \phi_\gamma, \tag{3.1}$$

$$B = SA. \tag{3.2}$$

Formally, S has elements referring to closed channels (for which k^2 is negative, k imaginary) as well as open; however, we shall usually be concerned only with the submatrix S^{++} referring to open channels. In fact, except in this section this will always be the case in this paper unless explicitly noted, and in other sections the superfix on S^{++} will be dropped and the reference to open channels only tacitly understood. When this is the case the closed channels are implicitly taken care of by the boundary conditions (no incoming waves in closed channels; see (A5)). When only two-particle channels are considered, the terms "ingoing" and "outgoing" waves for I and O are justified by calculating the current carried by the wavefunctions $I_\gamma \phi_\gamma, O_\gamma \phi_\gamma$; the normalization factor $m^{\frac{1}{4}} k^{-\frac{1}{2}}$ is then inserted either to normalize the basic solutions to unit flux (apart from a constant factor $\hbar$) or, equivalently, to make the scattering matrix S unitary. For many-particle channels the same reasons hold: I and O still represent ingoing and outgoing waves, and the normalization written down to keep the analogy with the two-particle functions complete ensures the unitarity of S.

The usual one-body particle-current operator is

$$\mathbf{J} = \frac{\hbar}{2mi} (\psi^* \nabla \psi - \psi \nabla \psi^*)$$

and we shall assume [5]) that the same form holds also for an M-body wavefunction,

$$\mathbf{J} = \frac{\hbar}{2i} \left(\psi^* \frac{\nabla}{m} \psi - \psi \frac{\nabla}{m} \psi^* \right), \tag{3.3}$$

∇/m denoting the $3M$ dimensional vector operator with components

$$\frac{1}{m_1}\frac{\partial}{\partial x_1}, \ldots \frac{1}{m_M}\frac{\partial}{\partial z_M}.$$

Equivalently we can write the mass current operator $\mathbf{J}_M$ as

$$\mathbf{J}_M = \frac{\hbar}{2i}(\psi^*\nabla\psi - \psi\nabla\psi^*). \tag{3.4}$$

If we operate with $\mathbf{J}_M$ on the "outgoing" part of (3.1) and integrate over the surface at infinity, we have

$$\int \mathbf{J}_M m^{\frac{1}{2}} k^{-\frac{1}{2}} BO\phi \mathrm{d}S = \frac{\hbar}{2i}\frac{m}{k} BB^* \left[O^* \frac{\mathrm{d}O}{\mathrm{d}r} - O\frac{\mathrm{d}O^*}{\mathrm{d}r}\right]_{r=\infty}$$
$$= \begin{cases} \hbar m BB^* & (k \text{ real}), \\ 0 & (k \text{ imaginary}), \end{cases} \tag{3.5}$$

where all the other terms involving derivatives of the surface function have disappeared as in the two-particle case, and we have used the asymptotic form of eq. (A5) for O. Similarly, for the particle current operator $\mathbf{J}$ we have

$$\int \mathbf{J}\left(\frac{m}{k}\right)^{\frac{1}{2}} BO\phi \mathrm{d}S = \begin{cases} \hbar BB^* & (k \text{ real}), \\ 0 & (k \text{ imaginary}). \end{cases} \tag{3.6}$$

This is in complete agreement with the usual two-particle result, and implies immediately (see, e.g., ref. [6])) that the submatrix of S referring to open channels only, S^{++}, is unitary. We note in passing that although the operator $\mathbf{J}$ acts on the individual bodies, it is the flux of particles which is given by (3.6); that is, $\hbar B_\gamma B_\gamma^*$ is the number of groups of N particles emitted per second in channel γ. This is of course due to the normalization of the surface wavefunctions to 1 rather than to N as would be done if attention were focussed on the bodies.

3.2. PROPERTIES OF THE SCATTERING MATRIX

The symmetry properties of the total scattering matrix S and the submatrix S^{++} referring to open channels only have been summarized by Lane and Thomas [6]) in the two-particle case. We give them here for the general case; the proofs, which we omit, are exactly as in Lane and Thomas apart from the occurrence of extra phase factors in places due to the possibility of half integral channel orders. Note that our set of wavefunctions I^-, O^- for negative energies is the analytic continuation of the set I^+, O^+ for positive energies and differs by a phase from that used by Lane and Thomas.

3.2.1. *Unitarity*

The matrix S^{++} is unitary

$$S^{++}(S^{++})^{*\mathrm{T}} = 1. \tag{3.7}$$

This property is independent of the coupling scheme used to define the surface functions; it depends only on the orthonormality of these functions and on the Wronskian (A7).

3.2.2. *Symmetry*

We obtain a further relation between S and S^{T} by considering the properties of Ψ under time reversal; however, these properties do depend on the coupling scheme used for the surface functions. For definiteness we assume one such scheme; that is, one in which all the angular momenta and spins are coupled (in any order) to give a surface function with a sharp total angular momentum J, z-component M, as in eq. (A25). Whether the generalized angular functions $Y(a, b, c; d)$ are recoupled in any way or not is immaterial, since these functions are real. We thus assume the surface functions to have the following behaviour under time reversal T:

$$\mathrm{T}\phi(J, M, \gamma) = (-1)^{J-M}\phi(J, -M, \gamma). \tag{3.8}$$

Then with the properties of O and I under T given by (A9), the arguments of Lane and Thomas can be carried through to give

$$S^{++}(S^{++})^* = 1, \quad (S^{-+})(S^{++})^* = -(S^{-+})^*, \tag{3.9}$$

and using (3.7)

$$S^{++} = (S^{++})^{\mathrm{T}}, \tag{3.10}$$

that is, S^{++} is symmetric.

3.2.3. *Properties in the complex plane*

Considering S as a function $S(k)$ of the channel wavenumbers k it is possible to find symmetry relations for $S(k)$ for complex k. These depend only on the symmetry properties of I and O under $k \to k^*$, $k \to -k$, since the surface functions do not involve k; these properties are

$$\begin{aligned} I_l(k^*) &= O_l^*(k), & I_l(-k) &= \mathrm{e}^{il\pi}O_l(k), \\ O_l(k^*) &= I_l^*(k), & O_l(-k) &= \mathrm{e}^{-il\pi}I_l(k), \end{aligned} \tag{3.11}$$

and using these we follow Lane and Thomas to obtain

$$S(k)[S(k^*)]^{*\mathrm{T}} = 1, \quad S(k)[S(k^*)]^* = 1, \tag{3.12}$$

and therefore

$$S(k)[S(k)^{\mathrm{T}}]^{-1} = 1, \tag{3.13}$$

so that not only S^{++} but also S is symmetric. We also find

$$e^{il\pi}S(-k)e^{2il\pi}S(k)e^{il\pi} = 1, \tag{3.14}$$

which for two-particle channels only (l integral) reduces to

$$S(-k)S(k) = 1.$$

From (3.14) and (3.12) we find

$$e^{2il\pi}S(-k)e^{2il\pi} = [S(k^*)]^*. \tag{3.15}$$

Eqs. (3.7), (3.10), (3.12), (3.13) are identical with the forms given by Lane and Thomas for two-particle channels; (3.14) and (3.15) differ by phase factors which reduce to 1 for two-particle channels.

3.3. DIAGONALIZATION OF S AND SOME ASSOCIATED MATRICES

Since S^{++} is symmetric and unitary, it can be diagonalized by a real orthogonal matrix; we write

$$S^{++} = T^{\mathrm{T}}e^{2i\delta}T, \quad T^{\mathrm{T}}T = 1, \tag{3.16}$$

where T and δ are both real.

It is sometimes convenient to include some or all closed channels in such a diagonalization. Since the total S-matrix S is symmetric, we can diagonalize a (square) submatrix S_{b} referring to any number of channels by an orthogonal matrix T_{b}:

$$S_{\mathrm{b}} = T_{\mathrm{b}}{}^{\mathrm{T}} \exp(2i\,\delta_{\mathrm{b}})T_{\mathrm{b}}, \quad T_{\mathrm{b}}{}^{\mathrm{T}}T_{\mathrm{b}} = 1. \tag{3.17}$$

In general, T_{b} and δ_{b} are not real.

It is not always convenient to work with S; we define two further matrices, the reaction matrix

$$R = 1-S,$$

and the matrix K which arises naturally from the choice of asymptotic form for a state wavefunction Ψ in channel γ (see eq. (2.10a)),

$$\Psi^{\gamma} = m_{\gamma}{}^{\frac{1}{2}}k_{\gamma}{}^{-\frac{1}{2}}[A_{\gamma}F_{\gamma}+B_{\gamma}G_{\gamma}]\phi_{\gamma}.$$

K is defined by $B = KA$ and is often called, somewhat confusingly in this field, the reactance matrix. It is related to S by

$$K = i\frac{1-S}{1+S}. \tag{3.18}$$

K^{++} can be diagonalized by the same matrix T which diagonalizes S^{++}:

$$K^{++} = T^{\mathrm{T}} \tan\,\delta T. \tag{3.19}$$

4. Discussion of the Formalism

4.1. THE ENERGY SPECTRUM OF THE EMITTED PARTICLES

So far we have shown that by using a suitable set of hyperspherical coordinates, N-particle channels can be treated in a completely equivalent manner to the two-particle channels. These coordinates involve the introduction of a set of "unphysical" angles, the α_i of (2.35); however, these angles and their eigenfunctions $Y(l_1, l_2, \lambda; \alpha_i)$ are directly related to a physical quantity of definite interest, the way in which the available energy is shared among the particles. To see this, it is convenient to consider the three-particle channels, for which there is only one such angle. Then labelling the particles 1, 2, 3, with the coordinates of paragraph 1, an outgoing wave in the three-particle channel defined by angular momenta $l_1 m_1$, $l_2 m_2$, and generalized angular momentum λ has the form

$$\psi = \left(\frac{m}{\hbar k}\right)^{\frac{1}{2}} r^{-\frac{1}{2}} \sin^{-1}\alpha \cos^{-1}\alpha O_i(kr)$$
$$Y_{l_1}^{m_1}(\Omega_1) Y_{l_2}^{m_2}(\Omega_2) Y(l_1, l_2, \lambda; \alpha) \psi_1(\text{int}) \psi_2(\text{int}) \psi_3(\text{int}). \quad (4.1)$$

This is normalized to unit flux over the whole surface at infinity; the three-particle flux into a given element of that surface

$$\mathrm{d}S = r^5 \sin^2\alpha \cos^2\alpha \sin\theta_1 \sin\theta_2 \,\mathrm{d}\theta_1 \,\mathrm{d}\theta_2 \,\mathrm{d}\phi_1 \,\mathrm{d}\phi_2 \,\mathrm{d}\alpha$$

is

$$|Y_1(\Omega_1) Y_2(\Omega_2) Y(l_1, l_2, \lambda; \alpha)|^2 \sin\theta_1 \sin\theta_2 \,\mathrm{d}\theta_1 \,\mathrm{d}\theta_2 \,\mathrm{d}\phi_1 \,\mathrm{d}\phi_2 \,\mathrm{d}\alpha,$$

or, if we integrate over Ω_1, Ω_2, the number of sets of particles per second emitted between α and $\alpha + \mathrm{d}\alpha$ is

$$|Y(l_1, l_2, \lambda; \alpha)|^2 \mathrm{d}\alpha.$$

The physical meaning of this is clear from the definition of α; we have from (2.14)

$$\tan\alpha = \left(\frac{\mu_2}{\mu_1}\right)^{\frac{1}{2}} \frac{r_1}{r_2}.$$

Now if particles 1 and 2 are emitted with relative velocity v_1, and particle 3 with velocity v_2 relative to the centre of mass of 1 and 2, then a measurement (at infinity) of r_1/r_2 will give

$$r_1/r_2 = v_1/v_2, \quad \tan\alpha = \mu_2^{\frac{1}{2}} v_1/(\mu_1^{\frac{1}{2}} v_2), \quad (4.2)$$

so that the distribution in α measures the distribution of energy between the three particles. We can convert the relations (4.2) into more convenient ones involving the centre of mass energies E_1, E_2, E_3 of 1, 2, 3. For a given total

channel energy E only one of these is independent. We find

$$\frac{E_1}{E}=\left[\frac{m_2}{m_1+m_2}\sin^2\alpha+\frac{m_1m_3\cos^2\alpha}{(m_1+m_2)(m_1+m_2+m_3)}-\frac{(m_1m_2m_3)^{\frac{1}{2}}\cos\alpha\sin\alpha\cos\theta_{12,3}}{(m_1+m_2)(m_1+m_2+m_3)^{\frac{1}{2}}}\right],$$

$$\frac{E_2}{E}=\left[\frac{m_1}{m_1+m_2}\sin^2\alpha+\frac{m_2m_3\cos^2\alpha}{(m_1+m_2)(m_1+m_2+m_3)}+\frac{(m_1m_2m_3)^{\frac{1}{2}}\cos\alpha\sin\alpha\cos\theta_{12,3}}{(m_1+m_2)(m_1+m_2+m_3)^{\frac{1}{2}}}\right], \tag{4.3}$$

$$\frac{E_3}{E}=\frac{m_1+m_2}{m_1+m_2+m_3}\cos^2\alpha,$$

where $\theta_{12,3}$ is the angle between $\mathbf{r}_1$ and $\mathbf{r}_2$; these formulae point up the inevitable asymmetry between particles 1 and 2 and particle 3 in these coordinates. The maximum value of E_i/E given by (4.3) is

$$\left(\frac{E_i}{E}\right)_{\max}=\frac{m_j+m_k}{m_1+m_2+m_3},$$

which is that obtained from purely kinematic reasoning when particles j, k come off together in the opposite direction from particle i.

Thus the distribution in α gives directly the energy spectrum of the emitted particles; in particular, if we write the results in terms of E_3, the number of sets of particles per second emitted with centre-of-mass energy for particle 3 between E_3 and $E_3+\mathrm{d}E_3$ for the wavefunction (4.1) is

$$\mathrm{d}\sigma(E_3)=\frac{|Y(l_1,l_2,\lambda;\cos^{-1}[E_3/E_{3\max}]^{\frac{1}{2}})|^2\,\mathrm{d}E_3}{[(E_3/E_{3\max})(1-E_3/E_{3\max})]^{\frac{1}{2}}} \tag{4.4}$$

$$\equiv f(l_1,l_2,\lambda,E_3/E_{3\max})\mathrm{d}E_3.$$

The energy spectrum $f(l_1,l_2,\lambda,E)$ is plotted in fig. 2 for various sets of l_1, l_2, λ.

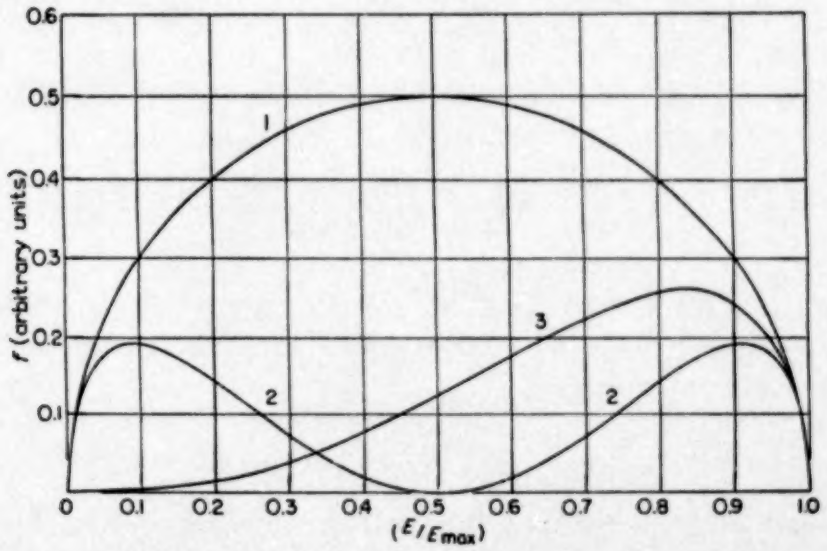

Fig. 2. Energy spectra $\sigma(E/E_{\max})=f(l_1,l_2,\lambda,E/E_{\max})$ for pure states $Y(l_1,l_2,\lambda;\alpha)$.
1. $l_1=l_2=\lambda=0$. 2. $l_1=l_2=0$, $\lambda=1$. 3. $l_1=\lambda=0$, $l_2=2$.

Of course, in general a physical situation is described by superposition of waves of various l_1, l_2, λ with definite phases, so that the measured energy spectrum will contain contributions from all these waves, including cross terms. However, it was shown in (I) that at threshold only the term with $\lambda = 0$ and the lowest possible l_1, l_2 consistent with any selection rules remains. The function f can be given explicitly as

$$f(l_1, l_2, 0; E) = E^{l_1+\frac{1}{2}}(1-E)^{l_2+\frac{1}{2}}. \tag{4.5}$$

In particular for $l_1 = l_2 = \lambda = 0$ we have

$$f(0, 0, 0; E) = E^{\frac{1}{2}}(1-E)^{\frac{1}{2}}.$$

This is just the usual result for the energy spectrum given by "phase-space" arguments, which appears automatically in our formalism. It also points up the limitation in the validity of such arguments; for nonzero energy other terms contribute, and may be important for even quite small energies.

4.2. METASTABLE STATES

As with the usual angular momentum partial wave analysis for two-particle reactions, the formalism is most useful for practical calculations if only a few values of l_1, l_2, λ are important. This will in general be the case at low energies, but circumstances can arise which enhance the role of the higher values of λ. In particular a reaction

$$A+B \to C+D+E$$

may go though an intermediate state involving an unstable particle F:

$$A+B \to F+E, \quad F \to C+D.$$

If F is sufficiently long-lived for this description to have any meaning, a reasonable first approximation to the wavefunction in the external region is the three-particle plane wave

$$\Psi = \exp i(\mathbf{k}_1 \cdot \mathbf{r}_1 + \mathbf{k}_2 \cdot \mathbf{r}_2),$$

where $\mathbf{k}_2$, the momentum carried by particle E, is determined by the almost sharp energy of the compound F. Such a wavefunction when expanded in terms of the set used here involves a sum over l_1, l_2, λ in which the higher values of these quantum numbers are important. The relevant expansion is given in the appendix, eq. (A24). It is probably better from a computational viewpoint to treat that part of the many-particle amplitude which arises from such intermediate states separately, in the plane wave representation, while the contribution from what is usually called "true many-body breakup" is treated with the formalism given here; however, in its simplest form the split is only

approximate, and becomes more so the shorter the lifetime of the unstable state. Such considerations have been treated more fully by Smith [7]).

4.3. GENERALIZED ANGULAR MOMENTUM

An interesting method of introducing the representation used here has also been given by Smith [8]). He points out that classically, for an exact three-body collision, we must have $r_{\min} = 0$, where r is the three-particle channel coordinate of (2.14). Considering r as a vector in the six dimensional channel space,

$$\mathbf{r} = \left(\left(\frac{\mu_1}{m}\right)^{\frac{1}{2}}\mathbf{r}_1, \left(\frac{\mu_2}{m}\right)^{\frac{1}{2}}\mathbf{r}_2\right) \equiv (x_1, \ldots, x_6),$$

with associated wave vector

$$\mathbf{k} = \left(\left(\frac{m}{\mu_1}\right)^{\frac{1}{2}}\mathbf{k}_1, \left(\frac{m}{\mu_2}\right)^{\frac{1}{2}}\mathbf{k}_2\right) \equiv (K_1, \ldots, K_6),$$

then for an exact classical three-body collision all the quantities

$$\Lambda_{ij} = x_i K_j - x_j K_i \quad (i, j = 1, \ldots, 6) \tag{4.6}$$

must vanish; the Λ_{ij} form the elements of what Smith calls the general angular momentum tensor Λ which is a direct generalization of the usual angular momentum operator for two-body channels. In the external region, outside the range of the interaction, Λ^2 is a constant of the motion with eigenvalues $(l+\frac{1}{2})(l+\frac{9}{2})$, where l is our three-particle channel order; its eigenfunctions are closely related to the angular parts of the surface functions in our formalism.

5. Long Range Effects in Many-Particle Channels

5.1. GENERAL

In (I) the form of the S matrix near threshold for one or more N-particle channels was derived, giving a generalization of the usual discussion of the behaviour of cross-sections and other observables in both new and old channels at such thresholds. The methods used give a rigorous proof of the results only for interactions which vanish identically beyond some finite radius in each new channel; but the results of course are expected to be valid for an interaction which, while not vanishing identically for large r, vanishes "sufficiently rapidly" at infinity. A necessary condition is that it vanish faster than r^{-2}, as otherwise the asymptotic form of the channel radial function is certainly changed; but this is already known in the single-channel two-particle case [9]) to be not sufficient. Rather in this case the interaction between the two particles must fall off faster than some inverse power of r, the power depending on the orbital angular momentum of the channel; and this is a non-trivial restriction since the Van der Waals potential between an electron and a neutral atom falls off as r^{-4},

giving a modified threshold behaviour for channels with $l \geqq 1$. We shall here derive similar restrictions in the many-channel, many-particle case; and we shall see that even if the interaction between any pair of particles in a many-particle channel is short-ranged, the threshold behaviour of the channel may be modified from that given in (I). Consider a system satisfying

$$(T+V-E)\Psi = 0. \tag{5.1}$$

We do not specify the nature of V; nor do we specify the number or kinds of channels open at energy E; if there are N such, then N independent solutions Ψ exist, and we pick a set ${}_K\Psi_\alpha$ ($\alpha = 1, \ldots, N$) which have the asymptotic form in channel γ

$$\begin{aligned} {}_K\Psi_\alpha{}^\gamma &= g_\alpha m_\gamma^{\frac{1}{2}} k_\gamma^{-\frac{1}{2}} (\delta_{\alpha\gamma} F_\gamma + K_{\gamma\alpha} G_\gamma)\phi_\gamma \\ &\equiv R_\alpha{}^\gamma \phi_\gamma. \end{aligned} \tag{5.2}$$

Here, $K_{\gamma\alpha}$ is an element of the reactance matrix (3.18) and g_α an energy-dependent normalizing constant chosen to keep Ψ finite at thresholds:

$$g_\alpha = \begin{cases} 1 & (\alpha \text{ old}), \\ k^{-l_\alpha - \frac{1}{2}} & (\alpha \text{ new}), \end{cases} \tag{5.3}$$

where $\hbar^2 k^2 = 2m(E-E_0)$ and E_0 is the energy at which we wish to determine the behaviour of K; a channel is new if it opens at energy E_0.

We also define the function

$$\xi_\alpha = g_\alpha m_\alpha^{\frac{1}{2}} k_\alpha^{-\frac{1}{2}} F_\alpha \phi_\alpha, \tag{5.4}$$

which obeys

$$(T+V'-E)\xi_\alpha = 0, \tag{5.5}$$

where V' includes only that part of the interaction V internal to each particle in channel α, and not the interaction between particles. Multiply (5.4) by ${}_K\Psi_\alpha$ on the left and (5.2) by ξ_α; add, and integrate over space:

$$\int (\xi_\alpha T\, {}_K\Psi_\alpha - {}_K\Psi_\alpha T \xi_\alpha)\mathrm{d}\tau = \int ({}_K\Psi_\alpha V' \xi_\alpha - \xi_\alpha V\, {}_K\Psi_\alpha)\mathrm{d}\tau. \tag{5.6}$$

The left hand side can be evaluated using Green's theorem to give

$$\begin{aligned} -g_\alpha \hbar^2 (4m_\alpha k_\alpha)^{-\frac{1}{2}} &\left[F_\alpha \frac{\mathrm{d}}{\mathrm{d}r} R_\alpha{}^\alpha - R_\alpha{}^\alpha \frac{\mathrm{d}}{\mathrm{d}r} F_\alpha \right]_{r=\infty} \\ &= g_\alpha{}^2 \hbar^2 (2k_\alpha)^{-1} K_{\alpha\alpha} [G_\alpha F'_\alpha - F_\alpha G'_\alpha]_{r=\infty} = g_\alpha{}^2 2^{-1} \hbar^2 K_{\alpha\alpha}, \end{aligned}$$

from the Wronskian (A7). The behaviour of $K_{\alpha\alpha}$ near threshold is thus contained in the integral on the right of (5.5), which is the usual integral relation for $K_{\alpha\alpha}$. Now this behaviour was given in (I) as †

$$K_{\alpha\beta} \to K_{0\alpha\beta} (g_\alpha\, g_\beta)^{-1},$$

† In fact these properties were listed in (I) for $R = 1-S$, but R and K have the same threshold behaviour.

where g_α, g_β are given by eq. (5.4). This property is then valid for interactions such that $K_{0\alpha\beta}$ is finite at E_0. For the diagonal terms therefore the threshold properties at E_0 are those given in (I) if

$$K_{0\alpha\alpha} = \lim_{E\to E_0} (g_\alpha{}^2 K_{\alpha\alpha}) = \lim_{E\to E_0} 2\hbar^{-2}\int ({}_K\Psi_\alpha V'\xi_\alpha - \xi_\alpha V\,{}_K\Psi_\alpha)\mathrm{d}\tau \qquad (5.6a)$$

is finite. The integrand in (5.6a) is finite everywhere, so that if the integral is to diverge the divergence must come from the behaviour at infinity, that is, in the external region. In this region the contribution to the integral is

$$I = -\lim_{E\to E_0} 2g_\alpha{}^2\hbar^{-2}\sum_{\gamma\delta}(m_\gamma m_\delta k_\gamma{}^{-1}k_\delta{}^{-1})^{\frac{1}{2}} \times\int^\infty \delta_{\alpha\gamma}F_\gamma(k_\gamma r)\delta V_{\gamma\delta}(r)[\delta_{\alpha\delta}F_\delta(k_\delta r)+K_{\delta\alpha}G_\delta(k_\delta r)]\mathrm{d}r, \qquad (5.7)$$

where

$$\delta V_{\alpha\beta}(r) = \int \phi_\alpha(V-V')\phi_\beta \mathrm{d}S \qquad (5.8)$$

is the effective interaction between channel α and channel β at large channel distances r; the diagonal elements $\delta V_{\alpha\alpha}(r)$ give the effective potential between the particles in channel α at radius r. For α old, (5.7) is always finite for the conditions assumed ($\delta V(r)$ falls off faster than r^{-2}). For α new, the results of (I) follow if we replace F and G by their form for small kr (see eq. (A6)) and g_α by (5.4). The least rapidly convergent term is that containing the diagonal element $V_{\alpha\alpha}(r)$, which is

$$I_{\alpha\alpha} \propto \int^\infty [r^{2l_\alpha+2}+O(r^{2l_\alpha-2})+K_{\alpha\alpha}O(r)]\delta V_{\alpha\alpha}(r)\mathrm{d}r, \qquad (5.7a)$$

and this integral converges (and $K_{0\alpha\alpha}$ is finite) if and only if $\delta V_{\alpha\alpha}(r)$ falls to zero faster than $r^{-(2l_\alpha+3)}$. This is then the condition on $\delta V(r)$ that the methods of (I) are valid, at least for the diagonal elements of K; we can also discuss the energy dependence of $K_{\alpha\alpha}$ when the condition is violated. In this case the major contribution to $K_{\alpha\alpha}$ for small k comes from large r; and at the threshold E_0 the whole of the leading term in $K_{\alpha\alpha}$ comes from these parts of space. Suppose that $\delta V_{\alpha\beta}(r)$ falls off for large r as $r^{-P_{\alpha\beta}}$,

$$\delta V_{\alpha\beta}(r) \underset{r\to\infty}{=} V_0 r^{-P_{\alpha\beta}}.$$

Then the integral $I_{\alpha\alpha}$ of (5.7a) can be written

$$I_{\alpha\alpha} = \lim_{E\to E_0} 2m_\alpha V_0 g_\alpha{}^2\hbar^{-2}k_\alpha{}^{P_{\alpha\alpha}-2}\int^\infty F_\alpha(x)x^{-P_{\alpha\alpha}}[F_\alpha(x)+K_{\alpha\alpha}G_\alpha(x)]\mathrm{d}x$$

and this integral converges. We thus have in general for α new

$$K_{\alpha\alpha} \propto \begin{cases} k^{2l_\alpha+1} & (P_{\alpha\alpha} \geqq 2l_\alpha+3), \\ k^{P_{\alpha\alpha}-2} & (P_{\alpha\alpha} \leqq 2l_\alpha+3). \end{cases} \qquad (5.9)$$

We can also discuss in the same way the off-diagonal elements of K; repeating the procedure which led to (5.6a), but with functions ${}_K\Psi_\alpha$, ξ_β, where ${}_K\Psi_\alpha$ is as before and

$$\xi_\beta = g_\beta m_\beta^{\frac{1}{2}} k_\beta^{-\frac{1}{2}} F_\beta \phi_\beta,$$

we find

$$g_\alpha g_\beta \hbar^2 2^{-1} K_{\beta\alpha} = \int ({}_K\Psi_\alpha V' \xi_\beta - \xi_\beta V {}_K\Psi_\alpha) \mathrm{d}\tau. \tag{5.10}$$

Thus again we have, taking the limit as $E \to E_0$,

$$K_{0\beta\alpha} = 2\hbar^{-2} \lim_{E \to E_0} \int ({}_K\Psi_\alpha V' \xi_\beta - \xi_\beta V {}_K\Psi_\alpha) \mathrm{d}\tau, \tag{5.10a}$$

and the results of (I) are valid if this integral is finite. As before, any divergence must come from distant regions; and we have for the contribution from such regions

$$I = -g_\alpha g_\beta \sum_{\gamma\delta} (m_\gamma m_\delta k_\gamma^{-1} k_\delta^{-1})^{\frac{1}{2}} \int^\infty \delta_{\beta\gamma} F_\gamma [\delta_{\alpha\delta} F_\gamma + K_{\delta\alpha} G_\delta] \delta V_{\gamma\delta}(r) \mathrm{d}r,$$

the least convergent term now being that with $\delta = \alpha$, $\gamma = \beta$, which is

$$I_{\beta\alpha} = -g_\alpha g_\beta (m_\alpha m_\beta k_\alpha^{-1} k_\beta^{-1})^{\frac{1}{2}} \int^\infty F_\alpha F_\beta \delta V_{\beta\alpha}(r) \mathrm{d}r, \tag{5.11}$$

and the discussion given for the diagonal elements follows through as before. There are four cases to be considered:

$$\begin{aligned}
&\text{a) } (\alpha \text{ old}, \ \beta \text{ old}) \quad K_{\beta\alpha} \text{ is finite at } E^0, \\
&\text{b) } (\alpha \text{ new}, \ \beta \text{ old}) \quad K_{\beta\alpha} \propto \begin{cases} k^{l_\alpha + \frac{1}{2}} & (P_{\beta\alpha} \geqq l_\alpha + 2), \\ k^{P_{\beta\alpha} - \frac{1}{2}} & (P_{\beta\alpha} \leqq l_\alpha + 2), \end{cases} \\
&\text{c) } (\alpha \text{ old}, \ \beta \text{ new}) \quad K_{\beta\alpha} \propto \begin{cases} k^{l_\beta + \frac{1}{2}} & (P_{\beta\alpha} \geqq l_\beta + 2), \\ k^{P_{\beta\alpha} - \frac{1}{2}} & (P_{\beta\alpha} \leqq l_\beta + 2), \end{cases} \\
&\text{d) } (\alpha \text{ new}, \ \beta \text{ new}) \quad K_{\beta\alpha} \propto \begin{cases} k^{l_\alpha + l_\beta + 1} & (P_{\beta\alpha} \geqq l_\alpha + l_\beta + 3), \\ k^{P_{\beta\alpha} - 2} & (P_{\beta\alpha} \leqq l_\alpha + l_\beta + 3). \end{cases}
\end{aligned} \tag{5.12}$$

As noted earlier, these restrictions on the potential for the usual threshold properties to be valid are non-trivial: for instance they affect the elastic scattering in other than S-states of electrons from neutron atoms, since in this case $P_{\alpha\alpha} = 4$. This (Van der Waals) potential is due to the underlying long-ranged two-body coulumb potentials; however, when many-particle channels are involved, even short-ranged two-particle forces will show the long range effects when integrated over the surface functions as in (5.8). This is easily seen by considering a three-particle channel with square well potentials of range a between each pair of particles: the contribution of V_{12} to the channel potential

$\delta V(r)$ is then proportional to

$$\int_0^x Y^2(l_1, l_2, \lambda; \alpha)\mathrm{d}\alpha,$$

where $r_{12} = r \sin\alpha$ and $x = \sin^{-1}(a/r)$. For large r, $x = a/r$ is small and for small α, $Y(l_1, l_2, \lambda; \alpha) = \alpha^{l_1+1}$ so that the contribution from V_{12} to $\delta V(r)$ is proportional to $r^{-(2l_1+3)}$ for large r. This long tail to the potential is enough to modify the threshold behaviour given in (I) for some three-particle channels (though not those of lowest channel order) and the modifications should be observable experimentally.

5.2. RELATION TO THE BORN APPROXIMATION

In the case that the potential $V_{\alpha\beta}(r)$ falls off slowly enough for the threshold behaviour of $K_{\alpha\beta}$ to be modified as above, we have seen that the main contribution to $K_{\alpha\beta}$ comes from large distances; and in this case the value of $K_{\alpha\beta}$ at threshold is independent of the form of the wavefunction in the internal region. We can write from (5.10), for both diagonal and off-diagonal elements,

$$\begin{aligned} K_{\alpha\beta} = {} & 2(g_\alpha g_\beta \hbar^2)^{-1} \int ({}_K\Psi_\beta V' \xi_\alpha - \xi_\alpha V {}_K\Psi_\beta)\mathrm{d}\tau \\ & + 2(m_\alpha m_\beta k_\alpha^{-1} k_\beta^{-1})^{\frac{1}{2}} \hbar^{-2} \int_0^\infty F_\alpha F_\beta \delta V_{\alpha\beta}(r)\mathrm{d}r \\ & - 2(m_\alpha m_\beta k_\alpha^{-1} k_\beta^{-1}) \hbar^{-2} \int_0^\infty F_\alpha F_\beta \delta V_{\alpha\beta}(r)\mathrm{d}r. \end{aligned} \tag{5.13}$$

The first two terms on the right hand side of this equation have integrands the leading terms of which cancel in the external region; the remainder represents an effective channel potential falling off faster than the $r^{-P_{\alpha\beta}}$ of $\delta V_{\alpha\beta}$, so that their contribution to $K_{\alpha\beta}$ vanishes with k faster than does $K_{\alpha\beta}$ itself; that is, at threshold (for α or β new) they contribute nothing to $K_{\alpha\beta}$ and we have

$$K_{\alpha\beta}|_{k=0} = \lim_{E \to E_0} -2\hbar^{-2}(m_\alpha m_\beta k_\alpha^{-1} k_\beta^{-1})^{\frac{1}{2}} \int_0^\infty F_\alpha F_\beta \delta V_{\alpha\beta}(r)\mathrm{d}r. \tag{5.14}$$

That is, the Born approximation is strictly valid at threshold independently of the potential strength, provided $\delta V_{\alpha\beta}$ is of sufficiently long range.

The results of this section have been proved more rigorously by Spruch (private communication) in the case of potential scattering by a potential of form $V_0 r^{-4}$ outside a finite radius.

6. Effective Range Expansions

In a previous paper[10]) effective range expansions for cot δ and the diagonalizing matrix T were given for the two-particle many-channel case. As a further example of the use of the formalism given here, we write down such expansions in a form valid also for many-particle channels, under the assumption that the

long-range modification of the threshold behaviour discussed in the previous paragraph does not occur in any channel at the energy about which the expansion is made. The expansions will be written down for what seem to be the two most useful matrices, K and cot δ; similar results exist for T. We do not give proofs here; they follow closely those given in ref. [10]), to which the reader is referred also for a discussion of such expansions in general.

We write then

$$\begin{aligned} K_{\alpha\beta} &= k^{(q_\alpha+q_\beta)}[K_{0\alpha\beta}+K_{2\alpha\beta}k^2+\ldots], \\ k^{2q_\alpha}\cot\delta_\alpha &= \delta_{0\alpha}+\delta_{1\alpha}k+\delta_{2\alpha}k^2+\ldots, \\ T_{\alpha\beta} &= g_{\alpha\beta}[T_{0\alpha\beta}+T_{1\alpha\beta}k+\ldots. \end{aligned} \tag{6.1}$$

The powers of k in the leading terms and the definition of $g_{\alpha\beta}$ are (introducing the channel order l_γ)

$$q_\gamma = \begin{cases} 0 & (\gamma \text{ old}), \\ l_\gamma+\frac{1}{2} & (\gamma \text{ new}), \end{cases} \qquad g_{\alpha\beta} = \begin{cases} 1 & (\alpha \text{ old}, \ \beta \text{ old}), \\ k^{l_\alpha+\frac{1}{2}} & (\alpha \text{ new}, \beta \text{ old}), \\ k^{l_\beta+\frac{1}{2}} & (\alpha \text{ old}, \ \beta \text{ new}), \\ k^{|l_\alpha-l_\beta|} & (\alpha \text{ new}, \beta \text{ new}). \end{cases} \tag{6.2}$$

The coefficients of these terms, $K_{0\alpha\beta}$, $\delta_{0\alpha}$ and $T_{0\alpha\beta}$ follow as shown in ref. [10]) from the asymptotic form of the wavefunction at the energy E_0 about which the expansions are made, and from which k is measured:

$$\hbar^2k^2 = 2m(E-E_0), \tag{6.3}$$

m being an arbitrary mass. k is related to k_γ for γ new by $m_\gamma k^2 = mk_\gamma{}^2$; for γ old, k_γ is finite at E_0. The form of the next terms up to terms of order k^2 also follow explicitly from the wavefunction at E_0; as indicated in (6.1) only terms of order k and or order k^2 appear. Moreover, the term of order k in K is missing; it can be shown indeed that $K_{\alpha\beta}$ is an even function of k when the term $k^{(q_\alpha+q_\beta)}$ has been removed. It was stated in ref. [10]) that the term $\delta_{1\alpha}$ in cot δ_α was zero also; however, cases can occur where this is not so, and they are noted here.

It is necessary to define first the set of wavefunctions we wish to use; for the reactance matrix K, these are the solutions ${}_K\Psi_\alpha$ of (5.2) having regular waves in only one channel:

$$\begin{aligned} {}_K\Psi_\alpha{}^\gamma &= g_\alpha m_\gamma{}^{\frac{1}{2}}k_\gamma{}^{-\frac{1}{2}}[\delta_{\alpha\gamma}F_\gamma+K_{\gamma\alpha}G_\gamma]\phi_\gamma \\ &\equiv {}_KR_{\alpha\gamma}\phi_\gamma \quad (\alpha = 1, \ldots, N). \end{aligned} \tag{6.4}$$

Here, ${}_KR_{\alpha\gamma}$ is the channel radial wavefunction for channel γ, and g_α is given by (5.4). We also define modified channel wavefunctions

$${}_K\bar{R}_{\alpha\gamma} = g_\alpha m_\gamma{}^{\frac{1}{2}}k_\gamma{}^{-\frac{1}{2}}[\delta_{\alpha\gamma}F_{2\gamma+1}+K_{\gamma\alpha}G_{l_\gamma+1}], \tag{6.5}$$

which have the channel order increased by one unit. Then, following the

procedure of ref. [10]), we have †

$$\frac{\mathrm{d}}{\mathrm{d}(k^2)}\left(k^{-2q_\alpha}K_{\alpha\alpha}\right)=\frac{1}{m}\left[\int {}_K\Psi_\alpha{}^2\mathrm{d}\tau-\sum_\gamma\int_{r_0}^{\infty}{}_KR_{\alpha\gamma}^2\mathrm{d}r\right]-\frac{q_\alpha K_{0\alpha\alpha}}{k^2}$$
$$+\sum_\gamma(2mk_\gamma)^{-1}[(2l_\gamma+1)\,{}_KR_{\alpha\gamma}\,{}_K\bar{R}_{\alpha\gamma}-k_\gamma r_0\{{}_KR_{\alpha\gamma}^2+{}_K\bar{R}_{\alpha\gamma}^2\}]_{r_0}\quad(6.6)$$

and the limit $k\to 0$ is to be taken. For α old, all the terms here are manifestly finite ($q_\alpha=0$), but for α new, terms of order k^{-2} are present in the sum on the right hand side of (6.6). Evaluating these explicitly by expanding the sum and using the form (A6) for $F(k_\gamma r)$ and $G(k_\gamma r)$ as $k_\gamma\to 0$, we find these terms to be

$$(2l_\alpha+1)K_{0\alpha\alpha}/2k^2,$$

cancelling the term $-q_\alpha K_{0\alpha\alpha}/k^2$. No terms of order k^{-1} are present, verifying the statement that no term of the form $K_{1\alpha\alpha}k$ appears in (6.1); and thus (6.6) is finite at E_0 and equal to $K_{2\alpha\alpha}$.

For the off-diagonal elements we proceed as for the off-diagonal elements of T in ref. [10]) and obtain

$$K_{2\alpha\beta}=\frac{\mathrm{d}}{\mathrm{d}(k^2)}\left[k^{-q_\alpha-q_\beta}K_{\alpha\beta}\right]$$
$$=\frac{1}{m}\left[\int {}_K\Psi_\alpha\,{}_K\Psi_\beta\mathrm{d}\tau-\sum_\gamma\int_{r_0}^{\infty}{}_KR_{\alpha\gamma}\,{}_KR_{\beta\gamma}\mathrm{d}r\right]-\frac{(q_\alpha+q_\beta)}{2k^2}K_{0\alpha\beta}$$
$$-\frac{1}{2m}\sum_\gamma\left[r_0\{{}_KR_{\alpha\gamma}\,{}_KR_{\beta\gamma}+{}_K\bar{R}_{\alpha\gamma}\,{}_K\bar{R}_{\beta\gamma}\}-\frac{{}_KR_{\alpha\gamma}\,{}_KR_{\beta\gamma}}{2k_\gamma}\left\{2l_\gamma+1+\frac{k_\gamma{}^2mg'_\alpha}{km_\gamma g_\alpha}-\frac{k_\gamma{}^2mg'_\beta}{km_\gamma g_\beta}\right\}\right.$$
$$\left.-\frac{{}_K\bar{R}_{\alpha\gamma}\,{}_K\bar{R}_{\beta\gamma}}{2k_\gamma}\left\{2l_\gamma+1+\frac{k_\gamma{}^2mg'_\beta}{km_\gamma g_\beta}-\frac{k_\gamma{}^2mg'_\alpha}{km_\gamma g_\alpha}\right\}\right]_{r_0},\quad(6.7)$$

where $g'_\alpha=\mathrm{d}g_\alpha/\mathrm{d}k$.

In equating (6.7) to $K_{2\alpha\beta}$ we have anticipated the fact, which is easily verified, that at E_0 terms of order k^{-2} always cancel, and no terms of order k^{-1} appear, so that $K_{1\alpha\beta}$ is zero. We can develop similar results for $\cot\delta_\alpha$; for this purpose we use the set Ψ_α of eigenfunctions of the scattering matrix (see ref. [10])) which have the asymptotic form in channel γ

$$\Psi_\alpha{}^\gamma=j_\alpha m_\gamma{}^{\frac{1}{2}}k_\gamma{}^{-\frac{1}{2}}T_{\alpha\gamma}[\cot\delta_\alpha F_\gamma+G_\gamma]\phi_\gamma$$
$$=R_{\alpha\gamma}\phi_\gamma.\quad(6.8)$$

The normalizing factor j_α is that used in ref. [10]) and is related to g_α of eq. (5.4) by

$$j_\alpha g_\alpha=1.$$

† Certain divergent terms which were cancelled in ref. [10]) by using modified channel functions are here avoided completely by using the form of the channel functions only outside the radius r_0: this seems more convenient from a computational standpoint.

It is inserted to assure that Ψ_α is finite at E_0. The $T_{\alpha\gamma}$ are the elements of T (3.16).

As for K, we define modified functions

$$\bar{R}_{\alpha\gamma} = j_\alpha m_\gamma^{\frac{1}{2}} k_\gamma^{-\frac{1}{2}} T_{\alpha\gamma}[\cot\delta_\alpha F_{l_\gamma+1}+G_{l_\gamma+1}]. \tag{6.9}$$

We find

$$\frac{\mathrm{d}}{\mathrm{d}(k^2)}(k^{2q_\alpha}\cot\delta_\alpha) = \frac{-1}{m}\left[\int \Psi_\alpha^2 \mathrm{d}\tau - \sum_\gamma \int_{r_0}^{\infty} R_{\alpha\gamma}^2 \mathrm{d}r\right] + \frac{q_\alpha \delta_{\alpha 0}}{k^2}$$
$$- \frac{1}{m}\sum_\gamma \left[\frac{2l_\gamma+1}{2k_\gamma} R_{\alpha\gamma}\bar{R}_{\alpha\gamma} - \tfrac{1}{2} r_0\{R_{\alpha\gamma}^2+\bar{R}_{\alpha\gamma}^2\}\right]_{r_0}. \tag{6.10}$$

In contrast to the situation with (6.6) and (6.7), the right hand side of (6.10) is not necessarily finite at E_0; as before, the terms of order k^{-2} all cancel, but in addition terms of order k^{-1} may be present; that is to say, $\delta_{\alpha 1}$ may be non-zero. We will only quote here the cases in which this may occur; these results follow simply by expanding (6.10).

For α old, terms in k^{-1} appear if and only if the α channel is coupled by non-zero $T_{\alpha\gamma}$ to new channels γ with $l_\gamma = 0$; these terms are

$$\frac{1}{2k}\sum_{\gamma\ \mathrm{new},\ l_\gamma=0} T_{0\alpha\gamma}^2 \delta_{\alpha 0},$$

so that in this case, from (6.10) and (6.1),

$$\delta_{\alpha 1} = -\sum_{\gamma\ \mathrm{new},\ l_\gamma=0} T_{0\alpha\gamma}^2 \delta_{\alpha 0} \quad (\alpha\ \mathrm{old}). \tag{6.11a}$$

For α new, terms of order k^{-1} appear if $l_\alpha = 0$ and α is coupled to old channels γ by non-zero $T_{\alpha\gamma}$; we find

$$\delta_{\alpha 1} = -\sum_{\gamma\ \mathrm{old}} T_{0\alpha\gamma}^2 \delta_{\alpha 0} \quad (\alpha\ \mathrm{new},\ l_\alpha = 0). \tag{6.11b}$$

In addition, such terms can appear in circumstances which are peculiar to many-particle channels; that is, if α is coupled to new channels γ whose channel orders differ from that of α by $\frac{1}{2}$. In this case we have

$$\delta_{\alpha 1} = 2\delta_{\alpha 0}\sum_{\gamma\ \mathrm{new},\ l_\gamma=l_\alpha\pm\frac{1}{2}} (l_\gamma - l_\alpha) T_{0\alpha\gamma}^2 \quad (\alpha\ \mathrm{new},\ l_\alpha \neq 0). \tag{6.11c}$$

The restriction $l_\alpha \neq 0$, making the overlap with (6.11b) zero, comes only from the absence of channel orders of $\frac{1}{2}$: $l_\alpha = 0, 1, \frac{3}{2}, 2, \frac{5}{2}, \ldots$. The possibility of such terms seems rather academic; they arise from the slow variation with k of $T_{\alpha\gamma}$ for such coupled channels (which have $T_{\alpha\gamma} \propto k^{\frac{1}{2}}$ at E_0).

Finally we have the finite expression for $\delta_{\alpha 2}$:

$$\delta_{\alpha 2} = -\frac{1}{m}\left[\int \Psi_\alpha{}^2 \mathrm{d}\tau - \sum_\gamma \int_{r_0}^{\infty} R_{\alpha\gamma}^2 \mathrm{d}r\right] + \frac{q_\alpha \delta_{\alpha 0}}{k^2} - \frac{\delta_{\alpha 1}}{2k} - \frac{1}{m}\sum_\gamma \left[\frac{2l_\gamma+1}{2k_\gamma} R_{\alpha\gamma}\bar{R}_{\alpha\gamma} - \tfrac{1}{2} r_0 \{R_{\alpha\gamma}^2 + \bar{R}_{\alpha\gamma}^2\}\right]_{r_0}. \quad (6.12)$$

Similar results can be given for T, but we shall not quote them here.

7. Many-Particle Bound States

Bound states of a system occur [13]) at energies such that one of the eigenphase-shifts, δ_α say, of the system passes through $i\infty$; that is, $\cot \delta_\alpha = i$. A bound state at such an energy can be characterized by the channel α whose eigenphase-shift passes through $i\infty$; and we can talk of an N-particle bound state if this is an N-particle channel.

It is well known that for two-particle bound states α lying sufficiently close to the threshold of α the energy of the bound state can be predicted well from the first two terms of the expansion (6.1) for $\cot \delta_\alpha$; we write

$$(ik)^{2l_\alpha+1} \cot \delta_\alpha = i^{2l_\alpha+2} k^{2l_\alpha+1} \approx \delta_{\alpha 0} + (ik)^2 \delta_{\alpha 2}, \quad (7.1)$$

where the bound state is at an energy E below the threshold of α and

$$\hbar^2 k^2 = 2mE.$$

For two-particle channels this gives

$$(-1)^{l+1} k^{2l+1} + k^2 \delta_{\alpha 2} - \delta_{\alpha 0} = 0, \quad (7.2)$$

which can be solved for k; the required root is the smallest positive one. However, for many-particle channels this procedure may fail; specifically, if the channel contains an odd number of particles, the first two leading terms (7.1) in $\cot \delta_\alpha$ below threshold for α are real ($2l_\alpha+1$ is even). However, $\cot \delta_\alpha$ in these cases is not wholly real; we shall show that below threshold it contains a constant term of magnitude i, so that for instance for three-particle states of low channel order three terms in the expansion (6.1) may be sufficient to define the bound state.

This result can be seen by considering a wholly real representation; above threshold, F and G are real, while below threshold the $\bar{F}$, $\bar{G}$ of eq. (A4) are real. Consider then a representation in which the channel functions are written

$$\Psi^\gamma = (A' X_\gamma + B' Y_\gamma)\phi_\gamma, \quad (7.1)$$

where

$$X_\gamma = \begin{cases} m_\gamma{}^{\frac{1}{2}} k_\gamma{}^{-\frac{1}{2}} F_\gamma & (k_\gamma \text{ real}), \\ m_\gamma{}^{\frac{1}{2}} |k_\gamma|^{-\frac{1}{2}} \bar{F}_\gamma & (k_\gamma \text{ imaginary}), \end{cases} \qquad Y_\gamma = \begin{cases} m_\gamma{}^{\frac{1}{2}} k_\gamma{}^{-\frac{1}{2}} G_\gamma & (k_\gamma \text{ real}), \\ m_\gamma{}^{\frac{1}{2}} |k_\gamma|^{-\frac{1}{2}} \bar{G}_\gamma & (k_\gamma \text{ imaginary}). \end{cases} \quad (7.2)$$

Then we can write

$$B' = S'A', \tag{7.3}$$

where S' is manifestly real since X, Y are real and is related to the reactance matrix K by

$$K^{-1} = \exp\left\{\tfrac{1}{4}i\pi(l+\tfrac{1}{2})\left(\frac{k^*-k}{k}\right)\right\} S'^{-1} \exp\left\{\tfrac{1}{4}i\pi(l+\tfrac{1}{2})\left(\frac{k^*-k}{k}\right)\right\} + \frac{k-k^*}{2k}\, i. \tag{7.4}$$

This result follows by noting that X, Y can be written

$$X = \exp\left\{\tfrac{1}{4}i\pi(l+\tfrac{1}{2})\left(\frac{k^*-k}{k}\right)\right\}\left(\frac{m}{k}\right)^{\frac{1}{2}} F,$$

$$Y = \left(\frac{k-k^*}{2k}\right)\exp\left\{\tfrac{1}{4}i\pi(l+\tfrac{3}{2})\left(\frac{k-k^*}{k}\right)\right\}\left(\frac{m}{k}\right)^{\frac{1}{2}} F \tag{7.5}$$

$$+ \exp\left\{\tfrac{1}{4}i\pi(l+\tfrac{1}{2})\left(\frac{k-k^*}{k}\right)\right\}\left(\frac{m}{k}\right)^{\frac{1}{2}} G.$$

If all channels considered are open, (7.4) implies of course that K is real. The behaviour of K implied by (7.4) when negative energy channels exist is most easily seen by considering the simplest case of a one-channel matrix; then $K = \tan\delta$ and (7.4) reads for negative energies

$$\cot\delta = \exp\{-\tfrac{1}{2}i\pi(2l+1)\}S'^{-1}+i, \tag{7.6}$$

where S' is real.

For integer l this gives

$$\cot\delta = i[1+(-1)^l S'^{-1}],$$

which is wholly imaginary; while for half-integer, $l = l_0+\frac{1}{2}$ say,

$$\cot\delta = i+(-1)^{l_0+1}S'^{-1}.$$

8. Summary

In this paper we have given in some detail a formalism for treating many-particle scattering states which yields a discrete scattering matrix; and we have tried to show that it is as easy to handle as the usual two-particle angular momentum formalism. The results obtained lend themselves to the same sort of approximations in performing practical calculations as are used in treating two-particle scatterings by compound systems, and it is hoped to report on some calculations of this sort at a later date.

I would like to thank Dr. R. J. Blin-Stoyle for his help and encouragement throughout this work, and Professor L. Spruch for stimulating discussions on

long-range potentials. Thanks are also due to Professor V. Weisskopf for making possible a stay at M.I.T., where much of this work was done.

Appendix

We list here some useful relations concerning the surface functions and radial functions for integral or half-integral channel order. These results are all well-known properties of the hypergeometric and Bessel functions involved and we merely state them here in the notation and with the normalization we have chosen; where it seemed desirable references are given. In general the possibility of half-integral l does not change the form of results as usually quoted; but some differences do arise.

A.1. THE RADIAL WAVE EQUATION

We consider solutions of

$$\left[\frac{\mathrm{d}^2}{\mathrm{d}r^2} - \frac{l(l+1)}{r^2} + k^2\right] R(r) = 0 \tag{A1}$$

for integral and half-integral values of l. This equation has two independent solutions, which can be chosen in various ways. One choice, used to define the scattering matrix, is the set of ingoing and outgoing waves I and O:

$$I_l(kr) = -i(\tfrac{1}{2}\pi kr)^{\frac{1}{2}} H^2_{l+\frac{1}{2}}(kr), \quad O_l(kr) = i(\tfrac{1}{2}\pi kr)^{\frac{1}{2}} H^1_{l+\frac{1}{2}}(kr), \tag{A2}$$

where $H_n^{1,2}(x)$ are the Hankel functions of order n as defined in Jahnke and Emde [11]).

A second set is that given by the "regular" and "irregular" solutions which define the reactance matrix:

$$\begin{aligned} F_l(kr) &= -\tfrac{1}{2}i[O_l(kr) - I_l(kr)] = (\tfrac{1}{2}\pi kr)^{\frac{1}{2}} J_{l+\frac{1}{2}}(kr), \\ G_l(kr) &= \tfrac{1}{2}[O_l(kr) + I_l(kr)] = -(\tfrac{1}{2}\pi kr)^{\frac{1}{2}} N_{l+\frac{1}{2}}(kr). \end{aligned} \tag{A3}$$

$J_n(z)$, $N_n(z)$ are the Bessel functions of the first and second kind defined in ref. [11]). F and G are real for real kr. In discussing the transition from open channels (k real) to closed channels (k pure imaginary and in the upper half plane) it is useful to have solutions which are real for imaginary kr. These are [12])

$$\bar{F}_l(ikr) = i^{-(l+1)} F_l(ikr), \quad \bar{G}_l(ikr) = i^l O_l(ikr). \tag{A4}$$

A.2. ASYMPTOTIC FORMS

For large r ($kr \gg l$) the solutions take the form

$$\begin{aligned}
&I_l(kr) \sim \mathrm{e}^{-i(kr-\frac{1}{2}l\pi)}[1+O(kr)^{-1}],\\
&O_l(kr) \sim \mathrm{e}^{i(kr-\frac{1}{2}l\pi)}[1+O(kr)^{-1}],\\
&F_l(kr) \sim \sin(kr-\tfrac{1}{2}l\pi)[1+O(kr)^{-2}]+\cos(kr-\tfrac{1}{2}l\pi)O(kr)^{-1},\\
&G_l(kr) \sim \cos(kr-\tfrac{1}{2}l\pi)[1+O(kr)^{-2}]+\sin(kr-\tfrac{1}{2}l\pi)O(kr)^{-1},\\
&\bar{F}_l(ikr) \sim \tfrac{1}{2}\mathrm{e}^{+kr}[1+O(kr)^{-1}],\\
&\bar{G}_l(ikr) \sim \mathrm{e}^{-kr}[1+O(kr)^{-1}],
\end{aligned} \tag{A5}$$

where $O(x)$ stands for terms of order x.

For small r ($kr \ll 1$) we have

$$\begin{aligned}
F_l(kr) &\approx \frac{\pi^{\frac{1}{2}}(kr)^{l+1}}{2^{l+1}(l+\frac{1}{2})!}\left[1-\frac{(kr)^2}{2(2l+3)}+O(kr)^4\right],\\
G_l(kr) &\approx \frac{2^l(l-\frac{1}{2})!}{\pi^{\frac{1}{2}}(kr)^l}\left[1-\frac{(kr)^2}{2(2l-1)}+O(kr)^4\right].
\end{aligned} \tag{A6}$$

These take for l integral the simpler forms

$$\begin{aligned}
F_l(kr) &\approx \frac{(kr)^{l+1}}{(2l+1)!!}\left[1-\frac{(kr)^2}{2(2l+3)}+O(kr)^4\right],\\
G_l(kr) &\approx \frac{(2l-1)!!}{(kr)^l}\left[1-\frac{(kr)^2}{2(2l-1)}+O(kr)^4\right].
\end{aligned}$$

A.3. WRONSKIANS

The solutions chosen have the following Wronskians; a prime denotes differentiation with respect to r

$$I_lO'_l-O_lI'_l = 2ik, \quad G_lF'_l-F_lG'_l = k. \tag{A7}$$

A.4. SYMMETRY RELATIONS AND BEHAVIOUR UNDER TIME REVERSAL

Considered as functions of k, O and I have the following symmetry properties

$$[O(k^*)]^*=I(k), \quad [I(k^*)]^*=O(k), \quad O(-k)=\mathrm{e}^{-il\pi}I(k), \quad I(-k)=\mathrm{e}^{il\pi}O(k). \tag{A8}$$

These imply the following behaviour of O and I under time reversal T:

$$\begin{aligned}
\mathrm{T}[O(k)] = [O(k)]^* &= \begin{cases} I(k) & k \text{ real: open channels),}\\ \mathrm{e}^{il\pi}O(k) & (k \text{ imaginary: closed channels),}\end{cases}\\
\mathrm{T}[I(k)] = [I(k)]^* &= \begin{cases} O(k) & (k \text{ real}),\\ \mathrm{e}^{-il\pi}I(k) & (k \text{ imaginary}).\end{cases}
\end{aligned} \tag{A9}$$

A.5. INTEGRAL AND DIFFERENTIAL RELATIONS; RECURRENCE RELATIONS

Writing $R_l(kr) = AF_l(kr)+BG_l(kr)$ where A, B are independent of l we have the properties

$$\int r^{-l}R_l(kr)\mathrm{d}r = -\frac{r^{-l}}{k}R_{l-1}(kr), \quad \int r^{l+1}R_l(kr)\mathrm{d}r = \frac{r^{l+1}}{k}R_{l+1}(kr), \quad \text{(A10)}$$

$$\frac{\mathrm{d}}{\mathrm{d}r}(R_l(kr)) = \frac{-l}{r}R_l(kr)+kR_{l-1}(kr) = \frac{l+1}{r}R_l(kr)-kR_{l+1}(kr), \quad \text{(A12)}$$

$$R_{l+1}(kr) = -R_{l-1}(kr)+\frac{2l+1}{kr}R_l(kr), \quad \text{(A12)}$$

$$\int R_l(k_1r)R_l(k_2r)\mathrm{d}r = [k_2R_l(k_1r)R_{l-1}(k_2r)-k_1R_{l-1}(k_1r)R_l(k_2r)](k_1^2-k_2^2)^{-1}$$
$$= [k_1R_l(k_2r)R_{l+1}(k_1r)-k_2R_{l+1}(k_2r)R_l(k_1r)](k_1^2-k_2^2)^{-1}. \quad \text{(A13)}$$

We also have from (A7) and (A12) the relation

$$F_l(kr)G_{l+1}(kr)-G_l(kr)F_{l+1}(kr) = 1. \quad \text{(A14)}$$

A.6. GENERALIZED SPHERICAL HARMONICS

The angular functions which occur in the treatment of many-particle channels are solutions $Y(a, b, c; \alpha)$ of

$$\left[\frac{\mathrm{d}^2}{\mathrm{d}\alpha^2}-\frac{a(a+1)}{\sin^2\alpha}-\frac{b(b+1)}{\cos^2\alpha}+(a+b+2c+2)^2\right]Y(a, b, c; \alpha) = 0, \quad \text{(A15)}$$

where a, b are integral or half integral and $c = 0, 1, 2, \ldots$.

The solution of (A15) which is finite for $0 \leqq \alpha \leqq \frac{1}{2}\pi$ is

$$Y(a, b, c; \alpha) = A_{abc}\sin^{a+1}\alpha\cos^{b+1}\alpha\,{}_2F_1(-c, a+b+c+2; a+\tfrac{3}{2}; \sin^2\alpha), \quad \text{(A16)}$$

where ${}_2F_1(p, q; r; x)$ is a hypergeometric function as defined in ref. [11]); for negative integral p, which is the only case with which we are concerned, it is a finite polynomial of degree $|p|$ in x, the Jacobi polynomial:

$${}_2F_1(p, q; r; x) = 1+\frac{pq}{r}\frac{x}{1!}+\frac{p(p+1)q(q+1)}{r(r+1)}\frac{x^2}{2!}+\ldots. \quad \text{(A17)}$$

We take the normalizing factor A_{abc} as

$$A_{abc} = \left[\frac{2(a+b+2c+2)(a+b+c+1)!(a+c+\frac{1}{2})!}{c![(a+\frac{1}{2})!]^2(b+c+\frac{1}{2})!}\right]^{\frac{1}{2}}. \quad \text{(A18)}$$

With this value for A the $Y(a, b, c; \alpha)$ are normalized between 0 and $\frac{1}{2}\pi$ with

unit weight function; moreover they are orthogonal in c:

$$\int_0^{\frac{1}{2}\pi} Y(a, b, c_1; \alpha)Y(a, b, c_2; \alpha)\mathrm{d}\alpha = \delta_{c_1 c_2}. \tag{A19}$$

They have the symmetry property

$$Y(a, b, c; \alpha) = (-1)^c Y(b, a, c; \tfrac{1}{2}\pi-\alpha). \tag{A20}$$

Two further relations which are not required in the text but are sufficiently useful to state here are

$$\cos\alpha Y(a, b, c; \alpha) = \left[\frac{(a+b+c+2)(b+c+\frac{3}{2})}{(a+b+2c+2)(a+b+2c+3)}\right]^{\frac{1}{2}} Y(a, b+1, c; \alpha)$$
$$+ \left[\frac{c(a+c+\frac{1}{2})}{(a+b+2c+2)(a+b+2c+1)}\right]^{\frac{1}{2}} Y(a, b+1, c-1; \alpha), \tag{A21}$$

$$\sin\alpha Y(a, b, c; \alpha) = \left[\frac{(a+b+c+2)(a+c+\frac{3}{2})}{(a+b+2c+2)(a+b+2c+3)}\right]^{\frac{1}{2}} Y(a+1, b, c; \alpha)$$
$$+ \left[\frac{c(b+c+\frac{1}{2})}{(a+b+2c+1)(a+b+2c+2)}\right]^{\frac{1}{2}} Y(a+1, b, c-1; \alpha). \tag{A22}$$

A.7. EXPANSIONS

It is possible to transform from the many-particle representation used here to a representation in which the particles have sharp relative momenta; the necessary relations were given in (I), but we repeat them here with the present notation, with which they have a particularly simple form

$$(k_1 r_1 k_2 r_2)^{-\frac{1}{2}} H_{l_1+\frac{1}{2}}(k_1 r_1) H_{l_2+\frac{1}{2}}(k_2 r_2) = (k^2 r^2 \cos\alpha \sin\alpha \cos\phi \sin\phi)^{-1}$$
$$\times \sum_{\lambda=0}^{\infty} (-1)^\lambda Y(l_1, l_2, \lambda; \alpha)Y(l_1, l_2, \lambda; \phi) H_{l_1+l_2+2\lambda+2}(kr), \tag{A23}$$

where

$$k_1 = k\sin\phi, \quad k_2 = k\cos\phi, \quad r_1 = r\sin\alpha, \quad r_2 = r\cos\alpha.$$

Similarly a three-particle plane wave representing particles 1 and 2 with relative momentum k_1, along the z axis, and particle 3 with momentum $\mathbf{k}_2$ relative to the centre of mass 1 and 2 can be expanded in the set given here

$$\mathrm{e}^{i(k_1 z_1 + \mathbf{k}_2\cdot\mathbf{r}_3)} = 2^{\frac{1}{2}}\pi^2 i (kr)^{-\frac{1}{2}} (\sin\alpha\cos\alpha\sin\phi\cos\phi)^{-1} \sum_{l_1 l_2 \lambda} (2l_1+1)^{\frac{1}{2}} (-1)^\lambda [I_P - O_P]$$
$$\times Y(l_1, l_2, \lambda; \alpha)Y(l_1, l_2, \lambda; \phi) Y^0_{l_1}(\Omega_1) \sum_{m_3} Y^{m_3}_{l_2}(\Theta, \Phi) Y^{m_3}_{l_3}(\Omega_2), \tag{A24}$$

where $P = l_1+l_2+2\lambda+\frac{3}{2}$, $\mathbf{r}_1 = (r_1, \Omega_1)$, $\mathbf{r}_2 = (r_2, \Omega_2)$ and the incident angle between $\mathbf{k}_1$ and $\mathbf{k}_2$ is (Θ, Φ).

A.8. RECOUPLING OF THE SURFACE FUNCTIONS

The N-particle surface functions given explicitly in the text (2.35) are eigenfunctions of the individual orbital angular momenta l_i and z-components $m_i (i = 1, \ldots, (N-1))$ and of the particle spins S_i and z-components $m_{si} (i = 1, \ldots, N)$ (as well as other quantities). In practice we will use surface functions which are eigenfunctions of the l_i and s_i, and of the total angular momentum $\mathbf{J}^2 = (\sum \mathbf{l}_i + \sum \mathbf{S}_i)^2$, its z-component M, and a set of intermediate quantum numbers depending on the order in which the angular momenta and spins are coupled together, We assume the recoupling is done using

$$\phi(l_1; l_2; l_{12}, m_{12}) = \sum_{m_1 m_2} (l_1 l_2 m_1 m_2 | l_1 l_2 l_{12} m_{12}) \phi(l_1 m_1; l_2 m_2) \qquad \text{(A25)}$$

successively on pairs of quantum numbers. Then if the individual orbital and spin wavefunctions appearing in (2.35) are phased to behave under time reversal as

$$\mathrm{T} Y_l^m(\Omega) = (-1)^{l-m} Y_l^{-m}(\Omega)$$

and similarly for the spins, the total recoupled surface functions satisfy

$$\mathrm{T}\phi(J, M, \gamma) = (-1)^{J-M} \phi(J, -M, \gamma), \qquad \text{(A26)}$$

which is the result we wish to assume.

References

1) L. M. Delves, Nuclear Physics **9** (1959) 391
2) See, e.g., Edmonds, Angular momentum in quantum mechanics (Princeton, 1957)
3) P. M. Morse and H. Feshbach, Methods of theoretical physics (McGraw Hill, 1953) Vol. II, p. 1731
4) D. Jepsen and J. O. Hirschfelder, Proc. Nat. Acad. Sci. U.S. **45** (1959) 249
5) E. Schrödinger, Ann. Physik **81** (1926) 109
6) A. M. Lane and R. G. Thomas, Rev. Mod. Physics **30** (1958) 257, section VI
7) F. T. Smith, Phys. Rev. **118** (1960) 349
8) F. T. Smith, to be published
9) B. H. Bransden, A. Dalgarno, T. L. John and M. J. Seaton, Proc. Phys. Soc. A **71** (1958) 882
10) L. M. Delves, Nuclear Physics **8** (1958) 358
11) E. Jahnke and F. Emde, Funktionentafeln (Teubner, 1933)
12) Watson, A treatise on the theory of Bessel functions (2nd ed., Cambridge, 1953)
13) L. M. Delves, Phys. Rev. **118** (1960) 1318

7.C

Nuclear Physics **20** (1960) 309—312; © *North-Holland Publishing Co., Amsterdam*

Not to be reproduced by photoprint or microfilm without written permission from the publisher

MULTIPLE PRODUCTION OF MESONS IN PION-NUCLEON COLLISIONS

WIESLAW CZYŻ

Institute for Nuclear Research, Krakow, Bronowice, Poland

and

SHELDON L. GLASHOW †

Institute for Theoretical Physics, University of Copenhagen, Denmark

and

CERN, Geneva, Switzerland

Received 25 June 1960

Abstract: The model of Czyz, Ericson and Glashow for multiple meson production in energetic nucleon-nucleon collisions is applied to the analogous pion-nucleon process. The angular distributions of the shower particles of such events are predicted to display a single-cone structure, and to be forward peaked in the centre-of-mass system at primary energies greater than 400 GeV. The model should be applicable for pion energies beyond 50 GeV.

In an earlier publication with T. Ericson [1]), we described a new model of the multiple production of mesons occurring in energetic nucleon-nucleon collisions. Visualizing the nucleon as a dense "core" surrounded by an extended meson "cloud", we attributed the meson production to a mesonic analogue of the Čerenkov effect. The existence of this effect requires a source of the meson field (the nucleon "core") rapidly moving through an extended region (another nucleon's "cloud") in which the refractive index for the propagation of pions is greater than one (caused, presumably, by an attractive pion-pion interaction). Each of the two participating nucleon cores, traversing the periphery of the other nucleon, was assumed to produce a cone of emitted mesons — just as a charged body, moving sufficiently rapidly through a dielectric medium, produces Čerenkov photons. A two-centre appearance of the angular distribution of shower particles emerges naturally, and more detailed predictions follow from the hypothesis that the mesonic Čerenkov effect, like its electrodynamic analogue, becomes energy-independent at extremely relativistic energies.

This note is an attempt to extend these notions to describe the multiple production attending pion-nucleon collisions, and is not logically independent of our earlier work ††. Again, the target nucleon "core" will play the role of a rapidly moving charge in the Čerenkov analogy. We shall assume that the incident pion does not possess a central core and cannot act as a source of the pion field.

† National Science Foundation Post-Doctoral Fellow.

†† Ref. [1]) will hereafter be referred to as A.

However, we shall regard the pion as a structure comparable in linear dimension with the Compton wavelength of the pion within which the refractive index for propagation of other pions is greater than one. Just as the pion cloud about the nucleon can be produced by the pion-nucleon coupling, so may a comparably extended pion result from a pion-pion interaction. We attribute the meson production in meson-nucleon collisions to the mesonic Čerenkov emission accompanying passage of the target nucleon core through the incident pion. As a most immediate consequence, the pion-nucleon events are expected to display a single-cone structure, unlike the two-centred appearance of nucleon-nucleon events.

With the spirit of A, let us further assume that at sufficiently high energies, the mesonic Čerenkov effect — depending only upon the velocity of the source with respect to the medium — becomes essentially energy-independent. Remembering that it is the incident pion that acts as a dielectric medium, we conclude that *the multiple production events will appear energy-independent in the Lorentz system in which the incident pion is at rest.* The experimenter with a target of pions at rest exposed to cosmic ray protons would be unable to distinguish events of widely different energies with observations of the shower particles alone. To the less fortunate experimenter, our result is not so striking, since an energy-dependence to the angular distribution is introduced by the transformation to the system wherein the nucleon is at rest. However, the average meson multiplicity and distribution of transverse momenta are unaffected by this transformation, and are consequently expected to remain independent of primary energy.

To some extent, the hypothesized energy-independence of the angular distribution persists in the laboratory system. Let $F_0(\theta')$ be the integral angular distribution of shower particles in the rest system of the pion. Then,

$$F(\theta, \gamma) = F_0(\pi) - F_0(\theta') \tag{1}$$

is the corresponding distribution in the laboratory system †, where θ' is expressed in terms of the laboratory angle,

$$\tan \theta = \frac{1}{\gamma} \cot \tfrac{1}{2}\theta'. \tag{2}$$

Here, γ is the Lorentz factor of the incident pion, and all velocities are assumed relativistic for (2) to be valid. It follows from the energy-independence of F_0 that F depends only upon $\gamma \tan \theta$. Hence, any plot of F, or a function of F, against log tan θ cannot depend upon energy other than by its position along the abscissa. We predict that there is no systematic variation of the shape of the Duller-Walker plot [2]) (log $F/1-F$ versus log tan θ) with primary energy for pion-nucleon events. This is to be contrasted with the predictions of our model in the case of nucleon-nucleon collisions (A, fig. 2).

† See A for further details about this transformation.

A useful parameter describing the angular distribution of a multiple production event might be called "the Castagnoli determination of the Lorentz factor of the centre-of-mass",

$$\log \gamma_C = -\frac{1}{n}\sum_{i=1}^{i=n} \log \tan \theta_i, \tag{3}$$

where the sum is extended (in principle) over all the shower particles, and θ_i is the angle between the direction of the primary and the i-th shower particle. If the event is symmetric in the centre-of-mass, γ_C becomes the Lorentz factor of the centre-of-mass. For forward peaked distributions γ_C yields an overestimate of the energy, while for backward peaked distributions γ_C yields an underestimate. In most models, one expects a symmetric distribution in the centre-of-mass, hence

$$E = 2\gamma_C{}^2 m_N c^2 \tag{4}$$

is a conventional estimation of the primary energy of a pion-nucleon event. With our model, it is convenient to re-express (3) in the pion rest system, wherein the energy-independence of the model is explicit. Using eq. (2), eq. (3) becomes

$$\log \gamma_C = \log \gamma + \log \tan \tfrac{1}{2}\theta_1, \tag{5}$$

where θ_1 is a mean opening angle of the Čerenkov cone in the pion rest system,

$$\log \tan \tfrac{1}{2}\theta_1 = \frac{1}{n}\sum_{i=1}^{n} \log \tan \tfrac{1}{2}\theta_i, \tag{6}$$

and is consequently independent of primary energy. The dependence of the primary pion energy upon γ_C is now linear rather than quadratic,

$$E = \gamma_C m_\pi c^2 \cot \tfrac{1}{2}\theta_1. \tag{7}$$

To be more concrete, we shall assume that the opening angle of the Čerenkov cone in the pion-nucleon process is the same as that of the nucleon-nucleon process, and we shall use the value $\theta_1 = 10^{-2}$ radians determined in A. Expressions (4) and (7) will coincide at primary energies near 400 GeV. At lower energies, (4) will be an under-estimate (by a factor of 4 at 100 GeV), while at higher energies it will be an over-estimate (by a factor of 4 at 1600 GeV).

The preceding paragraph could equivalently have been discussed in terms of the angular distributions of the shower particles. Our model predicts that the opening angle of the event will vary with γ^{-1} much more rapidly than one would expect with other models. Thus we anticipate a distribution backward peaked in the centre-of-mass at primary energies less than 400 GeV, and a forward peaked distribution at higher energies. However, the experimental detection of this effect presupposes a knowledge of the velocity of the centre-of-mass, and hence of the energy of the event. For this reason we have preferred to

emphasize the connection between the angular distribution and the primary energy obtained with our model. Should the experimenter discover that (7) rather than (4) is a superior estimate of primary energy, he will, in effect, have verified that the angular distributions behave as we assert.

For the mesonic Čerenkov mechanism to function requires a sufficiently rapid transit of the nucleon through the incident pion. The condition for coherence,

$$\cos\theta = (n\beta)^{-1},$$

where n is the refractive index of an extended pion, and β is the velocity of the pion, must be satisfied for some angle θ of production of shower particles. For $n\beta \leqq 1$, the mesonic Čerenkov effect cannot take place. Assuming that the mean refractive index about a pion is the same as that of the meson cloud of a nucleon (which is estimated in A to be 1.00005), we find that the break-down of the Čerenkov effect occurs at a pion lab energy of 15 GeV. This is a factor m_π/m_N lower than the corresponding energy limit of the nucleon-nucleon effect, since it is the relative velocity of the two particles which is relevant. However, even at considerably larger energies the Čerenkov mechanism is not yet fully operative. From A we know that the energy contained in a Čerenkov cone (in the system in which the medium is at rest) is about 600 GeV. We shall assume that a similar energy pertains to the Čerenkov cone produced in pion-nucleon collisions. In the rest system of the incident pion, this much energy will be available for Čerenkov emission only at energies in excess of 700 GeV. Thus for the full effect to be realized requires a pion energy of (m_π/m_N) 700 GeV $\approx$ 100 GeV, and the predictions based upon energy-independence apply only to primary energies greater than 100 GeV.

The energy content of the Čerenkov cone in the lab. system is

$$E_s = \gamma(1-\cos\theta_1)\ 600\ \text{GeV} = 0.03\,\gamma m_N c^2$$

for pion energy beyond 100 GeV. Thus about 20 % of the energy of the primary pion is expected to be transferred to the shower particles. At lower energies, the contribution to the inelasticity due to the Čerenkov process should decrease linearly, and should vanish at a primary energy of 15 GeV.

We wish to acknowledge several valuable discussions with Professor Miesowicz and his group. One of us (S. L. G.) thanks the CERN laboratories for their hospitality while part of this work was completed, and is very grateful both to the Institute for Theoretical Physics of the University of Copenhagen and to the Institute for Nuclear Research of the Polish Academy of Sciences for making possible his stay in Poland.

References

1) W. Czyż, T. Ericson and S. L. Glashow, Nuclear Physics **13** (1959) 516
2) N. M. Duller and W. D. Walker, Phys. Rev. **93** (1954) 215
3) C. Castagnoli *et al.*, Nuovo Cim. **10** (1953) 1539

2.G

Nuclear Physics **20** (1960) 313—320; © *North-Holland Publishing Co., Amsterdam*

Not to be reproduced by photoprint or microfilm without written permission from the publisher

A STUDY OF THE ANGULAR DISTRIBUTIONS OF NEUTRONS LEADING TO THE GROUND STATE IN THE REACTION $^{12}C(^3He, n)^{14}O$

N. H. GALE, J. B. GARG, J. M. CALVERT and K. RAMAVATARAM

The Physical Laboratories, The University, Manchester

Received 7 June 1960

Abstract: A pulsed beam time-of-flight neutron spectrometer has been used to study the neutrons emitted from a target of ^{12}C bombarded with singly ionized ^3He particles having energies of 4.09, 4.62, 5.16 and 5.70 MeV. The angular distributions of the neutron group leading to the ground state of ^{14}O have been compared with a double stripping theory, and good agreement has been obtained with the theoretical prediction for transfer of zero orbital angular momentum. It is emphasised that the angular distributions alone are insufficient to distinguish between a stripping process or a direct knock-out mechanism, but arguments are advanced which favour the former. On the assumption that the mechanism of the reaction is that of double-stripping the results lead to the assignment of a spin zero and even parity to the ^{14}O ground state.

1. Introduction

Although a considerable amount of work has now been carried out on (^3He, p) and (^3He, d) reactions [1–5]), little work has yet been reported on (^3He, n) reactions. In particular, few measurements have been made of neutron angular distributions, and those which have been reported are all for fairly low bombarding energies.

It has been suggested that (^3He, n) reactions, in common with (^3He, p), (^3He, d) and (t, p) reactions, may at sufficiently high bombarding energies proceed predominantly by a stripping mechanism analogous to that which has been established for (d, p) and (d, n) reactions. It therefore appeared to be of considerable interest to investigate the reaction mechanism for the (^3He, n) process, especially because of the recent development of a theoretical treatment of the double-stripping process by Newns [6]). The interest in the (^3He, n) reaction is considerably enhanced because of the unusually severe selection rules applicable to it if it does indeed proceed by the double stripping process. A further factor of importance is that it affords the possibility of studying many proton-rich nucleides which have as yet been little investigated owing to the absence of suitable alternative reactions. It is clear that if the (^3He, n) reaction can be established as proceeding by a double-stripping process (at least for sufficiently high energies), it may become a very useful spectroscopic tool.

In order to provide some information on the (^{3}He, n) reaction the ^{12}C(^{3}He, n)^{14}O reaction was studied for bombarding energies in the range 4—6 MeV. Previous reported work on this reaction included a measurement of the excitation function in the range $1.3 \leqq E(^3\text{He}) \leqq 3.75$ MeV, and a measurement of the ground state threshold energy [7]). The same workers have also measured angular distributions of the neutron group to the ^{14}O ground state at bombarding energies of 1.89, 2.16, 2.40 and 2.51 MeV. Isotropic distributions were found at the two lower energies, whilst at the higher energies single minima were found in the angular distributions which appeared to reflect residual resonance structure in the yield curve. It is perhaps not surprising that stripping processes appear to be of little importance at these low bombarding energies.

2. Experimental Details

Singly charged ^{3}He ions were accelerated by the University of Manchester 6 MV Van der Graaff accelerator, and were analyzed by a 90° deflecting magnet. The energy calibration was obtained in terms of the threshold energies of the Li^7(p, n) and F^{19}(p, n) reactions, the energy of the analysed beam being stablized to better than $\frac{1}{2}$ %.

The ^{3}He particles were used to bombard a carbon target which was 250 μg · cm^{-2} thick. The energy loss in the target for the ^{3}He energies used in this work was about 175 keV. The target was prepared by making a colloidal suspension of graphite in alcohol and spraying a uniform film on a 127 μm thick gold backing. The area of the deposit was defined by masking, and the thickness determined by weighing.

The neutron spectra were obtained with a pulsed beam time-of-flight spectrometer similar to that described by Cranberg and Levin [8]), the details of which will be described elsewhere. Even for the ^{12}C(^{3}He, n)^{14}O reaction where (for bombarding energies below about 6 MeV) only the ground state neutron group is present, this technique has important advantages because of the facility with which the neutron group is distinguished from background neutrons of either higher or lower energy. This feature is especially important when the neutron angular distributions are to be studied, and results in a clear superiority of the instrument over such an alternative as the long counter, which is sensitive to low and high energy neutrons.

The chopping frequency employed was 4 MHz. A peak beam deflecting field strength of only 5 kV/cm was used in these measurements, resulting in a pulse duration of $\approx$ 1.25 ns. Even with a pulse length as long as this the time resolution is governed chiefly by the characteristics of the neutron detector, using currently available photomultiplier and fluor combinations [9]). No attempt was made to secure optimum time (and hence energy) resolution, since only a single neutron group was to be studied.

The electronic apparatus was used in a conventional fast-slow coincidence system. The two channels of the slow coincidence unit were operated respectively by pulses from the slow side channel of the neutron detector and by pulses from a "negative time" elimination circuit similar in principle to those described by Green and Bell [10]) and by Neilson *et al.* [11]). Conventional amplifiers and discriminators were employed in each channel of the slow coincidence system.

The neutron detector was an NE211 cell † consisting of liquid fluor in a glass cylinder, 5.5 cm long by 7.8 cm diameter, bonded by a short truncated conical light guide to a 6810A photomultiplier tube. The detector was mounted on a trolley which could be set at any desired distance from the target and moved round in angle so as to obtain the angular distribution. Since resolution was not critical in the present experiment, a flight path of 50 cm was used throughout.

The neutron detection efficiency depends on the fluor and on the setting of the discriminator bias in the slow side channel from the detector. The variation of the fluor detection efficiency with neutron energy was calculated by adapting the work of Swartz, Owen and Ames [12]) for stilbene to the case of NE211, including both the effect of direct n—p scattering and that of single carbon scattering followed by n—p scattering. The effect of the side-channel discriminator bias was determined empirically by using the ^{7}Li(p, n)^{7}Be reaction as a source of neutrons of known energy in the range 1.5 MeV $\leqq E_n \leqq$ 3 MeV, observing at each neutron energy the variation of neutron counting rate with bias. It was found possible to extrapolate with small error the resulting curves of neutron counting rate against bias to zero bias, and hence obtain at a number of different neutron energies the variation of electronic counting efficiency with bias. By combining the empirical counting efficiency with the calculated fluor detection efficiency, a family of curves was constructed giving the variation of absolute neutron detection efficiency with energy for different settings of the side channel bias. Each angular distribution was corrected for the dependence of efficiency on neutron energy.

The charge striking the target was measured with a current integrator; the average ^{3}He current after beam pulsing was about 5×10^{-9} A.

3. Results

A typical neutron time-of-flight spectrum is presented in fig. 1. As can be seen, the true-to-background ratio is good, and the shape of the line due to the neutron group is undistorted and quite symmetrical, hence the number of counts in the peak can be obtained unambiguously.

Angular distributions for incident ^{3}He energies of 4.09, 4.62, 5.16 and 5.7 MeV are presented in figs. 2 to 5. It will be noted that all the distributions show strong forward peaking, although the peak to valley ratio is greatest for the highest

† Supplied by Nuclear Enterprises Ltd., Edinburgh.

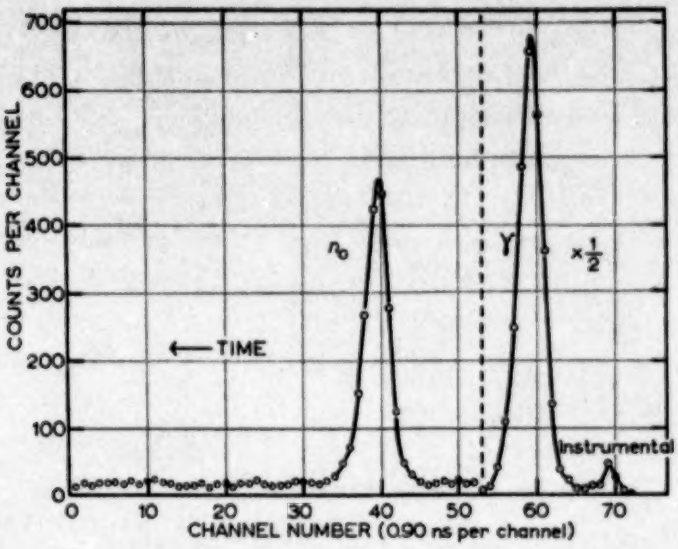

Fig. 1. Time-of-flight spectrum of neutrons and γ rays from the ^{3}He bombardment of ^{12}C at 5.70 MeV. The ground state group from the ^{12}C(^{3}He, n)^{14}O reaction is designated n_0. The time calibration is 0.90 ns per channel.

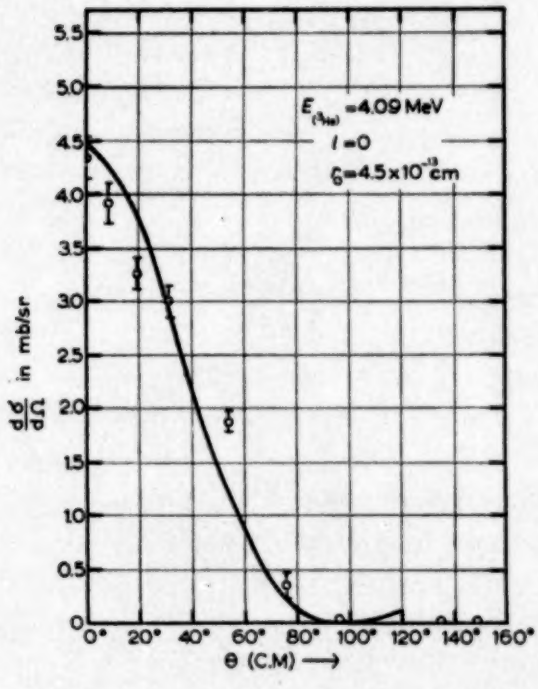

Fig. 2. Angular distribution of the neutron group corresponding to the ground state of ^{14}O from the reaction ^{12}C(^{3}He, n)^{14}O at a bombarding energy of 4.09 MeV. The solid curve is the zero order spherical Bessel function fit taking $r_0 = 4.5 \times 10^{-13}$ cm. The relative errors indicated on the figure are ± 4 %, but the error in the absolute differential cross section may be as large as ± 50 % (see text).

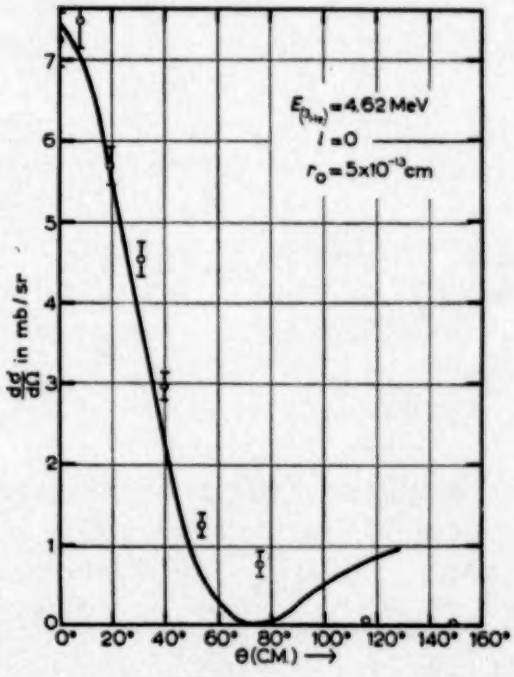

Fig. 3. Angular distribution of the ground state neutron group at a bombarding energy of 4.62 MeV. The solid curve is the fit for $l = 0$, $r_0 = 5 \times 10^{-13}$ cm.

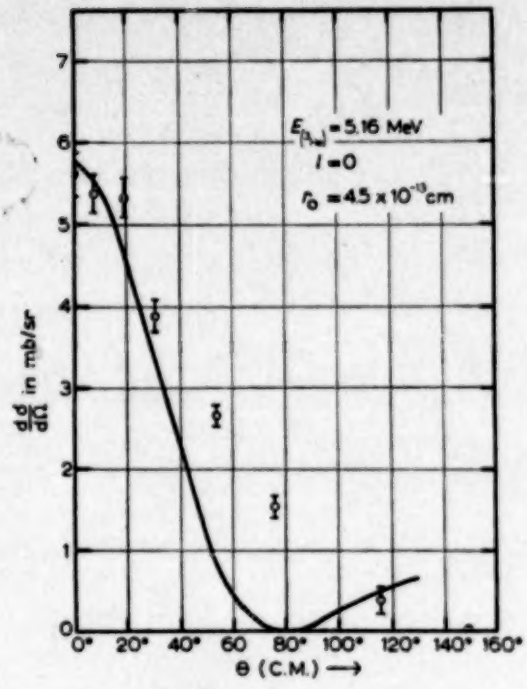

Fig. 4. Angular distribution of the ground state neutron group at a bombarding energy of 5.16 MeV. The solid curve is the fit for $l = 0, r_0 = 4.5 \times 10^{-13}$ cm.

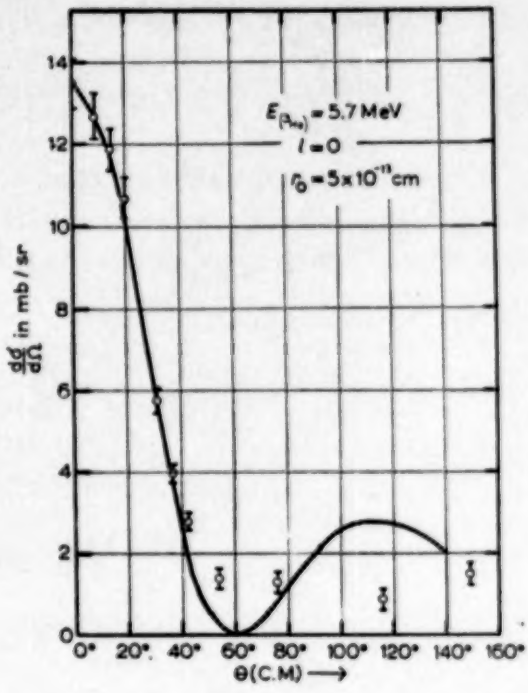

Fig. 5. Angular distribution of the ground state neutron group at a bombarding energy of 5.7 MeV. The solid curve is the fit for $l = 0, r_0 = 5 \times 10^{-13}$ cm.

bombarding energy investigated. The absolute differential cross sections may be in error by as much as ± 50 %, due to uncertainties in the calculated neutron detection efficiency, but the relative cross-sections are accurate to ± 4 %.

4. Discussion of Results

4.1. THEORY

Direct reactions other than the (d, p) and (d, n) stripping reactions have recently received a good deal of attention from both the theoretical and experimental aspects. Apart from heavy particle stripping, a considerable interest has been aroused in direct reactions proceeding by the transfer of two nucleons, such as the (^{3}He, p), (^{3}He, n), (t, p), (t, n) and (d, α) reactions. Newns [6]) has developed a theory for such reactions based on the assumption that they take place by a double-stripping process. The theory takes into account the structure of the stripped particles.

The result for the differential cross-section of the X(^{3}He, n)Y reaction is, in its most general form, difficult to compare with experiment. Newns gives several limiting forms which the cross-section assumes in various approximations. The differential cross-section in the limit that the ^{3}He nucleus is very

small is essentially of the form

$$\sum_l A_l\{j_l(Qr_0)\}^2,$$

where $j_l(Qr_0)$ is the spherical Bessel function of order l, Q is the absolute value of the momentum transfer vector $\mathbf{Q}$, and r_0 is the interaction radius. The momentum transfer vector is given by

$$\mathbf{Q} = \mathbf{k}(^3\mathrm{He}) - \frac{M_X}{M_Y}\mathbf{k}_n,$$

where the $\mathbf{k}$'s are the wave vectors of the incoming ^{3}He particle and the outgoing neutron. The allowed orders are found from the selection rule

$$\mathbf{J}_Y = \mathbf{J}_X + \mathbf{l} + \mathbf{S},$$

where $\mathbf{S}$ is the combined spin, and $\mathbf{l}$ the combined orbital angular momentum, of the captured protons. In addition, l is restricted to odd values if the parity of the residual nucleus differs from that of the target nucleus, and even values if it is the same. If more than one l value is allowed, the coefficients A_l depend on the configurations of the states involved.

In the case of (^{3}He, n) reactions (and also for (t, p) reactions, as has been remarked by Newns [6]), S can take only the value 0. Hence the selection rule is very restrictive, and in the special case where the spin of either initial or final states is zero at most one value of l is allowed. This immediately makes possible a unique spin assignment if that of either state is known beforehand to be zero. It also leads to the possibility of forbidden (^{3}He, n) double-stripping transitions; for example, a transition from a 0^+ state to a state of even spin and negative parity is forbidden by the double-stripping selection rules. It would appear important to investigate such cases to see whether or not the selection rules are obeyed.

It should be mentioned at this point that the knock-out reaction mechanism leads to an angular distribution experimentally indistinguishable from that predicted by the double stripping theory. The selection rules are less stringent than those applicable to double stripping. As for double-stripping, the angular distribution is essentially given by $j_1^2(Qr_0)$, where Q is now given by

$$\mathbf{Q} = \frac{M_X - M_n}{M_X}\left(\mathbf{k}(^3\mathrm{He}) - \frac{M_X}{M_Y}\mathbf{k}_n\right),$$

whilst the selection rule governing the allowed orders is

$$|\mathbf{J}_X + \mathbf{J}_Y + \mathbf{i}|_{\min} \leqq l \leqq J_X + J_Y + i,$$

where $\mathbf{i}$ is the vector sum of the spins of the entering and emerging particles.

4.2. OBSERVED ANGULAR DISTRIBUTIONS

The angular distributions presented in figs. 2 to 5 were analyzed by fitting to spherical Bessel functions $j_0^2(Qr_0)$; good fits were obtained with the interaction radii shown on the diagrams. The fit at the highest bombarding energy appears especially good, although in no case was there any evidence of a second maximum. No attempt was made to include the form factor proposed by Newns, since it appears that the error arising from the neglect of Coulomb and nuclear force distortions in the theory may easily outweigh the importance of this factor. In addition, no attempt was made to calculate the effect of the infinite series which appears in the full expression for the double-stripping differential cross-section. The justification for this is that calculations to allow for this effect have been made by Hinds and Middleton [1]) for the ^{9}Be(^{3}He, p)^{11}B reaction, and by Jaffe *et al.* [13]) for the reaction ^{16}O(t, p)^{18}O. In each case the inclusion of the correction had negligible effect on the shape of the theoretical angular distribution.

It is of some interest to compare the angular distributions for the ^{12}C(^{3}He, n)^{14}O reaction with those for the ^{12}C(t, p)^{14}C reaction. The (t, p) reaction has recently been studied by Jaffe *et al.* [13]) at a bombarding energy of 5.5 MeV. The angular distribution of protons leading to the ground state is quite similar to that obtained for the (^{3}He, n) ground state neutrons in the present work, and has been fitted to a spherical Bessel function with $l = 0$ and an interaction radius of 6.0×10^{-13} cm.

Since the angular distributions can be fitted by spherical Bessel functions $j_0^2(Qr_0)$, it is reasonable to conclude that in this experiment the reaction proceeds either by double-stripping or knock-on. As the ^{12}C nucleus is tightly bound, it appears plausible that the stripping process may be more probable than the knock-out process, but a theoretical calculation of the relative cross-sections for the two processes is necessary before a definite conclusion can be drawn.

Some further evidence favouring the stripping mechanism rather than the knock-out process is available from the work of Jaffe *et al.* on the analogous (t, p) reactions [13]). The selection rules for the knock-out process are less restrictive than those for the double-stripping process, and certain transitions forbidden by the latter are allowed on the knock-out interpretation. Several such cases occur in Jaffe's work, and in each case a spherical Bessel function angular distribution was not experimentally observed. In addition, the cross-sections for such transitions were found to be small compared with transitions to other states of the same nucleus allowed by the stripping selection rules. Two such cases occurred in the ^{12}C(t, p)^{14}C reaction.

If the ^{12}C(^{3}He, n)^{14}O reaction is assumed to proceed by the stripping process, then, since the ^{12}C ground state has spin zero, there is only one allowed value of l, and this must be equal to the previously unknown spin of the ^{14}O ground

state. The fit of the observed angular distributions with $l = 0$ thus gives the ground state spin of ^{14}O as zero, with even parity, in accordance with expectation from the general rule for the ground state in even nuclei, to which there is no known exception.

5. Conclusion

The four angular distributions obtained can be fitted quite well by the double-stripping theory, and lead to an assignment for the spin and parity of the ^{14}O ground state which is in accord with expectation. It appears that in this case the direct reaction mechanism predominates, but much more work is required to establish the (^{3}He, n) reaction as a useful and reliable spectroscopic tool. In particular, experimental and theoretical work is required to enable an unambiguous distinction to be made between the double-stripping and knock-out reaction mechanisms.

We are indebted to Dr. H. C. Newns and to Dr. A. A. Jaffe and his co-workers who have kindly communicated their work to us prior to publication.

References

1) S. Hinds and R. Middleton, Proc. Phys. Soc. **74** (1959) 196
2) S. Hinds and R. Middleton, Proc. Phys. Soc. **74** (1959) 762
3) P. D. Forsyth, F. de S. Barros, A. A. Jaffe, I. J. Taylor and S. Ramavataram, Proc. Phys. Soc. **75** (1960) 291
4) I. J. Taylor, F. de S. Barros, P. D. Forsyth, A. A. Jaffe and S. Ramavataram, Proc. Phys. Soc. (1960), In press
5) D. A. Bromley and E. Almquist, Chalk River Report C.R.P. 881 (1959)
6) H. C. Newns, (1960), to be published
7) D. A. Bromley, E. Almquist, H. E. Gove, A. E. Litherland, E. B. Paul and A. J. Ferguson, Phys. Rev. **105** (1957) 957
8) L. Cranberg and J. S. Levin, Phys. Rev. **100** (1955) 434
9) J. H. Neiler and W. M. Good, Fast neutron physics (Interscience, New York, 1960) Vol. 1, Ch. IV
10) R. F. Green and R. E. Bell, Nuclear Instruments **3** (1958) 127
11) G. C. Neilson, W. K. Dawson and Fl A. Johnson, Rev. Sci. Inst. **30** (1959) 963
12) C. D. Swartz, G. E. Owen and O. Ames, A.E.C. report NYO-2053
13) A. A. Jaffe, F. de S. Barros, P. D. Forsyth, J. Muto, I. J. Taylor and S. Ramavataram, Proc. Phys. Soc. (1960), in press

1.C:6B:
7.A

Nuclear Physics **20** (1960) 321—346; © *North-Holland Publishing Co., Amsterdam*
Not to be reproduced by photoprint or microfilm without written permission from the publisher

EXTENSION D'UNE FORMULE DE LAGRANGE À DES PROBLÈMES DE VALEURS PROPRES

JACQUES DES CLOIZEAUX

Service de Physique Mathématique, Centre d'Études Nucléaires de Saclay, Gif-sur-Yvette (S. et O.)

Reçu le 2 juin 1960

Abstract: An implicit eigenvalue equation may be transformed into an ordinary eigenvalue problem by generalizing the Lagrange formula to operators. A method is given to build a constant operator h which has the same eigenvalues and eigenvectors as the original equation. Moreover it is possible to find a hermitian operator K which has the same eigenvalues and whose eigenvectors are related in a simple way to the original ones.

The method is applied to the calculation of perturbation expansions for bound states starting from the Brillouin-Wigner formula. In this case, the eigenvectors of K have a simple geometric meaning and may be considered as good unperturbed wave functions.

1. Introduction

Dans divers problèmes de mécanique quantique, on rencontre des équations aux valeurs propres de la forme suivante:

$$[E-e-H(E)]|\varphi_E\rangle = 0. \tag{1}$$

Dans cette équation, e est une constante réelle, $H(\varepsilon)$ est un opérateur hermitique pour toutes les valeurs réelles de ε et $|\varphi_E\rangle$ est une fonction propre relative à la valeur propre E.

Parmi les nombreuses équations appartenant à ce type, nous pouvons citer la formule de Brillouin-Wigner [1]) utilisée en calcul des perturbations, l'équation de Bethe-Salpeter [2-3]) qui représente approximativement en théorie des champs l'interaction de deux particules habillées, et l'équation de Bloch-Horowitz [4]) qui permet de déterminer les premiers états d'un système de fermions lorsque l'état de base non perturbé est dégénéré.

En général, on peut trouver que l'ensemble des fonctions propres $|\varphi\rangle$, solutions de l'équation (1) forme un système complet de fonctions linéairement indépendantes. Il existe alors un opérateur linéaire h tel que les fonctions $|\varphi_E\rangle$, solutions de l'équation (1), soient fonctions propres de cet opérateur et tel que la valeur propre correspondante de h vaille $(E-e)$. Nous écrirons

$$(E-e-h)|\varphi_E\rangle = 0. \tag{2}$$

Soit alors $\sigma(\varepsilon)$ une valeur propre de l'opérateur $H(\varepsilon)$,

$$[H(\varepsilon)-\sigma(\varepsilon)]|\varphi_\varepsilon\rangle = 0, \tag{3}$$

l'équation (1) peut s'écrire

$$[E-e-\sigma(E)]|\varphi_E\rangle = 0$$

ou plus simplement

$$E-e-\sigma(E) = 0. \tag{4}$$

La valeur propre E, solution de cette équation, peut être calculée de façon explicite en utilisant la formule de Lagrange [5])

$$E-e-\sum_{n=1}^{\infty} \frac{1}{n!} \frac{\mathrm{d}^{n-1}}{\mathrm{d}e^{n-1}} [\sigma(e)]^n = 0. \tag{5}$$

Ainsi les valeurs propres de l'opérateur h s'expriment explicitement en fonction des valeurs propres de l'opérateur $H(\varepsilon)$. On peut alors se poser le problème suivant: Connaissant l'opérateur $H(\varepsilon)$ peut-on construire explicitement l'opérateur h?

Il existe un cas simple où la question peut être immédiatement résolue. Considérons en effet les opérateurs hermitiques $\Sigma(\varepsilon)$ qui restent diagonaux par rapport à une base orthogonale fixe lorsque ε varie. Autrement dit, $\Sigma(\varepsilon)$ et $\Sigma(\varepsilon')$ commutent quels que soient ε et ε'. Ces opérateurs $\Sigma(\varepsilon)$ sont analogues aux opérateurs de self-énergie.

Dans ce cas, on peut immédiatement généraliser la formule de Lagrange et l'on retrouve ainsi la formule (2) à condition de poser

$$h = \sum_{n=1}^{\infty} \frac{1}{n!} \frac{\mathrm{d}^{n-1}}{\mathrm{d}e^{n-1}} [\Sigma(\varepsilon)]^n. \tag{6}$$

Remarquons par ailleurs que dans ce cas, l'opérateur h est hermitique, les fonctions $|\varphi_E\rangle$ formant un système orthogonal.

Dans le cas général, l'extension de la formule de Lagrange est encore possible mais le résultat n'est pas trivial. Dans la suite de cet article, nous nous proposons de montrer comment on peut construire l'opérateur h dans tous les cas, au moins formellement. Les questions de convergence des développements ne seront qu'effleurées.

Par ailleurs, remarquons que dans le cas général, l'opérateur h n'est pas hermitique bien qu'il possède des valeurs propres réelles. En effet, il n'y a aucune raison pour que les fonctions propres $|\varphi_E\rangle$, solutions de l'équation (1), soient orthogonales.

Par conséquent, l'équation (2) n'est pas une véritable équation de Schrödinger. Son interprétation soulève quelques difficultés et ses solutions ne peuvent être considérées comme représentant exactement des états physiques au moins si l'on néglige les phénomènes de dissipation. En effet, le plus souvent, les équations du type (1) décrivent des interactions existant entre des états renormalisés ou habillés. Nous pensons que cet habillage peut théoriquement

être réalisé en effectuant sur l'hamiltonien complet du système une transformation canonique. Cette transformation conserve l'orthogonalité des fonctions d'onde. L'interaction entre les états habillés doit donc être décrite par une véritable équation de Schrödinger.

Cette remarque nous suggère de transformer l'équation (2). À chaque fonction $|\varphi\rangle$ nous ferons correspondre une fonction $|\phi\rangle$ par la transformation

$$|\phi\rangle = g|\varphi\rangle, \tag{7}$$

l'opérateur g étant un opérateur linéaire possédant un inverse.

Les nouvelles fonctions $|\phi\rangle$ sont fonctions propres de l'équation suivante:

$$(E-e-K)|\phi\rangle = 0, \tag{8}$$

avec

$$K = ghg^{-1}. \tag{9}$$

Nous montrerons plus loin qu'il est possible de choisir g de telle façon que l'opérateur K soit hermitique. Cet opérateur K joue alors le rôle d'un véritable hamiltonien et les fonctions propres $|\phi\rangle$ solutions de l'équation (8) forment un système orthonormé.

Par ailleurs, nous désirons que les fonctions $|\phi\rangle$ restent aussi voisines que possible des fonctions $|\varphi\rangle$. Cette condition sera réalisée si l'on exige que l'opérateur g soit hermitique. Ainsi la transformation (7) sera une simple affinité orthogonale réelle dans l'espace des fonctions d'onde.

Cette restriction ne suffit pas à déterminer exactement la forme de g. Toutefois, nous montrerons que l'on peut définir de façon naturelle des opérateurs K et g qui soient hermitiques. Ces opérateurs seront exprimés de manière explicite en fonction de $H(\varepsilon)$. Les développements obtenus constituent une deuxième extension de la formule de Lagrange.

L'établissement des lois de formation des opérateurs h, g et K formera la première partie de cet article. Ces opérateurs s'expriment facilement en fonction d'opérateurs hermitiques A et B qui s'expriment eux-mêmes en fonction de $H(\varepsilon)$ par des intégrales de contour dans le plan complexe. Dans la deuxième partie de cet article, ces résultats sont appliqués à l'étude des perturbations des états liés. Nous partirons de la formule de Brillouin-Wigner et nous montrerons que, dans ce cas, nos opérateurs A et B coïncident avec les opérateurs A et B définis par Kato[6]), tandis que l'opérateur h est identique à un opérateur $\mathscr{A}$ déjà calculé par Bloch[7]). En outre, il sera possible de donner aux fonctions $|\phi\rangle$, solutions de l'équation (8), une interprétation géométrique simple.

2. Systèmes de Vecteurs associés à un Ensemble de Vecteurs Non Orthogonaux

Les fonctions propres $|\varphi_E\rangle$ forment un système de vecteurs non orthogonaux. Par conséquent, il est utile d'étudier les propriétés géométriques de ces systèmes.

Soit donc n vecteurs $|\alpha\rangle$ linéairement indépendants mais quelconques qui définissent un espace Ω à n dimensions. Nous allons montrer qu'aux vecteurs $|\alpha\rangle$, on peut associer de façon naturelle deux autres systèmes de vecteurs que nous désignerons par les symboles $|\bar{\alpha}\rangle$ et $|\hat{\alpha}\rangle$.

Tout d'abord, dans l'espace Ω, nous pouvons associer aux vecteurs $|\alpha\rangle$, les vecteurs $|\bar{\alpha}\rangle$ qui forment avec les vecteurs $|\alpha\rangle$ un système biorthogonal, ce qui s'écrit ainsi:

$$\langle\bar{\beta}|\alpha\rangle = \langle\beta|\bar{\alpha}\rangle = \delta_{\alpha\beta}. \tag{10}$$

Les vecteurs $|\bar{\alpha}\rangle$ sont eux aussi linéairement indépendants. On peut généraliser la correspondance entre les vecteurs $|\alpha\rangle$ et les vecteurs $|\bar{\alpha}\rangle$. Soit en effet, dans Ω, un vecteur quelconque $|l\rangle$ donné par le développement

$$|l\rangle = \sum \lambda_\alpha |\alpha\rangle. \tag{11}$$

Nous pouvons lui faire correspondre le vecteur

$$|\bar{l}\rangle = \sum \lambda_\alpha |\bar{\alpha}\rangle. \tag{12}$$

Définissons alors dans Ω l'opérateur G

$$G = \sum_\alpha |\bar{\alpha}\rangle\langle\bar{\alpha}|. \tag{13}$$

Cet opérateur permet de passer des vecteurs $|l\rangle$ aux vecteurs $|\bar{l}\rangle$:

$$G|l\rangle = |\bar{l}\rangle. \tag{14}$$

L'opérateur G^{-1} inverse de G dans Ω se définit de façon analogue,

$$G^{-1} = \sum_\alpha |\alpha\rangle\langle\alpha|, \tag{15}$$

et l'on a évidemment

$$G^{-1}|\bar{l}\rangle = |l\rangle. \tag{16}$$

L'opérateur G est défini positif. En effet, $|l\rangle$ étant un vecteur non nul quelconque, défini par le développement (11), nous avons

$$\langle l|G|l\rangle = \sum |\lambda_\alpha|^2 > 0. \tag{17}$$

L'opérateur G possède donc n vecteurs propres orthogonaux associés à n valeurs propres positives.

Soit $|x_j\rangle$ l'un des vecteurs propres et S_j la valeur propre correspondante:

$$G|x_j\rangle = S_j|x_j\rangle = |\bar{x}_j\rangle. \tag{18}$$

Les vecteurs $|x_j\rangle$ et $|\bar{x}_j\rangle$ sont donc colinéaires.

Nous pouvons normer les vecteurs $|x_j\rangle$ de telle façon que les vecteurs $|x_j\rangle$ et $|\bar{x}_j\rangle$ forment un système biorthogonal.

Comme les vecteurs $|x_j\rangle$ et $|\bar{x}_j\rangle$ sont colinéaires et vecteurs propres d'un opérateur hermitique, il suffit de poser

$$\langle x_j|\bar{x}_j\rangle = \langle \bar{x}_j|x_j\rangle = 1. \tag{19}$$

De l'égalité (18) nous tirons alors

$$S_j = \langle \bar{x}_j|\bar{x}_j\rangle = (\langle x_j|x_j\rangle)^{-1}. \tag{20}$$

L'opérateur G peut maintenant s'écrire

$$G = \sum_j |\bar{x}_j\rangle\langle \bar{x}_j|, \tag{21}$$

et de même nous aurons

$$G^{-1} = \sum_j |x_j\rangle\langle x_j|. \tag{22}$$

Introduisons alors les vecteurs $|\hat{x}_j\rangle$ définis ainsi:

$$|\hat{x}_j\rangle = S_j^{\frac{1}{2}}|x_j\rangle = S_j^{-\frac{1}{2}}|\bar{x}_j\rangle. \tag{23}$$

Les vecteurs $|\hat{x}_j\rangle$ forment un système orthonormé. En effet

$$\langle \hat{x}_j|\hat{x}_j\rangle = \langle \bar{x}_j|x_j\rangle = 1. \tag{24}$$

Le système des vecteurs $|\hat{x}_j\rangle$ n'est défini de manière unique (à un facteur de phase près) que si les valeurs propres de G sont non dégénérées. Dans le cas contraire, le choix des vecteurs $|\hat{x}_j\rangle$ orthonormés reste soumis à un certain arbitraire. Toutefois les définitions des divers opérateurs et des transformations que nous considérons plus loin, sont indépendantes de ce choix.

En particulier, l'opérateur G s'exprime ainsi:

$$G = \sum_j |\hat{x}_j\rangle S_j \langle \hat{x}_j|. \tag{25}$$

Appliquer l'opérateur G à un vecteur $|l\rangle$ revient à effectuer une simple affinité orthogonale.

Nous pouvons maintenant introduire l'opérateur g tel que

$$G = g^2, \tag{26}$$

$$g = \sum_j |\hat{x}_j\rangle S_j^{\frac{1}{2}}\langle \hat{x}_j| = \sum_j |\hat{x}_j\rangle\langle \bar{x}_j| = \sum_j |\bar{x}_j\rangle\langle \hat{x}_j|, \tag{27}$$

$$g^{-1} = \sum_j |\hat{x}_j|\rangle S_j^{-\frac{1}{2}}\langle \hat{x}_j| = \sum_j |\hat{x}_j\rangle\langle x_j| = \sum_j |x_j\rangle\langle \hat{x}_j|. \tag{28}$$

L'opérateur g est défini positif.

Nous pouvons maintenant associer en toute généralité, aux vecteurs $|l\rangle$ et $|\hat{l}\rangle$, le vecteur $|\hat{l}\rangle$ défini par les égalités

$$|\hat{l}\rangle = g|l\rangle, \quad |\hat{l}\rangle = g|\hat{l}\rangle. \tag{29}$$

Les vecteurs $|\bar{l}\rangle$ sont intermédiaires entre les vecteurs $|l\rangle$ et les vecteurs $|\bar{\bar{l}}\rangle$.

En particulier, nous pouvons définir ainsi les vecteurs $|\hat{\alpha}\rangle$,

$$|\hat{\alpha}\rangle = g|\alpha\rangle, \quad |\bar{\alpha}\rangle = g|\hat{\alpha}\rangle. \tag{30}$$

Les vecteurs $|\hat{\alpha}\rangle$ sont orthonormés; en effet

$$\langle\hat{\beta}|\hat{\alpha}\rangle = \langle\bar{\beta}|g^{-1}g|\alpha\rangle = \langle\bar{\beta}|\alpha\rangle = \delta_{\alpha\beta}. \tag{31}$$

Les opérateurs g et g^{-1} s'expriment facilement en fonction des vecteurs $|\alpha\rangle$, $|\bar{\alpha}\rangle$ et $|\hat{\alpha}\rangle$,

$$g = \sum_{\alpha} |\hat{\alpha}\rangle\langle\bar{\alpha}| = \sum_{\alpha} |\bar{\alpha}\rangle\langle\hat{\alpha}|, \tag{32}$$

$$g^{-1} = \sum_{\alpha} |\hat{\alpha}\rangle\langle\alpha| = \sum_{\alpha} |\alpha\rangle\langle\hat{\alpha}|. \tag{33}$$

Les vecteurs $|\hat{\alpha}\rangle$ forment le système de vecteurs orthonormés le plus simple que l'on puisse associer aux vecteurs $|\alpha\rangle$.

Remarquons que lorsque les normes des vecteurs $|\alpha\rangle$ varient, la direction des vecteurs $|\bar{\alpha}\rangle$ reste fixe mais leurs normes varient; au contraire, dans ce cas, les normes des vecteurs $|\hat{\alpha}\rangle$ restent égales à l'unité mais leurs directions varient.

Toutefois, nous pensons que si les vecteurs $|\alpha\rangle$ représentent certaines solutions d'une équation aux valeurs propres, il existe en général un système bien défini de vecteurs $|\hat{\alpha}\rangle$ auxquels on peut attribuer une interprétation physique simple. Il en est d'ailleurs ainsi dans un cas particulier que nous étudierons plus loin.

3. Définition des Opérateurs *A* et *B*

Pour une valeur réelle de ε, l'opérateur $H(\varepsilon)$ est hermitique et en désignant par $|j, \varepsilon\rangle$ ses vecteurs propres et par $\sigma_j(\varepsilon)$ les valeurs propres correspondantes, on peut l'exprimer sous la forme

$$H(\varepsilon) = \sum_{j} |j, \varepsilon\rangle\sigma_j(\varepsilon)\langle j, \varepsilon|. \tag{34}$$

En général, cet opérateur pourra être prolongé dans le plan complexe. Soit $\mathscr{D}$ un domaine du plan complexe limité par la courbe $\mathscr{C}$ et tel que $H(\varepsilon)$ soit partout régulier dans $\mathscr{D}$ et sur la courbe $\mathscr{C}$ sauf peut-être en des points isolés (pôles). Le domaine $\mathscr{D}$ contient un certain nombre de valeurs propres E_α de l'équation (1). Les valeurs propres sont supposées isolées et non dégénérées (voir fig. 1).

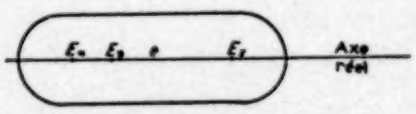

Fig. 1. Contour d'intégration dans le plan complexe pour le calcul des opérateurs *A* et *B*.

Les vecteurs propres correspondants sont les vecteurs $|\alpha\rangle$,

$$[E_\alpha - e - H(E_\alpha)]|\alpha\rangle = 0. \tag{35}$$

En particulier si, sur le contour $\mathscr{C}$, l'une des valeurs propres de $H(\varepsilon)$, soit $\sigma_1(\varepsilon)$, satisfait à la condition suivante:

$$|\sigma_1(\varepsilon)| < |\varepsilon - e|, \tag{36}$$

le théorème de Lagrange permet d'affirmer que l'équation

$$E - e - \sigma_1(E) = 0 \tag{37}$$

admet une racine E_α appartenant au domaine $\mathscr{D}$ et donnée par la formule

$$E_\alpha - e = \sum_{n=1}^{\infty} \frac{1}{n!} \frac{\mathrm{d}^{n-1}}{\mathrm{d}e^{n-1}} [\sigma_1(e)]^n. \tag{38}$$

De façon plus générale, lorsque ε tend vers une valeur propre E_α de l'équation (35), il existe un indice j, soit $j = 1$, tel que $[\varepsilon - e - \sigma_1(\varepsilon)] \to 0$ et tel que $|1, \varepsilon\rangle \to a|\alpha\rangle$ (a étant un coefficient de normalisation).

Cherchons maintenant à transformer les équations (35). Dans ce but, nous pouvons introduire les opérateurs A et B qui sont définis par des intégrales de contour (le contour $\mathscr{C}$ est décrit dans le sens trigonométrique),

$$A = \frac{1}{2\pi i} \int_{\mathscr{C}} \frac{\varepsilon - e}{\varepsilon - e - H(\varepsilon)} \, \mathrm{d}\varepsilon, \tag{39}$$

$$B = \frac{1}{2\pi i} \int_{\mathscr{C}} \frac{1}{\varepsilon - e - H(\varepsilon)} \, \mathrm{d}\varepsilon. \tag{40}$$

De l'égalité (34), nous pouvons tirer l'expression

$$[\varepsilon - e - H(\varepsilon)]^{-1} = \sum_j |j, \varepsilon\rangle [\varepsilon - e - \sigma_j(\varepsilon)]^{-1} \langle j, \varepsilon|. \tag{41}$$

Cet opérateur possède un pôle pour $\varepsilon = E_\alpha$ et pour des valeurs de ε voisines de ce pôle, on peut écrire

$$[\varepsilon - e - H(\varepsilon)]^{-1} \approx |\alpha\rangle |a|^2 [\varepsilon - E_\alpha]^{-1} [1 - \sigma'_1(E_\alpha)]^{-1} \langle\alpha|. \tag{42}$$

Nous pouvons encore simplifier cette expression.

Décrivons l'égalité (34) par rapport à ε, puis faisons tendre ε vers E_α. En prenant l'élément de matrice de $[1 - H'(E_\alpha)]$ par rapport à $|\alpha\rangle$, on obtient

$$\langle\alpha|1 - H'(E_\alpha)|\alpha\rangle = |a|^{-2} [1 - \sigma'_1(E_\alpha)]. \tag{43}$$

Des relations (42) et (43), on tire la partie principale de l'opérateur $[\varepsilon - e - H(\varepsilon)]^{-1}$ pour ε voisin de E_α,

$$[\varepsilon - e - H(\varepsilon)]^{-1} \approx |\alpha\rangle [\varepsilon - E_\alpha]^{-1} [\langle\alpha|1 - H'(E_\alpha)|\alpha\rangle]^{-1} \langle\alpha|. \tag{44}$$

Cet opérateur ne possède pas d'autres singularités que des poles aux points E_α. Les pôles de $H(\varepsilon)$ en effet ne sont pas des singularités pour l'opérateur $[\varepsilon - e - H(\varepsilon)]^{-1}$. En conséquence, les opérateurs A et B sont bien définis.

En utilisant les égalités (44), on peut les exprimer en fonction des vecteurs $|\alpha\rangle$,

$$A = \sum_\alpha |\alpha\rangle \frac{E_\alpha - e}{\langle\alpha|1 - H'(E_\alpha)|\alpha\rangle} \langle\alpha|, \tag{45}$$

$$B = \sum_\alpha |\alpha\rangle \frac{1}{\langle\alpha|1 - H'(E_\alpha)|\alpha\rangle} \langle\alpha|. \tag{46}$$

Ces représentations des opérateurs A et B permettent de montrer que les vecteurs $|\alpha\rangle$ sont solutions des équations aux valeurs propres suivantes:

$$[A - (E_\alpha - e)B]|\tilde{\alpha}\rangle = 0. \tag{47}$$

Les opérateurs A et B sont hermitiques.

4. Construction des Opérateurs h, g et K à partir des Opérateurs A et B

L'opérateur B admet dans l'espace Ω un inverse que l'on peut écrire

$$B^{-1} = \sum_\alpha |\tilde{\alpha}\rangle\langle\alpha|1 - H'(E_\alpha)|\alpha\rangle\langle\tilde{\alpha}|. \tag{48}$$

L'opérateur h peut être défini ainsi:

$$h = AB^{-1}. \tag{49}$$

Des expressions (45) et (48), nous tirons immédiatement une représentation de h:

$$h = \sum_\alpha |\alpha\rangle E_\alpha \langle\tilde{\alpha}|. \tag{50}$$

Les vecteurs $|\alpha\rangle$ sont donc solutions de l'équation aux valeurs propres suivante qui n'est autre que l'équation (2):

$$[h - (E_\alpha - e)]|\alpha\rangle = 0. \tag{51}$$

Nous allons maintenant montrer que si tous les éléments de matrice $\langle\alpha|1 - H'(E_\alpha)|\alpha\rangle$ sont positifs, il est possible d'associer aux vecteurs $|\alpha\rangle$ et de façon très naturelle un ensemble de vecteurs orthonormés $|\hat{\alpha}\rangle$.

L'élément de matrice $\langle\alpha|1 - H'(E_\alpha)|\alpha\rangle$ est positif, si l'on a $\sigma'_1(E_\alpha) < 1$. Cette condition est satisfaite, en particulier, si pour toutes les valeurs réelles de ε comprises dans le domaine $\mathscr{D}$, l'opérateur $H'(\varepsilon)$ est borné et si la borne est inférieure à l'unité. Cette circonstance n'est pas exceptionnelle et par exemple se présente lorsque l'opérateur $H(\varepsilon)$ est relativement petit et représente une perturbation.

Considérons le cas où tous les éléments de matrice $\langle\alpha|1-H'(E_\alpha)|\alpha\rangle$ sont positifs. Jusqu'ici, les normes des vecteurs $|\alpha\rangle$, solutions des équations (35), sont restées arbitraires. Si nous voulons définir des vecteurs $|\hat{\alpha}\rangle$ nous devons fixer ces normes. Un moyen commode consiste à poser

$$\langle\alpha|1-H'(E_\alpha)|\alpha\rangle = 1. \tag{52}$$

Les vecteurs $|\alpha\rangle$ étant bien définis, nous pouvons introduire un système de vecteurs orthonormés $|\hat{\alpha}\rangle$ comme nous l'avons fait à la section 2.

Remarquons alors que les conditions (52) assurent l'identité de l'opérateur B et de l'opérateur G^{-1} défini plus haut (cf. formules (15) et (46)). Dans le cas présent, l'opérateur B est par conséquent défini positif.

L'opérateur g défini positif peut être déterminé de manière unique par l'égalité

$$g^2 = B^{-1}, \tag{53}$$

ce que nous écrivons

$$g = B^{-\frac{1}{2}}. \tag{54}$$

Nous pouvons maintenant définir l'opérateur hermitique K

$$K = ghg^{-1} = B^{-\frac{1}{2}}hB^{\frac{1}{2}} = B^{-\frac{1}{2}}AB^{-\frac{1}{2}}. \tag{55}$$

Les opérateurs A, B, h, g et K sont maintenant bien déterminés. Cherchons à les exprimer explicitement par des développements en fonction de l'opérateur $H(\varepsilon)$.

5. Développement des Opérateurs A et B

Nous pouvons développer les opérateurs A et B en fonction de l'opérateur $H(e)$ et de ses dérivées successives $H^{(n)}(e)$ au point $\varepsilon = e$, si les énoncés suivants sont exacts:

1) Le point $\varepsilon = e$ est un point du domaine $\mathscr{D}$ circonscrit par la courbe $\mathscr{C}$.

2) Sur la courbe $\mathscr{C}$ l'opérateur $H(\varepsilon)$ est borné par le module de $(\varepsilon-e)$ ce que nous écrivons

$$|H(\varepsilon)| < |\varepsilon-e| \quad \text{sur} \quad \mathscr{C}. \tag{56}$$

(Cf. inégalité (36)).

Admettons que les conditions 1 et 2 soient réalisées, l'opérateur $[\varepsilon-e-H(\varepsilon)]^{-1}$ peut être développé en série entière:

$$[\varepsilon-e-H(\varepsilon)]^{-1} = \sum_{n=0}^{\infty} [H(\varepsilon)]^n [\varepsilon-e]^{-(n+1)}. \tag{57}$$

Les opérateurs A et B qui sont donnés par les intégrales de contour (39) et (40) s'expriment ainsi:

$$A = \sum_{n=0}^{\infty} \frac{1}{2\pi i} \int_{\mathscr{C}} \frac{[H(\varepsilon)]^n}{[\varepsilon-e]^n}\, d\varepsilon, \tag{58}$$

$$B = \sum_{n=0}^{\infty} \frac{1}{2\pi i} \int_{\mathscr{C}} \frac{[H(\varepsilon)]^n}{[\varepsilon - e]^{n+1}} \, d\varepsilon. \tag{59}$$

Ces intégrales se calculent par la méthode des résidus et l'on obtient

$$A = \sum_{n=1}^{\infty} \frac{1}{(n-1)!} \frac{d^{n-1}}{de^{n-1}} [H(e)]^n, \tag{60}$$

$$B = 1 + \sum_{n=1}^{\infty} \frac{1}{n!} \frac{d^n}{de^n} [H(e)]^n. \tag{61}$$

6. Représentation des Opérateurs par des Suites de Nombres; Définitions et Notations

Soit ω l'un des opérateurs que nous considérons dans cet article, par exemple A ou B. Moyennant certaines conditions, nous pouvons l'exprimer sous forme d'une série

$$\omega = \omega_0 + \omega_1 + \ldots + \omega_n + \ldots. \tag{62}$$

Chaque opérateur ω_n est constitué par un ensemble fini de termes de la forme suivante

$$R(\mu_1, \mu_2 \ldots \mu_n) H^{(\mu_1)}(e) H^{(\mu_2)}(e) \ldots H^{(\mu_n)}(e) / \mu_1! \mu_2! \ldots \mu_n!. \tag{63}$$

Dans cette expression $H^{(\mu)}(e)$ est la dérivée d'ordre μ de l'opérateur $H(e)$ et les coefficients $R(\mu_1, \mu_2 \ldots \mu_n)$ sont purement numériques.

À ces termes, nous pouvons faire correspondre des suites de nombres $\{\mu_1, \mu_2 \ldots \mu_n\}$, les nombres μ étant entiers, positifs ou nuls. L'opérateur ω est bien déterminé si l'on connaît d'une part la loi de formation des suites $\{\mu_1, \mu_2 \ldots \mu_n\}$ et d'autre part la valeur des coefficients numériques afférents.

En particulier, si l'opérateur ω correspond à des suites $\{\tau\}$ et si tous les coefficients numériques $R(\mu_1, \mu_2 \ldots \mu_n)$ sont égaux à l'unité, nous dirons que l'opérateur ω correspond „exactement" aux suites $\{\tau\}$ et nous écrirons

$$\omega \to \{\tau\}.$$

Ainsi par exemple $H(e) \to \{0\}$, $H'(e) \to \{1\}$ et $\frac{1}{2} H'(e) H''(e) \to \{1, 2\}$.

Par ailleurs, à toute suite

$$\{M\} \equiv \{\mu_1, \mu_2 \ldots \mu_n\} \equiv \{\nu_n \ldots \nu_2, \nu_1\}$$

nous associerons les sommes $S_{\mu, n}(p)$ et $S^+_{\mu, n}(p)$ définies comme suit:

$$S_{\mu, n}(p) = \sum_{r=1}^{r=p} \mu_r - p, \tag{64}$$

$$S^+_{\mu, n}(p) = \sum_{r=1}^{r=p} \nu_r - p. \tag{65}$$

Les lois de formation des suites $\{M\}$ figurant dans cet article s'exprimeront très simplement en fonction des sommes $S_{\mu,n}(p)$ ou $S^{+}_{\mu,n}(p)$.

7. Répresentation des Opérateurs A et B; Définition de l'Opérateur C

Il ressort des égalités (60) et (61) que les opérateurs A et $(B-1)$ correspondent exactement à des suites $\{A\}$ et $\{B-1\}$ définies par les critères suivants (pour chaque opérateur, le nombre n correspond au terme ω_n du développement (62)):

$$(A \to \{A\}) \quad S_{A,n}(n) = -1, \tag{66}$$

$$((B-1) \to \{B-1\}) \quad S_{B-1,n}(n)=0. \tag{67}$$

On vérifie facilement sur ces développements l'hermiticité de A et B.

Il est intéressant d'introduire un troisième opfirateur C qui est relié directement à l'opérateur B mais qui, à l'ordre n, possède moins de termes que celui-ci.

Par définition, l'opérateur C correspond exactement aux suites $\{C\}$ qui sont déterminées par les critères suivants (le nombre n correspond au terme ω_n du développement (62) et le nombre p peut prendre les valeurs 1, 2, . . ., $(n-1)$):

$$(C \to \{C\}) \quad \begin{cases} S_{C,n}(n) = 0, & (68) \\ S_{C,n}(p) \neq 0 \quad (p < n). & (69) \end{cases}$$

L'opérateur C est encore hermitique; en effet, si une suite $\{\mu_1, \mu_2 \ldots \mu_n\}$ est une suite C, il en est de même de la suite conjuguée $\{\mu_n \ldots \mu_1, \mu_2\}$.

La relation entre B et C découle immédiatement des définitions des suites associées à ces opérateurs

$$B = 1+C+C^2+ \ldots$$

ou encore

$$B^{-1} = 1-C. \tag{70}$$

8. Représentation de l'Opérateur h

L'opérateur h est défini par l'égalité (49),

$$h = AB^{-1}, \tag{71}$$

qui s'écrit encore

$$A = h+AC. \tag{72}$$

Cette dernière expression va nous servir à caractériser le développement de h.

Considérons les suites composées d'ordre n, soit $\{M_n\} \equiv \{\mu_1 \ldots \mu_p, \nu_1 \ldots \nu_{n-p}\}$, formées à partir d'une suite $\{A_p\} \equiv \{\mu_1, \ldots \mu_p\}$ et d'une suite $\{C_{n-p}\} \equiv \{\nu_1 \ldots \nu_{n-p}\}$. Ces suites sont des suites $\{A\}$ d'ordre n puisque des relations de définition des suites $\{A\}$ et $\{C\}$, on tire

$$S_{M,n}(n) = S_{A,p}(p)+S_{C,n-p}(n-p) = -1.$$

Réciproquement, soit une suite $\{A_n\} \equiv \{\mu_1, \mu_2 \ldots \mu_n\}$. Pour cette suite, nous aurons $S_{A,n}(n) = -1$.

S'il existe un nombre q inférieur à n tel que $S_{A,n}(q) = -1$, on peut décomposer la suite $\{A_n\}$ en deux suites, une suite $\{A\}$ d'ordre p soit $\{A_p\} \equiv \{\mu_1 \ldots \mu_p\}$, et une suite $\{C\}$ d'ordre $(n-p)$ soit $\{C_{n-p}\} \equiv \{\mu_{p+1} \ldots \mu_n\}$. De plus la décomposition est unique. En effet, pour que la suite $\{C_{n-p}\}$ satisfasse aux conditions (68) et (69), il faut et il suffit que le nombre p choisi soit le plus grand nombre q tel que $S_{A,n}(q) = -1$; ce choix assure l'unicité de la décomposition.

Au contraire, si la suite $\{A_n\} \equiv \{\mu_1, \mu_2 \ldots \mu_n\}$ est telle qu'il n'existe pas de nombre q inférieur à n tel que $S_{A,n}(q) = -1$, nous dirons que cette suite est une suite $\{h\}$.

Les suites $\{h\}$ sont donc définies par les critères suivants

$$(\{h\}) \quad \begin{aligned} S_{h,n}(n) &= -1, && (73) \\ S_{h,n}(p) &\neq -1 \quad (p < n). && (74) \end{aligned}$$

La discussion précédente montre que l'opérateur h défini par l'égalité (71) correspond exactement aux suites $\{h\}$.

La définition de ces suites peut être légèrement modifiée. En effet, soit une suite $\{h_n\} \equiv \{\mu_1, \mu_2 \ldots \mu_n\}$; comme il n'existe pas de nombre q inférieur à n tel que $S_{h,n}(q) = -1$, il ne peut exister de nombre p tel que $S_{h,n}(p) < -1$. Démontrons cette propriété par l'absurde. Pour $n > 1$, nous avons $S_{h,n}(1) > -1$. S'il existe un nombre p tel que $S_{A,n}(p) < -1$, lorsque varie de la valeur 1 à la valeur p, la somme $S_{A,n}(r)$ traverse au moins une fois la valeur (-1) en décroissant. Or si la somme $S_{A,n}(r)$ décroît lorsque r est changé en $(r+1)$, elle ne décroit que d'une unité (cf. définition (64)). Elle doit donc passer au moins une fois par la valeur (-1), pour une valeur de r comprise entre 1 et p, ce qui est contraire aux prémisses.

Cette remarque permet de définir l'opérateur h et les suites $\{h\}$ par des critères en apparence plus restrictifs que les conditions (73) en (74)

$$(h \to \{h\}) \quad \begin{aligned} S_{h,n}(n) &= -1, && (75) \\ S_{h,n}(p) &> -1 \quad (p < n). && (76) \end{aligned}$$

Ces critères peuvent s'exprimer encore sous une autre forme qu'il est commode d'utiliser pour construire explicitement les suites $\{h\}$

$$(h \to \{h\}) \quad \begin{aligned} S^+_{h,n}(n) &= -1, && (77) \\ S^+_{h,n}(p) &< 0. && (78) \end{aligned}$$

De ces conditions, il ressort en particulier que pour une suite $\{h_n\}$ avec $n > 0$, nous avons toujours $\mu_1 > 0$ et $\mu_n = 0$.

9. Calcul Direct du Développement de l'Opérateur h

Le développement de l'opérateur h peut se déduire directement de l'équation (1)

$$[E-e-H(E)]|\varphi_E> = 0. \tag{79}$$

Exprimons $H(E)$ par la formule de Taylor

$$(E-e)|\varphi_E\rangle = \left[H(e)+(E-e)H^{(1)}(e)+\ldots+\frac{(E-e)^n}{n!}H^{(n)}(e)+\ldots\right]|\varphi_E\rangle. \tag{80}$$

Mais par ailleurs l'équation (2) s'écrit

$$(E-e)|\varphi_E\rangle = h|\varphi_E\rangle. \tag{81}$$

Dans le deuxième membre de l'équation (80), nous pouvons remplacer les expressions $(E-e)|\varphi_E\rangle$ par $h|\varphi_E\rangle$, on obtient ainsi

$$(E-e)|\varphi_E\rangle = \sum_{n=0}^{\infty}\frac{H^{(n)}(e)}{n!}h^n|\varphi_E\rangle. \tag{82}$$

Identifions les équations (81) et (82). Nous en tirons une équation implicite pour h

$$h = \sum_{n=0}^{\infty}[H^{(n)}(e)/n!]h^n. \tag{83}$$

Nous pouvons alors développer h sous la forme suivante:

$$h = h_1+h_2+\ldots+h_n+\ldots,$$

le terme h_n étant un polynôme homogène d'ordre n par rapport à $H(e)$ et à ses dérivées.

Reportons le développement de h dans la formule (83) et identifions les termes d'ordre n. Nous trouvons ainsi une relation de récurrence qui permet d'exprimer h_n en fonction des opérateurs h_r de degré inférieur à n,

$$h_n = \sum_{p=1}^{p=n-1}[H^{(p)}(e)/p!]\sum_{\nu_1+\ldots+\nu_p=n-1}h_{\nu_1}h_{\nu_2}\ldots h_{\nu_p}. \tag{84}$$

Le signe $\sum_{\nu_1+\ldots+\nu_p=n-1}$ indique que l'on doit sommer tous les termes pour lesquels la condition $\nu_1+\ldots+\nu_p = n-1$ est satisfaite.

Les premiers termes du développement de h sont facilement calculables

$$h_1 = H(e),\quad h_2 = H^{(1)}(e)H(e),\quad h_3 = [H^{(1)}(e)]^2H(e)+\tfrac{1}{2}H^{(2)}(e)[H(e)]^2. \tag{85}$$

Ces premiers termes correspondent exactement aux suites $\{h_1\}$, $\{h_2\}$ et $\{h_3\}$ définies ci-dessus. En s'appuyant sur la relation de récurrence (84), il est facile de montrer que le terme général h_n calculé de proche en proche peut être représenté exactement par les suites $\{h_n\}$ (voir l'appendice).

Remarquons au passage que la formule (83) peut s'écrire sous une forme

condensée qui peut être utile dans certains problèmes:

$$h = \int_{\mathscr{C}} H(\varepsilon)\, \frac{1}{\varepsilon - e - h}\, \mathrm{d}\varepsilon. \tag{86}$$

10. Développement de l'Opérateur K

L'opérateur K s'exprime en fonction de A et C,

$$K = B^{-\frac{1}{2}} A B^{-\frac{1}{2}} = (1-C)^{\frac{1}{2}} A (1-C)^{\frac{1}{2}}. \tag{87}$$

Le développement de K en fonction de $H(e)$ et de ses dérivées peut être obtenu à partir des développements des opérateurs A et C. Malheureusement, l'expression générale du terme K_n d'ordre n n'est pas simple, et nous nous contentons de donner dans le paragraphe suivant les premiers termes du développement.

11. Tableau des Premiers Termes du Développement de h, C et K

Les opérateurs sont représentés par les suites qui leur sont associées. Pour l'opérateur K les coefficients $R(\mu_1, \mu_2 \ldots \mu_n)$ sont indiqués à côté des suites correspondantes. Pour les opérateurs h et C les coefficients sont égaux à l'unité. Les opérateurs A et B ne sont pas indiqués. En effet, leur construction est triviale mais le nombre de suites d'ordre n qui leur correspondent croît rapidement avec n.

h_1	{0}
h_2	{10}
h_3	{200} {110}
h_4	{3000} {2100} {2010} {1200} {1110}

K_1	{0}	1
K_2	{10}	$\frac{1}{2}$
	{01}	$\frac{1}{2}$
K_3	{110}	$\frac{3}{8}$
	{011}	$\frac{3}{8}$
	{101}	$\frac{1}{4}$
	{200}	$\frac{1}{2}$
	{002}	$\frac{1}{2}$
K_4	{1110}	$\frac{5}{16}$
	{0111}	$\frac{5}{16}$
	{1101}	$\frac{3}{16}$
	{1011}	$\frac{3}{16}$
	{1200}	$\frac{3}{8}$
	{0021}	$\frac{3}{8}$
	{1020}	$\frac{1}{8}$
	{0201}	$\frac{1}{8}$
	{1002}	$\frac{1}{4}$
	{2001}	$\frac{1}{4}$
	{0120}	$-\frac{1}{8}$
	{0210}	$-\frac{1}{8}$
	{0102}	$\frac{3}{8}$
	{2010}	$\frac{3}{8}$
	{0012}	$\frac{1}{2}$
	{2100}	$\frac{1}{2}$
	{3000}	$\frac{1}{2}$
	{0003}	$\frac{1}{2}$

C_1	{1}
C_2	{20} {02}
C_3	{012} {210} {300} {003} {030}

12. Application: Perturbation des États Liés

12.1 POSITION DU PROBLÈME

Considérons un système décrit par un hamiltonien H

$$H = H_0 + V,$$

où H_0 est l'hamiltonien non perturbé et V la perturbation.

Le calcul du spectre discret de l'opérateur H par des méthodes de perturbation présente quelques difficultés lorsque certains des niveaux correspondants de H_0 sont dégénérés.

Soit par exemple E_0 une valeur propre de l'opérateur H_0, correspondant à n fonctions dégénérées. Nous désignerons par Ω_0 l'espace à n dimensions défini par ces fonctions. L'introduction de la perturbation V va en général lever la dégénérescence et nous obtiendrons n fonctions orthogonales qui sont fonctions propres de H,

$$H|\alpha\rangle = E_\alpha|\alpha\rangle. \tag{88}$$

Soit Ω l'espace défini par les fonctions $|\alpha\rangle$. Une théorie de perturbation doit permettre de construire, dans l'espace Ω_0, un opérateur qui peut dépendre de l'énergie E et tel que ses n racines propres soient les valeurs E_α et que ses n fonctions propres soient „les bonnes fonctions non perturbées". Par ailleurs, elle doit permettre d'établir une correspondance entre les fonctions propres de H et les bonnes fonctions non perturbées. Le problème ainsi posé présente un grand degré d'arbitraire comme l'a remarqué Bloch [7]) qui a étudié la question en détail.

En particulier, à toute fonction $|l\rangle$ de Ω, on peut associer dans Ω_0

1) la projection $|l\rangle_0$ de la fonction $|l\rangle$ sur l'espace Ω_0,

2) la fonction $|\bar{l}\rangle_0$ de Ω_0 dont la projection sur l'espace Ω est la fonction $|l\rangle$.

En fait, ni les fonctions $|\alpha\rangle_0$, ni les fonctions $|\bar{\alpha}\rangle_0$ ne forment un système orthogonal et cette propriété n'incite guère à attribuer à l'un ou l'autre de ces systèmes le caractère de bonnes fonctions non perturbées. Toutefois, ces deux systèmes, pris dans leur ensemble, forment un système biorthogonal. Il est, en effet, facile de prouver les relations

$${}_0\langle\bar{\alpha}|\beta\rangle_0 = \langle\alpha|\bar{\beta}\rangle_0 = \delta_{\alpha\beta}. \tag{89}$$

En réalité, nous pensons qu'il serait plus juste de considérer comme bonnes fonctions non perturbées les fonctions orthonormées $|\hat{\alpha}\rangle_0$ que l'on peut associer, dans l'espace Ω_0, aux fonctions $|\alpha\rangle_0$ en suivant la méthode développée à la section 2.

Dans le cas présent, la signification des fonctions $|\hat{\alpha}\rangle_0$ est particulièrement simple. En effet, comme à la section 2, nous pouvons définir dans Ω_0, deux systèmes orthogonaux de vecteurs colinéaires $|x_j\rangle_0$ et $|\bar{x}_j\rangle_0$ formant un système

biorthogonal. Par définition, les vecteurs $|x_j\rangle_0$ sont les projections sur Ω_0 d'un système de vecteurs $|x_j\rangle$ de Ω qui eux-mêmes sont les projections sur Ω des vecteurs $|\bar{x}_j\rangle_0$. Les vecteurs $|x_j\rangle_0$ et $|\bar{x}_j\rangle_0$ formant un système biorthogonal, il s'ensuit que les vecteurs $|x_j\rangle$ sont orthonormés, car

$$\langle x_j|x_k\rangle = \langle x_j|\bar{x}_k\rangle_0 = {}_0\langle x_j|\bar{x}_k\rangle_0 = \delta_{jk}.$$

Ainsi les vecteurs $|x_j\rangle$ forment un système de vecteurs orthonormés dans Ω, qui se projettent sur Ω_0 suivant un système orthogonal de vecteurs. Un tel système est en général unique. Réciproquement, les vecteurs $|\hat{x}_j\rangle_0$ étant portés par les vecteurs $|\bar{x}_j\rangle_0$, forment le système de vecteurs orthonormés de Ω_0 qui se projette sur Ω suivant un système orthogonal de vecteurs. Les vecteurs $|\hat{x}_j\rangle$ sont donc obtenus à partir des vecteurs $|x_j\rangle$ en rabattant l'espace Ω sur l'espace Ω_0.

Pour plus de clarté, supposons que Ω et Ω_0 soient deux plans réels dans un espace à trois dimensions et soit L la droite commune aux deux plans. L'origine O se trouve naturellement sur la droite L. Les vecteurs de base $|x_1\rangle$ et $|\hat{x}_1\rangle$ seront confondus et portés par la droite L, les vecteurs de base $|x_2\rangle$ et $|\hat{x}_2\rangle$ seront orthogonaux à L et tracés respectivement dans les plans Ω et Ω_0 (voir fig. 2).

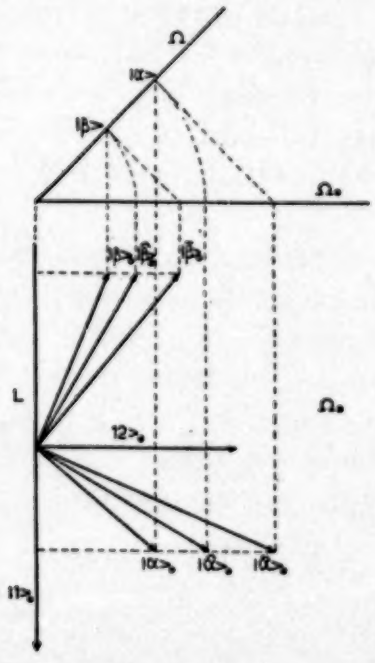

Fig. 2. Épure représentant deux plans Ω et Ω_0 et les divers vecteurs contenus dans ces deux plans.

Toute correspondance linéaire entre les vecteurs $|x\rangle$ et $|\hat{x}\rangle$ équivaut à un rabattement.

Dans le cas général, soit $|l\rangle$ un vecteur de l'espace Ω, défini par l'égalité

$$|l\rangle = \sum_j \lambda_j |x_j\rangle. \tag{90}$$

Par projection sur Ω_0, nous en tirons

$$|l\rangle_0 = \sum_j \lambda_j |x_j\rangle_0. \tag{91}$$

À tout vecteur $|l\rangle_0$ nous pouvons associer dans Ω_0 un vecteur $|\hat{l}\rangle_0$ en supposant que la correspondance est linéaire,

$$|\hat{l}\rangle_0 = \sum_j \lambda_j |\hat{x}_j\rangle_0. \tag{92}$$

Les vecteurs $|l\rangle$ et $|\hat{l}\rangle_0$ se correspondent donc par rabattement. En particulier, les vecteurs $|\hat{\alpha}\rangle_0$ correspondent aux vecteurs $|\alpha\rangle$ et l'interprétation géométrique de la transformation montre que le choix des vecteurs $|\hat{\alpha}\rangle_0$ comme bonnes fonctions non perturbées est particulièrement raisonnable.

12.2 APPLICATION DE LA FORMULE DE BRILLOUIN-WIGNER AU PROBLÈME DES ÉTATS LIÉS

L'équation aux valeurs propres à laquelle satisfont les fonctions $|\alpha\rangle$ s'écrit

$$(E_\alpha - H_0)|\alpha\rangle = V|\alpha\rangle. \tag{93}$$

Soit alors P_0 l'opérateur de projection sur l'espace Ω_0 et Q_0 l'opérateur complémentaire:

$$P_0 + Q_0 = 1. \tag{94}$$

Nous aurons

$$P_0|\alpha\rangle = |\alpha\rangle_0. \tag{95}$$

Les fonctions $|\alpha\rangle_0$ sont solutions de l'équation de Brillouin-Wigner [1])

$$\left[E_\alpha - E_0 - P_0 V \frac{1}{1 - \dfrac{Q_0}{E_\alpha - H_0} V} P_0\right] |\alpha\rangle_0 = 0. \tag{96}$$

La démonstration de cette formule est simple mais instructive et certains intermédiaires de calcul nous servirons plus loin. C'est pourquoi nous la répétons ici. De la formule (93) nous tirons aisément

$$Q_0|\alpha\rangle = \frac{Q_0}{E_\alpha - H_0} V|\alpha\rangle. \tag{97}$$

Ajoutons, membre à membre, les égalités (95) et (97), nous obtenons

$$|\alpha\rangle = |\alpha\rangle_0 + \frac{Q_0}{E_\alpha - H_0} V|\alpha\rangle, \tag{98}$$

ce qui s'écrit encore

$$|\alpha\rangle = \frac{1}{1 - \dfrac{Q_0}{E_\alpha - H_0} V} |\alpha\rangle_0. \tag{99}$$

Ainsi $|\alpha\rangle$ se trouve exprimé en fonction de $|\alpha\rangle_0$. Reportons cette expression dans le second membre de l'équation (93):

$$(E_\alpha - H_0)|\alpha\rangle = V \frac{1}{1-\frac{Q_0}{E_\alpha - H_0}V} P_0|\alpha\rangle_0. \tag{100}$$

Multiplions cette équation à gauche par P_0, nous obtenons

$$(E_\alpha - E_0)|\alpha\rangle_0 = P_0 V \frac{1}{1-\frac{Q_0}{E_\alpha - H_0}V} P_0|\alpha\rangle_0, \tag{101}$$

c'est l'équation de Brillouin-Wigner. Cette équation est de la forme

$$[E_\alpha - E_0 - H(E_\alpha)]|\alpha\rangle_0 = 0, \tag{102}$$

à condition de poser

$$H(E) \equiv P_0 V \frac{1}{1-\frac{Q_0}{E-H_0}V} P_0$$

$$= P_0 V P_0 + P_0 V \frac{Q_0}{E_0 - H_0} V P_0 + P_0 V \frac{Q_0}{E_0 - H_0} V \frac{Q_0}{E_0 - H_0} V P_0 + \ldots. \tag{103}$$

L'opérateur h que l'on peut associer à $H(E)$ s'écrit naturellement (cf. égalité (50)):

$$h = \sum_\alpha |\alpha\rangle_0 E_\alpha \, {}_0\langle\bar{\alpha}|. \tag{104}$$

Cet opérateur est donc identique à l'opérateur $\mathscr{H}$ défini par Bloch [7]).

Calculons maintenant l'élément de matrice ${}_0\langle\alpha|1-H'(E_\alpha)|\alpha\rangle_0$. De la définition (103) de $H(E)$ nous tirons immédiatement

$$H'(E) = -P_0 V \frac{1}{1-\frac{Q_0}{E-H_0}V} \frac{Q_0}{(E-H_0)^2} V \frac{1}{1-\frac{Q_0}{E-H_0}V} P_0. \tag{105}$$

Formons alors l'élément de matrice ${}_0\langle\alpha|1-H'(E_\alpha)|\alpha\rangle_0$ et tenons compte de la relation (100) et de la relation conjuguée; nous obtenons ainsi

$${}_0\langle\alpha|1-H'(E_\alpha)|\alpha\rangle_0 = {}_0\langle\alpha|\alpha\rangle_0 + \langle\alpha|Q_0|\alpha\rangle = \langle\alpha|P_0|\alpha\rangle + \langle\alpha|Q_0|\alpha\rangle. \tag{106}$$

Cette relation s'écrit encore

$${}_0\langle\alpha|1-H'(E_\alpha)|\alpha\rangle_0 = 1. \tag{107}$$

Cette égalité correspond exactement à la relation (52). Les opérateurs A et B

que l'on peut associer à $H(E)$ pourront donc s'exprimer ainsi:

$$A = \sum_{\alpha} |\alpha\rangle_0 (E_\alpha - E_0)_0 \langle\alpha|, \tag{108}$$

$$B = \sum_{\alpha} |\alpha\rangle_0 \, {}_0\langle\alpha|. \tag{109}$$

Ces opérateurs sont identiques aux opérateurs A et B définis par Kato.

De plus, l'existence de la relation (107) montre que les fonctions propres de l'opérateur K que l'on peut associer à l'opérateur $H(E)$ sont les vecteurs $|\hat{\alpha}\rangle_0$ que nous avons définis à la subsection 12.1 et qui se déduisent des fonctions $|\alpha\rangle$ par rabattement de l'espace Ω sur l'espace Ω_0:

$$K = \sum_{\alpha} |\hat{\alpha}\rangle_0 (E_\alpha - E_0)_0 \langle\hat{\alpha}|. \tag{110}$$

Il est satisfaisant de constater que les opérateurs A, B, h et K que nous avons définis de façon très générale possèdent, dans le cas particulier considéré, des interprétations géométriques simples. Ces opérateurs sont d'ailleurs directement reliés aux opérateurs de projection $\mathscr{U}$, $\mathscr{P}$ et $\mathscr{D}$ qui font passer des fonctions non perturbées $|\alpha\rangle_0$, $|\alpha\rangle_0$ et $|\hat{\alpha}\rangle_0$ aux fonctions $|\alpha\rangle$ et que l'on peut écrire ainsi:

$$\mathscr{U} = \sum_{\alpha} |\alpha\rangle \; {}_0\langle\bar{\alpha}|, \tag{111}$$

$$\mathscr{P} = \sum_{\alpha} |\alpha\rangle \; {}_0\langle\alpha|, \tag{112}$$

$$\mathscr{D} = \sum_{\alpha} |\alpha\rangle \; {}_0\langle\hat{\alpha}|. \tag{113}$$

En effet, comme l'a montré Bloch [7]), les opérateurs h, A et B peuvent s'exprimer ainsi (P_0 est l'opérateur de projection sur Ω_0)

$$h = P_0 V \mathscr{U}, \tag{114}$$

$$A = P_0 V \mathscr{P}, \quad B = P_0 \mathscr{P}. \tag{115}$$

De manière semblable, on peut définir des opérateurs a et b

$$a = P_0 V \mathscr{D}, \quad b = P_0 \mathscr{D}.$$

Pour une transformation simple, on obtient pour a et b les expressions

$$a = \sum_{\alpha} |\alpha\rangle_0 (E_\alpha - E_0)_0 \langle\hat{\alpha}|, \tag{116}$$

$$b = \sum_{\alpha} |\alpha\rangle_0 \, {}_0\langle\hat{\alpha}| = \sum_{\alpha} |\hat{\alpha}\rangle_0 \, {}_0\langle\alpha|. \tag{117}$$

Ces opérateurs jouent un rôle analogue aux opérateurs A et B. Ainsi, par exemple, les vecteurs $|\hat{\alpha}\rangle_0$ sont solutions de l'équation

$$[a - b(E_\alpha - E_0)]|\hat{\alpha}\rangle_0 = 0. \tag{118}$$

Quant aux opérateurs A, B, h et K, ils s'expriment facilement en fonction de a et b:

$$A = ab, \quad B = b^2, \quad h = ab^{-1}, \quad K = b^{-1}a. \tag{119}$$

12.3. CALCUL EXPLICITE DES OPÉRATEURS A, B et h

Comme nous l'avons vu, les opérateurs A, B et h s'expriment facilement à l'aide des projecteurs $\mathscr{P}$ et $\mathscr{U}$. Ceux-ci ont été calculés directement par Kato et Bloch. Les résultats s'expriment simplement en posant

$$\sigma_0 = -P_0, \quad \sigma_s = \frac{Q_0}{(E_0 - H_0)^s}$$

d'une part et d'autre part en associant aux suites $\{s_1, s_2 \ldots s_n\}$ les sommes

$$S_{s,n}(p) = \sum_{r=1}^{r=p} s_r - p.$$

Avec ces notations, on peut écrire

$$\mathscr{P} = P_0 + \sum_{u} \sigma_{u_1} V \sigma_{u_2} V \ldots \sigma_{u_n} V P_0, \tag{120}$$

les suites $\{u_1 \ldots u_n\}$ satisfaisant aux conditions

$$S_{u,n}(n) = 0,$$

et

$$\mathscr{U} = P_0 + \sum_{v} \sigma_{v_1} V \sigma_{v_2} V \ldots \sigma_{v_n} V P_0, \tag{121}$$

les suites $[v_1 \ldots v_n]$ satisfaisant aux conditions

$$S_{v,n}(n) = 0, \quad S_{v,n}(p) \geqq 0.$$

Nous pouvons facilement retrouver ces résultats à partir de l'opérateur $H(E)$ de Brillouin-Wigner, en utilisant la méthode générale développée dans la première partie de cet article. Ainsi, nous pouvons exprimer A et B sous une forme compacte en utilisant les formules (60) et (61),

$$A = \sum_{n=1}^{\infty} \frac{1}{(n-1)!} \frac{\mathrm{d}^{n-1}}{\mathrm{d}E_0^{n-1}} \left[P_0 V \frac{1}{1 - \dfrac{Q_0}{E_0 - H_0} V} P_0 \right]^n, \tag{122}$$

$$B = P_0 + \sum_{n=1}^{\infty} \frac{1}{n!} \frac{\mathrm{d}^n}{\mathrm{d}E_0^n} \left[P_0 V \frac{1}{1 - \dfrac{Q_0}{E_0 - H_0} V} P_0 \right]^n. \tag{123}$$

Les correspondances des opérateurs A, B et h avec certaines suites de nombres permettent d'écrire ces opérateurs sous une forme développée (voir formules

(66), (67), (75) et (76)). Ainsi l'opérateur A s'exprime ainsi:

$$A = \sum_{\mu} [H^{(\mu_1)}(E_0)/\mu_1!] \dots [H^{(\mu_m)}(E_0)/\mu_m!], \tag{124}$$

les suites $\{\mu_1, \dots \mu_n\}$ satisfaisant à la condition

$$S_{\mu, m}(m) = -1. \tag{125}$$

Soit alors $H_q(E)$ le terme de rang q dans le développement de $H(E)$ (cf. formule (103)),

$$H(E) = \sum_{q=0}^{\infty} H_q(E). \tag{126}$$

On peut écrire l'opérateur A sous la forme

$$A = \sum_{\mu, q} [H_{q_1}^{(\mu_1)}(E_0)/\mu_1!] \dots [H_{q_m}^{(\mu_m)}/\mu_m!].$$

Calculons les dérivées qui interviennent dans cette expression:

$$H_q^{(\mu)}(E_0) = (-1)^{\mu} \sum_{u} P_0 V \frac{Q_0}{(E_0 - H_0)^{u_1}} V \dots \frac{Q_0}{(E_0 - H_0)^{u_q}} V P_0, \tag{127}$$

les suites $\{u_1 \dots u_q\}$ satisfaisant aux conditions

$$u_r > 0, \quad S_{u, q}(q) = \mu. \tag{128}$$

Reportons les valeurs des dérivées dans le développement de l'opérateur A et utilisons les mêmes notations que précédemment; nous obtenons le résultat final suivant

$$A = P_0 V P_0 + \sum_{j} P_0 V \sigma_{s_1} V \dots \sigma_{s_n} V P_0, \tag{129}$$

les suites $\{s_1, s_2 \dots s_n\}$ satisfaisant aux conditions

$$S_{s, n}(n) = 0, \quad n > 0. \tag{130}$$

Ces dernières conditions s'obtiennent aisément à partir des conditions (125) et (128), en effet

$$S_{s, n}(n) = \sum_{r=1}^{r=m} S_{u_r, q_r}(q_r) - (m-1) = \sum_{r=1}^{r=m} \mu_r - (m-1) = S_{\mu, m}(m) + 1 = 0.$$

Les développements de B et h s'obtiennent de façon analogue:

$$B = P_0 + \sum_{s} P_0 V \sigma_{s_1} V \dots \sigma_{s_n} V P_0, \tag{131}$$

les suites $\{s_1, s_2 \dots s_n\}$ satisfaisant aux conditions

$$S_{s, n}(n) = 1, \quad n > 0; \tag{132}$$

et pour h on a

$$h = P_0VP_0 + \sum_s P_0V\sigma_{s_1}V \ldots \sigma_{s_n}VP_0, \tag{133}$$

les suites $\{s_1, s_2 \ldots s_n\}$ satisfaisant aux conditions

$$S_{s,n}(n) = 0, \quad S_{s,n}(p) \geqq 0. \tag{134}$$

12.4. PREMIERS TERMES DU DÉVELOPPEMENT DE h ET K

Le développement général de l'opérateur K n'est pas simple mais les premiers termes sont faciles à calculer à partir de l'expression de $H(E)$ donnée à la formule (103) et du tableau de la section [11]). (Remarquons en passant que dans l'espace Ω_0, on peut poser $P_0 = 1$).

Les développements de h et K jusqu'au troisième ordre s'écrivent ainsi:

$$h = P_0VP_0 + P_0V\frac{Q_0}{E_0-H_0}VP_0 + P_0V\frac{Q_0}{E_0-H_0}V\frac{Q_0}{E_0-H_0}VP_0 - P_0V\frac{Q_0}{(E_0-H_0)^2}VP_0VP_0 + \ldots, \tag{135}$$

$$K = P_0VP_0 + P_0V\frac{Q_0}{E_0-H_0}VP_0 + P_0V\frac{Q_0}{E_0-H_0}V\frac{Q_0}{E_0-H_0}VP_0 - \tfrac{1}{2}P_0V\frac{Q_0}{(E_0-H_0)^2}VP_0VP_0 - \tfrac{1}{2}P_0VP_0V\frac{Q_0}{(E_0-H_0)^2}VP_0 + \ldots. \tag{136}$$

Il est intéressant d'utiliser l'opérateur K lorsque l'hamiltonien initial H_0 est dégénéré. Dans le cas non dégénéré, l'espace Ω_0 ne comporte qu'une dimension. Les opérateurs h et K sont donc des nombres nécessairement égaux; il vaut alors mieux partir de l'expression de h qui est plus simple.

13. Conclusion

En résumé, l'essentiel de cet article consiste à montrer qu'un grand nombre de problèmes de valeurs propres que l'on rencontre en mécanique quantique peuvent se ramener au calcul du spectre d'un opérateur hermitique K indépendant de l'énergie. Les fonctions propres de cet opérateur doivent être considérées comme les bonnes fonctions non perturbées; elles correspondent en général aux états habillés du système complet. Dans ce cas, l'opérateur K représente l'interaction entre les états habillés.

Notre méthode peut s'appliquer à la perturbation des états liés, à partir de la formule de Brillouin-Wigner. Les bonnes fonctions non perturbées définies ci-dessus possèdent alors une interprétation géométrique simple.

Dans tout ce qui précède, nous n'avons pas tenu compte des phénomènes

dissipatifs. Nous pensons que, même dans ce cas, il doit être possible de définir de bonnes fonctions non perturbées qui puissent être reliées aux états quasi-stationnaires du système complet mais ce problème dépasse beaucoup le cadre de cet article.

L'auteur tient à remercier le Professeur Bloch qui lui a communiqué quelques suggestions relatives à ce travail.

Appendice

CALCUL DU DÉVELOPPEMENT DE h À PARTIR DE LA FORMULE (83)

L'opérateur h est donné par la formule (83). Il peut être développé en série sous la forme

$$h = h_1 + h_2 + \ldots + h_n + \ldots . \tag{A1}$$

Le terme h_n est un polynôme homogène d'ordre n par rapport à $H(e)$ et ses dérivées.

Il est alors possible d'exprimer h_n en fonction des opérateurs h_r de degré inférieur à n

$$h_n = \sum_{q=1}^{q=n-1} [H^{(q)}(e)/q!] \sum_{\mu_1+\ldots+\mu_q=n-1} h_{\mu_1} h_{\mu_2} \ldots h_{\mu_q}. \tag{A2}$$

Le deuxième signe $\sum$ indique que l'on doit sommer tous les termes tels que la condition $\mu_1+\mu_2+\ldots+\mu_q = n-1$ soit satisfaite.

Nous voulons montrer que l'opérateur h_n correspond „exactement" aux suites $\{h_n\}$ définiés par les critères (73) et (74), ou les critères équivalents (75) et (76). La formule (83) permet de calculer les premiers termes

$$h_1 = H(e), \quad h_2 = H^{(1)}(e)H(e).$$

Il est facile de vérifier que ces termes correspondent exactement aux suites $\{h_1\}$ et $\{h_2\}$. Pour montrer que le terme général h_n correspond exactement aux suites $\{h_n\}$, il suffit de prouver que si la propriété est vraie pour tous les ordres p inférieurs à n, elle est encore vraie à l'ordre n. L'opérateur h_n étant défini par la formule de récurrence (A3), il suffit pour arriver à ce résultat d'établir les deux propositions suivantes.

Proposition 1

Soit $\{a_1\}$, $\{a_2\} \ldots \{a_q\}$ un ensemble de q suites $\{h\}$ d'ordres μ_1, $\mu_2 \ldots \mu_q$. La suite $\{M\} \equiv \{q\}\{a_1\}\{a_2\} \ldots \{a_q\}$ formée à partir de ces suites et de la suite $\{q\}$ est une suite $\{h\}$ d'ordre n avec $n = \mu_1+\mu_2+\ldots+\mu_q+1$.

Démonstration

La suite $\{M\}$ satisfait au critère (75) car

$$S_{M,n}(n) = q-1+S_{a_2,\mu_1}(\mu_1)+S_{a_2,\mu_2}(\mu_2)+\ldots+S_{a_q,\mu_q}(\mu_q) = -1.$$

Examinons si elle satisfait au critère (76). En premier lieu, on vérifie que $S_{\mu,n}(1) = q-1 > -1$. Soit maintenant $1 < p < n$. Écrivons la suite $\{M\}$ sous la forme

$$\{M\} \equiv \{s_1, s_2 \ldots s_n\}.$$

Le nombre s_p figure dans une certaine suite $\{a_r\}$ où il occupe le rang l. Posons

$$\{a_r\} \equiv \{s_{r,1}, s_{r,2} \ldots s_{r,\mu_r}\},$$

nous aurons $s_p = s_{r,l}$ avec $p = 1+\mu_1+\mu_2+\ldots+\mu_{r-1}+l$. La somme $S_{M,n}(p)$ s'exprime ainsi:

$$S_{M,n}(p) = q-1+S_{a_1,\mu_1}(\mu_1)+\ldots+S_{a_{r-1},\mu_{r-1}}(\mu_{r-1})+S_{a_r,\mu_r}(l)$$
$$= q-r+S_{a_r,\mu_r}(l). \quad \text{(A3)}$$

Pour $r < q$, l'application des critères (75) et (76) à la suite $\{a_r\}$ fournit l'inégalité $S_{a_r,\mu_r} \geqq -1$. Par conséquent, dans ce cas, nous tirons de la formule (A3)

$$S_{M,n}(p) > -1.$$

Pour $r = q$, nous devons avoir $l \neq \mu_r = \mu_q$ sinon nous aurions $p = n$. L'application du critère (76) à la suite $\{a_q\}$ fornit l'inégalité

$$S_{a_q,\mu_q}(l) > -1.$$

Par conséquent dans ce cas, nous tirons de la formule (A3)

$$S_{M,n}(p) > -1.$$

Cette inégalité est donc valable pour tout nombre p inférieur à n. C'est le critère (76). La suite $\{M\}$ satisfaisant aux critères (75) et (76) est une suite $\{h\}$.

Proposition 2

Soit $\{M\} \equiv \{s_1, s_2 \ldots s_n\}$ une suite $\{h\}$ d'ordre n et soit $s_1 = q > 0$. Il est possible de trouver q suites $\{h\}$, soit $\{a_1\}$, $\{a_2\} \ldots \{a_q\}$ telles que l'on puisse écrire la suite $\{M\}$ sous la forme $\{M\} \equiv \{q\}\{a_1\}\{a_2\} \ldots \{a_q\}$. De plus la décomposition est unique.

Démonstration

Lorsque le nombre r inférieur à n est changé en $r+1$, si la somme $S_{M,n}(r)$ décroit, elle décroit au plus d'une unité à la fois. Or, $S_{M,n}(1) = q-1 > 0$ et $S_{M,n}(n) = -1$. Par conséquent, lorsque r varie, la somme $S_{M,n}(r)$ passe au

moins une fois par toutes les valeurs intermédiaires et l'on peut trouver une suite de nombres

$$1 = p_0 < p_1 < p_2 < \ldots < p_q = n$$

telle que

$$S_{M,n}(p_r) = q-1-r.$$

À ces nombres, nous pourrons faire correspondre q suites $\{a_1\}$, $\{a_2\} \ldots \{a_q\}$ définies ainsi:

$$\{a_r\} \equiv \{s_{p_{r-1}+1}, \ldots s_{p_r}\},$$

de telle façon que l'on puisse écrire

$$\{M\} \equiv \{q\}\{a_1\}\{a_2\} \ldots \{a_q\}.$$

Soit μ_r l'ordre de la suite $\{a_r\}$,

$$\mu_r = p_r - p_{r-1}.$$

Les nombres p_r ont été choisis de telle sorte que

$$S_{a_r,\mu_r}(\mu_r) = -1.$$

Les suites $\{a_r\}$ satisfont donc au critère (73). Pour qu'elles obéissent aussi au critère (74), il faut que pour tout nombre l inférieur à μ_r, nous ayons

$$S_{a_r,\mu_r}(l) \neq -1.$$

Pour que la suite $\{a_1\}$ satisfasse à cette condition, il faut et il suffit que le nombre p_1 choisi soit le plus petit nombre p tel que $S_{M,n}(p) = (q-1)-1$. De même pour que la suite $\{a_r\}$ satisfasse à cette condition, il faut que le nombre p_r choisi soit le plus petit nombre p supérieur à p_{r-1} tel que $S_{M,n}(p) = (q-1)-r$.

Dans ce cas, les suites $\{a_1\}$, $\{a_2\} \ldots \{a_{q-1}\}$ sont des suites $\{h\}$ et cette condition suffit à déterminer les nombres $p_1, p_2 \ldots p_q$.

Il reste à vérifier que la suite $\{a_q\}$ est elle aussi une suite $\{h\}$ c'est-à-dire qu'elle obéit au critère (75). Supposons alors que le nombre qui occupe le rang $l (l < \mu_q)$ dans la suite $\{a_q\}$ occupe le range p dans la suite $\{M\}$. Evaluons $S_{M,n}(p)$:

$$S_{M,n}(p) = q-1+S_{a_1,\mu_1}(\mu_1)+ \ldots +S_{a_{q-1},\mu_{q-1}}(\mu_{q-1})+S_{a_q,\mu_q}(l) = S_{a_q,\mu_q}(l).$$

Par définition, la suite $\{M\}$ est une suite $\{h\}$; par conséquent, elle obéit au critère (74). Ainsi, nous prouvons l'inégalité

$$S_{a_q,\mu_q}(l) \neq -1.$$

La suite $\{a_q\}$ est donc une suite $\{h\}$.

L'unicité du développement de $\{M\}$ résulte directement de la construction des suites $\{a_1\}$, $\{a_2\} \ldots \{a_q\}$.

Bibliographie

1) Voir par exemple P. M. Morse et H. Feshbach, Methods of theoretical physics (McGraw Hill, New York, 1953) II, p. 1001
2) E. E. Salpeter et H. A. Bethe, Phys. Rev. **93** (1951) 1094
3) M. Gell-Mann et F. Low, Phys. Rev. **84** (1951) 350
4) C. Bloch et J. Horowitz, Nuclear Physics **8** (1958) 91
5) Voir E. T. Whittaker et G. N. Watson, Modern analysis (Cambridge University Press, 1952) p. 133
6) T. Kato, Progr. Theor. Phys. **4** (1949) 514; **5** (1950) 95, 207
7) C. Bloch, Nuclear Physics **6** (1958) 329

3.A:4.E

Nuclear Physics **20** (1960) 347—359; © *North-Holland Publishing Co., Amsterdam*

Not to be reproduced by photoprint or microfilm without written permission from the publisher

THE DECAY OF Pb^{212}

P. G. ROETLING †, W. P. GANLEY ‡ and G. S. KLAIBER ††

University of Buffalo, N.Y.

Received 27 June 1960

Abstract: The gamma rays of Bi^{212} following the beta decay of 10 hour Pb^{212} have been studied using gamma response function analysis, coincidence spectroscopy and directional correlation techniques. The coincidence results agree in general with the level scheme proposed by Krisyouk *et al.* However a 177 keV gamma ray has been found, showing that transition to be M1 rather than E0. The weak 415 keV gamma radiation has been observed for the first time, and intensities assigned to all gamma radiations. Angular correlation experiments show the spins of the 415 keV and 300 keV levels to be 1 and 2 respectively, in disagreement with Krisyouk.

1. Introduction

The decay of Pb^{212} (Thorium B) has been studied by many observers by means of electron conversion techniques, and by one group by means of gamma ray coincidence techniques. Krisyouk *et al.* [1]) have proposed a decay scheme on the basis of conversion electron measurements, which is in disagreement with the scheme presented by earlier investigators. Demichelis *et al.* [2]) have found some gamma radiations that appear to substantiate the earlier work, but have been unable satisfactorily to demonstrate that these radiations actually come from Pb^{212}, in preference to one of the other daughters of Radiothorium.

2. Experimental Procedure

A 2 millicurie radiothorium source was available from which an active deposit of Pb^{212} could be obtained by electrostatic deposition upon aluminium foil. Recently developed chemical techniques [3]) were used to separate the 1 hour Bi^{212} from the parent Pb^{212}. Experiments were carried out both upon the daughter products and the parent, in order to demonstrate as strikingly as possible the origin of the various radiations observed. The chemical process was capable of separating about 99 % of the daughter products from the Pb^{212}, and experiments were performed upon the Lead for approximately 20 min without daughter product contamination being in excess of 20 %.

For the total gamma spectrum measurements, use was made of four single-channel analysers properly arranged to simultaneously scan various parts of the spectrum. The measured spectrum of the daughter products (corrected for decay) was then subtracted leaving the spectrum of Pb^{212}. Response function

† Now at Cornell Aeronautical Laboratory, Inc. Buffalo, N.Y.

‡ Now at the Wurlitzer Company, N. Tonawanda, N.Y.

†† Sponsored in part under a National Science Foundation Fellowship.

techniques were then applied to this spectrum [4,5]) in order to analyze the gamma ray intensities.

Coincidence measurements were taken by similar methods, using a fast-slow coincidence system having a resolving time of 40 ns. The detectors employed in this work were 4.4 cm × 5.1 cm NaI(Tl) crystals mounted on DuMont 6292 photomultiplier tubes. The analyzers were periodically calibrated to prevent electronic or photocathode drift.

Directional correlation work was carried out using four detectors and three fast-slow coincidence circuits similar to the ones described above. A master circuit allows one detector to be run in coincidence with three others. This technique permitted the measurement of correlation at three angles, simultaneously.

Preliminary experiments carried out with and without graded lead shields fitted around the counters demonstrated that counter-to-counter scattering did not affect the results of the work.

Since many runs had to be made, involving many sources of different strengths, the data from each counter was corrected for source strength.

The correlation apparatus was tested upon the well-known 1.17 MeV—1.33 MeV cascade in the Co^{60}—Ni^{60} decay. The results of each test run, and of all combined, agreed with various published data to within statistical errors.

Angular correlation work was performed upon Thorium B in equilibrium with its daughters, and separately in the same energy range upon the daughter products. Calibration of the equipment was made at each angle after each 15 min run. Spectra for Thorium B and its daughters were compared with spectra from the daughters alone, to determine the background counting rate present, and the correlation results were then properly adjusted to give the correlation due to coincidence from the 115—300 keV cascade in Pb^{212} alone.

3. Results

3.1. RESPONSE FUNCTION ANALYSIS OF TOTAL SPECTRUM

Fig. 1 shows the spectrum obtained from several runs on Separated Pb^{212}. The daughter product background present is about 20 % of the equilibrium intensity. Fig. 2 shows the spectrum for the daughter products. The strong 511 and 583 keV lines belong to 3.1 min Tl^{208} (daughter of Bi^{212}). The Bismuth spectrum, normalized to these two lines of Thallium, has been subtracted from the first spectrum, giving the results for pure Pb^{212} shown in fig. 3. The 415 keV line is seen in this spectrum, but the 177 keV line is obscured by the Compton edge of the 300 keV line which occurs at 162 keV. The 80 keV X-ray has been strongly reduced, since a 1 mm Cadmium absorber has been used in these experiments to eliminate the 160 keV sum peak.

The response functions [4]) for 239 and 300 keV were used to subtract the counts

due to these lines from the spectrum. The response of the spectrometer was measured for the single energy gamma radiations of Cr^{51}(320 keV) and Hg^{203} (279 keV). A curve of Gaussian form was fitted to the photopeak in each case

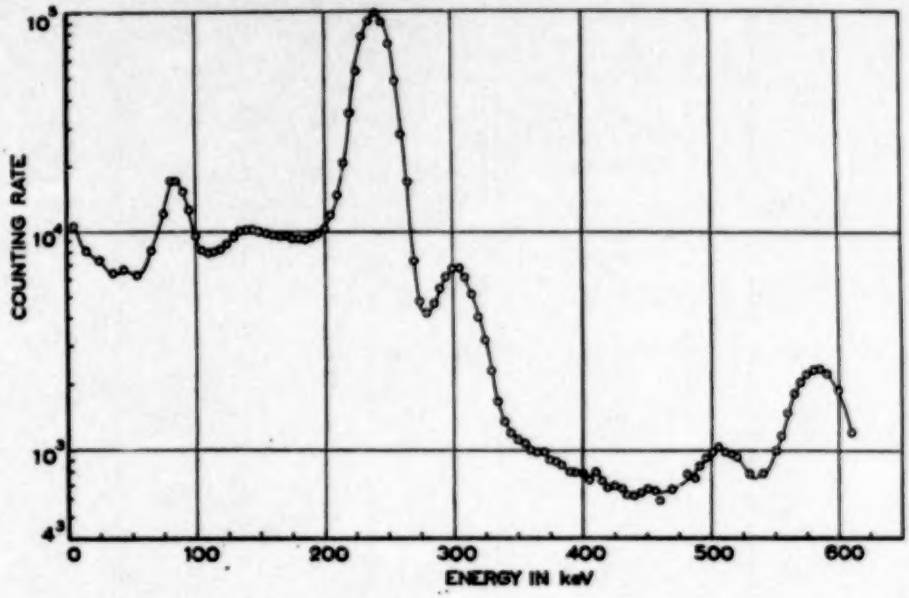

Fig. 1. Spectrum of Pb^{212} taken with 1 mm Cadmium absorber (20 % daughter background).

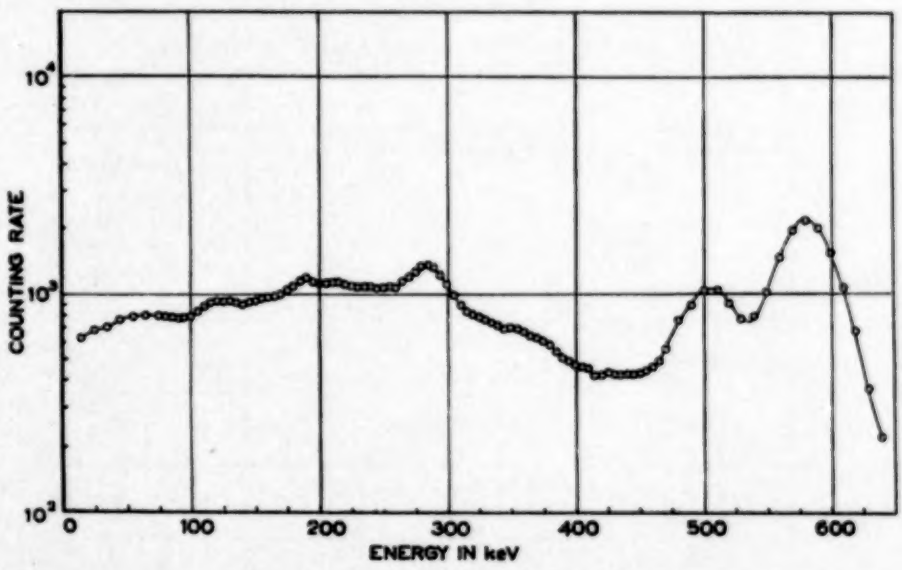

Fig. 2. Spectrum of the daughter products of Pb^{212} (with absorber).

and subtracted from the measured spectrum, the remainder being called the response functon. The response functions were normalized to the Compton edge energy. The response for 300 keV, shown in fig. 4, was obtained by linear interpolation and that for 239 keV was obtained by extrapolation.

The extrapolated response function for the 239 keV line is not considered to

be accurate below about 150 keV, and no attempt has been made to analyze the spectrum below this point. On subtracting the gaussian fits to the 239 keV peak and the 300 keV peak, as well as the response functions for these lines, the

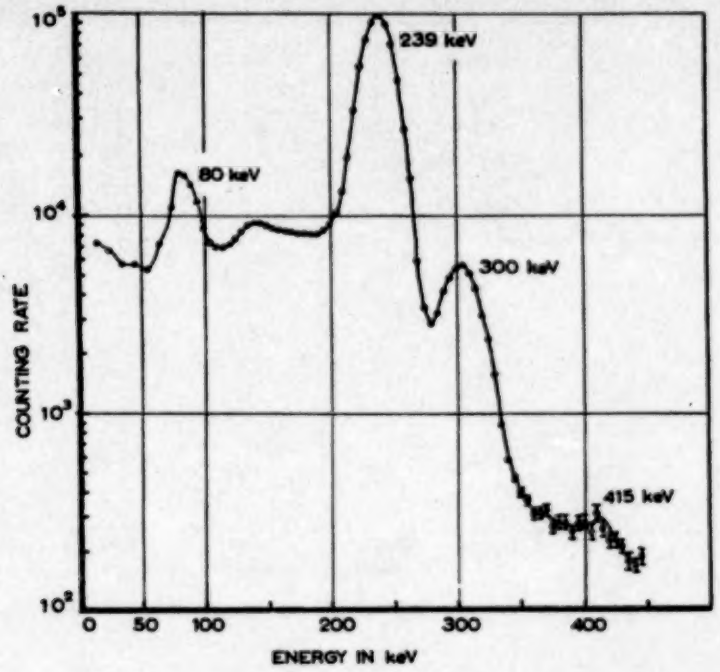

Fig. 3. Spectrum of Pb^{212} (background subtracted).

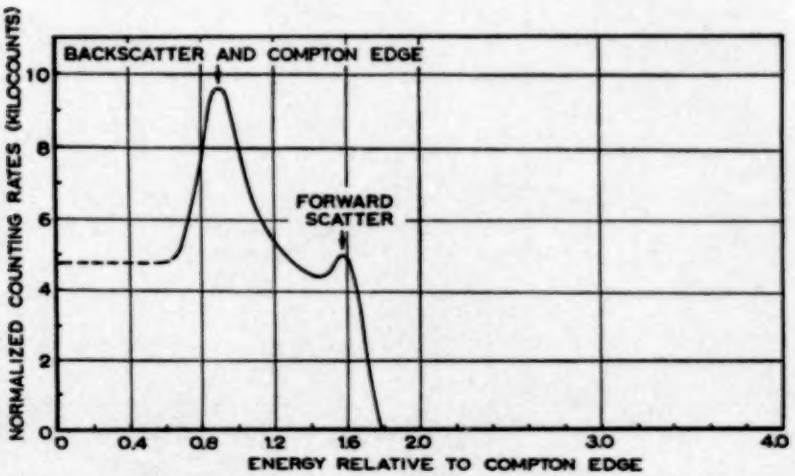

Fig. 4. Computed response function for 300 keV.

resulting spectra are shown in fig. 5. The very small peak at about 367 keV can be identified as a sum peak, and may be ignored. The peak at 177 keV is identifiable with the 177 keV peak observed in conversion electron investigtions, and the peak at 407 keV may be identified within experimental error with the

415 keV peak observed in the conversion electron experiments by Krisyouk *et al.* [1]).

The intensities of these lines, relative to the strong 239 keV peak, are given

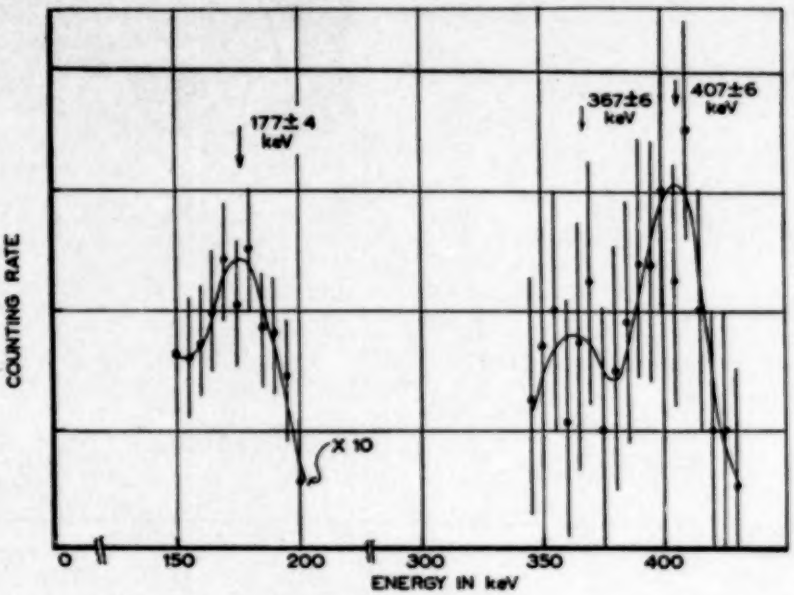

Fig. 5. Sections of the Pb^{212} spectrum after subtraction of the response functions and large peaks.

TABLE 1

Intensities of several lines in the Pb^{212} spectrum

Energy (keV)	Relative intensity (based on 239 keV)	Absolute intensity (photons/decay)	Theoretical or previous experimental value (photons/decay)
115	(observed in coincidence work only)		
164	not observed		
177	about 5×10^{-3}	about 3×10^{-3}	5×10^{-4} (ref. [1]))
239	1	$4.4\times10^{-1}\pm10$ %	about 0.3 (ref. [6]))
251	not observed		
300	$7.7\times10^{-2}\pm5$ %	$3.4\times10^{-2}\pm10$ %	about 0.03 (ref. [6]))
415	about 3×10^{-3}	about 2×10^{-3}	

in table 1. Only approximate values for the intensities of the lines at 177 keV and 415 keV have been given, in view of the large errors present in determining the intensity of a weak line superimposed upon a large background.

An approximate measure of the total decay rate may be obtained from the intensity of the 80 keV X-ray, the ground state beta decay [6]), the fluorescence yield [7]) and the various gamma intensities. From this, the absolute intensities in photons/decay may be computed, and are also given in table 1. The relatively simple decay scheme of Pb^{212} makes possible these computations from purely gamma radiation measurements.

3.2. COINCIDENCE RESULTS

Fig. 6 shows the spectrum in coincidence with the 300 keV line. This confirms

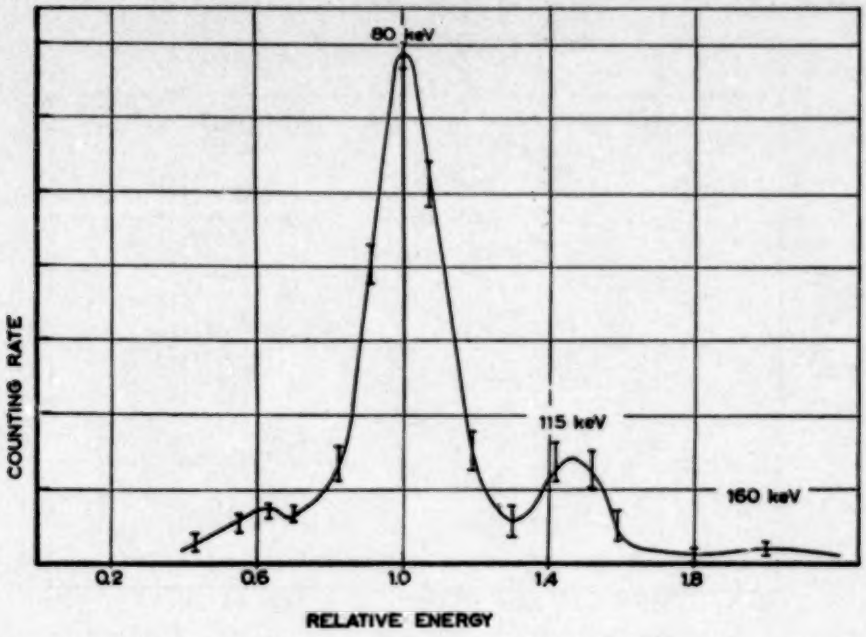

Fig. 6. The 300 keV coincidence spectrum of seperated Pb^{212}.

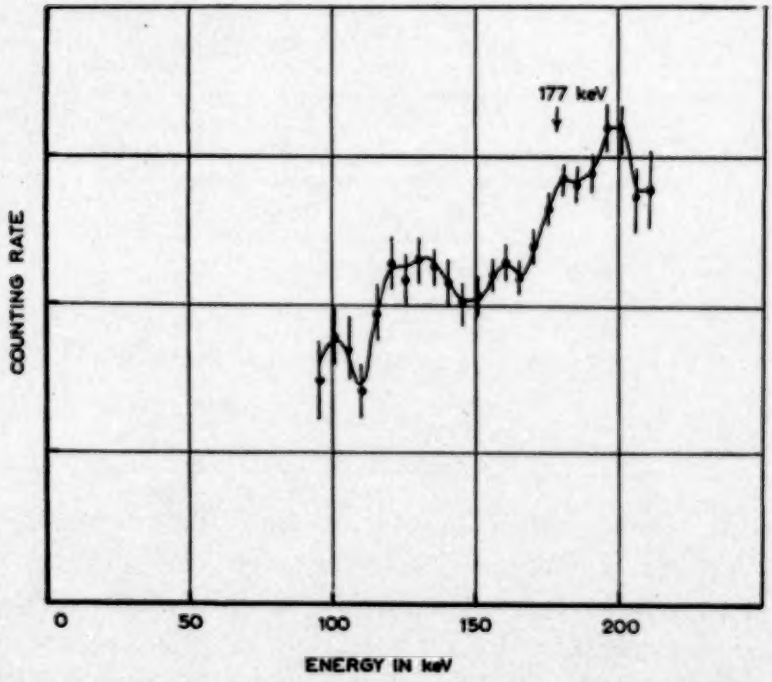

Fig. 7. The 239 keV coincidence spectrum of Pb^{212} and daughters (shielded).

the result of Demichelis *et al.* [2]), who apparently found this cascade in work performed on radiothorium. It is now seen definitely to come from Pb^{212}.

Fig. 7 shows the spectrum in coincidence with the 220—240 keV region of

Pb^{212} in equilibrium with its daughters. Fig. 8 shows a similar spectrum taken with only the daughters as a source. From a comparison of the two, is seen that only the bulge at about 177 keV appears to come from Pb^{212}. Experiments on

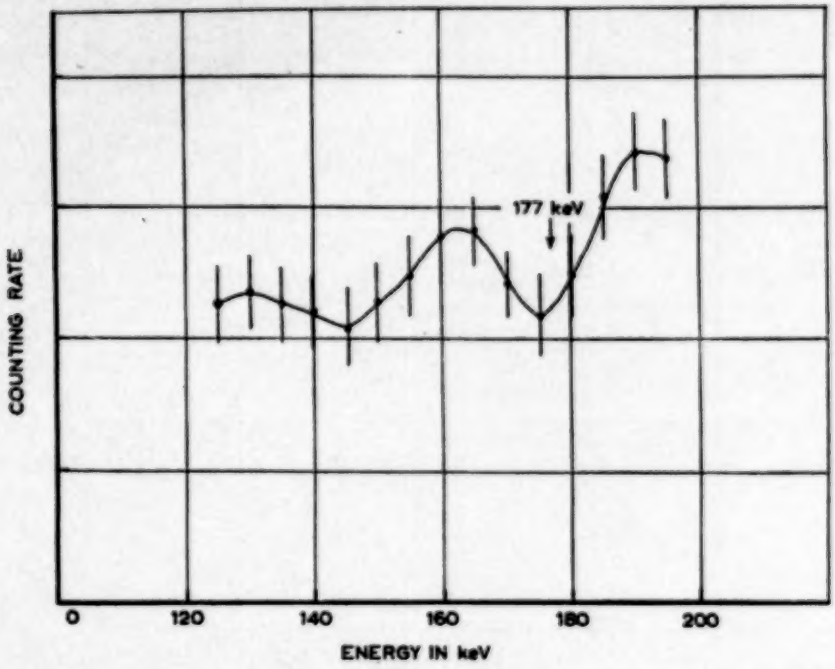

Fig. 8. The 239 keV coincidence spectrum of the daughters of Pb^{212} (shielded).

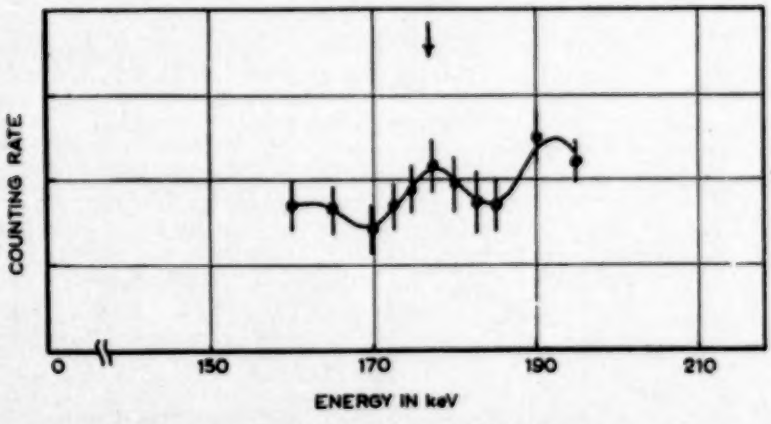

Fig. 9. The 239 keV coincidence spectrum of Pb^{212} with $\approx$ 10 % daughter contamination (shielded; 6 runs, 8 min after separation).

Pb^{212} with about 10 % daughter contamination show the definite existence of this weakly coincident line (fig. 9). Similar experiments were performed with the 250—270 keV region of these elements in an effort to locate the proposed 164—251 keV cascade. In agreement with the results of Krisyouk [1]) no such cascade was observed.

As a by-product of the experiments described above, one can compute the approximate values of the K conversion coefficients for the 239 keV line and the 115 keV line. From fig. 10 one may obtain the intensity ratio between the

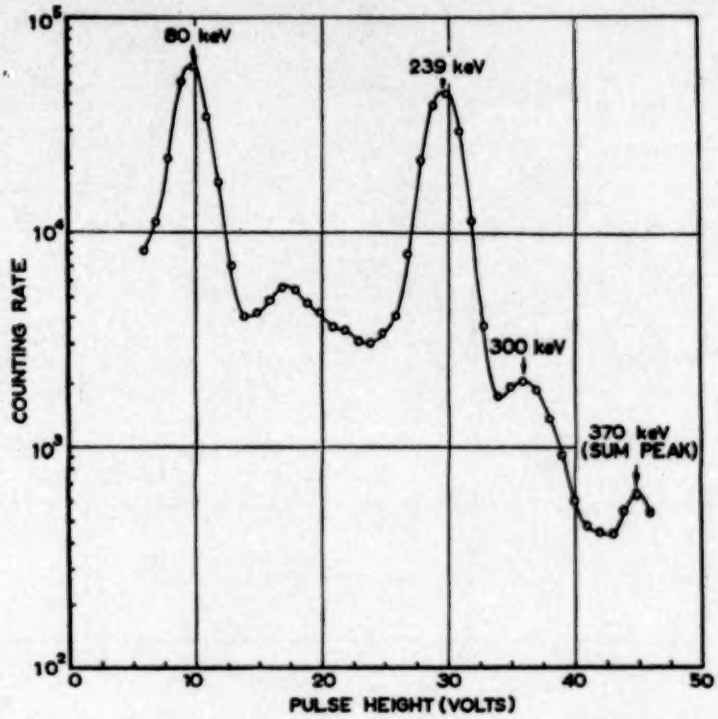

Fig. 10. Pulse-height spectrum of Pb^{212}, containing less than 25 % daughter background (no absorber).

TABLE 2

K conversion coefficients

Energy (keV)	Experimental value	Theoretical values (Rose [8]), Sliv and Band [9]))							
		E1		M1		E2		M2	
239	0.74±10 %	0.036	0.045	0.85	0.65	0.096	0.105	2.8	2.55
115	5.8 ±15 %	0.25	0.235	6.4	5.3	0.58	0.50	49	30.0

K conversion line (corrected for fluorescence yield) and the 239 keV gamma line, making the assumption that most of the X-rays arise from the very strong 239 keV conversion lines. Similarly, one may use the spectrum in fig. 6, to obtain this information for the 115 keV transition.

The experimental values of conversion coefficients are listed in table 2, along with the theoretical calculations, for some types of transitions, reported by Rose [8]) and Sliv and Band [9]). The transitions are seen to be essentially M1 in nature, in good agreement with the results of conversion electron measurements.

3.3. DIRECTIONAL CORRELATION RESULTS

Series of runs were taken at angles separated by 30°. At each angle, all the data collected were analyzed separately for each detector, as a check on the consistency of results. To obtain better statistics, all data from all detectors were combined in the final analysis.

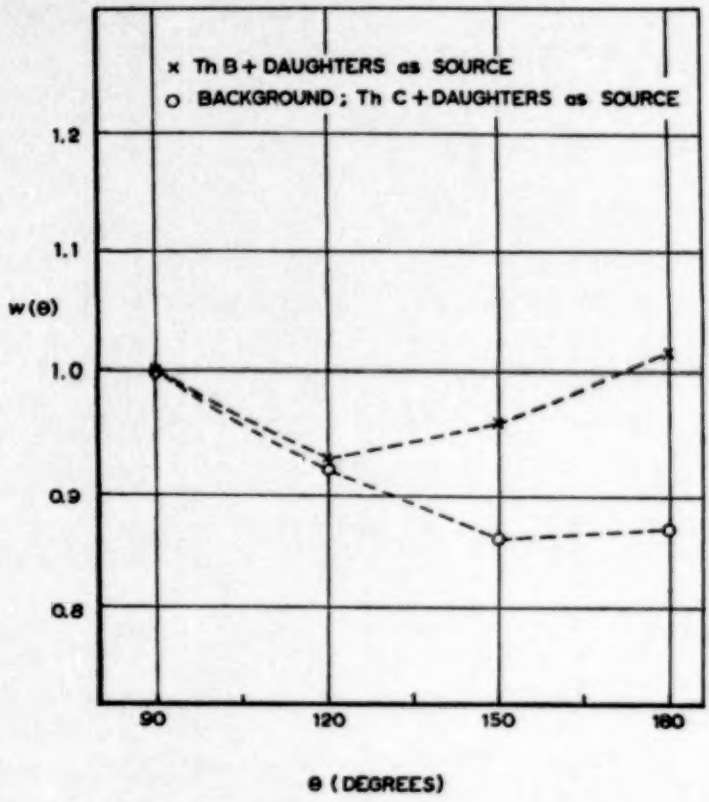

Fig. 11. Experimental angular correlations in Pb^{212} in equilibrium with its daughters and in the daughters alone (uncorrected and arbitrarily normalized data; unfitted).

Experiments were performed to measure the correlations in Thorium B in equilibrium with its daughters and in the daughters alone. The experimental points for the combined results are shown arbitrarily normalized in fig. 11.

No attempt has been made to fit a curve to either the Thorium B with daughters or the background due to the daughters as the correction due to this background is important. No runs were made with separated Thorium B as a source, since the daughter product contamination would increase significantly during the long counting times involved.

From fig. 2, the spectrum of the daughter products of Thorium B, and from fig. 12, the spectrum of Thorium B in equilibrium with its daughter products, one may obtain the ratio of counting rates between the daughter product "background" and Thorium B in equilibrium with daughter products, as used in the directional correlation experiments. This is accomplished by equating

the counting rates beyond 415 keV, as was done in the coincidence work. Around 300 keV within the acceptance range of the single-channel analyzers used, the ratio is found to be $B = 0.52 \pm 0.06$.

The directional correlation counting rates were normalized to the total counting rates in the separate channels which were set on the 300 keV line.

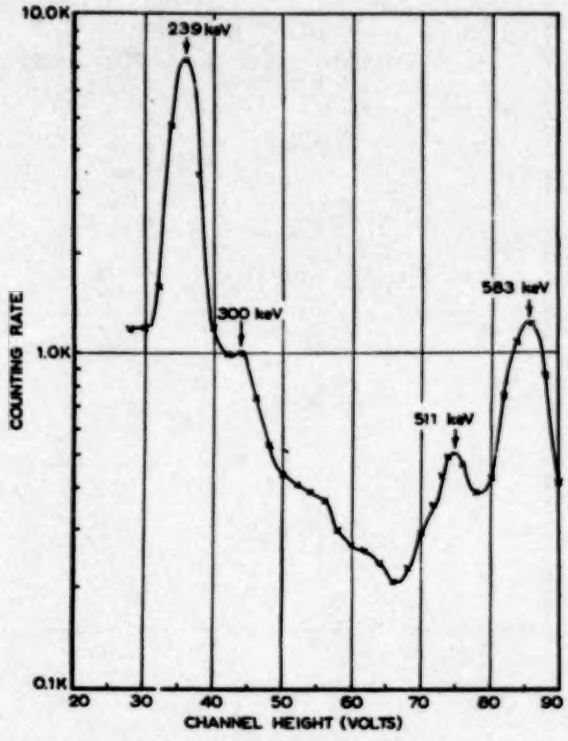

Fig. 12. Spectrum of Pb^{212} and daughters (with absorber).

The master channel was set on the 115 keV line. The background ratio found above was used as the centre of a range of values of background ratios, and the data were corrected for each ratio picked. The corrected data were fitted to

$$W(\theta) = 1 \pm A_2 P_2(\cos\theta) \tag{1}$$

and

$$W^1(\theta) = 1 + A_2^1 P_2(\cos\theta) + A_4^1 P_4(\cos\theta), \tag{2}$$

using an IBM 704 computer [10]) to carry out the least square curve fitting to the sum of Legendre polynomials. Since the errors in A_4^1 were in every case the same order of magnitude as A_4^1, the first fit (1) was assumed to be sufficient. This agrees with the well established M1 nature of the 115 keV and 300 keV radiation, as determined by conversion electron work [1]).

TABLE 3

Attenuated theoretical values of A_2

Cascade	A_2	Case
0(1)1(1)1	−0.236	(a)
1(1)0(1)1	0.000	(b)
1(1)1(1)1	0.118	(c)
1(1)2(1)1	0.165	(d)
2(1)1(1)1	−0.024	(e)
2(1)2(1)1	−0.165	(f)
3(1)2(1)1	0.047	(g)

TABLE 4

Assumed background ratios and experimental A_2 coefficients

Background ratio	A_2
0.40	0.1075 ± 0.0243
0.50	0.1543 ± 0.0271
0.55	0.1866 ± 0.0291
0.60	0.2290 ± 0.0317

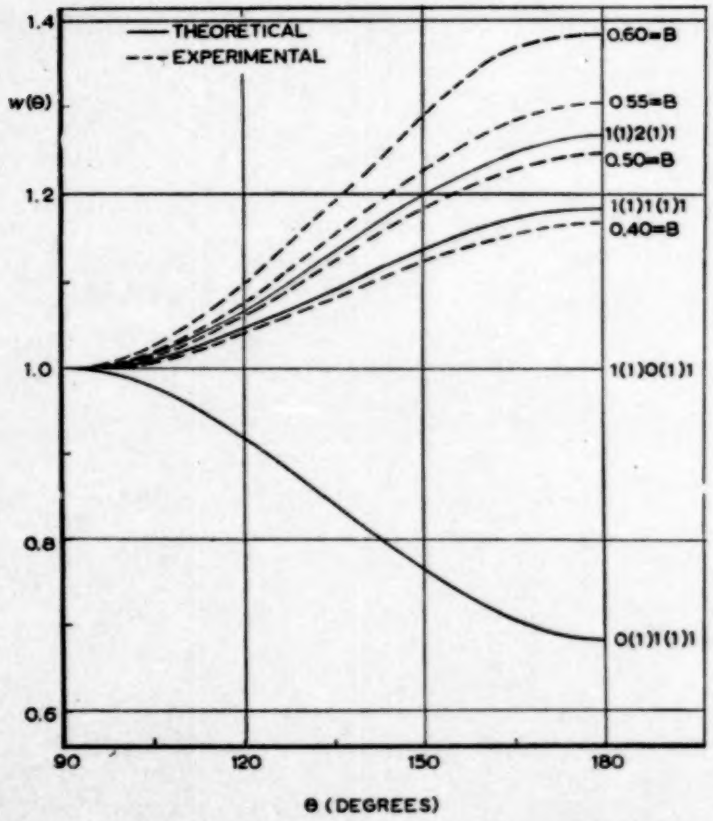

Fig. 13. Theoretical and experimental angular correlation curves for various assumed background ratios (115−300 keV cascade in Bi^{212}).

The coefficients [11]) for all cascades of the form $I_A(1)I_B(1)$ 1 are listed in table 3, corrected for the measured attenuation due to finite angular resolution in the detectors. The attenuation factor Q_2 was found by use of annihilation radiation[12]) to be 0.943 for the A_2 coefficient.

Comparison of values in table 3 with the experimental ratios shows that cases (a), (b), (e), (f), (g) may be ruled out without further consideration. Case (c) must be excluded, since the background ratio cannot be sufficiently in error to yield coefficients matching this case. Table 4 shows that this would require a background ratio of approximately 0.4, whereas the measured value was 0.52 ± 0.06. Fig. 13 shows the experimental curves for various assumed background ratios, and the various theoretical curves. Case (a) is included simply to show what would be predicted by previously assigned spins [1]).

Both the assumed backgrounds of 0.50 and 0.55 are within the probable error in the measured background, and both yield coefficients which match only the 1(1)2(1)1 cascade, within the experimental error.

4. Summary

The gamma rays following the decay of Pb^{212} to Bi^{212} have been examined by response function analysis, coincidence techniques and directional correla-

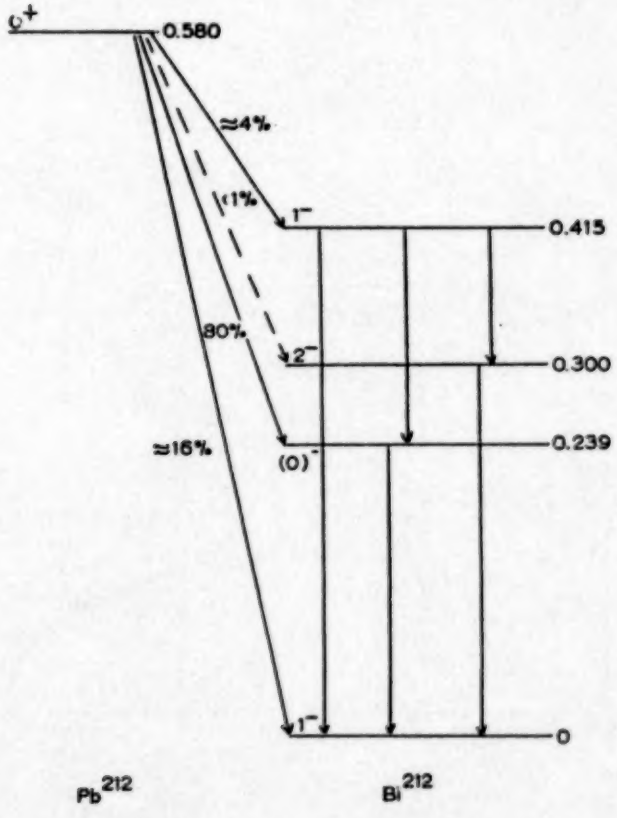

Fig. 14. Proposed decay scheme of Pb^{212}.

tion. The proposed decay scheme is shown in fig. 14. In accordance with electron conversion work [1]) the 251 keV level has been dropped, since no evidence could be found for either the 164 keV or 251 keV gamma transitions. The 115 keV, 177 keV and 415 keV lines were observed by gamma detection and definitely attributed to this decay. Where measured, intensities are listed in table 1. The K conversion coefficients have been estimated, showing again that the 239 keV and 115 keV lines are M1. The 115 keV and 300 keV lines are determined, by directional correlation, to be dipole. Spin 1 is assigned to the 415 keV level, and spin 2 for the 300 keV level, both by directional correlation. The results agree with electron conversion work, except for the spin assignments. Since the intensity of the 177 keV gamma ray is too low for directional correlation measurements, the spin of the 239 keV level remains in doubt. The 61 keV transition has been omitted from the decay scheme, since it was not found. If the 239 keV level has spin 0, the 61 keV transition from the 300 keV to the 239 keV level would be E2 so would not be expected to be observable.

The authors wish to thank IBM Corporation and Cornell Aeronautical Laboratory for the use of the IBM 704 Computer.

References

1) Krisyouk, Sergeyev, Latyskev and Vorobyov, Nuclear Physics **4** (1957) 579
2) Demichelis, Chinaglia and Trivero, Nuovo Cim. **8** (1958) 369
3) N. P. Rudenko, Journ. Anal. Chem. of the USSR **11** (1956) 4
4) Lazar, IRE Transactions NS-5 (1958) p. 58
5) Hubbell and Scofield, IRE Transactions NS-5 (1958) p. 156
6) Nuclear Data Tables (National Academy of Science, 1959) p. 1959-4118, 119, 120
7) Hagedorn and Wapstra, Nuclear Physics **15** (1960) 146
8) Rose, in Beta and gamma ray spectroscopy, ed. by K. Siegbahn (North-Holland Publishing Company, Amsterdam, 1955)
9) Sliv and Band, Univ. of Illinois, Report 571CCK1
10) SHARE program ANE 201, Least square Legendre polynomial fit (1959)
11) S. P. Lloyd, Phys. Rev. **83** (1951) 716
12) Church and Kraushaar, Phys. Rev. **88** (1952) 419

2.G

Nuclear Physics **20** (1960) 360—369; © *North-Holland Publishing Co., Amsterdam*

Not to be reproduced by photoprint or microfilm without written permission from the publisher

NUCLEAR STRUCTURE STUDIES IN THE LEAD REGION WITH (d, t) REACTIONS

BERNARD L. COHEN, SANTOS MAYO † and ROBERT E. PRICE

Radiation Laboratory, University of Pittsburgh, Pittsburgh, Pa. ††

Received 10 June 1960

Abstract: Energy distributions of tritons from (d, t) reactions in the isotopes of Pb, Bi and Tl were measured with ≈ 100 keV resolution. Evidence is given on the location of the missing $h_{\frac{9}{2}}$ state in Pb^{207}. As theoretically expected, the spectrum from Bi^{209}(d, t) is quantitatively similar to that from Pb^{208}(d, t) except that all levels are split into two or more components. The energies of the states excited by Pb^{207}(d, t) agree well with those predicted from the True and Ford calculation. The cross sections for exciting these agree reasonably well with calculations from the True and Ford wave functions; but several changes in the latter are suggested, including a reduction of the $(p_{\frac{1}{2}})^{-2}$ configuration in the ground state from 73 % to about 55 %. The long sought 0^+ state apparently occurs at 1.19 MeV. The spectra from Pb^{206}(d, t) and from Tl^{205}(d, t) show marked similarities to each other and a general similarity with the spectrum from Pb^{208}(d, t); it is shown that this is to be expected. In general, the shell model of nuclear structure with inverse stripping reaction theory gives a satisfactory quantitative explanation of all the data.

1. The Experiment

Neutron pick-up reactions have been used by Harvey [1]) and by Cohen and Mosko [2]) for nuclear structure studies in the region near the doubly closed shell Pb^{208}; in both cases, however, the resolution was rather poor (≈ 400 keV) and measurements were made at only a single angle, so that practically no quantitative conclusions could be reached. In this paper, studies of this type are reported using (d, t) reactions and employing much better resolution (≈ 100 keV). Data are reported at several angles and relatively detailed comparisons with theoretical predictions are made.

The experimental method has been described previously [3]). Thin targets were bombarded by 15 MeV deuterons from the University of Pittsburgh 119 cm cyclotron; reaction products are passed through a 60° wedge magnet spectrograph and into the emulsions of photographic plates located on the spectrograph focal plane. After the bombardment, the plates are developed, and the tracks at various positions in the photographic emulsions are counted under a microscope to obtain an energy spectrum. Only that region of the

† Presently at Laboratorio Sincrociclotron, Comision Nacional de Energia Atomica, Ao. Libertador Gral. San Martin, 8250, Buenos Aires, Argentina.

†† Work assisted by the National Science Foundation and the joint program of the Office of Naval Research and the U. S. Atomic Energy Commission.

spectrum where the magnetic rigidity for tritons is greater than that for any other reaction product was studied. An example of typical data is shown in fig. 1. Data were obtained at scattering angles of 45°, 60° and 90° for the Pb^{206},

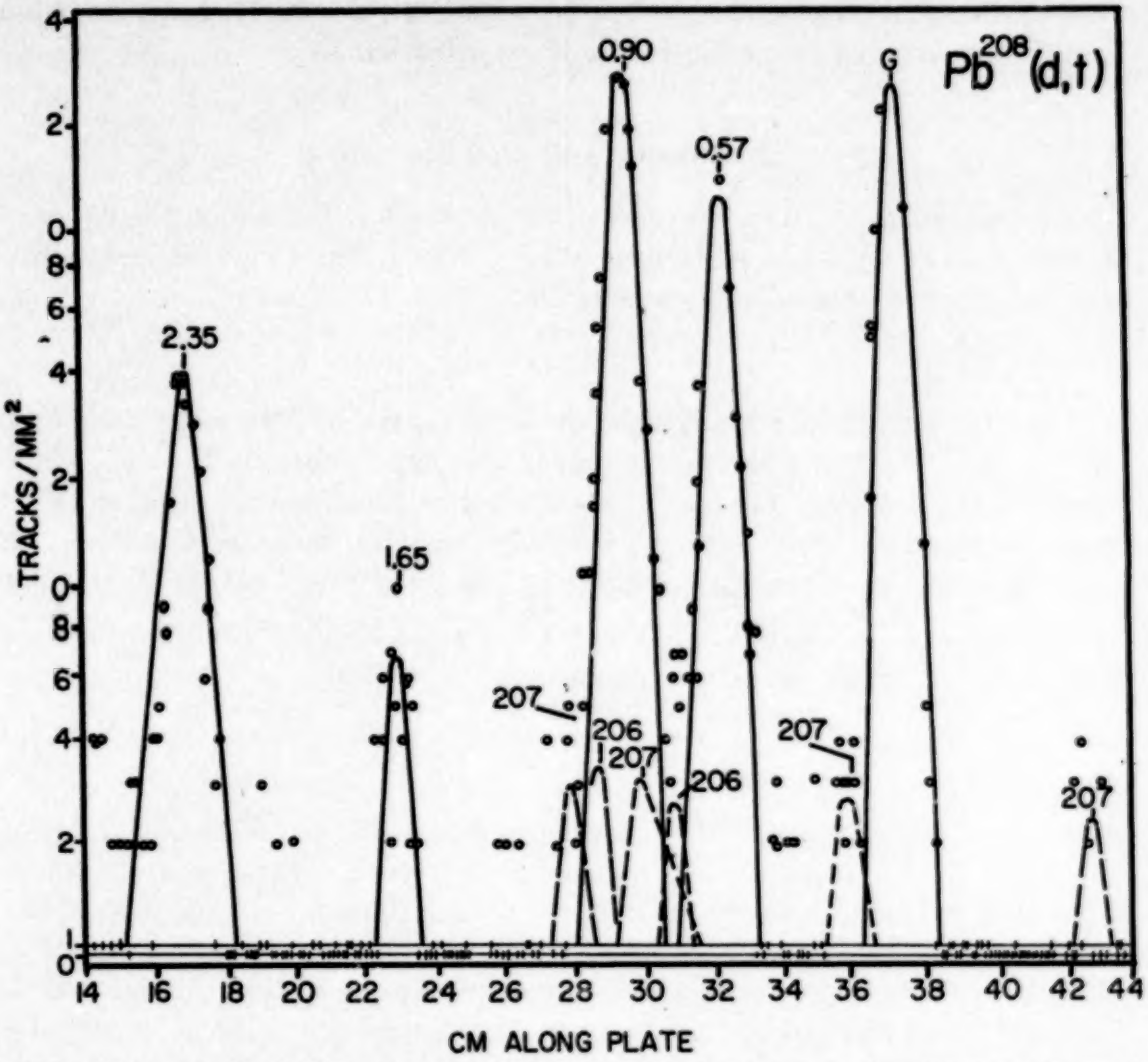

Fig. 1. Energy distribution of tritons from $Pb^{208}(d, t)Pb^{207}$. Angle of observation is 45°. Background at left side is from elastic deuterons, it is considerably lower at larger angles. Different symbols used for ordinates equal 0 and 1 are only to facilitate clarity in the figure.

Pb^{207} and Pb^{208} targets; and at 90° for the Bi and Tl targets. The lead isotope targets were not isotopically pure (isotopic analyses are shown in table 1)

TABLE 1

Composition of lead isotope targets

Designation	Composition (%)		
	Pb^{206}	Pb^{207}	Pb^{208}
Pb^{206}	80.4	11.7	7.9
Pb^{207}	3.5	71.5	25.0
Pb^{208}	1.2	2.8	96.0

so that careful corrections were necessary. In addition, the targets were thicker (11 mg/cm²) than is desirable for optimum energy resolution [4]). The bismuth target was 7 mg/cm² thick and was evaporated on 0.9 mg/cm² gold backing. The thallium target was TlO powder on a mylar backing [5]). There are no triton peaks from oxygen or carbon in the region studied.

2. Results and Conclusions

Surveys of the triton energy spectra are shown in figs. 2 and 3; the 90° data for the lead isotopes is qualitatively very similar to the 45° and 60° data but the resolution is considerably poorer [4]).

$Pb^{208}(d, t)Pb^{207}$

The most easily understood results are those for the $Pb^{208}(d, t)Pb^{207}$ reaction, as that reaction excites the well known single "hole" states in the shell which closes at 126 neutrons. The spins are known from other work, so that the shell model assignments may be made unambiguously as shown in figs. 2 and 3. The only difficulty is the absence of the $h_{\frac{9}{2}}$ hole state; it will now be shown that it very probably lies within 40 keV of the $f_{\frac{7}{2}}$ state. The differential cross section for a (d, t) reaction may be expressed as

$$\frac{d\sigma}{d\Omega} \propto f(l_n, Q, \theta) S c^2, \tag{1}$$

where S is the coefficient of fractional parentage, c is the overlap integral of the initial state minus a neutron and the final state, and f is a factor obtained from nuclear reaction theory. In Butler stripping theory, f is a function of the angular momentum l_n of the neutron in the nucleus, the energy Q, released in the reaction, the angle θ at which the triton is emitted, and the nuclear radius. This will be assumed to be the case here. The difference in nuclear size among the lead isotopes will be neglected. S may be simply calculated [6]) and for the $Pb^{208}(d, t)Pb^{207}$ reaction, $c = 1$ for all single hole states. Thus, the observed data may be used to determine f. The results at each angle are shown in fig. 4. In that figure, a linear dependence on a semi-log plot is assumed for interpolation or extrapolation purposes. Actually, fig. 4 is presented for use in later calculations where the interpolations and extrapolations are relatively small; however, it may be used to obtain at least a rough estimate of the expected intensity of the $h_{\frac{9}{2}}$ hole state as a function of its Q-value. From this it may be concluded that it would have been observed if its Q-value were greater than -4.3 MeV, unless it is almost coincident with another peak. Since that Q-value seems much too small (all other states in the shell have Q-values between -1.1 and -3.4 MeV), the latter situation seems more probable. It cannot be below the $i_{\frac{13}{2}}$ state, for if it were, the $i_{\frac{13}{2}}$ state would not be isomeric. It cannot be very

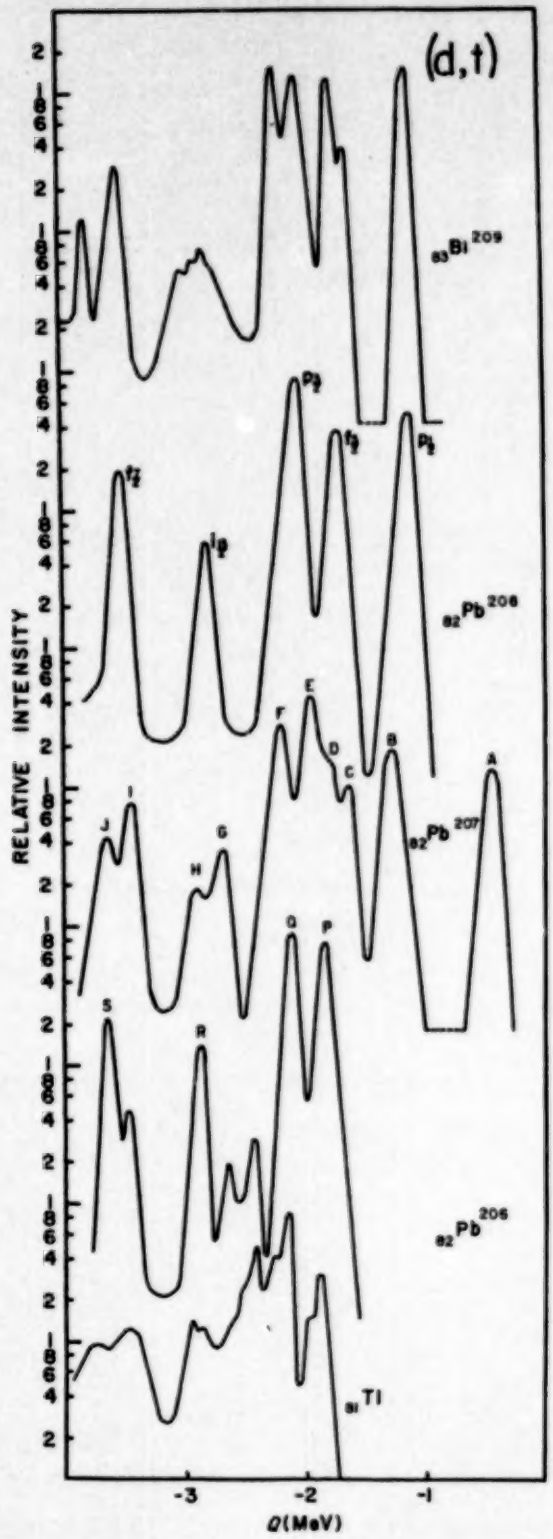

Fig. 2. Survey of energy spectra of tritons observed at 60° from (d, t) reactions in Pb isotopes, Bi and Tl.

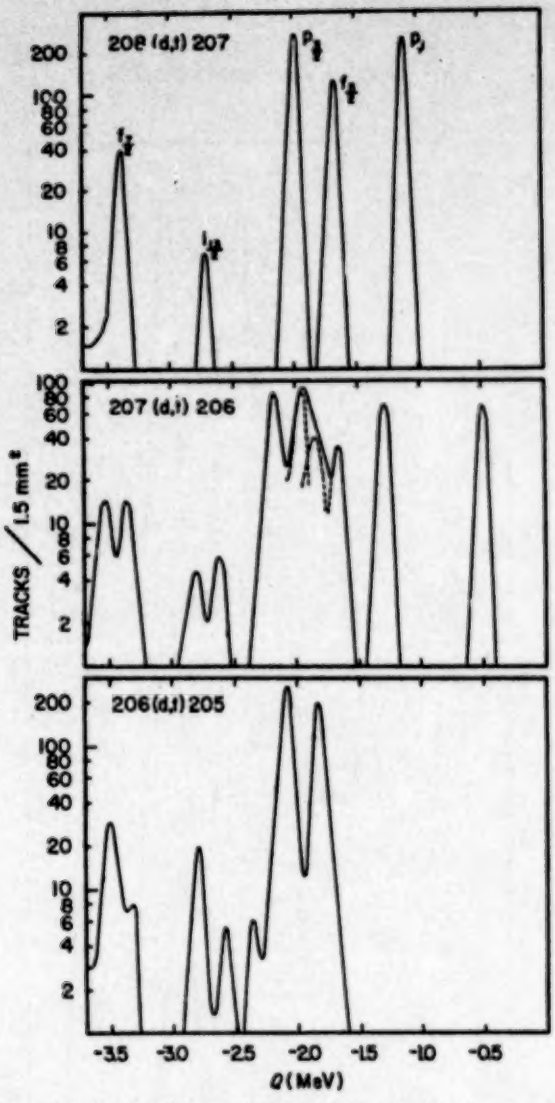

Fig. 3. Energy spectra of tritons observed at 45° from (d, t) reactions in the Pb isotopes.

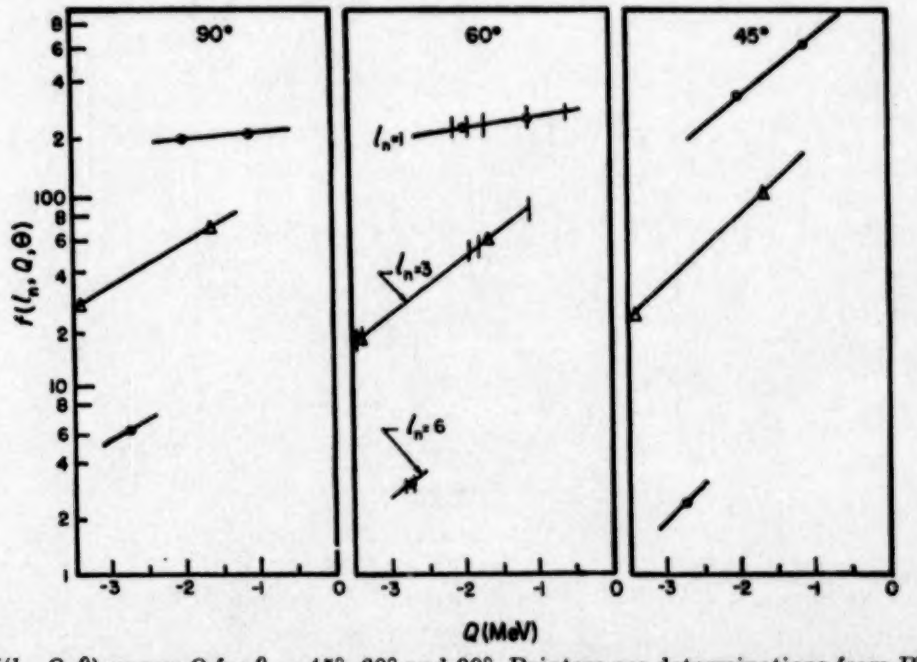

Fig. 4. $f(l_n, Q, \theta)$ versus Q for $\theta = 45°$, 60° and 90°. Pointers are determinations from Pb^{208}(d, t) Pb^{207}. Vertical lines in 60° data show values of Q for which these curves are used in calculation of intensities from Pb^{207}(d, t)Pb^{206} reactions.

close to the $i_{\frac{13}{2}}$ or else the Bi^{207} electron capture would decay almost exclusively to it rather than to the $i_{\frac{11}{2}}$. Thus the only alternative is to assume that the $h_{\frac{9}{2}}$ lies very close to the $f_{\frac{7}{2}}$.

The ratio of peak height to peak area is smaller for the $f_{\frac{7}{2}}$ state than for any of the other peaks in the spectrum, but it is only smaller than the average by about 6 %. While this is perhaps within the error of the determination, it lends at least some additional support to the conclusion, and indicates that the separation of the two levels must be less than 40 keV.

$Bi^{209}(d, t)Bi^{208}$

The next simplest reaction is $Bi^{209}(d, t)Bi^{208}$ as this again should excite single hole states in the 126 neutron shell. The spectrum should thus be identical with that from $Pb^{208}(d, t)$ except that for every level excited in the latter reaction there should be a group of levels corresponding to the various couplings of the extra $h_{\frac{9}{2}}$ proton in Bismuth to the single neutron hole. For example, the ground state which is $\frac{1}{2}^-$ in the Pb^{208} reaction, must be split into two states of spin 5^+ and 4^+ in the Bi reactions.

From fig. 2 both the correspondence between the two cases in the gross structure and the splitting in the Bi fine structure are clearly seen. The excitation energies of the states and the cross sections are listed in table 2. The

TABLE 2

Levels excited by (d, t) reactions in Pb^{208} and Bi^{209}

Excitation energy		$d\sigma/d\Omega$(mb/sr at 60°)		Designation in Pb^{208}	Peak height/area ratio in Bi
Bi^{209}	Pb^{208}	Bi^{209}	Pb^{208}		
0†	0	3.0	3.0	$p_{\frac{1}{2}}$	0.92
0.49 0.61	0.57	0.48 1.5 } 2.0	2.3	$f_{\frac{5}{2}}$	1.5 1.5
0.87† 1.05†	0.90	2.7 2.3 } 5.0	5.7	$p_{\frac{3}{2}}$	0.85 1.2
1.65†	1.64	0.28	0.28	$ir_{\frac{11}{2}}$	0.27
2.34† 2.60	2.35	0.43 0.13 } 0.56	1.0	$f_{\frac{7}{2}}$	1.0 1.4

† More than one level as indicated by last column

correspondence in both energies (averaged in the case of Bi) and cross sections is seen to be quite close for all cases except for the $f_{\frac{7}{2}}$ state where the Bi cross section is rather too small and the average energy is shifted. The simplest explanation would be that the splitting of this level is very large and some of the

components are not seen. This is difficult to reconcile with the facts that (1) there are no other sufficiently excited levels within 600 keV, and (2) the $f_{\frac{1}{2}}$ level is not strongly split and indeed none of the other levels is split by nearly as much as 600 keV. One interesting possibility is that a component of this level in Pb^{207} is $h_{\frac{1}{2}}$ as indicated by previous arguments and there is an extra strong coupling between the $h_{\frac{9}{2}}$ proton and the $h_{\frac{9}{2}}$ hole in the neutron shell. Such an interaction would be the analogue in isobaric spin space of the well known pairing interaction in ordinary spin space.

Also listed in table 2 are the ratios of peak height to areas under peaks for the various peaks in the Bi spectrum. A ratio of 1.5 is expected for a single isolated peak, so that the peaks for which this ratio is appreciably less than 1.5 are a combination of two or more unresolved peaks; the energies of these are marked by an asterisk in the table. In the case of the $i_{\frac{13}{2}}$, there must be at least 6 peaks if they are all of equal intensity, and since the spectrum indicates that the latter is not the case, there are probably 10 or more peaks.

Pb^{207}(d, t)Pb^{206}

The results for the reaction Pb^{207}(d, t)Pb^{206} are much more complex to analyze since there are strong couplings between two holes in the same major shell. However, nuclear structure calculations for Pb^{206} have been made by True and Ford [7]) and by Kearsley [8]), so that detailed comparisons with theory are possible. Since the True and Ford paper contains complete wave functions, comparisons will be made with it, but the results of the two papers are very similar.

Since the ground state of Pb^{207} is pure $(p_{\frac{1}{2}})^{-1}$, the states of Pb^{206} excited by the Pb^{207}(d, t) reaction are those with components in their wave functions of the form $(p_{\frac{1}{2}})^{-1}(x)^{-1}$ where x is $p_{\frac{1}{2}}$, $f_{\frac{5}{2}}$, etc. The states of this type from ref. [7]) are listed in table 3 together with their energies, spins, parities and the pertinent

TABLE 3

Energy levels excited by (d, t) reactions in Pb^{207}

Symbol	Excitation energy			Predicted I^π	True-Ford configuration
	This work	Alburger	Predicted		
A	0	0	0	0^+	0.73 $(p_{\frac{1}{2}})^2$
B	0.81	0.803	0.72	2^+	0.57 $p_{\frac{1}{2}} f_{\frac{5}{2}}$ +0.30 $p_{\frac{1}{2}} p_{\frac{3}{2}}$
C	1.19		1.36	0^+	0.18 $(p_{\frac{1}{2}})^2$
D	1.34	1.341	1.40	3^+	$p_{\frac{1}{2}} f_{\frac{5}{2}}$
E	1.49		1.39	2^+	0.37 $p_{\frac{1}{2}} f_{\frac{5}{2}}$ +0.60 $p_{\frac{1}{2}} p_{\frac{3}{2}}$
F	1.72		1.74	1^+	0.99 $p_{\frac{1}{2}} p_{\frac{3}{2}}$
G	2.19	2.200	2.17	7^-	0.90 $p_{\frac{1}{2}} i_{\frac{13}{2}}$
H	2.38	2.385	2.35	6^-	0.97 $p_{\frac{1}{2}} i_{\frac{13}{2}}$
I	2.95		3.01	4^+	0.90 $p_{\frac{1}{2}} f_{\frac{7}{2}}$
J	3.11		3.08	3^+	$p_{\frac{1}{2}} f_{\frac{7}{2}}$

part of their wave functions. The experimental energies from this work are also listed in table 3, and the agreement between theory and experiment is very good. In a few cases, levels known from other work [9]) are listed in table 3, and it is seen that the agreement between the experiments is quite satisfactory.

One important conclusion from table 3 is the identification of a 0^+ state at 1.19 MeV. From ref. [7]) alone, the 0^+ state could be the 1.19, 1.34 or 1.49 MeV state. However, the 1.34 MeV state is known to be 3^+ from ref. [9]), and the cross section results below would preclude the identification of the 1.49 MeV state as the 0^+.

The theoretically expected cross sections for exciting the various states in Pb^{206} may be calculated from eq. (1) by taking $f(l_n, Q, \theta)$ from fig. 4, c^2 from ref. [1]) (or table 3), and calculated values † of S. The values of f needed from fig. 4 are shown by the vertical cross lines in the 60° portion of that figure, and it is clear that interpolations and extrapolations from the data used in obtaining that figure are very small in all cases. This is most fortunate, as any large extrapolations would be very unreliable.

The results of the calculations are shown in table 4 where they are compared with the experimental values. The agreement is, in general, reasonably good. The most striking difficulty is in the $i_{\frac{13}{2}}$ level at forward angles. However, its intensity is very low at such angles, and the intensity is changing quite rapidly with angle. It is even possible that the level is excited by some other process to a sufficient extent to compete with the neutron pick-up reaction.

TABLE 4

Cross sections for excitation of various levels in $Pb^{207}(d, t)Pb^{206}$ reactions. All values are relative to the ground state transition from $Pb^{208}(d, t)Pb^{207}$ at that angle.

Level symbol	45°		60°		90°		meas./calc. ratio		
	meas.	calc.	meas.	calc.	meas.	calc.	45°	60°	90°
A	0.33	0.53	0.32	0.43	0.30	0.38	0.62	0.75	0.79
B	0.34	0.52	0.43	0.65	0.57	0.71	0.66	0.66	0.80
C	0.16	0.05	0.22	0.087	0.36	0.090	3.2	2.6	4.0
D	0.19	0.24	0.22	0.39	0.51	0.57	0.79	0.56	0.89
E	0.45	0.45	0.86	0.81	0.80	0.83	1.00	1.06	0.96
F	0.41	0.34	0.60	0.68	0.65	0.68	1.20	0.88	0.95
G	0.029	0.012	0.077	0.044	0.14	0.09	2.4	1.75	1.5
H	0.024	0.011	0.042	0.037	0.12	0.09	2.3	1.13	1.3
I	0.067	0.073	0.18	0.16	0.27	0.30	0.92	1.12	0.90
J	0.067	0.058	0.10	0.13	0.24	0.25	1.15	0.77	0.96

All other discrepancies between calculated and observed cross sections in table 4 may be explained as errors in the True and Ford wave function [7]); to remove these discrepancies, the amplitudes of the respective terms should be

† The authors are greatly indebted to J. B. French for his calculations of the S values for transitions between single hole and two hole states.

multiplied by the ratio of experimental to calculated cross sections. The most clear cut case of this type is the relative distribution of the $(p_{\frac{1}{2}})^{-2}$ state between the two 0^+ states (A and C): while the True and Ford wave function gives A to be 73 % $(p_{\frac{1}{2}})^{-2}$ and C to be 18 % $(p_{\frac{1}{2}})^{-2}$, the experiments indicate that each is about 55 % $(p_{\frac{1}{2}})^{-2}$. There is additional evidence from (d, p) reactions that A is definitely less than 73 % $(p_{\frac{1}{2}})^{-2}$ and 55 % is in reasonable agreement with those results. This will be discussed in the following paper [10]). Table 4 also indicates that the amplitude of $(p_{\frac{1}{2}} f_{\frac{5}{2}})_3$ in D should be decreased slightly, and that the amplitudes of one or both parts of the wave function for B should be decreased.

$Pb^{206}(d, t)Pb^{205}$

The energy levels of Pb^{205} excited by the (d, t) reaction on Pb^{206} are listed in table 5. The relative cross sections at 45° and 60° are also tabulated. According to either the True and Ford wave function or its modifications discussed above,

TABLE 5

Energy levels excited by (d, t) reactions in Pb^{206}

Excitation energy (MeV)	Relative intensity		Symbol
	45°	60°	
0	1.0	1.0	P
0.24	1.3	1.1	Q
0.54	0.031	0.038	
0.77	0.028	0.026	
0.99	0.10	0.19	R
1.53	0.039	0.060	
1.72	0.15	0.28	S

a large part of the time the ground state of Pb^{206} is the same as the ground state of Pb^{208} except that the $p_{\frac{1}{2}}$ shell is empty instead of full. Since there can be no interaction between either completely empty or completely full shells and other states, the spectrum from $Pb^{206}(d, t)$ should be largely identical with that from $Pb^{208}(d, t)$ except that the $p_{\frac{1}{2}}$ level should be missing. Qualitatively, such a similarity is apparent from figs. 2 and 3 in that the four large peaks from $Pb^{206}(d, t)$ seem to correspond to the $f_{\frac{5}{2}}$, $p_{\frac{3}{2}}$, $i_{\frac{13}{2}}$ and $f_{\frac{7}{2}}$ peaks from $Pb^{208}(d, t)$.

TABLE 6

Cross section ratios between corresponding levels from $Pb^{206}(d, t)$ and $Pb^{208}(d, t)$. Capital letters refer to states from Pb^{206} reaction (cf. table 5), and spectroscopic notation refers to states from $Pb^{208}(d, t)$.

Angle of observaiton	$P/f_{\frac{5}{2}}$	$Q/p_{\frac{3}{2}}$	$R/i_{\frac{13}{2}}$	$S/f_{\frac{7}{2}}$
45°	1.5	0.9	2.7	0.9
60°	1.1	0.7	2.2	1.0
90°	1.1	0.6	2.5	1.1

A quantitative test of the correspondence is shown in table 6, where the cross section ratios of corresponding levels from the two reactions are listed. If the True and Ford wave function were correct, all ratios in table 6 would be at least 0.73 whereas if the altered wave function deduced above is accepted, they should be at least 0.55. The evidence is far from conclusive, but there is perhaps some indication here that the True and Ford value is too high.

Tl(d, t)

Natural thallium is 70 % Tl^{205} which has the same number of neutrons as Pb^{206}. There is some evidence [11]) that an odd, low angular momentum proton coupling to a single-particle neutron state does not cause very wide splittings. Thus it might be hoped that the extra $s_{\frac{1}{2}}$ proton hole in Tl^{205} will not cause the spectrum from Tl^{205} (d, t) to differ markedly from the spectrum from Pb^{206}(d, t). It is evident from fig. 2 that this is indeed the case. There is essentially a one-to-one correspondence between the peaks in the two spectra, and there is at least a rough similarity in the relative intensities of the various peaks.

3. Discussion

From the results and their analyses described above, it is clear that the combination of the shell model description of nuclear structure and deuteron stripping reaction theory can successfully explain all the major features of the energy spectra of tritions from (d, t) reactions in the region near Pb^{208}. The energies are very well explained, and the cross sections can be at least semi-quantitatively calculated. A few problems arise, but these can always be explained away without major changes in the theory. The True and Ford wave functions [7]) for the states of Pb^{206} seem to be reasonably good, but several changes in them are suggested by the experimental results. No investigation has yet been made of what interactions are necessary in the theory to give these changes.

The authors would like to acknowledge the very important services of the cyclotron operations group and the plate reading group, some helpful discussions with E. Baranger, J. B. French and S. Meshkov, and the support and encouragement of A. J. Allen.

References

1) J. A. Harvey, Can. J. Phys. **31** (1953) 278
2) B. L. Cohen and S. W. Mosko, Phys. Rev. **106** (1957) 995
3) B. L. Cohen *et al.*, Phys. Rev. (in print)
4) B. L. Cohen, Rev. Sci. Instr. **30** (1959) 415
5) G. Fodor and B. L. Cohen, Rev. Sci. Instr. **31** (1960) 73
6) J. B. French, in Nuclear spectroscopy, to be published
7) W. W. True and K. W. Ford, Phys. Rev. **109** (1958) 1675
8) M. J. Kearsley, Nuclear Physics **4** (1957) 157
9) D. E. Alburger and A. W. Sunyar, Phys. Rev. **99** (1955) 695
10) B. L. Cohen, R. E. Price and S. Mayo, Nuclear Physics **20** (1960) 370
11) B. L. Cohen and R. E. Price, Nuclear Physics (in print)

2.G

Nuclear Physics **20** (1960) 370—381; © *North-Holland Publishing Co., Amsterdam*

Not to be reproduced by photoprint or microfilm without written permission from the publisher

NUCLEAR STRUCTURE STUDIES IN THE LEAD REGION WITH (d, p) REACTIONS

BERNARD L. COHEN, ROBERT E. PRICE and SANTOS MAYO †

Radiation Laboratory, University of Pittsburgh, Pittsburgh, Pa. ††

Received 10 June 1960

Abstract: Energy distributions of protons from (d, p) reactions in the isotopes of Pb and Bi were measured with ≈ 100 keV resolution and angular distributions of several of the groups were studied. The angular distribution from Pb^{207}(d, p)Pb^{208}(g.s.) agrees very well with the distorted wave Born approximation calculation of Tobocman and with measured angular distributions of $l_n = 1$ transitions in Pb^{206}(d, p)Pb^{207}. The difference from a measured $l_n = 3$ transition is quite large. From studies of the excitation of the various single hole states of Pb^{207} in Pb^{206}(d, p)Pb^{207}, the wave function of the ground state of Pb^{206} is determined to be approximately

$$\Psi_{206} = \sqrt{0.56}(p_{\frac{1}{2}})^{-2} + \sqrt{0.25}(f_{\frac{5}{2}})^{-2} + \sqrt{0.12}(p_{\frac{3}{2}})^{-2} + \sqrt{0.04}(i_{\frac{13}{2}})^{-2} + \sqrt{0.03}(f_{\frac{7}{2}})^{-2},$$

which has less $(p_{\frac{1}{2}})^{-2}$, and more $(f_{\frac{5}{2}})^{-2}$, $(i_{\frac{13}{2}})^{-2}$ and $(f_{\frac{7}{2}})^{-2}$ than the theoretical wave functions of True and Ford, and of Kearsley. A new low lying non-hole state of Pb^{207} is found. Extensive efforts to understand the spectrum from Pb^{208}(d, p)Pb^{209} are reported. The relative intensities of the various peaks are very difficult to explain.

1. Introduction

Deuteron stripping reactions have been used to study nuclear structure in the region of Pb^{208} by Harvey [1]) and by McEllistrem, Martin, Miller and Sampson [2]). While the first is an early low resolution survey at a single angle, the second is a reasonably detailed, good resolution experiment. However, the study reported here represents several improvements relative to it, namely: (1) it is carried out at 15 MeV bombarding energy as compared to 10 MeV in ref. [2]) so that Coulomb effects are less dominating; (2) the intensity relative to background is much higher so that several peaks are observed which were missed there; (3) this work includes Bi^{209} and large parts of the spectra from Pb^{207} and Pb^{208} which were not included in that study; and (4) the resolution is somewhat better.

In addition, the analysis is carried considerably further, and the conclusions are somewhat different.

† Now at Laboratorio Sincrociclotron Comision Nacional de Energia Atomica Ao. Libertador Gral. San Martin, 8250 Buenos Aires, Argentina.

†† Work assisted by the National Science Foundation and the joint program of the Office of Naval Research and the U. S. Atomic Energy Commission.

2. Experimental

The method of obtaining energy spectra with photographic plate detection was reviewed in the previous paper on (d,t) reactions [3]), so that it will not be repeated here. The only difference is that the reaction product analysing magnet is run at lower magnetic fields to pass protons, and since such fields also pass deuterons, tritons and alpha particles, an absorber is placed in front of the photographic plates to remove all particles except protons. Some typical data are shown in fig. 1. In some of the angular distribution studies where the best resolution is not needed, the photographic plates are replaced by a 0.32 cm wide $\times$ 2.54 cm high scintillation detector; data are then obtained by measuring

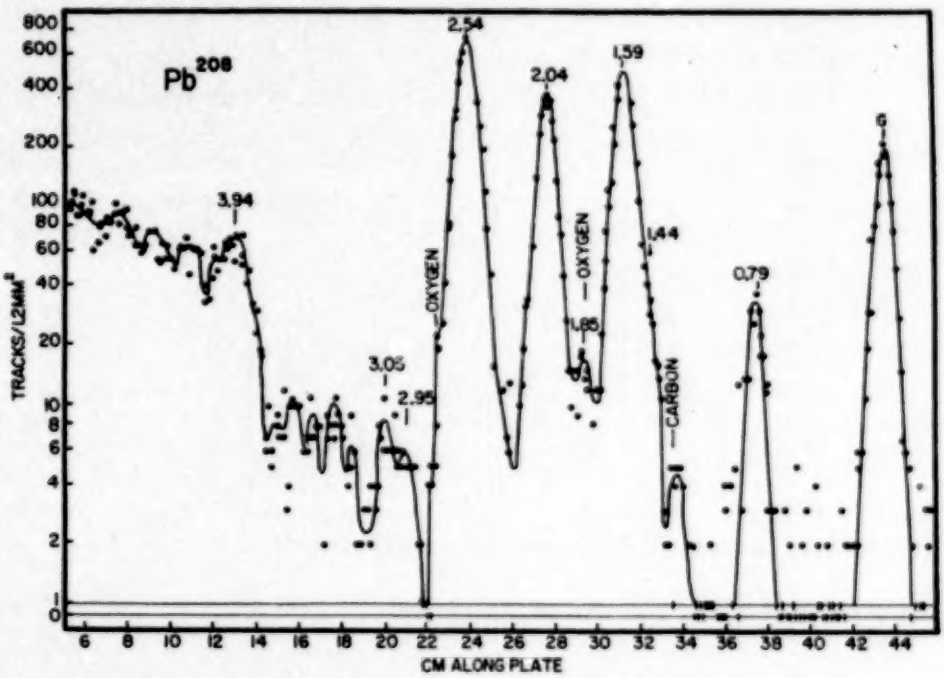

Fig. 1. Energy distribution of protons from Pb^{208}(d, p)Pb^{209}. Angle of observation is 60°. Different symbols for ordinates equal to 0 and 1 are only to facilitate clarity. Numbers are excitation energies of final states in MeV.

the counts per μC of the incident beam for various settings of the magnetic field.

3. Results and Conclusions ($N \leqq 126$ Shell)

It is natural to divide the results into two parts, those bearing on the $N \leqq 126$ shell (N is the neutron number) which will be discussed in this section, and those bearing on the $N > 126$ shell which will be taken up in the following section. The first group consists of data pertaining to the excitation of the low lying single hole states of Pb^{207} by Pb^{206}(d, p) and the excitation of the ground state of Pb^{208} by Pb^{207}(d, p). Two aspects of this work which are particularly

interesting are (1) the study of angular distributions of proton groups from these levels; since the neutron transfer angular momentum l_n is known, they can be compared with theoretical calculations from stripping theory and used as a test of the feasibility of using angular distributions for nuclear spectroscopy in this mass and energy region; and (2) the study of the True and Ford [4]) and Kearsley [5]) wave functions for the ground state of Pb^{208}.

3.1. ANGULAR DISTRIBUTIONS

The angular distribution of the ground state proton group from Pb^{207} (d, p)Pb^{208} is shown in fig. 2 together with the theoretical curve from the distorted wave Born approximation calculation of Tobocman [6]), and a previous measurement at this energy by Wall [7]). In so far as there is disagreement with the previous experimental results, it may be presumed that the results reported here are the more reliable as the detection method was more elaborate. Ref. [7]) does not give an absolute cross section so that the normalization to it is arbitrary.

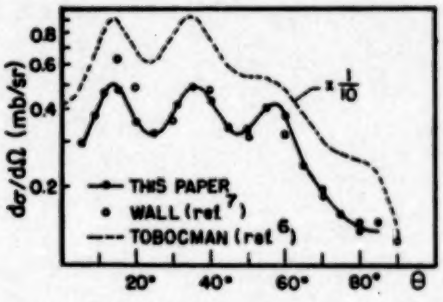

Fig. 2. Angular distribution of ground state proton group from Pb^{207}(d, p)Pb^{208}. Data from ref. [7]) are arbitrarily normalized to data from this paper.

The shape of the angular distribution is in very good agreement with the theory; the angular positions and relative heights of the two principle peaks agree almost perfectly, the angular position of the third peak is well reproduced, and there are even indications of agreement in the fourth peak. On the basis of shape, therefore, the fit of theory to experiment in fig. 2 is as good as almost any ever achieved in deuteron stripping investigations. A rather bad disagreement arises, however, in considering absolute cross sections; the theoretical cross section is larger than the experimental by about a factor of eighteen. It might be pointed out that the theoretical calculations were done with $j = \frac{3}{2}$ whereas the actual value of j here is $\frac{1}{2}$; this would reduce the absolute cross sections, but not nearly by a factor of 18; it would not affect the angular distribution.

Fig. 3 shows angular distributions of the three highest energy proton groups from Pb^{208}(d, p) which lead to the $p_{\frac{1}{2}}$, $f_{\frac{5}{2}}$ and $p_{\frac{3}{2}}$ states of Pb^{207}. These data were obtained from photographic plates so that the accuracy is not as good as in fig. 2, but it is apparent that the principle features of the angular distribution in that figure ($l_n = 1$, $Q = 5.4$ MeV) are retained here for the transition to the

$p_{\frac{1}{2}}$ state ($l_n = 1$, $Q = 4.6$ MeV) and are still recognizable for the transition to the $p_{\frac{3}{2}}$ state ($l_n = 1$, $Q = 3.7$ MeV), whereas the angular distribution for the transition to the $f_{\frac{5}{2}}$ state ($l_n = 3$, $Q = 4.0$ MeV) is quite different. This gives reasonable encouragement for attempting to do nuclear spectroscopy with (d, p) angular distribution studies in this region of mass and energy. It should be noted, however, that the angular distributions depend much more sensitively on Q than in usual stripping theory; a very noticeable feature of this type is the decrease of intensity of small angle peaks relative to large angle peaks as Q decreases.

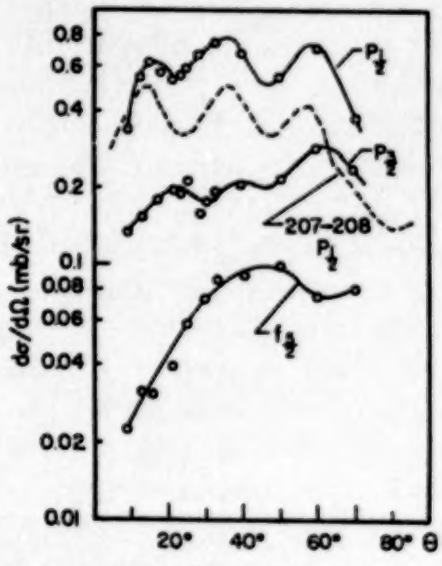

Fig. 3. Angular distributions of three highest energy proton groups from Pb^{208}(f, p)Pb^{207}. The curve through the data from fig. 2 is included for reference.

3.2. WAVE FUNCTIONS FOR GROUND STATES OF Pb^{208}

The cross section for a (d, p) reaction may be written [8])

$$\sigma \propto \frac{2I_f+1}{2I_i+1} f(l_n, Q, \theta)\, Sc^2, \tag{1}$$

where I_f and I_i are the spins of the initial and final states respectively, S is the coefficient of fractional parentage, c is the overlap integral between the initial and final states, and f is a quantity derived from nuclear reaction theory. In usual theories, f depends on l_n, the orbital angular momentum with which the "stripped" neutron enters the nucleus, the Q of the reaction, and the angle of observation. It also depends on the radius and charge of the target nucleus, but these are essentially the same for all cases considered in this paper. Since reaction theories in their present state cannot predict f and we have no direct way of determining it, we simplify (1) by assuming that the dependence of f on l_n and Q are separable as

$$f(l_n, Q, \theta) = F(l_n, \theta) g(Q). \tag{2}$$

The function $g(Q)$ can be very crudely estimated by comparing the intensities of the ground state group and the most intense groups from $Pb^{207}(d, p)$. The former is due to the filling of the $p_{\frac{1}{2}}$ single hole state, while the latter must be due to the excitation of the single particle $s_{\frac{1}{2}}$, $d_{\frac{3}{2}}$ and $d_{\frac{5}{2}}$ states (see below), so that c^2 is unity for all cases, S is always calculable [8]) and $F(l_n, \theta)$ should be about the average of $F(0, \theta)$ and $F(2, \theta)$. The result of this calculation is that $g(Q)$ increases by about a factor of 5 as Q decreases by 5 MeV. If we assume that $g(Q)$ varies logarithmically with Q, it increases by a factor of 1.35 per MeV decrease in Q.

This procedure is, of course, quite crude but there is little alternative except to ignore the dependence on Q (as was done in ref. [2])); it seems reasonably justifiable because it will be used only over relatively short intervals of Q so that it is never a very large correction. Furthermore, it agrees in direction, and roughly in magnitude with the prediction of Butler theory which is a factor of about 1.2 per MeV.

The function $F(l_n, \theta)$ is also not known. The dependence on θ is handled by determining all interesting quantities at each of several angles, and averaging over angles. The uncertainty introduced by this procedure may be judged by the straggling of the values which are used to compute the average; while this is far from insignificant, it is perhaps not unduly large. The dependence of F on l_n will be considered as a parameter in analysing results; however, the direction of the variation is certainly known, and its magnitude is known at least roughly.

The wave function of the ground state of Pb^{206} may be written

$$\Psi_{206} = a(p_{\frac{1}{2}})^{-2} + b(f_{\frac{5}{2}})^{-2} + d(p_{\frac{3}{2}})^{-2} + e(i_{\frac{13}{2}})^{-2} + f(f_{\frac{7}{2}})^{-2}. \quad (3)$$

According to (1) and (2), the coefficient a may be determined from the ratio of the cross sections for the ground state transitions in $Pb^{206}(d, p)$ and $Pb^{207}(d, p)$ as

$$\frac{\sigma(206)}{\sigma(207)} = 2.43\, a^2. \quad (4)$$

The values of this ratio at various angles is shown in table 1. A straight average of the values listed there is $\sigma(206)/\sigma(207) = 1.44$ which corresponds to

TABLE 1

Ratio of cross sections for ground state transitions in $Pb^{206}(d, p)$ and $Pb^{207}(d, p)$ reactions at various angles

θ	8°	11°	23°	30°	33°	40°	60°	70°
$\frac{\sigma(206)}{\sigma(207)}$	1.30	1.30	1.49	1.71	1.20	1.54	1.49	1.54

$a^2 = 0.59$; any other method of taking an average would not give an appreciably different result. The True and Ford prediction [4]) is $a^2 = 0.73$, whereas the experimental result from our study of (d, t) reactions [3]) was $a^2 \approx 0.56$.

By measuring the excitation of the various single hole states of Pb^{207} by Pb^{206}(d, p) all of the coefficients in (3) may be estimated. A typical spectrum of protons from this reaction is shown in fig. 4. It is seen that each of the single hole states in Pb^{207} is clearly resolved. Besides these, an additional state is observed at an excitation of 1.99 MeV; this will be discussed below. Spectra of this type were obtained at 30°, 45°, 60° and 90°, and the relative intensities of

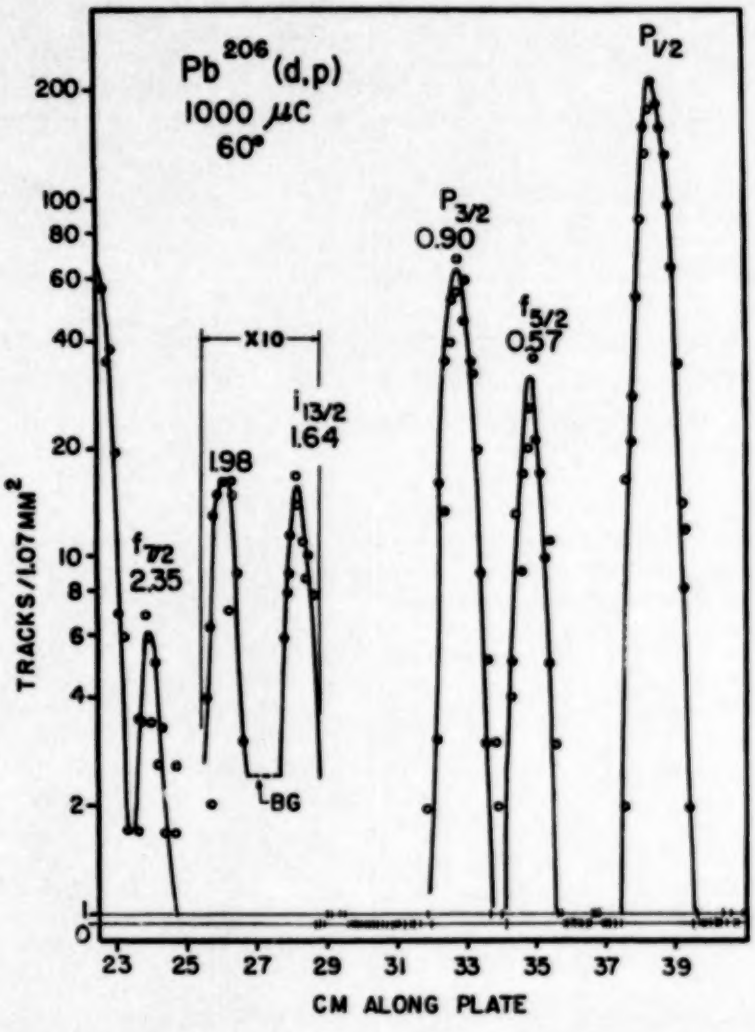

Fig. 4. Energy distribution of protons from Pb^{206}(d, p)Pb^{207} at 60°. This is the high energy end of the spectrum; the low energy part is very similar to that shown in fig. 5.

the various peaks are listed in table 2. From these, the quantity Fc^2 may be calculated from (1) and (2); it turns out that $\{(2I_f+1)/(2I_i+1)\}S$ is unity in cases, so that the only correction is for $g(Q)$. The results are listed in table 2 for each angle, and a weighted average over angles, $\bar{F}(l_n)$, is shown in the last column. In obtaining this average, angles where the intensity is highest are weighted most heavily.

TABLE 2

Relative intensities σ of transitions to various states of Pb^{207} from Pb^{206}(d, p) reactions and relative values of Fc^2 calculated from them using eqs. (1) and (2). The last column is $\bar{F}c^2$, obtained by averaging Fc^2 over angles as discussed in text.

State in Pb^{207}	30°		45°		60°		90°		$\bar{F}c^2$
	σ	Fc^2	σ	Fc^2	σ	Fc^2	σ	Fc^2	
$p_{\frac{1}{2}}$	1.0	1.0	1.0	1.0	1.0	1.0	1.0	1.0	1.0
$f_{\frac{5}{2}}$	0.12	0.10	0.23	0.19	0.15	0.13	0.31	0.26	0.18
$p_{\frac{3}{2}}$	0.26	0.20	0.28	0.21	0.29	0.22	0.47	0.36	0.22
$i_{\frac{13}{2}}$	0.009	0.006			0.009	0.006	0.018	0.011	0.008
$f_{\frac{7}{2}}$			0.05	0.025	0.03	0.015	0.09	0.045	0.025

To obtain c^2, some estimate must be made of $\bar{F}(l_n)$. For this purpose, we assume

$$\bar{F}(l_n) = 2^{-kl_n}, \tag{5}$$

which is an expression that has been used successfully in other mass regions. The values of the coefficient in (3) obtained for various values of k are listed in table 3, where in each case they have been normalized to sum to unity. To

TABLE 3

Values of coefficients in Pb^{208} ground state wave function of eq. (3) for various assumptions on the value of k in eq. (5). The "Best estimates" are obtained by choosing the value of k as discussed in text. The last two columns give values of these coefficients from theoretical calculations cited.

$(\text{coeff.})^2$	Hole pair state	Dependence of F on l_n			Best estimate	Calculated	
		$k = 0$	$k = \frac{1}{2}$	$k = 1$		True and Ford	Kearsley
a^2	$(p_{\frac{1}{2}})^{-2}$	0.70	0.60	0.43	0.56	0.73	0.70
b^2	$(f_{\frac{5}{2}})^{-2}$	0.13	0.22	0.32	0.25	0.13	0.11
d^2	$(p_{\frac{3}{2}})^{-2}$	0.15	0.13	0.09	0.12	0.13	0.14
e^2	$(i_{\frac{13}{2}})^{-2}$	0.006	0.02	0.12	0.04	0.009	0.02
f^2	$(f_{\frac{7}{2}})^{-2}$	0.017	0.03	0.04	0.03	0	0.02

assume $k = 0$, i.e. that the average cross section is independent of l_n, is contradictory to all experience in stripping reactions. In lighter nuclei, $k \approx 1$ is approximately correct and this is approximately the value found in (d, t) reactions in the Pb region. In (d, p) reactions in the Pb isotopes, an estimate of k may be obtained by comparing the $g_{\frac{9}{2}}$ ground state peaks from Pb^{208}(d, p) with the peaks which lead to the s and d single particle states; this gives $k \approx 0.8$. There is thus every reason to believe that k is considerably larger than zero, and very probably larger than $\frac{1}{2}$. From table 3, then, a^2 must be definitely less than 0.70, and very probably less than 0.60, which is in agreement with results discussed above.

In order to obtain the other coefficients in (3), it seems reasonable to choose the value of k to obtain agreement with the other determinations of a^2. This

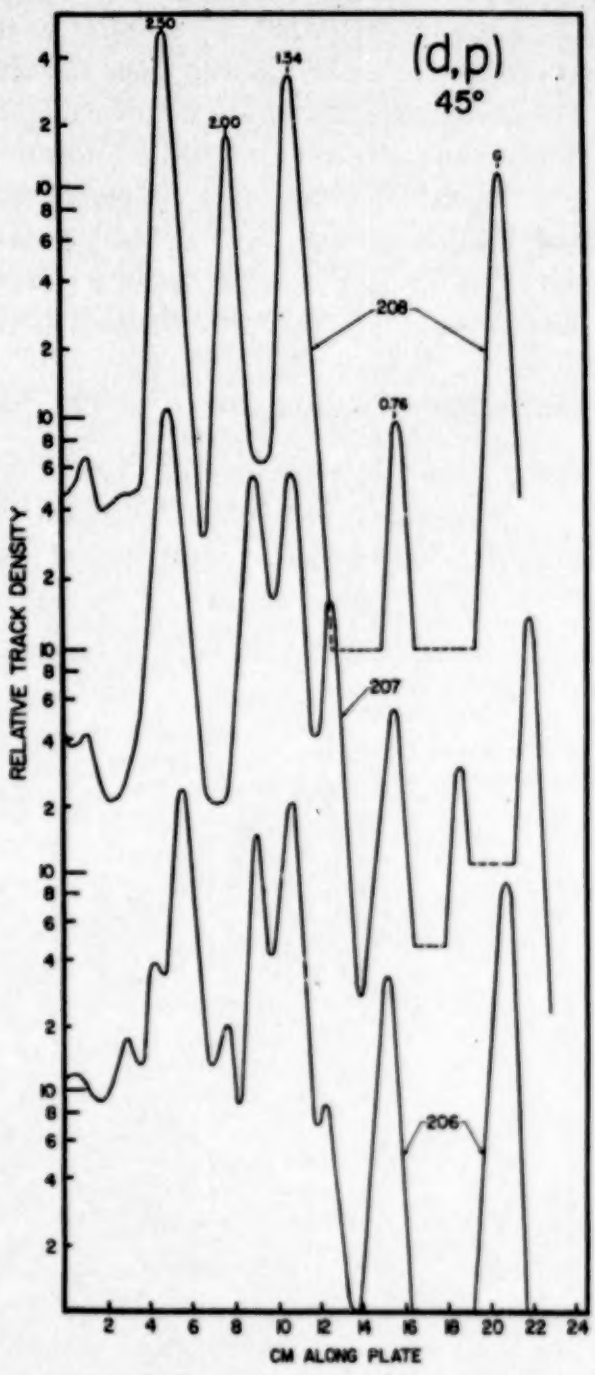

Fig. 5. Survey of energy distributions of protons from (d, p) reactions on Pb^{206}, Pb^{207} and Pb^{208} at 45°. Energies on peaks in spectrum from Pb^{209} are in MeV above the ground state (G). Upper end of spectrum from Pb^{207} contains only a single peak, and upper end of spectrum from Pb^{206} is as shown in fig. 4.

leads to the results listed in the "Best estimate" column of table 3. Also listed in table 3 are the values of these coefficients obtained from the calculated

wave functions of True and Ford [4]), and Kearsley [5]). The principal discrepancy seems to be that their wave functions have too much $(p_{\frac{1}{2}})^{-2}$.

Some comment is perhaps in order concerning the peak in fig. 5 at 1.99 MeV. It was observed at the same energy at 30°, 60° and 90°; it therefore cannot be due to an impurity of an element of mass less than 150 since centre of mass effects in elements lighter than this would cause noticeable shifts in the energy.

It would be very difficult to explain the intensity if it were due to an impurity with less then 0.2 % abundance, and no heavy element impurity of this abundance is known or expected to be present. It thus seems quite likely that this is a previously unknown level of Pb^{207}. Since it is not observed in Pb^{208}(d, t) reactions, it cannot be a hole level; it is thus the lowest lying non-hole level in Pb^{207}.

4. Results and Conclusions ($N > 126$ Shell)

The low energy part of the energy spectra of protons from (d, p) reactions on Pb^{206} and Pb^{207}, and the entire spectrum from Pb^{208} and Bi^{209} is due to excitation of particle states in the $N > 126$ shell. Some typical measured spectra are shown in figs. 5 and 6.

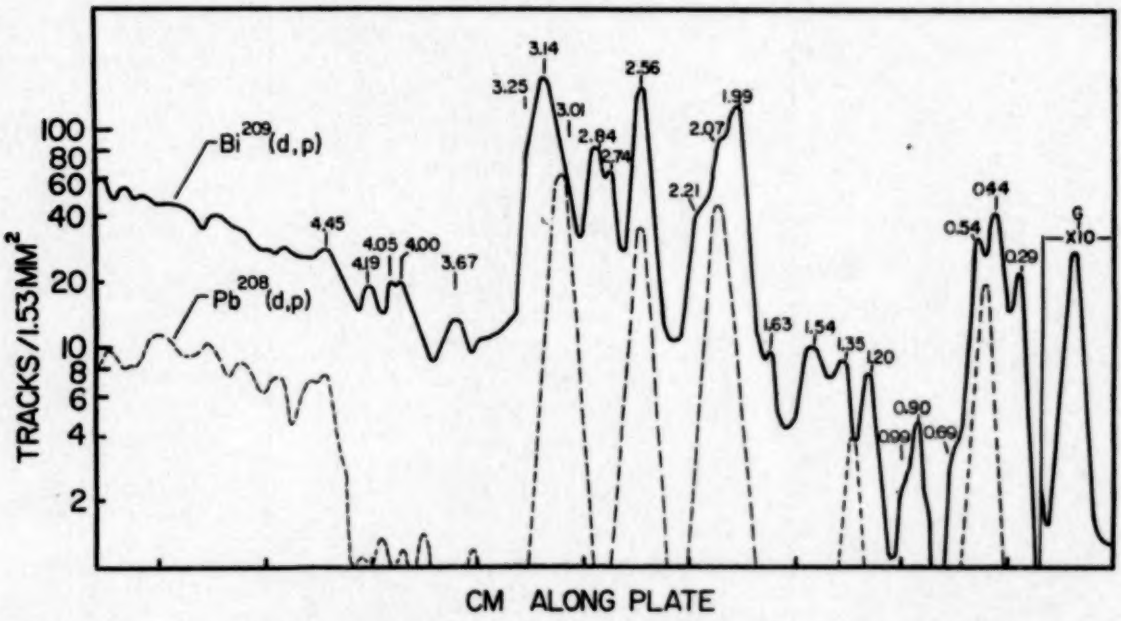

Fig. 6. Energy distribution of protons from Bi^{209}(d, p)Bi^{210} at 90°. Numbers attached to peaks are energies above the ground state in MeV; values in parentheses are from ref. [11]). The spectrum from Pb^{208}(d, p)Pb^{209} is shown for comparison.

The simplest spectrum to understand theoretically should be that from Pb^{208} (d, p)Pb^{209}, as in this case each single particle state should be a single nuclear level. Seven single particle levels are expected in this shell, namely those listed in the first column of table 4. This immediately raises a problem, as there are only five peaks in the spectrum (cf. figs. 1 and 5); the only simple explanation is

that two of the observed peaks are unresolved doublets. To test whether any of the peaks are wider than can be explained by the experimental resolution, the ratios of peak height to area were determined; they were found to be about 5 % less for the two lowest energy peaks (2.00 MeV and 2.50 MeV) than for the other three, which might indicate that the former are double. However, this small a difference could probably be explained by experimental error and small corrections, so that the evidence is far from conclusive.

TABLE 4

States of Pb^{209} expected to be excited by Pb^{208}(d, p) reactions. The last three columns are obtained under the following assumptions: (A) energies are as in column 2 of this table; (B) observed peaks in spectrum are G-$g_{\frac{9}{2}}$, 0.76-$i_{\frac{13}{2}}$+$j_{\frac{15}{2}}$, 1.54-$d_{\frac{5}{2}}$+$s_{\frac{1}{2}}$, 2.00-$g_{\frac{7}{2}}$, 250-$d_{\frac{5}{2}}$; (C) same as (B) except 1.54-$d_{\frac{5}{2}}$ and 2.50-$d_{\frac{5}{2}}$+$s_{\frac{1}{2}}$.

State	Expected energy (MeV)	Expected intensity (relative)		
		(A)	(B)	(C)
$s_{\frac{1}{2}}$	2.0	10	10	10
$d_{\frac{3}{2}}$	≈1.3	9	11	7
$d_{\frac{5}{2}}$	≈2.7	10	11	8
$g_{\frac{9}{2}}$	0	4	4	3
$g_{\frac{7}{2}}$	2.5	7	7	5
$i_{\frac{13}{2}}$	≈0.4	2	2	2
$j_{\frac{15}{2}}$	≈1.0	2	2	2

A more important, and somewhat related problem is the identification of the various single particle states. First estimates of the expected positions of these are listed in table 4; they were arrived at as follows:

(1) The location of the $s_{\frac{1}{2}}$ was estimated from the position of the neutron giant resonance at $A \approx 160$ and the rate of shift of this state with A as calculated from optical model and experimentally verified in lighter mass regions [9]).

(2) The location of the "centre of gravity" of the d-states was taken to be coincident with the s-state. This is the situation in the previous s-state (Zr^{91}) but there is no reason to expect it to be more than very roughly true here.

(3) The spin orbit splitting ΔE_{so} should be roughly given by

$$\Delta E_{so} = K(2l+1). \tag{6}$$

In Pb^{207}, eq. (6) is valid for the p-states and f-states with $K = 0.28$ MeV. This determines the location of the $g_{\frac{7}{2}}$ state if we accept the evidence [2]) that the ground state is $g_{\frac{9}{2}}$, and determines the location of the d-states if we accept the above crude arguments on the location of their centre of gravity.

(4) The $i_{\frac{11}{2}}$ and $j_{\frac{11}{2}}$ are located relative to the other states from Nillson's calculation [10]).

Given the expected energy, the expected relative intensity may be calculated from eqs. (1), (2) and (5) with $g(Q)$ and k taken as above. The results are listed in table 4 as "Expected intensities (A)".

In order to throw more light on the problem, angular distributions of the five peaks in the spectrum were measured. The results are shown in fig. 7; they are somewhat disappointing in that there are very few differences among angular distributions for various groups. The most noticeable feature is that the 2.00 MeV group is different from any of the others, and falls off very rapidly in the forward direction. The latter property plus the intensity discrepancy would

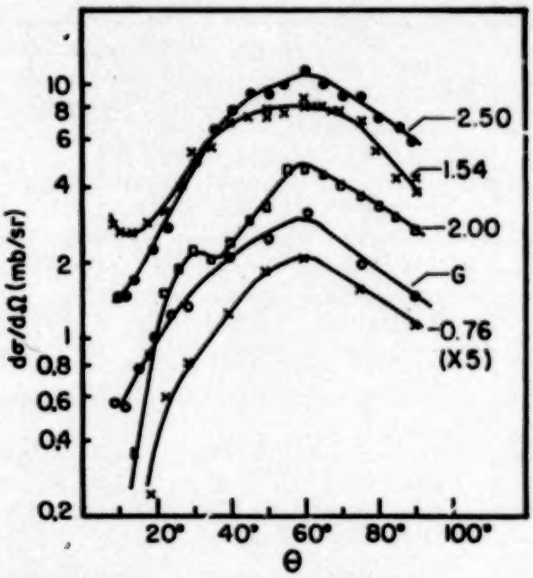

Fig. 7. Angular distributions of various peaks from $Pb^{208}(d, p)Pb^{209}$. All data shown are consistently normalized except those for the 0.76 MeV group which have been multiplied by 5.

indicate that it is not the $s_{\frac{1}{2}}$ state. Since angular distributions from the two d-states should be similar, it is very probably not a d-state. If it were, eq. (6) would also be badly violated, and the intensity fit would be poor. The only alternative at all consistent with its intensity would be to assign it as $g_{\frac{7}{2}}$. The difference between its angular distribution and that of the ground state group might be explained by the large difference in Q-value.

If we accept this, it seems obvious to assign the 1.54 and 2.50 MeV states as $d_{\frac{3}{2}}$ and $d_{\frac{5}{2}}$ respectively and assume that the $s_{\frac{1}{2}}$ is degenerate with one of them. In view of the angular distributions, it seems most natural to assume it to be degenerate with the 1.54 MeV state; the intensities calculated from this assumption are listed in table 4 as "Expected Intensities (B)". The discrepancy with measured intensities is quite bad; for example the ratio of the 1.54 to 2.50 MeV state intensities is expected to be ≈ 2 as compared to an average

value of 0.8 at large angles. While the intensity calculations are indeed crude, such a large discrepancy over such a short range of Q and l_n would be most unexpected.

The other alternative, that the $s_{\frac{1}{2}}$ is nearly coincident with the $d_{\frac{3}{2}}$ at 2.50 MeV gives the relative intensities listed in the last column of table 4. The expected intensity ratio of the two peaks is now about 0.4 which disagrees as badly with the experimental value (0.8) as the other assumption. In addition, the angular distributions can only be interpreted as indicating that the $l_n = 0$ angular distribution decreases rapidly at forward angles, which is most distasteful. Thus, there are important difficulties with any assignments we may make, and the resolution of this problem must await further experimental information.

The spectra from the other reactions studied show similarities to that from Pb^{208}, except that each level is split into two or more as expected. However, any detailed analysis is difficult without the solution to the Pb^{208} problem. It might be noted that the data show the ground state of Bi^{210} and Bi^{209}(d, p); this was only recently observed for the first time. From its low intensity, it has very little single particle component.

The authors are greatly indebted to the cyclotron operations and plate reading groups for their very important services, to E. Baranger, S. Meshkov, N. Austern and J. B. French for helpful discussions, and to A. J. Allen for support and encouragement.

References

1) J. A. Harvey, Can. J. Phys. **31** (1953) 278
2) M. T. McEllistrem, H. J. Martin, D. W. Miller and M. B. Sampson, Phys. Rev. **111** (1958) 1636
3) B. L. Cohen, S. Mayo and R. E. Price, Nuclear Physics **20** (1960) 360
4) W. W. True and K. W. Ford, Phys. Rev. **109** (1958) 1675
5) M. J. Kearsley, Nuclear Physics **4** (1957) 157
6) W. Tobocman, Phys. Rev. **115** (1959) 98
7) N. S. Wall, Phys. Rev. **96** (1954) 670
8) J. B. French, in Nuclear spectroscopy, to be published
9) B. L. Cohen and R. E. Price, Nuclear Physics (submitted)
10) S. G. Nillson, Mat. Fys. Medd. Dan. Vid. Selsk. **29**, No. 16 (1955)

3.A

Nuclear Physics **20** (1960) 382—394; © *North-Holland Publishing Co., Amsterdam*

Not to be reproduced by photoprint or microfilm without written permission from the publisher

A SEARCH FOR DOUBLE DIPOLE DE-EXCITATION IN C^{12}

G. J. McCALLUM †, D. A. BROMLEY and J. A. KUEHNER

Atomic Energy of Canada Limited, Chalk River, Ontario

Received 10 May 1960

Abstract: An experimental search for the simultaneous quanta which would result from double E1 electromagnetic de-excitation of the 4.43 MeV, 2^+ state in C^{12}, in competition with the normal E2 de-excitation, has yielded negative results. The 4.43 MeV state was populated via the resonant $N^{15}(p, \alpha)C^{12}$ reaction; competing proton capture reactions preclude the establishment of an experimental limit on the branching ratio Γ_{2E1}/Γ_{E2} of less than 1.7×10^{-4}. It is suggested that this limitation applies generally to reaction studies of this branching ratio. Recent theoretical studies of this process suggest that Γ_{2E1} vanishes in first order, consistent with the experimental observations.

1. Introduction

In studies of the electromagnetic de-excitation of nuclear levels it is customarily assumed that the de-excitation proceeds via the emission of a single quantum of unique energy given by the energy separation of the initial and final states. The possibility of a competing process involving the simultaneous emission of two quanta of fixed *total* energy was first considered theoretically by Goeppert-Mayer [1]), and was re-examined by Sachs [2]) as a possible de-excitation mode for isomeric states. More recently, Cameron [3]) has investigated the possible relevance of this two-quantum process to the de-excitation of low lying 0^+ states in even-even nucleides where direct gamma ray transitions are forbidden. The double quantum process may be thought of as a cascade de-excitation via the tails of broad levels at much higher excitations in the nucleus in question; thus the individual quanta would be expected to have continuous energy spectra.

In the case of 0^+ or 2^+ states in even-even nuclei the two-quantum process is assumed to involve excitation of the 1^- states centred in the giant resonance region at excitations $\approx$ 20 MeV and their subsequent de-excitation via E1 transitions.

The probability for double electric dipole emission W_{2E1} was given by Sachs as

$$W_{2E1} = \frac{16}{9}\frac{e^4 R_{ab}^2 R_{bc}^2}{\hbar^6 c^6}\int_0^{\nu_{ac}} (h\nu)^3 (E_{ac}-h\nu)^3 \left\{\frac{1}{h\nu_{bc}-h\nu}+\frac{1}{h\nu_{ab}+h\nu}\right\}^2 d\nu, \quad (1)$$

where a, b and c label the initial state, the intermediate (broad) state and the

† Seconded from Institute of Nuclear Sciences, Wellington, New Zealand.

final state respectively in the de-excitation; $h\nu$ is the energy of one of the quanta $E_{ac}-h\nu$ that of the other, where E_{ac} is the available energy. The electric dipole moments eR_{ij} are related to the widths for single quantum emission from the state b to states a and c by

$$e^2 R_{ij}^2 = \frac{3c^3 \Gamma_{ij}}{2\nu_{ij}^3} = 4.58\times 10^{-42} \frac{\Gamma(\mathrm{eV})}{[E_\gamma(\mathrm{MeV})]^3} \mathrm{erg}\cdot\mathrm{cm}^3. \qquad (2)$$

Only in isolated cases are the relevant widths Γ_{ij} available for substitution in eq. (2). In the case of the broad 1^- state at 17.22 MeV in C^{12}, Huus and Day have measured de-excitation widths to the 4.43 MeV and ground states, obtaining 20 and 40 eV respectively [4]).

Using these widths the integral in eq. (1) was evaluated numerically to obtain a value for the double dipole probability for de-excitation of the 4.43 MeV state via that at 17.22 MeV. The result thus obtained is

$$W_{2E1} = 1.2\times 10^7\ \mathrm{sec}^{-1}.$$

From the measured mean life [5]) of the 4.43 MeV state

$$\tau_m = (6.5\pm 1.2)\times 10^{-14}\ \mathrm{sec}\ ,$$

and neglecting any possible competing de-excitation modes, the electric quadrupole de-excitation probability is

$$W_{E2} = 1.54\times 10^{13}\ \mathrm{sec}^{-1}.$$

This leads to

$$\frac{\Gamma_{2E1}}{\Gamma_{E2}} = \frac{W_{2E1}}{W_{E2}} = 0.75\times 10^{-6}$$

as the predicted branching ratio for the de-excitation involving *only* the 17.22 MeV 1^- level. On this basis, it appeared reasonable to expect that when the contributions from all the giant resonance levels were included this branching ratio might increase by between one and two orders of magnitude and a direct measurement would become feasible.

Recent measurements of the Coulomb excitation of heavy elements by heavy ion bombardment have shown an anomalously high yield of relatively low energy radiation with a continuous energy spectrum. The intensity of this radiation exceeds that calculated for normal bremsstrahlung by a factor of 20 in the case of 20 to 80 MeV oxygen ions on tungsten for example [6]). The double dipole process, if sufficiently probable, would provide a possible explanation for these observations.

It was decided to undertake an experimental search for this process in order to determine whether, in fact, such an explanation was tenable and whether the formalism leading to eq. (1) was valid.

In view of the relatively large branching ratio anticipated for the 4.43 MeV state in C^{12} from preliminary calculations, the de-excitation of this state was selected for study. It has the marked advantage that it is populated by the resonant $N^{15}(p, \alpha)C^{12}$ reaction with a minimum number of competing reaction exit channels [7]).

Following completion of the measurements to be reported herein, however, a more exact theoretical study of the process was made by Lane and Soper [8])† which indicates that the double electric dipole process is much less probable than is suggested by eq. (1). Using properly antisymmetrized wave functions, Lane and Soper find that the double electric dipole process has zero probability in first order. Very rough estimates of the higher order terms suggest a branching ratio $\Gamma_{2E1}/\Gamma_{E2} \leqq 10^{-8}$. If the assumptions on which this estimate is based are valid, it follows that the double electric dipole process is not accessible to direct experimental observation by using currently available techniques. To the extent that the measurements reported herein establish an upper limit for the width of this process they support the calculations, leading to branching ratios $\lesssim 10^{-4}$.

It should be noted that in a double dipole de-excitation process involving a parity change between initial and final states, the antisymmetry requirements no longer obtain; an expression similar to eq. (1) may therefore legitimately be used to obtain the order of magnitude of the transition probability, namely

$$W_{E1M1} \approx \frac{4e^4 R_{ab}^2}{\hbar^4 M^2 c^8} \int_0^{\nu_{ac}} (h\nu)^3 (E_{ac} - h\nu)^3 \left\{ \frac{1}{h\nu_{ac} - h\nu} + \frac{1}{h\nu_{ab} + h\nu} \right\}^2 d\nu, \qquad (3)$$

where the magnetic moment of the proton $\approx 3e\hbar/2Mc$ has been used for the matrix element of the magnetic moment. Since magnetic moments are in general 2 to 3 orders of magnitude less than the corresponding electric moments de-excitation by mixed dipole radiation would be difficult to observe except perhaps in very favourable cases of radioactive decay.

Recent measurements on the decay of the 164 keV $\frac{1}{2}^-$ level in Xe^{131m} to the $\frac{3}{2}^+$ ground state [9]) indicate a double quadrupole de-excitation mechanism in competition with the expected M4 decay mode. A value of $\Gamma_{E2M2}/\Gamma_{M4} \approx 2 \times 10^{-3}$ was obtained.

2. Experimental Details

2.1. TARGET PREPARATION

Targets were prepared by nitriding 0.254 mm tantalum backings by induction heating in an atmosphere of NH_3 enriched to 60 % in N^{15}. The target preparation technique has been described previously [10]). The isotopically enriched NH_3 was prepared from enriched HNO_3 using the standard Devarda method [11]). An effective target thickness of approximately 18 keV for 1 MeV protons was used.

† *Note added in proof* The two quantum de-excitation process has also recently been discussed by Eichler and Jacob [23]).

2.2. DETECTION SYSTEM

A block diagram of the circuits used is shown in fig. 1. The crystals used were 13 cm diam. by 10 cm thick NaI(Tl) optically coupled to 6365 Dumont photomultipliers; these were mounted on opposite sides of the target at 90° to the incident proton beam with conical lead collimators inserted to minimize spurious coincidences between the crystals resulting from Compton scattering or annihilation quantum escape. The choice of this particular geometry, in which

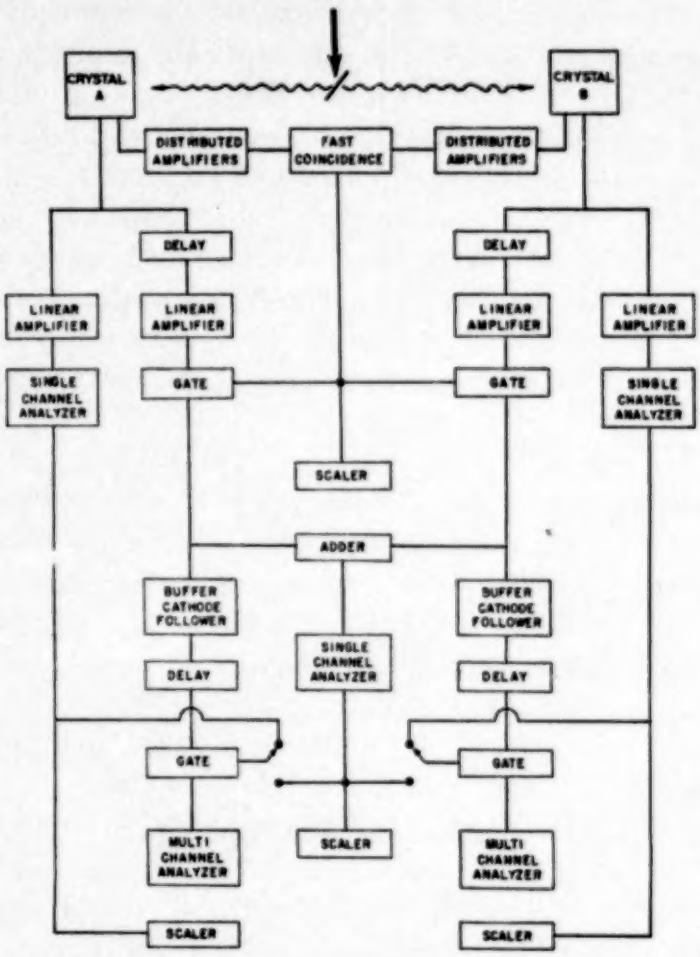

Fig. 1. Block diagram of electronic circuitry.

the dipole quanta are detected at 90° to the beam direction and at 180° to each other, was chosen since it allowed the two counters to subtend larger solid angles than was possible in any other arrangement. Furthermore, the calculated quadruple angular correlations, which are presented in the appendix, showed this to be the most favourable geometry. In this configuration these two factors combine to give a calculated efficiency for detecting double dipole events ≈ 10 times higher than in any other. The circuit of fig. 1 is a modification of that originally proposed by Hoogenboom [12]), in which a fast coincidence system [13]) has been added as shown. This coincidence circuit was operated with a resolving

time $2\tau = 25$ ns in these measurements. With the switches as shown, in their upper positions, the circuits are arranged for "self-gate" operation wherein only that portion of the pulse spectrum selected by the corresponding single channel analyzer is transmitted to the multi-channel analyzers. This feature is used to provide a convenient means of setting voltage gates on individual spectrum sections. In this case, it permitted the setting of a gate on the direct yield of 4.43 MeV E2 radiation which was recorded by the scalers shown.

With the switches in their lower positions, only pulses which corresponded to emission of two quanta from the target within the resolving time of the fast coincidence circuits and which have a *total* pulse height within the window set with the central single-channel analyzer, are transmitted for analysis. With this window set on a pulse region corresponding to the photopeak for a 4.43 MeV gamma ray, the circuit, in principle, rejects all direct 4.43 MeV quanta and transmits only members of pairs of quanta having this total energy. In practice, of course, because of finite resolving times and gate widths, there exists a significant background rate. As will be discussed later in this paper, this purely instrumental background does not constitute a limitation on the experiment.

2.3. EXPERIMENTAL RESULTS

The $N^{15}(p, \alpha)C^{12}$ reaction was used initially at the $E_p = 898$ keV resonance to populate preferentially the 4.43 MeV level in C^{12}. A gamma ray spectrum measured at this energy is shown in fig. 2. A partial cross section of 800 mb has been reported [14]) for this reaction. In some of the later measurements the 1.210 MeV resonance was used; although this resonance has a lower partial cross section for population of the 4.43 MeV state in C^{12} (425 mb), it has the advantage that the ratio of the yield of 4.43 MeV radiation to that of higher energy capture radiation is greater by a factor of 2 than at the 0.898 MeV resonance. This reduction is of particular relevance to the experimental limitations imposed by the competition from capture radiation, to be discussed later in this paper.

At the 1.210 MeV resonance the yield of radiation with $E_\gamma > 4.43$ MeV was negligible compared with that from the de-excitation of the 4.43 MeV state, consequently an integral rather than a differential bias was set on the direct spectrum at an energy corresponding to (4.43—1.02) MeV to include the first and second annihilation escape peaks as shown in fig. 2.

The double dipole process would be expected to contribute a continuous pulse height spectrum component extending in energy from zero to 4.43 MeV with its shape principally determined by the $E^3(E_0-E)^3$ factor in eq. (1). As well, because of the symmetry of the detection system as shown in fig. 1, the output spectrum from spurious events would be expected to be symmetric about a pulse height corresponding to one half of the maximum available energy. However, the dependence of the detector resolution on the gamma radiation energy leads to certain asymmetries.

Fig. 3 shows a coincidence spectrum measured at the 1.013 MeV $N^{15}(p, \alpha)C^{12}$ resonance with the adding circuit gate set to transmit a total energy loss in the

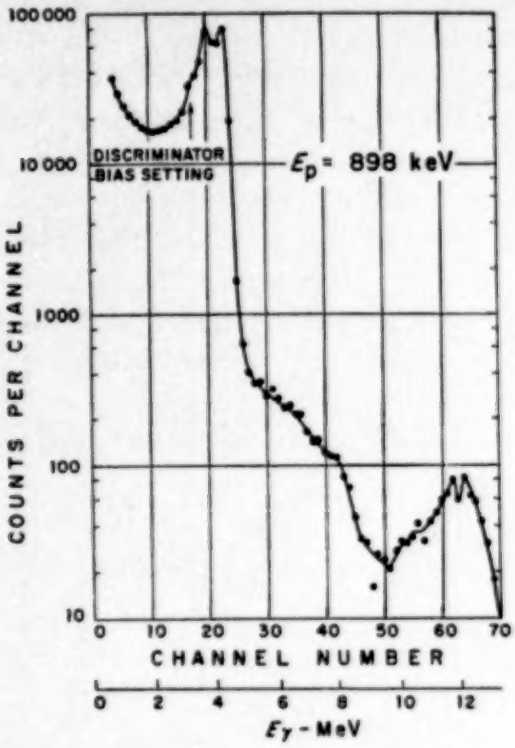

Fig. 2. Gamma ray spectrum of the $N^{15}(p, \alpha\gamma)C^{12}$ reaction taken at the 898 keV resonance.

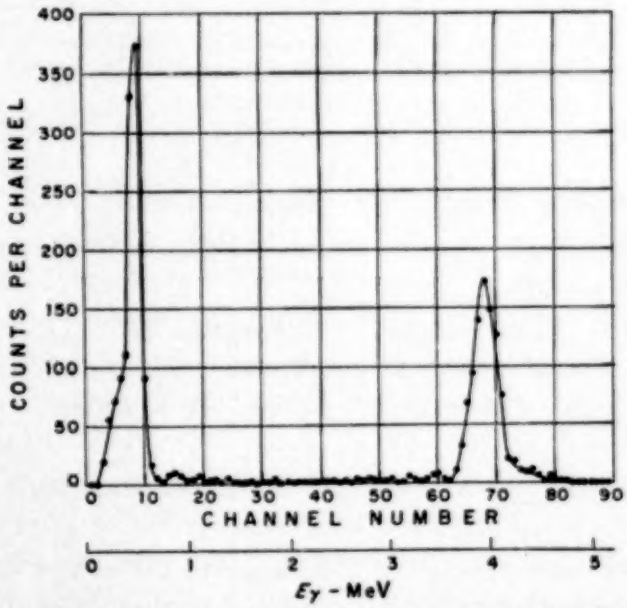

Fig. 3. Sum coincidence spectrum at the 1.013 MeV resonance obtained with switch in fig. 1 in "down" position. Sum set on energy range 4.18 to 4.68 MeV.

two crystals in the range 4.18 to 4.68 MeV. The two peaks appearing in this spectrum suggest the following process: a 4.43 MeV quantum interacts with one

of the crystals with the subsequent loss of one annihilation quantum which is in turn absorbed by the second crystal. This event satisfies all requirements set by the circuit as characteristic of true double dipole events.

The high probability of pair production in the absorption of 4.43 MeV gamma rays also makes feasible a second process other than the double dipole one which satisfies the circuitry restrictions imposed. Annihilation quanta from the targets and detectors have a high probability of producing a true fast coincidence event because of their $\approx 180°$ emission correlation; a correspondingly high background coincidence rate, reflecting the finite coincidence resolution of the electronic circuitry, is observed. To reduce this source of background, lead collimators were inserted to shield the crystals as much as possible from one another and the fast coincidence circuits were adjusted to eliminate coincidences between quanta unless each of their energies was greater than ≈ 600 keV. The spectrum observed under these latter conditions is shown in fig. 4.

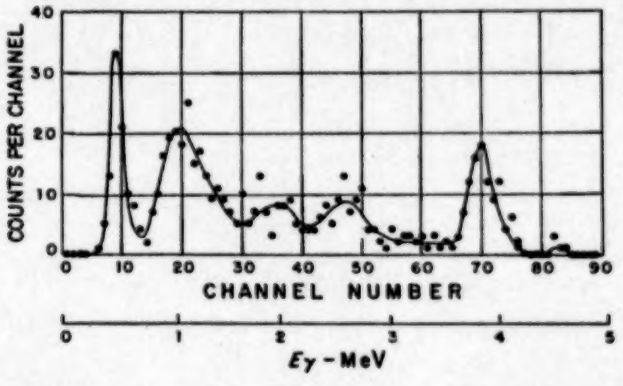

Fig. 4. Sum coincidence spectrum with conditions as in fig. 3 except that the fast coincidence circuit was operative only for gamma rays of energy $\gtrsim 600$ keV.

It is clear that the rejection is not complete and that a spurious peak corresponding to the simultaneous absorption of two annihilation quanta remains as well as an attenuated pair of peaks at ≈ 0.5 MeV and ≈ 4 MeV. These two processes, although serious, do not pose a fundamental limitation to the detection of the true double-dipole de-excitation mode since the latter leads to a continuous spectrum rather than to these characteristic symmetric pairs of peaks.

The spectrum observed with the adding circuit gate set to accept quantum energies between 5.05 and 5.55 MeV is shown in fig. 5. Figs. 4 and 5 have been normalized to the same number of counts in the direct spectrum corresponding to energies greater than (4.43—1.02) MeV. As shown, the total counts in both of these coincidence spectra, between channels 20 and 65, are comparable. It is this residual true coincidence effect, resulting from the cascade de-excitation of states produced by proton capture in the target which limits the applicability of this method for determining the double dipole branching ratio. The gamma

ray cascades from capture reactions satisfy all the criteria demanded by the circuitry when, for example, a gamma ray of energy E MeV is totally absorbed in one crystal and a gamma ray which simultaneously loses (4.43—E) MeV by Compton scattering is detected in the other crystal. In this case, the output spectra will yield peaks corresponding to energies of E MeV and (4.43—E) MeV respectively. Similarly two coincident Compton scattered gamma rays whose energy sum is 4.43 MeV are also counted; a continuous spectrum results from

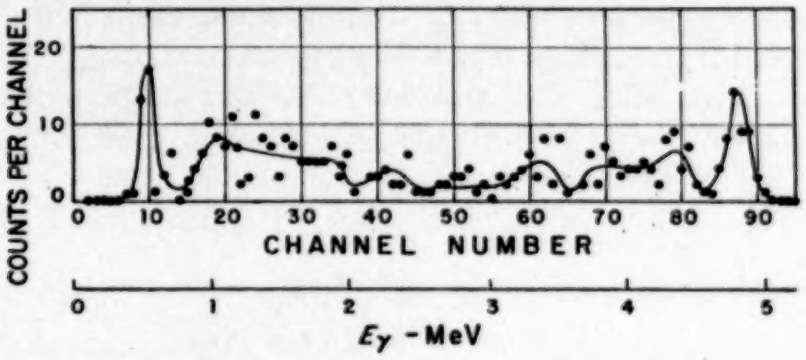

Fig. 5. Sum coincidence spectrum with sum set on energy range 5.05 to 5.55 MeV. Other conditions as in fig. 4.

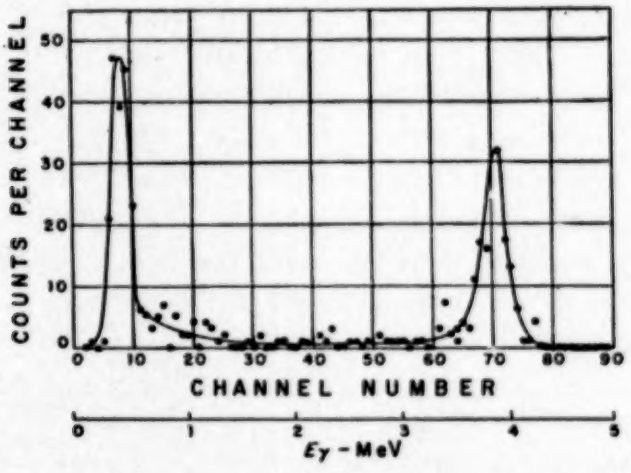

Fig. 6. Spectrum obtained with delay inserted in one channel of fast coincidence circuit. Other conditions as in fig. 4.

this latter contribution which is not separable experimentally from true double-dipole events.

For further examination of sources of spurious effects, a 50 ns delay was inserted in one of the channels of the fast coincidence system. Since the resolving time was 25 ns, the resulting spectra result entirely from random coincidence events; as expected the dominant spectrum peaks are those corresponding to $E_\gamma = 0.511$ and 3.92 MeV. A typical spectrum obtained under these conditions is shown in fig. 6.

2.4. EXTRACTION OF THE BRANCHING RATIO Γ_{2E1}/Γ_{E2}

From the data presented an upper limit for the ratio Γ_{2E1}/Γ_{E2} may be obtained as follows. Let N_1 be the assumed number of double dipole de-excitations per unit time and N_2 the number of electric quadrupole de-excitations in the same time interval. The number of counts per unit time recorded in the scaler recording the output from crystal A (fig. 1), N_A, is given by the expression

$$N_A = N_2 \varepsilon_A(E) f_A(\theta, \phi), \tag{4}$$

where $\varepsilon_A(E)$ is the efficiency of crystal A for detecting gamma rays of energy E under the geometry and discriminator bias conditions used; $f_A(\theta, \phi)$ is the ratio of the angular distribution of the 4.43 MeV radiation averaged over the effective detector aperture of crystal A to that of an isotropic distribution similarly averaged. A similar expression applies for scaler B. The total number of counts recorded by the multi-channel analyzer is

$$N_C = \int_0^{4.43} N(E)[\varepsilon_A(E)\varepsilon_B(4.43\text{-}E)g_A(\theta, \phi)h_B(\theta, \phi) + \varepsilon_A(4.43-E)\varepsilon_B(E)h_A(\theta, \phi)g_B(\theta, \phi)]\mathrm{d}E, \tag{5}$$

where $N(E)$ is the number of double dipole events in which gamma rays of energy E and $4.43-E$ are emitted simultaneously such that $\int_0^{4.43} N(E)\mathrm{d}E = N_1$. A correction to the observed coincidence count rate must be made to take into account the effect of finite resolving times; this is obtained experimentally by inserting a delay in one of the fast coincidence channels (see fig. 6).

The crystal efficiencies ε_j, were obtained from previous measurements using these crystals [15]) and were adjusted to correspond to the geometry in use using the efficiency calculations of Wolicki *et al.* [16]). The correlation factors $f_j(\theta, \phi)$, $g_j(\theta, \phi)$ and $h_j(\theta, \phi)$ were calculated from the known characteristics of the reaction resonances used. These calculations are described in the appendix.

As a result of the spurious effects arising from annihilation radiation it was not possible to integrate eq. (5) from 0 to 4.43 MeV; instead the results were integrated from 1.6 to 3.6 MeV and the complete integral computed on the assumption that the spectral shape is approximately of the predicted form, i.e. $E^3(E_0-E)^3$, as shown in eq. (1) and (3). Substituting the experimental values, the computed detector efficiencies ε_j, and the angular distribution factors, into eq. (4) and (5) a value of

$$\frac{\Gamma_{2E1}}{\Gamma_{E2}} \leqq 2.6 \times 10^{-4}$$

is obtained.

2.5. PROTON CAPTURE CONTAMINATION

In computing this value, no account has been taken of the background effects arising principally from the (p, γ) reactions. Since the capture reactions

in N^{14} and N^{15} in the target pose a fundamental limitation in this type of measurement the effects will be treated in some detail.

An estimate of the contribution from competing reactions can be made using presently available reaction data [7]). At 1.21 MeV the (p, γ) cross section in N^{15} arises principally from the resonance at 1.028 MeV where $\sigma_{p,\gamma} = 1000\ \mu b$ and $\Gamma_\gamma = 140$ keV. Hence $\sigma_{p,\gamma}$ at 1.21 MeV $> 125\ \mu b$. After proton capture the O^{16} is at an excitation of $\approx$ 13 MeV and de-excites by gamma-ray cascading. Since the target is 40 % N^{14}, the $N^{14}(p, \gamma)O^{15}$ cross section must also be considered. From the gamma-ray yield curve and parameters of the resonance at 1.064 MeV [7]) a capture cross section of $\approx 60\ \mu b$ is calculated. On the other hand, the reaction of interest, $N^{15}(p, \alpha\gamma_{4.43})C^{12}$, has a cross section of 425 mb at 1.21 MeV and a width of 22 keV, which is approximately the target thickness. The average cross section is therefore $\approx$ 300 mb. From these computations the ratio of the total capture cross section to the average $N^{15}(p, \alpha\gamma_{4.43})C^{12}$ cross section for a bombarding energy of 1.21 MeV is computed to be of the order of 5×10^{-4}. However, the efficiency of detection of the competing capture reactions will be less by some ratio P, say, than that of detection of the reaction of interest. In de-excitation of both O^{15} and O^{16} there will be one 5 to 7 MeV gamma ray and one or more low energy quanta since de-excitation by the emission of one gamma ray is less favoured than cascade de-excitation. To obtain an order of magnitude estimate for the relative efficiency of the electronic circuitry used for detection of cascade de-excitation, a 2 MeV quantum was assumed to be Compton scattered, losing $\approx$ 2 MeV energy, in the second crystal. It follows that the ratio P is given by the probability of a 6 MeV gamma ray losing 2 to 2.5 MeV divided by the probability of a 2 MeV gamma ray being totally absorbed in the same crystal. The 2 to 2.5 MeV figure arises from the fact that the adding circuit gate transmitted a 0.5 MeV band of energies. From the known efficiencies and standard spectral shapes measured with these crystals [15]) a value of $P = 0.12$ has been obtained. Ignoring all angular distribution effects and using a figure of 2.5 for the number of gamma rays per capture reaction we obtain the value of $\approx 10^{-4}$ for the ratio of the number of capture reactions detected per E2 de-excitation. We may set this value equal to the lowest limit of the ratio Γ_{2E1}/Γ_{E2} which the present equipment could measure directly.

An experimental check on the above estimate can be made by setting the adding circuit gate above 4.43 MeV where the entire real coincidence contribution would be expected to be due to proton-capture reactions. Thus, using results such as those shown in fig. 5 together with a computed value for P as described above, it is possible to determine the ratio of the number of cascade events detected to the number of electric quadrupole transitions with the adding circuit gate set to cover the energy range 5.05 to 5.55 MeV. To determine what this ratio would be if this gate were set on the range 4.18 to 4.68 MeV it can be assumed (to a first approximation only) that the ratios are proportional to the

mean of the energy limits of the adding circuit gate setting. The value of the ratio obtained in this way (0.9×10^{-4}) is close to the predicted value and is a lower limit, since lowering the energy of the sum coincidence condition would permit more cascades to satisfy the energy sum criterion. Taking the figure of 0.9×10^{-4} as background and subtracting this from the value for Γ_{2E1}/Γ_{E2} deduced above results in a limit

$$\frac{\Gamma_{2E1}}{\Gamma_{E2}} \leqq 1.7\times10^{-4}$$

It should be noted that the reaction chosen here i.e. $N^{15}(p, \alpha\gamma)C^{12}$, was selected because it provided by far the greatest ratio of relevant to background-producing reactions as determined by reaction data presently available. It can also be seen that the background figure of 0.9×10^{-4} computed above, arising from proton capture contamination, could well be too low by a factor of at least 2 and may indeed explain all the observed coincidence count rate. As a much more detailed investigation would be required to reduce the lower limit on the Γ_{2E1}/Γ_{E2} ratio by more than a factor of 2 no extension of these reaction measurements is planned.

3. Conclusions

A search for double dipole de-excitation of the 4.43 MeV state in C^{12}, in competition with the normal E2 de-excitation has yielded an upper limit to the width ratio for the two processes of

$$\frac{W(2E1)}{W(E2)} \leqq 1.7\times10^{-4}.$$

This limit is set by the presence of competing radiative capture processes in reaction studies.

On the basis of reaction information currently available, the $N^{15}(p, \alpha\gamma)C^{12}$ reaction used here has the least competing capture radiation. The fact that the presence of such radiation, even in this case, precludes the establishment of a more stringent limit on this branching ratio suggests that the only possibility of establishing a lower limit would involve studies on de-excitations associated with radioactive decays where the capture problem is obviated.

As noted previously, the most recent theoretical estimate of this ratio [8]) is $\approx 10^{-8}$ which is inaccessible to present experimental techniques although consistent with the limit quoted herein.

We are indebted to Dr. A. M. Lane for discussions concerning the work, and to Mr. W. Woytowich for assistance with target preparation.

Appendix

CALCULATION OF ANGULAR DISTRIBUTION FACTORS

The 1.210 MeV resonance for $N^{15}+p$ has been shown to have an assignment of 3^- both from analysis of the $N^{15}(p, p)N^{15}$ elastic scattering data [17]) and the α-γ correlation data; there is a remaining discrepancy in that the angular distributions of the alpha particles to this state have not yet been satisfactorily explained [18]). However, in the discussion herein it will be assumed that the 3^- assignment is a correct one.

Using standard correlation formalism [19]), for the angular distribution of the 4.43 MeV radiation, i.e. a triple correlation with the intermediate alpha radiation unobserved, the predicted correlation is

$$W(\theta) = P_0(\cos\theta)+0.49\,P_2(\cos\theta)-0.30\,P_4(\cos\theta),$$

where θ is measured relative to the proton beam direction and where formation by d-wave protons and de-excitation by p-wave alpha particles has been assumed; this is required by the elastic scattering and α—γ correlation data.

The experimentally measured angular distribution [20]) is given by

$$W(\theta) = P_0(\cos\theta)+(0.45\pm0.01)P_2(\cos\theta)-(0.30\pm0.01)P_4(\cos\theta),$$

in good agreement with this prediction. Using this angular distribution it can be shown readily that the factor $f_j(\theta, \phi)$ is given by

$$f(\theta, \phi) = 0.763+0.35\cos^2\theta_0-0.11\cos^4\theta_0,$$

where θ_0 is the effective half angle of the detectors ($\approx 35°$). In obtaining this expression from the angular correlation coefficients a correction has been applied for the finite detector aperture [21]).

Knowing the parameters for the resonance, it is similarly possible to calculate the quadruple correlation involving the two dipole radiations with the intermediate alpha particle unobserved. The appropriate correlation expression has been quoted in detail previously [22]). Three separate correlation calculations are relevant to the present measurements. The corresponding predictions are as follows:

(a) both dipole radiations detected at 90° to the beam but with variable azimuthal angle ϕ between the counters

$$W_1(\phi) = 1-0.013\,P_2(\cos\phi);$$

(b) The final dipole radiation detected at 90° to the beam and the penultimate radiation detected at an angle θ_{12} to the beam, in the same plane

$$W_2(\theta_{12}) = 1-0.29\,P_2(\cos\theta_{12});$$

(c) The penultimate dipole radiation detected at 90° to the beam and the final radiation detected at an angle θ_2 to the beam in the same plane

$$W_3(\theta_2) = 1+0.04\ P_2(\cos\theta_2).$$

The latter two correlations integrated over the detector apertures define the factors $g_j(\theta, \phi)$ and $h_j(\theta, \phi)$ appearing in eq. (5).

The selection of the 90° geometry used in these measurements followed obviously from these calculations as that giving the highest coincidence yield since the $W_2(\theta)$ correlation peaks more strongly in this geometry than does the $W_3(\theta)$ in that for $\theta=0°$. Since the $W_1(\phi)$ correlation is so weak it was convenient to leave the two detectors in the same plane. This arrangement allows greater bulk shielding of the crystal albeit at the expense of greater efficiency for detection of annihilation coincidence events.

References

1) M. Goeppert, Naturwissenschaften **17** (1929) 932;
M. Goeppert-Mayer, Ann. Physik **9** (1931) 273
2) R. G. Sachs, Phys. Rev. **57** (1940) 194
3) A. G. W. Cameron, Bull. Am. Phys. Soc. **3** (1958) 269
4) T. Huus and R. Day, Phys. Rev. **91** (1953) 599
5) Rasmussen, Metzger and Swann, Phys. Rev. **110** (1958) 154
6) J. O. Newton, Proceedings of the Gatlinburg Conference on the Interaction of Complex Ions, Gatlinbrug, Tenn., May 1958, Paper No. 25
7) F. Ajzenberg-Selove and T. Lauritsen, Nuclear Physics **11** (1959) 1
8) A. M. Lane and J. M. Soper, private communication
9) T. Alväger and H. Ryde, Phys. Rev. Lett. **4** (1960) 363
10) Bromley, Gove, Kuehner, Litherland and Almqvist, Phys. Rev. **114** (1959) 758
11) W. W. Scott, Standard Methods of Chemical Analysis (D. Van Nostrand, 1939)
12) A. M. Hoogenboom, Nuclear Instruments **3** (1958) 57
13) Graham, Bell and Petch, Can. J. Phys. **30** (1952) 35
14) Schardt, Fowler and Lauritsen, Phys. Rev. **86** (1952) 527
15) A. J. Ferguson, private communication
16) Wolicki, Jastrow and Brooks, U.S. Naval Research Laboratory Report 4833, October 1956
17) F. B. Hagedorn, Phys. Rev. **108** (1957) 735
18) Kraus, French, Fowler and Lauritsen, Phys. Rev. **89** (1953) 299
F. B. Hagedorn, Phys. Rev. **108** (1957) 735
19) Sharp, Kennedy, Sears and Hoyle, Chalk River Report CRT-556, August 1954, unpublished
20) S. Bashkin and R. R. Carlson, Phys. Rev. **106** (1957) 261
21) M. E. Rose, Phys. Rev. **91** (1953) 610;
H. E. Gove and A. R. Rutledge, Chalk River Report CRP-755, February 1958, unpublished
22) Bromley, Gove, Paul, Litherland and Almqvist, Can. J. Phys. **35** (1957) 1042
23) Eichler and Jacob, Zs. f. Physik **157** (1959) 286

2.D

Nuclear Physics **20** (1960) 395—407; © *North-Holland Publishing Co., Amsterdam*

Not to be reproduced by photoprint or microfilm without written permission from the publisher

NEUTRON EVAPORATION SPECTRA FROM (p, n) REACTIONS

RICHARD L. BRAMBLETT and T. W. BONNER

The Rice University, Houston, Texas †

Received 28 June 1960

Abstract: A new type of neutron spectrometer has been used to compare neutron spectra from (p, n) reactions in several medium weight nuclei with Weisskopf evaporation theory. The method is very sensitive to the shape of the spectrum from 0.1 to 2.0 MeV, and allows the determination of the exponent k and the parameter τ in the expression $E^k e^{-E/\tau}$ for the neutron spectrum. Measurements of the (p, n) spectra from targets of Sn^{120}, Co^{59}, In^{115}, Ag^{109}, Sb^{123}, Nb^{93}, Rh^{103}, Cd^{114} and Sn^{122} have been made with a proton bombarding energy of 5.30 MeV. The neutron spectra agree well with that predicted by evaporation theory ($k = 1$) for all of the reactions studied except Sn^{120}(p, n) and Co^{59}(p, n). The values of τ obtained for the remaining seven target nuclei are respectively 0.53, 0.56, 0.51, 0.57, 0.59, 0.49 and 0.46 MeV, with an estimated absolute error of 0.02 MeV. For those nuclei for which the neutron spectra agree with theory, the variation of the level density parameter with atomic weight is roughly $a \approx 0.094\ A\ (\mathrm{MeV})^{-1}$. Angular distributions were obtained for four representative target nuclei. The angular distributions of neutrons from Sn^{120}(p, n) and In^{115}(p, n) were isotropic to within 5 %, whereas those from Nb^{93}(p, n) and Co^{59}(p, n) were symmetric about 90° with dips at 90° of 5 % for Nb^{93} and 7 % for Co^{59}. The angular distributions, in conjunction with information about the neutron spectra at 0° and 135° show that the contribution of direct interaction to these (p, n) cross sections is less than 5 %.

1. Introduction

The energy distribution of particles emitted from the compound nucleus can give information about the variation of the energy level density of the residual nucleus with excitation energy. For excitation high enough to make a large number of levels available, the statistical theory of the decay of the compound nucleus, as formulated by Weisskopf [1]), relates the energy spectrum of emitted neutrons to the level density. Weisskopf's concept of nuclear temperature leads to a specific form for the energy distribution of emergent particles. The case in which the emergent particles are neutrons has most frequently been compared with theory, since the spectrum of neutrons is not distorted by Coulomb effects. The experiments described here test the applicability of the statistical theory to neutron spectra resulting from proton bombardment of several intermediate weight nuclei.

The statistical model predicts that the energy distribution of neutrons resulting from the decay of a compound nucleus at excitation E_e is, in the centre of mass system,

$$N(E) = \text{const.}\ \sigma_c E \omega(E_e), \tag{1}$$

† Work supported in part by the U. S. Atomic Energy Commission.

where σ_c is the cross section for the formation of a compound nucleus by interaction of a neutron of energy E with the residual nucleus which has excitation E_e, and $\omega(E_e)$ is the level density of the residual nucleus. Experimentally determined cross sections for nonelastic scattering of neutrons [2,3,4]) indicate that the formation cross section σ_c decreases less than 20 % from 2 to 7 MeV neutron energy, but these experiments give no information about σ_c at lower energies due to the competition of compound elastic scattering with nonelastic scattering. Nemirovski [5]), using a complex potential with rounded edges, has calculated variations of the order of ± 10 % per MeV in σ_c. For the analysis of the experimental data presented here, the effect of the energy dependence of σ_c will be neglected.

Weisskopf [1]) introduces the concept of nuclear temperature by considering the nucleus as a highly degenerate Fermi gas. The excitation energy is then, to a very rough approximation,

$$E_e \approx aT^2, \tag{2}$$

where T is the nuclear temperature and a is a slowly varying function of the atomic weight. Calculation of the entropy $S = \ln \omega = \int dE_e/T$, leads to

$$\omega(E_e) \approx \text{const. } e^{2\sqrt{aE_e}}. \tag{3}$$

Neglecting the energy dependence of σ_c, the neutron spectrum is then

$$N(E) \approx \text{const. } Ee^{2\sqrt{aE_e}}. \tag{4}$$

For the cases for which the ground state Q value is known, the residual excitation is determined by the projectile bombarding energy in the laboratory system E_a, and the neutron energy. In the centre of mass system

$$E_e = \frac{M}{M+m} E_a + Q - E = b - E, \tag{5}$$

where m and M are respectively the masses of the bombarding particle and the target nucleus, and b is the maximum excitation of the residual nucleus. The neutron spectrum becomes

$$N(E) \approx Ee^{2\sqrt{a(b-E)}}, \tag{6}$$

which will henceforth be called the Weisskopf distribution. If the average excitation of the residual nucleus is such that

$$\bar{E}_e \gg |\bar{E} - E|, \tag{7}$$

where $\bar{E}$ is the average value of E, the Weisskopf distribution becomes [6])

$$N(E) \approx Ee^{-E/\tau}, \tag{8}$$

where τ is an appropriate average nuclear temperature, $\tau = \sqrt{(E_e/a)}$. The latter

spectrum is called the evaporation spectrum, and is the one commonly used for analysis of experiments.

A large proportion of the experimental data [7,8]) on nuclear temperatures consist in measurements of the energy spectrum of inelastically scattered neutrons. Inelastic scattering of 14 MeV neutrons [7]) has shown that compound nucleus formation is much more probable than direction interaction, which leads to neutrons of higher energy, but the relation of the neutron spectrum obtained to the level density is obscured by the large contribution of (n, 2n) reactions. Inelastic scattering of neutrons below 7 MeV [8]) has been a primary source of experimental data on nuclear temperatures. The (p, n) reaction complements neutron inelastic scattering measurements of nuclear temperatures, since it provides an entirely different set of residual nuclei to be compared with theory. The conditions for performing (p, n) experiments are such that multiple scattering corrections are not required, and there is no source of primary neutrons to provide background, as in neutron inelastic scattering experiments. A disadvantage involved in the use of (p, n) reactions to measure nuclear temperatures is that the Q value is generally negative. Moreover, the Q value is often quite different for isotopes of the same element, requiring that isotopically pure targets be used. At present, relatively few measurements of (p, n) neutron spectra exist in the range of energy and atomic number for which the statistical model is expected to apply. The experiments of Gugelot [9]) were complicated by the (p, 2n) reaction, since the proton energy used was 16 MeV. Albert *et al.* [10]) used a proton bombarding energy of 8 MeV and determined the neutron spectra from several medium weight nuclei. Experiments on the (n, n') and (p, n) reactions have made use of the time-of-flight method to measure the emergent neutron spectrum, except for some earlier high energy experiments [7,9]) where the photographic plate technique was used.

The experiments described here were performed to determine the neutron spectra resulting from bombarding nine intermediate weight nuclei with 5.30 MeV protons. The maximum residual excitations were of the order of 3 to 4 MeV, which is sufficient for the statistical model to apply for intermediate weight nuclei. Since the most probable energy in an evaporation spectrum is often about 0.5 MeV, energy sensitivity below 0.5 MeV is very desirable. In the experiments reported in this paper a new type of neutron spectrometer [11]) has been used. This device has good energy sensitivity from 0.1 to 2 MeV, which covers the range of neutron energy in most evaporation spectra.

2. Experimental Method

Neutrons were detected in a small $Li^6I(Eu)$ scintillator placed at the centre of polyethylene moderating spheres with sizes ranging from 5 cm to 30 cm in diameter. The efficiency of this neutron counter has been experimentally determined [11]) using monoenergetic neutrons from thermal energies to 15 MeV.

Over the range of neutron energies of interest for the experiments described here, the efficiencies of the small counters decrease rapidly with increasing neutron energy, whereas the efficiencies of the large counters increase. The pronounced difference in the efficiencies of the five counters provides a means for accurate determination of neutron spectra †.

Protons from the Rice University 5.5 MeV Van de Graaff accelerator were used to bombard targets of Co^{59}, Nb^{93}, Rh^{103}, Ag^{109}, Cd^{114}, In^{115}, Sn^{120}, Sn^{122} and Sb^{123}. The resulting spectra of neutrons were observed at 90° to the incident proton beam, using 5 sizes of polyethylene spheres around the Li^6I(Eu) slow neutron detector. At this angle of observation, the neutron spectrum in the laboratory system is nearly the same as that in the centre of mass system. The targets used were either monoisotopic or isotopically enriched to greater than 90 % and were deposited on 0.020 inch thick gold discs. The bombarding protons lost about 0.3 MeV energy in traversing the targets when the energy was adjusted to be 5.30 MeV at the centre of the target.

For measurements at 90°, the targets were aligned 45° to the proton beam. The counter was positioned at 20 cm from the target when using the 5.1 cm and 7.6 cm diameter polyethylene spheres, and at 40 cm when using the larger spheres. In addition, measurements were made for each sphere at 100 cm from the target to determine background due to scattered neutrons. That fraction of the count not following the inverse square law was considered to be background. The nearest scattering material was the concrete floor, 370 cm away. Experiments were done using a cleaned gold blank to determine background due to neutrons from sources other than the target. Small corrections, less than 10 % with an average of 5 %, were made to correct the two types of background neutrons.

For the purpose of determining the shape of a neutron spectrum, the counting rates of several sizes of counters are obtained. These experimental count rates are ordinarily quite different for the various counters. Since the counting rate as a function of energy is known experimentally for monoenergetic neutrons, the counting rate of each counter can be calculated for any assumed spectrum. The calculated counting rates are then compared with the experimental counting rates. If they do not agree, a different spectrum is assumed and the counting rates are again calculated. This procedure is repeated until the calculated count rates agree with the experimental count rates. Table 1 shows the results of such a calculation for the spectrum of neutrons resulting from bombardment of Rh^{103} with 5.30 MeV protons. To eliminate normalization problems, the ratios of the counting rates of different spheres are used. It is important to note that in table 1 distinction is made between the evaporation spectrum $Ee^{-E/\tau}$ and the

† The neutron detector used for (p, n) neutron spectra was an earlier model than that described in ref. [11]). This model used a Li^6I(Eu) crystal 1 mm thick and 8 mm in diameter, and the counting rate curves are slightly different from those given in ref. [11]).

Maxwellian distribution $E^{\frac{1}{2}}e^{-E/\theta}$. If the neutron spectrum is assumed to be of the evaporation form, the parameter τ can be determined from the ratio of the counting rates of two counters. Since 5 sizes of counters were used, there are 4 independent determinations of τ. If these independent determinations agree, the algebraic form assumed is correct. If they do not, another form must be chosen. The first column of table 1 shows the ratio under consideration, the second column gives the value of τ determined by the ratio. The average value of τ is 0.586 MeV and the largest deviation is 0.009 MeV, which is less than the estimated experimental error of about 0.014 MeV. It is concluded that the spectrum of neutrons from Rh^{103}(p, n) fits the evaporation spectrum.

TABLE 1

Values of parameters required to fit experimental neutron spectrum from Rh^{103}(p, n)

Counters used	Assumed spectrum	
	Evaporation $Ee^{-E/\tau}$ τ(MeV)	Maxwellian $\sqrt{E}e^{-E/\theta}$ θ(MeV)
30 cm and 20 cm	0.582	0.792
30 cm and 13 cm	0.592	0.844
30 cm and 7.6 cm	0.581	0.856
30 cm and 5.1 cm	0.591	0.912
20 cm and 7.6 cm	0.577	0.908
20 cm and 5.1 cm	0.593	0.983
13 cm and 5.1 cm	0.587	1.042
Average	0.586	0.905

Another form that might fit the neutron spectrum is the Maxwellian distribution, with parameter θ. The attempt to fit this spectrum is shown in the third column of table 1. This spectrum does not fit the experimental data. The values of θ determined by the ratios differ by as much as 0.14 MeV from the average of 0.90 MeV. The expected experimental error in this case is about 0.03 MeV. The ratios are listed in a meaningful order, starting with ratios of large counters at the top and ending with small counters at the bottom. When arranged in this order, a misfit to the neutron spectrum results in a trend in the values of the parameters indicated by the ratios. The trend for the Maxwellian form is apparent. Even though there are only 4 independent ratios, the use of more than 4 ratios in this manner makes the analysis easier.

Fig. 1 shows the shapes of the spectra under consideration, and gives an idea of the sensitivity of the counter. The dashed curve is a Maxwellian distribution with $\theta = 0.900$ MeV. The solid curve is an evaporation spectrum with $\tau = 0.590$ MeV. These correspond to the evaporation spectrum that fits the Rh^{103} data of table 1, and the Maxwellian that most nearly fits. Recall that the Maxwellian does not fit the data, since the values of the parameter indicated by the ratios

show a trend that is about 5 times the expected experimental error. Even so, the two spectra are quite similar.

As regards the sensitivity of the counter, it is appropriate to point out that it is sensitive to all energies of neutrons. The results for Rh^{103}(p, n) presented in table 1 indicate that the neutron spectrum is well described by the evaporation spectrum down to about 0.10 MeV. This lower limit of measurement exists because the fraction of neutrons below 0.10 MeV is a very small portion of the total number of neutrons in the evaporation spectrum. For the 5.1 cm counter, the fraction below 0.10 MeV is responsible for about 6 % of the total number of counts.

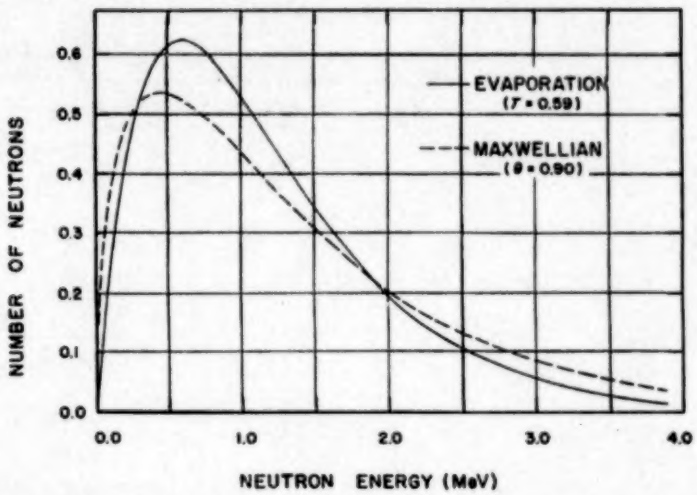

Fig. 1. Evaporation and Maxwellian spectra that most nearly fit the Rh^{103}(p, n) data. The evaporation spectrum agrees with the experimental data within the experimental error, the Maxwellian does not.

3. Neutron Spectra

The experimental counting rates of the various size counters, resulting from 5.30 MeV proton bombardment of 9 isotopes, were determined with a precision of about 1 %. Table 2 shows the values of the evaporation spectrum parameter τ indicated by the most sensitive ratios of counting rates. Except for Co^{59}, the 9 target nuclei are listed in order of the (p, n) Q value. It was found that the neutron spectra fit the evaporation spectrum very well in seven cases. The average values of τ listed in column 8 are estimated to be accurate to ± 0.02 MeV for all except the last two entries. Note that these temperatures are for the residual nuclei, which, contrary to the situation that exists in neutron inelastic scattering, are not the target nuclei.

The neutron spectra from the target nuclei Sn^{120} and Co^{59} did not fit the evaporation spectrum. For the case of Co^{59}, the misfit probably is due to the small number of levels available in the residual nucleus. Even though the maximum excitation of the residual nucleus was 3.35 MeV, the number of

levels accessible was much less than for the other nuclei under consideration, due to the relatively low atomic number of Co^{59}. From the Ni^{58}(d, p)Ni^{59} reaction [12]) it is known that there are about 30 levels accessible in Ni^{59} from Co^{59}(p, n)Ni^{59} at a proton bombarding energy of 5.30 MeV. Even at 8 MeV proton bombarding energy, the neutron spectrum from Co^{59}(p, n)Ni^{59} has been shown [10]) by time-of-flight methods to deviate from a smooth curve by 50 % at 3 MeV excitation in the residual nucleus.

TABLE 2

Nuclear temperatures from (p, n) reactions at 5.30 MeV

Target Isotope	(p, n) Q value (MeV)	Experimental evaporation spectrum temperatures (MeV) using						Level density parameter a $(MeV)^{-1}$
		30 cm and 13 cm counters	30 cm and 7.6 cm counters	30 cm and 5.1 cm counters	20 cm and 7.6 cm counters	20 cm and 5.1 cm counters	Average	
$_{49}In^{115}$	−0.28	0.514	0.522	0.513	0.559	0.535	0.529	14.0
$_{47}Ag^{109}$	−0.94	0.550	0.561	0.553	0.591	0.568	0.565	10.0
$_{51}Sb^{123}$	−1.0	0.493	0.503	0.498	0.525	0.514	0.507	13.3
$_{41}Nb^{93}$	−1.27	0.564	0.550	0.578	0.565	0.576	0.567	8.8
$_{45}Rh^{103}$	−1.35	0.592	0.581	0.591	0.577	0.593	0.587	7.9
$_{48}Cd^{114}$	−2.20	0.475	0.484	0.477	0.507	0.490	0.487	8.7
$_{50}Sn^{122}$	−2.33	0.470	0.473	0.478	0.433	0.456	0.462	9.4
$_{50}Sn^{120}$	−3.50	0.445	0.485	0.484	0.538	0.520	≈0.5	
$_{27}Co^{59}$	−1.86	0.98	0.93	0.86	0.92	0.82	≈0.9	

For the target nucleus Sn^{120}, the deviation from the evaporation spectrum is also possibly due to the small number of levels available. The (p, n) Q value is so unfavorable that the maximum excitation of the residual nucleus was only 1.75 MeV. Examination of the derivation of the evaporation spectum formula shows that an approximation eq. (7) was made which is particularly poor in the case of Sn^{120}(p, n)Sb^{120}. Consequently, the more exact Weisskopf distribution eq. (6) was used as a trial spectrum. The latter has fewer high energy neutrons than the evaporation spectrum. It was found that the neutron spectrum did not fit the Weisskopf distribution appreciably better than the evaporation spectrum.

The level density parameter a can be calculated from the (p, n) Q value and the average temperature determined from the fit to the evaporation spectrum. Since the average energy of the evaporation spectrum is 2τ, a is given by

$$a = \frac{b-2\tau}{\tau^2}. \tag{9}$$

Another more direct way to determine a is to fit the more exact Weisskopf distribution directly to the experimental data, hence avoiding the intermediate step involving average temperature. Although the Weisskopf distribution and the evaporation spectrum fit the experimental data equally well, the values of a

obtained are slightly different. For the neutron spectra measured in these experiments, use of the Weisskopf distribution results in values of a about 10 % lower than values determined using the evaporation spectrum. This difference corresponds to about 4 % in the nuclear temperature. The discrepancy in a due to the two methods of analysis is about the same size as the estimated experimental error in its absolute determination. Since the discrepancy is small, the value of a determined by the fit of the neutron spectrum to the evaporation spectrum eq. (9) will be used.

The values of a determined from the average nuclear temperatures are listed in order of the maximum excitation of the residual nucleus in table 2. These values are estimated to be correct to 10 %. The values of a obtained for $Nb^{93}(p, n)Mo^{93}$ and $In^{115}(p, n)Sn^{115}$ agree to within 10 % with values calculated from the data of Albert *et al.* [10]) who used time-of-flight techniques and a proton bombarding energy of 8 MeV. The value of a obtained for $Rh^{103}(p, n)Pd^{103}$ differs by 25% from that determined from the data of Albert *et al.* Theoretically, a should be independent of the excitation energy; and for Mo^{93}, Sn^{115}, and Pd^{103} this is true to within 25 %, which is roughly the combined experimental error of the two experiments. Cranberg *et al.* [8]), measuring spectra of inelastically scattered neutrons, has found nuclei for which a is dependent on excitation energy, in addition to nuclei for which a is constant.

The variation of a as a function of atomic weight is shown in fig. 2. The values from Albert *et al.* are included with those determined in this experiment. The values of a determined from the two (p, n) experiments follow the relation $a \approx 0.094A\,(\mathrm{MeV})^{-1}$ with an average deviation of 15 %. This is in agreement with theoretical calculations [13,14]) which indicate that a should be roughly proportional to atomic weight. Values of a obtained from neutron inelastic scattering experiments [8]) are somewhat larger, and fit the relation $a \approx 0.16A$

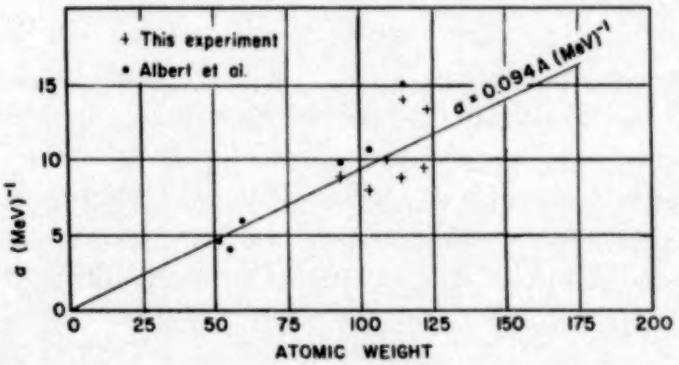

Fig. 2. Variation of the level density parameter a with atomic weight.

$(\mathrm{MeV})^{-1}$ with considerable fluctuations. Fong [15]) has obtained $a \approx 0.05A$ $(\mathrm{MeV})^{-1}$ for values of a calculated from 1 MeV neutron capture cross section data.

For his analysis, Fong, following a suggestion by Hurwitz and Bethe [16]), has calculated the excitation energy eq. (5), above a characteristic level rather than above the ground state. According to this suggestion the position of the ground state and low lying levels are influenced by odd-even and shell effects, whereas the higher levels are not. In the application of the statistical model the spacing of the higher levels is of primary importance, consequently a characteristic level was introduced to eliminate odd-even and shell effects. If this analysis due to Fong is applied to the present data, the corrections to a due to even-odd and shell effects are in the proper direction to remove fluctuations in a as a function of atomic weight, but they are too large. This might be expected for low excitation energies where the shell and even-odd effects on the level density are not completely absent. Application of the characteristic level concept to this experiment changes the rough relation between a and atomic weight to $a \approx 0.07A$, which is in better agreement with Fong's result for neutron capture.

In addition to measurements of neutron spectra at 90° to the beam of 5.30 MeV protons, the neutron spectrum from In^{115}(p, n) was measured at other angles and proton energies. In every case it was found that the laboratory system neutron spectrum could be fit by an evaporation spectrum. It is necessary to account for the change in τ due to centre of mass motion; however, the small change in τ can be calculated to within the accuracy of the experimental data. For the evaporation spectrum with $\tau = 0.50$ MeV, the calculated difference in τ between 0° and 135° in the laboratory system is 0.033 MeV. The average observed difference was 0.02 MeV. The results are summarized in table 3. The fourth column gives the nuclear temperatures corrected to the centre of mass system, and the fifth column gives the resulting values of a. The estimated relative errors in τ and a are respectively 2 and 5 %. The absolute errors are estimated to be 4 and 10 %.

TABLE 3

Supplementary In^{115}(p, n)Sn^{115} data

Proton energy (MeV)	Angle of observation	τ(MeV) (laboratory system)	τ(MeV) (centre of mass system)	a $(MeV)^{-1}$
5.50	0°	0.536	0.514	15.1
5.50	135°	0.517	0.529	
5.00	0°	0.516	0.494	15.2
5.00	135°	0.479	0.490	
4.50	0°	0.499	0.477	14.1

Two significant facts are revealed by the data in table 3. The first is that the neutron spectrum at 0° does not show any displacement to higher energy other

than that due to centre of mass motion. Displacement to higher energy at 0° would be expected if there were neutrons due to direct interaction processes which are strongly peaked at small angles. Assuming that neutrons due to direct interaction would have an energy of about 3 MeV, a 4 % contribution of direct interaction at 0° would cause 0.010 MeV change in τ. These results show that the contribution of direct interaction at 0° is less than 10 %. Further evidence that direct interaction is unimportant is given in the next section, where angular distributions are discussed. The second significant fact is that a is independent of bombarding energy from 4.50 MeV to 5.30 MeV. Since these values of a agree with that of Albert *et al.* [10]) at 8.0 MeV, it may be concluded that the level density in Sn^{115} is well described by evaporation theory from an average excitation of 3 to 6 MeV.

4. Angular Distributions and Cross Sections

Angular distributions of Co^{59}(p, n)Ni^{59}, Nb^{93}(p, n)Mo^{93}, In^{115}(p, n) Sn^{115} and Sn^{120}(p, n)Sb^{120} were obtained at 4.9 MeV using the 12.7 cm diameter counter at 40 cm from the target. The results, corrected to the centre of mass system, are shown in fig. 3. The cross sections in the centre of mass system at 0° were respectively 10, 2.1, 1.3 and 1.2 mb/sr. A small correction (less than 10 %) has been made for the variation of the efficiency of the counter due to the change in energy of the neutrons with angle. The angular distributions for Sn^{120} and In^{115} were isotropic to within 5 %, whereas those for Co^{59} and Nb^{93} showed slight dips at 90°. The dip was about 7 % for Co^{59} and 5 % for Nb^{93}. These angular distributions are those to be expected for reactions proceeding by compound nucleus formation. None of the angular distributions showed the peaking at small angles characteristic of direct interaction processes. For this reason it is estimated that the extent of direct interaction is less than 5 % of the cross section at 0°. This is in agreement with the upper limit of 10 % direct interaction in In^{115}(p, n) obtained in the previous section from the fact that the neutron spectrum is the same at 0° and 135° in the centre of mass system.

Cross sections at a proton energy of 5.30 MeV for all the reactions studied were obtained from the target weight and the known efficiency of the neutron detector. The values at 5.30 MeV given in table 4 are estimated to be correct to $\pm$10 %. The cross sections obtained for Sn^{122}, Sn^{120}, Ag^{109} and Rh^{103} are in excellent agreement with Blaser *et al.* [17]), but those for Cd^{114}, and especially for Nb^{93} are in very poor agreement. The cross sections for all except Sn^{122} and Sb^{123} agree well with the optical model cross sections calculated as a function atomic mass by Albert [18]) to fit his data.

The yield as a function of energy for the In^{115}(p, n)Sn^{115} reaction was obtained using the 7.6 cm diameter counter. This counter was positioned at 0° to the proton beam and subtended a half angle of 45° from the target. In addition, a

long counter was positioned directly behind the 7.6 cm counter, and at the same solid angle. The ratio of counts in the two counters was nearly constant from 3.6 MeV to 5.3 MeV, indicating that the average neutron energy remained nearly constant over this range of proton energy. This fact, in conjunction with the isotropic angular distribution, indicates that the count rate of the 7.6 cm

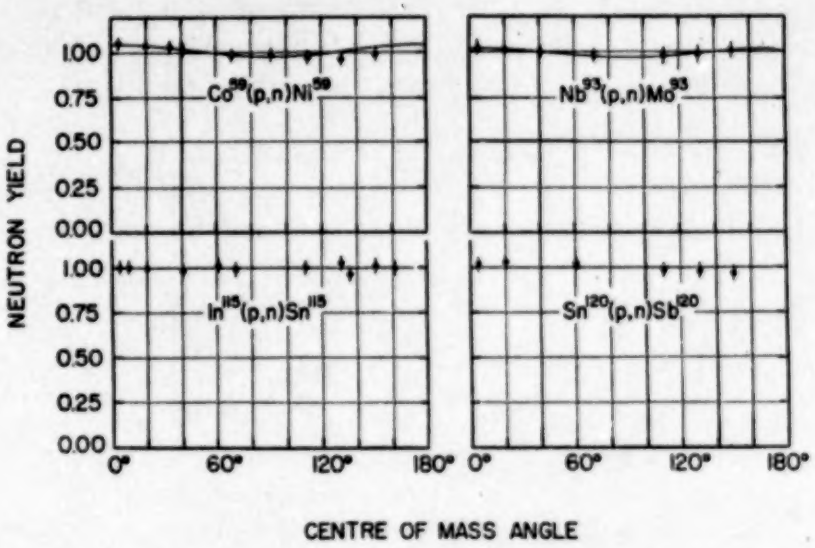

Fig. 3. Angular distributions of all neutrons from several (p, n) reactions obtained with 4.9 MeV protons.

TABLE 4

Results of (p, n) cross section measurements at 5.30 MeV

Target isotope	Cross section (mb)	Strength function (10^{-14} cm)
Sb^{123}	15	2.1
Sn^{122}	44	5.3
Sn^{120}	36	4.2
In^{115}	31	3.4
Cd^{114}	32	2.9
Ag^{109}	36	3.1
Rh^{103}	46	3.4
Nb^{93}	63	2.5
Co^{59}	246	2.9

counter at one angle was a good relative measure of the cross section. The cross section obtained at 5.30 MeV during the measurement of the neutron spectrum was used to obtain the absolute cross section. The resulting excitation curve is shown in fig. 4. The error in the cross sections given in fig. 4 is estimated to be ± 10 %.

The Coulomb and angular momentum effects can be removed from the cross sections and the excitation curves by introducing the strength function. Ex-

pressed as an average over resonances, the contribution to the average total reaction cross section from the partial wave denoted by l is [19])

$$\sigma_l = 4\pi^2(2l+1)\frac{\lambda\!\!\!^{-}}{A_l^2}(\gamma^2{}_{Jl}/D_J)_{\mathrm{AV}}. \tag{10}$$

The strength function $(\gamma^2{}_{Jl}/D_J)_{\mathrm{AV}}$, is the average ratio of reduced width to level spacing. By summing eq. (10) over l, it can be seen that the (p, n) cross section gives a strength function averaged with the weight factor $(2l+1)/A_l^2$,

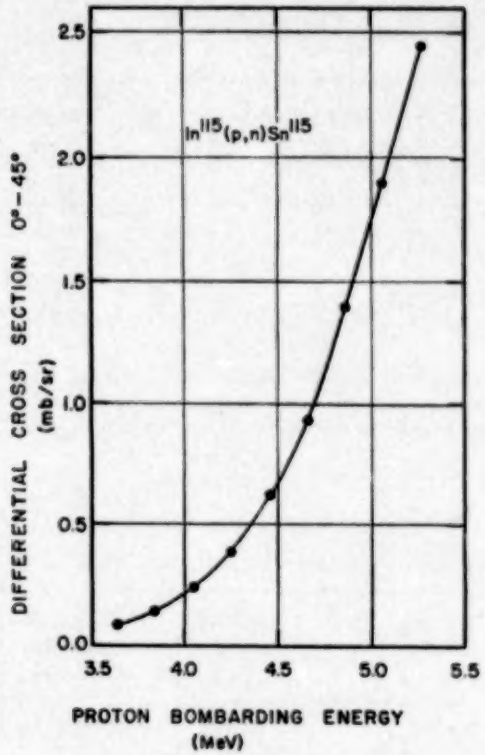

Fig. 4. Absolute yield of neutrons from the reaction In^{115}(p, n) as a function of proton energy.

$$\overline{S} = \frac{\sigma}{4\pi^2\lambda\!\!\!^{-}}\left[\sum_l \frac{2l+1}{A_l^2}\right]^{-1}. \tag{11}$$

The averaged strength function has been obtained from the In^{115}(p, n) excitation curve using penetrabilities for a nuclear radius of $1.45A^{\frac{1}{3}}10^{-13}$ cm. The averaged strength function obtained in this manner is nearly constant, which is consistent with measurements made by Jones [19]) on lighter nuclei.

Averaged strength functions eq. (11) calculated from the cross sections at 5.30 MeV are listed in table 4 for each target isotope. Again, a nuclear radius of $1.45\ A^{\frac{1}{3}}\ 10^{-13}$ cm was used to determine the penetrabilities. The strength functions for Co^{59}, Nb^{93}, Rh^{103} and Sn^{115} agree to within experimental error with measurements by Schiffer and Lee [20]), who used the same radius.

References

1) V. F. Weisskopf, Phys. Rev. **52** (1937) 295
2) Taylor, Lönsjö and Bonner, Phys. Rev. **100** (1955) 174
3) M. Walt and J. R. Beyster, Phys. Rev. **98** (1955) 677
4) Beyster, Henkel and Nobles, Phys. Rev. **97** (1955) 563
5) P. E. Nemirovski, Peaceful uses of atomic energy (United Nations, New York, 1956) Vol. 2, p. 86
6) James Terrell, Phys. Rev. **113** (1959) 527
7) L. Rosen, Peaceful uses of atomic energy (United Nations, New York, 1956) Vol. 4, p. 97
8) L. Cranberg and J. S. Levin, Phys. Rev. **109** (1958) 2063;
   L. Cranberg, Peaceful uses of atomic energy (United Nations, New York, 1956) Vol. 4, p. 40;
   D. B. Thompson and L. Cranberg, Bull. Am. Phys. Soc. **4** (1959) 258
9) P. C. Gugelot, Phys. Rev. **81** (1951) 51
10) Albert, Anderson, Wong, McClure and Walker, to be published
11) Bramblett, Ewing and Bonner, Nuclear Instruments and Methods **9** (1960) 1
12) C. H. Paris, MIT LNS Progr. Report, (1958) and (1959);
   C. H. Paris and W. W. Buechner, Bull. Am Phys. Soc. **3** (1958) 38
13) H. A. Bethe, Phys. Rev. **50** (1936) 332; Revs. Mod. Phys. **9** (1937) 69
14) J. M. B. Lang and K. J. LeCouteur, Proc. Phys. Soc. A **67** (1954) 586
15) Peter Fong, Phys. Rev. **102** (1956) 434
16) H. Hurwitz and H. A. Bethe, Phys. Rev. **81** (1951) 898
17) Blaser, Boehm, Marmier and Peaslee, Helv. Phys. Acta **24** (1951) 3
18) Richard D. Albert, Phys. Rev. **115** (1959) 925
19) G. A. Jones, Nuclear Physics **12** (1958) 167
20) J. P. Schiffer and L. L. Lee, Jr., Phys. Rev. **109** (1958) 2098

2.I

Nuclear Physics **20** (1960) 408—416; © *North-Holland Publishing Co., Amsterdam*

Not to be reproduced by photoprint or microfilm without written permission from the publisher

ENERGY SPECTRUM OF THE PHOTONEUTRONS FROM GOLD

R. F. ASKEW † and A. P. BATSON

Department of Physics, University of Virginia, Charlottesville, Virginia ††

Received 30 June 1960

Abstract: The energy spectrum of the neutrons produced at 90° to a gold target bombarded with 55 MeV bremsstrahlung has been measured. Nuclear emulsions were used to detect the photoneutrons. The spectrum shows two peaks. The large peak at 1.25 MeV can be interpreted as due to the statistical decay of the compound nucleus. The smaller peak at about 5.5 MeV is assumed to come from a "direct" transition, as described by the Wilkinson model.

In the appendix a new method is presented for the calculation of the corrections involved for those proton recoils which leave the emulsion.

1. Introduction

The photoneutron energy spectrum from gold has been previously measured by Cavallaro, Emma, Milone and Rubbino [1]), using bremsstrahlung with a maximum energy of 30 MeV. They found an energy distribution with a large peak for neutrons of about 2 MeV, decreasing smoothly with increasing neutron energy. Experiments with other elements, for example tantalum [2]), have given some evidence of additional peaks in the energy distribution at higher neutron energies. Such peaks can be interpreted as being due to "direct resonance" transitions, as described by Wilkinson [3]). The statistical accuracy of most previous experiments has been rather poor in the region of high neutron energies, and the present experiment gives better data in this energy range for gold, for the photoneutrons emitted at 90° to a 55 MeV bremsstrahlung beam.

2. Experimental Method

A gold cylinder, of diameter 1.232 cm and height 1.257 cm, was bombarded with a 55 MeV "thin target" bremsstrahlung beam from the University of Virginia electron synchrotron. The beam was defined by a lead collimator 30.5 cm long which had a tapered hole of square cross section, such that the photon beam just covered the target. Ilford C2 nuclear emulsions, 200 μm thick, were placed in a horizontal plane at 90° and 75° to the beam. The plane of each emulsion was vertical and made an angle of 5° to the line joining the centres of the target and the emulsion. Lead shields 0.32 cm thick were placed over each

† Now at Auburn University, Auburn, Alabama.

†† Supported by the U. S. Air Force Office of Scientific Research.

emulsion to screen it from low energy photons from the target. An exposure of 3000 roentgen was given to the target, and an equivalent exposure was given with a second set of plates, with the target removed, to obtain the background.

The processed emulsions were mounted on a micrometer stage, and viewed with a 97× oil immersion objective in conjunction with a 10× eyepiece. The recoil protons from the hydrogen contained in the emulsion were used to determine the neutron energy spectrum. If the length of the proton track and ψ, the angle it makes with the incident neutron, are known, then the energy of the neutron is given by

$$E_n = \frac{E_p}{\cos^2\psi}, \tag{1}$$

where E_p is determined from the range-energy curves given by Rotblat [4]). In practice, the scattering angle cannot be determined directly, but measurements were made of Φ, the dip angle of the track in the emulsion, and of θ, the angle which the projection of the observed proton track in the plane of the emulsion makes with the incident neutron direction. The scattering angle ψ is then given by

$$\cos\psi = \cos\theta\cos\Phi. \tag{2}$$

Two initial acceptance criteria were placed on all proton tracks. First they had to be of sufficient length to have been produced by a neutron with a minimum energy of 0.5 MeV, this length being 5 μm in the unprocessed emulsion, since shorter tracks have too great a probability of being missed if the dip angle is large. Secondly, the maximum acceptable value of θ or Φ was taken to be 20°. For each track that began and ended in the emulsion, θ was measured with a protractor in the eyepiece, and Φ by observing the lengrh of track in focus, the depth of field of the microscope having been previously determined. The coordinates of the beginning and end points of each track were then measured. The precision of the measurements was such that the length of the track could be determined to within 1 μm, and θ and Φ were known to better than $\frac{1}{2}$°.

Since it is known that nearly all of the photoneutrons have energies below 4 MeV, and it was desirable to obtain additional data at energies in excess of this, two sets of measurements were taken. All the tracks within a volume of 49.79 mm^3 on one plate at 90°, satisfying the above criteria, were measured. This will be referred to as the "slow scan." In adition, two plates, one at 90° and the other at 75° to the photon beam, were given a "fast scan", in which only proton recoils of length greater than 85 μm in the horizontal plane were measured. For this track length all of the proton recoils which were caused by neutrons of energy greater than 4 MeV were recorded. Similar measurements were made on the background plates, scanning an area of $\frac{1}{8}$ of that scanned on the target emulsions. The data were corrected for the shrinkage of the emulsion,

and the length and scattering angle of each track in the unprocessed emulsion were calculated.

It is necessary to correct for those tracks which, while falling within the angular criteria, do not end in the emulsion. The method generally used for making this correction is due to Richards [5]). This method suffers from the limitation that it assumes that the recoil proton receives all the energy of the incident neutron. For scattering angles of 20° this causes an error of about 12 % in E_n. A new method of making this correction, involving no approximations, has been derived, and is presented in the appendix. During the slow scan of the 90° plate, all the tracks within the angular criteria which left the emulsion were counted, and this number of tracks was compared with the additional tracks added by the above correction. The numbers, 102 and 99.5 respectively, are in excellent agreement.

Only those tracks which had a scattering angle $\psi \leqq 20°$ were actually included in the final data; the small number of additional tracks lying in the corners of the acceptance pyramid were rejected. For the fast scan, only those protons which were produced by neutrons of energy greater than 4 MeV were included in the sample.

The protons were then sorted into groups which corresponded to increments of 0.5 MeV neutron energy, with a 2° range of recoil proton angle. The appropriate correction factor for lost tracks was then applied to each group, and the resulting number of proton recoils in each energy interval was then summed over all angle intervals. This is permissible since their angular distribution is independent of neutron energy in this energy range. The results for each energy interval were then corrected for the attenuation of neutrons in the gold target and the lead shield round the emulsion. Finally, the number of events in each energy interval was divided by the appropriate neutron-proton scattering cross section.

3. Results and Discussion

The energy spectra for neutrons with $E_n > 4$ MeV found in the fast scans of the 75° and 90° plates were identical within the statistical limits, and also agreed well with the results from the slow scan in this energy range. Therefore, the data from the fast scan were combined with those from the slow scan, and the results are presented in tables 1 and 2 and fig. 1. The solid line in fig. 1 is the neutron energy spectrum calculated on the basis of the statistical model [6,7]) normalized to the experimental data at the peak of the distribution. The parameters used in this calculation are the same as those used by Cavallaro *et al.*, but with a 55 MeV Schiff bremsstrahlung spectrum. The agreement of the low energy data with the statistical model spectrum is seen to be good, which was not the case in the work of Cavallaro *et al.* A considerable excess of high energy

neutrons, compared with the statistical model predictions, is found in both experiments. These are interpreted as neutrons produced by a direct emission process.

TABLE 1

Number of observed tracks

	Number of tracks on target emulsions	Number of tracks on background emulsions †
Slow scan		
$E_n < 4$ MeV	3071	11
$E_n > 4$ MeV	217	0
Fast scan		
$E_n > 4$ MeV	838	0

† The numbers recorded in this column are the actual numbers of tracks observed in scanning one eighth the area scanned on the target emulsions.

TABLE 2

Relative photoneutron energy spectrum

E_n(MeV)	$I(E_n)$ [a]	Standard Deviation (%) [b]
0.75	1306	3.1
1.25	1386	3.5
1.75	1137	4.3
2.25	849	5.5
2.75	590	7.1
3.25	411	9.2
3.75	278	11.8
4.25	218	6.3
4.75	168	7.3
5.25	150	7.8
5.75	139	8.7
6.25	113	10.1
6.75	79	12.3
7.25	72	13.3
7.75	60	15.3
8.25	51	17.1
8.75	51	18.3
9.25	31	24.6
9.75	13	38.5
10.25	19	34.2

[a]) Corrected for absorption and the variation of σ(n, p) with energy.

[b]) Does not include the error involved in normalizing the fast and slow scans (7.5 %). This error will not affect the structure of the curve, except in the region of 4 MeV.

The most interesting piece of information that can be gleaned from an experiment of this type is an energy distribution for the "direct" neutrons mentioned

above. For neutron energies greater than about 5 MeV this is simple to obtain from the data, since the contribution by the evaporated neutrons to the spectrum is small at high energies. The situation for $E_n < 5$ MeV is much more difficult to resolve, however, since the fraction of the neutrons which are produced by the direct process is not known. Also, the shape of the statistical spectrum may be in error, even though it appears to fit the low energy data well.

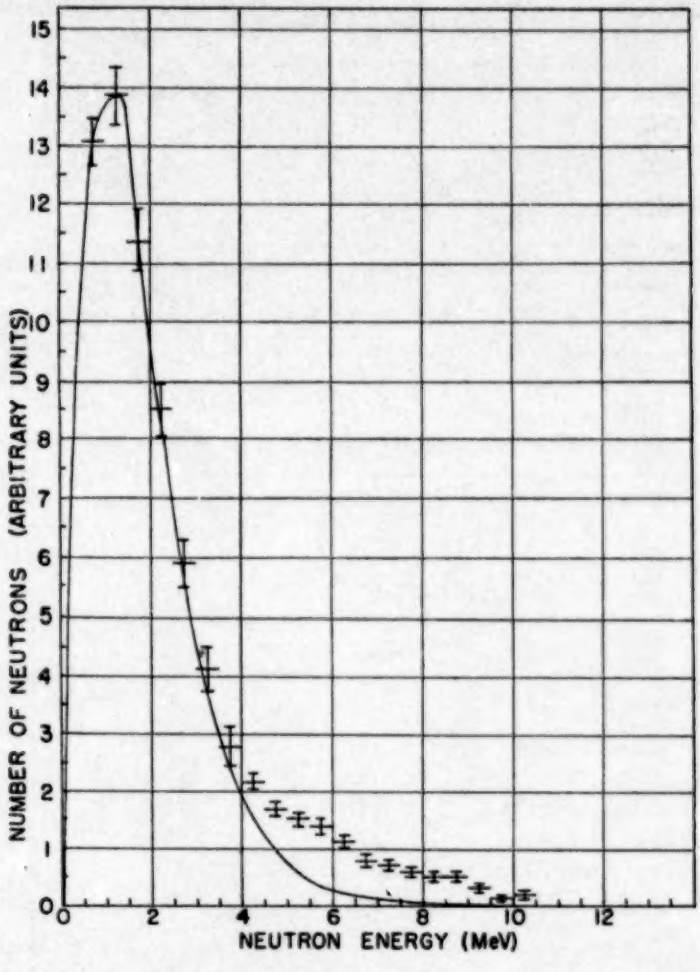

Fig. 1. Relative photoneutron energy spectrum. The solid curve is the statistical theory prediction.

Nevertheless, if this spectrum is assumed to be correct, and is fitted to the low energy data as in fig. 1, then 12.4 % of the neutrons are found to be produced by a direct process. The energy distribution of these neutrons is shown in fig. 2(a). The most notable feature of this distribution is the peak at about 5.5 MeV. There can be little doubt that there is a peak at this neutron energy, whatever assumptions are made for the parameters of the statistical theory spectrum, since it is clearly present in the raw data shown in fig. 1. Figs 2(b) and 2(c) show the direct neutron spectra if it is assumed that 20 % and 30 % of the neutrons are of this type, All these, of course, still show the 5.5 MeV peak.

A simple calculation of the neutron energies to be expected on the basis of

the Wilkinson model has been made, assigning energy levels to the gold nucleus by an interpolation between a square well and a simple harmonic oscillator potential. An effective mass of half the nucleon mass was used for each nucleon, in order that the giant resonance should appear at the observed energy. The transition strengths were computed for all major transitions, using the enhancement factors and radial overlap integrals tabulated by Wilkinson. It is found

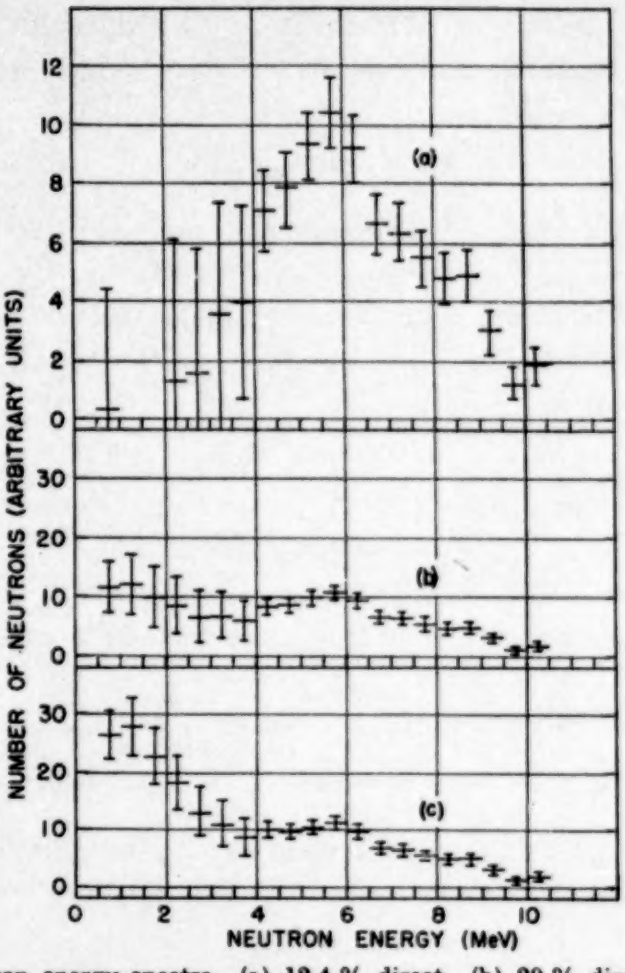

Fig. 2. Direct neutron energy spectra. (a) 12.4 % direct, (b) 20 % direct, (c) 30 % direct.

that the strongest direct transition is from the $2f_{\frac{5}{2}}$ to the $2g_{\frac{7}{2}}$ level, corresponding to a neutron energy of approximately 5 MeV, in good agreement with the experimental data shown in fig. 2. However, more detailed work, both theoretical and experimental, must be carried out before the direct transitions can be unambiguously identified.

This experiment was initiated by Dr. W. D. Whitehead, and we wish to express our appreciation for his contribution to the work. We are also grateful to R. S. Tickle and P. A. Flournoy for many valuable discussions and in particular to G. C. Reinhardt for discussions and for the calculation of the direct neutron transition strengths referred to in sect. 3.

Appendix. Correction for tracks which leave the emulsion.

A.1. $\psi < \theta_0, \Phi_0$

Let d be the thickness of the emulsion, and the latitude and longitude maxima criteria be Φ_0 and θ_0 respectively. The end-points of all tracks of length l scattered at angle ψ from a given origin lie on a circle of radius $l \sin \psi$ (see fig. 3). The total number of tracks of length l at angles from ψ to $\psi+\mathrm{d}\psi$, emitted from an emulsion depth between z and $z+\mathrm{d}z$ is proportional to the circumference of this circle, i.e.

$$N = \rho\, 2\pi\, l \sin \psi\, \mathrm{d}z.$$

Due to the up-down symmetry of the system, the same number of tracks will be lost at the bottom of the emulsion as at the top, so it is only necessary to consider those tracks in the upper semicircle. Thus, the number of tracks N is redefined as

$$N = \rho \pi l \sin \psi\, \mathrm{d}z,$$

and $\mathrm{d}n$, the number lost at depth z, is given by

$$\mathrm{d}n = \rho \pi l \sin \psi \frac{2\lambda}{\pi} \mathrm{d}z.$$

Thus the total number lost from the upper semicircle, is given by

$$n = 2\rho\, l \sin \psi \int_{z=0}^{z_{\max}} \cos^{-1} \frac{z}{l \sin \psi}\, \mathrm{d}z.$$

Case A. $l \sin \psi < d$

In this case the upper limit of integration is $l \sin \psi$, since beyond this depth no tracks are lost. The expression for n then reduces to

$$n = 2\rho\, l^2 \sin^2 \psi,$$

and f, the fraction of tracks lost, is given by

$$f = \frac{n}{N} = \frac{2l \sin \psi}{\pi d}.$$

Case B. $l \sin \psi > d$

In this case, no simplification of the expression is possible, and

$$f = \frac{2}{\pi x} \left[x \cos^{-1} x + 1 - (1-x^2)^{\frac{1}{2}}\right],$$

where

$$x = \frac{d}{l \sin \psi}.$$

(The above corrections were the only ones used in the present work, since all tracks with $\psi > 20°$ were rejected).

A.2. $\psi > \theta_0, \Phi_0$

The general case of $\theta_0 \neq \Phi_0$ will be considered here. Fig. 4 shows one quadrant of the circle of radius $l \sin \psi$, with the angular criteria cutting this circle.

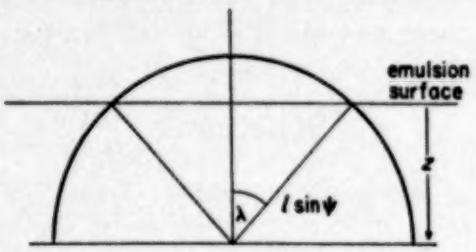

Fig. 3.

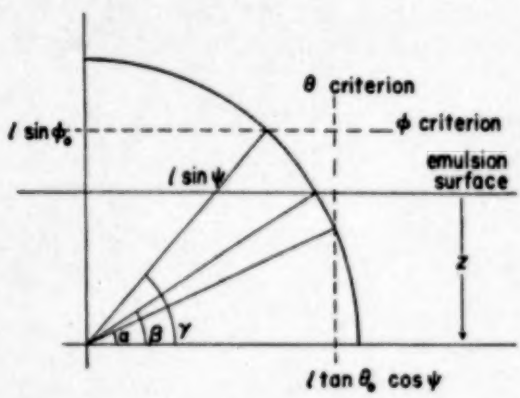

Fig. 4.

If $\eta\, dz$ is the number of events per unit angle around the quadrant which start from a point between z and $z+dz$ below the emulsion surface, then the number of available tracks lost between the θ_0, Φ_0 criteria is

$$n = \eta \int (\gamma - \beta) dz,$$

and since $\sin \beta = z/l \sin \psi$

then

$$n = \eta \{\gamma d - l \sin \psi [\beta \sin \beta + \cos \beta]_{\beta_1}^{\beta_2}\}.$$

Case A. $l \sin \Phi_0 < d$

Then the integration must be carried up to the criteria, i.e. f, the fraction of tracks within the criteria that do not end in the emulsion, is given by

$$f = \frac{\gamma d - l \sin \psi [\beta \sin \beta + \cos \beta]_{\beta=\alpha}^{\beta=\gamma}}{(\gamma - \alpha)\, d},$$

where $\cos \alpha = \tan \theta_0 \cot \psi$ and $\sin \gamma = \sin \Phi_0 \operatorname{cosec} \psi$.

Case B. $l \sin \Phi_0 > d$

Here the upper limit of integration over β will be given by

$$\sin \beta_{\max} = \frac{d}{l \sin \psi}.$$

For both case A and B the number of tracks scattered at angle ψ can then be determined from the corrected number found between the criteria.

References

1) S. Cavallaro, V. Emma, C. Milone and A. Rubbino, Nuovo Cim. **9** (1958) 736
2) G. Cortini, C. Milone and A. Rubbino, Nuovo Cim. **9** (1958) 85
3) D. H. Wilkinson, Physica **22** (1956) 1039
4) J. Rotblat, Nature **167** (1951) 550
5) H. T. Richards, Phys. Rev. **59** (1941) 796
6) V. Weisskopf and D. Ewing, Phys. Rev. **57** (1940) 472
7) J. Blatt and V. Weisskopf, Theoretical nuclear physics (Wiley, New York, 1952) Ch. 8

8.B

Nuclear Physics **20** (1960) 417—439; © *North-Holland Publishing Co., Amsterdam*

Not to be reproduced by photoprint or microfilm without written permission from the publisher

K-MESON-NUCLEON SCATTERING AND RELATIVISTIC DISPERSION RELATIONS

P. K. ROY

Physics Department, University College of Science, Calcutta

Received 22 June 1960

Abstract: Relativistic K-meson-nucleon dispersion relations are subjected to the type of analysis which leads one to expect a resonance in the pion-nucleon system. The P-wave equations for scalar mesons show no indication of any resonance. But the S-wave equations strongly suggest a resonant K^+-p scattering and a repulsive $\overline{K}$-nucleon potential, both in contradiction with experiment. However, for pseudo-scalar K-particles, analogous to the pion, the P-wave equations are consistent with a resonance in the $I = 1$, $j = \frac{3}{2}$ and one of the $I = 0$ states. This conclusion is not borne out by the present experimental findings and calls for detailed information about the angular distributions and the high energy behaviour of the scattering cross-section to decide the issue. For the $\overline{K}$ particles no such resonance states are found.

For the pseudoscalar K particles it is concluded, in the absence of the "accidental cancellation" which characterizes the pion case, that the $I = 1$ phase-shift at threshold should be given correctly by the "Born" term corresponding to a repulsive interaction, in agreement with experiment. No definitive conclusion about the S-wave behaviour of the $\overline{K}$ particles can really be drawn for reasons mentioned below.

The main conclusion of the present work is thus that the dispersion theoretic analysis of *non-forward* scattering is capable of discriminating between a scalar and pseudoscalar K-meson on *qualitative* grounds alone; it strongly indicates that these mesons are pseudoscalar.

1. Introduction

In the course of the last few years much attention has been devoted to the study of relativistic dispersion relations both for boson-fermion [1]) and fermion-fermion [2]) scattering. In the "truncated" form of the dispersion relations the most striking success has been scored in pion-nucleon scattering [3]), in photo-pion production [4]) and in electro-pion production [5]). For pion-nucleon scattering in the low energy region the equations for the P-wave amplitudes have been found to be consistent only with the assumption of a resonance in the 33-state. These relativistic relations have also successfully reproduced the experimental smallness of the S-wave scattering amplitudes as a consequence of the assumption of the 33-resonance.

Recently considerable information about K-meson-nucleon scattering has been obtained [6]). In contrast to the pion, the present experimental data do not conclusively determine the intrinsic parity of the K-mesons. However, these data do show that up to rather high energy the scattering of K-particles in the $I = 1$ state is characterized by the predominance of S-waves with a negative scattering length at threshold. For the $\overline{K}$-particles there are virtually no data beyond 200 MeV, but the low energy scattering is again characterized by the

predominance of S-waves with positive scattering lengths at threshold; however, in this case, there is an indication of some P-waves from about 100 MeV onwards [7]). Thus, although the pions and the K-mesons are both bosons with spin zero, they behave quite differently in their interaction with nucleons.

Accordingly, in this paper, we propose to examine to what extent the dispersion theoretic methods, combined with the experimental information on the relative importance of S and P waves, are capable of discriminating between a scalar and a pseudoscalar K-meson. To be more explicit, the present work has been motivated by the desire to find out whether the Gell-Mann-Nishijima scheme for the strange particles, together with the selection rules arising from strangeness conservation governing strong interaction, is capable of introducing the necessary variation from the situation in the pion-nucleon case with regard to the relative importance of S and P waves; and, in the process, leading to a determination of the relative parities of the particles involved. This is an amplification, from a rather different standpoint, of work which has been briefly reported elsewhere [8]) †.

The success of the approach of "truncated" dispersion relations has naturally prompted us to extend the method of Chew *et al.* [3]) to the case of K-meson-nucleon scattering. The problem to be treated here is certainly much more complicated than the one in ref. [3]). Nevertheless, under conditions to be discussed below, we have obtained the following results. To find out whether the dispersion relations yield any P-wave resonant state, we first make the assumption that the P-states not only dominate but also exhaust the dispersion integrals; we, however, find that such an assumption does not lead to a self-consistent picture, at least for negative K-meson scattering. The above conclusion is true for both scalar and pseudoscalar $\overline{\mathrm{K}}$-mesons.

For the K-particle scattering the P-wave equations for the pseudoscalar case are found to be consistent with the assumption of a resonance in the $I = 1$, $j = \frac{3}{2}$ and one of the $I = 0$ states. For the scalar case no such resonances are allowed.

The consequences of the above P-wave analysis on the S-wave scattering have also been examined. It is clear that, for a scalar meson, even the moderately high energy scattering should be dominated by the S-waves; the $I = 1$ S-wave scattering length for K-particles is found to be positive, while those for the $\overline{\mathrm{K}}$-particles are negative. Furthermore, the $I = 1$ S-wave scattering amplitude for K-particles satisfies an equation of the Chew-Low type, very similar to the equation for the 33-state in pion-nucleon scattering, and there is thus a strong suggestion of a resonance in this state. In fact, the effective range corresponding to this state is positive definite. All these conclusions are in contradiction with experiment. The nature of the $I = 0$ S-wave for the scattering of

† The present work should replace the analysis reported in ref. [8]). The author is grateful to Dr. S. Barshay for having pointed out the possibility of a systematic error in the previous analysis.

K-particles again depends on the relative strength of two coupling constants.

For pseudoscalar mesons it is shown, from qualitative arguments, that the scattering of positive K-mesons on protons should be characterized by the predominance of S-wave with negative scattering length determined mainly by the Born approximation term. The present experimental situation favours such a repulsive S-wave interaction. The nature of the $I = 0$ S-wave is dependent on the relative strength of the two coupling constants referred to above. For the $\overline{K}$-particles such an analysis for the S-waves is not really permissible in the absence of any detailed information about the K-nucleon scattering in the energy region where one expects the strong P-wave effects to show up. Besides, the question of the ***absolute*** magnitudes of the coupling constants becomes significant here. Nevertheless, it is possible to conclude that there is no reason to expect that the S-wave scattering should be determined, as in the case of positive K-meson scattering on proton, by the "Born" terms which also correspond to negative scattering lengths. The S-wave behaviour of the negative K-mesons may well reflect the characteristic of that of the π-mesons, namely the cancellation of the "Born" terms by the contributions from the resonance states. This (negative) conclusion is again consistent with the present experimental knowledge.

Thus the main conclusion of the present work is that the dispersion theoretic analysis of ***non-forward*** scattering is capable of discriminating between a scalar and pseudoscalar K-meson on ***qualitative*** grounds alone. The validity of this remark rests, of course, upon the applicability of the "truncated" form of the dispersion relations. These equations, without a cut-off, are not convergent. But the surprising agreement with experiment of a similar analysis in the pion case is certainly suggestive. Experimentally, the interaction of K^+ with proton is repulsive in nature (negative scattering length) and the scattering cross-section is almost constant with energy. This experimental information, combined with the dispersion relations, certainly indicates that the K-mesons are pseudoscalar. An attractive interaction between negative K-mesons and proton also leads to the same conclusion. In this connection it is worth remarking that all attempts so far made to determine the intrinsic parity of these mesons by using forward scattering dispersion relations alone have proved to be inconclusive [9]), though they indicate a pseudoscalar K-meson. It should, however, be stated here that the question of applicability of the dispersion theoretic method in the K-nucleon scattering case will finally be resolved by a detailed study of the behaviour of the K^+ particle scattering cross-section and the angular distribution, for, only then the P-wave conclusions obtained above can be decisively tested.

In sect. 2 quite well-known kinematical details are given for ready reference. Starting with the exact formula for the scattering matrix, symmetry properties are derived by extending the approach of Goldberger *et al.* [2]) to our problem;

the general form of the dispersion relations for the eight invariant amplitudes are also given. It should, however, be stated that relativistic dispersion relations have already been written down by several authors [10]); but we give an heuristic derivation in a form most suitable for our purpose. The general character of the unphysical region is just mentioned in the next section but the contributions from the discrete states are explicitly evaluated there. In sect. 4 the dispersion relations for the invariant amplitudes are transformed into those for the physical amplitudes which characterize the scattering process. In the next section, following the conventional approach of 1/N and Legendre polynomial expansion, a partial wave analysis is made; the algebra of this section is not very complicated and the main results are summarized in eqs. (5.7), (5.14), (5.16), which are exact analogues of the pion-nucleon case. In the last section the results are briefly summarized and the limitations of the present approach are discussed.

2. Scattering Kinematics

The four-momenta of the incident and outgoing meson are denoted by k_1 and k_2 respectively; those of the final nucleon by p_1 and p_2. Then conservation of energy-momentum expressed by $p_2+k_2 = p_1+k_1$ implies that only three of the four-vectors are independent. (The four-dimensional inner product is $p \cdot k = p_\nu k_\nu = \mathbf{p} \cdot \mathbf{k} - p_0 k_0$ and we have set $\hbar = c = \mathrm{K} = 1$; the masses of the particles are denoted by their first letters.) These independent vectors are taken to be

$$P = \tfrac{1}{2}(p_1+p_2), \quad K = \tfrac{1}{2}(k_1+k_2), \quad Q = k_1-k_2 = p_2-p_1. \tag{2.1}$$

The mass-shell restrictions ${p_1}^2 = {p_2}^2 = -\mathrm{N}^2$, ${k_1}^2 = {k_2}^2 = -1$ yield

$$P \cdot Q = K \cdot Q = 0, \quad P^2+\tfrac{1}{4}Q^2 = -\mathrm{N}^2, \quad K^2+\tfrac{1}{4}Q^2 = -1,$$

so that there are only two independent scalars which we choose to be $\nu = -P \cdot K/\mathrm{N}$ and Q^2. The first of these variables is related to the meson energy ν_L in the laboratory system by the relation

$$\nu = \nu_\mathrm{L} - Q^2/4\mathrm{N}; \tag{2.2}$$

the second is, as is well-known, the square of the momentum transferred

$$Q^2 = (k_1-k_2)^2 = 2q^2(1-\cos\theta), \tag{2.3}$$

where q is the magnitude of the three-momentum of the meson and θ the scattering angle in the barycentric system.

The scattering matrix is written as

$$\langle \mathrm{f}|S|\mathrm{i}\rangle = \langle \mathrm{f}|\mathrm{i}\rangle - (2\pi)^4 i\delta^4(p_2+k_2-p_1-k_1)(\mathrm{N}^2/4p_{10}p_{20}k_{10}k_{20})^{\frac{1}{2}}\langle \mathrm{f}|M|\mathrm{i}\rangle,$$

where the spinor normalization is the standard one. Following Lehmann *et al.* [11]) the causal K-meson-nucleon scattering amplitude is given by

$$F_{\beta\alpha}(p_2, k_2; p_1, k_1) = i(2\pi)^3(p_{10}p_{20}/N^2)^{\frac{1}{2}}\int d^4x e^{-iK\cdot x}\eta(x_0)\langle p_2|[\bar{j}_\beta(\tfrac{1}{2}x), j_\alpha(-\tfrac{1}{2}x)]|p_1\rangle, \quad (2.4)$$

where we have assumed a three-particle interaction; as a consequence, the equal-time commutator is absent. $\eta(x_0)$ is the usual step-function which vanishes for $x_0 < 0$ and is unity for $x_0 > 0$; the current operators $\bar{j}_\alpha$, j_α are defined in terms of Heisenberg field variables $\bar{\Phi}_\alpha$, Φ_α by

$$(\Box^2-1)\bar{\Phi}_\alpha = -\bar{j}_\alpha, \quad (\Box^2-1)\Phi_\alpha = -j_\alpha. \quad (2.5)$$

Later on we shall find it necessary to use, in addition to F, the causal amplitude for the scattering of the meson by the anti-target, or equivalently due to invariance under charge conjugation, the scattering of the anti-projectile by the target. Let us denote this amplitude by F^c. This is formed from eq. (2.4) by replacing the states $|p\rangle$ by the states $|p\rangle^c = U|p\rangle$; here U is the unitary operator which effects the charge conjugation of the state vectors. It also induces a transformation on the field operators according to $O(x) \to O'(x) = U^{-1}O(x)U$. For the boson

$$\Phi_\alpha(x) \to \bar{\Phi}_\alpha(x) = U^{-1}\Phi_\alpha(x)U, \quad \bar{\Phi}_\alpha(x) \to \Phi_\alpha(x) = U^{-1}\bar{\Phi}_\alpha(x)U. \quad (2.6)$$

Thus the evaluation of the causal commutator between the charge-conjugated state vectors is equivalent to that of the charge-conjugated causal commutator between the particle states; so that we have

$$F^c_{\beta\alpha}(p_2, k_2; p_1, k_1) = i(2\pi)^3(p_{10}p_{20}/N^2)^{\frac{1}{2}}\int d^4x e^{-iK\cdot x}\eta(x_0)\langle p_2|[j_\beta(\tfrac{1}{2}x), \bar{j}_\alpha(-\tfrac{1}{2}x)]|p_1\rangle. \quad (2.7)$$

Introducing the covariant quantity $\mathcal{J}$ which is a matrix in the spinor space, we have

$$F = \bar{u}_\beta(p_2)\mathcal{J}_{\beta\alpha}u_\alpha(p_1). \quad (2.8)$$

It is well-known that $\mathcal{J}$ may be written, suppressing spinor indices, as

$$\mathcal{J} = \sum_{j=1}^{2} X_j(i\gamma\cdot K)^{j-1}, \quad (2.9)$$

where the $X_j(\nu, Q^2)$ are invariant functions of the scalars ν and Q^2. There is an analogous set of functions $X_j^c(\nu, Q^2)$ for $\overline{K}$-scattering.

At this stage we further break up the X's in the isobaric spin space. Since both the interacting particles are isospinors, we get

$$X_j = X_j^{(+)} + \tau\cdot\tau^N X_j^{(-)} \quad (2.10a)$$

and

$$X_j^c = X_j^{c(+)} + \tau^c \cdot \tau^N X_j^{c(-)}, \tag{2.10b}$$

where $\tau^c = \tau_2 \tau \tau_2 = -\tau^t$ is the relation between the isospins τ of the particle and τ^c of the anti-particle, τ^N is the isospin of the nucleon and the superscript t means transposition. If X_j^1 and X_j^0 are the projections of X_j into states of total isospin one and zero respectively, one obtains the relations

$$X_j^{(+)} = \tfrac{1}{4}(X_j^0 + 3X_j^1), \quad X_j^{(-)} = \tfrac{1}{4}(X_j^1 - X_j^0); \tag{2.11a}$$

in other words

$$X_j^0 = X_j^{(+)} - 3X_j^{(-)}), \quad X_j^1 = X_j^{(+)} + X_j^{(-)}. \tag{2.11b}$$

Similar relations hold for $X_j^{c(+)}$ and $X_j^{c(-)}$.

As a necessary preliminary to the application of the dispersion relations to scattering phenomena, we first obtain the general form of the dispersion relations for the eight invariant amplitudes $X_j^{(\pm)}(\nu, Q^2)$ and $X_j^{c(\pm)}(\nu, Q^2)$. The simplest and most convenient quantities are the combinations

$$X_{j\pm}^{(+)} = \tfrac{1}{2}(X_j^{(+)} \pm X_j^{c(+)}), \quad X_{j\pm}^{(-)} = \tfrac{1}{2}(X_j^{(-)} \pm X_j^{c(-)}); \tag{2.12}$$

for, as we shall find, they have simple behaviour as $\nu \to -\nu$. To show this we introduce the quantity

$$\mathcal{J}_\pm = \tfrac{1}{2}(\mathcal{J} \pm \mathcal{J}^c).$$

We first note that

$$\tilde{F}^*(p_2, k_2; p_1, k_1) = F^c(p_1, -k_2; p_2, -k_1), \tag{2.13}$$

where $\sim$ means transposition of the spin and isospin labels of the target and the asterisk stands for complex conjugation. The transformation $p_1 \leftrightarrow p_2$, $k_j \leftrightarrow -k_j (j = 1, 2)$ leaves P invariant but changes the sign of Q and K.

Using eqs. (2.8) and (2.13), we get

$$X_{j\pm}(\nu, Q^2) = \pm(-1)^{j-1} X_{j\pm}^{t*}(-\nu, Q^2), \tag{2.14}$$

which, combined with eqs. (2.10) and (2.12), yields

$$\begin{aligned} X_{j\pm}^{(+)}(\nu, Q^2) &= \pm(-1)^{j-1} X_{j\pm}^{(+)*}(-\nu, Q^2), \\ X_{j\pm}^{(-)}(\nu, Q^2) &= \mp(-1)^{j-1} X_{j\pm}^{(-)*}(-\nu, Q^2). \end{aligned} \tag{2.15}$$

In eq. (2.14) the superscript t means transposition of the target isospin label.

Let us denote the eight amplitudes by $T_\alpha(\nu, Q^2)$. The form that the dispersion relations take depends on the behaviour of $T_\alpha(\nu, Q^2)$ for very large values of ν. Following the work of ref. [3]) we make the most optimist assumption about the behaviour of these amplitudes for large values of ν, leading to the following

dispersion type relations

$$\mathrm{Re}\, T_\alpha(\nu, Q^2) = \frac{1}{\pi} \mathrm{P} \int_{-\infty}^{\infty} \mathrm{d}\nu' \frac{\mathrm{Im}\, T_\alpha(\nu', Q^2)}{\nu' - \nu}, \tag{2.16}$$

where P stands for the principal value of the integral. This may be written as an integral from zero to infinity by using the known even-odd character of the particular T_α; that is

$$\mathrm{Re}\, T_\alpha(\nu, Q^2) = \frac{1}{\pi} \mathrm{P} \int_0^{\infty} \mathrm{d}\nu'\, \mathrm{Im}\, T_\alpha(\nu', Q^2) \left(\frac{1}{\nu' - \nu} \pm \frac{1}{\nu' + \nu} \right), \tag{2.17}$$

the upper sign going with the even and the lower one with the odd character of the amplitude.

3. The Unphysical Region and the Discrete States

In the discussion of the unphysical region and the mass spectra the causal amplitude is split into a dispersive and an absorptive part. The absorptive part is given by

$$A_{\beta\alpha}(p_2, k_2; p_1, k_1) = \tfrac{1}{2}(2\pi)^3 \left(\frac{p_{10} p_{20}}{\mathrm{N}^2} \right)^{\frac{1}{2}} \int \mathrm{d}^4x \langle p_2 | [j_\beta(\tfrac{1}{2}x), j_\alpha(-\tfrac{1}{2}x)] | p_1 \rangle \tag{3.1}$$

and there is a similar representation for A^c. There is a corresponding decomposition for the invariant amplitudes $X_{j\pm}^{(\pm)}$; that is

$$X_{j\pm} = d_{j\pm} + i a_{j\pm}, \tag{3.2}$$

where d, a and the corresponding charge-conjugated quantities can easily be shown to be real functions of ν and Q^2. Using reality and symmetry properties one obtains

$$a_{j\pm}^{(+)}(\nu, Q^2) = \mp(-1)^{j-1} a_{j\pm}^{(+)}(-\nu, Q^2), \quad a_{j\pm}^{(-)}(\nu, Q^2) = \pm(-1)^{j-1} a_{j\pm}^{(-)}(-\nu, Q^2). \tag{3.3}$$

Eqs. (3.3) imply that, for discussing the spectrum, one may conveniently restrict oneself to a_j only.

The decomposition of A follows the conventional procedure [2]). It is characterized by the existence of a Q-continuum [2]) which collapses for $Q = 0$; expressed in terms of ν such a continuum is defined by the region $\nu(\mathrm{N}+1) \leqq \nu \leqq \nu_\mathrm{p}$. Here $\nu(m)$ is defined by

$$\nu(m) = \frac{m^2}{2\mathrm{N}} - \frac{\mathrm{N}^2+1}{2\mathrm{N}} - \frac{Q^2}{4\mathrm{N}}, \tag{3.4}$$

m being the "mass" of the intermediate state; so that $\nu(\mathrm{N}+1) = 1 - Q^2/4\mathrm{N}$ and $\nu_\mathrm{p} = 1 + Q^2/4\mathrm{N}$. However, besides the Q-continuum, there is an additional

continuum in the unphysical range

$$\frac{-1+Q^2}{4N} = -\nu(N+1) \leqq \nu \leqq -\nu(Y+n\Pi) = \frac{N^2+1}{2N} - \frac{(Y+n\Pi)^2}{2N} + \frac{Q^2}{4N}, \quad (3.5)$$

which survives even for $Q = 0$. It is mainly due to states of one Y-hyperon ($Y = \Lambda, \Sigma$) and $n(= 1, 2)$ pions whose relative kinetic energy is limited by $m < N+1$.

Apart from these continua there are two discrete contributions from the unphysical region. They correspond to the one Y-hyperon states. But, in order to use these contributions A_Y, we must express them in terms of the covariant quantities $a_{j\pm}^{(\pm)}(\nu, Q^2)$. For this purpose it is necessary to write A_Y explicitly in terms of the isospin indices. The evaluation of these contributions is, otherwise, quite straightforward and yields

$$(A_Y)_{\beta\alpha} = \pi[\bar{u}_\sigma(p_2)\tau^\mu_{\sigma\alpha}\tau^\mu_{\beta\rho}Lu_\rho(p_1)], \quad (3.6)$$

where L is an operator in the spinor space and is given by

$$L = -g_Y^{r^2}\frac{N+\varepsilon Y+i\gamma\cdot K}{2N}. \quad (3.7)$$

Here ε is equal to plus or minus one according as the meson is scalar or pseudoscalar and g_Y^r is the rationalized coupling constant renormalized according to the Watson-Lepore convention; note that we have used the same coupling constant symbol for both the scalar and the pseudoscalar case. These coupling constants, however, include some charge factors if one assumes charge independence [10]). The early Greek letters like α, β refer to the mesic degree of freedom while the later ones to the nucleonic degree. τ^4 is the 2×2 identity and $\tau_\mu(\mu \neq 4)$ are the usual Pauli matrices.

Our next problem is to express $\tau^\mu_{\sigma\alpha}\tau^\mu_{\beta\rho}$ in terms of the matrices in the KK—NN space. We give below a sketch of the method; we assume, for example, that for $\mu = 4$, that is for $\tau^4 = \delta$, that

$$\delta_{\sigma\alpha}\delta_{\beta\rho} = a\delta_{\beta\alpha}\delta_{\sigma\rho}+b\tau_{\beta\alpha}\cdot\tau_{\sigma\rho}. \quad (3.8)$$

The constants a and b are easily determined as follows: multiply both sides of eq. (3.8) by $\delta_{\alpha\beta}\delta_{\rho\sigma}$ and sum over the repeated indices. We obtain $\delta_{\sigma\sigma} = a\delta_{\sigma\sigma}\delta_{\alpha\alpha}+b\tau_{\sigma\sigma}\cdot\tau_{\alpha\alpha}$, so that $a = \frac{1}{2}$; here we have used the relations $\tau_{\sigma\sigma} = 0$, $\delta_{\alpha\alpha} = 2$. To determine b we again multiply both sides of eq. (3.8) by $\tau^1_{\alpha\beta}\tau^1_{\rho\sigma}$, sum as before and we obtain $\tau^1_{\rho\beta}\tau^1_{\beta\rho} = b(\tau^1)^2_{\alpha\alpha}(\tau^1)^2_{\sigma\sigma}$, so that $b = \frac{1}{2}$; in deriving this result we have used the relations $\tau\times\tau = 2i\tau$ and $(\tau^r)^2_{\alpha\alpha} = 2$ for all r.

For the rest of the terms we assume, as before, that

$$\tau_{\sigma\alpha}\cdot\tau_{\beta\rho} = a\delta_{\beta\alpha}\delta_{\sigma\rho}+b\tau_{\beta\alpha}\cdot\tau_{\sigma\rho}. \quad (3.9)$$

To determine a, first multiply both sides of eq. (3.9) by $\delta_{\alpha\beta}\delta_{\rho\sigma}$ and sum over the repeated indices; we get $(\tau\cdot\tau)_{\sigma\sigma}=a\delta_{\alpha\alpha}\delta_{\sigma\sigma}$, so that $a=\frac{3}{2}$. To find b, multiply both sides of eq. (3.9) by $\tau^1_{\alpha\beta}\tau^1_{\rho\sigma}$ and proceed, as before, to obtain

$$(\tau^1)^4_{\sigma\sigma}+i^2(\tau^2)^2_{\sigma\sigma}+i^2(\tau^3)^2_{\sigma\sigma}=b(\tau^1)^2_{\sigma\sigma}(\tau^1)^2_{\alpha\alpha}.$$

Thus we finally obtain

$$\tau_{\sigma\alpha}\cdot\tau_{\beta\rho}=\tfrac{3}{2}\tau^4_{\beta\alpha}\tau^4_{\sigma\rho}-\tfrac{1}{2}\tau_{\beta\alpha}\cdot\tau_{\sigma\rho},\qquad \tau^4_{\sigma\alpha}\tau^4_{\beta\rho}=\tfrac{1}{2}\tau^4_{\beta\alpha}\tau^4_{\sigma\rho}+\tfrac{1}{2}\tau_{\beta\alpha}\cdot\tau_{\sigma\rho}. \quad (3.10)$$

With the help of eqs. (3.10), (3.6) and (3.3) the discrete contributions to the absorptive part can be written as

$$\begin{aligned} a^{(+)}_{j\pm}&=\sum_{Y=\Lambda,\Sigma}\frac{G_r{}^2\pi}{2N}(N+\varepsilon Y)^{2-j}\{\delta(\nu+\nu_Y)\mp(-1)^{j-1}\delta(\nu-\nu_Y)\},\\ a^{(-)}_{j\pm}&=\sum_{Y=\Lambda,\Sigma}\frac{\mathscr{G}_r{}^2\pi}{2N}(N+\varepsilon Y)^{2-j}\{\delta(\nu+\nu_Y)\pm(-1)^{j-1}\delta(\nu-\nu_Y)\}, \end{aligned} \quad (3.11)$$

where

$$G_r{}^2=\tfrac{1}{4}(g_\Lambda{}^{r^2}+3g_\Sigma{}^{r^2}),\quad \mathscr{G}_r{}^2=(g_\Lambda{}^{r^2}-g_\Sigma{}^{r^2}), \quad (3.12)$$

and

$$\nu_Y=(Y^2-N^2-1-\tfrac{1}{2}Q^2)/2N. \quad (3.13)$$

4. Transformation of the Dispersion Relations

Having completed the evaluation of the discrete contributions to the unphysical region we write below the dispersion relations for the eight invariant amplitudes. They are

$$\begin{aligned} \mathrm{Re}\,X^{(+)}_{1\pm}(\nu,Q^2)&=\sum_{Y=\Lambda,\Sigma}\frac{G_r{}^2}{2N}(N+\varepsilon Y)\left(\mp\frac{1}{\nu_Y-\nu}-\frac{1}{\nu_Y+\nu}\right)\\ &\quad+\frac{1}{\pi}\int d\nu'\,\mathrm{Im}\,X^{(+)}_{1\pm}(\nu',Q^2)\left(\frac{1}{\nu'-\nu}\pm\frac{1}{\nu'+\nu}\right), \end{aligned} \quad (4.1^+)$$

$$\begin{aligned} \mathrm{Re}\,X^{(+)}_{2\pm}(\nu,Q^2)&=\sum_{Y}\frac{G_r{}^2}{2N}\left(\pm\frac{1}{\nu_Y-\nu}-\frac{1}{\nu_Y+\nu}\right)\\ &\quad+\frac{1}{\pi}\int d\nu'\,\mathrm{Im}\,X^{(+)}_{2\pm}(\nu',Q^2)\left(\frac{1}{\nu-\nu}\mp\frac{1}{\nu'+\nu}\right), \end{aligned} \quad (4.2^+)$$

$$\begin{aligned} \mathrm{Re}\,X^{(-)}_{1\pm}(\nu,Q^2)&=\sum_{Y}\frac{\mathscr{G}_r{}^2}{2N}(N+\varepsilon Y)\left(\pm\frac{1}{\nu_Y-\nu}-\frac{1}{\nu_Y+\nu}\right)\\ &\quad+\frac{1}{\pi}\int d\nu'\,\mathrm{Im}\,X^{(-)}_{1\pm}(\nu',Q^2)\left(\frac{1}{\nu'-\nu}\mp\frac{1}{\nu'+\nu}\right), \end{aligned} \quad (4.1^-)$$

$$\operatorname{Re} X^{(-)}_{2\pm}(\nu, Q^2) = \sum_{\mathrm{Y}} \frac{\mathscr{G}_{\mathrm{r}}^2}{2\mathrm{N}} \left(\mp \frac{1}{\nu_{\mathrm{Y}} - \nu} - \frac{1}{\nu_{\mathrm{Y}} + \nu} \right)$$
$$+ \frac{1}{\pi} \int \mathrm{d}\nu' \operatorname{Im} X^{(-)}_{2\pm}(\nu', Q^2) \left(\frac{1}{\nu' - \nu} \pm \frac{1}{\nu' + \nu} \right). \quad (4.2^-)$$

The final task to be completed, before we can go into a discussion of low energy scattering, is to relate the eight invariant amplitudes $T_\alpha(\nu, Q^2)$ to those which should be used in the description of the scattering in the barycentric system. Consequently, let us first attend to the necessary preliminary of writing the dispersion relations for the physical amplitudes.

The case of particular interest is where the initial and the final states are chosen with respect to the total angular momentum J and parity P in the centre-of-mass system. These two quantities are good quantum numbers in strong interaction; therefore a representation in which they are diagonal is of great importance. It is, however, well-known that the invariant amplitudes are connected to those for well-defined J and P by the following relations:

$$\frac{1}{4\pi} X_1 = (W - \mathrm{N}) F_2 - (W + \mathrm{N}) F_1, \quad \frac{1}{4\pi} X_2 = F_1 + F_2, \quad (4.3)$$

where

$$F_1 = \frac{1}{E+N} \sum_{l=0}^{\infty} [f(l_+) P'_{l+1}(x) - f(l_-) P'_{l-1}(x)],$$
$$F_2 = \frac{1}{E-N} \sum_{l=0}^{\infty} [f(l_-) - f(l_+)] P'_l(x). \quad (4.4)$$

Here, W is the total energy of the system, E the energy of the nucleon. The quantities $P'_l(x)$ are the derivatives of the Legendre polynomials; the argument x, being the cosine of the angle of scattering, is given by eq. (2.3). All the quantities referred to here are measured in the barycentric system.

The partial wave amplitudes $f(l_\pm)$ are eigenstates of J and P, belonging to orbital angular momentum l and total angular momentum $l \pm \frac{1}{2}$. Expressed in terms of phase-shifts

$$f^{(\pm)}(l_\pm) = \frac{\mathrm{e}^{i\delta(l_\pm)} \sin \delta^{(\pm)}(l_\pm)}{q}, \quad (4.5)$$

where the isospin decomposition is given by

$$f^{(+)}(l_\pm) = \tfrac{1}{4}[f^0(l_\pm) + 3f^1(l_\pm)], \quad f^{(-)}(l_\pm) = \tfrac{1}{4}[f^1(l_\pm) - f^0(l_\pm)]. \quad (4.6)$$

In the absence of inelastic processes the phase-shifts $\delta(l_\pm)$ are real; otherwise they are complex. In any case, we have

$$\operatorname{Im} f^{(\pm)}(l_\pm) = \frac{q}{4\pi} \sigma^{(\pm)}(l_\pm), \quad (4.7)$$

$\sigma^{(\pm)}(l_\pm)$ being the corresponding partial cross-sections for scattering in states of well-defined J and P.

Relations similar to the above exist for the charge-conjugated amplitudes. *For quantities evaluated at the same centre-of-mass values* one obtains

$$\frac{1}{4\pi}X^{(\gamma)}_{1\pm} = (W-\mathrm{N})F^{(\gamma)}_{2\pm} - (W+\mathrm{N})F^{(\gamma)}_{1\pm},$$
$$\frac{1}{4\pi}X^{(\gamma)}_{2\pm} = F^{(\gamma)}_{1\pm} + F^{(\gamma)}_{2\pm}, \qquad (\gamma = +,-). \tag{4.8}$$

Inverting the relations (4.8) we get

$$F^{(\gamma)}_{1\pm} = \frac{1}{2W}\frac{1}{4\pi}[-X^{(\gamma)}_{1\pm} + (W-\mathrm{N})X^{(\gamma)}_{2\pm}],$$
$$F^{(\gamma)}_{2\pm} = \frac{1}{2W}\frac{1}{4\pi}[X^{(\gamma)}_{1\pm} + (W+\mathrm{N})X^{(\gamma)}_{2\pm}]. \tag{4.9}$$

With the help of eq. (4.9) one can easily transform eqs. (4.1–2) into dispersion-type equations for the physical amplitudes. These equations may, however, be expressed in terms of W, the connexion between W and ν being given by

$$2\mathrm{N}\nu = W^2 - \mathrm{N}^2 - 1 - \tfrac{1}{2}Q^2. \tag{4.10}$$

This considerably simplifies, as we shall find, the work in the last section. The dispersion relations take the final form [12] †

$$\mathrm{Re}\, F^{(+)}_{1\pm}(W,Q^2) = \frac{G^2}{2W}\left(\mp\frac{\mathrm{N}+\varepsilon\mathrm{Y}+W-\mathrm{N}}{W^2-\mathrm{Y}^2} + \frac{\mathrm{N}+\varepsilon\mathrm{Y}-(W-\mathrm{N})}{W^2+\mathrm{Y}^2-2(\mathrm{N}^2+1+\frac{1}{2}Q^2)}\right)$$
$$+\frac{1}{\pi}\int \mathrm{d}W'(W'/W)\ \mathrm{Im}\, F^{(+)}_{1\pm}(W',Q^2)\left(\frac{1}{W'-W} \pm \frac{W'-W+2\mathrm{N}}{W^2+W'^2-2(\mathrm{N}^2+1+\frac{1}{2}Q^2)}\right)$$
$$-\frac{1}{\pi}\int \mathrm{d}W'(W'/W)\ \mathrm{Im}\, F^{(+)}_{2\pm}(W',Q^2)\left(\frac{1}{W'+W} \pm \frac{W'+W-2\mathrm{N}}{W^2+W'^2-2(\mathrm{N}^2+1+\frac{1}{2}Q^2)}\right), \tag{4.11$^+$}$$

$$\mathrm{Re}\, F^{(+)}_{2\pm}(W,Q^2) = \sum_{\mathrm{Y}}\frac{G^2}{2W}\left(\pm\frac{\mathrm{N}+\varepsilon\mathrm{Y}-(W+\mathrm{N})}{W^2-\mathrm{Y}^2} - \frac{\mathrm{N}+\varepsilon\mathrm{Y}+W+\mathrm{N}}{W^2+\mathrm{Y}^2-2(\mathrm{N}^2+1+\frac{1}{2}Q^2)}\right)$$
$$+\frac{1}{\pi}\int \mathrm{d}W'(W'/W)\ \mathrm{Im}\, F^{(+)}_{2\pm}(W',Q^2)\left(\frac{1}{W'-W} \pm \frac{W'-W-2\mathrm{N}}{W^2+W'^2-2(\mathrm{N}^2+1+\frac{1}{2}Q^2)}\right)$$
$$-\frac{1}{\pi}\int \mathrm{d}W'(W'/W)\ \mathrm{Im}\, F^{(+)}_{1\pm}(W',Q^2)\left(\frac{1}{W'+W} \pm \frac{W'+W+2\mathrm{N}}{W^2+W'^2-2(\mathrm{N}^2+1+\frac{1}{2}Q^2)}\right), \tag{4.12$^+$}$$

† In the pion case, similar equations have been inferred by using Nambu's representation [12]. The author is deeply indebted to Prof. Chew for sending the preprint along with a private communication after the present work was first reported. They have considerably helped in reformulating some of the ideas contained in this section and particularly in the following one.

and

$$\text{Re } F_{1\pm}^{(-)}(W, Q^2) = \sum_{\text{Y}} \frac{\mathscr{G}^2}{2W}\left(\pm\frac{\text{N}+\varepsilon\text{Y}+W-\text{N}}{W^2-\text{Y}^2}+\frac{\text{N}+\varepsilon\text{Y}-(W-\text{N})}{W^2+\text{Y}^2-2(\text{N}^2+1+\frac{1}{2}Q^2)}\right)$$

$$+\frac{1}{\pi}\int dW(W'/W)\ \text{Im}\ F_{1\pm}^{(-)}(W', Q^2)\left(\frac{1}{W'-W}\mp\frac{W'-W+2\text{N}}{W^2+W'^2-2(\text{N}^2+1+\frac{1}{2}Q^2)}\right)$$

$$-\frac{1}{\pi}\int dW(W'/W)\ \text{Im}\ F_{2\pm}^{(-)}(W', Q^2)\left(\frac{1}{W'+W}\mp\frac{W'+W-2\text{N}}{W^2+W'^2-2(\text{N}^2+1+\frac{1}{2}Q^2)}\right), \quad (4.11^-)$$

$$\text{Re } F_{2\pm}^{(-)}(W, Q^2) = \sum_{\text{Y}} \frac{\mathscr{G}^2}{2W}\left(\mp\frac{\text{N}+\varepsilon\text{Y}-(W+\text{N})}{W^2-\text{Y}^2}-\frac{\text{N}+\varepsilon\text{Y}+W+\text{N}}{W^2+\text{Y}^2-2(\text{N}^2+1+\frac{1}{2}Q^2)}\right)$$

$$+\frac{1}{\pi}\int dW(W'/W)\ \text{Im}\ F_{2\pm}^{(-)}(W', Q^2)\left(\frac{1}{W'-W}\mp\frac{W'-W-2\text{N}}{W^2+W'^2-2(\text{N}^2+1+\frac{1}{2}Q^2)}\right)$$

$$-\frac{1}{\pi}\int dW(W'/W)\ \text{Im}\ F_{1\pm}^{(-)}(W', Q^2)\left(\frac{1}{W'+W}\right)\mp\frac{W'+W+2\text{N}}{W^2+W'^2-2(\text{N}^2+1+\frac{1}{2}Q^2)}\Big). \quad (4.12^-)$$

Here $G^2 = \frac{1}{4}(g_\Lambda{}^2+3g_\Sigma{}^2)$, $\mathscr{G}^2 = \frac{1}{4}(g_\Lambda{}^2-g_\Sigma{}^2)$, where g_Y are the renormalized but nonrationalized coupling constants so that $g_\text{Y}{}^2 = g_\text{Y}{}^{r^2}/4\pi$. The complete separation of the amplitudes F_1 and F_2 under the integrals in eqs. (4.11—12) has been achieved by using identities like

$$X_1(W')\pm(W+\text{N})X_2(W')$$
$$= y[-X_1(W')+(W'-\text{N})X_2(W')]+x[X_1(W')+(W'+\text{N})X_2(W')], \quad (4.13a)$$

where

$$x = (W'+W)/2W', \quad y = -(W'-W)/2W' \quad \text{for the upper sign,} \quad (4.13b)$$

and

$$x = (W'-W-2\text{N})/2W',\ y = -(W'+W+\text{N})/2W' \text{ for the lower sign.} \quad (4.13c)$$

Use has also been made of eq. (3.13) in deriving eqs. (4.11—12).

5. Partial Wave Analysis

We have at last been led to a form of the dispersion relations where it would now be more convenient to project out any desired partial waves on the left hand sides of eqs. (4.11—12). In this we follow the conventional procedure: expand in powers of 1/N, or rather ω/N, retaining terms of the desired order only. Here ω is the total centre-of-mass energy in the barycentric system, excluding the rest energy of the nucleon, and is defined by $\omega = W-\text{N}$.

Inside the integrals we retain the P-waves only; for we want to find out first whether equations, as in the pion case, can be obtained so that one can conclude the existence of a resonance in any of the P-states. The task of projecting out the partial waves is achieved by repeated application of the relations

$$(1-x^2)P_l(x) = lP_{l-1}(x) - lxP_l(x) \tag{5.1}$$

and the orthonormalization conditions of the Legendre polynomials expressed in

$$\int_{-1}^{+1} \mathrm{d}x P_l(x) P_k(x) = 2\delta_{lk}/2l+1. \tag{5.2}$$

The pure $j = \frac{3}{2}$ state is first projected out. Recalling that $x = P_1$, $x^2 = \frac{1}{3}(2P_2(x)+1)$, eqs. (4.11±) suggest that to project out the $j = \frac{3}{2}$ states one has to multiply these equations by $x(1-x^2)$ and integrate between the limits $+1$ and -1. Inside the integrals one uses the covariant relation (2.3) $q'^2(1-x') = q^2(1-x)$.

For the *pseudoscalar* case the result is

$$\mathrm{Re}\, h_{3\pm}^{(+)}(\omega) = \frac{2f_1^2}{3\omega} + \frac{1}{\pi}\int \mathrm{d}\omega'\, \mathrm{Im}\, h_{3\pm}^{(+)}(\omega') \left(\frac{1}{\omega'-\omega} + \frac{1}{\mathrm{N}} \pm \frac{1}{3(\omega'+\omega)}\right)$$
$$\pm \frac{2}{3\pi}\int \mathrm{d}\omega' \mathrm{Im}\, h_{1\pm}^{(+)}(\omega') \frac{1}{\omega'+\omega}, \tag{5.3$^+$}$$

$$\mathrm{Re}\, h_{3\pm}^{(-)}(\omega) = \frac{2f_2^2}{3\omega} + \frac{1}{\pi}\int \mathrm{d}\omega'\, \mathrm{Im}\, h_{3\pm}^{(-)}(\omega') \left(\frac{1}{\omega'-\omega} + \frac{1}{\mathrm{N}} \mp \frac{1}{3(\omega'+\omega)}\right)$$
$$\mp \frac{2}{3\pi}\int \mathrm{d}\omega'\, \mathrm{Im}\, h_{1\pm}^{(-)}(\omega') \frac{1}{\omega'+\omega}. \tag{5.3$^-$}$$

Here $f_1^2 = \frac{1}{4}(f_A^2+3f_\Sigma^2)$, $f_2^2 = \frac{1}{4}(f_A^2-f_\Sigma^2)$, where f_Y is the nonrationalized but renormalized pseudovector coupling constant such that $f_\mathrm{Y}^2 = g_\mathrm{Y}^2/4\mathrm{N}^2$. The partial amplitudes $h(\omega)$ are given by

$$h_\alpha(\omega) = f_\alpha(\omega)/q^2 \equiv \mathrm{e}^{i\delta_\alpha(\omega)} \sin \delta_\alpha(\omega)/q^3. \tag{5.4}$$

To project out the $l = 1$ states from the other relations it is evident that one needs to multiply eqs. (4.12±) by $(1-x^2)$ and proceed as before. One thus projects out a linear combination of the $j = \frac{3}{2}$ and the $j = \frac{1}{2}$ states. Using eqs. (5.3±) to eliminate the $j = \frac{3}{2}$ states from these new relations, one finally obtains

$$\mathrm{Re}\, h_{1+}^{(+)}(\omega) = -\frac{4f_1^2}{3\omega} + \frac{f_1^2}{\mathrm{N}} + \frac{1}{\pi}\int \mathrm{d}\omega'\, \mathrm{Im}\, h_{1+}^{(+)}(\omega') \left(\frac{1}{\omega'-\omega} + \frac{1}{\mathrm{N}} - \frac{1}{3(\omega'+\omega)}\right)$$
$$+ \frac{4}{3\pi}\int \mathrm{d}\omega'\, \mathrm{Im}\, h_{3+}^{(+)}(\omega') \frac{1}{\omega'+\omega}, \tag{5.5$^+$}$$

$$\operatorname{Re} h_{1-}^{(+)}(\omega) = \frac{2f_1^2}{3\omega} - \frac{f_1^2}{N} + \frac{1}{\pi}\int d\omega' \operatorname{Im} h_{1-}^{(+)}(\omega') \left(\frac{1}{\omega'-\omega} + \frac{1}{N} + \frac{1}{3(\omega'+\omega)}\right) - \frac{4}{3\pi}\int d\omega' \operatorname{Im} h_{3-}^{(+)}(\omega') \frac{1}{\omega'+\omega}; \quad (5.6^+)$$

and

$$\operatorname{Re} h_{1+}^{(-)}(\omega) = \frac{2f_2^2}{3\omega} - \frac{f_2^2}{N} + \frac{1}{\pi}\int d\omega' \operatorname{Im} h_{1+}^{(-)}(\omega') \left(\frac{1}{\omega'-\omega} + \frac{1}{N} + \frac{1}{3(\omega'+\omega)}\right) - \frac{4}{3\pi}\int d\omega' \operatorname{Im} h_{3+}^{(-)}(\omega') \frac{1}{\omega'+\omega}, \quad (5.5^-)$$

$$\operatorname{Re} h_{1-}^{(-)}(\omega) = -\frac{4f_2^2}{3\omega} + \frac{f_2^2}{N} + \frac{1}{\pi}\int d\omega' \operatorname{Im} h_{1-}^{(-)}(\omega') \left(\frac{1}{\omega'-\omega} + \frac{1}{N} - \frac{1}{3(\omega'+\omega)}\right) + \frac{4}{3\pi}\int d\omega' \operatorname{Im} h_{3-}^{(-)}(\omega') \frac{1}{\omega'+\omega}. \quad (5.6^-)$$

We now use the relations (4.6) and introduce the suffix α such that $\alpha = 1, 2, 3, 4$ refer to the 01, 03, 11, 13 $(I, 2J)$ states respectively; the first suffix refers to the isobaric state and the other to the angular momentum one. Then the eight P-wave equations, under the assumed dominance of the P-states in the dispersion integrals, can be compactly written as

$$\operatorname{Re} h_\alpha(\omega) = \frac{\lambda_\alpha}{\omega} + \frac{1}{\pi}\int d\omega' \left[\operatorname{Im} h_\alpha(\omega') \left(\frac{1}{\omega'-\omega} + \frac{1}{N}\right) + A_{\alpha\beta} \operatorname{Im} h_\beta^{c}(\omega') \frac{1}{\omega'+\omega}\right], \quad (5.7a)$$

$$\operatorname{Re} h_\alpha^{c}(\omega) = \frac{\lambda_\alpha^{c}}{\omega} + \frac{\mu_\alpha^{c}}{N} + \frac{1}{\pi}\int d\omega' \left[\operatorname{Im} h_\alpha^{c}(\omega') \left(\frac{1}{\omega'-\omega} + \frac{1}{N}\right) + A_{\alpha\beta} \operatorname{Im} h_\beta(\omega') \frac{1}{\omega'+\omega}\right], \quad (5.7b)$$

where

$$\mu_\alpha^{c} = \begin{pmatrix} 2f_\Lambda^2 \\ 0 \\ 2f_\Sigma^2 \\ 0 \end{pmatrix}, \quad \lambda_\alpha^{c} = -\mu_\alpha^{c}, \quad \lambda_\alpha = \tfrac{1}{3}\begin{pmatrix} -(3f_\Sigma^2 - f_\Lambda^2) \\ 2(3f_\Sigma^2 - f_\Lambda^2) \\ -(f_\Sigma^2 + f_\Lambda^2) \\ 2(f_\Sigma^2 + f_\Lambda^2) \end{pmatrix} \quad (5.8a)$$

and

$$A_{\alpha\beta} = \tfrac{1}{6}\begin{pmatrix} 1 & -4 & -3 & 12 \\ -2 & -1 & 6 & 3 \\ -1 & 4 & -1 & 4 \\ 2 & 1 & 2 & 1 \end{pmatrix}. \quad (5.8b)$$

The 4×4 matrix $A_{\alpha\beta}$ is the present analog of the P-wave crossing matrix in the pion-nucleon case; it has the property $A^2 = 1$.

The foregoing P-wave equations have a number of interesting properties in comparison with those for the pion-nucleon case. For an analysis similar to the effective range one in the pion case, these P-wave equations are expressed, in the approximation in which one can ignore the absorption processes, in the form

$$\mathrm{Re}\, h_\alpha(\omega) = \frac{\lambda_\alpha}{\omega} + \int \mathrm{d}\omega' F_\alpha(\sigma_\alpha(\omega'), \quad \sigma_\beta^{\mathrm{c}}(\omega'), \omega', \omega) \tag{5.9a}$$

$$= \frac{\lambda_\alpha}{\omega} + r_\alpha \lambda_\alpha + \ldots, \quad |\omega| < 1. \tag{5.9b}$$

Comparing eq. (5.9b) with eq. (5.9a) one readily expresses the effective ranges r_α in terms of integrals over the various partial cross-sections for both particle and anti-particle states. The final expression (5.9b) can be approximately inverted to give the Chew-Low type equation

$$\frac{\lambda_\alpha}{\omega} \mathrm{Re}\, h_\alpha^{-1}(\omega) = 1 - r_\alpha \omega. \tag{5.10}$$

For a resonance in an α state, it is clear that r_α must be positive; for only then does the cotangent of the (real) phaseshift δ_α pass through zero. Conversely, if it is assumed that r_α is positive in one particular state, it is implied that the corresponding partial cross-section should dominate in the various $F_\alpha(\sigma)$; this, in turn, should determine the signs of all the r_α, thereby checking the consistency of the original assumption.

Before we go into the details of an effective range type of analysis, let us note the following characteristic features of eqs. (5.7). In sect. 3 we introduced ν as the crossing variable; but the P-wave equations are expressed in terms of ω. On the face of it, no crossing relation is satisfied by these equations because of the existence of the 1/N terms. A similar situation exists in the pion case and has been discussed by Chew [12]). As in the pion case, if these terms are removed, these equations also obey the following crossing relations:

$$\lambda_\alpha = -A_{\alpha\beta}\lambda_\beta^{\mathrm{c}}, \quad \lambda_\alpha r_\alpha = A_{\alpha\beta}\lambda_\beta^{\mathrm{c}} r_\beta^{\mathrm{c}}. \tag{5.11}$$

The relations (5.11) for the effective ranges imply that these effective ranges are not all independent; and, further, all the 1/N dependences of the functional form of the P-wave amplitudes may then be looked upon as confined to the values of the effective ranges. We further note that, for the $\overline{\mathrm{K}}$-particles, the scattering lengths in the $j = \frac{3}{2}$ states are both zero in the approximation used

in this paper. This relative weakness of the $j = \frac{3}{2}$ interaction is not altered by the consideration of orders of approximation higher than 1/N. This corresponds to the absence of crossed Feynman graph for $\overline{\text{K}}$-nucleon interaction.

We now return to the question of resonant state. As an application of the reasoning sketched above, we first consider the $\overline{\text{K}}$-particles. For these particles the scattering is complicated by the production processes even at the threshold. But if one ignores them for the time being, one can get some insight into the behaviour of these particles. For this purpose we first express the effective ranges in terms of the partial cross-sections,

$$\begin{aligned} r_1^{\,c} &= -\frac{1}{8\pi^2 f_\Lambda^{\,2}} \int \frac{d\omega}{\omega} \frac{\sigma_1^{\,c} + \frac{1}{6}(\sigma_1 - 4\sigma_2 - 3\sigma_3 + 12\sigma_4)}{q}, \\ r_3^{\,c} &= -\frac{1}{8\pi^2 f_\Sigma^{\,2}} \int \frac{d\omega}{\omega} \frac{\sigma_3^{\,c} + \frac{1}{6}(-\sigma_1 + 4\sigma_2 - \sigma_3 + 4\sigma_4)}{q}. \end{aligned} \tag{5.12a}$$

The most interesting point that emerges is that these relations do not produce any positive effective range. The scattering lengths in the $j = \frac{3}{2}$ states being zero, the question of resonance in those states does not arise. Moreover, in order that $r_3^{\,c}$, say, may be positive one must assume that the $\alpha = 3$ state does not dominate and that either the 01 or 11 state of the K-particles should dominate. The first condition certainly contradicts the original assumption, while the second one is at variance with eq. (5.7a) in the effective range approximation, as our subsequent discussion about K-particles will show. One can similarly show that $r_1^{\,c}$ is also not positive. It is evident that our conclusions about the $\overline{\text{K}}$-particles do not depend upon the difficult question of the "unphysical contributions" or of the "production processes" associated with these particles. Thus a significant conclusion of our analysis of the pseudoscalar $\overline{\text{K}}$-particles is that the dispersion relations give no grounds to expect any resonance in the P-states in spite of the similar space properties of π and $\overline{\text{K}}$ mesons †. This is largely in qualitative agreement with the present experimental findings [13]).

In the case of the K-particles the effective ranges are given by

$$\begin{aligned} r_1 &= -\frac{3}{4\pi^2(3f_\Sigma^{\,2} - f_\Lambda^{\,2})} \int \frac{d\omega}{\omega} \frac{\sigma_1 + \frac{1}{6}(\sigma_1^{\,c} - 4\sigma_2^{\,c} - 3\sigma_3^{\,c} + 12\sigma_4^{\,c})}{q}, \\ r_2 &= \frac{3}{8\pi^2(3f_\Sigma^{\,2} - f_\Lambda^{\,2})} \int \frac{d\omega}{\omega} \frac{\sigma_2 + \frac{1}{6}(-2\sigma_1^{\,c} - \sigma_2^{\,c} + 6\sigma_3^{\,c} + 3\sigma_4^{\,c})}{q}, \\ r_3 &= -\frac{3}{4\pi^2(f_\Sigma^{\,2} + f_\Lambda^{\,2})} \int \frac{d\omega}{\omega} \frac{\sigma_3 + \frac{1}{6}(-\sigma_1^{\,c} + 4\sigma_2^{\,c} - \sigma_3^{\,c} + 4\sigma_4^{\,c})}{q}, \\ r_4 &= \frac{3}{8\pi^2(f_\Sigma^{\,2} + f_\Lambda^{\,2})} \int \frac{d\omega}{\omega} \frac{\sigma_4 + \frac{1}{6}(2\sigma_1^{\,c} + \sigma_2^{\,c} + 2\sigma_3^{\,c} + \sigma_4^{\,c})}{q}. \end{aligned} \tag{5.12b}$$

† On the basis of this type of argument one can single out, in the pion-nucleon case, the 33 state as the only consistent resonant state. Chew leaves open the question of resonances in the other states [12]).

An examination of the fourth relation in (5.12b) immediately shows that the $\alpha = 4$ state is certainly a candidate for resonance, for all the terms on the right hand side are positive; that is, r_4 is positive definite. This is an exact analog of the 33 state in pion physics. But there is one remarkable difference in our case. The absence of a strong P-state for the $\overline{\mathrm{K}}$-particles leads to an overall positive contribution by the integrals on the right hand sides of eq. (5.12b). Since λ_1 or λ_2 is the only other positive scattering length depending upon whether $3f_\Sigma^2$ is smaller or greater than f_Λ^2, one of the zero isospin state can equally claim to be a resonance state provided the coupling is strong. It should be noted that the suggestion of a resonance in the $I = 1, j = \frac{3}{2}$ state does not depend on the relative strength of the coupling constants. Moreover, if one looks upon the $\overline{\mathrm{K}}$ contributions in eq. (5.7a) as modifications to the particle states, one readily finds that our conclusions about the K particles are not invalidated by the difficult question of the so-called "unphysical contributions". We are thus led to conclude that the positive π and K mesons, at least, whose space-time properties are similar, behave quite similarly in their interaction with nucleons. That is, the dispersion equations for the K^+ particles scattering from nucleons are consistent, as in the π^+ case, with the assumption of a resonance in the $I = 1, j = \frac{3}{2}$ state. This conclusion is not borne out by the present experimental findings. A more detailed study than has been made of the behaviour of the scattering cross-section in the energy region of interest is called for to decide this point.

One can perform an analogous calculation with scalar K mesons. One then finds that *none* of the P-states is eligible for resonance. That is, for both types of scalar K mesons the dispersion relations give no suggestion of a resonance in any of the P states.

We now investigate the effect of the preceding analysis on the S waves. Accordingly, we first proceed to project out the S-wave parts of the left-hand sides of eq. (4.11±); note that the relations (4.12±) do not contain any S-wave part on the left side. We further decide, on the basis of our P-wave analysis, to retain only the $l = 0,1$ states under the dispersion integrals for pseudoscalar K but only the $l = 0$ states for scalar K. As the scalar case is the simpler one, we first discuss the scalar S-waves.

For the scalar K-mesons we have

$$\mathrm{Re}\, f_{0\pm}^{(+)}(\omega) = g_1^2\left(\mp\frac{1}{\omega}+\frac{1}{\omega}\right)+\frac{1}{\pi}\int d\omega'\, \mathrm{Im}\, f_{0\pm}^{(+)}(\omega')\left(\frac{1}{\omega'-\omega}+\frac{1}{\mathrm{N}}\pm\frac{1}{\omega'+\omega}\right), \quad (5.13^+)$$

$$\mathrm{Re}\, f_{0\pm}^{(-)}(\omega) = g_2^2\left(\pm\frac{1}{\omega}+\frac{1}{\omega}\right)+\frac{1}{\pi}\int d\omega'\, \mathrm{Im}\, f_{0\pm}^{(-)}(\omega')\left(\frac{1}{\omega'-\omega}+\frac{1}{\mathrm{N}}\mp\frac{1}{\omega'+\omega}\right). \quad (5.13^-)$$

Eqs. (5.13) have been obtained by multiplying eqs. (4.11) by $1-x^2$ and integrating as before; here $g_1^2 = \frac{1}{4}(g_\Lambda^2+3g_\Sigma^2)$, $g_2^2 = \frac{1}{4}(g_\Lambda^2-g_\Sigma^2)$.

Expressed in terms of well-defined isospin states the scalar S-wave equations are given by

$$\begin{aligned} \mathrm{Re}\, f_{0\alpha}(\omega) &= \frac{\lambda_{0\alpha}}{\omega} + \frac{1}{\pi}\int d\omega' \left[\mathrm{Im}\, f_{0\alpha}(\omega')\left(\frac{1}{\omega'-\omega}+\frac{1}{N}\right) + A^S_{\alpha\beta}\frac{\mathrm{Im}\, f^c_{0\beta}(\omega')}{\omega'+\omega}\right], \\ \mathrm{Re}\, f^c_{0\alpha}(\omega) &= \frac{\lambda^c_{\alpha}}{\omega} + \frac{1}{\pi}\int d\omega' \left[\mathrm{Im}\, f^c_{0\alpha}(\omega')\left(\frac{1}{\omega'-\omega}+\frac{1}{N}\right) + A^S_{\alpha\beta}\frac{\mathrm{Im}\, f_{0\beta}(\omega')}{\omega'+\omega}\right], \end{aligned} \tag{5.14}$$

where

$$\lambda_{0\alpha} = \begin{pmatrix} 3g_\Sigma^2-g_\Lambda^2 \\ g_\Sigma^2+g_\Lambda^2 \end{pmatrix}, \quad \lambda^c_{0\alpha} = -\begin{pmatrix} 2g_\Lambda^2 \\ 2g_\Sigma^2 \end{pmatrix}, \tag{5.15a}$$

and the S-wave crossing matrix A^S is given by

$$A^S_{\alpha\beta} = \frac{1}{2}\begin{pmatrix} -1 & 3 \\ 1 & 1 \end{pmatrix}. \tag{5.15b}$$

Here $\alpha = 0,1$ refer to the two isospin states.

These scalar S-wave equations possess a very interesting property. If one subjects them to the Chew-Low type of analysis as done above, then one can easily show that the $I = 1$ S-wave is a certain candidate for resonance; for the corresponding S-wave effective range is positive *definite*. All the experimental evidence about the positive K-meson interaction with the proton contradicts such an attractive, let alone a resonant, S-state. More precisely, it implies a *repulsive* S-wave interaction and that the scattering cross-section, up to a rather high energy, is almost constant. If one assumes that the present approach is reasonably valid, then the appearance of a resonant, or even an attractive, $I = 1$ S-state for K^+ interaction with proton points conclusively against the scalar nature of the K-mesons. We would like to emphasize that this conclusion is absolutely independent of the question of the magnitude of the coupling constants.

For the scalar $\overline{K}$ particles, in the absence of any strong P-state interaction, one concludes that even the moderately high energy scattering should be characterized by the predominance of the S-waves. Further, given the experimental behaviour of the K particles, these S-waves, at threshold, are determined by the Born approximation terms. In other words, the present analysis predicts a repulsive $\overline{K}$-nucleon potential, provided, of course, the scalar coupling constants are not very weak. The above conclusions are all in disagreement with the presently available experimental data [6]). Thus the present experimental data, combined with the dispersion theoretic approach of ref. [3]), seem to rule out scalar K-mesons.

We conclude this section with a discussion about the *pseudoscalar* S-wave

equations. These equations are given by

$$\begin{aligned}\mathrm{Re}\, f_{0\alpha}(\omega) = \lambda_{0\alpha} &+ \frac{2N}{\pi}\int \frac{d\omega'}{q'^2}\left(1+\frac{2\omega'}{N}+\frac{\omega}{N}\right)\mathrm{Im}\, f_{3\alpha}(\omega') \\ &+ \frac{2N}{\pi}\int \frac{d\omega'}{q'^2}\left(1+\frac{2\omega'}{N}-\frac{\omega}{N}\right)A^S_{\alpha\beta}\,\mathrm{Im}\, f^c_{3\beta}(\omega') \\ &+ \frac{1}{\pi}\int d\omega'\,\mathrm{Im}\, f_{0\alpha}(\omega')\left(\frac{1}{\omega'-\omega}+\frac{1}{N}\right)+A^S_{\alpha\beta}\frac{\mathrm{Im}\, f^c_{0\beta}(\omega')}{\omega'+\omega}\Bigg), \quad (5.16a)\end{aligned}$$

$$\begin{aligned}\mathrm{Re}\, f^c_{0\alpha}(\omega) = \lambda^c_{0\alpha} &+ \frac{2N}{\pi}\int \frac{d\omega'}{q'^2}\left(1+\frac{2\omega'}{N}+\frac{\omega}{N}\right)\mathrm{Im}\, f^c_{3\alpha}(\omega') \\ &+ \frac{2N}{\pi}\int \frac{d\omega'}{q'^2}\left(1+\frac{2\omega'}{N}-\frac{\omega}{N}\right)A^S_{\alpha\beta}\,\mathrm{Im}\, f_{3\beta}(\omega') \\ &+ \frac{1}{\pi}\int d\omega'\,\mathrm{Im}\, f^c_{0\alpha}(\omega')\left(\frac{1}{\omega'-\omega}+\frac{1}{N}\right)A^S_{\alpha\beta}\frac{\mathrm{Im}\, f_{0\beta}(\omega')}{\omega'+\omega}. \quad (5.16b)\end{aligned}$$

Here,

$$\lambda_{0\alpha} = -\frac{(1+\omega/2N)}{2N}\begin{pmatrix}3g_\Sigma{}^2-g_\Lambda{}^2\\ g_\Sigma{}^2+g_\Lambda{}^2\end{pmatrix}, \quad \lambda^c_{0\alpha} = -\frac{(1-\omega/2N)}{2N}\begin{pmatrix}2g_\Lambda{}^2\\ 2g_\Sigma{}^2\end{pmatrix}. \quad (5.17)$$

The above S-wave equations make an interesting reading when compared with those for pion-nucleon scattering. For a clearer understanding it is necessary to restate the characteristic elements of the S-wave analysis in the latter case within the present framework. Here the equations analogous to eqs. (5.16) are

$$\begin{aligned}\mathrm{Re}\, f_{0\alpha}(\omega) = \lambda_{0\alpha} &+ \frac{2N}{\pi}\int \frac{d\omega'}{q'^2}\left(1+\frac{2\omega'}{N}+\frac{\omega}{N}\right)\mathrm{Im}\, f_{3\alpha}(\omega') \\ &+ \frac{2N}{\pi}\int d\omega'/q^2\left(1+\frac{2\omega'}{N}-\frac{\omega}{N}\right)A^S_{\alpha\beta}\,\mathrm{Im}\, f_{3\beta}(\omega') \\ &+ \frac{1}{\pi}\int d\omega'\,\mathrm{Im}\, f_{0\alpha}(\omega)\left(\frac{1}{\omega'-\omega}+\frac{1}{N}\right)+A^S_{\alpha\beta}\frac{\mathrm{Im}\, f_{0\beta}(\omega)}{\omega'+\omega},\end{aligned}$$

where

$$\lambda_{0\alpha} = -\frac{g^2}{N}\begin{pmatrix}1-\omega/2N\\ 1+\omega/2N\end{pmatrix}, \quad A^S_{\alpha\beta} = \frac{1}{3}\begin{pmatrix}-1 & 4\\ 2 & 1\end{pmatrix}.$$

Here $\alpha = 1,3$ refer to the two isospin states.

The most striking feature about these pion equations is that if one had compared the "Born" terms here with those in the P-wave equations, then one would have expected the S-waves to dominate the low energy scattering and they would have been repulsive in nature; for the S-wave "Born" terms are

N($\approx$ 7 at threshold!) times larger. But such is not the case experimentally. The experimental smallness of the S-waves is adequately accounted for by a cancellation arising from the 33 resonance. One first notes that the resonance integrals have the correct sign for the desired cancellation; furthermore, given the right order of magnitude, they are capable of reproducing the experimental situation. It is worth recalling that the large value of g does not lead to a correspondingly large value for the "Born" terms ($g^2/\mathrm{N} \approx 2$) and that the resonance integrals make a large contribution as they are multiplied by factors such as 2N($\approx$ 14) or 4N †.

We now turn our attention to the K particle case. It is obvious that the "Born" terms in eqs. (5.7) and (5.16) retain the qualitative characteristics of their counterparts in the pion case. Although the coupling is relatively weak here, the "Born" terms are not correspondingly small; for example, for $g_Y^2 = \frac{1}{10^5} g^2$ they are almost of the order of unity. Besides, the contributions from the K-resonance integrals, even for values comparable to those in the pion case, are much smaller; for they are multiplied by reduced factors such as 2N($\approx$ 4, here). Accordingly it is concluded that in the low energy region the K^+-proton scattering is effectively determined by the "Born" term in eq. (5.16a). In other words, the low energy scattering in the $I = 1$ state is dominated by S-wave and the corresponding phase-shift, at threshold, is negative, corresponding to a K^+-proton nuclear potential. The relative strength and nature of the two S-waves can be effectively determined only when one obtains the requisite information about resonant scattering and the relative magnitude of the two coupling constants. For example, should the $I = 1$ resonance be the stronger one, then the magnitude of the $I = 0$ S-wave scattering length would be greater than the other. It is even possible † to have an attractive S-wave in the $I = 0$ state for $g_\Lambda^2 > 3g_\Sigma^2$.

For the $\overline{\mathrm{K}}$ particles it is not possible to give any qualitative analysis along the above lines; such an analysis is so intimately linked with the question of the nature of the resonances and the absolute magnitudes of the coupling constants. However, one finds from eqs. (5.16) that, at threshold, the "Born" terms for the K particles are three times larger than those for the $\overline{\mathrm{K}}$ particle scattering. Further, the contributions from the S-wave terms for $\overline{\mathrm{K}}$-nucleon interaction in (5.16b) (these S-wave terms are experimentally quite large) are much larger than those in (5.16a). These qualitative arguments imply only that the S-wave scattering of the $\overline{\mathrm{K}}$ particles need not necessarily be determined by the "Born" terms. These "Born" terms correspond, as in the scalar case, to a repulsive

† The present argument about the cancellation of the large "Born" term is a generalization of Haber-Schaim's result for forward scattering [14]). The qualitative aspects of this simplified argument are most probably independent of the question of the existence of the unsubtracted dispersion equations. For example, on the basis of the above qualitative analysis one finds that the pion S-wave equations imply that a_1 should be *algebraically* greater than a_3, the a's being the two S-wave scattering lengths. This agrees with experiment.

$\overline{K}$-nucleon potential. The situation may turn out to be quite analogous to the pion case in this respect. This rather negative result for the $\overline{K}$ particles is yet in agreement with experiment. However, the discussion given above strongly underline the necessity of a detailed information about K-nucleon scattering and angular distribution in the energy range where the strong P-wave effects, if any, are expected to show up.

There is yet another property of the pseudoscalar S-wave equations. As in the case of the P-wave equtions, they also satisfy a crossing relation.

Again, it is possible to deal with the cases where the relative parity of (Y, N) may be odd or even. But these cases do not generally yield any information worth mentioning. Only if the scalar coupling constants are of the same order of magnitude as the pseudoscalar ones, then one easily finds that it is the scalar case which really determines the whole situation. For, by comparing the "Born" terms in eqs. (5.14) and (5.16), one finds that the scalar terms are larger than the pseudoscalar ones by a factor of N at threshold. In other cases no conclusion can be drawn.

6. Summary and Discussion

For the sake of convenience let us summarize the results obtained in this work.

(1) The "truncated" dispersion relations imply the absence of any P-wave resonance for scalar K-mesons and the consequent predominance of S-waves in scattering up to moderately high energies. The phase-shifts, at threshold, are accordingly determined by the "Born" terms. For the K particles there are strong indications that the $I = 1$ S-state should have a resonance and the phase-shift, at threshold, is positive, corresponding to an attractive potential. For the $\overline{K}$ particles, however, the phase-shifts, at threshold, are negative, indicating a repulsive potential. All these predictions are in contradiction with the present experimental data.

(2) These relations further imply that for pseudoscalar K^+ particles there is a strong suggestion of a resonance in the $j = \frac{3}{2}$ and $I = 1$ state. It is however inferred, on qualitative grounds, that the S-wave phase-shift at threshold should be determined by the "Born" term, as a cancellation analogous to that in pion physics is unlikely to occur. That is, the phase-shift should be negative corresponding to a repulsive K^+-proton nuclear potential. The nature of the other P and S waves depends on the relative strength of the coupling constants. The P-wave conclusions are *not* borne out by the present experimental findings which are, however, meagre in the high energy region. Detailed information about the angular distributions and the high energy behaviour of the scattering cross-section is thus really needed to decide the issue. The S-wave conclusions about the K^+ particles are, however, in agreement with experiment.

For the $\overline{K}$ particles the theory suggests no resonance in the P-states. Never-

theless, if the K-nucleon resonances are found to occur, then an eventual cancellation of the "Born" terms may not be ruled out. Thus there is no reason to expect the sign of the S-wave scattering lengths to be given correctly by the "Born" terms. These negative results are again in agreement with experiment.

For the scalar mesons the theory implies absence of any P-wave resonance. But it strongly suggests a resonance in the S-state for K^+-proton interaction. Besides, it leads one to expect a repulsive $\overline{K}$-nucleon potential. All these conclusions go against the present experimental data.

Thus the main and significant conclusion of the present work is that the dispersion theoretic analysis, in the "truncated" form, of non-forward scattering is capable of discriminating between a scalar and pseudoscalar K-meson on *qualitative* grounds alone. The results strongly indicate that the K-mesons are pseudoscalar. The validity of this conclusion rests, of course, upon the applicability of the "truncated" form of the dispersion relations. These equations, without a cut-off, are divergent. But what has emboldened the author to make this remark is the analogous situation in the pion-nucleon case. If one carries through a similar analysis there, then the "truncated" dispersion relations for scalar π-mesons do not yield any resonance in the P-states; this is, as is well-known, in contradiction with experiment.

The present analysis is, to be sure, based on a very rough approximation when compared with the pion-nucleon case. This is particularly so for the $\overline{K}$ particles. The question of validity of the unsubtracted dispersion equations apart, there are some serious limitations. One is the application of the 1/N ($\approx \frac{1}{2}$) expansion; this is completely unjustified inside the integrals in eqs. (4.11—12). The second is the neglect of the production processes altogether. The former may be minimized by taking into consideration the higher order approximations. But such improvements are of very little practical significance unless the second defect is effectively removed.

The author would like to express his best thanks to Prof. A. Salam and Dr. P. T. Matthews for suggesting the problem and for many instructive discussions. He is, in particular, indebted to Dr. Matthews, without whose continued interest the present work would not have been completed. He would also like to thank Dr. Riazuddin for some useful discussions. The author is indebted to Prof. S. N. Bose for a fellowship which enabled him to submit this revised version.

References

1) R. H. Capps and G. Takeda, Phys. Rev. **103** (1956) 1877, where further references are given
2) M. L. Goldberger, Y. Nambu and R. Oehme, Ann. Phys. **2** (1957) 226
3) G. F. Chew, F. E. Low, M. L. Goldberger and Y. Nambu, Phys. Rev. **106** (1957) 1337

4) G. F. Chew, F. E. Low, M. L. Goldberger and Y. Nambu, Phys. Rev. **106** (1957) 1345
5) S. Fubini, Y. Nambu and V. Wataghin, Phys. Rev. **111** (1958) 329
6) D. Keefe *et al.*, Nuovo Cim. **12** (1959) 241, where further references are given
7) A. Salam, private communication
8) P. K. Roy, Phys. Rev. Lett. **2** (1959) 364
9) R. Karplus, L. Kerth and T. Kycia, Phys. Rev. Lett. **2** (1959) 510
10) J. J. Sakurai, Bull. Am. Phys. Soc. **2** (1957) 177;
D. Amati and B. Vitale, Nuovo Cim. **7** (1958) 190;
P. T. Matthews and A. Salam, Phys. Rev. **110** (1958) 565, 569
11) H. Lehmann, K. Symanzik and W. Zimmermann, Nuovo Cim. **6** (1955) 205
12) G. F. Chew, UCRL Misc. 1957–45 (Preprint)
13) M. F. Kaplon, in Proc. of the 1958 Annual International Conference on High-Energy Physics at CERN, edited by B. Ferreti (CERN, Geneva, 1958), p. 171
14) U. Haber-Schaim, Phys. Rev. **104** (1956) 1113

2.F

Nuclear Physics **20** (1960) 440—454; © *North-Holland Publishing Co., Amsterdam*

Not to be reproduced by photoprint or microfilm without written permission from the publisher

QUASI-FREE DIFFRACTION SCATTERING

GERHARD JACOB and TH. A. J. MARIS †

Instituto de Física and Faculdade de Filosofia, Universidade do Rio Grande do Sul, Pôrto Alegre, Brasil

Received 16 May 1960

Abstract: It is shown that a certain type of non-coplanar quasi-free proton-proton scattering on heavy and medium nuclei is able to give direct and clear information on the structure of the target nucleus and the mechanism of the interaction. It is expected that the parities and orbital angular momenta of the occupied single particle states in the least bound shell, and for some cases in the stronger bound shells, can be determined. In addition the radial extension of the surface interaction zone and its distance from the centre of the nucleus would follow immediately from the expected interference patterns.

1. Introduction

This paper is concerned with the study of processes of the type

$$N_A{}^Z(\mathrm{p}, 2\mathrm{p})N_{A-1}^{Z-1},$$

in which, loosely speaking, an incoming proton of intermediate energy (50—500 MeV) knocks another proton out of a nucleus without any additional violent interaction of the incoming or the two emerging protons with the nucleus taking place.

Such a definition can have only an exact meaning in the extreme independent particle model. For a real nucleus the removal of one nucleon will strongly influence all other particles of the nucleus. Therefore, more precisely expressed, "quasi-free" †† proton-proton scattering is a knock-out process, resulting in the one or more states of the nucleus N_{A-1}^{Z-1} which in the shell model corresponds to the ground state of the original nucleus $N_A{}^Z$ with one proton hole.

Experimentally these events are recognizable by the more or less sharp peaks they cause in the spectrum of the summed energies of the two emerging protons, corresponding to the binding energies of the shell model state of the ejected proton. The peaks are superimposed on a background caused by multiple scattered protons and by excitations from rearrangements in the residual nucleus. This background will start at the energy corresponding to the

† On leave of absence from The Florida State University.

†† We prefer this name to the more usual "quasi-elastic" scattering. This last expression is increasingly used for inelastic scattering with a small energy loss (see for example ref. [22])). It is also practical to have a name for the quasi-free inelastic processes occurring at energies over the meson production threshold.

ground state of the residual nucleus and rise with excitation energy. In general it will increase with increasing atomic number of the target nucleus and with decreasing bombarding energy. The separation of quasi-free events will become impossible if a structure in the background becomes comparable to the height of the peaks caused by quasi-free collisions. For heavy and medium nuclei at all energies and at energies of 50—100 MeV also for rather light nuclei, interactions leading to quasi-free scattering events will mainly take place at the nuclear surface. For events occurring nearer to the centre of the nucleus the chance of a multiple collision becomes over-whelmingly large. Because of the sloping edges of the shell model potential and because of the influence of the binding energy on the exponential tail of a single-particle wavefunction the surface of a nucleus consists predominantly of particles from the upper shells. Consequently, "clean" knock-out processes will, in case of strong absorption, mainly involve protons from the upper shell. This fact, together with the relatively small number of occupying particles, the location of the peaks in the energy spectrum over a continuum, and the considerable width of the peaks, explains why the detection of events caused by knock-out processes from stronger bound shells has, up to now, only been achieved for high bombarding energies and light nuclei. We shall now briefly review the present status of our experimental and theoretical knowledge of the reaction in question †.

At high energies the first experiments on quasi-free proton-proton collisions were performed in Berkeley [1–3]) bombarding light nuclei with 340 MeV protons. By measuring the angular correlation between emerging proton pairs or the energy spectrum of one of the protons, momentum distributions of the protons in the nucleus with an average momentum corresponding to about 20 MeV were obtained. Angular correlation studies [4]) at 925 MeV in photographic plates and at 660 MeV by magnetic analysis gave similar results.

The energies of each of two protons coincidently emerging at definite angles were measured in Uppsala with 185 MeV bombarding energy [5, 6]). Clear peaks in the energy spectrum demonstrated the shell structure of the light target nuclei and gave values for the binding energies of the protons in the 1s and 1p shells. These results were confirmed by experiments at 150 MeV performed in Harwell [7]) and at 440 MeV performed in Chicago ††. These measurements were carried out for various values of the correlation angles, and a sharp structure of the correlation cross sections, corresponding to the momentum distributions of the protons in the different shells, was observed.

As for the theory, a qualitative interpretation of the interaction between high energy nucleons and nuclei was given by Serber [8]) who suggested that the interaction can be regarded as taking place between the incident particle and

† Our references are far from complete; in particular, the relevant Russian literature was not available.

†† We thank Dr. H. Tyrén and Mr. P. Isacsson for sending us these results prior to publication.

the individual nuclear particles. Chew [9]) treated this idea quantitatively and reduced by his impulse approximation the scattering amplitude for a quasi-free event to the product of the scattering amplitude for free nucleon-nucleon scattering with the probability amplitude for finding a nucleon in the nucleus having the momentum required by momentum conservation. Wolff [10]) applied the impulse approximation to a calculation of the momentum distribution in C^{12} from experimental results at 340 MeV. For a quantitative calculation it is important to take the influence of the nucleus on the incoming and the two outgoing protons into account; a general treatment of this problem has been given by Watson [11]).

The consequences of the nuclear shell structure for quasi-free scattering and the possibilities of these measurements for the investigation of the shell structure were discussed in ref. [12]). A calculation of the expected angular correlation distribution at 200 and 400 MeV for $A = 7$, using the impulse approximation with distorted waves, was given in ref. [13]) and extended to the case $A = 12$ and other values of the parameters by Riley *et al.* [14]).

At lower energies quasi-free collisions become difficult to recognize because the chance for additional interactions with the residual nucleus increases. This is partially caused by the shorter mean free path in the nucleus and partially by the fact that the interactions are not any longer sufficiently localized if the de Broglie wavelength λ is of the same order of magnitude as the internucleon distance.

Cohen [15]) measured for 20 MeV protons on nickel angular correlations between two outgoing protons as a function of their energy. Excited states of the residual nucleus show up by peaks and breaks in the spectrum of the summed energies. Other careful experiments have been performed by Griffiths and Eisberg [16]) with 40 MeV protons on nickel, copper and lead. Because of the small cross sections no structure was resolved in the summed energy spectrum which rises steadily towards increasing excitation energy of the residual nucleus. As remarked earlier, quasi-free knockout processes at this energy will in most cases only cost the binding energy of a proton in the least bound shell. It seems, therefore, that most of the protons detected in the Minnesota experiments, although originating from direct processes, have suffered a multiple interaction with the nucleus. Interpretations, assuming quasi-free interactions, seem somewhat doubtful.

A classical theory of quasi-free collisions at low energies, giving the connection between the distribution of the (tangential) momenta in the nuclear surface and the angular correlation of the emerging proton pairs, has been developed by McCarthy *et al.* [17]). A recent paper by Green and Brown [18]) applies the usual surface interaction formalism [19]) on the low energy quasi-free scattering, assuming that the interaction takes place over the whole nuclear surface. For reasons which will become clear later, this assumption does not appear correct to us.

For an unpolarized incoming beam of definite energy and a definite target nucleus the correlation cross section of quasi-free scattering is, not counting final polarizations, dependent on five parameters. This should be compared with the two variables occurring in the cross section of nearly all common reactions like inelastic scattering, pick-up processes etc. To cover the domain of every variable by only 10 values, one needs for each energy and nucleus 10^5 measurements in the quasi-free case against 10^2 for usual reactions. This situation opens the (perhaps) unpleasant perspective of a nearly unlimited amount of experimental and computational work to be done. On the other hand it might happen, that the unusual freedom available allows for the possibility of choosing a set of measurements which gives very direct and clear information on the nucleus and the reaction mechanism. It is the purpose of the present paper to show that this is indeed the case. It becomes, however, necessary to deviate from a common praxis in nearly all published measurements (an exception is ref.[1])) of only choosing coplanar events.

In the case of strong absorption, the region in the nucleus where interactions can lead to quasi-free scattering is severely limited (compare the analogous situation in other surface processes[19])). It will be shown that this limitation should give rise to an angular correlation distribution which varies fast and regularly with the angle between the incoming beam and the plane of the two emerging protons. The observation of these patterns would directly give the quantum numbers of the states from which the protons are knocked out and also the location and radial extension of the interaction zone.

First the simple physical idea will be exposed, then an explicit calculation of the expected distributions for different l-values, energies and target-nuclei is performed, some corrections are considered and the results of the calculations are discussed.

2. General Considerations

Consider a quasi-free (p, 2p) process in a heavy or medium nucleus. As often is the case in direct interactions[19]) with strong absorption, mean free path considerations restrict the effective collisions to a very limited part of the nuclear surface. Suppose the case of zero momentum transfer is realized, which means that the emerging protons are so selected that the sum of their momenta equals the momentum of the incoming proton. The momenta of the emerging protons are then approximately orthogonal and are coplanar with and symmetric in respect to the momentum of the incoming proton. Simple physical reasoning on the basis of the path lengths in the nucleus of the involved protons shows that the effective interaction region consists mainly of two pole caps at the ends of the nuclear symmetry axis orthogonal to the scattering plane. If a proton is knocked out of a state of even parity, the contributions of the two

pole caps will interfere constructively. If, however, the proton is knocked out of a state of odd parity, the interference is destructive and the cross section will be strongly suppressed.

If a small variable angle is introduced between the incoming beam and the plane of the emerging particles, a phase difference will occur between the contributions of the pole caps. If their thickness is small as compared to their mutual distance (which presumably is true of the heavy and medium nuclei) one should be able to observe an interference pattern with an angular period equal to the ratio of the incoming wavelength to the distance between the pole caps. In the case of 400 MeV protons on a nucleus with $A = 80$ this period is about 7° and the angular resolution necessary to observe it is at present experimentally obtainable. In this way important information, such as the distance between the interaction regions and the parity of the involved state, could be obtained.

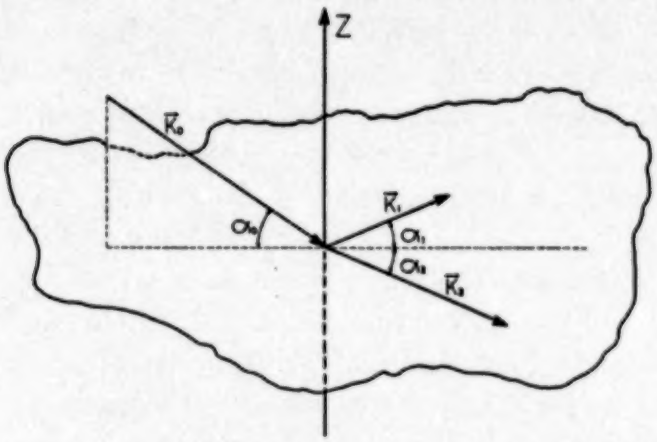

Fig. 1. Definition of angles.

By choosing a suitable angle between the incoming proton and the plane of the emerging protons, the two contributions from an inner shell state of certain parity can be made to interfere constructively and the study of these shells could eventually become possible also in the case of strong absorption. This consideration will now be generalized to the case of non-zero momentum transfer.

We investigate the idealized process in which a bombarding proton ejects a proton from a single-particle state of a shell model nucleus. The treatment can immediately be extended to the case of linear combinations of such states. The absorption, refraction and reflection of the incoming and emerging protons by the nucleus are taken into account by deforming the corresponding plane waves by a suitable complex potential.

The following notation will be used: the indices 0, 1 and 2 refer to the incoming and the two emerging protons; $\mathbf{k}$ is a momentum; α_i is the angle between $\mathbf{k}_i$ and the projection of $\mathbf{k}_0$ on the plane through $\mathbf{k}_1$ and $\mathbf{k}_2$ (see fig. 1).

First we consider the coplanar case ($\alpha_0 = 0$) and neglect the spin of the

particles. Angular momenta will be quantized along the Z-axis which is taken through the centre of the nucleus orthogonal to the scattering plane.

The matrix-element in the impulse approximation, using distorted waves, is

$$T(\mathbf{k}_1, \mathbf{k}_2, \mathbf{k}_0) g_i'^m(\mathbf{k}_0, \mathbf{k}_1, \mathbf{k}_2),$$

with

$$g_i'^m(\mathbf{k}_0, \mathbf{k}_1, \mathbf{k}_2) = \int \psi_1^{-*}(\mathbf{r}) \psi_2^{-*}(\mathbf{r}) \psi_0^{+}(\mathbf{r}) \psi_i^{m}(\mathbf{r}) \, d\mathbf{r}. \tag{1}$$

The symbols have the following meaning: $T(\mathbf{k}_1, \mathbf{k}_2, \mathbf{k}_0)$ is the relevant matrix element for free scattering; ψ_0^+, ψ_1^- and ψ_2^- are deformed waves asymptotically equal to the plane incoming and outgoing waves, ψ_i^m is the single-particle state which the knocked-out particle originally had in the nucleus. We have omitted a constant factor giving the overlap between the ground state of the original nucleus and the considered final state of the residual one. Compare the values of the integrand of (1) in the two points (x, y, z) and $(x, y, -z)$ or, in polar coordinates, in (r, θ, φ) and $(r, \pi-\theta, \varphi)$. Because of the symmetries of the situation these two values differ only by the sign factor $(-1)^{l+m}$ arising from the relation

$$Y_l^m(\pi-\theta, \varphi) = (-1)^{l+m} Y_l^m(\theta, \varphi).$$

It follows that for this coplanar case only shell model states with even $l+m$ give a non-zero integral.

For a small non-zero value of α_0, the values of the integrand at the two points (x, y, z) and $(x, y, -z)$ differ in the semi-classical approximation (up to terms of higher than first order in α_0) by the factor

$$(-1)^{l+m} e^{i2k_0 z z_0}. \tag{2}$$

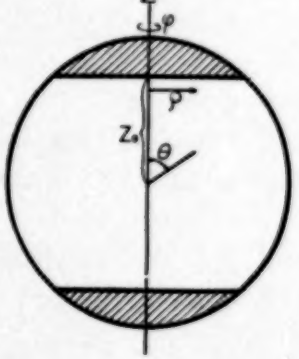

Fig. 2. Coordinate system used and location of pole caps.

As remarked in the introduction, in the case of strong absorption the most important contributions to the integral (1) arise from the two pole caps at both ends of the nuclear symmetry axis orthogonal to the plane through $\mathbf{k}_1$ and $\mathbf{k}_2$; z in (2) can then be replaced by an average value R of the distance of the pole caps from this plane (fig. 2).

We write

$$g_l'^m = G_{1l}^m + G_{2l}^m,$$

G_{1l}^m and G_{2l}^m being the separate contributions of the two pole caps. Then we have

$$G_{2l}^m \approx G_{1l}^m e^{i\{2k_0 R\alpha_0 + (l+m)\pi\}}$$

and

$$g_l'^m \approx G_{1l}^m [1 + e^{i\{2k_0 R\alpha_0 + (l+m)\pi\}}],$$

thus

$$|g_l'^m|^2 \approx 4|G_{1l}^m|^2 \cos^2 [k_0 R\alpha_0 + \tfrac{1}{2}(l+m)\pi]. \tag{3}$$

This function and the corresponding cross section show, for varying α_0,

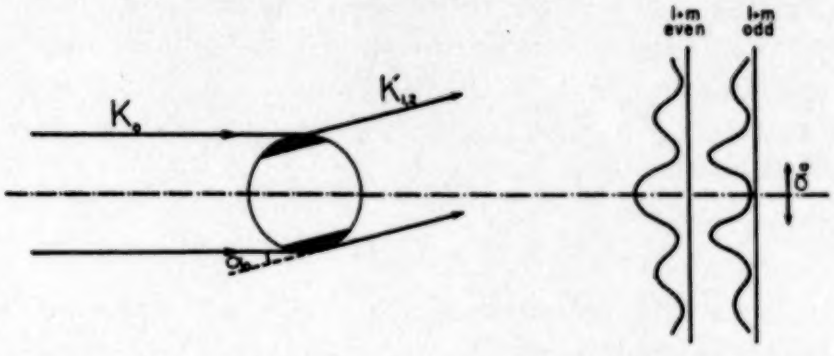

Fig. 3. Schematic presentation of interference. The plane of the figure goes through the centre of the nucleus and is parallel to $\mathbf{k}_0$ and orthogonal to the plane through $\mathbf{k}_1$ and $\mathbf{k}_2$.

an interference pattern with a period of $\pi/k_0 R$ radians. In the scattering plane and for the angles

$$\alpha_0 = \frac{n\pi}{2k_0 R} \quad (n \text{ integer}), \tag{4}$$

one will find the summed cross sections for only even $l+m$, if n is even and for only odd $l+m$ if n is odd. As the angular correlation distribution for processes involving ψ_l^m's with different m-values is different, the interference will in general be observable. Such an observation should give the location of the interaction, the parity and the l-value of the nuclear state concerned and could help separating the knocked-out protons coming from states with different quantum numbers.

The α_0-dependent interference pattern for states with a certain l-value is modulated by the function $\sum_m |G_{1l}^m|^2$. This function represents a kind of distorted distribution of the radial momenta introduced by the limitation of the interaction zone. An angular width $2\overline{\Delta\alpha_0}$ of the modulation curve corresponds to a radial extension

$$\tfrac{1}{2}d \approx \frac{1}{\overline{\Delta\alpha_0}\, k_0} \text{ (cm)}$$

of the interaction region, which in this way could be estimated from experimental data, even without resolving the interference pattern.

If we take spins and spin-orbit coupling into account, Y_l^m's with odd and even $(l+m)$-values will be mixed in one state of given j. This fact does not alter our conclusions: for the even values of n in (4) only the Y_l^m's with even $l+m$, and for the odd n-values only the ones with odd $l+m$ will contribute. In the next section we will calculate the angular correlation cross sections for the ψ_l^m's with l up to 4.

3. Determination of the Cross Sections

The integral (1) of the previous section will now be estimated by taking a perhaps somewhat oversimplified volume of integration, consisting of the two afore-mentioned pole caps limited by planes parallel to $\mathbf{k}_1$ and $\mathbf{k}_2$. Although the main conclusions will have a more general validity, we shall neglect in what follows the absorption, refraction and reflection in the pole caps, i.e., the incoming and outgoing wave functions will be taken as plane waves at the pole caps and zero elsewhere in the nucleus.

The wave function at the edge of the nucleus for the bound proton will be of the form

$$\psi_l^m(\mathbf{r}) = c h_l(i\kappa r)\, e^{im\varphi} \overline{P_l^m}(\cos\theta), \tag{5}$$

where $h_l(i\kappa r)$ is the spherical Hankel function of the first kind with $\kappa = \sqrt{2m_p B}/\hbar$; B denotes the (positive) binding energy of the proton; $\overline{P_l^m}(\cos\theta)$ is the associated Legendre function, normalized as in ref. [20]).

Thus, we have for G_{1l}^m in (3)

$$G_{1l}^m = c \int e^{-i\mathbf{k}\cdot\mathbf{r}} e^{im\varphi} h_l(i\kappa r) \overline{P_l^m}(\cos\theta) d\mathbf{r}, \tag{6}$$

$$\mathbf{k} = \mathbf{k}_1 + \mathbf{k}_2 - \mathbf{k}_0$$

being the momentum transfer †. Because of the symmetry of the problem it is natural to use cylindrical coordinates (ρ, z, φ), with the z-axis orthogonal to the plane through $\mathbf{k}_1$ and $\mathbf{k}_2$. Developing the plane waves in terms of cylindrical Bessel functions, and performing the integral over φ one gets

$$G_{1l}^m = 2\pi c(-i)^m \int_{z_0}^{\infty} dz \int_0^{\infty} J_m(k\rho)\, \overline{P_l^m}\left(\frac{z}{\sqrt{z^2+\rho^2}}\right) h_l(i\kappa\sqrt{z^2+\rho^2})\, \rho d\rho, \tag{7}$$

where $z = z_0$ is the plane which limits the pole cap. The integral over ρ can be approximately evaluated in a closed form, as shown in the Appendix and then $|g_l'^m|^2$ follows from (3). In the approximation of this section $|G_{1l}^m|^2$ is only a function of the absolute value of the momentum transfer $\mathbf{k}$.

† Green and Brown [18]) take the integral in (6) over the whole nuclear surface. This procedure is mathematically simple, because of the orthogonality of the Y_l^m's, but most of the physical contents of the present problem gets lost by it.

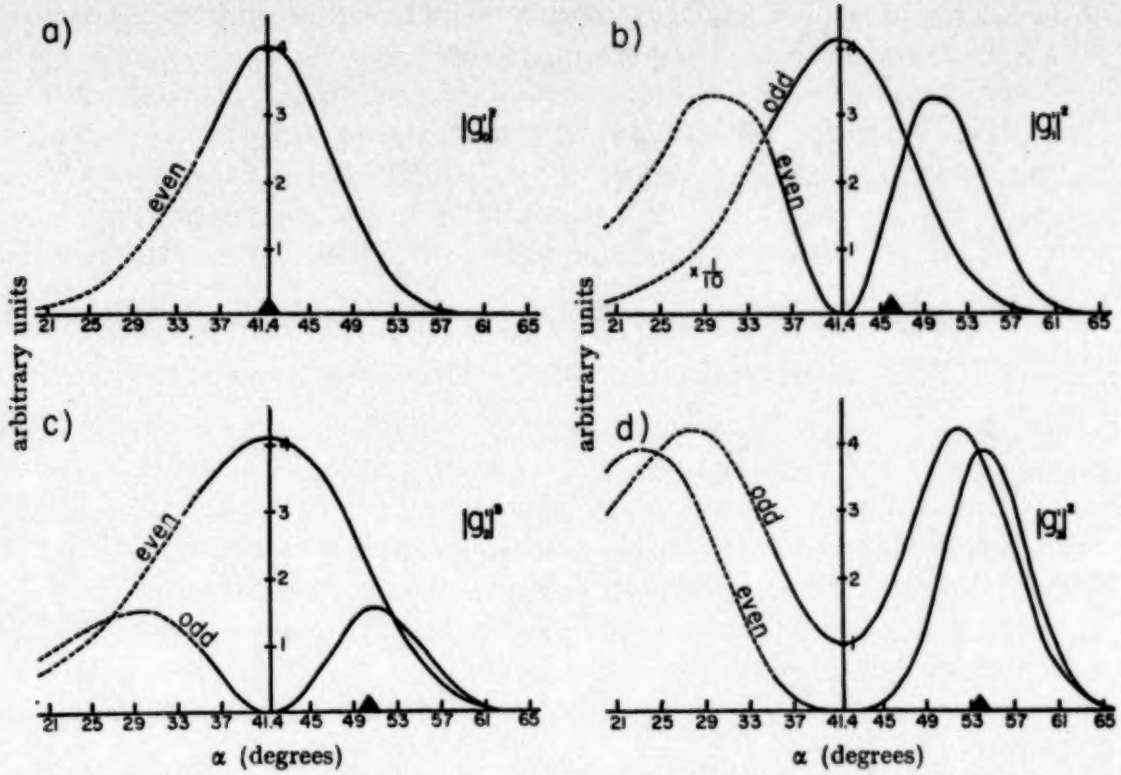

Fig. 4. Correlation curves for varying $\alpha_1 = \alpha_2 = \alpha$, $E_1 = E_2$ and constant α_0 in the case $A = 40$, $E_0 = 150$ MeV for various l-values. $\alpha_0 = \frac{1}{2}n\pi/k_0 R$, n even and odd. The dotted parts of the curves are uncertain, because the rim of the nucleus may become penetrable. The triangles denote the value $\frac{1}{2}l\,\pi/k_0 R\sqrt{2}$.

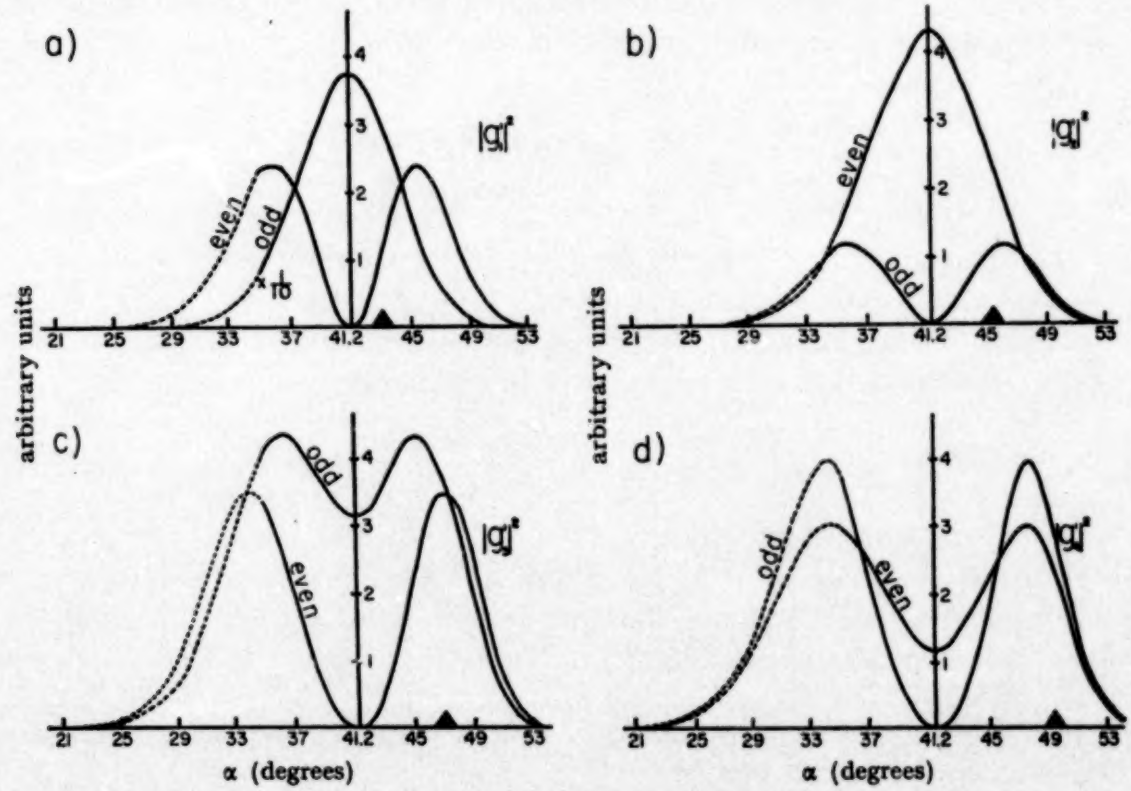

Fig. 5. Same as fig. 4 for $A = 80$, $E_0 = 400$ MeV.

The contributions from different m-values add incoherently; thus the differential cross section is essentially proportional to

$$\sum_{m=-l}^{+l} |g_l'^m|^2 = |g_0'^0|^2 + 2\sum_{m=1}^{l} |g_l'^m|^2 = |g'_l|^2.$$

In figs. 4 and 5 $|g'_l|^2$ is plotted for the symmetric case ($\alpha_1 = \alpha_2 = \alpha$; $E_1 = E_2$) as a function of α for a constant $\alpha_0 = \frac{1}{2}\, n\pi/k_0 R$, ($n = 0$ and 1), in the two cases $A = 40$, $E_0 = 150$ MeV and $A = 80$, $E_0 = 400$ MeV, E_0 being the bombarding energy. We used $1.5A^{\frac{1}{3}} \times 10^{-13}$ cm for the mean distance R and $B = 11$ MeV as a mean binding energy for a proton in the upper shell. In particular the case $A = 40$ represents too light a nucleus for our approximation to be good.

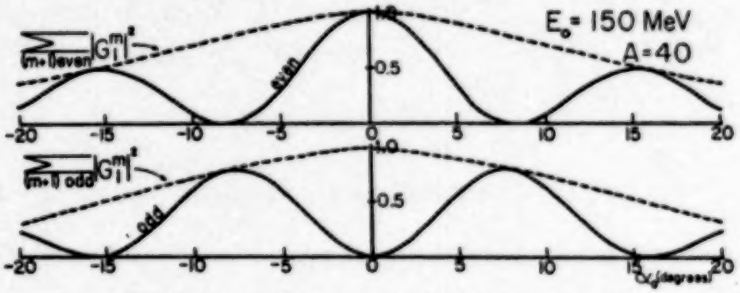

Fig. 6. The interference pattern for varying α_0 and constant α_1 and α_2, $A = 40$, $E_0 = 150$ MeV, in the cases of even and odd $l+m$ or, for zero momentum transfer, even and odd l ($m = 0$).

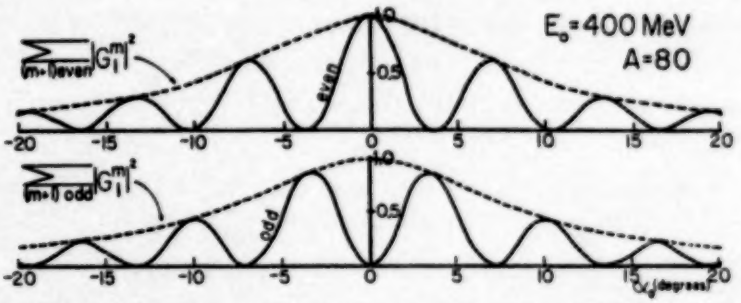

Fig. 7. Same as fig. 6 for $A = 80$, $E_0 = 400$ MeV.

It is given as an example because the required experimental angular and energy resolution is more easily obtained for the lighter nuclei, for which the relative cross section is larger, than for the heavier ones. The curves, with some modifications, mainly in the angular scale, are also applicable to somewhat different values of the parameters.

As we saw in (3), for varying α_0 and constant α_1, α_2 an interference pattern of the $\cos^2$-type, modulated because of the finite extension of the interaction zone, will be obtained. To get an impression of the type of curve that has to be expected, we have taken the simple model in which the tail of the nuclear wave function, taken to be a pure exponential, is cut off abruptly at the plane $z = z_0$ as a result of the strong absorption. The resulting patterns are shown in figs. 6 and 7 for the cases $A = 40$ and $A = 80$ with the same parameters as before, both for $(l+m)$ even and odd.

For $\alpha_0 = 0$, $\alpha_1 = \alpha_2$ and $E_1 = E_2$ the relation between the cross section and $|g'_l|^2$ is given by [13])

$$\frac{\mathrm{d}\sigma}{\mathrm{d}\Omega_1 \mathrm{d}\Omega_2 \mathrm{d}E_1} = \frac{4k_1^2}{\hbar v_0} \frac{k_1^2 \sin^2\alpha + \dfrac{m^2c^2}{\hbar^2}}{2k_1^2 \sin^2\alpha + \dfrac{m^2c^2}{\hbar^2}} \frac{\mathrm{d}\sigma_{free}}{\mathrm{d}\Omega'} \frac{N}{2l+1} |g'_l|^2, \tag{8}$$

with the same notation as in ref. [13]); N denotes the number of protons in the considered single particle state. Eq. (8) will be still valid for small values of α_0. For the asymmetric case, another relativistic factor [14]) and the free cross section for polarized protons should be taken. In general, the behaviour of the cross section is governed by $|g'_l|^2$ because the multiplying factors are smoothly varying functions of the angles.

4. Discussion of Results

It is convenient to distinguish two types of angular correlation distributions:

a) those with constant α_1 and α_2 and varying α_0 (figs. 6 and 7);
b) those with varying α_1 and α_2 and constant α_0 (figs. 4 and 5).

We saw already that the interference pattern expected for a) determines by its *phase* the *parity* of the shell model state from which the proton is knocked out, by its *period* the *location* of the interaction zones and by the width of its *modulation* the *extension* in the z-direction of the interaction zones.

From (6) it follows for small α_0 that the curves b) give a momentum distribution in the nuclear surface [16, 17]), namely the one of the momenta in the pole caps parallel to the cut-off plane. This statement is not in contradiction with the uncertainty principle, because the mentioned momenta commute with the coordinate which defines the position of the cut-off plane. Although in reality the distortion of the incoming and outgoing waves in the pole caps will deform the correlation distributions, we neglect this effect in the following discussion of the curves in figs. 4 and 5, because it was also neglected in the calculation of the curves.

The momentum distribution parallel to the cut-off plane is mainly made up of the tangential momenta of protons in the nuclear surface, although there are also components of the radial momentum involved because of the considerable diameter of the pole caps. It is possible to understand the general features of the curves of figs. 4 and 5 from the tangential momentum distributions (at the surface) of the various wavefunctions.

Firstly it is clear that the tangential momenta increase with increasing l. This is reflected by the fact that for increasing l the curves extend farther away from the angle of zero momentum transfer. Somewhat more quantitatively, in a

semi-classical model, one may calculate that the average absolute value of the tangential momentum of a particle with an arbitrarily directed angular momentum of magnitude $l\hbar$ on a distance R from the origin equals $\frac{1}{2}\pi l\hbar/R$. The average value of one of the two orthogonal tangential momentum components is therefore about equal to $\frac{1}{2}\pi l\hbar/\sqrt{2}R$. In the symmetric case, the momentum transfer for a deviation $\Delta\alpha$ of the momenta of the emerging protons from the angle of zero momentum transfer corresponds to a momentum transfer of about $k_0\hbar\Delta\alpha$. Our semi-classical expectation for the mean deviation of the correlation angle from the angle of zero momentum transfer is therefore

$$\overline{\Delta\alpha} \approx \frac{l}{2\sqrt{2}} \frac{\pi}{k_0 R}.$$

These values are indicated in the figures and are in qualitative agreement with the trend of the curves.

Finally we shall give some rather disconnected remarks on the curves of figs. 4 and 5. The wave-function for $l = 0$ has only zero tangential momentum components. Therefore the correlation curve in fig. 4a gives a measure of the influence of the radial components on the momentum distribution under consideration.

The only zero momentum components occur for $m = 0$, because the factor $e^{im\varphi}$ in the wave function gives otherwise always a non-zero momentum. Consequently, the curves with odd $(l+m)$, even l and even $(l+m)$, odd l vanish for zero momentum transfer.

The vertical scale in the figures is arbitrary, but the ratio between the two curves of even and odd $(l+m)$ for the same l-value is meaningful.

The contributions from states with low m-values tend to be larger than the curves with high m-values, because the centrifugal force tries to push the particles with high m-values away from the pole caps. This effect is more serious for low l-values, as the wavefunction for high l-values is able to restore itself faster from its zero value in the Z-axis, because it contains higher tangential momentum components.

If the distortion of the curves by the absorption in the pole caps would not be unexpectedly strong, it would from figs. 4 and 5 seem to be rather easy to distinguish the different l-values, because of their typical angular dependences.

5. Corrections

The following corrections will modify the quantitative results of section 3:

a) The limitation of the interaction zone to two pole caps is an idealization and the transparency of other regions is not negligible. This effect is strongly dependent on factors like the bombarding energy, size of the nucleus, diffuseness of the surface and geometry of the experiment. With increasing transparency

the interference pattern will become more and more faded out and the situation will go over into the more general one of a partially penetrable nucleus as treated in refs. [13, 14]).

b) The absorption in the effective interaction regions (the two pole caps), has been neglected. From our general symmetry considerations it is clear that this effect will not mix the distributions for different $(-1)^{l+m}$ values. However, the curves calculated in section 3 will be influenced. The different m-components from which the curves are made up will get a different weight, because they are differently absorbed, and every m-component will be modified. Although detailed calculations with distorted waves are necessary for a precise prediction, we expect that the main characteristics of the calculated curves will be unaltered. In particular, it seems likely that, for zero momentum transfer in the plane through $\mathbf{k}_1$ and $\mathbf{k}_2$ and for $\alpha_0 = \frac{1}{2}n\pi/k_0R$ the cross sections for even $l+n$ will be appreciably larger than for odd $l+n$, n being an integer.

c) For α_0 different from zero, the physical situation is not anymore mirror-symmetric with respect to the plane through $\mathbf{k}_1$ and $\mathbf{k}_2$. This means that the contributions to the matrix elements from the pole caps are no longer equal in magnitude. This effect should not be important for small α_0 and will in that case result in some smearing out of the interference patterns by a slight mixing of the distributions of different $(l+m)$-parities. Rather naïve geometrical considerations give for a medium nucleus a value of about 20° for the angle α_0 at which the interference pattern would begin to be appreciably disturbed.

6. Concluding Remarks

The extra degree of freedom of "going-out of the scattering plane" gives in quasi-free scattering an important possibility for the investigation of nuclear structure and the mechanism of direct interactions.

The essential assumptions on which the obtained results are based are those of a rather sharply located region where the direct interaction takes place and of the approximate validity of the shell model. For a liquid drop model, for example, no simple result of the interference between the contributions of the pole caps should be expected. The observation of the interference pattern would be an interesting confirmation of the mentioned assumptions.

The angular period and the modulation of the expected interference pattern for varying α_0 and constant α_1 and α_2 would directly give the location and radial extension of the relevant interaction zone; from the phase at zero momentum transfer the parity of the states involved can be determined. The orbital angular momentum might be deduced from the angular correlation curves taken for constant α_0. By making a systematic study of nuclei with successive atomic numbers the filling up of the upper proton shell could be studied.

Finally, energy measurements of a small cross section from an inner or the upper shell could be facilitated by choosing values of α_i appropriate to the l—value involved (see figs. 4—7).

One of the authors (T. M.) wants to thank the Rector of the University, Prof. Elyseu Paglioli, the Director of the Instituto de Física, Prof. Saviniano de Castro Marques, and the members of the Institute for the great hospitality he received. It is a pleasure for us to thank Prof. Darcy Dillenburg for his stimulating interest. This work was partially supported by Comissão Supervisionadora dos Institutos and Conselho Nacional de Pesquisas, Brasil and by the National Science Foundation, USA.

Added note: After the completion of this paper we received a publication of Kromminga and McCarthy [23]), in which they remark that the limitation of the interaction zone emphasizes the importance of the tangential momentum distribution for coplanar scattering.

Appendix

In this appendix we approximate the integral (7):

$$G_{1l}^{m} = 2\pi c(-i)^m \int_{z_0}^{\infty} \mathrm{d}z \int_0^{\infty} J_m(k\rho) \overline{P_l^m}\left(\frac{z}{\sqrt{z^2+\rho^2}}\right) h_l(i\kappa\sqrt{z^2+\rho^2})\rho \mathrm{d}\rho. \quad \text{(A1)}$$

Setting $\rho/z = y$ we take

$$y\overline{P_l^m}\left(\frac{z}{\sqrt{z^2+\rho^2}}\right) = [a_l^{m,m+1} y^{m+1} + a_l^{m,m+3} y^{m+3}], \quad \text{(A2)}$$

with, for the region of interest, graphically determined values of $a_l^{m,m+1}$ and $a_l^{m,m+3}$, and replace

$$h_l(i\kappa\sqrt{z^2+\rho^2}) \quad \text{by} \quad \mathrm{e}^{-\frac{1}{2}\kappa z y^2} h_l(i\kappa z). \quad \text{(A3)}$$

Substituting (A2) and (A3) in (A1) one gets

$$G_{1l}^{m} = 2\pi c(-i)^m \int_{z_0}^{\infty} h_l(i\kappa z) z^2 \mathrm{d}z \times \int_0^{\infty} J_m(zky)\mathrm{e}^{-\frac{1}{2}\kappa z y^2}[a_l^{m,m+1} y^{m+1} + a_l^{m,m+3} y^{m+3}]\mathrm{d}y. \quad \text{(A4)}$$

The variation over z in (A4) is mainly due to the Hankel function $h_l(i\kappa z)$ so that, to a good approximation, we may in the integral over y set z equal to an average value $R \approx z_0 + 1/\kappa$. Thus setting

$$2\pi c(-i)^m \int_0^{\infty} h_l(i\kappa z) z^2 \mathrm{d}z = (-i)^m c_l(\kappa), \quad \kappa R = 2\beta^2, \; kR = \alpha, \quad \text{(A5)}$$

we find

$$G_{1l}^{m} = (-i)^m c_l(\kappa) \int_0^\infty J_m(\alpha y) \mathrm{e}^{-\beta^2 y^2} [a_l^{m,m+1} y^{m+1} + a_l^{m,m+3} y^{m+3}] \mathrm{d}y. \qquad \text{(A6)}$$

The integral (A6) can be evaluated in closed form [21]), leading to the result

$$G_{1l}^{m} = (-i)^m c_l(\kappa) \left\{ a_l^{m,m+1} \frac{\alpha^m \mathrm{e}^{-\frac{\alpha^2}{4\beta^2}}}{(2\beta^2)^{m+1}} + a_l^{m,m+3} \frac{\alpha^m \mathrm{e}^{-\frac{\alpha^2}{4\beta^2}}}{(2\beta^2)^{m+1}\beta^2} \left[m+1-\frac{\alpha^2}{4\beta^2} \right] \right\}, \qquad \text{(A7)}$$

and thus

$$|G_{1l}^{m}|^2 = |c_l(\kappa)|^2 \{ d(\delta, m, \beta)[b(l, m, \beta)]^2 - 2a_l^{m,m+3} d(\delta, m+1, \beta) b(l, m, \beta) + d(\delta, m+2, \beta)[a_l^{m,m+3}]^2 \}, \qquad \text{(A8)}$$

where

$$\delta^2 = \frac{\alpha^2}{2\beta^2} = \frac{R}{\kappa} k^2, \quad d(\delta, n, \beta) = \frac{\delta^{2n} \mathrm{e}^{-\delta^2}}{(2\beta^2)^{n+2}}, \quad b(l, m, \beta) = a_l^{m,m+1} + \frac{2(m+1) a_l^{m,m+3}}{2\beta^2}.$$

The result (A8) is plotted in figs. 4 and 5.

References

1) O. Chamberlain and E. Segré, Phys. Rev. **87** (1952) 81
2) J. B. Cladis, W. N. Hess and B. J. Moyer, Phys. Rev. **87** (1952) 425
3) J. M. Wilcox and B. J. Moyer, Phys. Rev. **99** (1955) 875
4) J. C. McEwen, W. M. Gibson and P. J. Duke, Phil. Mag. **2** (1957) 231;
   L. S. Azhgirey, I. K. Vzorov, V. P. Zrelov, M. G. Mescheryakov, B. S. Neganov, R. M. Ryndin and A. F. Shabudin, Nuclear Physics **13** (1959) 258
5) H. Tyrén, Th. A. J. Maris and P. Hillman, Nuovo Cimento **6** (1957) 1507
6) H. Tyrén, P. Hillman and Th. A. J. Maris, Nuclear Physics **7** (1958) 10
7) T. J. Gooding and H. G. Pugh, preprint
8) R. Serber, Phys. Rev. **72** (1947) 1114
9) G. F. Chew, Phys. Rev. **80** (1950) 196
10) P. A. Wolff, Phys. Rev. **87** (1952) 434
11) K. M. Watson, Phys. Rev. **89** (1953) 575
12) Th. A. J. Maris, P. Hillman and H. Tyrén, Nuclear Physics **7** (1958) 1
13) Th. A. J. Maris, Nuclear Physics **9** (1958/59) 577
14) K. F. Riley, Nuclear Physics **13** (1959) 407;
   K. F. Riley, H. G. Pugh and T. J. Gooding, preprint
15) B. L. Cohen, Phys. Rev. **108** (1957) 768
16) R. J. Griffiths and R. M. Eisberg, Nuclear Physics **12** (1959) 225
17) I. E. McCarthy, E. V. Jezak and A. J. Kromminga, Nuclear Physics **12** (1959) 274
18) A. M. Green and G. E. Brown, preprint
19) S. T. Butler, Phys. Rev. **106** (1957) 272;
   S. T. Butler, N. Austern and C. Pearson, Phys. Rev. **112** (1958) 1227;
   L. R. B. Elton and L. C. Gomes, Phys. Rev. **105** (1957) 1027
20) E. Jahnke and F. Emde, Tables of Functions (Dover Publications, 1945) p. 116
21) I. N. Sneddon, Special Functions of Mathematical Physics and Chemistry (Oliver and Boyd, 1956) p. 113
22) T. K. Fowler and K. M. Watson, Nuclear Physics **13** (1959) 549
23) A. J. Kromminga and McCarthy, Phys. Rev. Letters **4** (1960) 288

1.D.1

Nuclear Physics **20** (1958) 455—463; © *North-Holland Publishing Co., Amsterdam*

Not to be reproduced by photoprint or microfilm without written permission from the publisher

NUCLEAR SPECTROSCOPY WITH NON-LOCAL POTENTIALS

A. N. MITRA

Physics Department, Muslim University, Aligarh U.P., India

and

S. P. PANDYA

Physical Research Laboratory, Ahmedabad, India

Received 1 June 1960

Abstract: A non-local separable potential derived earlier by one of us (A. N. M.) has been used to calculate the $T = 0$ energy levels of the shell model configuration $(d_{\frac{5}{2}})^2$. The results are satisfactory, and the advantages of such a realistic and well-behaved potential over the other potentials, local but invoking singularities, hard cores etc., for calculating nuclear energy levels are pointed out.

1. Introduction

One of the main formal successes of Brueckner theory is perhaps the realisation that the nuclear shell model can be understood qualitatively within its broad premises which seek to explain the nuclear structure with the help of two-body potentials adjusted to fit scattering data. Such two-body potentials (we shall call them "realistic" in what follows) usually have short ranges, hard cores etc., and are quite different from the smooth, long range effective interactions used in the conventional shell model calculations. The Brueckner theory attempts to bridge the considerable gap between such widely divergent types of potentials with the introduction of the reaction matrix which is free from hard cores, singularities etc. However, it is not at all clear so far to what extent the reaction matrix, even qualitatively, approximates the known features of the phenomenological shell model potentials. Banerjee and Dutta-Roy [1]) have carried out a shell model calculation, using the Gammel-Thaler potential, essentially in the spirit of the Brueckner theory. This calculation very appropriately shows up the practical difficulties of the formalism which is rather involved in spite of a number of simplifying assumptions, and as for the detailed agreement with experimental results, we are not quite certain of the advantages such a calculation has over the more prosaic shell model calculations. We, however, feel that there is still a strong case for testing the validity of the realistic potentials in shell model type calculations. The purpose of the present note is to report one such calculation.

One of the authors (A. N. M.) was associated with a recent derivation [2] † of a non-local, separable, Yamaguchi-type potential, operative in the $T = 0$, $l = 0$, 2 states, which fitted the deuteron parameters (including the magnetic moment anomaly) and the low energy two-body scattering data. This potential was also found to account semi-quantitatively for the spin-orbit splittings in nuclei such as O^{17} or Ca^{41}, the $\mathbf{L} \cdot \mathbf{S}$ term in it playing a decisive role. The only additional term in this potential which was expected to be important at moderate energies was the one corresponding to the singlet P-state, and this has since been worked out by Mitra and Naqvi [3], to fit the phase-shift analysis of Phillips [4] up to about 100 MeV. Together with this term, the potential derived in A may be thought of as providing a fairly complete description of the interaction at low and moderate energies in the $T = 0$ state of two nucleons, and may, in principle, be used to test some phenomena depending on this interaction.

It may be of some interest to apply this $T = 0$ potential to a calculation of the energy levels of some simple nuclei to see how far such a "realistic" potential (in contrast to the empirical two-body potentials used in the shell model) may successfully predict the observed level schemes. As we do not know of any other shell-model calculations with such non-local potentials carried out in momentum space, we hope that some of the calculational techniques developed here may also be of some inherent value.

The choice of a suitable nucleus for such calculations has been motivated primarily by the necessity to avoid as far as possible assumptions which would increase the ambiguity in the value of the final results and agreement with experiments. It is known that near the mass number $A = 40$, the jj coupling scheme is a fairly good approximation for predicting the energy levels, and the configuration mixing effects are reasonably small [5]. Hence we choose to calculate the levels of the $(d_{\frac{3}{2}})^2$ configuration, which one may expect to see in Cl^{34} or K^{38}. The only $T = 0$ states of this configuration are $J = 1, 3$.

For obvious reasons we have made a shell model calculation rather than a calculation in the Brueckner spirit, i.e. we have not solved the self-consistency problem, nor do we evaluate the reaction matrix. Perhaps it is not unreasonable to approximate the reaction matrix by the potential matrix for such well-behaved potentials, as was discussed by Bethe [6]. In absence of the self-consistent wave functions (which may not be very serious for shell model calculations as pointed out by Banerjee and Dutta-Roy [1]), we choose harmonic oscillator wave functions for the nucleons [7]. The knowledge of the self-consistent single particle energies is in any case not required for our calculation.

In section 2 we outline the derivation of the formula for the V-matrix elements, relegating some of the details to a couple of appendices. Section 3 is then devoted to a discussion of the numerical results and some qualitative conclusions that can be drawn within the limitations of our calculation.

† This paper will be referred to as A.

2. Calculation of the Energy Levels

The $T = 0$ part of the two-body potential may be written in the centre of mass (c.m.) system as

$$(\mathbf{p}|V|\mathbf{p}') = (\mathbf{p}|V_{\text{even}}|\mathbf{p}')+(\mathbf{p}|V_{\text{odd}}|\mathbf{p}'), \tag{2.1}$$

where V_{even} is the even (triplet) part of the potential defined by eqs. (2.2), (3.2), (3.24), and (6.31) of A, and V_{odd} is the odd (singlet) part given by [3])

$$(\mathbf{p}|V_{\text{odd}}|\mathbf{p}') = -\frac{4\pi\lambda_1}{M} v_1(p)v_1(p') \sum_m Y_1^{m*}(\hat{p})Y_1^m(\hat{p}'), \tag{2.2}$$

$$v_1(p) = p(b^2+p^2)^{-1}, \tag{2.3}$$

$$\lambda_1 = -1.7\alpha, \quad b = 5\alpha. \tag{2.4}$$

It may be noted that while V_{even} was found in A to be an overall attractive potential, V_{odd} is repulsive, λ_1 being negative.

We have to evaluate the matrix element of (2.1) for the states $|(j)^2 JM\rangle$. The first step is to transform these states to the LS coupling representation by the relation

$$|(lsj)^2 JM\rangle = \sum_{LS} A \begin{pmatrix} l & s & j \\ l & s & j \\ L & S & J \end{pmatrix} |(l)^2 L(s)^2 SJM\rangle, \tag{2.5}$$

where $A(LSJ)$ are the well known $jj-LS$ transformation coefficients [8]) and

$$|LSJM\rangle = \sum_{m_L m_S} \langle Lm_L Sm_S|JM\rangle \Phi_{Lm_L}(\mathbf{p}_1, \mathbf{p}_2)\chi_{Sm_S}, \tag{2.6}$$

$$\Phi_{Lm_L}(\mathbf{p}_1, \mathbf{p}_2) = \sum_{m_1 m_2} \langle lm_1 lm_2|Lm_L\rangle \phi_{lm_1}(\mathbf{p}_1)\phi_{lm_2}(\mathbf{p}_2). \tag{2.7}$$

Here χ_{Sm_S} is the spin eigenfunction of the two particles, $S = 0, 1$, the quantity Φ is the space part of the two-particle eigenfunction, and $\phi_{lm}(\mathbf{p})$ is the single particle harmonic oscillator wave function; $\langle j_1 m_1 j_2 m_2|JM\rangle$ denotes the Clebsch-Gordan coefficient. As the non-local potential is most easily described in momentum space, the subsequent calculations and the single particle wave functions are also worked out in momentum space. The explicit form of $\phi_{lm}(\mathbf{p})$ required in the following is ($l = 2$)

$$\phi_{2m}(\mathbf{p}) = Ne^{-\mu p^2} p^2 Y_2^m(\hat{p}), \tag{2.8}$$

$$N^2 = 16(2\mu)^{\frac{7}{2}}/15\sqrt{\pi}. \tag{2.9}$$

The parameter $\sqrt{2\mu}$ measures the extension of the wave function.

It follows from the symmetry of the wave function that the terms in series (2.5) may be broken up into two groups (a) $S = 1$, $L = 0, 2, 4$, and (b) $S = 0$, $L = 1, 3$. It is then obvious from the structure of the potential (2.1) that the matrix elements of V_{even} are non-zero only for group (a), and of V_{odd} only for group (b). This introduces considerable simplicity in subsequent calculations, as the centre-of-mass transformation may be carried out separately for odd and even parts of the wave function. For evaluation of matrix elements with local potentials $V(|\mathbf{r}|) = V(|\mathbf{r}_2-\mathbf{r}_1|)$, one generally expands the potential in a Legendre series with coefficients $V_k(r_1, r_2)$. However, for our non-local, separable potential, it is more convenient to transform the two-particle wave functions to express them in terms of the c.m. and relative momenta. We define

$$\mathbf{P} = \mathbf{p}_1+\mathbf{p}_2, \quad 2\mathbf{p} = \mathbf{p}_2-\mathbf{p}_1, \quad \mathbf{P}' = \mathbf{p}'_1+\mathbf{p}'_2, \quad 2\mathbf{p}' = \mathbf{p}'_2-\mathbf{p}'_1. \tag{2.10}$$

The details of the c.m. transformation are shown in Appendix 1. The results are:

(A) *Triplet states* ($L = 0, 2, 4$)

$$\begin{aligned}\Phi_{Lm_L}(\mathbf{p}_1, \mathbf{p}_2) = N^2 e^{-\frac{1}{2}\mu P^2-2\mu p^2}\Big[&\frac{D_{22L}}{\sqrt{4\pi}}\left(\tfrac{1}{16}P^4 Y_L^{m_L}(P)+p^4 Y_L^{m_L}(\hat{p})\right)\\ &+P^2p^2\sum_{l_1 l_2 \mu_1 \mu_2} B_{l_1 l_2 L}\langle l_1\mu_1 l_2\mu_2|Lm_L\rangle Y_{l_1}^{\mu_1}(\hat{P})Y_{l_2}^{\mu_2}(\hat{p})\Big],\end{aligned} \tag{2.11}$$

$$D_{l_1 l_2 L} = [(2l_1+1)(2l_2+1)/(2L+1)]^{\frac{1}{2}}\langle l_1 0 l_2 0|L0\rangle, \tag{2.12}$$

$$B_{l_1 l_2 L} = \tfrac{1}{2}\delta_{2l_1}\delta_{2l_2}-\tfrac{5}{6}D_{11l_1}D_{11l_2}A\begin{pmatrix}1 & 1 & l_1\\ 1 & 1 & l_2\\ 2 & 2 & L\end{pmatrix}; \tag{2.13}$$

(B) *Singlet states* ($L = 1, 3$)

$$\begin{aligned}\Phi_{Lm_L}(\mathbf{p}_1, \mathbf{p}_2) = N^2 e^{-\frac{1}{2}\mu P^2-2\mu p^2}\delta_{LJ}&\\ \times\sum_{l\mu_1\mu_2}\left[\frac{25(2l+1)}{6}\right]^{\frac{1}{2}} D_{12l}W(11J2;2l)\langle l\mu_1 1\mu_2|JM\rangle&\\ \times[\tfrac{1}{2}P^3 p Y_l^{\mu_1}(P)Y_1^{\mu_2}(\hat{p})+2Pp^3 Y_l^{\mu_1}(\hat{p})Y_1^{\mu_2}(P)].&\end{aligned} \tag{2.14}$$

The matrix-element of (2.1) in the state (2.5) is now

$$\begin{aligned}\langle J|V|J\rangle = \int \Psi^*_{JM}(\mathbf{p}_1, \mathbf{p}_2)(\mathbf{p}_1\mathbf{p}_2)|V|\mathbf{p}'_1\mathbf{p}'_2)\Psi_{JM}(\mathbf{p}'_1, \mathbf{p}'_2)&\\ \times d\mathbf{p}_1 d\mathbf{p}_2 d\mathbf{p}'_1 d\mathbf{p}'_2,&\end{aligned} \tag{2.15}$$

$$(\mathbf{p}_1\mathbf{p}_2|V|\mathbf{p}'_1\mathbf{p}'_2) = \delta(\mathbf{P}-\mathbf{P}')(\mathbf{p}|V|\mathbf{p}'). \tag{2.16}$$

The most interesting feature of this matrix element is that the separability of our potential in relative momenta $\mathbf{p}$ and $\mathbf{p}'$ greatly facilitates the evaluation of (2.15), as the $\mathbf{p}$ and $\mathbf{p}'$ integrations are completely decoupled from each other.

Indeed, the initial and the final states are directly connected only through the **P** integration which is vary simple. This type of feature has no analogue in the usual shell model calculations, and we feel that it may have some interesting consequences.

Further evaluation of (2.15) is carried out as follows. The spin-dependent part of $(\mathbf{p}|V|\mathbf{p}')$ is first eliminated by evaluating

$$\chi^*_{Sm_S}(\mathbf{p}|V|\mathbf{p}')\chi_{Sm'_S}, \tag{2.17}$$

with the help of the relations

$$\frac{1}{\sqrt{8}}S(\hat{p})\chi_{m_S} = \sqrt{4\pi}\sum_{\nu} Y_2{}^{\nu}(\hat{p})\chi_{m_S-\nu}\langle 2\nu 1m_s-\nu|1m_s\rangle \tag{2.18}$$

and

$$\begin{aligned}\sum_{\nu}\chi^*_{m_S}Y_2{}^{\nu *}(\hat{p})(\mathbf{L}_{p'}\cdot\mathbf{S})Y_2{}^{\nu}(\hat{p}')\chi_{m_{S'}}&\\ = \sum_{\nu}\sqrt{12}(-1)^{m'_S-m_S}\langle 2\,\nu+m'_S-m_S\;1\;m_S-m'_S|2\nu\rangle&\\ \times\langle 1m_S\,1\,m'_S-m_S|1m'_S\rangle Y_2{}^{\nu *}(\hat{p})Y_2{}^{\nu+m'_S-m_S}(\hat{p}'),&\end{aligned} \tag{2.19}$$

where $S(\hat{p})$ is the tensor operator defined in A.

Next, the angular integrations over **p**, **p'** and **P** are carried out in a straightforward manner. The few Clebsch-Gordan coefficients appearing in the formula, through summation over magnetic quantum numbers, give rise to at most Racah coefficients. Finally, the result of integration over the magnitudes of p, p' and P is expressed in terms of integrals of the following types:

$$J_{2n} = \mu^n\int_0^\infty P^{(2n+2)}\mathrm{e}^{-\mu P^2}\mathrm{d}P, \tag{2.20}$$

$$X_{2n} = \int_0^\infty p^{(2n+2)}(\beta^2+p^2)^{-1}\mathrm{e}^{-2\mu P^2}\mathrm{d}p, \tag{2.21}$$

$$X'_{2n} = \int_0^\infty p^{(2n+2)}(b^2+p^2)^{-1}\mathrm{e}^{-2\mu p^2}\mathrm{d}p, \tag{2.22}$$

$$Y_{2n} = \int_0^\infty p^{(2n+4)}(\gamma^2+p^2)^{-2}\mathrm{e}^{-2\mu p^2}\mathrm{d}p. \tag{2.23}$$

Evaluation of these integrals is discussed in Appendix 2.

The final results for the V-matrix are given in table 1 in which the contributions from (a) triplet (central, central-tensor, tensor, spin-orbit) and (b) singlet forces are shown separately for $J = 1, 3$.

For numerical evaluation of the matrix elements we use the values of the potential parameters derived in refs. [2, 3]), and the value of μ is adjusted to fit the radius of the core nucleus which in this case we choose as Ca^{40}. This gives $\sqrt{2\mu} = 2.24\times10^{-13}$ cm. Table 2 shows the numerical contributions of the different terms in the potential to the energy of the states $J = 1, 3$.

TABLE 1

The various contributions to $(J|V|J)$, apart from the factor $(-\lambda/M)N^4(\pi/\mu)^3$

		$J=1$	$J=3$
(A) Triplet	Central	$\frac{567}{2048}\frac{X_0^2}{\mu^4}+\frac{7X_0X_2}{32\mu^3}+\frac{33X_2^2}{16\mu^2}+\frac{3X_0X_4}{16\mu^2}-\frac{X_2X_4}{\mu}$	$\frac{567}{2048}\frac{X_0^2}{\mu^4}+\frac{3X_0X_2}{128\mu^3}+\frac{X_2^2}{32\mu^2}$
	Central-Tensor	$\frac{4\sqrt{2}}{5}X_4Y_4t+\frac{3\sqrt{2}}{16\mu^2}X_0Y_4t-\frac{\sqrt{2}}{\mu}tX_2Y_4+\frac{7\sqrt{2}}{10\mu}X_4Y_2t+\frac{77\sqrt{2}}{640\mu^3}tX_0Y_2-\frac{259\sqrt{2}}{120\mu^2}X_2Y_2t$	$-\frac{3\sqrt{2}}{40\mu^3}tX_0Y_2-\frac{\sqrt{2}}{5\mu^2}X_2Y_2t$
	Tensor	$\frac{4}{5}Y_4^2t^2+\frac{14}{10\mu}Y_2Y_4t^2+\left(\frac{49}{48}+\frac{6}{25}\right)\frac{t^2Y_2^2}{\mu^2}$	$\frac{16}{25}t^2\frac{Y_2^2}{\mu^2}$
	Spin-Orbit	$\left(\frac{\lambda_2}{\lambda}\right)\left[\frac{357}{80\mu^2}Y_2^2+\frac{12}{5}Y_4^2+\frac{21}{5\mu}Y_2Y_4\right]$	$\left(\frac{\lambda_2}{\lambda}\right)\left[-\frac{12}{245}Y_4^2-\frac{3}{35}\frac{Y_2Y_4}{\mu}+\frac{147}{80\mu^2}Y_2^2\right]$
(B) Singlet		$\left(\frac{\lambda_2}{\lambda}\right)\left[\frac{189}{64}\frac{X_2'^2}{\mu^3}+\frac{6X_4'^2}{\mu}-\frac{15}{2\mu^2}X'_2X'_4\right]$	$\frac{3}{8\mu^3}X_2'^2$

TABLE 2

$(J|V|J)$ in MeV, with $\sqrt{2\mu}=2.24\times10^{-13}$ cm

		$J=1$	$J=3$
(A) Triplet	Central	−5.20	−1.05
	Central-tensor	0.28	0.11
	Tensor	−0.17	−0.02
	Spin-Orbit	0.74	0.09
(B) Singlet		5.60	0.75
(A)+(B)		1.25	−0.12

3. Discussion

Certain qualitative features of the data in table 2 may be noted. While the triplet potential is predominantly attractive, the singlet part is repulsive. Almost the entire triplet contribution comes from the central interaction, which perhaps justifies the simple conventional shell model calculations carried out with central potentials only. The tensor force, in particular, gives a very small contribution to the energy of the state. The contribution of the spin-orbit forces is relatively larger, and in the desired direction since it raises $J = 1$ state above $J = 3$, as experimentally observed. Since the contributions of the central triplet and singlet interactions are large but of opposite signs, the role of spin-orbit force is of some interest. However, one may not arrive at very general conclusions from an isolated calculation.

Thus, the overall result of the calculation is that the $J = 1$ state is predicted about 1.3 MeV above the $J = 3$ state. As we have earlier mentioned, one may expect to see these states in nuclei K^{38} and Cl^{34}, the simple shell model configurations for nucleons outside (or holes in) the core being $(d_{\frac{3}{2}})^{-2}$ and $(d_{\frac{3}{2}})^2$ respectively. Unfortunately the $J = 1$ state is not yet clearly identified in either of these nuclei. In Cl^{34}, the first excited state at 0.14 MeV is known to have $J = 3$, $T = 0$ [9]). There are good theoretical reasons to believe that the next excited state at 1.1 MeV is a $J = 1, T = 0$ state [5]). On the other hand, in K^{38} the ground state has been identified as $J = 3, T = 0$, and the large $Ca^{40}(d, \alpha)$ cross section for the 0.44 MeV state in K^{38} suggests that it may have $T = 0$, $J = 1$ [10]). Qualitatively therefore, there is agreement between theory and experiment.

The lack of quantitative agreement of the calculations should not be very disturbing. We note that besides a small uncertainty in the value of μ (which would be different for Cl^{34} and K^{38}), the parameters of the singlet potential which were obtained only from n–p scattering phase shifts, are not as precisely known as the triplet parameters which were much better specified by the analysis of A. We may also expect some improvement in the result if the reaction matrix G is used in place of the potential matrix in the following way. The singlet part being repulsive, the G-matrix element would be reduced, whereas for the attractive triplet part, it would be increased. It is obvious that even a small correction ($\approx 10\,\%$) would substantially improve the agreements between theory and experiment. Finally, we would like to emphasise that our purpose is not to make a detailed prediction of the energy levels, but to test the consequences of a reasonable realistic two-body interaction in the frame work of the shell model. It is gratifying that a satisfactory qualitative agreement is obtained. One may be encouraged to believe that such well-behaved non-local realistic potentials may be further used to give reasonable estimates of the nuclear parameters with much less efforts than would be possible with the usual local potentials having hard cores etc.

One of us (A. N. M.) is grateful to Professor P. S. Gill for his interest in this work. We are indebted to H. J. Naqvi for making available to us the results for the singlet potential prior to publication.

Appendix 1

We outline here the main steps leading to eqs. (2.11) to (2.14) of the text. We define the spherical vector

$$p^{(m)} = \sqrt{4\pi/3}\, pY_1^m(\hat{p}). \tag{A.1}$$

Thus from (2.10), we have

$$p_1^{(m)} = \tfrac{1}{2}P^{(m)} - p^{(m)}, \quad p_2^{(m)} = \tfrac{1}{2}P^{(m)} + p^{(m)}. \tag{A.2}$$

Further, we may use the well-known relation

$$Y_{l_1}^{m_1}(\theta\phi)Y_{l_2}^{m_2}(\theta\phi) = \sum_{LM} \frac{1}{\sqrt{4\pi}} D_{l_1 l_2 L}\langle l_1 m_1 l_2 m_2 | LM\rangle Y_L^M(\theta\phi) \tag{A.3}$$

to write

$$\begin{aligned} p_1^2 Y_2^m(\hat{p}_1) &= \sqrt{10\pi/3} \sum_{m_1 m_2} \langle 1m_1 1m_2 | 2m\rangle p_1^{(m_1)} p_1^{(m_2)}, \\ p_2^2 Y_2^{m'}(\hat{p}_2) &= \sqrt{10\pi/3} \sum_{m'_1 m'_2} \langle 1m'_1 1m'_2 | 2m'\rangle p_2^{(m'_1)} p_2^{(m'_2)}. \end{aligned} \tag{A.4}$$

Clearly then, substituting (A.2) on the left side of (A.4), we obtain an expression for the wave function $p_1^2 Y_2^m(\hat{p}_1) p_2^2 Y_2^{m'}(\hat{p}_2)$ in terms of products of $P^{(m)}$ and $p^{(m)}$. Finally, in each term of the resulting expression we collect all the various Y_1^m having the same argument, and recouple them together by repeated application of (A.3); the Clebsch-Gordan coefficients appearing in this process are easily summed into various $6j$- and $9j$-coefficients, giving the results in the form shown in the text.

After these calculations were done, a number of authors [11]) have shown how the centre-of-mass transformations can be carried out in a more general fashion. Our procedure is almost similar to the work of Moshinsky, but owing to our ignorance of eq. (46) of his paper, we have carried out the transformation for our special case in a rather naive and straightforward (but in practice very simple) way. We have found by explicit calculations that for most of the cases of interest, at least in the region of light and medium nuclei, our prescription enables one to calculate the c.m. transformation in a very simple and direct way.

Appendix 2

The integrals (2.20) are simply given by

$$J_{2n} = \frac{(2n+1)!!}{2^n} J_0, \tag{A.5}$$

$$J_0 = \tfrac{1}{4}\sqrt{\pi}\, \mu^{-\frac{3}{2}}. \tag{A.6}$$

For the evaluation of X_{2n}, defined by (2.21), we write $t = 2\mu p^2$ and $x = (2\mu\beta^2)^{-1}$, so that

$$X_{2n} = \frac{x}{2\,(2\mu)^{n+\frac{1}{2}}} \int_0^\infty t^{n+\frac{1}{2}} e^{-t}(1+xt)^{-1} dt. \tag{A.7}$$

Now the values of β, μ for our case are such that $x \approx 0.1$. Still it is not a good approximation to expand $(1+xt)^{-1}$ in powers of xt, in spite of the convergence factor e^{-t} in (A.7). On the other hand, the following approximation turns out to be quite good. We write

$$(1+xt)^{-1} = e^{-\ln(1+xt)} \approx e^{-xt}[1+\tfrac{1}{2}x^2t^2-\tfrac{1}{3}x^3t^3+\ldots]. \tag{A.8}$$

Thus we finally obtain

$$X_{2n} = \tfrac{1}{2}x \frac{\Gamma(n+\frac{3}{2})}{(2\mu)^{n+\frac{1}{2}}} \frac{1}{(1+x)^{n+\frac{1}{2}}} \left[1+\tfrac{1}{2}(n+\tfrac{3}{2})(n+\tfrac{5}{2})\left(\frac{x}{1+x}\right)^2 - \ldots\right]. \tag{A.9}$$

Similarly, with $y = (2\mu\gamma^2)^{-1}$,

$$Y_{2n} = \tfrac{1}{2}y^2 \frac{\Gamma(n+\frac{5}{2})}{(2\mu)^{n+\frac{1}{2}}} \frac{1}{(1+2y)^{n+\frac{1}{2}}} \left[1+(n+\tfrac{5}{2})(n+\tfrac{7}{2})\left(\frac{y}{1+2y}\right)^2 - \ldots\right]. \tag{A.10}$$

The above approximation deteriorates with increasing n, and is somewhat better for X_{2n} than for Y_{2n}. However, for the worst case occurring in table 1, viz. Y_4, it has been found by actual numerical evaluation of the integral that the formula (A.10) with the inclusion of the second term gives a value differing by only 1.5 % from the true value.

References

1) M. K. Banerjee and B. Dutta Roy, Ann. of Phys. **7** (1959) 484
2) A. N. Mitra and V. L. Narasimham, Nuclear Physics **14** (1959–60) 407
3) A. N. Mitra and J. H. Naqvi, Nuclear Physics (to be published)
4) R. J. N. Phillips, Rep. Prog. Phys. **22** (1959) 562
5) S. P. Pandya, Phys. Rev. **103** (1956) 956;
   S. Goldstein and I. Talmi, Phys. Rev. **102** (1956) 589
6) H. A. Bethe, Phys. Rev. **103** (1956) 1353
7) I. Talmi, Helv. Phys. Acta **25** (1952) 185
8) H. A. Jahn and J. Hope, Phys. Rev. **93** (1954) 318;
   J. M. Kennedy and M. J. Cliff, CRT-609, Atomic Energy of Canada Ltd., Chalk River, Ontario (1955)
9) P. M. Endt and C. M. Braams, Revs. Mod. Phys. **29** (1957) 683
10) Y. Hashimoto and W. P. Alford, Phys. Rev. **116** (1959) 981
11) M. Moshinsky, Nuclear Physics **13** (1959) 104;
   A. Arima and T. Terasawa, Prog. Theor. Phys. **23** (1960) 115;
   R. D. Lawson and M. Goeppert-Mayer, Phys. Rev. **117** (1960) 174

8.B

Nuclear Physics **20** (1960) 464—474; © *North-Holland Publishing Co., Amsterdam*

Not to be reproduced by photoprint or microfilm without written permission from the publisher

THE PHENOMENOLOGICAL BARYON-BARYON SCATTERING THEORY AND THE RELATIVE PARITY DETERMINATION

A. DELOFF and J. WRZECIONKO
Institute for Nuclear Research, Warsaw

Received 11 April 1960

Abstract: The reactions a+b → c+d with four baryons are considered. Two cases of relative intrinsic parities $I_aI_b = \pm I_cI_d$ are taken into account; the phenomenological S-matrix technique is used for obtaining the cross section and polarizations. An approximation in which in the initial state only the S wave is present is discussed. In this approximation the cross section for unpolarized particles is isotropic and the polarizations in the final state are zero when $I_aI_b = I_cI_d$ and proportional to $\sin 2\theta$ when $I_aI_b = -I_cI_d$. Some experimental tests for the relative parity determination are proposed.

1. Introduction

Within the last few years great attention has been paid to the parity determination of strange particles. Some experiments have been suggested by which the relative paritis could be detected. In general we can divide these experiments into two classes. To the first class belong strange particle production reactions in which the K particles take part, e.g. [1]) $K+N \to \Sigma(\Lambda)+\pi$. As an effective test for the parity determination one can take here also reactions with three (or more) particles in the final state as for instance [2]) $K^-+p \to \Lambda+\pi+\pi$. Other possibilities are discussed by Bilenky and Ryndin, and A. Bohr [3]). In the second class are reactions of the type a+b → c+d in which only baryons are involved. These were discussed also by several authors [4–6]). Pais and Treiman [4]) consider the reaction $\Sigma^-+p \to \Lambda+n$ from the bound (Σ^-, p)state. They calculate the polarization change in this reaction, assuming that the transition takes place from the lowest state (S or P). The polarization of the final state particles depends on the relative (Λ, Σ) parity, as the latter determines the type of transition. Barshay [5]) takes into account the reaction $N+\overline{N} \to \Lambda+\overline{\Sigma}$ for energies which sligtly exceed the threshold and makes the plausible assumption that the hyperons are produced in the S-state. If the particles in the initial state are polarized some conclusions about (Λ, Σ) relative parity can be drawn by observing the subsequent decay of $\Lambda(\Sigma)$. Treiman [6]) considers the Ξ^- capture in hydrogen $\Xi^-+p \to \Lambda+\Lambda$ and the cascade decay of Λ from which information about the relative parity is obtainable.

In this paper we are interested in the second class of processes. Denoting by I_a, I_b, I_c, I_d the intrinsic parities of the particles involved we apply the phenomenological S matrix technique for the two cases $I_aI_b = \pm I_cI_d$, i.e. for even

(+) or (−) odd relative parity. The method used consists of a generalisation of the well known procedure applied in the NN scattering analysis [7–9]). From the very general conservation laws the transition matrix T is constructed. All measurable qualitities are expressed in terms of T^J submatrices (reaction amplitudes) which could be parametrized by means of the usual phase shifts and mixing parameters [10]). Hence, the obtained results could be a starting point for the phase shift analysis in a nucleon-hyperon scattering problem; however, here we are rather interested in the possibilities of the parity determination. For this purpose we apply our formalism to low energy collisions (with respect to the threshold) where it seems reasonable that only the S state enters into the initial or the final state. In a reaction in which the threshold is rather high (the total rest mass produced in the final state is considerably larger then the total rest mass in the initial state) we assume that in the final state only the S state is present. The reaction examined by Barshay belongs to this category.

The reaction $\Xi^- + p \to \Lambda + n$ in the low energy region is an example of a reaction with zero threshold in which the initial state is assumed to be the S state only. Reactions with high threshold considered in the S state approximation give no possibility of distinguishing between the parities, even when reactions with polarized particles are taken into account. There are some arguments that if one includes the P wave one can expect to obtain a difference in the angular correlations or at least in the polarizations. The authors believe that it will be possible to show this.

Much more useful experiments are the zero threshold reactions. In the S state approximation (S state taken as an initial state) the cross section for unpolarized particles is isotropic for both values of relative parity. The final polarization is different from zero only in the case of odd relative parity ($I_a I_b = I_c I_d$). Both particles (c and d) are in this case polarized perpendicularly to the reaction plane opposite to each other. The polarization is proportional to sin 2θ (θ is the c.m. scattering angle). One can expect that reactions with polarized particles lead also to some further effects determining the relative parity. The formalism given below yields all the quantities important for the experiment, but we did not consider reactions with polarized particles, which are extremely difficult to realize in the experiment.

2. The T Matrix

The general theory of collisions of the type $a+b \to c+d$ has been discussed several times [10–12]). We make use of the very simple treatment given recently by Jacob and Wick [12]), who consider the T matrix

$$\langle \mathbf{p}' \lambda_c \lambda_d \alpha' | T | \mathbf{p} \lambda_a \lambda_b \alpha \rangle, \tag{1}$$

where $\mathbf{p}$ and $\mathbf{p}'$ are the c.m. initial and final momenta respectively, λ_a, λ_b, λ_c, λ_d

are helicities of the involved particles, and α and α' are some channel indices denoting the sort of particles in the initial and the final state respectively. The T matrix is so normalized that for the cross section for the process $\alpha \to \alpha'$ we have

$$\mathrm{d}\sigma(\alpha \to \alpha') = \left(\frac{2\pi}{p}\right)^2 |\langle \mathbf{p}'\lambda_c\lambda_d\alpha'|T|\mathbf{p}\lambda_a\lambda_b\,\alpha\rangle|^2 \mathrm{d}\Omega. \tag{2}$$

Jacob and Wick introduce further the total angular momentum and helicity representation $\langle J'M'\lambda_c\lambda_d|T|JM\lambda_a\lambda_b\rangle$. In our case, when the relative parity of particles can be quite arbitrary, it seems more convenient to apply the standard $SLJM$ representation [9, 10]) (S, L are total spin and orbital quantum numbers).

Our new representation can be constructed by introducing the orbital quantum number L and adding it to the total spin S:

$$|\mathbf{p}\lambda_a\lambda_b\alpha\rangle = \sum_{SLJm} C(LSJ;\, m,\, \lambda)C(s_a s_b S;\, \lambda_a,\, -\lambda_b)\langle Lm|\mathbf{p}\rangle|LSJM\rangle, \tag{3}$$

where $\lambda = \lambda_a - \lambda_b$; $M = m + \lambda$; the $C(LSJ;\, m,\, \lambda)$ and $C(s_a s_b S;\, \lambda_a,\, -\lambda_b)$ are the Clebsch-Gordan coefficients in the notation of Rose [13]), s_a and s_b the spins of the particles a and b, m the projection quantum number of L. The $\langle Lm|\mathbf{p}\rangle$ matrix is the transformation matrix from the $|\mathbf{p}\rangle$ to the $|Lm\rangle$ representation. This matrix can be found by application of the well known prescription (see ref. [14]) and the appendix of ref. [12])), according to which the $|Lm\rangle$ state is expanded in the $|\mathbf{p}\rangle$ states as

$$i^L|Lm\rangle = N_L \int D^{L*}_{m0}(\phi,\, \theta,\, 0) R_{\phi\theta 0} \mathrm{e}^{ip(Z_a - Z_b)} \mathrm{d}\Omega, \tag{4}$$

where $R_{\phi\theta 0}$ is the rotation operator (θ and ϕ are the polar angles of $\mathbf{p}$), D^L_{m0} the matrix corresponding to $R_{\phi\theta 0}$ in the irreducible representation D^L; $N_L = [(2L+1)/4\pi]^{\frac{1}{2}}$; $\mathrm{d}\Omega = \sin\theta\ \mathrm{d}\theta\ \mathrm{d}\phi$. The expression (4) differs by a factor i^L from the formula ($B4$) given in the appendix of ref. [12]). This factor is necessary to make the T matrix symmetric, as was pointed out by Huby [15]). From (4) we obtain the transformation matrix

$$\langle \mathbf{p}|Lm\rangle = i^{-L} N_L D^{L*}_{m0}(\phi,\, \theta,\, 0) = i^{-L} Y_{Lm}(\mathbf{p}), \tag{5}$$

where Y_{Lm} are the spherical harmonics defined in ref. [13]).

Having in mind eqs. (3) and (5) we can rewrite eq. (1) in the $LSJM$ representation,

$$\langle \mathbf{p}'\lambda_c\lambda_d\alpha'|T|\mathbf{p}\lambda_a\lambda_b\alpha\rangle = \sum_{S,S',L'L,J,m,m'} C(s_a s_b S;\, \lambda_a,\, -\lambda_b)C(s_c s_d S';\, \lambda_c,\, -\lambda_d)$$
$$\times C(LSJ;\, m,\, \lambda)C(L'S'J;\, m',\, \mu) i^{L-L'} Y_{Lm}(\mathbf{p}) Y^*_{L'm'}(\mathbf{p}') \langle L'S'\alpha'|T^J|LS\alpha\rangle. \tag{6}$$

In eq. (6) we made use of the $\mathbf{J}^2$ and J_z conservation:

$$\langle L'S'J'M'\alpha'|T|LSJM\alpha\rangle = \delta_{JJ'}\delta_{MM'}\langle L'S'\alpha'|T^J|LS\alpha\rangle.$$

Expression (6), apart from the normalization and helicities used instead of spins projections, is identical with the corresponding one obtained by Chou and Shirokov [11]). Takig the **p** direction as the z axis of our coordinate system we have

$$Y_{Lm}(\mathbf{p}) = [(2L+1)/4\pi]^{\frac{1}{2}}\delta_{m0} \quad \text{and} \quad m' = \lambda - \mu.$$

Multiplying (6) by $C(s_a s_b S;\ \lambda_a, -\lambda_b)C(s_c s_d S';\ \lambda_c, \lambda_d)$ and summing over all helicities we obtain the T matrix in the representation of the total spin and its projection,

$$\langle S'\mu\alpha'\mathbf{p}'|T|S\lambda\alpha p_z\rangle = \sum_{JLL'} [(2L+1)/4\pi]^{\frac{1}{2}} i^{L-L'} Y_{L'\lambda-\mu}(\mathbf{p}')C(LSJ;\ 0,\ \lambda) \times C(L'S'J;\ \lambda-\mu,\ \mu)\langle L'S'\alpha'|T^J|LS\alpha\rangle. \quad (7)$$

Up to this point the theory is valid for particles of arbitrary spin. The expression (7) will be the starting point of our calculation, in which the particles a, b, c, d are spin $\frac{1}{2}$ fermions. If the relative parity is even $I_a I_b = I_c I_d$, we have for $\Delta L = L - L'$ the usual selection rule $\Delta L = 0, \pm 2$; when the relative parity is odd, $I_a I_b = -I_c I_d$, the corresponding selection rule is $\Delta L = \pm 1$. The above selection rules give rise to some relations between the matrix elements (7), which is a consequence of the parity conservation. The invariance under time reversal makes T^J symmetric in all indices [10, 15]).

Usually it is convenient to eliminate the ϕ dependence from the T matrix. This could be done by introducing the abbreviations

$$\frac{2\pi}{p}\langle S'\mu\alpha'\mathbf{p}'|T|S\lambda\alpha p_z\rangle = T^{(\pm)}_{ki} = e^{i(\lambda-\mu)\phi} M^{(\pm)}_{ki}, \quad (8)$$

where the superscript $+$ $(-)$ refers to the even (odd) relative parity and $k(l)$ are both either s for singlet state, or $\lambda(\mu)$ for the triplet state, for example $(2\pi/p)\langle 00\alpha'\mathbf{p}'|T|1, -1, \alpha p_z\rangle = T^{(\pm)}_{s,-1}$. This notation is adopted from the N—N scattering theory [8]), which follows here as a particular case. Changing signs of λ and μ in (7) we have

$$\langle S', -\mu, \alpha', \mathbf{p}'|T|S, -\lambda\alpha p_z\rangle = \sum_{JLL'} (-1)^{S+S'+L+L'+\lambda-\mu} Y^*_{L'\lambda-\mu}(\mathbf{p}') \times C(LSJ;\ 0,\lambda)C(L'S'J;\ \lambda-\mu,\ \mu)\langle S'L'\alpha'|T^J|SL\alpha\rangle. \quad (9)$$

To obtain (9) we applied the symmetry relation of the Clebsch-Gordan coefficients [13])

$$C(j_1 j_2 j;\ -m_1, -m_2) = (-1)^{j_1+j_2-j} C(j_1, j_2, j;\ m_1, m_2) \text{ and } Y_{L,-m} = (-1)^m Y^*_{L,m}.$$

Using the selection rules, and comparing (7) and (9) we get the following relations between the $T^{(\pm)}_{ki}$:

$$T^{(\pm}_{-k-i}(\theta, \phi) = \pm(-1)^{S+S'+\lambda-\mu} T^{(\pm)}_{ki}(\theta, -\phi), \quad (10)$$

TABLE 1

Matrix elements $M_{s't'}^{(\pm)}$ (the channel indices are omitted)

$M_{ss}^{(+)}$	$\frac{1}{2p}\sum_L P_L^0(\theta)[2L+1]\langle 0, L\|T^L\|0, L\rangle$
$M_{00}^{(+)}$	$\frac{1}{2p}\sum_L P_L^0(\theta)\{L\langle 1, L\|T^{L-1}\|1, L\rangle+(L+1)\langle 1, L\|T^{L+1}\|1, L\rangle$ $+[L(L+1)]^{\frac{1}{2}}\langle 1, L\|T^{L-1}\|1, L-2\rangle+[(L+1)(L+2)]^{\frac{1}{2}}\langle 1, L\|T^{L+1}\|1, L+2\rangle\}$
$M_{11}^{(+)}$	$\frac{1}{4p}\sum_L P_L^0(\theta)\{(L-1)\langle 1, L\|T^{L-1}\|1, L\rangle+(2L+1)\langle 1, L\|T^L\|1, L\rangle$ $+(L+2)\langle 1, L\|T^{L+1}\|1, L\rangle-[(L+1)(L+2)]^{\frac{1}{2}}\langle 1, L\|T^{L+1}\|1, L+2\rangle$ $-[L(L-1)]^{\frac{1}{2}}\langle 1, L\|T^{L-1}\|1, L-2\rangle\}$
$M_{10}^{(+)}$	$\frac{\sqrt{2}}{4p}\sum_L P_L^1(\theta)\{\langle 1, L\|T^{L+1}\|1, L\rangle-\langle 1, L\|T^{L-1}\|1, L\rangle$ $+\left[\frac{L+2}{L+1}\right]^{\frac{1}{2}}\langle 1, L\|T^{L+1}\|1, L+2\rangle-\left[\frac{L-1}{L}\right]^{\frac{1}{2}}\langle 1, L\|T^{L-1}\|1, L-2\rangle\}$
$M_{01}^{(+)}$	$\frac{\sqrt{2}}{4p}\sum_L P_L^1(\theta)\left\{\frac{L-1}{L}\langle 1, L\|T^{L-1}\|1, L\rangle+\frac{2L+1}{L(L+1)}\langle 1, L\|T^L\|1, L\rangle\right.$ $-\frac{L+2}{L+1}\langle 1, L\|T^{L+1}\|1, L\rangle+\left[\frac{L+2}{L+1}\right]^{\frac{1}{2}}\langle 1, L\|T^{L+1}\|1, L+2\rangle$ $\left.-\left[\frac{L-1}{L}\right]^{\frac{1}{2}}\langle 1, L\|T^{L-1}\|1, L-2\rangle\right\}$
$M_{1-1}^{(+)}$	$\frac{1}{4p}\sum_L P_L^2(\theta)\left\{\frac{1}{L}\langle 1, L\|T^{L-1}\|1, L\rangle-\frac{2L+1}{L(L+1)}\langle 1, L\|T^L\|1, L\rangle+\frac{1}{L+1}\langle 1, L\|T^{L+1}\|1, L\rangle\right.$ $\left.-[L(L-1)]^{-\frac{1}{2}}\langle 1, L\|T^{L-1}\|1, L-2\rangle-[(L+1)(L+2)]^{-\frac{1}{2}}\langle 1, L\|T^{L+1}\|1, L+2\rangle\right\}$
$M_{1s}^{(+)}$	$\frac{\sqrt{2}}{4p}\sum_L P_L^1(\theta)\frac{2L+1}{[L(L+1)]^{\frac{1}{2}}}\langle 1, L\|T^L\|0, L\rangle$
$M_{s1}^{(+)}$	$\frac{1}{2p}\sum_L P_L^1(\theta)\frac{2L+1}{L(L+1)}\langle 0, L\|T^L\|1, L\rangle$
$M_{11}^{(-)}$	$\frac{i}{4p}\sum_L P_L^0(\theta)\{-[L(2L+1)]^{\frac{1}{2}}\langle 1, L\|T^L\|1, L+1\rangle-[(L+2)(2L+3)]^{\frac{1}{2}}\langle 1, L\|T^{L+1}\|1, L+1\rangle$ $+[(L+1)(2L+1)]^{\frac{1}{2}}\langle 1, L\|T^L\|1, L-1\rangle+[(L-1)(2L-1)]^{\frac{1}{2}}\langle 1, L\|T^{L-1}\|1, L-1\rangle\}$
$M_{10}^{(-)}$	$\frac{i\sqrt{2}}{4p}\sum_L P_L^1(\theta)\left\{-\left[\frac{2L+1}{L}\right]^{\frac{1}{2}}\langle 1, L\|T^L\|1, L+1\rangle+\left[\frac{2L+1}{L+1}\right]^{\frac{1}{2}}\langle 1, L\|T^L\|1, L-1\rangle\right\}$
$M_{01}^{(-)}$	$\frac{i\sqrt{2}}{4p}\sum_L P_L^1(\theta)\left\{\frac{1}{L+1}\left[\frac{2L+1}{L}\right]^{\frac{1}{2}}\langle 1, L\|T^L\|1, L+1\rangle-\frac{1}{L}\left[\frac{2L+1}{L+1}\right]^{\frac{1}{2}}\langle 1, L\|T^L\|1, L-1\rangle\right.$ $\left.-\frac{1}{L+1}[(2L+3)(L+2)]^{\frac{1}{2}}\langle 1, L\|T^{L+1}\|1, L+1\rangle-\frac{1}{L}[(2L-1)(L-1)]^{\frac{1}{2}}\langle 1, L\|T^{L-1}\|1, L-1\rangle\right\}$

TABLE 1
(continued)

$M^{(-)}_{1-1}$	$\frac{i}{4p}\sum_L P_L^{\,2}(\theta)\left\{-\frac{1}{L+1}\left[\frac{2L+1}{L}\right]^{\frac{1}{2}}\langle 1, L\|T^L\|1, L+1\rangle + \frac{1}{L+1}\left[\frac{2L+3}{L+2}\right]^{\frac{1}{2}}\langle 1, L\|T^{L+1}\|1, L+1\rangle + \frac{1}{L}\left[\frac{2L+1}{L+1}\right]^{\frac{1}{2}}\langle 1, L\|T^L\|1, L-1\rangle - \frac{1}{L}\left[\frac{2L-1}{L-1}\right]^{\frac{1}{2}}\langle 1, L\|T^{L-1}\|1, L-1\rangle\right\}$
$M^{(-)}_{1s}$	$\frac{i\sqrt{2}}{4p}\sum_L P_L^{\,1}(\theta)\left\{\left[\frac{2L+3}{L+1}\right]^{\frac{1}{2}}\langle 1, L\|T^{L+1}\|0, L+1\rangle - \left[\frac{2L-1}{L}\right]^{\frac{1}{2}}\langle 1, L\|T^{L-1}\|0, L-1\rangle\right\}$
$M^{(-)}_{s1}$	$\frac{i\sqrt{2}}{4p}\sum_L P_L^{\,1}(\theta)\left\{\left[\frac{2L+1}{L+1}\right]^{\frac{1}{2}}\langle 0, L\|T^L\|1, L+1\rangle - \left[\frac{2L+1}{L}\right]^{\frac{1}{2}}\langle 0, L\|T^L\|1, L-1\rangle\right\}$
$M^{(-)}_{0s}$	$\frac{i}{2p}\sum_L P_L^{\,0}(\theta)\{[(L+1)(2L+3)]^{\frac{1}{2}}\langle 1, L\|T^{L+1}\|0, L+1\rangle - [L(2L-1)]^{\frac{1}{2}}\langle 1, L\|T^{L-1}\|0, L-1\rangle\}$
$M^{(-)}_{s0}$	$-\frac{i}{2p}\sum_L P_L^{\,0}(\theta)\{[(2L+1)(L+1)]^{\frac{1}{2}}\langle 0, L\|T^L\|1, L+1\rangle + [L(2L+1)]^{\frac{1}{2}}\langle 0, L\|T^L\|1, L-1\rangle\}$

and corresponding relations for $M^{(\pm)}_{kl}$:

$$M^{(\pm)}_{-k-l} = \pm(-1)^{S+S'+\lambda-\mu} M^{(\pm)}_{kl}. \tag{11}$$

The relation (11) reduces the number of independent $M^{(\pm)}_{kl}$ to 8 for each case of relative parity. The full expressions for them are given in table 1. The elements of the submatrix T^J are not all independent. Making use of the time reversal and unitarity conditions one could parametrize the T^J in terms of the phase shifts and mixing parameters according to the well known prescription of Blatt and Biedenharn [10]). We should notice also that in spite of the fact that our representation determines a particular frame of reference the calculation is relativistically correct. This question was raised in ref. [11]).

3. The Generalised Wolfenstein-Ashkin Matrix

In this section we give the general form of our transition T matrix in the m_{s_1}, m_{s_2} representation, i.e. in terms of the Pauli spin matrices for the particles involved in the reaction. This form is a useful starting point for obtaining the expressions which correspond to various experiments with polarized particles.

Similarly as in the N—N scattering theory [15, 17]) let us introduce three mutually orthogonal unit vectors $\mathbf{m}$, $\mathbf{l}$, $\mathbf{n}$ defined by

$$\mathbf{m} = \frac{\mathbf{p}_i - \mathbf{p}_f}{2\sin\frac{1}{2}\theta}, \quad \mathbf{l} = \frac{\mathbf{p}_i + \mathbf{p}_f}{2\cos\frac{1}{2}\theta}, \quad \mathbf{n} = \frac{\mathbf{p}_i \times \mathbf{p}_f}{\sin\theta}, \tag{12}$$

where $\mathbf{p}_i$ and $\mathbf{p}_f$ are unit vectors in the direction of the incident and outgoing c.m. momentum and θ is the scattering angle. The T matrix (7) can be written in terms of the vectors (12) and the two Pauli $\boldsymbol{\sigma}_1$ and $\boldsymbol{\sigma}_2$ matrices. An arbitrary matrix in the m_{s_1}, m_{s_2} representation contains 16 elements; in our case this number is reduced to -8 owing to the parity conservation. From the vectors (12) and $\boldsymbol{\sigma}_1$, $\boldsymbol{\sigma}_2$ we can construct 16 operators, 8 scalar and 8 pseudoscalar quantities: Scalars:

$$\mathbf{1}, \quad \boldsymbol{\sigma}_1\cdot\mathbf{n}, \quad \boldsymbol{\sigma}_2\cdot\mathbf{n}, \quad \boldsymbol{\sigma}_1\cdot\mathbf{n}\,\boldsymbol{\sigma}_2\cdot\mathbf{n}, \quad \boldsymbol{\sigma}_1\cdot\mathbf{m}\,\boldsymbol{\sigma}_2\cdot\mathbf{m}, \quad \boldsymbol{\sigma}_1\cdot\mathbf{l}\,\boldsymbol{\sigma}_2\cdot\mathbf{l},$$
$$\boldsymbol{\sigma}_1\cdot\mathbf{l}\,\boldsymbol{\sigma}_2\cdot\mathbf{m}, \quad \boldsymbol{\sigma}_1\cdot\mathbf{m}\,\boldsymbol{\sigma}_2\cdot\mathbf{l}; \quad (13)$$

Pseudo scalars:

$$\boldsymbol{\sigma}_1\cdot\mathbf{l}, \quad \boldsymbol{\sigma}_2\cdot\mathbf{l}, \quad \boldsymbol{\sigma}_1\cdot\mathbf{l}\,\boldsymbol{\sigma}_2\cdot\mathbf{n}, \quad \boldsymbol{\sigma}_1\cdot\mathbf{n}\,\boldsymbol{\sigma}_2\cdot\mathbf{l}, \quad \boldsymbol{\sigma}_1\cdot\mathbf{m}, \quad \boldsymbol{\sigma}_2\cdot\mathbf{m},$$
$$\boldsymbol{\sigma}_1\cdot\mathbf{m}\,\boldsymbol{\sigma}_2\cdot\mathbf{n}, \quad \boldsymbol{\sigma}_1\cdot\mathbf{n}\,\boldsymbol{\sigma}_2\cdot\mathbf{m}. \quad (14)$$

The operators (13) and (14) are mutually orthogonal, i.e. they have the property

$$\tfrac{1}{4}\,\mathrm{Tr}\,O_iO_j = \delta_{ij},$$

where O_i and O_j are arbitrary operators of the respective types (13) and (14).

A general T matrix would contain all 16 operators given by (13) and (14) multiplied by some functions of θ and energy E. The number of these functions is the same as the number of independent elements of $T^{(\pm)}_{kl}$. In our case the $T^{(\pm)}$ matrix contains 8 independent elements and is to be expressed by 8 operators. If the relative parity of the particles is even we take the set (13), whereas operators (14) are used when the relative parity is odd. Thus, the scalar and pseudoscalar quantities do not enter the $T^{(\pm)}$ matrix simultaneously, which is of course necessary in a parity conserving theory. Thus, we have in the even parity case

$$T^{(+)} = A+B\boldsymbol{\sigma}_1\cdot\mathbf{n}+C\boldsymbol{\sigma}_2\cdot\mathbf{n}+D\boldsymbol{\sigma}_1\cdot\mathbf{n}\boldsymbol{\sigma}_2\cdot\mathbf{n}+E\boldsymbol{\sigma}_1\cdot\mathbf{m}\,\boldsymbol{\sigma}_2\cdot\mathbf{m}$$
$$+F\boldsymbol{\sigma}_1\cdot\mathbf{l}\,\boldsymbol{\sigma}_2\cdot\mathbf{l}+G\boldsymbol{\sigma}_1\cdot\mathbf{l}\,\boldsymbol{\sigma}_2\cdot\mathbf{m}+H\boldsymbol{\sigma}_1\cdot\mathbf{m}\,\boldsymbol{\sigma}_2\cdot\mathbf{l}, \quad (15)$$

and correspondingly for the odd relative parity

$$T^{(-)} = A'\boldsymbol{\sigma}_1\cdot\mathbf{1}+B'\boldsymbol{\sigma}_2\cdot\mathbf{1}+C'\boldsymbol{\sigma}_1\cdot\mathbf{l}\,\boldsymbol{\sigma}_2\cdot\mathbf{n}+D'\boldsymbol{\sigma}_1\cdot\mathbf{n}\,\boldsymbol{\sigma}_2\cdot\mathbf{l}$$
$$+E'\boldsymbol{\sigma}_1\cdot\mathbf{m}+F'\boldsymbol{\sigma}_2\cdot\mathbf{m}+G'\boldsymbol{\sigma}_1\cdot\mathbf{m}\,\boldsymbol{\sigma}_2\cdot\mathbf{n}+H'\boldsymbol{\sigma}_1\cdot\mathbf{n}\,\boldsymbol{\sigma}_2\cdot\mathbf{m}, \quad (16)$$

where $A, \ldots, H$ and $A', \ldots, H'$ are ordinary scalar functions depending on θ and E. These functions are related to the matrix elements given in table 1. In table 2 we have epressed them all by $M^{(\pm)}_{kl}$. For the N—N problem $B = C$ and G, H together with all primed functions vanish †. We have checked our formulae by comparing them for this particular case with the results of Stapp

† This is true in a P and T conserving theory. A theory in which P and T are not conserved was considered by Woodruff [18]).

et al. [9]). Operators proportional to G, H, E', F', G', H' are time pseudoscalars; however, their presence does not violate the time reversal invariance. The latter is here assured by the symmetry of T^J in all indices, the channel index α included.

TABLE 2

The scalar coefficients of the T matrix

$4A$	$2M_{11}^{(+)}+M_{00}^{(+)}+M_{ss}^{(+)}$
$4B$	$i\sqrt{2}\left[M_{01}^{(+)}-M_{10}^{(+)}+M_{1s}^{(+)}-M_{s1}^{(+)}\right]$
$4C$	$i\sqrt{2}\left[M_{01}^{(+)}-M_{10}^{(+)}-M_{1s}^{(+)}+M_{s1}^{(+)}\right]$
$4D$	$\left[M_{00}^{(+)}-2M_{1-1}^{(+)}-M_{ss}^{(+)}\right]$
$4E$	$\left[M_{11}^{(+)}+M_{1-1}^{(+)}-M_{ss}^{(+)}\right]-\left[M_{11}^{(+)}-M_{1-1}^{(+)}-M_{00}^{(+)}\right]\cos\theta-\sqrt{2}\sin\theta\left[M_{10}^{(+)}+M_{01}^{(+)}\right]$
$4F$	$\left[M_{11}^{(+)}+M_{1-1}^{(+)}-M_{ss}^{(+)}\right]+\left[M_{11}^{(+)}-M_{1-1}^{(+)}-M_{00}^{(+)}\right]\cos\theta+\sqrt{2}\left[\sin\theta\left[M_{10}^{(+)}+M_{01}^{(+)}\right]\right.$
$4G$	$\sin\theta\left[M_{11}^{(+)}-M_{1-1}^{(+)}-M_{00}^{(+)}\right]-\sqrt{2}\cos\theta\left[M_{10}^{(+)}+M_{01}^{(+)}\right]-\sqrt{2}\left[M_{s1}^{(+)}+M_{1s}^{(+)}\right]$
$4H$	$\sin\theta\left[M_{11}^{(+)}-M_{1-1}^{(+)}-M_{00}^{(+)}\right]-\sqrt{2}\cos\theta\left[M_{10}^{(+)}+M_{01}^{(+)}\right]+\sqrt{2}\left[M_{s1}^{(+)}+M_{1s}^{(+)}\right]$
$4A'$	$\cos\frac{1}{2}\theta\left[2M_{11}^{(-)}+M_{s0}^{(-)}+M_{0s}^{(-)}\right]+\sqrt{2}\sin\frac{1}{2}\theta\left[M_{10}^{(-)}+M_{01}^{(-)}-M_{s1}^{(-)}-M_{1s}^{(-)}\right]$
$4B'$	$\cos\frac{1}{2}\theta\left[2M_{11}^{(-)}-M_{s0}^{(-)}-M_{0s}^{(-)}\right]+\sqrt{2}\sin\frac{1}{2}\theta\left[M_{10}^{(-)}+M_{01}^{(-)}+M_{s1}^{(-)}+M_{1s}^{(-)}\right]$
$4C'$	$i\sqrt{2}\cos\frac{1}{2}\theta\left[M_{10}^{(-)}-M_{01}^{(-)}+M_{1s}^{(-)}-M_{s1}^{(-)}\right]+i\sin\frac{1}{2}\theta\left[2M_{1-1}^{(-)}+M_{0s}^{(-)}-M_{s0}^{(-)}\right]$
$4D'$	$i\sqrt{2}\cos\frac{1}{2}\theta\left[M_{10}^{(-)}-M_{01}^{(-)}-M_{1s}^{(-)}+M_{s1}^{(-)}\right]+i\sin\frac{1}{2}\theta\left[2M_{1-1}^{(-)}-M_{0s}^{(-)}+M_{s0}^{(-)}\right]$
$4E'$	$\sin\frac{1}{2}\theta\left[2M_{11}^{(-)}+M_{s0}^{(-)}+M_{0s}^{(-)}\right]-\sqrt{2}\cos\frac{1}{2}\theta\left[M_{10}^{(-)}+M_{01}^{(-)}-M_{s1}^{(-)}-M_{1s}^{(-)}\right]$
$4F'$	$\sin\frac{1}{2}\theta\left[2M_{11}^{(-)}-M_{s0}^{(-)}-M_{0s}^{(-)}\right]-\sqrt{2}\cos\frac{1}{2}\theta\left[M_{10}^{(-)}+M_{01}^{(-)}+M_{s1}^{(-)}+M_{1s}^{(-)}\right]$
$4G'$	$i\sqrt{2}\sin\frac{1}{2}\theta\left[M_{10}^{(-)}-M_{01}^{(-)}+M_{1s}^{(-)}-M_{s1}^{(-)}\right]-i\cos\frac{1}{2}\theta\left[2M_{1-1}^{(-)}+M_{0s}^{(-)}-M_{s0}^{(-)}\right]$
$4H'$	$i\sqrt{2}\sin\frac{1}{2}\theta\left[M_{10}^{(-)}-M_{01}^{(-)}-M_{1s}^{(-)}+M_{s1}^{(-)}\right]-i\cos\frac{1}{2}\theta\left[2M_{1-1}^{(-)}-M_{0s}^{(-)}+M_{s0}^{(-)}\right]$

4. The Cross Section and Polarization

With the help of the $T^{(\pm)}$ matrix one can easily find the cross section and all quantities important for the polarization analysis. The prescription is here identical to that in the N—N problem. The cross section for the unpolarized particles in the channel $\alpha \to \alpha'$ is obtained by averaging over all spins:

$$\sigma^{(\pm)}(\alpha \to \alpha') = \tfrac{1}{4}\mathrm{Tr}[T^{(\pm)}T^{(\pm)\dagger}]. \tag{17}$$

Taking $T^{(\pm)}$ as given by (15) and (16) we have

$$\sigma^{(+)}(\alpha \to \alpha') = |A|^2+|B|^2+|C|^2+|D|^2+|E|^2+|F|^2+|G|^2+|H|^2; \tag{18}$$

$$\sigma^{(-)}(\alpha \to \alpha') = |A'|^2+|B'|^2+|C'|^2+|D'|^2+|E'|^2+|F'|^2+|G'|^2+|H'|^2. \tag{19}$$

Since polarized hyperons (antinucleons) are not available in the laboratory we are not interested here in scattering experiments with polarized particles; however, all measurable quantities can be obtained easily from (15) and (16). We calculate only the polarizations of the particles in the final state from a reaction with unpolarized beam and target. Let the vectors $\mathbf{P}_c$ and $\mathbf{P}_d$ denote the polarization of the particles c and d. If the particles a and b are unpolarized we have [17])

$$\mathbf{P}_c^{(\pm)} = \mathrm{Tr}[T^{(\pm)}T^{(\pm)\dagger}\boldsymbol{\sigma}_1]/\mathrm{Tr}\,[T^{(\pm)}T^{(\pm)\dagger}] \tag{20}$$

and a corresponding expression for $\mathbf{P}_d^{(\pm)}$, in which $\boldsymbol{\sigma}_1$ is replaced by $\boldsymbol{\sigma}_2$. A simple calculation shows that $\mathbf{P}_c^{(\pm)}$ and $\mathbf{P}_d^{(\pm)}$ are both proportional to the vector $\mathbf{n}$; we give below the formulae for the magnitudes of $\mathbf{P}_c^{(\pm)}$ and $\mathbf{P}_d^{(\pm)}$:

$$\begin{aligned} P_c^{(+)} &= \frac{2}{\sigma^{(+)}}\,[\mathrm{Re}(AB^*)+\mathrm{Re}(CD^*)+\mathrm{Im}(GE^*)+\mathrm{Im}(FH^*)], \\ P_c^{(-)} &= \frac{2}{\sigma^{(-)}}\,[\mathrm{Re}(B'D'^*)+\mathrm{Re}(F'H'^*)+\mathrm{Im}(A'E'^*)+\mathrm{Im}(C'G'^*)] \end{aligned} \tag{21}$$

$$\begin{aligned} P_d^{(+)} &= \frac{2}{\sigma^{(+)}}\,[\mathrm{Re}(AC^*)+\mathrm{Re}(BD^*)+\mathrm{Im}(HE^*)+\mathrm{Im}(FG^*)] \\ P_d^{(-)} &= \frac{2}{\sigma^{(-)}}\,[\mathrm{Re}(A'C'^*)+\mathrm{Re}(E'G'^*)+\mathrm{Im}(B'F'^*)+\mathrm{Im}(D'H'^*)] \end{aligned} \tag{22}$$

Using the results of table 2 one could express $P_c^{(\pm)}$ and $P_d^{(\pm)}$ in terms of $M_{kl}^{(\pm)}$.

5. The S-State Approximation

In this section we examine more closely the simplest case of a reaction in which a transition occurs only *from* or to the S-state. For the reaction with a high threshold, as for example the reaction $\mathrm{N}+\overline{\mathrm{N}} \to \Lambda+\overline{\Sigma}$, it seems reasonable to assume that the $(\Lambda\Sigma)$ production takes place in the S-state (for energies not larger than about $\approx$ 1 GeV). This process was considered in this approximation by Barshay [5]). Disregarding the subsequent decay of $(\Lambda\Sigma)$ any conclusion can be drawn about parities $(\Lambda\Sigma)$ only from the cross section and the polarizations as given by (21) and (22). The cross section for both cases of relative parity is isotropic and the polarizations (21) and (22) are equal to zero, which is obvious without any calculation.

A much more interesting class of reactions are those in which the threshold is zero and the total rest mass produced in the final state is considerably smaller than that in the initial state. As an example we can take the reaction $\Sigma^-+\mathrm{p} \to \Lambda+\mathrm{n}$. We examine these reactions in the low energy region where the assumption that the transition goes only from the S state is justified. In this

approximation we have in each case of relative parity only three matrix elements T^J different from zero, given in table 3.

TABLE 3

Matrix elements of T^J (the channel indices are omitted)

Relative parity even $I_aI_b = I_cI_d$		Relative parity odd $I_aI_b = -I_cI_d$	
transition	matrix element	transtition	matrix element
$^1S_0 \to {}^1S_0$	$\langle 00\|T^0\|00\rangle \equiv a$	$^3S_1 \to {}^3P_1$	$\langle 11\|T^1\|10\rangle \equiv \alpha$
$^3S_1 \to {}^3S_1$	$\langle 10\|T^1\|10\rangle \equiv b$	$^1S_0 \to {}^3P_0$	$\langle 11\|T^0\|00\rangle \equiv \beta$
$^3S_1 \to {}^3D_1$	$\langle 12\|T^1\|10\rangle \equiv c$	$^3S_1 \to {}^1P_1$	$\langle 01\|T^1\|10\rangle \equiv \gamma$

The cross section in both cases is isotropic;

$$\sigma^{(+)} = \frac{1}{16p^2}(|a|^2+3|b|^2+3|c|^2), \quad \sigma^{(-)} = \frac{1}{16p^2}(|\gamma|^2+3|\alpha|^2+3|\beta|^2). \tag{23}$$

For even relative parity the polarizations of the final particles are equal to zero. This is not the case for odd relative parity if only the matrix elements α and β do not vanish. One obtains

$$P_c^{(-)} \approx \frac{3\sqrt{2}}{16p^2\sigma^{(-)}} \sin 2\theta \, \mathrm{Im}(\beta\alpha^*), \quad P_d^{(-)} = -P_c^{(-)}. \tag{24}$$

The polarizations $P_c^{(-)}$ and $P_d^{(-)}$ are opposite in sign and they change sign when θ passes through $\frac{1}{2}\pi$. Fig. 1 represents the angular dependence of the polarizations.

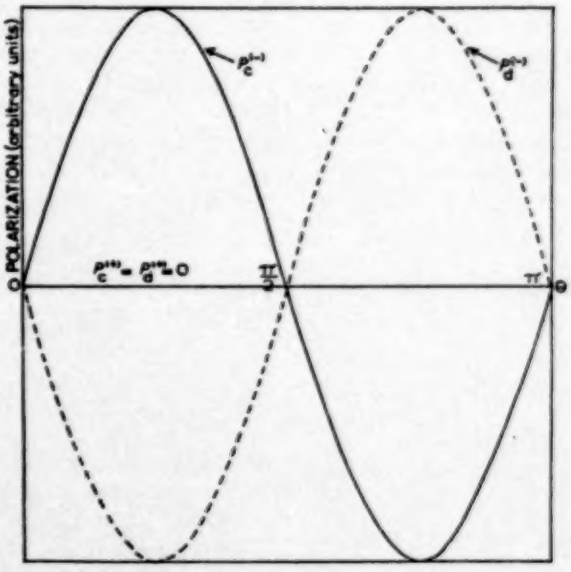

Fig. 1. The angular dependence of the polarizations.

6. Conclusions

In this paper we propose an experimental test for the determination of the relative parity of barions in a reaction a+b → c+d. We considered a reaction with zero threshold, in which in the initial state only the S-wave is taken into account. This assumption being justified in the low energy region can be checked by experiment. Only reactions with unpolarized particles were discussed and it is found that the final state particles are unpolarized if relative parity is even ($I_aI_b = I_cI_d$), and polarized perpendicular to the reaction plane if the relative parity is odd ($I_aI_b = -I_cI_d$). The angular dependence of the polarization is given in fig. 1. This result can serve as a test for the determination of the parity; the isotropy of the cross section and the existence or non-existence of a polarization determines whether we have $I_aI_b = I_cI_d$ or $I_aI_b = -I_cI_d$.

References

1) S. M. Bilenky, Nuovo Cim. **10** (1958) 1049
2) L. W. Okun and I. J. Pomerantschuk, JETP **34** (1958) 997
3) S. M. Bilenky and R. M. Ryndin, Nuovo Cim. **12** (1959) 106;
A. Bohr, Nuclear Physics **10** (1959) 486
4) A. Pais and S. B. Treiman, Phys. Rev. **109** (1958) 1759
5) S. Barshay, Phys. Rev. **113** (1959) 349
6) S. B. Treiman, Phys. Rev. **113** (1959) 355
7) S. C. Wright, Phys. Rev. **99** (1955) 996
8) H. P. Stapp, University of California, thesis, UCRL 3098 (1955)
9) H. P. Stapp, T. J. Ypsilantis and N. Metropolis, Phys. Rev. **105** (1957) 302
10) J. M. Blatt and L. C. Biedenharn, Phys. Rev. **86** (1952) 399; Revs. Mod. Phys. **24** (1952)258
11) Chou Kuang-Chao and M. I. Shirokov, JETP **34** (1958) 1230
12) M. Jacob and G. C. Wick, Annals of Physics **7** (1959) 404
13) M. E. Rose, Elementary Theory of Angular Momentum Wiley, New York, 1957)
14) E. P. Wigner, Gruppen theorie und ihre Anwendung auf die Quantenmechanik der Atomspektren (Edwards, Ann Arbor, Michigan, 1944) Ch. XII
15) R. Huby, Proc. Phys. Soc. A **67** (1954) 1103
16) L. Wolfenstein and J. Ashkin, Phys. Rev. **85** (1952) 947
17) R. Oehme, Phys. Rev. **98** (1955) 147
18) A. E. Woodruff, Annals of Physics **7** (1959) 65

8.A

Nuclear Physics **20** (1960) 475—486; © *North-Holland Publishing Co., Amsterdam*

Not to be reproduced by photoprint or microfilm without written permission from the publisher

LONGITUDINAL POLARIZATION OF BETA-ELECTRONS

P. E. SPIVAK and L. A. MIKAELIAN

I. V. Kurchatov Atomic Energy Institute, USSR Academy of Sciences, Moscow, USSR

Received 26 April 1960

Abstract: The longitudinal polarization of beta-electrons of P^{32}, In^{114}, Sm^{153}, Lu^{177}, Ho^{166} and Au^{198} has been measured by the Mott scattering method at 300 to 340 keV. Differences up to 10 % have been detect in the degree of polarization for the isotopes under investigation. It has also been found that the absolute polarization values lie in the interval $-(0.86—0.97)\ v/c$. The error in absolute measurements, ± 3 %, does not include possible inaccuracies of theoretical calculation connecting the degree of polarization and scattering asymmetry.

1. Introduction

The discovery of non-conservation of parity in weak interaction [1, 2]) led to a revision of the pattern of beta-decay. Thus, it appeared that according to the two-component neutrino theory [3, 4, 5]), the beta-decay electrons of non-polarized nuclei must be longitudinally polarized. This phenomenon was soon discovered in the first experiments [6, 7, 8]) conducted with this purpose in view. It was shown that the effect within an accuracy of ± 15 to 20 % agreed with the estimated value $\pm v/c$ for negatons and positons. During three subsequent years more than 20 papers [9]) were published, various methods being used and nuclei with different Z and transition types studied. A considerable number of these investigations had an accuracy which did not exceed ± 15 %. Most of the results of those (refs. [10–17]), for example) which had a higher degree of accuracy, lie approximately in the interval (0.9 to 1) v/c.

The current opinion was that the deviations from v/c were most likely attributable to systematic experimental errors, and that as the experiments grew more accurate it would appear that the polarization of electrons emitted by different nuclei would be the same and equal to v/c (with the exception of special cases, such as RaE). Yet at present, few authors indicate an accuracy of 3 to 5 % for their measurements, and if the value $P = (1.0 \pm 3\ \%) v/c$ [12]) is obtained for P^{32}, the ratio of the electron polarization of Au^{198} to that of Co^{60} proves to be $(0.87 \pm 5\ \%)$ [13]).

Our principal aim in the present paper is to decide, with the highest possible accuracy, at least whether the electron polarizations in the beta-decay of different nuclei are different. The accuracy of our relative measurements has proved to be sufficient to show that these differences actually exist for the allowed transitions of P^{32} and In^{114} and the Coulomb transitions of Au^{198}, Lu^{177}, Sm^{153}

and Ho^{166}. As to the deviation of the polarization from v/c, the accuracy of absolute measurements also performed will be dealt with in section 5.

2. Method

The Mott scattering method was used in the present experiment. Longitudinal polarization was transformed into transverse in cross fields and measured by scattering asymmetry on gold.

In this case polarization is connected with asymmetry through the expression

$$\frac{P}{\beta} = \frac{A}{\beta S}, \quad A = \frac{I_1/I_2 - 1}{I_1/I_2 + 1},$$

where I_1 and I_2 are the intensities of "right"-"left" scattering and S is a function of the angle and energy.

With the optimum choice of energies (300 to 500 keV), the angle of observation of scattered electrons (110° to 140°) and the thickness of scatterer (equal to several tenths of mg/cm²), the ratio of scattering intensities $I_1/I_2 \approx 1.6$.

A relatively high asymmetry makes this method especially attractive as compared with others. Yet even in this case the measurements of polarization with good accuracy, ± 3 % for example, is quite a problem. The accuracy of results is indeed limited mainly by the methodical errors in determining apparatus asymmetry, multiple scattering, depolarization in the source and other quantities. Yet to obtain these quantities it is necessary to conduct repeated measurements of scattering asymmetry, the error of which is double that of the scattering intensity ratio: with $I_1/I_2 = 1.6$, one has $\delta(A)/A = 2\delta(I_1/I_2)/(I_1/I_2)$.

In other known methods the requirements of accuracy of the measurements are even more rigorous owing to a smaller difference in the readings for polarized and non-polarized electrons.

Relative measurements, however, can be made with greater accuracy if depolarization in the sources is small while the energetical and angular distribution of the electrons impinging onto the scatterer is constant no matter which source is investigated. In this case the errors of numerous corrections entering into absolute measurements become negligibly small for the polarization ratio.

3. Main Specification of Apparatus and Check Experiments

3.1. EXPERIMENTAL SET-UP

The installation is represented schematically in fig. 1. The sources were installed about 10 cm upward of the axis of the instrument in the position shown in the figure. The electrons deflected by a transverse magnetic field at an angle $\approx 90°$, passed through a collimator enclosed in an iron pipe, a magnetic shield, until they reached the cross fields. Then the longitudinal polarized flux

of electrons again passed through the magnetic shield and the collimator enclosed in it until it reached the scatterer. The scattered electrons were detected by telescopes with axes at 120° with respect to the direction of the electron flux. Each telescope consisted of two Geiger counters in coincidence with a filter about 25 mg/cm² thick between them. The bodies of the counters were plexiglass rings (10 to 12 mm high and 20 and 25 mm in diameter) coated with a conductive layer of graphite. The volume of the counters was separated from vacuum with a thick film of about 0.3 mg/cm² thick. The sources and scatterers were installed in a strictly fixed position and could be changed without violating the high vacuum.

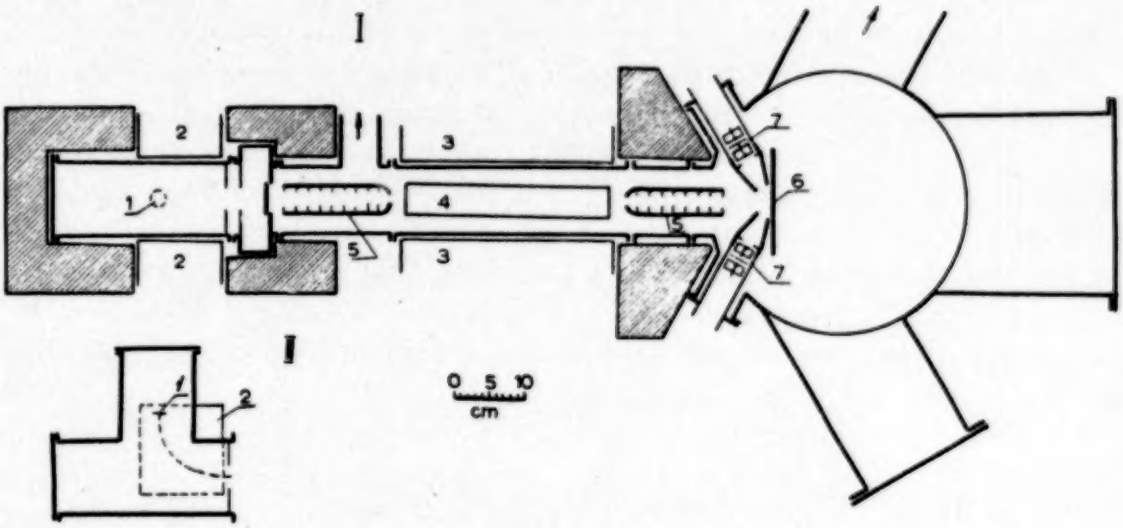

Fig. 1. Schematic plan of set up.
I. Horizontal cross section.
II. Vertical section of the chamber with a source.
1. A source. 2. Magnet poles of preliminary selection. 3. Magnet poles of the cross-field system. 4. Electrostatic plates of the cross-field system. 5. Magnetic shields with diaphragms. 6. A scatterer. 7. Telescopes.

3.2. CALIBRATION OF THE SYSTEM OF CROSS FIELDS

The strengths of the magnetic field H and electric field E necessary for the rotation of the spin of electrons with momentum p at an angle φ were determined from the relations

$$\varphi = \frac{eHL(1-\beta^2)^{\frac{1}{2}}}{pc}, \quad E = \beta H,$$

where L is the length of the region of cross fields (about 300 mm). The calibration of the instrument which controlled the difference of potentials between the plates was carried out by the well-known values of magnetic fields and the energy of conversion electrons passing the cross fields (the In^{114} 187 keV line was used). The value of the applied fields corresponded to a 90° spin rotation.

Therefore, a relatively large error which might occur in the spin rotation due to the error in determining the effective length L of cross fields did not lead to any appreciable error in the asymmetry measured. The test experiment in which the spin angle was deflected from 90° by $\pm 15°$ showed that the choice of the values of fields was correct: in both cases the asymmetry declined by 3 ± 2 %.

3.3. SOURCES

All sources were deposited on 6μm aluminium foil and had a diameter of 20 mm. The sources of Sm, Lu, Ho and In were made of finely dispersed non-active powder of the oxides of these elements. The sources of Sm and In were enriched by the isotopes Sm^{152}(98 %) and In^{113} (75 %).

The layers were deposited by evaporating the suspension of these powders in alcohol with an admixture of bakelite. The layers thus obtained reliably adhered to the mount after being dried at a temperature of about 200°C. A layer of gold was deposited by evaporation in vacuum. The sources were sealed in aluminium containers and irradiated in a reactor. P^{32} was made by repeatedly dabbing and evaporating an active nitric acid solution. The thickness of sources varied within 0.6 to 1.3 mg/cm^2. The low aperture ratio of the instrument precluded measurements with sources possessing a low specific activity. The most intense source Sm has an activity of up to 3 c. The activity of In amounted to approximately 100 mc.

3.4. SPECTRA OF ELECTRONS

The spectra of each source were carefully investigated to check that in the selected region of energies there are no conversion lines which might be

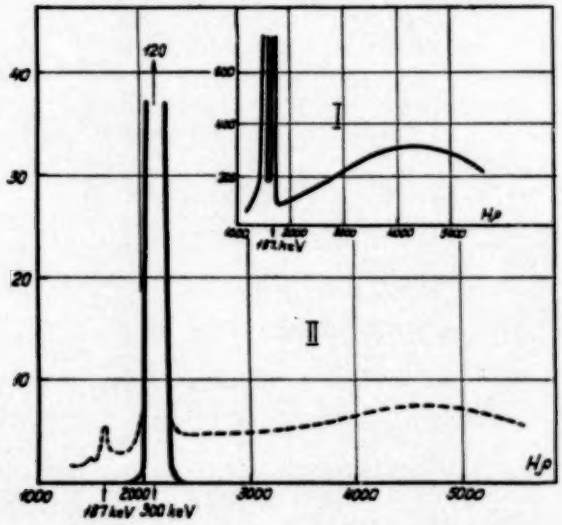

Fig. 2. Spectra of electrons.
I. In^{114} electron spectrum.
II. The spectrum of In^{114} electrons having passed through the cross-field system: a solid line—with preliminary selection of energy and the dotted line—without preliminary selection.

connected with the admixture of extraneous elements. Relative measurements of polarization were conducted at 340 keV for all sources except for gold. This energy was close to the maximal value which we could produce by the cross fields with a 90° spin deflection, the spectrum of the electrons entering the region of cross fields extending approximately from 240 to 440 keV. Fig. 2 exemplifies the spectra for the In^{114} source. Owing to the preliminary selection, the spectrum of the electrons impinging onto the scatterer did not depend on the shape of the spectrum of the source and had the form of a line standard for all sources, with a half width of 40 keV and a relative intensity less than 1 % outside the region 340 ± 40 keV. This made it possible to dispense with not easily estimated corrections which would have arisen in comparing sources with sharply different shapes of spectra.

3.5. EXCLUSION OF DIFFERENCES IN THE EFFICIENCY OF COUNTERS

Measurements of electron scattering asymmetry should allow for the differences in the efficiency of the counters. The cross-field method makes it possible easily to eliminate the efficiency of the counters from the results obtained. If the signs of electric and magnetic fields change simultaneously, the spin of the electrons impinging onto the scatterer is reversed from the position "upward" ($\uparrow$) into the position "downward" ($\downarrow$). The ratio of scattering intensities I_1/I_2, obtained from the measurement for the two spin directions, $I_1/I_2 = ((I_L/I_K)^{\uparrow}(I_K/I_L)^{\downarrow})^{\frac{1}{2}}$, does not contain the coefficients of efficiency of the counters. The effect of slow changes in the latter's efficiency (which could reach 3 to 5 % during the experiment) was eliminated by performing many sets of measurements with alternation of the signs of the fields.

3.6. BACKGROUND OF COUNTERS

The low sensitivity of counters to gamma-rays and a good protection of the source and counters made it possible to obtain a low level of background: 60 to 70 coincidences an hour. The background value was determined mainly by cosmic rays and radioactive solutions and changed little even when to most intense sources were investigated. Owing to the preliminary selection of electrons in a transverse magnetic field, there was no direct visibility from the source to the scatterer, and the gamma-rays of the source could not get into the latter. The test experiments showed that the background remains constant in two different methods of measurement: a) the beam passes into the chamber, the scatterer is removed; b) the scatterer is in place while the direction of one of the fields has been reversed and the beam did not pass.

The low level of background facilitated measurements with relatively weak sources and thin scatterers and to a certain extent compensated for the small aperture ratio of the instrument.

3.7. STABILITY OF RESULTS

In using the method of transforming longitudinal electron polarization into transverse in cross fields, it is necessary to take measures ensuring the independence of the scattering angle of electrons impinging onto the scatterer, and consequently of apparatus asymmetry, from the position of the source and the value of the field. One of the methods to achieve this is a sufficiently rigid collimation of the beam, which was used in the apparatus described. The adequate degree of collimation of the beam and the adjustment of the equipment were selected as a result of experiments to measure the dependence of asymmetry on the position of the source and the deviations of the field values from the established quantities. These experiments were conducted with the aid of the most intense source of Sm, making it possible to obtain an adequate statistical accuracy within a short time. As a result, the asymmetry value changed no more than by (1 to 1.5 %) as the current of the preliminary magnet changed by ± 15 %, and remained constant within 1 % as the strength of the cross fields changed by a value several times greater than the possible inaccuracy in their positioning.

Careful experiments showed that the asymmetry does not depend on how accurately the source is established in its effective position. For a sufficiently large displacement of the source the intensity of the beam hitting the scatterer declined sharply because of the rigid collimation. The scattering asymmetry, on the other hand, did not change to any perceptible degree. As a result of the above experiments in investigating the stability of apparatus asymmetry, and the subsequent measurements in which the scattering asymmetry of Sm electrons was compared with the asymmetry for other sources, it was possible to analyze about 20 measurements of Sm beta-electron scattering asymmetry, each of which had a statistical error approximately equal to 2 %. This analysis revealed non-statistical fluctuations, the maximum value of which was set at ± 1 %.

3.8. ELECTRON DEPOLARIZATION IN SOURCES

Depolarization in the sources was determined by several test experiments. The comparison of the sources of Sm 0.8 mg/cm^2 and 0.2 mg/cm^2 thick and of Au of the same thicknesses showed no difference in the asymmetry value within a measurement accuracy of ± 2 %. In the subsequent experiments layers of gold, silver and aluminium of varying thickness up to 10 mg/cm^2 were deposited on both sides of the source. The observed decrease of asymmetry made it possible to make a more accurate estimate of the depolarization in the sources, which proved to be equal to

$(1.7\pm0.5)\%$ for Au of 0.8 mg/cm^2,
$(1\ \pm0.5)\%$ for Sm of (0.9 ± 0.2) mg/cm^2,
$(1.2\pm0.5)\%$ for Lu of (1.6 ± 0.3) mg/cm^2,
$(1.3\pm0.5)\%$ for Lu of (0.9 ± 0.2) mg/cm^2,
$(1\ \pm0.5)\%$ for Ho of (0.8 ± 0.2) mg/cm^2
and $(0.8\pm0.5)\%$ for P of (1.8 ± 0.3) mg/cm^2.

3.9. THE ROLE OF ELECTRONS SCATTERED OFF THE WALL OF THE INSTRUMENT

To decrease the scattering of electrons, the walls of the chambers in which the sources and the scatterer were placed, were coated with plexiglass covered with a thin conductivity layer of graphite and grounded.

A number of test experiments showed that electron scattering in the chamber with a source and scattering at the edges of the first diaphragms leads to a depolarization, the value of which was set at 0.5 %.

Considerable difficulties had to be overcome to decrease the role of scattering at the edges of the chamber in which the counters and the scatterer were placed. In passing through a layer of gold practically all electrons of the beam hit the walls and in scattering off the latter the probability to hit the counters directly or through the scatterer was not so small as it seemed at first. In the absolute polarization values that we have published before [18]) account had to be taken of this effect and a correction of $(3\pm1.5)\%$ was introduced. In the equipment described here the dimensions of the chamber were considerably larger: the chamber was a cylinder of 350 mm in diameter and about 400 mm in height with deep baffles opposite each of the counters and on the path of the beam. A number of test experiments were carried out to determine the role of scattering off the chamber walls in conditions close to those in which the asymmetry was measured. These experiments with a very high sensitivity showed that corrections had to be introduced into the quantity of asymmetry: 0.4 % due to scattering off the chamber walls and 0.1 % due to scattering off the plexiglass ends of the counters.

4. Measurements and Results

4.1. RELATIVE MEASUREMENTS OF POLARIZATION

Relative polarization values were obtained by comparing the scattering asymmetry of each source under investigation with that of Sm^{153}. The measurements were conducted on the same scatterer with the same energy and a spin deflection of 90°. The results of the above test experiments, showing that the spectra of scatterer-hitting electrons and apparatus asymmetry do not change with the change of sources, suggest that polarizations were compared in strictly identical conditions.

From 3 to 5 series of measurements were performed for each source on and off during several months. Each series included measurements for the investigated source accurate to 2—3 % and measurements for Sm^{153} performed at the beginning, in the middle and at the end of the series. Table 1 represents relative polarization values obtained from the ratio $p/p_{Sm} = \Delta/\Delta_{Sm}$.

TABLE 1

Results of relative measurements of polarization

	340 keV					240 keV	
Isotope	Sm^{153}	P^{32}	In^{114}	Lu^{177}	Ho^{166}	Sm^{153}	Au^{198}
P	1.00	1.05±1.8 %	0.96±3.2 %	0.95±1.8 %	0.94±1.8 %	1.00	0.97±1.8 %

These ratios are readjusted for differences in depolarization in the sources in accordance with the values obtained before. Errors of the polarization ratios obtained include:

a) errors Δ for Sm: ±1 %;

b) error Δ for Lu, Ho, P and Au: 1.5 %; and for In: 2.5 %;

c) error of relative depolarization values in the sources: ±0.5 %.

The polarization ratios given need no correction: those corrections which are attributable to apparatus asymmetry, electron depolarization on the path from the source to the scatterer, the final angle of observation of scattered electrons, etc., are completely eliminated from the polarization ratio.

4.2. ABSOLUTE MEASUREMENTS

Absolute measurements were performed for the most intense source: Sm^{153}, at an electron energy of 300 keV. They consisted in determining the role of multiple scattering in the scatterer and the apparatus asymmetry.

The apparatus asymmetry was determined by experiments in which a gold scatterer was replaced by an aluminium one. Since the angular scattering distributions for gold and aluminium differ it was necessary to bring the apparatus asymmetry close to zero (as is indicated below, its value amounted to 0.01 in the final measurements). Preliminary experiments showed that thick layers of aluminium (of the order of 5 mg/cm²) were totally unsuitable for correct measurements of apparatus asymmetry. In further experiments, therefore the apparatus asymmetry was artificially changed by about 5 % and the changes were controlled with a very thin scatterer of aluminium (≈ 0.5 mg/cm²). Simultaneously, the apparatus asymmetry was measured with thicker scatterers (2, 3, 5 mg/cm²). As a result of these experiments it was shown that a 2 mg/cm² scatterer still reproduced the changes in apparatus asymmetry correctly. Measurements with a 3 mg/cm² scatterer already led to a slight error while the results obtained with 0.5 mg/cm² and 5 mg/cm² scatterers differed by ≈ 0.1.

The effects observed are accounted for by the angular scattering distribution caused by multiple electron scattering in aluminium. This is borne out by the fact that only for sufficiently thin layers the intensity increases practically linearly with the thickness of the scatterer (the absolute values of the thickness being determined by weighing with an accuracy better than 1 %). For a 3 mg/cm² scatterer, when the distortions of measurements of apparatus asymmetry are already perceptible, the deviations from linear dependence reach ≈ 15 %.

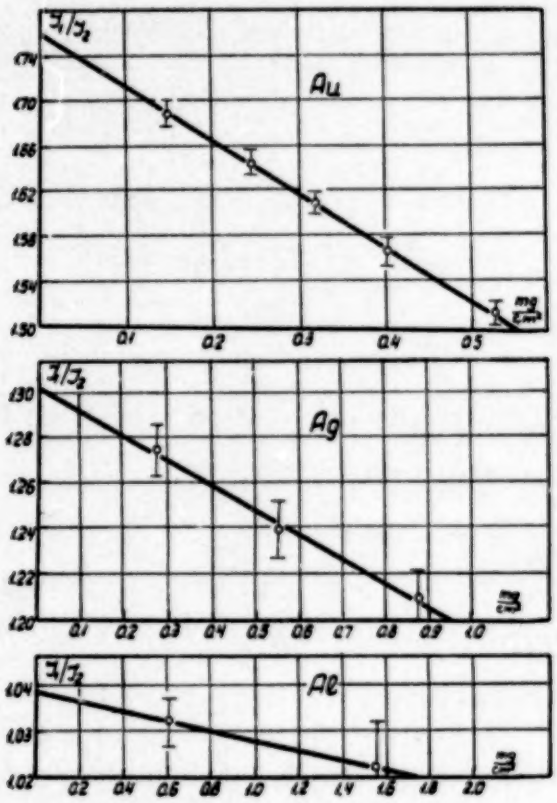

Fig. 3. The ratio of "left-right" scattering intensities depending on the thickness of gold, silver and aluminium scatterers.

For gold scatterers the absolute values of thickness could not be determined by sufficiently accurate weighing. Yet only relative thicknesses of layers need be known for correct extrapolation to zero. For finding relative thicknesses, intensities for various scatterers were compared at the operational energy of 300 keV and at a higher energy of 500 keV. It was found for which scatterers deviations from linear dependence of intensity increase are not too great.

For measuring the asymmetry we confined ourselves to the maximum thickness of 1.6 mg/cm² for aluminium and 0.5 mg/cm² for gold scatterers, for which the above-mentioned deviations do not exceed 8 to 10 %.

Fig. 3 shows the results of measurement of the intensity ratios I_1/I_2 for

Al, Ag and Au. The counting rates for the thinnest scatterers of Au, Ag and Al amounted approximately to 126, 60 and 30 counts per min respectively. The background, the effect of the sublayer scatterer film and the effect of scattering off the chamber walls, which, all combined, did not exceed 2 % of the quantities I for the thinnest gold, were subtracted from the quantities I_1 and I_2. The extrapolated values of I_1/I_2 and the corresponding asymetry values Δ are represented in table 2. The same table lists the values of S at $\beta = 0.776$ and

TABLE 2

Extrapolated intensity ratios and corresponding asymmetries

Scatterers	Au	Ag	Al
I_1/I_2	1.765±0.8 %	1.305±1 %	1.039±0.8 %
Δ	0.277±1.6 %	0.132±5 %	0.019±20 %
S at $\beta = 0.776$	0.427	0.208	0.038
Δ_{th}	0.331	0.161	0.0295

the quantity $\beta S = \Delta_{th}$ taken from N. Sherman's tables. The following corrections were introduced into the polarization value from the data of table 2:

depolarization in the source: $(1\pm0.5)\%$;

depolarization on the path from the source to the scatterer: $(2\pm1)\%$;

final size of the scatterer and the angles of observation: $(1.5\pm0.5)\%$;

error in determining the effective value βS: $(\pm1)\%$.

As a result, the polarization of electrons emitted in the beta-decay of Sm^{153} at 300 keV proved equal to $0.92\beta\pm2.5$ %. Apparatus asymmetry in these measurements was not great: 0.01. The asymmetry value for silver scatterers yields the same polarization value but with lower accuracy: 6 to 7 %.

TABLE 3

Absolute values of longitudinal polarization

Isotope	Sm^{153}	P^{132}	In^{114}	Lu^{177}	Ho^{166}	Au^{198}
$-P/v/c$	0.92±2.7 %	0.97±3.4 %	0.88±4.2 %	0.87±3.4 %	0.86±3.4 %	0.89±3.4 %

Table 3 shows electron polarization for the isotopes investigated. The quantities were obtained with the help of the results of relative measurement. It will be recollected in this connection that relative measurements for Au^{198} were performed at 240 keV and for the remaining isotopes at 340 keV.

5. Discussion of Results

The results of relative measurements show that electron polarizations are different for the isotopes investigated. It is noteworthy that polarizations for P^{32} and In^{114}, transitions in which are allowed and belong to the Gamow-Teller type, differ by roughly 10 %. The values obtained for P^{32} and Au^{198} within error coincide with the data of the refs. [12, 13]).

Though we tried with utmost care to track all possible causes which might lead to an underestimation of polarization, it seems to us that the absolute values obtained cannot be regarded as finally established. To begin with, it is necessary to check the theoretical calculations of the function S representing the connection between scattering asymmetry and polarization value. Unfortunately, experiments on non-polarized double electron scattering do not yield a better accuracy than 10 % for the value of S. We intend to repeat these experiments at the earliest opportunity for electrons with energies from 200 to 300 keV. We also hope to check the correctness of the estimate of depolarization on the path of the beam from the source to the scatterer in the installation used in the present paper.

It is impossible to predict the results of these experiments. If it turns out that the polarization corrections are great and reach 10 %, the polarization values in this case will shift to the interval $(0.95—1.05)v/c$. Then the deviations from the value v/c would not exceed 5 % which would obviously facilitate the explanation of this effect by the influence of the nuclear structure. If, on the other hand, the true polarization values are close to those obtained in the present work, it would be interesting to carry out measurements of longitudinal polarization for the simplest nucleus, tritium (for the neutron it is probably practically impossible). These measurements could show whether the influence of the nuclear structure is the only cause of the deviations observed, provided, of course, it were known beforehand that very small deviations from v/c ought so be expected for tritium, just as for the neutron [20]): it is highly desirable that tuch quantitative estimates for tritium should be performed.

The authors are indebted to V. I. Levin and his colleagues who prepared the source of P^{32} and the personnel of the RFT who ensured the irradiation of sources for a considerable period of time.

References

1) T. D. Lee and C. N. Yang, Phys. Rev. **104** (1956) 254
2) C. S. Wu, E. Ambler, R. H. Hayward, D. D. Hoppes and R. P. Hudson, Phys. Rev. **106** (1957) 1361
3) L. D. Landau, JETP **32** (1957) 405, 407; Nuclear Physics **3** (1957) 127
4) T. D. Lee and C. N. Yang, Phys. Rev. **105** (1957) 1671

5) A. Salam, Nuovo Cimento **5** (1957) 299
6) H. Frauenfelder, R. Bobone, E. von Goeler, N. Levine, H. R. Lewis, R. N. Peacock, A. Rossi and G. de Pasquale, Phys. Rev. **106** (1957) 386
7) A. I. Alikhanov, G. P. Eliseyev and V. A. Liubimov, JETP **34** (1958) 785
8) M. E. Vishnevsky, B. K. Grigoriev, V. A. Ermakov, S. I. Nikitin, E. V. Pushkin and Yu. V. Trebukhovsky, Nuclear Physics **4** (1957) 271
9) Ya. Smorodinsky, Uspekhi Fiz. Nauk. **57** (1959) 44
10) I. S. Geiger, G. T. Ewan, R. L. Graham and D. R. Mackenzie, Phys. Rev. **112** (1958) 1684
11) A. I. Alikhanov, G. P. Eliseiev and V. A. Liubimov, JETP **34** (1958) 1045
12) A. I. Alikhanov, G. P. Eliseiev and V. A. Liubimov, Nuclear Physics **7** (1958) 655
13) B. H. Ketelle, A. R. Rossi, A. Galonsky and H. B. Willard, Bull. Amer. Phys. Soc. **4** (1959) 76
14) I. F. Turner, G. A. Gard and P. E. Cavanagh, Bull. Amer. Phys. Soc. **4** (1959) 77
15) R. L. Gluerstern and V. W. Hoghes, Bull. Amer. Phys. Soc. **4** (1959) 76
16) M. Bernardini, P. Brovertto, S. Ferrani and A. Pasquarelly, Nuovo Cimento **14** (1959) 787
17) U. Amaldi, Nuovo Cimento **11** (1959) 415
18) P. E. Cavanagh, I. F. Turner, C. F. Colemans, G. A. Gard and B. W. Ridley, Phil. Mag. **2** (1959) 1105
19) L. A. Mikaelyan and P. E. Spivak, JETP **37** (1959) 1168
20) N. Sherman, Phys. Rev. **103** (1956) 1601
21) S. M. Bilenky, R. M. Ryndin, Ya. A. Smorodinsky and Ho Tzo-Hsiu, JETP **37** (1959) 1758

2.A.1

Nuclear Physics **20** (1959) 487—490; © *North-Holland Publishing Co., Amsterdam*

Not to be reproduced by photoprint or microfilm without written permission from the publisher

(n, α) AND (n, p) REACTIONS IN Na^{23}

L. VARGA

Central Research Institute of Physics, Budapest

Received 15 June 1960

Abstract: From the decay curve of the radioactive nuclei produced in the (n, α) and (n, p) reactions occurring in a NaJ(Tl) scintillation crystal irradiated by neutrons of 14 MeV energy the ratio $\sigma(n, \alpha)/\sigma(n, p)$ of the Na^{23} nucleus was computed and found to be 2.4 ± 10 % as compared with 3.1 obtained from the evaporation theory.

A NaJ(Tl) crystal of 1 cm thickness and 2.6 cm diameter was irradiated by neutrons of 14.3 MeV energy produced in T(d, n)He^4 nuclear reaction. The bombarding deuteron beam was accelerated to about 300 keV energy by the radiofrequency-heated Cockroft-Walton generator of our Institute and a T—Ti target, 2.54 cm in diameter, was used.

The Ne^{23} isotope produced by the Na^{23}(n, p) reaction in NaJ crystals decays with a half-life of $t_{\frac{1}{2}} = 36.6 \pm 0.1$ s, emitting β-rays of 4.4 MeV and 3.95 MeV energy with intensities of 67 and 32 % respectively, and γ-rays of 0.44 MeV energy [1]). The Na^{23}(n, α) reaction leads to F^{20} with a half-life of $t_{\frac{1}{2}} = 10.7 \pm 0.2$ s and its 91.5 % β-decay with a maximum energy of a 5.40 MeV is followed by a 1.6 MeV γ-transition to the ground state [2, 3]).

The activated NaJ crystal which acts as a 4π detector was used with a RCA type 5819 photomultiplier, the pulses of which were amplified and transmitted to an integral discriminator adjusted to an acceptance level of 250 keV. The electrons of energies $E > 250$ keV were scaled down in the counting process by a factor of 10^4. Since the major part of the radiation spectrum of both residual nuclei is above 250 keV, in order to minimize the background, the part below 250 keV can be neglected in the calculations of relative cross sections. In addition, so as to reduce the background, the NaJ crystal was placed in a sealed lead container in a nitrogen atmosphere instead of in the usual Al container with MgO reflector. Its surface was slightly dissolved and dried to obtain a thin microcrystalline NaJ reflecting layer.

The decay curve was measured as follows: The counter was turned on for a time interval of about 1 s by periodically operating programming device which caused a photograph to be taken in the following second and subsequently set the counter to zero. The statistical fluctuation in the turning on and off of the counter amounted to about 0.002 s.

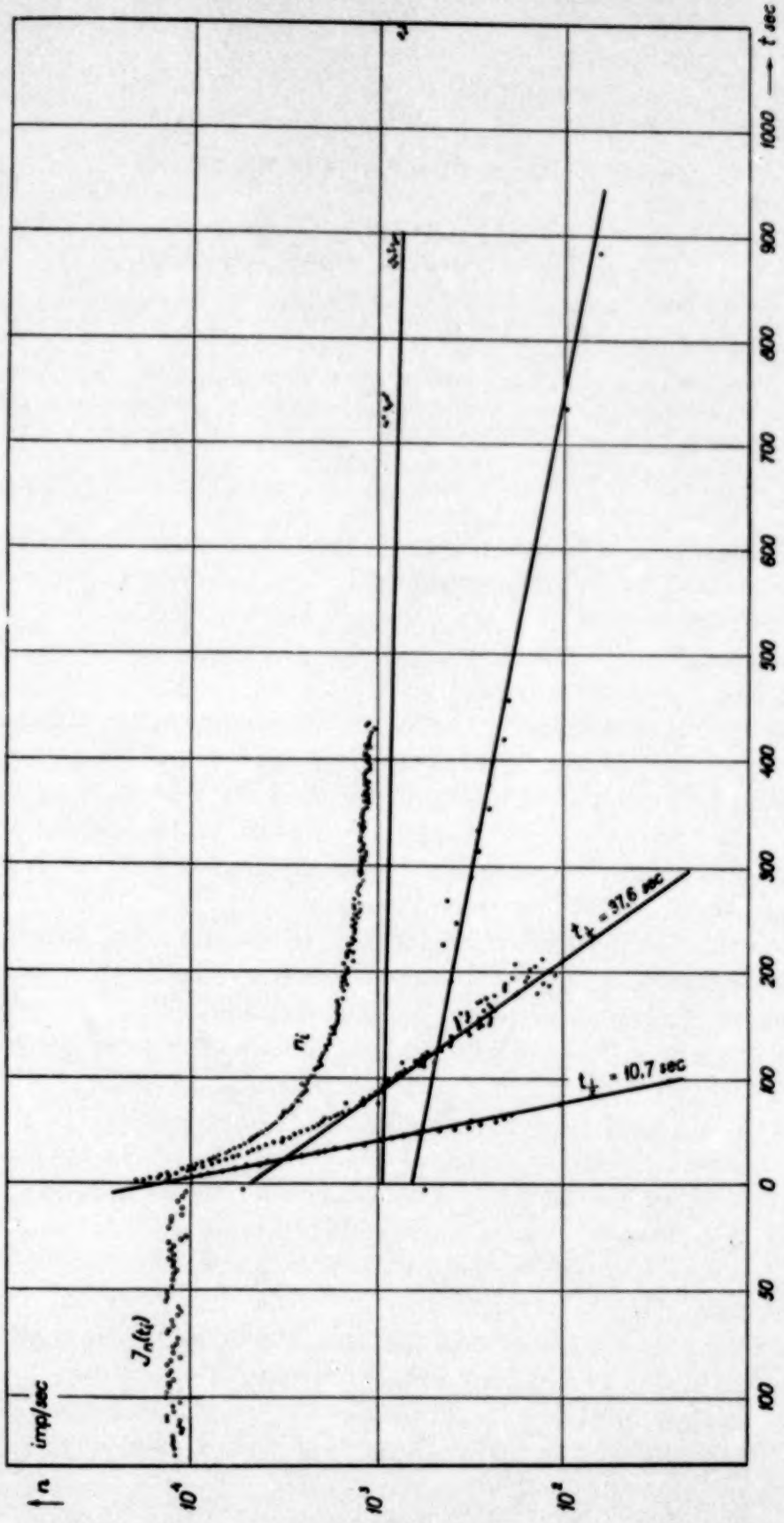

Fig. 1. Decay curve of NaJ activated by 14 MeV neutrons.

The same timing device was used for measuring the neutron flux. Plastic phosphor, 2.54 cm in diameter and 2.54 cm long, was used as target.

Na^{23} was activated for about 120 s, during the last half period of counting the oscillator of the accelerator was switched off and the ion current immediately interrupted. By comparing then the number of counts in this latter half period with that of the preceding ones, the starting time of the decay process can be accurately determined. During the subsequent period of photographing the counter was switched over to the NaJ channel to record again the number of disintegrations of NaJ in the next counting interval.

For greater accuracy the data had to be corrected for dead time. The dead time of the counter was determined by the two-samples method and was found to be 8.88 ± 0.07 μs.

Analysing the decay curve in the usual way the background could be approximated with sufficient accuracy by the calculation of two components. In fig. 1 the plots show the number of counts proportional to the neutron flux as well as the decay curve. The components with half-lives of 10.7 s and 37.6 s, remaining after subtraction of the two background components, are clearly seen.

From simple considerations it follows that the ratio of the yields of the $Na^{23}(n, \alpha)F^{20}$ and $Na^{23}(n, p)Ne^{23}$ reactions is

$$\frac{\sigma(n, \alpha)}{\sigma(n, p)} = \frac{\sum_i I_n(t_i) e^{-\alpha_2 t_i}}{\sum_i I_n(t_i) e^{-\alpha_1 t_i}} \frac{A_1}{A_2} \frac{\alpha_1}{\alpha_2} \frac{1 - e^{-\alpha_2 \Delta t}}{1 - e^{-\alpha_1 \Delta t}},$$

where the first fraction is the correction factor for fluctuations in the neutron flux. Here $I_n(t_i)$ is the number of counts proportional to the neutron flux as measured at the time t_i prior to the termination of the irradiation. α_1 and α_2 are the decay constants, A_1 and A_2 the initial values of the components of the decay curve due to F^{20} and Ne^{23}, respectively.

The result of our measurement was found to be

$$\frac{\sigma(n, \alpha)}{\sigma(n, p)} = 2.4 \pm 10\ \%.$$

For the relative cross sections computing with a rounded-off potential given in K. J. Le Couteur's paper [4]) we obtained $\sigma(n, \alpha)/\sigma(n, p) = 3.1$. This means that the evaporation theory covers only partly the $Na^{23}(n, p)Ne^{23}$ reaction. It seems probable that part of the protons is released by direct reaction.

I have to thank Professor L. Jánossy for valuable remarks in connection with the statistical analysis, Judith Németh for helpful theoretical discussions and Erzsébet Rupp for her assistance in the statistical evaluation.

References

1) J. R. Penning and F. H. Schmidt, Phys. Rev. **105** (1957) 647
2) S. C. Snowdon, Phys. Rev. **78** (1950) 299
3) F. Ajzenberg and T. Lauritsen, Revs. Mod. Phys. **27** (1955) 77
4) K. J. Le Couteur, Proc. Phys. Soc. A **63** (1949) 259

7.C

Nuclear Physics **20** (1960) 491—498; © *North-Holland Publishing Co., Amsterdam*

Not to be reproduced by photoprint or microfilm without written permission from the publisher

A NOTE ON π—π INTERACTION

A. N. MITRA, R. P. SAXENA and P. NARAYANASWAMY

Department of Physics, Muslim University, Aligarh (U.P.), India

Received 16 June 1960

Abstract: Some qualitative aspects of the π—π interaction have been studied with the help of a simple model which incorporates the essential features of the Bethe-Salpeter integral equation for π—π interaction as had been obtained by us some time ago. It is found (i) that a contact type ϕ^4 term does not affect the nature of the interaction which is attractive, and (ii) that the energy at which a resonance occurs increases with the effective $\pi-\pi$ coupling parameter. The numerical solutions of the π—π equations derived in ref. [7]) agree qualitatively with these predictions, and suggest that the $I = 0$ interaction (which has a larger coupling parameter) gives a resonance at a much higher energy than $I = 2$.

1. Introduction

At present there seems to be a considerable amount of theoretical interest on the problem of π—π interaction, especially after the work of Chew and Mandelstam [1]) on the subject. The main difficulty about drawing any firm conclusion from a theoretical study of this interaction is that its experimental verification is largely indirect, viz. through its effects on phenomena like π—N and N—N scattering, τ-decay and so forth. Under such circumstances, a good deal of speculative element is bound to come into the picture, especially because the present-day theories do not yet afford a clear-cut answer to important questions like the occurrence of resonances, or even whether the interaction is attractive or repulsive. Chew *et al.* [2]) have recently given theoretical limits on the s-wave π—π coupling constant, so that their π—π integral equation which had been derived under rather general conditions [1]), may have consistent solutions. It is interesting to note that these limits allow both attractive and repulsive solutions.

Even an appeal to experimental data may not be able to resolve this ambiguity. For example, the s-wave π—π interaction is believed to have an important role in producing the observed energy and angular distributions of the pions in τ-decay. Now one of us has recently made a detailed phenomenological study of this role [3]) and found that the observed distributions seem to admit of a variety of possible π—π mechanisms, even in the domain of attractive interactions, the $I = 0$ force playing a more important role than hitherto assumed [4,5]). On the other hand, Khuri and Treiman [6]) have found recently that the τ-decay data are also compatible with repulsive π—π interactions in $I = 0$ and $I = 2$.

It appears therefore that specific questions like attraction or repulsion cannot be answered without explicit appeal to some specific model. In this respect, the most ideal arrangement would of course have been to study the predictions of the usual pseudoscalar theory, had it not been for our incapacity to go beyond the usually crude approximations which largely tend to obscure the implications of the theory. Nevertheless, the advantages of specific predictions are so great in the absence of adequate experimental information that these alone should justify reasonable approximations on meson theory, of which the old-fashioned non-perturbation treatments are about the best available, especially at low energies. It may be of interest to note that one such treatment carried out by us some time ago [7]), gave the following predictions:

i) Both the s-state interactions $I = 0$ and $I = 2$ were attractive, the former appreciably more than the latter;

ii) $I = 2$ was resonant at a fairly low energy, but $I = 0$ was "too strong" for a low energy resonance.

These results were obtained with the neglect of the (repulsive) π—π divergence.

Without attaching much quantitative significance to these results, we wish to assert (1) that the stronger $I = 0$ interaction is in harmony with the findings of Chew *et al.* [1]) † and (2) that the attractive nature of these interactions is not affected by the presence of the meson-meson divergence. While the first assertion is essentially a consequence of isobaric spin considerations and is largely model-independent, the second statement concerns the role of the repulsive π—π divergence and as such needs further study.

In this paper we have first tried to make a study of the π—π interaction with the help of a soluble model which incorporates the basic features of the π—π integral equation derived in MS, so as to provide a qualitatively clearer understanding of questions like the occurrence of resonances as functions of energy and coupling constant, role of the π—π divergences etc. Secondly, in view of the importance of the $I = 0$ state with respect to τ-decay data as found recently [3]), we have made a further numerical analysis of the $I = 0$ equation of MS, in order to ascertain the implications of pseudoscalar theory in this regard. These two questions are dealt with successively in sections 2 and 3.

2. The Model π—π Integral Equation

In the notation of MS, and using the units of the pion mass, the model equation is chosen as

$$sg(s) = \lambda^2 \int_1^\infty (\ln s_> - a) \left[P \frac{s'}{s'-k} g(s') - \delta(s'-k) \right] ds', \qquad (1)$$

† Indeed from an inspection of the asymptotic kernels for the $I = 0$ and 2 states in MS, it appears that these are roughly in the ratio of 5 : 2, a result also in accord with that of ref. [1])

where λ^2 plays the role of a coupling constant, having different values for $I = 0$ and 2, and $s_>$ is the larger of s and s'. This equation has the following features:

i) The interaction is attractive as it stands. For repulsive interaction, λ should be changed to $i\lambda$.

ii) In this equation, no distinction is made between momentum and energy for simplicity, so that the lower limit of integration is taken as 1 rather than 0.

iii) The energy singularity appears at the correct place.

iv) The equation has essentially the same asymptotic form as those of MS (see eqs. (38) and (41)).

v) The constant term a obviously corresponds to the meson-meson divergence $\ln(\Lambda^2/m^2)$ which, it may be recalled, had appeared as an additive modification of the terms $\mathscr{R}_I$ of MS (eqs. (19)—(21)). The negative sign before it indicates its repulsive nature. We shall show below that, as long as a is an absolute constant, it has no effect on the final solution of (1).

The phase shift is given by the usual formula

$$\tan\delta = -\pi g(k). \tag{2}$$

We now turn to the solution of (1). Converting (1) into a differential equation in the usual manner [8]) we have

$$s^2g''+3sg'+g = \frac{\lambda^2 s}{s-k}g. \tag{3}$$

Substitution of

$$sg(s) = u(s) \tag{4}$$

brings (1) into the standard hypergeometric form

$$s(s-k)u''+(s-k)u'-\lambda^2 u = 0, \tag{5}$$

whose solution, finite for small s, is

$$F(-\lambda, \lambda; 1; s/k). \tag{6}$$

Now to solve (1), we need the solution of (5) also for large s, viz., one that will fall off as $s \to \infty$. For this purpose, we use the substitution

$$x = k/s, \tag{7}$$

which transforms (5) into

$$x^2(1-x)\frac{\mathrm{d}^2u}{\mathrm{d}x^2}+x(1-x)\frac{\mathrm{d}u}{\mathrm{d}x}-\lambda^2 u = 0. \tag{8}$$

The solution of (8) which remains finite as $x \to 0$, is

$$u = C\frac{\Gamma^2(\lambda)}{\Gamma(2\lambda+1)}x^\lambda F(\lambda, \lambda; 2\lambda+1; x). \tag{9}$$

This solution is valid for $0 \leqq x \leqq 1$, corresponding to $k \leqq s \leqq \infty$. For $x \geqq 1$, the complete solution of (5), including the one that becomes singular at $s = 0$ †, is found in the usual manner as

$$u = Af(x)+Bh(x), \tag{10}$$

where

$$f(x) = \Gamma(-\lambda)\Gamma(\lambda)F(-\lambda, \lambda; 1; x^{-1}), \tag{11}$$

$$h(x) = \sum_n x^{-n} \frac{\Gamma(n+\lambda)\Gamma(n-\lambda)}{\Gamma^2(n+1)} [-\ln x+\Psi(n+\lambda)+\Psi(n-\lambda)-2\Psi(n+1)], \tag{12}$$

and

$$\Psi(Z) = \frac{\mathrm{d}}{\mathrm{d}Z} \ln \Gamma(Z). \tag{13}$$

The condition of "matching" at $x = 1$ gives, from eqs. (4), (9)—(12),

$$-\lambda^{-2}A+BI_\lambda = \lambda^{-2}C \tag{14}$$

and

$$-\lambda^{-2}A+A\lambda^2\Gamma(\lambda)\Gamma(-\lambda)F(1-\lambda, 1+\lambda; 2; 1)+BJ_\lambda = \frac{C(\lambda+1)}{\lambda^2} + \frac{C\Gamma^2(\lambda+1)}{\Gamma(2\lambda+2)} F(\lambda+1, \lambda+1; 2\lambda+2; 1), \tag{15}$$

where

$$I_\lambda = \sum_n \frac{\Gamma(n+\lambda)\Gamma(n-\lambda)}{\Gamma^2(n+1)} [\Psi(n+\lambda)+\Psi(n-\lambda)-2\Psi(n+1)], \tag{16a}$$

and

$$J_\lambda = -\sum_n \frac{\Gamma(n+\lambda)\Gamma(n-\lambda)}{\Gamma^2(n+1)} [1+(n-1)\{\Psi(n+\lambda)+\Psi(n-\lambda)-2\Psi(n+1)\}]. \tag{16b}$$

In deriving these equations we have made use of some familiar properties of hypergeometric functions. It is easily seen that the two hypergeometric functions appearing in (15) are logarithmically divergent. In order therefore that (15) may be satisfied at all, the coefficients of these divergences must at least tally. Using in (15) the result [9])

$$F(a, b; a+b; 1-\varepsilon) \approx \frac{\Gamma(a+b)}{\Gamma(a)\Gamma(b)} \ln \frac{1}{\varepsilon} \qquad (\varepsilon \to 0), \tag{17}$$

we find immediately

$$A = -C, \tag{18}$$

since the other quantities, including J_λ, are finite. From (14) and (18) we then have

$$B = 0, \tag{19}$$

† Since the lower limit of s is 1, the "singular" solution should not be discarded.

since I_λ is also finite. The solution is thus greatly simplified by the complete elimination of the term $h(x)$ in (10).

Now our integral equation (1) may be transformed, witn the help of (7), to

$$u(x) = \frac{\lambda^2}{k}\left(a - \ln\frac{k}{x_<}\right) + \lambda^2 \int_0^k \frac{dx'}{x'}\left(\ln\frac{k}{x'_<} - a\right)\frac{u(x')}{1-x'}, \tag{20}$$

where $x'_<$ is the smaller of x and x', and $x_<$ is the smaller of x and 1. The solution expressed by eqs. (9), (10), (18) and (19) must now be substituted in (20). The integration of the hypergeometric functions on the right hand side of (20) is greatly facilitated by using the relation

$$F(a, b; c; x) = (1-x)^{c-a-b} F(c-a, c-b; c; x), \tag{21}$$

in both the equations (9) and (10), for which the relation $c-a-b = 1$ is satisfied, so as to *cancel* out the energy denominator $(1-x')$ in (20). The rest of the procedure is quite straightforward, though somewhat lengthy. We find that both sides of (20) are identical provided

$$C^{-1} = -\Gamma(\lambda)\Gamma(-\lambda)F(1-\lambda, 1+\lambda; 2; k^{-1}). \tag{22}$$

It may also be noted that the a terms in (20), give the contribution

$$\frac{\lambda^2 a}{k} - \frac{aC}{k}\Gamma(1+\lambda)\Gamma(1-\lambda)F(1-\lambda, 1+\lambda; 2; k^{-1}), \tag{23}$$

which vanishes identically as a result of (22).

Finally, the phase shift is given from eqs. (3), (9) and (22) by

$$\cot\delta = -\lambda \operatorname{cosec} \pi\lambda \, F(1-\lambda, 1+\lambda; 2; k^{-1}). \tag{24}$$

For the corresponding bound state problem, it is clear from the standard principles of quantum mechanics, that its solution, in conjunction with (24), is

$$F(1-\lambda, 1+\lambda; 2; k^{-1}) = 0. \tag{25}$$

This equation, which of course corresponds to the resonances of (24), may be thought of as giving the "eigenvalues" of k for fixed λ, or vice versa.

The identical vanishing of the a terms represented by (23) justifies our earlier statement that the π—π divergence does not in any way influence the physically observable effects of the interaction. It may be noted that this result is a direct consequence of the fact that the π—π divergence is an absolute constant, *independent* of the momenta. This corresponds to a contact δ-function interaction in coordinate space. Any spread of such an interaction, however small, (e.g., a repulsive "core" with a small non-zero radius), might very well make the over-all interaction repulsive [10]). We, however, prefer to maintain the conventional view that the π—π divergence, to be renormalizable, should be of the "contact" type, rather than non-local. Only such a situation is covered by our present analysis.

3. Numerical Results

Before considering the numerical results for the $I = 0$ integral equation of MS, we first discuss a few qualitative features of the solution given by (24).

It is of interest to note that for integral values of λ, eq. (24) gives $\delta = n\pi$, irrespective of k. This means that according to this model, integral values of λ do not give resonances, but rather something like a Ramsauer-Townsend effect. Again, for the minimum value of k on this model, viz., $k = 1$, the hypergeometric function in (24) diverges, leading to precisely the same situation as is obtained for integral λ. Finally, it is clear that the hypergeometric function in (24) remains positive for all values of $k > 1$, unless $\lambda > 1$, so that $\lambda = 1$ is a natural *lower limit* on the coupling parameter λ for the occurrence of resonances (or bound states).

Within the limitations set by the above conditions, we have tried to find approximate locations of the resonances for some typical pre-assigned values of λ. The results are given in table 1. It is immediately seen that the resonance

TABLE 1

$\tan\delta$ for certain values of k and λ

λ \ k	1.1	8.0	9.0	35	38
1.5	+132.0				
5.5		−6.41	+8.47		
10.5				+2.01	−7.31

energy *increases* with λ, implying that the stronger the attraction the larger is the resonance energy. Now, the values $\lambda = 5.5$ and 10.5 correspond roughly to the asymptotic cases of $I = 0$ and $I = 2$ respectively of MS (see eqs. (41)). If therefore such a model has any physical significance one would expect from this that the resonance for the $I = 0$ state considered in MS should occur at a substantially higher energy than for $I = 2$.

Guided by these considerations, we have calculated the phase shifts for the $I = 0$ integral equation of MS, at the additional c.m. momenta $k = 0.3M$ ($\approx 2\mu$) and $k = 0.45M$ ($\approx 3\mu$). The results which are given in table 2, do show that the resonance shifts to a higher energy, in accordance with the qualitative conclusions based on our model. Further, it may be noted that the phase shift of the actual interaction starts decreasing from the value π at $k = 0$, to lower values as k is gradually increased, and this also accords with the findings of our model.

We have also worked out the wave function for the $I = 0$ interaction for the different energies considered. Fig. 1 indicates its variation with the c.m. momentum k. Each of these curves shown in fig. 1 is characterized by pronounced

TABLE 2

The $I = 0$ phase shifts from MS

k	0.1 M	0.3 M	0.45 M
$\tan\delta$	−0.0152	−1.3850	+14.7700
δ	179° 8′	125° 50′	86° 6′

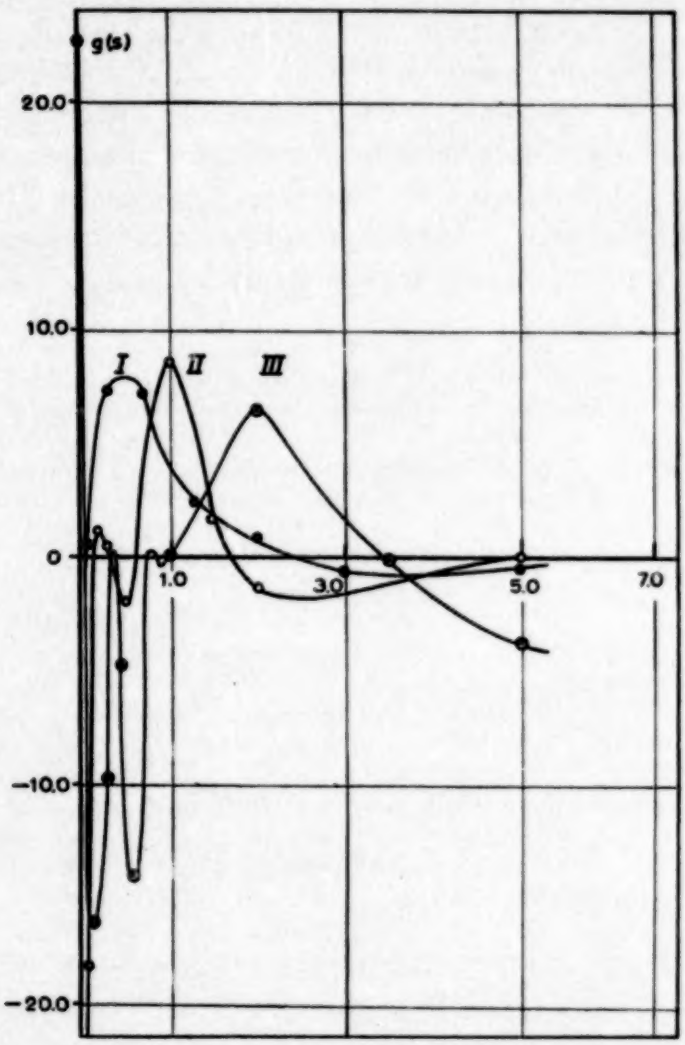

Fig. 1. The π—π wave function for $I = 0$. Curves *I*, *II*, *III* correspond respectively to $k = 0.1\ M$, $0.3\ M$ and $0.45\ M$ (for $k = 0.1\ M$, the ordinate scale is enlarged 100 times)

oscillations to the left of the main maximum beyond which there is a general tapering off. The number of these oscillations (viz., 1, 2 and 3) obviously increases with k, and the main maximum correspondingly shifts to the right. As a result, the importance of the high momentum region increases substantially with k.

It may be of interest to examine the implications of these results with respect to bound state formation. From our model, we find that the scattering length is given by

$$-a^{-1} = \lim_{k\to 1}(k-1)\cot\delta = 0, \tag{26}$$

since the hypergeometric function in (24) diverges logarithmically as $k \to 1$, according to eq. (17). The model therefore predicts an infinite scattering length, thus ruling out any stable bound state. As for the $I = 0$ interaction of MS, the above result for the model may be taken to hold qualitatively for this case as well; this means that the possible bound states can at most be unstable, being formed at *positive* energies only. Even a resonance width of $\approx$ 1 MeV would make the life time for such a state too small to be observed, viz., $\approx 10^{-21}$ s. On the other hand 1 MeV is too small an estimate of the width in the present case †. All this would suggest that the occurrence of π—π resonances need not pose any practical problem regarding the formation of bound states which still remain to be observed.

† The width may be crudely estimated as follows. Taking the equation $\tan\delta = \frac{1}{2}\Gamma(\omega_k - \omega_r)$, we see from table 2 that $r = 0.45\ M$. Next, from the usual relations of effective range theory (see ref. [3])) we note that $\Gamma \propto k$, which roughly holds for the value $k = 0.1\ M$. Therefore, setting $\Gamma = \gamma k$, where γ is nearly constant [3]), we find from the case $k = 0.1\ M$ of table 2 that $\gamma \approx 0.09$. This gives the width Γ_r at resonance as $\Gamma_r = \gamma r \approx 35$ MeV, corresponding to a life time of $\approx 10^{-23}$s.

References

1) G. Chew and S. Mandelstam, UCRL-8728, April 1958 (preprint); also G. Chew, Proceedings of the 9th International conference on High Energy Physics, Kiev (USSR), 1959
2) Chew *et al.*, UCRL-9001, November 1959 (preprint)
3) A. N. Mitra, Nuclear Physics (to be published)
4) A. N. Mitra, Nuclear Physics **6** (1958) 404
5) B. Thomas and W. Holladay, Phys. Rev. **115** (1959) 1329
6) N. Khuri and S. Treiman (preprint)
7) A. N. Mitra and R. P. Saxena, Phys. Rev. **108** (1957) 1083 (referred to as MS)
8) H. A. Bethe and F. de Hoffmann, Mesons and fields (Row, Peterson and Co., Evanston, 1955), Vol. II
9) Whittaker and Watson, A course of modern analysis (Cambridge University Press, 1915)
10) G. Allcock and A. Kamel (preprint)

1.D.2

Nuclear Physics **20** (1960) 499—508; © *North-Holland Publishing Co., Amsterdam*

Not to be reproduced by photoprint or microfilm without written permission from the publisher

ROTATION-VIBRATION INTERACTION IN NON-AXIAL EVEN NUCLEI

A. S. DAVYDOV and A. A. CHABAN

Department of Electrodynamics and Quantum Theory, Moscow State University, Moscow, USSR

Received 4 April 1960

Abstract: Collective excitations of even nuclei are investigated without dividing the excitations into rotational and vibrational. The conditions which enable one to distinguish between rotational and vibrational excitations are investigated. Correction terms are determined which take into account the interaction between both types of excited states. Level energies are determined for non-spherical nuclei for which division of the excitations into rotational and vibrational ones is meaningless.

1. Introduction

In the papers of Davydov and Filippov [1]) and Davydov and Rostovsky [2]) a theory of the rotational states of non-axial even nuclei was developed in the adiabatic approximation which assumes that rotation of the nucleus takes place without a change of its intrinsic state. In the general case violation of the adiabatic condition during rotation can be due to Coriolis interaction between the angular momentum and single-nucleon states and to centrifugal interaction which leads to a change of the shape of the nucleus during rotation and hence to a change of the moments of inertia of the nucleus.

The mean values of the total angular momentum projections of the outer nucleons on an arbitrary direction in the nucleus are zero in even non-spherical nuclei in the ground state (with respect to the outer nucleons); transition to an excited single-nucleon state, on the other hand, requires a large energy and therefore there is no Coriolis interaction. In order to investigate the coupling between rotational and vibrational motions due to centrifugal forces we shall take into account only β vibrations and thus assume that the nucleus is rigid with respcet to a change of the equilibrium value of the parameter γ which determines the deviation of the nuclear shape from axial symmetry. The so-called γ vibrations deserve a special study as the vibrations which some authors considered to be of this type in reality correspond, according to refs. [1, 2]), to rotation of a non-axial nucleus.

2. Collective Excitation Energy of Even Nuclei

The classical energy corresponding to β vibrations of the nuclear surface and to rotation of the nucleus can be written in the form

$$E = \tfrac{1}{2}B\dot{\beta}^2 + V(\beta) + \tfrac{1}{2}\sum_{\lambda=1}^{3}\frac{M_\lambda^2}{4B\beta^2\sin^2(\gamma-\frac{2}{3}\pi\lambda)}, \tag{2.1}$$

where B is the mass parameter which determines the kinetic energy of the β vibrations, $V(\beta)$ is the potential energy of the vibrations, $4B\beta^2\sin^2(\gamma-\frac{2}{3}\pi\lambda)$ and M_λ are respectively the three principal moments of inertia of the nucleus † and the projections of the angular momentum on the principal directions of the nucleus. The adiabatic approximation in the theory of rotational and vibrational motions corresponds to substitution of the equilibrium value β_0 for β in the moments of inertia.

Changing in (2.1) from classical quantities to operators in accordance with the general rules of quantum mechanics, for the case of a curvilinear system of coordinates [4]) we obtain the Hamiltonian operator of the nucleus in the form

$$H = -\frac{\hbar^2}{2B}\left[\frac{1}{\beta^3}\frac{\partial}{\partial\beta}\left(\beta^3\frac{\partial}{\partial\beta}\right) - \sum_\lambda \frac{J_\lambda^2}{4\beta^2\sin^2(\gamma-\frac{2}{3}\pi\lambda)}\right] + V(\beta),$$

where $\hbar J_\lambda$ are projections of the total angular momentum operator on the principal nuclear axes. The operator H commutes with the operator $\mathbf{J}^2$ of the square of the total angular momentum and hence the square of the angular momentum is an integral of motion. In order to determine the eigenfunctions and eigenvalues of the operator H we put

$$\Psi_J(\beta, \theta_i) = \varphi_J(\beta)\Phi_J(\theta_i).$$

The functions φ_J and Φ_J must then satisfy the equations

$$\left[\tfrac{1}{2}\sum_\lambda \frac{J_\lambda^2}{\sin^2(\gamma-\frac{2}{3}\pi\lambda)} - \mathscr{E}(J)\right]\Phi_J(\theta_i) = 0, \tag{2.2}$$

$$\left\{-\frac{\hbar^2}{2B}\frac{1}{\beta^3}\frac{\partial}{\partial\beta}\left(\beta^3\frac{\partial}{\partial\beta}\right) + V(\beta) + \frac{\hbar^2}{4B\beta^2}\mathscr{E}(J) - E_J\right\}\varphi_J(\beta) = 0. \tag{2.3}$$

The solutions of eq. (2.2) have been investigated in refs. [1, 2]). Generally speaking, several values of $\mathscr{E}_K(J)$ which we denote by the subscript K, correspond to each value of J and the parameter γ. For $J = 2$, $K = 1,2$; for $J = 3$, $K = 1$; for $J = 4$, $K = 1, 2, 3$ etc.

It is convenient to carry out the following transformation in eq. (2.3):

$$\varphi_{KJ}(\beta) = \beta^{-\frac{3}{2}}U_{KJ}(\beta).$$

The functions $U_{KJ}(\beta)$ will then be solutions of the equation

$$\left\{-\frac{\hbar^2}{2B}\frac{\mathrm{d}^2}{\mathrm{d}\beta^2} + W_{KJ}(\beta) - E_J\right\}U_{KJ}(\beta) = 0, \quad 0 \leqq \beta < \infty, \tag{2.4}$$

with the boundary condition $U_{KJ}(0) = 0$.

† The possibility of employing such expressions for the nuclear moments in calculating the rotational states has been investigated in a paper by Davydov, Rabotnov and Chaban [3]).

The potential energy operator in eq. (2.4) is defined by the equation

$$W_{KJ}(\beta) = \tfrac{1}{2}C(\beta-\beta_0)^2+\frac{\hbar^2}{4B\beta^2}\mathscr{E}_K(J)+\ldots,$$

where C and β_0 are respectively the elasticity constant and a parameter which determines the equilibrium shape of the nucleus for $J = 0$. Expanding $W_{KJ}(\beta)$ into a series and retaining only terms up to the square of the deviation from the new equilibrium position we can write

$$W_{KJ}(\beta) = W_{KJ}(\beta_{KJ})+\tfrac{1}{2}C_{KJ}(\beta-\beta_{KJ})^2, \tag{2.5}$$

where

$$\beta_{KJ} = \beta_0+\frac{\hbar^2\mathscr{E}_K(J)}{2BC\beta_{KJ}^3}, \tag{2.6}$$

$$C_{KJ} = C\left[1+\frac{3\hbar^2\mathscr{E}_K(J)}{2BC\beta_{KJ}^4}\right]. \tag{2.7}$$

Introducing $\omega_0 = \sqrt{C/B}$ and the dimensionless parameters $p = \beta_{KJ}/\beta_0 \geqq 1$ and $\mu^2 = 2(\beta_{00}/\beta_0)^2 = \hbar\omega_0/C\beta_0{}^2$, where $\beta_{00}^2 = \tfrac{1}{2}\hbar\sqrt{BC}$ is the mean value of the square of the zero vibration amplitude of the nuclear surface for $J = 0$, one can transform eqs. (2.6) and (2.7) to the form

$$(p-1)p^3 = \tfrac{1}{2}\mathscr{E}_K(J)\mu^4, \tag{2.6a}$$

$$C_{KJ} = C\left[1+\frac{3\mathscr{E}_K(J)\mu^4}{2p^4}\right]. \tag{2.7a}$$

Here

$$W_{KJ}(\beta_{KJ}) = \hbar\omega_0\left[\frac{(p-1)^2}{2\mu^2}+\frac{\mathscr{E}_K(J)\mu^2}{4p^2}\right].$$

Inserting (2.5) into (2.4) we obtain the equation

$$\left\{-\frac{\hbar^2}{2B}\frac{\mathrm{d}^2}{\mathrm{d}\beta^2}+\tfrac{1}{2}C_{KJ}(\beta-\beta_{KJ})^2-[E_{KJ}-W_{KJ}(\beta_{KJ})]\right\}U_{KJ}(\beta) = 0.$$

We now introduce a new variable

$$\zeta = \frac{p}{\mu_1}\frac{\beta-\beta_{KJ}}{\beta_{KJ}}, \quad \mu_1{}^4 = \mu^4\frac{C}{C_{KJ}}, \tag{2.8}$$

which varies in the interval $-p/\mu_1 \leqq \zeta < \infty$ and a new function $V(\zeta) = U(\beta)\exp\{\tfrac{1}{2}\zeta^2\}$. The function V will then satisfy the equation

$$\frac{\mathrm{d}^2V}{\mathrm{d}\zeta^2}-2\zeta\frac{\mathrm{d}V}{\mathrm{d}\zeta}+2\nu V = 0, \tag{2.9}$$

and the boundary conditions

$$V\left(-\frac{p}{\mu_1}\right)=0, \quad \exp\{-\tfrac{1}{2}\zeta^2\}V(\zeta)\to 0 \quad \text{for} \quad \zeta\to\infty. \tag{2.10}$$

The value of ν in (2.9) is determined by the equation

$$\nu=\frac{E_{KJ}-W_{KJ}(\beta_{KJ})}{\hbar\omega_{KJ}}-\tfrac{1}{2}, \quad \omega_{KJ}=\sqrt{\frac{C_{KJ}}{B}}.$$

The solution of equation (2.9) can be written in the form

$$V(\zeta)=NH_\nu(\zeta),$$

where N is a normalizing factor and

$$H_\nu(\zeta)=[2\Gamma(-\nu)]^{-1}\sum_{k=0}^{\infty}\frac{(-1)^k}{k!}\,\Gamma\left(\frac{k-\nu}{2}\right)(2\zeta)^k,$$

$\Gamma(x)$ being a gamma function. In this case the energy of collective nuclear excitations corresponding to a total angular momentum J will be given by the formula

$$E_{K\nu}(J)=\hbar\omega_0\left\{(\nu+\tfrac{1}{2})\sqrt{1+\tfrac{3}{2}\left(\frac{\mu}{p}\right)^4\mathscr{E}_K(J)}+\tfrac{1}{4}\left(\frac{\mu}{p}\right)^2\mathscr{E}_K(J)+\frac{(p-1)^2}{2\mu^2}\right\}, \tag{2.11}$$

where the quantum number ν (which in general is not an integer) is the root of the transcendental equation

$$H_\nu\left(-\frac{p}{\mu_1}\right)=0. \tag{2.12}$$

Since p and μ_1 can be expressed with the aid of formulas (2.6a) and (2.8) in terms of μ and $\mathscr{E}_K(J)$ which depends only on γ, one finds that for certain values of K and J the energy of collective excited states will be expressed only through two parameters, the "non-axiality" parameter γ and the "non-adiabaticity" parameter μ.

In the general case, collective excitation corresponding to a definite value of the total angular momentum J is a complicated combination of vibrational and rotational motions. Under certain conditions these two types of motion can be approximately separated. Thus, for $\mu<\frac{1}{3}$ one has $\mu_1\approx\mu$ and the quantum number ν in the transcendental equation (2.12) assumes values which are close to integers $\nu\approx n=0, 1, 2, \ldots$. Furthermore, for $\mu<\frac{1}{3}$ it follows from (2.6a) that

$$p=1+\tfrac{1}{2}\mu^4\mathscr{E}_K(J)+\ldots.$$

Inserting this value into (2.11) and expanding the expression thus obtained into

a series in powers of the small parameter μ, we find

$$E_{Kn}(J) = \hbar\omega_0(n+\tfrac{1}{2}) + \frac{\hbar^2}{4B\beta_0^2}\mathscr{E}_K(J)[1+3\mu^2(n+\tfrac{1}{2})] - D\frac{\hbar^2}{4B\beta_0^2}[\mathscr{E}_K(J)]^2, \quad (2.13)$$

where $D = \frac{1}{2}\mu^4[1+\frac{57}{4}(n+\frac{1}{2})\mu^2]$ is a small quantity which takes into account the coupling between rotation and vibration of the nuclear surface. The first term in (2.13) determines the energy of vibrations and the second, for $\mu = 0$, determines the energy of rotation in the adiabatic approximation. As a result of comparing the theory of rotational states of non-axial nuclei with the experiments Mallman and Kerman [5]) previously suggested the introduction of corrections corresponding to the third term in (2.13) and containing D, regarded as a parameter.

For $\mu > \frac{1}{3}$ the nucleus is "soft". The distinction of rotational and vibrational motions for such nuclei is very conventional and formula (2.13) is a rough approximation. For calculation of the energy of the excited states one should employ expression (2.11) in which ν is not an integer. Determining the smallest value of $\nu = \nu_1$ from eq. (2.12) and employing the values of $\mathscr{E}_K(J)$ given in refs. [1, 2]) we can find with the aid of (2.11) a sequence of energy levels of the "first band" possessing spins 0, 2, 3, ...

We introduce the ratio

$$R_{K1}(J) = \frac{E_{K\nu_1}(J) - E_{1\nu_1}(0)}{\Delta}$$

where $\Delta = E_{1\nu_1}(2) - E_{1\nu_1}(0)$ is the energy of the first excited state. The subscript in R specifies the number of the energy level $\mathscr{E}_K(J)$ corresponding to adiabatic rotation with angular momentum J and the second subscript numbers the values of ν corresponding to successive roots of eq. (2.12).

The values of $R_{11}(4)$ and $R_{11}(6)$ as functions of $R_{21}(2)$ i.e., of the ratio of the excitation energies of two spin 2 levels, are plotted in fig. 1 and 2 for various values of the non-adiabaticity parameter μ (solid lines) and non-axiality parameter γ (broken lines).

The value of $R_{21}(2)$ for $\gamma = 30°$ was a minimum, equal to 2 in the adiabatic approximation theory ($\mu = 0$). If the coupling between the rotation and vibrations of the nuclear surface are taken into account, $R_{21}(2)$ may assume values below 2. For example for $\mu = 1$ the minimum value of $R_{21}(2)$ is 1.6. In the absence of rotation-vibration coupling between rotation and nuclear surface vibrations the ratio $R_{11}(4)$ in an axially symmetric nucleus equals $\frac{10}{3}$. In a non-axial nucleus with $\gamma = 30°$ this ratio is $\frac{8}{3}$. Rotation-vibrational interaction diminishes this value to 2.25 for axial nuclei with $\mu = 1$ and to $R_{11}(4) = 1.95$ for nuclei with $\gamma = 30°$.

In fig. 1 the experimental ratios $R_{11}(4)$ for some nuclei are denoted by circles. It follows from the figure that values $\mu > 0.5$ correspond to the nuclei of

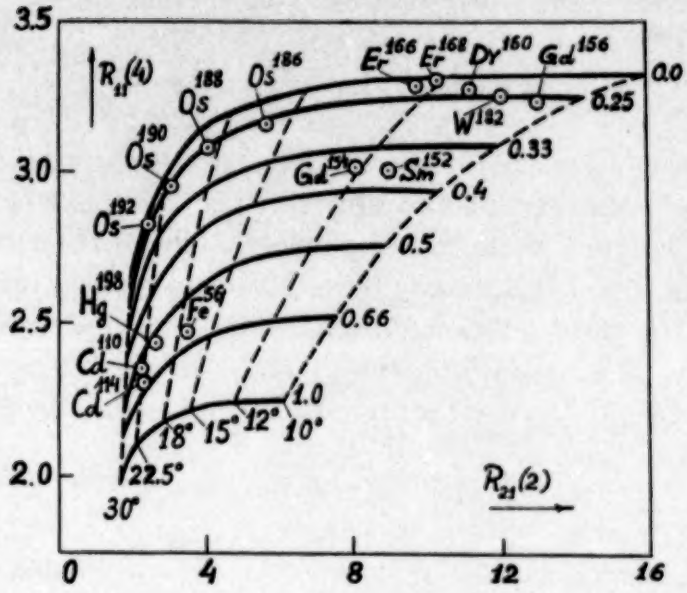

Fig. 1. Dependence of $R_{11}(4)$ (the ratio of the first energy level of spin 4 to the energy of the first excited level of spin 2) on $R_{21}(2)$ (the ratio of the energies of the first two spin 2 levels) for various values of the non-adiabaticity parameter μ (solid lines) and non-axiality parameter γ (broken lines). The circles denote the experimental values.

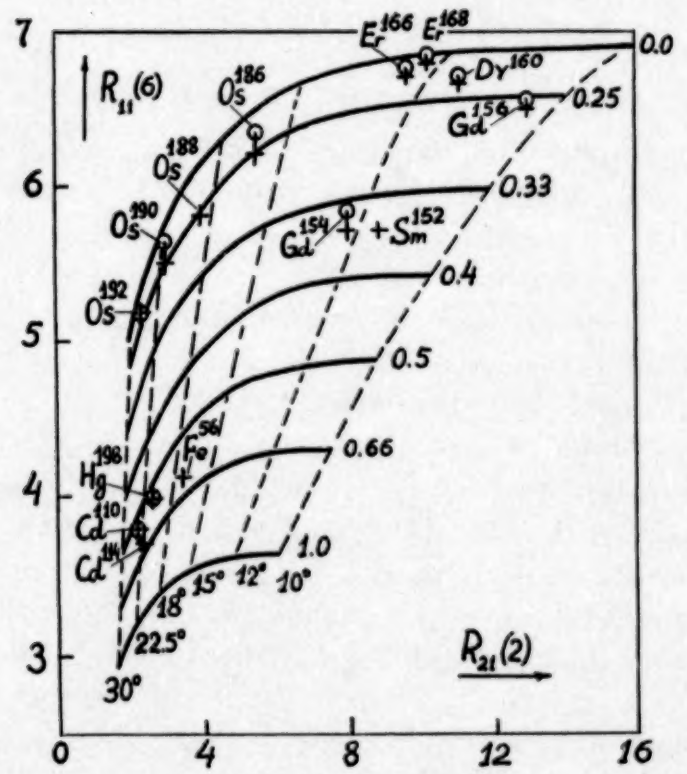

Fig. 2. Dependence of $R_{11}(6)$ (ratio of energy of first spin 6 level to energy of first excited level of spin 2) on $R_{21}(2)$ for various values of the non-adiabaticity parameter μ (solid lines) and non-axiality parameter γ (broken lines). The circles denote the experimental values. The theoretical values for the corresponding nuclei are denoted by the crosses.

Fe^{56}, Cd^{110}, Cd^{114}, and Hg^{198}. For these nuclei division into rotational and vibrational motions is quite conventional. Values of $\mu < 0.3$ are observed in nuclei of Gd^{156}, Dy^{160}, Er^{166}, Er^{168}, Os^{186}, Os^{188}, Os^{190} and Os^{192}. Rotational excitations are comparatively distinct in these nuclei. Corrections due to coupling between the rotation and vibrations can be taken into account with the help of formula (2.13). Nuclei of the type of Sm^{152} or Gd^{154} occupy an intermediate region and values of μ lying in the interval $0.3 < \mu < 0.5$ correspond to them.

As shown in ref. [1]), the position of the spin 3 level is determined in the adiabatic approximation by the simple formula

$$R_{11}(3) = 1 + R_{21}(2).$$

This relation is found to be relatively insensitive to non-adiabaticity corrections even for nuclei with $\mu > 0.3$.

With the aid of the values of the parameters γ and μ for separate nuclei derived from fig. 1, the theoretical values of the energies of other excited states of the nuclei may be computed. Values of γ and μ found on the basis of the experimental values of $R_{11}(4)$ and also the theoretical and experimental values

TABLE 1

Experimental and theoretical values of the ratios R

Nucleus	$R_{21}(2)$	$R_{11}(4)$	γ	μ	$R_{21}(4)$		$R_{11}(6)$		Ref.
					theory	exp.	theory	exp.	
Fe^{56}	3.49	2.47	17	0.61	4.67	4.85	4.7		[7])
Cd^{110}	2.10	2.35	22.5	0.58	3.8		3.8	3.8	[8]), [9])
Cd^{114}	2.18	2.30	22.5	0.54	3.8		3.7		[10])
Sm^{152}	8.92	3.01	11.4	0.37	10.3	11.68	5.7		[10]), [11]), [14])
Gd^{154}	8.10	3.02	11.8	0.36	5.7	5.84	5.7	5.84	[10]), [14])
Gd^{156}	13.01	3.24	10.5	0.26	14.9	15.34	6.5	6.56	[10]), [11]), [14])
Dy^{160}	11.16	3.27	11.4	0.2	13.2	13.35	6.6	6.70	[10]), [11])
Er^{166}	9.76	3.29	12.4	0.12	12.0	11.87	6.7	6.76	[12])
Er^{168}	10.29	3.31	12.2	0.05	12.7	12.47	6.8	6.86	[12])
W^{182}	12.11	3.26	10.8	0.25	14.0	14.68	6.6		[10]), [14])
Os^{186}	5.60	3.16	15.9	0.26	7.7	7.73	6.2	6.33	[13]), [14])
Os^{188}	4.09	3.08	18.5	0.25	6.3	6.17	5.8		[13]), [14])
Os^{190}	2.99	2.95	21.9	0.25	5.6	5.14	5.5	5.63	[14])
Os^{192}	2.37	2.82	24.5	0.1	5.4		5.2	5.17	[10]), [11])
Hg^{198}	2.65	2.43	21.0	0.54	4.1		4.0	3.97	[10]), [11])

of $R_{21}(4)$ and $R_{11}(6)$ which correspond to them are presented in table 1. The variation of the ratios $R_{11}(6)$ on $R_{21}(2)$ for various values of μ and γ is depicted in fig. 2. The crosses and circles in the figure denote respectively the theoretical and experimental values of the same ratios for some nuclei.

A "second band" of excited states with a spin sequence 0, 2, . . . will corre-

spond to the second root $\nu = \nu_2$ of the transcendental equation (2.12). The ratio

$$R_{12}(0) = \frac{E_{1\nu_2}(0) - E_{1\nu_1}(0)}{\Delta}$$

of the first level of this band (spin 0) to the energy of the first excited state of the first band is depicted in fig. 3. The crosses in the same figure denote the

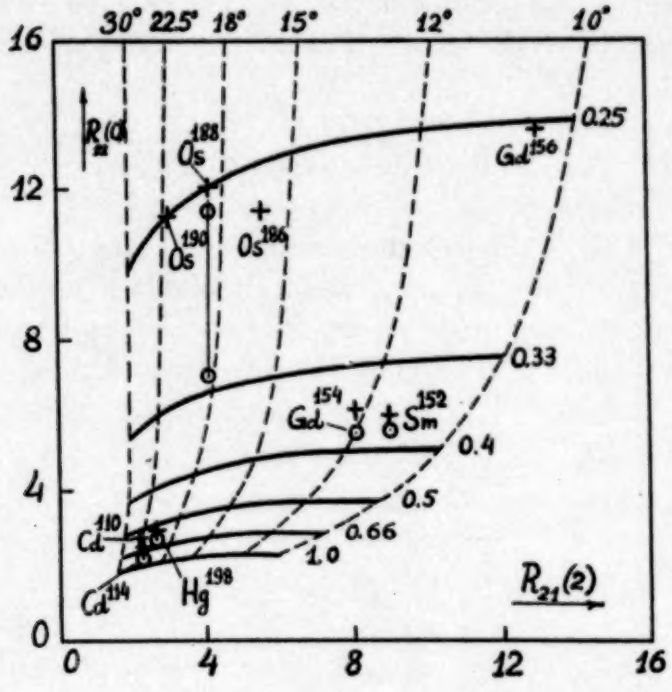

Fig. 3. Dependence of the ratio of the energy of the first excited level of spin 0 to the energy of the first excited level of spin 2 on the ratio $R_{21}(2)$ for various values of μ and γ. The crosses denote the theoretical values for some nuclei. The experimental values are denoted by the circles.

theoretical values of the ratio for values of γ and μ corresponding to the nuclei indicated in fig. 1. The circles denote ratios of the experimental values of the energy of zero spin and positive parity excited states to the energy of the first excited state. It can be seen from fig. 3 that for $R_{12}(0) > 7$ one gets $\mu < 0.3$. Thus, the possibility of separating the rotational and vibrational excitations can roughly be appraised on the basis of the position of the 0^+ excited level.

It can be seen from fig. 3 that the theory predicts quite satisfactorily the position of the 0^+ excited state for the Cd^{114}, Sm^{152}, Gd^{154}, Hg^{198} nuclei. The position (12.1) of the 0^+ level of the Os^{188} nucleus predicted by the theory does not differ noticeably from the value 11.4 found by King and Johns [6]) for the second spin 0^+ excited state and differs from the value 7 found in the same paper for the first excited level of spin 0.

3. Probabilities for Quadrupole Electric Transitions Between Collective Excitations of Even Nuclei

The collective excited states of even nuclei considered in the preceding section possess a positive parity and are characterized by the wave functions

$$\Psi_{JK\nu}(\beta, \theta_i) = e^{-\frac{1}{2}\zeta^2} V_\nu(\zeta)\beta^{-\frac{1}{2}}\Phi_{JK}(\theta_i), \tag{3.1}$$

where θ_i are Eulerian angles and ζ is defined by formula (2.8).

A calculation of the reduced E2 transition probabilities between the states defined by functions (3.1) shows that these probabilities can be represented by the formula

$$B(\mathrm{E2}; JK\nu \to J'K'\nu') = B_a(\mathrm{E2}; JK \to J'K')S, \tag{3.2}$$

where the $B_a(\mathrm{E2}; JK \to J'K')$ are the reduced transition probabilities computed in the adiabatic approximation [1,2]) and

$$S = \beta_0^{-2}|(JK\nu|\beta|J'K'\nu')|^2$$

is a correction factor which accounts for coupling between the rotation and vibrations of the nuclear surface.

Thus the change in the reduced transition probabilities which appears when account is taken of coupling between the rotations and vibrations may be due to two circumstances. First of all account of the coupling entails a change in the value of γ which corresponds to the given nucleus: as a consequence, the value of $B_a(\mathrm{E2}; JK \to J'K')$ also changes. Secondly, the factor S appears. For $\mu < 0.5$ the factor S does not significantly differ from unity and the main change in the reduced transition probabilities due to the interaction between the vibration and rotation will be determined by the change in the values of γ.

The experimental determinations of the probabilities for electromagnetic transitions between excited states are as yet not very precise (the errors are of the order of 20—40 %). In some cases the data of various authors may differ by a factor of several units. For this reason it does no seem to be very reasonable to introduce the small corrections due to the interaction between the rotation and vibrations in the theoretical estimations of the transition probabilities. For $\mu > 1$ the corrections may be large. However, in this case the theory developed in the present paper must apparently be modified since it does not seem probable that such nuclei are rigid with respect to γ vibrations.

References

1) A. S. Davydov and G. F. Filippov, JETP **35** (1958) 440; Nuclear Physics **8** (1959) 237
2) A. S. Davydov and V. S. Rostovsky, JETP **36** (1959) 1788; Nuclear Physics **12** (1958) 58
3) A. S. Davydov, N. S. Rabotnov and A. A. Chaban, JETP **38** (1960) 1311; Nuclear Physics **17** (1960) 169

4) W. Pauli, Handbuch d. Phys. **24/1** (1933) 120
5) C. Mallman and A. Kerman, Nuclear Physics **16** (1960) 105
6) W. J. King and M. W. Johns, Canad. J. Phys. **37** (1959) 755
7) Sharp Cook, Nuclear Physics **7** (1958) 480
8) D. Strominger, J. Hollander and G. Seaborg, Revs. Mod. Phys. **30** (1958) 585
9) H. W. Taylor and W. R. Frisken, Phys. Rev. **114** (1959) 127
10) B. S. Dželepov and L. K. Peker, Decay Schemes of Radioactive Nuclei (USSR Acad. Sci., 1958)
11) E. P. Grigoriev and M. P. Avotina, Izv. Akad. Nauk SSSR **24** (1960) 324
12) K. Jacob, J. Mihelich, B. Harmatz and T. Handey, Bull. Amer. Phys. Soc. **3** (1958) 558
13) R. Diamond and J. Hollander, Nuclear Physics **8** (1958) 143
14) B. S. Dželepov and A. K. Peker, Excited States of Deformed Nuclei (Joint Institute for Nuclear Research), P. 288

1.D.1:
1.E.1

Nuclear Physics **20** (1960) 509—512; © *North-Holland Publishing Co., Amsterdam*
Not to be reproduced by photoprint or microfilm without written permission from the publisher

NUCLEAR SPINS OF NEODYMIUM-147 AND PROMETHIUM-147

A. CABEZAS, I. LINDGREN, E. LIPWORTH, R. MARRUS and M. RUBINSTEIN

Lawrence Radiation Laboratory and Department of Physics, University of California, Berkeley, California †

Received 13 June 1960

Abstract: The nuclear spins of 11 d Nd^{147} and 2.6 y Pm^{147} have been measured to be $I = \frac{5}{2}$ and $I = \frac{7}{2}$ respectively by the atomic beam magnetic resonance method. The result for Nd^{147} confirms an earlier measurement made by paramagnetic resonance. The result for Pm^{147} is surprising in view of the fact that no beta transition has been observed between the ground states of these two isotopes.

Several investigations of the beta decay of Nd^{147} to the excited states of Pm^{147} have all been characterized by the failure to observe any direct beta transition to the ground state [1]). The most intense beta line is a first-forbidden transition to the first excited state, which then decays to the ground state by an M1 gamma-ray transition. These observations are very difficult to explain, in view of a recent measurement [2]), by paramagnetic resonance, of $\frac{5}{2}$ for the ground-state spin of Nd^{147} and the probable assignment of the ground-state of Pm^{147} on the basis of the single-particle shell model [3]). In the hope of improving our knowledge concerning this situation, we have undertaken to measure, by the method of atomic beams, the spins of these isobars. Our results confirm the paramagnetic resonance measurement of $I = \frac{5}{2}$ for Nd^{147} and yield $I = \frac{7}{2}$ for Pm^{147}.

Prior atomic-beam measurements on stable neodymium have established [4]) the existence of a low-lying electronic state characterized by $J = 4$ and $g_J = 0.603$. Such an electronic state is coupled by the hyperfine-structure interaction to a nuclear spin of $I = \frac{5}{2}$ to result in six nondegenerate levels of the total angular momentum F with Landé splitting factors given by

$$g_F \approx 0.603 \frac{F(F+1)+\frac{55}{4}}{2F(F+1)}. \qquad (1)$$

where a term in the nuclear moment has been neglected.

In an atomic-beam apparatus with flop-in magnet geometry and normal ordering of the F states, transitions in the highest four F states are observable.

† This research sponsored under the auspices of the U.S. Atomic Energy Commission and the Office of Naval Research.

We have observed transitions in the $F = \frac{13}{2}, \frac{11}{2}$ and $\frac{9}{2}$ states at two magnetic fields. The g_F values corresponding to the observed resonant frequencies are given in table 1 along with the values predicted from eq. (1). The discrepancies

TABLE 1

Observed resonances in Nd^{147} The calculated g_F's are based on the previously measured g_J's[4]

$\mu_0 H/h$ (MHz)	Transition		
	$I = \frac{5}{2}, J = 4, F = \frac{13}{2}$	$I = \frac{5}{2}, J = 4, F = \frac{11}{2}$	$I = \frac{5}{2}, J = 4, F = \frac{9}{2}$
5.880	0.371 ±0.018	0.394 ±0.020	0.438 ±0.021
9.679	0.3755±0.0021	0.4008±0.0026	0.4452±0.0025
mean experimental g_F	0.3755±0.0021	0.4008±0.0026	0.4452±0.0025
calculated g_F	0.3710	0.3943	0.4385

between the calculated and experimental g_F values are probably due to quadratic shift resulting from a small hyperfine structure. The failure to observe the transition in the $F = \frac{7}{2}$ state is probably due to the inability of the apparatus to refocus transitions for which $\Delta m_J = \pm 1$ for such low g_J values.

The Nd^{147} used in these runs was produced by neutron irradiation of commercially obtained material which was spectroscopically verified to be $> 99\,\%$ neodymium by weight. The method of production, together with the 11.5 d half-life established for the decay of a foil exposed to the neodymium beam at resonance and the g_J value, uniquely determines the material to be Nd^{147}.

The Pm^{147} used in these experiments was obtained in a weak HCl solution from Oak Ridge National Laboratory, and is guaranteed by the supplier to be $> 99\,\%$ pure. It is found that a satisfactory procedure for obtaining a beam of atomic promethium is to convert the material to the nitrate and mix the nitrate salt with an excess of lanthanum metal in the atomic-beam oven. The oven is then heated slowly up to operating temperature (about 1000°C), at which temperature a beam of atomic promethium is formed. The mechanism for the reaction is believed to be the initial decomposition (at low temperatures) of promethium nitrate to promethium oxide, then the reduction by the lanthanum (at some higher temperature) to the metal.

Since no prior information concerning the electronic ground state of promethium existed, a systematic search was initiated at low magnetic fields to observe resonances within the range of g values $0 \leqq g \leqq 2.0$. Three resonances were observed, each of which was followed up in field to a maximum field of 38.2 G. Table 2 gives the g_F values corresponding to the observed resonant frequencies.

Interpretation of these data is based on the assumption that the ground-state configuration of promethium is $(4f)^5$. This hypothesis is supported by the fact that the ground-state configuration of $_{60}$Nd and $_{62}$Sm are known [5,6]) to be $(4f)^4$ and $(4f)^6$, respectively. A calculation of the electrostatic energies indi-

TABLE 2

Observed resonances in Pm^{147} The calculated g_F's are based on the assumption of pure L—S coupling among the electrons of the configuration f^5 to the Hund's Rule term ^6H

$\mu_0 H/h$ (MHz)	Transition		
	$I=\frac{7}{2}$, $J=\frac{7}{2}$, All F	$I=\frac{7}{2}$, $J=\frac{9}{2}$, $F=8$	$I=\frac{7}{2}$, $J=\frac{9}{2}$, $F=7$
15.208	0.416 ±0.002	0.600 ±0.003	0.620 ±0.003
29.050		0.602 ±0.002	0.623 ±0.002
53.528	0.4164±0.0010	0.6044±0.0015	0.6230±0.0015
mean experimental g_F	0.4164±0.0010	0.6037±0.0015	0.6230±0.0015
calculated g_F	0.4127	0.6023	0.6214

cates that the Hund's Rule term ^6H is expected to be the ground state. The spin-orbit interaction will split this term into six J states, with the $J=\frac{5}{2}$ state lying lowest. An estimate of the separations can be obtained [6]) from the fine-structure splitting constant, measured in the optical spectrum of samarium to be about $a_{4f} \approx 1700\ cm^{-1}$. This indicates that the $J=\frac{5}{2}$, $\frac{7}{2}$ and $\frac{9}{2}$ states should all be present in measurable amounts in the beam. The $J=\frac{7}{2}$ and $J=\frac{9}{2}$ states are easily refocussed, and the L—S coupled g_J values are given in table 2 and compared with the values inferred from the experimental data on the assumption $I=\frac{7}{2}$. The state $J=\frac{5}{2}$ is not observed, for the g_J value of atoms in this state is too low to allow refocussing in our apparatus.

In analogy with the other rare earth elements, the only possible ground-state configuration besides $(4f)^5$ could be $(4f)^4$ (5d). An attempt to exclude the possibility of a data fit for the configuration $(4f)^4$ (5d) can be made on the following basis. Judd has calculated the electrostatic energies for f^4d and has shown that for this configuration the Hund's Rule term should lie lowest [7]). This term will give rise to states with all half-integral J values from $J=\frac{11}{2}$ to $J=\frac{21}{2}$, of which several would be present in the beam. An attempt has been made to fit the observed data in a g_J-independent way, i.e., by trying to fit ratios of the observed frequencies to ratios of the cosine factors $\{F(F+1)+J(J+1)-I(I+1)\}/2F(F+1)$ that arise from all possible F's corresponding to a given I and J. All values of I from $\frac{3}{2}$ to $\frac{13}{2}$ and all values of J from $\frac{3}{2}$ to $\frac{21}{2}$ were tried. No fit was obtained to all of the data for a single I and J. We are also able to exclude the case of two resonances occurring in one electronic state, and the third resonance occurring in another, except for the assigned I and J's. Hence we conclude that the spin of Pm^{147} is $\frac{7}{2}$, that $(4f)^5$ is the ground-state configuration, and that L—S coupling to the Hund's Rule ground-state gives an excellent approximation to the observed g values. It is of interest to note [8]) that the ground-state configuration of neptunium, the actinide homologue of promethium, is $(5f)^4$ $(6d)^1$.

The most plausible shell-model interpretation of the observed spin of Pm^{147} is to assign the 61st proton to the level $1g_{\frac{7}{2}}$. This implies that the $2d_{\frac{3}{2}}$ level lies

lower than the $1g_{\frac{7}{2}}$ level. The measured spins [9,10]) of $_{59}Pr^{141}$ and $_{63}Eu^{151,153}$ are all $\frac{5}{2}$, which indicates that for these nuclei the converse is true. The configuration $(d_{\frac{5}{2}})^3$ coupling to $J = \frac{7}{2}$ is forbidden by the Pauli principle.

The measured spins of the ground states of Nd^{147} and Pm^{147}, taken along with the beta decay information, indicate that the spin of the first excited state of Pm^{147} is either $\frac{5}{2}$ or $\frac{7}{2}$. It is difficult to understand the failure to observe the direct beta decay between the ground states of Nd^{147} and Pm^{147} on the basis of the now known spins, and the ordinary selection rules governing beta decay. It is possible that in this particular case some unusual effect results in a modification of the selection rules.

References

1) W. C. Rutledge, J. M. Cork and S. B. Burson, Phys. Rev. **86** (1952) 775;
P. R. Evans, Phil. Mag. **3** (1958) 1061;
A. C. G Mitchell, C. B. Creager and C. W. Kocker, Phys. Rev. **111** (1958) 1343
2) R. W. Kedzie, M. Abraham and C. D. Jeffries, Phys. Rev. **108** (1957) 54
3) M. G. Mayer, S. A. Moszkowski and L. W. Nordheim, Revs. Mod. Phys. **23** (1951) 315
4) K. F. Smith and I. Spalding (Cambridge University), private communication
5) Ph. Schummans, Physica **11** (1946) 419
6) W. E. Albertson, Phys. Rev. **47** (1935) 370
7) Bryan Judd (Lawrence Radiation Laboratory), private communication
8) J. C. Hubbs and R. Marrus, Phys. Rev. **110** (1958) 287
9) J. E. Mack, Revs. Mod. Phys. **22** (1950) 64
10) B. Bleaney and W. Low, Proc. Phys. Soc. A **68** (1955) 55

1.C

Nuclear Physics **20** (1960) 513—532; © *North-Holland Publishing Co., Amsterdam*

Not to be reproduced by photoprint or microfilm without written permission from the publisher

SUR LE DÉVELOPPEMENT DE LA GRANDE FONCTION DE PARTITION POUR DES SYSTÈMES DE PARTICULES IDENTIQUES

M. GAUDIN

Centre d'Études Nucléaires de Saclay, Gif-sur-Yvette (S. et O.)

Reçu le 23 juin 1960

Abstract: We start from the perturbation expansion of the grand partition function. The general n^{th} order term is described by a pair of two permutations and its contribution is presented in a compact form of a sum of n^{th} order permanents. The procedure is applied to a system of fermions interacting via a two-body separable potential. The form of the series suggests a partial summation which gives the known result for the thermodynamic potential in the superconducting state.

1. Introduction

Nous considérons la fonction de partition Z d'un système de particules identiques, développée en puissances de l'interaction. Le formalisme de la seconde quantification et l'utilisation du théorème de Wick [1]) pour le calcul des valeurs moyennes de produits d'opérateurs permettent de représenter par un diagramme chaque système de contractions. L'examen de leurs propriétés de symétrie [2]) dans les opérations d'échange conduit à décrire les systèmes de contractions à l'aide d'un couple de permutations. Le développement de Z ainsi obtenu, groupe les éléments de matrice de l'interaction sous forme de permanents qui rassemblent les contributions de diagrammes en général non connexes. Ce résultat pourrait sans doute être atteint par la méthode de Caïaniello [3]), l'opérateur densité jouant ici le rôle de la matrice S.

Nous appliquons ensuite ce développement au calcul du potentiel de Gibbs d'un système de fermions. Les termes de la fonction de partition se trouvent classés de façon à suggérer l'approximation simple qui consiste à ne conserver l'interaction qu'entre paires de fermions dans l'état singulet, d'impulsion totale nulle, et aussi d',,énergie'' totale nulle. Nous appelons ,,énergie'' la variable entière attachée à chaque ligne de particules, qui fut introduite dans le formalisme par Montroll et Ward [4]). Dans le cas d'un potentiel séparable, il est simple de sommer la série partielle ainsi extraite de la série initiale qui définit Z et d'étudier la limite du volume infini. On retrouve ainsi le potentiel thermodynamique obtenu par Bardeen, Cooper et Schrieffer [5]) et ensuite par divers auteurs avec la méthode des transformations canoniques [6]) et celle des fonctions de

November (3) 1960

Green [7]). Il paraît au contraire difficile de traiter le cas d'une interaction de paires quelconque, non séparable, alors que la méthode de Bogoliubov le permet.

Dans le cas répulsif et au-dessus de la température critique dans le cas attractif, cette série partielle redonne la contribution qui vient des „échelles généralisées" [8]), calculée avec la restriction des paires „d'énergie" nulle. La sommation des termes importants pour l'énergie libre de l'état superconducteur n'apporte donc pas de trouble dans les cas où la série de perturbation en diagrammes connexes est convergente.

2. Formalisme Général

2.1. LA SÉRIE DE PERTURBATION

L'hamiltonien H d'un système de particules identiques en interaction instantanée peut s'écrire sous la forme

$$H = H_0+V = \sum_k \varepsilon_k a_k^\dagger a_k+\tfrac{1}{4}\sum_{rsmn}\langle rs|v|mn\rangle a_r^\dagger a_s^\dagger a_n a_m, \tag{1}$$

où $\varepsilon_k = E_k-\lambda$ (la quantité E_k est l'énergie d'une particule libre dans l'état k, enclose dans un volume Ω, et λ est le potentiel chimique). Les éléments de matrice de l'interaction sont symétrisés ou antisymétrisés.

La grande fonction de partition $Z = \operatorname{tr} e^{-\beta H}$ admet le développement suivant:

$$Z = Z_0\sum_{n=0}^{\infty}\frac{(-1)^n}{n!}\int_0^\beta du_1\ldots\int_0^\beta du_n\langle TV(u_1)V(u_2)\ldots V(u_n)\rangle, \tag{2}$$

où la notation $\langle\ \rangle$ désigne la valeur moyenne au sens de la mécanique statistique, c'est-à-dire

$$\langle A\rangle = \frac{1}{Z_0}\operatorname{tr}\{Ae^{-\beta H_0}\},$$

avec $Z_0 = \operatorname{tr} e^{-\beta H_0}$. Enfin, $V(u)$ est exprimé dans la représentation de l'interaction en fonction des opérateurs $a_k(u)$ et $a_k^\dagger(u)$ tels que

$$a_k(u) = a_k e^{-\varepsilon_k u},\quad a_k^\dagger(u) = a_k^\dagger e^{\varepsilon_k u}.$$

En substituant l'expression de $V(u)$ dans (2), nous obtenons

$$\frac{Z}{Z_0} = \sum_{n=0}^{\infty}\frac{(-1)^n}{n!}\sum_{r_i s_i m_i n_i}\tfrac{1}{4}\langle r_1 s_1|v|m_1 n_1\rangle\langle r_2 s_2|v|m_2 n_2\rangle\ldots$$
$$\times\int_0^\beta du_1\ldots\int_0^\beta du_n\langle Ta_{r_1}^\dagger(u_1)a_{s_1}^\dagger(u_1)a_{n_1}(u_1)a_{m_1}(u_1)a_{r_2}^\dagger(u_2)a_{s_2}^\dagger(u_2)a_{n_2}(u_2)a_{m_2}(u_2)\ldots\rangle. \tag{3}$$

2.2. LA REPRÉSENTATION EN DIAGRAMMES DES TERMES DE Z

Nous portons maintenant notre attention sur la valeur moyenne d'un produit chronologique de $4n$ opérateurs a ou $a^\dagger$, intervenant dans le terme d'ordre n de la formule (3), soit

$$T_n = \langle T a^\dagger_{r_1} a^\dagger_{s_1} a_{n_1} a_{m_1} a^\dagger_{r_2} a^\dagger_{s_2} a_{n_2} a_{m_2} \ldots a^\dagger_{r_n} a^\dagger_{s_n} a_{n_n} a_{m_n} \rangle. \tag{4}$$

Les sous-indices 1, 2, . . ., n, suffisent à repérer les temps u_1, u_2, . . ., . . . u_n. Le théorème de Wick décompose T_n en $2n!$ systèmes de contractions distincts. En effet, les contractions sont du type $\langle T a^\dagger a \rangle$ et l'on obtient tous les systèmes en associant de toutes les façons possibles les $2n$ opérateurs a à chacun des $2n$ opérateurs $a^\dagger$.

La représentation d'un système de contractions par un diagramme est connue [1]): on dessine les unes au-dessous des autres n lignes horizontales numérotées 1, 2, . . . n, qui correspondent aux interactions $V(u_1)$, $V(u_2)$, . . ., $V(u_n)$. On affecte à la partie gauche des lignes d'interaction les opérateurs $a_r^\dagger$ et a_m et à la partie droite les opérateurs $a_s^\dagger$ et a_n, que l'on représente par des extrémités de lignes orientées (fig. 1).

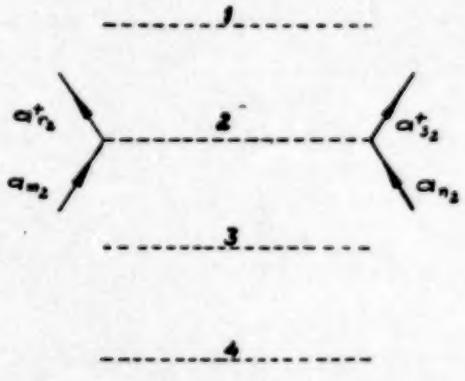

Fig. 1. Représentation des interactions.

Fig. 2. Ligne représentant la contraction $\langle T a^\dagger_{s_1} a_{m_2} \rangle$

On obtient tous les diagrammes en joignant entre elles de toutes les façons possibles les extrémités gauches ou droites des interactions (fig. 2).

Les éléments de matrice $\langle rs|v|mn \rangle$ ont un caractère de symétrie défini, pour l'échange des états m et n, ou l'échange des états r et s.

Les systèmes de contractions différant seulement par l'échange des opérateurs a_n et a_m ou $a_r^\dagger$ et $a_s^\dagger$, à l'intérieur des contractions, donnent donc la même contribution après sommation sur les indices. Par exemple, la fig. 3 montre l'échange de m_1 et n_1, où le produit

$$\langle T a^\dagger_{r_2} a_{m_1} \rangle \langle T a^\dagger_{s_2} a_{n_1} \rangle$$

est remplacé par

$$\varepsilon \langle T a^\dagger_{r_2} a_{n_1} \rangle \langle T a^\dagger_{s_2} a_{m_1} \rangle.$$

L'arrivée des deux lignes à l'interaction 1 est inversée. La valeur de ε est $+1$ ou -1 suivant qu'il s'agit de bosons ou de fermions.

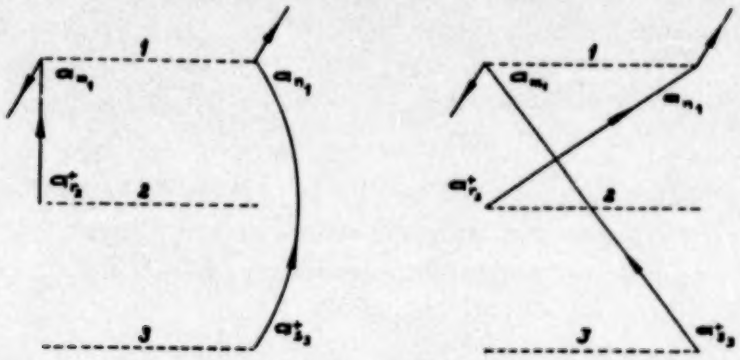

Fig. 3. Echange de a_{m_1} et de a_{n_1}.

Fig. 4. Dédoublement de la ligne d'interaction 1.

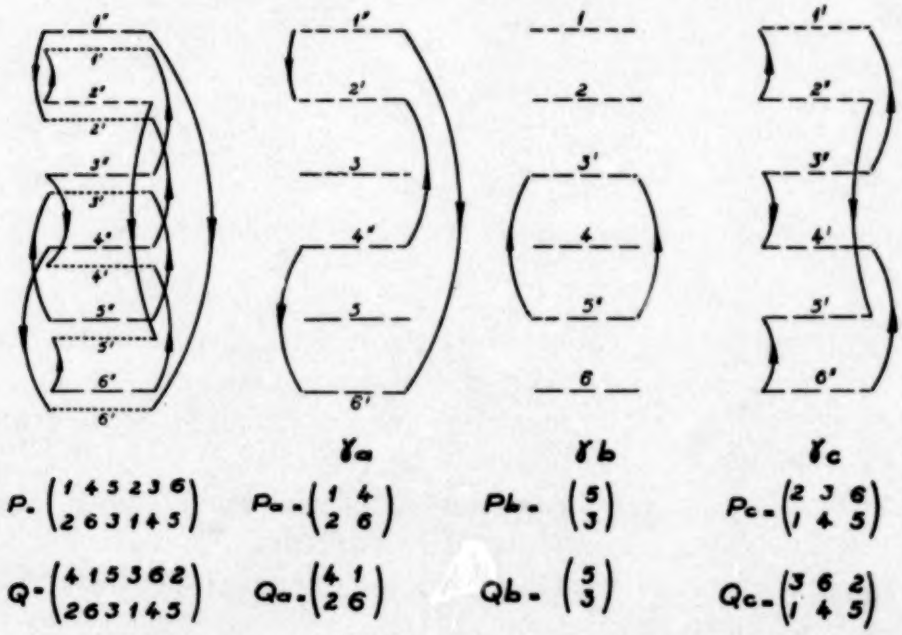

Fig. 5. Les cycles γ_a, γ_b, γ_c correspondant aux cycles (26), (3), (145) de $R' = QP^{-1}$.

De même pour un échange de r_1 et s_1, il suffit d'inverser les points de départ des deux lignes issues de l'interaction 1. Afin de rendre ces opérations d'échange

plus claires, nous allons „dédoubler" chaque interaction en deux lignes voisines que noterons 1′ et 1″ pour l'interaction 1. La ligne pointillée 1′ joint les opérateurs d'absorption et la ligne pointillée 1″ joint les opérateurs de création, comme si l'émission et l'absorption se faisaient à des temps différents (fig. 4).

L'échange de m_1 et n_1 se traduit alors par une symétrie gauche-droite sur l'interaction 1′ et l'échange de r_1 et s_1 par une symétrie analogue sur l'interaction 1″.

Le premier effet de ce dédoublement est de disconnecter le diagramme en un certain nombre de cycles (γ), indépendants les uns des autres quant aux opérations d'échange. Ces cycles, non orientés, sont déterminés de façon unique par le diagramme. Ils sont composés de lignes alternativement orientées dans un sens et dans l'autre, séparées par des lignes d'interaction V' et V'' (fig. 5).

2.3. NOUVELLE DESCRIPTION DES DIAGRAMMES

Définissons maintenant une classe (C) de diagrammes, à partir de laquelle tous les autres seront obtenus par échange de m et n ou de r et s. Décidons de n'effectuer les contractions qu'entre opérateurs $a_r^\dagger$ et a_m d'une part, et entre $a_s^\dagger$ et a_n d'autre part. Sur le diagramme, les extrémités gauches des interactions sont réunies par des lignes, de même que les extrémités droites, mais il n'y a pas de liaison gauche-droite. Pour décrire un tel diagramme, il suffit de deux permutations de n objets P et Q.

La permutation $i \to Pi$ fait correspondre l'opérateur a_{mPi} à $a^\dagger_{ri}$ dans la contraction $\langle Ta^\dagger_{ri} a_{mPi}\rangle$, et la permutation $i \to Qi$, a_{nQi} à $a^\dagger_{si}$.

Sur les diagrammes de (C), on reconnaît à gauche les cycles de P et à droite ceux de Q. Il y a donc correspondance biunivoque entre les systèmes de (C) et les couples (P, Q): leur nombre est $(n!)^2$. Pour cette classe (C), les „cycles" (γ) sont liés de façon très simple aux cycles de la permutation $R' = QP^{-1}$ ou à ceux de $R'' = P^{-1}Q$: les sommets consécutifs de (γ) notés V' décrivent les cycles de R'.

Si l'on isole un cycle de R' soit $(\alpha\beta\gamma \ldots \delta)$, on pourra écrire les "parties contigües" de R' à P et Q sous la forme

$$P = \begin{pmatrix} i & j & k \ldots & l \\ \alpha & \beta & \gamma \ldots & \delta \end{pmatrix}, \quad Q = \begin{pmatrix} j & k & \ldots & l & i \\ \alpha & \beta & \gamma \ldots & & \delta \end{pmatrix}.$$

Il faut noter que nous n'avons pas écrit P et Q tout entier, mais seulement les parties relatives à R' ou à (γ).

La fig. 5 montre un exemple de diagramme construit avec

$$P = \begin{pmatrix} 1 & 2 & 3 & 4 & 5 & 6 \\ 2 & 1 & 4 & 6 & 3 & 5 \end{pmatrix} \text{ ou } \left(\begin{array}{cc|c|ccc} 1 & 4 & 5 & 2 & 3 & 6 \\ 2 & 6 & 3 & 1 & 4 & 5 \end{array}\right),$$

$$Q = \begin{pmatrix} 1 & 2 & 3 & 4 & 5 & 6 \\ 6 & 5 & 1 & 2 & 3 & 4 \end{pmatrix} \text{ ou } \left(\begin{array}{cc|c|ccc} 4 & 1 & 5 & 3 & 6 & 2 \\ 2 & 6 & 3 & 1 & 4 & 5 \end{array}\right),$$

et, sous forme cyclique,

$$QP^{-1} = R' = (26)\,(3)\,(145),$$

où la seconde notation met en évidence les trois cycles (26), (3), (145) de R' et les „parties contigües" de P et Q correspondantes, que nous avons notées P_a, Q_a; P_b, Q_b; P_c, Q_c sur la fig. 5.

Avant d'effectuer les opérations de symétrisation sur les cyles (γ) à partir des diagrammes du type (C), nous remarquons que les seuls (γ) symétriques sont relatifs à des cycles de longueur 1 de R. En effet, si le cycle est symétrique, les parties contigües de P et Q au cycle correspondant de R sont identiques; le troisième diagramme de la fig. 5 illustre ce seul cas.

Soit donc un cycle (γ) non symétrique relatif à un cycle $(\alpha\beta\gamma \ldots \delta)$ de R', de longueur $p \neq 1$. On peut effectuer sur (γ), $2^{2p} = 4^p$ groupes d'échanges distincts, qui donnent donc lieu à autant de diagrammes distincts.

Inversement un cycle (γ) quelconque, du type (C) ou non, donne lieu à deux cycles (γ') et (γ'') du type (C): (γ') et (γ'') sont symétriques l'un de l'autre et ils engendrent le même ensemble de diagrammes après symétrisation (fig. 6).

Si les parties contigües de P et Q relatives au cycle $(\alpha\beta\gamma \ldots \delta)$ de R' décrivent (γ') et s'écrivent respectivement

$$(\gamma'): \quad P' = \begin{pmatrix} i & j & k \ldots l \\ \alpha & \beta & \gamma \ldots \delta \end{pmatrix}, \quad Q' = \begin{pmatrix} j & k & \ldots l & i \\ \alpha & \beta & \gamma \ldots & \delta \end{pmatrix},$$

nous aurons pour (γ'') à échanger le rôle des parties contigües P' et Q' (les autres parties de P et Q restent évidemment les mêmes)

$$(\gamma''): \quad P'' = Q' = \begin{pmatrix} j & k & \ldots l & i \\ \alpha & \beta & \gamma \ldots & \delta \end{pmatrix}, \quad Q'' = P' = \begin{pmatrix} i & j & k \ldots l \\ \alpha & \beta & \gamma \ldots \delta \end{pmatrix}.$$

On voit aisément sur la fig. 6 qu'il n'y a pas d'autres couples de permutation pour représenter un diagramme que les deux décrits ci-dessus. Si nous adoptons la convention de Hugenholtz [1]) de ramener la ligne d'interaction en un point, un diagramme détermine les cycles de R' (ou de R'') à l'orientation près, sauf pour les cycles de longueur 1, qui correspondent aux „doubles lignes". Aux deux choix d'orientation correspondent deux parties contigües possibles de P et Q relatives au cycle correspondant de R' (ou de R'').

En résumé, pour considérer l'ensemble des contributions auxquelles donnent lieu les $2n!$ systèmes de contractions, il suffit de choisir seulement les systèmes (C) définis par les couples (P, Q) à condition d'attribuer à la contribution de ce couple le poids $4^n(\frac{1}{2})^\nu$, où ν est le nombre de cycles de la permutation $R = QP^{-1}$.

En effet dans une sommation faite indépendamment sur P et Q, pour un cycle (γ) de R', le couple $(P, Q)_\gamma$ et le couple $(Q, P)_\gamma$ donneront la même contribution. Si R a pour longueur 1, le couple (P, Q) n'interviendra qu'une

seule fois dans la somme, mais au lieu d'avoir 4 diagrammes distincts par symétrisation, nous en aurons seulement 2.

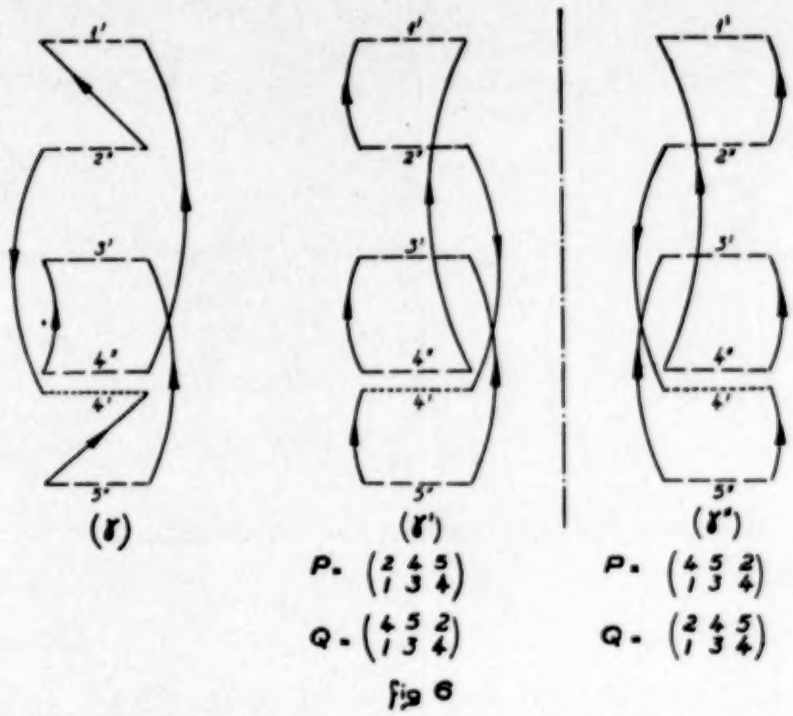

Fig. 6. Les symétries gauche-droite effectuées sur les interactions 2'', 4' de (γ') ou sur les interactions 1'. 3', 4', 5'' de (γ'') donnent le même diagramme (γ).

En règle générale, nous aurons le seul facteur de poids $(\frac{1}{2})^{\nu}$, le facteur $\frac{1}{4}$ devant chaque élément de matrice de (3) disparaissant.

2.4. DÉNOMBREMENT

Afin de montrer que nous avons obtenu tous les systèmes de contractions possibles, nous effectuons maintenant leur dénombrement.

Nous définirons par A_n le nombre de systèmes de contractions comptés avec la règle du paragraphe précédent:

$$A_n = \sum_{P,Q} \left(\frac{4}{2}\right)^{\nu_1} \left(\frac{4^2}{2}\right)^{\nu_2} \left(\frac{4^3}{2}\right)^{\nu_3} \dots,$$

où l'ensemble $\nu_1, \nu_2, \nu_3, \dots$ définit la classe de la permutation $R = QP^{-1}$ et la notation $\sum_{(\nu)}$ signifie la somme sur toutes les valeurs de $\nu_1, \nu_2, \dots$ telles que

$$\nu_1 + 2\nu_2 + 3\nu_3 + \dots = n.$$

Sommons sur les permutations P, à R fixé,

$$A_n = \sum_{P,R} \prod_p \left(\frac{4^p}{2}\right)^{\nu_p} = n! \sum_R \prod_p \left(\frac{4^p}{2}\right)^{\nu_p},$$

puis sur les permutations R de la même classe:

$$A_n = n! \sum_{(\nu)} \prod_p \left(\frac{4^p}{2}\right)^{\nu_p} \frac{1}{\nu_p! p^{\nu_p}} n!. \tag{5}$$

Introduisons la fonction génératrice $f(z)$ définie par la série entière

$$f(z) = \sum_{n=0}^{\infty} \frac{A_n}{(n!)^2} z^n. \tag{6}$$

En substituant la valeur de A_n donnée par l'expression (5), nous obtenons

$$f(z) = \sum_{\nu_1 \nu_2 \ldots} \prod_{p=1}^{\infty} \left\{\frac{(4z)^p}{2p}\right\}^{\nu_p} \frac{1}{\nu_p!} = \prod_{p=1}^{\infty} \exp \frac{(4z)^p}{2p} = \exp -\tfrac{1}{2} \log (1-4z),$$

soit

$$f(z) = (1-4z)^{-\frac{1}{2}}.$$

Cette fonction, développée par la formule du binôme, s'écrit

$$f(z) = \sum_{n=0}^{\infty} \frac{2n!}{(n!)^2} z^n. \tag{7}$$

L'identification des séries (6) et (7) permet de conclure

$$A_n = 2n!,$$

qui est en effet le nombre de tous les systèmes de contraction auxquels donne lieu le produit T_n du paragraphe 2.2.

2.5. EXPRESSION GÉNÉRALE D'UN SYSTÈME DE CONTRACTIONS

Pour les fermions, il nous reste à déterminer le signe à placer en tête de chaque système du type (C).

Écrivons la contribution, au signe près, d'un couple (P, Q), nous obtenons

$$(\tfrac{1}{2})^{\nu} \prod_{i=1}^{n} \langle T a^{\dagger}_{r_i} a_{m_{Pi}} \rangle \langle T a^{\dagger}_{s_i} a_{n_{Qi}} \rangle. \tag{8}$$

L'écriture de (8) fait apparaître les opérateurs dans l'ordre

$$a^{\dagger}_{r_1} a_{m_{P1}} a^{\dagger}_{s_1} a_{n_{Q1}} a^{\dagger}_{r_2} a_{m_{P2}} a^{\dagger}_{s_2} a_{n_{Q2}} \ldots, \tag{9}$$

que nous comparons à l'ordre suivant:

$$a^{\dagger}_{r_1} a_{m_1} a^{\dagger}_{s_1} a_{n_1} a^{\dagger}_{r_2} a_{m_2} a^{\dagger}_{s_2} a_{n_2} \ldots. \tag{10}$$

On remonte de (10) à (9) en effectuant d'abord les transpositions sur les a_m et ensuite sur les a_n. Or toute transposition sur les a_m, considérée comme permu-

tation de $4n$ objets est impaire, puisqu'il y a toujours un nombre impair d'objets entre deux a_m.

La permutation de $4n$ objets qui fait passer de (10) à (9) a donc la même parité que la permutation de n objets qui fait passer de l'ordre $m_1, m_2, m_3, \ldots$ à l'ordre $m_{P1}, m_{P2}, \ldots$, ce qui nous donne un facteur $I(P)$; le même raisonnement s'applique aux opérateurs a_n et donne un facteur $I(Q)$. Le signe cherché est donc $I(P)I(Q) = I(R) = (-1)^{n+\nu}$.

L'expression (4) s'écrit donc

$$T_n = \sum_{P,Q} f(R) \prod_{i=1}^{n} \langle T a^\dagger_{r_i} a_{m_{Pi}} \rangle \langle T a^\dagger_{s_i} a_{n_{Qi}} \rangle,$$

avec

$$f(R) = \begin{cases} (-1)^n (-\frac{1}{2})^\nu & \text{(fermions)}, \\ (\frac{1}{2})^\nu & \text{(bosons)}, \end{cases}$$

où ν est le nombre de cycles de la permutation $R = QP^{-1}$.

3. Forme du Développement dans la Représentation Indépendante du Temps

Le résultat précédent permet d'écrire l'expression (3) de Z sous la forme suivante:

$$\frac{Z}{Z_0} = \sum_{n=0}^{\infty} \frac{(-1)^n}{n!} \sum_{r_i s_i m_i n_i} \sum_{P,Q} f(R) \times \int_0^\beta du_1 \ldots \int_0^\beta du_n \prod_{i=1}^{n} \langle r_i s_i | v | m_i n_i \rangle \langle T a^\dagger_{r_i} a_{m_{Pi}} \rangle \langle T a^\dagger_{s_i} a_{n_{Qi}} \rangle.$$

Connaissant les propagateurs libres

$$\langle T a_k^\dagger(u) a_{k'}(u') \rangle = \delta_{kk'} G_k(u-u'),$$

nous sommons sur les indices r et s:

$$\frac{Z}{Z_0} = \sum_{n=0}^{\infty} \frac{(-1)^n}{n!} \sum_{m_i n_i} \sum_{P,Q} f(R) \times \int_0^\beta du_1 \ldots \int_0^\beta du_n \prod_{i=1}^{n} G_{m_{Pi}}(u_i - u_{Pi}) G_{n_{Qi}}(u_i - u_{Qi}) \langle m_{Pi} n_{Qi} | v | m_i n_i \rangle.$$

Afin d'effectuer l'intégration sur les variables u_i, nous utiliserons le développement connu [4]) de $G_k(u-u')$ en série de Fourier de période 2β. Nous avons

$$G_k(u) = \begin{cases} f_k^+ e^{-\varepsilon_k u} & \text{dans l'intervalle} \quad 0 < u \leqq \beta, \\ \varepsilon f_k^- e^{-\varepsilon_k u} & \text{dans l'intervalle} \quad -\beta < u \leqq 0, \end{cases}$$

avec $f_k^- = (e^{\beta\varepsilon_k} - \varepsilon)^{-1}$.

La fonctionad met un développement de Fourier, convergeant vers $G_k(u)$ pour $u \neq 0$ et $|u| \neq \beta$.

Posons

$$g_k(u) = \sum_l{}' c_k(l) e^{\frac{\pi i l}{\beta} u},$$

avec

$$c_k(l) = (\beta \varepsilon_k + \pi i l)^{-1},$$

où la somme est étendue aux valeurs paires ou impaires de l'entier l suivant qu'il s'agit de bosons ou de fermions. Les propriétés des séries de Fourier permettent de montrer que

$$g_k(u) = G_k(u) \quad \text{pour} \quad u \neq 0 \quad \text{et} \quad |u| \neq \beta,$$
$$g_k(+0) = f_k^+, \quad g_k(-0) = \varepsilon f_k^-, \quad g_k(0) = \tfrac{1}{2}(f_k^+ - \varepsilon f_k^-).$$

On pourra cependant utiliser dans tout l'intervalle la fonction $g_k(u)$ en écrivant

$$G_k(u) = \lim_{\tau \to 0} g_k(u-\tau), \quad \tau > 0.$$

Après avoir introduit deux suites d'entiers p_i et q_i, l'intégration sur les variables u_i est immédiate:

$$\int_0^\beta du_1 \ldots \int_0^\beta du_n \prod_{i=1}^n G_{m_{P_i}}(u_i - u_{P_i}) G_{n_{Q_i}}(u_i - u_{Q_i})$$
$$= \lim_{\tau \to 0} \sum_{p_i}{}' \sum_{q_i}{}' \int_0^\beta du_1 \ldots \int_0^\beta du_n \prod_{i=1}^n c_{m_{P_i}}(p_{P_i}) c_{n_{Q_i}}(q_{Q_i})$$
$$\times \exp\left\{\frac{\pi i}{\beta}(p_{P_i} + q_{Q_i} - p_i - q_i) - \frac{\pi i}{\beta}\tau(p_i + q_i)\right\}$$
$$= \lim_{\tau \to 0} \beta^n \sum_{p_i q_i}{}' \prod_{i=1}^n c_{m_i}(p_i) c_{n_i}(q_i) \delta_{kr}(p_{P_i} + q_{Q_i} - p_i - q_i) \exp - \frac{\pi i \tau}{\beta}\left(\sum_i p_i + q_i\right).$$

On pourra omettre le dernier facteur exponentiel qui dépend de τ et écrire $c_m(p)$ au lieu de $c_m(p)\, e^{\pi i \tau p/\beta}$.

Par commodité, nous définissons un élément de matrice

$$\langle p' q' | V | pq \rangle = \langle m' n' | v | mn \rangle \delta(p' + q' - p - q),$$

où la lettre p désigne à la fois l'état m et la variable entière p. Dans le cas d'un système infini, $\langle |V| \rangle$ contient donc à la fois la conservation de l'impulsion et de „l'énergie".

La fonction de partition prend alors la forme

$$\frac{Z}{Z_0} = \sum_{n=0}^\infty \frac{(-\beta)^n}{n!} \sum_{PQ} f(R) \sum_{p_i q_i} \prod_{i=1}^n c(p_i) c(q_i) \langle p_{P_i} q_{Q_i} | V | p_i q_i \rangle. \qquad (12)$$

Cette dernière forme de Z montre que les sommations sur P et Q portent seulement sur les produits d'éléments de matrice

$$\sum_{P,Q} f(R) \prod_{i=1}^{n} \langle p_{P_i} q_{Q_i} | V | p_i q_i \rangle,$$

que nous pouvons écrire

$$\sum_{R} f(R) \sum_{P} \prod_{i=1}^{n} \langle p_i q_{R_i} | V | p_{P_i} q_{P_i} \rangle.$$

Nous remarquons maintenant que les permutations R qui appartiennent à une même classe donnent la même contribution, après sommation sur les variables P et Q.

Effectuons le changement de variables

$$p'_{C_i} = p_i, \quad q'_{C_i} = q_i,$$

où C désigne une permutation quelconque. Nous avons

$$\prod_{i=1}^{n} \langle p_i q_{R_i} | V | p_{P_i} q_{P_i} \rangle = \prod_{i=1}^{n} \langle p'_{C_i} q'_{CR_i} | V | p'_{CP_i} q'_{CP_i} \rangle$$

$$= \prod_{i=1}^{n} \langle p'_i q'_{CRC^{-1}i} | V | p'_{CPC^{-1}i} q'_{CPC^{-1}i} \rangle,$$

d'où l'on déduit le résultat annoncé

$$\sum_{pq} \sum_{P} \prod_{i} \langle p_i q_{R_i} | V | p_{P_i} q_{P_i} \rangle c(p_i) c(q_i) = \sum_{p'q'} \sum_{P} \prod_{i} \langle p'_i q'_{CRC^{-1}i} | V | p'_{P_i} q'_{P_i} \rangle c(p'_i) c(q'_i).$$

On pourra donc restreindre la sommation aux différentes classes de R, que nous noterons $\{R\}$, à condition de multiplier par $\mathcal{N}(R)$, égal au nombre de permutations de la classe $\{R\}$ considérée. Si $\{R\}$ contient ν_p cycles de longueur p,

$$\mathcal{N}(R) = n! \prod_{p} \frac{1}{\nu_p!\, p^{\nu_p}}, \quad \sum_{p} p\nu_p = n.$$

Le résultat final s'écrit donc

$$\frac{Z}{Z_0} = \sum_{n=0}^{\infty} \frac{(-\beta)^n}{n!} \sum_{\{R\}} f(R) \mathcal{N}(R) \times \sum_{pq} \sum_{P} \prod_{i=1}^{n} \langle p_i q_{R_i} | V | p_{P_i} q_{P_i} \rangle c(p_i) c(q_i). \quad (13)$$

A l'ordre n, les différents produits d'éléments de matrice se groupent donc, pour chaque classe $\{R\}$, en une combinaison symétrique qui est un permanent $n \times n$ et que nous appèlerons Δ_R

Soient $C_1, C_2, \ldots, C_\alpha, \ldots$, les cycles de R, de longueurs $l_1, l_2, \ldots, l_\alpha, \ldots,$

avec $l_1 \leqq l_2 \leqq \ldots \leqq l_\nu$, le permanent a l'aspect suivant:

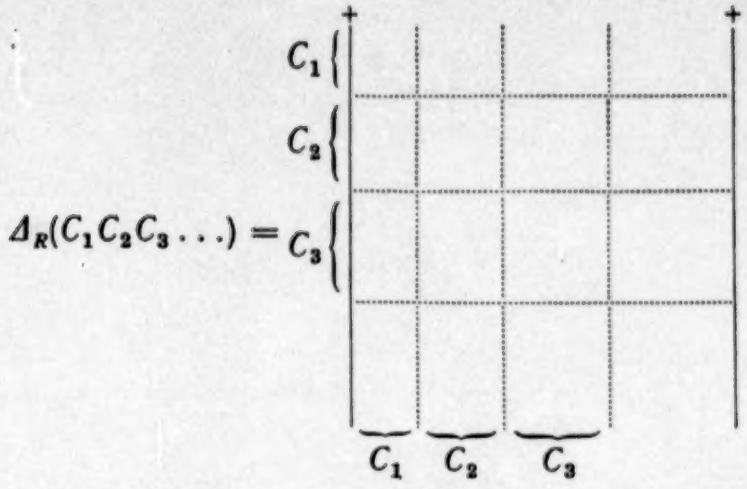

Si nous appelons $p_1^\alpha, p_2^\alpha, \ldots, p_{i_\alpha}^\alpha, q_1^\alpha, q_2^\alpha, \ldots, q_{i_\alpha}^\alpha$, les variables relatives au cycle C_α, la matrice dont les lignes appartiennent à C_α et les colonnes à C_λ s'écrit

$$C_\alpha \left\{ \begin{array}{|l} \langle p_1^\alpha q_2^\alpha | V | p_1^\lambda q_1^\lambda \rangle \langle p_1^\alpha q_2^\alpha | V | p_2^\lambda q_2^\lambda \rangle \ldots \langle p_1^\alpha q_2^\alpha | V | p_{i_\lambda}^\lambda q_{i_\lambda}^\lambda \rangle \\ \langle p_2^\alpha q_3^\alpha | V | p_1^\lambda q_1^\lambda \rangle \langle p_2^\alpha q_3^\alpha | V | p_2^\lambda q_2^\lambda \rangle \ldots \langle p_2^\alpha q_3^\alpha | V | p_{i_\lambda}^\lambda q_{i_\lambda}^\lambda \rangle \\ \langle p_3^\alpha q_4^\alpha | V | p_1^\lambda q_1^\lambda \rangle \ldots \ldots \ldots \langle p_3^\alpha q_4^\alpha | V | p_{i_\lambda}^\lambda q_{i_\lambda}^\lambda \rangle \\ \ldots\ldots\ldots\ldots\ldots\ldots\ldots\ldots\ldots\ldots\ldots\ldots\ldots\ldots\ldots\ldots\ldots\ldots \\ \ldots\ldots\ldots\ldots\ldots\ldots\ldots\ldots\ldots\ldots\ldots\ldots\ldots\ldots\ldots\ldots\ldots\ldots \\ \langle p_{i_\alpha}^\alpha q_1^\alpha | V | p_1^\lambda q_1^\lambda \rangle \ldots \ldots \ldots \ldots \ldots \langle p_{i_\alpha}^\alpha q_1^\alpha | V | p_{i_\lambda}^\lambda q_{i_\lambda}^\lambda \rangle \end{array} \right\} C_\lambda$$

Nous pouvons alors revenir à la représentation en diagramme de la manière suivante: dessinons les cycles (γ), disjoints, en confondant en un seul point les lignes d'interactions. Ces cycles sont formés de lignes alternativement orientées dans un sens et dans l'autre (fig. 7). Il existe deux sortes de sommets, les uns notés V' où convergent deux lignes, les autres notés V'' d'où partent deux lignes. À l'ordre n, on a $2n$ lignes et $2n$ sommets. On connecte ensuite les cycles (γ) de toutes les façons possibles en joignant les sommets V' aux sommets V'' par des lignes pointillées orientées qui représentent un élément de matrice et transfèrent l'impulsion et l'énergie totale de la paire en interaction. Nous allons justement porter notre attention dans les paragraphes suivants au cas où l'on impose que ces transferts soient nuls (fig. 8).

Cette représentation peut être commode, pour calculer les contributions des diagrammes connexes. On peut, en effet, montrer que la formule exponentielle permet d'écrire le potentiel de Gibbs sous une forme identique à (13) mais en

restreignant les sommations sur les permutations P qui forment une configuration connexe avec R. Les facteurs de poids ne dépendent toujours que de R.

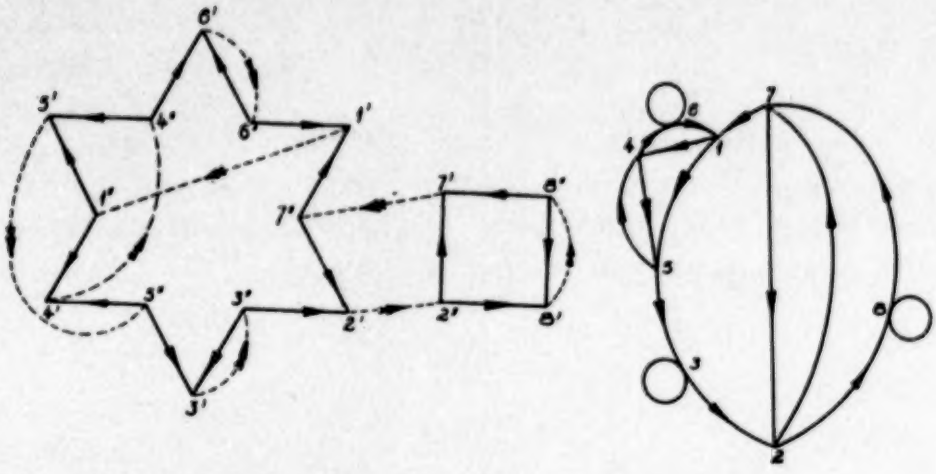

Fig. 7. Représentation d'un diagramme contenant deux cycles (γ)
avec $R = (123456)\ (78)$, et $P = \begin{pmatrix}12345678\\47253618\end{pmatrix}$;
à droite, le même diagramme dans la description de Hugenholtz.

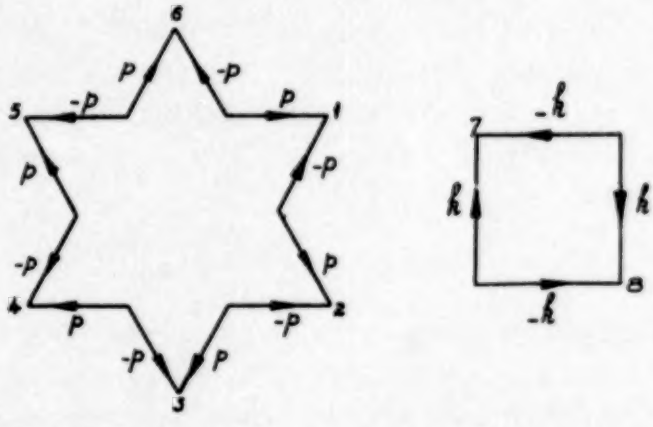

Fig. 8. Les deux seuls cycles d'impulsion et d' „énergie" non nulle du diagramme précédent.

4. Application à un Système de Fermions de Spin $\frac{1}{2}$

4.1. HYPOTHÈSES

Nous considérons un système de fermions enclos dans un grand volume Ω; les états individuels sont repérés par l'impulsion $\mathbf{p}$ et une composante de spin notée $\uparrow$ ou $\downarrow$. A la limite Ω infini, l'impulsion est conservée à chaque interaction dont nous écrivons les éléments de matrice sous la forme

$$\frac{1}{\Omega}\langle \mathbf{rs}|v|\mathbf{nm}\rangle \delta(\mathbf{r}+\mathbf{s}-\mathbf{n}-\mathbf{m}).$$

D'autre part, nous omettons toujours de noter la sommation sur les spins, qui sera comprise dans la notation

$$\sum_{\mathbf{p}} \sim \frac{2\Omega}{(2\pi)^3}\int \mathrm{d}^3\mathbf{p}.$$

Partons de l'expression (13) de $\zeta \equiv Z/Z_0$. Nous allons extraire de ζ une série partielle $\zeta_1 = Z_1/Z_0$, dont nous évaluerons exactement la contribution dans le cas d'une interaction séparable. Cette série partielle est définie de façon à ne contenir que des éléments de matrice du type

$$\langle p\uparrow, -p\downarrow|V|p'\uparrow, -p'\downarrow\rangle = -\langle p\downarrow, -p\uparrow|V|p'\uparrow, -p'\downarrow\rangle$$
$$= \frac{1}{\Omega}\langle \mathbf{p}, -\mathbf{p}|v|\mathbf{p}', -\mathbf{p}'\rangle.$$

Comme plus haut, p désigne l'ensemble de la variable d'impulsion $\mathbf{p}$ et de la variable d',,énergie'' notée encore p. Nous retenons donc seulement les termes de l'hamiltonien modèle de Bardeen [5]) où l'interaction n'a lieu qu'entre paires d'impulsion totale nulle dans l'état singulet, mais nous imposons de plus la condition d',,énergie'' totale nulle. Ce traitement symétrique est naturel dans une représentation indépendante du temps. En termes de diagrammes, au lieu de sommer sur les variables attachées à un système de cycles indépendants pour chaque partie connexe, nous nous limitons aux seuls cycles (γ) (fig. 8).

Afin d'effectuer la sommation de la série $\zeta_1 = Z_1/Z_0$ sans autre approximation, nous prendrons

$$\langle \mathbf{p}, -\mathbf{p}|v|\mathbf{p}', -\mathbf{p}'\rangle = g v_p v_{p'},$$

où v_p est une fonction de $|\mathbf{p}|$, et g est positif ou négatif suivant que le potentiel est répulsif ou attractif. On voit alors comment l'introduction du potentiel séparable permet de factoriser les contributions des différents cycles (γ) quelque soit la façon dont les interactions les connectent.

4.2. SOMMATION DE Z_1/Z_0

Selon (13), les éléments de matrice de V interviennent dans le produit

$$\prod_{i=1}^{n} \langle p_i q_{Ri}|V|p_{Pi} q_{Pi}\rangle.$$

D'après les hypothèses de la paragraphe 4.1, nous aurons, quel que soit l'indice i,

$$p_i = -q_{Ri}, \quad p_i = -q_i,$$

ce qui entraîne

$$p_i = p_{Ri}.$$

La sommation sur les variables q_i peut être effectuée:

$$\sum_{q_i} \prod_{i=1}^{n} c(p_i)c(q_i)\langle p_i q_{Ri}|V|p_{Pi}q_{Pi}\rangle = \left(\frac{g}{\Omega}\right)^n \prod_{i=1}^{n} c(p_i)c(-p_i)v_{p_i}^2\delta(p_i-p_{Ri}).$$

Cette expression est indépendante de la permutation P. Si nous la substituons dans la série (13), avec

$$c(p) = (\beta\varepsilon_{\mathbf{p}}+\pi i l)^{-1}, \quad p \to (\mathbf{p}, l),$$

le facteur $1/n!$ disparaît après sommation sur les diverses P et nous obtenons

$$\zeta_1 = \sum_{n=0}^{\infty}\left(\frac{-g\beta}{\Omega}\right)^n \sum_{\{R\}} f(R)\mathcal{N}(R) \sum_{\mathbf{p}_i l_i}{}' \prod_{i=1}^{n} \frac{v_{p_i}^2}{\beta^2\varepsilon_{p_i}^2+\pi^2 l_i^2}\delta(p_i-p_{Ri}).$$

Écrivons maintenant une permutation de la classe $\{R\}$ sous forme cyclique: soit $(\alpha\beta\gamma\ldots\delta)$ l'un des cycles. Le produit des fonctions $\delta(p_i-p_{Ri})$ fournit un facteur $\delta(p_\alpha-p_\beta)\delta(p_\beta-p_\gamma)\ldots\delta(p_\delta-p_\alpha)$; c'est-à-dire après sommation sur toutes les variables sauf une par cycle, nous devons attribuer un ensemble $\mathbf{p}, l$ de variables indépendantes à chaque cycle de R. Si nous repérons la classe de R par $\nu_1, \nu_2, \ldots, \nu_p, \ldots$ où les ν_p sont liés par la relation

$$\nu_1+2\nu_2+3\nu_3+\ldots = n,$$

la série $\zeta_1 = Z_1/Z_0$ devient

$$\zeta_1 = \sum_{n=0}^{\infty}\left(\frac{-g\beta}{\Omega}\right)^n \sum_{(\nu)} (-1)^n(-\tfrac{1}{2})^{\nu_1+\nu_3+\cdots} n! \prod_{k=1}^{\infty} \frac{1}{k^{\nu_k}\nu_k!}\left\{\sum_{\mathbf{p},l}{}'\left(\frac{v_p{}^2}{\beta^2\varepsilon_p{}^2+\pi^2 l^2}\right)^k\right\}^{\nu_k}$$

$$= \sum_{n=0}^{\infty} n! \sum_{(\nu)} \prod_k \frac{1}{\nu_k!}\left\{-\frac{1}{2k}\sum_{\mathbf{p},l}\left(\frac{1}{\Omega}\frac{g\beta v_p{}^2}{\beta^2\varepsilon_p{}^2+\pi^2 l^2}\right)^k\right\}^{\nu_k}.$$

Si l'on définit les fonctions $h_k(\rho)$ d'une variable ρ,

$$h_k(\rho) = -\frac{1}{2k}\sum_{\mathbf{p},l}{}'\left(\frac{g\beta\rho}{\Omega}\frac{v_p{}^2}{\beta^2\varepsilon_p{}^2+\pi^2 l^2}\right)^k,$$

et les nombres $h_k = h_k(\rho = 1)$, ζ_1 s'écrit

$$\zeta_1 = \sum_n n! \sum_{(\nu)} \prod_{k=1}^{\infty} \frac{1}{\nu_k!} h_k{}^{\nu_k}.$$

Nous pouvons sommer cette série en définissant $n!$ par l'égalité

$$n! = \int_0^\infty \mathrm{e}^{-\rho}\rho^n \mathrm{d}\rho,$$

d'où, formellement:

$$\zeta_1 = \int_0^\infty \mathrm{d}\rho\, \mathrm{e}^{-\rho} \prod_{k=1}^{\infty} \sum_{\nu_k} \frac{1}{\nu_k!} h_k{}^{\nu_k}(\rho) = \int_0^\infty \exp\left(-\rho+\sum_{k=1}^{\infty} h_k(\rho)\right)\mathrm{d}\rho, \qquad (14)$$

avec

$$\sum_k h_k(\rho) = -\sum_k \frac{1}{2k} \sum_{p,l}{}' \left(\frac{g\beta\rho}{\Omega} \frac{v_p^2}{\beta^2\varepsilon_p^2+\pi^2 l^2} \right)^k = \sum_{p,l>0} \log \left(1 - \frac{g\beta\rho}{\Omega} \frac{v_p^2}{\beta^2\varepsilon_p^2+\pi^2 l^2} \right). \quad (15)$$

Nous remarquons que la série précédente envisagée comme fonction analytique de ρ (ou de g) n'est pas uniforme. Cette difficulté est levée en considérant la fonction exp $\sum_k h_k(\rho)$ qui intervient seulement et qui s'écrit dans tous les cas

$$\prod_{p,l>0} \left(1 - \frac{g\beta\rho}{\Omega} \frac{v_p^2}{\beta^2\varepsilon_p^2+\pi^2 l^2} \right).$$

Le produit infini sur l impair positif a pour valeur

$$\operatorname{ch} \tfrac{1}{2}\beta\omega_p / \operatorname{ch} \tfrac{1}{2}\beta\varepsilon_p,$$

où l'on a posé

$$\omega_p^2 = \varepsilon_p^2 - \frac{g\rho}{\beta\Omega} v_p^2.$$

Si g est positif (cas répulsif), ω_p^2 peut prendre des valeurs négatives lorsque ρ varie de 0 à $+\infty$, et ch $\frac{1}{2}\beta\omega_p$ doit être écrit

$$\cos \tfrac{1}{2}\beta \left(\frac{g\rho}{\beta\Omega} v_p^2 - \varepsilon_p^2 \right)^{\frac{1}{2}}.$$

Le produit infini sur $\mathbf{p}$ a la forme suivante:

$$\left\{ \prod_k \cos \tfrac{1}{2}\beta \left(\frac{g\rho}{\beta\Omega} v_k^2 - \varepsilon_k^2 \right)^{\frac{1}{2}} \Big/ \operatorname{ch} \tfrac{1}{2}\beta\varepsilon_k \right\} \times \left\{ \prod_q \operatorname{ch} \tfrac{1}{2}\beta\omega_q / \operatorname{ch} \tfrac{1}{2}\beta\varepsilon_q \right\}. \quad (16)$$

La première parenthèse enferme un produit fini, puisqu'il est restreint aux valeurs de $\mathbf{k}$ telles que $|\varepsilon_k| < v_k(g\rho/\beta\Omega)^{\frac{1}{2}}$. Le second produit est étendu aux valeurs de $\mathbf{q}$ telles que $|\varepsilon_q| > v_q(g\rho/\beta\Omega)^{\frac{1}{2}}$ et converge avec l'intégrale $\int v_q^2 \mathrm{d}q$. Nous supposerons donc que v_q décroît convenablement à l'infini. Dans la région d'intégration $\rho \geqq 0$, le prolongement analytique des fonctions à intégrer est donc défini sans ambiguité, essentiellement à volume fini.

4.3. LE COMPORTEMENT ASYMPTOTIQUE DE Z_1/Z_0

L'étude du comportement asymptotique de $\zeta_1 = Z_1/Z_0$ lorsque Ω augmente indéfiniment, nous amène à traiter séparément les cas attractif et répulsif. Dans le premier cas, $g < 0$, il existe une valeur critique β_c, au-dessus de laquelle la quantité

$$\mathscr{P} = -\lim_{\Omega\to\infty} (\beta\Omega)^{-1} \log (Z_1/Z_0)$$

n'est pas nulle et détermine l'énergie libre de la phase superconductrice. Au-dessous de la valeur β_c, pour $g < 0$ et quel que soit β pour $g > 0$, $\mathscr{P} = 0$ et ζ_1

est indépendant du volume: on obtient alors la seule contribution dite des „échelles généralisées" calculées dans l'hypothèse des paires d'énergie nulle. On sait que dans la série des diagrammes connexes qui définissent le potentiel thermodynamique ce sont les échelles qui donnent la contribution maximum, indépendante du volume. Elles ont été sommées en toute généralité [8]) et convergent si g est positif, pour $\beta < \beta_c$, si g est négatif. C'est cependant le terme dû aux paires „d'énergie" nulle qui présente la première singularité, en β_c, lorsque β augmente. On peut donc penser que cette hypothèse des paires est valable dans le voisinage de la température critique.

4.3.1. Cas attractif, $g < 0$.

D'après (14) et (15), nous écrivons Z_1/Z_0 sous la forme

$$\frac{Z_1}{Z_0} = \int_0^\infty \exp\left\{-\rho + \sum_{\mathbf{p},l>0} \log\left(1 - \frac{g\beta\rho}{\Omega}\,\frac{v_p^{\,2}}{\beta^2\varepsilon_p^{\,2}+\pi^2 l^2}\right)\right\} \mathrm{d}\rho$$

$$= \int_0^\infty \exp\left\{-\rho + \sum_{\mathbf{p}} \log(\mathrm{ch}\,\tfrac{1}{2}\beta\omega_p/\mathrm{ch}\,\tfrac{1}{2}\beta\varepsilon_p)\right\}\mathrm{d}\rho. \quad (17)$$

La somme sur $\mathbf{p}$ converge quel que soit ρ avec l'intégrale $\int v_p^{\,2}\mathrm{d}p$. Changeons de variable pour l'intégration en ρ en posant

$$x = \frac{|g|\rho}{\Omega\beta}.$$

D'autre part, à la limite du volume infini,

$$\frac{1}{\Omega}\sum_{\mathbf{p}} \to \frac{2}{(2\pi)^3}\int \mathrm{d}^3\mathrm{p}.$$

Définissons $f(x)$ par l'égalité suivante:

$$f(x) = -\frac{1}{|g|}\beta x + \frac{2}{(2\pi)^3}\int \mathrm{d}^3\mathbf{p} \sum_{l>0} \log\left(1 + \frac{x\beta^2 v_p^{\,2}}{\beta^2\varepsilon_p^{\,2}+\pi^2 l^2}\right).$$

Nous avons, pour le logarithme des deux membres de (17),

$$\frac{1}{\Omega}\log(Z_1/Z_0) = \frac{1}{\Omega}\log\frac{\Omega}{|g|\beta} + \frac{1}{\Omega}\log\int_0^\infty \mathrm{d}x\, \mathrm{e}^{\Omega f(x)}.$$

La méthode de Laplace conduit à rechercher le maximum absolu de $f(x)$ pour $x \geqq 0$, et à calculer sa dérivée:

$$f'(x) = -\frac{\beta}{|g|} + \beta^2\frac{2}{(2\pi)^3}\int \mathrm{d}^3\mathbf{p} \sum_{l>0} \frac{v_p^{\,2}}{\beta^2\varepsilon_p^{\,2}+\pi^2 l^2}.$$

Sous cette forme, on voit que la dérivée seconde est toujours négative. Si

l'équation $f'(x) = 0$, possède une solution ξ, celle-ci est unique. L'équation pour ξ s'écrit donc

$$1 = \frac{|g|}{2(2\pi)^3}\int \mathrm{d}^3\mathbf{p}\ \ v_p^2\,\frac{1}{\omega_p}\,\mathrm{th}\,\tfrac{1}{2}\beta\omega_p, \tag{18}$$

avec

$$\omega_p^2 = \varepsilon_p^2 + \xi v_p^2.$$

On reconnaît en (18) l'équation connue qui détermine le „gap" $\Delta_p^2 = \xi v_p^2$, en fonction de β. Il existe une valeur β_c telle que la solution $\xi(\beta)$ existe pour $\beta \geqq \beta_c$. Plaçons-nous d'abord dans ce cas. Nous obtenons

$$\mathscr{P} = \lim_{\Omega\to\infty} -\frac{1}{\beta\Omega}\log\,(Z_1/Z_0) = -\frac{1}{\beta}f(\xi).$$

C'est-à-dire, pour le potentiel thermodynamique $\Omega\psi$,

$$\psi = \lim_{\Omega\to\infty} -\frac{1}{\beta\Omega}\log Z_1 = -\frac{1}{\beta\Omega}\log Z_0 - \frac{1}{\beta}f(\xi),$$

$$= -\frac{1}{\beta}\frac{2}{(2\pi)^3}\int \mathrm{d}^3\mathbf{p}\log(1+\mathrm{e}^{-\beta\varepsilon_p}) + \frac{\xi}{|g|} - \frac{2}{(2\pi)^3}\,\frac{1}{\beta}\int \mathrm{d}^3\mathbf{p}\,\log\,(\mathrm{ch}\,\tfrac{1}{2}\beta\omega_p/\mathrm{ch}\,\tfrac{1}{2}\beta\varepsilon_p),$$

ou

$$\psi = \frac{\xi}{|g|} - \frac{2}{(2\pi)^3}\,\frac{1}{\beta}\int \mathrm{d}^3\mathbf{p}\,\log\,(1+\mathrm{e}^{-\beta\omega_p}) - \frac{1}{(2\pi)^3}\int \mathrm{d}^3\mathbf{p}\,(\omega_p - \varepsilon_p).$$

Cette formule est la spécialisation au cas du potentiel séparable du résultat plus général donné par Bogoliubov, Zubarev et Tserkovnikov [6]).

Considérons maintenant le domaine $\beta < \beta_c$, où l'équation (18) n'a pas de solution. Le maximum de $f(x)$ est atteint pour $x = 0$ et l'on trouve $\mathscr{P} = 0$. Si l'on veut obtenir la limite de Z_1/Z_0, il faut revenir à l'expression (17) qui est uniformément convergente par rapport à Ω et l'on obtient

$$\lim Z_1/Z_0 = \int_0^\infty \exp\left\{-\rho - \frac{g\beta\rho}{\Omega}\sum_{\mathbf{p},l}\frac{v_p^2}{\beta^2\varepsilon_p^2+\pi^2l^2}\right\}\mathrm{d}\rho = \frac{1}{1+gF(\beta)},$$

avec la définition suivante de $F(\beta)$:

$$F(\beta) = \frac{\beta}{\Omega}\sum_{\mathbf{p},l>0}\frac{v_p^2}{\beta^2\varepsilon_p^2+\pi^2l^2} = \frac{1}{2(2\pi)^3}\int \mathrm{d}^3\mathbf{p}\ \ v_p^2\,\frac{1}{\varepsilon_p}\,\mathrm{th}\,\tfrac{1}{2}\beta\varepsilon_p.$$

Si l'on effectue la sommation des échelles on obtient effectivement $\log Z = \log Z_0 - \log(1+gF(\beta)) + \ldots$. La singularité en β_c est déterminée par l'équation $1 = -gF(\beta_c)$, qui coïncide avec (18) pour $\xi = 0$.

4.3.2. Cas répulsif, $g > 0$

Nous montrons ici la convergence uniforme par rapport au volume de l'expression (14) que nous devons écrire

$$\zeta_1 = \frac{Z_1}{Z_0} = \int_0^\infty e^{-\rho} \prod_{\mathbf{p}} (\operatorname{ch} \tfrac{1}{2}\beta\omega_{\mathbf{p}} / \operatorname{ch} \tfrac{1}{2}\beta\varepsilon_{\mathbf{p}}) d\rho,$$

où le produit $\prod_{\mathbf{p}}(\ldots)$ est défini par (16). Chaque facteur de ce produit est en valeur absolue inférieur à 1, nous avons donc $|\prod_{\mathbf{p}}(\ldots)| \leqq 1$.

Divisons l'intégrale sur ρ qui définit ζ_1 en deux parts

$$\zeta_1 = \int_0^\infty e^{-\rho} \prod_{\mathbf{p}} (\ldots) d\rho = \int_0^R + \int_R^\infty. \tag{19}$$

La seconde intégrale est inférieure en module à e^{-R}. Nous pouvons étudier la première pour $\Omega \to \infty$. Elle s'écrit, d'après (16),

$$\int_0^R d\rho e^{-\rho} \prod_{\mathbf{p}} (\ldots) = \int_0^R d\rho\, e^{-\rho} \prod_{\mathbf{k}} (\ldots) \times \prod_{\mathbf{q}} (\ldots).$$

Le premier produit $\prod_{\mathbf{k}}$ est restreint au domaine $|\varepsilon_{\mathbf{k}}| < v_k (g\rho/\beta\Omega)^{\frac{1}{2}}$.

Le domaine du produit sur $\mathbf{k}$ et l'argument du cos $(\ldots)$ tendent vers zéro uniformément par rapport à ρ,

$$\frac{|\varepsilon_{\mathbf{k}}|}{v_k} \leqq \left(\frac{g\rho}{\beta\Omega}\right)^{\frac{1}{2}} \leqq \left(\frac{gR}{\beta\Omega}\right)^{\frac{1}{2}}.$$

On peut donc remplacer $\prod_{\mathbf{k}}(\ldots)$ par l'unité sous l'intégrale $\int_0^R$, qui peut s'écrire maintenant

$$\int_0^R d\rho \exp\{-\rho + \sum_{\mathbf{q}} \log (\operatorname{ch} \tfrac{1}{2}\beta\omega_{\mathbf{q}} / \operatorname{ch} \tfrac{1}{2}\beta\varepsilon_{\mathbf{q}})\}, \tag{20}$$

avec

$$|\varepsilon_{\mathbf{q}}| > v_q (g\rho/\beta\Omega)^{\frac{1}{2}}.$$

Comme dans le cas attractif, si Ω tend vers l'infini, on obtient par un développement limité au terme en $1/\Omega$,

$$\sum_{\mathbf{q}} (\ldots) \sim \frac{2\Omega}{(2\pi)^3} \int \operatorname{th} \tfrac{1}{2}\beta\varepsilon_q \left(-\frac{g\rho}{4\Omega} \frac{v_q^2}{\varepsilon_q}\right) d^3\mathbf{q} = -g\rho F(\beta).$$

C'est-à-dire, après substitution dans (20),

$$\left|\zeta_1 - \int_0^R d\rho\, e^{-\rho(1+gF(\beta))}\right| < e^{-R}.$$

D'après (19), R est arbitraire, la limite de ζ_1 est donc $(1+gF(\beta))^{-1}$.

Dans les deux cas, ce résultat s'obtient en ne conservant que le premier

terme $h_1(\rho)$ de la série $\sum_{k=1}^{\infty} h_k(\rho)$ dans (14). Ce terme correspond en effet aux cycles de $\{R\}$ de longueur 1, les seuls à retenir pour la définition des diagrammes en échelles.

5. Conclusion

Sans qu'une justification plus précise en soit donnée, nous avons vu dans ce papier comment une écriture nouvelle de la série de perturbation de Z/Z_0 et la représentation correspondante des diagrammes, permet de reconnaître le rôle particulier joué par les termes de l'hamiltonien modèle de Bardeen et d'extraire la série partielle qui donne le résultat connu. La sommation exacte est possible grâce au potentiel séparable, sans lequel il faudrait évaluer de façon approchée les permanents qui rassemblent les éléments de matrice, afin de retrouver la solution plus générale de Bololiubov [6]).

Je remercie le Professeur C. Bloch et Monsieur R. Balian pour les nombreux conseils et remarques qui m'ont aidé dans ce travail.

Bibliographie

1) N. M. Hugenholtz, Physica **23** (1957) 481;
J. Goldstone, Proc. Roy. Soc. A **239** (1957) 267;
C. Bloch et C. De Dominicis, Nuclear Physics **7** (1958) 459
2) R. Balian, Rapport S.P.M. no 468, Saclay
3) E. R. Caïaniello, Nuovo Cim. **9** (1958) 569
4) E. W. Montroll et J. C. Ward, Physics of Fluids **1** (1958) 55
5) J. Bardeen, L. N. Cooper et J. R. Schrieffer, Phys. Rev. **108** (1957) 1175
6) N. N. Bogoliubov, Soviet Physics JETP **7** (1958) 51;
Bogoliubov, Zubarev et Tserkovnikov, Soviet Physics (Doklady) **2** (1958) 535
7) L. P. Gorkhov, Soviet Physics JETP **7** (1958) 505
8) D. J. Thouless, UCRL 8884;
M. L. Mehta, Nuclear Physics **20** (1960) 533

1.C

Nuclear Physics **20** (1960) 533—542; © *North-Holland Publishing Co., Amsterdam*

Not to be reproduced by photoprint or microfilm without written permission from the publisher

ON THE SUMMATION OF GENERALIZED LADDERS FOR A MANY-FERMION SYSTEM

M. L. MEHTA †

Centre d'Études Nucléaires de Saclay, Gif-sur-Yvette (S. et O.), France

Received 23 june 1960

Abstract: The analogy between an interacting fermion system and a system in an external potential, which may be non-hermitian, is employed to show why the generalized ladder approximation for an interaction attractive near the Fermi-surface diverges.

1. Introduction

In the study of large interacting systems, several difficulties, such as due to hard cores, were removed by making a partial summation of all particle-particle interactions [1]), giving the so-called "ladder approximation". However, the *t*-matrix introduced thus may have in the case of attractive potentials, one or more singularities below the Fermi-surface yielding divergent integrals in the expression of the binding energy [2]). The idea [3]) of summing all hole-hole as well as particle-particle interactions, hereafter called the "mixed ladder approximation", in defining the *t*-matrix has been shown [4]) to lead to the same type of divergence difficulties as the previous one.

A still better approximation will consist in summing all symmetric double looped graphs, hereafter called the "generalized ladder approximation". A typical example of such a graph is shown in fig. 1. One can systematically write down an integral equation for this class of graphs and solve it exactly. The reason of this simplicity is seen in the presence of the following underlying one-body problem.

As noticed by several authors [5]) the problem of a system of fermions in an external field is similar to the problem of a system of fermions interacting via two-body forces. The two problems are, in fact, exactly equivalent only up to the generalized ladder approximation. Fig. 2 shows the graph in the external potential case which corresponds to that of fig. 1. In the external field problem these are all the possible graphs, and their sum must therefore be equal to the exact energy value determined directly, which can easily be checked. The problem of interacting fermions, however, contains many more graphs, such as for

† On leave of absence from the Tata Institute of Fundamental Research, Apollo Pier, Bombay.

example those shown in fig. 3, which have no equivalent in the external field case.

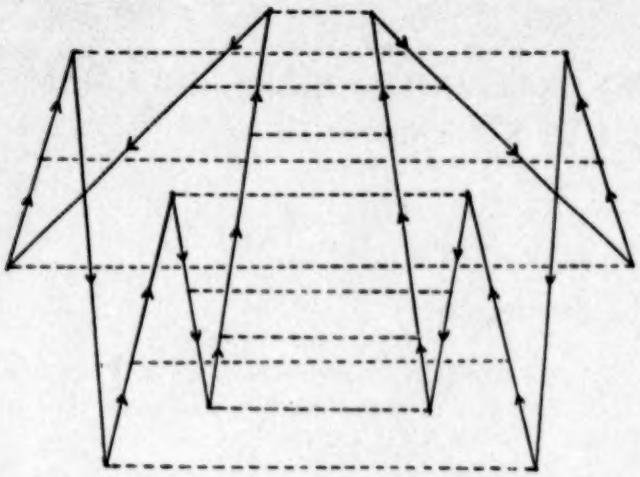

Fig. 1. A generalised ladder graph contributing to the ground-state energy of an interacting fermion system.

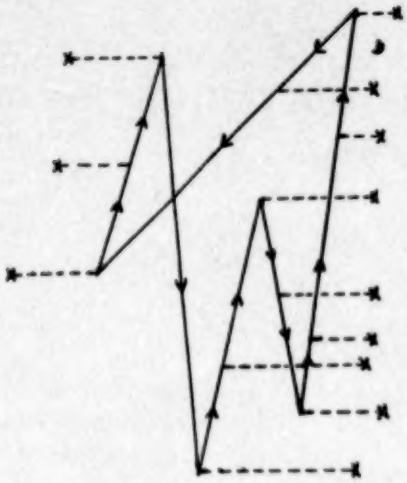

Fig. 2. The graph corresponding to that in fig. 1 for the fermions in an external field.

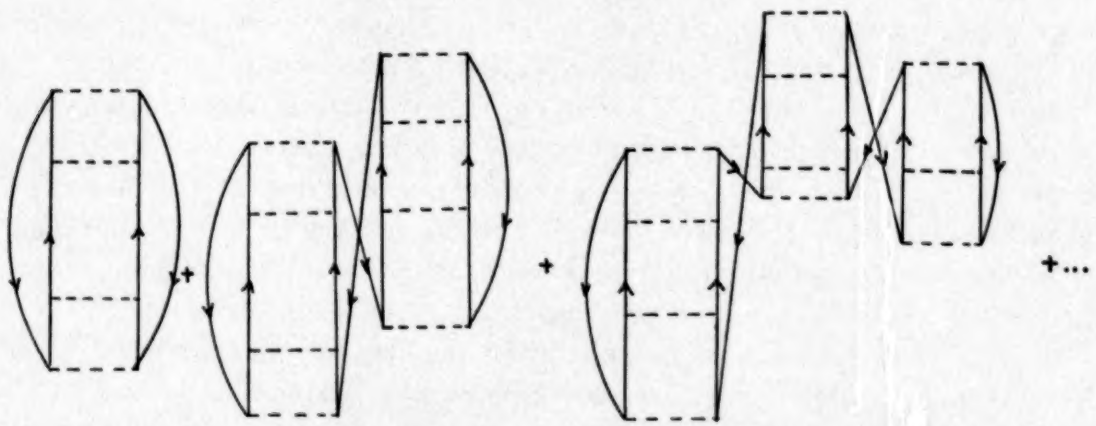

Fig. 3. Some graphs contributing to the ground-state energy of an interacting fermion system. These have no corresponding graphs in the external field case.

We shall take a separable potential and consider only the states of total momentum zero. We will then show that

1) for the problem of fermions in an external field:

a) the "ladder approximation" is not sufficient, as in some cases the binding energy is singular for arbitrarily small external potentials;

b) the "mixed ladder approximation" is also not sufficient for the same reasons;

c) The "generalized ladder approximation", which contains all the possible graphs in this case, gives a finite radius of convergence to the binding energy series, the sum of this series being equal to the exact result;

2) for the problem of interacting fermions:

a), b) the conclusions about "ladder" as well as "mixed ladder" approximations are the same as in the previous problem;

c) the "generalized ladder approximation" also has a radius of convergence tending to zero as the unperturbed single-particle levels become more and more dense in momentum space.

2. A System of Fermions in an External Field

This is obviously a one-body problem, as the Pauli principle can be taken into account by putting the fermions one by one in each of the lowest one-body states of the hamiltonian, until all of them are exhausted; the ground state energy being the sum of the energies of the occupied states.

We record in sect. 3 the straightforward solution to this problem, in various approximations, for the sake of completeness and for later comparison as the corresponding approximations in the pair interaction problem are obtained by allowing the potential to become imaginary for some states.

The hamiltonian is taken in the second quantized form as

$$H = H_0+H_1+H_2 = (H_0^+ + H_0^-)+(H_1^+ + H_1^-)+H_2, \tag{1}$$

where in terms of the usual creation and annihilation fermion operators, we have

$$\begin{aligned} H_0^+ &= \sum_k \varepsilon_k \xi_k^* \xi_k, \quad H_0^- = \sum_m \varepsilon_m \xi_m^* \xi_m, \\ H_1^+ &= -\sum_{k,k'} \langle k|V|k'\rangle \xi_k^* \xi_{k'}, \quad H_1^- = -\sum_{m,m'} \langle m|V|m'\rangle \xi_m^* \xi_{m'}, \\ H_2 &= -\sum_{k,m} \{\langle k|V|m\rangle \xi_k^* \xi_m + \langle m|V|k\rangle \xi_m^* \xi_k\}, \end{aligned} \tag{2}$$

with the convention that $k > k_F$ and $m < k_F$ (k_F being the Fermi-momentum).

The ladder approximation consists in taking

$$H = H_0+H_1^+,$$

and an interaction at each end of the ladder which scatters a particle into a hole state or vice-versa. The mixed ladder approximation is obtained by including H_1^- also

$$H = H_0+H_1,$$

and completing the graph, as before, by one interaction at each end connecting a particle and a hole state. We will get the generalized ladder approximation, if we take the full hamiltonian

$$H = H_0+H_1+H_2.$$

3. Diagonalization

As $H_0^+ + H_1^+$ and $H_0^- + H_1^-$ are completely disconnected, we can diagonalize them separately. For $H_0^+ + H_1^+$, the Schrodinger equation is

$$(H_0^+ + H_1^+) \sum_k B_{ik} \xi_k^* = \varepsilon_i^+ \sum_k B_{ik} \xi_k^*,$$

or

$$B_{ik} = \frac{1}{\varepsilon_k - \varepsilon_i^+} \sum_{k'} \langle k|V|k'\rangle B_{ik'}. \tag{3}$$

This equation is immediately solved for a separable potential †

$$\langle l|V|l'\rangle = V(l)V(l'), \tag{4}$$

on multiplying both sides of it by $V(k)$, summing over k and assuming that the common factor does not vanish. Thus we see that ε_i^+ are the roots of

$$\psi(\varepsilon^+) = \sum_k \frac{V^2(k)}{\varepsilon_k - \varepsilon^+} = 1. \tag{5}$$

Similarly ε_j^-, the eigenvalues of $H_0^- + H_1^-$ are the roots of

$$\phi(\varepsilon^-) = \sum_m \frac{V^2(m)}{\varepsilon_m - \varepsilon^-} = 1. \tag{6}$$

Let us denote by $\eta_{\alpha\pm}^*$, $\eta_{\alpha\pm}$ the creation and annihilation operators for the eigenstates of $H_0^\pm + H_1^\pm$ corresponding to the eigenvalues $\varepsilon_\alpha^\pm$. The orthogonality of the transformations and the normalization of the eigenstates allow us to write simply

$$\begin{aligned} \xi_k &= \sum_i (B^{-1})_{ki} \eta_{i+} = \sum_i \frac{V(k)}{\varepsilon_k - \varepsilon_i^+} \sqrt{a_i}\, \eta_{i+}, \\ \xi_m &= \sum_j (B^{-1})_{mj} \eta_{j-} = \sum_j \frac{V(m)}{\varepsilon_m - \varepsilon_j^-} \sqrt{b_j}\, \eta_{j-}, \end{aligned} \tag{7}$$

where a_i and b_j are given by

$$a_i^{-1} = \psi'(\varepsilon_i^+) = \left(\frac{\mathrm{d}\psi}{\mathrm{d}\varepsilon}\right)_{\varepsilon=\varepsilon_i^+}, \quad \text{and} \quad b_j^{-1} = \phi'(\varepsilon_j^-) = \left(\frac{\mathrm{d}\phi}{\mathrm{d}\varepsilon}\right)_{\varepsilon=\varepsilon_j^-}. \tag{8}$$

Changing the representation from ξ to η, we have

$$\begin{aligned} H_0 + H_1 &= \sum_i \varepsilon_i^+ \eta_{i+}^* \eta_{i+} + \sum_j \varepsilon_j^- \eta_{j-}^* \eta_{j-}, \\ H_2 &= -\sum_{i,j} \sqrt{a_i b_j} (\eta_{i+}^* \eta_{j-} + \eta_{j-}^* \eta_{i+}). \end{aligned}$$

† For the potential with a negative sign in eq. (4), trivial changes in the right hand sides of eqs. (5), (6), (7) and (9) are needed.

Now the Schrödinger equation

$$(H_0+H_1+H_2)\zeta_r^* = E_r\zeta_r^*$$

can be solved in exactly the same way. In the above equation put

$$\zeta_r = \sum_i L_i\eta_{i+}+\sum_j L_j\eta_{j-},$$

to get

$$(\varepsilon_i^+-E_r)L_i = \sqrt{a_i}\sum_j \sqrt{b_j}L_j, \quad (\varepsilon_j^--E_r)L_j = \sqrt{b_j}\sum_i \sqrt{a_i}L_i.$$

Eliminating the quantities

$$P_+ = \sum_i \sqrt{a_i}L_i, \quad P_- = \sum_j \sqrt{b_j}L_j,$$

we see that E_r are the roots of the equation

$$\sum_{i,j}\frac{a_ib_j}{(\varepsilon_i^+-E)(\varepsilon_j^--E)} = 1.$$

We may put this equation in a somewhat more convenient form. Note that

$$\sum_i \frac{a_i}{\varepsilon_i^+-E} = \frac{1}{2\pi i}\oint \frac{1}{\psi(z)-1}\frac{dz}{z-E} - \frac{1}{\psi(E)-1}$$
$$= -1-\frac{1}{\psi(E)-1} = -\frac{\psi(E)-1}{\psi(E)},$$

where in the middle member above, the contour of integration is large enough to enclose all finite singularities of the integrand, which are simple poles; and this contour may be made to tend to infinity for later evaluation.

Similarly we have

$$\sum_j \frac{b_j}{\varepsilon_j^--E} = -\frac{\phi(E)-1}{\phi(E)}.$$

Therefore, the eigenvalues E_r of H are the roots of

$$\psi(E)+\phi(E) = 1. \tag{9}$$

4. Interacting Fermions

In the approximations where some or all of the symmetrical double looped graphs are taken, i.e. in any of the three approximations considered above, the terms in the perturbation series of the ground state energy for the problem of interacting fermions are equal, except possibly for the sign, to the corresponding terms for the problem of fermions in an external field. The possible change in sign is due to the difference in the number of hole lines as well as the number of closed loops.

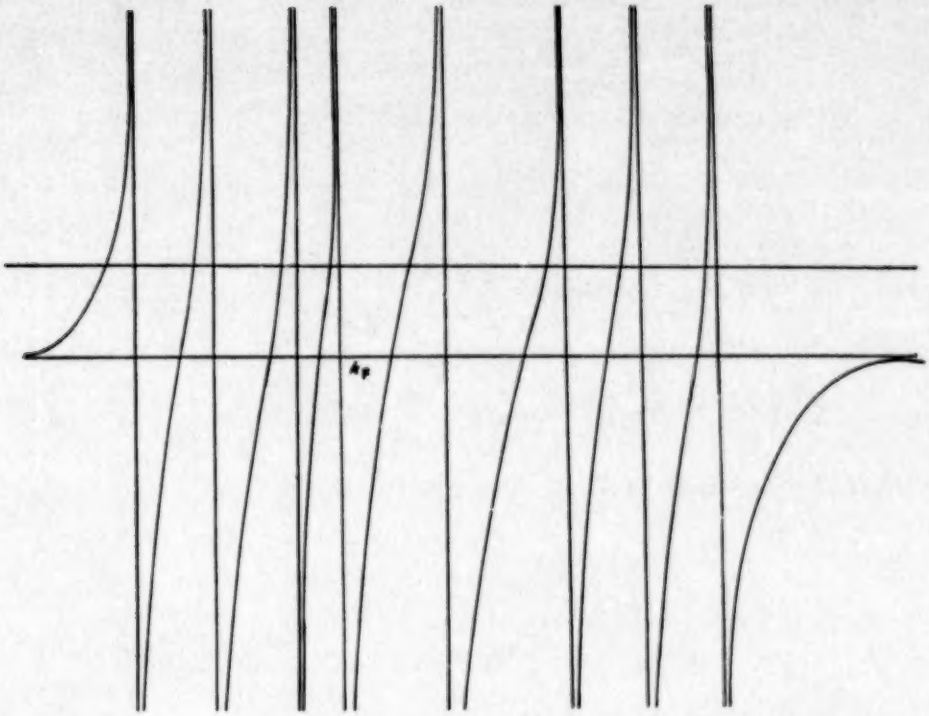

Fig. 4. The function $\psi(E)+\phi(E)$ when the potential has the form (12).

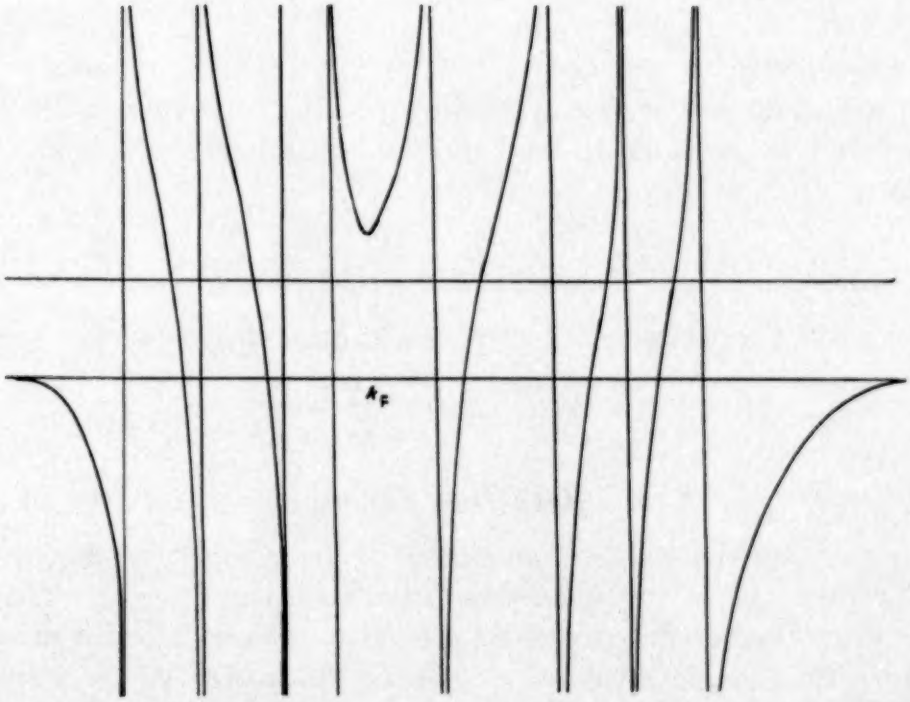

Fig. 5. The function $\psi(E)+\phi(E)$ when the potential has the form (10).

These signs can be properly accounted for, as can be seen from eq. (4) by letting the potential become imaginary in certain states, so that finally there is a relative sign change between $V^2(m)$ and $V^2(k)$. Let us put

$$V(l) = \lambda_l v_l,$$

with v_l real. Then if we take

$$\lambda_k = 1, \quad \lambda_m = i, \tag{10}$$

we shall be getting terms for an attractive two-body interaction; while if we take

$$\lambda_k = i, \quad \lambda_m = 1, \tag{11}$$

we will be getting those for a repulsive two-body interaction. The situation

$$\lambda_k = \lambda_m = 1, \quad (\text{or } \lambda_k = \lambda_m = i), \tag{12}$$

is the real external potential problem.

The function $\psi(E)+\phi(E)$ is drawn in figs. 4 and 5 for the cases (12) and (10) respectively. For the case (11) one should turn fig. 5 upside down. The intersections of these curves with the line at a unit distance up give the roots of eq. (9).

5. Discussion

It is a well-known fact that for a system of free fermions, the ground state energy is singular in the ladder approximation if the unperturbed states are dense enough near the Fermi-energy and have a negative external potential [6]). The same conclusion is immediately derived for the mixed ladder approximation by drawing a graph corresponding to fig. 1 of ref. [4]) for this case and the remarks at the end of sect. 2 there.

For attracting fermions also, the ladder as well as mixed ladder approximation lead to similar singularities [2, 4]).

For the generalized ladder approximation, it is shown in the appendix that the perturbation series when summed formally has the proper behaviour if all the roots E_r of eq. (9) are real and has a singular behaviour if some of the roots become complex.

Now for the case of fermions in an external field, we see from fig. 4 that all the roots E_r are real for arbitrary values of the coupling constant. Hence we conclude that the formal sum of the series is always non-singular and this sum is seen to give the exact result by comparison.

For repelling fermions, inverting fig. 5, we see that all the roots E_r are real for arbitrary values of the coupling constant and hence a proper behaviour of the formal sum is concluded.

On the other hand, for attracting fermions, fig. 5 shows that all the roots E_r

are real except the two near the Fermi-energy, which eventually become complex if the coupling constant is increased past a certain critical value g_c, say. And $g_c \to 0$ as the levels near the Fermi-energy become more and more dense. Hence a singularity appears for arbitrarily small attractions of levels dense enough near the Fermi-energy.

Thus it is seen that in the generalized ladder approximation, the system of interacting fermions is equivalent to a system of fermions in an external *non-hermitian* potential; and though the problem is exactly solvable, the perturbation treatment diverges due to the appearance of complex energy eigenvalues in the latter problem, giving an exponential behaviour rather than an oscillating one.

I want to thank Professor C. Bloch for suggesting the problem, guidance and helpful critisism throughout the work; to R. Balian, M. Gaudin and J. Lascoux for many interesting discussions, to Service de Coopération Technique for a maintenance grant during the Summer of 1959 when this work was done and to Commissariat à l'Énergie Atomique for the kind hospitality at Saclay.

Appendix

In this appendix we shall give briefly the steps and the main consequences of the time-dependent perturbation method. Following the general theory we first write down the integral equation for the particle propagator, i.e. symbolically:

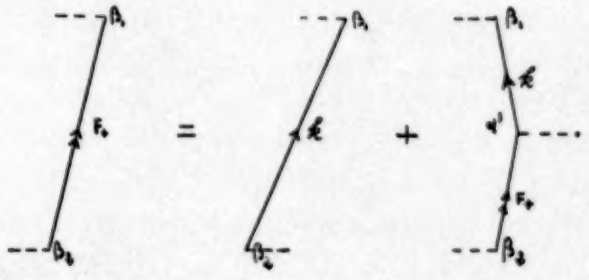

Taking as new variables

$$\Delta = \beta_1 - \beta_2, \quad \alpha = \alpha' - \beta_2,$$

it is easy to solve the linear equation to get

$$F_+(\Delta) = \sum_i a_i e^{-\varepsilon_i^+ \Delta},$$

with a_i and ε_i^+ as defined by the eqs. (5) and (8).

The same holds for the hole-propagator

$$F_-(\Delta) = \sum_j b_j e^{-\varepsilon_j^- \Delta},$$

with b_j and ε_j^- as given by eqs. (6) and (8).

Incidently we note that by closing F_+ with a hole-line we get the ladder approximation, while by closing it with an F_- line we get the mixed ladder approximation.

Writing the equation for the generalized ladders is now easy. It is symbolically:

It can be shown that this integral equation is equivalent to a linear differential equation with constant coefficients. Putting

$$\Delta = \beta_1 - \beta_2, \quad \gamma = \beta - \beta_2,$$

one has then the explicit solution

$$T_+(\gamma, \Delta) = \sum_r A_r(\gamma) \mathrm{e}^{-E_r \Delta},$$

where E_r are determined by eq. (9) and A_r are the roots of

$$1 - \sum_r \frac{\phi(E_r)}{\phi(E_r) - 1} \frac{A_r}{E_r - \varepsilon_i^+} = 0, \tag{A.1}$$

$$\sum_r A_r \frac{\mathrm{e}^{-E_r \gamma}}{E_r - \varepsilon_j^-} = 0. \tag{A.2}$$

Closing T_+ with an F_- line and integrating over β_1 and β_2 from 0 to β we get

$$\frac{1}{\beta} \langle 0|U(\beta)|0\rangle_c = \frac{1}{\beta} \sum_r c_r \int_0^\beta A_r \mathrm{d}\gamma, \tag{A.3}$$

where $\langle 0|U(\beta)|0\rangle_c$ is defined after Bloch [7]), the subscript c meaning the generalized ladder graphs; we have put

$$\frac{\phi(E_r)}{\phi(E_r) - 1} = c_r.$$

With a little reasoning on the linear dependence or independence of the coefficients in eqs. (A.1) and (A.2), one can prove that

1) if all the roots E_r are real, then the limit of the right hand side of eq. (A.3) exists for $\beta \to \infty$.

2) if a pair of roots E_r is complex, then the right hand side of eq. (A.3) does not have any limit as $\beta \to \infty$, because it will then be an integral of a function having poles almost periodically on the positive β axis.

In the case where the limit exists, we will have for the shift in energy

$$\begin{aligned} \Delta E &= -\lim_{\beta\to\infty} \frac{1}{\beta} \langle 0|U(\beta)|0\rangle_c \\ &= (\varepsilon_1^+ + \ldots + \varepsilon_{n_+}^+ - E_1 - \ldots - E_{n_+}) \\ &= (E'_1 + \ldots + E'_{n_-} - \varepsilon_1^- - \ldots - \varepsilon_{n_-}^-), \end{aligned}$$

if the roots are ordered as

$$E_1 > E_2 > \ldots > E_{n_+} > E'_1 > E'_2 > \ldots > E'_{n_-},$$

the integers n_+ and n_- being respectively the number of unperturbed levels above and below the Fermi-energy.

References

1) Reviews of the method and lists of references are given by H. A. Bethe, Phys. Rev. **103** (1956) 1353 and K. A. Brueckner and J. L. Gammel, Phys. Rev. **109** (1958) 1023

2) L. N. Cooper, Phys. Rev. **104** (1956) 1189;
A. Bohr, B. R. Mottelson and D. Pines, Phys. Rev. **110** (1958) 936;
J. Goldstone, Thesis, Cambridge University;
K. Gottfried, CERN report (unpublished);
L. van Hove, Physica **25** (1959) 849, Lecture at the International summer School of Physics, Naples (1960);
C. Bloch, C. R. du Congrès International de Physique Nucléaire, Paris, July 1958 (Dunod, Paris, 1959) 243

3) J. S. R. Chisholm and E. J. Squires, A.E.R.E. Harwell report; also Nuclear Physics **13** (1959) 156

4) M. L. Mehta, Nuclear Physics **12** (1959) 333

5) J. S. Bell, Proc. Phys. Soc. **73** (1959) 118;
A. Katz, Int. Summer School of Physics, Naples (1960)

6) J. S. Bell, ref. [5]) above

7) C. Bloch, Nuclear Physics **7** (1958) 451

8.B

Nuclear Physics **20** (1960) 543—556; © *North-Holland Publishing Co., Amsterdam*

Not to be reproduced by photoprint or microfilm without written permission from the publisher

TESTS EXPÉRIMENTAUX DE CERTAINES HYPOTHÈSES DE SYMÉTRIE RELATIVES AUX INTERACTIONS FORTES

B. D'ESPAGNAT, A. MARTIN et J. PRENTKI

CERN, Genève

Reçu le 6 juillet 1960

Abstract: Various tests for the global symmetry and for the Salam-Polkinghorne assumption are proposed. In the high energy reactions considered, such as antibaryon production, it is expected that the global symmetry might be more apparent than in reactions involving K mesons at low energies. While the tests for the universality of the pion-hyperon coupling are described by equalities, those which apply to a comparison between the pion-hyperon and pion-nucleon couplings are expressed in terms of inequalities between cross-sections for different processes. This is a consequence of indiscernibility and of the presence of the target nucleon in the initial state. These inequalities might, however, prove to give rather simple tests as they hold independently of the number of emitted pions. The tests for the Salam-Polkinghorne assumption are chosen so as to give a lower limit on the number of Ξ's appearing in a reaction, while the previously proposed tests gave an upper limit. Finally phase space effects are briefly discussed.

1. Introduction

Dans un travail précédent [1]) deux d'entre nous ont indiqué quelques tests expérimentaux de l'hypothèse de la „symétrie restreinte" dans les interactions fortes mésons-baryons (hypothèse $g_2 = g_3$ dans l'expression (2) ci-dessous, $m_{\Sigma^0} = m_{\Lambda^0}$). Nous avons fait remarquer que la possibilité d'observer des créations de paires d'hypérons dans les collisions π—p, p—p, et ausi p—$\bar{\text{p}}$ fournit un bon moyen de vérification de cette hypothèse qui conduit à des relations simples entre les nombres de paires produites, à savoir

$$\begin{aligned}
&\sigma(\bar{\Sigma}^-\Sigma^0) \approx \sigma(\bar{\Sigma}^-\Lambda) \approx \sigma(\bar{\Sigma}^0\Sigma^+) \approx \sigma(\bar{\Lambda}\Sigma^+),\\
&\sigma(\bar{\Sigma}^+\Sigma^0) \approx \sigma(\bar{\Sigma}^+\Lambda) \approx \sigma(\bar{\Sigma}^0\Sigma^-) \approx \sigma(\bar{\Lambda}\Sigma^-),\\
&\sigma(\bar{\Sigma}^+\Sigma^+)+\sigma(\bar{\Sigma}^-\Sigma^-) \approx 2[\sigma(\bar{\Sigma}^0\Lambda)+\sigma(\bar{\Lambda}\Lambda)],\\
&\sigma(\bar{\Sigma}^0\Sigma^0) \approx \sigma(\bar{\Lambda}\Lambda), \quad \sigma(\bar{\Lambda}\Sigma^0) = \sigma(\bar{\Sigma}^0\Lambda).
\end{aligned} \tag{1}$$

Ici nous voulons appliquer des considérations analogues au problème de la „symétrie globale" [2]) des interactions méson π-baryon et également indiquer quelques tests du schéma de Salam et Polkinghorne [3]). On peut évidemment se demander pourquoi chercher encore des tests de la symétrie globale puisque celle-ci paraît en désaccord avec les données expérimentales sur l'absorption et la diffusion des $\bar{\text{K}}$ par des nucléons à faible énergie [4]). La réponse à cette

question est qu'il est fort possible que la symétrie globale existe et soit simplement masquée par les interactions K-nucléon-hypéron. Dans cette hypothèse il n'est nullement exclu qu'un souvenir plus précis de la symétrie globale se manifeste dans les processus qui peuvent avoir lieu sans aucune intervention directe des interactions K.

Afin de préciser les idées nous écrivons l'hamiltonien des interactions fortes sous la forme †

$$g_1\bar{\mathrm{N}}\tau\mathrm{N}\pi+g_2\Lambda\Sigma\pi+\frac{1}{2i}g_3\bar{\Sigma}\times\Sigma\pi+g_4\bar{\Xi}\tau\Xi\pi \\ +g_5\bar{\mathrm{N}}\mathrm{K}\Lambda+g_6\bar{\mathrm{N}}\tau\mathrm{K}\Sigma+g_7\bar{\Xi}\dot{\mathrm{K}}\Lambda+g_8\bar{\Xi}\tau\dot{\mathrm{K}}\Sigma+\mathrm{h.c.} \tag{2}$$

La symétrie restreinte correspond à

$$g_2=g_3,\quad g_{\mathrm{K}}\ll g_\pi,\quad M_\Sigma\approx M_\Lambda, \tag{3}$$

la symétrie globale correspond à

$$g_1=g_2=g_3=g_4,\quad g_{\mathrm{K}}\ll g_\pi,\quad M_{\mathrm{N}}\approx M_\Sigma\approx M_\Lambda\approx M_\Xi, \tag{4}$$

et le schéma de Salam et Polkinghorne se caractérise par

$$g_1\approx g_4,\quad g_5\approx g_7,\quad g_6\approx g_8,\quad M_{\mathrm{N}}\approx M_\Xi. \tag{5}$$

2. Tests de $g_2=g_3=g_4$, $g_{\mathrm{K}}\ll g_\pi$

Il y a une très grande différence entre la vérification expérimentale de $g_i=g_k(i,k=2,3,4)$ et celle de $g_i=g_1$ parce que les cibles utilisées sont nécessairement constituées de nucléons. Le cas $g_2=g_3=g_4$ se révèle particulièrement simple. Dans cette hypothèse l'hamiltonien d'interactions π s'écrit

$$g_1\mathrm{N}\tau\mathrm{N}\pi+g(\bar{Y}\tau\mathrm{Y}+\bar{\mathrm{Z}}\tau\mathrm{Z}+\bar{\Xi}\tau\Xi)\pi, \tag{6}$$

avec

$$\mathrm{Y}=\begin{pmatrix}\Sigma^+\\ \mathrm{Y}^0\end{pmatrix},\quad \mathrm{Z}=\begin{pmatrix}\mathrm{Z}^0\\ \Sigma^-\end{pmatrix}\quad\text{et}\quad \mathrm{Y}^0=\frac{\Lambda-\Sigma^0}{\sqrt{2}},\quad \mathrm{Z}^0=\frac{\Lambda+\Sigma^0}{\sqrt{2}}.$$

L'hamiltonien d'interaction (6) est invariant dans les substitutions

$$\mathrm{Z}\leftrightarrow\Xi,\quad \mathrm{N}\leftrightarrow\mathrm{N},\quad \pi\leftrightarrow\pi,\quad \mathrm{Y}\leftrightarrow\mathrm{Y}, \tag{8}$$

$$\mathrm{Y}\leftrightarrow\Xi,\quad \mathrm{N}\leftrightarrow\mathrm{N},\quad \pi\leftrightarrow\pi,\quad \mathrm{Z}\leftrightarrow\mathrm{Z}. \tag{8'}$$

L'hamiltonien libre est également invariant si les différences de masses entre le Σ le Λ et le Ξ sont négligées.

† La structure spatiale de l'interaction a été omise. On emploie la notation $\dot{\mathrm{K}}=i\tau_2\mathrm{K}^*$.

On peut tirer de là les égalités suivantes † valables pour des collisions πN, NN ou $\bar{\text{N}}$N:

$$(\text{nombre de } \bar{\Xi}^- \text{ créés}) \approx (\text{nombre de } \bar{\Sigma}^-), \tag{9}$$

$$(\text{nombre de } \bar{\Xi}^0 \text{ créés}) \approx (\text{nombre de } \bar{\Sigma}^+). \tag{10}$$

Ces relations sont valables quel que soit le nombre de mésons créés dans la collision, pourvu que des mésons K n'apparaissent pas. En combinant (9) et (10) avec les relations (1) on obtient un ensemble complet de tests de $g_2 = g_3 = g_4$.

3. Tests de $g_1 = g_2 = g_3$, $g_K \ll g_\pi$

La difficulté rencontrée ici vient, nous l'avons dit, du fait que quelle que soit la réaction considérée l'état initial contient des nucléons. Il n'est donc pas possible de démontrer des égalités entre sections efficaces par des substitutions analogues à celles faites dans la section 2. car alors on modifierait non seulement

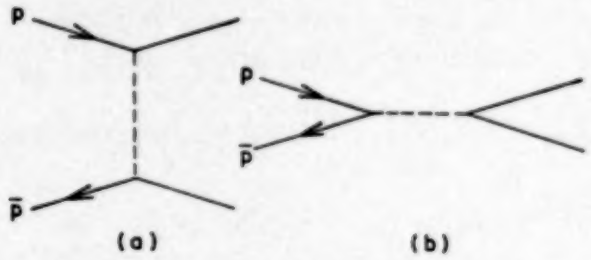

Fig. 1. Graphiques pour la diffusion nucléon-antinucléon.

l'état final mais aussi l'état initial de la réaction considérée. Ainsi il est impossible de prévoir une relation entre les réactions †† $\text{p}+\bar{\text{p}} \to \text{p}+\bar{\text{p}}$ et $\text{p}+\bar{\text{p}} \to \Sigma+\bar{\Sigma}$; ceci est d'ailleurs bien évident dans un calcul de perturbations: des deux graphiques (a) et (b) (fig. 1) pour la diffusion nucléon-antinucléon, seul (b) a un analogue dans la production de paires de Σ à partir d'un système nucléon-antinucléon.

Certaines prédictions sont cependant possibles pour d'autres réactions, mais on ne peut les obtenir qu'en mettant clairement en évidence la structure mathématique résultant des symétries $g_1 = g_2 = g_3$. L'hamiltonien (2) peut alors s'écrire (les interactions K sont négligées)

$$g_1\sqrt{2}[\bar{\text{N}}_k\pi_k{}^m\text{N}_m+\bar{\Sigma}_k{}^1\pi_k{}^m\Sigma_m{}^1+\bar{\Sigma}_k{}^2\pi_k{}^m\Sigma_m{}^2]+g_4\sqrt{2}\bar{\Xi}_k\pi_k{}^m\Xi_m, \tag{11}$$

† L'égalité (10) est vraie, bien entendu, si l'on néglige la différence entre les masses des Σ et des Ξ et la différence entre les volumes disponibles dans l'espace de phase qui en découlent. Ceci sera discuté brièvement dans la section VI. Cette remarque s'applique également aux sections III, IV et V.

†† Bien entendu si des hypothèses plus précises sont faites sur la forme du potentiel $\text{N}\bar{\text{N}}$ on peut néanmoins faire des prédictions [8]).

avec

$$\Sigma_k^1 = Z_k, \quad \Sigma_k^2 = Y_k, \quad (\pi_k^m) = \begin{pmatrix} 2^{-\frac{1}{2}}\pi^0 & \pi^+ \\ \pi^- & -2^{-\frac{1}{2}}\pi^0 \end{pmatrix}.$$

Le haut degré de symétrie de cet hamiltonien entraîne des propriétés d'invariance dans un grand nombre d'espaces de spin isobarique. Par exemple, écrivant (11) sous la forme

$$g_1\sqrt{2}\bar{N}_k\pi_k^m N_m + g_1\sqrt{2}\bar{\Sigma}_k^i\pi_k^m\Sigma_m^i + g_4\sqrt{2}\bar{\Xi}_k\pi_k^m\Xi_m, \tag{12}$$

nous pouvons introduire deux spins isobariques I_a et I_b correspondant aux indices non-pointés et pointés, N et Ξ appartenant à la représentation $\mathscr{D}(\frac{1}{2}0)$ (c'est-à-dire, $I_a = \frac{1}{2}$, $I_b = 0$), Σ_k^i à la représentation $\mathscr{D}(\frac{1}{2}\frac{1}{2})$ et π à la représentation $\mathscr{D}(10)$. Cet espace est précisément l'espace de la symétrie restreinte et la conservation de I_a et de I_b conduit aux relations (1) obtenues dans la référence[1]); pour cela il suffit d'exploiter le fait que dans I_b $(\Sigma^+ Z^0)$ et $(Y^0\Sigma^-)$ sont des spineurs alors que les autres particules sont des scalaires.

Par un groupement différent des termes du hamiltonien (11) on peut mettre en évidence d'autres propriétés d'invariance. Ainsi (11) peut s'écrire

$$g_1\sqrt{2}\bar{C}_k^i\pi_k^m C_m^i + g_1\sqrt{2}\bar{Z}_k\pi_k^m Z_m + g_4\sqrt{2}\bar{\Xi}_k\pi_k^m\Xi_m, \tag{13}$$

ou

$$g_1\sqrt{2}\bar{D}_k^i\pi_k^m D_m^i + g_1\sqrt{2}\bar{Y}_k\pi_k^m Y_m + g_4\sqrt{2}\bar{\Xi}_k^m\pi_k^m\Xi_m, \tag{14}$$

avec

$$C_k^{\dot{1}} = N_k, \quad C_k^{\dot{2}} = Y_k, \quad D_k^{\dot{1}} = N_k, \quad D_k^{\dot{2}} = Z_k.$$

Le mode d'écriture (13) montre que N et Y sont, dans un certain espace I'_b, les composantes $C^{\dot{1}}$, $C^{\dot{2}}$ d'un spineur, c'est à dire que, de façon plus précise, (13) est invariant dans toutes les rotations d'un espace à trois dimensions I'_b dans lequel (p, Σ^+) et (n, Y^0) se transforment chacun comme des spineurs, les autres particules étant des scalaires. Le mode d'écriture (14) met en évidence une propriété toute similaire relative aux spineurs (p, Z^0), (n, Σ^-) dans un espace I''_b. Nous allons maintenant exploiter ces propriétés et en tirer des tests de $g_1 = g_2 = g_3$.

3.1. PRODUCTION DE PAIRES $\bar{N}N$ ET $\bar{\Sigma}\Sigma$ DANS LES COLLISIONS π—p

Il s'agit de comparer les réactions

$$\pi + p \to N + N + \bar{N} + n\pi \quad \text{et} \quad \pi + p \to N + \Sigma + \bar{\Sigma} + n\pi.$$

On utilisera la conservation de I'_b ou de I''_b selon les états de charge des particules finales. L'état initial $p\pi$ est caractérisé par

$$I'_b = I''_b = \tfrac{1}{2}, \quad I'_{b3} = I''_{b3} = +\tfrac{1}{2}.$$

Les trois baryons présents dans l'état final sont des composantes de spineurs tandis que les mésons π sont des scalaires, aussi bien dans I'_b que dans I''_b. Nous allons donc traiter d'abord le problème suivant:

Partant d'un état $|\frac{1}{2}\frac{1}{2}\rangle$ on aboutit à un système de trois particules spinorielles,

$$A=\begin{pmatrix}A_1\\A_2\end{pmatrix},\quad B=\begin{pmatrix}B_1\\B_2\end{pmatrix},\quad C=\begin{pmatrix}C_1\\C_2\end{pmatrix}. \tag{15}$$

La conservation de I_{b3} (nous supprimons les signes ′ et ″) permet les réactions

$$|\tfrac{1}{2}\tfrac{1}{2}\rangle \to \begin{cases}A_2+B_2+C_1, & \text{(a)}\\ A_2+B_1+C_2, & \text{(b)}\\ A_1+B_2+C_2. & \text{(c)}\end{cases} \tag{16}$$

Les éléments de matrice pour les réactions (a), (b) et (c) sont respectivement

$$\begin{aligned}T_a &= \sqrt{\tfrac{1}{3}}T_{1,\frac{1}{2}}+\sqrt{\tfrac{1}{6}}T_{1,\frac{1}{2}}+\sqrt{\tfrac{1}{2}}T_{0,\frac{1}{2}},\\ T_b &= \sqrt{\tfrac{1}{3}}T_{1,\frac{1}{2}}+\sqrt{\tfrac{1}{6}}T_{1,\frac{1}{2}}-\sqrt{\tfrac{1}{2}}T_{0,\frac{1}{2}},\\ T_c &= \sqrt{\tfrac{1}{3}}T_{1,\frac{1}{2}}-\sqrt{\tfrac{2}{3}}T_{1,\frac{1}{2}},\end{aligned} \tag{17}$$

où $T_{i',i}$ est défini comme l'élément de matrice de transition de l'état $|\frac{1}{2}\frac{1}{2}\rangle$ vers un état final obtenu en combinant les particules BC en un état de spin isobarique i', cet état étant combiné lui-même avec la particule A pour donner un spin isobarique total i. Comme $I_b=\frac{1}{2}$ dans l'état initial,

$$T_{i',\frac{1}{2}}=0. \tag{18}$$

Combinant (17) et (18) on trouve finalement

$$T_a+T_b+T_c=0. \tag{19}$$

Ceci conduit à des relations triangulaires entre sections efficaces, du type

$$(\sigma_a)^{\frac{1}{2}}-(\sigma_b)^{\frac{1}{2}} \leqq (\sigma_c)^{\frac{1}{2}} \leqq (\sigma_a)^{\frac{1}{2}}+(\sigma_b)^{\frac{1}{2}}. \tag{20}$$

Comme les π sont des scalaires dans I_b, les relations (19) et (20) sont valables lorsque n mésons π sont présents dans l'état final de chacune des trois réactions. Malheureusement, la vérification des inégalités (20) exige des mesures de sections efficaces pour n fixé, ce qui n'est pas toujours facile. On peut cependant noter que de (20) découle l'inégalité moins restrictive:

$$\tfrac{1}{2}\sigma_c \leqq \sigma_a+\sigma_b. \tag{21}$$

On peut alors ajouter membre à membre les inégalités correspondant à l'émission d'un nombre donné de mésons π et obtenir une inégalité valable pour les sections efficaces de création des états (a), (b) et (c) indépendamment du nombre des π émis, notées par Σ_a, Σ_b, Σ_c,

$$\tfrac{1}{2}\Sigma_c \leqq \Sigma_a+\Sigma_b. \tag{22}$$

Dans le passage de (20) à (22) on perd de l'information mais l'analyse expérimentale peut s'en trouver grandement facilitée. Par ailleurs, cette relation est vraie aussi bien pour les sections efficaces totales que pour les sections efficaces différentielles.

Appliquons maintenant ces considérations à la production des anti Σ^+. D'après (13) c'est l'invariance dans I'_b qui doit être utilisée et, par suite de l'association $(\Sigma^+ p)$ c'est avec la production *d'antiprotons* qu'on devra faire la comparaison. Deux cas sont à distinguer:

1) Dans la réaction de production des antiprotons les deux nucléons présents dans l'état final sont différents. On doit alors associer les réactions

$$\pi+p\to\begin{cases} p+\bar{\Sigma}^+ + Y + n\pi & \text{(a)},\\ \Sigma^+ + \bar{\Sigma}^+ + n + n\pi & \text{(b)},\\ p+\bar{p}+n+n\pi & \text{(c)},\end{cases} \tag{23}$$

ici †

$$A=\begin{pmatrix} p\\ \Sigma^+\end{pmatrix},\quad B=\begin{pmatrix} -\bar{\Sigma}^+\\ \bar{p}\end{pmatrix},\quad C=\begin{pmatrix} n\\ Y\end{pmatrix}. \tag{24}$$

En comparant (22) et (23) on obtient immédiatement

$$(\text{nombre de } \bar{\Sigma}^+) \geqq \tfrac{1}{2}(\text{nombre de } \bar{p}).$$

Cette relation est valable aussi bien pour des antiparticules de quantité de mouvement donnée que pour l'ensemble des antiparticules produites.

2) Les deux nucléons présents dans l'état final de la réaction de production des antiprotons sont identiques. S'il s'agit de deux protons on devra faire l'association suivante:

$$\pi+p\to\begin{cases} p+\bar{\Sigma}^+ + \Sigma^+ + n & \text{(a)},\\ \Sigma^+ + \bar{\Sigma}^+ + p + n & \text{(b)},\\ p+\bar{p}+p+n & \text{(c)}.\end{cases} \tag{25}$$

Les produits finals sont du type A+B+A où A et B sont définis par (24). A partir de (17) et (18) on obtient aisément

$$|T_a(\mathbf{k}_1\mathbf{k}_2\mathbf{k}_3)|^2+|T_b(\mathbf{k}_1\mathbf{k}_2\mathbf{k}_3)|^2 \geqq \tfrac{1}{2}|T_c(\mathbf{k}_1\mathbf{k}_2\mathbf{k}_3)|^2, \tag{26}$$

où $\mathbf{k}_1$, $\mathbf{k}_2$, $\mathbf{k}_3$ désignent les moments des particules apparaissant dans les réactions (25). (a) et (b) représentent des états finals identiques aux quantités de mouvement près:

$$|T_a(\mathbf{k}_1\mathbf{k}_2\mathbf{k}_3)|^2 = |T_b(\mathbf{k}_3\mathbf{k}_2\mathbf{k}_1)|^2.$$

† Si $\binom{p}{\Sigma^+}$ se transforme comme un spineur, $\binom{-\bar{\Sigma}^+}{\bar{p}}$ se transforme comme un spineur de *même* espèce.

En sommant (26) sur toutes les valeurs possibles de $\mathbf{k}_1$ et $\mathbf{k}_3$, à $\mathbf{k}_2$ fixé, on obtient, à gauche, deux fois le nombre de $\bar{\Sigma}^+$ de moment $\mathbf{k}_2$ et, à droite, une fois le nombre $\bar{\mathrm{p}}$ de moment $\mathbf{k}_2$, compte tenu de l'indiscernabilité des 2 protons présents †. On obtient finalement, par conséquent, à la même relation que dans le cas 1), à savoir

$$(\text{nombre de } \bar{\Sigma}^+) \geqq \tfrac{1}{2}(\text{nombre de } \bar{\mathrm{p}}). \tag{27}$$

Cette relation est valable, aux corrections d'espace de phase près, quel que soit l'état de charge des particules finales. Elle est vraie pour un nombre donné de mésons π émis et aussi indépendamment des mésons π émis. On peut soit s'intéresser au nombre total d'antiparticules produites, soit fixer leur quantité de mouvement; par contre notre raisonnement exige que l'on somme sur les quantités de mouvement des deux autres baryons présents.

De la même façon les propriétés d'invariance dans I_{b}'' conduisent à l'inégalité

$$(\text{nombre de } \bar{\Sigma}^- \text{ produits}) \geqq \tfrac{1}{2}(\text{nombre de } \bar{\mathrm{n}}), \tag{28}$$

valable dans les mêmes conditions. Par combinaison de (27) et (28) avec les relations (1) on obtient des relations entre les nombres de $\bar{\Lambda}$ et $\bar{\Sigma}^0$ créés et les nombres de $\bar{\mathrm{n}}$ et $\bar{\mathrm{p}}$ créés.

3.2. PRODUCTION DE PAIRES $\bar{\mathrm{N}}\mathrm{N}$ ET $\bar{\Sigma}\Sigma$ DANS LES COLLISIONS p—p

Ici les états finals ont du type $\mathrm{NN}\bar{\Sigma}\Sigma$ et $\mathrm{NN}\bar{\mathrm{N}}\mathrm{N}$. Les différences essentielles avec le cas précédent sont que l'état initial est du type $I_{\mathrm{b}}' = I_{\mathrm{b}}'' = I_{\mathrm{b3}}' = I_{\mathrm{b3}}'' = 1$ et que trois particules identiques peuvent être présentes dans l'état final. Cependant la même méthode est applicable: on doit construire un vecteur à partir de quatre spineurs du type (24) et tenir compte des effets d'indiscernabilité. On obtient ainsi (voir l'appendice):

$$\begin{aligned} (\text{nombre de } \bar{\Sigma}^+) &\geqq \tfrac{1}{3}(\text{nombre de } \bar{\mathrm{p}}), \\ (\text{nombre de } \bar{\Sigma}^- &\geqq \tfrac{1}{3}(\text{nombre de } \bar{\mathrm{n}}), \end{aligned} \tag{29}$$

ceci quel que soit le nombre de mésons π émis et sans tenir compte des effets d'espace de phase.

3.3. COMPARAISON DES COLLISIONS p—p ET Σ^+—p

On peut traiter ce problème en utilisant la technique introduite dans a). Néanmoins, si l'on s'intéresse seulement aux sections efficaces totales on peut arriver au résultat plus rapidement. La section efficace p—p est proportionnelle à

$$\langle \mathrm{pp}|TT^+|\mathrm{pp}\rangle,$$

† En sommant sur toutes les directions des deux protons émis dans la réaction (c) la section efficace différentielle on obtient deux fois la section efficace totale. Un cas analogue a été traité en détail par E. Fermi dans les cours d'été de Varenna [9]).

la section efficace Σ^+—p est proportionnelle à

$$\langle \Sigma^+ \mathrm{p} | TT^+ | \Sigma^+ \mathrm{p} \rangle.$$

Dans l'espace I'_b l'état $|\mathrm{pp}\rangle = |V_1\rangle$ est la composante $+1$ d'un vecteur, alors que l'état Σ^+p est la superposition d'un vecteur et d'un scalaire:

$$|\Sigma^+ \mathrm{p}\rangle = \frac{1}{\sqrt{2}} |V_0 + S\rangle.$$

Par suite,

$$\sigma_{\mathrm{pp}} \propto \langle V | TT^+ | V \rangle = v,$$

$$\sigma_{\Sigma^+ \mathrm{p}} \propto \tfrac{1}{2} \langle V+S | TT^+ | V+\mathrm{S} \rangle = \tfrac{1}{2} v + \tfrac{1}{2} s,$$

car la conservation de I'_b entraîne

$$\langle V | TT^+ | S \rangle = \langle S | TT^+ | V \rangle = 0.$$

Par conséquent

$$\sigma_{\Sigma^+ \mathrm{p}} \geqq \tfrac{1}{2} \sigma_{\mathrm{pp}}. \tag{30}$$

Cette relation est peut-être l'un des meilleurs tests de la symétrie globale †. Pour remplacer l'inégalité (30) par des égalités il faudrait faire une analyse en déphasages de la diffusion Σ^+p ce qui semble impossible dans un avenir proche.

4. Tests de $g_1 = g_4$, $g_k \ll g_\pi$.

Lorsque $g_1 = g_4$ les interactions N—π et Ξ—π peuvent s'écrire sous la forme

$$B_k{}^i \pi_k{}^m B_m{}^i, \quad \text{avec} \quad (B_k{}^i) = \begin{pmatrix} \Xi^0, & \mathrm{p} \\ \Xi^-, & \mathrm{n} \end{pmatrix}. \tag{31}$$

Dans un espace I^-, $\binom{\mathrm{p}}{\Xi^0}$ et $\binom{\mathrm{n}}{\Xi^-}$ forment donc des spineurs. Par des considérations analogues à celles de la section 3, nous pouvons comparer la production des paires $\bar{\Xi}\Xi$ à la production de paires $\bar{\mathrm{N}}\mathrm{N}$.

Dans les collisions πN on a

$$\begin{aligned} &(\text{nombre de } \bar{\Xi}^0) \geqq \tfrac{1}{2}(\text{nombre de } \bar{\mathrm{p}}), \\ &(\text{nombre de } \bar{\Xi}^-) \geqq \tfrac{1}{2}(\text{nombre de } \bar{\mathrm{n}}), \end{aligned} \tag{32}$$

et dans les collisons p—p

$$\begin{aligned} &(\text{nombre de } \bar{\Xi}^0) \geqq \tfrac{1}{3}(\text{nombre de } \bar{\mathrm{p}}), \\ &(\text{nombre de } \bar{\Xi}^-) \geqq \tfrac{1}{3}(\text{nombre de } \bar{\mathrm{n}}). \end{aligned} \tag{33}$$

Bien entendu nous faisons les réserves habituelles en raison de l'effet de l'espace de phase.

† Voir la note sur épreuves.

5. Tests de l'Hypothèse de Salam et Polkinghorne

Il semble approprié de faire ici un bref rappel de ce que nous appellerons l'hypothèse de Salam et Polkinghorne [4]). Considérons l'hamiltonien d'interaction des N et des Ξ avec les mésons π:

$$\tfrac{1}{2}(g_1+g_4)[\bar{\mathrm{N}}\tau\mathrm{N}\pi+\bar{\Xi}\tau\Xi\pi]+\tfrac{1}{2}(g_1-g_4)[\bar{\mathrm{N}}\tau\mathrm{N}\pi-\bar{\Xi}\tau\Xi\pi].$$

Dans l'hypothèse de Salam et Polkinghorne $|g_1+g_4| \gg |g_1-g_4|$, c'est à dire que $g_1 \approx g_4$ (cas précédemment traité sous la condition $g_K \ll g_\pi$). Ici les interactions K ne sont plus négligées mais soumises à une condition similaire:

$$g_5 \approx g_7, \quad g_6 \approx g_8;$$

($g_5 \ldots g_8$ peuvent être de l'ordre de g_1 et g_4).

Les masses du Ξ et du nucléon sont supposées égales en l'absence des interactions en g_1-g_4, g_5-g_7, g_6-g_8. L'hamiltonien d'interaction se décompose en deux parties: H_{TF} hamiltonien des interactions très fortes et H_{MF} hamiltonien des interactions moyennement fortes responsables de la différence de masse $M_\Xi - M_\mathrm{N}$; H_{TF} est invariant dans les rotations d'un espace isobarique à quatre dimensions qui est le produit direct de deux expaces à trois dimensions, i^+, espace du spin isobarique ordinaire, et i^-, espace de l'étrangeté. Les particules appartiennent aux représentations irréductibles dans cet espace $\mathscr{D}(i^+, i^-)$; les attributions sont les suivantes: $(\mathrm{N}\Xi)$ et $(\mathrm{K}\dot{\mathrm{K}})$ appartiennent à $\mathscr{D}(\frac{1}{2}\frac{1}{2})$; Λ, Σ et π à $\mathscr{D}(0, 0)$, $\mathscr{D}(1, 0)$, $\mathscr{D}(1, 0)$ respectivement. Dans i^-, Λ, Σ et π sont des scalaires tandis qu'à partir de N, Ξ et $\dot{\mathrm{K}}$, K on construit les spineurs suivants:

$$\begin{pmatrix} \mathrm{p} \\ \Xi^0 \end{pmatrix}, \quad \begin{pmatrix} \mathrm{n} \\ \Xi^- \end{pmatrix}, \quad \begin{pmatrix} \mathrm{K}^+ \\ -\bar{\mathrm{K}}^0 \end{pmatrix}, \quad \begin{pmatrix} \mathrm{K}^0 \\ \mathrm{K}^- \end{pmatrix}. \tag{34}$$

On peut alors appliquer des méthodes analogues à celles employées dans les sections 3 et 4 pour faire certaines prédictions.

Evidemment les relations (32) et (33) fournissent un test de $g_1 = g_4$ valable non seulement pour $g_K \ll g_\pi$ mais aussi pour $g_5 = g_7$, $g_6 = g_8$, de l'ordre de g_1, mais ce test n'est pas spécifique de l'hypothèse de Salam et Polkinghorne. Il est donc nécessaire d'envisager par ailleurs des réactions dans lesquelles interviennent des mésons K.

Une série de tests de ce genre a été proposée par Feldman [7]); on trouve par exemple pour les réactions

$$\bar{\mathrm{K}}\mathrm{N} \to \bar{\mathrm{K}}\mathrm{N} \quad \text{(a)}, \quad \bar{\mathrm{K}}\mathrm{N} \to \mathrm{K}\Xi \quad \text{(b)}, \quad \mathrm{K}\mathrm{N} \to \mathrm{K}\mathrm{N} \quad \text{(c)}, \tag{35}$$

des inégalités triangulaires entre les racines des sections efficaces. Il faut cependant remarquer que dans les tests envisagés par Feldman on n'obtient pas de limite inférieure du nombre de Ξ produits en fonction des sections efficaces des autres réactions. Ainsi, dans l'exemple (33) on peut fort bien avoir

$\sigma_a = \sigma_c$, $\sigma_b = 0$. Il serait donc intéressant de donner quelques tests tels que si dans deux réactions comparées apparaissent des Ξ et des nucléons on ait une condition du type

$$(\text{nombre de } \Xi) \geqq \alpha(\text{nombre des nucléons}),$$

où α est un coefficient de l'ordre de l'unité. Les expériences que nous proposons sont certainement très difficiles mais il y a quelque espoir qu'elles puissent être un jour effectuées.

Si le nombre de Ξ produits par les grandes machines est appréciable, on peut tenter le test suivant:

$$\begin{aligned} \Xi^- + p &\to \Sigma(\text{ou } \Lambda) + \bar{K} + N + n\pi \quad (a), \\ \Xi^- + p &\to \Sigma(\text{ou } \Lambda) + K + \Xi + n\pi \quad (b), \\ n + p &\to \Sigma(\text{ou } \Lambda) + K + N + n\pi \quad (c). \end{aligned} \tag{36}$$

Utilisant les méthodes de la section 3 et tenant compte du caractère spinoriel des quantités (34) dans I^- nous obtenons, en précisant convenablement les états de charge des particules finales, des inégalités triangulaires entre les racines des sections efficaces pour (a), (b) et (c); de là on passe à des inégalités entre sections efficaces indépendantes du nombre de mésons π émis et de la charge des particules finales:

$$\sigma\left(\Xi^- + p \to \begin{matrix} \Sigma(\Lambda) + K + \Xi \\ \Sigma(\Lambda) + \bar{K} + N \end{matrix}\right) \geqq \tfrac{1}{4}\sigma(n + p \to \Sigma(\Lambda) + K + N). \tag{37}$$

On peut aussi examiner des réactions du type

$$\Sigma + N \to \begin{matrix} N + N + \bar{K} + n\pi, \\ N + \Xi + K + n\pi. \end{matrix}$$

Ainsi:

$$\Sigma^- + p \to \begin{matrix} \Xi^- + K^+ + p + n\pi \\ n + K^+ + \Xi^0 + n\pi \\ n + \bar{K}^0 + p + n\pi \end{matrix} \text{ ou bien } \to \begin{matrix} \Xi^0 + K^0 + p + n\pi & (a), \\ p + K^0 + \Xi^0 + n\pi & (b), \\ p + K^- + p + n\pi & (c). \end{matrix} \tag{38}$$

Nous sommes en présence de réactions du type (16) déjà traité dans la section 3, où A, B et C sont choisis parmi les spineurs (34). Les deux cas (particules toutes différentes dans chacun des trois états finals ou deux particules identiques dans l'un des états finals) conduisent, nous l'avons vu, au même résultat qui devient, ici:

$$\Sigma_a + \Sigma_b \geqq \tfrac{1}{2}\Sigma_c, \tag{39}$$

que l'on peut exprimer par

$$(\text{nombre de } \Xi) \geqq \tfrac{1}{2}(\text{nombre de } \bar{K}), \tag{39'}$$

ou encore par d'autres relations équivalentes.

Enfin, indiquons un dernier test concernant la production d'antihypérons accompagnés de mésons K. Si il s'avérait que l'hypothèse fondamentale de la symétrie globale, $g_\pi \gg g_K$, est fausse, c'est à dire que le nombre de paires $\bar{\Sigma}\Sigma$ produites n'est pas notablement plus grand que le nombre de paires du type $\bar{\Sigma}N$ accompagnées d'un méson K il serait intéressant de considérer les réactions

$$\pi+p \to \begin{cases} \bar{\Sigma}+\Xi+K+N+n\pi & \text{(a)}, \\ \bar{\Sigma}+N+K+\Xi+n\pi & \text{(b)}, \\ \bar{\Sigma}+N+\bar{K}+N+n\pi & \text{(c)}. \end{cases} \tag{40}$$

Il n'y a pas de différence formelle entre ce cas et le cas précédemment traité (38) car le π et le Σ étant des scalaires dans I^- peuvent passer de l'état initial à l'état final et inversément sans que le raisonnement soit modifié. On obtient donc encore (39): $\Sigma_a+\Sigma_b \geqq \frac{1}{2}\Sigma_c$; en particulier

$$(\text{nombre de } \Xi) \geqq \tfrac{1}{2}(\text{nombre de } \bar{K}). \tag{39'}$$

6. Corrections dues à la Variation des Densités d'États Finals par suite des Différences de Masses entre Baryons

Dans toutes les prédictions faites ci-dessus les différences de masses entre baryons sont négligées. Nous sommes bien obligés de supposer que l'effet de ces différences de masses sur les éléments de matrice des diverses réactions envisagées est petit, mais la variation du volume disponible dans l'espace de phase d'une réaction à l'autre est trop grande pour être négligée. C'est certainement dans les réactions de production de paires de baryons considérées dans les sections 2, 3 et 4 que cet effet sera le plus important. Nous ne voulons pas donner ici une étude complète des effets d'espace de phase mais seulement montrer leur importance par quelques exemples.

Pour la production de paires de baryons dans les collisions nucléon-nucléon, la densité d'états finals intégrée a déjà été calculée par Hagedorn [8]) pour une énergie de 25 GeV dans le système du laboratoire. Nous nous contentons de donner les résultats dans le tableau 1.

TABLEAU 1

Résultats des calculations de Hagedorn (n désigne le nombre de mésons π émis)

Rapports des densités \ n	0	1	2	3	4	5
$N\bar{N}/\Sigma\bar{\Sigma}$	1.5	2	3	4.3	6.5	9.5
$N\bar{N}/\Xi\bar{\Xi}$	2.3	3.9	7.2	17	28	112

On note que les rapports des densités d'états finals dépendent très fortement du nombre de mésons π émis. Ceci est désagréable car on est alors placé devant une alternative: ou bien renoncer à employer les inégalités que nous avons données indépendamment du nombre de mésons π émis est séparer les événements correspondant à des nombres n de π fixés, en revenant, lorsqu'on le peut, aux inégalités triangulaires de départ, ou bien se faire une idée du nombre n au dessus duquel la section efficace devient négligeable et appliquer la correction d'espace de phase correspondant au cas le plus défavorable.

Illustrons cette dernière possibilité par un exemple: si la production de quatre mésons π est appréciable, l'inégalité (27) devra être remplacée par

$$(\text{nombre de } \bar{\Sigma}^+) \geqq \tfrac{1}{20}(\text{nombre de } \bar{\text{p}});$$

l'inégalité devient donc beaucoup moins restrictive, donc moins intéressante.

Nous n'avons pas jugé utile de faire une étude aussi complète dans le cas de la production de paires de baryons dans les collisions π—p (on pourra le faire lorsque le besoin s'en fera sentir). Dans le cas simple où il n'y a aucun méson π dans l'état final nous obtenons

$$\text{densité } \text{N}\bar{\text{N}}/\text{densité } \Sigma\bar{\Sigma} = \begin{cases} 1.2 \text{ pour } E_{\text{lab}} = 25 \text{ GeV}, \\ 1.3 \text{ pour } E_{\text{lab}} = 18 \text{ GeV}, \end{cases}$$

$$\text{densité } \text{N}\bar{\text{N}}/\text{densité } \Xi\bar{\Xi} = \begin{cases} 1.4 \text{ pour } E_{\text{lab}} = 25 \text{ GeV}, \\ 1.6 \text{ pour } E_{\text{lab}} = 18 \text{ GeV}. \end{cases}$$

Par comparaison avec la première colonne du tableau 1, nous voyons que pour des mésons π et des nucléons de même énergie, le rapport des densités d'états finals est plus favorable pour les mésons π, ce qu'on devrait d'ailleurs attendre. Les mésons π de haute énergie semblent donc plus commodes, même si leur intensité est plus faible que celle des protons, car de telles expériences ne semblent possibles qu'à l'aide de chambres à bulles.

La comparaison de sections efficaces de diffusion, par exemple, pp et Σ^+p n'est pas affectée comme les réactions de production de paires par les effets d'espace de phase et semble donc, à ce point de vue, devoir donner des résultats beaucoup plus nets.

Nous tenons à remercier le professeur V. Glaser pour une discussion fructueuse et simplificatrice, le Dr. R. Hagedorn pour nous avoir communiqué ses résultats détaillés, et M. W. Klein pour des calculs numériques.

Appendice

PRODUCTION DE PAIRES $\Sigma\bar{\Sigma}$ ET $\text{N}\bar{\text{N}}$ DANS LES COLLISIONS p—p

Considérons la réaction

$$\text{p}+\text{p} \rightarrow \bar{\text{n}}+\text{n}+\text{p}+\text{p}. \quad \text{(a)}$$

On lui associera

$$p+p \to \begin{cases} \bar{\Sigma}^- + \Sigma^- + p + p & \text{(b)}, \\ \bar{\Sigma}^- + n + Z^0 + p & \text{(c)}, \\ \bar{\Sigma}^- + n + p + Z^0 & \text{(d)}. \end{cases}$$

Ces trois réactions sont du type

$$|11\rangle \to A+B+C+C,$$

où

$$A = \begin{pmatrix} -\bar{\Sigma}^- \\ \bar{n} \end{pmatrix}, \quad B = \begin{pmatrix} n \\ \Sigma^- \end{pmatrix}, \quad C = \begin{pmatrix} p \\ Z \end{pmatrix}.$$

Les amplitudes de transition pour ces quatre réactions sont des combinaisons linéaires d'amplitudes

$$T_{i_1 i_2},$$

où i_1 est le spin „isobarique" des deux premières particules (0 ou 1) et i_2 le spin „isobarique" des deux dernières (0 ou 1). i_1 et i_2 sont combinés pour donner un spin „isobarique" résultant $i = 1$; par suite

$$T_{00} = 0, \quad T_a = -\frac{1}{\sqrt{2}} T_{01} - \frac{1}{\sqrt{2}} T_{11}, \quad T_b = -\frac{1}{\sqrt{2}} T_{01} + \frac{1}{\sqrt{2}} T_{11},$$

$$T_c = \frac{1}{\sqrt{2}} T_{10} - \frac{1}{\sqrt{2}} T_{11}, \quad T_d = -\frac{1}{\sqrt{2}} T_{10} - \frac{1}{\sqrt{2}} T_{11},$$

d'où l'on tire

$$T_a - T_b - T_c - T_d = 0,$$

relation analogue à la relation (19), d'où

$$|T_a| \leqq |T_b| + |T_c| + |T_d|.$$

Utilisant l'identité

$$3(x^2+y^2+z^2) \equiv (x+y+z)^2 + (x-y)^2 + (y-z)^2 + (x-z)^2,$$

on obtient

$$\tfrac{1}{3}|T_a|^2 \leqq |T_b|^2 + |T_c|^2 + |T_d|^2.$$

Les réactions (c) et (d) sont identiques à l'échange des quantités de mouvement près; les réactions (a) et (b) contiennent chacune dans leur état final deux particules identiques. Laissant fixe la quantité de mouvement des antiparticules et sommant sur les autres quantités de mouvement nous obtenons donc (voir réf. [6]))

$$(\text{nombre de } \bar{n}) \leqq \tfrac{1}{3}(\text{nombre de } \bar{\Sigma}^-).$$

La démonstration complète exigerait que l'on considère les autres états de charge finals possibles, par exemple $\bar{n}+p+p+p$ et les états associés, mais il n'y a pas de difficulté de principe nouvelle.

Note sur épreuves: Notre attention a été récemment attirée sur le fait que les mesures de diffusion Λ-nucléon sont maintenant possibles. Par des méthodes analogues à celles qui conduisent à (30) mais en utilisant les propriétés de l'espace I_b'' on prouve

$$\sigma_{\Sigma^- p} \geqq \tfrac{1}{2}\sigma_{np}. \tag{30'}$$

D'autre part la symétrie restreinte (espace I_b) conduit à la relation

$$\tfrac{1}{2}(\sigma_{\Sigma^- p}+\sigma_{\Sigma^+ p}) = \sigma_{\Lambda p}. \tag{30''}$$

(30), (30') et (30'') donnent pour les sections efficaces totales

$$\sigma_{\Lambda p} \geqq \tfrac{1}{4}[\sigma_{np}+\sigma_{pp}]. \tag{30'''}$$

Les relations (30), (30') et (30''') sont probablement les meilleurs tests de la symétrie globale. En effet, l'influence de l'espace des phases n'est pas très importante et les sections efficaces attendues sont grandes. Quant à l'égalité (30'') elle est valable sous les conditions beaucoup moins restrictives de la symétrie restreinte et sa vérification expérimentale n'en présente que plus d'intérêt.

Bibliographie

1) B. d'Espagnat et J. Prentki, Nuclear Physics **9** (1958—59) 326
2) E. Wigner, Proc. Nat. Acad. Sci. **38** (1952) 449;
   M. Gell-Mann, Phys. Rev. **106** (1957) 1296;
   J. Schwinger, Proceedings of the Seventh Annual Conference on High Energy Physics, Rochester conference (1957)
3) A. Salam et J. Polkinghorne, Nuovo Cim. **2** (1955) 685
4) A. Salam, Conférence de Kiev (juillet 1959);
   D. Amati et B. Vitale, Nuovo Cim. **9** (1958) 895
   B. d'Espagnat et J. Prentki, Nuovo Cim. **15** (1960) 130
   M. H. Ross et G. L. Shaw, Phys. Rev. **115** (1959) 1773
   M. L. Gupta, Nuovo Cim. **16** (1960) 737
   R. H. Capps, Phys. Rev. **118** (1960) 1097
5) D. Lichtenberg, Phys. Rev. **113** (1959) 1309
6) E. Fermi, Nuovo Cim. Suppl. **2** (1955) 67
7) D. Feldman, Phys. Rev. **103** (1956) 254
8) R. Hagedorn, communication privée

3.A

Nuclear Physics **20** (1960) 557—560; © *North-Holland Publishing Co., Amsterdam*

Not to be reproduced by photoprint or microfilm without written permission from the publisher

A NEW ISOMERIC STATE OF Cs^{131}

E. BODENSTEDT, H. J. KÖRNER, C. GÜNTER, D. HOVESTADT and J. RADELOFF

II. *Institut für Experimentalphysik der Universität Hamburg*

Received 27 June 1960

Abstract: A new isomeric state at 133 keV was found. The half life was determined as $T_{\frac{1}{2}} = 13.3 \pm 0.5$ ns. The level is interpreted as the $g_{\frac{7}{2}}$ shell model state. A new determination of the half life of the 124 keV level gave $T_{\frac{1}{2}} = 3.77 \pm 0.05$ ns.

The decay of the 11.5 d Ba^{131} was investigated by several authors [1–4]). The decay scheme according to August *et al.* [4]) is shown in fig. 1a. We confirmed this decay scheme by gamma-gamma coincidence measurements. All of the gamma-gamma cascades of fig. 1a were found. In particular, the 487 keV—216 keV cascade could be detected in agreement with the recent result of August *et al.* [4]).

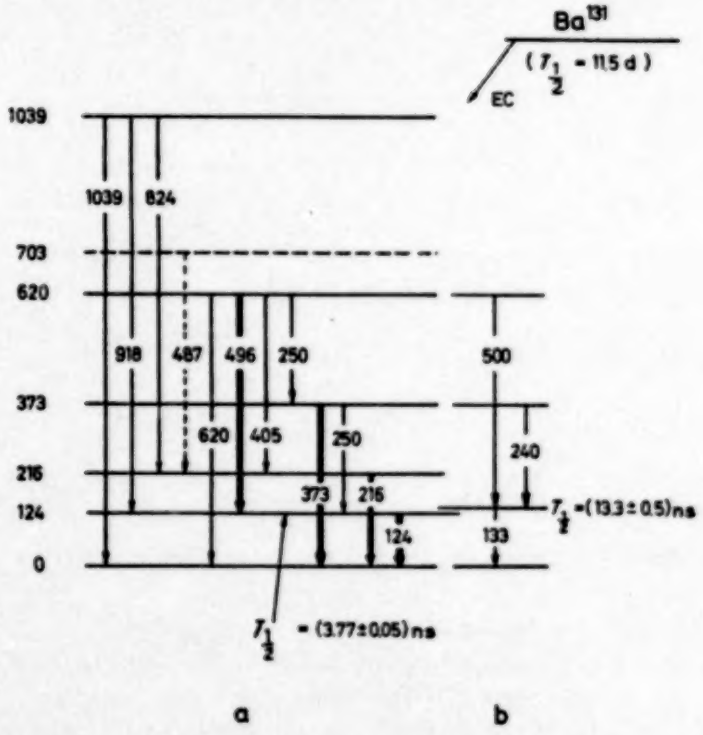

Fig. 1. Decay scheme of Ba^{131}.

Additional gamma lines of 133.4 keV and 239.3 keV were only found in the conversion spectrum by Cork *et al.* [1]) and August *et al.* [4]). The position of these

transitions in the level scheme has not yet been fixed. As the sum of the precisely known energies of these two lines agrees very well with the energy of the 373 keV level it is probable that they form a cascade between this level and the ground state.

The half life of the 124 keV state was determined by Coleman [5]) as

$$T_{\frac{1}{2}} = 4.1 \pm 0.5 \text{ ns}$$

and by Vartapetian *et al.* [3]) as

$$T_{\frac{1}{2}} = 4.0 \pm 0.3 \text{ ns}.$$

When we repeated the measurement of this half life we obtained the curve shown in fig. 2. We used a "fast- slow"-coincidence circuit with a resolving time

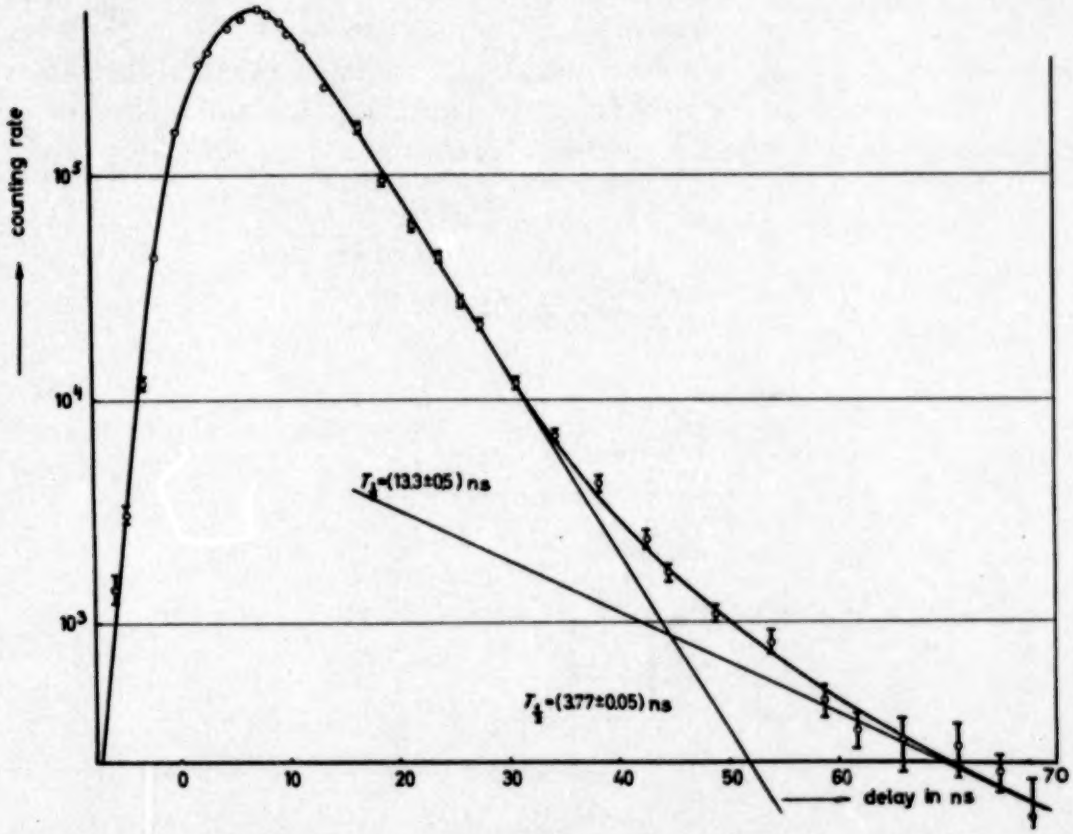

Fig. 2. Half life measurement by the method of delayed coincidences. The single-channel analysers accept radiations with energies of 500±40 keV and 125±15 keV respectively. The straight lines are the result of a least square fit for the two different half lives.

of $2\tau = 9$ ns. The single-channel analysers were set on the photo peaks at 124 keV and 500 keV.

The result shows the existence of two different half lives. They were deter-

mined by a least square fit of three independent measurements as

$$T_{\frac{1}{2}}(\mathrm{I}) = 3.77 \pm 0.05 \text{ ns}$$

and

$$T_{\frac{1}{2}}(\mathrm{II}) = 13.3 \pm 0.5 \text{ ns}.$$

The first value must be attributed to the intense 124 keV-transition. The coincidence spectrum was measured at a delay of 55 ns where contributions of the 3.77 ns cascade are negligibly small. It could be shown that the low intensity admixture is a cascade of two gamma lines with energies of 500 ± 30 keV and 133 ± 5 keV.

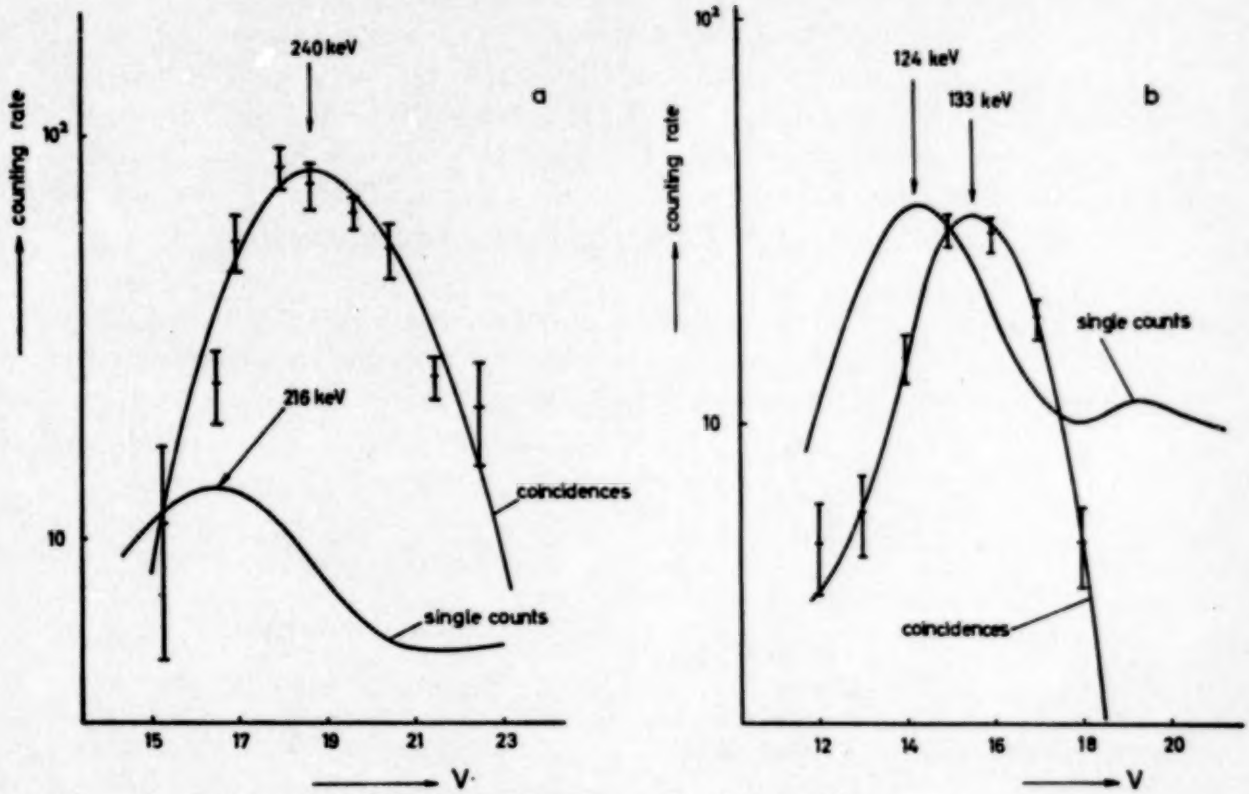

Fig. 3. Coincidence spectra at 55 ns delay.
a. Coincidences with the 133 keV radiation.
b. Coincidences with the 240 keV radiation.

A repetition of the measurement of the half life curve after 60 days showed no change, thus proving that the new half life is not due to impurities of the source.

It is proposed that the new 133 keV transition is identical with the 133.4 keV conversion line and leads from a 133.4 keV isomeric state of 13.3 ns of Cs^{131} to the ground state. In addition, coincidences between the 133 keV gamma line and a line at 240 ± 5 keV have been detected at a delay of 55 ns (fig. 3). This radiation can be identified as the 239.3 keV conversion line and confirms the proposed decay scheme of fig. 1b. Measurements at different delays also showed the new half life of 13.3 ns.

The spin of the ground state of Cs^{131} has been determined by Bellamy and Smith [7]) and Nierenberg *et al.* [8]) as $\frac{5}{2}^+$. Angular correlation measurements on the 496 keV—124 keV-cascade by Lindqvist and Karlsson [9]) showed an anisotropy of about +1 %.

Preliminary angular correlation measurements of the same cascade at different delays showed however that the admixed cascade of 500 keV—133 keV has an anisotropy of about +100 % and that the 496 keV−124 keV angular correlation is probably isotropic. A liquid source of $BaCl_2$ in aqueous solution was used for these measurements.

Our results suggest the spin $\frac{1}{2}^+$ for the 124 keV level and the spin $\frac{7}{2}^+$ for the 133 keV level which can be interpreted as the $g_{\frac{7}{2}}$ shell model state. From these spin assignments it follows that the 124 keV transition is pure E2, which is in agreement with the known value of the K/L ratio [1]). The half life corresponds to a single-particle E2 transition. The 133 keV radiation is the *l*-forbidden M1 transition between the shell model states $g_{\frac{7}{2}}$ and $d_{\frac{5}{2}}$. This interpretation also agrees with the observed K/L ratio [1]) and the expected half life.

The authors are indebted to Prof. W. Jentschke for his interest in this investigation. The financial funds submitted by the Bundesministerium für Atomkernenergie und Wasserwirtschaft are gratefully acknowledged.

References

1) J. M. Cork, J. M. LeBlanc, W. H. Nester and M. K. Brice, Phys. Rev. **91** (1953) 76
2) W. C. Beggs, D. L. Robinson and R. W. Fink, Phys. Rev. **110** (1956) 149
3) M. H. Vartapetian, Compt. Rend. **243** (1956) 1512
4) L. S. August, R. W. Campell and M. Goodrich, Bull. Am. Phys. Soc. **2** (1957) 231
5) C. Coleman, Phil. Mag. **96** (1955) 1135
6) H. Vartapetian, L. Dick, R. Foucher and N. Perrin, Compt. Rend. **242** (1956) 103
7) E. H. Bellamy and K. F. Smith, Phil. Mag. **44** (1953) 33
8) W. A. Nierenberg, J. C. Hubbs, H. A. Shugart, H. B. Silsbee and P. O. Strom, Bull. Am. Phys. Soc. **1** (1956) 343
9) T. Lindqvist and E. Karlsson, Ark. f. Fysik **12** (1957) 519

2.B

Nuclear Physics **20** (1960) 561—584; © *North-Holland Publishing Co., Amsterdam*

Not to be reproduced by photoprint or microfilm without written permission from the publisher

THÉORIE DES CORRÉLATIONS MULTIPLES PERTURBÉES

VINCENT GILLET

Service de Physique Mathématique, Centre d'Études Nucléaires de Saclay, Gif-sur-Yvette (S. & O.)

Reçu le 25 Mai 1960

Abstract: Techniques using irreducible tensorial sets for the calculation of multiple correlated processes are extended to the case when the degeneracies of one or several component states are removed. The irreducible representation of an operator acting on a state perturbed through an interaction with a classical or quantal system is first given in a quite general form. The irreducible product of two operators is then easily generalized when one of the operators is acting on a space of non-degenerate states, the states of the tensor product space being non-degenerate also. This permits the construction of the most general density matrices for perturbed nuclear states prepared from perturbed states initially oriented through the absorption or the emission of a radiation of known polarization. Provisions are also made for taking into account any partial depolarization in external fields of the incident or emitted particles before absorption or detection. A detailed discussion is made of perturbed double and triple nuclear correlations, the polarizations of the nuclear states and of the absorbed (or emitted) radiations being specified (or analyzed), the perturbing systems being oriented or not. For double angular distributions with axial measurements only, one obtains well known results. The infinite limit is discussed in detail; in particular, for non-oriented perturbing fields, the residual anisotropy, independent of the orientation of the observation plane (the "hard core" of double angular correlations), is calculated for triple correlation processes; it is shown to be a function of the multipolarities of the intermediate radiation except in the case of axial perturbing fields.

1. Introduction

Le calcul de valeur moyenne d'opérateurs sur des états nucléaires préparés a été grandement simplifié par l'introduction de techniques utilisant systématiquement les ensembles tensoriels irréductibles et leur algèbre [1–3]). Nous étendons ces méthodes lorsqu'il existe des perturbations levant la dégénérescence des états sur lesquels sont construites les représentations irréductibles des opérateurs considérés. Pour ce faire, nous redéfinissons pour l'opérateur agissant sur un espace perturbé, une représentation tensorielle irréductible dont les éléments de matrice sont donnés par un développement sur les éléments de matrice de l'opérateur dans une représentation irréductible lorsque la dégénérescence de l'espace de représentation n'est pas levée. Les coefficients de ce développement dépendants ou indépendants du temps, indépendants des nombres quantiques magnétiques, sont donnés par une sommation sur deux coefficients de Clebsch-Gordan multipliés par un terme dépendant de l'interaction et du recouvrement des états propres du système perturbateur et du système perturbé. La formulation donnée est tout à fait générale et elle s'applique

aussi bien à des systèmes perturbateurs décrits quantiquement que classiquement. Nous généralisons ensuite la formule de composition l'opérateurs agissant sur deux espaces distincts lorsque les dégénérescences de l'un de ces deux espaces et de l'espace produit direct sont levées par des interactions avec des systèmes perturbateurs.

Généralisant au cas perturbé une expression de U. Fano et G. Racah [1]), nous donnons la matrice densité d'un état perturbé pendant un temps donné, sachant que cet état a été formé par la désintégration d'un premier état lui-même perturbé pendant un certain temps, et qu'une mesure de polarisation et de direction angulaire est effectuée sur le produit de la désintégration. Si le produit de la désintégration est partiellement dépolarisé par un champ externe, nous donnons les modifications de la formule précédente qui en résultent. Ces expressions servent de point de départ à tout calcul de processus multiples atténués par des perturbations, dès que l'on connaît, en l'absence de perturbations, les éléments de matrice dans des représentations irréductibles des opérateurs densité décrivant les divers systèmes interagissant et des opérateurs associés aux observables.

Nous appliquons les résultats précédents aux corrélations nucléaires, doubles ou triples [4–8]) lorsque le ou les états nucléaires intermédiaires ont leur dégénérescence levée par des champs perturbateurs classiques ou quantiques, orientés au hasard ou non, pour des mesures à symétrie axiale ou de type plus général (mesures de polarisation), pour des coïncidences retardées ou effectuées en moyenne sur le temps de vie du ou des états intermédiaires. Dans le cas des corrélations doubles, pour des mesures purement axiales, nous obtenons des résultats bien connus [9–12]). En particulier lorsque les champs perturbateurs sont orientés au hasard, la corrélation double perturbée s'exprime simplement en fonction des termes du développement de la corrélation non perturbée, chaque terme étant multiplié par un facteur d'atténuation indépendant des multipolarités des rayonnements absorbés ou émis [9–11]) pourvu que l'état nucléaire initial ne soit pas polarisé et qu'on n'observe pas la polarisation de l'état nucléaire final. Nous généralisons ce résultat au cas des corrélations triples, les facteurs d'atténuation sont alors fonctions des multipolarités du rayonnement de la transition intermédiaire mais ils sont indépendants des multipolarités des rayonnements de la première et de la dernière transition, si les polarisations de l'état nucléaire initial et de l'état nucléaire final ne sont pas spécifiées ou mesurées. Nous discutons en détail la limite des perturbations infinies. Si le ou les champs perturbateurs sont orientés, l'anisotropie résiduelle des corrélations perturbées doubles ou triples est une fonction de l'orientation relative du plan d'observation et du ou des systèmes perturbateurs. L'anisotropie ne peut être complètement effacée que dans le cas particulier de champs perturbateurs axials, pour des mesures purement axiales, le plan d'observation étant perpendiculaire à l'axe de symétrie du ou des systèmes perturbateurs.

Si le ou les champs perturbateurs sont orientés au hasard, l'anisotropie résiduelle, à la limite des perturbations infinies, est indépendante de l'orientation du plan d'observation: c'est le „cœur dur" étudié pour les distributions angulaires doubles par K. Alder [10]) et A. Abragam et R. V. Pound [11]). Nous étendons ce résultat au cas des corrélations triples. La limite du „cœur dur" pour les corrélations doubles est indépendante des multipolarités des rayonnements absorbés ou émis. Pour les corrélations triples, elle dépend en général de la multipolarité du rayonnement intermédiaire. Dans ce dernier cas cependant, si les systèmes perturbateurs dans les deux états nucléaires intermédiaires présentent la symétrie axiale, l'anisotropie résiduelle devient également indépendante des multipolarités du rayonnement intermédiaire.

2. Formalisme Général

2.1. REPRÉSENTATIONS IRRÉDUCTIBLES D'OPÉRATEURS SUR UN ESPACE PERTURBÉ

Soit un système physique caractérisé par les nombres quantiques α_j et j, dégénéré d'ordre $(2j+1)$. Pour ce qui suit, il est suffisant de se limiter aux observables associées à ce système qui sont représentées par des opérateurs scalaires O. Un opérateur O a pour représentation sur la base des états propres $|\alpha_j jm\rangle$ de $\mathbf{j}$ les matrices d'éléments $\langle\alpha_j jm|O|\alpha_j jm'\rangle$. Il est plus commode d'adopter une représentation équivalente irréductible ayant pour éléments de matrice

$$[(\alpha_j j|O|\alpha_j j)]_\mu^\nu = \sum_{m,m'} (-)^{j-m'}(jjm-m'|\nu\mu)\langle\alpha_j jm|O|\alpha_j jm'\rangle. \qquad (1)$$

Les notations et définitions utilisées sont celles de U. Fano et G. Racah [1]). Pour les coefficients de recouplage géométrique voir également A. Messiah [13]) et A. Edmonds [14]).

La dégénérescence $(2j+1)$ de l'état α_j, j est en fait levée partiellement ou complètement par une perturbation. Celle-ci peut être constituée par la précession du moment magnétique dipolaire du système dans un champ magnétique constant externe, par le couplage de ce moment magnétique avec le moment magnétique dipolaire d'un système perturbateur quantique (structure hyperfine), ou encore par le couplage du moment électrique quadrupolaire du système avec un gradient de champ électrique cristallin etc. . . . L'observable O devient maintenant une fonction de la perturbation appliquée, et nous nous proposons d'étudier la modification qui en résulte pour son expression dans une représentation irréductible.

Le couplage du système α_j, j avec le champ perturbateur appliqué est représenté par l'hamiltonien K. Soient $|k\rangle$, $k = 1$ à $n (n \leqq 2j+1)$, les états propres de K correspondant aux énergies E_k. Si le système perturbateur est

quantique, les états $|k\rangle$ sont des combinaisons linéaires de produits des états propres du système perturbateur avec ceux du système perturbé. Par exemple, dans le cas simple de la structure hyperfine des atomes libres: $K = \gamma \mathbf{j} \cdot \mathbf{I}$ (où $\mathbf{j}$ et $\mathbf{I}$ représentent respectivement les moments angulaires nucléaire et électronique), l'on a

$$|k\rangle = |\mathcal{F}\mathcal{M}\rangle = \sum_{mM} (jImM|\mathcal{F}\mathcal{M})|jm\rangle|IM\rangle. \tag{2}$$

Souvent le champ perturbateur peut être décrit classiquement (champ magnétique constant externe couplé au moment magnétique dipolaire du système perturbé, gradient du champ électrique du réseau cristallin couplé au moment électrique quadrupolaire etc. . . .). Seules les variables quantiques du système perturbé figurent dans la description des états propres de K. Ceux-ci sont alors donnés par un développement du type

$$|k\rangle = \sum_{m} C_{mk}|jm\rangle. \tag{3}$$

Dans le cas fréquent d'un champ perturbateur classique invariant par rotation autour d'un axe, l'hamiltonien K commute avec $\mathbf{j}$ et ses états propres sont identiques à ceux de $\mathbf{j}$.

En représentation interaction pour l'hamiltonien K, l'observable O devient une fonction de K et du temps t

$$O(K, t) = U^{\dagger}(K, t)OU(K, t). \tag{4}$$

Pour un champ perturbateur statique

$$U(K, t) = \mathrm{e}^{-\frac{iKt}{\hbar}} \tag{5}$$

la représentation irréductible, dépendante du temps, de $O(t)$, est donnée par le développement

$$[(\alpha_j j|O(K, t)|\alpha_j j)]^{\nu}_{\mu} = \sum_{\bar{\nu}\bar{\mu}} A^{j}_{\bar{\nu}\bar{\mu}\nu\mu}(K, t)[(\alpha_j j|O|\alpha_j j)]^{\bar{\nu}}_{\bar{\mu}}. \tag{6}$$

Les coefficients d'atténuation dépendants du temps $A^{j}_{\bar{\nu}\bar{\mu}\nu\mu}(K, t)$ sont obtenus en inversant la relation (1)

$$\langle \alpha_j j\tilde{m}|O|\alpha_j jm\rangle = (-)^{j-m} \sum_{\bar{\nu}\bar{\mu}} (jj\tilde{m}-m|\bar{\nu}\bar{\mu})[(\alpha_j j|O|\alpha_j j)]^{\bar{\nu}}_{\bar{\mu}},$$

en appliquant la transformation (4)

$$\langle \alpha_j j\tilde{m}|O(K, t)|\alpha_j jm\rangle = \sum_{m\tilde{m}} \sum_{k\tilde{k}} \langle \tilde{m}'|\tilde{k}\rangle \mathrm{e}^{iE_{\tilde{k}}t/\hbar}\langle \tilde{k}|\tilde{m}\rangle \times \langle \alpha_j j\tilde{m}|O|\alpha_j jm\rangle\langle m|k\rangle \mathrm{e}^{-iE_k t/\hbar}\langle k|m'\rangle,$$

puis en repassant dans une représentation irréductible à l'aide de (1). Il vient

$$A^{j}_{\bar{\nu}\bar{\mu}\nu\mu}(K,t) = \sum_{\substack{m\tilde{m}\\ m'\tilde{m}'}} (-)^{2j-m-m'}(jj\tilde{m}'-m'|\nu\mu)(jj\tilde{m}-m|\bar{\nu}\bar{\mu}) \times \sum_{k\tilde{k}} r^{j}(\tilde{m}'\tilde{k}\tilde{m};mkm')\mathrm{e}^{-i(E_k-E_{\tilde{k}})t/\hbar}$$
$$= \sum_{k\tilde{k}} a^{jk\tilde{k}}_{\bar{\nu}\bar{\mu}\nu\mu}\mathrm{e}^{-i(E_k-E_{\tilde{k}})t/\hbar}. \qquad (7)$$

Pour un champ perturbateur décrit classiquement, sans symétrie particulière

$$r^{j}(\tilde{m}'\tilde{k}\tilde{m};mkm') = \langle j\tilde{m}'|\tilde{k}\rangle\langle\tilde{k}|j\tilde{m}\rangle\langle jm|k\rangle\langle k|jm'\rangle, \qquad (8a)$$

où les vecteurs $|k\rangle$ sont donnés par le développement (3). Quant au facteur en énergie, il demande la résolution d'une équation séculaire. Si les énergies de la perturbation sont faibles, $\Delta t(E_k-E_{\tilde{k}})/\hbar \ll 1$, où Δt est l'imprécision sur l'instant de mesure, on peut utiliser le premier ordre du développement en puissance de K de l'expression (4). (Cf. réf. [11]), équation (7)). Pour un système perturbateur décrit classiquement et invariant par rotation autour d'un axe

$$r^{j}(\tilde{m}'\tilde{k}\tilde{m};mkm') = \delta_{\tilde{m}'\tilde{k}}\delta_{\tilde{k}\tilde{m}}\delta_{mk}\delta_{km'}, \qquad (8b)$$

de sorte que

$$a^{jk\tilde{k}}_{\bar{\nu}\bar{\mu}\nu\mu} = a^{jm\tilde{m}}_{\bar{\nu}\bar{\mu}\nu\mu}\delta_{\bar{\mu}\mu} = (jj\tilde{m}-m|\nu\mu)(jj\tilde{m}-m|\bar{\nu}\mu)\delta_{\bar{\mu}\mu}. \qquad (9a)$$

L'expression du facteur en énergie est alors simple. Par exemple pour le couplage du moment quadrupolaire électrique nucléaire $\mathbf{Q}$ avec le gradient de champ électrique cristallin ∇E

$$\frac{1}{\hbar}(E_m-E_{\tilde{m}}) = \frac{1}{\hbar}\left(\frac{3}{4j(2j-1)}\mathrm{e}\mathbf{Q}\cdot\nabla E\right)(m^2-\tilde{m}^2) = \omega_Q(m^2-\tilde{m}^2); \qquad (10a)$$

pour le couplage du moment dipolaire magnétique nucléaire $g M_N \mathbf{j}$ (où M_N est le magnéton nucléaire) avec un champ magnétique statique externe $\mathbf{H}$

$$\frac{1}{\hbar}(E_m-E_{\tilde{m}}) = \frac{1}{\hbar}gM_N H(m-\tilde{m}) = \omega_L(m-\tilde{m}). \qquad (10b)$$

Si ces deux types de perturbation à symétrie axiale existent simultanément, la situation est encore simple si l'une est prépondérante. En prenant pour axe de quantification l'axe de symétrie de la perturbation dominante, et en supposant que seules les valeurs propres et non les états propres de cette dernière sont modifiées par la seconde perturbation il vient (cf. réf. [11]): pour une interaction quadrupolaire électrique dominante

$$\frac{1}{\hbar}(E_m-E_{\tilde{m}}) = \omega_Q(m^2-\tilde{m}^2)\left\{1+\frac{\omega_L\cos\delta}{\omega_Q(m+\tilde{m})}\right\}, \qquad (10c)$$

et pour une interaction dipolaire magnétique dominante

$$\frac{1}{\hbar}(E_m - E_{\tilde{m}}) = \omega_L(m-\tilde{m})\left\{1+\frac{\omega_Q(m+\tilde{m})\cos\delta}{\omega_L}\right\}, \tag{10d}$$

où δ est l'angle que font entre eux les axes de symétrie de la perturbation électrique et de la perturbation magnétique.

La généralisation à un système perturbateur quantique est simple (K. Alder[10]). Ainsi, si en plus d'un champ perturbateur magnétique externe **H**, on introduit le couplage hyperfin entre les moments magnétiques dipolaires nucléaire et électronique ($K = \mathbf{j}\cdot(\gamma\mathbf{I}+gM\mathbf{H})$ et $|k\rangle = |\mathcal{F}\mathcal{M}\rangle$, expression (2))

$$r^j(\tilde{m}'\tilde{k}\tilde{m};\, mkm') = (jI\tilde{m}M|\tilde{\mathcal{F}}\tilde{\mathcal{M}})^2(jImM|\mathcal{F}\mathcal{M})^2\delta_{\tilde{m}'\tilde{m}}\delta_{mm'}, \tag{8c}$$

puisque l'opérateur O n'agit que sur le système α_j, j. Donc

$$\begin{aligned} a^{jk\tilde{k}}_{\bar{\nu}\bar{\mu}\nu\mu} &= a^{j\mathcal{F}\mathcal{M}\tilde{\mathcal{F}}\tilde{\mathcal{M}}}_{\bar{\nu}\mu\nu\mu}\delta_{\bar{\mu}\mu} \\ &= \left(\frac{(2j+1)}{\sum\limits_{\mathcal{F}'}(2\mathcal{F}'+1)}\right)(2\mathcal{F}+1)(2\tilde{\mathcal{F}}+1)(\mathcal{F}\tilde{\mathcal{F}}-\mathcal{M}\tilde{\mathcal{M}}|\nu\mu) \\ &\qquad \times(\mathcal{F}\tilde{\mathcal{F}}-\mathcal{M}\tilde{\mathcal{M}}|\bar{\nu}\mu)\begin{Bmatrix}\mathcal{F} & \tilde{\mathcal{F}} & \nu\\ j & j & I\end{Bmatrix}\begin{Bmatrix}\mathcal{F} & \tilde{\mathcal{F}} & \bar{\nu}\\ j & j & I\end{Bmatrix}, \end{aligned} \tag{9b}$$

où la constante $(2j+1)/\sum_{\mathcal{F}'}(2\mathcal{F}'+1)$ est introduite pour des raisons de normalisation (voir plus loin expressions (12a) et (12b)). Si le champ magnétique externe est nul, la séparation hyperfine des sous-niveaux ne dépend plus que de $\mathcal{F}$, $(E_{\mathcal{F}\mathcal{M}}-E_{\tilde{\mathcal{F}}\tilde{\mathcal{M}}})/\hbar = \omega_{\mathcal{F}\tilde{\mathcal{F}}}\delta_{\mathcal{M}\tilde{\mathcal{M}}}$. Les $\omega_{\mathcal{F}\tilde{\mathcal{F}}}$ ont été calculés par ailleurs [20]) et l'expression précédente se réduit à

$$a^{j\mathcal{F}\tilde{\mathcal{F}}}_{\bar{\nu}\mu\nu\mu} = \left(\frac{(2j+1)}{\sum\limits_{\mathcal{F}'}(2\mathcal{F}'+1)}\right)(2\mathcal{F}+1)(2\tilde{\mathcal{F}}+1)\begin{Bmatrix}\mathcal{F} & \tilde{\mathcal{F}} & \nu\\ j & j & I\end{Bmatrix}^2\delta_{\bar{\nu}\nu}. \tag{9c}$$

Le plus souvent on ne s'intéresse pas à la représentation de l'observable $O(t)$ à l'instant t, mais à la représentation de sa valeur moyenne $\bar{O}$ dans le temps sachant que le système α_j, j de temps de vie τ a la probabilité $\{\exp(-t/\tau)\}/\tau$ de se désintégrer à l'instant t. Les coefficients d'atténuation indépendants du temps qui doivent alors être introduits dans le développement (6) sont

$$\mathscr{A}^j_{\bar{\nu}\bar{\mu}\nu\mu}(K) = \int_0^\infty A^j_{\bar{\nu}\bar{\mu}\nu\mu}(K,t)\mathrm{e}^{-t/\tau}\frac{\mathrm{d}t}{\tau} = \sum_{k\tilde{k}} a^{jk\tilde{k}}_{\bar{\nu}\bar{\mu}\nu\mu}\left[\left(1+\frac{i\tau}{\hbar}(E_k-E_{\tilde{k}})\right)\right]^{-1}. \tag{11}$$

Les conventions adoptées pour définir les coefficients $A^j_{\bar{\nu}\bar{\mu}\nu\mu}(K,t)$ et $\mathscr{A}^j_{\bar{\nu}\bar{\mu}\nu\mu}(K)$ sont telles que

$$A^j_{00\nu\mu}(K,t) = \mathscr{A}^j_{00\nu\mu}(K) = \delta_{\nu 0}\delta_{\mu 0} \tag{12a}$$

et

$$\lim_{K\to 0} A^{j}_{\bar{\nu}\bar{\mu}\nu\mu}(K,t) = \lim_{K\to 0} \mathscr{A}^{j}_{\bar{\nu}\bar{\mu}\nu\mu}(K) = \delta_{\underset{\sim}{\bar{\nu}\nu}}\delta_{\bar{\mu}\mu}. \tag{12b}$$

Par ailleurs, lorsque le champ perturbateur, classique ou quantique, présente une symétrie axiale, on a la relation utile suivante, indépendante de la perturbation:

$$\sum_{\mu} A^{j}_{\bar{\nu}\mu\nu\mu}(K,t)\delta_{\mu 0} = \sum_{\mu} \mathscr{A}^{j}_{\bar{\nu}\mu\nu\mu}(K)\delta_{\mu 0} = \delta_{\bar{\nu}\nu}. \tag{13}$$

Lorsque la perturbation devient infinie, c'est-à-dire pour des coïncidences différées lorsque

$$\frac{E_k}{\hbar} \gg \Delta t^{-1}, \tag{14a}$$

où Δt est l'imprécision sur l'instant de mesure et pour des coïncidences intégrées sur le temps de vie lorsque

$$\frac{E_k}{\hbar} \gg \tau^{-1}, \tag{14b}$$

quel que soit k, les coefficients d'atténuation dépendants du temps (7) tendent vers une limite finie, indépendante du temps, identique à la limite des coefficients indépendants du temps (11). En effet, dans le premier cas, la mesure étant intégrée sur l'intervalle Δt, les termes du développement (7) tels que $(\Delta t/\hbar)(E_k - E_{\tilde{k}}) \to \pm\infty$ donnent une contribution nulle. Il en est de même dans le développement (11). Il ne reste que la contribution des termes dans lesquels $k = \tilde{k}$. Si l'hamiltonien K ne présente pas de symétrie particulière

$$\lim_{K\to\infty} A^{j}_{\bar{\nu}\bar{\mu}\nu\mu}(K,t) = \lim_{K\to\infty} \mathscr{A}^{j}_{\bar{\nu}\bar{\mu}\nu\mu}(K) = \sum_{\substack{\tilde{m}m \\ \tilde{m}'m'}} (-)^{2j-m-m'}(jj\tilde{m}'-m'|\nu\mu)$$
$$(j\tilde{m}-m|\bar{\nu}\bar{\mu}) \sum_{k,\tilde{k}} r^{j}(\tilde{m}'k\tilde{m};mkm')\delta_{k\tilde{k}}. \tag{15a}$$

Si la perturbation est décrite classiquement et présente une symétrie axiale

$$\lim_{K\to\infty} A^{j}_{\bar{\nu}\mu\nu\mu}(K,t) = \lim_{K\to\infty} \mathscr{A}^{j}_{\bar{\nu}\mu\nu\mu}(K) = \delta_{\mu 0}\delta_{\bar{\nu}\nu}. \tag{15b}$$

Si la perturbation est quantique et présente une symétrie axiale, par exemple dans le cas précédent (9b) d'un champ magnétique axial externe superposé au couplage magnétique dipolaire hyperfin entre le noyau et le cortège électronique

$$\lim_{K\to\infty} A^{j}_{\bar{\nu}\mu\nu\mu}(K,t) = \lim_{K\to\infty} \mathscr{A}^{j}_{\bar{\nu}\mu\nu\mu}(K)$$
$$= \left(\frac{(2j+1)}{\sum_{\mathscr{F}'}(2\mathscr{F}'+1)}\right) \sum_{\mathscr{F}} (2\mathscr{F}+1)^2 \begin{Bmatrix} \mathscr{F} & \mathscr{F} & \nu \\ j & j & I \end{Bmatrix}^2 \delta_{\mu 0}\delta_{\bar{\nu}\nu}. \tag{15c}$$

Dans ces deux derniers cas, nous voyons que les éléments de matrice de la représentation irréductible de l'opérateur perturbé O se réduisent aux éléments de matrice invariants par rotation autour d'un axe $[(\alpha_j j|O|\alpha_j j)]_0^\nu$ de l'opérateur non perturbé, à un facteur de proportionnalité géométrique près dans le cas quantique.

2.2. REPRÉSENTATION IRRÉDUCTIBLE DE PRODUITS D'OPÉRATEURS SUR DES ESPACES PERTURBÉS

La construction des coefficients géométriques associés aux processus corrélés les plus compliqués repose sur la formation des représentations irréductibles du produit de deux opérateurs dans l'espace produit direct, connaissant leurs représentations irréductibles dans leurs espaces propres. Pour fixer les idées, nous considérons l'opérateur O_1 agissant sur l'espace † $|\alpha_1 j_1\}$ et ayant pour éléments de matrice irréductibles $[(\alpha_1 j_1|O_1|\alpha_1 j_1)]_{\mu_1}^{\nu_1}$, l'opérateur O_2 agissant sur l'espace $\sum_{\alpha_2 j_2}|\alpha_2 j_2\}$ et ayant pour éléments de matrice irréductibles $[(\tilde{\alpha}_2 \tilde{j}_2|O_2|\alpha_2 j_2)]_{\mu_2}^{\nu_2}$. Leur produit $O_1 O_2$ agit sur l'espace produit direct $|\alpha j\} = \sum_{\alpha_2 j_2}|\alpha_1 j_1\}\otimes|\alpha_2 j_2\}$, et les éléments de matrice $[(\alpha_1 j_1 \tilde{\alpha}_2 \tilde{j}_2 j|O_1 O_2|\alpha_1 j_1 \alpha_2 j_2 j)]_\mu^\nu$ de sa représentation irréductible sont donnés par la formule de composition

$$[(\alpha_1 j_1 \tilde{\alpha}_2 \tilde{j}_2 j|O_1 O_2|\alpha_1 j_1 \alpha_2 j_2 j)]_\mu^\nu = \sum_{\nu_1\mu_1\nu_2\mu_2} \begin{bmatrix} j_1 & \tilde{j}_2 & j \\ j_1 & j_2 & j \\ \nu_1 & \nu_2 & \nu \\ \mu_1 & \mu_2 & \mu \end{bmatrix} \times [(\alpha_1 j_1|O_1|\alpha_1 j_1)]_{\mu_1}^{\nu_1} [(\tilde{\alpha}_2 \tilde{j}_2|O_2|\alpha_2 j_2)]_{\mu_2}^{\nu_2}, \quad (16)$$

où nous avons posé pour simplifier l'écriture

$$\begin{bmatrix} j_1 & \tilde{j}_2 & \tilde{j} \\ j_1 & j_2 & j \\ \nu_1 & \nu_2 & \nu \\ \mu_1 & \mu_2 & \mu \end{bmatrix} = [(2j+1)(2\tilde{j}+1)(2\nu_1+1)(2\nu_2+1)]^{\frac{1}{2}} \begin{pmatrix} j_1 & \tilde{j}_2 & \tilde{j} \\ j_1 & j_2 & \nu \\ \nu_1 & \nu_2 & \nu \end{pmatrix} (\nu_1 \nu_2 \mu_1 \mu_2|\nu\mu). \quad (17)$$

Dans l'expression (16) les éléments $[(\alpha_1 j_1 \tilde{\alpha}_2 \tilde{j}_2 j|O_1 O_2|\alpha_1 j_1 \alpha_2 j_2 j)]_\mu^\nu$, $[(\alpha_1 j_1|O_1|\alpha_1 j_1)]_{\mu_1}^{\nu_1}$ et $[(\tilde{\alpha}_2 \tilde{j}_2|O_2|\alpha_2 j_2)]_{\mu_2}^{\nu_2}$ sont tous trois exprimés dans le même système d'axes de coordonnées.

Nous supposons maintenant que les dégénérescences $(2j+1)$ et $(2j_1+1)$ des espaces $|\alpha j\}$ et $|\alpha_1 j_1\}$ sont respectivement levées par des perturbations représentées par les hamiltoniens K et K_1. Ainsi que nous le verrons dans les applications pratiques, nous n'aurons jamais à considérer la levée de la dégénérescence de l'espace $\sum_{\alpha_2 j_2}|\alpha_2 j_2\}$. Les perturbations K et K_1 ne sont pas nécessairement de même nature, et elles opèrent pendant des temps égaux à t_1 et $t-t_1$. La représentation irréductible perturbée dépendante du temps du produit

† Par $|\alpha_1 j_1\}$ nous désignons l'espace des états du système $\alpha_1 j_1$ dégénéré $(2j_1+1)$ fois.

de deux opérateurs O_1O_2 qui généralise (16) est

$$[(\alpha_1 j_1 \tilde{\alpha}_2 \tilde{j}_2 j|(O_1(K_1, t_1)O_2)(K, t)|\alpha_1 j_1 \alpha_2 j_2 j)]^{\nu}_{\mu} = \sum_{\substack{\nu_1\nu_2 \\ \mu_1\mu_2}} \sum_{\substack{\bar{\nu}_1\bar{\nu} \\ \bar{\mu}_1\bar{\mu}}} A^{j}_{\bar{\nu}\bar{\mu}\nu\mu}(K, t-t_1)$$

$$\times \begin{bmatrix} j_1 & \tilde{j}_2 & j \\ j_1 & j_2 & j \\ \tilde{\nu}_1 & \nu_2 & \tilde{\nu} \\ \bar{\mu}_1 & \mu_2 & \bar{\mu} \end{bmatrix} A^{j_1}_{\nu_1\mu_1\bar{\nu}_1\bar{\mu}_1}(K_1, t_1)[(\alpha_1 j_1|O_1|\alpha_1 j_1)]^{\nu_1}_{\mu_1}[(\tilde{\alpha}_2 \tilde{j}_2|O_2|\alpha_2 j_2)]^{\nu_2}_{\mu_2}. \quad (18)$$

Souvent on s'intéresse à la valeur moyenne des éléments de matrice (18) prise sur le temps, sachant que le système $\alpha_1 j_1$ et le système composé α, j ont des temps de vie respectivement égaux à τ_1 et τ, l'origine des temps pour le second système étant l'instant de désintégration t_1 du premier. Les facteurs dépendants du temps dans l'expression précédente doivent alors être simplement remplacés par

$$\int_0^{\infty} \mathrm{d}t_1 \int_{t_1}^{\infty} \mathrm{d}t A^{j}_{\bar{\nu}\bar{\mu}\nu\mu}(K, t-t_1) \frac{\mathrm{e}^{-\frac{t-t_1}{\tau}}}{\tau} A^{j_1}_{\nu_1\mu_1\bar{\nu}_1\bar{\mu}_1}(K_1, t_1) \frac{\mathrm{e}^{-\frac{t_1}{\tau_1}}}{\tau_1}$$

$$= \mathscr{A}^{j}_{\bar{\nu}\bar{\mu}\nu\mu}(K)\mathscr{A}^{j_1}_{\nu_1\mu_1\bar{\nu}_1\bar{\mu}_1}(K_1). \quad (19)$$

Les systèmes α_1, j_1 et α, j peuvent être stables, le système α_1, j_1 subissant une dépolarisation pendant un temps bien défini Δt correspondant par exemple à son temps de parcours dans un champ externe, avant détection par un analyseur. Les éléments de matrice (18) deviennent une fonction de Δt en remplaçant les facteurs

$$A^{j}_{\bar{\nu}\bar{\mu}\nu\mu}(K, t-t_1)A^{j}_{\nu_1\mu_1\bar{\nu}_1\bar{\mu}_1}(K_1 t_1) \text{ par } \delta_{\bar{\nu}\nu}\delta_{\bar{\mu}\mu}A^{j}_{\nu_1\mu_1\bar{\nu}_1\bar{\mu}_1}(K, \Delta t).$$

On vérifie immédiatement avec (12b) que l'expression (18) a pour limite (16) lorsque les perturbations tendent vers 0.

2.3. MATRICE DENSITÉ D'ÉTATS NUCLÉAIRES PRÉPARÉS PERTURBÉS

Comme application, nous généralisons aux cas de perturbations corrélées, c'est-à-dire de perturbations dans deux états nucléaires successifs, une expression de U. Fano et G. Racah pour la construction de la matrice densité d'états nucléaires préparés (voir ch. 19 réf. [1]). Nous conservons leur notation.

Nous cherchons l'expression dépendante du temps de la matrice densité $\rho_b(K_a, K_b, t_1, t_2)$ d'un état nucléaire $\alpha_b j_b$, soumis pendant le temps t_2-t_1 à une perturbation représentée par l'hamiltonien K_b, sachant que cet état $\alpha_b j_b$ a été formé à l'instant t_1 par la désintégration d'un état nucléaire α_a, j_a décrit en $t = 0$ par l'opérateur densité ρ_a et soumis pendant le temps t_1 à une perturbation K_a. Nous savons en outre que le produit de la désintégration $\alpha_a j_a \to \alpha_b j_b$ a été détecté en direction et en polarisation par un analyseur dont la réponse est représentée par l'opérateur D_r. L'indice r désigne l'ensemble des

variables quantiques caractérisant le rayonnement émis, c'est-à-dire l'espace sur lequel opère D_r. Soit T l'opérateur responsable de la transition $\alpha_a j_a \to \alpha_b j_b$. La matrice densité de l'état intermédiaire $\rho_b(K_a, K_b, t_1, t_2)$ après obtention de l'information D_r est donnée par

$$\rho(K_a, K_b, t_1, t_2) = \sum_{r,a} U^\dagger(K_b, t_2-t_1)(T^\dagger U^\dagger(K_a, t_1)\rho_a U(K_a, t_1)T)_{r,a} D_r U(K_b, t_2-t_1). \quad (20)$$

Soient $[(\alpha_a j_a|\rho_a|\alpha_a j_a)]^{\nu_a}_{\mu_a}$ les éléments de matrice irréductible de l'opérateur densité ρ_a décrivant l'état $\alpha_a j_a$ en l'absence de perturbation, c'est-à-dire à l'instant $t = 0$, et soient $[(\tilde{\alpha}_r \tilde{j}_r|D_r|\alpha_r j_r)]^{\nu_r}_{\mu_r}$ les éléments de matrice de D_r également dans une représentation irréductible. Soient $R(\Omega_a)$, $R(\Omega_r)$ et $R(\Omega_b)$ les rotations définies par les systèmes d'angles d'Euler Ω_a, Ω_r et Ω_b venant faire coincider le système de coordonnées de référence (attaché au laboratoire) avec les systèmes de coordonnées dans lesquels sont exprimés respectivement les éléments de matrice de ρ_a, D_r et ρ_b. On obtient en appliquant directement (18)

$$\begin{aligned}
&[(\alpha_b j_b|\rho_b(K_a, K_b, t_1, t_2)|\alpha_b j_b)]^{\nu_b}_{\mu_b} \\
&\quad = \sum_{\mu'_b} \mathscr{J}^{(\nu_b)}_{\mu'_b \mu_b}(\Omega_b) \sum_{\substack{\alpha_r \tilde{\alpha}_r \\ j_r \tilde{j}_r}} (\alpha_r j_r \alpha_b j_b j_a|T|\alpha_a j_a)(\alpha_a j_a|T^\dagger|\tilde{\alpha}_r \tilde{j}_r \alpha_b j_b j_a) \\
&\quad \times \sum_{\substack{\nu_a \nu_r \\ \mu'_a \mu'_r}} \sum_{\substack{\bar{\nu}_a \bar{\nu}_b \\ \bar{\mu}_a \bar{\mu}_b}} A^{j_b}_{\bar{\nu}_b \bar{\mu}_b \nu_b \mu'_b}(K_b, t_2-t_1) \begin{bmatrix} j_a & \tilde{j}_r & j_b \\ j_a & j_r & j_b \\ \bar{\nu}_a & \nu_r & \bar{\nu}_b \\ \bar{\mu}_a & \mu'_r & \bar{\mu}_b \end{bmatrix} \sum_{\mu_a \mu'_a} A^{j_a}_{\nu_a \mu'_a \bar{\nu}_a \bar{\mu}_a}(K_a, t_1) \\
&\quad \times \mathscr{J}^{(\nu_a)-1}_{\mu_a \mu'_a}(\Omega_a)[(\alpha_a j_a|\rho_a|\alpha_a j_a)]^{\nu_a}_{\mu_a} \sum_{\mu_r} \mathscr{J}^{(\nu_r)-1}_{\mu_r \mu'_r}(\Omega_r)[(\tilde{\alpha}_r \tilde{j}_r|D_r|\alpha_r j_r)]^{\nu_r}_{\mu_r}.
\end{aligned} \quad (21)$$

Si on a effectué sur l'état $\alpha_b j_b$ avant désintégration à l'instant t_3 une mesure G_b concernant sa polarisation à l'instant t_2 sa matrice densité devient

$$\begin{aligned}
[(\alpha_b j_b|\rho_b(K_a, K_b, t_1, t_2, t_3|\alpha_b j_b)]^{\nu_b}_{\mu_b} &= \sum_{\bar{\nu}'_b \bar{\mu}'_b} A^{j}_{\bar{\nu}'_b \bar{\mu}'_b \nu_b \mu_b}(K_b, t_3-t_2) \\
&\quad \times [(\alpha_b j_b|G_b|\alpha_b j_b)]^{\bar{\nu}'_b}_{\bar{\mu}'_b}[(\alpha_b j_b|\rho_b(K_a, K_b, t_1, t_2)|\alpha_b j_b)]^{\bar{\nu}'_b}_{\bar{\mu}'_b},
\end{aligned} \quad (22)$$

où les éléments de matrice de G_b sont exprimés dans le même système de coordonnées que $\rho_a(K_a, K_b, t_1, t_2)$. La matrice de ρ_a entrant dans l'expression (21) peut elle même être donnée par une expression analogue à (21) conformément au mode de préparation de l'état $\alpha_a j_a$. Par conséquent, cette formule de complication maximum sert de point de départ à tout calcul de processus multiple perturbé.

Si l'état α_a, j_a n'est pas polarisé, sa matrice densité se réduit à l'élément tel que $\nu_a = 0$. En utilisant la propriété (12a), l'expression (21) se simplifie,

l'opérateur densité de l'état α_b, j_b devenant uniquement une fonction de K_b comme il se doit:

$$[(\alpha_b j_b|\rho_b(K,t)|\alpha_b j_b)]^{\nu}_{\mu}$$

$$= \sum_{\mu'} \mathscr{J}^{(\nu)}_{\mu'\mu}(\Omega_b) \sum_{\substack{\alpha_r \tilde{\alpha}_r \\ j_r \tilde{j}_r}} (\alpha_r j_r \alpha_b j_b j_a|T|\alpha_a j_a)(\alpha_a j_a|T^{\dagger}|\tilde{\alpha}_r \tilde{j}_r \alpha_b j_b j_a) \tag{23}$$

$$\times \sum_{\bar{\nu}\bar{\mu}} A^{j}_{\bar{\nu}\bar{\mu}\nu\mu'}(K_b,t)(-)^{\tilde{j}_r+j_a+j_b+\bar{\nu}} \frac{2j_b+1}{2j_a+1} \begin{Bmatrix} j_b & j_b & \bar{\nu} \\ j_r & \tilde{j}_r & j_a \end{Bmatrix} \sum_{\mu_r} \mathscr{J}^{(\bar{\nu})-1}_{\bar{\mu}_r\bar{\mu}}(\Omega_r)[(\tilde{\alpha}_r \tilde{j}_r|D_r|\alpha_r j_r)]^{\bar{\nu}}_{\mu_r}.$$

Si la transition α_a, $j_a \to \alpha_b$, j_b est constituée par l'absorption d'un rayonnement et non de son émission, les éléments de matrice de l'opérateur densité perturbé de l'état α_b, j_b sont donnés par des expressions identiques à (21) et (23) en y remplaçant l'opérateur D_r associé à la réponse de l'analyseur par l'opérateur ρ_r décrivant le flux de particules incident.

Les éléments de matrice dans une représentation irréductible de D_r ou de ρ_r entrant dans les expressions générales (21) et (23) sont donnés dans la littérature pour divers cas d'intérêt, par exemple par W. T. Sharp [3]). Mais pour la construction explicite des expressions de corrélations multiples perturbées les plus générales, il faut également connaître l'expression des éléments de matrice de l'opérateur $D_r(K, \Delta t)$ lorsque le flux de particules émis traverse un champ dépolarisateur pendant un temps Δt avant d'être reçu par le système analyseur D_r (ce qui est le cas pour une expérience de type Stern-Gerlach), ainsi que pour l'opérateur $\rho_r(K, \Delta t)$ lorsque le flux incident initialement décrit par ρ_r est dépolarisé partiellement pendant un temps de parcours Δt avant son absorption par le système nucléaire. Dans ce dernier cas, par exemple, soient $[(\alpha_p j_p|\rho_p|\alpha_p j_p)]^{\nu_p}_{\mu_p}$ les éléments de matrice de l'opérateur ρ_p décrivant la polarisation des particules et $[(\tilde{j}_F|\rho_F|j_F)]_0^{\nu_F} = (-)^{j_F}\sqrt{(2j_F+1)(2\tilde{j}_F+1)}(j_F \tilde{j}_F 00|\nu_F 0)$ les éléments de matrice de l'opérateur ρ_F décrivant la décomposition harmonique de l'onde plane [3]). Les éléments de matrice densité de l'opérateur $\rho(K, \Delta t)$ décrivant le flux de particules partiellement dépolarisées est alors

$$[(\alpha_p \tilde{j}_r|\rho_r(K,\Delta t)|\alpha_p j_r)]^{\nu_r}_{\bar{\mu}_r} = \sum_{\substack{\nu_p \bar{\nu}_p \\ \mu_p \bar{\mu}_p}} \sum_{\nu_r j_r \tilde{j}_r} \delta_{\bar{\mu}_p \mu_r} \begin{bmatrix} j_p & \tilde{j}_F & \tilde{j}_r \\ j_p & j_F & j_r \\ \bar{\nu}_p & \nu_F & \nu_r \\ \bar{\mu}_p & 0 & \mu_r \end{bmatrix} A^{j_p}_{\nu_p \mu_p \bar{\nu}_p \bar{\mu}_p}(K, \Delta t)$$

$$\times [(\alpha_p j_p|\rho_p|\alpha_p j_p)]^{\nu_p}_{\mu_p}[(\tilde{j}_F|\rho_F|j_F)]^{\nu_F}_0. \tag{24}$$

Les éléments de matrice de l'expression précédente sont évidemment exprimés dans le même système de coordonnées. Si l'on considère l'émission d'un flux de particules polarisées, la représentation irréductible de l'opérateur $D_r(K, \Delta t)$

associé à la détection une fois que les particules ont été soumises pendant un temps Δt à un champ perturbateur est représentée par une expression analogue; les opérateurs densité ρ_p et ρ_F sont respectivement remplacés alors par les projecteurs D_p et D_F représentant la réponse du détecteur à la polarisation et à la direction du flux reçu.

3. Application au Calcul des Corrélations Angulaires Perturbées

3.1. CORRÉLATIONS DOUBLES

Nous considérons tout d'abord à titre d'exemple le cas simple des corrélations nucléaires doubles lorsque l'état intermédiaire excité du noyau est perturbé. Les expressions sont obtenues pour des mesures du type le plus général, c'est-à-dire à la fois de polarisation et de distribution angulaire. Elles redonnent, dans le cas de mesures angulaires seules, des résultats bien connus. (Cf. G. Goertzel [9]), K. Alder [10]), A. Abragam et R. V. Pound [11])).

Soit un système nucléaire subissant les transitions $\alpha_0, j_0 \to \alpha, j \to \alpha_f, j_f$ auxquelles sont associés respectivement les opérateurs T_1 et T_2. Pour fixer les idées, nous supposons que la transition $\alpha_0, j_0 \to \alpha, j$ est obtenue par absorption par le système initial, décrit par l'opérateur densité ρ_0, d'un rayonnement incident représenté par l'opérateur densité ρ_{r_1}. Avant de se désexciter, l'état intermédiaire α, j est soumis pendant le temps t à une perturbation représentée par l'hamiltonien K. Le rayonnement émis est détecté par un appareil d'observation auquel est associé l'opérateur D_{r_2}. Le résultat de la mesure de corrélation double perturbée est la valeur moyenne de D_{r_2} sur l'état final soit

$$\langle D_{r_2}(K,t)\rangle = \mathrm{Tr}\, T_2^\dagger [U^\dagger(K,t)(T_1^\dagger \rho_0 \rho_{r_1} T_1) U(K,t)] T_2 D_{r_2}. \tag{25}$$

Pour simplifier, nous supposons que l'état initial α_0, j_0 du système nucléaire n'est pas polarisé. Avec cette condition, les éléments de matrice $[(\alpha j|\rho|\alpha j)]_\mu^\nu$ dans une représentation irréductible de l'opérateur ρ décrivant l'état intermédiaire non perturbé α, j sont directement proportionnels aux éléments de matrice supposés connus $[(\tilde\beta_1 \tilde L_1|\rho_{r_1}|\beta_1 L_1)]_{\bar\mu}^{\bar\nu}$ dans une représentation irréductible de l'opérateur ρ_{r_1} décrivant l'analyse harmonique et la polarisation du flux incident. En utilisant (23) il vient pour les éléments de matrice irréductible de l'opérateur perturbé $\rho(K,t)$

$$\begin{aligned}
&[(\alpha j|\rho(K,t)|\alpha j)]_\mu^\nu \\
&= \sum_{\bar\nu\bar\mu} A^j_{\bar\nu\bar\mu\nu\mu}(K,t) \sum_{\substack{\beta_1\tilde\beta_1 \\ L_1\tilde L_1}} (\alpha_0 j_0 \beta_1 L_1 j|T_1^\dagger|\alpha j)(\alpha j|T_1|\alpha_0 j_0 \tilde\beta_1 \tilde L_1 j) \\
&\quad \times (-)^{j_0+j+\tilde L_1+\nu} \frac{2j+1}{2j_0+1} \begin{Bmatrix} j & j & \nu \\ L_1 & \tilde L_1 & j_0 \end{Bmatrix} \sum_{\bar\mu'} \mathscr{I}^{(\bar\nu)-1}_{\bar\mu'\bar\mu}(\Omega_1)[(\tilde\beta_1 \tilde L_1|\rho_{r_1}|\beta_1 L_1)]_{\bar\mu'}^{\bar\nu} \\
&= \sum_{\bar\nu\bar\mu} A^j_{\bar\nu\bar\mu\nu\mu}(K,t) \sum_{\substack{\beta_1\tilde\beta_1 \\ L_1\tilde L_1}} C_1(\alpha_0 j_0 \alpha_1 j_1 \beta_1 \tilde\beta_1 L_1 \tilde L_1 \nu) \sum_{\bar\mu'} \mathscr{I}^{(\bar\nu)-1}_{\bar\mu'\bar\mu}(\Omega_1)[(\tilde\beta_1 \tilde L_1|\rho_{r_1}|\beta_1 L_1)]_{\bar\mu'}^{\bar\nu}.
\end{aligned} \tag{26}$$

Les trois angles d'Euler Ω_1 définissent la rotation qui vient faire coïncider le système des coordonnées du laboratoire avec le système de coordonnées dans lequel sont exprimés les $[(\tilde{\beta}_1\tilde{L}_1|\rho_{r_1}|\beta_1 L_1)]_\mu^\nu$. Le coefficient $C_1(\alpha_0 j_0 \alpha_1 j_1 \beta_1 \tilde{\beta}_1 L_1 \tilde{L}_1 \nu)$ qui est le produit des éléments de matrice réduite par le coefficient de dépolarisation n'est posé que pour simplifier l'écriture. Toujours pour simplifier, nous supposons que la polarisation de l'état nucléaire final α_t, j_t n'est pas observée. Dans ce cas les éléments de matrice $[(\tilde{\beta}_2\tilde{L}_2|\rho_{r_2}|\beta_2 L_2)]_\mu^\nu$ de l'opérateur densité ρ_{r_2} décrivant le rayonnement émis sont directement proportionnels aux éléments de matrice précédents $[(\alpha j|\rho(K,t)|\alpha j)]_\mu^\nu$. La corrélation double perturbée, dépendante du temps, correspondant au résultat de mesure (25), peut être représentée par $W_K(\Omega_1, \Omega_2, \rho_{r_1}, D_{r_2}, t)$, où Ω_2 est le système d'angles d'Euler venant faire coïncider les axes du laboratoire avec le système de coordonnées dans lequel sont exprimés les éléments de matrice de l'opérateur D_{r_2} du détecteur, et où ρ_{r_1} et D_{r_2} indiquent que, outre les directions Ω_1 et Ω_2, on spécifie les polarisations des particules incidentes et des particules détectées. Explicitement on a

$$\begin{aligned} W_K(\Omega_1, \Omega_2, \rho_{r_1}, D_{r_2}, t) &= \sum_{\nu} \sum_{\mu\bar{\mu}\mu'\bar{\mu}'} \sum_{\substack{\beta_1\tilde{\beta}_1\beta_2\tilde{\beta}_2 \\ L_1\tilde{L}_1L_2\tilde{L}_2}} C_{\mathrm{I}}^*(\alpha_0 j_0 \alpha j \beta_1 \tilde{\beta}_1 L_1 \tilde{L}_1 \nu) C_{\mathrm{II}}^*(\alpha j \alpha_t j_t \beta_2 \tilde{\beta}_2 L_2 \tilde{L}_2 \nu) \\ &\times [(\beta_1 L_1|\rho_{r_1}|\tilde{\beta}_1\tilde{L}_1)]_{\bar{\mu}}^{\bar{\nu}*} \mathscr{J}_{\bar{\mu}'\bar{\mu}}^{(\bar{\nu})-1*}(\Omega_1) A_{\bar{\nu}\bar{\mu}\nu\mu}^{j*}(K,t) \mathscr{J}_{\mu'\mu}^{(\nu)-1}(\Omega_2) [(\beta_2 L_2|D_{r_2}|\tilde{\beta}_2\tilde{L}_2)]_{\mu'}^{\nu}. \end{aligned} \tag{27}$$

Comme précédemment on a réuni les éléments de matrice réduite et le facteur de dépolarisation de la transition finale dans le coefficient $C_{\mathrm{II}}(\alpha j \alpha_t j_t \beta_2 \tilde{\beta}_2 L_2 \tilde{L}_2 \nu)$ afin d'alléger l'écriture

$$\begin{aligned} C_{\mathrm{II}}(\alpha j \alpha_t j_t \beta_2 \tilde{\beta}_2 L_2 \tilde{L}_2 \nu) &= (\alpha j|T_2^\dagger|\beta_2 L_2 \alpha_t j_t j) \\ &\times (\tilde{\beta}_2 \tilde{L}_2 \alpha_t j_t j|T_2|\alpha j)(-)^{j+j_t+L_2+\nu}(2j+1) \begin{Bmatrix} j & j & \nu \\ \tilde{L}_2 & L_2 & j_t \end{Bmatrix}. \end{aligned} \tag{28}$$

Si la mesure est prise en moyenne sur le temps de vie τ de l'état intermédiaire, la corrélation perturbée correspondante indépendante du temps $\mathscr{W}_K(\Omega_1, \Omega_2, \rho_{r_1}, D_{r_2})$ s'obtient simplement en remplaçant les coefficients dépendants du temps $A_{\bar{\nu}\bar{\mu}\nu\mu}^j(K,t)$ par les coefficients indépendants du temps $\mathscr{A}_{\bar{\nu}\bar{\mu}\nu\mu}^j(K)$ de l'expression (11).

Lorsque l'hamiltonien perturbateur présente une symétrie axiale, il est normal de prendre un système de référence dont l'axe O_z coïncide avec cet axe de symétrie. Si le flux incident est parallèle à cet axe, celui-ci devient également axe de symétrie pour le système observé, de sorte qu'on a soit $\bar{\mu} = 0$, soit $\mu = 0$ respectivement dans (27). L'application des relations (13) montre immédiatement que la corrélation (27) se réduit à la corrélation non perturbée, conformément à un résultat bien connu.

Si l'information connue sur le flux incident est purement angulaire, les éléments de matrice de ρ_{r_1} dans une représentation irréductible se réduisent aux éléments $[(\tilde{\beta}_1\tilde{L}_1|\rho_{r_1}|\beta_1 L_1)]_0^{\bar{\nu}}$ $(\bar{\mu}'=0)$ dans un système de coordonnées dont l'axe O_z coïncide avec l'axe de symétrie du flux. De même, si le détecteur n'est pas sensible à la polarisation du rayonnement émis, les éléments de matrice de D_{r_2} se réduisent aux éléments $[(\tilde{\beta}_2\tilde{L}_2|D_{r_2}|\beta_2 L_2)]_0^{\nu}$ $(\mu'=0)$. Lorsque nous avons simultanément $\bar{\mu}'=\mu'=0$ nous retrouvons le résultat d'Abragam et Pound (éq. 12 et 15, réf. [11]))

$$W_K(\omega_1,\omega_2,t)=\sum_{\bar{\nu}\bar{\mu}\nu\mu}\sum_{\substack{\beta_1\tilde{\beta}_1\beta_2\tilde{\beta}_2\\ L_1\tilde{L}_1L_2\tilde{L}_2}}\frac{4\pi}{\sqrt{(2\bar{\nu}+1)(2\nu+1)}}C_{\mathrm{I}}^*(\alpha_0 j_0\alpha j\beta_1\tilde{\beta}_1L_1\tilde{L}_1\nu)$$
$$\times C_{\mathrm{II}}^*(\alpha j\alpha_t j_t\beta_2\tilde{\beta}_2L_2\tilde{L}_2\nu)[(\beta_1L_1|\rho_{r_1}|\tilde{\beta}_1\tilde{L}_1)]_0^{\bar{\nu}*}$$
$$\times[(\beta_2L_2|D_{r_2}|\tilde{\beta}_2\tilde{L}_2)]_0^{\nu}A^{j*}_{\bar{\nu}\bar{\mu}\nu\mu}(K,t)Y^{\bar{\mu}}_{\bar{\nu}}(\omega_1)Y^{\mu}_{\nu}(\omega_2). \quad (29)$$

Lorsque la perturbation tend vers zéro, le théorème d'addition des harmoniques sphériques, appliqué à l'expression précédente, redonne l'expression usuelle de la distribution angulaire (polarisations non observées)

$$W_0(\theta)=\sum_{\nu}\sum_{\substack{\beta_1\tilde{\beta}_1\beta_2\tilde{\beta}_2\\ L_1\tilde{L}_1L_2\tilde{L}_2}}C_{\mathrm{I}}(\alpha_0 j_0\alpha j\beta_1\tilde{\beta}_1L_1\tilde{L}_1\nu)^*C_{\mathrm{II}}(\alpha j\alpha_t j_t\beta_2\tilde{\beta}_2L_2\tilde{L}_2\nu)^*$$
$$\times[(\beta_1L_1|\rho_{r_1}|\tilde{\beta}_1\tilde{L}_1)]_0^{\nu*}[(\beta_2L_2|D_{r_2}|\tilde{\beta}_2\tilde{L}_2)]_0^{\nu}P_\nu(\cos\theta),$$

θ étant l'angle que font entre elles les directions ω_1 et ω_2.

Nous examinons maintenant ce que deviennent les expressions des corrélations doubles (27) et (29) à la limite d'une perturbation infinie.

Dans le cas général d'un hamiltonien perturbateur classique sans symétrie particulière, les coefficients $A^j_{\bar{\nu}\bar{\mu}\nu\mu}(K,t)$ et $\mathscr{A}^j_{\bar{\nu}\bar{\mu}\nu\mu}(K)$ tendent tous vers des limites finies non nulles, données par l'expression (15a) et dans lesquelles n'interviennent que des sommes sur des produits de coefficients de Clesh-Gordan multipliés par des produits d'intégrales de recouvrement. Donc, quel que soit le plan d'observation, il reste une anisotropie qui est une fonction de l'orientation relative du plan d'observation par rapport au système perturbateur.

Si le système perturbateur présente une symétrie axiale, cet axe étant choisi comme axe O_z du système de coordonnées de référence, la limite de la perturbation infinie prend une forme très simple. En effet, en appliquant la relation (15b), il vient pour l'expression (27), dans le cas classique

$$\lim_{K\to\infty}W_K(\Omega_1,\Omega_2,\rho_{r_1},D_{r_2},t)=W_\infty(\omega_1,\omega_2,\rho_{r_1},D_{r_2})$$
$$=\sum_{\nu\mu\mu'}\sum_{\substack{\beta_1\tilde{\beta}_1\beta_2\tilde{\beta}_2\\ L_1\tilde{L}_1L_2\tilde{L}_2}}\frac{4\pi}{(2\nu+1)}C_{\mathrm{I}}^*(\alpha_0 j_0\alpha j\beta_1\tilde{\beta}_1L_1\tilde{L}_1\nu)C_{\mathrm{II}}^*(\alpha j\alpha_t j_t\beta_2\tilde{\beta}_2L_2\tilde{L}_2\nu)$$
$$\times[(\beta_1L_1|\rho_{r_1}|\tilde{\beta}_1\tilde{L}_1)]^{\nu*}_{\mu}[(\beta_2L_2|D_{r_2}|\tilde{\beta}_2\tilde{L}_2)]^{\nu}_{\mu'}Y_{\nu}{}^{\mu}(\omega_1)Y_{\nu}{}^{\mu'}(\omega_2), \quad (30)$$

et pour l'expression (29), lorsque les polarisations des divers rayonnements

sont ignorées

$$\lim_{K\to\infty} W_K(\omega_1, \omega_2, t) = W_\infty(\theta_1, \theta_2)$$
$$= \sum_\nu \sum_{\substack{\beta_1\tilde\beta_1\beta_2\tilde\beta_2 \\ L_1\tilde L_1 L_2\tilde L_2}} C_{\mathrm{I}}^*(\alpha_0 j_0 \alpha j \beta_1\tilde\beta_1 L_1\tilde L_1 \nu) C_{\mathrm{II}}^*(\alpha j \alpha_t j_t \beta_2\tilde\beta_2 L_2\tilde L_2 \nu)$$
$$\times [(\beta_1 L_1|\rho_{r_1}|\tilde\beta_1\tilde L_1)]_0^{\nu *} [(\beta_2 L_2|D_{r_2}|\tilde\beta_2\tilde L_2)]_0^{\nu} P_\nu(\cos\theta_1) P_\nu(\cos\theta_2). \quad (31)$$

Si en plus du champ classique axial nous considérons le couplage hyperfin magnétique dipolaire du noyau avec les électrons du cortège, les valeurs limites pour $K = \infty$ de $W_K(\Omega_1, \Omega_2, \rho_{r_1}, D_{r_2}, t)$ et $W_K(\omega_1, \omega_2, t)$ sont données par des développements analogues à (30) et (31) dont les différents termes sont multipliés par les valeurs asymtotiques purement géométriques (15c) des coefficients d'atténuation.

Par conséquent, nous avons le résultat suivant: si l'on effectue une mesure de corrélation double, les polarisations des rayonnements initiaux et finaux étant spécifiées ou analysées, en présence d'une perturbation infinie axiale, expression (30), il reste encore une anisotropie quelle que soit l'orientation du plan d'observation par rapport à la direction de l'axe de symétrie du système perturbateur, la valeur de l'anisotropie dépendant de l'orientation du plan d'observation par rapport à cet axe. Par contre, si l'on effectue uniquement des mesures à symétrie axiale, expression (31), l'anisotropie est complètement effacée dans le plan perpendiculaire à l'axe de symétrie du système perturbateur; dans tout autre plan il reste une anisotropie déterminée uniquement par les angles que font respectivement la direction du flux incident et la direction d'observation avec la direction du champ perturbateur.

Nous considérons maintenant le cas important des systèmes perturbateurs orientés au hasard, par exemple les gradients de champs électriques dans une poudre microcristalline, les moments magnétiques dipolaires électroniques d'atomes libres etc. . . . Soit Ω les angles d'Euler amenant le système d'axes de coordonnées dans lequel sont exprimés les éléments de matrice de ρ_{r_1} en coïncidence avec le système d'axes de coordonnées du détecteur. On a $\Omega' = \Omega_1^{-1}\Omega_2$. La moyenne sur l'orientation au hasard de la perturbation peut être faite sur Ω_1 en gardant Ω' fixe; elle donne le facteur

$$\frac{1}{8\pi^2}\int \mathrm{d}\Omega_1 \mathscr{J}^{(\bar\nu)-1*}_{\bar\mu'\bar\mu}(\Omega_1) \sum_\varepsilon \mathscr{J}^{(\nu)-1}_{\varepsilon\mu}(\Omega_1) \mathscr{J}^{(\nu)-1}_{\mu'\varepsilon}(\Omega') = \frac{1}{2\nu+1}\delta_{\bar\nu\nu}\delta_{\bar\mu\mu}\mathscr{J}^{(\nu)-1}_{\mu'\bar\mu'}(\Omega').$$

En effectuant un changement simple d'indice, la corrélation perturbée qui ne dépend plus que de Ω' devient

$$\overline{W}_K(\Omega', \rho_{r_1}, D_{r_2}, t) = \sum_\nu B_\nu^j(K, t) \sum_{\substack{\beta_1\tilde\beta_1\beta_2\tilde\beta_2 \\ L_1\tilde L_1 L_2\tilde L_2}} C_{\mathrm{I}}^*(\alpha_0 j_0 \alpha j \beta_1\tilde\beta_1 L_1\tilde L_1 \nu)$$
$$\times C_{\mathrm{II}}^*(\alpha j \alpha_t j_t \beta_2\tilde\beta_2 L_2\tilde L_2 \nu) \sum_{\mu\mu'} [(\beta_1 L_1|\rho_{r_1}|\tilde\beta_1\tilde L_1)]_\mu^{\nu *} [(\beta_2 L_2|D_{r_2}|\tilde\beta_2\tilde L_2)]_{\mu'}^{\nu} \mathscr{J}^{(\nu)-1}_{\mu'\mu}(\Omega'). \quad (32)$$

Aux coefficients atténuateurs $B_\nu^j(K,t)$ près, elle est identique à la corrélation non perturbée. Les nouveaux coefficients $B_\nu^j(K,t)$ dépendants du temps ont pour définition

$$B_\nu^j(K,t) = \frac{1}{2\nu+1} \sum_{\mu=-\nu}^{+\nu} A^j_{\nu\mu\nu\mu}(K,t). \tag{33}$$

Les $B_\nu^j(K,t)$ sont similaires aux coefficients $G_\nu(t)$ d'Alder [10]) et d'Abragam et Pound [11]) et l'expression générale (32) se réduit à l'expression (17), ref. [11]), lorsqu'on ignore la polarisation des divers rayonnements, c'est-à-dire lorsque ρ_{r_1} et D_{r_2} présentent tous deux la symétrie axiale

$$\overline{W}_K(\theta,t) = \sum_\nu B_\nu^j(K,t) \sum_{\substack{\beta_1\tilde{\beta}_1\beta_2\tilde{\beta}_2 \\ L_1\tilde{L}_1L_2\tilde{L}_2}} C_1^*(\alpha_0 j_0 \alpha j \beta_1 \tilde{\beta}_1 L_1 \tilde{L}_1 \nu) C_{II}^*(\alpha j \alpha_1 j_1 \beta_2 \tilde{\beta}_2 L_2 \tilde{L}_2 \nu)$$
$$\times [(\beta_1 L_1 | \rho_{r_1} | \tilde{\beta}_1 \tilde{L}_1)]_0^{\nu *} [(\beta_2 L_2 | D_{r_2} | \tilde{\beta}_2 \tilde{L}_2)]_0^{\nu} P_\nu(\cos\theta), \tag{34}$$

où θ est l'angle amenant la direction du flux incident sur l'axe de symétrie du détecteur.

Si, au lieu de coincidences retardées, la mesure est effectuée en moyenne sur le temps de vie de l'état intermédiaire, la corrélation correspondante est obtenue en remplaçant dans (32) ou dans (34), suivant le cas, les coefficients $B_\nu^j(K,t)$ par les coefficients indépendants du temps $\mathscr{B}_\nu^j(K)$ donnés par l'expression (33) lorsqu'on y porte les $\mathscr{A}^j_{\nu\mu\nu\mu}(K)$ de la formule (11).

On a par ailleurs, quel que soit l'hamiltonien perturbateur K, avec les définitions adoptées,

$$B_0^j(K,t) = \mathscr{B}_0^j(K) = 1,$$

et à la limite d'une perturbation nulle

$$\lim_{K\to 0} B_\nu^j(K,t) = \lim_{K\to 0} \mathscr{B}_\nu^j(K) = 1, \quad (\nu \text{ quelconque}).$$

A la limite de la perturbation infinie, conditions (14a) et (14b) dans le cas des systèmes perturbateurs orientés au hasard, nous obtenons encore une anisotropie résiduelle, mais maintenant elle est évidemment indépendante de l'orientation du plan d'observation. Elle n'est fonction que de l'angle relatif des directions d'observation, c'est le „cœur dur" d'Abragam et Pound [11]), et Alder [10]). Explicitement la limite pour $K \to \infty$ des corrélations doubles (32) ou (34) s'obtient en portant dans ces expressions la valeur limite pour $K \to \infty$ des coefficients $B_\nu^j(K,t)$ ou $\mathscr{B}_\nu^j(K)$ suivant le cas, soit pour un système pertnrbateur sans symétrie particulière

$$\lim_{K\to\infty} B_\nu^j(K,t) = \lim_{K\to\infty} \mathscr{B}_\nu^j(K) = \frac{1}{2\nu+1} \sum_{\substack{\mu,k \\ m,m'}} (-)^{2j-m-m'} (jj\tilde{m}' - m' | \nu\mu)$$
$$\times (jj\tilde{m} - m | \nu\mu) r^j(\tilde{m}' k\tilde{m}; m' k m), \tag{35a}$$

pour un système perturbateur classique à symétrie axiale

$$\lim_{K\to\infty} B_\nu^j(K,t) = \lim_{K\to\infty} \mathscr{B}_\nu^j(K) = \frac{1}{2\nu+1} \tag{35b}$$

(l'atténuation devient indépendante du spin de l'état nucléaire intermédiaire α, j),

et pour un système perturbateur quantique en reprenant l'exemple du couplage magnétique hyperfin (2)

$$\lim_{K\to\infty} B_\nu^j(K,t) = \lim_{K\to\infty} \mathscr{B}_\nu^j(K,t) = \frac{1}{2\nu+1}\left(\frac{(2j+1)}{\sum_{\mathscr{F}'}(2\mathscr{F}'+1)}\right)\sum_{\mathscr{F}}(2\mathscr{F}+1)^2 \begin{Bmatrix} \mathscr{F} & \mathscr{F} & \nu \\ j & j & I \end{Bmatrix}^2. \tag{35c}$$

3.2. CORRÉLATIONS TRIPLES PERTURBÉES

A titre d'exemple, nous considérons le processus suivant:

Un système nucléaire, initialement dans l'état α_0, j_0 non polarisé, est excité vers un premier état intermédiaire α_1, j_1 par absorption d'un rayonnement dont l'analyse harmonique et la polarisation sont décrites par l'opérateur densité ρ_{r_1}. Soit T_1 l'opérateur responsable de la transition $\alpha_0, j_0 \to \alpha_1, j_1$. La dégénérescence d'ordre $(2j_1+1)$ de l'état intermédiaire α_1, j_1 est levée partiellement ou complètement par une perturbation représentée par l'hamiltonien K_1 agissant depuis l'instant $t=0$ de la transition $\alpha_0, j_0 \to \alpha_1, j_1$ jusqu'à l'instant $t=t_1$ de la transition $\alpha_1, j_1 \to \alpha_2, j_2$ induite par l'opérateur T_2. Cette dernière correspond à la désexcitation du niveau intermédiaire α_1, j_1 vers le second niveau excité intermédiaire α_2, j_2 par émission d'un rayonnement qui est observé par un détecteur dont la réponse est représentée par l'opérateur D_{r_3}. La dégénérescence du second état nucléaire intermédiaire α_2, j_2 est également levée par une perturbation représentée par l'hamiltonien K_2. Ce dernier agit depuis l'instant $t=t_1$ de la transition $\alpha_1, j_1 \to \alpha_2, j_2$ jusqu'à l'instant $t=t_2$ de la transition $\alpha_2, j_2 \to \alpha_f, j_f$ induite vers l'état nucléaire final α_f, j_f par l'opérateur T_3. La polarisation de l'état nucléaire final α_f, j_f n'est pas observée mais le rayonnement émis au cours de cette dernière transition est détecté par un système de mesure, dont la réponse est représentée par l'opérateur D_{r_3}. Le résultat de cette mesure de corrélation triple doublement perturbée est représenté par

$$\sum_{r_3} T_3^\dagger\{U_2^\dagger(K_2, t_2-t_1)[\sum_{r_2} T_2^\dagger U_1^\dagger(K_1,t_1)(\sum_{r_1} T_1^\dagger \rho_0\rho_{r_1} T_1)U_1(K_1,t_1)T_2 D_{r_2}] \times U_2(K_2,t_2-t_1)\}T_3 D_{r_3}. \tag{36}$$

Dans cette expression $U_1(K_1,t)$ et $U_2(K_2,t)$ sont les opérateurs d'évolution (5) associés aux hamiltoniens K_1 et K_2 respectivement. Soient $[(\tilde{\beta}_1\tilde{L}_1|\rho_{r_1}|\beta_1 L_1)]^{\nu_1}_{\mu_1}$ les éléments de matrice de ρ_{r_1} dans une représentation irréductible. Comme ρ_0 décrit un état non polarisé, les éléments de matrice dans une représentation irréductible de l'opérateur densité $T_1^\dagger\rho_0\rho_{r_1}T_1$, décrivant le système nucléaire

et le rayonnement en interaction à l'instant $t = 0$, sont directement proportionnels aux éléments $[(\tilde{\beta}_1\tilde{L}_1|\rho_{r_1}|\beta_1 L_1)]^{\nu_1}_{\mu_1}$ aux coefficients $C_I(\alpha_0 j_0 \alpha_1 j_1 \beta_1 \tilde{\beta}_1 L_1 \tilde{L}_1 \nu)$ près, définis par l'expression (26). L'opérateur densité $T_1^\dagger \rho_0 \rho_{r_1} T_1$ joue le rôle de l'opérateur ρ_a dans l'expression (21). Cette dernière nous permet de construire explicitement les éléments de matrice $[(\alpha_2 j_2|\rho_2(K_1, K_2, t_1, t_2)|\alpha_2 j_2)]^{\nu_2}_{\mu_2}$ de l'opérateur densité du second état nucléaire intermédiaire α_2, j_2 perturbé par K_2 pendant un temps $t_2 - t_1$, le premier état initialement décrit par $\sum_{r_1} T_1^\dagger \rho_0 \rho_{r_1} T_1$ ayant été perturbé pendant le temps t_1 par K_1 et une observation D_{r_2} ayant été effectuée sur le rayonnement émis. Enfin comme la polarisation de l'état nucléaire final α_f, j_f n'est pas observée, les éléments de matrice dans une représentation irréductible de l'opérateur densité $T_3^\dagger \rho_2(K_1, K_2, t_1, t_2) T_3$ décrivant le système nucléaire final et le rayonnement émis dans la transition $\alpha_2, j_2 \to \alpha_f, j_f$ sont directement proportionnels aux éléments $[(\alpha_2, j_2|\rho_2(K_1, K_2, t_1, t_2)\ |\alpha_2, j_2)]^{\nu_3}_{\mu_3}$ aux coefficients $C_{II}(\alpha_2 j_2 \alpha_f j_f \beta_3 \tilde{\beta}_3 L_3 \tilde{L}_3 \nu_3)$ près, définis précédemment dans l'expression (28).

On peut désigner le résultat de la mesure par $W_{K_1,K_2}(\Omega_1, \Omega_2, \Omega_3, \rho_{r_1}, D_{r_2}, D_{r_3}, t_1, t_2)$, où Ω_1, Ω_2 et Ω_3 sont les trois systèmes d'angles d'Euler qui viennent faire coïncider le système d'axes de coordonnées de référence (associé au laboratoire) avec respectivement les systèmes d'axes de coordonnées associés au flux incident et aux deux détecteurs, et où ρ_{r_1}, D_{r_2}, D_{r_3} indiquent que le flux incident est polarisé et que les deux détecteurs analysent les polarisations des rayonnements émis. Nous obtenons

$$W_{K_1,K_2}(\Omega_1, \Omega_2, \Omega_3; \rho_{r_1}, D_{r_2}, D_{r_3}; t_1, t_2) = \sum_{\substack{\nu_1\nu_2\nu_3 \\ \mu_1\mu_2\mu_3 \\ \mu'_1\mu'_2\mu'_3}} \sum_{\substack{\bar{\nu}_1\bar{\nu}_2 \\ \bar{\mu}_1\bar{\mu}_2}} \sum_{\beta_1\tilde{\beta}_1\beta_2\tilde{\beta}_2\beta_3\tilde{\beta}_3}$$

$$C_I^*(\alpha_0 j_0 \alpha_1 j_1 \beta_1 \tilde{\beta}_1 L_1 \tilde{L}_1 \nu_1) C_{II}(\alpha_2 j_2 \alpha_f j_f \beta_3 \tilde{\beta}_3 L_3 \tilde{L}_3 \nu_3) C_{III}^*(\alpha_1 j_1 \alpha_2 j_2 \beta_2 \tilde{\beta}_2 L_2 \tilde{L}_2 \nu_2)$$
$$\times [(\beta_1 L_1|\rho_{r_1}|\tilde{\beta}_1 \tilde{L}_1)]^{\nu_1 *}_{\mu_1} \mathscr{J}^{(\nu_1)-1*}_{\mu_1\mu'_1}(\Omega_1) A^{j_1 *}_{\nu_1\mu'_1\bar{\nu}_1\bar{\mu}_1}(K_1, t_1)$$
$$\times \begin{bmatrix} j_1 & \tilde{L}_2 & j_2 \\ j_1 & L_2 & j_2 \\ \bar{\nu}_1 & \nu_2 & \bar{\nu}_3 \\ \bar{\mu}_1 & \mu'_2 & \bar{\mu}_3 \end{bmatrix} \mathscr{J}^{(\nu_2)-1*}_{\mu_2\mu'_2}(\Omega_2) [(\beta_2 L_2|D_{r_2}|\tilde{\beta}_2 \tilde{L}_2)]^{\nu_2 *}_{\mu_2} A^{j_2 *}_{\nu_2\bar{\mu}_3\nu_3\mu'_3}(K_2, t_2 - t_1)$$
$$\times \mathscr{J}^{(\nu_3)-1}_{\mu_3\mu'_3}(\Omega_3) [(\beta_3 L_3|D_{r_3}|\tilde{\beta}_3 \tilde{L}_3)]^{\nu_3}_{\mu_3}, \tag{37}$$

où nous avons posé pour simplifier l'écriture

$$C_{III}(\alpha_1 j_1 \alpha_2 j_2 \beta_2 \tilde{\beta}_2 L_2 \tilde{L}_2 \nu_2) = (\beta_2 L_2 \alpha_2 j_2 j_1|T_2|\alpha_1 j_1)(\alpha_1 j_1|T_2^\dagger|\tilde{\beta}_2 \tilde{L}_2 \alpha_2 j_2 j_1)$$

Si l'un (ou plusieurs) des rayonnements est absorbé (ou émis) après interaction pendant un temps Δt avec un champ externe (expérience du type Stern-Gerlach), l'expression correspondante des éléments de matrice de ρ_r ou de D_r, doit être remplacée par les éléments de matrice de $\rho_r(K, \Delta t)$ ou de $D_r(K, \Delta t)$ correspondants donnés, précédemment (24). Si l'état nucléaire initial est polarisé, ou si l'on observe la polarisation de l'état nucléaire final ou d'un état

intermédiaire, les éléments de matrice de ρ_0 ou de ρ_{r_3} doivent être calculés avec une formule du type général (21) ou (22) avec ou sans perturbation suivant le cas.

La formule précédente (37) correspond à une mesure utilisant des coïncidences retardées. Si la mesure au contraire est effectuée en moyenne sur les temps de vie τ_1 et τ_2 des états nucléaires intermédiaires α_1, j_1 et α_2, j_2 (coïncidences intégrées sur le temps), la corrélation perturbée indépendante du temps est obtenue en remplaçant dans (37)

$$A^{j}_{\nu_1\mu'_1\bar{\nu}_1\bar{\mu}_1}(K_1, t_2)A^{j_2}_{\bar{\nu}_2\bar{\mu}_2\nu_2\mu'_2}(K_2, t_2-t_1) \quad \text{par} \quad \mathscr{A}^{j_1}_{\nu_1\mu'_1\bar{\nu}_1\bar{\mu}_1}(K_1)\mathscr{A}^{j_2}_{\bar{\nu}_2\bar{\mu}_2\nu_2\mu'_2}(K_2)$$

d'après le résultat de l'expression (19). Si l'on effectue des coincidences retardées uniquement sur le premier ou le second rayonnement émis, l'autre étant détecté quel que soit l'instant de son émission, on doit utiliser alors respectivement

$$A^{j_1}_{\nu_1\mu'_1\bar{\nu}_1\bar{\mu}_1}(K_1, t)\mathscr{A}^{j_2}_{\bar{\nu}_2\bar{\mu}_2\nu_2\mu'_2}(K_2) \quad \text{ou} \quad \mathscr{A}^{j_1}_{\nu_1\mu'_1\bar{\nu}_1\bar{\mu}_1}(K_1)A^{j_2}_{\bar{\nu}_2\bar{\mu}_2\nu_2\mu'_2}(K_2, t).$$

Les hamiltoniens K_1 et K_2 peuvent être différents, mais ils ont en général les mêmes caractères de symétrie. Considérons le cas où ils présentent tous deux la symétrie axiale autour d'une direction commune. On peut prendre cet axe comme axe O_z du système de coordonnées de référence. Nous obtenons immédiatement avec les relations (13) les résultats suivants: Si la direction du rayonnement incident coïncide avec l'axe de symétrie, la corrélation devient indépendante du couplage K_1 dans le premier état intermédiaire. De même, si le dernier rayonnement émis est détecté dans cette direction, la corrélation devient indépendante du couplage K_2 dans le second état intermédiaire. Par conséquent, si la direction du détecteur pour le dernier rayonnement émis, ainsi que la direction du rayonnement incident sont confondues avec l'axe de symétrie commun des hamiltoniens K_1 et K_2, la corrélation angulaire pour le rayonnement intermédiaire est identique à la corrélation en l'absence de perturbations. Par contre, il n'existe aucune propriété particulière si le rayonnement intermédiaire est détecté dans la direction de l'axe de symétrie.

Lorsque les polarisations des divers rayonnements ne sont pas spécifiées ou mesurées, l'expression (37) se simplifie ($\mu_1 = \mu_2 = \mu_3 = 0$)

$$\begin{aligned}
W_{K_1,K_2}(\omega_1, \omega_2, \omega_3; t_1, t_2) = {} & \sum_{\substack{\nu_1\ \nu_2\ \nu_3 \\ \mu'_1\mu'_2\mu'_3}} \sum_{\substack{\bar{\nu}_1\bar{\nu}_2 \\ \bar{\mu}_1\bar{\mu}_2}} \sum_{\substack{\beta_1\tilde{\beta}_1\beta_2\tilde{\beta}_2\beta_3\tilde{\beta}_3 \\ L_1\tilde{L}_1L_2\tilde{L}_2L_3\tilde{L}_3}} \frac{(4\pi)^{\frac{3}{2}}}{\sqrt{(2\nu_1+1)(2\nu_2+1)(2\nu_3+1)}} \\
& \times C_{\mathrm{I}}^{*}(\alpha_0 j_0 \alpha_1 j_1 \beta_1\tilde{\beta}_1 L_1\tilde{L}_1\nu_1) C_{\mathrm{II}}(\alpha_2 j_2 \alpha_t j_t \beta_3\tilde{\beta}_3 L_3\tilde{L}_3\nu_3) C^{*}_{\mathrm{III}}(\alpha_1 j_1 \alpha_2\beta_2\tilde{\beta}_2 L_2\tilde{L}_2\nu_2) \\
& \times A^{j_1*}_{\nu_1\mu'_1\bar{\nu}_1\bar{\mu}_1}(K_1, t_1) \begin{bmatrix} j_1 & \tilde{L}_2 & j_2 \\ j_1 & L_2 & j_2 \\ \bar{\nu}_1 & \nu_2 & \bar{\nu}_3 \\ \bar{\mu}_1 & \mu'_2 & \bar{\mu}_3 \end{bmatrix} A^{j_2*}_{\bar{\nu}_2\bar{\mu}_3\nu_3\mu'_3}(K_2, t_2-t_1) \\
& \times [(\beta_1 L_1|\rho_{r_1}|\tilde{\beta}_1\tilde{L}_1)]^{\nu_1*}_0 [(\beta_2 L_2|D_{r_2}|\tilde{\beta}_2\tilde{L}_2)]^{\nu_2*}_0 [(\beta_3 L_3|D_{r_3}|\tilde{\beta}_3\tilde{L}_3)]^{\nu_3}_0 \\
& \times Y^{-\mu'_1*}_{\nu_1}(\omega_1) Y^{-\mu'_2*}_{\nu_2}(\omega_2) Y^{-\mu'_3}_{\nu_3}(\omega_3).
\end{aligned} \tag{38}$$

Comme précédemment à la limite des perturbations infinies, $K_1 \to \infty$ et $K_2 \to \infty$ lorsque le champ perturbateur ne présente pas de symétrie particulière, les expressions du cas général (37) tendent vers des limites finies, obtenues en y portant les valeurs asymptotiques (15). L'anisotropie résiduelle est fonction des orientations des détecteurs et du flux incident, relativement aux systèmes perturbateurs, mais quelle que soit la géométrie de la mesure, cette anisotropie résiduelle n'est jamais nulle.

Si les hamiltoniens perturbateurs K_1 et K_2 sont tous deux à symétrie axiale et s'ils admettent le même axe de symétrie, cet axe étant pris comme axe O_z du système de référence, et si les états de polarisations des divers rayonnements sont spécifiés ou mesurés, l'expression générale (37) devient, à l'aide de (15b) dans le cas de perturbations décrites classiquement

$$\lim_{K_1, K_2 \to \infty} W_{K_1, K_2}(\Omega_1, \Omega_2, \Omega_3; \rho_{r_1}, D_{r_2}, D_{r_3}; t_1, t_2) = W_\infty(\omega_1, \omega_2, \omega_3; \rho_{r_1}, D_{r_2}, D_{r_3})$$

$$= \sum_{\substack{\nu_1\nu_2\nu_3 \\ \mu_1\mu_2\mu_3}} \sum_{\substack{\beta_1\tilde{\beta}_1\beta_2\tilde{\beta}_2\beta_3\tilde{\beta}_3 \\ L_1\tilde{L}_1L_2\tilde{L}_2L_3\tilde{L}_3}} \frac{(4\pi)^{\frac{3}{2}}}{\sqrt{(2\nu_1+1)(2\nu_2+1)(2\nu_3+1)}} C_{\mathrm{I}}^*(\alpha_0 j_0 \alpha_1 j_1 \beta_1 \tilde{\beta}_1 L_1 \tilde{L}_1 \nu_1)$$

$$\times C_{\mathrm{II}}(\alpha_2 j_2 \alpha_1 j_1 \beta_3 \tilde{\beta}_3 L_3 \tilde{L}_3 \nu_3) C_{\mathrm{III}}^*(\alpha_1 j_1 \alpha_2 j_2 \beta_2 \tilde{\beta}_2 L_2 \tilde{L}_2 \nu_2) \begin{bmatrix} j_1 & \tilde{L}_2 & j_2 \\ j_1 & L_2 & j_2 \\ \nu_1 & \nu_2 & \nu_3 \\ 0 & 0 & 0 \end{bmatrix}$$

$$\times [(\beta_1 L_1 | \rho_{r_1} | \tilde{\beta}_1 \tilde{L}_1)]_{\mu_1}^{\nu_1 *} [(\beta_2 L_2 | D_{r_2} | \tilde{\beta}_2 \tilde{L}_2)]_{\mu_2}^{\nu_2 *} [(\beta_3 L_3 | D_{r_3} | \tilde{\beta}_3 \tilde{L}_3)]_{\mu_3}^{\nu_3}$$

$$\times Y_{\nu_1}^{\mu_1}(\omega_1) Y_{\nu_2}^{\mu_2}(\omega_2) Y_{\nu_3}^{\mu_3 *}(\omega_3), \tag{39}$$

et si les polarisations des rayonnements sont ignorées

$$\lim_{K_1, K_2 \to \infty} W_{K_1, K_2}(\omega_1, \omega_2, \omega_3; t_1, t_2) = W_\infty(\theta_1 \theta_2 \theta_3)$$

$$= \sum_{\nu_1\nu_2\nu_3} \sum_{\substack{\beta_1\tilde{\beta}_1\beta_2\tilde{\beta}_2\beta_3\tilde{\beta}_3 \\ L_1\tilde{L}_1L_2\tilde{L}_2L_3\tilde{L}_3}} C_{\mathrm{I}}^*(\alpha_0 j_0 \alpha_1 j_1 \beta_1 \tilde{\beta}_1 L_1 \tilde{L}_1 \nu_1) C_{\mathrm{II}}(\alpha_2 j_2 \alpha_1 j_1 \beta_3 \tilde{\beta}_3 L_3 \tilde{L}_3 \nu_3)$$

$$\times C_{\mathrm{III}}^*(\alpha_1 j_1 \alpha_2 j_2 \beta_2 \tilde{\beta}_2 L_2 \tilde{L}_2 \nu_2) \begin{bmatrix} j_1 & \tilde{L}_2 & j_2 \\ j_1 & L_2 & j_2 \\ \nu_1 & \nu_2 & \nu_3 \\ 0 & 0 & 0 \end{bmatrix} [(\beta_1 L_1 | \rho_{r_1} | \tilde{\beta}_1 \tilde{L}_1)]_0^{\nu_1 *} [\beta_2 L_2 | D_{r_2} | \tilde{\beta}_2 \tilde{L}_2)]_0^{\nu_2 *}$$

$$\times [(\beta_3 L_3 | D_{r_3} | \tilde{\beta}_3 \tilde{L}_3)]_0^{\nu_3} P_{\nu_1}(\cos\theta_1) P_{\nu_2}(\cos\theta_2) P_{\nu_3}(\cos\theta_3). \tag{40}$$

S'il existe en plus du couplage avec le champ externe axial un couplage magnétique dipolaire hyperfin entre le noyau et le cortège électronique, la valeur limite de la corrélation triple perturbée, pour des perturbations infinies, est encore donnée par les développements (39) et (40), chacun de leur termes étant en outre multiplié par le facteur correspondant (15c).

Nous avons donc les résultats suivants pour la limite des perturbations infinies lorsqu'elles sont à symétrie axiale:

Si les polarisations sont observées, il reste une anisotropie, quelle que soit la géométrie de l'expérience, qui dépend entre autres de l'orientation du flux incident et des détecteurs relativement au système perturbateur. Si les polarisations ne sont pas observées, l'anisotropie résiduelle dépend uniquement des angles entre les directions des rayonnements absorbés ou émis et la direction de l'axe de symétrie commun des systèmes perturbateurs. Par conséquent, si le plan d'observation est perpendiculaire à la direction des champs perturbateurs, la corrélation triple devient isotrope. Nous retrouvons donc des résultats analogues à ceux des corrélations doubles.

Nous reprenons maintenant le cas de systèmes perturbateurs orientés au hasard. Comme précédemment, nous effectuons la moyenne de l'expression (37) sur les diverses orientations possibles des systèmes perturbateurs en exprimant les directions des rayonnements intermédiaire et final dans le système de coordonnées du rayonnement incident initial. Soient $\Omega'_2 = \Omega_1^{-1}\Omega_2$ et $\Omega'_3 = \Omega_1^{-1}\Omega_3$ les systèmes d'angles d'Euler amenant le système de coordonnées du rayonnement initial sur les systèmes de coordonnées du rayonnement intermédiaire et du rayonnement final respectivement. La moyenne effectuée sur la partie angulaire donne

$$\frac{1}{8\pi^2}\int d\Omega_1 \mathscr{T}^{(\nu_1)-1*}_{\mu_1\mu'_1}(\Omega_1)\sum_{\varepsilon}\mathscr{T}^{(\nu_2)-1*}_{\varepsilon\mu'_2}(\Omega_1)\mathscr{T}^{(\nu_2)-1*}_{\mu_2\varepsilon}(\Omega_2)\sum_{\eta}\mathscr{T}^{(\nu_2)-1}_{\eta\mu'_3}(\Omega_1)\mathscr{T}^{(\nu_3)-1}_{\mu_3\eta}(\Omega_3)$$

$$= \frac{1}{2\nu_3+1}(\nu_1\nu_2\mu'_1\mu'_2|\nu_3\mu'_3)\sum_{\varepsilon,\eta}(\nu_1\nu_2\mu_1\varepsilon|\nu_3\eta)\mathscr{T}^{(\nu_2)-1*}_{\mu_2\varepsilon}(\Omega'_2)\mathscr{T}^{(\nu_3)-1}_{\mu_3\eta}(\Omega'_3)$$

de sorte que la corrélation triple perturbée dans les deux états intermédiaires lorsque les systèmes perturbateurs sont orientés au hasard et que les polarisations des rayonnements sont spécifiées ou mesurées, est

$$\begin{aligned}
&\overline{W}_{K_1K_2}(\Omega'_2, \Omega'_3; \rho_{r_1}, D_{r_2}, D_{r_3}; t_1, t_2)\\
&= \sum_{\nu_1\nu_2\nu_3}\sum_{\substack{\beta_1\tilde{\beta}_1\beta_2\tilde{\beta}_2\beta_3\tilde{\beta}_3\\ L_1\tilde{L}_1L_2\tilde{L}_2L_3\tilde{L}_3}} C_I^*(\alpha_0 j_0\alpha_1 j_1\beta_1\tilde{\beta}_1 L_1\tilde{L}_1\nu_1)C_{II}(\alpha_2 j_2\alpha_t j_t\beta_3\tilde{\beta}_3 L_3\tilde{L}_3\nu_3)\\
&\times C^*_{III}(\alpha_1 j_1\alpha_2 j_2\beta_2\tilde{\beta}_2 L_2\tilde{L}_2\nu_2)\left(\frac{1}{2\nu_3+1}\sum_{\substack{\bar{\nu}_1\bar{\nu}_2\\ \bar{\mu}_1\bar{\mu}_2}}\sum_{\mu'_1\mu'_2\mu'_3} A^{j_1}_{\nu_1\mu'_1\bar{\nu}_1\bar{\mu}_1}(K_1, t_1)\begin{bmatrix} j_1 & \tilde{L}_2 & j_2\\ j_1 & L_2 & j_2\\ \bar{\nu}_1 & \nu_2 & \bar{\nu}_3\\ \bar{\mu}'_1 & \mu'_2 & \bar{\mu}'_3\end{bmatrix}\right.\\
&\left.\times A^{j_2}_{\bar{\nu}_2\bar{\mu}_2\nu_2\mu'_2}(K_2, t_2-t_1)(\nu_1\nu_2\mu'_1\mu'_2|\nu_3\mu'_3)\right)\sum_{\mu_1\mu_2\mu_3}[(\beta_1 L_1|\rho_{r_1}|\tilde{\beta}_1\tilde{L}_1)]^{\nu_1*}_{\mu_1}\\
&\times[(\beta_2 L_2|D_{r_2}|\tilde{\beta}_2\tilde{L}_2)]^{\nu_2*}_{\mu_2}[(\beta_3 L_3|D_{r_3}|\tilde{\beta}_3\tilde{L}_3)]^{\nu_3}_{\mu_3}\sum_{\varepsilon,\eta}(\nu_1\nu_2\mu_1\varepsilon|\nu_3\eta)\mathscr{T}^{(\nu_2)-1*}_{\mu_2\varepsilon}(\Omega'_2)\mathscr{T}^{(\nu_3)-1}_{\mu_3\eta}(\Omega'_3).
\end{aligned} \tag{41}$$

Dans l'expression précédente, il apparaît le facteur

$$b^{j_1 j_2}_{\nu_1\nu_2\nu_3 L_2\tilde{L}_2}(K_1, K_2, t_1, t_2) = \frac{1}{2\nu_3+1} \sum_{\mu'_1\mu'_2\mu'_3} \sum_{\bar{\mu}_1\bar{\mu}_3}$$

$$\times A^{j_1}_{\nu_1\mu'_1\bar{\nu}_1\bar{\mu}_1}(K_1, t_1) \begin{bmatrix} j_1 & \tilde{L}_2 & j_2 \\ j_1 & L_2 & j_2 \\ \nu_1 & \nu_2 & \nu_3 \\ \bar{\mu}_1 & \mu'_2 & \bar{\mu}_3 \end{bmatrix} A^{j_2}_{\bar{\nu}_3\bar{\mu}_2\nu_3\mu'_3}(K_2, t_2-t_1)(\nu_1\nu_2\mu'_1\mu'_2|\nu_3\mu'_3), \qquad (42)$$

qui, à la limite des perturbations nulles, devient à l'aide de la relation (12b)

$$\lim_{\substack{K_1\to 0 \\ K_2\to 0}} b^{j_1 j_2}_{\nu_1\nu_2\nu_3 L_2\tilde{L}_2}(K_1, K_2, t_1, t_2) = (2j_2+1)\sqrt{(2\nu_1+1)(2\nu_2+1)} \begin{Bmatrix} j_1 & \tilde{L}_2 & j_2 \\ j_1 & L_2 & j_2 \\ \nu_1 & \nu_2 & \nu_3 \end{Bmatrix},$$

de sorte qu'en posant

$$B^{j_1 j_2}_{\nu_1\nu_2\nu_3 L_2\tilde{L}_2}(K_1, K_2, t_1, t_2) = \frac{b^{j_1 j_2}_{\nu_1\nu_2\nu_3 L_2\tilde{L}_2}(K_1, K_2, t_1, t_2)}{(2j_2+1)\sqrt{(2\nu_1+1)(2\nu_2+1)} \begin{Bmatrix} j_1 & \tilde{L}_2 & j_2 \\ j_1 & L_2 & j_2 \\ \nu_1 & \nu_2 & \nu_3 \end{Bmatrix}} \qquad (43)$$

la corrélation triple doublement perturbeé (41) peut s'exprimer par un développement analogue à (32) en fonction de la corrélation triple non perturbée

$$\overline{W}_{K_1K_2}(\Omega'_2, \Omega'_3; \rho_{r_1}, D_{r_2}, D_{r_3}; t_1, t_2) = \sum_{\nu_1\nu_2\nu_3 L_2\tilde{L}_2}$$

$$\times B^{j_1 j_2}_{\nu_1\nu_2\nu_3 L_2\tilde{L}_2}(K_1, K_2, t_1, t_2) \sum_{\substack{\beta_1\tilde{\beta}_1\beta_2\tilde{\beta}_2\beta_3\tilde{\beta}_3 \\ L_1\tilde{L}_1 \quad L_3\tilde{L}_3}} C_1^*(\alpha_0 j_0 \alpha_1 j_1 \beta_1\tilde{\beta}_1 L_1\tilde{L}_1\nu_1)$$

$$\times C_{II}(\alpha_2 j_2 \alpha_1 j_1 \beta_3\tilde{\beta}_3 L_3\tilde{L}_3\nu_3) C^*_{III}(\alpha_1 j_1 \alpha_2 j_2 \beta_2\tilde{\beta}_2 L_2\tilde{L}_2\nu_2) \sum_{\mu_1\mu_2\mu_3} [(\beta_1 L_1|\rho_{r_1}|\tilde{\beta}_1\tilde{L}_1)]^{\nu_1 *}_{\mu_1}$$

$$\times [(\beta_2 L_2|D_{r_2}|\tilde{\beta}_2\tilde{L}_2)]^{\nu_2 *}_{\mu_2} [(\beta_3 L_3|D_{r_3}|\tilde{\beta}_3\tilde{L}_3)]^{\nu_3}_{\mu_3} \sum_{\varepsilon\eta} \begin{bmatrix} j_1 & \tilde{L}_2 & j_2 \\ j_1 & L_2 & j_2 \\ \nu_1 & \nu_2 & \nu_3 \\ \mu_1 & \varepsilon & \eta \end{bmatrix}$$

$$\times \mathscr{J}^{(\nu_2)-1*}_{\mu_2\varepsilon}(\Omega'_2) \mathscr{J}^{(\nu_3)-1}_{\mu_3\eta}(\Omega'_3). \qquad (44)$$

Les coefficients d'atténuation $B^{j_1 j_2}_{\nu_1\nu_2\nu_3 L_2\tilde{L}_2}(K_1, K_2, t_1, t_2)$ généralisent au cas des corrélations triples les coefficients $B^j_\nu(K, t)$ définis précédemment pour les corrélations doubles. Mais alors que ces derniers sont indépendants de la multipolarité des rayonnements, les $B^{j_1 j_2}_{\nu_1\nu_2\nu_3 L_2\tilde{L}_2}(K_1, K_2, t_1, t_2)$ sont des fonctions des multipolarités du rayonnement intermédiaire. Si les mesures sont faites en moyenne sur les temps de vie τ_1 et τ_2 des deux états nucléaires intermédiaires (coïncidences différées), l'expression de la corrélation triple est donnée par le même développement (44) lorsqu'on y porte les coefficients d'atténuation double

indépendants du temps $\mathscr{B}^{j_1 j_2}_{\nu_1\nu_2\nu_3 L_2\tilde{L}_2}(K_1, K_2)$ obtenus à l'aide des expressions (42) et (43) en remplaçant les $A^{j}_{\bar{\nu}\bar{\mu}\nu\mu}(K, t)$ par les $\mathscr{A}^{j}_{\bar{\nu}\bar{\mu}\nu\mu}(K)$.

Par définition, quels que soient ν_1, ν_2, ν_3, L_2, $\tilde{L}_2$,

$$\lim_{\substack{K_1\to 0\\ K_2\to 0}} B^{j_1 j_2}_{\nu_1\nu_2\nu_3 L_2\tilde{L}_2}(K_1, K_2, t_1, t_2) = \lim_{\substack{K_1\to 0\\ K_2\to 0}} \mathscr{B}^{j_1 j_2}_{\nu_1\nu_2\nu_3 L_2\tilde{L}_2}(K_1, K_2) = 1, \tag{45a}$$

et par ailleurs, quels que soient K_1, K_2, L_2 et $\tilde{L}_2$,

$$B^{j_1 j_2}_{000 L_2\tilde{L}_2}(K_1, K_2, t_1, t_2) = \mathscr{B}^{j_1 j_2}_{000 L_2\tilde{L}_2}(K_1, K_2) = 1. \tag{45b}$$

Si le flux de particules incident n'est pas polarisé ($\mu_1 = 0$) et si les polarisations des rayonnements émis ne sont pas détectées ($\mu_2 = \mu_3 = 0$) l'expression (44) se simplifie avec $\varepsilon = \eta = \mu$

$$\begin{aligned}\overline{W}_{K_1K_2}(\omega'_2, \omega'_3, t_1, t_2) = \sum_{\nu_1\nu_2\nu_3 L_2\tilde{L}_2} B^{j_1 j_2}_{\nu_1\nu_2\nu_3 L_2\tilde{L}_2}(K_1, K_2, t_1, t_2) \sum_{\substack{\beta_1\tilde{\beta}_1\beta_2\tilde{\beta}_2\beta_3\tilde{\beta}_3\\ L_1\tilde{L}_1 \quad L_3\tilde{L}_3}}\\ \times C_{\mathrm{I}}^{*}(\alpha_0 j_0 \alpha_1 j_1 \beta_1\tilde{\beta}_1 L_1\tilde{L}_1\nu_1) C_{\mathrm{II}}(\alpha_2 j_2 \alpha_t j_t \beta_3\tilde{\beta}_3 L_3\tilde{L}_3\nu_3) C^{*}_{\mathrm{III}}(\alpha_1 j_1 \alpha_2 j_2 \beta_2\tilde{\beta}_2 L_2\tilde{L}_2\nu_2)\\ \times [(\beta_1 L_1|\rho_{r_1}|\tilde{\beta}_1\tilde{L}_1)]^{\nu_1 *}_{0} [(\beta_2 L_2|D_{r_2}|\tilde{\beta}_2\tilde{L}_2)]^{\nu_2 *}_{0} [(\beta_3 L_3|D_{r_3}|\tilde{\beta}_3\tilde{L}_3)]^{\nu_3}_{0}\\ \times \sum_{\mu} \begin{bmatrix} j_1 & \tilde{L}_2 & j_2\\ j_1 & L_2 & j_2\\ \nu_1 & \nu_2 & \nu_3\\ 0 & \mu & \mu \end{bmatrix} \frac{4\pi}{\sqrt{(2\nu_2+1)(2\nu_3+1)}} Y^{-\mu *}_{\nu_2}(\omega'_2) Y^{-\mu}_{\nu_3}(\omega'_3).\end{aligned} \tag{47}$$

Nous considérons maintenant ce que deviennent les expressions (44) et (47) lorsque les perturbations K_1 et K_2 tendent toutes deux vers l'infini. Il suffit de considérer la limite de $B^{j_1 j_2}_{\nu_1\nu_2\nu_3 L_2\tilde{L}_2}(K_1, K_2, t_1, t_2)$ ou de $\mathscr{B}^{j_1 j_2}_{\nu_1\nu_2\nu_3 L_2\tilde{L}_2}(K_1, K_2)$ pour $K_1 \to \infty$ et $K_2 \to \infty$. Si les systèmes perturbateurs ne présentent pas de symétrie particulière, cette limite est relativement compliquée. Elle est obtenue en portant les valeurs limites (15a) de $A^{j}_{\bar{\nu}\bar{\mu}\nu\mu}(K, t)$ ou de $\mathscr{A}^{j}_{\bar{\nu}\bar{\mu}\nu\mu}(K)$ dans (42). Mais si les deux perturbations sont toutes deux à symétrie axiale et si elles admettent le même axe de symétrie on a le résultat simple dans le cas classique

$$\lim_{\substack{K_1\to\infty\\ K_2\to\infty}} B^{j_1 j_2}_{\nu_1\nu_2\nu_3 L_2\tilde{L}_2}(K_1, K_2, t_1, t_2) = \lim_{\substack{K_1\to\infty\\ K_2\to\infty}} \mathscr{B}^{j_1 j_2}_{\nu_1\nu_2\nu_3 L_2\tilde{L}_2}(K_1, K_2) = \frac{(\nu_1\nu_2 00|\nu_3 0)^2}{2\nu_3+1}, \tag{48}$$

qui généralise au cas des corrélations triples le „cœur dur" $1/(2\nu+1)$ des corrélations doubles. Remarquons encore dans cet exemple précis que si $K_1 \to \infty$ et $K_2 = 0$ ou si $K_1 = 0$ et $K_2 \to \infty$ on a respectivement pour limite

$$\begin{aligned}\lim_{\substack{K_1\to\infty\\ K_2=0}} B^{j_1 j_2}_{\nu_1\nu_2\nu_3 L_2\tilde{L}_2}(K_1, K_2, t_1, t_2) = \lim_{\substack{K_1\to\infty\\ K_2=0}} \mathscr{B}^{j_1 j_2}_{\nu_1\nu_2\nu_3 L_2\tilde{L}_2}(K_1, K_2) = \frac{1}{2\nu_2+1},\\ \lim_{\substack{K_1=0\\ K_2\to\infty}} B^{j_1 j_2}_{\nu_1\nu_2\nu_3 L_2\tilde{L}_2}(K_1, K_2, t_1, t_2) = \lim_{\substack{K_1=0\\ K_2\to\infty}} \mathscr{B}^{j_1 j_2}_{\nu_1\nu_2\nu_3 L_2\tilde{L}_2}(K_1, K_2) = \frac{1}{2\nu_3+1}.\end{aligned} \tag{49}$$

Les expressions (48) et (49) montrent que la limite du „cœur dur" dans une corrélation triple, lorsque les systèmes perturbateurs présentent la symétrie axiale et sont orientés au hasard, est indépendante des multipolarités du rayonnement intermédiaire. Dans tous les autres cas, à la limite infinie ou non, les facteurs d'atténuations (43) sont des fonctions des multipolarités du rayonnement intermédiaire.

L'auteur remercie MM. A. Abragam, R. Barloutaud, P. G. de Gennes et P. Lehman pour d'utiles suggestions et discussions concernant diverses applications du problème qui sont actuellement en cours de calcul au Centre d'Études Nucléaires de Saclay.

Bibliographie

1) U. Fano et G. Racah, Irreducible Tensorial Sets (Academic Press, New-York, 1959)
2) U. Fano, Revs. Mod. Physics **29** (1957) 74
3) W. T. Sharp, The quantum theory angular momentum, AECL report no 465 (1957)
4) L. C. Biedenharm et M. E. Rose, Revs. Mod. Phys. **25** (1953) 729;
H. Frauenfelder, in Beta and Gamma ray Spectroscopy, edited by K. Siegbahn (North-Holland Publishing Company, Amsterdam, 1955) Ch. XIX (I)
5) R. J. Blin-Stoyle et M. A. Grace, Handbuch d. Phys. **42** (1957)
6) S. Devons et L. J. B. Goldfarb, Handbuch d. Phys. **42** (1957)
7) A. Simon, Phys. Rev. **92** (1953) 1050
8) F. Coester et J. M. Jauch, Helv. Phys. Acta **26** (1953) 3
9) G. Goertzel, Phys. Rev. **70** (1946) 897
10) K. Alder, Helv. Phys. Acta **25** (1952) 235
11) A. Abragam et R. V. Pound, Phys. Rev. **92** (1953) 943
12) E. Heer et T. B. Novey, Solid State Physics **9** (1959) 199
13) A. Messiah, Mécanique Quantique (Dunod, Paris, 1959) Vol. II, App. C
14) A. R. Edmonds, Angular Momentum in Quantum Mechanics (Princeton University Press, Princeton, 1957)
15) H. Kopferman, Nuclear moments (Academic Press, New-York, 1958)

3.A

Nuclear Physics **20** (1960) 585—589; © *North-Holland Publishing Co., Amsterdam*

Not to be reproduced by photoprint or microfilm without written permission from the publisher

EXCEPTIONS TO GAMMA INTENSITY RULES IN NUCLEAR ROTATIONAL SPECTRA

K. HELMERS

Physikalisches Staatsinstitut, Hamburg

Received 28 June 1960

Abstract: The usual gamma intensity rules in nuclear rotational spectra can be proved only for transition operators that do not depend on collective angular momentum. It is shown that in the Bohr-Mottelson nuclear model only the magnetic dipole and magnetic octupole operators do not satisfy this condition and thus may give rise to unusual branching ratios.

Intensity rules for gamma transitions between nuclear rotational states have been derived some years ago by Alaga, Alder, Bohr and Mottelson (ref. [1]), eqs. (12), (13)). In order to see whether there are any exceptions to these rules, let us examine the essential steps in the proof.

We employ here the simplest version of the hydrodynamical model which partly disregards the non-distinguishability of the nucleons and the exclusion principle †. The "inner" nucleons are replaced by an irrotationally flowing liquid with only five degrees of freedom α_ν ($\nu = 0, \pm 1, \pm 2$) that describe in a well-known manner [4]) the surface shape of the liquid drop. For the "outer" nucleons, however, all the cartesian coordinates x are retained. The spin variables of these nucleons will in the following be omitted for the sake of simplicity; it is possible to include them without changing the main results.

We are considering the case of strong coupling [4]) between liquid drop and outer nucleons, hence it is convenient to use Bohr's coordinates θ_1, θ_2, θ_3 (Eulerian angles), β, γ in place of the α_ν. The transformation between the two sets is given by ††

$$\alpha_\nu = \sum_{\rho=-2}^{2} a_\rho(\beta, \gamma) \mathscr{D}^{(2)*}_{\rho\nu}(\theta_1, \theta_2, \theta_3), \tag{1}$$

with the auxiliary quantities

$$a_{\pm 2} \equiv 2^{-\frac{1}{2}} \beta \sin\gamma, \quad a_{\pm 1} \equiv 0, \quad a_0 \equiv \beta \cos\gamma. \tag{2}$$

† The alternative version, with collective coordinates being *symmetric* functions of the nucleon coordinates, is more correct in this respect, but it leads to difficulties in splitting angular momentum and multipole operators into a "collective" and a "particle" term.

†† For the quantities of angular momentum formalism Edmonds' notation [3]) is used; this implies, e.g., a reversed order of the lower indices of the representative matrices $\mathscr{D}^{(j)}_{m'm}$ as compared to refs. [1, 2, 4]).

The wave function in the initial and final states is then of the product type (eq. (118) of ref. [4]))

$$|IMK\tau\rangle = \left(\frac{2I+1}{8\pi^2}\right)^{\frac{1}{2}} \varphi_{\tau K}(\beta, \gamma, x')\mathscr{D}^{(I)}_{KM}(\theta_1, \theta_2, \theta_3), \tag{3}$$

x' representing the cartesian coordinates of the outer nucleons in the "primed" system of coordinates defined by the Eulerian angles θ. Strictly speaking, one would yet have to *symmetrize* this expression by adding another product of the same type [4]). We shall return to this point at the end of this paper.

The multipole tensor operator $\mathfrak{M}_{\lambda\mu}$ (λ is the multipole order, μ the number of the component) will in general depend on θ, β, γ, x as well as on $\partial/\partial\theta$, $\partial/\partial\beta$, $\partial/\partial\gamma$, $\partial/\partial x$. We disregard nucleon spin also in this place. Let us, first of all, introduce into $\mathfrak{M}_{\lambda\mu}$ the components R_k ($k = 1, 2, 3$) in the laboratory system of the liquid drop angular momentum $\mathbf{R}$ instead of the $\partial/\partial\theta_i$ ($i = 1, 2, 3$).

Now †

$$\mathbf{R} = \mathbf{I}-\mathbf{J}, \tag{4}$$

where $\mathbf{I}$ is the total angular momentum and $\mathbf{J}$ the angular momentum of the outer nucleons. The J_k ($k = 1, 2, 3$) are functions of x and $\partial/\partial x$, and therefore eq. (4) enables us to introduce I_k ($k = 1, 2, 3$) into $\mathfrak{M}_{\lambda\mu}$ in place of R_k. Finally, we pass to components I'_k, x', $\partial/\partial x'$ in the "primed" frame and obtain $\mathfrak{M}_{\lambda\mu}$ as a function of θ_i, β, γ, x' and of I'_k, $\partial/\partial\beta$, $\partial/\partial\gamma$, $\partial/\partial x'$. Except the θ, these are all scalar operators. From the tensor operator property of $\mathfrak{M}_{\lambda\mu}$ and the completeness of the symmetric top eigenfunctions $\mathscr{D}^{(I)}_{m'm}$ we get the following expansion:

$$\mathfrak{M}_{\lambda\mu}(\theta, \beta, \gamma, x', I'_k, \partial/\partial\beta, \partial/\partial\gamma, \partial/\partial x') = \sum_{\mu'=-\lambda}^{\lambda} \mathfrak{M}'_{\lambda\mu'}(\beta, \gamma, x', I'_k, \partial/\partial\beta, \partial/\partial\gamma, \partial/\partial x')\mathscr{D}^{(\lambda)}_{\mu'\mu}(\theta), \tag{5}$$

in terms of the coefficients $\mathfrak{M}'_{\lambda\mu'}$ which no longer depend explicitly on the angles θ. As usual, the I'_k are functions of θ_i and of $\partial/\partial\theta_i$, where the differentiation is carried out for fixed β, γ, x'.

The problem is now to calculate the matrix element of the operator (5) between states of type (3):

$$\langle I_1 M_1 K_1 \tau_1|\mathfrak{M}_{\lambda\mu}|I_f M_f K_f \tau_f\rangle = \frac{(2I_1+1)^{\frac{1}{2}}(2I_f+1)^{\frac{1}{2}}}{8\pi^2} \sum_{\mu'=-\lambda}^{\lambda} \int \mathrm{d}(\beta\gamma x')\mathrm{d}(\theta)\varphi^*_{\tau_1 K_1}(\beta, \gamma, x')\mathscr{D}^{(I_1)*}_{K_1 M_1}(\theta)\mathfrak{M}'_{\lambda\mu'}\mathscr{D}^{(\lambda)}_{\mu'\mu}(\theta)\varphi_{\tau_f K_f}(\beta, \gamma, x')\mathscr{D}^{(I_f)}_{K_f M_f}(\theta). \tag{6}$$

If in eq. (5) $\mathfrak{M}_{\lambda\mu}$ and thus $\mathfrak{M}'_{\lambda\mu'}$ are *independent of the* I'_k, we have the especially simple and important case discussed by Alaga *et al.* [1]). The integral in (6) may then be factorized into an integral over β, γ, x' which is independent of the

† Cf. footnote on the first page of this article.

spins I_1 and I_f, and an integral over θ. The latter contains the whole dependence on I_1 and I_f and equals

$$\frac{(2I_1+1)^{\frac{1}{2}}(2I_f+1)^{\frac{1}{2}}}{8\pi^2}\int \mathrm{d}(\theta)\,\mathscr{D}^{(I_1)*}_{K_1M_1}(\theta)\,\mathscr{D}^{(\lambda)}_{\mu'\mu}(\theta)\,\mathscr{D}^{(I_f)}_{K_fM_f}(\theta)$$

$$= (2I_1+1)^{\frac{1}{2}}(2I_f+1)^{\frac{1}{2}}(-)^{K_1-M_1}\begin{pmatrix} I_1 & \lambda & I_f \\ -K_1 & \mu' & K_f\end{pmatrix}\begin{pmatrix} I_1 & \lambda & I_f \\ -M_1 & \mu & M_f\end{pmatrix}. \qquad (7)$$

The right-hand side † of (7) immediately leads to the *intensity rule*, eq. (12) of ref. [1]).

The *multipole operators* in the hydrodynamical model have been given by Bohr and Mottelson (eqs. (VII.5), (VII.6) of ref. [2])). It is possible to transform them into the standard form corresponding to the right-hand side of (5). One then sees that the *electrical* transition operators belong to the class treated by Alaga *et al.*, i.e. they do not depend on the I'_k. The same is true of the contribution of the outer nucleons to the *magnetic* transition operators.

The *contribution of the liquid drop* to the *magnetic* multipole operator, however, does not fall under the scheme of ref. [1]) and wants therefore special consideration. It is, after ref. [2]),

$$\mathfrak{M}_{\lambda\mu} = \frac{2\mu_B g_R}{\lambda+1}\int \mathbf{R}(\mathbf{r})\cdot\nabla[r^\lambda Y_{\lambda\mu}(\vartheta,\varphi)]\mathrm{d}\mathbf{r}, \qquad (8)$$

μ_B being the nuclear Bohr magneton, g_R the hydrodynamical g-factor, $\mathbf{R}(\mathbf{r})$ the density of angular momentum in the liquid drop and $Y_{\lambda\mu}$ a spherical harmonic [3]). Using the formulas of ref. [4]), one can, as a first step, express $\mathfrak{M}_{\lambda\mu}$ in terms of the α_ν and their time derivatives $\dot{\alpha}_\nu$. A somewhat tedious calculation leads to the following result ††:

$$\mathfrak{M}_{\lambda\mu} = K_\lambda \sum_{\nu'\nu}\begin{pmatrix} 2 & 2 & \lambda \\ \nu' & \nu & \mu\end{pmatrix}\alpha_\nu\dot{\alpha}_{\nu'} = K_\lambda\sum_{\nu'\nu}\begin{pmatrix} 2 & 2 & \lambda \\ \nu' & \nu & \mu\end{pmatrix}\dot{\alpha}_{\nu'}\alpha_\nu \qquad (9)$$

up to first order in α_ν, with a proportionality constant †††

$$K_\lambda = -5i\left(\frac{30}{\pi}\right)^{\frac{1}{2}}\frac{\lambda^{\frac{1}{2}}(2\lambda-1)^{\frac{1}{2}}(2\lambda+1)}{\lambda+1}\begin{Bmatrix} 2 & 2 & 1 \\ \lambda & \lambda-1 & 2\end{Bmatrix}\begin{pmatrix} 2 & 2 & \lambda-1 \\ 0 & 0 & 0\end{pmatrix}B\mu_B g_R r_0^{\lambda-1}, \qquad (10)$$

where

$$B \equiv \tfrac{1}{2}\rho_0 r_0^5, \qquad (11)$$

ρ_0 being the mass density, r_0 the equilibrium radius of the liquid drop. According to these equations, $\mathfrak{M}_{\lambda\mu}$ *vanishes* for $\lambda > 4$, as the 3-j symbol in (9) is

† Two 3-j symbols here occur [3]).

†† In deriving eq. (9) it was assumed as usual that in the classical Lagrangian $L(\alpha, \dot{\alpha}, x, \dot{x})$ of the nucleus the $\dot{\alpha}$ occur only in the kinetic energy $\frac{1}{2}B\,\Sigma\dot{\alpha}_\mu^*\,\dot{\alpha}_\mu$ of the liquid drop. This assumption is also used in the proof of (15).

††† The curly brackets here denote a 6-j symbol [3]).

then zero; also $\mathfrak{M}_{\lambda\mu} = 0$ for *even* λ, as then the $3-j$ symbol (in 10) vanishes. *Therefore, in the framework of the present nuclear model the intensity rules of ref.* [1]) *can be violated for* M1 *and* M3 *transitions only.*

In order to obtain the standard form (5) for $\mathfrak{M}_{\lambda\mu}$ form (9) we have to pass from the α_ν to the $\theta_1, \theta_2, \theta_3, \beta, \gamma$. This step again involves a lengthy but elementary calculation which we shall not reproduce here. At various stages additive terms can be split off from $\mathfrak{M}_{\lambda\mu}$ that do not depend on the I'_k and the matrix elements of which can therefore be calculated by the procedure of ref. [1]) outlined above. As those terms are of no interest in the present context, we treat here explicitly only *the non-trivial rest term* $\mathfrak{N}_{\lambda\mu}$ of $\mathfrak{M}_{\lambda\mu}$. It is found to have the following standard form of type (5):

$$\mathfrak{N}_{\lambda\mu} = \sum_{\mu'=-\lambda}^{\lambda} \mathfrak{N}'_{\lambda\mu'} \mathscr{D}^{(\lambda)}_{\mu'\mu}(\theta), \tag{12}$$

where, for $\lambda = 1$,

$$\mathfrak{N}'_{1\mu'} = \left(\frac{3}{4\pi}\right)^{\frac{1}{2}} \mu_B g_R I'_{\mu'} \quad (\mu' = 0, \pm 1), \tag{13}$$

i.e.

$$\mathfrak{N}_{1\mu} = \left(\frac{3}{4\pi}\right)^{\frac{1}{2}} \mu_B g_R I_\mu \quad (\mu = 0, \pm 1), \tag{14}$$

and, for $\lambda = 3$,

$$\begin{aligned}
\mathfrak{N}'_{3,\pm 3} &= 2^{-\frac{1}{2}} N \left(\mp \frac{I'_{(1)}}{\varepsilon_1} + i \frac{I'_{(2)}}{\varepsilon_2} \right) \varepsilon_3, \\
\mathfrak{N}'_{3,\pm 2} &= 3^{-\frac{1}{2}} N \frac{I'_{(3)}}{\varepsilon_3} (\varepsilon_1 - \varepsilon_2), \\
\mathfrak{N}'_{3,\pm 1} &= 30^{-\frac{1}{2}} N \left[\pm \frac{I'_{(1)}}{\varepsilon_1} (4\varepsilon_2 - \varepsilon_3) + i \frac{I'_{(2)}}{\varepsilon_2} (4\varepsilon_1 - \varepsilon_3) \right], \\
\mathfrak{N}'_{3,0} &= -(\tfrac{2}{5})^{+\frac{1}{2}} N I'_{(3)},
\end{aligned} \tag{15}$$

with

$$N = \tfrac{3}{8} \left(\frac{5}{7\pi}\right)^{\frac{1}{2}} \mu_B g_R r_0^2, \quad \varepsilon_k = \beta \sin(\gamma - \tfrac{2}{3}\pi k) \quad (k = 1, 2, 3). \tag{16}$$

In eqs. (13)—(15), I'_0, $I'_{\pm 1}$ are *spherical*, and $I'_{(1)}$, $I'_{(2)}$, $I'_{(3)}$ the *cartesian* components of **I** in the "primed" coordinate system. I_0, $I_{\pm 1}$ are the spherical components of **I** in the *laboratory* system.

By (13) and (15), we have proved the existence of angular momentum dependent transition operators.

Let us briefly discuss the calculation of their *matrix elements*. For that purpose we have in eq. (6) to replace $\mathfrak{M}$ by $\mathfrak{N}$. Substitution of (13) or (15),

respectively, into the right-hand side of (6) shows that the integral factorizes for $\lambda = 1$, and is, for $\lambda = 3$, either factorizable or a sum of two factorizable integrals. The dependence on I_1 and I_f is again contained in the θ integral which has the following form, different from (7):

$$\frac{(2I_1+1)^{\frac{1}{2}}(2I_f+1)^{\frac{1}{2}}}{8\pi^2}\int \mathrm{d}(\theta)\mathscr{D}^{(I_1)*}_{K_1M_1}(\theta)I'_\rho\mathscr{D}^{(\lambda)}_{\mu'\mu}(\theta)\mathscr{D}^{(I_f)}_{K_fM_f}(\theta) = (-)^{-I_1+M_1} \tag{17}$$

$$\times(2I_f+1)^{\frac{1}{2}}(2I_1+1)(I_1+1)^{\frac{1}{2}}I_1^{\frac{1}{2}}\begin{pmatrix} I_1 & 1 & I_1 \\ -K_1 & -\rho & K_1+\rho\end{pmatrix}\begin{pmatrix} I_1 & \lambda & I_f \\ -K_1-\rho & \mu' & K_f\end{pmatrix}\begin{pmatrix} I_1 & \lambda & I_f \\ -M_1 & \mu & M_f\end{pmatrix}.$$

In the case $\lambda = 3$ (M3 transitions) no manageable formula for the matrix element (6) results because the expressions (15) are so complicated, and we content ourselves with stating that the gamma intensities will, in general, not satisfy the simple rules of ref. [1]).

For M1 transitions ($\lambda = 1$), however, the matrix element of $\mathfrak{R}_{1\mu}$ may be calculated directly from (14), with the result

$$\langle I_1M_1K_1\tau_1|\mathfrak{R}_{1\mu}|I_fM_fK_f\tau_f\rangle = \left(\frac{3}{4\pi}\right)^{\frac{1}{2}}\mu_B g_R\int \mathrm{d}(\beta\gamma x')\varphi^*_{\tau_1K_1}\varphi_{\tau_fK_f}$$

$$\times(-)^{I_1-M_1}[(2I_1+1)(I_1+1)I_1]^{\frac{1}{2}}\delta_{K_1K_f}\delta_{I_1I_f}\begin{pmatrix} I_1 & 1 & I_f \\ -M_1 & \mu & M_f\end{pmatrix}. \tag{18}$$

One immediately sees that the characteristic first 3-j symbol of eq. (7) is here absent and that therefore the usual intensity rule [1]) has to be modified. Because of the selection rule $\Delta K = 0$, $\Delta I = 0$ contained in (18), this modification will be necessary and experimentally detectable only for pairs of transitions between *different* bands ($\tau_1 \neq \tau_f$) of *equal* K. But then the factor $\int \mathrm{d}(\beta\gamma x')\varphi^*_{\tau_1K}\varphi_{\tau_fK}$ in (18) is small, which will also make the anomalous transition probability small.

The matrix elements of the transition operators between properly *symmetrized* [4]) wave functions are, as usual, *sums* of matrix elements of the type (6) between unsymmetrized wave functions and will thus be modified, too, if the latter are modified through dependence of the transition operator on the I'_k.

The author wishes to thank Prof. A. Bohr for correspondence and Prof. G. Süssmann for valuable criticism.

References

1) G. Alaga, K. Alder, A. Bohr and B. R. Mottelson, Mat. Fys. Medd. Dan. Vid. Selsk. **29**, No. 9 (1955)
2) A. Bohr and B. R. Mottelson, Mat. Fys. Medd. Dan. Vid. Selsk. **27**, No. 16 (1953)
3) A. R. Edmonds, Angular momentum in quantum mechanics (Princeton University Press, 1957)
4) A. Bohr, Mat. Fys. Medd. Dan. Vid. Selsk. **26**, No. 14 (1952)

2.A.2

Nuclear Physics **20** (1960) 590—600; © *North-Holland Publishing Co., Amsterdam*

Not to be reproduced by photoprint or microfilm without written permission from the publisher

CLASSICAL TREATMENT OF NUCLEAR REACTIONS INDUCED BY FAST NUCLEONS

KEN KIKUCHI †

School of Physics, University of Minnesota, Minneapolis, Minnesota ††

Received 26 June 1960

Abstract: The direct process in nuclear reactions is studied using a simplified classical model. The process of the usual inelastic scattering type is found to give a contribution of 10 to 25 % to the total cross section. The more complicated processes, in which two or more collisions take place, seem to contribute 10 % to the absorption cross section.

1. Introduction

A nuclear reaction induced by particles of intermediate energies is considered to proceed through the direct and the compound processes. The optical model had made it possible to calculate the total absorption cross section, but it remains to calculate the cross section for the direct process. As far as the low-lying excited states are concerned, it seems to be adequate to make a quantum mechanical calculation for the direct process. However, the features of the direct process are extremely complicated in the intermediate energy range, and are difficult to analyze because of our scanty knowledge about wave functions of a number of residual states. A similar difficulty lies in calculating higher terms in the perturbation expansion, since a large number of intermediate states take part in the process. In order to avoid these complications in the quantum mechanical calculation, we adopt in this paper a simplified classical model for the collision between a fast nucleon and a complex nucleus. The incident nucleon with moderately high energy is assumed to travel in a straight line following its initial direction upon entering the target nucleus. The nucleons in the target nucleus are considered to be free Fermi particles moving in the nuclear potential. The interaction between the impinging nucleon and the target nucleus is considered to take place through two-body collisions between the incident particle and those in the target nucleus. In this picture the incident particle is described by the kinetic energy and the impact parameter; the nucleus acts as an absorbing medium to the incident beam and is characterized by the absorption coefficient for the incident nucleon and by the spatial distribution of the absorption coefficient. Here the energies of the incident particle and of

† On leave of absence from the Institute for Nuclear Study, University of Tokyo, Japan.

†† Work supported in part by the U. S. Atomic Energy Commission.

target nucleons are measured from the bottom of the nuclear potential. Now we may outline the procedure of the calculation:

(1) First of all, we calculate the total absorption cross section σ_{abs}, in which the absorption coefficient and its distribution are involved as adjustable parameters. The comparison between the total absorption cross section thus calculated and the experimental data allows us to determine both the absorption coefficient and its adequate distribution.

(2) We next consider a simplified one-dimensional problem and calculate how many two-body collisions take place when the incident particle travels in the absorbing medium whose distribution is given. Then we know the probability $f_n(x)$ that the incident nucleon suffers n collisions when it has passed through the thickness x of the nuclear medium.

(3) Then, we apply the probability $f_n(x)$ to the three dimensional nucleus and calculate the probability F_n that the incident nucleon undergoes n collisions when it has passed through the actual nuclear medium. The probability F_n takes into account the absorption coefficient and the parameters involved in the distribution formula of the absorption coefficient.

(4) Now we can set a more realistic question: "How many collisions take place up to the point that the incident particle with energy E_0 has passed through the actual nucleus, or has been trapped by the nuclear potential?" To give an answer to this question, we calculate the probability P_n that the incident particle after passing through the target nucleus suffers n collisions and still has enough energy to escape from the nuclear potential. This quantity P_n is given as the product of two quantities in the form

$$P_n = F_n G_n(E_0), \tag{1}$$

where F_n is defined in (3) and $G_n(E_0)$ is the probability that the incident nucleon has enough energy to escape from the nuclear potential after suffering n collisions, and depends on the magnitudes of the incident energy E_0 and of the depth of the nuclear potential. Roughly speaking, the quantity P_n corresponds, within certain uncertainties, to the contribution from the n-th order term in the perturbation expansion.

(5) Finally from the probability P_n and the total absorption cross section σ_{abs} we are able to calculate the cross section σ_d for the direct process. Let us define the n collisions cross section $\sigma_d^{(n)}$ by $\sigma_d^{(n)} = \sigma_{abs} P_n$. Then one can see that $\sigma_d^{(1)}$ expresses the cross section of the direct process in usual sense, in which a single nucleon is excited in the residual nucleus. The general $\sigma_d^{(n)}$ ($n \geqq 2$) is a cross section for a more complicated process in which two or three nucleons are excited in the residual nucleus. The cross section σ_d for the direct process is given by the sum of all $\sigma_d^{(n)}$'s and the cross section σ_c for the formation of the compound nucleus can easily be obtained by omitting the compound elastic cross section.

2. Collision Probability f_n in a One-Dimensional Model

For simplicity, we assume that the absorption coefficient K is constant in all regions of the absorbing medium. Let x_i be the position where the i-th collision takes place; then the probability $f_n(x)$ that the incident particle suffers n collisions after having passed through the thickness x of the medium is given by

$$f_n(x) = \int_0^x K\,\mathrm{d}x_n \int_0^{x_n} K\,\mathrm{d}x_{n-1} \cdots \int_0^{x_2} K\,\mathrm{d}x_1 \mathrm{e}^{-K\sum_{i=0}^{n}(x_{i+1}-x_i)} \tag{2}$$

with $x = x_{n+1} \geqq x_n \geqq x_{n-1} \geqq \ldots \geqq x_1 \geqq x_0 = 0$. Here the small quantities $\mathrm{d}x_i$ in the exponent are neglected. A straightforward calculation leads to

$$f_n(x) = \frac{1}{n!}(Kx)^n \mathrm{e}^{-x}. \tag{3}$$

Let us mention several characteristics of this function. Obviously $f_0(x)$ is the usual formula for the penetrating probability, i.e. the probability that no collisions take place. Also $f_n(x)$ satisfies the equation

$$\sum_{n=0}^{\infty} f_n(x) = 1, \tag{4}$$

as should be expected from the property of the probability. $f_n(x)$, as a function of distance x, has its maximum at $x = nK^{-1}$, as would be expected from the physical point of view since the reciprocal of K is the mean free path.

3. Collision Probability F_n in the Spherical Nucleus

In this section we calculate the probability F_n that the incident particle makes n collisions when it passes through the nuclear medium of given distribution of absorption. Before calculating the probability F_n, it is necessary to assume an adequate distribution of the absorption coefficient. Since the actual distribution of the absorption coefficient is so complicated as to make further

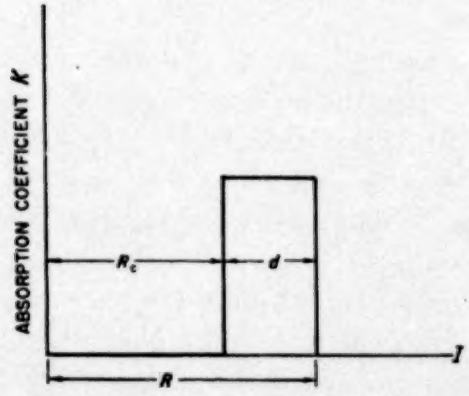

Fig. 1. The simplified distribution of the absorption coefficient employed in our calculation.

analytical calculation impossible, we use a spherical shell for the distribution, which is described by two parameters R and d. R is the outer boundary of the distribution, which is not necessarily equal to the nuclear radius, and d is the thickness of the spherical shell. The absorption coefficient K is assumed to be constant between the inner and the outer boundaries of the shell. This extremely crude approximation may be adequate because of simplifications made in other parts of our calculation. As can be seen in fig. 1, this distribution includes the uniform spherical distribution as an extreme case of $R_c \equiv R-d = 0$. With this distribution, the probability F_n is given by the integral

$$F_n = \frac{2}{R^2}\int_0^R s\,\mathrm{d}s\, f_n(x), \tag{5}$$

where x is the function of the impact parameter s of the incident particle and given by

$$x = \begin{cases} 2(\sqrt{R^2-s^2}-\sqrt{R_c^2-s^2}) & \text{for} \quad s \leqq R_c, \\ 2\sqrt{R^2-s^2} & \text{for} \quad R \geqq s \geqq R_c. \end{cases} \tag{6}$$

An elementary calculation gives the following formula for F_n:

$$F_n = \frac{(n+1)}{2\gamma^2}\left[3\Gamma_{n+2}(\gamma_1)+\Gamma_{n+2}(\gamma_2)+\gamma_1{}^4 I_n(\gamma_1, \gamma_2)\right], \tag{7}$$

with

$$\gamma = 2KR, \quad \gamma_1 = 2K\sqrt{R^2-R_c^2}, \quad \gamma_2 = 2K(R-R_c). \tag{8}$$

Here $\Gamma_n(a)$ is the incomplete gamma function defined by

$$\Gamma_n(a) = \int_0^a \frac{t^n \mathrm{e}^{-t}}{(n+1)!}\,\mathrm{d}t$$

and the function I_n is given by the integral

$$I_n = \frac{1}{(n+1)!}\int_{\gamma_2}^{\gamma_1} t^{n-3}\mathrm{e}^{-t}\mathrm{d}t = g_n(t)\Big|_{\gamma_2}^{\gamma_1}, \tag{9}$$

which turns out to be †

$$\begin{aligned} &g_0(t) = \frac{\mathrm{e}^{-t}}{2t}\left(1-\frac{1}{t}\right)+\tfrac{1}{2}Ei(-t), \quad g_1(t) = -\frac{\mathrm{e}^{-t}}{2t}-\tfrac{1}{2}Ei(-t), \\ &g_2(t) = \tfrac{1}{6}Ei(-t), \quad g_3(t) = -\tfrac{1}{24}\mathrm{e}^{-x}. \end{aligned} \tag{10}$$

As mentioned in the introduction, F_n involves the absorption coefficient K and parameters R and d.

† The function $Ei(-t)$ is tabulated in ref. [1]).

4. Total Absorption Cross Section

Since the quantity $F_0(n=0)$, derived in sect. 3, stands for the penetrating probability, the total absorption cross section σ_{abs} is immediately obtained from the equation

$$\sigma_{abs} = \pi R^2(1-F_0). \tag{11}$$

One can see easily that, if one puts $R_c = 0$ in the above expression, one can obtain the well-known formula derived by Fernbach, Serber and Taylor [2]),

$$\sigma_{abs} = \pi R^2\left[1-\frac{1-e^{-2KR}(1+2KR)}{2K^2R^2}\right] \quad \text{for} \quad R_c = 0. \tag{12}$$

Our procedure is to determine the parameters involved in the expression of the total absorption cross section by using the experimental data. The available experimental data [3]) are shown in fig. 2.

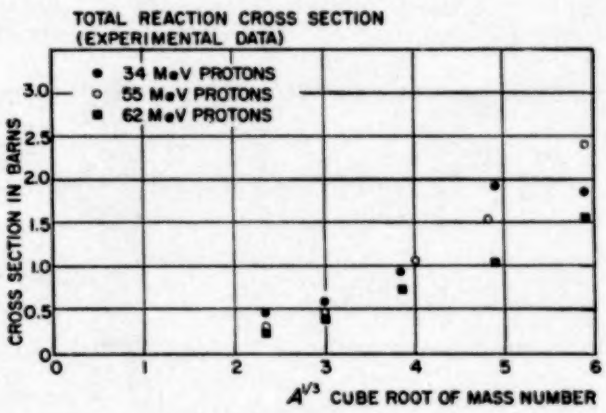

Fig. 2. Available experimental data on total absorption cross sections.

TABLE 1

Total absorption cross section

Nucleon energy	$A^{\frac{1}{3}}$	σ_{abs} (mb)			Parameters
		Exp.	Unif. (A)	Spher. sh. (B)	
55 MeV neutrons	3	500	660	661	$R = (1.33\,A^{\frac{1}{3}}+1.0)\times 10^{-13}$ cm
	4	1100	1110	1090	(A) $d = R$, $K^{-1} = 3.1\times 10^{-13}$ cm
	5	1700	1690	1620	(B) $d = 2$, $K^{-1} = 2.5\times 10^{-13}$ cm
	6	2300	2380	2250	
62 MeV protons	3	430	460	470	$R = (1.33\,A^{\frac{1}{3}}+0.25)\times 10^{-13}$ cm
	4	850	860	840	(A) $d = R$, $K^{-1} = 3.2\times 10^{-13}$ cm
	5	1320	1360	1310	(B) $d = 2$, $K^{-1} = 2.5\times 10^{-13}$ cm
	6	1980	2010	1900	

In our model, since the absorption coefficient K should be independent of the nuclear mass number, it has been fixed for a given energy. The calculations are made for 55 MeV neutrons and 62 MeV protons employing two values for d; $d = R$ and $d = 2\times10^{-13}$ cm. The results, as shown in table 1, are in fair agreement with the measurements. As far as the total absorption cross section is concerned, either type of distribution for the absorption coefficient is acceptable, if the values of parameters are suitably chosen.

5. Energy Integral $G_n(E_0)$

The quantity F_n, except for $n = 0$, does not tell whether or not the incident particle has enough energy to escape from the nuclear potential when it reaches the exit boundary of the nucleus. Therefore we introduce another probability $G_n(E_0)$ that the incident particle has enough energy to escape from the nuclear potential after n collisions. $G_n(E_0)$ is a quantity with a somewhat formal definition, since we do not know which particle in the collision between identical particles we are observing in the experiment. Leaving out discussions of the actual form of the energy distribution, let $w(E, E')\mathrm{d}E'$ be the energy distribution after a single two-body collision in the nuclear medium. Here E and E' refer to the energies of the particle concerned, before and after a collision, respectively. Then the probability $G_n(E_0)$ is given by the integral

$$G_n(E_0) = \int_{E_c}^{E_0} w(E_0, E_1)\mathrm{d}E_1 \int_{E_c}^{E_1} w(E_1, E_2)\mathrm{d}E_2 \cdots \int_{E_c}^{E_{n-1}} w(E_{n-1}, E_n)\mathrm{d}E_n, \quad (13)$$

with $E_0 \geqq E_1 \geqq E_2 \geqq \ldots \geqq E_n \geqq E_c$, where E_i is the energy of the particle after i collisions and E_c is the minimum energy which is necessary to escape from the nuclear potential.

The actual form of $w(E, E')$ can be obtained by taking summation over all possible final states of the collision partner and integrating over all scattering angle of the particle concerned since we are dealing with the one-dimensional model. The energy distribution function w should be normalized as follows

$$\int_{E_F}^{E} w(E, E')\,\mathrm{d}E' = 1. \quad (14)$$

The lower limit is the Fermi energy E_F because the Pauli principle prohibits occupying any states under the Fermi surface after a inelastic two-body collision. In order to make the calculation, we must know the actual form of the function w. For the Fermi gas model and assuming an energy-independent cross section for free nucleon-nucleon collisions, we can obtain

$$w(E, E') = (\text{const.}) \begin{cases} 1 & \text{for} \quad E' \leqq E - E_F, \\ 1 - \left(1 - \dfrac{E - E'}{E_F}\right)^{\frac{3}{2}} & \text{for} \quad E' \leqq E - E_F. \end{cases} \quad (15)$$

This formula can be obtained by performing a tedious integration of the formulas derived in previous papers [4, 5]). This can give, for instance, the same result for the average kinetic energy after a single collision as that derived by a different method [5]). Unfortunately this expression seems to fail to give a realistic form for the energy distribution, since the actual contribution from particles leading to low excited states is much bigger than that predicted by formula (15). This is partly due to the large contribution from collective excitations in these states, and partly due to the distortion of the wave functions of nucleons in the target nucleus. Therefore it is not unreasonable to assume the form for the energy distribution as

$$w(E, E')\mathrm{d}E' = C_m \left(\frac{E'}{E}\right)^m \left(1-\frac{E'}{E}\right)\frac{\mathrm{d}E'}{E}, \tag{16}$$

where m is an adjustable parameter and C_m is the normalization constant determined by the condition (14). For our simplified model, in which all nucleons in the target nucleus are considered to be Fermi particles moving in a constant nuclear potential, the average kinetic energy $\langle E' \rangle$ after a collision, defined by

$$\langle E' \rangle = \int_{E_F}^{E} E' w(E, E')\, \mathrm{d}E', \tag{17}$$

must satisfy the requirement

$$E_F \leqq \langle E' \rangle \leqq \tfrac{1}{2}(E+E_F), \tag{18}$$

which follows from the conservation of energy. The condition (18) gives a restric-

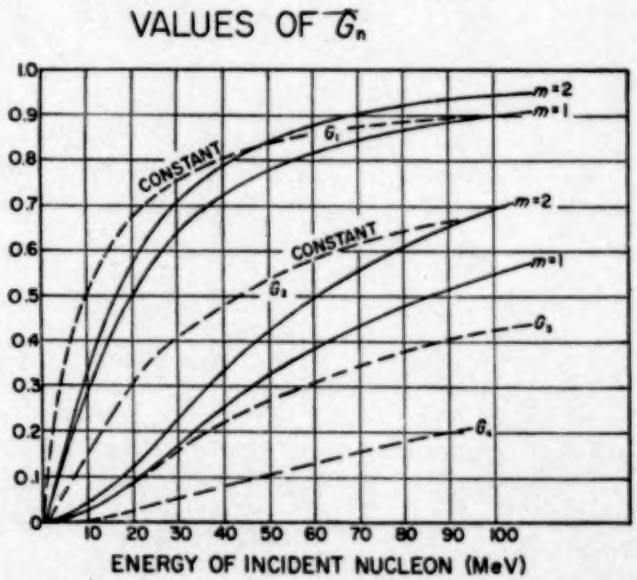

Fig. 3. Values of G_n versus the energy of the incident nucleon. The nuclear potential and the Fermi energy are assumed to be 50 MeV and 40 MeV respectively. The solid curves indicate the value of G_n calculated for the energy distribution (16) and values of m are attached to respective curves. The dashed-curves indicate those calculated for the energy independent energy distribution.

tion on the choice of arbitrary values of m. The actual distribution seems to be realized approximately by choosing m between 1 and 2. The values of G_1 and G_2 calculated for $m = 1$ and $m = 2$ are shown in fig. 3 and one can see that the ambiguity contained in the choice of values of m does not make a large difference in our conclusions. The values G_3 and G_4 shown are estimated by using an energy independent, i.e. constant, energy distribution. In these calculations the values $E_F = 40$ MeV and $E_c = 50$ MeV are employed.

6. Cross Section for n-Collisions

According to the procedure mentioned in the introduction, we define by eq. (1) the probability P_n that the incident nucleon leaves the residual nucleus after exciting n nucleons; and also we define the corresponding cross section $\sigma_d^{(n)}$ by

$$\sigma_d^{(n)} = \sigma_{abs} P_n. \tag{19}$$

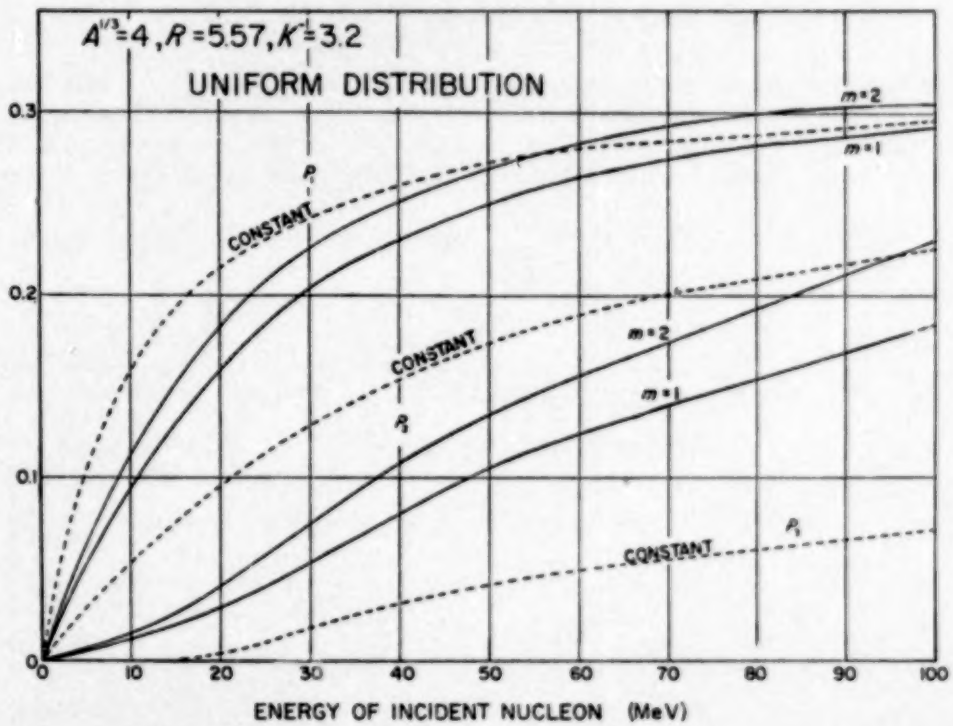

Fig. 4. Values of P_n versus the energy of the incident nucleon. These are calculated for $A^{\frac{1}{3}} = 4$ assuming the uniform distribution for the absorption coefficient. The labels $m = 1$ or 2 indicate the value of parameters in the expression (16) of the energy distribution. The label "constant" refers to the results calculated for the energy-independent energy distribution.

Typical values of P_n are shown in figs. 4—7. The cross section σ_d for the direct process is given by

$$\sigma_d = \sum_{n=1}^{\infty} \sigma_d^{(n)} = \sigma_{abs} \sum_{n=1}^{\infty} P_n, \tag{20}$$

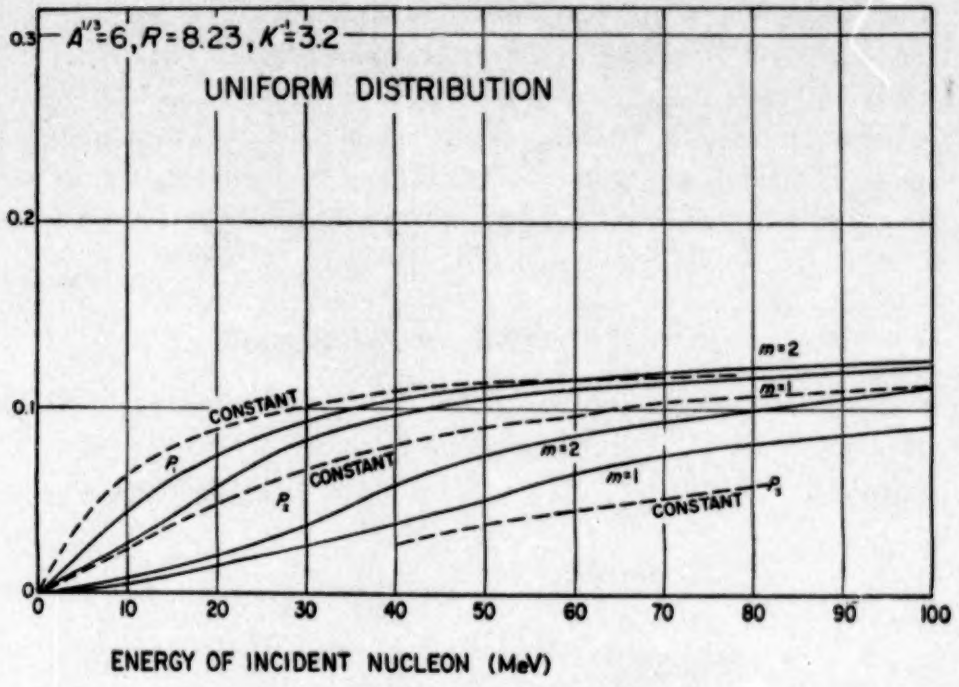

Fig. 5. Values of P_n versus the energy of the incident nucleon. These are calculated for $A^{\frac{1}{3}} = 4$ assuming the spherical shell distribution for the absorption coefficient. The labels $m = 1$ or 2 indicate the value of parameters in the experession (16) of the energy distribution. The label "constant" refers to the results calculated for the energy-independent energy distribution.

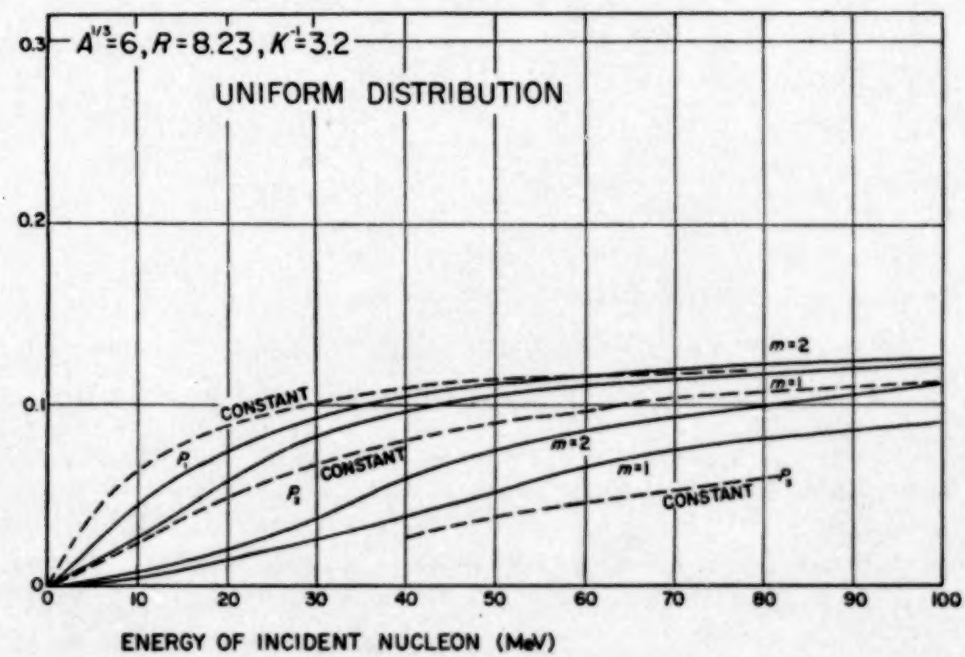

Fig. 6. The same as fig. 4 with $A^{\frac{1}{3}} = 6$.

which turns out to be, for the energy range of 30 to 60 MeV,

$$\sigma_d \approx (20 \text{ to } 35\ \%) \text{ of } \sigma_{abs}.$$

Furthermore, the cross section σ_c for the formation of the compound nucleus † is

$$\sigma_c = \sigma_{abs} - \sigma_d = \sigma_{abs}\left(1 - \sum_{n=1}^{\infty} P_n\right) \approx (80 \text{ to } 65\ \%) \text{ of } \sigma_{abs}. \tag{21}$$

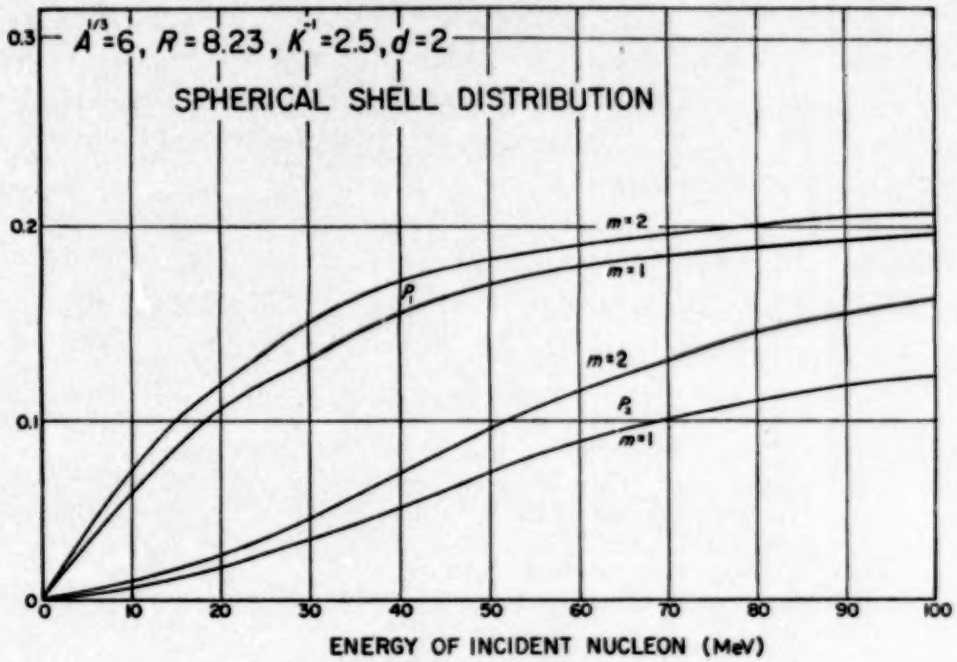

Fig. 7. The same as fig. 5 with $A^{\frac{1}{3}} = 6$.

7. Discussion and Remarks

It has been found that the probability P_2, which essentially corresponds to the second order process, can give a fairly large contribution in actual nuclear reactions for the energy range from 30 to 60 MeV. This process is especially important in the analysis of the energy spectrum observed in the experiments. In heavy nuclei high Coulomb barriers make the emission of protons from the compound nucleus less pronounced, but the protons produced by the direct process are less affected by the Coulomb barrier since the direct process is supposed to take place near the nuclear surface ††. Since the nucleons emitted as a result of multiple collisions have rather small kinetic energy, they may form the low energy portion of the energy spectrum. In fact the previous theoretical calculations [6, 7]) fail to explain the low energy portion of the energy spectrum, whereas the agreement between the theory and experiment is fair in

† Here the compound nucleus refers to the one with the highest possible excitation energy, which can be formed before any particle is emitted from it.

†† As to this point, another investigation on a similar model is now being made.

the high energy part of the energy spectrum. Although the transmission effect at the nuclear boundary has been neglected in our calculation, it does not seem to alter our conclusion, because the main contribution to the whole direct process comes from the surface region of the nucleus as discussed by Eisberg, McCarthy and Spurrier [8]). In order to see these effect more precisely, it would be worth while making a similar calculation with a more suitable distribution of the absorption coefficient. P_3 and higher terms can be neglected in the nuclear reactions of this energy range. Processes involving three or more successive collisions result in the formation of so-called compound nucleus, in which a number of nucleons are excited and a mixed-up condition is obtained. Further calculations on the energy spectrum, in which successive collisions are taken into account, will be published.

The author would like to express his sincere thanks to Professor R. M. Eisberg for his helpful discussions and careful reading of the manuscript.

References

1) E. Jahnke and F. Emde, Tables of functions
2) Fernbach, Serber and Taylor, Phys. Rev. **75** (1949) 1352
3) R. M. Eisberg, Proceedings of the International Conference on the Nuclear Optical Model, (1959) p. 67
4) M. L. Goldberger, Phys. Rev. **74** (1948) 1269
5) Hayakawa, Kawai and Kikuchi, Prog. Theor. Phys. **13** (1955) 415
6) L. R. B. Elton and L. C. Gomes, Phys. Rev. **105** (1957) 1027
7) N. Oda and K. Harada, Nuclear Physics **7** (1958) 251
8) Eisberg, McCarthy and Spurrier, Minnesota Linear Accelerator Progress Report (1959)

2.A.2

Nuclear Physics **20** (1960) 601—613; © *North-Holland Publishing Co., Amsterdam*

Not to be reproduced by photoprint or microfilm without written permission from the publisher

EXCITATION OF HEAVY NUCLEI BY FAST NUCLEONS

KEN KIKUCHI †

School of Physics, University of Minnesota, Minneapolis, Minnesota ††

Received 26 June 1960

Abstract: Nuclear reactions induced by fast nucleons are studied on the basis of a classical model. A formula is obtained to calculate the energy spectrum of all nucleons emitted, taking account of the successive collisions between the incident nucleon and the nucleons in the target nucleus. The result is compared with the energy spectrum predicted by the statistical theory. Calculated energy spectra and cross sections are found to be in fair agreement with the experimental results.

1. Introduction

In a previous paper [1]), cited as (I), it has been found that successive collisions cannot be neglected in nuclear reactions of the intermediate energy range. This paper deals with the excitation of nuclei bombarded by fast nucleons, taking account of successive collisions on the basis of a semiclassical model. The dissipation of the incident energy in the nuclear medium is reminiscent of the diffusion of neutrons in an absorbing medium. Proceeding by analogy, we develop a diffusion equation for the energy and spatial distributions of the incident beam and for the nucleons excited by the incident nucleon, supposing that the differential cross section for nucleon-nucleon scattering in the nucleus is known. For simplicity we consider a one-dimensional problem, in which the energy distribution of nucleons in the excited states is given as a function of the distance. In order to make calculations easier, we make the following assumptions:

[1] First, the number of excited nucleons above the Fermi surface is assumed to be much smaller than the number of nucleons in the Fermi sea. Therefore we neglect the effect of holes in the nucleon states beneath the Fermi surface produced by the two-body collision. This implies that the density distribution of the target nucleus does not change in the couse of interaction between the incident nucleon and the target; and that the total number of nucleons in the system is not conserved.

[2] Secondly we neglect the interaction between excited nucleons above the Fermi surface. Therefore the mean free path of a nucleon travelling in the excited nuclear medium is the same as the one for the ground state, because we ignore the holes in the Fermi sea.

† On leave of absence from the Institute for Nuclear Study, University of Tokyo, Japan.

†† Work supported in part by the U. S. Atomic Energy Commission.

[3] We assume that the cross section for nucleon-nucleon collisions in the nuclear medium is independent of energy [2, 3]). This assumption is quite valid for the energy range of importance, since we are interested in nucleons that are capable of exceeding the nuclear potential barrier. Then the mean free path of a nucleon travelling in the nuclear medium is dependent only on the nuclear density.

[4] Densities of neutrons and protons are assumed to be the same; that is, we neglect the neutron excess. However, we take account of the difference between n—p and p—p interactions and use the fact that the cross section for n—p scattering is about three times larger than that for p—p scattering in the energy range concerned here.

In order to develop the diffusion equation for the energy-spatial distribution of nucleons, it is necessary to know the energy distribution of two nucleons after a single collision in a nuclear medium. Leaving out discussion of the practical form of the energy distribution for the moment, we introduce the energy distribution function $w(E, E')\mathrm{d}E'$ as in (I), which satisfies the normalization condition

$$\int_{E_F}^{E} w(E, E')\mathrm{d}E' = 1. \tag{1}$$

Here E and E' are the energies before and after a collision, and the lower limit E_F of the integral is the Fermi energy since the Pauli principle prohibits the occupation of any state under the Fermi surface. Throughout this paper the particle energy E is measured from the bottom of the Fermi sea. We also assume the following simplified relation:

$$E = V+\varepsilon = E_F+B+\varepsilon, \tag{2}$$

where ε is the corresponding energy of the particle outside the nucleus, V is the depth of the nuclear potential, and B is the binding energy.

In order to make analytical calculations easier, we assume that the kinetic energy of a particle is independent of the distance x. This assumption is valid for infinite nuclear matter, in which the Fermi energy is constant over all regions of nuclear matter. In the case of finite nuclei, the kinetic energy of a particle and the Fermi energy are supposed to be functions of nuclear density and then vary with the distance as in a classical picture. This assumption implies that a particle at any position is described by its kinetic energy measured from the bottom of the Fermi sea and that the energy distribution function w is dependent on the distance. Therefore it is necessary to pay special attention to the effect of the nuclear surface when we apply the theory to the analysis of the experimental data.

2. Formulation

We deal with the case of proton-induced reactions; but it is easy to apply the solution of our problem to neutron induced reactions. Let P and N be the

energy and spatial distributions of protons and neutrons; they are functions of energy E and of distance x. $P(E, x)\mathrm{d}E$ is the number of protons at distance x with energy between E and $E+\mathrm{d}E$, and $N(E, x)\mathrm{d}E$ is the same for neutrons. Since, by assumption [1], P and N are always uniform under the Fermi surface, we observe only their behaviour above the Fermi surface. By use of the assumptions made, we can develop the following equations for P and N:

$$\frac{\partial P}{\partial x} = -\frac{P}{L(x)} + \frac{1}{(1+k)L(x)} \int_E^\infty \{kN(E')+(2+k)P(E')\}w(E', E)\mathrm{d}E', \quad (3)$$

$$\frac{\partial N}{\partial x} = -\frac{N}{L(x)} + \frac{1}{(1+k)L(x)} \int_E^\infty \{(2+k)N(E')+kP(E')\}w(E', E)\mathrm{d}E', \quad (4)$$

where k is the ratio σ_{pn}/σ_{pp} of p—n and p—p cross sections, σ_{nn} is assumed to be equal to σ_{pp}, and L is the mean free path which is a function of x. In the equations (3) and (4) the first term expresses the decrease of nucleon number due to attenuation and the second integral expresses the increase due to two-body collisions; the terms kN and kP are due to n—p collisions and the terms $(2+k)N$ and $(2+k)P$ are due to n—n and p—p collisions. If we introduce the total number of nucleons $I(E, x)$, we have

$$\frac{\partial I}{\partial x} = -\frac{I}{L(x)} + \frac{2}{L(x)} \int_E^\infty I(E', x)w(E', E)\mathrm{d}E'. \quad (5)$$

The factor 2 in the second term represents the fact that a two-body (inelastic) collision in the nuclear medium creates one nucleon above the Fermi surface.

Upon introducing the attenuation factor

$$X(x) = \int_{-\infty}^{x} \frac{\mathrm{d}x}{L(x)} \quad (6)$$

and after several manipulations, the equations can be rewritten in the integral form

$$P(E, X) = \frac{\mathrm{e}^{-X}}{1+k} \int_0^X \mathrm{e}^X \mathrm{d}X \int_E^{E_0} \{(2+k)P(E')+kN(E')\}w(E', E)\mathrm{d}E', \quad (7)$$

$$N(E, X) = \frac{\mathrm{e}^{-X}}{1+k} \int_0^X \mathrm{e}^X \mathrm{d}x \int_E^{E_0} \{(2+k)N(E')+kP(E')\}w(E', E)\mathrm{d}E', \quad (8)$$

$$I(E, X) = 2\mathrm{e}^{-X} \int_0^X \mathrm{e}^X \mathrm{d}X \int_E^{E_0} I(E', X)w(E', E)\mathrm{d}E', \quad (9)$$

where E_0 is the energy of the incident proton beam. For $E = E_0$, the solution is

$$I(E_0, X) = P(E_0, X) = \mathrm{e}^{-X}\delta(E-E_0), \quad (10)$$

which represents the attenuation of the incident proton beam. The set of

equations can be solved in an iteration method by regarding (10) as the zero-order solution. The solutions are found to take the form

$$I(E, X) = \mathrm{e}^{-X}\delta(E-E_0)+\sum_{n=0}^{\infty} 2^{n+1}\Phi_n, \tag{11}$$

$$P(E, X) = \mathrm{e}^{-X}\delta(E-E_0)+\sum_{n=0}^{\infty} C_P{}^{(n)}\Phi_n, \tag{12}$$

$$N(E, X) = \sum_{n=0}^{\infty} C_N{}^{(n)}\Phi_n, \tag{13}$$

with

$$\Phi_n = \mathrm{e}^{-X}\sum_{j=0}^{n}\frac{X^j}{j!}\varphi_j(E_0, E). \tag{14}$$

Here the quantities φ_j are the energy integrals

$$\begin{aligned}
&\varphi_0 = w(E_0, E),\\
&\varphi_1 = \int_E^{E_0} w(E_0, E_1)w(E_1, E)\mathrm{d}E_1,\\
&\cdots\cdots\cdots\cdots\cdots\cdots\cdots\cdots\cdots\cdots\\
&\varphi_j = \int_E^{E_0}\mathrm{d}E_j w(E_j, E)\int_{E_j}^{E_0}\mathrm{d}E_{j-1}w(E_{j-1}, E_j)\cdots\int_{E_2}^{E_0}\mathrm{d}E_1 w(E_0, E_1)w(E_1, E_2),
\end{aligned} \tag{15}$$

and $C_P{}^{(n)}$ and $C_N{}^{(n)}$ are coefficients given by

$$\begin{aligned}
&C_P{}^{(n)}+C_N{}^{(n)} = 2^{n+1},\\
&C_P{}^{(0)} = (2+k)/(1+k), \quad C_P{}^{(1)} = 4(2+2k+k^2)/(1+k)^2,\\
&C_P{}^{(2)} = 2(4+2k+5k^2+2k^3)/(1+k^3),\\
&C_P{}^{(n)} \approx C_N{}^{(n)} \quad \text{for} \quad n \gtrsim 3.
\end{aligned}$$

From the physical point of view, the j-th term in the expansion of the solution corresponds to the contribution due to $(j+1)$ two-body collisions. Therefore, as predicted in (I), only the first few terms in the summation are appreciable when applying the theory to nuclear reactions in the intermediate energy range.

3. Application to Nuclear Reactions

We can apply the theory to the actual nuclear phenomena, if we know the distribution of the absorption coefficient $L(x)^{-1}$, which is closely related with the imaginary part of the optical potential. For low incident energies the distribution of the absorption coefficient is considered to be peaked at the nuclear surface; however, this peak does not seem to be so pronounced for intermediate energies. In our calculation we adopt the previous theoretical result [7] for the

distribution of the absorption coefficient, which is almost the same as the Wood-Saxon type distribution. As in (I), we take the simplified model in which the incident nucleon with moderately high energy travels in a straight line following its initial direction upon entering the target nucleus. In this picture the incident particle is described by the kinetic energy and the impact parameter s. With this model it is easy to calculate the attenuation factor

$$\int_{-\infty}^{\infty} \frac{\mathrm{d}x}{L(x)} = X(s) \tag{16}$$

for a particle with given impact parameter s. This model can be modified, if we use the results obtained by Eisberg, McCarthy and Spurrier [6]) and take account of the focusing effect of the incident beam. They show that this modification in our model makes the magnitude of $X(s)$ larger, but the attenuation factor $X(s)$ calculated by the quantum mechanical method is found to be smaller than the classical one for particles which go through the neighbourhood of the nuclear boundary. After considering both of these effects, the magnitude of $X(s)$ calculated in our model is probably not very different from the actual one.

The energy spectrum of nucleons observed in the experiment is given by the superposition of different beams with different impact parameters. Since we have started from the one-dimensional model, only the energy spectrum integrated over all angles is of interest. The whole energy spectrum integrated over the angle is given by

$$\frac{\partial \sigma_P}{\partial E} = 2\pi \int_0^{\infty} s\mathrm{d}s P(E, X(s)) \tag{17}$$

for protons. We can get the spectrum of neutrons $(\partial \sigma_N / \partial E)$ by replacing P by N in the above expression.

Obviously, the most striking difference between the spectra of protons and neutrons lies in the elastic peak which is due to the δ-function in the solution $P(E, X)$.

The complexity in the practical calculation arises from the evaluation of the energy integrals given by (15). Let us first see the overall behaviour of the solutions of the equation in a simplified case, namely, the case of the energy-independent distribution function

$$w(E, E') = \frac{1}{E - E_F}. \tag{18}$$

The energy integral φ_j can be calculated analytically. The result is

$$\varphi_j = \frac{1}{j!} \frac{1}{E_0 - E_F} \left(\log \frac{E_0 - E_F}{E - E_F} \right)^j. \tag{19}$$

In this particular case, if we use the relation (2), the solution does not depend upon the magnitude of the Fermi energy, so that our solutions are complete. The energy distribution (18) gives

$$\langle E' \rangle = \tfrac{1}{2}(E+E_F) \tag{20}$$

for the average kinetic energy $\langle E' \rangle$ after a single collision, which is the upper limit of the condition (18) given in (I). Physically this corresponds to the average kinetic energy after a collision between the incident particle and a target nucleon located at the Fermi surface. The actual magnitude of $\langle E' \rangle$ should be slightly smaller than $\frac{1}{2}(E+E_F)$ and is about equal to half of $E+\frac{3}{5}E_F$ for high incident energies on the basis of the Fermi gas model. For lower incident

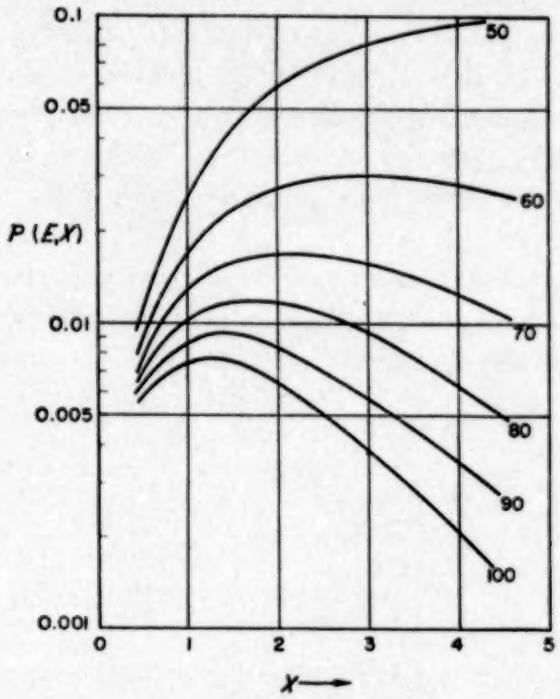

Fig. 1. Solution $P(E, X)$ of eq. (7) for the case of 60 MeV (110 MeV inside the nucleus) incident protons and for the constant energy distribution (18) versus the attenuation factor X defined by (16). The figures attached to respective curves indicate the energy E of the protons inside the nucleus.

energies $\langle E' \rangle$ approaches $\frac{1}{2}(E+E_F)$, since the Pauli principle prohibits collisions between the incident nucleon and the nucleons near the bottom of the Fermi sea. Thus the energy distribution (18) seems to be adequate to discuss the overall behaviour of the reaction phenomena. The numerical calculations for more reasonable energy distributions will be made in later sections.

The solutions of our equations are shown in figs. 1 and 2 for the case of 60 MeV incident protons and for the constant energy distribution. We apply these solutions to nuclear reactions occurring in the spherical uniform nucleus, in which the mean free path L and the Fermi energy E_F are constant over all the

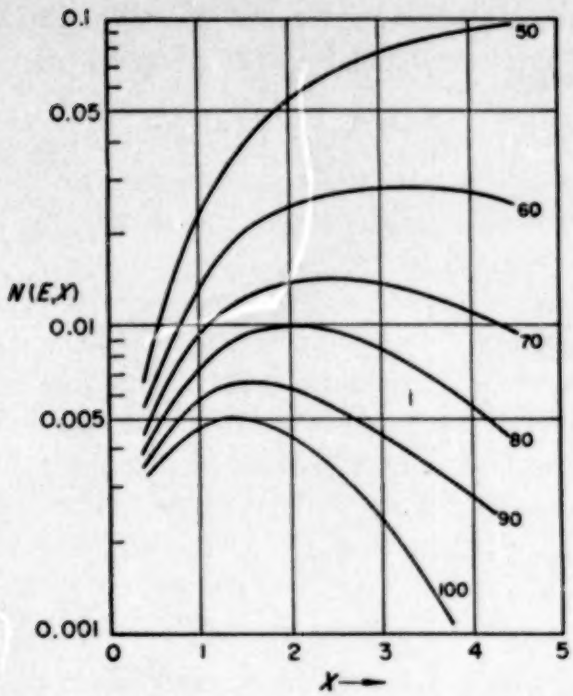

Fig. 2. Solution $N(E, X)$ of eq. (8) for the case of 60 MeV (110 MeV inside the nucleus) incident protons and for the constant energy distribution (18) versus the attenuation factor X defined by (16). The figures attached to respective curves indicate the energy E of the neutrons inside the nucleus.

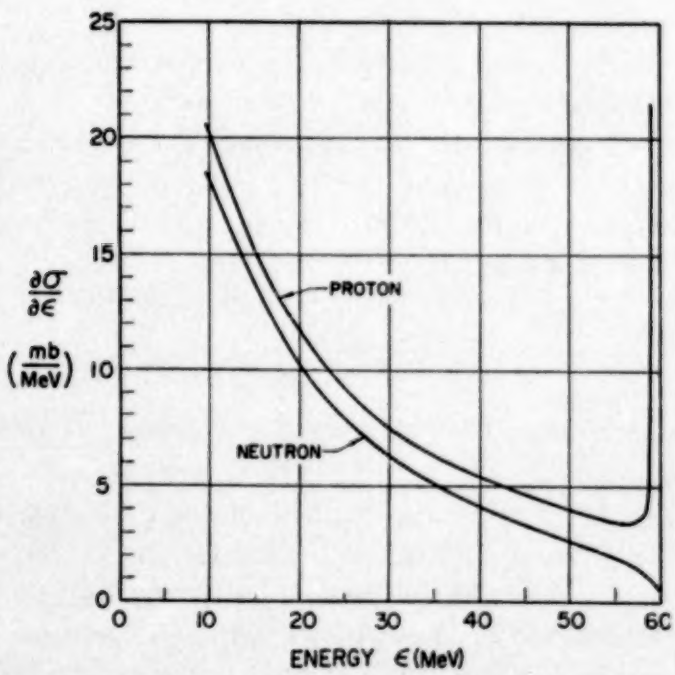

Fig. 3. Energy spectra of protons and neutrons emitted from an $R = 5\times10^{-13}$ cm nucleus bombarded by 60 MeV protons. A spherical symmetric and uniform distribution is assumed for the nuclear medium and the mean free path is taken to be 3×10^{-13} cm.

nuclear medium where the absorption takes place. The attenuation factor $X(s)$ for a particle with impact parameter s is given by

$$X(s) = 2\sqrt{R^2-s^2}/L, \tag{20}$$

where R is the radius of nuclear medium. Numerical calculations are made for $R = 5\times10^{-13}$ cm and $L = 3\times10^{-13}$ cm. The energy spectra of protons and neutrons emitted are shown in fig. 3.

The energy spectrum observed in the experiment is peaked, since most of low energy particles cannot emerge from the nucleus because of the nuclear potential barrier. We have assumed a spherical uniform distribution with a sharp edge for the nuclear medium in the calculation shown in fig. 3, so that we have less yield for the high energy portion of the spectrum. The high energy portion is mainly due to the surface processes, which correspond to small magnitudes of $X(s)$. The calculations for the nucleus with a diffuse surface will be made in a later section.

4. Comparison with the Energy Spectrum due to the Evaporation Theory

The energy spectrum of particles emitted from the compound nucleus is given by [4])

$$\frac{\partial\sigma}{\partial\varepsilon} \propto \varepsilon \exp(-\varepsilon/T), \tag{21}$$

where ε is the kinetic energy (outside the nucleus) of the particles and T is the nuclear temperature. Here the penetration factor is omitted, since it is also neglected in our calculation. It is interesting to see the difference between the energy spectra of particles predicted by the evaporation theory and obtained here. Since the energy spectrum differs for different values of attenuation factor X in our case, we plot the quantity

$$\eta = \frac{1}{E-V} P(E,X) \propto \frac{1}{\varepsilon}\frac{\partial\sigma}{\partial\varepsilon} \tag{22}$$

as a function of energy $\varepsilon = E-V$ for different values of X, and then compare η with the expression $\exp(-\varepsilon/T)$ of (21). The numerical calculation is made for the case of 60 MeV incident protons with the constant energy distribution, for which solutions have been given in the last section. As can be seen from fig. 4, η decreases almost linearly with increasing energy for $X \gtrsim 2$. This shows that there is no large difference in results between the evaporation theory and ours. The mean free path for nucleons of intermediate energy is about 2 to 3×10^{-13} cm, so the condition $X \gtrsim 2$ is easily satisfied for medium and heavy nuclei. This fact suggests that the incident nucleons with impact parameter small

compared to the radius of target nucleus do not exhibit the character of so-called direct process, even if they are not emitted from the compound nucleus. It seems that even at $X = 2$ it is hard to distinguish the energy spectra of particles due to the direct process from those due to the evaporation process, except for the particle groups leading to the low lying excited states of the residual nucleus, with which we are not concerned here.

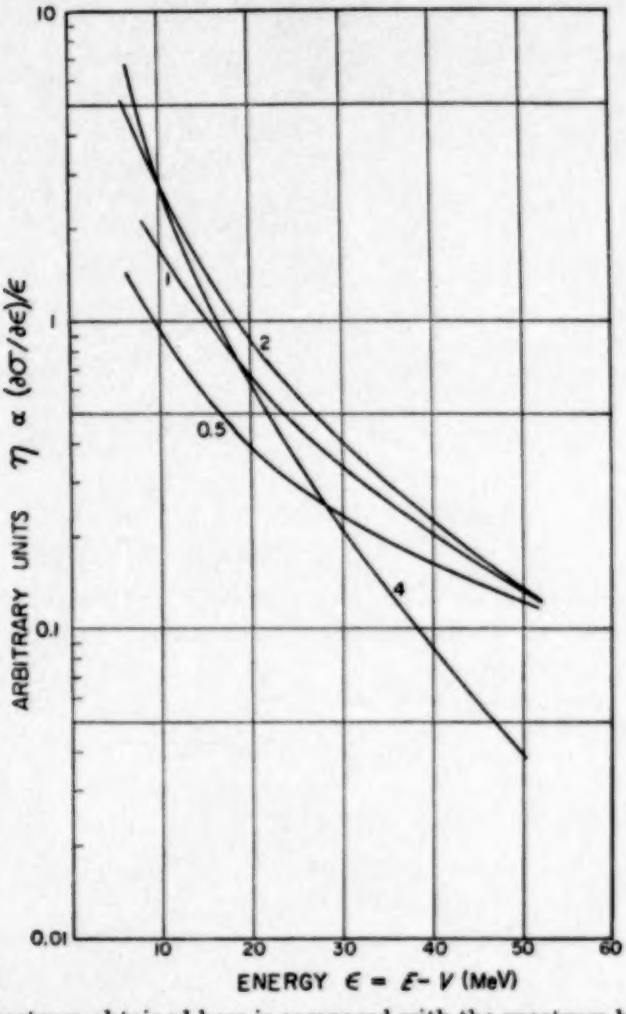

Fig. 4. The energy spectrum obtained here is compared with the spectrum based upon the evaporation theory. The quantity η may be compared with $\exp(-\varepsilon/T)$, T being the nuclear temperature. The gradient of each curve represents the reciprocal of the nuclear temperature.

Since we have neglected the effects of holes in the Fermi sea, the total number of nucleons is not conserved but increases with increasing distance X. Hence we are not able to discuss how fast the Maxwellian distribution can be achieved in the target nucleus bombarded by the incident nucleon.

5. Comparison with the Experimental Results

The most desirable experiment so far, to which our calculation is to be compared, has been done by using the fast proton beam from the Minnesota Linear

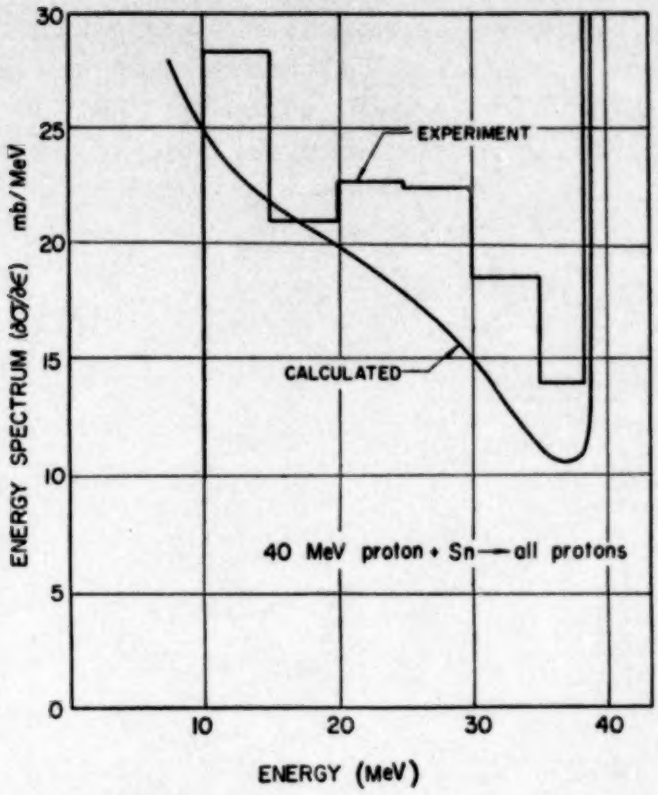

Fig. 5. The energy spectrum of all protons emitted from Sn bombarded by 40 MeV protons. The block diagram shows experimental data and the solid curve is the calculated result.

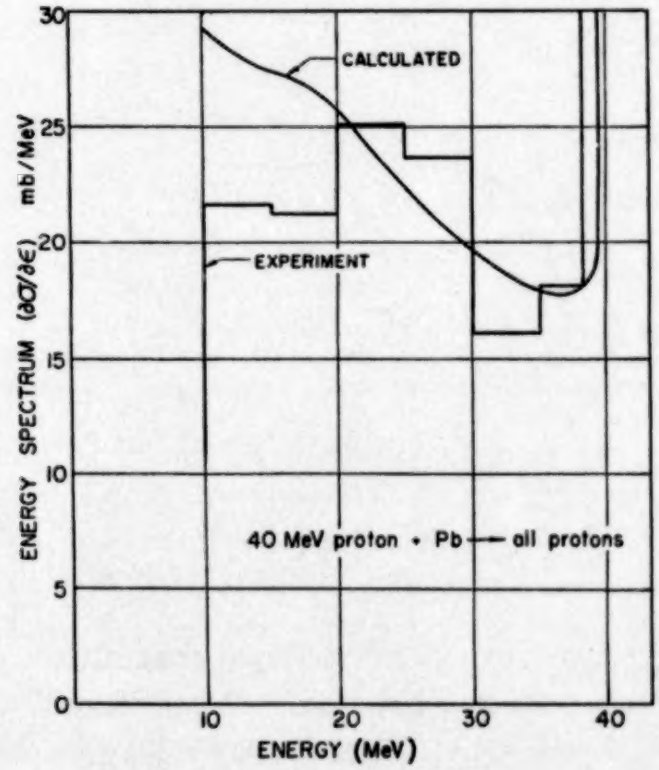

Fig. 6. The energy spectrum of all protons emitted from Pb bombarded by 40 MeV protons. The block diagram shows experimental data and the solid curve is the calculated result.

Accelerator. The numerical calculations are made for the energy spectra of protons emitted from Sn and Pb bombarded by 40 MeV protons [5]). Here the energy distribution

$$w(E, E') \propto \left(\frac{E'}{E}\right)^2 \left(1 - \frac{E'}{E}\right) \frac{1}{E}$$

has employed as in (I). Since we use the nuclear distribution with a diffuse surface this time, it is necessary to pay special attention to the fact that the

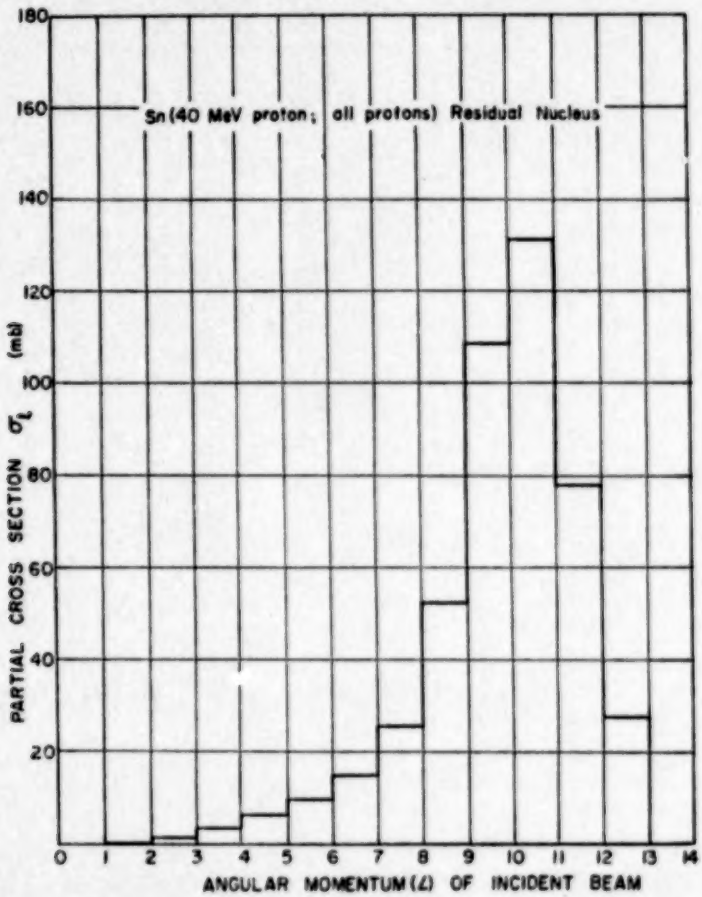

Fig. 7. Partial cross sections defined by (23) versus the angular momentum of the incident nucleon for the case of the reaction induced by 40 MeV protons on Sn. R indicates the average nuclear radius.

energy distribution function, involving the Fermi energy as a parameter, is no longer independent on the distance x. Therefore it is not possible to obtain solutions to the equations in the form given by (12) and (13). The Fermi energy varies as a function of nuclear density, when particles move in the nuclear medium, and it has a maximum value at the middle of the whole path, supposing that the incident particle always goes straight ahead in the nucleus. In order to make an approximate calculation, we make the assumption that we can omit the Fermi energy in the expression for the energy distribution if its maximum

value at the middle of the path is less than half of Fermi energy $E_F(0)$ at the centre of the nucleus, and that on the other hand, we can put it equal to $E_F(0)$ if it is larger than half of $E_F(0)$. In other words, this assumption is equivalent to the following: we neglect the effect of the Pauli principle for the particles whose impact parameter is larger than about $R-0.34\times10^{-13}$ cm, and the Pauli principle is taken into account, usually too strictly, for particles with smaller impact parameters. We can expect that effects of these two approximations partly cancel each other and then the result is not so much different from the exact calculation. With the above assumptions, we are able to use the Wood-

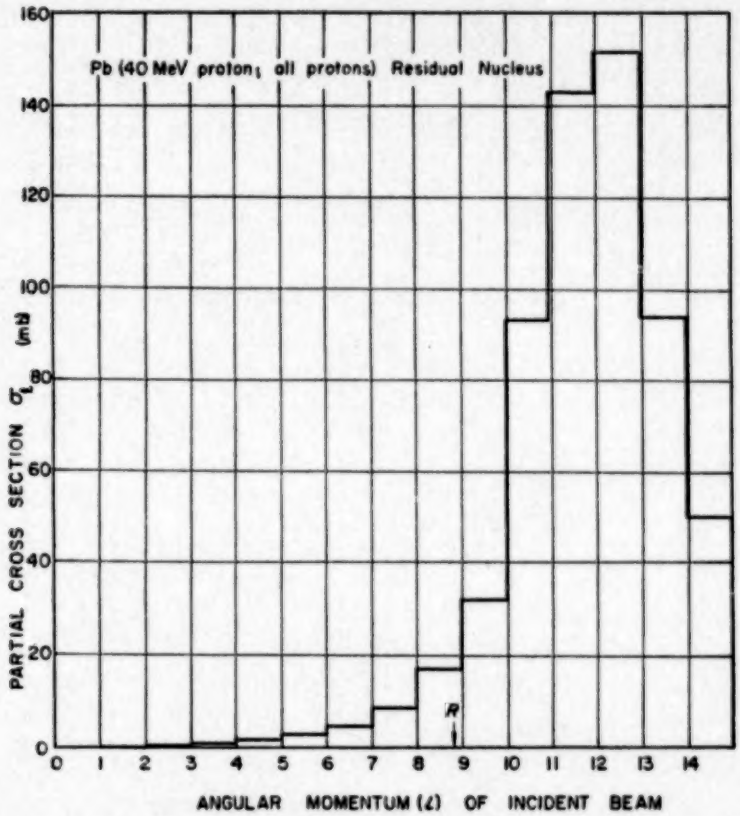

Fig. 8. Partial cross sections defined by (23) versus the angular momentum of the incident nucleon for the case of reactions induced by 40 MeV protons on Pb. R indicates the average nuclear radius.

Saxon distribution for the nuclear density and the corresponding distribution of the absorption coefficient obtained by the previous theoretical calculation [7]). Calculated curves are in fair agreement with the experimental results as can be seen in figs. 5 and 6. The main contribution to the spectrum, especially to the high energy portion, is due to the collisions occurring around the nuclear surface. This fact is mainly due to the large attenuation, which the incident particle with small impact parameter undergoes, as predicted by Eisberg, McCarthy and Spurrier [6]) in their detailed study of the behaviour of the incident flux in the optical potential. In our formulation this corresponds to

the fact that the solutions P and N have their maxima around $X = 0.5$ to 1 for values of energies which are large enough to exceed the nuclear potential barrier. In order to see the effect of surface processes, we calculate the partial cross section σ_l from the equation

$$\sigma_l = \int_{l\lambda}^{(l+1)\lambda} 2\pi s\,ds \int_{10\,\mathrm{MeV}}^{35\,\mathrm{MeV}} P(E, X(s))\,d\varepsilon \approx (2l+1)\pi\lambda^2 \int_{10\,\mathrm{MeV}}^{35\,\mathrm{MeV}} P(E, \bar{X})\,d\varepsilon, \quad (23)$$

which expresses the contribution to the cross section from the incident beam with angular momentum l. Here X is the average attenuation factor for the incident beam with angular momentum l. Calculated partial cross sections are shown in figs. 7 and 8. The total cross section for the production of protons, defined by

$$\sigma_t = \sum_l \sigma_l, \quad (24)$$

is also in fair agreement with the experimental data as be seen in table 1.

TABLE 1

Comparison between theory and experiment

Target nucleus	Total cross section σ_t (mb)	
	Experimental	Calculated
Sn	570±10 %	470
Pb	536±10 %	590

From the comparison between the theory and the experiment, our method seems to be fairly useful for calculating energy spectra and total cross sections. These predictions should be helpful in the study of nuclear events of intermediate and high energies. So far as the concept of successive two-body collisions is valid, our method can be applied to high energy nuclear reactions, to which the classical treatment is still useful. The theoretical calculations for such cases may be simpler, since the Pauli principle is less effective for high energy incident nucleons.

The author would like to express his sincere thanks to Professor R. M. Eisberg for his helpful discussions and creaful reading of the manuscript.

References

1) K. Kikuchi, Nuclear Physics **20** (1960) 590
2) Hayakawa, Kawai and Kikuchi, Prog. Theor. Phys. **13** (1955) 415
3) M. L. Goldberger, Phys. Rev. **74** (1948) 1269
4) J. M. Blatt and V. F. Weisskopf, Theoretical nuclear physics (Wiley, New York, 1952)
5) S. W. Chen and N. M. Hintz, Minnesota Linear Accelerator Progress Report (1958)
6) Eisberg, McCarthy and Spurrier, Nuclear Physics **10** (1959) 571
7) K. Kikuchi, Nuclear Physics **12** (1959) 305

2.F

Nuclear Physics **20** (1960) 614—620; © *North-Holland Publishing Co., Amsterdam*

Not to be reproduced by photoprint or microfilm without written permission from the publisher

SECTION EFFICACE DIFFÉRENTIELLE DE LA RÉACTION C^{13} (He^3, α) C^{12} à 1.8 MeV

ROBERT BARJON †, MICHEL LAMBERT et JEAN SCHMOUKER †

Laboratoire de Physique, École Polytechnique, Paris

Reçu le 18 juillet 1960

Abstract: The differential cross section of the reaction $C^{13}(He^3, \alpha)C^{13}$ has been studied by means of 1.8 MeV He^3 ions provided by a Van de Graaff accelerator, using scintillation-counters to count the α-particles.

1. Introduction

Depuis quelques années, la théorie de l'intéraction directe a été appliquée avec succès à l'étude de certaines réactions nucléaires. Les réactions (He^3, α) constituent un outil de choix pour l'étude de tel processus, le mécanisme de „pick-up" pouvant être prédominant. Dans ce cas, un neutron du noyau cible est capturé au passage par l'ion He^3, sans que ce dernier interagisse avec le reste du noyau. La distribution angulaire des particules α observées a un rendement important vers l'avant. Elle peut présenter divers maximum et minimum, mais vers l'arrière le rendement est nul.

Il est naturel de choisir pour cible un noyau qui possède un neutron faiblement lié comme le carbone 13. La réaction $C^{13}(He^3, \alpha)C^{12}$ n'a été étudiée que pour deux énergies des ions incidents: 2 MeV et 4.5 MeV [1]), à l'aide d'émulsions nucléaires. Nous avons poursuivi cette étude à plus basse énergie, en utilisant la technique de comptage par scintillations.

L'absorption de l'ion He^3 par le noyau C^{13} conduit à une énergie d'excitation élevée du noyau composé O^{16} de 22.77 MeV.

Parmi les diverses voies possibles de la réaction $C^{13}+He^3$, deux d'entre elles ont des valeurs de Q élevées, 15.62 MeV pour (He^3, α) et 10.66 MeV pour (He^3, p). Pour une énergie des ions He^3 de 1.8 MeV, et lorsqu'on observe à 0° vers l'avant, on doit s'attendre à trouver des α de 14.7 MeV, 11.3 MeV, etc., conduisant aux différents niveaux du C^{12} et des protons de 12.3 MeV, 7.2 MeV, 6.3 MeV, etc. . . ., amenant aux niveaux de N^{15}. L'émission d'autres particules (neutrons et deuterons) se fait avec des énergies plus faibles.

† Actuellement à l'Institut d'Études Nucléaires d'Alger.

2. Dispositif Expérimental

2.1. LE FAISCEAU

Le gaz Hélium 3, fourni par le Laboratoire National de Oak Ridge (500 cm^3) contenait une très légère contamination de Tritium, inférieure à une partie par million. Le gaz He^3 diffusait très lentement (quelques cm^3 par heure) dans la source à ionisation haute fréquence par l'intermédiaire d'un robinet à fuite réglable à commande électrique [2]).

Les ions He^3 ionisés une fois, étaient accélérés dans le Van de Graaff de l'École Polytechnique dont l'énergie maximum est de 2 MeV. Un déflecteur électrostatique assure une précision en énergie de un millième. Un petit déflecteur magnétique permet la séparation des ions de masses différentes.
Avant de pénétrer dans la boîte à cible, le faisceau devait traverser une série de 4 diaphragmes de 1.5 mm de diamètre. L'intensité était de 3 à 5 μA avant les diaphragmes et de 1 à 2 μA après.

2.2. LA BOÎTE À CIBLES

Le schéma de la boîte à cibles se trouve à la figure 1. La cible est située au centre géométrique du boitier, dont la partie inférieure est fixe. Le couvercle mobile peut tourner sur lui-même, entraînant un détecteur, tout en maintenant le vide dans l'enceinte.

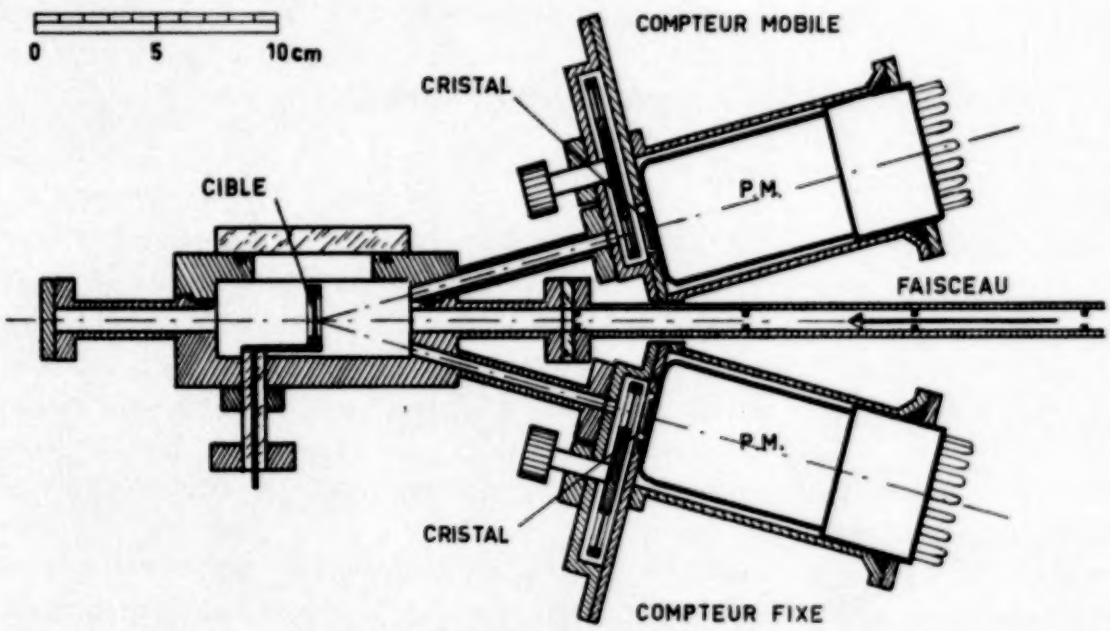

Fig. 1. Boîte à cibles et détecteurs.

L'étanchéité est assurée par un joint torique sur lequel s'appuie le couvercle. Le mouvement de rotation se fait aisément sans roulement à billes, grâce à la faible dimension de l'appareil: diamètre du joint 92 mm. L'angle d'observation peut varier de 15° à 165° autour du faisceau incident. L'angle solide d'observation, défini par des diaphragmes est de 8×10^{-4} sr.

Les deux cibles utilisées, enrichies à 65 % de carbone 13, ont été fournies par les Laboratoires de Harwell. L'une avait une épaisseur de 84 $\mu g/cm^2$, sur un support en or de 0.0004 pouce; l'autre 200 $\mu g/cm^2$ sur 0.003 pouce de cuivre. La cible est disposée à 45° du faisceau incident, la face contenant le carbone étant dirigée vers celui-ci. Pour les observations vers l'avant, les particules secondaires doivent traverser le support, ce qu'elles n'ont pas à faire pour les angles d'observation supérieurs à 90°.

La cible est isolée électriquement du boitier qui peut être lui-même isolé du reste de l'installation. La cible est reliée à un intégrateur de courant.

Un disque de quartz mobile qu'on peut disposer à la place de la cible, permet de contrôler la position du point d'impact du faisceau sur la cible.

Un détecteur fixe permet un comptage de référence à 165°.

2.3. LA DÉTECTION

Les particules chargées sont détectées par un cristal mince d'iodure de Césium et un photomultiplicateur Dumont 6292. Le cristal est placé sous vide et l'étanchéité est assurée par un joint torique qui appuie directement sur la photocathode plate du photomultiplicateur. Un disque mobile permet d'interposer entre cible et cristal un des 6 écrans d'aluminium d'épaisseur variable, dont il est muni (fig. 1).

Les impulsions qui sortent du photomultiplicateur sont envoyées, après amplification, dans un sélecteur d'amplitudes à 10 canaux, à bande variable, qui permet d'explorer en six opérations successives, un spectre d'impulsions comprises entre 10 et 100 V.

2.4. ÉTALONNAGE

L'appareillage a subi toute une série d'étalonnages. L'énergie des ions incidents a été calibrée par comparaison avec les résonances fines, bien connues [3]) de la réaction $F^{19}(p, \gamma)$. La boîte à cible a été vérifiée en retrouvant les distributions angulaires connues [4]) des deux résonances de 1.370 et 1.712 keV de la réaction $F^{19}(p, \alpha_0)O^{16}$. La linéarité de la réponse de la chaîne de détection a été soigneusement mesurée à l'aide d'un générateur d'impulsions étalonné. L'étalonnage du cristal a été réalisé en utilisant les α de la radioactivité naturelle (dépôt actif du thorium) 6.06 et 8.77 MeV, ainsi que les α produits par les réactions $F^{19}(p, \alpha_0)O^{16}$ et $Li^7(p, \alpha)He^4$, dont on peut faire varier les énergies respectivement de 8.7 à 6.9 MeV et de 11.2 à 7.6 MeV, en faisant varier l'angle d'observation de 0° à 180° pour une énergie de protons de 1.37 MeV.

3. Résultats

3.1. SPECTRE DES PARTICULES

Le rendement de la réaction $C^{13}(He^3, p)N^{15}$ est beaucoup plus important que celui de la réaction $C^{13}(He^3, \alpha)C^{12}$. Il faut donc distinguer les rares α parmi un grand nombre de groupes de protons, moins énergiques. Mais, comme le rende-

ment d'un cristal de Iodure de Césium est deux fois plus faible pour les α que pour les protons [5]), les impulsions dues aux α les plus énergiques ont des amplitudes du même ordre de grandeur que celles dues aux protons moins énergiques. Le spectre observé avec un cristal de ICs de 0.7 mm nous a montré que l'on ne pouvait séparer les α.

Nous avons alors utilisé un cristal beaucoup plus mince: 0.15 mm d'épaisseur. Des particules α de 15 MeV y perdent toute leur énergie, mais les protons ne peuvent y perdre qu'une faible partie de leur énergie. Un exemple typique d'un spectre, obtenu avec un tel cristal se trouve à la fig. 2. Le pic des α_0 qui conduisent à l'état fondamental du C^{12} est très bien isolé.

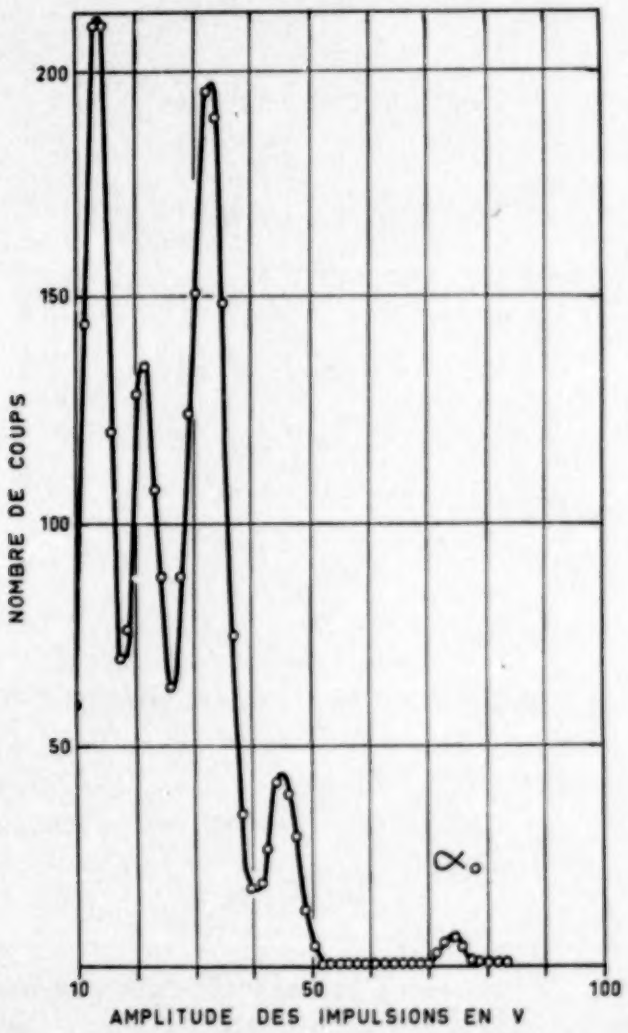

Fig. 2. Spectre caractéristique des particules de la réaction $C^{13}+He^3$.

3.2. COURBE D'EXCITATION

Elle a été étudiée pour un angle: 165° dans le Laboratoire (166° 15′ dans le système du centre de masse). Les mesures ont été „croisées" en recommançant périodiquement un comptage à une même énergie pour détecter un éventuel

appauvrissement de la cible en C^{13}. Les résultats sont reportés à la fig. 3. Les erreurs représentées sont celles dues à la statistique du comptage. La section efficace est donnée en millibarn par stéradian.

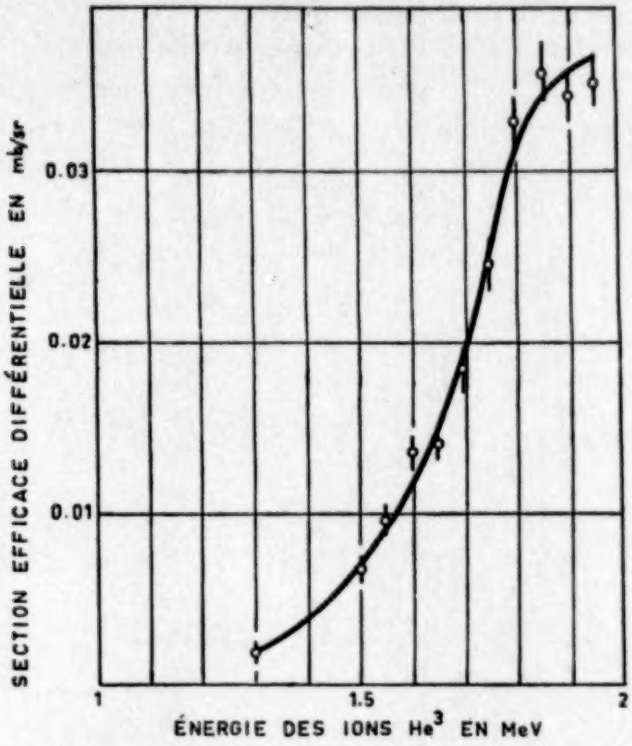

Fig. 3. Courbe d'excitation de la réaction $C^{13}(He^3, \alpha)\ C^{13}$ à 166° 15′ (système du centre de masse).

Holmgren donne à 2 MeV, une valeur environ deux fois plus grande que la nôtre. Mais l'incertitude est importante, car il est difficile de connaître avec précision la quantité de C^{13} présente dans la cible. Il n'y a pas de résonance entre 1 et 2 MeV. La section efficace augmente régulièrement et la courbe présente un point d'inflexion vers 1.75 MeV.

3.3. DISTRIBUTION ANGULAIRE DES α_0

La section efficace différentielle a été mesurée pour une énergie de 1.8 MeV des ions He^3 incidents. Les résultats sont portés sur la fig. 4. Les erreurs portées sont également celles dues à la statistique du comptage, de beaucoup la plus importante, à cause du faible rendement de la réaction. La statistique est meilleure pour les angles supérieurs à 90°, car nous avons pu utiliser la cible qui contenait davantage de C^{13}, mais possédait un support trop épais pour faire des mesures vers l'avant. Pour les angles inférieurs à 90°, la cible utilisée avait un support mince, mais contenait moins de C^{13}.

Il n'y a pas de symétrie par rapport à 90°. Le rendement est important vers l'avant. Il y a un minimum prononcé à 60°, suivi d'une remontée d'un palier vers 120° et d'une forte remontée vers l'arrière.

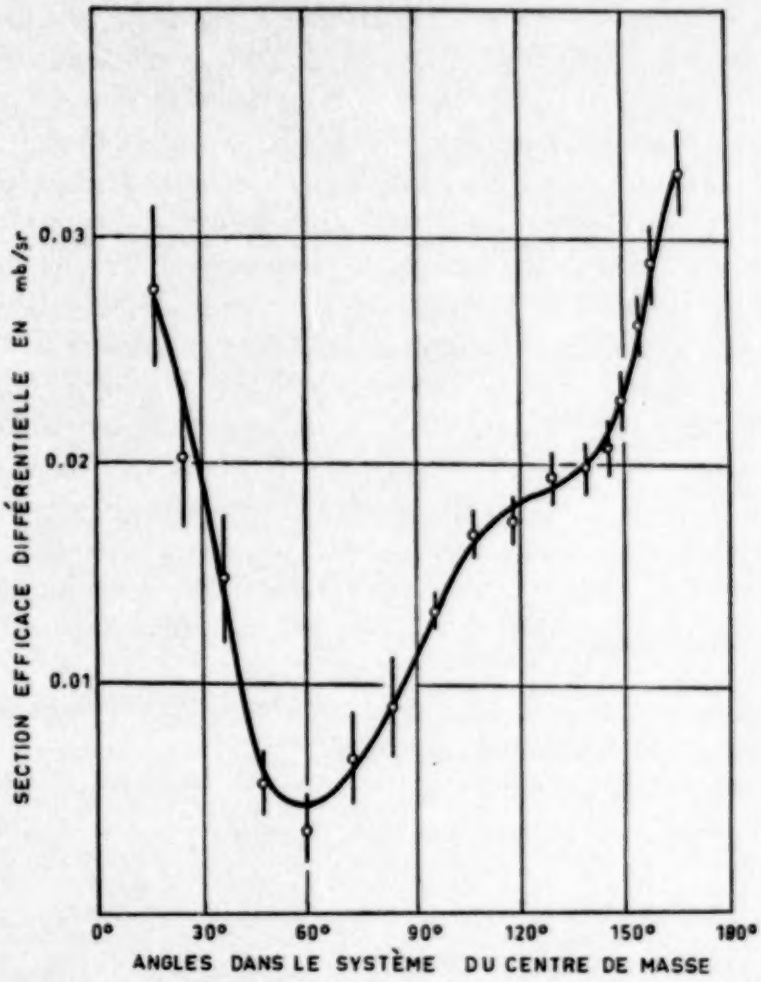

Fig. 4. Distribution angulaire de la réaction $C^{13}(He^3, \alpha_0)C^{12}$ à 1.8 MeV.

4. Discussion

Les contaminations possibles pouvaient être de deux sortes. La très faible quantité de tritium présente, dans le réservoir pouvait provoquer une réaction (He^3, α), sur les noyaux présents dans la cible, essentiellement C^{13} et C^{12}. Heureusement, les Q de ces réactions sont faibles, (2.266 MeV et 3.853 MeV) devant celui de la réaction $C^{13}(He^3, \alpha)$: 15.62 MeV, et ces α parasites ont une énergie beaucoup plus petite.

Il en est de même pour la réaction $C^{12}(He^3, \alpha)$ dont le Q est égal à 1.855 MeV.

Quant aux autres particules qui pourraient être émises par la cible, ce sont essentiellement des protons qui ne peuvent perdre qu'une faible partie de leur

énergie dans le cristal, dont l'épaisseur est moindre que leur parcours. Ils donneront donc des impulsions nettement plus faibles. Ce ne sont bien que des α de 14 MeV que nous pouvions compter dans les derniers canaux du sélecteur.

La forme de la distribution angulaire trouvée à 1.8 MeV ressemble à celle trouvée à 2 MeV par Holmgren. Le fait que la distribution angulaire change peu avec l'énergie, fait pour lequel Holmgren avait des indices, et que confirme, d'une part, la forme très voisine de la distribution angulaire à 1.8 et 2 MeV et, d'autre part, la variation lente et continue de la section efficace à 165° semble indiquer qu'il faut renoncer à une explication de cette réaction, par un processus de noyau composé. Holmgren a tenté, sans succès, d'interpréter la réaction comme un pur phénomène de pick-up [1]). Ce processus en effet, ne prévoit pas de rendement vers l'arrière. Owen plus récemment [6]) a essayé de rendre compte du phénomène, en faisant intervenir deux voies possibles pour la réaction: le „pick-up" et le „stripping de particule α" où l'He^3 est capturé entièrement par le noyau C^{13}, alors qu'une particule α, préexistante à l'intérieur de ce noyau, est éjectée. Ce processus permet d'expliquer le rendement élevé vers l'arrière. Divers paramètres, permettent d'ajuster la courbe théorique, avec les points expérimentaux. L'accord semble bon, mais paraît très sensible au choix de certains paramètres. Il y a là une voie intéressante de recherche, qui reste à perfectionner, en tenant compte notamment des effets Coulombiens.

Nous remercions vivement Monsieur le Professeur Leprince-Ringuet qui a assuré la direction scientifique de ce travail Nous remercions également Monsieur le Professeur Vignal pour l'aide qui nous a été donnée dans son laboratoire ainsi que Monsieur Brachet pour le soutien et les encouragements qu'il a accordé à nos expériences.

Références

1) Holmgren, Geer, Johnston et Wolicki, Phys. Rev. **106** (1957) 100, 102
2) Roubeau, Garin et Prugne, Le Vide **66** (1956) 453
3) Hunt et Firth, Phys. Rev. **99** (1955) 786
4) Clarke et Paul, Canadian Journal of Physics **35** (1957) 155
5) Bashkin, Carlson, Douglas et Jacobs, Phys. Rev. **109** (1958) 434
6) Owen, Madansky et Steve Edwards, Phys. Rev. **113** (1959) 575

7.A

Nuclear Physics **20** (1960) 621—629; © *North-Holland Publishing Co., Amsterdam*

Not to be reproduced by photoprint or microfilm without written permission from the publisher

INVARIANCE AND THE S-MATRIX (II)

Y. TAKAHASHI

Dublin Institute for Advanced Studies, Dublin, Ireland

Received 8 July 1960

Abstract: A formal method is proposed for handling an interaction, which is *not* invariant under a certain transformation. It is proved that a linearly dependent relation of the "invariance deficiencies" yields a selection rule for the S-matrix element constructed from the non-invariant interaction.

1. Introduction

We have discussed in a previous paper [1]) (hereafter quoted as (I)) how the S-matrix transforms under infinitesimal transformations. The condition for the S-matrix to be invariant is obtained in an integral form which may be less restrictive than the ordinary differential conservation laws in the Heisenberg picture [1]). We have further shown that there exists a constant of collision associated with the transformation, which leaves the S-matrix invariant.

In this paper, we shall discuss the case where the S-matrix is "almost invariant". It is interesting to formulate such a case, in view of the fact that it is experimentally confirmed that a certain type of symmetry is destroyed in weak interactions, and that this leads to selection rules, such as $\Delta S = \pm 1$ or $\Delta T = \pm\frac{1}{2}$, etc. Let us consider the meaning of an "almost invariant" S-matrix. If the S-matrix is not invariant, there will be no conserved quantity. But, to what extent is the invariance destroyed? Is it completely at random? Or, is it systematically destroyed? We shall introduce the quantity "invariance deficiency" in order to examine the above questions. As will be seen in the next section, the linearly dependent relation between invariance deficiencies of various orders furnishes us with the measure of the deviation from the strict invariance of the S-matrix. The linearly dependent relation contains, of course, the invariance condition as a special case. We shall not discuss, however, the mathematical criterion of the linear dependence of the invariance deficiencies.

It will be illustrated in sect. 3 that some of the known selection rules can be derived systematically in our formalism, and that the selection rule has meaning only when the interaction is weak. This situation is quite similar to that in which a selection rule is derived from the multipole expansion of the radiation-atom system, where the wave length of radiation is assumed to be long compared with the size of an atom.

2. The S-Matrix and the Selection Rule

It is our purpose to present a general theory of the S-matrix which may provide a framework capable of admitting non-invariant interactions. In (I) we have formulated the S-matrix theory, starting from the Schrödinger equation in the interaction picture, without recourse to the Heisenberg picture. The condition for the invariant S-matrix is obtained in an integral form, which is less restrictive than the ordinary one usually given in a differential form. We shall find it useful first to review briefly some matters which we had developed in paper (I).

We consider an infinitesimal transformation such that the interaction Hamiltonian $H(\tau)$ transforms

$$H(\tau) \to H'(\tau) = H(\tau)+K(\tau), \tag{2.1}$$

where $K(\tau)$ is a first order infinitesimal, and is generated by an infinitesimal Hermitian operator F^0 as

$$K(\tau) = i[F^0, H(\tau)]. \tag{2.2}$$

The S-matrix transforms under (2.1) as

$$S \to S' = \{1-iF(\infty)\}S = S+i[F^0, S], \tag{2.3}$$

that is,

$$[F^0, S] = -F(\infty)S, \tag{2.3'}$$

where

$$-F(\infty)S = -S\int_{-\infty}^{\infty} d\tau U^{-1}(\tau)K(\tau)U(\tau) \equiv J_{(0,1)}, \tag{2.4}$$

with

$$U(\tau) = I-i\int_{-\infty}^{\tau} d\tau' H(\tau')U(\tau'). \tag{2.5}$$

The quantity $J_{(0,1)}$ which we shall refer to as the (0,1)-th order invariance deficiency, can be given in powers of the coupling constant as

$$J_{(0,1)} = -\sum_{n=0}^{\infty} \frac{(-i)^n}{n!} \int_{-\infty}^{\infty} d\tau\, d\tau_1 \ldots d\tau_n T\{K(\tau), H(\tau_1), \ldots, H(\tau_n)\}. \tag{2.6}$$

As was shown in (I), the necessary and sufficient condition for the S-matrix to be invariant under (2.1) is

$$J_{(0,1)} = 0. \tag{2.7}$$

There exists a *constant of collision* associated with (2.1), if and only if (2.7) holds. In the representation in which F^0 is diagonal, that is,

$$F^0|f_i) = f_i|f_i) \quad (i = 1, 2, \ldots, N), \tag{2.8}$$

the S-matrix is also diagonal, since from (2.8), (2.7) and (2.3), it follows

$$(f'-f)(f'|S|f) = 0. \tag{2.9}$$

Here f and f' are any of $f_1, f_2, \ldots, f_N$.

We next consider the case where $J_{(0,1)}$ does not vanish. In order to treat this case systematically, one introduces quantities

$$J^{(l,m)} \equiv \underbrace{F^0 \ldots F^0}_{l} R \underbrace{F^0 \ldots F^0}_{m} \quad (l, m = 0, 1, 2, \ldots), \tag{2.10}$$

where $R = S - I$.

The matrix element of $J^{(l,m)}$ between $(f'|$ and $|f)$ is

$$(f'|J^{(l,m)}|f) = f'^l f^m (f'|R|f). \tag{2.11}$$

Since the $f'^l f^m$'s are linearly independent if $l, m \leqq N-1$, a linear relation

$$\sum_{l,m \leqq N-2} C^{(l,m)} f'^l f^m (f'|R|f) = 0 \tag{2.12}$$

gives the selection rule such that

$$(f'|R|f) = 0, \tag{2.13}$$

unless

$$\sum_{l,m \leqq N-1} C^{(l,m)} f'^l f^m = 0. \tag{2.14}$$

This equation furnishes the connection which must exist between f' and f in order that the R-matrix element $(f'|R|f)$ may not vanish. The equation (2.12) can be written in the operator form

$$\sum_{l,m \leqq N-1} C^{(l,m)} J^{(l,m)} = 0, \tag{2.15}$$

which implies the quantities $J^{(l,m)}$'s are linearly dependent. Conversely, if $(f'|R|f)$ obeys an absolute selection rule, one can find a linearly dependent relation (2.15).

From this standpoint, the invariance condition (2.7) is a special case of (2.15), namely,

$$J_{(0,1)} \equiv J^{(1,0)} - J^{(0,1)} = 0. \tag{2.16}$$

As is seen above, the violation of invariance is systematic, if there exists a linearly dependent relation between $J^{(l,m)}$'s. If all the $J^{(l,m)}$'s $(l, m \leqq N-1)$ are linearly independent, the selection rule does not follow. This case may be called the random violation of invariance.

If there exists more than one linearly dependent relation, say,

$$\sum_{l,m \leqq N-1} C^{(l,m)} J^{(l,m)} = 0, \quad \sum_{l,m \leqq N-1} C'^{(l,m)} J^{(l,m)} = 0, \tag{2.17}$$

the selection rule is given by the common roots of the equations

$$\sum_{l,m \leqq N-1} C^{(l,m)} f'^l f^m = 0, \quad \sum_{l,m \leqq N-1} C'^{(l,m)} f'^l f^m = 0. \tag{2.18}$$

The quantity $J^{(l,m)}$ introduced above is not convenient, however, for practical purposes, since it is usually difficult to calculate the multiple product of F^0 and R. We therefore define, instead of $J^{(l,m)}$, quantities

$$J_{(l,m)} \equiv \{\underbrace{F^0\{\ldots\{F^0}_{l}[\underbrace{F^0[\ldots[F^0}_{m}, R]\ldots]\}\ldots\}, \tag{2.19}$$

where l and m stand for the number of anti-commutators and commutators respectively. The order of anti-commutation and commutation does not matter, since, for two arbitrary operators A and B, we have

$$\{A[A, B]\} = [A\{A, B\}]. \tag{2.20}$$

The quantity $J_{(l,m)}$ will be referred to as the (l, m)-th order "invariance deficiency".

The relation between $J^{(l,m)}$ and $J_{(l',m')}$ can readily be found as

$$J^{(l,m)} = (\tfrac{1}{2})^{l+m} \sum_{l',m'} [l, m|l', m']J_{(l',m')} \tag{2.21}$$

or

$$J_{(l,m)} = \sum_{l',m'} [l, m|l', m']J^{(l',m')}, \tag{2.22}$$

where

$$[l, m|l', m'] \equiv \sum_{i=0}^{l'} \binom{l}{i}\binom{m}{l'-i}(-1)^{m-l'+i}\delta_{l+m,\,l'+m'} \tag{2.23}$$

with

$$\binom{l}{i} = \begin{cases} \dfrac{l!}{(l-i)!\,i!} & \text{for } l \geqq i, \\ 0 & \text{for } l < i. \end{cases} \tag{2.24}$$

We now suppose there exists a linearly dependent relation

$$\sum_{l=0}^{L}\sum_{m=0}^{M} C_{(l,m)}J_{(l,m)} = 0. \tag{2.25}$$

By using the transformation formula (2.22), one obtains

$$\sum_{l=0}^{L}\sum_{m=0}^{M}\sum_{l'=0}^{\infty}\sum_{m'=0}^{\infty} C_{(l,m)}[l, m|l', m']J^{(l',m')} = \sum_{l'=0}^{\infty}\sum_{m'=0}^{\infty} C^{(L,M)}_{(l',m')}J^{(l',m')} = 0, \tag{2.26}$$

which turns out to be

$$\sum_{l'=0}^{\infty}\sum_{m'=0}^{\infty} C^{(L,M)}_{(l',m')}f^{l'}f^{m'}(f'|R|f) = 0, \tag{2.27}$$

where

$$C^{(L,M)}_{(l',m')} \equiv \sum_{l=0}^{L}\sum_{m=0}^{M} C_{(l,m)}[l, m|l', m']. \tag{2.28}$$

It should be noticed, however, that one cannot immediately derive the selection rule from (2.27), because the $f^{\prime l'} f^{m'}$'s are linearly independent only when l' and m' are less than N †. This condition is always satisfied if

$$L+M \leqq N-1 \tag{2.29}$$

(sufficient condition).

We may therefore say that the linear relation (2.25) gives the selection rule when the relation (2.29) is fulfilled. For infinite N, any relation of the type (2.25) leads to the selection rule, as long as L and M are finite.

Summarizing our argument, one can state as follows:

(1) The S-matrix is invariant and F^0 is a constant of collision, if the relation

$$J_{(0,1)} = 0 \tag{2.30}$$

holds.

(2) If a relation

$$\sum_{l=0}^{L} \sum_{m=0}^{M} C_{(l,m)} J_{(l,m)} = 0 \tag{2.31}$$

holds for $C_{(l,m)}$ which are not identically zero ($J_{(0,1)} \neq 0$), the S-matrix is not invariant, but the violation of invariance is systematic. The selection rule follows from (2.31).

(3) If all the $J_{(l,m)}$'s are linearly independent, the invariance of the S-matrix is violated at random.

The above argument holds for $N = \infty$.

3. Examples

Some well-known examples will be discussed in this section, in order to illustrate the method presented in the previous section.

3.1. THE NUMBER OPERATOR

It is well known that the number of free particles is not conserved in the presence of an interaction. We shall show how this problem is fitted into our formalism.

Consider an infinitesimal phase transformation

$$\begin{aligned} \phi^{(+)}(x) \to \phi'^{(+)}(x) &= \phi^{(+)}(x)(1-i\alpha), \\ \phi^{(-)}(x) \to \phi'^{(-)}(x) &= \phi^{(-)}(x)(1+i\alpha), \end{aligned} \tag{3.1}$$

where $\phi^{(+)}$ and $\phi^{(-)}$ are positive and negative frequency parts of a neutral boson field $\phi(x)$, and α is an infinitesimal parameter. The number operator N^0 is introduced as

$$\begin{aligned} \phi'^{(+)}(x) &= (1+i\alpha N^0)\phi^{(+)}(x)(1-i\alpha N^0), \\ \phi'^{(-)}(x) &= (1+i\alpha N^0)\phi^{(-)}(x)(1-i\alpha N^0). \end{aligned} \tag{3.2}$$

† See subsection 3.3.

The comparison of (3.2) with (3.1) yields

$$[N^0, \phi^{(+)}(x)] = -\phi^{(+)}(x), \quad [N^0, \phi^{(-)}(x)] = \phi^{(-)}(x), \tag{3.3}$$

or

$$[N^0, \phi(x)] = i\phi^{(1)}(x), \quad [N^0, \phi^{(1)}(x)] = -i\phi(x), \tag{3.4}$$

where

$$\phi^{(1)}(x) = i[\phi^{(+)}(x) - \phi^{(-)}(x)]. \tag{3.5}$$

The S-matrix in iteration form is

$$S = 1 + R^{(1)} + R^{(2)} + \ldots \tag{3.6}$$

with

$$R^{(1)} = -i\int_{-\infty}^{\infty} \mathrm{d}^4x \mathscr{H}(x), \quad R^{(2)} = \frac{(-i)^2}{2!}\int_{-\infty}^{\infty} \mathrm{d}^4x_1 \mathrm{d}^4x_2 T[\mathscr{H}(x_1), \mathscr{H}(x_2)], \ldots, \tag{3.7}$$

where the interaction Hamiltonian density is assumed to be given by

$$\mathscr{H}(x) = \rho(x)\phi(x), \tag{3.8}$$

with a source function $\rho(x)$ which does not contain $\phi(x)$.

As is easily verified, $R^{(1)}$ satisfies

$$[N^0, [N^0, R^{(1)}]] = R^{(1)}, \tag{3.9}$$

which is a linearly dependent relation

$$J_{(0,2)} - J_{(0,0)} = 0. \tag{3.10}$$

We obtain therefore

$$\{(n'-n)^2 - 1\}(n'|R^{(1)}|n) = 0. \tag{3.11}$$

Hence, the selection rule is given by

$$\Delta n \equiv n' - n = \pm 1, \tag{3.12}$$

which agrees with the direct calculation of the $R^{(1)}$-matrix elements.

To obtain the selection rule for $R^{(2)}$, one calculates quantities

$$\begin{aligned}
&[N^0, \phi(x_1)\phi(x_2)] = i\phi^{(1)}(x_1)\phi(x_2) + i\phi(x_1)\phi^{(1)}(x_2), \\
&[N^0, [N^0, \phi(x_1)\phi(x_2)]] = 2\phi(x_1)\phi(x_2) - \phi^{(1)}(x_1)\phi^{(1)}(x_2), \\
&[N^0, [N^0, [N^0, \phi(x_1)\phi(x_2)]]] \\
&\qquad = 2[N^0, \phi(x_1)\phi(x_2)] + 2i\phi(x_1)\phi^{(1)}(x_2) + 2i\phi^{(1)}(x_1)\phi(x_2).
\end{aligned} \tag{3.13}$$

We thus arrive at the relation

$$[N^0, [N^0, [N^0, \phi(x_1)\phi(x_2)]]] = 4[N^0, \phi(x_1)\phi(x_2)]. \tag{3.14}$$

From (3.14) there follows the linearly dependent relation

$$J_{(0,3)} - 4J_{(0,1)} = 0. \tag{3.15}$$

The selection rule is consequently given by

$$(n'-n)^3-4(n'-n) = 0, \tag{3.16}$$

that is,

$$\Delta n \equiv n'-n = 0 \quad \text{or} \quad \Delta n = \pm 2. \tag{3.17}$$

It is remarked that the linearly dependent relation becomes complicated as the order of the R-matrix increases, and one cannot obtain any linear relation for the total R-matrix by a finite number of operations.

3.2. THE ISO-SPIN OPERATOR IN THE NUCLEON-PHOTON SYSTEM

We take the interaction

$$\mathscr{H}(x) = ie\bar{\psi}(x)\tfrac{1}{2}(1+\tau_3)\gamma_\mu\psi(x)A_\mu(x), \tag{3.18}$$

where $\psi(x)$ and $A_\mu(x)$ are nucleon and photon fields, respectively, and τ_3 the 3-rd component of iso-spin matrices which satisfy

$$[\tau_1, \tau_2] = 2i\tau_3 \quad \text{(cyclic)}. \tag{3.19}$$

The iso-spin operator T_i is defined by

$$T_i = \tfrac{1}{2}i\int \mathrm{d}\sigma_\mu\bar{\psi}(x)\gamma_\mu\tau_i\psi(x) \qquad (i = 1, 2, 3) \tag{3.20}$$

and

$$T^2 = T_1^2+T_2^2+T_3^2. \tag{3.21}$$

A short calculation shows that the equations

$$[T^2[T^2, \mathscr{H}_3(x)]] = 2\{T^2, \mathscr{H}_3(x)\}, \quad [T^2, \mathscr{H}_0(x)] = 0 \tag{3.22}$$

hold for

$$\mathscr{H}_3(x) = ie\bar{\psi}(x)\tfrac{1}{2}\tau_3\gamma_\mu\psi(x)A_\mu(x), \quad \mathscr{H}_0(x) = ie\bar{\psi}(x)\tfrac{1}{2}\gamma_\mu\psi(x)A_\mu(x). \tag{3.23}$$

Consequently, we have

$$[T^2[T^2[T^2, R^{(1)}]]] = 2[T^2\{T^2, R^{(1)}\}], \tag{3.24}$$

since

$$R^{(1)} = -i\int_{-\infty}^{\infty} \mathrm{d}^4x\{\mathscr{H}_0(x)+\mathscr{H}_3(x)\}. \tag{3.25}$$

Eq. (3.24) is, in terms of $J_{(t,m)}$,

$$J_{(3,0)}-2J_{(1,1)} = 0, \tag{3.26}$$

which gives the selection rule

$$\{t'(t'+1)-t(t+1)\}^3-2\{t'(t'+1)-t(t+1)\}\{t'(t'+1)+t(t+1)\} = 0, \tag{3.27}$$

that is,

$$(t'+t+1)(t'+t+2)(t'+t)(t'-t)(t'-t-1)(t'-t+1) = 0. \tag{3.28}$$

Since t and t' are non-negative, (3.28) is fulfilled if

$$\Delta t \equiv t'-t = 0 \quad \text{or} \quad \Delta t = \pm 1. \tag{3.29}$$

3.3. THE SELECTION RULE FOR A FINITE MATRIX

As an example of N being finite, we wish to discuss a simple operator, such that

$$F^0 = \begin{pmatrix} 1 & 0 \\ 0 & -1 \end{pmatrix}. \tag{3.30}$$

We now suppose relations

$$J_{(1,0)} = \{F^0, R\} = 0, \quad J_{(0,1)} - 2J_{(0,0)} = [F^0, R] - 2R = 0, \tag{3.31}$$

are fulfilled. From (3.30) and (3.31), we obtain

$$(f'+f)(f'|R|f) = 0, \quad (f'-f-2)(f'|R|f) = 0. \tag{3.32}$$

Therefore, $(f'|R|f)$ vanishes, unless

$$f'+f = 0, \quad f'-f = 2, \tag{3.33}$$

that is,

$$f' = 1, \quad f = -1. \tag{3.34}$$

The R-matrix therefore has the form

$$R = \begin{pmatrix} 0 & R_{12} \\ 0 & 0 \end{pmatrix}. \tag{3.35}$$

Notice here that the relations (3.31) fulfil the condition $L+M \leqq N-1$, since

$$L+M = 1, \quad N-1 = 1. \tag{3.36}$$

Thus the selection rule (3.34) has been obtained. One can, however, find a relation

$$J_{(1,1)} = [F^0\{F^0, R\}] = [F^0 F^0, R] = 0, \tag{3.37}$$

since

$$F^0 F^0 = \begin{pmatrix} 1 & 0 \\ 0 & 1 \end{pmatrix}. \tag{3.38}$$

Such a relation (3.37) is an identity which does not fulfil $L+M \leqq N-1$, and therefore leads to no selection rule.

4. Discussion

We have formulated a general kinematical method of handling the non-invariant S-matrix. Although this formulation may not be very useful from the practical viewpoint, it furnishes us with an interesting aspect of the S-matrix

theory in view of the fact that it is observed that, in weak interaction between elementary particles, some of the invariance properties are destroyed. A selection rule such as $\Delta S = \pm 1$ in the weak interaction indicates that the invariance deficiencies introduced in sect. 2 are not all linearly independent. It is noticed, however, from the examples given in sect. 3 that the selection rule has a meaning only in an approximate sense, as long as one uses the ordinary definition of the S-matrix given by the interaction Hamiltonian. The reason is that the unitarity of the S-matrix, which is a kind of non-linear relation, is not compatible with a linear relation such as (2.15). This may be a clue to understanding the reason why "the stronger the interaction, the greater the number of symmetries it will possess".

Let us suppose there be a strong interaction which is not invariant. Since the interaction is strong, the perturbation expansion would not be valid, and the higher order terms become more and more important. Consequently, the linearly dependent relation of the invariance deficiencies will become very complicated, or may not exist at all. Therefore, it would become useless to think about such a transformation to assign a quantum number. In other words, one gives up, from the beginning, discussing any transformation under which strong interactions are not invariant. Such an example is discussed in subsection 3.1, where the interaction is not invariant under (3.1). This may be one of the reasons why the strong interaction seems to be more symmetric than the weak interaction.

We recall finally the important role played by the selection rules in the correspondence theory before quantum mechanics was discovered, where the simple quantum condition was interrupted by various selection rules to give only particular couplings of spectrum terms. The present situation of the phenomenology of elementary particles might be similar to that of atomic spectra at the dawn of quantum mechanics, as most physicists may expect. It is hoped that the investigation of the selection rule along the line described in this paper may clarify one aspect of the S-matrix theory.

Reference

1) S. Kamefuchi and Y. Takahashi, Nuclear Physics **17** (1960) 686;
See also: E. Arnous, W. Heitler and Y. Takahashi, Nuovo Cim. **16** (1960) 671

3.B

Nuclear Physics **20** (1960) 630—647; © *North-Holland Publishing Co., Amsterdam*

Not to be reproduced by photoprint or microfilm without written permission from the publisher

THE ELECTRON SPECTRUM OF $_{81}Tl^{199}$

B. JUNG and J. SVEDBERG

The Gustaf Werner Institute for Nuclear Chemistry, University of Uppsala, Uppsala

Received 12 July 1960

Abstract: The electron spectrum between 5.75 and 950 keV of mass separated Tl^{199} sources was studied in a double focusing β-spectrometer, adjusted to a momentum resolution of about 0.4 %. The experimental findings are in accordance with the following level sequence in Hg^{199}: ground state $(\frac{1}{2}-)$, 158.4 $(\frac{3}{2}-)$, 208.2 $(\frac{3}{2}-)$, 403.4 $(\frac{1}{2}-)$, 455.4 $(\frac{1}{2}-)$ and 492.2 keV $(\frac{5}{2}-)$. The half-life of Tl^{199} was measured as 7.42 ± 0.08 h. The K- and L-Auger spectra of mercury are briefly discussed.

1. Introduction

In the region of spherical nuclei around Pb^{208} only those very close to the doubly magic nucleus are susceptible to a detailed theoretical analysis, particularly of the energies of the excited states. For a synthetic description of the other nuclei in this region, the systematic treatment of characteristics of nucleides differing by two neutrons or protons [1, 2]) seems to offer rather promising properties, pending a more fundamental theoretical approach. As recently discussed by Herrlander *et al.* [3]) such a treatment of the low-lying, low-spin states of odd mass mercury isotopes demands a more detailed knowledge of the level schemes than is now available. In order to fill this need the present investigation was undertaken. It will be followed by a similar study, almost finished, of the levels in Hg^{197}, and it is our intention also to study the levels in Hg^{195}. We hope that after finishing this series the information will be sufficient for a systematic analysis.

Tl^{199} was first reported by Orth *et al.* [4]). The conversion electron spectrum has been studied by Israel and Wilkinson [5]) and by Bergström *et al.* [6]). The latter group also proposed a decay scheme. However, a reinvestigation of the decay of Tl^{199} was considered worthwhile as the earlier investigators have given very limited information on the intensities of the γ-transitions. Also the mass separation facilities at this institute would put us in a favoured position with regard to the purities of the sources.

It should be remarked that some of the excited levels of Hg^{199} also can be studied in the decays of Hg^{199m} (42 min) and Au^{199} (3.15 d). Recent precision measurements by Bäckström *et al.* [7]) of conversion lines in the decay of Au^{199} have provided suitable internal energy standards.

2. Experimental Procedures

2.1. SOURCE PREPARATIONS

All sources were prepared in the electromagnetic mass separator [8, 9]) of this institute. The activities were fed to the ion source oven as TlCl, and the Tl^{199+} ion current was collected directly on 2 mg/cm² aluminium foils, having dimensions of approximately 1.5×25 mm. This yields carrier-free sources, but the finite penetration of the ions into the backing material [10]) might give rise to energy straggling of the emerging electrons. As the penetration depth can be calculated to be about 3 μg/cm², this effect is certainly rather limited. The energy straggling will be most easily detected for low electron energies, and as an indication of the weakness of the effect, it can be mentioned, that a 22 and a 201 keV conversion line, when measured in the same run, were obtained with half-widths of 0.52 and 0.46 %, respectively. The L-Auger lines with an energy of about 7 keV appear, however, to be considerably broadened. The L-Auger spectrum is very complex, and it is therefore difficult to judge whether the broadening is caused by source thickness effects or a superposition of lines. The overall efficiency resulting from the mass separation as well as the amount of admixture of adjacent isotopes in the sources has been discussed in connection with a study [11]) similar to the present one.

The thallium activities were normally produced by bombardments of natural mercurous chloride with 55 MeV protons in the Werner synchrocyclotron. Standard procedures were applied for the chemical separations [12]). Sources of this kind will be referred to as *type A*. As it was found that impurities of Tl^{198m} (1.9 h) in these sources gave conversion lines interfering with important lines in the Tl^{199} spectrum, two special sources, referred to as *type B* were prepared. The thallium activities fed to the ion source of the mass separator, when preparing these sources, were obtained in the decay of lead activities produced by bombardments of natural thallium with 85 MeV protons. As the isomeric level in Tl^{198} is not fed to a detectable degree in the decay of Pb^{198} (2.4 h) [13]), these sources were free from Tl^{198m} impurities. The chemical procedures applied have been described elsewhere [14]).

For the energy calibration of the electron spectrum a source of type A was used, on which an active deposit of ThB (Pb^{212}) had been collected prior to the mass separation by the usual electrostatic deposition method in a vessel containing RdTh (Th^{228}). Care was taken that both activities were placed on the same area of the aluminium strip. This source will be referred to as *type C*.

2.2. β-SPECTROMETER MEASUREMENTS

The double focusing β-spectrometer [15]) of this institute has recently been equipped with an automatic device for recording the electron spectrum. The spectrometer current is changed in equal steps, and in each position the number of counts during a preset time is numerically printed out. The equipment

allows 500 successive points to be measured without manual operation, except for spectrometer current readings measured manually at suitable intervals. A detailed description of the new outfit will appear elsewhere [16]).

Full advantage of the automatic operation was taken in the present investigation, although a few calibration lines were measured manually. It was found that the stepping device was linear within the limits of error in the current measurements and in order to use this fact a least squares fit of the spectrometer current as a linear function of the step number was made for each automatic run. To illustrate the linearity of the automatic stepping device it can be mentioned that in one run, when the spectrometer current in 42, evenly spaced, steps was measured, the deviation between the measured values and those obtained from the least squares analysis was found to be less than 1 part in 10^4 for 23 steps and less than 2 parts in 10^4 for 41 steps. The spectrometer was adjusted to a momentum resolution of about 0.4 %, so that it was found favourable to spread the 500 automatically recorded points over a momentum interval with a ratio of about 1.4 between the last and first setting in order to have a convenient number of points over each conversion line. The counting time per point varied between 19 and 49 s depending on the source strength and the energy region being studied, the lower energy region usually giving higher counting rates. The decays of the lines were followed by repeated measurements and from the half-lives obtained it was often possible to discriminate against impurities in the sources. Fig. 1 has been included in order to show the general appearance of the automatic runs.

The energy calibration of the electron spectrum was made with the type C source. The ThA, ThB, ThF and ThI lines (in the notation used by Siegbahn and Gerholm [17])) were measured in the same run as L_I 36, L_I 50, K 158, L_{II} 158, K 247, L 208, K 334 and K 455 in the decay of Tl^{199} (cf. table 1). As always, the spectrometer current was increased monotonically during the run. From corresponding values of the spectrometer current I and the magnetic rigidity $B\rho$ of the measured ThB lines, as given by Siegbahn and Gerholm [17]) a curve of $B\rho/I$ versus log I was constructed. It has been shown by Arbman [18]) that this procedure yields a straight line in the energy region of interest here. The energy values obtained from this calibration curve for the 50, 158 and 208 keV transitions (cf. subsection 3.1) agreed well within the limits of error with those given by Bäckström *et al.* [7]), who studied Au^{199} sources. Their energies, being more accurate than ours, were adopted as energy standards and used together with our energies for the other Tl^{199} lines measured with the type C source for the energy calibration of the individual, automatically recorded parts of the spectrum.

The K 208 and K 455 keV conversion lines served as intensity standards and were recorded for every source. The relative intensities of the conversion lines were obtained from the plots by the use of a planimeter and corrections

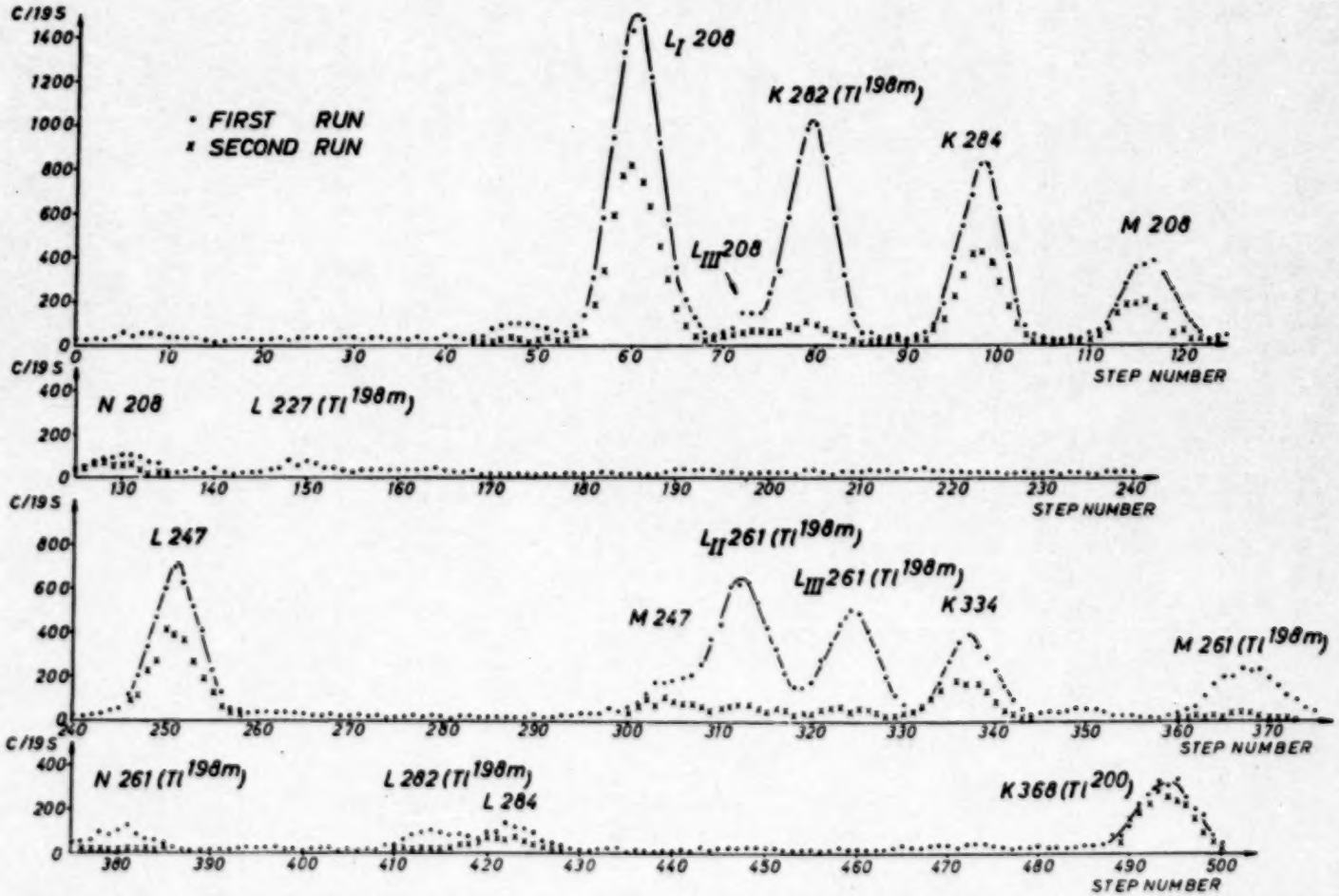

Fig. 1. Automatically recorded part of the conversion electron spectrum. Counting time per point is 19 s. Time elapsed between consecutive steps is 20 s. The second run was started 404 min after the start of the first run. For convenience only parts of the second run have been plotted. Step number 0 corresponds to $B\rho = 1557$ G · cm, step number 500 to $B\rho = 2042$ G · cm.

TABLE 1

Internal conversion lines in the decay of Tl^{199}.

Conversion ratios within parentheses are interpolated from Rose [33]) and Sliv and Band [34]) for the suggested multipole order. Mean values are given where the two theoretical calculations differ. The transitions are commented on in the text.

Adopted energy and multipole order	Conv. shell	Electron energy (keV)	Rel. electron intensity (K 208 = 100)	Half-life (h)	Conversion ratios		
36.83 ±0.03	L_I	21.99 ±0.03	2.3±0.3	≈7	L_I/L_{II}	≈ 10	(10)
M1	M_I	33.32 ±0.08	0.8±0.2		L/M	= 3 ± 1	
49.817±0.015	L_I	(34.974±0.015)	39.5±4.0	7.8 ±0.5	L_I/L_{III}	= 61 ±12	(99)
M1+(0.1 % E2)?	L_{II}	35.59 ±0.07	3.9±0.5		L_{II}/L_{III}	= 6 ± 2	(10)
	L_{III}	37.58 ±0.11	0.7±0.2		L/M	= 4.8± 0.5	
	M_I	46.27 ±0.14	9.1±1.4	7.4 ±1.0	M/N	= 3.1± 0.3	
	N_I	49.07 ±0.14	2.9±0.6		N/O	= 5 ± 2	
	O_I	49.79 ±0.14	0.6±0.2				
51.93 ±0.06	L_I	37.08 ±0.06	2.0±0.4	7 ±2	L_I/L_{III}	> 5	
M1	M_I	48.40 ±0.13	0.7±0.2		L/M	= 3 ± 1	
158.359±0.025	K	(75.265±0.025)	15.0±2.3	7.4 ±0.7	K/L	= 0.6± 0.2	(0.63)
E2	L_{II}	(144.145±0.025)	15.8±2.3	8.1 ±0.8	L_I/L_{II}	< 0.3	(0.15)
	L_{III}	(146.073±0.025)	9.3±1.0	7.4 ±0.7	L_I+L_{II}/L_{III}	= 1.7± 0.3	(1.64)
	M_{II}	155.2 ±0.2	7.0±1.0	7.7 ±1.0	L/M	= 3.6± 0.4	
	N_{II}	157.6 ±0.3	1.6±0.4	8.3 ±2.0	M/N	= 4.4± 1.0	
195.1 ±0.2	K	112.0 ±0.2	2.8±0.4	6 ±2	K/L	= 5.3± 1.0	(6.1)
M1	L_I	180.1 ±0.5	0.5±0.1				
208.176±0.030	K	(125.086±0.030)	100	7.42±0.08	K/L	= 5.1± 0.6	(5.6)
89 % M1+11 %E2	L_I	(193.328±0.030)	18.6±1.9	7.6 ±0.8	L_I/L_{III}	= 20 ±10	(22)
	L_{III}	195.7 ±0.6	1.1±0.4		L/M	= 4.4± 0.5	
	M_I	204.5 ±0.2	4.4±0.7	6.6 ±1.0	M/N	= 4.4± 1.0	
	N_I	207.4 ±0.3	1.0±0.3	9 ±2			
247.2 ±0.1	K	164.1 ±0.1	48.5±5.0	6.7 ±0.7	K/L	= 5.4± 1.1	(6.2)
M1	L_I	232.2 ±0.3	9.0±1.5		L_I/L_{II}	> 20	
284.0 ±0.1	K	200.9 ±0.1	8.7±0.9	7.6 ±0.7	K/L	= 5.8± 1.5	(6.2)
M1	L_I	269.2 ±0.5	1.5±0.4				
333.9 ±0.2	K	250.8 ±0.2	4.2±0.6	≈7	K/M	> 16	
M1							
403.5 ±0.4	K	320.4 ±0.4	2.6±0.8	7 ±1	K/L	> 3	
M1	L_I	388.6 ±0.7	0.5±0.2				
455.1 ±0.5	K	371.9 ±0.5	14.8±0.8	7.4 ±0.7	K/L	= 5.3± 1.3	(6.1)
M1	L_I	440.0 ±1.1	2.8±0.6		L/M	= 4.0± 1.2	
	M_I	451.6 ±1.1	0.7±0.2				
491.8 ±0.8	K	408.7 ±0.8	1.0±0.4		K/L	≈ 3	
M1	L_I	477 ±2	0.3±0.2				

for decay were applied. As the counter window was made of 0.9 mg/cm² Mylar film when electrons of energies larger than 100 keV were measured and of about 0.05 mg/cm² VYNS for electrons below this energy, only the L 37 keV conversion line had to be corrected for the absorption of electrons in the counter window [19]). Also the L-Auger spectrum should be corrected for this effect but as the correction in this case would be rather uncertain because of the low energy it has not been applied. The appreciable broadening of the lines in this spectrum might be caused by source thickness effects which should also influence the measured intensity distribution in a way, difficult to correct.

3. Results and Discussion

3.1. CONVERSION ELECTRON SPECTRUM

The information on γ-transitions in the decay of Tl^{199}, gained in the present investigation, is listed in table 1. The limits of error given in the table are meant to be maximal. The accurate values for the energies of the 50, 158 and 208 keV transitions are taken from the work of Bäckström *et al.* [7]) and the energies of the conversion lines of these transitions, which served as energy standards are put in parentheses. It should be remarked that very recently Bäckström *et al.* [20]) have recalculated these transition energies as 49.830, 158.396 and 208.226 keV. The influence of these changes on our results is certainly rather limited and it was not considered worthwhile to recalculate our energies, especially as the situation regarding the energy of the 158 keV transition is not very clear at present, de Vries [21]) having reported a value of 158.335±0.015 keV. Like Bäckström *et al.* [7]), de Vries measured Au^{199} sources. From comparison of the conversion ratios and the transition energies we are confident in treating the 50, 158 and 208 keV transitions in the decays of Au^{199} and Tl^{199} as identical. With the type C source we obtained the energy values 49.74±0.04, 158.36±0.05 and 208.11±0.13 keV. The somewhat low value of the first transition may be explained by interference from a 48 keV transition in the decay of Tl^{198m} [12]), this nucleide being present in the source as an impurity.

The following remarks apply to the different transitions.

37 keV

This is a new transition. The mass assignment of the L 37 keV conversion line must be considered well established. Impurities of Tl^{198} and Tl^{200} are the only ones expected, and the latter can be excluded by the half-life, the former by the fact that the L 37 keV line was found to be about the same intensity as the K 412 keV line in the decay of Tl^{198} [6, 11]) when measured with a type B source. An upper limit of L_I 37/K 412 of 0.01 can be calculated from the original spectra obtained by Jung [11]) of mass separated Pb^{198} sources with grown-in Tl^{198} activity. The relative intensity of the L_I 37 keV line was found

to be the same within 30 % when measured with type A and type B sources. The conversion shell assignment of this line is, however, less certain. Conversion in the M or N shell can be excluded as corresponding N or M lines would then have been found, but conversion in the K shell cannot be ruled out. We prefer the L_I assignment because a corresponding M_I line was found as well as a very weak indication of an L_{II} line. The M line was measured with a type B source and possible influence from the near-lying L_I 48 keV line in the decay of Tl^{198m} [12]) was thus eliminated. It should be remarked, however, that the line interpreted as M 37 might be explained as a K 116.5 keV line in the decay of Tl^{200} [22]). Israel and Wilkinson [5]) seem to prefer a K shell assignment as they ascribe a 103 keV γ-transition to the decay of Tl^{199}, the K conversion line of which may be identical with our L_I 37. The 37 keV transition fits nicely into the proposed decay scheme (cf. fig. 5) which may be taken as a further indication that our interpretation is correct. It should be pointed out, however, that although Bergström *et al.* [6]) expected a transition at this place in the level scheme, they did not find any corresponding conversion lines. The M1 multipole order follows from the high L_I/L_{II} ratio.

50 keV

L_{III} 50 and L_{II} 52 coincide and the intensity of L_{III} 50 has been corrected for an L_I/L_{II} ratio of the 52 keV transition equal to 10. Bäckström *et al.* [7]) found a (0.19 ± 0.06) % admixture of E2 into the mainly M1 transition and our L_I/L_{III} ratio, which is somewhat too low for a pure M1 transition (cf. the theoretical ratio in table 1), indicates a similar amount of admixture, namely 0.1 %. Very recently Nall *et al.* [23]) have reported a $(3.3\pm1)\times10^{-4}$ E2 admixture.

52 keV

The mass assignment of the L conversion line of this new transition is well established. The measured half-life is incompatible with a Tl^{200} assignment and Tl^{198} can be excluded since the K 412 keV conversion line in this decay was found to have about the same intensity as L 52 when measured with a type B source. From the measurements by Jung [11]) the intensity ratio L 52/K 412 in the decay of Tl^{198} (5.3 h) can be estimated as less than 0.02. The relative intensity of the L 52 keV line was found to be constant within 30 % when measured with type A and B sources. For this line conversion in the K shell cannot be ruled out, but we prefer the L_I assignment as a corresponding M_I line was found and as the proposed decay scheme nicely accommodates a 52 keV transition. The M1 multipole order follows from the high L_I/L_{III} ratio. The L_{II} line is hidden in L_{III} 50.

158 keV

The L_{II} intensity given in table 1 also includes a possible L_I conversion line.

195 keV

Bergström *et al.* [6]) associate a 195 keV transition with the decay of Tl^{198} (5.3 h). Knight and Baker [24]) report a short-lived component of the same transition, thus indicating that it is also fed in the decay of Tl^{198m} (1.9 h). We are, however, convinced that the 195 keV transition belongs to the decay of Tl^{199}. The K and L conversion lines were studied both with type A and B sources, and the relative intensities were found to be the same within 30 % in both cases. With the type B source we found a ratio of about 1 between K 195 and K 412 in the decay of Tl^{198}. A renewed inspection of the primary conversion electron spectra recorded in the study of the decay of Pb^{198} [11]) revealed that the intensity of a possible K 195 keV conversion line in the decay of Tl^{198} (5.3 h) is less than 2 % of K 412. Nor does there seem to be a 195 keV transition in the decay of Tl^{198m} (1.9 h). A conversion electron spectrum obtained from a mass separated source in a study of Tl^{198m} [2]) was reinvestigated and although a weak indication of a line which could be K 195 was found, the intensity of this line could well be explained by the presence of Tl^{199} impurities in the source, as judged from the intensity of other Tl^{199} conversion lines in the spectrum.

208 keV

The K line of this transition was chosen for the measurement of the half-life of Tl^{199}. The line was focused in the β-spectrometer and the decay was followed for 7 half-lives as can be seen from fig. 2. A least squares analysis of the decay

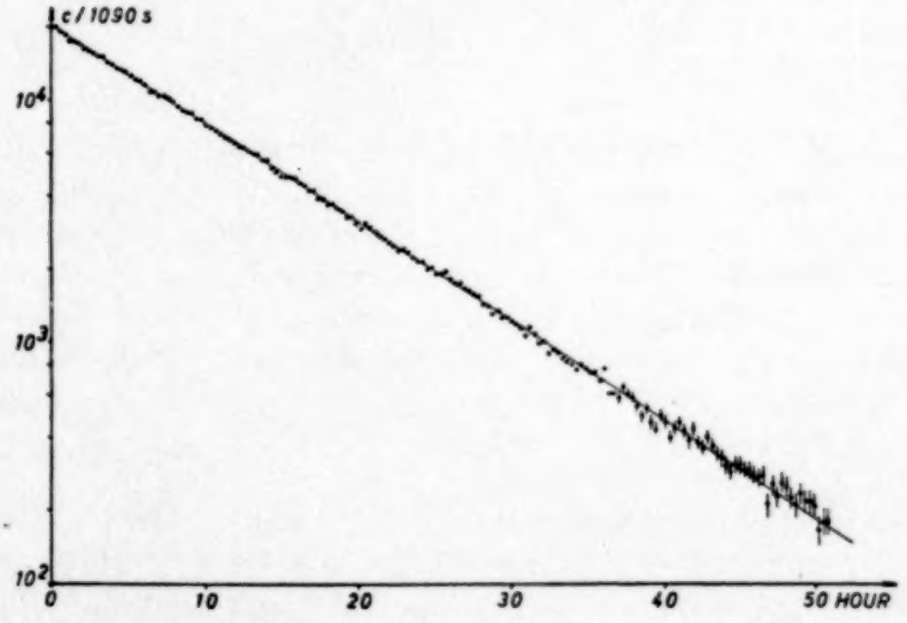

Fig. 2. Semilogarithmic plot of the decay curve of K 208 keV. Counting time per point is 1090 s, time elapsed between consecutive points is 1100 s. Correction has been applied for a background of 300 counts/1090 s.

curve yielded a half-life of 7.42 ± 0.08 h, three fourths of the error in which arises from possible shifts in line positioning and counter efficiency. The new value is in good agreement with the earlier value 7.4 ± 0.2 h reported by Michel and Templeton [25]). Bäckström *et al.* [7]) found an (11 ± 3) % E2 admixture in this transition and Nall *et al.* [23]) (11.3 ± 1) %. We cannot obtain the mixing ratio with this high an accuracy and have therefore adopted a value of 11 % when calculating the total transition intensity of the 208 keV transition.

247 keV

The assignment of the multipole order is strengthened by the measurements of Bergström *et al.* [6]) who report an L_I/L_{II} ratio of about 10 and no indication of an L_{III} line. We found an indication of an M line, the L/M ratio being about 4.

284 keV

Bergström *et al.* [6]) and Knight and Baker [24]) have reported a transition of this energy in the decay of Tl^{198} (5.3 h). Our half-life for the K line indicates, however, that the transition belongs to the decay of Tl^{199}; the fact that the K line showed up with an intensity about 6 times that of the intense K 412 keV line in the decay of Tl^{198} when measured with a type B source also confirms this assignment. This ratio is about 300 times higher than that which can be obtained from the measurements of mass separated $Pb^{198}+Tl^{198}$ sources by Jung [11]). The relative intensity of the K 284 keV line was found to be constant within 30 % when measured with type A and B sources. We are thus confident in the assignment of a 284 keV transition to the decay of Tl^{199}. An indication of an M line was found, having an intensity about $\frac{1}{4}$ of the L line.

334 keV

From a measurement of the K/L ratio of this transition by Wilkinson [26]), Bergström *et al.* [6]) suggested an E2 assignment. The apparently low K/L ratio seems, however, to be caused by a K 404 keV conversion line, superimposed on the L 334 keV line. We have found a lower limit of 16 for the K/M ratio of the 334 keV transition, which when taken together with the empirical thumb-rule $L/M \approx 3$ gives the lower limit of the K/L ratio as 5, thus suggesting an M1 multipole order.

404 keV

As discussed in connection with the 334 keV transition, the K 404 keV conversion line coincides with the L 334 keV line. A 402 keV transition, probably identical with our 404 keV transition, has earlier been ascribed to the decay of Tl^{198} [6]), but we are strongly in favour of an assignment to the decay of Tl^{199} since the half-life of the K 404+L 334 complex was measured as 7 ± 1 h and since a type B source gave a ratio of 2 between this complex and the K 412 keV

line in the decay of Tl^{198} [6, 11]). This ratio can be calculated as less than 0.002 from the spectra of Jung [11]). The relative intensity of K 404+L 334 was found to be constant within 30 % when measured with type A and B sources. In table 1 the intensity of the K 404 keV line has been corrected for a K/L ratio of the 334 keV transition of 6.

492 keV

The K and L lines were measured with rather poor statistics and the M 412 conversion line in the decay of Tl^{198} [6, 11]) interfered with the K line. The M1 assignment is strengthened by the measurement of Bergström *et al.* [6]) who report the absence of an L_{III} conversion line.

Table 1 contains all transitions interpreted by Bergström *et al.* [6]) to be involved in the decay of Tl^{199}. Israel and Wilkinson [5]) report two additional ones, namely 78 and 103 keV transitions. The conversion line which they interpret as K 103 might be identical with our L_I 37. An L 103 conversion line would have an intensity less than 1 % of K 208. An L 78 keV conversion line has an upper intensity limit of 1 % of K 208, if it is not hidden in the KLM-Auger group. An M_I 78 keV conversion line could be hidden in K 158. We thus conclude that evidence was found neither for a 78 nor for a 103 keV transition in the decay of Tl^{199}.

TABLE 2

Interpretation of lines identified as due to impurities

Nucleide	Transition energy (keV)	Lines observed
Tl^{198} (5.3 h)	227	K, L
	412	K, L, M
	676	K
Tl^{198m} (1.9 h)	48	L, M, N
	260	K
	261	K, L, M, N
	283	K, L, M
	442	K
	586	K
	635	K
Tl^{200} (26 h)	368	K, L, M, N
	579	K, L
	629	K
	829	K, L

Table 2 contains those conversion lines which were interpreted as due to impurities. As the lines were recorded from different sources it is not worthwhile giving any intensity relations.

3.2. K-AUGER SPECTRUM

With the resolution used in the present work the KLL-lines could at least partially be resolved. Less structure was, however, found in the KLM etc.

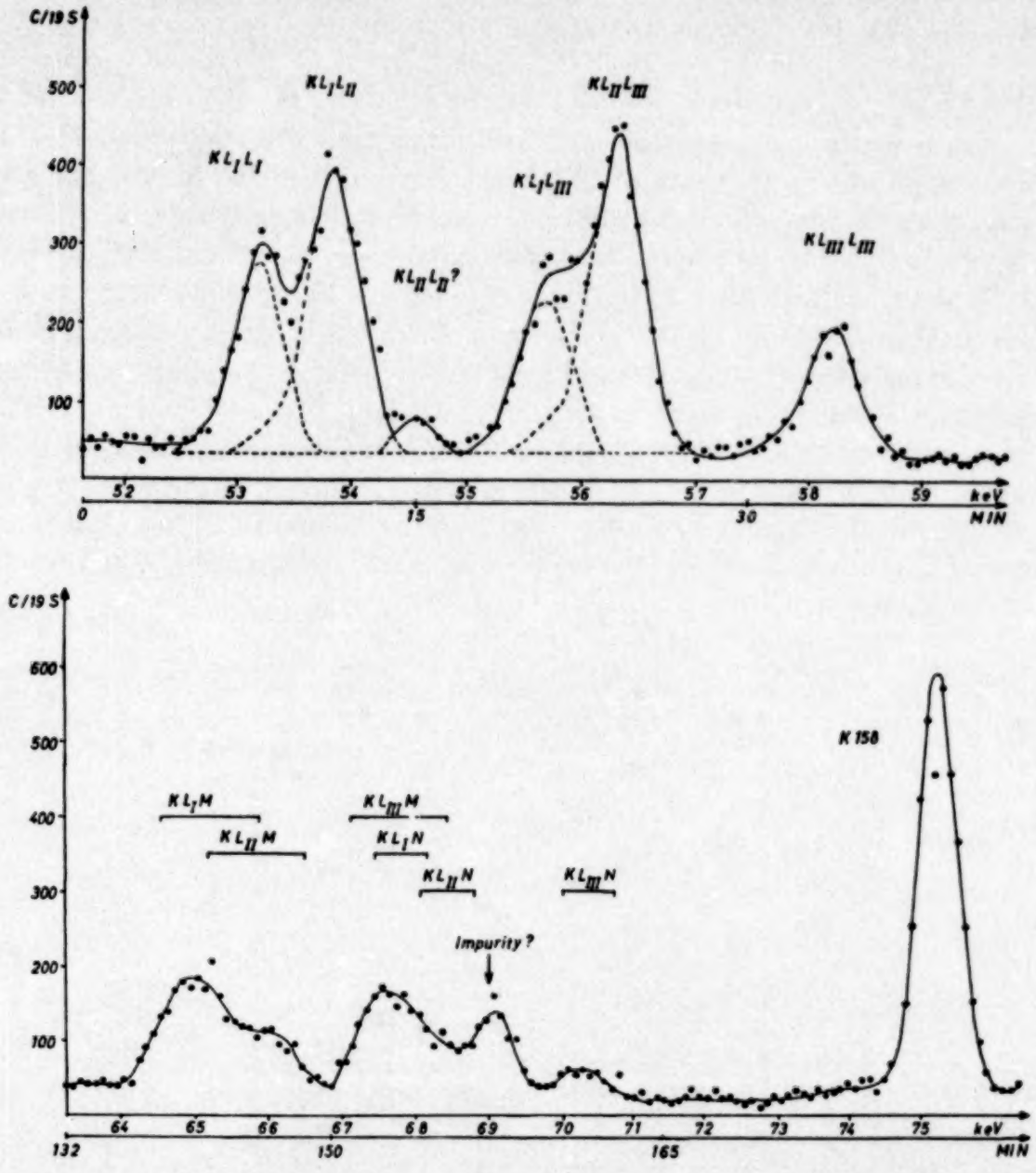

Fig. 3. The K-Auger spectrum of a Tl^{199} source. The abscissa is actually linear in the spectrometer current, but for convenience the energy scale has been indicated. The figure is composed of parts of two automatic runs, which explains the break in the time scale. The counting time per point is 19 s. The peak marked "impurity" has a half-life of less than 3.5 h.

groups as can be seen from fig. 3, where the K 158 keV conversion line is included for intensity comparison. It should be remarked that owing to the presence of impurities in the source the intensity comparison is not very exact.

TABLE 3

The KLL-Auger spectrum of mercury

Transition	Energy (keV)				Relative intensity †			
	Calculated Asaad [27])	Experimental			Calculated Asaad [27])	Experimental		
		Bergström and Hill [28])	Nall *et al.* [22])	this work		Herrlander *et al.* [3])	Nall *et al.* [22])	this work
KL_IL_I	53.293	53.18±0.04	53.56	53.12±0.07	1.00	0.88±0.09	1.00	1.00
KL_IL_{II}	53.713	53.79±0.04	54.19	53.80±0.07	1.44	1.48±0.11	1.32±0.1	1.48±0.11
KL_IL_{III}	55.780	55.71±0.04	56.15	55.67±0.14	0.82	0.75±0.09	0.85±0.06	0.79±0.08
$KL_{II}L_{II}$	54.133	54.32	55.07	54.5 ±0.2	0.09	0.12±0.06	0.40±0.03	0.19±0.10
$KL_{II}L_{III}$	56.199	56.35±0.05	56.73	56.34±0.07	1.46	1.62±0.13	1.28±0.08	1.69±0.16
$KL_{III}L_{III}$	58.266	58.27±0.05	58.70	58.27±0.07	0.66	0.67±0.07	0.76±0.05	0.69±0.07

† Herrlander *et al.* [3]) give the relative intensities in a scale adjusted to Asaad's values by a weighted mean-square method, the other relative intensities are normalized to $KL_IL_I = 1.00$

Asaad [27]) has made a relativistic calculation of the energies and relative intensities of the lines in the KLL-Auger spectrum of mercury. The theoretical results are compared in table 3 with the experimental findings of Bergström and Hill [27]), Herrlander *et al.* [3]), Nall *et al.* [23]) and the present work. Bergström and Hill concentrated on the energies of the lines which they obtained from what seems to have been a mixture of thallium isotopes. Herrlander *et al.* measured Tl^{201} sources and report only on the relative intensities of the lines and Nall *et al.* studied sources of Au^{199}.

In general there is a good agreement between theory and experiment, and only for the $KL_{II}L_{II}$ line there seems to be a slight discrepancy both regarding the relative intensity and the energy. It should be remarked, however, that if the $KL_{II}L_{II}$ line has the energy given by Asaad [27]), it might well be hidden in the much stronger $KL_{I}L_{II}$ line in our measurement. One would then have to find another explanation for the line interpreted here as $KL_{II}L_{II}$. The fact that it shows up at about the same position in the present work as in the measurements by the three other groups [3, 23, 28]) strongly suggests that it is of Auger origin since the four measurements were performed on different decays. Preliminary results on a measurement [29]) of the K-Auger spectrum emitted in the decay of Tl^{197} supports this conclusion.

3.3. L-AUGER SPECTRUM

Although we were by no means able to resolve the complicated L-Auger spectrum, our findings might be of some value, as there appears to be very limited information regarding this spectrum in the literature. Haynes and Achor [30]) have measured the L-Auger spectrum emitted in the decay of Au^{199} but their resolution was inferior to ours. Very recently Nall *et al.* [23]) have measured the same spectrum with a resolution of about 1 % which is somewhat higher than ours (approximately 1.5 %). As our spectrum was measured in a different decay, it is still of some interest.

Sujkowski and Slätis [31]) have studied the L-Auger spectrum of ThB sources, and as they used a high resolution spectrograph (resolution better than 0.1 %) they were able to resolve and interpret the more prominent lines in the L-Auger spectra of bismuth and thallium. Neglecting a possible dependence on atomic number, our spectrum should resemble that of Sujkowski and Slätis [31]) when the relative intensity distribution of Auger-lines caused by the same L-shell vacancies is compared. The distribution of primary L-shell vacancies cannot, however, be expected to be the same, as they are generated in different processes.

We refrain from any attempts to analyse the spectrum but give in fig. 4 merely the measured intensity distribution. No correction was applied for the absorption of the electrons in the counter window (about 0.05 mg/cm^2) although this correction is not negligible. The expected positions of the more prominent lines as judged from the work of Sujkowski and Slätis [31]) are indicated. The

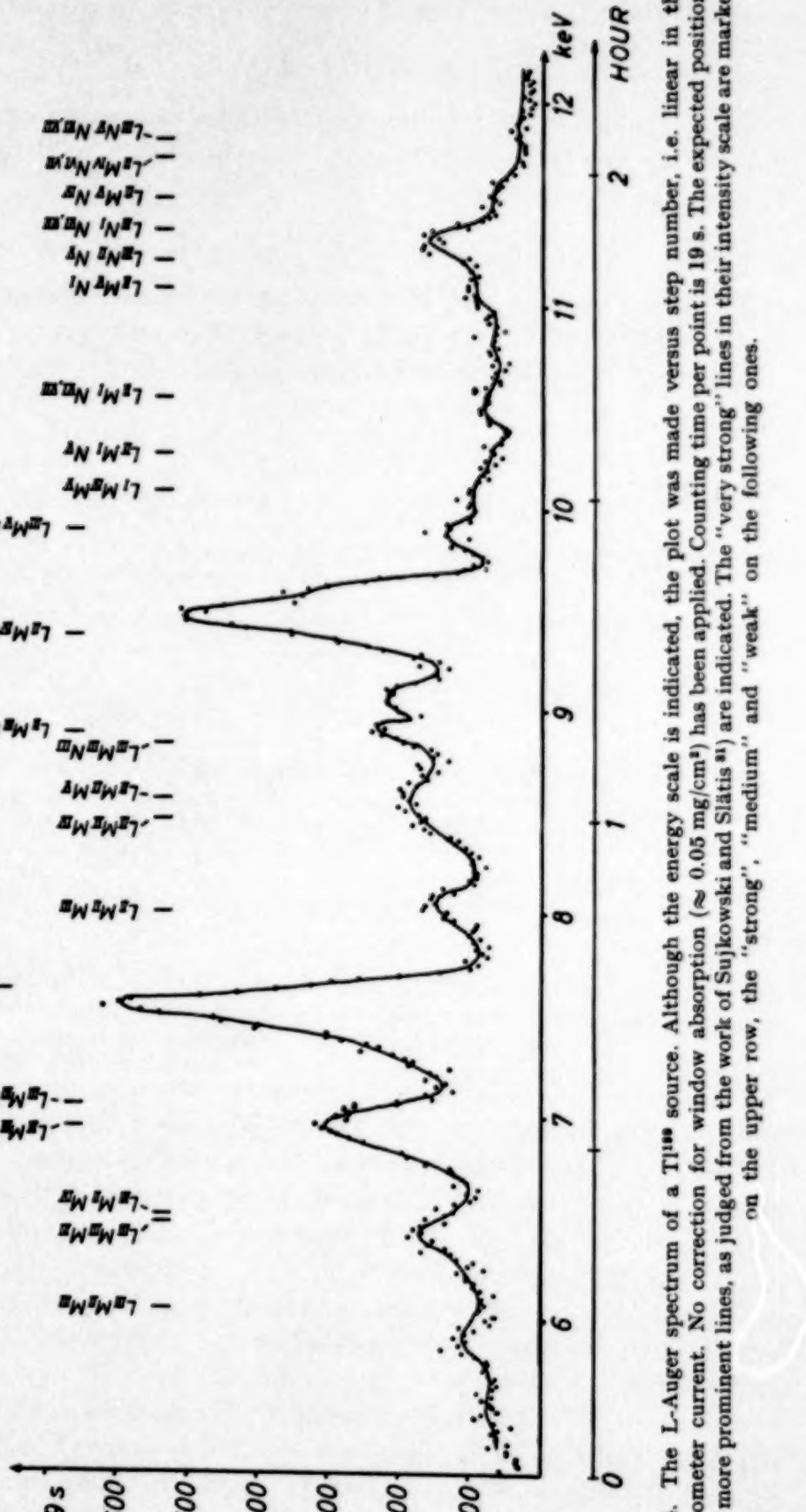

Fig. 4. The L-Auger spectrum of a Tl^{199} source. Although the energy scale is indicated, the plot was made versus step number, i.e. linear in the spectrometer current. No correction for window absorption (≈ 0.05 mg/cm^2) has been applied. Counting time per point is 19 s. The expected positions of the more prominent lines, as judged from the work of Sujkowski and Slätis [21]) are indicated. The "very strong" lines in their intensity scale are marked on the upper row, the "strong", "medium" and "weak" on the following ones.

energies of the L-Auger lines of mercury were calculated from the formula

$$E_{XYZ} = B_X(\mathrm{Hg}) - B_Y(\mathrm{Hg}) - B_Z(\mathrm{Tl}),$$

where B stands for the binding energies of the electrons in the X, Y and Z subshells. As can be seen from the figure there appears to be a gross agreement between the two measurements.

3.4. LEVEL SCHEME OF Hg^{199}

Only minor modifications were needed in the level scheme of Hg^{199} proposed by Bergström *et al.* [6]) to make it accommodate all transitions found in the present work. In fig. 5 we give the decay scheme of Tl^{199} obtained by us together

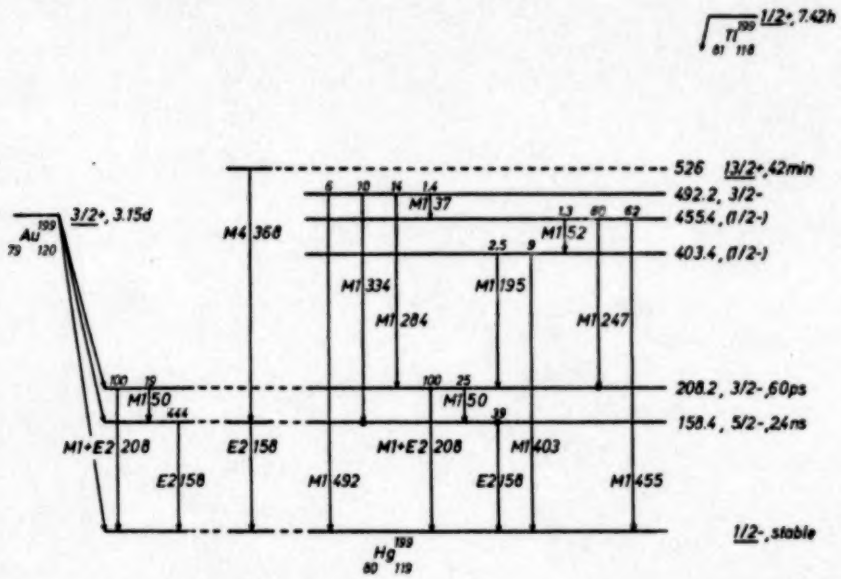

Fig. 5. The level scheme of Hg^{199}. The present work is confined to the right part of the figure. All energies are given in keV and the total transition intensities, normalized to the 208 keV transition, are indicated at the tails of the transition arrows.

with those of Au^{199} and Hg^{199m}. The information on the last two decays was taken mainly from the Nuclear Data Sheets [32]). The figures at the tails of the transition arrows represent the total transition intensities normalized to the intensity of the 208 keV transition and were calculated with the theoretical conversion coefficients of Rose [33]) and Sliv and Band [34]). The errors can be taken from the relative intensities of the conversion lines in table 1. The relative total transition intensities in the decay of Au^{199} were obtained from the work of Bäckström *et al.* [7]).

When the different transitions were placed in the level scheme, it was possible to make a least squares fit of the level energies. In order to decrease the numerical work the energies of the two lowest excited levels were regarded to be fixed,

as they have been accurately measured by Bäckström *et al.* [7]). The adopted level scheme was found to be consistent with the measured transition energies and the values for the energies of the levels resulting from the calculation will be given below in the discussion of the individual levels.

The spin of the ground state of Tl^{199} has been measured by Brink *et al.* [35]) as $\frac{1}{2}$, and the shell model predicts positive parity for this state. The ground state spin of Hg^{199} has been reported to be $\frac{1}{2}$ both by Schüler and Keyston [36]) and by Proctor and Yu [37]). The shell model predicts negative parity for this level.

The following remarks apply to the different levels.

158.4 keV

The 158 keV transition depopulating this level is pure E2 (less than 1 % M1 according to Nall *et al.* [23])) which indicates a spin-parity of $\frac{5}{2}-$. This assignment is further supported by the strong branch from the $\frac{3}{2}+$ ground state of Au^{199} [7, 23]), whereas the feeding from the Tl^{199} ground state ($\frac{1}{2}+$) is apparently rather weak (cf. fig. 5).

208.2 keV

A spin-parity of $\frac{3}{2}-$ is suggested by the 208 keV (89 % M1+11 % E2) transition to the ground state and the 50 keV M1 transition to the 158 keV level. The difference in the intensity ratio between the 50 and 208 keV transitions in the decay of Au^{199} and Tl^{199} (cf. fig. 5) may be explained by experimental uncertainties. Nall *et al.* [23]) obtained a branching ratio of 0.25 ± 0.03 for the Au^{199} decay, which is in better agreement with our value.

403.40±0.10 keV

This is the only new level and it was added to the decay scheme given by Bergström *et al.* [6]) in order to allow for the new 52, 195 and 404 keV transitions found in the present work. The existence of the level is rather well established by the three transitions feeding or depopulating it. As discussed below no transition was found between the 403 keV level and the $\frac{5}{2}-$ level at 158 keV. This may indicate a spin-parity of $\frac{1}{2}-$ since transitions of M1 multipole character were observed both to the $\frac{1}{2}-$ ground state and to the $\frac{3}{2}-$ state at 208 keV. The decay energy of Au^{199} (460 ± 10 keV) [32]) is just high enough to allow a β^--branch to the 403 keV level. No such transition has, however, been found [32]). Nall *et al.* [23]) report an upward deviation of the Fermi plot for the β^--group to the 208 keV level in the decay of Au^{199} for energies less than about 45 keV and this may be an indication of the presence of a β^--group to the 403 keV level. They state, however, that this upward deviation undoubtedly is due to source thickness effects, as Haynes and Achor [30]) found the Fermi plot to be straight down to 20 keV. Because of the very low energy available, the feeding of the 403 keV level in the decay of Au^{199} must be expected to be very weak.

455.39±0.08 keV

This level has most probably a spin-parity of $\frac{1}{2}-$ as no transition was found to the $\frac{5}{2}-$ level at 158 keV although strong transitions both to the $\frac{1}{2}-$ ground state and the $\frac{3}{2}-$ level at 208 keV were observed.

492.17±0.07 keV

Since the 334 keV transition was found by us to be of M1 character rather than E2, the spin of this level is most probably $\frac{3}{2}$ and not $\frac{1}{2}$ as proposed by Bergström *et al.* [6]). Negative parity follows from the M1 multipole order of the transitions depopulating the level.

The level scheme is consistent with the coincidence measurements by Wilkinson [26]). He found that the 158 keV transition coincides both with the 247 keV and the 334 keV transitions.

The conversion electron spectrum was searched for conversion lines of transitions between the 492 and 403 keV, the 455 and 158 keV and the 403 and 158 keV levels, which are missing in the level scheme. No indications of these transitions were found and in table 4 upper intensity limits of conversion lines of these transitions are given.

TABLE 4

Unobserved transitions between levels in the level scheme (intensity scale: K 208 keV = 100)

Initial and final level (keV)	Transition energy (keV)	Upper intensity limit
492–403	88.8	$L_1 < 1$
455–158	297.0	$K < 0.2$, $L < 0.3$
403–158	245.0	$K < 0.4$

As a final remark we should like to point out the striking difference between the level schemes of Hg^{201} and Hg^{199}. The former scheme has recently been studied by Herrlander *et al.* [3]) who found excited levels at 1.6, 32 and 167 keV. No unambiguous spin assignments could be given to the levels. It is hoped that further work in progress on the level schemes of the more neutron deficient mercury isotopes will make clear whether the difference between the schemes merely indicates a break in the systematics or whether the low spin levels in the different mercury isotopes cannot be correlated at all. The levels involved in the decays by internal transitions of the isomeric levels of Hg^{193}, Hg^{195}, Hg^{197} and Hg^{199} have, however, been successfully treated with the systematic approach [1, 3]).

We are most indepted to Professor The Svedberg for excellent working conditions and for various facilities put at our disposal. The numerous sources were prepared by the joint efforts of ing. Å. Svanheden and his cyclotron staff, fil. mag. I. B. Häller, and fil. kand. T. Stenström, who made the chemical separations, and ing. R. Ringh and Mr. H. G. Rikner, who operated the mass separator, and their cooperation is gratefully acknowledged. The work has been financially supported by the Swedish Atomic Research Council.

References

1) I. Bergström and G. Andersson, Arkiv Fysik **2** (1957) 415
2) B. Jung and G. Andersson, Nuclear Physics **15** (1960) 108
3) C. J. Herrlander, R. Stockendal and R. K. Gupta, Arkiv Fysik **17** (1960) 315
4) D. A. Orth, L. Marques, W. J. Heiman and D. H. Templeton, Phys. Rev. **75** (1949) 1100
5) H. I. Israel and R. G. Wilkinson, Phys. Rev. **83** (1951) 1051
6) I. Bergström, R. D. Hill and G. de Pasquali, Phys. Rev. **92** (1953) 918
7) G. Bäckström, O. Bergman and J. Burde, Nuclear Physics **7** (1958) 263
8) G. Andersson, Arkiv Fysik **12** (1957) 331
9) J. O. Burgman and G. Andersson, Nuclear Instruments **3** (1958) 33
10) K. O. Nielsen, Proc. 1955 Harwell Isotope Conf., Ch. 9
11) B. Jung, Nuclear Physics **10** (1959) 440
12) G. Andersson and I. Bergström, Nuclear Physics **3** (1957) 506
13) G. Andersson, E. Arbman and B. Jung, Arkiv Fysik **11** (1957) 297
14) G. Andersson, P. A. Tove, B. Jung and I. B. Svensson, Nuclear Physics **3** (1957) 493
15) E. Arbman and N. Svartholm, Arkiv Fysik **10** (1956) 1
16) E. Arbman and B. Jung (to be published)
17) K. Siegbahn and T. R. Gerholm, in Beta- and gamma-ray spectroscopy, ed. by K. Siegbahn (North-Holland Publishing Co., Amsterdam 1955) Appendix 7.
18) E. Arbman, Thesis, University of Uppsala (1958)
19) D. Saxon, Phys. Rev. **81** (1951) 639
20) G. Bäckström, O. Bergman, J. Burde and J. Lindskog, Nuclear Physics **15** (1960) 566
21) C. de Vries, Thesis, University of Amsterdam (1960)
22) C. J. Herrlander and T. R. Gerholm, Nuclear Physics **3** (1957) 161
23) J. C. Nall, Q. L. Baird and S. K. Haynes, Phys. Rev. **118** (1960) 1278
24) J. D. Knight and E. W. Baker, Phys. Rev. **100** (1955) 1334
25) M. C. Michel and D. H. Templeton, Phys. Rev. **93** (1954) 1422
26) R. G. Wilkinson, quoted by Bergström *et al.* [6])
27) W. N. Asaad, Proc. Roy. Soc. A **249** (1959) 555
28) I. Bergström and R. D. Hill, Arkiv Fysik **8** (1954) 21
29) B. Jung and J. Svedberg, work in progress
30) S. K. Haynes and W. T. Achor, J. Phys. Radium **16** (1955) 635
31) Z. Sujkowski and H. Slätis, Arkiv Fysik **14** (1958) 101
32) K. Way *et al.*, Nuclear Data Sheets, National Academy of Sciences-National Research Council (Washington, D.C., 1958, 1959)
33) M. E. Rose, Internal conversion coefficients (North-Holland Publishing Co., Amsterdam, 1958)
34) L. A. Sliv and I. M. Band, Tables of internal conversion coefficients of gamma rays (Academy of Sciences Press, Moscow-Leningrad), I. K-shell (1956); II. L-shell (1958)
35) G. O. Brink, J. C. Hubbs, W. A. Nierenberg and J. L. Worcester, Phys. Rev. **107** (1957) 189; Bull. Am. Phys. Soc. **1** (1956) 343
36) H. Schüler and J. E. Keyston, Z. Physik **72** (1931) 423
37) W. G. Proctor and F. C. Yu, Phys. Rev. **81** (1951) 20, **76** (1949) 1728

1.D.3

Nuclear Physics **20** (1960) 648—662; © *North-Holland Publishing Co., Amsterdam*

Not to be reproduced by photoprint or microfilm without written permission from the publisher

A TWO-BODY CLUSTER MODEL OF THE NUCLEUS

T. A. TOMBRELLO † and G. C. PHILLIPS

The Rice Institute, Houston, Texas ††

Received 20 June 1960

Abstract: Calculations are presented for coupled Schrödinger equations which develop the detailed behavior predicted by the two-body cluster model described in a preceding paper. The results show that: 1) narrow resonances in the scattering cross section may be quantitatively described by this model, 2) the cross section in the neighborhood of the threshold of another channel shows the Wigner cusp, and 3) the configuration mixing of bound states is a necessary consequence of the model. As an example, the model is used as a means of parameterizing the lowest $J = \frac{1}{2}^+$ states in C^{13}. This method allows a fit to the scattering phase shift and the level structure, at the same time making a definite prediction of the fractional parentage of the $\frac{1}{2}^+$ bound state.

1. Introduction

A preceding paper [1]) presented a phenomenological model of the nucleus describing two-body cluster states in terms of coupled Schrödinger equations. It is the purpose of this paper to investigate the characteristics of such a model. Several nuclear models exist which adequately describe the gross properties of nuclear structure and to some extent describe those broad excited states which correspond to states of two-body motion. In these models narrow states are frequently classified, *ad hoc*, as "many particle" excitations. Until now no simple model has proved capable of explaining the existence of both types of states simultaneously or has provided any means of making quantitative predictions about the properties of such states.

The proposed cluster model not only allows an explanation of these narrow states, but also can describe simple nuclear reactions, behavior near thresholds, configuration mixing in bound states, and the enhancement of some electromagnetic transitions. This paper will consider these aspects of the cluster model.

2. Description of the Model

As noted in the preceding paper the nuclear wave function at low energies may be approximated by an expansion in the wave functions that represent all the possible states of two-body motion. In practice this expansion will consist

† National Science Foundation Fellow in Physics.

†† Work supported in part by the U. S. Atomic Energy Commission.

of only that finite number of configurations that are energetically possible (or almost energetically possible) in the energy range considered. Those states of motion corresponding to much higher excitations will necessarily be neglected.

To a first (linear) approximation it will be assumed that the Hamiltonian for the system is given by

$$H = \begin{pmatrix} H_{11} V_{12} \cdots V_{1n} \\ V_{21} H_{22} \cdots \\ . \\ . \\ . \end{pmatrix},$$

and the wave function is

$$\Psi = \begin{pmatrix} \theta_1 \psi_1 \\ \theta_2 \psi_2 \\ . \\ . \\ . \end{pmatrix}.$$

$\theta_i \psi_i$ represents the wave function for the i_{th} state of two-body motion, and H_{ii} is the (unperturbed) Hamiltonian for this state. $V_{ij} (i \neq j)$ is the interaction between this two-body state and the j^{th} state of two-body motion.

The general behavior of such a system of coupled equations is easily seen by considering the time dependent Schrödinger equation,

$$H\Psi = -\frac{\hbar}{i} \frac{\partial \Psi}{\partial t}.$$

For the case of only two states of motion this becomes

$$\begin{pmatrix} T_1+V_{11} & V_{12} \\ V_{21} & T_2+V_{22} \end{pmatrix} \begin{pmatrix} \theta_1 \psi_1 \\ \theta_2 \psi_2 \end{pmatrix} = -\frac{\hbar}{i} \begin{pmatrix} \dot{\theta}_1 \psi_1 \\ \dot{\theta}_2 \psi_2 \end{pmatrix}.$$

If the ψ_i are normalized such that $\int |\psi_i|^2 dV = 1$, the matrix equation may be rewritten as

$$\dot{\theta}_1 = -i[\omega_1 \theta_1 + \alpha \ \theta_2],$$
$$\dot{\theta}_2 = -i[\omega_2 \theta_2 + \alpha^* \theta_1],$$

with $\alpha = \hbar^{-1} \langle 1 | V_{12} | 2 \rangle$ and $\omega_i = \hbar^{-1} \langle i | T_i + V_{ii} | i \rangle$.

Solving these equations gives

$$\theta_1 = e^{-i\lambda t} \left[\theta_1(0) \cos \nu t + i \frac{\sin \nu t}{\nu} \left(\frac{\theta_1(0)\omega_2 - \theta_2(0)\alpha}{\hbar} - \theta_1(0)\lambda \right) \right],$$

$$\theta_2 = e^{-i\lambda t} \left[\theta_2(0) \cos \nu t + i \frac{\sin \nu t}{\nu} \left(\frac{\theta_2(0)\omega_1 - \theta_1(0)\alpha^*}{\hbar} - \theta_2(0)\lambda \right) \right],$$

where

$$\lambda = \frac{\omega_1+\omega_2}{2\hbar}, \quad \text{and} \quad \nu = \frac{\sqrt{(\omega_1-\omega_2)^2+4|\alpha|^2}}{2\hbar}.$$

If it is assumed that the system is initially entirely in one state of motion (i.e. $\theta_1(0) = 0$, $\theta_2(0) = 1$) and the time average is taken, then

$$\overline{|\theta_2|^2} = \tfrac{1}{2}\left(1+\frac{(\omega_1-\omega_2)^2}{(\omega_1-\omega_2)^2+4|\alpha|^2}\right), \quad \text{and} \quad \overline{|\theta_1|^2} = \frac{2|\alpha|^2}{(\omega_1-\omega_2)^2+4|\alpha|^2}.$$

A necessary and sufficient condition for $|\theta_2|^2$ to be near unity is that

$$|\langle 1|T_1+V_{11}|1\rangle-\langle 2|T_2+V_{22}|2\rangle|^2 \gg 4|\langle 1|V_{12}|2\rangle|^2.$$

This inequality gives the conditions for the occurrence of a state of high purity in channel 2, and may be satisfied in either of two ways:

(a) If $|\langle 1|T_1+V_{11}|1\rangle-\langle 2|T_2+V_{22}|2\rangle|^2$ is very large. Such a situation will occur if the unperturbed eigenvalues of the two channels are far apart in energy. If the channel interactions V_{ii} are not too large, but the difference of binding energy of the two cluster arrangements is large, then pure states of channel 2 may be expected near in energy to the dissociation energy of channel 2.

(b) If $\langle 1|V_{12}|2\rangle$ is small. This condition will occur if either V_{12} represents a weak interaction, or if V_{12} is strong only in spatial regions where the wave functions are small.

One would thus expect to find the majority of nearly pure states of a particular parentage near to the dissociation energy for that two-body parentage form. States that are further away in energy would in general be of mixed parentage, the degree of mixing being determined by the coupling potential V_{12} and by the relative binding energy of the two parentage forms.

3. Solution of the Coupled Equations

For the purpose of calculation consider a system which may be described by two two-body states of motion. For this system the Schrödinger equation is

$$\begin{pmatrix} H_{11} & V_{12} \\ V_{21} & H_{22} \end{pmatrix} \begin{pmatrix} \theta_1\psi_1 \\ \theta_2\psi_2 \end{pmatrix} = \begin{pmatrix} E_1 & 0 \\ 0 & E_2 \end{pmatrix} \begin{pmatrix} \theta_1\psi_1 \\ \theta_2\psi_2 \end{pmatrix}.$$

Because of the short range nature of nuclear forces, it is required that V_{ij} and the nuclear part of V_{ii} have a finite range that is approximately that of the nuclear radius. Thus, outside the range of the nuclear forces the equations are uncoupled. In the calculations that are described in this paper all of the V_{ii} and V_{ij} were taken to be square wells whose ranges were equal to the nuclear radius.

Making the change of variable $u_i = r\theta_i\psi_i$ the coupled equations become:

$$\frac{d^2u_1}{dr^2}+\frac{2\mu_1}{\hbar^2}(E_1-V_{11})u_1-\frac{2\mu_1}{\hbar^2}V_{12}u_2=0,$$

and

$$\frac{d^2u_2}{dr^2}+\frac{2\mu_2}{\hbar^2}(E_2-V_{22})u_2-\frac{2\mu_2}{\hbar^2}V_{21}u_1=0,$$

where $E_1 = E_2+$ the difference of binding energy of the two clusters. Defining

$$K_{11}^2=\frac{2\mu_1}{\hbar^2}(E_1-V_{11}),\quad K_{22}^2=\frac{2\mu_2}{\hbar^2}(E_2-V_{22}),\quad K_{12}^2=\frac{2\mu_1}{\hbar^2}V_{12},$$

$$K_{21}^2=\frac{2\mu_2}{\hbar^2}V_{21},\quad K_1^2=\tfrac{1}{2}(K_{11}^2+K_{22}^2)+\tfrac{1}{2}\sqrt{(K_{11}^2-K_{22}^2)^2+4K_{12}^2K_{21}^2},$$

and

$$K_2^2=\tfrac{1}{2}(K_{11}^2+K_{22}^2)-\tfrac{1}{2}\sqrt{(K_{11}^2-K_{22}^2)^2+4K_{12}^2K_{21}^2},$$

the solutions u_1 and u_2 for cluster separations less than the nuclear radius, are

$$u_1=\frac{K_1^2C_1-(C_1K_{22}^2+K_{12}^2C_2)}{K_1(K_1^2-K_2^2)}\sin K_1r+\frac{(C_1K_{22}^2+K_{12}^2C_2)-C_1K_2^2}{K_2(K_1^2-K_2^2)}\sin K_2r,$$

$$u_2=\frac{K_1^2C_2-(C_2K_{11}^2+C_1K_{21}^2)}{K_1(K_1^2-K_2^2)}\sin K_1r+\frac{(C_2K_{11}^2+K_{21}^2C_1)-C_2K_2^2}{K_2(K_1^2-K_2^2)}\sin K_2r,$$

where

$$u_1(0)=0,\quad u'_1(0)=C_1,\quad u_2(0)=0,\quad \text{and}\quad u'_2(0)=C_2.$$

Since the two types of motion may correspond to either energetically bound or free states, the solutions in the region outside the nucleus have either an oscillatory or decreasing exponential character. The exact form of these solutions depends on the value of the orbital angular momentum as well as on the presence or absence of the Coulomb field.

Three cases are possible: 1) both channels are closed, 2) one channel is open, the other closed, 3) both channels are open. In the following section sample calculations for these three cases will be discussed.

4. Calculations

4.1. BOTH CHANNELS ARE CLOSED

Where both channels are bound, the exterior solutions were taken to be decreasing exponentials. For this case the boundary conditions can only be satisfied at certain energies, and discrete eigenstates result. The values of V_{11} and V_{22} were chosen so that in the absence of coupling, each channel has a

bound state in the energy range considered. The quantities of interest are the energy separation of the two eigenstates and the relative mixture of the cluster wave functions in the eigenfunctions, studied as functions of the coupling potential †.

For an example we have chosen the case of C^{13}. For this nucleus the clusters at low energy are $C^{12}+n$ and $C^{12*}+n$. In choosing this example it is not our immediate goal to explain the experimental results in detail, but rather to provide a physically reasonable background for exploring the properties of the model.

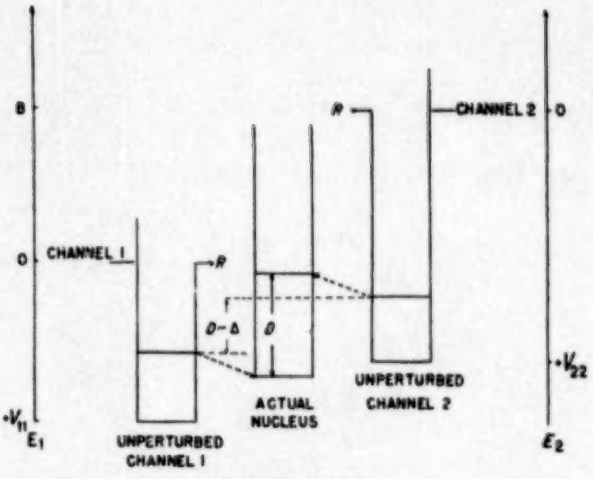

Fig. 1. An energy level diagram of a nucleus requiring only two cluster arrangements. Bound states corresponding to the two possible modes of motion are shown. The diagram indicates the unperturbed positions of the eigenstates in potential wells for each cluster form and shows how the levels are shifted by the coupling between channels. The coupling tends to increase the energy separation D of the states by an amount Δ.

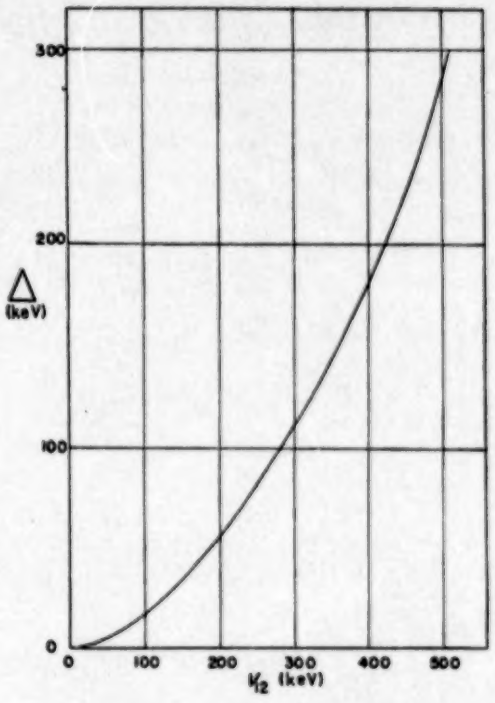

Fig. 2. The change in the energy separation of a pair of two-body cluster bound states as a function of the coupling potential, V_{12}. The difference Δ between the actual separation of the two states and their unperturbed separation is given as a function of V_{12}. ($V_{11}=-5.00$ MeV, $V_{22}=-9.50$ MeV, $R=4.5\times10^{-13}$ cm; see text for the definition of symbols.)

The results of the calculation are shown in figs. 1, 2 and 3. The first of these figures shows the energy diagram of the nucleus. The second figure shows how the energy separation of the two types of eigenstates is affected by changing the coupling potential. The calculations show that the two eigenstates are forced apart in energy with increased coupling. Fig. 3 shows the mixing of the cluster wave functions that is obtained by increasing the coupling. θ_i^2 is defined

† It is interesting to note that in this section, as well as in the following ones, the results are dependent only upon the magnitude of V_{12}, and not upon its sign or complex phase. This is a consequence of the Hermitean property of the Hamiltonian.

by $\int |\theta_i \psi_i|^2 dV$ (the integration taking place over all space), subject to the normalization condition

$$\int_{\substack{\text{all}\\\text{space}}} |\theta_1 \psi_1|^2 dV + \int_{\substack{\text{all}\\\text{space}}} |\theta_2 \psi_2|^2 dV = 1.$$

The reason that θ_1^2 appears to be more greatly affected by the coupling, is that V_{11} was chosen -5.00 MeV, while V_{22} was taken -9.50 MeV, Thus, the coupling potential represents a much stronger perturbation on the less strongly bound state. It is apparent that this model allows the representation of bound states of any degree of cluster purity.

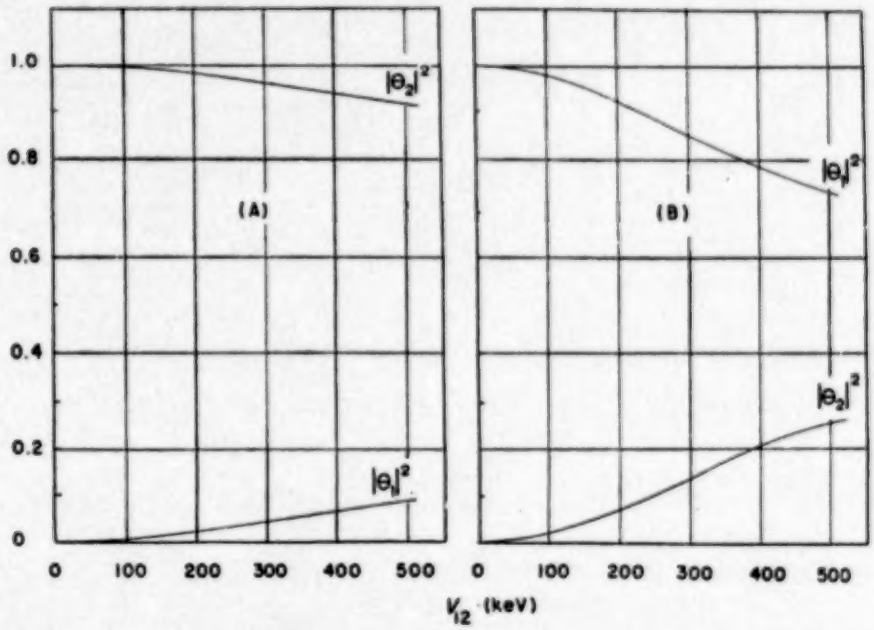

Fig. 3. The cluster mixing of bound states as related to the coupling potential. Section (A) shows a state that for zero coupling is purely of type 2 parentage. Section (B) shows a similar state of initially pure type 1 parentage. The fractional parentage coefficients, $|\theta_i|^2$, are given as functions of the coupling potential V_{12} for both of these cases. For a full discussion see the text. ($V_{11} = -5.00$ MeV, $V_{12} = -9.50$ MeV, $R = 4.5 \times 10^{-13}$ cm.)

4.2. ONE CHANNEL IS OPEN

For the case where one of the channels is open, the problem becomes that of elastic scattering. This energy region corresponds to $0 \leqq E_1 \leqq B$ in fig 1. The wave function in the open channel was matched to an incoming plane wave plus an outgoing spherical wave at the nuclear surface, while the exterior solution in the closed channel was again of a decreasing exponential character. Each partial wave, characteristic of the square of total angular momentum, was separately examined. Scattering resonances of single-particle width are provided by the virtual states of the central potential V_{11} of the open channel. In most energy regions the behavior of the cross section is well described by scattering

from the central potential V_{11}. However, in the energy regions corresponding to the bound eigenstates of the closed channel anomalous scattering behavior occurs. These anomalies take the form of very narrow scattering resonances, whose widths may be shown to be approximately proportional to $|V_{12}|^2$. The overall character of the cross section is best demonstrated by the following simplified treatment.

Rewriting Schrödinger's equation for the two-channel system as

$$(T_1+V_{11})\theta_1\psi_1+V_{12}\theta_2\psi_2 = E_1\theta_1\psi_1,$$

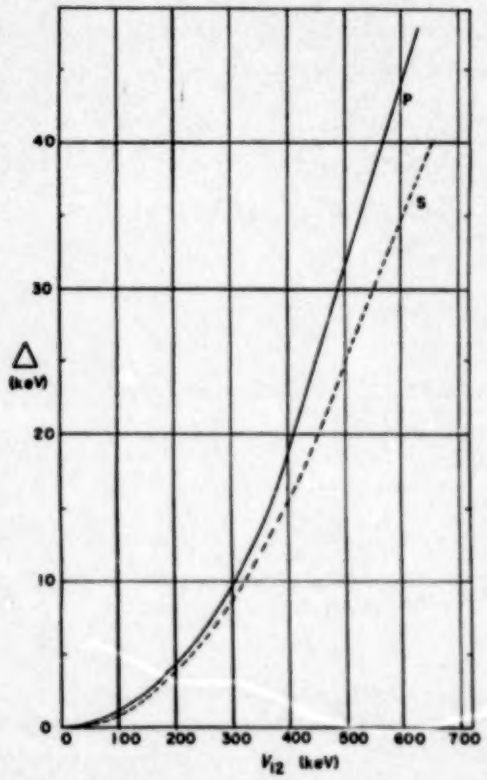

Fig. 4. The shift in the resonance energy as a function of V_{12}. The level shift Δ is shown as a function of the coupling potential V_{12}. The dotted curve gives Δ for an S-wave resonance, the solid curve for an P-wave resonance. ($V_{11}=V_{22}=-7.25$ MeV, $R=4.5\times10^{-13}$ cm.)

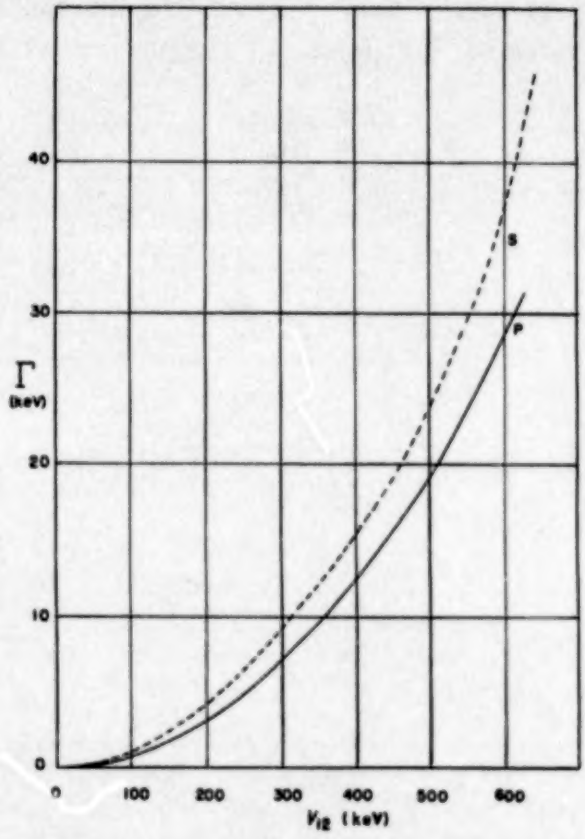

Fig. 5. The resonance width as a function of V_{12}. The width of a resonance (of type 2) is given as a function of V_{12}. The parameters and curves are labeled as in fig. 4.

$$(T_2+V_{22})\theta_2\psi_2+V_{21}\theta_1\psi_1 = (E_1-B)\theta_2\psi_2,$$

and assuming that near the eigenstate of channel 2 the function ψ_2 is not greatly perturbed by the coupling to channel 1, i.e. $(T_2+V_{22})\psi_2 \approx \mathcal{E}_2\psi_2$, the following approximate relation is obtained:

$$\left(T_1+V_{11}+\frac{V_{12}V_{21}}{E_1-B-\mathcal{E}_2}\right)\psi_1 = H_{1,\text{approx.}}\,\psi_1 \approx E_1\psi_1.$$

The third term in $H_{1,\text{approx.}}$ is small if V_{12} is small and if E_1 is not near $\mathscr{E}_2+B$. Thus, ψ_1 will not be very different from the uncoupled ψ_1. However, when E_1 is near $\mathscr{E}_2+B$ the third term in the Hamiltonian will dominate, and ψ_1 will become small within the range of the nuclear force. This exclusion of the wave function of channel 1 from the region of nuclear interaction will appear as a resonance in the scattering: the resonant width is approximately

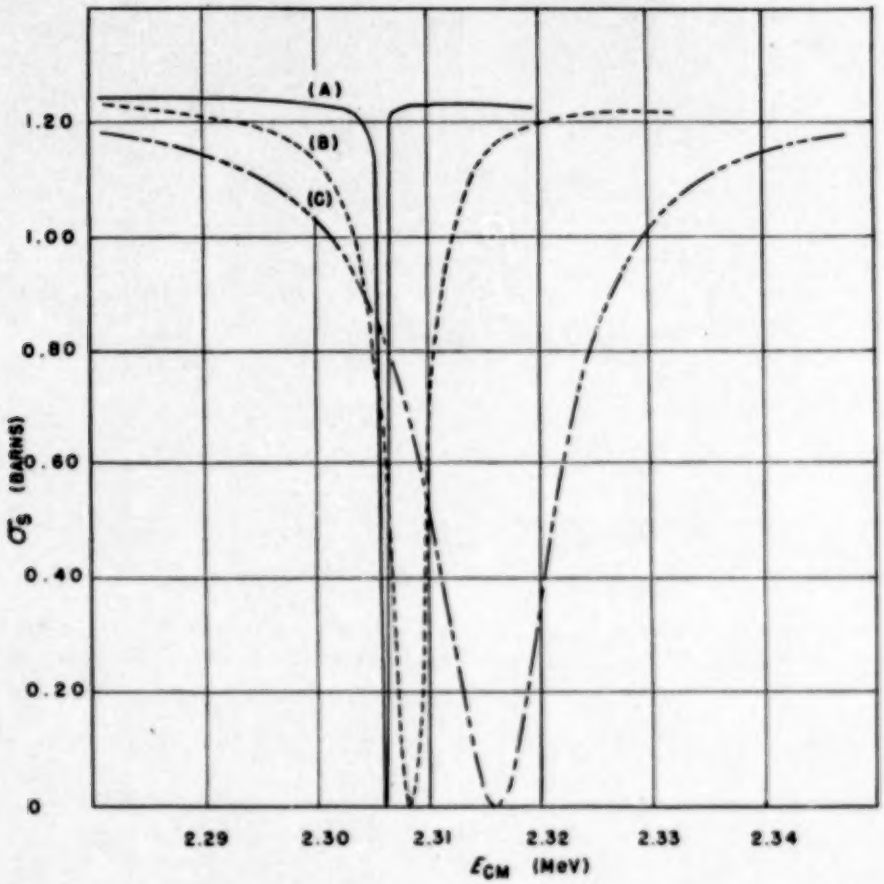

Fig. 6. S-wave resonance shapes. The S-wave partial cross section curves are given for several values of V_{12}. $V_{11} = V_{22} = -7.25$ MeV, $R = 4.5\times10^{-13}$ cm; (A) $V_{12} = 50$ keV, (B) $V_{12} = 200$ keV, (C) $V_{12} = 350$ keV.

$$\Gamma \approx \frac{\langle 1|V_{12}V_{21}|1\rangle}{B+\mathscr{E}_2}.$$

Exact numerical results are summarized in figs. 4 to 10. In these cases, as in the previous ones, the eigenstates tend to be pushed apart with increasing value of the coupling as is shown in fig. 4. The behavior of the width of the narrow resonances as a function of the coupling potential is shown in fig. 5. As previously noted the width of the resonance varies approximately as $|V_{12}|^2$. The resonance shapes are shown in figs. 6 and 7 for S-wave and P-wave scattering respectively. Calculations have shown that these shapes correspond closely to those

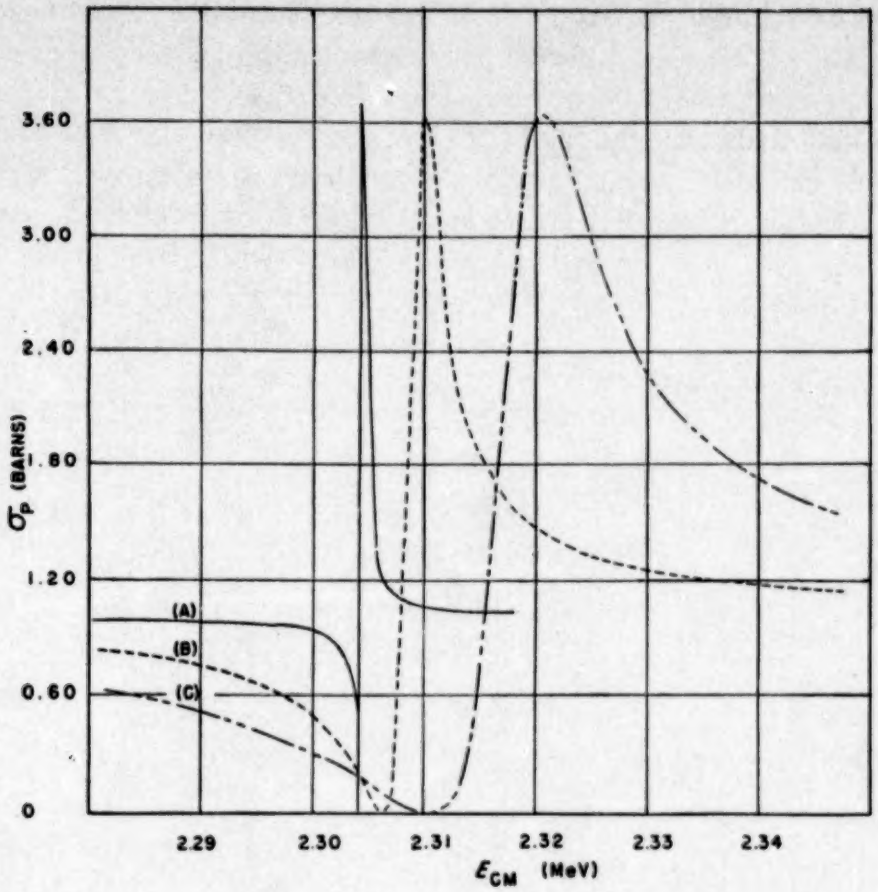

Fig 7. P-wave resonance shapes. The P-wave partial cross section curves are given for several values of V_{12}. The parameters and curve labels are the same as in fig. 6.

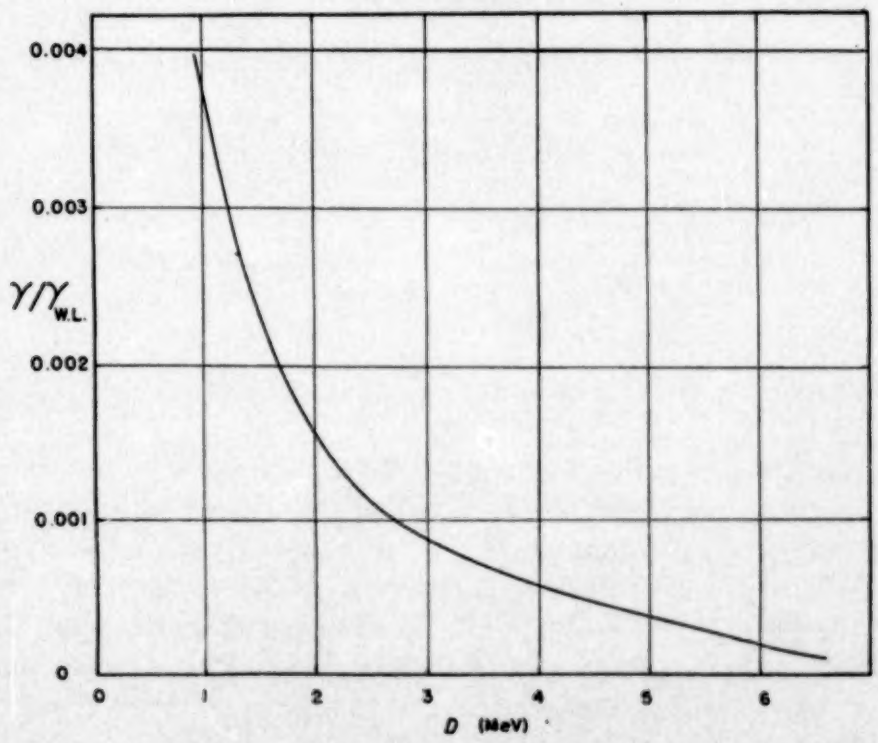

Fig. 8. The ratio of the reduced width γ to the Wigner limit $\gamma_{W.L.}$ as a function of the energy separation D of the two levels. ($V_{12} = 200$ keV, $R = 4.5 \times 10^{-13}$ cm.)

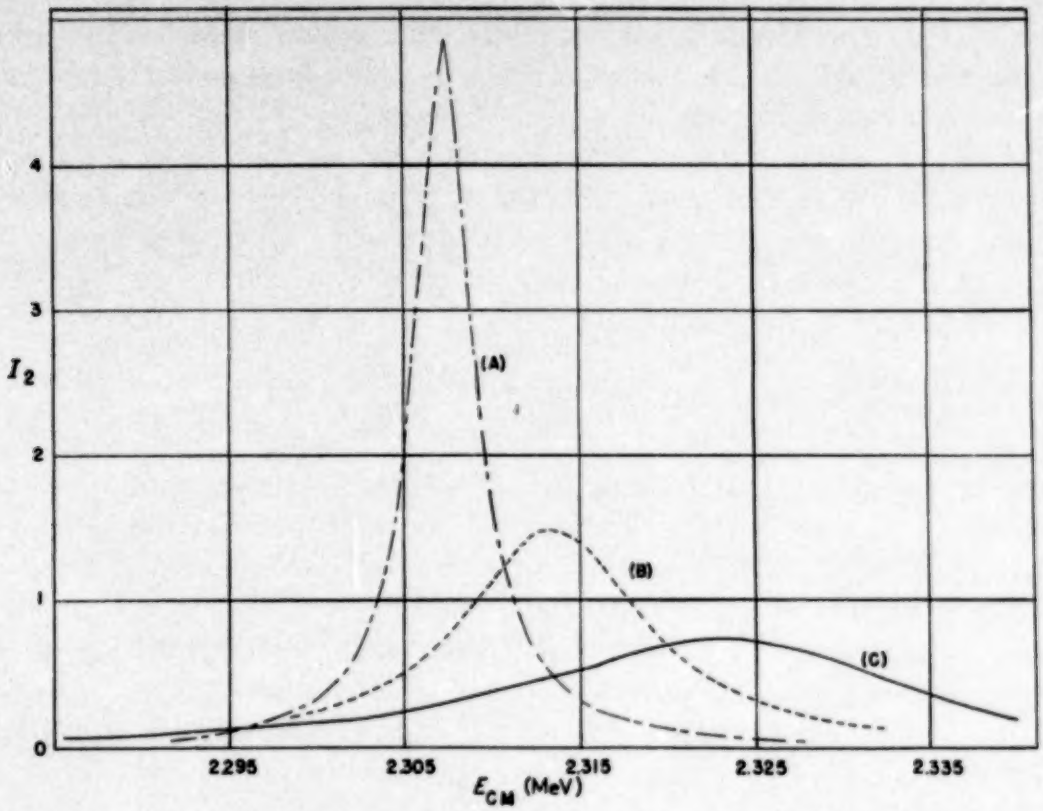

Fig. 9. I_2 as a function of the centre-of-mass energy for several values of the coupling potential V_{12}. $V_{11} = V_{22} = -7.25$ MeV, $R = 4.5 \times 10^{-13}$ cm; (A) $V_{12} = 200$ keV, (B) $V_{12} = 350$ keV, (C) $V_{12} = 500$ keV. (I_2 is given in arbitrary units and is defined in the text.)

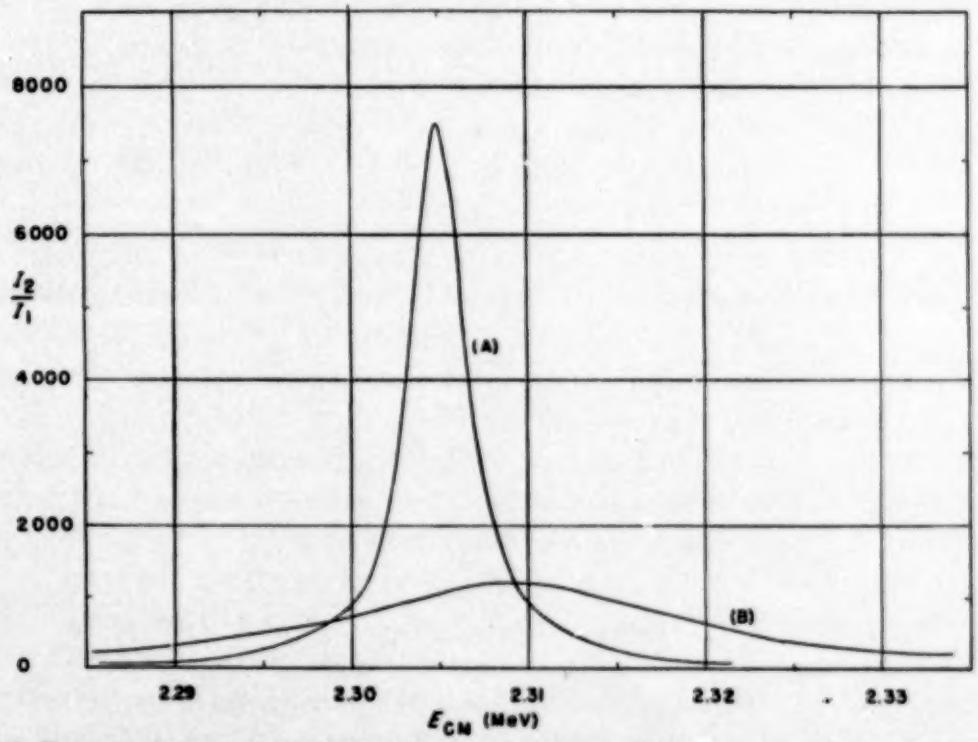

Fig. 10. The ratio I_2/I_1, defined in the text, *versus* the centre-of-mass energy. $V_{11} = V_{22} = -7.25$ MeV, $R = 4.5 \times 10^{-13}$ cm; (A) $V_{12} = 200$ keV, (B) $V_{12} = 500$ keV.

given by the single-level dispersion formula. For these comparisons the radius used in the single level formula was taken to be that of the potential well, and the resonance energy-widths were made to coincide.

The reduced width of such narrow resonances as a function of the energy separation of the eigenstates of the two channels is shown in fig. 8. As the eigenstates in the two channels are made to approach each other in energy, the width of the resonance approaches single-particle width.

If one considers the quantities

$$I_1 = \int_{\text{nucleus}} |\theta_1 \psi_1|^2 dV \quad \text{and} \quad I_2 = \int_{\text{all space}} |\theta_2 \psi_2|^2 dV$$

it may be seen in fig. 9 that in the neighborhood of one of these narrow resonance I_2 shows a peak whose width is equal to the width of the scattering resonance In addition, the ratio I_2/I_1 becomes large at resonance as is exhibited in fig. 10. These facts reveal that at resonance the favored mode of motion for the system is that corresponding to the closed channel. Because of this large increase in the amplitude of ψ_2, the overlap integrals of this wave function with channel 2 eigenfunctions of lower energy is increased. Thus, at resonance the probability for an electromagnetic transition to lower states of the same two-body parentage is greatly enhanced.

4.3. BOTH CHANNELS ARE OPEN

For the case of C^{12}+n and C^{12*}+n both channels are open above $E_1 = 4.43$ MeV. The behavior of the cross section and phase shift in the neighborhood of the threshold is of special interest. For S-wave scattering there is a marked discontinuity in the slope of the scattering cross section as the threshold is crossed. This is the cusp effect predicted by Wigner [2]), and its manifestation is shown in fig. 11.

If there are no resonances near the threshold energy, the behavior of the phase shift is continuous across the region. However, the modulus of the "phase shift" is no longer required to be unity and in general will decrease with increasing energy. A discussion of the resonance behavior of the "phase shift" in this region will be taken up later in this section.

The cross section of channel 2 is strongly influenced by the presence of a state (of type 2) near the threshold; as the position of the state approaches the threshold energy, the maximum value of the reaction cross section passes through a sharp maximum. This effect is seen in figs. 12 and 13, and may be used, in some cases, to explain anomalously large reaction cross sections near thresholds.

Resonance shapes above threshold due to an eigenstate in channel 2 for $l_1 = 0, l_2 = 2$ are shown in figs. 14 and 15. The states remain relatively narrow because of the presence of the centrifugal barrier. Both the scattering resonances

and the resonance in the reaction cross section have the same width, but their maximum values are strongly affected by the barrier. For resonances only slightly above threshold the maximum value attained by the reaction cross section is relatively small; however, at higher energies the reaction cross section may dominate.

It should be noted that the elastic scattering cross section does not pass through zero at these resonances; this is a consequence of the complex nature of the "phase shift". At resonance the complex phase angle of this generalized "phase shift" changes by 180°; however, at the same time the modulus goes through a minimum. This effect causes a distortion of the resonance shape

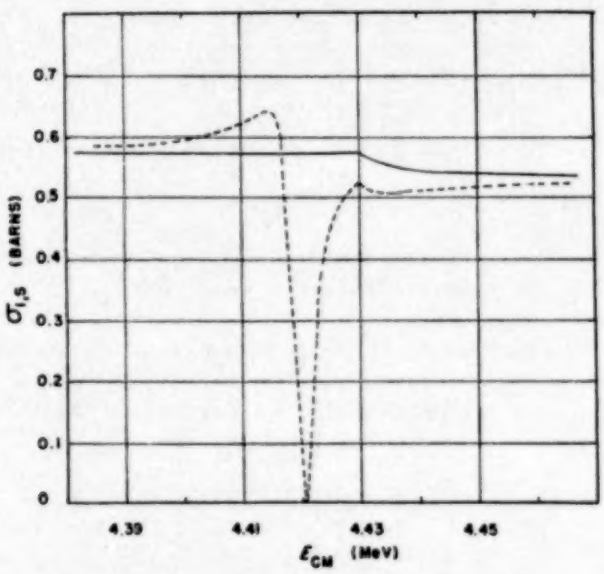

Fig. 11. The Wigner cusp. The elastic S-wave scattering cross section in channel 1 is shown in the neighborhood of the threshold for channel 2. The solid curve gives the cross section for the case where there is no state near the threshold energy. ($V_{11} = -7.25$ MeV, $V_{22} = -2.5$ MeV, $V_{12} = 0.500$ MeV, $R = 4.5 \times 10^{-13}$ cm.) The dotted curve gives the cross section when there is a state (of type 2) slightly below threshold. ($V_{11} = -7.25$ MeV, $V_{22} = -3.0$ MeV, $V_{12} = 0.500$ MeV, $R = 4.5 \times 10^{-13}$ cm.) The threshold energy was taken to be exactly 4.43 MeV.

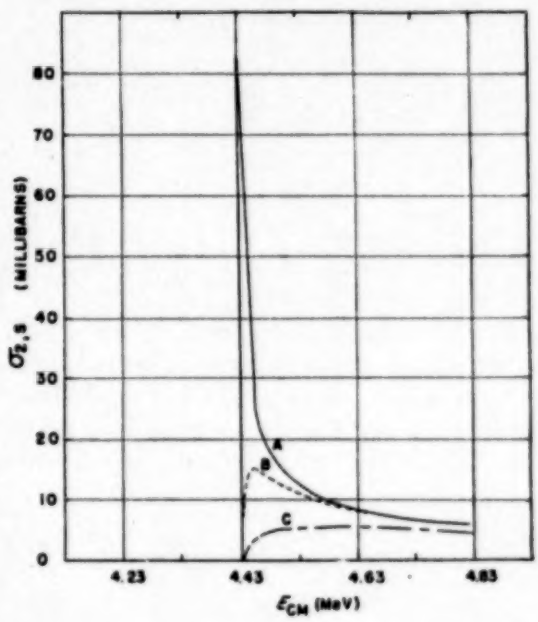

Fig. 12. The reaction cross section in the neighborhood of the threshold. $V_{11} = -7.25$ MeV, $V_{12} = 0.500$ MeV, $R = 4.5 \times 10^{-13}$ cm; (A) $V_{22} = -2.75$ MeV, (B) $V_{22} = -2.5$ MeV, (C) $V_{22} = -2.0$ MeV.

from that predicted by single level dispersion theory: since the modulus is not necessarily unity when the phase angle goes through 90°, the cross section curve does not go through zero. A polar plot of the "phase shift" for a typical resonance is shown in fig. 16.

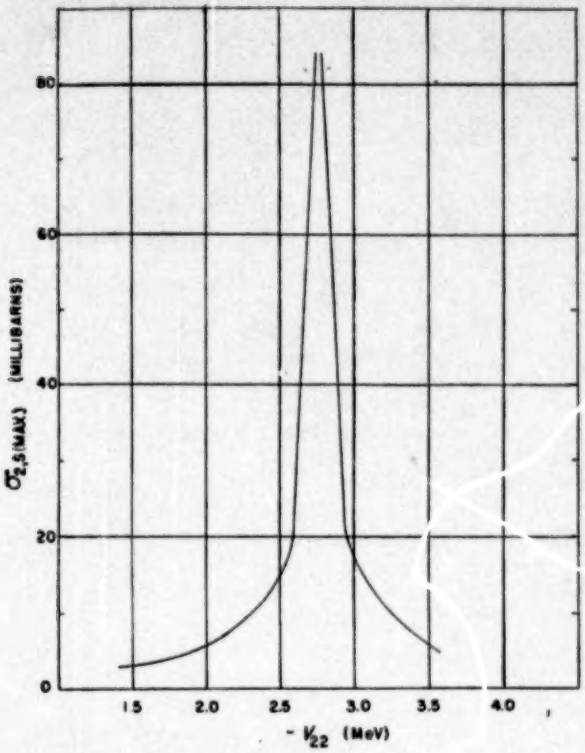

Fig. 13. The maximum value of the reaction cross section where a resonance (of type 2) occurs near threshold energy as a function of $-V_{22}$. ($V_{11} = -7.25$ MeV, $V_{12} = 0.500$ MeV, $R = 4.5 \times 10^{-13}$ cm.)

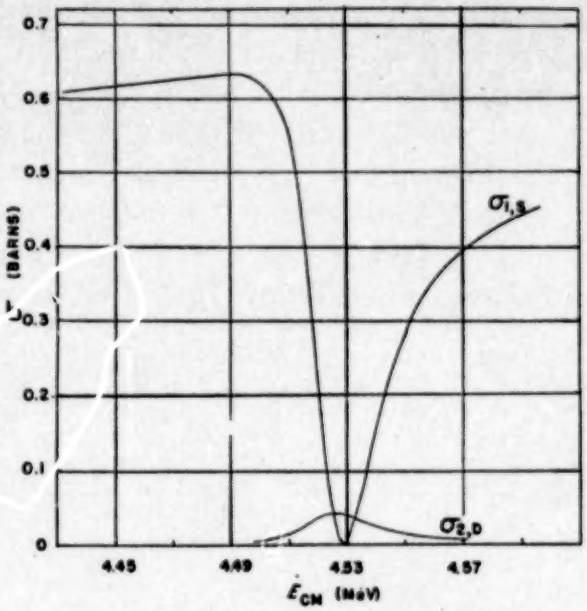

Fig. 14. The elastic scattering cross section $\sigma_{1,S}$ and the reaction cross section $\sigma_{2,D}$. The resonance is of type 2. The S and D refer to the values of the orbital angular momentum in the two channels. ($V_{11} = -7.25$ MeV, $V_{22} = -5.75$ MeV, $V_{12} = 0.500$ MeV, $R = 4.5 \times 10^{-13}$ cm.)

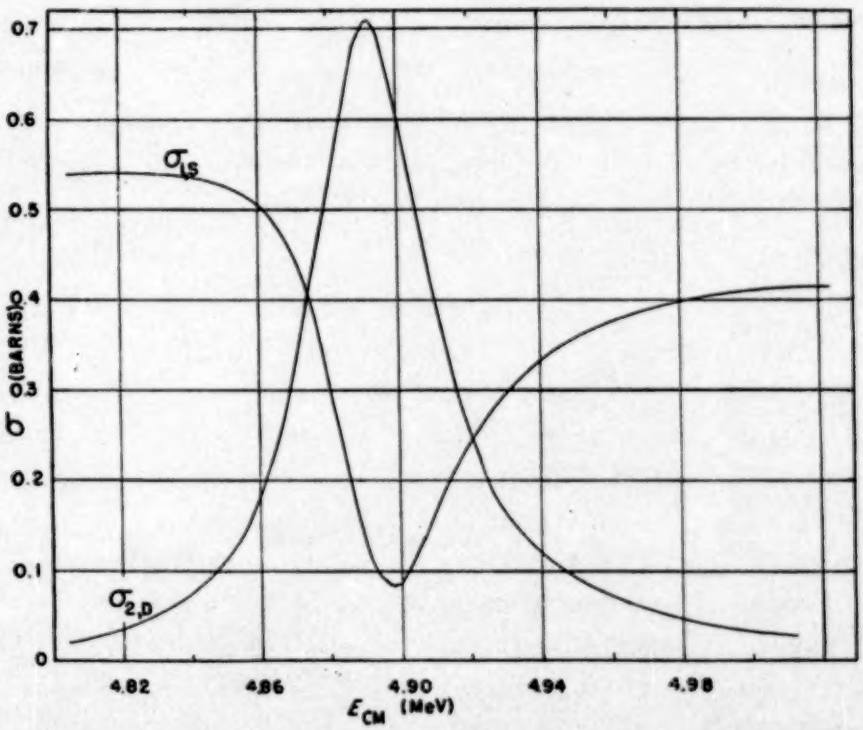

Fig. 15. Same as fig. 14, but for a resonance at a higher energy, ($V_{11} = -7.25$ MeV, $V_{22} = -5.25$ MeV, $V_{12} = 0.500$ MeV, $R = 4.5 \times 10^{-13}$ cm.)

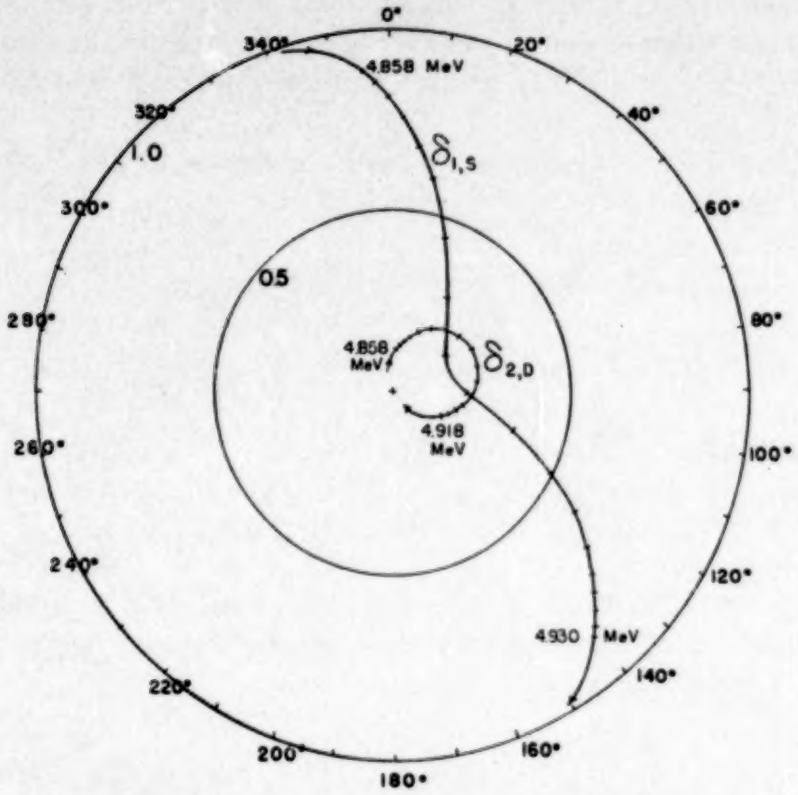

Fig. 16. The complex phase shifts for the resonance shown in fig. 15. $\delta_{1,S}$ is the elastic scattering phase shift; $\delta_{2,D}$ is the reaction phase shift. The modulus is given by the distance to a point on the curve from the origin; the phase is given by the angular displacement from the vertical. The energy scale is provided by the hash marks along the curves. The distance between two adjacent marks corresponds to an energy interval of 4 keV. The energies given refer to the initial and final hash marks on the curves.

5. Application of the Model

One aim of future investigation is to fit the energy levels and the scattering phase shifts for the C^{13}—N^{13} system [3]). As a step in this direction a fit to the $J = \frac{5}{2}^+$ levels and scattering parameters of C^{13} was attempted. In this nucleus there is a $\frac{5}{2}^+$ bound state of parentage $C^{12}+n$ at $E_{CM} = 3.85$ MeV and a narrow $\frac{5}{2}^+$ scattering level at a positive neutron energy of 2.076 MeV of the parentage $C^{12*}(2^+$ state$)+n$.

The position of the bound state is controlled chiefly by V_{11}; the position of the virtual state by V_{22} and its width by V_{12}. By adjusting these three parameters the bound state was set at the proper energy, and the $J = \frac{5}{2}^+$ phase shift was fitted within the experimental error from $E_n = 1.5$ MeV to $E_n = 4.0$ MeV [3]). The nuclear radius for all potentials was taken be to 4.5×10^{-13} cm.

One additional piece of previously unavailable information was provided by this analysis. From the parameters obtained in fitting the data the purity of the bound state could be determined. The final results are summarized in table 1.

TABLE 1

Derived parameters for the $\frac{1}{2}^+$ states in C^{13}. The two $\frac{1}{2}^+$ states have been fitted by the potential parameters shown, and the fractional parentage coefficients of the bound state deduced.

1. Data given Resonance energy (Lab): 2.076 MeV Resonance width (Lab): 7 keV Bound state energy (C.M.): 3.85 MeV
2. Derived values of the parameters V_{11}: −6.50 MeV V_{22}: −7.85 MeV V_{12}: 0.45 MeV
3. Purity of the 3.85 MeV level $\|\theta_1\|^2 = 0.986$ (C^{12}+n) $\|\theta_2\|^2 = 0.014$ (C^{12*}+n)

The authors wish to thank Dr. Noyes Smith and Arnold Romberg of the Shell Development Company for their generosity in allowing us free use of their IBM-650 and other computational facilities.

References

1) G. C. Phillips and T. A. Tombrello, to be published
2) E. P. Wigner, Phys. Rev. **73** (1948) 1002
3) Wills, Bair, Cohn and Willard, Phys. Rev. **109** (1958) 891;
Reich, Phillips and Russell, Phys. Rev. **104** (1956) 143

1.C

Nuclear Physics **20** (1960) 663—689; © *North-Holland Publishing Co., Amsterdam*

Not to be reproduced by photoprint or microfilm without written permission from the publisher

MANY-BODY PERTURBATION METHODS IN A SOLUBLE MODEL

AMNON KATZ

Department of Physics, The Weizmann Institute of Science, Rehovoth, Israel †

Received 11 May 1960

Abstract: It is pointed out that because statistics should not be obeyed in Goldstone's perturbation expansion there exist two-body contributions from diagrams other than ladders. The role of diagrams with "wrong" statistics is investigated in a model in which the perturbation is a single particle potential. A summation of all diagrams is carried out in this model and compared to the sum of all ladders. It is found that the "wrong statistics" contributions are important in deciding the region of convergence of the series and the location and nature of the singularities which limit it. While the region of convergence of the series of ladders is limited by a pole on the real axis, the radius of convergence of the complete series (which is smaller) is marked off by two branching points off the real axis. The formal sum of all diagrams displays a finite discontinuity at that point of the real axis where the ladders have a pole, thus changing from one branch to another. Each branch can be continued analytically through this discontinuity which is not a singularity of either branch. The ladders approximate only one branch, turning the finite discontinuity into a pole and thus one branch corresponding to the Cooper state, is lost. The remaining branch is described quite well by Brueckner's ladders even outside the region of convergence of the power series. It corresponds to the "normal" state. In the case of two-body interactions with short range and low density the most important contributions with wrong statistics are the two-body contributions of "many-body diagrams". Their inclusion is equivalent to using the Cooper type solution of a Bethe-Goldstone equation.

Introduction

The ground state of a system of many fermions with a wide range of attractive interactions is known to be "superconducting". The properties of such a state can be readily derived by the method of Bardeen, Cooper and Schrieffer (BCS) [1]). It is then found that the distribution of fermions over single-fermion states in the superconducting state deviates considerably from the Fermi step function. Its energy, in the case of an infinite system, is found, in the BCS method, to be non analytically dependent on the strength of the interaction g at $g = 0$, and is therefore unobtainable by perturbation expansion near $g = 0$. In the case of a finite system, however, the dependence of the ground state energy on g is analytic. The perturbation series may not be convergent, but there is no reason why its analytic continuation from the region of convergence should not reproduce the BCS state and energy. Yet Brueckner's method which

† The research reported in this paper has been sponsored in part by the Air Force Office of Scientific Research of the Air Research and Development Command, U. S. Air Force, through its European office.

Goldstone [3]) was able to derive from his perturbation expansion, fails to yield them. It is the purpose of this paper to investigate why. We shall try to see if there is any connection between Goldstone's perturbation expansion in its region of convergence and the BCS results for the fermion-system ground state.

Goldstone's [3]) main idea was to retain in his perturbation series only terms (diagrams) due to the interaction of two particles alone. All terms in which three or more particles interact simultaneously were to be neglected. This can be justified when the range of the interaction is short compared to the relative distance between the particles in the system. Yet, it soon proved that this choice of diagrams, namely the ascending ladders, was not always satisfactory as it gave rise to a non-physical singularity in the expression for the energy. This was realized by several authors [4, 12, 13]), some of whom (Chisholm and Squires [4])) tried to remedy the deficiency by the inclusion of more diagrams, namely the descending ladders. This was also done by Goldstone (unpublished). By this procedure we establish in our solution a complete symmetry between particles and holes which is characteristic of the BCS result. But otherwise it suffers all the shortcomings of Brueckner's original approximation. The next step in this direction would have been the summation over mixed ladders as well as over ascending and descending ones. To the best of our knowledge this has not yet been done. Yet, as will be shown below, it is not all these diagrams which are really wanting in our approximation. Descending and mixed ladders are not even proper two-body contributions. The successive scattering of a pair of holes is really a successive scattering of different pairs of particles.

But there is another proper two-body contribution. There are the contributions of many-body diagrams in which some of the line labels are identical. In the Goldstone perturbation series the summation on the labels of particle and hole lines should be carried out without any restrictions due to statistics. Therefore any diagram contributes something to the two-body part of the interaction for some choice of line indices. The best argument to show that these are proper two-body contributions is the fact that, as we shall see, they must be included even when we are dealing with a system which consists of only two particles. In a system of many particles there are also many particle contributions corresponding to similar diagrams which are of the same order of magnitude and must be included as well. Yet even the introduction of the two-body contributions alone is enough to make the characteristics of the superfluid state appear.

We can see that the nature of the super-conducting state is determined by these special many-body diagrams with repeated labels if we examine more closely the BG equation. This is an equation for a pair of fermions immersed in a sea of other fermions which, however, do not interact among themselves or with the pair except via the Pauli principle.

The BG procedure is equivalent to summation over all diagrams with no more than two hole labels in them. This sum includes, of course, all ascending ladders

and also all contributions from diagrams with more than two hole lines provided they have no more than two hole labels. It is in this last contribution that the BG method differs from that of Brueckner, and this difference must therefore account for the existence of Cooper-type solutions [6, 14]) to the BG equations and to their absence in the method of Brueckner. The Cooper-type solution is a bound pair state which has comparable probability amplitudes in all available unperturbed states. The dependence of its energy on the strength of the interaction, in the limit of an infinite system is non-analytic in a similar way to that of the BCS energy. We see therefore that the peculiarities of the BCS result appear already in the BG equation. The latter is of course not symmetrical in particles and holes and is not self consistent; it starts from a Fermi distribution of non-interacting fermions and after the inclusion of the interaction it winds up with a different distribution. Yet the inclusion of two-body contributions from many-body diagrams is enough to introduce some of the peculiarities of the BCS theory. It may be hoped that if *all* many-body contributions were to be taken into account the solution, which would be symmetric in particles and holes, would still feature the BCS characteristics and would yield the correct result.

In order to illustrate this idea we shall introduce a model on which we shall try the Goldstone perturbation method. We shall achieve an expression for the energy in a case where the total contribution is due to a Cooper type state. We shall derive the result by the Goldstone perturbation expansion although, in that case, it does not converge. We shall also see that in our model the inclusion of all ladders would have contributed nothing to the energy. All the energy of a Cooper state therefore lies in the contributions of many body diagrams.

We shall also see in our model what the "technical" role of the contributions from many body diagrams is. It is well known [4, 12, 13]) that the Brueckner expression for the energy displays a singularity at that value of the parameters of the problem where the Cooper solution starts to yield lower energy than the normal solution. This singularity is a pole, and marks, of course, the boundary of the region of convergence of Brueckner's expansion. This expansion, however, can easily be continued beyond the pole. The continuation then describes the "normal" solution. If we include the contributions of many-body diagrams (or even only two-body contributions thereof) we get an expression for the energy which is not much different than Brueckner's expression either inside or outside the region of convergence of the latter. It does, however, differ greatly from Brueckner's expression where the latter displays its pole. Instead of the infinite discontinuity of the pole we get a finite discontinuity (see fig. 7). The value of the energy remains finite on every side of the discontinuity corresponding to the "normal" and "superconducting" energies of the system at that value of the interaction. Moreover, the expression constitutes a two-valued analytic function. It can be continued analytically through the discontinuity

from either side (figs. 5, 6) to form the values of two possible energy levels of the system for any strength of the interaction. One of them is always lower than the other but the titles "normal" and "superconducting" are changed. This is the well known phenomenon that energy levels do not cross, rather they change names. This is illustrated in fig. 1 which is a curve of the energies of both states versus the strength of the interaction.

For the sake of illustration we shall also carry through a parallel treatment of the problem by the Wigner Brillouin [8]) perturbation method. In this method statistics should not be disregarded and therefore the ladders do include all two body contributions. As we shall see the Wigner-Brillouin ladders are a correct (although implicit) representation of the Cooper state.

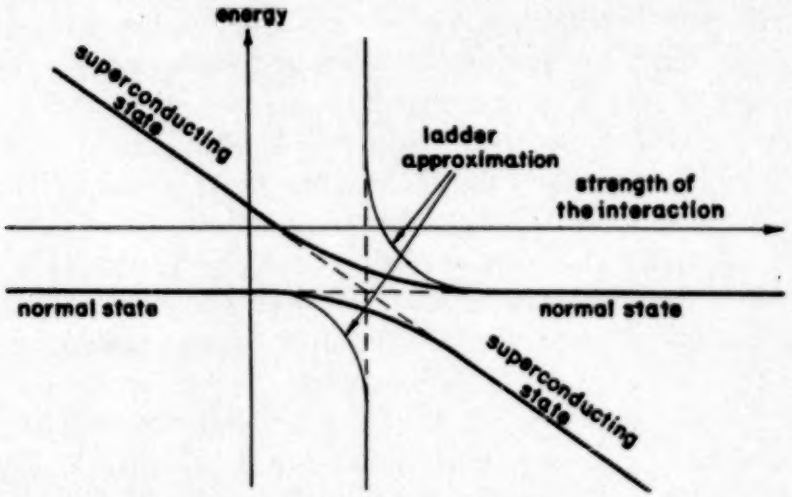

Fig. 1. Energies of the superconducting state and lowest normal state vs. the strength of the interaction. The broken line is Brueckner's approximation.

In the model that we shall introduce the perturbation will be a single-particle force [4]). Most of the considerations of the usual two-body forces in perturbation theory remain valid also in this simpler case. It enables us therefore to obtain a clearer picture of the role played by various terms in the perturbation series. The analogue of a two-body contribution is now a one-body contribution. This is the contribution of a process in which only one particle is in the active range of the external force which we use for perturbation. We shall see, that a single-particle Bethe-Goldstone procedure gives a reasonable approximation to both branches of the energy. But our main concern here is to stress the role of diagrams with "wrong" statistics. These include two-body contributions of many-body diagrams as well as many-body contributions of more-body diagrams.

Before we end the introduction and proceed to describe the perturbation methods and the model, some remarks are due about what happens when the system becomes infinite. In an infinite system the superconducting state is

orthogonal to the unperturbed states of the system; it is therefore inaccessible to the perturbation methods of either Wigner Brillouin or Goldstone. The Goldstone method yields the lowest state which is not orthogonal to the unperturbed ground state, and therefore the lowest "normal "state. What happens in the power expansion as the system goes to infinity is that the contributions of many-body diagrams become negligible separately in every order in comparison to the contributions of ladders of the same order. This has led to their neglect in the Brueckner theory. But the smallness of these contributions is not due to the smallness of the physical phenomenon which they describe; it is rather due to the fact that the mathematical device which we use, namely Goldstone's method, ceases to describe this phenomenon and "switches over" from the superconducting state to the normal state. If we want to have the physical phenomenon in our calculation, we must include the contribution, however small in every order. If we must go to the limit of an infinite system an order of limits should be devised, such that the physical phenomenon will not escape us.

1. The Wigner Brillouin Perturbation Theory

In the Wigner Brillouin expansion [8]) the difference between the true energy E and the unperturbed energy U of the system is given by

$$E-U = (0|v+v\frac{P}{E-H_0}v+v\frac{P}{E-H_0}v\frac{P}{E-H_0}v+\ldots|0), \tag{1.1}$$

where $|0)$ is the unperturbed state from which we begin and H_0 the unperturbed hamiltonian, for which

$$H_0|0) = U|0). \tag{1.2}$$

In eq. (1.1), v is the interaction; the complete hamiltonian is

$$H = H_0+v. \tag{1.3}$$

P is a projection operator which eliminates the unperturbed state $|0)$:

$$P|0) = 0, \quad P|\psi) = |\psi) \quad \text{if} \quad (\psi|0) = 0. \tag{1.4}$$

The true state $|E)$, which satisfies

$$H|E) = E|E), \tag{1.5}$$

is given by

$$|E) = \left[1+\frac{P}{E-H_0}v+\frac{P}{E-H_0}v\frac{P}{E-H_0}v+\ldots\right]|0). \tag{1.6}$$

In eq. (1.6) we have assumed that the state $|E)$ is not degenerate. Even if it is, then $|E)$ of eq. (1.6) is still a solution of eq. (1.5) and the energy equation (1.1)

is still valid. Another assumption implied in eq. (1.6) is that the true state $|E)$ is not orthogonal to the unperturbed state $|0)$. This assumption is essential. Apart from it the choice of $|E)$ and $|0)$ is quite arbitrary. Provided the correspondence between the state $|E)$ and the energy E and between the state $|0)$ and the operator P be correct, we may start with any state $|0)$ and end with any state $|E)$ not orthogonal to it. The operator series (1.1) and (1.6) are geometric series and as such may be readily summed, giving

$$E-U=(0|v\frac{1}{1-\frac{P}{E-H_0}v}|0), \tag{1.7}$$

$$|E)=\frac{1}{1-\frac{P}{E-H_0}v}|0). \tag{1.8}$$

The validity of the expressions for E and $|E)$ can be easily checked by applying $H=H_0+v$ to either (1.6) or (1.8). The "closed" forms (1.7) and (1.8) have little practical value for they contain the inverse of a complicated operator, the evaluation of which is equivalent in difficulty as well as in principle to the solution of the original Schroedinger equation. The importance of these closed forms lies however in that they show that the perturbation method may be carried over to regions where the original series does not converge by means of analytic continuation. We shall use this idea later on.

2. Diagrams

In a system of many particles the various contributions to any perturbation series may be classified by the use of diagrams [3, 9, 10]. The intermediate states are denoted by directed lines for particles and holes. "Particles" are extra particles to a certain agreed unperturbed state which we choose as "vacuum", and "holes" are missing particles in this same vacuum. External lines carry labels of the states they stand for while a summation on all states is implied for internal lines. The interactions are represented by dotted lines [3, 10] or dots [9] where lines start and end. Usually the interaction v is a two-body force so that four lines meet at every matrix element. In order to simplify the proceedings we shall treat a case where both H_0 and v are single-body operators. This case does not need in principle a perturbation expansion for its solution. Once the total hamiltonian of a single particle is diagonalized, we can construct the ground state and its energy by putting each particle in a definite state. We put one fermion in each state, in order of ascending eigenvalues starting with the lowest, until we have exhausted the particles. Still, in order to study the details of the various perturbation methods we can examine them for the case in which

a single body external potential is the perturbation; this case is simpler than the case of two body interaction. This device was used by Chisholm and Squires [4]) who attribute it to Bell [4]).

For a single-body perturbation only two lines meet at each interaction. A typical diagram is:

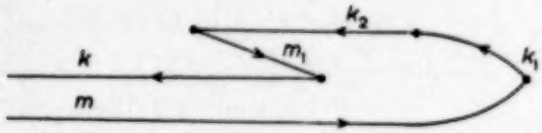

(2.1)

It is a contribution to the matrix element of the entity for which we use the perturbation expansion, which, for definiteness, we choose to be the operator of eq. (1.6), between tne "vacuum" and the state with particle k and hole m. (We shall go on using the label k for particles and m for holes). It stands for the expression

$$\sum_{k_1 k_2 m_1} (0|a_k a_m^\dagger \frac{1}{E-(U+\varepsilon_k-\varepsilon_m)} v_{m_1 k_2} a_{m_1}^\dagger a_{k_2} \frac{1}{E-(U+\varepsilon_{k_2}+\varepsilon_k-\varepsilon_m-\varepsilon_{m_1})}$$

$$\times v_{k m_1} a_k^\dagger a_{m_1} \frac{1}{E-(U+\varepsilon_{k_2}-\varepsilon_m)} v_{k_2 k_1} a_{k_2}^\dagger a_{k_1} \frac{1}{E-(U+\varepsilon_{k_1}-\varepsilon_m)} v_{k_1 m} a_{k_1}^\dagger a_m|0)$$

$$= \sum_{k_1 k_2 m_1} (0|a_k a_m^\dagger a_{m_1}^\dagger a_{k_2} a_k^\dagger a_{m_1} a_{k_2}^\dagger a_{k_1} a_{k_1}^\dagger a_m|0) \frac{1}{E-(U+\varepsilon_k-\varepsilon_m)} \tag{2.2}$$

$$\times v_{m_1 k_2} \frac{1}{E-(U+\varepsilon_{k_2}+\varepsilon_k-\varepsilon_m-\varepsilon_{m_1})} v_{k m_1}$$

$$\cdot \frac{1}{E-(U+\varepsilon_{k_2}-\varepsilon_m)} v_{k_2 k_1} \frac{1}{E-(U+\varepsilon_{k_1}-\varepsilon_m)} v_{k_1 m}.$$

Here $v_{ll'}$ is the matrix element of the total perturbation v between the single-particle states l and l':

$$v_{ll'} = (l|v|l'). \tag{2.3}$$

The ε's are the unperturbed single-particle energies.

The total perturbation is therefore given by

$$v = \sum v_{ll'} a_l^\dagger a_{l'}. \tag{2.4}$$

This was used in (2.2). We have omitted the projection operator P appearing in the expression (1.6). If, as is normally done, we choose for the vacuum $|0)$ of (2.2) the unperturbed state which goes over into the perturbed state in question in (1.6), then the operator P just implies that diagrams with an "empty" intermediate state be excluded. Diagram (2.5) for instance,

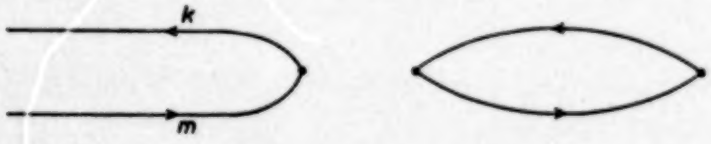

(2.5)

should not be counted, while one like (2.1) remains unaltered. The use of topological properties of diagrams in the formulation of theorems is the basic tool of the Goldstone method to be described presently.

A remark about statistics may be adequate at this stage. The effects of statistics in eq. (2.2) is contained in the commutation relations of the creation and annihilation operators. For fermions it follows from these commutation relations that the matrix element in the last row of (2.2) may in general assume one of the values $+1$, 0, -1. For a diagram of a given topology however, there are only two possible values: $+1$ and 0 or -1 and 0.

In the case of the diagram (2.1) the possible values are $+1$ and 0. The latter value occurs when some particle or hole appears twice in the same intermediate state. For instance when $k_2 = k$ or when $m_1 = m$. When all labels are different we have the value $+1$; we therefore call this diagram a "positive diagram".

It is well known that statistics may be disregarded in summations over diagrams. We may replace the matrix element of the a's and $a^\dagger$'s by $+1$ when the topology of the diagram makes it positive and by -1 when it is negative even if there are repeated indices. The contribution of a diagram like (2.1) is then considered to be

$$\sum_{m_1 k_1 k_2} \frac{1}{E-(U+\varepsilon_k-\varepsilon_m)} v_{m_1 k_2} \frac{1}{E-(U+\varepsilon_{k_2}+\varepsilon_k-\varepsilon_m-\varepsilon_{m_1})} \cdot v_{k m_1} \frac{1}{E-(U+\varepsilon_{k_2}-\varepsilon_m)} v_{m_2 m_1} \frac{1}{E-(U+\varepsilon_{k_1}-\varepsilon_m)} v_{k_1 m},$$

taken with the appropriate sign and without any restrictions on the values of k_1 and k_2 (i.e. it includes the terms with $k = k_2$ which do not contribute to (2.2) since $a_k a_k = 0$). The superfluous contributions thereby included in positive diagrams are cancelled by equal superfluous contributions in negative diagrams.

This is displayed in (2.6). The drawing represents

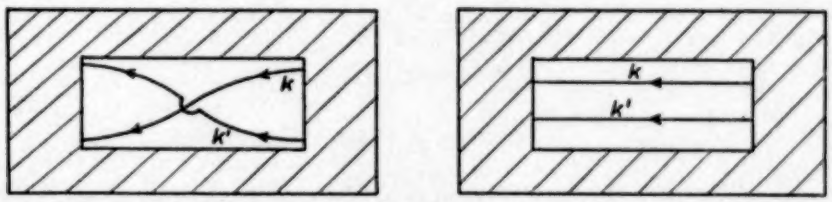

(2.6)

two diagrams which are identical except for the crossing over of the particle lines k and k' appearing in some intermediate state. The two diagrams have opposite signs because the cross-connection of the lines implies that in the matrix element of a's and $a^\dagger$'s the operators a_k and $a_{k'}$ appear in inverse order for the two diagrams. If we observe statistics the case $k = k'$ should be exluded from the summation in both diagrams. But if statistics is disregarded in both diagrams the two contributions cancel because of the opposite signs, the formal contributions being of course equal.

There is another case where a restriction exists in the summation over line labels though it is not a question of intermediate states. This is the case of the contributions of diagonal matrix elements of holes, $v_{mm} = (m|v|m)$. These give rise to diagrams of the form

(2.7)

Such diagrams, although they contribute nothing to intermediate states, cannot, because of statistics, coexist with an m hole line. In order to lift this restriction it is necessary to introduce the non-existent process of forward scattering of the hole line m by the matrix element v_{mm}. The matrix element v_{mm} refers to a state of the system in which the single-particle state m is occupied, while the m line denotes that this state is free. As v_{mm} refers to a state of the system opposed to the one implied by the m line no forward scattering of the m line by v_{mm} is possible. Formally, v_{mm} appears in (2.4) accompanied by the operator $a_m^\dagger a_m$, therefore all it can scatter forward is "vacuum" as it does in (2.7). Nevertheless, once we introduce this fictitious hole scattering, the superfluous contribution of diagrams of the type of (2.7) coexisting with the corresponding hole lines is exactly cancelled. (A hole scattering always implies a minus sign because the operators $a_m^\dagger a_m$ first create the new hole and only then destroy the old one). The cancellation is demonstrated in (2.8) where the two diagrams whose contributions cancel are represented. That

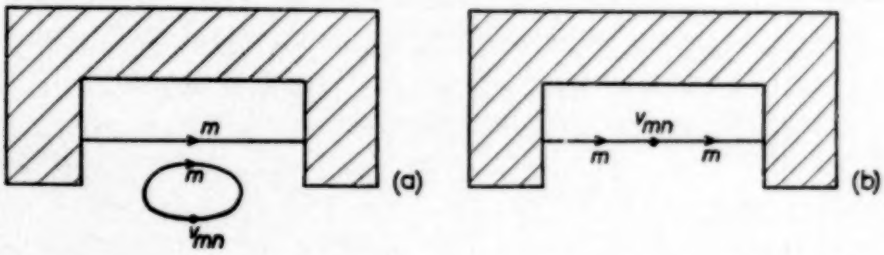

(2.8)

this cancellation is similar in nature to the one demonstrated in (2.6), i.e. due to cross-connection of lines with identical labels, can be seen in (2.9) where (2.8)(b) is drawn in a somewhat different fashion:

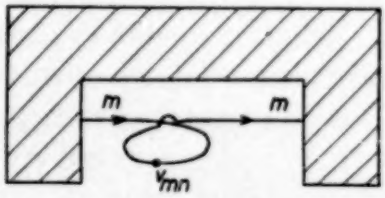

(2.9)

We may therefore lift every restriction due to statistics in our summations over line labels provided we include also fictitious processes. This of course implies the addition of many terms which just cancel one another and that should

never have been in the summation to begin with. In the discussion of the special model we shall prefer not to lift the statistics restriction, as long as we are dealing with the Wigner-Brillouin perturbation series. With the Goldstone perturbation series, however, this is no longer a matter of choice.

3. The Goldstone Theorem

A theorem due to Goldstone [3, 9, 10]) states that if our "vacuum" $|0)$ is chosen to be the unperturbed ground state and provided it is not degenerate, the lowest state which is not orthogonal to $|0)$ is given by

$$|\psi) = \Omega(U)_{\mathrm{L}}|0) \tag{3.1}$$

and its energy E by

$$E = U + (0|G(U)|0)_{\mathrm{C}}. \tag{3.2}$$

Here,

$$\Omega(\varepsilon) = 1 + \frac{1}{\varepsilon - H_0} v + \frac{1}{\varepsilon - H_0} v \frac{1}{\varepsilon - H_0} v + \ldots, \tag{3.3}$$

$$G(\varepsilon) = v\Omega(\varepsilon) = v + v \frac{1}{\varepsilon - H_0} v + \ldots, \tag{3.4}$$

and U is the unperturbed energy of the unperturbed ground state (1.2). The subscripts L and C mean that only contributions of linked diagrams or connected diagrams respectively should be taken into account. (Linked diagrams are those into every part of which one can get through external lines and along the lines of the diagram. Diagrams without external lines but in which every part is connected with every other by internal lines are connected diagrams. The empty diagram corresponding to the term 1 in (3.3) is considered linked). It can also be proved [9, 10]) that

$$|(\psi|0)|^2 = \exp \frac{\mathrm{d}}{\mathrm{d}\varepsilon} (0|G(\varepsilon)|0)_{\mathrm{C}}|_{\varepsilon = U}. \tag{3.5}$$

The various proofs of the above results are not valid unless the summation on the line labels in a diagram expansion of the operators (3.3) (3.4) is carried out independently for every label, i.e. we must abandon the restrictions of statistics and introduce forward scattering of holes as explained in section 2. Once we have separated connected and linked diagrams from the rest of the diagrams we cannot go back and limit ourselves to diagrams which obey statistics. For in a pair of cancelling superfluous contributions of the type shown in (2.6) and (2.8) one diagram may be linked or connected while the other is not and does not appear any more in the restricted summation over linked or con-

nected diagrams. In the pair of diagrams (3.6),

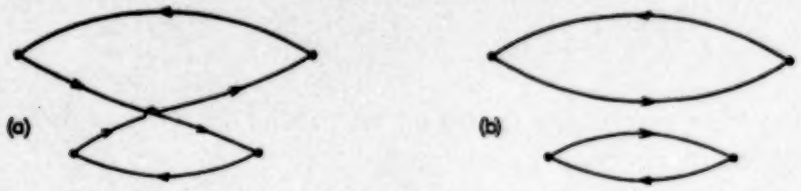

(3.6)

(a) is a connected diagram. It contributes to the energy expression (3.2) even when the two-hole lines carry the same label. This contribution is no longer cancelled by (3.6) (b) because the latter, being disconnected, does not appear in the summation. We see that since we restrict the diagrams in (3.1) and (3.2) to be linked or connected respectively we must lift all statistical restrictions and allow all forward scattering of holes. Therefore the restrictions in Goldstone's expansion are not necessarily stronger than those in the Wigner-Brillouin expansion and the number of diagrams included is not necessarily smaller. In the next section we shall study a model in which the whole Wigner-Brillouin expansion consists of a single diagram while Goldstone's expansion includes an infinity of them.

4. The Two-State Model

Let us consider a quantum system with two single particle states populated by one particle. The operators H_0 and v, which are both single particle operators, will be chosen as

$$H_0 = \begin{bmatrix} \varepsilon & 0 \\ 0 & 0 \end{bmatrix}, \tag{4.1}$$

$$v = \begin{bmatrix} 0 & v \\ v^* & 0 \end{bmatrix}, \tag{4.2}$$

$$H = H_0 + v = \begin{bmatrix} \varepsilon & v \\ v^* & 0 \end{bmatrix}. \tag{4.3}$$

Let us, for the time being, assume that $\varepsilon > 0$, in which case the unperturbed ground state, and consequently also the "vacuum" for our diagrams, is the state of the system in which the particle occupies the single particle state corresponding to the eigenvalue 0 of H_0. Since the system is composed of a single particle and the operators (4.1), (4.2) and (4.3) are single-particle operators we may simply say in the language of first quantization that the state of H_0 with eigenvalue 0 is the unperturbed ground state. The unperturbed energy U is 0.

The energy of the true ground state E is a root of the equation

$$\begin{vmatrix} \varepsilon - E & v \\ v^* & -E \end{vmatrix} = (E-\varepsilon)E - |v|^2 = 0. \tag{4.4}$$

Implicitly E is therefore given by

$$E = v^* \frac{1}{E-\varepsilon} v. \tag{4.5}$$

This is the whole Wigner-Brillouin expansion (1.1). It contains the contribution of the single diagram

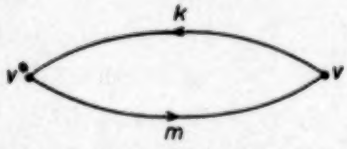

(4.6)

This is obviously the only diagram possible. The interaction v as given by (4.2) can take a particle from the state 0 to the state ε. In the language of diagrams it creates from the vacuum a pair, a particle k and a hole m. v is the only non vanishing matrix element of the interaction which connects the vacuum with anything. Once we are in the state ε the only matrix element we can use is v^* which takes us back to the ground state and there the game is over, because "vacuum" cannot serve as an intermediate state in the Wigner-Brillouin expansion. If we try to use Goldstone's expansion, however, there are many more diagrams to consider. As statistics must be disregarded we must include the possibility of creating a second pair after the first one, though it contains the same particle and hole as the first. Then we may destroy the two pairs in one order or the other. This give rise to the diagrams:

(4.7)

The number of possible pairs is of course unlimited and so is the number of diagrams. Let us now try to sum them all. Consider first the sign of each diagram. The diagram (4.6) is positive. The diagrams (4.7) could be achieved by cross connecting two diagrams of the type (4.6); therefore they are negative. In general the sign of a diagram of the order (number of interactions) $2p$ is $(-)^{p-1}$. Only even orders appear, for every pair must be first created then annihilated and there are no other interactions. As v appears once for every creation and v^* once for every annihilation the contribution of the diagram of order $2p$ is proportional to $|v|^{2p}$. The energy denominator in the state with κ pairs is $U-\kappa(\varepsilon-0) = -\kappa\varepsilon$. The whole contribution of a diagram of order $2p$ with a series of energy denominators $\{\kappa_i\}$ is therefore equal to

$$(-)^{p-1} \frac{1}{\prod \kappa_i} \frac{|v|^{2p}}{(-\varepsilon)^{2p-1}} = (-)^p \frac{1}{\prod \kappa_i} \frac{|v|^{2p}}{\varepsilon^{2p-1}}; \tag{4.8}$$

$\prod \kappa_i$ is the product of the κ's, i.e. numbers of pairs, in the intermediate states involved. The κ_i's are a series of positive integers differing by ± 1 from one another (since a pair must be created or annihilated in every interaction).

For $p = 3$, for instance, we have the following possibilities:

$$\begin{aligned} &\text{(a)} \quad (\kappa_1, \kappa_2, \ldots, \kappa_5) = (\overbrace{1, 2}, \overbrace{3}, \underbrace{2, 1}), \\ &\text{(b)} \quad (\kappa_1, \kappa_2, \ldots, \kappa_5) = (\overbrace{1}, \underbrace{2}, \overbrace{1}, \underbrace{2}, 1). \end{aligned} \tag{4.9}$$

Every such series of κ_i's corresponds, in general, to a number of different diagrams. If we take for instance the series (4.9a) and try to construct the corresponding diagrams, we see that, starting from the right, whenever κ_i increases we must create another pair and that part of the diagram is unique. We thus reach the first part of the diagram which is:

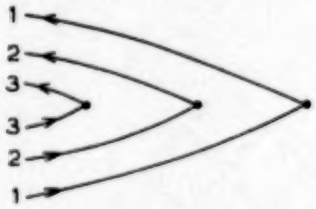

The sequence of κ_i in (4.9a) now tells us that the number of pairs has to be reduced by one. To do this we can pick on any of the κ_i particle lines (i.e. in the above example particle line 1, 2 or 3) and connect it with a hole line. We should, however, be careful not to connect a particle line with the *same* hole line with which it was created since this will lead to a disconnected diagram (i.e. in the above example particle line 1 should not be connected to hole line 1 etc.). Thus every time κ_i *decreases* (counting from the right) in a series like (4.9a) there are $\kappa_i(\kappa_i-1)$ different possible diagrams. The total number of possibilities may be arrived at by going over the series of κ_i from the right and multiplying together all pairs $\kappa_i\kappa_{i+1}$ for which $\kappa_{i+1} = \kappa_i+1$. The κ_i's so multiplied together are indicated in (4.9) by a $\frown$ joining them from above. (Some of the κ_i's of course get into the product twice). We may have used a similar logic starting from the left again obtaining the same number of possible diagrams. The κ'_i's we would have multiplied together then are indicated by a $\smile$ from below in (4.9). If we multiply together the first product of the κ_i's with the second, every one of the κ_i's appears exactly twice except for the first and the last which are unity and do not affect the product. Therefore this product, which is the square of the number of all possible diagrams corresponding to the series $\{\kappa_i\}$, is $\Pi\kappa_i^2$. The number of possible diagrams is therefore $\prod\kappa_i$. The contribution of all diagrams of order $2p$ corresponding to a series $\{\kappa_i\}$ is (4.8) multiplied by $\prod\kappa_i$, i.e.

$$(-)^p \frac{|v|^{2p}}{\varepsilon^{2p-1}}. \tag{4.10}$$

We see that the contribution of all possible diagrams with energy denominators represented by the series $\{\kappa_i\}$ is independent of the choice of this series. Every

series $\{\kappa_i\}$ gives the same contribution (4.10). To obtain the total contribution of diagrams of order $2p$ all we have to do now is to count the number of different series of κ_i's which are possible in such diagrams.

To derive an expression for this number, which we shall denote by T_p, let us consider the drawing in fig. 2. Every path from I to F along the heavy lines in the direction of the arrows corresponds to a series of κ_i's. The heavy segments represent addition of pairs when they slope up and their annihilation when they slope down, while the values of κ_i for intermediate states are represented by the points of intersection, κ_i being the height of the point above the diagonal IF. The drawing is completed by the thin lines into a square the side of which is p segments long (in the drawing $p = 5$).

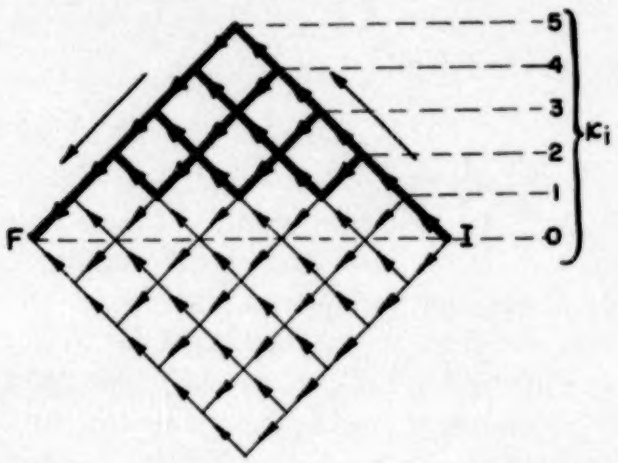

Fig. 2. Each way from I to F along the heavy lines corresponds to a series of intermediate states in a diagram. κ_i is the number of pairs. A segment sloping upwards represents the creation of a pair. A segment sloping downwards is the destruction of a pair and the points of intersection are possible intermediate states.

The number of possible ways from I to F along the lines of the complete square in the direction of the arrows is easy to calculate. One has to make p steps sloping up and p steps sloping down and the choice of the relative order of these steps is free; the number of choices of p up sloping steps from the total $2p$ is $\binom{2p}{p}$. This result can be expressed with the help of $T_{p'}$'s with $1 \leqq p' \leqq p$. Dividing the interval p into ν segments of length p_i, $1 \leqq p_i \leqq p$, $\sum p_i = p$, the number of ways from I to F which lie above the diagonal IF and touch it at intervals p_i (for instance the ways along the heavy lines of fig. 3 for the case $p_1 = 2$, $p_2 = 3$, $p_1 + p_2 = p = 5$) is

$$T_{p_1} T_{p_2} \dots T_{p_\nu}. \tag{4.11}$$

The number of ways from I to F touching the diagonal at intervals p_i but lying on any side of it (fig. 4 for the same p_i's as fig. 3) is 2^ν larger, ν being the

number of intervals, for in any interval the way may lie either above or bellow the diagonal.

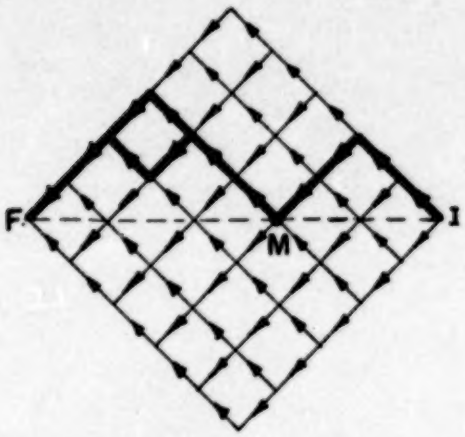

Fig. 3. The ways from I to F touching the diagonal only at M and lying above it.

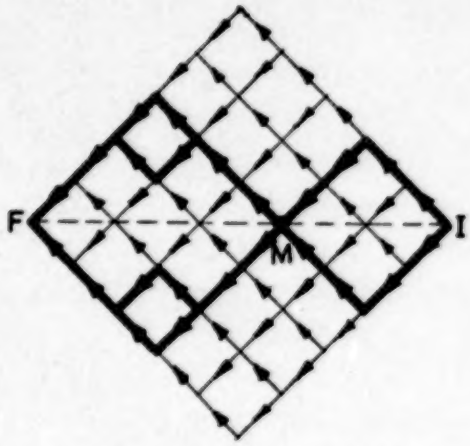

Fig. 4. All ways from I to F touching the diagonal only at M.

It is therefore

$$T_{p_1} T_{p_2} \dots T_{p_\nu} 2^\nu. \tag{4.12}$$

Summing on all numbers ν of intervals and on all the possible divisions of p into $p_1 + \dots + p_\nu = p$ for every ν, we have counted all possible paths from I to F. These, as we said, must add up to $\binom{2p}{p}$, and hence

$$\binom{2p}{p} = \sum_{\nu=1}^{\infty} \sum_{p_1+\dots p_\nu=p} T_{p_1} T_{p_2} \dots T_{p_\nu} 2^\nu. \tag{4.13}$$

(It is convenient to extend the summation on ν up to ∞; the contributions of values of $\nu > p$ vanish since then there is no possible division of p in p_i's satisfying $p_i \geqq 1$).

Let us now transform (4.13) into the space of generating functions, defined as

$$S(z) = \sum_{p=0}^{\infty} \binom{2p}{p} z^p, \tag{4.14}$$

$$T(z) = \sum_{p=1}^{\infty} T_p z^p. \tag{4.15}$$

By the use of the identity

$$\binom{2p}{p} = (-4)^p \binom{-\frac{1}{2}}{p}, \tag{4.16}$$

(4.14) can be summed up to yield

$$S(z) = \sum_{p=0}^{\infty} \binom{-\frac{1}{2}}{p} (-4z)^p = \frac{1}{\sqrt{1-4z}}. \tag{4.17}$$

On the other hand, using (4.13) one gets

$$\begin{aligned} S(z) &= 1+\sum_{p=1}^{\infty} z^p \sum_{\nu=1}^{\infty} \sum_{p_1+\cdots+p_\nu=p} T_{p_1} T_{p_2} \cdots T_{p_\nu} 2^\nu \\ &= 1+\sum_{\nu=1}^{\infty} 2^\nu \sum_{p=1}^{\infty} \sum_{p_1+\cdots+p_\nu=p} T_{p_1} z^{p_1} T_{p_2} z^{p_2} \cdots T_{p_\nu} z^{p_\nu} \qquad (4.18) \\ &= 1+\sum_{\nu=1}^{\infty} 2^\nu T(z)^\nu = \sum_{\nu=0}^{\infty} (2T(z))^\nu = \frac{1}{1-2T(z)}. \end{aligned}$$

Equating (4.18) with (4.17) we get

$$T(z) = \tfrac{1}{2}(1-\sqrt{1-4z}). \qquad (4.19)$$

Returning now to the Goldstone expansion of the ground state energy, let us remember that T_p was the number of series $\{\kappa_i\}$ of energy denominators possible for the diagrams of order $2p$. The contributions of all series $\{\kappa_i\}$ are the same and are given, for each one of them, by (4.10):

$$(-)^p \frac{|v|^{2p}}{\varepsilon^{2p-1}}. \qquad (4.10)$$

As there are T_p such contributions in the diagrams of order $2p$ the complete Goldstone expansion gives for the energy

$$\begin{aligned} E &= \sum_{p=1}^{\infty} T_p (-)^p \frac{|v|^{2p}}{\varepsilon^{2p-1}} = \varepsilon \sum_{p=1}^{\infty} T_p \left(-\frac{|v|^2}{\varepsilon^2}\right)^p \\ &= \varepsilon T\left(-\frac{|v|^2}{\varepsilon^2}\right) = \tfrac{1}{2}\varepsilon\left(1-\sqrt{1+4\frac{|v|^2}{\varepsilon^2}}\right), \end{aligned} \qquad (4.20)$$

where in the last step we have used (4.19).

As can be easily checked the expression (4.20) is a root of the quadratic equation (4.4). The second root displays the plus sign before the square root:

$$E' = \tfrac{1}{2}\varepsilon\left(1+\sqrt{1+4\frac{|v|^2}{\varepsilon^2}}\right). \qquad (4.21)$$

E is the ground state in the case we have assumed, that is $\varepsilon > 0$. In the case $\varepsilon < 0$ the ground state is E'. It can be reached through the Goldstone expansion in very much the same way which we have followed.

We have derived a closed expression for E. The expansion as a power series in $|v|^2$ converges only when $2|v| < |\varepsilon|$. Yet the closed formula (4.20) is a correct solution in all cases as it is a root of (4.4). In general one may say that in a system with a finite number of states the energy is an analytic function of the parameters of the problem (ε and $|v|$ in our case) and the meaning of a power

series can be extended to regions where it does not converge by means of analytic continuation. When we were summing the diagrams in this section we made no remark about convergence. It was enough to sum the series *formally* into a closed expression. This is a great advantage of a summation of the complete series. The formal sum of the complete series conserves its meaning even in regions where the series does not converge and where, therefore, approximations to any finite order have no meaning.

5. Scattering in the Two-State Model

Scattering is a process in which a particle makes a transition to another particle state or a hole to another hole state. As there is only one possible particle label in our model and only one hole label, any scattering is necessarily forward scattering. In order to introduce this phenomenon into our discussion let us modify the interaction (4.2) into

$$v_1 = \begin{bmatrix} u & v \\ v^* & 0 \end{bmatrix}. \tag{5.1}$$

The complete hamiltonian now is

$$H = \begin{bmatrix} \varepsilon+u & v \\ v^* & 0 \end{bmatrix}. \tag{5.2}$$

The quadratic equation (4.4) which the true energy satisfies becomes

$$(E-(\varepsilon+u))E-|v|^2 = 0. \tag{5.3}$$

The implicit (Wigner Brillouin) expression for the energy now reads

$$E = v^* \frac{1}{E-(\varepsilon+u)} v. \tag{5.4}$$

The corresponding Goldstone expression is

$$E = \tfrac{1}{2}(\varepsilon+u)\left(1-\sqrt{1+\frac{4|v|^2}{(\varepsilon+u)^2}}\right). \tag{5.5}$$

Both these expressions may be obtained from their counterparts of section 4 by the substitution

$$\varepsilon \to \varepsilon+u. \tag{5.6}$$

The energy denominators now become, in the Wigner Brillouin case for instance, $1/(E-(\varepsilon+u))$ which, when developed in powers of u, gives

$$E = \frac{|v|^2}{E-(\varepsilon+u)} = \frac{|v|^2}{E-\varepsilon}\,\frac{1}{1-\dfrac{u}{E-\varepsilon}} \tag{5.7}$$

$$= v\,\frac{1}{E-\varepsilon}\,v + v\,\frac{1}{E-\varepsilon}\,u\,\frac{1}{E-\varepsilon}\,v + v\,\frac{1}{E-\varepsilon}\,u\,\frac{1}{E-\varepsilon}\,u\,\frac{1}{E-\varepsilon}\,v + \ldots.$$

The Wigner Brillouin series has now contributions from all possible diagrams (statistics observed) in (5.8),

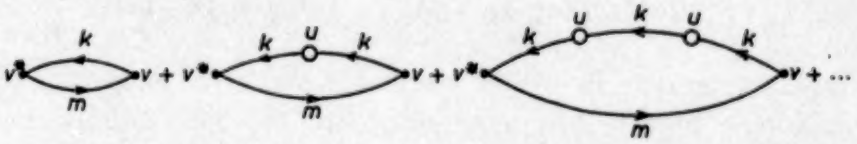

(5.8)

where the dot signifies v interaction (creation or annihilation of pairs) and the open circle u interaction (a particle forward scattering).

The effect of the transformation (5.6) in the Goldstone case is very similar. There too it introduces the contributions of all possible scatterings in the particle lines of the former diagrams of section 4. It should be noted however that in the Goldstone case where the development of the energy denominators in powers of u is

$$\frac{1}{0-(\varepsilon+u)} = \frac{1}{-\varepsilon}\,\frac{1}{1-\dfrac{u}{(-\varepsilon)}} \tag{5.9}$$

$$= \frac{1}{(-\varepsilon)} + \frac{1}{(-\varepsilon)}\,u\,\frac{1}{(-\varepsilon)} + \frac{1}{(-\varepsilon)}\,u\,\frac{1}{(-\varepsilon)}\,u\,\frac{1}{(-\varepsilon)} + \ldots.$$

There may be κ particle lines present between two v or v^* elements. In such a case the scattering may be performed on every line giving κ separate contributions. On the other hand the energy denominator is in that case $\kappa(0-\varepsilon)$. Every scattering therefore introduces the expression

$$\kappa u\,\frac{1}{\kappa(-\varepsilon)} = u\,\frac{1}{(-\varepsilon)}. \tag{5.10}$$

Thus we see that (5.9) accounts correctly for these contributions.

Let us now consider instead of v_1 given by (5.1) the perturbation v_2 given by

$$v_2 = \begin{bmatrix} 0 & v \\ v^* & w \end{bmatrix}. \tag{5.11}$$

Here only holes can be scattered forward. Now the quadratic equation is

$$(E-\varepsilon)(E-w)-|v|^2 = 0 \tag{5.12}$$

and the Wigner Brillouin expression is

$$E = w + v^* \frac{1}{E-\varepsilon} v. \tag{5.13}$$

It accounts for the diagrams:

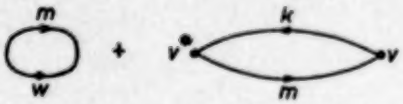

(5.14)

These are all diagrams allowed. The matrix element w refers to the vacuum and can cause no forward scattering of the state where a particle and a hole are present, which is the *second* state of the system. The pair state is the ε state, while w refers to the 0 state. This was explained in section 2. But in section 3 it was explained why in the Goldstone case such forward scattering does appear. Indeed we see that the total hamiltonian now is

$$H = \begin{bmatrix} \varepsilon & v \\ v^* & w \end{bmatrix} = w + \begin{bmatrix} \varepsilon - w & v \\ v^* & 0 \end{bmatrix}. \tag{5.15}$$

The transformation which it is now necessary to perform on the Goldstone expression (4.20) in order to get the correct energy is the addition of a term w which accounts for the first diagram in (5.14) and the substitution $\varepsilon \to \varepsilon - w$. The first of these appears in the Wigner Brillouin case as well. The last part accounts for all the scattering done by w on the hole lines. Every such scattering is accompanied with the sign minus as is appropriate for the scattering of a hole (section 2). As a last example in this section we shall treat the interaction v_3, given by

$$v_3 = \begin{bmatrix} u & v \\ v^* & w \end{bmatrix}. \tag{5.16}$$

In this case besides the addition of the term w, as before, the necessary transformation is

$$\varepsilon \to \varepsilon + u - w. \tag{5.17}$$

In this case the contributions of the matrix elements u and w to a sequence of n scatterings is

$$(u-w)^n = \sum \binom{n}{\nu} u^\nu (-w)^{n-\nu}. \tag{5.18}$$

It results from the choice of ν particle scattering amongs the total number of n scatterings which can be done in $\binom{n}{\nu}$ possible ways, leaving us with $n-\nu$ hole scatterings, and then summing over all values of ν.

6. A Many-State Model

The considerations of the preceding sections can be easily generalized to a limited case of a system with $K+M$ single-particle states populated by M fermions.

We choose H_0 as

$$H_0 = \begin{bmatrix} \varepsilon & & & & 0 \\ & \ddots & & & \\ & & \varepsilon & & \\ & & & 0 & \\ & & & & \ddots \\ 0 & & & & 0 \end{bmatrix}, \quad \varepsilon > 0. \tag{6.1}$$

On the diagonal of this matrix, the element ε occurs K times whereas the value 0 occurs M times. The equality between the number of particles and the number of eigenvalues 0 of H_0 is essential. It ensures a non-degenerate unperturbed ground state, without which Goldstone's theorem is not valid. For the interaction we shall take for the time being

$$v = \begin{bmatrix} 0 \ldots & 0 & v & v \ldots v \\ \cdot & & v & v \ldots \\ \cdot & & \cdot & \\ \cdot & & \cdot & \\ \cdot & & \cdot & \\ 0 \ldots & 0 & v & v \ldots v \\ v^* & v^* \ldots v^* & 0 \ldots & 0 \\ \cdot & & \cdot & \\ \cdot & & \cdot & \\ \cdot & & \cdot & \\ v^* & v^* \ldots v^* & 0 \ldots & 0 \end{bmatrix} \begin{matrix} \} K \\ \\ \\ \\ \\ \\ \} M \\ \\ \\ \\ \end{matrix} \tag{6.2}$$

$$\underbrace{\qquad\qquad}_{K} \quad \underbrace{\qquad\qquad}_{M}$$

This interaction can bring about the creation or annihilation of any pair but it causes no scattering. The diagrams involved are the same as those involved in section 4 (with the hamiltonian (4.3)), but every diagram must be counted many times, for every particle line may carry any one of K labels and any hole lines any of M. Every creation matrix element v in a given diagram may be chosen freely out of the KM possibilities (all of them contributing equally) so as to create any of the KM possible pairs. But once we have specified all the creation matrix elements in a diagram, all lines have been given labels and the annihilation matrix elements must be chosen uniquely so as to annihilate the existing pairs. From this we see that the multiplicity of the contributions of the various diagrams may be accounted for correctly by applying to the energy

expression (4.20) the transformation

$$v \to KMv, \quad v^* \to v^*, \quad |v|^2 \to KM|v|^2. \tag{6.3}$$

The energy is therefore given by

$$E = \tfrac{1}{2}\varepsilon\left(1 - \sqrt{1+4KM\frac{|v|^2}{\varepsilon^2}}\right). \tag{6.4}$$

If we take instead of (6.2) an interaction with scattering given by

$$v = \begin{bmatrix} \overbrace{v \quad v \ldots v}^{K+M} \\ v \quad v \ldots v \\ \cdot \\ \cdot \\ \cdot \\ v \ldots \quad v \end{bmatrix}, \tag{6.5}$$

v being real and negative, we can use considerations similar to those of section 5 and show that the energy is obtained by the substitution

$$\varepsilon \to \varepsilon + (K-M)v. \tag{6.6}$$

One also has to account for diagrams of the form of the first diagram in (5.14). This is done by the addition of the term Mv. The complete energy thus is

$$E = Mv + \tfrac{1}{2}(\varepsilon + (K-M)v)\left(1 - \sqrt{1+\frac{4KMv^2}{(\varepsilon+(K-M)v)^2}}\right). \tag{6.7}$$

We shall now take E to the limit $\varepsilon \to 0$. In this limit, which is known as a "degenerate shell", the Goldstone theorem is not valid on account of the degeneracy of the unperturbed ground state. The limit $\varepsilon = 0$ also lies far out of the region of convergence of the power series which has for limitation $|\varepsilon| > |(K+M)v|$. Yet if we use the analyticity of (6.7) we may use it all the same for $\varepsilon = 0$. This does not necessarily imply the substitution $\varepsilon = 0$ in (6.7), because the latter has a discontinuity at $\varepsilon + (K-M)v = 0$ (fig. 5(a)). This corresponds to the fact that as an analytic function (6.7) has two branches and the formal expression (6.7) describes only one of them for any value of ε.

Starting with $\varepsilon > (K+M)|v|$ in order to get expression (6.7) we may use it as its own analytic continuation down to $\varepsilon = -(K-M)v$. But beyond this point (6.7) jumps to a different branch. The continuation of the branch we started with is given by (6.8) which was obtained from (6.7) by changing the minus sign before the square root to plus:

$$E = Mv + \tfrac{1}{2}(\varepsilon + (K-M)v)\left(1 + \sqrt{1+\frac{4KMv^2}{(\varepsilon+(K-M)v)^2}}\right). \tag{6.8}$$

E of (6.8) also has a discontinuity at $\varepsilon = -(K-M)v$ (fig. 5(b)). Each of its parts is the direct continuation of the opposite part of (6.7). The complete

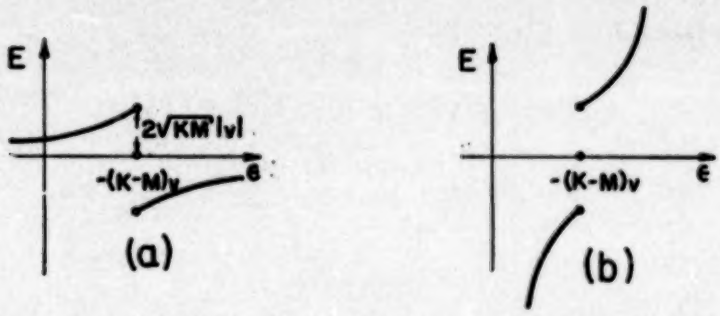

Fig. 5. The energies given by (6.7) (a) and (6.8) (b) versus the value of ε. The two branches display a discontinuity at $\varepsilon = -(K-M)v$. The continuation of the graphs in (a) across the discontinuity are the graphs in (b) and vice versa.

analytic expression for the ground state energy E as continued from the region of convergence consists of (6.7) for $\varepsilon > -(K-M)v$ and of (6.8) for $\varepsilon < -(K-M)v$. This recipe may be put into one formal expression namely

$$E = Mv+\tfrac{1}{2}(\varepsilon+(K-M)v-\sqrt{(\varepsilon+(K-M)v)^2+4KMv^2}). \tag{6.9}$$

The curve of expression (6.9) is shown by the heavy line in fig. 6, the dotted line shows what we would get by changing the minus sign in (6.9) into plus. Eq.

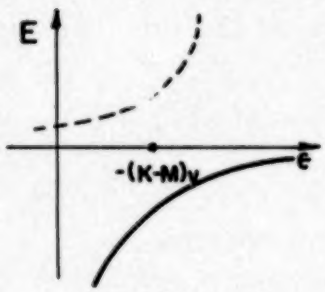

Fig. 6. The ground state energy given by (6.9) versus ε. The dotted line is the energy of the excited state.

(6.9) is the complete expression for the ground state energy in any region. It is here that we should substitute $\varepsilon = 0$ in order to get the energy of the degenerate shell. Doing so we get

$$\begin{aligned} E_{\text{deg. shell}} &= Mv+\tfrac{1}{2}(K-M)v-\sqrt{(K-M)^2v^2+4KMv^2}) \\ &= Mv+\tfrac{1}{2}((K-M)v-(K+M)|v|). \end{aligned} \tag{6.10}$$

As we are interested in $v < 0$, i.e. $|v| = -v$ (attractive perturbation), we get

$$E_{\text{deg. shell}} = Mv+\tfrac{1}{2}v((K-M)+(K+M)) = (K+M)v. \tag{6.11}$$

This obviously is the correct solution. Our single particle hamiltonian when $\varepsilon = 0$ is (6.5) .The matrix (6.5) is of rank one. Therefore it has only one non-

vanishing eigenvalue which equals the trace $(K+M)v$. We have to distribute the M fermions over the eigenvalues of H. One fermion gets the eigenvalue $(K+M)v$ and all the others have zero energy. The total energy is therefore $(K+M)v$.

The whole energy is due to the state with eigenvalue $(K+M)v$. The corresponding state vector is $(1, 1, \ldots 1)$. It spans all unperturbed states. If the unperturbed states are momentum eigenstates then the true state with eigenvalue $(K+M)v$ is highly localized. This is the bound Cooper-type state. The dependence of its energy on v seems quite analytic, in fact it is linear. But this linearity is the limit of a non-analytic expression as the unperturbed states become degenerate. (e.g. $\varepsilon/[1-\exp(-\varepsilon/v)] \to v$ as $\varepsilon \to 0$). In the next section we shall see how the energy $(K+M)v$ due to the Cooper state quite escapes ladder approximations. The ladders, as we shall see, always approximate the negative square root branch of (6.7).

7. Ladder Approximation to the Many-State Model

Let us consider our model as the description of a physical system of low density in which the average distance between particles is larger than the range of the perturbing potential. In momentum space this would mean that the range of momenta for which the matrix elements of v do not vanish (namely the $K+M$ states) extends far beyond the Fermi sea (which consists of M states). We therefore assume that

$$K \gg M. \tag{7.1}$$

As the line labels of any diagram must be summed upon without restriction, a diagram with κ particle lines and μ hole lines is counted $K^\kappa M^\mu$ times. A diagram of order n has n lines of which κ are particle lines and $\mu = n-\kappa$ are hole lines. Since $K \gg M$, the diagrams have more weight the greater their κ is. The Brueckner approximation consists of counting only diagrams with $\kappa = n-1$ and neglecting all others. The diagrams we count in this approximation are thus:

(7.2)

They are known as ascending ladders. There is one of them in every order. Their sum in the model of section 6 is

$$Mv+KMv\frac{1}{0-(\varepsilon+Kv)}v. \tag{7.3}$$

If instead of the ascending ladders of (7.2) we sum all ladders (ascending, descending and mixed):

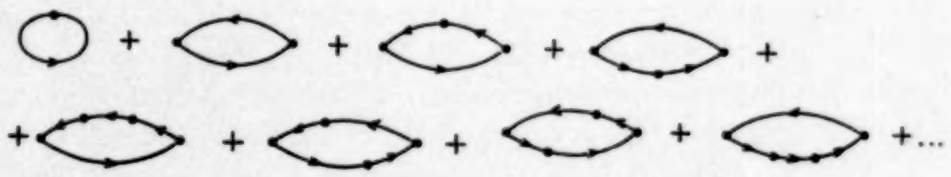

(7.4)

we get the result

$$Mv-\frac{KMv^2}{\varepsilon+(K-M)v} \tag{7.5}$$

instead of (7.3). The difference between (7.3) and (7.5) is small when $K \gg M$. Expression (7.5) can be obtained from the formal sum of all diagrams (6.7)

$$E = Mv+(\varepsilon+(K-M)v)\left(1-\sqrt{1+\frac{4KMv^2}{(\varepsilon+(K-M)v)^2}}\right) \tag{6.7}$$

by expanding the square root to first order. Such an expansion is legitimate whenever $4KMv^2/(\varepsilon+(K-M)v)^2 \ll 1$. This condition is satisfied provided we keep away from the point $\varepsilon+(K-M)v = 0$. At the neighbourhood of this point (7.5) approximates (6.7) very badly (see fig. 7). (7.5) becomes infinite and has

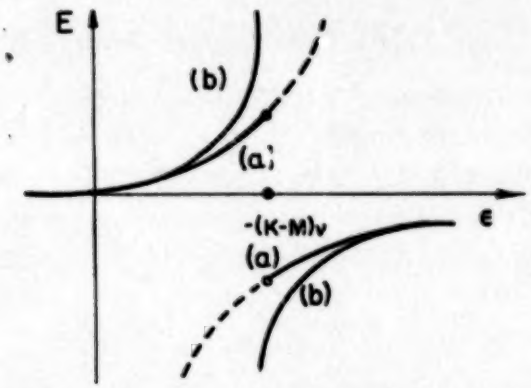

Fig. 7. The energies given by the closed sum of all diagrams (a) and Brueckner's approximation to it (b) versus ε.

an infinite discontinuity whereas (6.7) has just a finite discontinuity. At the point $\varepsilon = 0$, corresponding to the degenerate shell, $4KMv^2/(\varepsilon+(K-M)v)^2 \approx \approx 4M/K \ll 1$, and consequently in this case the ladders approximate (6.7) very well. Unfortunately (6.7) no longer gives the ground state energy as ε becomes smaller than $-(K-M)v$. The ground state energy is given by the continuation of (6.7) from the region of large ε, i.e. by (6.8) and (6.9), rather than by the formal expression (6.7).

Although the closed sum of ladders gives a good approximation to the closed sum of all diagrams both inside and outside the region of convergence of the power series in v, it fails in one important way: it does not reproduce the features of the sum of all diagrams as an analytic function of the parameters. Instead of a two-valued function we get a single-value done. Instead of a finite discontinuity which is only a transition from one branch of the function to another, and not really a singularity, we have an infinite discontinuity which is a pole of the sum of ladders. We thus lose completely one branch of the function and are not able to perform correctly the analytic continuation of our expression through

the discontinuity. The connection of the different parts of the function in the complex plane is completely altered.

All this was brought about by the neglect of the diagrams other than ladders. Although small in every order, it is these diagrams that determine the features of the energy as an analytic function of the parameters. These are determined mainly by the singularities which mark off the region of convergence of the power series which we sum. For the series of ladders this singularity is the pole which we have mentioned above. For the complete series describing (6.9) these singularities are a pair of branching points at $\varepsilon = -(K-M)v \pm 2i\sqrt{KM}v$. The nature of the singularities is in turn determined by the high order terms of the series. They are unaffected by the change of any finite number of terms. In the high order terms most of the diagrams have many hole lines. As the number of hole lines per diagram is bound to surpass M as we go along the series, most of the diagrams have wrong statistics. It is these diagrams with wrong statistics which decide the nature of the series as an analytic function of its parameters.

As was remarked earlier, we are not going in this paper to decide which of the many diagrams with wrong statistics are the most important. Still we shall briefly indicate a single-particle BG procedure which approximates the energy of our system well when $K \gg M$ (that is when only one particle at a time is inside the range of the perturbation). This procedure consists of taking into account only diagrams with a single hole label, adding the passive hole diagrams (first diagram in (7.2)) of all other labels and averaging over the chosen label. In our case all labels are equivalent, it is therefore enough to calculate with one arbitrarily chosen label. The result is

$$v+\tfrac{1}{2}(\varepsilon+(K-1)v)\left(1-\sqrt{1+\frac{4Kv^2}{(\varepsilon+(K-1)v)^2}}\right)+(M-1)v. \tag{8.6}$$

It has the same analytic properties as (6.7). It can be continued into two branches the lower one being

$$Mv+\tfrac{1}{2}(\varepsilon+(K-1)v-\sqrt{(\varepsilon+(K-1)v)^2+4Kv^2}). \tag{7.7}$$

For $\varepsilon = 0$ (7.7) gives the correct energy $(K+M)v$.

8. The Case of Two-Body Interaction

In this case four lines meet at every point in the diagrams (we draw the diagrams after Hugenholtz [9]). All ascending ladders are now:

(8.1)

They are pure two-body contributions to the perturbation series. As an example

for a many-body diagram let us consider (8.2):

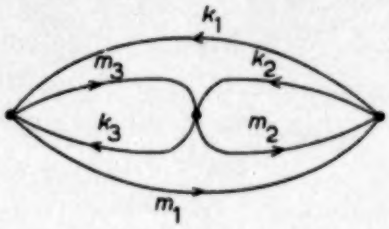

(8.2)

In this diagram there appear three hole labels: namely m_1, m_2, m_3. In a physical process no two of them can be equal, but for $m_2 = m_3$ we have a contribution to Goldstone's series. The whole contribution of (8.2) is smaller than that of an ascending ladder of the same order, because the former contains more hole lines for which the summation is very limited in the low density case (see section 7). But the two-body contribution of (8.2) is even smaller because then $m_2 = m_3$ and there is one less index to sum on. This makes the two body contribution of (8.4) smaller than that of a ladder by a factor of one over the volume of the system. When the volume increases to infinity it seems justified to drop these contributions in every order. But if we do so, we may again lose energies due to a Cooper state.

For illustration we may suggest the case of a degenerate shell with BCS interaction [11]). Let us choose H_0 as

$$H_0 = \varepsilon \sum_{k>0} (a_k^\dagger a_k + a_{-k}^\dagger a_{-k}), \tag{8.5}$$

$\pm k$ being a single fermion state label. Our system has $2K$ single-particle states with $H_0 = \varepsilon$ and $2M$ states with $H_0 = 0$. The former are labelled by $\pm k$ (k having K values), the latter by $\pm m$ (m having M values). The BCS interaction is

$$v = v\Big(\sum_{k>0} a_k^\dagger a_{-k}^\dagger + \sum_{m>0} a_m^\dagger a_{-m}^\dagger\Big)\Big(\sum_{k'>0} a_{-k'} a_{k'} + \sum_{m'>0} a_{-m'} a_{m'}\Big). \tag{8.6}$$

The sum of all ladders is expressed by

$$Mv + KMv \frac{1}{0 - (\varepsilon + (K-M)v)} v, \tag{8.7}$$

which is identical with (7.5). Just like the latter it tends to zero when $\varepsilon \to 0$, $K/M \gg 1$. In the opposite case of $K/M \gg 1$ it gives $(K+M)v$ which is the energy of a Cooper state occupied by a single pair. But pair statistics allow the Cooper state to be occupied by many pairs and the true ground state energy in the limit is [11])

$$M(K+1)v, \tag{8.8}$$

which is larger by a factor M, the number of interacting pairs. (8.8) cannot be achieved by any limit of (8.7), because the latter approximates only one branch of the energy function while (8.8) corresponds to another. The correct energy cannot be achieved without including a class of wrong statistics diagrams.

It can be shown that in the limit (for $\varepsilon = 0$) the two-body contributions from all diagrams are enough [15]).

9. Conclusion

We have concentrated our attention in this paper on a group of contributions which, to the best of our knowledge, have so far been neglected, namely the contribution of diagrams with wrong statistics. We have seen that though small in magnitude, and therefore negligible in the region of convergence of the perturbation expansion, these contributions decide the nature of the singularity which limits this region. We have seen an example where the inclusion of such contributions introduced a branching in the analytic expression for the energy. One of the branches represented the lowest energy while the ladders in many cases approximated the other branch. Whenever a system possesses a superconducting state and a normal state, it may be expected that the energies of the two states form different branches of the same analytic function of the parameters. It may be necessary to include the contributions of many-body diagrams with wrong statistics in order that the branching be correctly described. The two-body contributions of this kind are in some cases enough.

I want to thank Professor A. de-Shalit for his interest in this work and for the time he devoted to going over the manuscript of this paper. I also wish to thank Dr. P. Benioff who read the manuscript for errors of English. I am also indebted to Mr. I. Unna, my roommate, who patiently listened to partial expositions of the work while it was in the making.

References

1) J. Bardeen, L. N. Cooper and J. R. Schrieffer, Phys. Rev. **108** (1957) 1175
2) K. A. Brueckner, C. A. Levinson and H. Mahmoud, Phys. Rev. **95** (1954) 217;
K. A. Brueckner, Phys. Rev. **96** (1954) 508;
K. A. Brueckner and C. Levinson, Phys. Rev. **97** (1955) 1344;
K. A. Brueckner, Phys. Rev. **97** (1955) 1353;
L. S. Rodberg, Annals of Phys. **2** (1957) 199
3) J. Goldstone, Proc. Roy. Soc. A **239** (1957) 267
4) J. S. R. Chisholm and E. J. Squires, Nuclear Physics **13** (1959) 156
J. S. Bell, Proc. Phys. Soc. **73** (1959) 118
5) H. A. Bethe and J. Goldstone, Proc. Roy. Soc. A **238** (1957) 551
6) L. N. Cooper, Phys. Rev. **104** (1956) 1189
7) A. Katz, Nuclear Physics (to be published)
8) E. Wigner, Math. Naturn. Awz. Ungar. Akad. Wiss. **53** (1935) 477;
L. Brillouin, J. Phys. Radium (7) **3** (1935) 373
9) N. M. Hugenholtz, Physica **23** (1957) 481
10) C. Bloch, Nuclear Physics **7** (1958) 451
11) B. Mottelson, The many-body problem (Dunod, Paris, 1959)
12) C. Bloch and C. De Dominicis, Nuclear Physics **10** (1959) 509
13) L. Van Hove, Physica **25** (1959) 849
14) K. Gottfried (unpublished)
15) A. Katz, A. de Shalit and I. Talmi, Nuovo Cim. **16** (1960) 485

1.D.1

Nuclear Physics **20** (1960) 690—697; © *North-Holland Publishing Co., Amsterdam*

Not to be reproduced by photoprint or microfilm without written permission from the publisher

CLASSIFICATION OF ALPHA PARTICLE WAVE FUNCTIONS

L. COHEN

Mathematics Department, University of Southampton

Received 28 June 1960

Abstract: A classification is given of the functions which can occur in the alpha particle ground state wave function. Isobaric spin functions, spin and orbital angular momentum functions, and internal functions are classified according to their behaviour under the permutation group of four particles, and combined to form completely antisymmetric functions. Three S-state functions, eight P-state functions, and six D-state functions are obtained.

1. Introduction

When non-central forces are present the only good quantum numbers in the alpha particle ground state are the total angular momentum $J = 0$, the parity, which is even, and the z-component of the isobaric spin $T_3 = 0$. Neglecting the Coulomb interaction, the total isobaric spin is also a good quantum number $T = 0$. The Coulomb interaction causes a slight admixture of charge triplet and quintet terms which are neglected.

There are twelve position coordinates of the four nucleons. Removal of the centre of gravity leaves nine position coordinates which can be expressed in terms of vectors joining pairs of particles. A convenient choice of three independent vectors is

$$\mathbf{r} = \tfrac{1}{2}(\mathbf{R}_4+\mathbf{R}_3-\mathbf{R}_2-\mathbf{R}_1), \quad \boldsymbol{\varrho}_1 = \frac{1}{\sqrt{2}}(\mathbf{R}_2-\mathbf{R}_1), \quad \boldsymbol{\varrho}_2 = \frac{1}{\sqrt{2}}(\mathbf{R}_4-\mathbf{R}_3), \quad (1)$$

where $\mathbf{R}_i$ is the position vector of the ith nucleon relative to a fixed origin.

In classifying the wave functions there are two ways of proceeding. One method would be to separate each wave function into an isobaric spin part, a spin part, an orbital angular momentum part and an internal part. This requires the further reduction of the nine relative coordinates to three Euler angles and six interparticle distances, as has been carried out in a previous paper [1]). The orbital angular momentum part must then be expressed in terms of Euler angle wave functions. Such an approach has been adopted by Blatt and Derrick [2]) in classifying the triton wave functions. It gives rise to considerable difficulties in the case of the alpha particle. If a choice of "standard" position of the nucleus is made so that the Euler angle wave functions behave simply under permutations (for example by taking the axes of coordinates along the

principle axes of inertia of the nucleus) the kinetic energy operator becomes immensely complicated. (Even in the case of triton the working is by no means simple [3])). On the other hand if a choice of coordinate axes is made so as to simplify the kinetic energy operator, the Euler angle wave functions behave in a complicated way under permutations of the particles (and hence corresponding rotations of the axes), and the construction of eigenfunctions of total orbital angular momentum is also made more difficult.

An alternative approach, which is the one adopted here, separates each wave function into an isobaric spin part, a combined spin and orbital angular momentum part and an "internal" part. The spin and orbital part is constructed using the operator method introduced by Gerjuoy and Schwinger [4]), and contains the vectors $\mathbf{r}$, $\boldsymbol{\varrho}_1$, $\boldsymbol{\varrho}_2$. The "internal" part is a function of interparticle distances only. The symmetry properties of each part are discussed, and functions of appropriate symmetry combined to form totally antisymmetric wave functions. In applying the kinetic energy operator one can now choose whichever coordinate system is most convenient for separately carrying out differentiations on either part containing the distances, without having to worry about the symmetry properties of the coordinate systems. In this way the kinetic energy matrix elements can be evaluated without difficulty, as will be reported in a later paper; after summing over spins, the Euler angles (which are only used in an intermediate step in the calculation) disappear, as one should expect.

After summing over spins and isobaric spins, all matrix elements are integrals over the interparticle distances. Techniques for dealing with these six-dimensional integrals over a complicated region of space have been developed in an earlier paper [1]) †. We will use the following notation: χ denotes isobaric spin wave functions, ϕ the spin and angular momentum parts of the wave functions, ψ the direct products of χ and ϕ, f the internal parts of the wave functions and Ψ the totally antisymmetric wave functions.

2. Permutation Symmetry

There are five irreducible representations of the permutation group of four particles. There are two one-dimensional representations corresponding to partitions [4] (completely symmetric), and [1111] (completely antisymmetric). There is one two-dimensional representation corresponding to partition [22];

† The fact there are two possible configurations of the nucleus for a given set of interparticle distances can be dealt with by introducing a further two-valued coordinate μ, which might be called the "stereo-isomeric parity". This coordinate can be given the value $+1$ or -1 according as particle 4 is in a clockwise or anticlockwise direction relative to traversing the triangle formed by the other three in the order 1, 2, 3. Interchange of a pair of particles changes one value of μ into the other. Since the Hamiltonian is μ-independent (except that possible 4-body forces could depend on μ), we can without loss of generality work only with wave functions of the form $\psi^+ = \psi(\mu = 1) + \psi(\mu = -1)$. Clearly therefore μ need not be explicitly considered.

we denote the components of this representation by ([22], aa) and ([22], ss), where the first a or s refer to antisymmetry or symmetry with respect to particles 1 and 2, and the second a or s refer to antisymmetry or symmetry with respect to particles 3 and 4. Finally there are two three-dimensional representations corresponding to partitions [31] and [211], the components of which are denoted by

$$([31], \text{as}), \quad ([31], \text{sa}), \quad ([31], \text{ss})$$

and

$$([211], \text{sa}), \quad ([211], \text{as}), \quad ([211], \text{aa}).$$

(In general a component of a representation is denoted by $([\lambda], \kappa)$ where $[\lambda]$ refers to the partition and κ to the row).

The discussion which follows is concerned with direct products of representations of the permutation group, and these are fully elaborated in table 13 of the paper by Jahn [5]).

3. Internal Wave Functions

Using the operator method functions with $J = 0$ and given L values ($L = 0$, 1 or 2) can be formed. The L and J values are unaltered on multiplying by any scalar function of position vectors. Such scalar functions must be expressible as functions of scalar products of the vectors $\mathbf{r}$, $\boldsymbol{\varrho}_1$, $\boldsymbol{\varrho}_2$, and since all such scalar products can be expressed in terms of interparticle distances only, the functions that are needed are functions of interparticle distances. If one assumes that the part of the internal function which determines its symmetry character can be expressed as a power series in interparticle distances, a convenient way of generating functions of the required symmetry can be obtained as follows.

The six interparticle distances r_{ij} span a six-dimensional representation of the permutation group, whose irreducible components are

$$\begin{aligned}
g_1 &= g([4]) &&= \frac{1}{\sqrt{6}}\,(r_{12}+r_{13}+r_{14}+r_{23}+r_{24}+r_{34}),\\
g_2 &= g([22], \text{aa}) &&= \tfrac{1}{2}\,(r_{14}+r_{23}-r_{13}-r_{24}),\\
g_3 &= g([22], \text{ss}) &&= \frac{1}{2\sqrt{3}}\,(r_{13}+r_{14}+r_{23}+r_{24}-2r_{12}-2r_{34}),\\
g_4 &= g([31], \text{as}) &&= \tfrac{1}{2}\,(r_{13}+r_{14}-r_{23}-r_{24}),\\
g_5 &= g([31], \text{sa}) &&= \tfrac{1}{2}\,(r_{13}+r_{23}-r_{14}-r_{24}),\\
g_6 &= g([31], \text{ss}) &&= \frac{1}{\sqrt{2}}\,(r_{12}-r_{34}).
\end{aligned} \tag{2}$$

All irreducible representations whose components are polynomials of given degree in the r_{ij} can be obtained as repeated direct products of these linear

representations. (This follows by noting that the r_{ij} can be considered as a vector in 6-dimensional space, and the polynomials of degree n in the r_{ij} are then the components of a tensor of rank n).

To form totally antisymmetric D-states we require representations corresponding to [211] and [1111]. The simplest representation corresponding to [211] is quadratic in the r_{ij} and can readily be obtained as

$$\begin{aligned} g([211], \text{sa}) &= \tfrac{1}{2} g_2 g_4 + \tfrac{1}{2} \sqrt{3} g_3 g_5 \\ g([211], \text{as}) &= \tfrac{1}{2} \sqrt{3} g_3 g_4 + \tfrac{1}{2} g_2 g_5, \\ g([211], \text{aa}) &= -g_2 g_6. \end{aligned} \tag{3}$$

Similarly the simplest totally antisymmetric function of interparticle distances is cubic in the r_{ij} and is

$$\begin{aligned} g([1111]) = (r_{13}-r_{24})^2(r_{14}+r_{23}-r_{12}-r_{34}) + (r_{14}-r_{23})^2(r_{12}+r_{34}-r_{13}-r_{24}) \\ + (r_{12}-r_{34})^2(r_{13}+r_{24}-r_{14}-r_{23}). \end{aligned} \tag{4}$$

Multiplying by a completely symmetric function does not affect the symmetry type. It would be natural therefore in carrying out a variation calculation, to use internal functions of lowest degree with the symmetry required to produce a totally antisymmetric function, and multiply this by a convenient completely symmetric function (e.g. a product of functions of each r_{ij} separately).

4. Iobaric Spin Wave Functions

There are two isobaric spin wave functions corresponding to $T = 0$, $T_3 = 0$, spanning a two-dimensional representation corresponding to the partition [22]. They can be written as

$$\begin{aligned} \chi_1 \equiv \chi([22], \text{aa}) &= \tfrac{1}{2} (\zeta_1^+ \zeta_2^- - \zeta_1^- \zeta_2^+)(\zeta_3^+ \zeta_4^- - \zeta_3^- \zeta_4^+), \\ \chi_2 \equiv \chi([22], \text{ss}) &= -\frac{1}{\sqrt{3}} (\boldsymbol{\tau}_1 \cdot \boldsymbol{\tau}_3)\chi_1, \end{aligned} \tag{5}$$

where ζ_i^+, ζ_i^- are the two isobaric spin wave functions of the ith nucleon.

5. S-state Wave Functions

In the same way there are two $S = 0$ spin wave functions, denoted by

$$\begin{aligned} \phi_1 \equiv \phi([22], \text{aa}) &= \tfrac{1}{2} (\alpha_1 \beta_2 - \beta_1 \alpha_2)(\alpha_3 \beta_4 - \beta_3 \alpha_4), \\ \phi_2 \equiv \phi([22], \text{ss}) &= -\frac{1}{\sqrt{3}} (\boldsymbol{\sigma}_1 \cdot \boldsymbol{\sigma}_3)\phi_1, \end{aligned} \tag{6}$$

where α, β are the spin wave functions for each particle.

Possible combined charge-spin wave functions are given by direct products of

isobaric spin and ordinary spin irreducible representations, and are

$$\begin{aligned} \psi_S([4]) &= \frac{1}{\sqrt{2}}(\phi_1\chi_1+\phi_2\chi_2), \quad \psi_S([1111]) = \frac{1}{\sqrt{2}}(\phi_1\chi_2-\phi_2\chi_1), \\ \psi_S([22], \text{aa}) &= \frac{1}{\sqrt{2}}(\phi_1\chi_2+\phi_2\chi_1), \quad \psi_S([22], \text{ss}) = \frac{1}{\sqrt{2}}(\phi_1\chi_1-\phi_2\chi_2). \end{aligned} \tag{7}$$

The first two functions are completely symmetric and completely antisymmetric respectively, and the last two are the components of the representation belonging to the partition [22].

The totally antisymmetric S-state wave functions are now obtained by combining these with internal functions of the correct symmetry. If we denote the latter by $f_S([\lambda], \kappa)$, then there are three totally antisymmetric S-state functions

$$\begin{aligned} \Psi_S^{(1)} &= \psi_S([1111])f_S([4]), \\ \Psi_S^{(2)} &= \psi_S([22], \text{aa})f_S([22], \text{ss}) - \psi_S([22], \text{ss})f_S([22], \text{aa}), \\ \Psi_S^{(3)} &= \psi_S([4])f_S([1111]). \end{aligned} \tag{8}$$

If the nuclear forces are central and independent of spin only $\Psi_S^{(1)}$ appears in the ground state.

6. P-state Wave Functions

The alpha particle ground state is of even parity and $J = 0$. Consequently P-state wave functions can be formed [3]) using scalar products of spin vectors with vectors formed from any two of $\mathbf{r}$, $\boldsymbol{\rho}_1$, $\boldsymbol{\rho}_2$. The resultant spin operator can then operate on any spin zero wave function. There are nine linearly independent quantities which can be formed

$$\begin{aligned} a_1 &= (\boldsymbol{\sigma}_1 \cdot \mathbf{r} \wedge \boldsymbol{\rho}_1)\phi_1, & b_1 &= (\boldsymbol{\sigma}_1 \cdot \mathbf{r} \wedge \boldsymbol{\rho}_2)\phi_1, & c_1 &= (\boldsymbol{\sigma}_1 \cdot \boldsymbol{\rho}_1 \wedge \boldsymbol{\rho}_2)\phi_1, \\ a_2 &= (\boldsymbol{\sigma}_3 \cdot \mathbf{r} \wedge \boldsymbol{\rho}_1)\phi_1, & b_2 &= (\boldsymbol{\sigma}_3 \cdot \mathbf{r} \wedge \boldsymbol{\rho}_2)\phi_1, & c_2 &= (\boldsymbol{\sigma}_3 \cdot \boldsymbol{\rho}_1 \wedge \boldsymbol{\rho}_2)\phi_1, \\ a_3 &= i(\boldsymbol{\sigma}_1 \wedge \boldsymbol{\sigma}_3 \cdot \mathbf{r} \wedge \boldsymbol{\rho}_1)\phi_1, & b_3 &= i(\boldsymbol{\sigma}_1 \wedge \boldsymbol{\sigma}_3 \cdot \mathbf{r} \wedge \boldsymbol{\rho}_2)\phi_1, & c_3 &= i(\boldsymbol{\sigma}_1 \wedge \boldsymbol{\sigma}_3 \cdot \boldsymbol{\rho}_1 \wedge \boldsymbol{\rho}_2)\phi_1. \end{aligned} \tag{9}$$

These span a nine-dimensional representation of the permutation group, which can be reduced to one one-dimensional, one two-dimensional and two three-dimensional irreducible representations as follows

$$\begin{aligned} \phi_P([1111]) &= a_1 - b_2 + \frac{1}{\sqrt{2}}c_3, \\ \phi_P([22], \text{aa}) &= \frac{1}{\sqrt{3}}(a_1 - b_2 - \sqrt{2}c_3), \quad \phi_P([22], \text{ss}) = a_2 - b_1, \end{aligned} \tag{10}$$

$$\begin{aligned}
\phi_P([31],\,as) &= c_1 - \frac{1}{\sqrt{2}}a_3, & \phi_P([211],sa) &= \frac{1}{\sqrt{2}}b_3 - c_2,\\
\phi_P([31],\,sa) &= -c_2 - \frac{1}{\sqrt{2}}b_3, & \phi_P([211],\,as) &= c_1 + \frac{1}{\sqrt{2}}a_3,\\
\phi_P([31],\,ss) &= a_2 + b_1, & \phi_P([211],\,aa) &= a_1 + b_2.
\end{aligned} \tag{10}$$

These can be combined with the isobaric spin wave functions to give eight irreducible representations, one [4], one [1111], two [22], two [31], two [211] as follows

$$\psi_P^{(i)}([\lambda],\,\kappa) = \sum_{\kappa',\kappa''} \begin{pmatrix} [\lambda'] & [22] & [\lambda] \\ \kappa' & \kappa'' & \kappa \end{pmatrix} \phi_P([\lambda'],\,\kappa')\chi([22],\,\kappa''), \tag{11}$$

where the coefficients in this summation can be extracted from table 13 of the paper by Jahn [5]). The quantity (i) can take the values 1 and 2 when $[\lambda] = [31]$, $[211]$ and $[22]$, since the representations $[31]$ and $[211]$ can both arise from $[31]\times[22]$ and $[211]\times[22]$, and the representation $[22]$ can arise from $[1111]\times[22]$ and $[22]\times[22]$.

These functions must now be combined with internal functions $f_P([\lambda],\,\kappa)$ of the correct symmetry to give eight totally antisymmetric P-states of the form

$$\Psi_P = \sum_{\kappa} \psi_P^{(i)}([\lambda],\,\kappa) f_P^{(i)}([\tilde{\lambda}],\,\tilde{\kappa}), \tag{12}$$

where the tilde denotes the adjoint symmetry.

There is only one P-state in which the internal function is totally symmetric,

$$\Psi_P^{(1)} = [(a_2 - b_1) + \tfrac{1}{3}(a_1 - b_2 - \sqrt{2}c_3)(\boldsymbol{\tau}_1 \cdot \boldsymbol{\tau}_3)]\chi_1 f_P([4]). \tag{13}$$

7. D-state Wave Functions

Since the symmetrical tensor $x_i y_j + x_j y_i - \frac{2}{3}\delta_{ij} x_k y_k$ transforms like a spherical harmonic of order 2 if x_i, y_i are vectors, we can form [3]) D-state wave functions by constructing all such tensors from any two of the vectors $\mathbf{r}$, $\boldsymbol{\varrho}_1$, $\boldsymbol{\varrho}_2$, and obtain scalar products by contracting these tensors with spin vectors or vector products. The resultant spin operator can operate on any spin zero wave function. There are only six linearly independent quantities which can be formed

$$D(\boldsymbol{\varrho}_1, \boldsymbol{\varrho}_2),\quad D(\mathbf{r}, \boldsymbol{\varrho}_1),\quad D(\mathbf{r}, \boldsymbol{\varrho}_2),\quad D(\mathbf{r}, \mathbf{r}),\quad D(\boldsymbol{\varrho}_1, \boldsymbol{\varrho}_1),\quad D(\boldsymbol{\varrho}_2, \boldsymbol{\varrho}_2),$$

where

$$D(\mathbf{a}, \mathbf{b}) = [(\boldsymbol{\sigma}_1 \cdot \mathbf{a})(\boldsymbol{\sigma}_3 \cdot \mathbf{b}) + (\boldsymbol{\sigma}_1 \cdot \mathbf{b})(\boldsymbol{\sigma}_3 \cdot \mathbf{a}) - \tfrac{2}{3}(\boldsymbol{\sigma}_1 \cdot \boldsymbol{\sigma}_3)(\mathbf{a} \cdot \mathbf{b})]\phi_1. \tag{14}$$

These span a six-dimensional representation of the permutation group which can be reduced to one [4], one [22], and one [31] representations

$$\begin{aligned}
\phi_D([4]) &= D(\mathbf{r},\mathbf{r})+D(\boldsymbol{\varrho}_1,\boldsymbol{\varrho}_1)+D(\boldsymbol{\varrho}_2,\boldsymbol{\varrho}_2),\\
\phi_D([22],\mathrm{aa}) &= D(\boldsymbol{\varrho}_1,\boldsymbol{\varrho}_2),\\
\phi_D([22],\mathrm{ss}) &= \frac{1}{\sqrt{3}}\left[D(\mathbf{r},\mathbf{r})-\tfrac{1}{2}D(\boldsymbol{\varrho}_1,\boldsymbol{\varrho}_1)-\tfrac{1}{2}D(\boldsymbol{\varrho}_2,\boldsymbol{\varrho}_2)\right],\\
\phi_D([31],\mathrm{as}) &= D(\mathbf{r},\boldsymbol{\varrho}_1),\quad \phi_D([31],\mathrm{sa}) = -D(\mathbf{r},\boldsymbol{\varrho}_2)\\
\phi_D([31],\mathrm{ss}) &= \tfrac{1}{2}D(\boldsymbol{\varrho}_1,\boldsymbol{\varrho}_1)-D(\boldsymbol{\varrho}_2,\boldsymbol{\varrho}_2).
\end{aligned} \tag{15}$$

These can be combined with the isobaric spin wave functions to give six irreducible representations, one [1111], one [4], two [22], one [31], and one [211] as follows

$$\psi_D^{(i)}([\lambda],\kappa) = \sum_{\kappa',\kappa''}\begin{pmatrix}[\lambda'][22][\lambda]\\ \kappa' \quad \kappa'' \quad \kappa\end{pmatrix}\phi_D([\lambda'],\kappa')\chi([22],\kappa''). \tag{16}$$

The quantity (i) can take the values 1 and 2 when $[\lambda]=[22]$, since the representation [22] can arise from $[4]\times[22]$ and $[22]\times[22]$.

These functions are now combined with internal functions $f_D([\lambda],\kappa)$ in exactly the same way as for the P-states to give six totally antisymmetric D-states.

There is only one D-state in which the internal function is totally symmetric

$$\Psi_D^{(1)}=[-D(\mathbf{r},\mathbf{r})+\tfrac{1}{2}D(\boldsymbol{\varrho}_1,\boldsymbol{\varrho}_1)+\tfrac{1}{2}D(\boldsymbol{\varrho}_2,\boldsymbol{\varrho}_2)-D(\boldsymbol{\rho}_1,\boldsymbol{\rho}_2)(\boldsymbol{\tau}_1\cdot\boldsymbol{\tau}_3)]\chi_1 f_D([4]). \tag{18}$$

8. Discussion

Of the seventeen functions contributing to the wave function of the alpha particle ground state there is only one S-state, one P-state and one D-state in

TABLE 1

Classification of alpha particle wave functions

Spectroscopic classification	L	S	Permutation symmetry		
			Internal	Spin-orbit	Isobaric spin
$^{11}S_0$	0	0	[4]	[22]	[22]
	0	0	[22]	[22]	[22]
	0	0	[1111]	[22]	[22]
$^{13}P_0$	1	1	[4]	[22]	[22]
	1	1	[22]	[22]	[22]
	1	1	[22]	[1111]	[22]
	1	1	[31]	[211]	[22]
	1	1	[31]	[31]	[22]
	1	1	[211]	[31]	[22]
	1	1	[211]	[211]	[22]
	1	1	[1111]	[22]	[22]
$^{15}D_0$	2	2	[4]	[22]	[22]
	2	2	[22]	[22]	[22]
	2	2	[22]	[4]	[22]
	2	2	[31]	[31]	[22]
	2	2	[211]	[31]	[22]
	2	2	[1111]	[22]	[22]

which the internal function is completely symmetric (the "principal" states). If only central, spin-independent forces are present, only $\Psi_S^{(1)}$ occurs. The complete set of states is listed in table 1.

The introduction of a tensor force couples the D-states to this S-state. The P-states only occur in second order, coupled to the D-states, and are usually neglected in a variation calculation. One might expect the principal D-state to be the most important one, but calculations indicate that other D-states also make a significant contribution to the binding energy [6]).

In general a convenient guide to constructing trial wave functions (neglecting P-states) would be to commence with the principal S- and D-states. In the next stage all states which can be formed using only linear functions of the r_{ij} to provide the correct symmetry could be included; this would give two further S-states and four further D-states. One could proceed systematically using higher powers of the r_{ij} at each stage.

It is a pleasure to acknowledge many helpful discussions with Dr. J. B. Willis and Dr. J. P. Elliott.

References

1) L. Cohen and J. B. Willis, Nuclear Physics **13** (1959) 125
2) G. Derrick and J. M. Blatt, Nuclear Physics **8** (1958) 310
3) G. Derrick, Nuclear Physics **16** (1960) 405
4) E. Gerjuoy and J. Schwinger, Phys. Rev. **61** (1942) 138
5) H. A. Jahn, Proc. Roy. Soc. A **205** (1951) 192
6) G. Abraham, L. Cohen and A. S. Roberts, Proc. Phys. Soc. A **68** (1955) 265

10.D *Nuclear Physics* **20** (1960) 698—699; © *North-Holland Publishing Co., Amsterdam*

BOOK REVIEWS

M. RUSSELL WEHR and JAMES A. RICHARDS, JR., *Physics of the atom* (Addison-Wesley Publishing Company, Reading, Mass., 1960. xi—420 pp. $ 8,50)

This book is intended as an introduction to atomic physics for students of other branches of science. It is a well-composed, instructive book, presenting its subject-matter in a lucid exposition. Each chapter contains a number of problems, many of them consisting in simple calculations meant to give the reader an idea of the magnitudes of atomic quantities. Besides there are lists of literature to which the student is referred for a profounder study of the subjects dealt with in the individual chapters. These references, which are adapted to the level of knowledge of the prospective readers, comprise not only books and survey articles, but also works describing the historical development and the human background (including Mr. Tompkins' explorations in dreams of the world of atoms!).

The authors have had the good idea of appending a chronological list of discoveries bearing on the development of the present atomic theories. It ranges from about 550 B.C. to the most recent years and provides — as intended — a striking illustration of the international character of science. Of course the selection of names for such a chronology is a matter of personal judgment; the present list is, however, both copious and representative. Unfortunately it is marred by too many errors and inaccuracies, especially in the indications of the countries in which the various scientists worked: in many cases these indications are even not identical in different entries about the same person. A similar defect impairs the chronological list of Nobel Prize winners in physics and chemistry, also to be found in the appendix. Against each name a country is mentioned without any explanation. In some cases it seems to be the country of origin, in others the country in which the person concerned worked at the time when the prize was awarded to him, but in others again it is neither one nor the other (1943, George de Hevesy; Germany). These lists should be carefully examined with a view to correcting such inaccuracies in a later edition.

Stefan Rozental

R. F. SAXE, *Approaches to Thermonuclear Power* (Temple Press Limited, London, 1960. ix—65 p. 12s. 6d.)

"Nuclear Engineering" Monographs is a series of books intended for students, research assistants and qualified technicians who want to get a basic knowledge in those topics of nuclear engineering outside their own field of study. This book deals with the work that is being done to obtain power from controlled thermonuclear processes.

In chapter one the fusion processes and the conditions under which one could hope to get power from them on a reasonable scale are discussed. Chapter two deals with the behaviour of a plasma at high temperatures giving the physical background necessary to understand the pinch-effect, the principles in a magnetic bottle and instabilities in a plasma. In chapter three, four and five are described the principles and the results obtained by the linear pinch devices, the torioidal machines and the mirror machines. Except for the first part of chapter two, students and research assistants will find the book clear and easily understandable. The treatment of the physical properties of a plasma in the beginning of chapter two is rather complicated and it seems to be outside the scope of this series of monographs. Fortunately, the reader can leave out this part of the book without losing the broad understanding of the problems which the book gives.

This book can be recommended to people with some physical knowledge who want to know about the problems in controlled thermonuclear research.

V. O. Jensen

N. Robert Nilsson (Editor) *Proceedings of the Fourth International Conference on Ionization Phenomena in Gases.* (North-Holland Publishing Company, Amsterdam 1960. Vol. I and II, 1210 p. Glds. 130.–)

It is a great pleasure for one who has participated in the Fourth Ionization Conference in Uppsala in August 1959 that proceedings from the conference have been printed so quickly and nicely. The two volumes contain nearly all the papers (more than 200) given at the conference.

The papers are placed in subject order as they were presented at the conference. They are divided in four main subject groups, namely, in Volume I: 1) Fundamental Processes in Gas Discharges, and 2) Different types of Discharges and Applications, and in Volume II: 3) Theoretical and Experimental Studies in Plasma Physics, and 4) Production, Confinement and Heating of Plasmas. Within these four groups a further subject division is made. This division of the papers makes it very easy to find the papers in which one is interested.

As the standard of the papers is very high, the books are very useful for people working in that branch of physics.

Torkil Hesselberg Jensen

J. S. Levinger, *Nuclear Photo-Disintegration* (Oxford University Press, 1960. 144 pages, 15s.)

The student desiring to learn about photonuclear reactions will find a solid and sensibly-presented exposition of the subject here. The author quite rightly begins by stressing the importance of sum rules and other model-independent features. This is fortunate, because the models discussed in Chapter V and the reaction mechanisms in Chapter VI are now understood much better than at the time the book was written.

With respect to Chapter V, I could never share the author's equanimity towards different nuclear models, feeling that there must be one model more completely truthful than the others, that one should love best of all. Recent work on the particle-hole interaction has moved, I feel, towards such a model and has shown that more or less equal mixtures of the various models proposed are contained in the giant dipole state, although it is closest to the plasma oscillation of Ferentz, Gell-Mann and Pines, skipped over lightly on page 88.

As inevitable in any rapidly progressing subject there have been many developments both experimental and theoretical since this book was put into press. On the experimental side, exciting work on photon scattering by deformed nuclei has been carried out by Fuller and Hayward, at the Bureau of Standards and theoretical analyses have been made by Baldin and coworkers in Moscow. In general, experimental work has progressed greatly in the accuracy with which quantitative measurements have been carried out. Because of the many recent developments, the last part of the book was, therefore, outdated before it appeared. However, I believe that the first four chapters will remain a classic on the subject for some time. After the above critical remarks, it is only fair to say that, as a whole, the book is by far the best treatment in print on the subject.

G. E. Brown

10.B

Nuclear Physics **20** (1960) 700; © *North-Holland Publishing Co., Amsterdam*

REPORT

INTERNATIONAL CONGRESS ON MANY-PARTICLE PROBLEMS

(Utrecht, 13—18 June 1960)

A congress on many-particle problems was held in the Physics Laboratory of the State University of Utrecht, 13—18 June, 1960. It was initiated by Professor L. Van Hove (Utrecht).

The first lecture was by N. N. Bogolyubov, who reported on advances in solving the BCS reduced Hamiltonian rigorously. J. R. Schrieffer surveyed the latest developments in superconductivity, and showed how collective excitations (excitons), lying below the gap, are obtained. P. W. Anderson presented an extension of the BCS theory to He^3, A. F. Siegert discussed the use of averages of functionals of Gaussian random functions in partition functions, and G. E. Uhlenbeck presented a suggested graphology, which all subsequent speakers proceeded to ignore. A dynamical derivation of equilibrium statistical mechanics was presented by I. Prigogine.

A survey of work initiated by Lee and Yang on the imperfect Bose gases was presented by C. N. Yang. C. Bloch discussed the expansion of the grand partition function of an imperfect Fermi gas. C. T. De Dominicis discussed a general quasiparticle formulation, and showed the relation of Landau's expression for the entropy to the result obtained by summing certain classes of graphs. The correlation energy and other aspects of an electron gas were discussed by E. W. Montroll, and D. Pines talked on plasma oscillations. N. M. Hugenholtz lectured on interacting bosons at zero temperature.

In lectures devoted to experiment and applications, G. Careri discussed the influence of foreign particles in He II, and H. C. Kramers discussed its flow properties. W. M. Fairbank talked on the low temperature properties of He 3.

Nuclear problems were covered in talks by J. Dąbrowski and G. E. Brown. The former dealt with the optical model and correlations at relatively high-energies; the latter, with vibrational states in nuclei.

S. T. Belyaev and V. M. Galitskii dealt with collective oscillations in Fermi systems which they treated using Green's function techniques. Belyaev concentrated on the nuclear problem, whereas Galitskii dealt mainly with zero sound. L. Van Hove discussed difficulties in the ground-state theory of Fermi systems.

On the last morning, K. M. Watson discussed cooperative interactions in plasmas, and J. Korringa, perturbation theory of antiferromagnetism.

The proceedings of the congress, edited by Dr. van Kampen, will be published as a separate issue of Physica.

E. Verboven

AUTHOR INDEX

ASKEW, R. F. and A. P. BATSON, Energy spectrum of the photoneutrons from gold 408

BARJON, ROBERT, MICHEL LAMBERT et JEAN SCHMOUKER, Section efficace différentielle de la réaction $C^{13}(He^3, \alpha)C^{12}$ à 1.8 MeV 614

BATSON, A. P., *see* ASKEW

BODENSTEDT, E., H. J. KÖRNER, C. GÜNTER, D. HOVESTADT and J. RADELOFF, A new isomeric state of Cs^{131} 557

BONNER, T. W., *see* BRAMBLETT

BRAMBLETT, RICHARD L. and T. W. BONNER, Neutron evaporation spectra from (p, n) reactions 395

BREIT, G. and R. L. GLUCKSTERN, Effect of finite life of upper level on probability of Coulomb excitation 188

BROMLEY, D. A., *see* MCCALLUM

BUTCHER, J. C. and H. MESSEL, Electron number distribution in electron-photon showers in air and aluminium absorbers 15

CABEZAS, A., I. LINDGREN, E. LIPWORTH, R. MARRUS and M. RUBINSTEIN, Nuclear spins of neodymium-147 and promethium-147 . . . 509

CALVERT, J. M., *see* GALE

CHABAN, A. A., *see* DAVYDOV

CLOIZEAUX, JAQUES DES, Extension d'une formule de Lagrange à des problèmes de valeurs propres 321

COHEN, BERNARD L., SANTOS MAYO and ROBERT E. PRICE, Nuclear structure studies in the lead region with (d, t) reactions 360

COHEN, BERNARD L., ROBERT E. PRICE and SANTOS MAYO, Nuclear structure studies in the lead region with (d, p) reactions 370

COHEN, L., Classification of alpha particle wave functions 690

COOK, C. W., *see* SCHMITT

CZYŻ, WIESLAW and SHELDON L. GLASHOW, Multiple production of mesons in pion-nucleon collisions 309

DAVYDOV, A. S. and A. A. CHABAN, Rotation-vibration interaction in non-axial even nuclei 499

DELOFF, A. and J. WRZECIONKO, The phenomenological baryon-baryon scattering theory and the relative parity determination 464

DELVES, L. M., Tertiary and general-order collisions (II) 275

EASTERDAY, H. T. and R. L. SMITH, Balanced ion chamber measurement of half-lives of several radioisotopes 155

D'ESPAGNAT, B., A. MARTIN et J. PRENTKI, Tests expérimentaux de certaines hypothèses de symétrie relatives aux interactions fortes . . . 543

FORKMAN, BENGT and SVEN A. E. JOHANSSON, Angular distributions in photofission of uranium 136
GALE, N. H., J. B. GARG, J. M. CALVERT and K. RAMAVATARAM, A study of the angular distributions of neutrons leading to the ground state in the reaction $^{12}C(^{3}He, n)^{14}O$ 313
GANLEY, W. P., *see* ROETLING
GARG, J. B., *see* GALE
GAUDIN, M., Sur le développement de la grande fonction de partition pour des systèmes de particules identiques 513
GILL, P. S., *see* HANS
GILLET, VINCENT, Théorie des corrélations multiples perturbées 561
GLASHOW, SHELDON L., *see* CZYŻ
GLUCKSTERN, R. L., *see* BREIT
GRABOWSKI, Z., S. GUSTAFSSON, I. MARKLUND and I. B. HÄLLER, Angular correlation measurements in Ba^{136} 159
GÜNTER, C., *see* BODENSTEDT
GUSTAFSSON, S., *see* GRABOWSKI
HÄLLER, I. B., *see* GRABOWSKI
HANS, H. S., M. L. SEHGAL and P. S. GILL, Thermal neutron cross sections for producing isomers (II) 183
HARVEY, JOHN A., Donald J. Hughes (1915—1960) 1
HELMERS, K., Exceptions to gamma intensity rules in nuclear rotational spectra. 585
HOVESTADT, D., *see* BODENSTEDT
JACOB, GERHARD and TH. A. J. MARIS, Quasi-free diffraction scattering . 440
JOHANSSON, SVEN A. E., *see* FORKMAN
JUNG, B. and J. SVEDBERG, The electron spectrum of $_{81}Tl^{199}$ 630
KATZ, AMNON, Many-body perturbation methods in a soluble model . . 663
KIKUCHI, KEN, Classical treatment of nuclear reactions induced by fast nucleons 590
KIKUCHI, KEN, Excitation of heavy nuclei by fast nucleons 601
KLAIBER, G. S., *see* ROETLING
KLEINHEINZ, PETER, *see* WENDT
KÖRNER, H. J., *see* BODENSTEDT
KUEHNER, J. A., *see* MCCALLUM
LAMBERT, MICHEL, *see* BARJON
LANDSHOFF, P. V., A discussion of dual diagrams in perturbation theory 129
LINDGREN, I., *see* CABEZAS
LIPWORTH, E., *see* CABEZAS
MARIS, TH. A. J., *see* JACOB
MARKLUND, I., *see* GRABOWSKI
MARRUS, R., *see* CABEZAS

MARTIN, A., *see* D'ESPAGNAT
MAYO, SANTOS, *see* COHEN
MCCALLUM, G. J., D. A. BROMLEY and J. A. KUEHNER, A search for double dipole de-excitation in C^{12}. 382
MEHTA, M. L., On the summation of generalized ladders for a many-fermion system 533
MESSEL, H., *see* BUTCHER
MIKAELIAN, L. A., *see* SPIVAK
MITRA, A. N. and S. P. PANDYA, Nuclear spectroscopy with non-local potentials 455
MITRA, A. N., R. P. SAXENA and P. NARAYANASWAMY, A note on π–π interaction 491
NARAYANASWAMY, P., *see* MITRA
PANDYA, S. P., *see* MITRA
PHILLIPS, G. C., *see* TOMBRELLO
PRENTKI, J., *see* D'ESPAGNAT
PRICE, ROBERT E., *see* COHEN
PÜSCHEL, W., Die mittlere Lebensdauer geladener Σ-Hyperonen und Untersuchungen über weitere Eigenschaften dieser Teilchen 254
RADELOFF, J., *see* BODENSTEDT
RAMAVATARAM, K., *see* GALE
ROETLING, P. G., W. P. GANLEY and G. S. KLAIBER, The decay of Pb^{212} . 347
ROTH, B. and K. WILDERMUTH, Reduced widths in O^{16} and gamma transition probabilities in F^{19} 10
ROY, P. K., K-meson-nucleon scattering and relativistic dispersion relations 417
RUBINSTEIN, M., *see* CABEZAS
SAXENA, R. P., *see* MITRA
SCHMITT, H. W. and C. W. COOK, Absolute neutron absorption cross sections for Sb-Be photoneutrons. 202
SCHMITT, H. W., Determination of the energy of antimony-beryllium photoneutrons 220
SCHMOUKER, JEAN, *see* BARJON
SEHGAL, M. L., *see* HANS
SMITH, R. L., *see* EASTERDAY
SPIVAK, P. E. and L. A. MIKAELIAN, Longitudinal polarization of beta-electrons 475
SVEDBERG, J., *see* JUNG
TAKAHASHI, Y., Invariance and the *S*-matrix (II) 621
TIETGE, J., Eine systematische Untersuchung π^--mesonisch zerfallender Hyperfragmente, die durch K^--Mesonen erzeugt wurden 227
TOMBRELLO, T. A. and G. C. PHILLIPS, A two-body cluster model of the

nucleus 648
VARGA, L., (n, α) and (n, p) reactions in Na^{23} 487
WENDT, HANS-DIETRICH und PETER KLEINHEINZ, Der β-Zerfall des Neodym-147 169
WILDERMUTH, K., *see* ROTH
WRZECIONKO, J., *see* DELOFF

SUBJECT INDEX

1. Nuclear Structure

1.C *Many-particle systems*

Extension d'une formule de Lagrange à des problèmes de valeurs propres, Jacques des Cloizeaux 321
Sur le développement de la grande fonction de partition pour des systèmes de particules identiques, M. Gaudin 513
On the summation of generalized ladders for a many-fermion system, M. L. Mehta 533
Many-body perturbation methods in a soluble model, Amnon Katz 663

1.D *Nuclear models*

1.D.1 *Shell model*

Nuclear spectroscopy with non-local potentials, A. N. Mitra and S. P. Pandya 455
Nuclear spins of neodymium-147 and promethium-147, A. Cabezas, I. Lindgren, E. Lipworth, R. Marrus and M. Rubinstein 509
Classification of alpha particle wave functions, L. Cohen 690

1.D.2 *Collective model*

Rotation-vibration interaction in non-axial even nuclei, A. S. Davydov and A. A. Chaban 499

1.D.3 *Other models*

Reduced widths in O^{18} and gamma transition probabilities in F^{19}, B. Roth and K. Wildermuth 10
A two-body cluster model of the nucleus, T. A. Tombrello and G. C. Phillips 648

1.E *Properties of nuclei*

1.E.1 *Energy levels*

Der β-Zerfall des Neodym-147, Hans-Dietrich Wendt und Peter Kleinheinz 169
Nuclear spins of neodymium-147 and promethium-147, A. Cabezas, I. Lindgren, E. Lipworth, R. Marrus and M. Rubinstein 509

1.E.4 *Transition probabilities; cross sections*

Reduced widths in O^{18} and gamma transition probabilities in F^{19}, B. Roth and K. Wildermuth 10

2. Nuclear Reactions

2.A *General properties*

2.A.1 *Cross-sections, energy relations*

Thermal neutron cross sections for producing isomers (II), H. S. Hans, M. L. Sehgal and P. S. Gill 183

Absolute neutron absorption cross sections for Sb-Be photoneutrons, H. W. Schmitt and C. W. Cook 202
Determination of the energy of antimony-beryllium photoneutrons, H. W. Schmitt 220
(n, α) and (n, p) reactions in Na^{23}, L. Varga 487

2.A.2 *General theory*

Classical treatment of nuclear reactions induced by fast nucleons, Ken Kikuchi 590
Excitation of heavy nuclei by fast nucleons, Ken Kikuchi 601

2.B *Angular distributions; correlations; polarization*

Angular correlation measurements in Ba^{138}, Z. Grabowski, S. Gustafsson, I. Marklund and I. B. Häller 159
Théorie des corrélations multiples perturbées, Vincent Gillet 561

2.C *Resonance reactions; R-matrix theory*

Tertiary and general-order collisions (II), L. M. Delves 275

2D. *Statistical model*

Neutron evaporation spectra from (p, n) reactions, Richard L. Bramblett and T. W. Bonner 395

2.F *Direct interaction (other than stripping)*

Quasi-free diffraction scattering, Gerhard Jacob and Th. A. J. Maris 440
Section efficace différentielle de la réaction $C^{13}(He^3, \alpha)C^{12}$ à 1.8 MeV, Robert Barjon, Michel Lambert et Jean Schmouker 614

2.G *Stripping and pick-up*

A study of the angular distributions of neutrons leading to the ground state in the reaction $^{12}C(^3He, n)^{14}O$, N. H. Gale, J. B. Garg, J. M. Calvert and K. Ramavataram 313
Nuclear structure studies in the lead region with (d, t) reactions, Bernard L. Cohen, Santos Mayo and Robert E. Price 360
Nuclear structure studies in the lead region with (d, p) reactions, Bernard L. Cohen, Robert E. Price and Santos Mayo 370

2.H *Coulomb excitation*

Effect of finite life of upper level on probability of Coulomb excitation, G. Breit and R. L. Gluckstern 188

2.I *Photonuclear processes*

Angular distributions in photofission of uranium, Bengt Forkman and Sven A. E. Johansson 136
Energy spectrum of the photoneutrons from gold, R. F. Askew and A. P. Batson 408

2.J *Fission and spallation*

Angular distributions in photofission of uranium, Bengt Forkman and Sven A. E. Johansson 136

3. Electromagnetic Radiation

3.A *Gamma radiation*

The decay of Pb^{212}, P. G. Roetling, W. P. Ganley and G. S. Klaiber 347
A search for double dipole de-excitation in C^{12}, G. J. McCallum, D. A. Bromley and J. A. Kuehner 382
A new isomeric state of Cs^{131}, E. Bodenstedt, H. J. Körner, C. Günter, D. Hovestadt and J. Radeloff 557
Exceptions to gamma intensity rules in nuclear rotational spectra, K. Helmers 585

3.B *Internal conversion*

The electron spectrum of $_{81}Tl^{199}$, B. Jung and J. Svedberg 630

4. Beta Decay; Parity

4.E *Analysis of data*

Balanced ion chamber measurement of half-lives of several radioisotopes, H. T. Easterday and R. L. Smith 155
Der β-Zerfall des Neodym-147, Hans-Dietrich Wendt und Peter Kleinheinz . 169
The decay of Pb^{212}, P. G. Roetling, W. P. Ganley and G. S. Klaiber 347

6. Methods and Instruments

6.A *Experimental*

Balanced ion chamber measurement of half-lives of several radioisotopes, H T. Easterday and R. L. Smith 155

6.B *Theoretical*

Extension d'une formule de Lagrange à des problèmes de valeurs propres, Jacques des Cloizeaux 321

7. Quantum Field Theory

7.A *General*

A discussion of dual diagrams in perturbation theory, P. V. Landshoff . . . 129
Extension d'une formule de Lagrange à des problèmes de valeurs propres, Jacques des Cloizeaux 321
Invariance and the S-matrix (II), Y. Takahashi 621

7.C π-meson field (*scattering and nuclear forces*)

Multiple production of mesons in pion-nucleon collisions, Wieslaw Czyż and L. Glashow 309
A note on π—π interaction, A. N. Mitra, R. P. Saxena and P. Narayanaswamy. 491

8. Elementary Particles

8.A *Experimental*

Eine systematische Untersuchung π^--mesonisch zerfallender Hyperfragmente, die durch K^--Mesonen erzeugt wurden, J. Tietge 227

Die mittlere Lebensdauer geladener Σ-Hyperonen und Untersuchungen über weitere Eigenschaften dieser Teilchen, W. Püschel 254
Longitudinal polarization of beta-electrons, P. E. Spivak and L. A. Mikaelian . 475

8.B *Theory, interactions, transformation properties*

K-meson-nucleon scattering and relativistic dispersion relations, P. K. Roy . 417
The phenomenological baryon-baryon scattering theory and the relative parity determination, A. Deloff and J. Wrzecionko 464
Tests expérimentaux de certaines hypothèses de symétrie relatives aux interactions fortes, B. d'Espagnat, A. Martin et J. Prentki 543

9. Cosmic Radiation

9.B *Passage of particles through matter*

Electron number distribution in electron-photon showers in air and aluminium absorbers, J. C. Butcher and H. Messel 15

10. News Items

10.B *Reports on conferences and congresses*

International congress on many-particle problems (Utrecht, 13—18 June 1960), E. Verboven. 700

10.C *Obituaries*

Donald J. Hughes (1915—1960), John A. Harvey 1

10.D *Book Reviews*

M. Russell Wehr and James A. Richards, Jr., Physics of the atom (Stefan Rozental) 698
R. F. Saxe, Approaches to thermonuclear power (V. O. Jensen) 698
N. Robert Nilsson (Editor) Proceedings of the fourth international conference on ionization phenomena in gases (Torkil Hesselberg Jensen) 699
J. S. Levinger, Nuclear photo-disintegration (G. E. Brown) 699